



Pavement Cracking

Mechanisms, Modeling, Detection, Testing, and Case Histories

Editors

Imad L. Al-Qadi, Tom Scarpas & Andreas Loizos

 **CRC Press**
Taylor & Francis Group
A BALKEMA BOOK

PAVEMENT CRACKING

PROCEEDINGS OF THE 6TH RILEM INTERNATIONAL CONFERENCE ON CRACKING
IN PAVEMENTS, CHICAGO, USA, 16–18 JUNE 2008

Pavement Cracking

*Mechanisms, Modeling, Detection,
Testing and Case Histories*

Editors

Imad L. Al-Qadi

University of Illinois at Urbana Champaign, Urbana, Illinois, USA

Tom Scarpas

Delft University of Technology, Delft, The Netherlands

Andreas Loizos

National Technical University of Athens, Athens, Greece



CRC Press

Taylor & Francis Group

Boca Raton London New York Leiden

CRC Press is an imprint of the
Taylor & Francis Group, an **informa** business

A BALKEMA BOOK

CRC Press/Balkema is an imprint of the Taylor & Francis Group, an informa business

© 2008 Taylor & Francis Group, London, UK

Typeset by Charon Tec Ltd (A Macmillan Company), Chennai, India
Printed and bound in the USA by Edwards Brothers, Inc, Lillington, NC.

All rights reserved. No part of this publication or the information contained herein may be reproduced, stored in a retrieval system, or transmitted in any form or by any means, electronic, mechanical, by photocopying, recording or otherwise, without written prior permission from the publishers.

Although all care is taken to ensure integrity and the quality of this publication and the information herein, no responsibility is assumed by the publishers nor the author for any damage to the property or persons as a result of operation or use of this publication and/or the information contained herein.

Published by: CRC Press/Balkema
P.O. Box 447, 2300 AK Leiden, The Netherlands
e-mail: Pub.NL@taylorandfrancis.com
www.crcpress.com – www.taylorandfrancis.co.uk – www.balkema.nl

ISBN 13: 978-0-415-47575-4 (Hbk + CD-rom)

Table of contents

Preface	xiii
Organization	xv
<i>1. Accelerated pavement testing to assess pavement structure, interface bonding and reflective cracking</i>	
Evaluation of reflective cracking performance of asphalt mixes with asphalt rubber binder using HVS tests and non-local continuum damage mechanics <i>R.Z. Wu & J.T. Harvey</i>	3
The LCPC's ALT facility contribution to pavement cracking knowledge <i>P. Hornyh, J.P. Kerzreho, A. Chabot, D. Bodin, J.M. Balay & L. Deloffre</i>	13
Pavement strength measured by full scale test <i>E.H. Guo, L. Ricalde & F. Petch</i>	25
Fatigue cracking characteristics of accelerated testing pavements with modified binders <i>X. Qi, N. Gibson & J. Youtcheff</i>	35
An overview of an accelerated pavement testing experiment to assess the use of modified binders to limit reflective cracking in thin asphalt concrete overlays <i>D. Jones, J.T. Harvey & T. Bressette</i>	45
Accelerated pavement cracking testing: experimental and finite element analysis <i>S.A. Pérez, J.M. Balay, P. Tamagny, A. Chabot, Ch. Petit, A. Millien & L. Wendling</i>	55
<i>2. Analytical and experimental investigations of concrete joints</i>	
Influence of the coefficient of thermal expansion on the cracking of jointed concrete pavements <i>E. Kohler & V. Kannekanti</i>	69
An analytical approach to computing joint opening in concrete pavements <i>J.R. Roesler & D. Wang</i>	79
Experimental behavior of construction joints in FRC pavements <i>L. Cominoli, A. Meda & G.A. Plizzari</i>	89
Induction of joints in concrete pavements <i>J.R. Vázquez</i>	99
Numerical assessment of saw-cutting: The influence on stress development and cracking <i>K. Raoufi, J. Weiss & T. Nantung</i>	109
Moisture warping in slabs on grade <i>Y. Wei, W. Hansen & E. Schlagen</i>	119

<i>3. Performance of concrete pavements and white topping</i>	
Cracking in concrete pavements – an interaction of various influences <i>R. Breitenbücher & C. Sievering</i>	127
Consequences of fracture mechanics for size effect, crack spacing and crack width in concrete pavements <i>C.G. Hoover & Z.P. Bazant</i>	137
Assessment and mitigation of early-age cracking in concrete pavements due to restrained movement <i>S.S. Tyson, S.D. Tayabji & H.T. Yu</i>	145
The effect of different axle configurations on the fatigue life of plain cement concrete <i>K. Chatti, N.A. Brake, H. Salama & S.W. Haider</i>	155
Evaluation of factors influencing distress development in ultra-thin whitetopping <i>S.A. Newbolds & J. Olek</i>	167
Restrained shrinkage cracking of fiber-reinforced self-consolidating concrete <i>S.H. Kwon, R.P. Ferron, Y. Akkaya & S.P. Shah</i>	179
<i>4. Cracking in semi-rigid and stabilized-base pavements</i>	
Prediction of fatigue cracking in cement treated base courses <i>A.A.A. Molenaar & B. Pu</i>	189
Cracking response and service life prediction of flexible and semi-rigid road pavements implementing M-E PDG 2002 code <i>M. la Agostinacchio, D. Ciampa & S. Olita</i>	201
A prediction procedure of reflective cracking growth life for cement stabilized base asphalt pavement <i>F.-J. Ni & Q. Li</i>	211
Cracking survey on freeways using asphalt pavement with semi-rigid base in Jiangsu <i>J. Yang, H. Lu & Y. Yang</i>	221
Asphalt sand stress absorbing interlayer used in asphalt pavement with semi-rigid base <i>J. Yang, P. Dai, B. Yu & Y. Yang</i>	229
Effectiveness of slab stabilization in mitigating reflective cracking in HMA overlays: A case-history <i>F.G. Praticò & M. Losa</i>	239
Fatigue performance of self cementing base courses <i>A.A.A. Molenaar</i>	251
<i>5. Fatigue cracking and damage characterization of HMA</i>	
A five point bending test for asphalt cracking on steel plates <i>A. Houel & L. Arnaud</i>	261

FE evaluation of 4-point bending test for fatigue cracking assessment <i>M. Coni, S. Portas, R. Isola & J.R.M. Oliveira</i>	271
Investigation of cracking in bituminous mixtures with a 4 points bending test <i>M.L. Nguyen, C. Sauzeat, H. Di Benedetto & L. Wendling</i>	283
A micromechanics-based computational model and testing protocols to characterize damage-dependent mechanical responses of asphalt mixtures in flexible pavements <i>Y.-R. Kim, F.A.C. de Freitas & D.H. Allen</i>	295
Use of pseudostress and pseudostrain concepts for characterization of asphalt fatigue tests <i>M.E. Kutay, N.H. Gibson & J. Youtcheff</i>	305
Viscoelastic continuum damage model based finite element analysis of fatigue cracking <i>C. Baek, B.S. Underwood, V. Subramanian, M.N. Guddati, Y.R. Kim & K. Lee</i>	315
 <i>6. Top-down cracking in flexible pavements</i>	
Finite element analysis of top-down cracking in semi-rigid pavement structure <i>P. Wang, X.-M. Huang, Q.-F. Li & Z.-T. Yang</i>	327
Investigation of fatigue cracking: Bottom-up or top-down <i>X. Hu, S. Hu, L. Sun & L.F. Walubita</i>	333
Strength theory, a better explanation for top-down cracking in asphalt pavement <i>L. Jia, L. Sun, X. Hu & X. Hu</i>	345
Modeling shear properties of airport asphalt mixes using different test methods <i>A. El-Desouky, A. Mostafa, S. Easa & A.O. Abd El Halim</i>	357
 <i>7. Low temperature cracking in HMA</i>	
Integration of laboratory testing, field performance data and numerical simulations for the study of low-temperature cracking <i>E.V. Dave, A.F. Braham, W.G. Buttlar, G.H. Paulino & A. Zofka</i>	369
Thermal cracking prediction using artificial neural network <i>M. Zeghal</i>	379
Effect of aggregate grading on low temperature cracking resistance in asphalt mixtures base on mathematical statistic <i>Y.-Q. Tan, H.-N. Xu, Z.-J. Dong & W.-Q. Gong</i>	387
Discrete element modelling of low temperature monotonic compression tests in an idealised asphalt mixture <i>J. Wu, A. Collop & G. McDowell</i>	395
Investigation of low temperature cracking in asphalt mixtures using TSRST <i>R. Velásquez, M. Turos, M. Marasteanu, N. Gibson & T. Clyne</i>	405

<i>8. Binder and HMA laboratory characterization for cracking potential</i>	
Measurement and effective evaluation of crack growth in asphalt mixtures <i>H.A. Khalid & I. Artamendi</i>	417
Evaluation of fracture properties of hot mix asphalt <i>L.N. Mohammad, M.D. Kabir & S. Saadeh</i>	427
Crack propagation performance evaluation of asphaltic mixes using a new procedure based on cyclic semi-circular bending tests <i>R.C. van Rooijen & A.H. de Bondt</i>	437
A new laboratory test for reflective cracking in mode I and/or mode II <i>D. Perraton, G. Guissi, P. Pierre & G. Doré</i>	447
New procedure to evaluate fatigue of bituminous mastics using an annular shear rheometer prototype <i>B. Delaporte, J. Van Rompu, H. Di Benedetto, P. Chaverot & G. Gauthier</i>	457
Thermo-volumetric properties of asphalt binders and mixtures <i>J.O. Ojo, D. Fratta, H.U. Bahia, C. Daranga & M. Marasteanu</i>	469
Low temperature behavior of very hard bituminous binder material for road applications <i>R.N. Khedoe, A.A.A. Molenaar & M.F.C. v.d. Ven</i>	481
Comparison of the modulus of high-modulus asphalt mixtures – experimental determination and calculation <i>F. Vervaecke, J. Maeck & A. Vanelstraete</i>	491
Acoustic emission in asphalt mixture IDT creep and strength tests <i>X. Li, M.O. Marasteanu & J.F. Labuz</i>	501
The effects of different waveforms and rest period in cyclic loading on the fatigue behavior of the asphalt mixtures <i>K. Kogo & K. Himeno</i>	509
Evaluation of cracking in recycled pavements with foamed asphalt and cement stabilization <i>A. Loizos & V. Papavasiliou</i>	519
The effects of cracking type and location on the choice of asphalt pavement recycling method <i>S.W. Haider, G.Y. Baladi, T. Akram & A. Hussain</i>	529
Cracks in porous European mixes: A theoretical and experimental study <i>F.G. Praticò, R. Ammendola & A. Moro</i>	539
<i>9. Pavement modeling-response, crack analysis, and damage prediction</i>	
Reflective cracking behavior for traffic and temperature effects <i>M.J.C. Minhoto, J.C. Pais & P.A.A. Pereira</i>	551
Mechanism of overlay reinforcement to retard reflective cracking under moving vehicular loading <i>J. Baek & I.L. Al-Qadi</i>	563
Virtual testing procedure for cracking performance prediction of HMA <i>Z. Feng, P. Zhang, M.N. Guddati, Y.R. Kim & D.N. Little</i>	575

Structural impact and dynamics response in brittle materials <i>M. Buonsanti, G. Leonardi & F. Scopelliti</i>	587
Multiscale computational modeling for predicting evolution of damage in asphaltic pavements <i>R.F. Soares, Y.-R. Kim & D.H. Allen</i>	599
Finite element modeling of fatigue shear tests: Contribution to pavement lifetime design under traffic loading <i>F. Bouhas, A. Millien & C. Petit</i>	609
Shift factor model evaluations using tested data from PMA at low temperatures and data reductions methods for IDT and HT-BBR testing <i>B.-Q. Bai</i>	617
An experimental investigation of the fracture mechanics of bitumen and asphalt <i>O. Portillo & D. Cebon</i>	627
Using semi-analytical finite element method to evaluate stress intensity factors in pavement structure <i>S. Hu, X. Hu & F. Zhou</i>	637
<i>10. Pavement interface testing and modeling</i>	
Interface fatigue cracking in multilayered pavements: Experimental analysis <i>M. Diakhaté, Ch. Petit, A. Millien, A. Phelipot-Mardelé, B. Pouteau & H. Goacolou</i>	649
A fracture-based constitutive model for pavement interface characterization <i>H. Ozer, I.L. Al-Qadi & Z. Leng</i>	661
FABAC accelerated loading test of bond between cement overlay and asphalt layers <i>A. Chabot, J.M. Balay, B. Pouteau & F. de Larrard</i>	671
Low temperature cracking in asphalt overlays bonded to rigid pavements <i>H.M. Yin, W.G. Buttlar & G.H. Paulino</i>	683
<i>11. Interlayer system effectiveness in reducing reflective cracking in pavements</i>	
Techniques to mitigate reflective cracking in asphalt overlay <i>H. Wen & W. Shitangkoon</i>	695
Proper installation of paving fabric interlayers when placed prior to chip sealing <i>L. Davis & J. Dendurant</i>	703
The use of geogrids to retard reflective cracking on airport runways, taxiways and aprons <i>J. Penman & K.D. Hook</i>	713
Evaluation of fiber reinforced bituminous interlayers for pavement preservation <i>C. Palacios, G.R. Chehab, F. Chaignon & M. Thompson</i>	721

Installation and performance of a fiberglass geogrid interlayer on the NCAT Pavement Test Track <i>R.B. Powell</i>	731
Evaluation of reflective cracking performance of AC mixes with asphalt rubber binder using HVS tests and recursive mechanistic-empirical analysis <i>P. Ullidtz, J. Harvey, D. Jones & B.-W. Tsai</i>	741
Fatigue investigations of asphalt concrete beams reinforced with geosynthetics interlayer <i>P. Zieliński</i>	751
On site validation and long term performance of anti-cracking interfaces <i>F. Vervaecke, J. Maeck & A. Vanelstraete</i>	761
Laboratory study of geogrid reinforcement in Portland cement concrete <i>X. Tang, G.R. Chehab & S. Kim</i>	769
Performance and service life prediction of crack preventative joint systems <i>C. Recknagel, S. Pirskawetz & F. Lüddecke</i>	779
Anti-reflective cracking solutions for asphalt overlays: 8 years performance monitoring <i>M.L. Antunes, S. Fontul & A.M. Pinelo</i>	791
 <i>12. Field investigation of pavement cracking</i>	
Development of reflective cracking index to determine the effectiveness and service life of strip interlayer systems <i>I.L. Al-Qadi, J. Baek & W.G. Buttlar</i>	801
The use of digital image correlation for accurate determination of fracture energy density in Hot Mix Asphalt (HMA) <i>B. Birgisson, A. Montepara, E. Romeo, R. Roncella, G. Tebaldi & R. Roque</i>	811
Mitigating reflective cracking under Nevada's conditions <i>N.E. Morian, E.Y. Hajj & P.E. Sebaaly</i>	821
A practical methodology for the performance-based selection of bituminous mixtures for concrete overlays <i>T. Bennert & A. Maher</i>	833
Case history on surface initiated cracks on urban thoroughfare pavements <i>L.A. Cooley, Jr., I.L. Howard, G. Baumgardner & M. Ross</i>	843
Investigation of transverse cracking of asphalt pavements in the North-Eastern Poland <i>M. Pszczoła, J. Judycki & B. Dołżycki</i>	853
Evaluation of relationships between deflection-based indices and flexible pavement cracking field performance <i>S.W. Haider & K. Chatti</i>	861
 <i>13. Pavement cracking detection</i>	
Photogrammetric pavement detection system <i>T. Lovas, I. Kertész, I. Fi & A. Barsi</i>	873

Automated cracking survey <i>K.C.P. Wang, W. Gong & Z. Hou</i>	881
Crack detection and classification in asphalt pavement using image processing <i>A. Hassani & H. Ghasemzadeh Tehrani</i>	891
<i>14. Cracking control in concrete and bridge decks</i>	
Experimental and numerical simulation study on the crack of steel orthotropic bridge deck pavement <i>W. Xu & X.-N. Zhang</i>	899
Cracking of wearing courses on steel orthotropic bridge decks <i>X. Chen, W. Huang, J. Yang, X. Wang & G. Cheng</i>	907
Author Index	913

Preface

Pavement cracking is a major pavement distress, and its rehabilitation cost is astronomical. Because the mechanisms and the causes of cracking in concrete, flexible, and composite pavements are still not well understood, this RILEM Conference is both timely and necessary. The Conference addresses several issues including pavement crack initiation and propagation mechanisms, modeling, laboratory evaluation, field validation, and detection techniques.

The Conference is the sixth in a series of RILEM Conferences on cracking in pavements. The first four focused on reflective cracking while the fifth and sixth have a focus on pavement cracking. The following is a historical summary of the past conferences:

- RC1989 Liège: Pointed out the main factors and mechanisms involved in the initiation and propagation of cracks.
- RC1993 Liège: Focused on the theoretical and experimental research needed to optimize solutions.
- RC1996 Maastricht: Presented the importance of utilizing the appropriate interlayer systems and their applications. Introduced the benefits expected from modeling and the needs for structural design of overlays.
- RC2000 Ottawa: Shared the experiences of North America in reflective cracking.
- RC2004 Limoges: Shifted the focus to pavement cracking and advanced modeling; Established the RILEM technical committee on reflective cracking.

The 6th RILEM International Conference on Cracking in Pavements marks the first time the Conference is held in the United States. We are very pleased to host the Conference considering the growing interest in this topic in North America as was evidenced during RC2004 Limoges. The submitted papers were rigorously peer reviewed, and only 89 papers from 20 different countries were accepted for presentation and publication indicating the international nature of the Conference. The Conference Proceedings provide both a state-of-the-art and state-of-the practice record on modeling of cracking in pavements, experimental approaches, field investigations, case histories, and interlayer system effectiveness.

Due to the large number of papers, the Conference includes three parallel tracks. In addition, four events are taking place in conjunction with the Conference: a workshop on reflective cracking immediately prior to the Conference; an exhibition during the Conference, with several manufacturers and services related to pavement crack detection, rehabilitation, and material testing; a meeting of the RILEM Technical Committee on Reflective Cracking; and the mid-term meeting of the FHWA Expert Task Group on Fundamental Properties and Advanced Models.

Finally, we would like to acknowledge the Scientific and Organizing Committees for their continuing input and suggestions throughout the Conference planning and the many individuals who helped review the papers.

Imad L. Al-Qadi, Conference Chair
Tom Scarpas, Co-Chair
Andreas Loizos, Co-Chair
Chicago, June 2008

Organization

Chairmen

Imad Al-Qadi, Chairman
Tom Scarpas, Co-Chairman
Andreas Loizos, Co-Chairman

University of Illinois at Urbana-Champaign, USA
Delft University of Technology, The Netherlands
National Technical University of Athens, Greece

Scientific Committee

Chairman
Secretary

Imad Al-Qadi, USA
Leslie Elble, USA

Gordon Airey, UK
Hussain Al-Khalid, UK
Hussain Bahia, USA
Bill Buttlar, USA
Samuel Carpenter, USA
Armelle Chabot, France
Emmanuel Chailleux, France
Andrew Collop, UK
Mauro Coni, Italy
Morris de Beer, South Africa
Arian De Bondt, The Netherlands
Herve Di Benedetto, France
Guy Dore, Canada
Mostafa Elseifi, USA
Ali Farhang, Sweden
Edward Guo, USA
A. Abdel Halim, Canada
Will Hansen, USA
Gerry Huber, USA
Anastasios Ioannides, USA
Ilan Ishai, Israel
Elin Jensen, USA
Lev Khazanovich, USA
Richard Kim, USA
Niki Kringos, The Netherlands
Samer Lahouar, Tunisia

Xueyan Liu, The Netherlands
Bob Lytton, USA
Johan Maeck, Belgium
Mihai Marasteanu, USA
Mark Marienfeld, USA
Eyad Masad, USA
Ann Millien, France
Andre Molenaar, The Netherlands
Antonio Montepara, Italy
Jorge Pais, Portugal
Manfred Partl, Switzerland
Glaucio Paulino, USA
Daniel Perraton, Canada
Christophe Petit, France
Katherine Petros, USA
Annabelle Phelipot, France
Rob Rasmussen, USA
Jeff Roesler, USA
Reynaldo Roque, USA
Johan Silfwerbrand, Sweden
Jorge Soares, Brazil
Dariusz Sybilski, Poland
Gabriele Tebaldi, Italy
Erol Tutumluer, USA
Jacob Uzan, Israel
Tom Van Dam, USA
Julie Vandenbossche, USA

Organizing Committee

Imad Al-Qadi, USA
Jongeeun Baek, USA
William Buttlar, USA
Leslie Elble, USA
Eli Fini, USA
Zhen Leng, USA
Hasan Ozer, USA

Geoff Roberts, USA
Jeff Roesler, USA
Tom Scarpas, The Netherlands
Leslie Sweet Myrick, USA
Erol Tutumluer, USA
Hao Wang, USA

1. Accelerated pavement testing to assess pavement structure, interface bonding and reflective cracking

Evaluation of reflective cracking performance of asphalt mixes with asphalt rubber binder using HVS tests and non-local continuum damage mechanics

R.Z. Wu & J.T. Harvey

University of California Pavement Research Center, Davis, USA

ABSTRACT: A major research project has been conducted at the University of California Pavement Research Center to evaluate the performance of several asphalt mixes that contain binders with recycled rubber. This paper presents the analysis results with respect to reflection cracking using a mechanistic model based on non-local continuum damage mechanics and the finite element method. The damage evolution law parameters were identified using laboratory fatigue test data. The Finite Element model was validated by simulating full-scale pavement testing using a Heavy Vehicle Simulator. The ranking of different asphalt mixes with respect to reflective cracking was then determined by simulating overlay systems with different asphalt mixes for the overlay but the same mechanical properties for all the underlying layers including old asphalt, aggregate base and subgrade.

1 INTRODUCTION

1.1 *Background*

A major research project has been conducted at the University of California Pavement Research Center to evaluate the performances of several asphalt mixes that contain asphalt rubber binder. A key component of the research effort was the evaluation of reflective cracking performance using a Heavy Vehicle Simulator (HVS). Specifically, the HVS testing program involved running full-scale accelerated pavement tests on asphalt overlay systems that have different material types and layer thicknesses for the overlay. Although the underlying pavement systems were designed to be the same, it was found that the in-situ conditions of the underlying layers varied significantly among different HVS test sections. This variation makes it questionable to rank reflective cracking performance of different asphalt mixes based on the HVS test results directly.

This paper presents an alternative method to rank different asphalt mixes using HVS test results. This was made possible through simulations of HVS tests using non-local continuum damage mechanics (NLCDM) implemented in the finite element method (FEM).

The simulations were divided into two stages: (1) Calibrate the simulation procedure using in-situ conditions of different overlays as model inputs and match model predictions with observed reflective cracking performance; (2) Predict reflective cracking performance of different asphalt overlays placed on various given underlying structures. The first stage simulations serve as validation of the FEM procedure. The results obtained in the second stage simulations provide objective ranking of different asphalt overlays with respect to reflective cracking performance without the influence of underlying conditions.

1.2 *FEM simulation using NLCDM*

The FEM simulation procedure used here is essentially the same as the one developed by Wu (2005, 2006). Cracking damage in asphalt mix caused by truck wheel trafficking is represented by asphalt

mix stiffness reduction. The rate of stiffness reduction (i.e., damage evolution) is controlled by a spatially averaged value of principal tensile strain. The radius of the area for spatial averaging is related to the maximum aggregate size of asphalt mix. The averaging operation is performed by concurrently solving a differential equation in addition to equilibrium. It is called non-local because of the use of average strain for driving damage evolution.

NLCDM describes asphalt material cracking behavior, while FEM takes into account the effects of structure features (e.g., cracks) and loading conditions. By implementing the NLCDM as a material constitutive model into a general FEM framework, a mechanistic model is obtained that can predict crack propagation in general asphalt pavement structures. The specific formulation used in this paper is based on the work (Peerlings, Borst et al., 1998), developed for general composite materials. Similar approach has been used by (Bodin, Pijaudier-Cabot et al., 2004) for asphalt mixes and (Bazant and Jirasek, 2002) for PCC. A more extensive review on the approach can be found in (Wu, 2005).

2 DEVELOPMENT OF MODEL INPUTS

2.1 General assumptions

The design pavement structure for the HVS test sections is shown in Figure 1. Each HVS test section is eight meters long and one meter wide. All of the test sections have the same structure, i.e. asphalt overlay on top of an old cracked asphalt pavement. The underlying old cracked asphalt pavements were resulted from Phase I HVS testing of this project (Bejarano, et al., 2005). The general methodology and model assumptions are listed below:

- The pavement system is analyzed as a 2D plain strain model with considerations to account for the 3D nature of HVS wheel load.
- AC overlays are assumed to be linear elastic with loading time and temperature dependent stiffness and subjected to damage driven by a measure of strain.

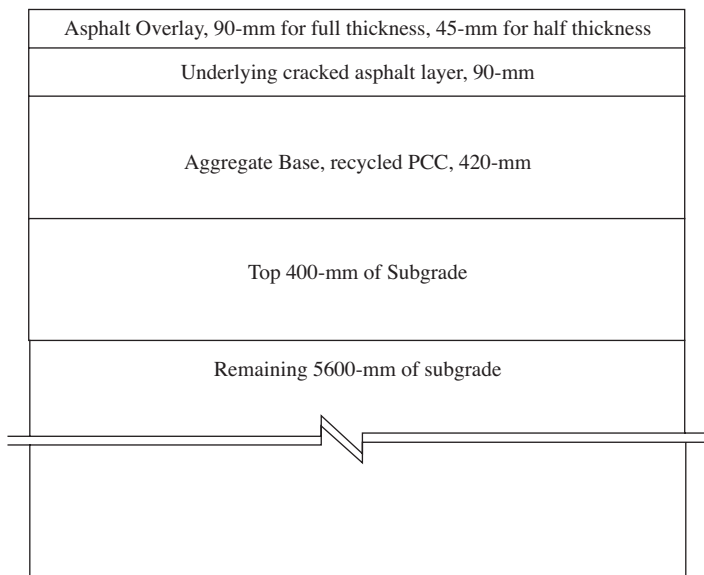


Figure 1. Design structure of HVS test sections (actually layer thickness may vary).

- The underlying cracked asphalt layer is assumed to be linear elastic with stiffness that are functions of loading time and temperature. Cracks are modeled directly with empty spaces in the underlying asphalt layer. The underlying asphalt layer is not subjected to damage because of the extensive existing cracks.
- Aggregate base (AB) and subgrade (SG) are assumed to be linear elastic with stiffness degradation determined by back-calculation from surface deflections measured during HVS tests using Road Surface Deflectometer (RSD). AB and SG layers can not sustain tensile strains larger than 0.1 percent, in which case their stiffness along the tensile direction is reduced to 10 percent of the original value.
- Subgrade is assumed to be 6000-mm deep and is subdivided into two layers: the top 400-mm and the remaining 5600-mm.

2.2 Environmental conditions

All of the HVS test sections were enclosed with a temperature chamber. The pavement temperature at 50-mm depth were controlled to be $20 \pm 2^\circ\text{C}$ for the first million load repetitions and $15 \pm 2^\circ\text{C}$ for the rest of the tests.

2.3 Loading history

HVS trafficking was applied with dual wheel truck tires running at a speed of about 9.6 km/h. The range of wheel loads used during the test was between 60 kN and 90 kN.

2.4 Underlying crack spacing

In the FEM model, crack spacing is assumed to be constant for each individual simulation. It was observed that the majority of the cracks are in transverse direction. Accordingly, the crack spacing is referred to as the distance between cracks in the longitudinal direction. Each HVS test section is divided into five subsections with center at Stations 4, 6, 8, 10 and 12 respectively (i.e. at 2, 3, 4, 5 and 6 meter marks along the longitudinal direction of the test section). Crack spacing for each subsection is calculated by counting the number of transverse cracks within $\pm 0.5\text{m}$ range to subsection center. For example, the crack spacing is $1000/(n - 1)$ mm if n cracks are counted. Table 1 lists the number of cracks counted for each subsection of the six HVS test sections.

2.5 AC overlay characterization

The asphalt overlay was treated as a linear elastic material with loading time and temperature dependent stiffness, and with damage (stiffness reduction) evolution caused by repetitive HVS

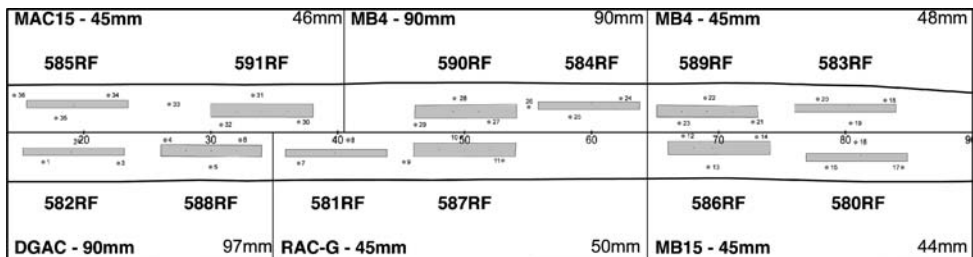


Figure 2. Overall layout of the test site, 586RF to 591RF are under discussion in the paper; MB4, MB15, MAC15, RAC-G and DGAC indicate different mix types, 45-mm and 90-mm (in bold font) indicate overlay thicknesses, actual overlay thicknesses are also indicated in normal font.

Table 1. Number of cracks counted for different locations on the surface of the underlying DGAC old pavement.

Subsection center station	4	6	8	10	12
586RF over 567RF	9	6	9	8	9
587RF over 568RF	8	9	10	9	9
588RF over 569RF	1	0	4/0*	9	7
589RF over 571RF	4/2*	7	8	9	11
590RF over 572RF	10	9	9	0/3*	4/2*
591RF over 573RF	3/2*	6	7	11	9

* These subsections have significantly different crack densities for the two sides of the subsection center and therefore the crack numbers are counted separately.

trafficking. Asphalt mixture stiffness master curves were developed from laboratory bending beam frequency sweep test.

Damage evolution parameters (three in total) were identified using laboratory bending beam fatigue test data. Fatigue tests were simulated using FEM to obtain the predicted stiffness degradation curve corresponding to a given set of damage evolution parameters. The set of parameters that led to good match between predicted and measured stiffness degradation curves were recorded and used in later HVS test simulation. This matching process is still conducted manually and no optimization method is used so far.

One set of damage evolution parameters were obtained for each temperature under which fatigue tests were conducted. Damage evolution parameters for temperatures other than 10, 20 and 30°C were determined using linear interpolation.

2.6 AB and SG characterization

AB and SG were treated as linear elastic materials with stiffnesses determined from back-calculation using surface deflection data measured by RSD (road surface deflectometer).

Neither aggregate base nor subgrade can sustain large tensile stress. A special material model was used in the analysis to describe this behavior. Specifically, the normal stiffness for AB and SG in certain direction will be reduced to 0.1 of its normal value if it is subjected to tensile strain greater than 0.1 percent (i.e. 1000 microstrain) in that direction.

Back-calculation results indicate that stiffness for AB and the top 400-mm of SG decreased significantly under HVS trafficking. This decrease is described by the following exponential function:

$$E(n) = E_0 \exp(-\alpha \cdot n) \quad (1)$$

where E is the stiffness, and n is the number of load repetitions. The variables E_0 and α are regression constant representing initial stiffness and rate of stiffness degradation, respectively. There are significant differences in AB and SG stiffness among the six HVS test sections.

2.7 FEM model

Figure 3 shows the overall FEM mesh, while Figure 4 shows a close up look of the mesh around the crack tip. During initial simulations, it was found that cracks would propagate horizontally first to debond the overlay from the old AC layer if the overlay is soft. Although debonding is likely to occur in actual HVS test, it is regarded less important than vertical crack propagation. It is therefore decided to prevent cracks from propagating horizontally at the beginning of each HVS test simulation.

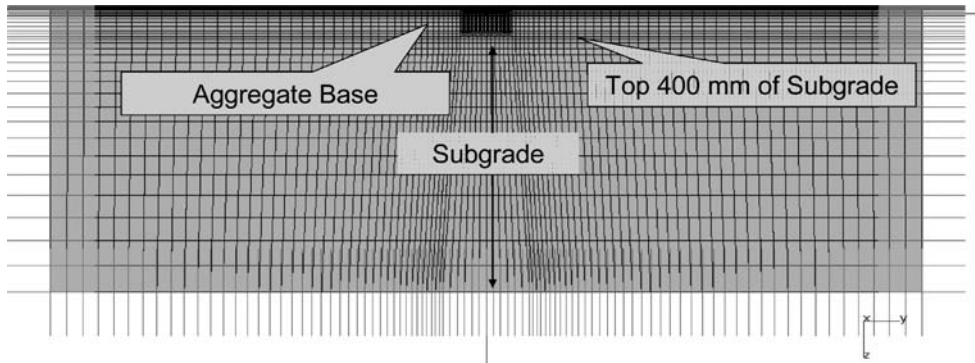


Figure 3. Overall FEM mesh for a typical HVS simulation, red lines at the left, right and bottom boundary indicate confinements in the direction of the lines, colors of the mesh indicate material specifications.

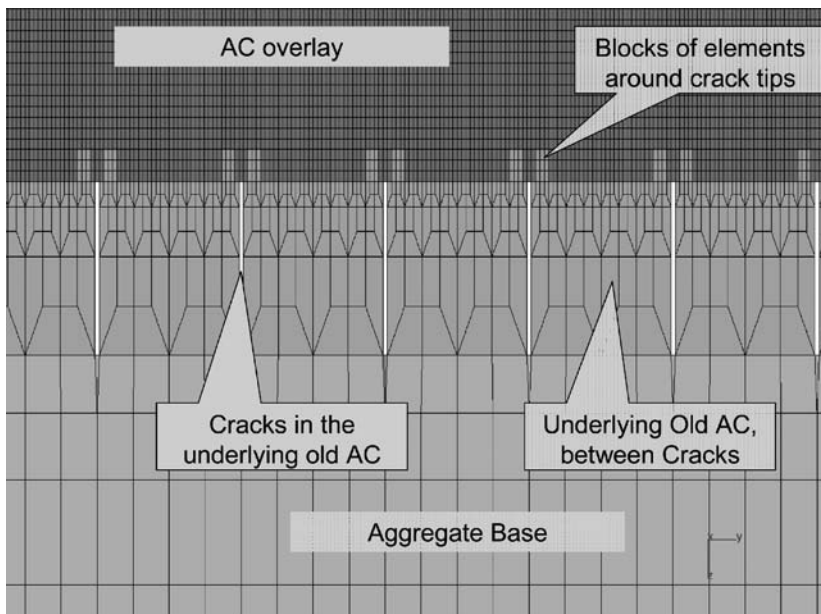


Figure 4. A further close up look of the FEM mesh shown in Figure 3, the green blocks in the overlay around the tip of the underlying cracks indicate areas that are not subjected to damage. These blocks are necessary to force cracks to propagate upwards instead of sideways.

2.8 Simulation procedure

The overall procedure for FEM simulation of reflective cracking in asphalt overlay is described in detailed in (Wu, 2006). In summary, the simulation procedure follows the steps below:

- (a) Establish the intact (undamaged) stiffness of different layers based on current pavement temperature, and the aggregate base and subgrade stiffness based on current accumulated traffic count.
- (b) Calculate the non-local strain field for part of the overlay that are near an underlying crack.

- (c) Calculate the damage induced by ΔN additional HVS traffic repetitions using the non-local strain calculated in Step (b). Step size ΔN is determined in adaptive manner using current maximum damage rate within the overlay.
- (d) Apply the damage to asphalt overlay, which leads to decrease in stiffness.
- (e) Remove an element and propagate the crack once the stiffness at all gauss points within certain element have been reduced to 1 percent of their intact value.
- (f) Repeat Steps (a) to (e) until cracks reach the surface of the overlay.

2.9 Some details

The 2D plane strain FEM model used in simulations is a simplification of the actual HVS test, which is essentially three-dimensional in nature. To make the strain calculated in a 2D-FEM model approximately equal to the actual strain experienced by the overlay in the HVS tests, the load pressure is scaled by a factor. This load pressure scale factor is calculated as the ratio between actual surface deflection measured by RSD and the calculated surface deflection from 2D FEM analysis. When measured surface deflections are not available, they were replaced by values calculated using multilayer elastic theory using ELSYM5 with the underlying cracks ignored. In the HVS simulations for this project, load pressure scale factors were mostly around 0.20. This procedure was shown to work well in (Wu, 2005).

HVS wheels apply dynamic loads on pavement systems. The inertia effect of the dynamic wheel load was ignored because the wheels were moving at fairly constant speeds except only when they make turns at both ends of the test section, which were not analyzed.

Another effect of the moving wheel is that different points in the overlay may not reach maximum strain simultaneously. This implies that fixing wheels at any specific location may lead to an underestimation of the strain field and hence underestimate the damage rate. The detailed procedure used to account for this effect of moving wheels can be found in (Wu, 2005). The procedure essentially calculate the envelop of non-local strain for any given point during a passage of truck wheels and use the envelop value for driving damage.

In summary, the maximum strain any point experienced during a passage of the wheels is used to drive the damage evolution at that point in the FEM simulations.

3 MODEL VALIDATION

3.1 Comparison between observed and predicted reflective cracking life

Reflective cracking life is defined here as the time required for cracks to appear on the surface of an overlay. Comparison of observed and predicted reflective cracking lives for different HVS test sections are listed in Table 2. As shown in the table, the predicted reflective cracking lives are not exactly the same but the differences between them are mostly within 0.3 million when they can be calculated. For sections that did not reach the end of their reflective cracking lives in the HVS tests, namely sections 586RF, 589RF, 590RF and 591RF, the predicted reflective cracking lives are mostly compatible with the observations. It is concluded that the simulation procedure provides reasonable predictions for reflective cracking lives on asphalt overlays with similar structures as those in this project.

3.2 Reflective crack propagation plots

During simulations of all of the HVS sections, except 586RF, cracks initiated from the bottom of the overlay and propagated upward until they reached the surface. In other words, all of the cracks in the HVS sections were bottom-up cracks except 586RF, which has no crack initiated after 10-million load repetitions.

A typical set of crack propagation history plots are shown in Figure 5 for HVS Section 589RF. Note that crack height was calculated using the bottom of the overlay as the reference. As shown in

Table 2. Reflective cracking life in millions for different stations within each HVS section (repetitions in millions).

Section		4	6	8	10	12
586RF (MB15)	Observed	No crack after 2.49 million load repetitions				
	Calculated	No crack after 10.0 million load repetitions				
587RF (RACG)	Observed	1.52	1.49	1.55	2.08	2.94
	Calculated	1.52	1.72	1.52	1.82	1.89
588RF (AR4000)	Observed	0.51	>1.4	0.51	0.51	0.51
	Calculated	0.48	0.94	0.31	0.21	0.26
589RF (MB4)	Observed	No crack after 2.09 million load repetitions				
	Calculated	3.19	4.44	3.59	2.03	1.49
590RF (MB4)	Observed	No crack after 1.98 million load repetitions				
	Calculated	2.35	2.24	1.84	1.63	1.63
591RF (MAC15)	Observed	No crack after 2.55 million load repetitions				
	Calculated	2.92	2.77	2.67	3.31	3.03

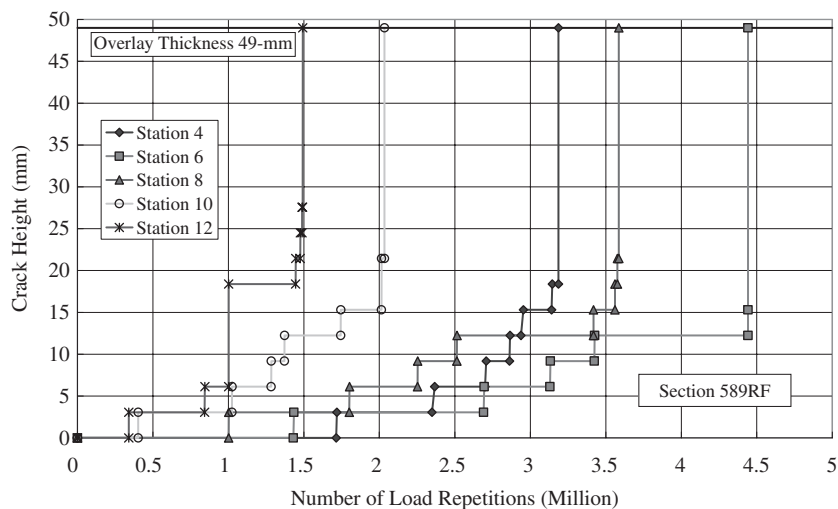


Figure 5. Evolution of height of crack tip with number of load repetitions for sub-sections of HVS section 588RF.

the figure, reflective cracking performance can vary significantly even for different locations within the same HVS test section. This variation came from the fact that conditions of the underlying layers (including the old asphalt layer, aggregate base and subgrade layers) varied significantly among different stations within each test section.

4 PERFORMANCE RANKING

The procedure validated in the first stage simulations was used to predict reflective cracking performance of different asphalt overlays placed on the same underlying layers. As discussed in Section 1.2, these analyses are referred to as second stage simulations and are used to rank the relative performance of different asphalt overlays used in this project with respect to reflective cracking.

4.1 Methodology

To rank their reflective cracking performance, different overlays were placed on the same underlying structures and their reflective cracking lives were calculated using the procedure validated in the first-stage simulations. Different underlying structures were included to determine the sensitivity of the performance ranking with respect to overlay thickness, and aggregate base stiffness. The variations of different quantities considered in these simulations are shown below in Table 3, while all the other common quantities are listed in Table 4.

4.2 Simulation results

This section presents the second stage simulation results. Note that these results were based on a specific pavement structure and environment condition as described in Table 3 and Table 4.

The effects of overlay thickness on reflective cracking life are shown in Figure 6. As shown in the figure, increasing overlay thickness from 45 mm to 90 mm increases reflective cracking lives by 30 to 70 percent for all the mixes except AR4000, whose reflective cracking lives are very close for both overlay thicknesses and can not be distinguished by the model used.

The effects of aggregate base (AB) stiffness are shown in Figure 7. As shown in the figure, increasing AB stiffness (from 150 to 300 MPa) increases reflective cracking lives significantly for all the asphalt mixes. The improvements in reflective cracking lives ranges from 80 percent for AR4000 mix to 230 percent for MAC15 mix.

According to the results shown in Figure 6 and Figure 7, increasing asphalt overlay thickness from 45 to 90 mm is not as effective in improving reflective cracking performance as increasing AB stiffness from 150 to 300 MPa. The simulation results also indicate the overall ranking of reflective cracking performance as listed in Table 5.

Table 3. Variations of quantities considered in second-stage simulations.

Quantity	Variations	Number of levels
Mix Type	AR4000, RACG, MB4, MB15, MAC15	5
Overlay Thickness (mm)	45, 90	2
Base Stiffness (MPa)	300, 150, both degraded to 80	2
	Total	20

Table 4. Values of common quantities for second-stage simulations.

Quantity	Value
Loading	Same as in HVS test section 588RF, except that the trafficking did not stop until the overlay has failed
Pavement Temperature	20°C
Mix Air Void Content	6%
Mix Aging	No aging
Mix Gradation	DGAC for AR4000, OGAC for all others
Mix Preparation Method	Field mix lab compact
Underlying Old Asphalt Stiffness	30% of intact stiffness
Crack Spacing (mm)	100 mm
Old DGAC Thickness	90 mm
Aggregate Base Thickness	400 mm
Stiffness of Top 400-mm of Subgrade	50 MPa
Stiffness of Remaining subgrade	300 MPa

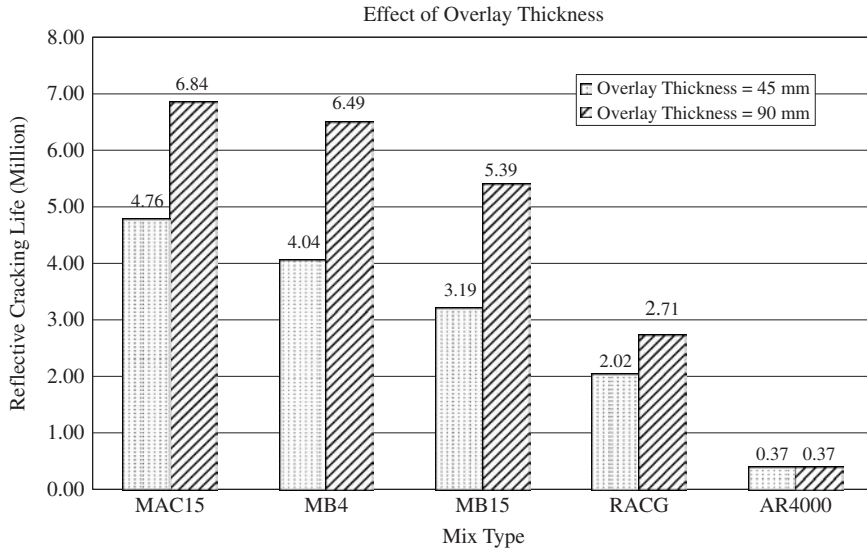


Figure 6. Effects of AC overlay thickness on reflective cracking life for different AC mixes.

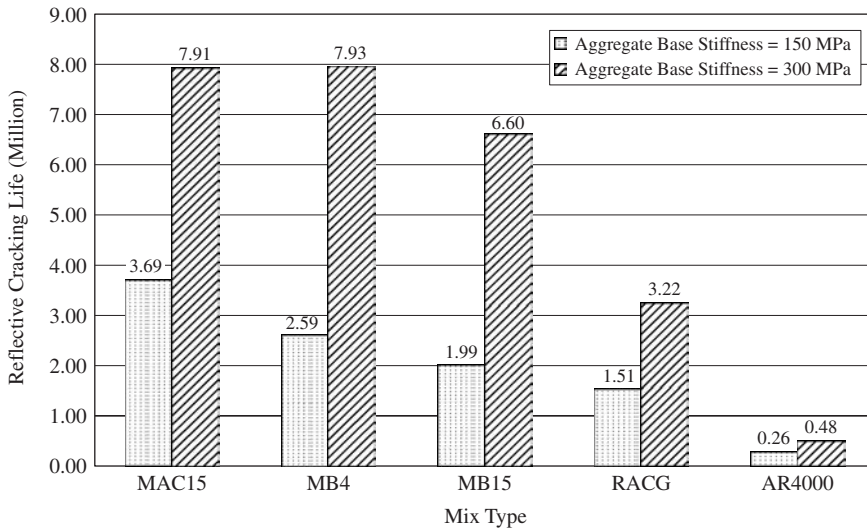


Figure 7. Effects of aggregate base stiffness on reflective cracking life for different AC mixes.

Table 5. Reflective cracking performance ranking of asphalt mixes.

Performance ranking	AC overlay mix type	Normalized reflective cracking life
1	MAC15	1.00
2	MB4	0.91
3	MB15	0.74
4	RAC-G	0.41
5	AR4000	0.06

5 SUMMARY AND CONCLUSIONS

In summary, this paper presents the following analyses:

- First stage simulations: validate a FEM simulation procedure based on non-local continuum damage mechanics with actual performance data collected during HVS tests.
- Second stage simulations: predict reflective cracking performance of different mixes in asphalt overlays under the HVS testing conditions, using uniform underlying structure.

Based on the results from the simulations in the two stages, the proposed analysis procedure provides a rational alternative for interpreting HVS test results. This alternative is able to remove the effects of variations in underlying support on reflective cracking performance.

The proposed analysis procedure requires laboratory fatigue test data for identifying damage evolution parameters for given asphalt mix. Since fatigue test data are usually available, model parameters for the proposed analyses procedure is easy to obtain. It is therefore believed that the propose procedure is a practical tool that can help evaluate reflective cracking performance of asphalt overlays.

The recommended third stage, which was performed for this study, but not included in this paper, is to use the validated model to evaluate the relative performance of the different overlays under different climate, load and underlying structure conditions expected in highway applications.

REFERENCES

- Bazant, Z. P. & M. Jirasek (2002). Nonlocal Integral Formulations of Plasticity and Damage: Survey of Progress. *Journal of Engineering Mechanics* 128(11): 1119–1149.
- Bejarano, M., Morton, B. & Scheffy, C. 2005. *Summary of Construction Activities and Results from Six Initial Accelerated Pavement Tests Conducted on Asphalt Concrete Pavement Sections for Modified Binder Overlay*. Pavement Research Center, Institute of Transportation Studies, University of California Berkeley.
- Bodin, D., G. Pijaudier-Cabot, et al. (2004). Continuum Damage Approach to Asphalt Concrete Fatigue Modeling. *Journal of Engineering Mechanics* 130(6): 700–708.
- Peerlings, R. & R. D. Borst, et al. (1998). Gradient-enhanced damage modelling of concrete fracture. *Mechanics of Cohesive-Frictional Materials* 3(4): 323–342.
- Wu, R. 2005. *Finite Element Analysis of Reflective Cracking in Asphalt Concrete Overlays*. Ph.D. Thesis, University of California, Berkeley.
- Wu, R., Harvey, J. & Monismith, C. 2006. Towards a Mechanics Model for Reflective Cracking in Asphalt Concrete Overlays. *Journal of Asphalt Paving Technologists*, 491–534.

The LCPC's ALT facility contribution to pavement cracking knowledge

P. Hornych, J.P. Kerzreho, A. Chabot, D. Bodin, J.M. Balay & L. Deloffre
Laboratoire Central des Ponts et Chaussées, Nantes, France

ABSTRACT: The full scale observation of damage and failure mechanisms of pavements due to traffic is quite essential for the improvement of road materials and construction methods, as well as for the development and the validation of modelling tools and pavement design methods. An alternative to the survey of real roads over long periods consists in performing accelerated pavement tests (APT). LCPC has today more than 20 years of experience in APT applied to study of pavement deterioration and cracking. Since 2006, in relation with an LCPC research program to update the French pavement design method, a detailed analysis of existing data of LCPC APT tests is being carried out. The objective of this work is to improve the understanding and modelling of the development of rutting and fatigue in different types of pavements. This paper presents the first conclusions of this synthesis, in relation to fatigue cracking, for the purpose of the RILEM Technical Committee – Cracking in Asphalt Pavements (TC-CAP).

1 INTRODUCTION

To improve the understanding and modelling of fatigue mechanisms and crack localization and propagation phenomena in bituminous pavements, it is necessary to rely on observations of real pavement behaviour. Data on pavement performance can be obtained from road data bases. This data can be used to derive laws of evolution of distresses, depending on the type of structures, traffic and successive maintenance operations (Kobisch 2000, Brillet et al. 2006). However, it is necessary to complement this statistical approach with mechanical data, including accurate information on materials, description of applied loads and instrumentation of the pavements. The feedback from real pavements is also considerably delayed, because of the long service life of these structures (20 to 30 years on the French national network).

The interest of accelerated loading tests is to allow the development and the observation of deterioration mechanisms of full scale pavements, in a much shorter time than on the real road network. In addition, these tests are performed in controlled conditions, and on instrumented pavements, and thus provide more complete data.

At LCPC, in Nantes, two accelerated pavement testing facilities are in operation: A large scale accelerated testing facility, the LCPC fatigue test track (Autret et al. 1987, 1988, www.lcpc.fr), and a small scale linear accelerated testing facility, the FABAC machine (Balay et al. 1998, Perez et al. 2007, Chabot et al. 2008, www.lcpc.fr).

Within the framework of numerous partnerships with the French road authority, motorway companies, pavement contractors or bitumen producers, LCPC has performed a great number of fatigue experiments with its large outdoor ALT facility, since its commissioning in 1984. Approximately 60 new pavement structures, and 15 pavement reinforcements, have been tested. This installation allows to test pavements up to their failure, and to follow the evolution of pavement distress (rutting, cracking) with traffic loading. Depending on the types of materials and pavement structures,

different rates of evolution and types of cracking are observed: longitudinal or transversal cracks, bottom up or top down cracking.

This paper describes cracking mechanisms observed on 16 pavement structures tested on the LCPC large ALT facility, which are all low traffic pavements, with less than 12 cm of bituminous materials, and a granular base. A detailed study of the damage of those structures has been made by means of trenches and cores. Comparisons of the observed behaviour with predictions obtained with the French pavement design method (LCPC, SETRA 1994), based on multi-layer linear elastic analysis, are also discussed. The results are presented in two parts, concerning respectively:

- Pavements with a very thin bituminous wearing course (less than 6 cm), presented in part 4;
- Pavements with a thicker wearing course (between 6 and 12 cm), presented in part 5.

2 THE LCPC FATIGUE TEST TRACK

The LCPC accelerated pavement testing facility, in Nantes, is an outdoor circular carousel, with a diameter of 40 meters (see Figure 1). The installation comprises a central 750 kW motor unit and four arms carrying the wheel loads, which can reach a maximum speed of 100 km/h. The experimental pavement has a mean radius of 17.5 m and a width of 6 m, and thus a total length of approximately 110 m. The position of the load can be adjusted at a different radius on each arm, for instance to test simultaneously the effect of different load configurations. During loading, a lateral wandering of the loads can be applied (Autret & Gramsammer 1990).

The arms can be equipped with various load configurations: single or dual wheel, single, tandem or triple axles. A large range of loads can be applied: between 45 and 80 kN on a single half axle, up to 135 kN with multiple axles. A very low stiffness suspension system allows to continue to run on pavements presenting severe deteriorations.

The test facilities comprise three circular tracks where the pavements are built, one of them equipped with a waterproof concrete pit, allowing to control the water table level in the subgrade by means of pumps. The loading system can be moved from one ring to another within approximately one week. The pavement structures are built using normal road-building equipment and in general, 4 different structures are tested simultaneously in each experiment, including in general a reference structure with well known behaviour.



Figure 1. View of the LCPC fatigue test track.

3 PAVEMENT INSTRUMENTATION AND MONITORING

The experiments presented in this paper have all been performed with a dual wheel 65 kN load, (standard French equivalent axle load, shown in Figure 2), and a loading speed of 70 km/h. Generally, bituminous layers are instrumented during construction with thermocouples and strain gage sensors, measuring longitudinal and transversal (horizontal) tensile strains at the bottom of the layers. Vertical strains in unbound layers and subgrade, and also vertical displacements of the pavement surface are measured using displacement transducers. In situ tests and distress measurements are also performed after different levels of traffic, including measurements of deflections, transversal profile and visual survey of surface cracking.

In this study, it is proposed to examine mainly the extent of cracking, defined as the percentage of the length of the pavement section showing visible cracking. (see Figure 2). A transversal crack is assumed to have a length of 50 cm.

Typical examples of measurements of longitudinal and transversal strain variations at bottom of bituminous layers, in pavements with a bituminous wearing course and a granular base are shown in Figure 3.

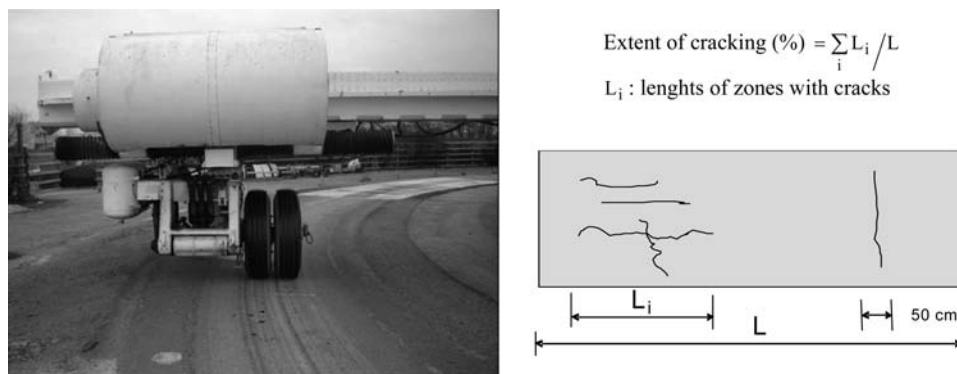


Figure 2. Dual wheel 65 kN load applied in the experiments and assessment of the extent of cracking.

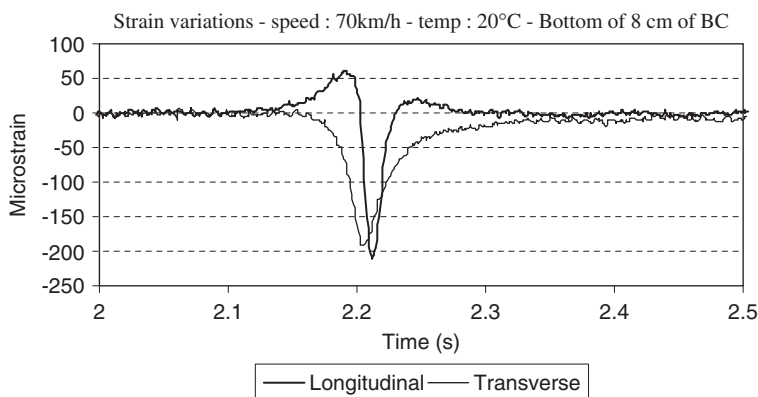


Figure 3. Typical measurements of longitudinal and transversal strains at the bottom of a thin bituminous surface layer (compressive strains positive).

Table 1. Main characteristics of the pavement structures with 5 cm thick wearing courses.

Experiment	Name	Layer thickness (cm)		Soil modulus (MPa)	AC composition (in %)					Deflection 0.01 mm
		BC	UGM		%bit	6/10	2/6	0/2	Fines	
S1	Ex B0	5.0	45	60	6.45	43	15	41	1	100–140
S2	TP Sor	5.0	40	60	6.05	28	30	42	–	65–75
S3	TP Pom	5.0	40	60	6.05	28	30	42	–	90–110
S4	TP Poe	5.0	55	60	6.05	28	30	42	–	80–105
S5	DR1 p1	5.0	20	110	6.20	38	24	36	2	70–85
S6	DR1 p2	5.0	35	80	6.20	38	24	36	2	70–80
S7	DR2 p1	5.0	20	110	6.20	38	24	36	2	85–95
S8	DR2 p2	5.0	35	80	6.20	38	24	36	2	85–95

4 PAVEMENTS WITH LESS THAN 6 CM THICK BITUMINOUS WEARING COURSES

4.1 Experimental results

Eight pavements of this type have been analysed. Table 1 gives the main characteristics of the pavement structures, and of the bituminous materials. The levels of deflection of each pavement, under the standard 65 kN dual wheel load, at the start of the experiments, are also indicated. The bituminous mixes used in all these experiments are mixes specified in France for low traffic pavements, presenting high bitumen contents (between 6 and 6.45% of grade 50/70 bitumen); their standard elastic moduli (at 15°C and 10 Hz) vary from 4000 MPa to 5000 MPa. The experiments S2, S3 and S4 have been analysed by Odéon et al. (1994).

On these structures, the first distress observed was rutting, and cracks started to develop only when the rut depth exceeded 12 to 15 mm. Investigations performed at the end of the experiments indicated that the rutting was mainly due to permanent deformations of the unbound granular layers and not only of the subgrade, contrary to what is assumed in the French pavement design method, where the only design criterion for rutting is the maximum vertical elastic strain ϵ_z at the top of the subgrade.

For these very thin pavements, the measurements indicate that maximum tensile strains at the bottom of the bituminous layers are generally transversal, and located under the centre of each wheel. They are generally 1.2 to 1.5 times higher than longitudinal strains. This probably explains why the cracks observed in these experiments were mainly longitudinal (assuming bottom-up cracking), except on structures S5, S6 and S8. Figure 4 shows a typical example of the crack patterns observed on these structures.

On structures S5 and S6, cores taken after observation of the first cracks indicated that the cracks were superficial, and stopped a few millimetres below the surface. These first transversal cracks were short (20 to 40 cm) and very thin, and led to a production of fines due to attrition. Visco-elastic calculations performed on similar pavement structures (Heck et al. 1998, Duhamel et al. 2005) have shown that visco-elastic behaviour can generate significant tensile stresses at the top of the thin bituminous layer, near the wheel, and this could be one possible explanation of the top down cracking.

Table 2 describes the experimental conditions, and the distresses observed on the 8 pavement structures. The evolution of cracking with the number of loads is shown in Figure 5. Although the pavement structures are similar, two types of evolution can be seen: On structures S1 to S4, and also S7, the first cracks appear early (between 50 000 and 200 000 cycles), and cracking develops rapidly to failure (more than 90% cracking after 100 000 to 500 000 cycles). On structures S5, S6 and S8, development of cracking is much slower (50% cracking is attained after 750 000 to 1 million loads). Two main factors probably explain these differences:

- The bearing capacity of the soil: In experiments S1 to S4, the soil (clayey sand) had an elastic modulus of about 60 MPa after construction. In comparison, in experiments S5 to S8, a stiffer



Figure 4. Illustration of cracks observed on structure S1 at the end of the experiment.

Table 2. Distresses observed on the pavements with 5 cm thick wearing courses.

Experiment	First cracks	Number of loads (millions) leading to		Rut depth at 10% cracking (mm)	Temperature in BC (°C)	Rainfall (mm)	Soil modulus (MPa)
		10% cracking	50% cracking				
S1	Longitudinal	0.350	0.450	22	10–30°C	Medium	60
S2	Longitudinal	0.180	0.300	12	5–20°C	Abundant	60
S3	Longitudinal	0.100	0.110	12	5–20°C	Abundant	60
S4	Longitudinal	0.060	0.080	12	5–20°C	Abundant	60
S5	Transversal	0.500	0.950	20	20–55°C	Dry	110
S6	Transversal	0.590	1.050	20	20–55°C	Dry	110
S7	Longitudinal	0.050	0.200	15	0–45°C	Medium	80
S8	Transversal	0.300	0.750	20	0–45°C	Medium	80

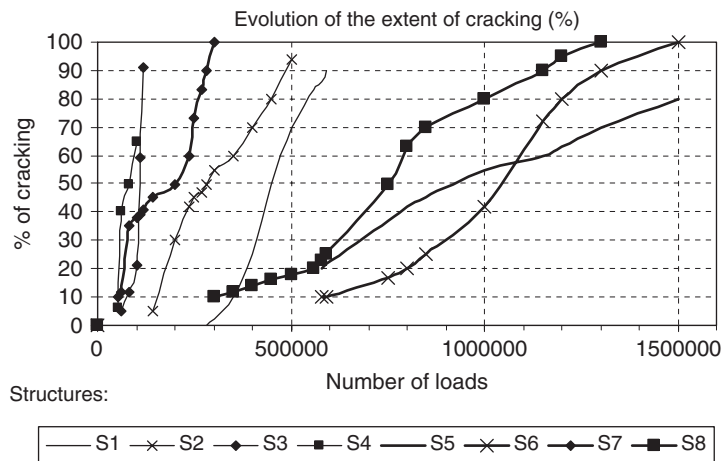


Figure 5. Evolution of the extent of cracking on the pavements with 5 cm thick wearing courses.

Table 3. Comparison of predicted and observed lives of the experimental pavements (number of 130 kN axle loads NE).

	S1	S2	S3	S4	S5	S6	S7	S8
Standard design NE	14600	902000	492000	2610000	28400	224000	28400	224000
Design with back calculated moduli NE	118000	388000	61000	1180000	150000	450000	160000	520000
Experimental NE	36000	340000	115000	95000	430000	800000	80000	900000

soil with levels of modulus varying between 80 and 110 MPa was used. This is in accordance with the French design method, where a penalization factor is applied to low bearing capacity soils.

- The climatic conditions. Structures S1 to S4 were tested in autumn or winter, with mild temperatures and heavy rainfall, leading to high moisture contents in the unbound layers. Structures S5 and S6 were tested during summer with high temperatures and practically no rainfall. Structures S7 and S8 were tested in Summer and autumn, with a high water table level in the soil. Dry and hot conditions certainly contributed to the good performance and slow evolution of cracks on structures S5, S6. Structures S7 and S8, with high water table level, present a different behaviour. On structure S7, with a thin granular base (20 cm) cracking developed much earlier than on section S8, with a 35 cm thick granular base.

4.2 Predictions of pavement lives and conclusions

The observations on the low traffic pavements with less than 6 cm thick bituminous wearing course clearly show that the main distress mode of these pavements is rutting, mainly localized in the granular layers and subgrade. In the French design method, based on a multi-layer linear elastic model, the design criterion used for these pavements with a thin surface layer is only a rutting criterion. No bituminous layer fatigue criterion is used, and this is coherent with the observed behaviour. The rutting criterion is expressed by:

$$\varepsilon_z \leq 16000(\text{NE})^{-0,222} \quad (1)$$

where ε_z : the maximum vertical strain at the top of the subgrade

NE the number of equivalent standard axle loads (130 kN axle).

In these pavements with a thin surface layer, cracking was observed only after a significant level of rutting, and then contributed to the degradation of the pavement, in particular by facilitating infiltration of water. This good resistance to cracking is probably due to the use of specific bituminous mixes, specified in France for low traffic pavements, which a high bitumen content, and this confirms the interest of these materials.

To evaluate the French design method, design calculations have been performed, with the rutting criterion, for the 8 experimental pavements. For each pavement, two calculations have been performed. The first one was performed with standard values of elastic moduli of the unbound granular layers and subgrade, defined from empirical criteria (standard design procedure). The second calculation was performed with values of elastic moduli back-calculated from in situ measurements (FWD or deflection tests). The results of the design predictions (number of axle loads NE to failure) are presented in Table 3. In general, better predictions are obtained with the back-calculated layer moduli. These last predictions are reasonable for all structures except S4, with ratios between the experimental and predicted design life varying between 1.1 and 3.3. The only exception is structure S4, where the real life is largely over-predicted. This structure differs by its very thick granular base (55 cm). With such a thick granular layer, the subgrade strain ε_z becomes low, and the subgrade strain criterion is not any more applicable. Clearly, for structure S4, another design criterion is required (rutting criterion for the granular layer).

Table 4. Main characteristics of the pavement structures with 6 to 12 cm thick wearing courses.

Experiment	Name	Layer thickness (cm)		Soil modulus (MPa)	AC composition (in %)						Deflection 0.01 mm
		BC	UGM		%bit	10/14	6/10	2/6	0/2	Fines	
S9	Enr ph1 str1	7.0	40	50/70	5.40	29	16	22	32	1	90–100
S10	Enr ph1 str2	7.5	40	50/70	5.40	29	16	22	32	1	110–120
S11	Enr ph2 str1	9.0	40	50/70	5.40	29	16	22	32	1	100–120
S12	Enr ph2 str2	7.5	40	50/70	5.40	29	16	22	32	1	130–140
S19	Enr ph1 str4	11.0	40	50/70	4.60	29	16	22	32	1	70–90
S20	Enr ph 2 str3	11.0	40	50/70	4.60	29	16	22	32	1	90–110
S22	Enr ph 1 str3	8.0	40	10/20	6.20	29	16	22	31	2	70–80
S23	Enr ph 2 str4	6.0	40	10/20	6.20	29	16	22	31	2	100–120

To improve the rutting predictions, further research is carried out at LCPC to develop a finite element model, for calculation of permanent deformations in these low traffic pavements (Finite element program ORNI, Hornych et al., 2007).

5 PAVEMENTS WITH 6 TO 12 CM THICK BITUMINOUS WEARING COURSES

5.1 *Experimental results*

Eight pavement structures with more than 6 cm thick bituminous layers have been analysed. The main characteristics of the pavement structures and materials are given in Table 4. In these experiments, different bituminous mixes have been tested:

- Classical bituminous concretes (BBSG) in structures S9 to S12, with elastic moduli at 15°C and 10 Hz varying between 6000 and 7000 MPa.
- Road base bituminous materials (GB) in structures S19 and S20 with elastic moduli at 15°C and 10 Hz varying between 9000 and 12000 MPa. On structure S19 this material was covered by a 2 cm very thin bituminous concrete layer; no wearing course was used on S20.
- High modulus bituminous mixes (EME) in structures S22 and S23, with elastic moduli at 15°C and 10 Hz varying between 12000 and 13000 MPa.

For all these structures, the main mode of distress is cracking of the bituminous layers. When the extent of cracking attains 10%, the rut depth remains low, varying generally between 3 and 7 mm. Moreover, the type of bituminous mix influences the mode of cracking observed.

Table 5 describes the experimental conditions, and the distresses observed on the pavement structures with 6 to 12 cm thick bituminous layers. The evolution of cracking on these structures is summarised in Figure 7. For structures S9 to S12, with a standard bituminous concrete, the first cracks were in all cases transversal (an example is shown in Figure 6), and there was evidence that some of them initiated at the top of the layer, and propagated downwards. For these structures, measurements indicated that the longitudinal and transversal tensile strains, at the bottom of the bituminous layer were of the same level. Cores taken on structures S9 and S10, after the observation of the first cracks, indicated that these cracks were superficial, and went only a few millimetres below the surface. Later, the cracks propagated through the whole bituminous layer. The first cracks appeared for levels of rut depth of about 4 to 7 mm.

For structures S19 and S20 (road base bituminous material, with a relatively low bitumen content), cracks were also transversal. They started to appear for levels of rut depth of 3 to 5 mm, and rapidly crossed the whole layer.

Table 5. Distresses observed on the pavement structures with 6 to 12 cm thick wearing courses.

Exp	First cracks	Number of loads (millions) leading to		Rutting at 10% cracking (mm)	Temperature AC in °C	Rainfall (mm)
		10% cracking	50% cracking			
S9	Transverse	1.000	1.300	7	5–40°C	Medium
S10	Transverse	1.000	1.700	7	5–40°C	Medium
S11	Transverse	0.250	1.000	4	5–30°C	Medium
S12	Transverse	0.250	0.300	5	5–30°C	Medium
S19	Transverse	2.300	2.700	5	5–40°C	Medium
S20	Transverse	0.250	0.400	3	5–30°C	Medium
S22	Transverse	1.200	1.750	3	5–40°C	Medium
S23	Transverse	0.200	0.300	3	5–30°C	Medium



Figure 6. Transversal cracking observed on structure 9.

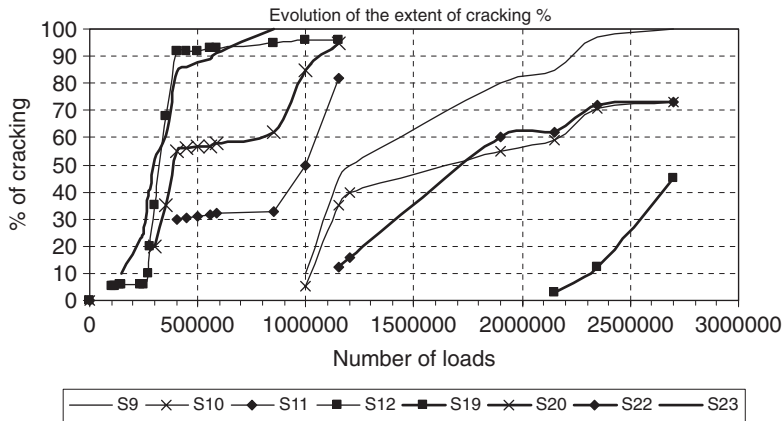


Figure 7. Evolution of the extent of cracking on the pavements with 6 to 12 cm thick wearing courses.

Structures S22 and S23 were built with high modulus bituminous mixes. Usually, these materials are used for base course, and are covered with a wearing course, but on the test track, they were tested without wearing course. In these stiff materials, the cracks (again mainly transversal) appeared for low levels of rutting (2 to 4 mm) and developed rapidly.

Structures S9, S10, S19 and S22 present a long life (between 1.3 and 2.6 million loads to reach 50% of cracking), see Figure 7. Structures S11, S12, S20 and S23 present a much shorter life (0.3 to 1 million loads), despite the fact that they were built to have the same characteristics (S11 was identical to S9, etc.). However, the structures S11, S12 and S20 were built on a layer of crushed gravel which had been extracted and recompacted, and which had a low density. In addition, structure 23, with high modulus bituminous mix, had a thinner bituminous layer (6 cm instead of 8 cm).

5.2 Predictions of pavement lives and conclusions

For these pavements, design calculations were performed, in order to predict the pavement life, and make comparisons with the observed behaviour. For these bituminous pavements, two design criteria are applied, in the French pavement design method: the rutting criterion limiting the maximum vertical strain at the top of the subgrade (equation 1), and a fatigue criterion limiting the maximum tensile strain ε_t at the bottom of the bituminous layer. However, the relevant design criterion is generally the fatigue criterion, expressed as follows:

$$\varepsilon_t \leq \varepsilon_6(10^\circ C, 25 Hz) \times \left(\frac{NE}{10^6} \right)^{-1/b} \times \sqrt{\frac{E(10^\circ C)}{E(\theta eq)}} \times kr \times kc \times ks \quad (2)$$

where: ε_6 the strain leading to a fatigue life of 10^6 cycles, determined at $10^\circ C$ and 25 Hz,
 b : the slope of the fatigue line,
 NE the number of equivalent standard axle loads (130 kN dual wheel axle loads),
 $E(10^\circ C)$: the modulus of the bituminous material at $10^\circ C$ and 10 Hz,
 $E(\theta)$: the modulus of the bituminous material at the design temperature θ and 10 Hz,
 kr , ks and kc are coefficients related respectively with the risk of failure, the penalization for low bearing capacity soils and the calibration of the model (comparison between predictions of the model and behaviour observed on real pavements).

This fatigue design criterion was applied, for the 8 pavement structures, using fatigue parameters determined from two-point bending fatigue laboratory tests. Two calculations were performed for each pavement structure: in the first one, a constant temperature of $15^\circ C$ (generally adopted for standard design) was used. In the second calculation, the temperature variations were considered, by cumulating the fatigue damage occurring at each temperature θ (by intervals of $5^\circ C$), using the Miner hypothesis for damage accumulation.

Comparisons of the design lives predicted with these two approaches with the experimental pavement lives (number of loads leading to an extent of cracking of 50%, assumed equal to the design risk of failure) are given in Table 6. Clearly, for these pavements, the two design approaches lead to unrealistically low design lives. It must be stressed that all the pavements are tested in accelerated conditions, without normal seasonal variations, and material ageing, which could be favorable. But, nevertheless, the application of the fatigue criteria, based on laboratory tests, leads here to very poor predictions. This could mean that:

- For these relatively thin pavements, the conventional fatigue criterion (assuming bottom up cracking) does not describe correctly the failure mechanisms.
- The laboratory fatigue tests are not representative of the in situ behaviour. The bending test, without confinement, may be too severe compared with the in situ stress conditions, as well as the continuous high frequency loading (25 Hz). For instance, studies performed by de la Roche et al. (1994) have shown the strong influence of rest periods on fatigue behaviour.

Table 6. Comparison of predicted and observed lives of the experimental pavements (degradation level 50%).

	S9	S10	S11	S12	S20	S21	S22	S23
Standard design ($\theta = 15^{\circ}\text{C}$) NE	69000	14500	50000	63000	153000	102000	169000	29900
Design with variable temperature NE	68000	6400	11700	8700	30700	7400	328000	11600
Experimental NE	1250000	1687500	995000	322000	2700000	385500	1750000	294500

- The fatigue criterion (based on parameters determined at 10°C , equation 2) is probably not sufficient to take into account the thermal susceptibility of the materials, and this is at present a subject under research at LCPC.
- It is probable that, due to the absence of ageing and seasonal variations, the accelerated tests lead to higher pavement lives than on real roads. This effect may be corrected by considering the relative performance in comparison with a reference pavement.

6 CONCLUSIONS

The paper presents a synthesis of pavement deterioration mechanisms observed in APT experiments, on the LCPC fatigue carousel, on low traffic pavement structures, with unbound granular bases. The experiments lead to similar deterioration mechanisms as on real pavements. The main deterioration mechanism depends on the thickness of the bituminous surfacing (less than 6 cm, or between 6 and 12 cm). For the pavements with very thin bituminous layers, the main deterioration mechanism is rutting due to permanent deformations of the unbound layers, and significant cracking appears only after 10 to 15 mm of rutting; this cracking is mainly longitudinal. For the pavements with thicker bituminous layers (6–12 cm), the main deterioration is cracking, and rutting remains much more limited (3 to 7 mm). In this case, the cracking is mainly transversal, contrary to the longitudinal cracking generally observed on real pavements.

For the two types of structures, design calculations have been performed with the French design method. For the very thin pavements, reasonable predictions of the service life are obtained, despite the simplifications of the model (subgrade rutting criterion only). For the thicker pavements, where bituminous layer fatigue is the design criterion, however, the design method leads to a large underestimation of the observed pavement life, showing the limits of the conventional fatigue criterion. These results show the necessity:

- to improve the modelling of fatigue damage in pavements. Research is presently carried out at LCPC on development of a damage model for bituminous materials in pavement structures (Bodin et al., 2004a, b) and on modelling of pavements with vertical discontinuities, to understand crack propagation phenomena (Chabot et al., 2007).
- to study the real representativity of accelerated tests, which do not take into account ageing of materials, climatic effects and variability of loads, regarding fatigue mechanisms.
- to develop specific sensors to survey development of cracking in pavements.

REFERENCES

Autret, P., de Boissoudy, A.B. & Gramsammer, J.C. 1987. The circular test track of the Laboratoire Central des Ponts et Chaussées – First Results. *Proc. 6th Intern. Conf. on Structural Design of Asphalt Pavements, Ann Arbor, June 13–17 1997*, 1: 550–561.

- Autret P., Baucheron de Boissoudy, A. & Gramsammer, J.C. 1988. Le manège de fatigue du Laboratoire Central des Ponts et Chaussées: Premiers résultats. *Bulletin de liaison des Laboratoires des Ponts et Chaussées*, (155): 33–45.
- Balay, J.M. & Gramsammer, J.C. 1990. Le manège de fatigue du LCPC et l'innovation. *Revue Générale des Routes* (680): 13–18.
- Balay, J.M. & Aunis, J. 1998. An applied research program on continuous reinforced concrete pavement: the Fabac project, *8th International conference on Concrete Roads, 1998, Lisbon*.
- Bodin, D., de La Roche, C. & Chabot, A. 2004. Prediction of bituminous mixes fatigue behavior during laboratory fatigue tests. *3rd Euraspalt & Eurobitume Congress, 12-14 may, Vienna*, 2: 1935–1945.
- Bodin, D., Pijaudier-Cabot, G., de La Roche, C., Piau, J.M. & Chabot, A. 2004. Continuum Damage Approach to Asphalt Concrete Fatigue Modeling. *Journal of Engin. Mechanics (ASCE)* 130(6): 700–708.
- Brillet, F., Lorino, T. & Dumeix, T. 2006. Analysis of road maintenance sequences according to the evolution of Distresses. *10th International Conference on Asphalt Pavements, Québec, August 12–17*.
- Chabot, A., Tran Q. D. & Ehrlacher A. 2007. A modeling to understand where a vertical crack can propagate in pavements. In Taylor & Francis Group Proceedings, *Internat. Conf. on Advanced Characterization of Pavement and Soil Engineering Materials, Athens, June 20–22 2007*, 1: 431–440.
- Chabot, A., Pouteau, B., Balay, J. M. & de Larrard, F. 2008. FABAC Accelerated Loading Test of Bond between Cement and Asphalt Material Layers. Proposed to the *Sixth International RILEM Conference on Cracking in Pavements, Chicago, June 16–18*.
- De La Roche, C. & Corté, J. F. & Gramsammer, J. C. & Odéon, H. & Tiret, L. & Caroff, G. 1994. Etude de la fatigue des enrobés bitumineux à l'aide du manège de fatigue du LCPC. *Revue Générale des Routes* (716): 62–75.
- Duhamel, D., Chabot, A., Tamagny, P. & Harfouche, L. 2005. Viscoroute: Visco-elastic modeling for asphalt pavements – Viscoroute : Modélisation des chaussées bitumineuses. *Bulletin des Laboratoires des Ponts et chaussées* (258–259): 89–103.
- Heck, J.V., Piau, J.M., Gramsammer, J.C., Kerzreho, J.P. & Odeon, H. 1998. Thermo-visco-elastic modelling of pavement behaviour and comparison with experimental data from the LCPC test track. *Proceedings of the 5th BCRA, Trondheim*.
- Hornych, P., Chazallon, C. & Allou, F. & El Abd, E. 2007. Prediction of permanent deformations of unbound granular materials in low traffic pavements. *Roads Materials and Pavement Design*. To be published.
- Kobisch, R. 2000. Comportement et modélisation des structures de chaussées. Base de données des sections tests «SHRP» françaises no de Dossier 980238.
- LCPC-SETRA, 1994. Conception et dimensionnement des structures de chaussée. *Guide Technique LCPC-SETRA*.
- Odéon, H., Kerzrého, J.P., Kobish, R. & Paute, J.L. 1994. Expérimentation de trois graves non traitées sur le manège de fatigue du LCPC. *Bulletin de Liaison Labo P. et Ch.*, 189.
- Pérez, S. A. & Balay, J. M. & Tamagny, P. & Petit, C. 2007. Accelerated pavement testing and modeling of reflective cracking in pavements. *Engineering Failure Analysis*, 14 (8): 1526–1537.

Pavement strength measured by full scale test

E.H. Guo & L. Ricalde

SRA International, Egg Harbor TWP, New Jersey, USA

F. Petch

Airport Technology Research and Development, Technical Center, FAA, Atlantic City, New Jersey, USA

ABSTRACT: Pavement strength is defined as the maximum stress that leads to crack initialization in a concrete pavement. Full-scale static step-loads were applied at the free edge of concrete slabs to induce bottom-up and top-down cracks, and then to determine the pavement strength. Both top-down and bottom-up crack initializations were successfully detected. Then the pavement strength was estimated using the collected test data and two assumptions: the pavement strength is similar at the slab top and bottom, and the residual stress at the slab top and bottom has the same magnitude but different signs. It has been found that the laboratory flexural strength of the cast beam was higher than the pavement strength in full-scale tests, while the flexural strength of the saw-cut beams from the slabs was lower than it.

1 INTRODUCTION

The concept of concrete pavement strength is very different from the strength of concrete used to build the pavement. Most failure models used in concrete pavement design are based on Miner's fatigue model (Miner et al., 1945). For the simplest case, single type load, the following equation is used

$$N = f(\sigma / R) \quad (1)$$

Where N is the load coverage to pavement failure; σ is the critical stress predicted in the pavement under a specific load and R is the flexural strength of the concrete mix. The value N is very sensitive to value R . In Miner's work, σ and R were obtained from the same type of test specimen. Therefore, when $\sigma = R$, $N = 1$, then strength failure occurs. When $\sigma < R$, $N > 1$, more load repetitions will lead to the specimen failure. It is unrealistic to use "pavement strength" for pavement design so the strength obtained from a specimen has to be used. Therefore different test standards such as ASTM C39, C78 and C496 were developed simulating different stress states. Currently, the flexural strength of concrete is widely used in concrete pavement design procedures. However, it is interesting to compare the strength from a specimen and from the pavement itself since the later makes the application of the fatigue equation closer to the assumptions in Miner's model.

Full scale tests were conducted at the FAA's National Airport Pavement Test Facility (NAPTF) in April and May, 2005 to observe crack behavior on Portland Cement Concrete (PCC) slabs. During the period the pavement strength was obtained and compared to the "beam flexural strength" from the laboratory tests. The full-scale testing was conducted on three rigid test items with different cross sections as shown in Figure 1. Each test item contained twenty 4.6 m by 4.6 m (15 ft. by 15 ft.) slabs, four slabs in the transverse direction and five slabs in the longitudinal direction. The test items were built on a medium strength subgrade with CBR values of 7 to 8 and the 30.5 cm (12 in) slab thickness. The three structures only difference was the subbase layer material: conventional

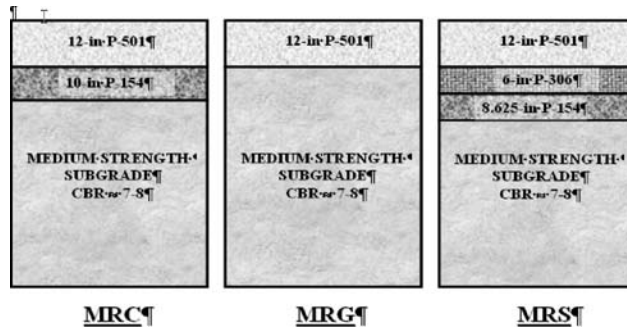


Figure 1. Cross section of rigid structures tested at the FAA's NAPTF.



Figure 2. Strip 30.5 cm (12 inch) wide by 22.86 m (5 slabs length, 75 ft) were saw-cut and removed.

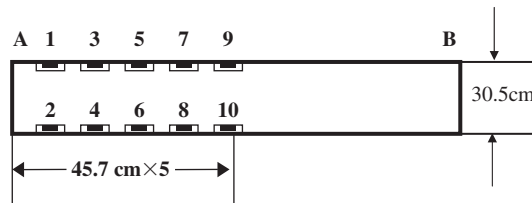
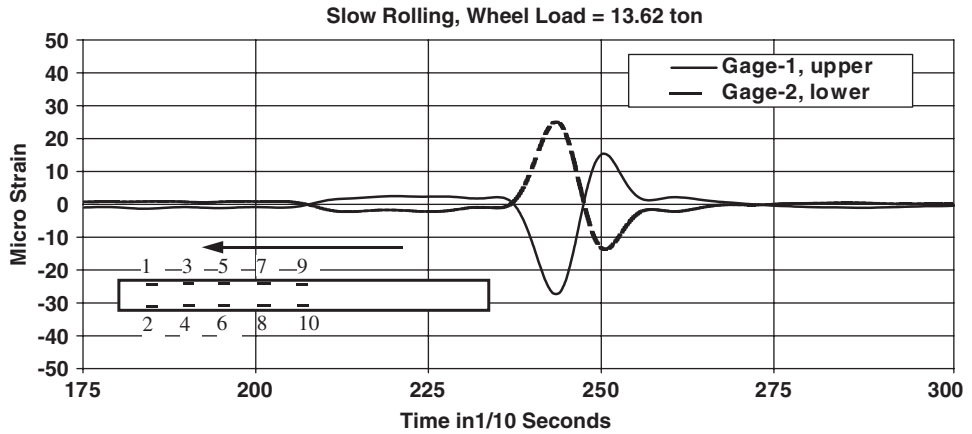


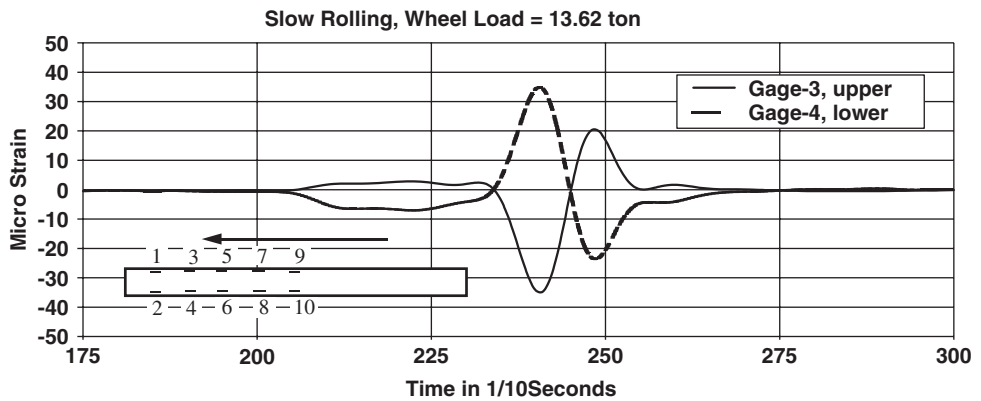
Figure 3. Ten strain gages mounted on slab S11 free edge.

(granular) for MRC and stabilized for MRS, there was no subbase for MRG where the slab was placed on grade.

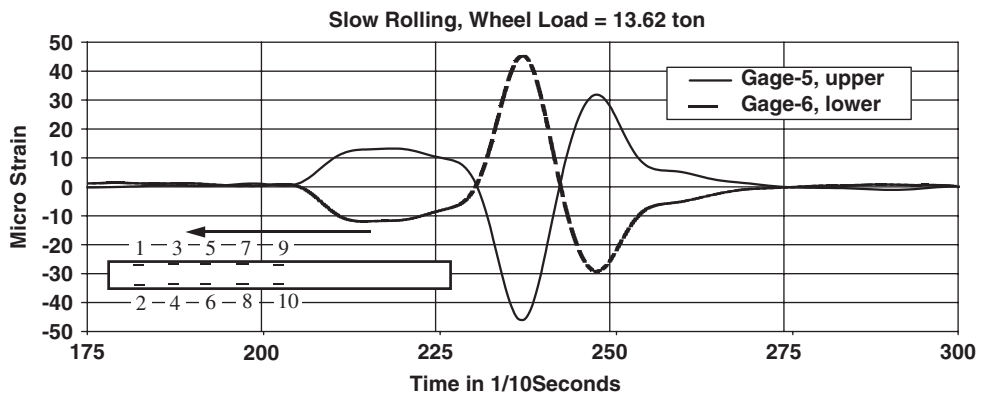
The three structures were built to contribute in the calibration of the FAA's new rigid pavement design model for airports (Brill 2006). After the traffic testing was completed, all the slabs located in the loading/traffic area next to the longitudinal side joint (north and south sections) were severely distressed. However, no cracks were observed at longitudinal joint next to the center line since no load was applied in that area. A 30.5 cm (12 in) wide and 22.86 m (75 ft) long (slabs S11, S12, S13, S14 and S15) strip was cut in test item MRC, south of the center line longitudinal joint as shown in Figure 2. Strain gages were mounted on the free edge of the cut slabs. The strain gage locations on slab S11 are shown in Figure 3. The distance from the upper and lower gages to the slab top and bottom respectively was 3.8 cm (1.5 in). Heavy static and slow rolling loads were applied along the free edge of the tested slabs. Both, bottom-up and top-down cracks were induced as planned and their propagation histories were not only collected from the strain gages but recorded using a camcorder. The major effects affecting the pavement cracking behavior in the tested slabs have been analyzed and summarized in this paper.



(a) Strain histories of gages 1 and 2



(b) Strain histories of gages 3 and 4



(c) Strain histories of gages 5 and 6

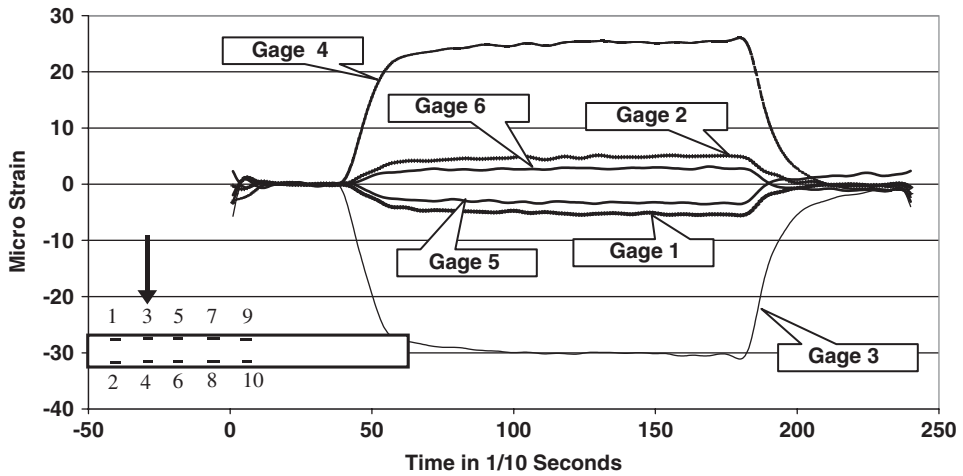
Figure 4. Strain histories under a slow rolling load.

2 RELIABILITY OF TEST DATA

Before the execution of the test plan the strain gage reliability was evaluated. Figure 4 shows the recorded history of strain gages 1 to 6 under a 13.2 ton (30,000 lbs) single wheel moving load in

slab S11 in direction from B to A in Figure 3. The results show symmetric records received by the upper (1, 3 and 5) and lower (2, 4 and 6) gages. Comparing the three histories in Figure 4 it can be observed that the magnitude of the strain recorded by gages 5 and 6 were the highest, and the lowest were recorded by gages 1 and 2, when the wheel load was sitting exactly above the gages. Figure 4 also shows the inverse bending strain variation when the single wheel was moving from point B to A. Gages 5 and 6 recorded the highest inverse bending strain and gages 1 and 2 the lowest. This can be explained because the wheel load moved out of the tested slab shortly after rolling over gages 1 and 2, but remained on the slab enough time to allow the development of the inverse strain for gages 5 and 6 after rolling over them.

Figure 5a shows the strain histories of gages 1 to 6 under a static single wheel load on gages 3 and 4, and Figure 5b is an actual picture taken during the static loading of gages 5 and 6. The single wheel was loaded on a specific location, held position for about 10 seconds and then unloaded.



(a) Strain histories of gages 1 to 6 under a static single wheel load



(b) The 13.2 ton (30,000 lbs) singlewheel load was above gages 5 and 6

Figure 5. Strain histories of gage 1 to 6 under a static single wheel load.

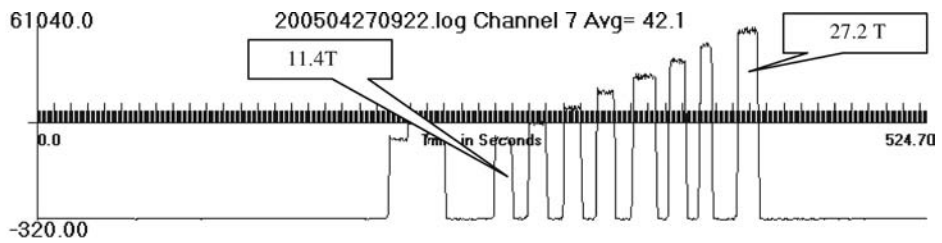
During the holding period, the recorded data was relatively stable. The average five-second data shown in Figure 5a is defined as the “static strain” under the static load.

The results shown in Figures 4 and 5 verify the reliability of the collected data. Slab S11 was selected to conduct several tests due to its accessibility and good structural condition. Eight of the ten mounted gages were verified reliable, including gages 1 to 6. Gages 7 and 10 recorded data was unreliable and it has not been used in this paper. The first crack initialization was observed between gages 3 and 5, from the slab top down to the slab bottom. Since all six gages were reliable, the collected data could be used for crack behavior analysis, and later for the calculation of the pavement strength.

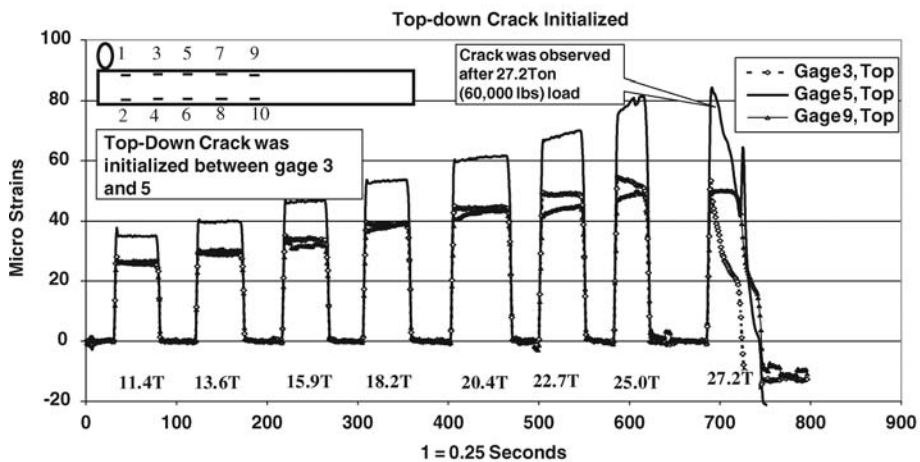
3 INITIALIZATION OF TOP-DOWN CRACK UNDER A STATIC LOAD

An incremental load of 2270 kg (5,000 lbs) was applied to the left corner of slab S11. The collected load records in shown in Figure 6a and the strain history in Figure 6b. The test consisted in loading the single wheel up to 11,350 kg (25,000 lbs), holding position for few seconds, unloading the wheel and then waiting for few seconds before the application of the next incremental load until 13,620 kg (30,000 lbs) was reached. During the waiting period after unloading, the slab was surveyed to investigate whether a top-down crack had been developed.

During the incremental load test at slab S11 corner, a top-down crack was visually observed shortly after the single wheel was loaded to 27,240 kg (60,000 lbs). The researchers clearly noticed



(a) Record of static loading, from 11,350kg (25,000 lbs) to 27,240kg (60,000 lbs), incremental load 2,270kg (5,000 lbs)



(b) Records of strains of gages 3, 5 and 9

Figure 6. Initialization of top-down crack in slab S11 detected by strain gage records.

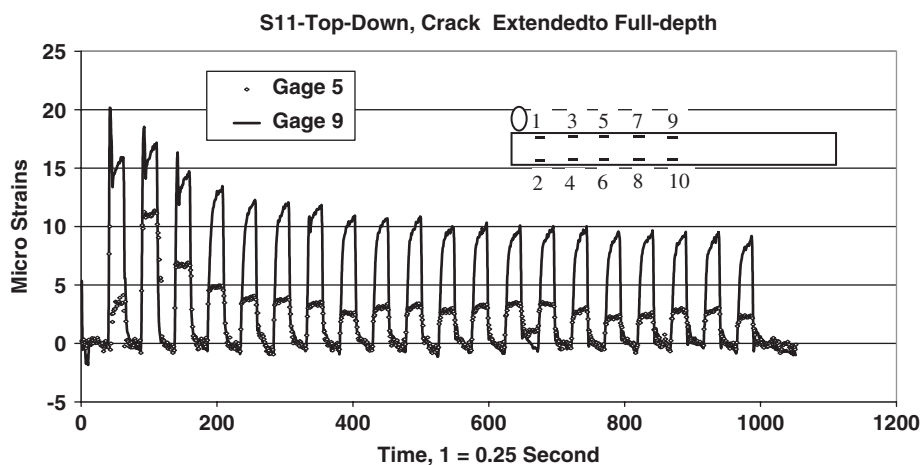


Figure 7. Propagation of a top-down crack in slab S11 recorded by strain gages.

the occurrence of the crack even before the wheel was unloaded. After the test was completed, the strain records were analyzed and presented in Fig. 6b. After 22,700 kg (50,000 lbs) load was applied, the strain values gradually increased during the load holding period. The increase in strain might indicate the development of a micro crack near the slab surface. The micro crack width continuously increased while the load was held. However, the crack propagation during this time was not significant for visual observation. The macro crack was observed when the wheel was loaded up to 27,240 kg (60,000 lbs).

4 PROPAGATION OF TOP-DOWN CRACK INTO FULL DEPTH UNDER A STATIC LOAD

After the top-down crack was initialized in slab S11, it was visible to the naked eye. The crack was located between gages 3 and 5, about 12.7 cm (5 in) away from gage 5. Since the crack did not propagate to full depth, the 27,240 kg (60,000 lbs) static wheel load was repeatedly applied (twenty times) to induce full depth propagation, the strain records for gages 5 and 9 are presented in Figure 7. The strain data in gage 9 was showing a higher value than the strain data in gage 5, just reverse of what was happening before the crack was initialized, when the strain in gage 5 was the highest (Fig. 6b). It can be observed the readings were relatively stable for the two gages after ten repetitions of incremental loads. The change in strain readings from unstable to stable is an indication that a full depth crack was developed. During the crack propagation, the pavement structure continuously changed after every load, and after the full-depth crack was developed, a new stable pavement structure was formed. Therefore, all strain gage readings became stable. Not only the crack initialization, but also the completion of a full depth crack was detected in the test. The application of the finding will be discussed in section 7.

5 BEHAVIOR OF BOTTOM-UP CRACK UNDER A STATIC LOAD

Slab S12 in test item MRC was selected to run bottom-up crack testing (Fig. 8). The single wheel was loaded at the middle of the free edge. After 24,970 kg (55,000 lbs) wheel load was applied, a very fine crack was observed at the slab bottom. The crack was initialized near the strain gage but did not propagate through the gage. The strain histories under the same incremental load for slab S15 show a similar crack behavior as shown in Figure 9a. Although the initialization of bottom-up

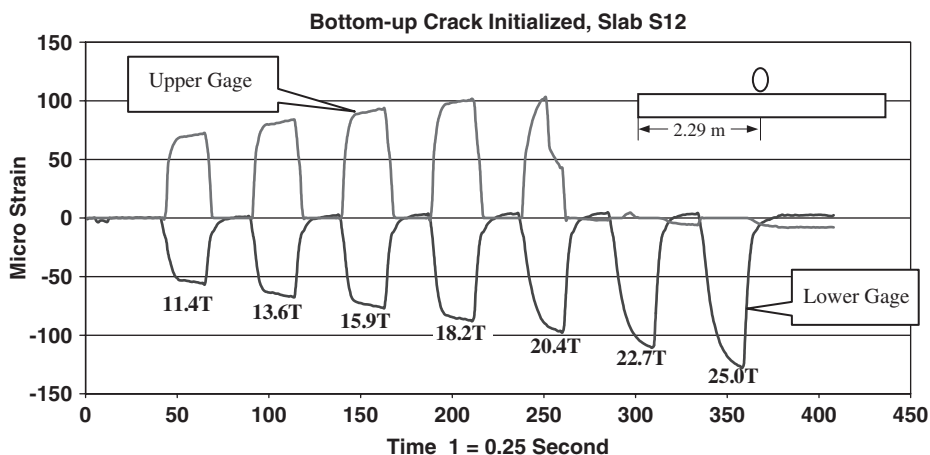


Figure 8. Initialization of bottom-up crack in slab S12 detected by strain records.

crack was visually observed after the 24,970 kg (55,000 lbs) wheel load was applied, it is obvious that the crack was initialized before that loading.

If the crack initialization occurred when the loading was 20,430 kg (45,000 lbs), the corresponding strain was about 105 micro strains (Figs. 8, 9a).

Hoping to induce and record the crack propagation history for the bottom-up crack, a static incremental load test series were conducted in slab S12. The initial single wheel load was 27,240 kg (60,000 lbs) with increments of 2270 kg (5,000 lbs) up to 43,130 kg (95,000 lbs). The strain histories presented in Figure 10 are a continuation of Figure 8. There was no crack propagation to full-depth even under application of extremely heavy single wheel load. The lack of crack propagation was verified by visual survey, and collected strain histories. The strain gage readings at the top of the slab in Figure 10 continued increasing and did not reach stable values. No full depth crack was developed. Similar behavior was observed while testing slab S15 (Fig. 9b).

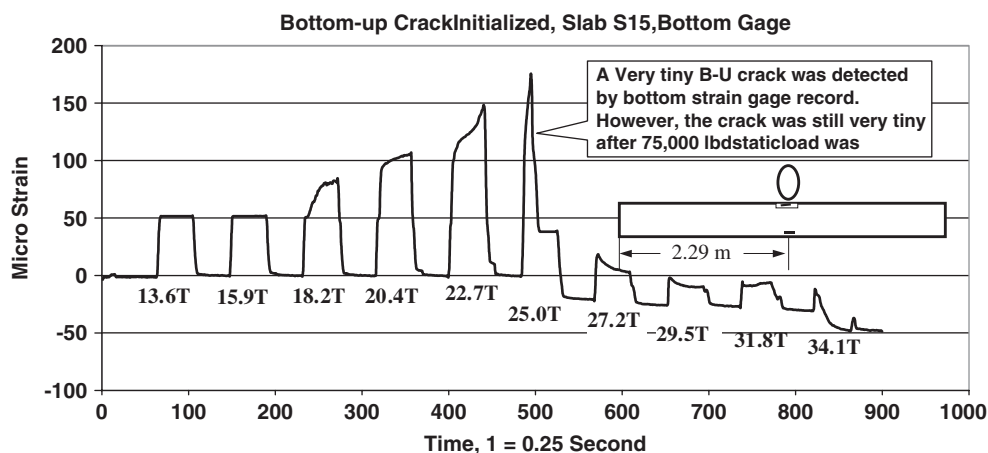
6 ESTIMATION OF PAVEMENT STRENGTH

Since strain histories were recorded covering the entire process of concrete cracking, we may estimate the pavement strength using two additional assumptions: (1) both, the top-down and bottom-up cracks share the same concrete pavement strength; (2) the residual stress in the slab due to the long term environmental effects are the same at slab top and bottom.

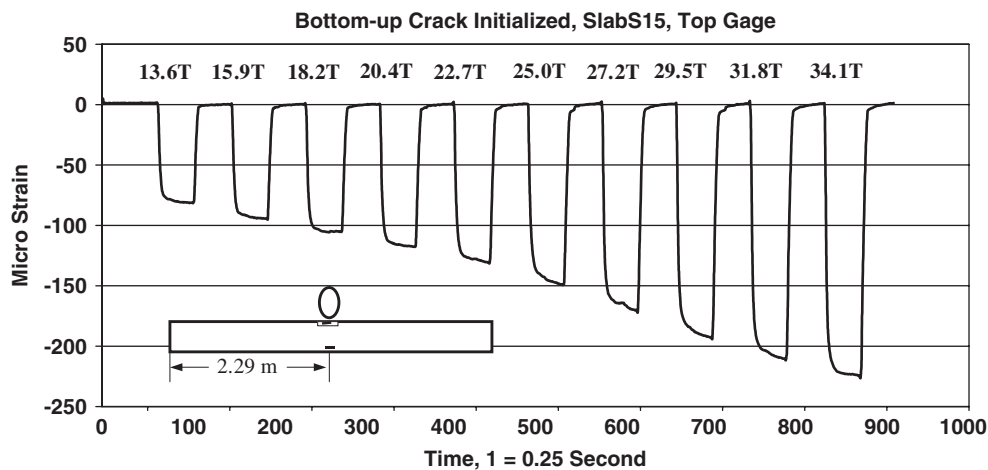
A few dozens of beams 15.3 cm (6 in) wide, 50.8 cm (20 in) long and 30.5 cm (12 in) thick were saw-cut from the full scale rigid test items. Then the beams were saw-cut in half (thickness) to satisfy ASTM C78 requirement for flexural strength testing. Some beams were tested such that the bottom of the slab remained as the bottom of the specimen. Others were tested using the middle of the slab as the bottom of the specimen. The final group was tested setting the top of the slab as the bottom of the specimen. Laboratory tests following ASTM C78 showed that the flexural strengths for the three groups had similar values. Therefore, assumption (1) can be used.

Residual stress is a very complicated topic since there is no direct testing procedure in existence that can measure residual stress in a concrete pavement due to a long term environmental effects before a load is applied. A simple and realistic way is to assume that the magnitudes of the maximum residual stress at the slab top and bottom are similar but with different signs – the residual stress at the slab top is in tension and at the slab bottom is in compression, after all the joints have been formed (Dong 2003).

The concrete modulus value E selected was 37,930 MPa (5,500,000 psi), This value was measured using the Portable Seismic Pavement Analyzer, PSPA (Nazarian et al. 1997). The micro strain



(a) Bottom Gage



(b) Top Gage

Figure 9. Strain histories under static step loads, slab S15, MRC.

detected by strain gage under the 22,700 kg (50,000 lbs) wheel load in Figure 6 was 68 micro strain at the gage located 3.8 cm (1.5 in) from the slab surface. Extrapolating to the slab surface: $[\sigma] = 3.44 \text{ MPa}$ (499 psi). The macro crack observed at wheel load 27,240 kg (60,000 lbs) recorded 84 micro strains. Extrapolating to the slab surface: $[\sigma] = 4.25 \text{ MPa}$ (616 psi). Based on the micro strain detected by strain gage under the wheel load 20,430 kg (45,000 lbs), 105 micro strain at the gage located 3.8 cm (1.5 in) from the slab bottom was recorded in both slabs S12 and S15 (Figs. 8 and 9a): $[\sigma] = 5.31 \text{ MPa}$ (770 psi).

Using assumption (2), the magnitudes of residual stress at the slab top and bottom are the same, the pavement strength defined as the total stress that cracks a pavement is ranged from $(5.31 + 3.44) \div 2 = 4.375 \text{ MPa}$ (635 psi) to $(5.31 + 4.25) \div 2 = 4.78 \text{ MPa}$ (693 psi). The 28-day laboratory flexural strength (ASTM C78) was 5.13 MPa (744 psi), and the average flexural strength

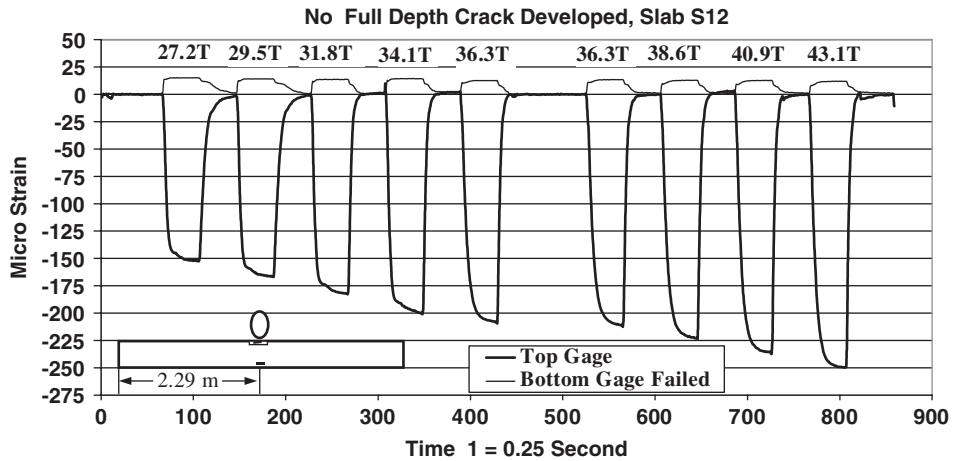


Figure 10. Strain records in slab S12 from load 27,240 kg (60,000 lbs) to 41,130 kg (95,000 lbs).

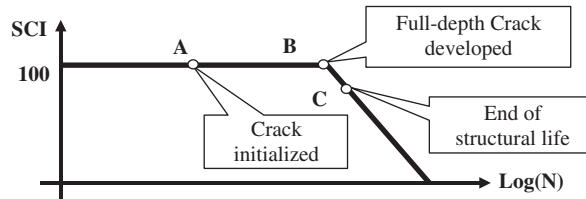


Figure 11. Failure model in FAA's current design procedure for PCC airport pavements.

obtained from the saw-cut beams in non-traffic area was 4.25 MPa (617 psi) (Ricalde et al., 2005). It can be concluded that the flexural strength for the cast beams over-estimated the pavement strength and the flexural strength for the saw-cut beams under-estimated the pavement strength, both test specimens followed the same ASTM C78 standard.

7 POTENTIAL APPLICATION FOR CALIBRATING DESIGN PROCEDURE

The new FAA design procedure for rigid pavements (FAARFIELD) selected the failure model proposed by Rollings in 1988. Structural Condition Index (SCI) is used to define the structural condition of a pavement in service. SCI = 100 is defined for a new constructed pavement until the first full-depth crack is developed as seen in Figure 11. SCI = 80 is defined as the end of pavement structural life. N in Figure 11 represents the number of the load coverage that produces the maximum calculated critical stress in the pavement. Point A indicates the pavement crack initialization. It is worth to know not only how many load repetitions lead to the end of the pavement structural life, but also how many load repetitions a new pavement require for the initialization of the first crack, and propagation of the crack initialization to the full depth.

The results presented in this paper are concentrated on the pavement strength under static incremental loads. Some pavement strengths under slow rolling loads have also been measured in MRC, MRG and MRS at the FAA's NAPTF. The detailed failure description and analysis may be found in Brill 2006 and Ricalde et al. 2005. When sufficient full scale test data are obtained, the final design failure model would be calibrated using the collected full scale data.

ACKNOWLEDGEMENT

This work was supported by the FAA Airport Technology Research and Development Branch, Manager, Dr. Satish K. Agrawal. Special thanks are given to Dr. Gordon F. Hayhoe for his technical leadership in test planning and organization, and to Mr. Chuck Teubert for his test management. The authors would also like to express their appreciation to Mr. Hector Diautolo and Mr. Murphy Flynn for their assistance in testing. The contents of the paper reflect the views of the authors, who are responsible for the facts and accuracy of the data presented within. The contents do not necessarily reflect the official views and policies of the FAA. The paper does not constitute a standard, specification, or regulation.

REFERENCES

- ASTM C39. Standard Test Method for Compressive Strength of Cylinder Concrete Specimens.
- ASTM C78. Standard Test Method for Flexural Strength of Concrete (Using Simple Beam with Third-Point Loading).
- ASTM C496. Standard Test Method for Splitting Tensile Strength of Cylindrical Concrete Specimens.
- Brill, D.R., 2006. Performance of Rigid airport Pavements Incorporating Full-Scale Test Data from the FAA National Airport Pavement Test Facility. *Proceedings of the 6th DUT-Worshop on Fundamental Modeling of Design and Performance of Concrete Pavements*.
- Dong, M., 2003. Analysis of Test Strip Data. *FAA Airport Pavement Working Group Meeting, 2003*.
- FAA 2001, AC 150-5370/10A. Standards For Specifying Construction Of Airports.
- Miner, M. A. and S. Monica, June 1945. Cumulative Damage in Fatigue. *Meeting of Aviation Division, Los Angeles, California, of the American Society of Mechanical Engineering*.
- Nazarian, S., D., M., Baker and K. Crain, 1997. Assessing Quality of Concrete with Wave Propagation Techniques, *ACI Material Journal*, page 296–305, July–August, 1997.
- Ricalde, L. and H. Daiutolo, 2005. New Rigid Pavement Construction and Testing at the FAA National Airport Pavement Test Facility (NAPTF). *Proceeding of 5th ICPT, Seoul, Korea*, page 759–768.
- Rollings, R.S., 1988. Design of Overlays for Rigid Airport Pavements. *FAA Report DOT/FAA/PM-87/19, April 1988*.

Fatigue cracking characteristics of accelerated testing pavements with modified binders

X. Qi

SES Group/Turner-Fairbank Highway Research Center, FHWA, McLean, Virginia, USA

N. Gibson & J. Youtcheff

Federal Highway Administration, McLean, Virginia, USA

ABSTRACT: A wide range of fatigue performance has been observed from the 12 full-scale lanes of FHWA's ALF pavements constructed with various modified binders. ALF fatigue experiment is an important part of a new transportation pooled fund study to validate and refine changes in the Superpave binder specification and mixture simple performance tests. This paper first presents the fatigue cracking data in both crack length and percent area crack obtained from these 12 lanes of ALF testing pavements. Then an evaluation of the fatigue cracking characteristics is followed, which include correlation between crack length and area cracked, surface cracking initiation and cracking rate, crack length variations within the ALF test site, cracking orientation, and cracking initiation location.

1 INTRODUCTION

In the summer of 2002, under a new transportation pooled fund study TPF-5(019), 12 full-scale lanes of pavements with various modified asphalts were constructed at the Federal Highway Administration's (FHWA) Pavement Testing Facility (PTF) in Virginia. The primary goal of the study is to use FHWA's two Accelerated Loading Facility (ALF) machines to validate and refine changes being proposed in the Superpave binder specification to properly grade modified binders. The study will also provide valuable data to test new features of the Mechanistic-Empirical Pavement Design Guide as well as other pavement technologies. During the construction, all 12 lanes were instrumented with strain gauges and differential survey plates. Pavement strain responses were measured after the construction (1) and during the course of ALF loading in the pavement fatigue tests (2). Full-scale accelerated loading testing started a month later after construction to induce both rutting and fatigue distresses. Rutting test results have been reported previously (3). Fatigue tests have been just completed for all 12 pavement lanes conducted at 19°C temperature and 74 kN load. A wide range of fatigue performance has been observed from these pavements. This paper presents these fatigue test results and an evaluation of the fatigue cracking data obtained to date.

2 ALF PAVEMENT TESTING EXPERIMENT

FHWA's PTF consists of two ALF machines (Figure 1) on about 3420 m² of grounds that provide space for 12 pavement test lanes. The ALF machines simulate traffic loading at controlled loading and pavement temperatures and are 29-m long frames with rails to direct rolling wheel loads. Each machine is capable of applying an average of 35,000 wheel passes per week from a half-axle load ranging from 33 to 84 kN. The current layout of the 12 as-built pavement lanes is presented in



Figure 1. The FHWA two ALF machines loading pavements at PTF site.

Lane 1	2	3	4	5	6	7	8	9	10	11	12
CR-AZ	PG 70-22	Air-Blown	SBS-LG	CR-TB	Ter-polymer	1.1 Fiber	PG 70-22	SBS 64-40	Air-Blown	SBS LG	Ter-polymer
Removed 100 mm Of Existing CAB							100 mm of New No. 21A CAB Under All 12 Lanes				
							Removed 50 mm of Existing CAB				
Existing VDOT No. 21A Crushed Aggregate Base (CAB) (25-mm Nominal Maximum Aggregate Size)											
Bottom of CAB to Pavement Surface is 660 mm											
Re-compacted AASHTO A-4 Subgrade Soil											

- PG 70-22 = Unmodified Asphalt Binder Control
- CR-AZ = Crumb Rubber Asphalt Binder, Arizona DOT Wet Process
- CR-TB = Crumb Rubber Asphalt Binder, Terminal Blend
- Terpolymer = Ethylene Terpolymer Modified Asphalt Binder
- SBS LG = Styrene-Butadiene-Styrene Modified Asphalt Binder with Linear Grafting
- SBS 64-40 = Styrene-Butadiene-Styrene Modified Asphalt Binder Graded to be a PG 64-40
- Air-Blown = Air-Blown Asphalt Binder
- Fiber = Unmodified PG 70-22 Asphalt Binder with 0.2 Percent Polyester Fiber by Mass of the Aggregate.

Figure 2. Layout and cross-section of the 12 as-built pavement lanes.

Figure 2. Each pavement lane is 4 m wide and 50 m long, and is divided into four test sites. All pavement lanes consist of a hot-mix asphalt (HMA) layer and a dense-graded, crushed aggregate base (CAB) course over a uniformly prepared, AASHTO A-4 subgrade soil (silty clay). The total thickness of the HMA and CAB layers is 660 mm. Lanes 1 through 7 were constructed with a 100-mm thick layer of HMA, while lanes 8 through 12 were constructed with 150 mm of HMA. The HMA is a dense graded mixture with a 12.5 mm maximum nominal aggregate size. The binders used in each lane are also listed in Figure 2. Note that the control binder (PG 70-22) and three modified binders (Air-Blown, SBS-LG, and Terpolymer) are used in both 100-mm and 150-mm thick lanes.

Each pavement lane has four test sites available allowing full-scale testing for two failure modes; rutting (sites 1 and 2) at 64 and 74°C without transverse wander, and fatigue cracking (sites 3 and 4) at 19 and 28°C with transverse wander. The performance data will be compared to the extensive

laboratory material characterization of the binders and mixtures to achieve the overall project objectives.

For fatigue test, cracks were manually traced onto clear plastic Mylar sheets as they formed at the surface of the pavements. Different color pens were used to correspond to the number of load repetitions. Two approaches were used to process the data. One was to measure the total crack length and the other was to measure the percentage of area cracked in the loaded area.

3 FATIGUE TESTING RESULTS

The ALF fatigue tests at 19°C and 74 kN have been completed for all 12 pavement lanes. Figure 3 graphically presents the fatigue cracking data at various ALF passes. The cumulative crack length and the percentage of the area cracked are shown in Figure 3 (a) for 100-mm HMA pavements and in Figure 3 (b) for 150-mm HMA pavements. As shown in the figure, the fatigue performance rankings are identical by both crack length and crack area. As expected, a wide range of fatigue performance can be observed from both figures. Based on these original measured cracking data, the fatigue performance rankings are quite evident: for the 100-mm HMA pavements, Lane 1 with CR-AZ binder, showed the best fatigue cracking resistance, i.e., no crack was found on the pavement surface after 300,000 ALF passes; followed by Lane 7 with fibers, Lane 4 with SBS-LG, Lane 6 with Terpolymer, Lane 5 with CR-TB, Lane 2 with control binder, and the worst fatigue performance for Lane 3 with air-blown binder. For lanes 8 to 12 with 150-mm HMA pavements, after more than 300,000 ALF load passes, Lane 10 (air blown) has significant cracks; Lanes 8 (control) and 9 (SBS 64-40) showed minor cracking; Lane 11 (SBS LG) and 12 (Terpolymer) have not shown any crack yet. It is recommended that more ALF loads be added to the 150-mm pavements in the next year winter period to at least obtain the cracking initiation for both Lane 11 and Lane 12. It should also be pointed out that some construction variations in HMA layer air void, thickness, and base layer support may have effect on the fatigue performance. For example, Lane 1 has a stiffer aggregate base layer indicated by the FWD testing conducted during construction, which may have a significantly influence on the pavement fatigue performance (4). The effect of the variations in the as-built properties is being quantified through the mechanistic pavement modeling predictions and will be included in the final data analysis report.

4 EVALUATION

4.1 *Correlation between crack length and area cracked*

Since both the crack length and the percentage of area cracked have been measured, the correlation between these two measurements can be established so that when the crack length is evaluated, its correspondent cracking level in percent area will be known. Figure 4 shows the plot of the two measurements from all cracking data obtained in this study. As seen from the figure, the coefficient of correlation is about 0.94 and the slope of regression line is close to 1, which indicates a good correlation between two measurements and the cumulative crack length in meter is approximately equal to cumulative percentage of area cracked. Therefore, only one of the measurements will be further analyzed in the following subsections.

4.2 *Surface cracking initiation and cracking rate*

In order to facilitate the comparison of HMA fatigue performance between ALF pavement testing and laboratory binder and mixture testing, a linear model was selected to fit the cumulative crack length at different ALF loading passes for the 100-mm HMA pavements. In this linear model, the intercept of the regression line represents the ALF loading pass at the surface cracking initiation and the reciprocal of the slope of the regression line represents the cracking rate. Table 1 summarizes

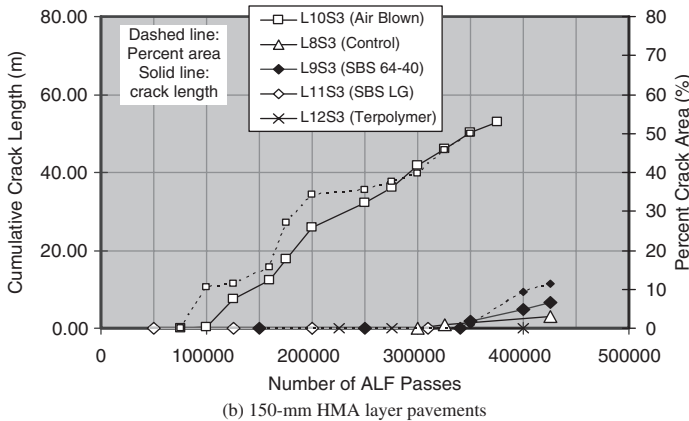
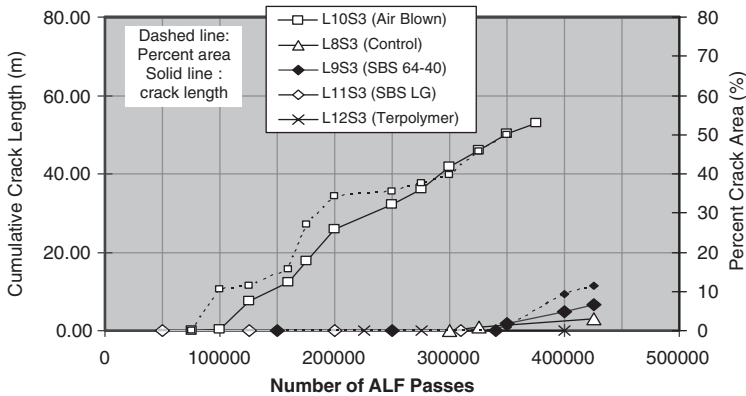
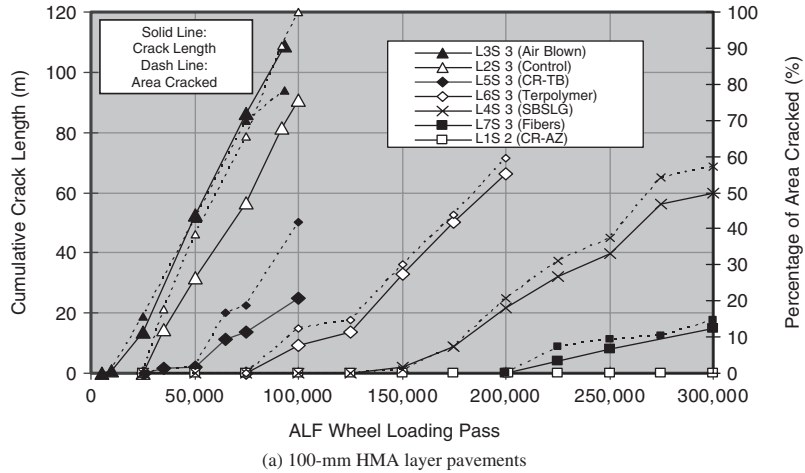


Figure 3. ALF pavement fatigue cracking data at 19°C and 74 kN.

the regression parameters. Rowe number 4 in the table gives very high coefficient of correlation (R^2) for each fatigue test, which indicates the linear model fits the cracking data very well.

There is a general trend: the higher the cracking initiation ALF pass (intercept) is, the lower the cracking rate is, except for lanes 6 and 5. Modified binder pavements have higher cracking initiation

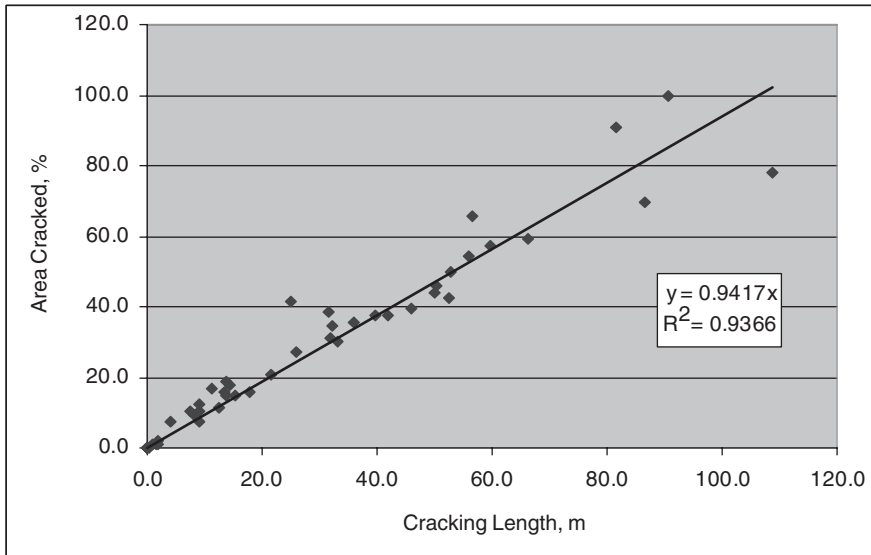


Figure 4. Correlation between crack length and percent area cracked.

Table 1. Linear regression parameters.

Lane/Site (Binder)	L7S3 (Fiber)	L4S3 (SBS LG)	L6S3 (Terpolymer)	L5S3 (CR-TB)	L2S3 (Control)	L3S3 (Air Blown)
Intercept	197414	148879	94306	43811	23709	9343
Slope	7636	2423	1617.3	2216.8	851.39	772.59
R ²	0.95	0.99	0.97	0.99	0.99	0.99
Cracking Rate (m/pass)	1.31E-04	4.13E-04	6.18E-04	4.51E-04	1.17E-03	1.29E-03

ALF pass and the lower cracking rate. Therefore, they have more fatigue cracking resistance than control and air-blown.

With these developed linear models, the predicted ALF load pass for various levels of fatigue crack length can be calculated as shown in Table 2. All these 6 lanes have the same fatigue performance rankings at all levels of crack length except for the 100 m crack length where Lanes 5 and 6 have changed their rankings. Therefore, the rankings are almost independent to the cracking levels. A comprehensive comparison of HMA fatigue performance between ALF and laboratory tests has been performed and reported in a separate paper (5).

An assessment of correlation between the ALF pass at various levels of crack length and ALF pass at surface crack initiation was also made and graphically shown in the Figure 5. The coefficient of correlation R² is shown in the figure with the legends of crack length. For 10 m to 25 m cracking level (10 to 25% area cracked), the R² value ranges 0.98 to 0.93 while for 50 m to 100 m cracking level (50 to 100% area cracked) the R² ranges 0.87 to 0.81. This indicates the surface crack initiations are well correlated to the cracking length at various levels. This finding will especially benefit the APT when the loading time is too constrained to generate a significant level of cracking, the cracking initiation may be used to reasonably rank the pavement fatigue performance. For example, Lanes 11 and 12 in the current ALF project are not cracked yet after more than 300,000 ALF passes and they are recommended to be loaded to the surface cracking initiation so that all 150-mm HMA pavements can be ranked.

Table 2. ALF load pass vs. crack length.

Crack Length (m)	L7S3 (Fiber)	L4S3 (SBS LG)	L6S3 (Terpolymer)	L5S3 (CR-TB)	L2S3 (Control)	L3S3 (Air Blown)
10	273774	173,109	110,479	65,979	32,223	17,069
20	350134	197,339	126,652	88,147	40,737	24,795
25	388314	209,454	134,739	99,231	44,994	28,658
50	579214	270,029	175,171	154,651	66,279	47,973
75	770114	330,604	215,604	210,071	87,563	67,288
100	961014	391,179	256,036	265,491	108,848	86,602

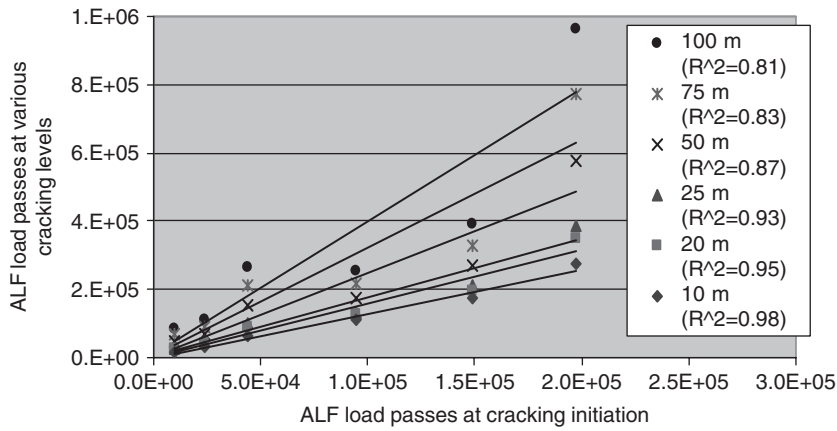


Figure 5. ALF pass at different cracking levels vs. cracking initiation.

4.3 Cracking variations within ALF test site

One of motivations to evaluate the fatigue cracking variation within the ALF test site is to see if it is feasible to have different treatments within the test site such as different surface materials or different surface coatings for fatigue testing experiment, which will certainly save significant loading time and have the same loading environmental conditions for different treatments. However, the variation level is a major concern: if the variation within the test site is too high it will shield the effect of the different treatments.

In order to assess the variation, the total recorded loading area of each test site was divided into 8 subsections and the cumulative crack length at different ALF passes were measured for each subsection. Figure 6 shows these cracking data for 6 lanes of 100-mm HMA pavements. In the figure, the legends in each plot show the correspondent ALF pass. The #1 subsection is the closest to the ALF load landing area while the #8 subsection is the closest to the ALF load lifting area. It is obvious that significant variations exist among the subsections at all levels of ALF load passes for all 6 pavement lanes. It can also be observed that those subsections close to both ALF landing and lifting areas (examples, #1 and #8 subsections) always have less cracks except for lane 5 having the #1 subsection most cracked. The possible sources of this systematic cracking variation can include the construction variations in HMA layer thickness, air void, and base layer support; the ALF dynamic loading characteristics at landing and lifting may also be a factor of influence. A new hydraulic load lifting system has been proposed to both FHWA ALF machines which may reduce the dynamic loading significantly and therefore may reduce the fatigue cracking variation within the test site.

Statistics in terms of mean, standard deviation, and coefficient of variation (CV) were calculated for each line of data points from Figure 6 and they are presented in Figure 7. As shown by the legends

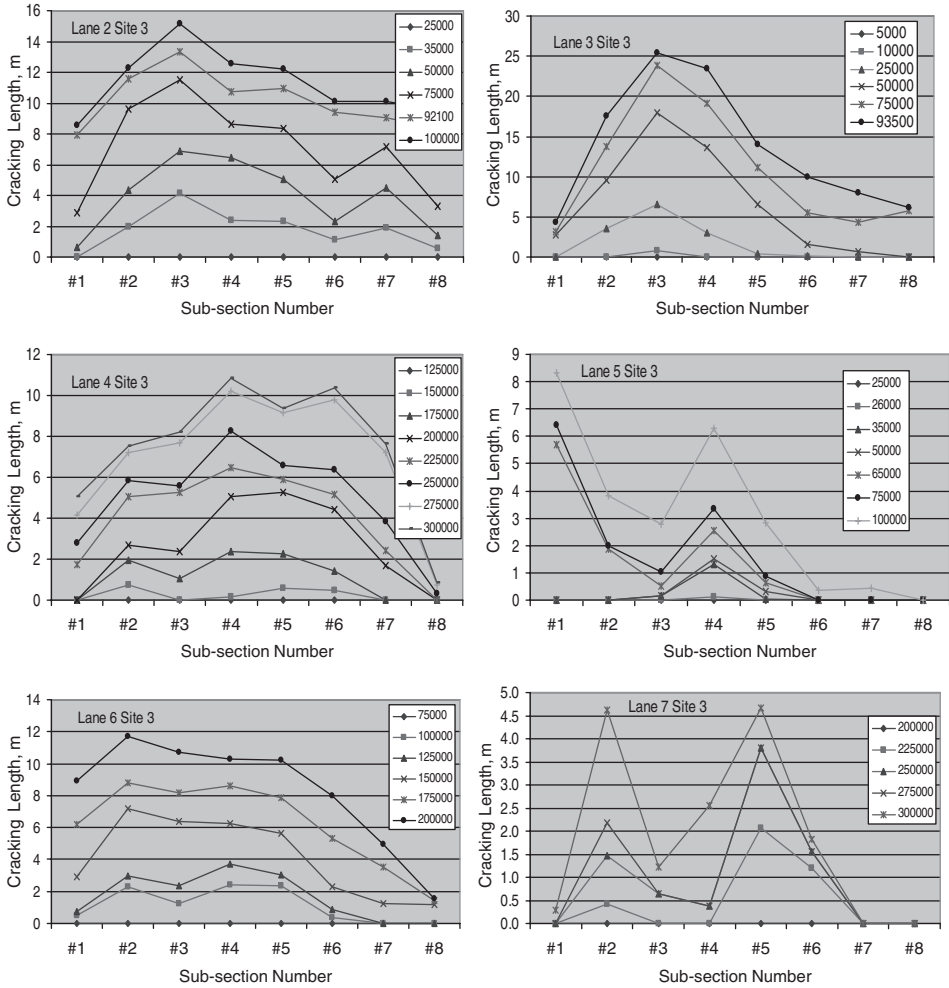


Figure 6. Cracking length at each sub-sections for different ALF load passes.

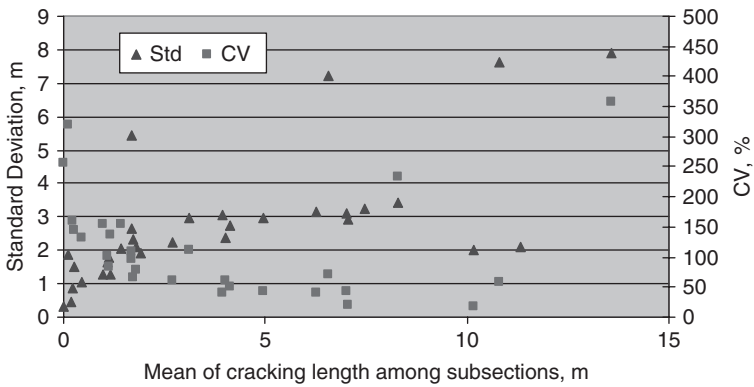


Figure 7. Standard deviation/CV vs. mean of cracking length among the subsections.

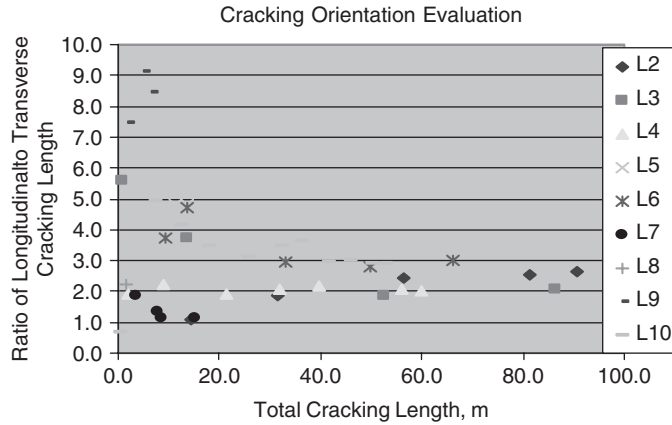


Figure 8. Cracking orientation evaluation.

in the figure, the triangle represents standard deviation and the square represents CV. Although these two statistics showed different trends: the standard deviation increasing with increase in mean while the CV decreasing with mean, they both showed the very high variation in crack length among subsections. With such a high variation, it is not recommended to use different treatments within the ALF test site for the future fatigue experiment unless a significant improvement has been made in reduction of both ALF dynamic loading and pavement construction variation.

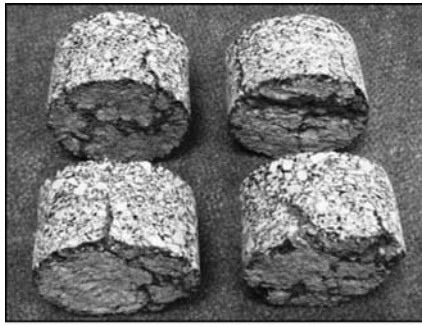
4.4 Cracking orientation

In this study, as the first step to evaluate the cracking orientation, the crack length was measured in such a way: if the angle between a crack and the longitudinal direction is less than 45° , the crack then is classified as longitudinal oriented; if the angle is greater than 45° , the crack classified as transverse. The sum of the both types of cracks is the total crack length. Figure 8 shows the ratio of longitudinal to transverse crack length vs. the total crack length. As seen from the figure, most of measurements have the value of ratio above 1 (mean = 3.2 with range of 0.7 to 9.1), which means cracks are more longitudinal oriented. At lower side of total crack length, the ratio tends to be higher, which means at the early cracking stage the longitudinal cracks are dominated. The next step to further evaluate the crack orientation is to digitize all the cracking maps then more types of orientation crack can be defined and calculated.

4.5 Cracking initiation location

In a previous ALF project post mortem study (6), trenching and coring were conduct to investigate the cracking initiation location within the HMA layer after the completion of pavement fatigue tests. It was found that cracks initiated from the bottom of pavement inside the ALF wheel path while cracks initiated from the top of pavements just outside the wheel path. For the current ALF project, cores have been cut inside the wheel path from most of fatigue test lanes after the end of ALF loading. Again, the cracks were found to initiate from the bottom of pavements. However, the cores cut from Lane 1 and Lane 8 showed some special characteristics (see Figure 9).

As shown in Figure 2, Lane 1 HMA layer was constructed with a 50-mm Arizona ARM in the top lift and a 50-mm control mix in the bottom lift. No crack was found on the pavement surface at the end of ALF loading. In order to investigate any cracks inside the pavement layer, 4 cores were cut from the loaded area (Figure 9 (a)). All cores exhibited bottom-up cracks and the cracks are limited in the bottom lift. This cracking pattern may indicate the higher fatigue cracking resistance in the top lift Arizona ARM.



(a) Cores from Lane 1 Site 2



(b) Cores from Lane 8 Site 2

Figure 9. Photos of pavement cores cut at the end of ALF loading.

Figure 9 (b) shows the cores cut from Lane 8 at the end of ALF loading. The top 4 cores were cut inside wheel path while bottom 3 cores from outside wheel path. Clearly, delaminating has occurred at the interface of two lifts. It should be loading associated since no delamination took place in the cores outside wheel path. A investigation is under way to find out the possible causes of this type of distress during the fatigue testing.

5 SUMMARY AND CONCLUSIONS

- A wide range of fatigue performance has been observed from the 12 lanes of FHWA's ALF pavements constructed with various modified binders. For lanes 1 to 7 with 100-mm HMA pavements, the pavements modified with polymers and AR binders exhibited better fatigue performance than those with air blown and control binders. For lanes 8 to 12 with 150-mm HMA pavements, after more than 300,000 ALF load passes, Lane 10 (air blown) has significant cracks; Lanes 8 (control) and 9 (SBS 64-40) showed minor cracking; Lane 11 (SBS LG) and 12 (Terpolymer) have not shown any crack yet.
- Both crack length and percent area cracked were used to measure the cracking level. The two measurements were found well correlated and the cumulative crack length in meter is approximately equal to the cumulative percent area cracked. The fatigue performance rankings are identical by both measurements.
- A linear model was found to well fit the crack length at different ALF passes for the 100-mm HMA pavements. The intercept of the linear model represents the ALF pass at the surface crack initiation while the reciprocal of the slope of the model represents the cracking rate. A general trend shows the higher the ALF pass at surface cracking initiation, the lower the cracking rate is. The cracking initiation also showed a good correlation with various levels of crack length, which indicates the cracking initiation may be used to reasonably rank the ALF pavement fatigue performance.
- High variation in crack length within the ALF test site have been observed from the plots of cumulative crack length in each of 8 subsections for all 6 lanes of 100-mm HMA pavements. The subsections close to both ALF load landing and lifting areas have always less cracks. The ALF dynamic loading effect and construction variations may be responsible for this. Both standard variation and CV values calculated for 8 subsections are very high, which suggests that it is not feasible to have different treatments within the ALF test site for future fatigue experiments.
- The ratio of longitudinal to transverse oriented crack length showed the cracks measured from this project are more longitudinal oriented, and at the early cracking stage the longitudinal cracks become dominated. Digitizing the cracking maps and further analysis on cracking orientation are planned.

- Pavement cores have been cut inside the ALF wheel path to investigate the cracking initiation location. The cracks were found to initiate from the bottom of pavements, which is consistent with the findings from a previous ALF project post mortem study. However, Lanes 1 and 8 showed some special characteristics: 4 cores from Lane 1 showed cracks are limited in the bottom lift (AR in top lift and control in bottom lift); and 3 cores from Lane 8 showed delamination at the interface of two lifts.

ACKNOWLEDGEMENT

The work presented here was conducted as part of national pooled fund study TPF-5(019), which is partially funded by 15 State highway agencies (CT, FL, IL, IN, KS, MD, MI, MS, MT, NE, NV, NJ, NM, NY, and TX) with materials provided by the asphalt industry; funds are also provided by the FHWA, and the study is staffed by FHWA and its contractors

REFERENCES

1. Qi, X., Mitchell, T. Stuart, K., Youtcheff, J., Harman, T., Petros, K., Al-Khateeb, G. "Strain Responses in ALF Modified-Binder Pavement Study" Proceedings of 2nd IAPT, Minneapolis, September 2004.
2. Qi, X., Gibson, G., Youtcheff, J. "Strain response and fatigue performance from the FHWA ALF modified binder pavements" Proceedings of the International Conference on Advanced Characterization of Pavement and Soil Engineering Materials, 20–22 June, 2007 Athens, Greece.
3. Mitchell, T. Stuart, K., Qi, X., Al-Khateeb, G., Youtcheff, J., Harman, T. "ALF Testing for Development of Improved Superpave Binder Specification", Proceedings of 2nd IAPT, Minneapolis, September 2004.
4. Qi, X., Mitchell, T., Harman, T. "Evaluation of Aggregate Base Course for the FHWA's New Pooled. Fund Accelerated Testing Pavements." Proceedings of the 5th International Conference of Transportation Professionals, Xian, China, 2005
5. Qi, X., Shenoy, A., Kutay, E., Gibson, G., Youtcheff, J., Harman, T. "Update on FHWA ALF Accelerated Pavement Tests of Modified Binders Experiment", paper submitted to 3rd International Conference on APT held in Madrid, 2008.
6. Sherwood, J., Qi, X., Romero, Stuart, Thomas, Shashidar and Mogawer "Full-Scale Pavement Fatigue Testing from FHWA Superpave Validation Study" Proceedings of 1st IAPT, Reno, September 1999.

An overview of an accelerated pavement testing experiment to assess the use of modified binders to limit reflective cracking in thin asphalt concrete overlays

D. Jones & J.T. Harvey

University of California Pavement Research Center, Davis, California, USA

T. Bressette

California Department of Transportation, Sacramento, California, USA

ABSTRACT: A comprehensive laboratory and accelerated pavement testing study has recently been completed on the use of modified binders to limit reflective cracking in thin asphalt concrete overlays at the University of California Pavement Research Center. The experiment entailed the construction of a 90 m test road consisting of compacted clay subgrade, a 410 mm aggregate base and 90 mm dense graded asphalt concrete surface. A Heavy Vehicle Simulator (HVS) was used to induce fatigue cracking on six, eight-by-one metre sections. Trafficking on each section was stopped when crack density exceeded 2.5 m/m². Six different overlays, including a dense graded asphalt concrete control section, and five different rubber modified binder sections, were then placed on the road. The original six section locations were precisely mapped onto the overlays and the HVS used to assess reflective cracking in each. Pavement temperatures were controlled using a temperature chamber. Separate rutting studies were also carried out on the overlays on sections adjacent to the fatigue sections. In conjunction with the HVS testing, laboratory shear and fatigue testing was carried out on field-mixed/field-compacted, field-mixed/laboratory-compacted, and laboratory-mixed/laboratory-compacted specimens. The findings have shown a good relationship between HVS and laboratory results, with the modified binder overlays limiting reflective cracking significantly better than the conventional mix. This paper provides an overview of the experiment and summary of the results. Specific discussions on the various components of the study will be published elsewhere.

1 INTRODUCTION

California, like most other states in the USA, has a mature road network that requires ongoing maintenance and rehabilitation. On that part of the network surfaced with asphalt concrete, fatigue cracking is a common distress, which is typically maintained by placing a thin overlay of dense-graded asphalt concrete (DGAC) or gap-graded rubberized asphalt concrete (RAC-G). Milling of the upper 50 mm to 100 mm of the old wearing course may be carried out prior to overlaying to maintain the existing surface elevation. The life of these overlays depends in large part on the extent of fatigue cracking in the original surface, and the support provided by the underlying layers. With a view to extending the life of overlays, a study comprising accelerated pavement testing and associated laboratory testing was initiated by the California Department of Transportation (Caltrans) and the University of California Pavement Research Center (UCPRC) to evaluate the reflection cracking performance of asphalt mixes used in the state (Caltrans, 2005).

The main objective of this investigation was to compare the performance of three maintenance overlays using modified binder (MB) mixes against two control maintenance overlay mixes (DGAC

and RAC-G), essentially asking the question “*Will gap-graded modified binder (MB-G) mixes provide performance equal to gap-graded rubberized asphalt concrete (RAC-G) mixes in half-thickness applications?*” (UCPRC 2003). MB binders are asphalt binders modified with polymers and recycled tire rubber and blended at the refinery (terminal blend) meeting a Caltrans performance related specification. This study, termed the MB-Road study, is part of a larger study to develop improved rehabilitation designs for reflection cracking for California. The objectives of this study will have been met after completion of four tasks:

1. Develop improved mechanistic models of reflection cracking in California
2. Calibrate and verify these models using laboratory and HVS testing
3. Evaluate the most effective strategies for reflection cracking
4. Provide recommendations for reflection cracking strategies

This paper describes part of the work undertaken to complete Task 2 and includes a summary of the project experimental design, accelerated pavement testing, laboratory testing, and preliminary findings. Results of the other tasks are described in other reports and papers.

2 EXPERIMENTAL DESIGN

2.1 Test summary

The MB-Road study was divided into three phases (Jones, et al., 2007a):

- Phase 1 covered construction of a uniform test pavement, demarcating six uniform test sections, trafficking these sections with a Heavy Vehicle Simulator (HVS) to induce fatigue cracking on the asphalt concrete layer, then overlaying the test track with the following six overlays:
 - Half-thickness (45 mm) MB4 gap-graded overlay;
 - Full-thickness (90 mm) MB4 gap-graded overlay;
 - Half-thickness (45 mm) MB4 gap-graded overlay with minimum 15 percent recycled tire rubber, termed MB15-G in this paper;
 - Half-thickness (45 mm) MAC15TR gap-graded overlay, termed MAC15-G in this paper;
 - Half-thickness (45 mm) rubberized asphalt concrete gap-graded overlay (RAC-G), included as a control for performance comparison purposes; and
 - Full-thickness (90 mm) dense-graded asphalt concrete (DGAC) overlay, included as a control for performance comparison purposes. The binder used was AR-4000, approximately equivalent to PG64-16.
- Phase 2 involved a total of 12 HVS tests, including six reflection cracking tests at moderate temperature on sections positioned precisely over the cracked original six tests on the underlying DGAC, and six rutting tests at high temperature on sections adjacent to the fatigue sections.
- Phase 3, run concurrently with the HVS tests, entailed a comprehensive laboratory investigation to relate laboratory rutting and fatigue performance to performance under the HVS. Experiments were conducted on samples removed from the road, on field-mix/laboratory-compacted (FMLC) samples, and on laboratory-mixed/laboratory-compacted (LMLC) samples.

2.2 Section layout

The MB-Road experiment is shown in Figure 1.

2.3 Instrumentation

Instrumentation of the test sections consisted of the following:

- Multi-Depth Deflectometers (MDD): used to measure elastic vertical deflections and permanent vertical deformations at various levels in the pavement structure, relative to a reference depth located in the subgrade.

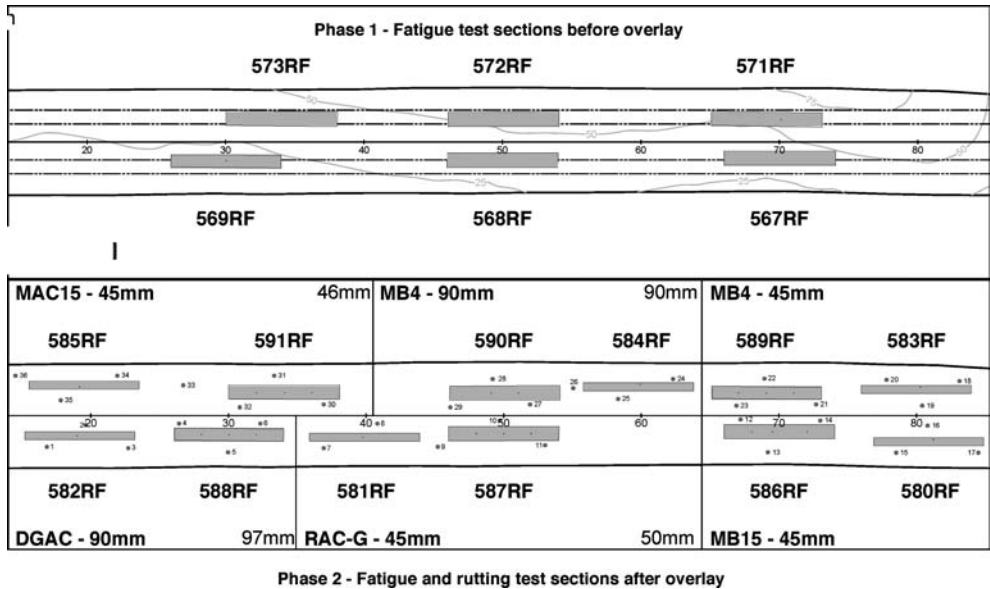


Figure 1. MB-Road layout.

- Road Surface Deflectometer (RSD): used to measure elastic vertical deflections at the surface of the pavement.
- Laser Profilometer and Straight Edge: used to measure the transverse profile of the pavement surface to determine surface rutting.
- Thermocouples used to measure temperatures at various depths in the asphalt bound materials.
- Time Domain Reflectometer: used to monitor the changes in water content in the unbound layers just outside the trafficked area during testing of the section.

The following testing was also undertaken:

- Digital Crack Imaging: used to measure surface cracking.
- Falling Weight Deflectometer (FWD): used to measure elastic vertical deflections at the surface of the pavement before and after HVS testing and on areas not trafficked to monitor asphalt aging and seasonal changes in unbound layer moduli.
- Dynamic Cone Penetrometer (DCP): used to measure the relative shear resistance of unbound layers.
- Trenching: To determine final rut depths in each layer and assess final condition of the pavement layers after completion of HVS trafficking.

3 PHASE 1: CONSTRUCTION, INITIAL HVS TRAFFICKING, AND OVERLAYS

The test road was designed following standard Caltrans procedures and incorporated a 410 mm Class 2 aggregate base (recycled construction waste) on a clay subgrade with a 90 mm dense-graded asphalt concrete (DGAC) surface. Design thickness was based on a subgrade R-value of 5 and a California Traffic Index of 7 (~131,000 equivalent standard axle loads, or ESALs). The road was constructed in 2001 by a commercial contractor (selected based on low-bid) using conventional equipment.

Six sections on this structure were trafficked with the HVS between February 2002 and April 2003 to induce fatigue cracking. A total of approximately 3.3 million load repetitions – equating to about 17.7 million equivalent standard axles (ESALs) using the Caltrans 4.2 exponent – were

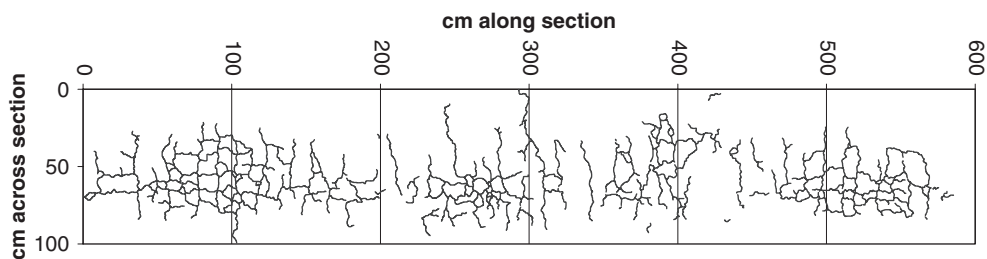


Figure 2. Fatigue cracking on one section after Phase 1 HVS testing.

applied to the six sections to induce a minimum of 2.5 m^2 fatigue cracking on each section (Jones, et al., 2007a). An example of the fatigue cracking measured on one of the sections is shown in Figure 2. In June 2003, the road was overlaid with six different treatments. The thickness for the control DGAC overlay was determined according to Caltrans Test Method 356. The other overlay thicknesses were either the same or half of the DGAC overlay thickness.

4 PHASE 2: HVS RUTTING AND FATIGUE TESTING

The second phase of HVS tests consisted of two sub-phases. In the first, a rutting study on sections adjacent to the fatigue sections was carried out to assess the susceptibility of the mixes to early rutting at high pavement temperatures (50°C at 50 mm pavement depth). In the second, a fatigue study was carried out to assess the effectiveness of the overlays in limiting reflective cracking at moderate temperatures (20°C then 15°C at 50 mm pavement depth). The fatigue sections were precisely positioned on top of the sections already trafficked on the underlying pavement during Phase 1 (see Figure 1).

4.1 Rutting study

The overlay rutting sections were trafficked with the HVS between September and December 2003. During this period a total of about 80,000 60 kN channelized, unidirectional load repetitions with a dual tire (720 kPa pressure) were applied across the sections, equating to approximately 455,000 ESALs. A temperature chamber was used to maintain the pavement temperature at $50^\circ\text{C} \pm 4^\circ\text{C}$ at 50 mm depth. Measurements taken at regular intervals throughout the test included air and pavement temperatures, in-depth elastic deflection, and surface and in-depth permanent deformation. An average maximum rut of 12.5 mm was set as the failure criterion. Results of the test are summarized in Table 1. Rankings are from best to worst. It should be noted that most of the rutting was in the underlying DGAC layer and not in the overlay (Steven, et al., 2007).

4.2 Fatigue study

HVS trafficking of the overlay fatigue sections took place between January 2004 and June 2007. During this period a total of approximately 12.5 million load repetitions at loads varying between 60 kN and 100 kN, depending on the stage in the test plan, were applied across the sections, which equates to about 385 million ESALs. A temperature chamber was used to maintain the pavement temperature on each section at $20^\circ\text{C} \pm 4^\circ\text{C}$ for the first one million repetitions, then at $15^\circ\text{C} \pm 4^\circ\text{C}$ for the remainder of the test. A dual tire (720 kPa pressure) in a bidirectional loading pattern with lateral wander was used for all experiments. Measurements taken at regular intervals throughout the test included air and pavement temperatures, surface and in-depth elastic deflection, surface and in-depth permanent deformation, and cracking. A crack density of 2.5 m^2 was set as the failure criteria. FWD measurements were taken before and after HVS testing. Figure 3 shows the outcome of one of the fatigue experiments. Results of the test are summarized in Table 2. Rankings are from

Table 1. Summary of HVS rutting study results.

Rank	Section	Repetitions to 12.5 mm rut
1	90 mm AR-4000 DGAC	8,266
2	45 mm MB4-G	3,043
3	45 mm RAC-G	2,324
4	90 mm MB4-G	1,522
5	45 mm MB15-G	914
6	45 mm MAC15-G	726

Table 2. Summary of HVS fatigue study results.

Rank	Section	ESALs to 2.5 m/m ² reflection cracking
1	45 mm MAC15-G	No cracking after 91 million
2	45 mm MB15-G	No cracking after 88 million
3	45 mm MB4-G	No cracking after 66 million
4	90 mm MB4-G	No cracking after 37 million
5	45 mm RAC-G	60 million
6	90 mm DGAC	16 million



Figure 3. Typical fatigue cracking on HVS test section (RAC-G section).

best to worst. It should be noted that no fatigue cracking was recorded on the MB4-G, MB15-G and the MAC15-G sections. Ranking of these mixes is therefore based on the number of repetitions actually applied and not on cracking performance (Jones, et al., 2007a). Figure 4 shows the cracking patterns of the underlying DGAC and RAC-G overlay.

4.3 Forensic investigation

A forensic investigation was carried out after HVS testing. This included excavation and assessment of 18 test pits, coring, density and moisture determination, Dynamic Cone Penetrometer (DCP) measurements, and microscope studies of material sampled from the pits. Observations revealed that most of the permanent deformation measured in the rutting study occurred in the underlying DGAC (Figure 5). Studies of the asphalt layers, including fractured cores, showed that cracking in

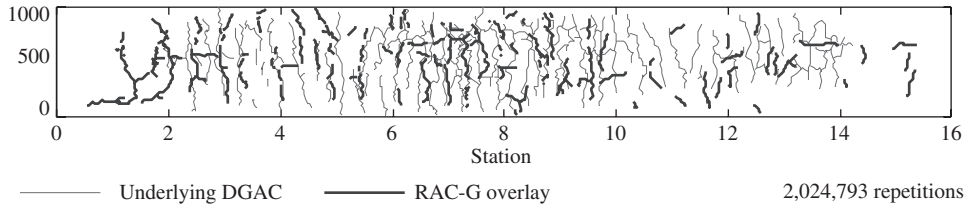


Figure 4. Phase 1 and Phase 2 cracking after HVS testing (RAC-G section).

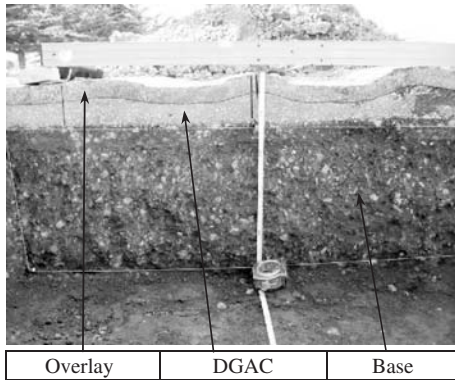


Figure 5. Rutting section forensic.

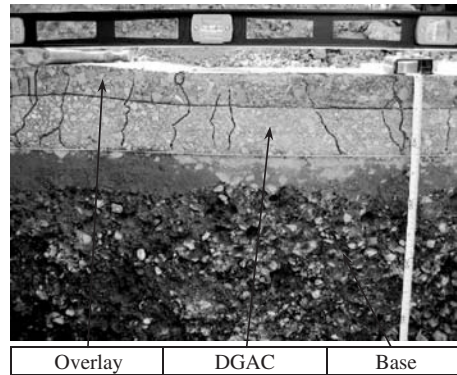


Figure 6. Fatigue section forensic (cracks are highlighted with marker pen).

the DGAC and RAC-G overlays had mostly reflected from the underlying DGAC layer (Figure 6). There was no observed cracking on the surface of the MB sections. There was some variation in layer thicknesses over the length of the experiment. DCP measurements and scanning electron microscope studies indicated that the stiffness of the recycled aggregate base varied somewhat between sections due to some re-cementation of the recycled construction waste that occurred after construction. The strongest part of the base was typically between 100 mm and 250 mm below the asphalt concrete (Jones, et al., 2007b).

5 PHASE 3: LABORATORY STUDY

Laboratory fatigue and shear studies were conducted in parallel with Phase 2 HVS testing.

5.1 Laboratory fatigue

In the cracking study, flexural frequency sweeps (stiffness at different temperatures and period of loading related to traffic speed and climate) and flexural beam tests were carried out to assess cracking resistance of the overlay mixes. The experiment design was formulated to quantify the effects of mix temperatures, air-void content, aging, mixing and compaction conditions, aggregate gradation, and time of loading (load frequency). To test a full factorial considering all the variables, a total of 1,440 tests would have been required. Because of time and fund constraints, a partial factorial experiment was completed with 172 tests. Rolling wheel compaction was used to prepare slab specimens of the various mixes, from which beams were cut for flexural fatigue testing and stiffness (frequency sweep) determinations following the AASHTO 321 procedure (four point bending). Fatigue tests were all conducted at 10 Hz and temperatures of 10°C, 20°C and 30°C. Stiffness measurements were conducted over the range of 15 Hz to 0.01 Hz and at temperatures

of 10°C, 20°C, and 30°C to define the effect of time-of-loading and temperature on this mix characteristic. Results are described below (Tsai, et al., 2006).

– Summary of Binder Tests

- Based on Bending Beam Rheometer (BBR) test results conducted by FHWA, the ranking of propensity to low temperature thermal cracking is listed below, from best to worst. The RAC binder was not tested.
 1. MB4 → 2. MB15 → 3. MAC15 → 4. AR4000.
- The order of thermal cracking potential was closely matched with the order of initial stiffness in the fatigue beam tests and flexural frequency sweep results; hence a mix with a higher initial stiffness might have a higher thermal cracking potential.
- The Dynamic Shear Rheometer (DSR) test results indicated that:
 - (a) According to the Superpave specification, the ranking of fatigue resistance capacity, from best to worst, is in the order listed below, which is the same ranking obtained for initial stiffness during laboratory mix fatigue tests.
 1. MB4 → 2. MB15 → 3. MAC15 → 4. AR4000
 - (b) MB4 and MB15 binders have better rutting resistance capacities than AR4000 binder.

– Construction and Environment Effects

- The binder type had an overall effect on all the response variables including initial phase angle, initial stiffness, and fatigue life. As expected, the temperature effect on all three response variables was immediately apparent. The other effects assessed at 20°C (for comparison with HVS testing) revealed that:
 - (a) Air-void content had a significant effect for some parts of the experiment, such as the FMLC mixes at 20°C, but the effect was not significant for many of the mixes and test conditions for all of the response variables (stiffness, fatigue life and shear resistance).
 - (b) The effect of long-term oven aging at 85°C for 6 days (SHRP I procedure) was only significant for initial phase angle and stiffness but not for fatigue life.

– Ranking of Initial Stiffness and Fatigue Performance

- The ranking of predicted initial stiffness (most to least stiff) and fatigue life (longest to shortest) under various specimen preparation and testing conditions, and specifically for the controlled strain mode of loading used in this experiment, was normally in the order listed below. For initial stiffness, no apparent differences exist between MB15-G and MB4-G mixes, while for fatigue life, no apparent differences exist between MAC15-G and MB15-G mixes. As expected, the two orders are reverse mirror images of each other.

Initial stiffness	Fatigue life
1 AR-4000-D	1 MB4-G
2 RAC-G	2 MAC15-G
3 MAC15-G	3 MB15-G
4 MB15-G	4 RAC-G
5 MB4-G	5 AR-4000-D

- Fatigue test results indicate that initial stiffness and fatigue life are moderately negative-correlated ($\rho = -0.604$), confirming a general observation that lower stiffnesses equate to higher fatigue life at a given tensile strain under controlled-strain testing when ranking fatigue life performance against initial stiffness or vice versa. When using this observation, consideration must also be given to rutting, as mixes with low stiffness are generally susceptible to this distress. *It must be emphasized that cracking performance can only be assessed from simulation considering overlay thickness, stiffness, laboratory fatigue life, climate and traffic, and not directly from these laboratory fatigue life test rankings.*
- Preliminary analysis of stiffness versus strain repetition curves using three-stage Weibull analysis indicated differences in crack initiation and propagation. The AR4000-D mix had

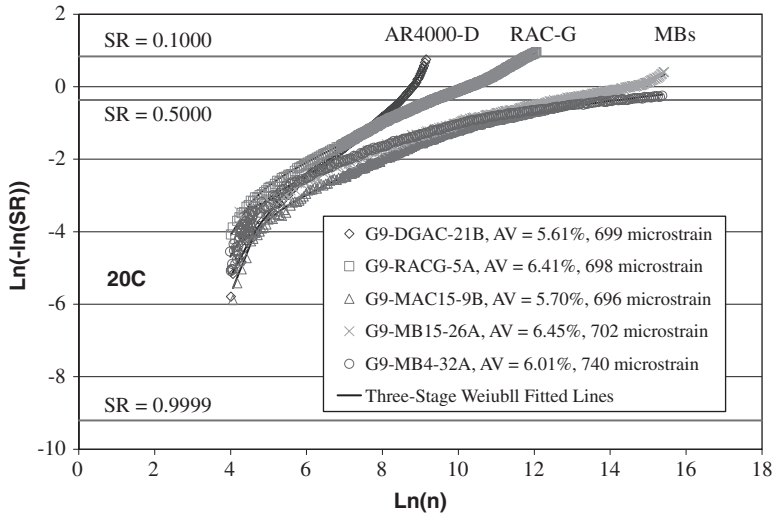


Figure 7. Typical Weibull curves for Reflection Cracking Study mixes.

different behavior from that of the RAC-G mix, while the RAC-G mix performed differently than the MB4-G, MB15-G, and MAC15-G mixes. The results indicate that damage may slow during the propagation phase of the latter four mixes, while it accelerates for the AR4000-D mix (Figure 7).

– Dense-Graded versus Gap-Graded Mixes

- The optimum binder contents used in the mix designs for the MAC15, MB15, and MB4 dense-graded mixes (6.0, 6.0, and 6.3 percent respectively) were lower than the optimum binder contents used in the mix designs of the gap-graded mixes (7.4, 7.1, and 7.2 percent respectively).
- Limited fatigue testing of modified binders in dense-graded mixes led to the following observations:
 - (a) The initial stiffnesses of the dense-graded mixes were generally greater than those of the corresponding gap-graded mixes but less than those of the AR4000-D and RAC-G mixes. The beam fatigue life at a given tensile strain of the dense-graded mixes was generally less than those of the corresponding gap-graded mixes, but greater than those of the AR4000-D and RAC-G mixes.
 - (b) The mix ranking of the E^* master curves, from most to least stiff, for laboratory mixed, laboratory compacted specimens at 6 percent air-voids was:
 1. AR4000-D → 2. MAC15-D → 3. RAC-G → 4. MB15-D → 5. MB4-D → 6. MAC15-G → 7. MB15-G → 8. MB4-G
 - (c) The mix ranking (longest to shortest) for the same conditions for beam fatigue life at 400 microstrain shows exactly the reverse trend from the above except that MAC15-D and RAC-G change places:
 1. MAC15-G → 2. MB4-G → 3. MB15-G → 4. MB4-D → 5. MB15-D → 6. MAC15-D → 7. RAC-G → 8. AR4000-D

– E^* Master Curves of Mixes

- E^* master curves from flexural frequency sweep tests showed mix stiffnesses for a wide range of temperature and time of loading conditions. Initial stiffnesses determined from beam fatigue tests were only for 10 Hz and the temperature at which the fatigue test was performed. Nevertheless, the mix ranking of E^* master curves under various combinations of material properties and testing conditions was generally in the order listed below (most to least stiff), and was

comparable to the overall general ranking of beam fatigue performance in the controlled-strain testing (longest to shortest life). The MB4 and MB15 mixes showed no significant difference in E^* master curves.

Initial stiffness	Fatigue life
1 AR-4000-D	1 MB4G
2 RAC-G	2 MB15-G
3 MAC15-G	3 MAC15-G
4 MB15-G	4 RAC-G
5 MB4-G	5 AR-4000-D

- The ranking of E^* master curves (most to least stiff) for dense-graded mixes considering the effect of gradation is in the order below, with no significant difference between the MB4 and MB15 mixes:

1. MAC15-D → 2. MB4-D → 3. MB15-D

5.2 Laboratory shear

In the shear study, stiffnesses and permanent deformation at high temperatures were used to evaluate rutting resistance. Tests were carried out on field-mixed/field-compacted (FMFC), field-mixed/laboratory-compacted (FMLC – rolling wheel compaction), and laboratory-mixed/laboratory compacted (LMLC – rolling wheel compaction) specimens.

Laboratory results were statistically analyzed to identify the significant variables affecting stiffness, fatigue and permanent shear deformation performance (Guada et al., 2006). The effects of aggregate gradation, long-term aging, air-void content, mix temperature, and strain/stress level were the focus of the study, with both field- and laboratory-prepared specimens compared. Regression models were developed to portray the effects of the significant variables on the performance-related properties. Test criteria for the shear study included Cycles to 5 Percent Permanent Shear Strain, Permanent Shear Strain at 5,000 Cycles, and Resilient Shear Modulus (G^*). Detailed results are not provided in this paper. The ranking of performance, from best to worst, based on an average of the results from all tests results (Permanent Shear Strain at 5,000 cycles and Cycles to 5 percent Permanent Shear Strain) is as follows:

1. AR4000-D → 2. MAC15-G → 3. RAC-G → 4. MB4-G → 5. MB15

Use of the MAC15, MB4 and MB15 binders with dense gradations increased shear test performance and stiffness in the laboratory tests compared to gap-graded mixes with the same binders.

5.3 Simulation

Simulation models developed for Caltrans by the UCPRC were used to extrapolate HVS results to identical test and in-service pavement conditions. Two approaches were used:

- A recursive mechanistic-empirical design model for rutting and reflection cracking included in the *CalME* (California Mechanistic Empirical Design) software (Ullidtz et al., 2006). This was used with laboratory shear, fatigue and frequency sweep tests results to simulate rutting and fatigue cracking performance on the HVS sections and then in three California climate regions (Desert, Valley, South Coast) at various traffic levels, with two truck traffic speeds (10 km/h and 70 km/h).
- A continuum damage mechanics model using finite element method calculation of strains for simulation of reflection crack initiation and propagation. This was used with laboratory fatigue characterization of the materials to simulate the HVS sections as tested, and then with identical underlying pavement structures and cracking patterns to eliminate differences in as-built conditions and to extrapolate results to other conditions.

Detailed analysis and results are not discussed in this paper.

6 CONCLUSIONS

A comprehensive laboratory and accelerated pavement testing experiment comparing gap-graded, terminal blend modified binder mixes with gap-graded rubberized asphalt concrete and conventional dense-graded asphalt concrete (using an equivalent PG64-16 binder) has recently been completed in California. The results indicate that gap-graded mixes with MB4, MB4 with 15 percent recycled rubber, and MAC15TR with 15 percent recycled rubber binders will provide superior performance in terms of reflection cracking compared to the same half thickness of RAC-G and full thickness of DGAC, when used in thin overlays on cracked asphalt pavements. With regard to rutting performance, conventional dense-graded asphalt concrete was clearly superior to all other mixes, followed by the RAC-G, and then the modified binder mixes. Most of the rutting in the HVS test sections occurred in the DGAC layer below the overlays, and not in the overlay itself.

The following interim recommendations were made with regard to implementation, based on the findings of this task of the study. More detailed recommendations will be made on completion of the second-level analysis and simulations.

- MB4, MB4 with 15 percent rubber, and MAC15TR binders can be used in appropriately designed half-thickness overlay mixes for reflection cracking applications where RAC-G would normally be considered. There is potentially a greater risk of rutting compared to RAC-G if these mixes are used under slow moving, heavy truck traffic in hot climates, hence they should not be used in locations with these conditions until proven in pilot projects on in-service highways.
- Simulation models calibrated with the HVS results should be used to assess the performance of other mixes or changes in binder specifications and to validate future mix and thickness design changes.
- Long-term performance monitoring (rutting, cracking, forensic coring and assessment of the interactions of underlying pavement and thin overlays) of in-service test sections should be continued to relate long-term performance to the laboratory and HVS findings.

ACKNOWLEDGEMENTS

This research study was financially supported by the California Department of Transportation. Caltrans sponsorship is gratefully acknowledged. The contents of this paper reflect the views of the authors and do not reflect the official views or policies of the State of California.

REFERENCES

- California Department of Transportation (Caltrans). 2005. *Generic experimental design for product/strategy evaluation – crumb rubber modified materials*. Sacramento, CA.
- Guada, I., Signore, J., Tsai, B., Jones, D., Harvey, J. and Monismith, C. 2006. *Reflective cracking study: First-level report on laboratory shear testing*. Davis & Berkeley, CA: University of California Pavement Research Center (UCPRC-RR-2006-11).
- Jones, D., Harvey, J. and Monismith, C. 2007a. *Reflective cracking study: Summary report*. Davis & Berkeley, CA: University of California Pavement Research Center. (UCPRC-SR-2007-01).
- Jones, D., Steven, B. and Harvey, J. 2007b. *Reflective cracking study: HVS test section forensic investigation*. Davis & Berkeley, CA: University of California Pavement Research Center. (UCPRC-RR-2007-05).
- Steven, B., Jones, D. and Harvey, J. 2007. *Reflective cracking study: First-level report on the HVS rutting experiment*. Davis & Berkeley, CA: University of California Pavement Research Center (UCPRC-RR-2007-06).
- Tsai, B. Jones, D. Harvey, J. and Monismith, C. 2006. *Reflective Cracking Study: First-level report on laboratory fatigue testing*. Davis & Berkeley, CA: University of California Pavement Research Center. (UCPRC-RR-2006-08).
- Ullidtz, P. Harvey, T. Tsai, B. and Monismith, C.L. 2006. *Calibration of incremental-recursive flexible damage models in CalME using HVS experiments*. Davis & Berkeley, CA: University of California Pavement Research Center. (UCPRC-RR-2005-06).
- University of California Pavement Research Center (UCPRC). 2003. *Comparison of MB, RAC-G and DGAC Mixes Under HVS and Laboratory Testing*. Davis and Berkeley, CA. (Project Workplan).

Accelerated pavement cracking testing: experimental and finite element analysis

S.A. Pérez, J.M. Balay, P. Tamagny & A. Chabot

Laboratoire Central des Ponts et Chaussées, Nantes, France

Ch. Petit & A. Millien

Université de Limoges, Limoges, France

L. Wendling

Laboratoire Régional d'Autun, Autun, France

ABSTRACT: In the domain of pavement reinforcement, one of the major problems is the frequent incidence of reflective cracking over the top asphalt new layer. One experiment using an Accelerated Pavement Testing (APT) facility has been done to evaluate this type of damage. The experiment was performed on a full scale test track with three types of surface layers. Transversal joints were established in the base layer and were charged with heavy traffic loads to promote reflective cracking in the surface layer. Many sensors measuring deformations, temperature, vertical displacements and crack evolution were used. The experimental data has been compared with numerical computation results made with the CESAR-LCPC's FEA software. This comparison had lead to a validation of the calculation hypothesis and a better understanding of the reflective cracking failure mechanism. The main perspective is to use those results to define a new laboratory test equipment to evaluate reflective cracking on pavement bituminous complexes.

1 INTRODUCTION

1.1 *Context*

One of the main mechanism of deterioration in semi-rigid roadways and the repaired pavement is bottom-top propagation cracking into the surface bituminous layers of the base layer's cracks. In both situations, semi-rigid and reinforced pavement, the cracking damage mechanism has the same characteristics. A semi-rigid pavement structure has a base layer treated with hydraulic binders covered with and asphalt concrete surface layer. This base layer is expected to crack. Cracks on this kind of material are normal and they appear because of the thermal shrinkage. The reinforced pavement has a bituminous overlay on top of a cracked pavement. The relationship established between the bituminous layer and the cracked layer in both cases is then alike and leads into a reflective cracking deterioration. In spite of the great number of roadways concerned, there is no reliable method to predict the development of reflective cracking as a function of the traffic and to determine the minimal thickness of the bituminous overlay necessary to reinforce a given damaged pavement. There are few records of an operational test that can quantify the effectiveness of bituminous surface layer complex in reflective crack cases. Furthermore, neither the French Guide (SETRA-LCPC, 1994), nor American Guides (NCHRP1-37A 2005, NCHRP 9-19 2005) specifically addresses tests on this matter (Zhou & Scullion 2005). Many authors agreed that there is a lack of methods and simple and rapid tests equipments to characterize reflective cracking.

Some of the latest developments on this way are the Texas Transportation Institute Overlay Tester of the Texas Department of Transportation (Zhou & Scullion 2005) and the Wheel Reflective

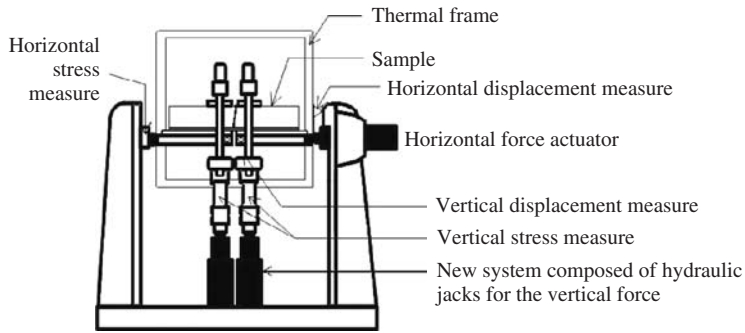


Figure 1. New laboratory test based on the equipment MEFISTO.

Cracking of the Universidad Politécnica de Madrid (Gallego & Prieto 2006). In both cases the test can be classified as a behavior-related test but a behavior-based test is still needed.

The Laboratoire Central des Ponts et Chaussées (LCPC) is developing in France a new reflective cracking laboratory test based on the already existing test equipment called MEFISTO. The dimensions of the tested samples are the same as in the precedent test (560 × 100 × 100 mm). The final objectives are to predict reflective cracking and quantify life time service of different layer complexes used as surface layer on semi-rigid new pavements or in reinforced cracked pavements. This quantification of life time service depends on how realistic is the strain field reproduced on the sample and how close it is to the one induced by the traffic loads in the roadways. Therefore the MEFISTO test has been improved by modifying its configuration. From a displacement controlled test it has been changed into a force controlled test by adding two vertical hydraulic jacks. Due to this modification, in order to reproduce a realistic strain field on the sample, loading protocols must be defined to simulate the passage of the wheel.

To define these protocols the LCPC has worked on two main aspects. On the one hand, the simulation of strain fields leading to reflective cracking requires validated numerical tools related to the phenomenon of multi-layer material cracking. On the other hand it also requires accurate experimental data on the behavior and the damage of materials subjected to this phenomenon in a heavy loaded roadway.

1.2 Objectives of the Accelerated Pavement Testing

The experience made with the LCPC's linear APT facility (FABAC) was defined to study in a full scale test track the behavior of three complexes subjected to the reflective cracking damage. The collected data of the cracking propagation, the strains and the displacements are used to identify the good assumptions and the choice of numerical values leading to a satisfactory simulation of the reflective cracking in pavement, using the Finite Element Analysis (FEA).

The FEA numerical simulations are made with the software CESAR-LCPC (CESAR-LCPC 2001). The module used in this study is TACT – TACT stands for conTACT – which introduces different boundary conditions at the interface between the two top layers of the pavement. In the present work, after describing the APT experience, focus is made only on the results concerning reflective cracking initiation and its relevance for the model validation.

A successful validation of the model will allow its use into further numerical calculations of reflective cracking damages in other pavement structures. The next modeling steps are the evaluation of reflective cracking into a real pavement geometry and then into a sample laboratory test geometry. This final modeling will allow the definition of the loading protocols of the new laboratory equipment, reproducing a realistic strain field on the sample, leading into reflective cracking damages.

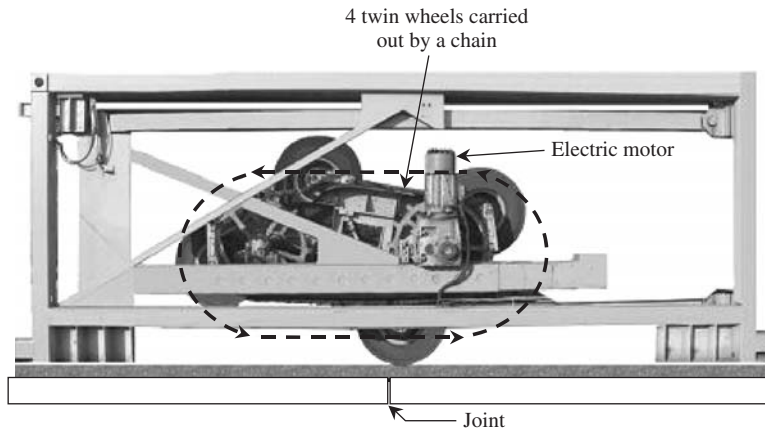


Figure 2. APT equipment used for reflective cracking test on full scale pavement structures at the LCPC.

2 EXPERIENCE WITH THE APT FACILITY

2.1 *Equipment characteristics*

The LCPC has two FABAC machines. They are small heavy traffic simulators built in 1995. Their characteristics make them optimal for structural pavement researches. The main advantage of the LCPC facility is the possibility to apply the equivalent of 10 to 20 years (according to the real traffic intensity) of heavy loadings on a full scale pavement structure in less than two months.

The load applied by the twin wheel of this equipment is 65 kN, namely one half of the reference load of 13 tons on one single axle. Each machine has 4 twin wheels which are carried by a chain to apply the load in 2 meters of the test track (Fig. 2). Two experiences can be done at the same time but the size of the machines imposes a particular disposition of the surface layers.

2.2 *Test track configuration*

The pavement structure was specially adapted for reflective cracking testing. There were 3 main particular improvements implemented on the track for the present test. Those improvements concern the pavement structure, the transversal cross section and the instrumentation.

2.2.1 *The pavement structure*

The test is performed on a 30 meters long track with eight discontinuities on the base layers. The pavement base is composed of three layers. The one at the bottom is a sand concrete cemented ribbon, over this one there is a granular asphalted layer and on top a concrete ribbon. This 2 meters width concrete ribbon is composed of nine adjacent slabs. The eight joints between them pass through all the base layer thickness simulating the crack in the pavement base layer. Their role is to avoid transfer displacements as cracks in semi-rigid base layer or in an old damaged pavement do.

Three different overlays have been placed over the pre-existing concrete pavement, constructed for a previous research (Pouteau 2004). The distribution of the different types of overlay over the total length of the concrete ribbon was determined taking into account the fact that the two machines had to run simultaneously on the two locations chosen for a given test, avoiding any obstruction between them.

Four of the structures have a surface layer composed of 6 cm of standard bituminous layer without any additional material (joints J3, J4, J5 and J8). These structures are set as the reference ones (referred to here as BBC). Two joints, J1 and J2, are covered with a composite layer made of 2 cm of sand bituminous mixed layer and 4 cm of regular bituminous layer (referred to here as SB + BBC).

Table 1. Characteristics of all the layer materials.

Pavement layer	Young Modulus E (MPa)			Poisson Ratio ν	Thickness e (cm)
	Temperature				
	20°C	10°C	0°C		
Bituminous layer	2000	8000	12,000	0.35	6
Concrete Slab	35,000	35,000	35,000	0.25	8
Granular bituminous layer	5000	10,000	17,000	0.35	10
Sand concrete cemented layer	2000	2000	2000	0.25	15
Soil	110	110	110	0.35	–

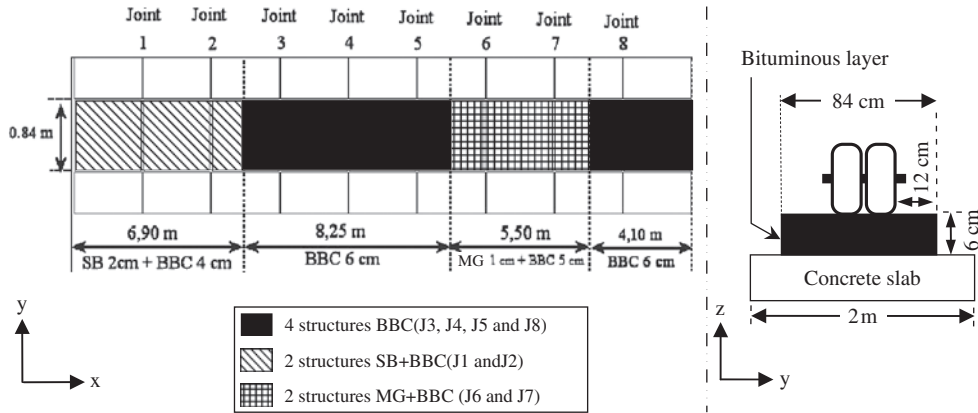


Figure 3. Position of the different surface layers on the tested track.

Finally the last two structures have 1 cm of a bituminous layer added with a Metallic Grid and 5 cm of regular bituminous layer (referred to here as MG + BBC).

The characteristics of all the materials were determined with classical laboratory tests made in the LCPC. The summary of the characteristics used on the FEA numerical simulations are shown in Table 1: the Young modulus in MPa (E), the Poisson ratio (ν) and the layer thickness in cm. The Young modulus of these materials was determined with the complex modulus laboratory test which defines the Young Modulus as a function of the temperature and the frequency of loadings. The first modulus value shown in the table 1 is the modulus of the bituminous layer for 20°C and 0.5 Hz. This frequency is defined by the velocity of passage of the wheels (1 m/s) and the longitude of the tested surface (2 m). To extrapolate calculations to real weather conditions, the Young modulus was also used in 10° and 0°C simulations (also shown in table 1).

2.2.2 The transversal cross section

Before setting the instrumentation, one improvement has been made to the track concerning its geometry. The best way to get information of the propagation of the crack under the loading application zone is the observation of the lateral faces of the track.

In order to obtain reliable data of the reflective cracking the track's width was reduced. The precise length over the twin wheel width was defined as the double of the thickness of the layer (Fig. 3). This reduction was optimized not only to facilitate the observation of the crack propagation, but also to avoid any creep of the material.

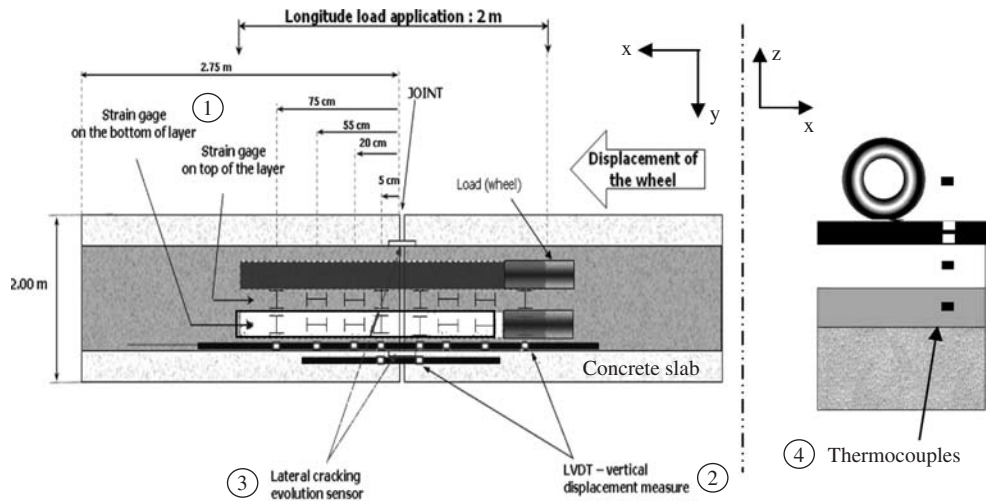


Figure 4. Instrumentation placed on each tested joint.

2.2.3 The instrumentation of the test track

The main objective of the APT is to obtain accurate data to understand the structure behavior under rolling load making a parametrical study and validate the model in FEA numerical simulations. To ensure the correct and detailed acquisition of data associated to stress fields, vertical displacements, cracking propagation and thermal conditions, a large amount of sensors has been placed in the bituminous overlay. Four main types of sensors have been placed on the test track: strain gages for the transversal and longitudinal strains in the surface layer, LVDT for vertical displacement of the surface bituminous layer and the concrete slabs, lateral cracking evolution sensors for the propagation of the crack in the surface layer and thermocouples for the temperature inside and outside the pavement layers. The figure 4 shows the position of these sensors on each joint.

The strain gages at top of the surface layer are placed between the twin wheels without any cover material. The ones at the bottom of the surface layer are the so called H-shaped sensors consisting of horizontal strain gages protected by a resin coating. Two aluminum bars are attached to the extremity of the gage in order to ensure that the sensor is properly anchored to the material in which it is embedded. The LVDT sensors for measuring vertical displacement are fixed on a metallic beam. The cracking sensors consist of a horizontal net of silver paint made on the lateral face of the surface bituminous layer to detect the crack propagation. The acquisitions of those three types of measurement were realized two times per day during 40 loading cycles. The measurement of the temperature was made each 15 minutes.

2.3 Test procedure and reflective cracking with APT facility

Three series of tests have been performed until now. The principal restrictions to carry out the APT experiences are high temperatures. To avoid rutting and creep of the bituminous material, to be representative of the whole thermal condition over the total life duration of the real pavement, and also because high temperature considerably reduces reflective cracking, the tests have to be made in the cold periods of the year.

Schedule and final number of passages for the different experiences were different for each one of the series of tests:

- The joints no 3 and no 7 were tested between March and April 2005. The experience was stopped after 600,000 loading.

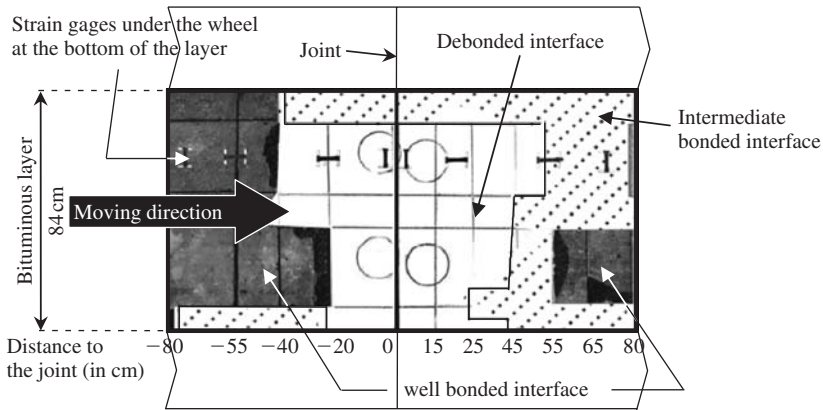


Figure 5. Example of collected data of the bonding properties of the interface (joint no 5).

- The joints no 2 and no 6 were tested between end September and beginning of November 2005. The experience was stopped after 1,000,000 loading.
- The joints no 1 and no 5 were tested between January and February 2006 and between May and June. The last part of the third series was made at night to avoid high temperatures. A breakdown of an APT machine had stopped the experience for two months. The experience was stopped after 1,000,000 loading.

After each test, bonding properties between surface layer and concrete slab were studied near the joint by sawing and extracting the entire tested bituminous surface layer in small samples. For each sample the bonding condition was qualitatively defined as debonded, intermediate bonded or well bonded. From the observed interface and the collected samples, it is possible to conclude that three general bonding conditions were present:

- In some joints the contact between base layers and the surface layer presents large debonded zones. All strain gages related to the joint are in the debonded zone or at least in a transitional debonded zone. The joints concerned by this kind of debonding conditions are J3, J6 and J7. The two MG structures belong to this description. Those structures have been reinforced with a metal grid but they both cracked as fast as one of the baseline structures. Bonding interface properties had proved bigger influence on reflective cracks development than reinforcement of the layer.
- In one of the structures (J5 baseline structure) the debonded zone existed in a relatively short distance near to the joint. Half of the strain gages placed near to the joint were in a debonded zone and the other half in a well bonded zone or in an intermediate bonded zone (Fig. 5). Because of the big temperature variations during the third test series, the comparison between baseline structures J3 and J5 cannot be made without further analysis.
- One joint presented better bond conditions. Only very near to the Joint no 1 the interface had intermediate or bad bonding properties but the rest of the interface presented good bonding properties. The sand bituminous structure is already used as a reflective cracking retarding. This type of layer has a high thermal susceptibility and sometimes it can present other type of damages like creeping or rutting. After one millions of cycles the Joint no 1 didn't present any crack.

The expected reflective cracking in thin asphalt overlay over existing Portland cement concrete is a double reflective cracking (Zhou & Sun 2002, Zhou & Scullion 2005). This cracking occurs only at joints with significant vertical movement, like in the cases of the joints no 3, no 6 and no 7. The magnitudes of verticals movements are also related to the bonding interface characteristics.

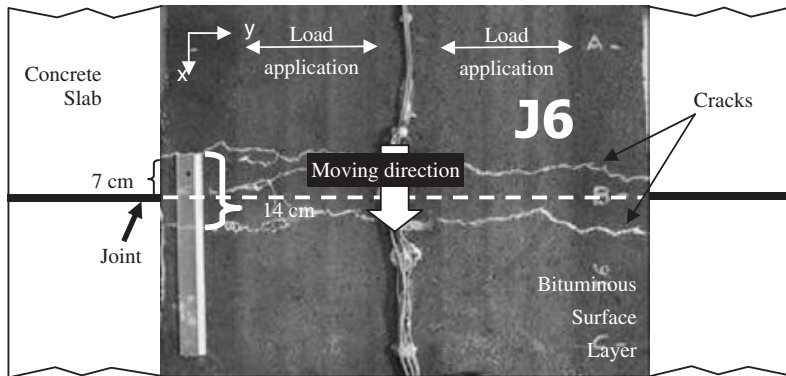


Figure 6. Top view of double reflective cracking over the tested joint no 6.

Table 2. Summary of the characteristics of the tested joints.

Series	Joint	Type of structure	Average Temperature	Visual observation of Reflective cracking (Cycle number)
1	J3	Bituminous baseline structure (BBC)	12°C	450,000
	J7	Metallic Grid (MG)		450,000
2	J2	Sand bituminous mixed layer (SB + BBC)	16°C	Creep
	J6	Metallic Grid (MG)		450,000
3	J1	Sand bituminous mixed layer (SB + BBC)	7°C and 21°C	No crack
	J5	Bituminous baseline structure (BBC)		500,000

As in joint no 5, a better bonded surface layer reduced them and the structure presented only one reflective crack. The double reflective cracking can be appreciated in Figure 6.

The Table 2 shows a summary of some of the results of the different tests. The temperature of the bituminous layer is calculated as the average of the temperature given by the two thermocouples in this layer. The average temperature shown in the table was calculated as the average of the temperature in the bituminous layer during the whole experiment.

3 NUMERICAL FINITE ELEMENT ANALYSIS OF THE APT EXPERIENCE

3.1 CESAR FEA and its TACT module for contact calculations

CESAR-LCPC is a finite element software, developed at the LCPC since 1981 (CESAR LCPC 2001), particularly adapted to the resolution of Civil Engineer problems (soil mechanics, structures calculations, etc). This program is composed of modules of data management and modules of execution. The module which is used here to solve contact calculation between two elastic layers is the module TACT.

The standard mesh for 3D calculations of CESAR-LCPC's finite elements code is made up mainly with parallelepipedic isoparametric elements with 20 nodes. Those elements easily support automatic generation of volumes and definition of uniform multi-layer solids. The final 3D mesh made with this kind of elements also allows the use of flat contact element with 16 nodes. These

elements were used to simulate the interface behavior. The module TACT is based on the method of penalization, which was particularly developed in CESAR software for contact element approach. The method of penalization introduces a very specific and variable rigidity matrix at the level of the interface. The reason of its variability is because the matrix depends on the state of the interface on each iteration (Salasca 1998).

3.2 Numerical simulation parameters and series of calculations

3.2.1 Load characteristics

A static vertical load is placed on the surface elements to calculate the strain and stress fields caused by the wheel on a particular position. To simulate the passage of the wheel, the load is placed on 9 different positions. The wheel shape is associated to a rectangle of 0.3 m × 0.2 m and the uniform pressure is 0.541 MN/m².

3.2.2 Bonded and debonded zones for calculations

In the APT experiences it was found that the bonding interface properties between the surface layer and the concrete slab ribbon were particularly determinant in the reflective cracking. For the numerical simulations with CESAR software this parameter can be taken into account using the TACT module. This module permits to introduce double bar elements which can simulate two main bonding conditions. In the perfect bonded condition the continuity of the whole stress field is assured. In the perfect debonded condition the elements introduced assure the normal and tangential displacements and two tests are made: the first one to avoid interpenetration of the materials and the second to verify the normal stress value (which must be superior or equal to 0).

To define bonded and debonded zones the interface was divided in 6 zones on each side of the joint. The contact elements placed in these zones allow setting bonding interface properties in a chosen distance on each side of the joint. Calculations were made with the whole bonded interface and with different debonded distances from the joint: 0.05 m, 0.25 m, 0.45 m, 1.75 m. Combinations of symmetrical and non symmetrical debonded areas were calculated using these distances.

3.2.3 Number of load positions for calculations

To simulate the passage of the wheel over the joint, 9 positions of the load were define for symmetrical debonded calculations and 17 positions were defined for non symmetrical calculations. Some of the load positions correspond also to a captor position.

3.2.4 Materials and mesh characteristics

For each position of the load one mesh must be established. In order to optimize the software capacity only the pavement under the load and near the joint had a very dense mesh. To simplify calculations only one half of the track was considered in the modeling by using the existing symmetry to the xz plane. This means that only one wheel of FABAC's twin wheel was modeled. To take into account the effect of the other adjacent discontinuities, 3 concrete slabs were set in the calculation meshes. The discontinuities were set geometrically by defining a void at the position of the joint. The properties of the materials are the ones defined before in table 1. Three different calculations changing the Young Modulus for temperatures of 0°C, 10° C and 20° C were made for each position of the load for each combination of debonded zone.

3.2.5 Summary of the combination made of calculations

Each data acquisition taken during the test has a specific temperature and bonded area, so a vast number of calculations should be made. These parameters were then combined to guarantee a complete analyze of the accelerated pavement test. At least four symmetrical debonded calculations were made for three temperatures (243 FEM individual calculations) and two non symmetrical debonded calculations for the same three temperatures (102 FEM calculations).

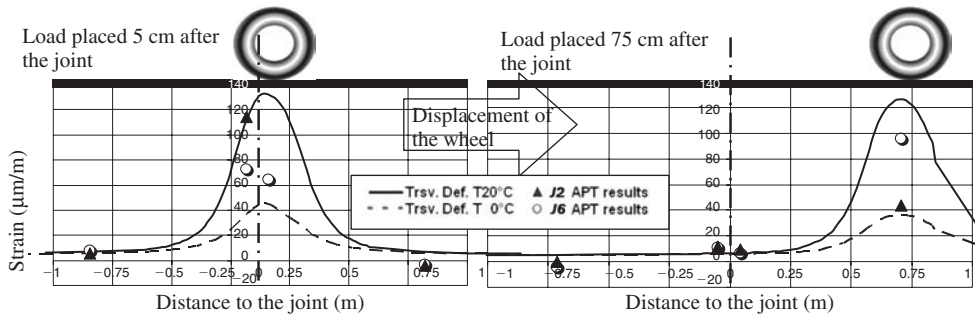


Figure 7. CESAR calculations for 2 positions of the load compared to punctual values obtained with the strain gages at 75 and 5 cm before the joint. Temperature of the acquisition: 17.5°C.

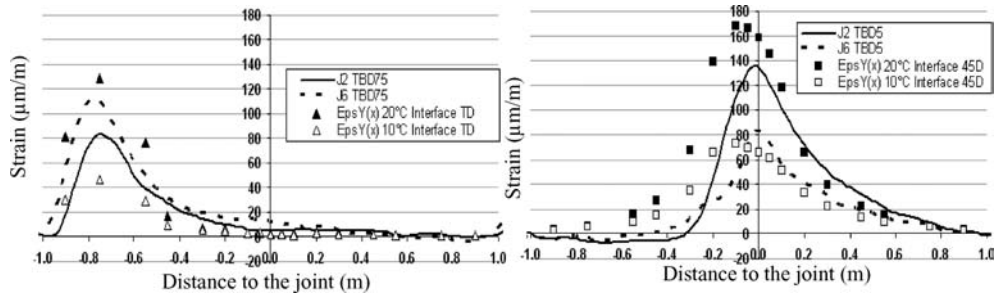


Figure 8. Comparison between an APT strain gage acquisition data placed 75 cm and 5 cm before the joint for one passage of the load (Temperature 17.5°C) and CESAR results for 10°C and 20°C.

3.3 Validations results

The number of measures realized for each test was about 100 data acquisitions. In each data acquisition, 20 passages of Fabac wheels were stored for the 31 captors placed in the test track (strain gages, LVDTs, thermocouples, cracking sensors).

The thermocouples information will be always implicitly linked to the other captor's data. In the initial phase, before cracking reflection, the vertical displacement data is used only to pre-calibrate the model.

To study the initial strain/stress conditions leading to the reflective crack initiation the strain gages measurements at the bottom of the surface layer were used. These captors were able to record small changes and their behavior can be associated to the bond interface evolution properties.

First calculations were compared to single position response of the captor on the track (Fig. 7). The strain values of the joints presenting debonded interfaces during the test were coherent with the CESAR's calculations debonded case.

In figure 7, results present the existing static strain field in the entire section for a position of the load on each case. The CESAR curves represent limit control values of the calculations since one of the curves is issued from the 0°C calculation and the other one from the 20°C calculation. For this particular measure of the strain in the test track, the temperature was 17.5°C. The strain gages placed on the bottom of the surface layer were placed at 75 cm and 5 cm after the joint. As it is shown in the figure 7 strain gages data results are mostly placed in between the two limits established by the FEA calculations.

The next step to completely define the initial strain field on the test track is to make, for the whole passage of the load, FEA calculations and confront them to the whole captor's response. An example of this comparison is shown in figure 8. In this figure the curve represents the response of the strain gage placed 75 cm before the joint as the wheel passes over the slabs and the joint no 2 and no 6.

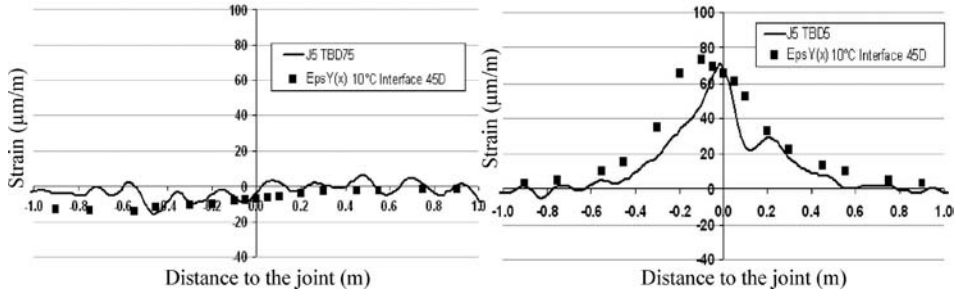


Figure 9. Comparison between an APT strain gage acquisition data placed 75 cm and 5 cm before the joint for one passage of the load (temperature 11°C) and CESAR calculations results for 10°C.

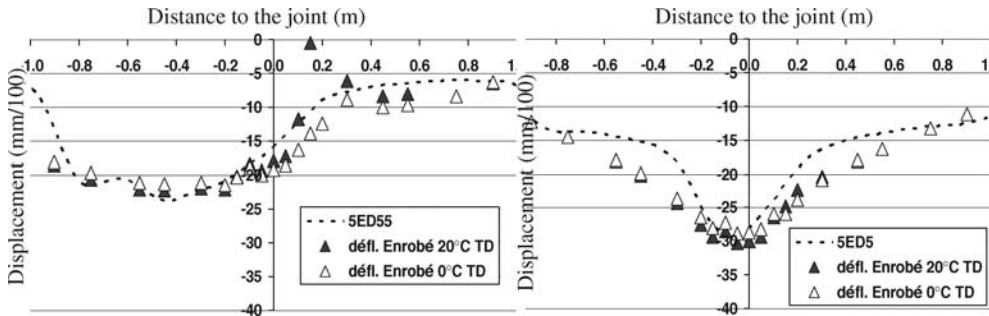


Figure 10. Comparison between an APT deflection acquisition data placed 55 cm and 5 cm before the joint for one passage of the load (temperature 11°C) and CESAR calculations results for 10°C and 20°C.

The temperature of APT Joint no 2 and no 6 data is 17.5°C and the calculations temperatures are 10°C and 20°C. The test results are correctly placed between 10°C and 20°C validating calculation hypothesis concerning the bonding properties of the layers and the material properties.

For all the initial strain fields in all the tested joints the same exercise was done and the same good correlation between observed bonding conditions and bonding calculation hypothesis were obtained.

As an example, Figures 9 and 10 show the case of a partially debonded joint (§2.3 and Fig. 5). In this case, bad bonding properties were observed only very near of the joint. Here the temperature test was 11°C. In this case, the measured data fits very well with the 10° C CESAR calculation for a partially debonded condition of the interface (only 45 cm debonded interface on both sides of the joint). All the other strain gages under the twin wheel present similar good correlations between experience and calculation when bonding properties are correctly defined.

4 CONCLUSIONS AND PROSPECTS

The large amount of precise and accurate experimental data has demonstrated the utility of the Accelerated Pavement Testing in the reflective cracking simulations. There is no record of an APT reflective cracking test using neither the kind nor the amount of instrumentation used for the present test.

For the first time it was possible to record and to visualize cinematically, in a full scale pavement structure, the reflective cracking propagation, using very simple instrumentation by optimizing its position on the pavement structure. The advantage to be able to put the instrumentation very close to the loaded road is an advantage only given by the APT facility and it wouldn't be probably possible in a real pavement. Also, concerning the acquisition of strain data, the test presents some

new punctual data values of the strain field occurring on a full scale pavement. With this data the initial strain and stress field could be deduced.

Conclusions of the impact of bonding interface properties in the reflective cracking evolution were then confirmed using the FEM code of calculation CESAR and its contact module (TACT) simulating the structure test pavement including the bonding interface properties.

The calculations results match particularly well to the strain data obtained from the test. Furthermore, theoretical types of cracking evolutions depending on bonding interface conditions were also confirmed by crossing experimental failure data (test recorded data and failure observation conclusions) and strain field calculation data. Namely when single or double reflective cracking occurs, the specific causes are detected and their relationship is coherent in the experiment and the numerical simulations.

Finally, since the FEA software is validated for the reflective cracking Accelerated Pavement Test, further simulations have been made to reproduce on the MEFISTO sample, the results from this APT reflective cracking experience. The next step is to optimize the position of the vertical hydraulic jacks and the magnitude of the forces that must be applied on the laboratory test sample to simulate the loading leading to reflective cracking.

REFERENCES

- CESAR-LCPC 3.3 2001. Le code de calcul CESAR. 2e édition – Mode d’emploi.
- Gallego, J. & Prieto, J. N., 2006. New Laboratory Equipment for Study of Reflective Cracking in Asphalt Overlays. 2006 Annual Meeting of the Transportation Research Board of the National Academies. ISSN 0361-1981. Issue Volume 1970 / 2006. DOI 10.3141/1970-25. Pages 215-222.
- NCHRP 1-37A, 2005. Development of the 2002 Guide for the Design of New and Rehabilitated Pavement Structures: Phase II. College Station, Texas, Mar. 1, 2005.
- NCHRP 9-19, 2005. Superpave Support and Performance Models Management. College Station, Texas, Mar. 1, 2005.
- Pouteau, B. 2004, Durabilité mécanique du collage blanc sur noir dans les chaussées. Thèse de Doctorat. Ecole Central de Nantes, Université de Nantes. France.
- Salasca, S. 1998; Phénomènes de contact dans les chaussées en béton : modélisation théorique et validation expérimentale. Thèse de Doctorat. Ecole Central de Nantes, Université de Nantes. France.
- SETRA-LCPC, 1994. Conception et dimensionnement des structures de chaussée. Guide Technique. Ministère de l’équipement des Transport et du Tourisme. Paris, France.
- Zhou, F. & Sun, L. 2002. Reflection Cracking in Asphalt Overlay on Existing PCC, Proceedings of the 9th International Conference on Asphalt Pavements, Copenhagen.
- Zhou, F. & Scullion, T. 2005. Overlay tester: a rapid performance related crack resistance test. Texas Transportation Institute & The Texas A&M University System, USA.

2. Analytical and experimental investigations of concrete joints

Influence of the coefficient of thermal expansion on the cracking of jointed concrete pavements

E. Kohler & V. Kannekanti

Dynatest Consulting Inc, Formerly with the University of California Pavement Research Center, Davis, California, USA

ABSTRACT: The influence of the coefficient of thermal expansion (CTE) on cracking of jointed concrete pavements is investigated in this study, based on crack survey data and laboratory evaluation of samples from approximately one hundred sections of in-service highway pavements throughout the state of California. The CTE values found in the experiment ranges from 4.8 to 6.7 microstrain/°F. The reason for the experiment resides in the lack of empirical information that confirms the effect of CTE on cracking. Adequate account of this factor is necessary for calibration and refinements of mechanistic-empirical pavement performance models. The sections' cracking data was obtained from the Caltrans pavement management database, and consisted of first stage cracking, third stage cracking, and corner cracking. Condition data for sections up to 46 years old was included. Taking into account the slabs on all traffic lanes of all sections and the time histories of cracking data, the number of cases investigated in the study exceeded 3,400. It was found that CTE does affect crack development on jointed concrete pavements. Despite the difficulties of subjective cracking data, the pavements with CTE higher than 5.7 microstrain/°F showed more cracking than those with CTE lower than this value.

1 INTRODUCTION

The coefficient of thermal expansion (CTE) is an important parameter that might affect the service life of concrete pavements. In Jointed Plain Concrete Pavements (JPCP), the CTE controls joint opening, which affects load transfer through joints and cracks. It also affects joint sealant performance, development of spalling, and even controls the potential for catastrophic failures such as blow ups. The extent of longitudinal, transverse, and corner cracking associated with thermal curling on jointed concrete pavements is believed to depend on the CTE of the concrete. For continuously reinforced pavements the CTE has a strong effect on crack spacing and crack width, which in turn also control pavement performance. Because of increased awareness of this parameter, the California Department of Transportation (Caltrans), through the University of California Pavement Research Center (UCPRC) began CTE testing of concrete pavements throughout the state in 2005. This paper provides details on the testing procedures used in the study to gather CTE and cracking information, followed by an analysis of the effect of CTE on cracking of JPCP. Since CTE is not the only parameter affecting the cracking levels of a given pavement, other studies are being conducted to try to take into account all the major variables that affect the service life of a pavement structure. The focus of this article is the effect of CTE in JPCP cracking, and therefore all other factors are assumed to be influencing the formation and progression of crack in similar ways on all the pavement sections included in the study, regardless of the CTE values of such sections.

2 PAST STUDIES ON CTE AND CONCRETE PAVEMENTS

Although theoretically correct, there is no tangible evidence that the CTE really affects the level of cracking in concrete pavements. The Federal Highway Administration (FHWA) developed a test method and has been testing CTE on a great number of concrete pavement cores from sections in the Long-Term Pavement Performance (LTPP) program. The results from about 670 tests indicate that CTE ranges between 5.0 and 7.0 microstrain/°F (Mallela et al. 2005). The average CTE of the entire data set was 5.7 microstrain/°F. The motivation for the FHWA's study resides in validating data for the Mechanistic-Empirical Pavement Design Guide (NCHRP 2004). The Texas Department of Transportation has also been testing CTE (Won 2005) mostly to evaluate concretes made with aggregates from different sources in the state of Texas. Sensitivity analyses using the models of the Mechanistic-Empirical Pavement Design Guide have indicated that transverse crack predictions are highly dependent on the assumed CTE value (Kannekanti & Harvey 2002, Mallela et al. 2005, Tanesi et al. 2006).

The Texas study reported a large variance in CTE values with concretes made with river gravels, as opposed to crushed limestone aggregates. The research also evaluated CTE values of early age concrete, and confirmed previous results (Alungbe et al. 1992) in that the CTE does not change with age and that specimen size has a negligible effect on CTE (Won 2005). The other motivation of the Texas study was to improve reinforcement design and construction specifications to extend continuously reinforced concrete pavement (CRCP) service life. Analysis done in Minnesota from an instrumented pavement section at MnRoad concluded that in-situ CTE values are similar to those obtained in a laboratory (Burnham 2001), which agrees with results from Texas and Illinois.

3 METHODOLOGY

3.1 *Coefficient of thermal expansion of California pavements*

A total of one hundred and four concrete pavement sections were selected for this study, and drilled cores were subjected to CTE testing at the UCPRC laboratory in Davis. The test equipment for the method developed by FHWA was not yet commercially available at the beginning of this study, and therefore hardware components were assembled based on FHWA and TXDOT setups, and a computer application was written to automatically run the experiments. The CTE testing procedure followed in this study is based on amendments proposed by Won (2005) to the AASHTO temporary protocol known as TP60, adopted from the development at FHWA. The main features of the CTE testing as performed for this study are summarized as follows.

The cores from the field are cut in order to have flat and parallel surfaces at top and bottom of the cylinders. The specimens are approximately 100 mm (4-in) in diameter, with the length varying anywhere between 170 and 200 mm. They are submerged in limewater for at least 5 days, for conditioning before the testing. The exact length of the specimen is measured, and the cylinder is placed in a testing frame and submerged in a water tank. A Linear Variable Displacement Transducer (LVDT) attached to the frame measures the change in length of the specimen. The frame consists of vertical members made of Invar and horizontal members made of stainless steel.

Figure 1 shows the LVDT, frame, water tank and a concrete pavement specimen during the process to determine the CTE. A computer controls the test and automatically varies the water temperature in order to subject the specimen to a thermal change from 10°C to 50°C, and back to 10°C. The system collects temperature and displacement data at 60-seconds intervals. The thermal cycling is automatically repeated three times to obtain more stable readings (Kohler 2007). As explained, each cycle consists of a rising temperature ramp (heating) and a falling temperature ramp (cooling). Each cycle spans 6 hours with the entire test taking 18 hours.

Figure 2 presents a summary of the results of CTE for the approximately 100 sections of the study. The CTE values found in the experiment range from 4.8 to 6.7 microstrain/°F (8.6 to 12.0

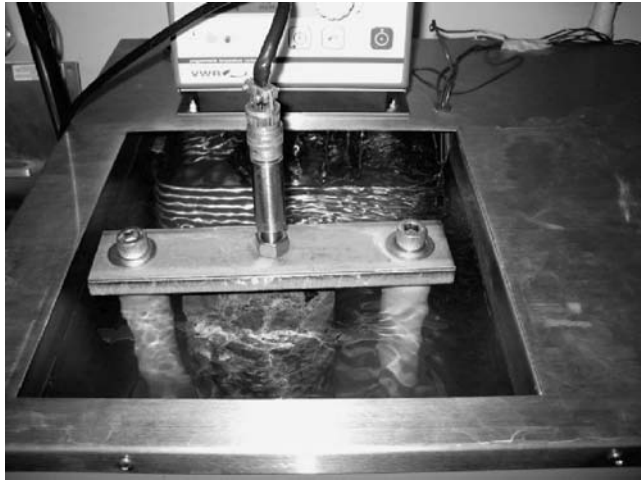


Figure 1. Concrete specimen during test, showing frame, LVDT, and water tank.

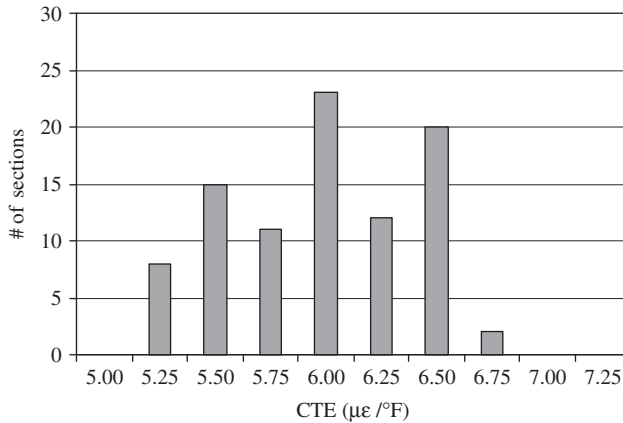


Figure 2. Histogram of CTE for all the sections in the study.

microstrain/°C). The CTE of each section was generally determined from the CTE results of two cores, although in some cases up to four cores from a given section were tested. A total of 185 cores were tested.

3.2 Pavement condition information

The California Department of Transportation was one of the first few states in the nation to adopt a Pavement Management System (PMS) in 1979 (Finn 1998). The purpose behind developing Caltrans' PMS was to "monitor deteriorating pavement, to disseminate repair strategy information, to substantiate cost-effective rehabilitation strategies, and to be used as a basis for managing existing pavements in the State highway system" (Bartell and Kampe 1978).

Caltrans has been conducting almost every year an inventory of the surface condition of the entire state highway network. Jointed concrete pavements are surveyed by counting each slab that exhibits triggering levels of distresses. Slab cracking is reported as a percentage based on the

number of cracked slabs over the surveyed distance. Three types of cracking levels are included in the data collected by Caltrans, and examples are shown in Figure 1:

- First Stage Cracks (FSC) are transverse, longitudinal, or diagonal cracks that do not intersect, which divide the slab into two or more large pieces.
- Third Stage Cracks (TSC) are interconnected cracks that divide the slab into three or more large pieces. Fragmented slabs are characterized by interconnected irregular multiple cracks and breaks. First stage cracking and third stage cracking cannot co-exist in the same slab.
- Corner Cracks (CC) are diagonal cracks that meet both a longitudinal and transverse joint within six feet, and over two feet, at the same slab corner. A slab can have as many as four corner cracks. For rating purposes, regardless of the amount of corner cracks in a slab, only one count is logged. Corner Cracks may co-exist with 1st and 3rd Stage Cracking.

The survey results are the percentage of slabs in a given section displaying FSC, TSC, and CC. The length of the sample location ranges from 0.1 to 1.5 miles for a given homogenous section. For this study the surface roughness data was also sought, in addition to the cracking levels, because the effect of CTE on cracking should reflect through the measurement of ride quality. However, the low level of reliability was found to be associated with this data.

Approximately half of the sections of the study had been overlaid with asphalt pavements, but were anyway selected in order to obtain an experimental factorial that covered the major climate regions in the state, plus typical ranges of highway traffic levels, support conditions, and other parameters to allow for a balanced set of sections. In addition to satisfy factorial requirements, the overlaid sections exhibited high levels of cracking, which was useful for this investigation.

The structural design of concrete pavements in California has changed over time, which makes the pavements from older sections somehow different from the slabs in newer sections. Changes in the joint spacing, allowable thicknesses, and/or base layer material occurred in 1964, 1967, and 1983 (Harvey et al. 2000). The types of material that constitutes the layer under the slabs varies from cement treated bases, some asphalt permeable treated bases, unbound granular bases, and a few sections that had 50 mm asphalt between PCC and cement treated base. Detailed information for every section of the study is not included in this article, but it was obtained and is being used in other studies. This includes complete pavement structure (materials and thicknesses), geometry, location (climate), traffic from weight in motion. Even on a few sections, where the field work occurred during day time lane closures, the sunlight absorptivity on the concrete pavement surface was measured using an albedo meter.

3.3 Data processing

A database was organized for the sections of this study according to yearly information of pavement condition. Records of pavement condition were available for years 1978 to 2004. Using year of construction and year of condition survey, a table of distresses versus pavement age was generated, including every lane of each section. A total of over 3,400 records were generated given that up to 26 years of data were in some cases available for the 104 sections of the study, and all the concrete pavement lanes were included for every section.

Analysis of condition survey data revealed that the cracking levels not always followed the expected trends. Figure 3 presents examples of pavement cracking from two sections. The figure includes FSC, TSC and CC. Examples with high levels of cracking were selected, but some of the sections not shown have remained for long time with very low cracking.

Rehabilitation by slab replacements explains some cases in which a transient decrease in percent of cracked slabs is observed. Also, as the pavement condition deteriorates, individual cracks become interconnected cracks, thus FSC become TSC. It should be noted that condition surveys are subjective, and there might be a large degree of variability associated with ratings of the percent of slabs with any type of cracks (measurement error). To get past the problem of unexplained oscillations in the amount of cracking, the years of condition surveys were arranged in groups. Separate data subsets were created for target ages in increments of 5 years. Each subset consisted



Figure 3. Examples of FSC, TSC, and CC.

not only of the target age, but also ± 2 years, i.e. records from 8 to 12 years were combined into the 10-year old subset.

The fact that some of the sections were overlaid with asphalt was not an issue as historical cracking data was available and actual CTE values could be obtained from the concrete pavement part (bottom) of the cores. One problem encountered with composite pavements in this investigation was the fact that during construction the concrete slabs were “crack and seated” to prevent later reflection of joints and cracks. The concrete core samples obtained from this type of sections were in some cases cracked. The presence of cracks altered the results of the CTE tests, and it was not possible to obtain CTE results for those sections where all the cores were cracked. CTE values could actually be measured for 87 of the 104 sections. The CTE for the remaining sections was assumed to be equal to the average of nearby sections (less than 1 mile apart). Since cores were obtained only from the outer lane in all the sections, there could be an inconsistency when the same CTE was assumed for all the lanes. This is because there are cases in which one or two inside lanes were built years earlier than the outer lane. Although the concrete in older and newer lanes is most certainly different, there is a good chance that the aggregates used in the production of the concrete came from the same or similar source, which is determined from proximity to the pavement section and concrete plant.

4 RESULTS AND ANALYSIS

Information was organized according to the pavement age at the time of each condition survey, given that this factor is critical on the progression of all types of cracks (FSC, TSC, and CC). As expected, almost no cracking was reported on pavement with ages below 5 years. FSC in general starts developing when the pavement is around 3 years old and progresses steadily until about 20 years. After about 15 to 20 years, some of the FSC have turned into TSC as they become interconnected cracks. If no new FSC are developing, the percentage of slabs with FSC should drop and TSC should increase. With regard to CC, the data indicates that very few slabs develop CC before 15 years. It must be kept in mind that the sections, and the number of them, are not the same for every age group analyzed. It should also be noted that the number of records (data points) is not the same across the range of CTE values, but they come from a set of sections with the CTE distribution shown in Figure 1.

Figure 4 presents the results of cracking levels versus CTE for pavements that are 15, 25, and 35 years old. The charts on the left side show FSC added to TSC, while the charts on the right side show CC. The vertical axis is the percentage of cracked slabs. The figure shows that higher levels of cracking are observed from sections with higher CTE. For CC at 25 year the plot shows clearly an increase of cracking with CTE. The cracking goes beyond 10 percent when CTE is greater than 6.25 microstrains/ $^{\circ}$ F, while at the same time the cracking levels are very minimal for CTE lower than approximately 5.90 microstrain/ $^{\circ}$ F. For the case of FSC combined with TSC, the same trend seems to hold, especially for the data at 15 and 25 years. Slab replacement and reconstruction probably explains the fact that the most cracked sections disappear from the database as time progresses.

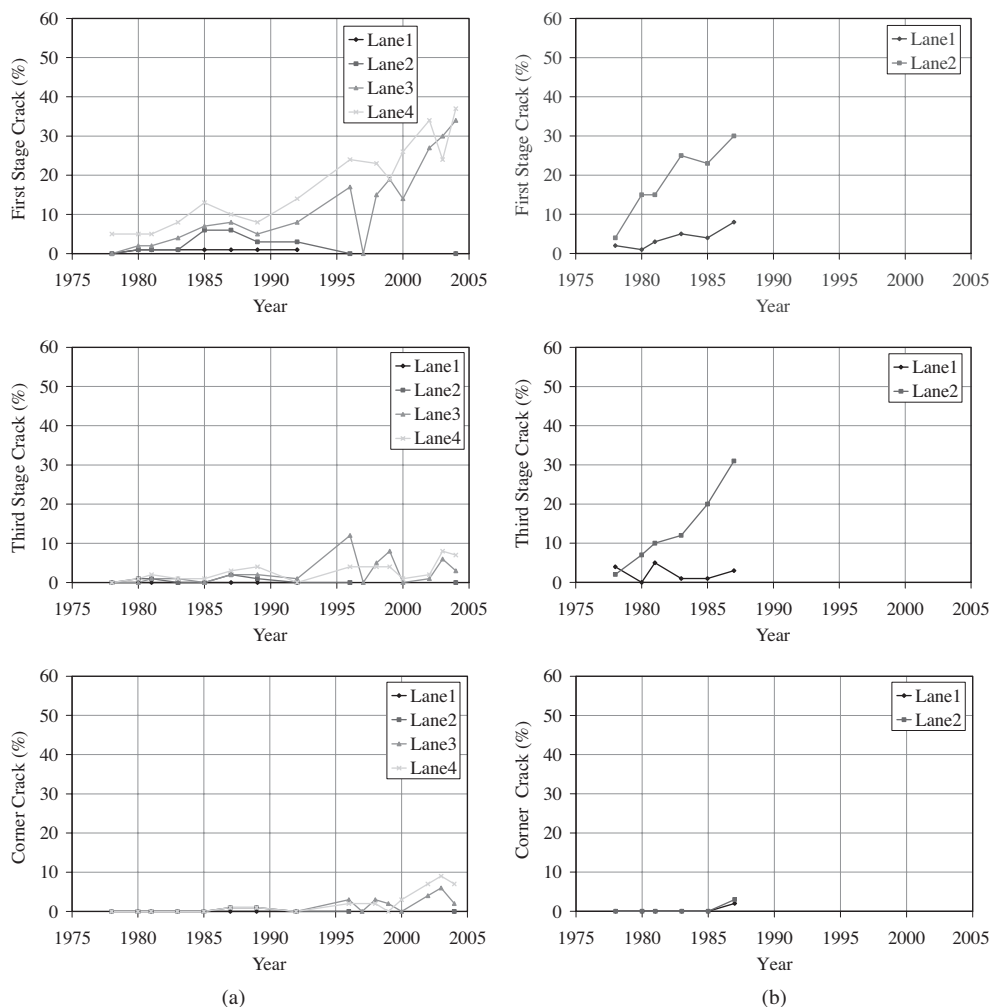


Figure 4. Examples of crack progression in (a) a four-lane highway that still has a concrete surface, and (b) a two-lane highway overlaid in 1988.

The analysis in the preceding paragraph would be more robust if the distribution of sections over the range of CTE was uniform, i.e. if approximately the same number of sections was available for each CTE level. To overcome this limitation the following procedure was used. First all the cracking below 1 percent was removed so as to keep only sections that show some cracking. The number of data points on each side of an arbitrary limit of CTE was then computed. The last step consisted on calculating the ratio of cracked slabs as indicated in Equation 1

$$K = \frac{\text{Nr. of sections with cracking} \geq 10 \text{ percent}}{\text{Nr. of sections with cracking} \geq 1 \text{ percent}} \quad (1)$$

The 10 percent limit was used for FSC and TSC. A 5 percent limit was used for CC. In both cases κ represents what could be called the proportion of severely cracked sections with respect to the total number of sections. This ratio was computed using two chosen CTE values to separate the data into two groups, low and high CTE. The selected CTE limit values were 5.7 and 6.0 microstrains/°F,

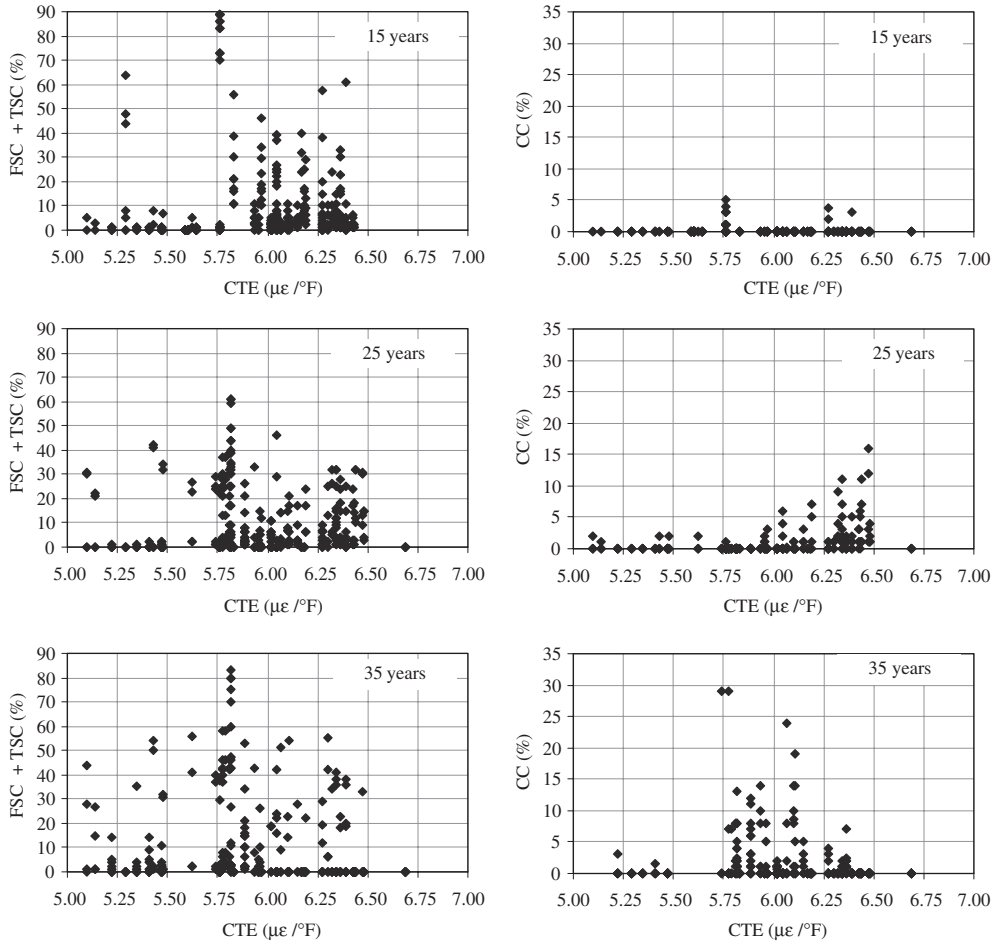


Figure 5. Percentage of slabs cracked versus CTE for concrete pavements at 15, 25, and 35 years of age.

which come from simple visual assessments of all the charts of the type shown in Figure 4. Figure 5 shows the comparison of cracking trends for pavements with low and high CTE. Linear trends are included in the charts, in addition to highly scattered points. It must be noted that the regression lines were forced to pass at the origin (zero crack at zero years). It can be seen from the figures that when the limit between low and high CTE is 5.7 the cracking trends in the two groups are drastically different. For all types of cracks, the group with high CTE develops more cracks over time than the group with low CTE. When the limit between high and low CTE is 6.0 instead of 5.7 the results show only a minor difference.

5 SUMMARY AND CONCLUSIONS

This paper presented the analysis of cracking on jointed concrete pavements against the coefficient of thermal expansion (CTE). The CTE from more than 100 pavement sections was measured using a modified version of the AASHTO TP-60 method. Cracking data obtained from Caltrans' pavement management system was used, and the percentage of cracked slabs for each section, and each traffic lane, over the entire life of the pavement, was studied. The analysis of the effect of the

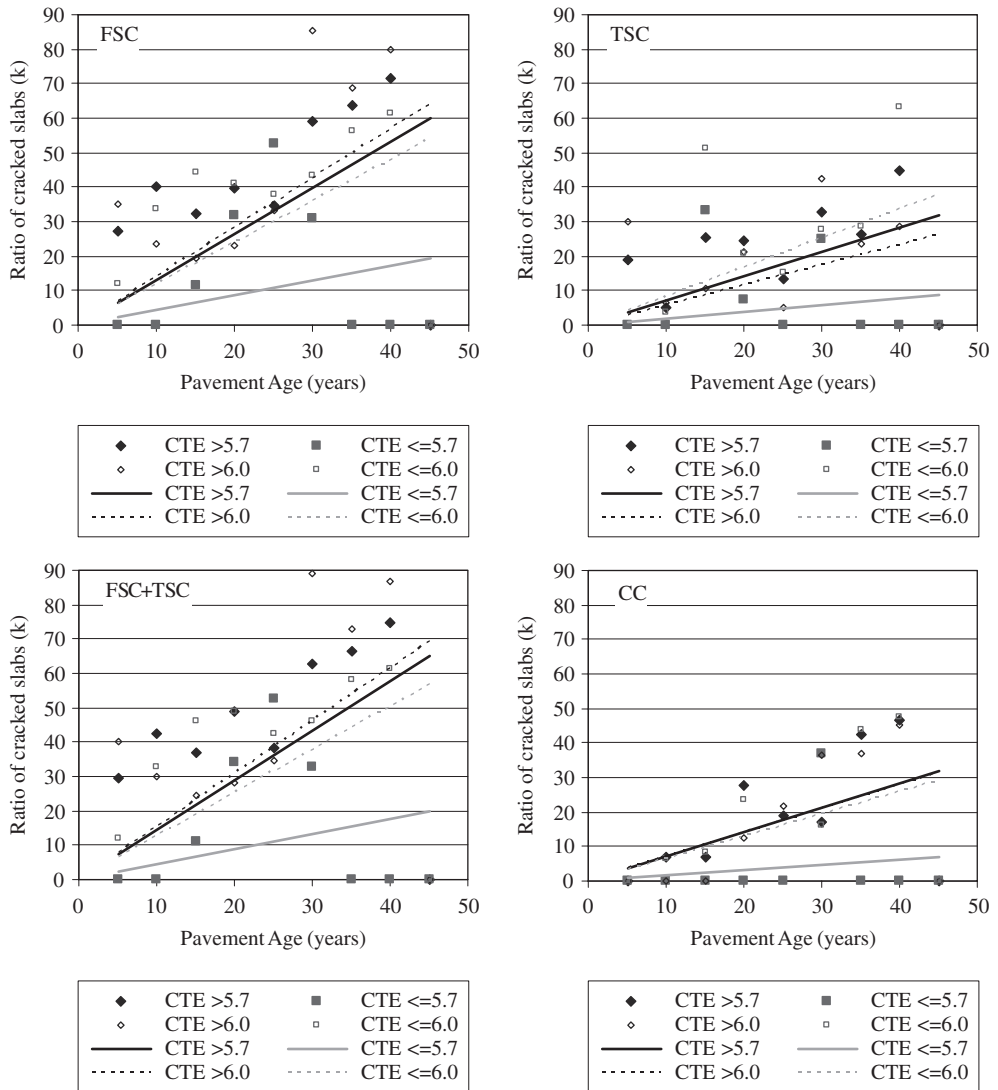


Figure 6. Comparison of ratio of cracked slabs for cases for pavements with high and low CTE (arbitrary limits at CTE = 5.7 and alternatively at CTE = 6.0).

CTE on cracking on concrete pavement revealed that in fact greater CTE is associated with the most cracked slabs. Due to imbalances in the number of sections for low and high CTE values, a ratio of severely cracked sections over the total number of cracked sections was used. This analysis illustrated that for CTE greater than 5.7 microstrains/ $^{\circ}$ F the cracking is considerable larger than otherwise.

The results presented in this work strongly suggest that longer lasting concrete pavements can be expected in the future if low CTE is specified. Cost restrictions will probable continue to control the selection of aggregates and therefore the CTE of the concrete, but CTE should be considered by highway agencies and designers as one simple factor that could reduce cracking over the life of jointed concrete pavements.

ACKNOWLEDGEMENTS

This work was carried at the University of California Pavement Research Center (UCPRC), based upon work supported by the California Department of Transportation, and under the direction of Professor John T. Harvey of the Civil and Environmental Engineering Department at UC Davis. Others from the UCPRC participated by collecting data and field samples, assisting with laboratory tests, and by carrying out data reduction from archival databases. Any opinions, findings, and conclusions or recommendations expressed in this publication are those of the authors and do not necessarily reflect the views of Caltrans.

REFERENCES

- Alungbe, G.D., Tia, M. and Bloomquist, D.G. 1992. Effects of Aggregate, Water/Cement Ratio, and Curing on the Coefficient of Linear Thermal Expansion of Concrete. In *Transp. Research Record: Journal of the Transp. Research Board, No. 1335*, TRB, National Research Council, Washington, D.C., 1992.
- Burnham, T. and Koubaa, A.A. 2001. New Approach To Estimate The In-Situ Thermal Coefficient And Drying Shrinkage For Jointed Concrete Pavement. *Seventh International Conference on Concrete Pavements*. Orlando, Florida.
- Bartell, C. and Kampe, K. 1978. Development of the California Pavement Management System Volume I: System Description. California Department of Transportation, Division of Maintenance. Final Report. FHWA-CA-HM-7139-78-03.
- Caltrans. 2000. Pavement Survey Evaluation Manual. California Department of Transportation. Sacramento, California. p. 112
- Finn, F. 1998. Pavement Management Systems – Past, Present, and Future. *Public Roads magazine*. Vol. 62 n. 1 p. 16
- Kannekanti, V. and Harvey, J. 2006. Sensitivity Analysis of 2002 Design Guide Jointed Plain Concrete Pavement Distress Prediction Models, *Proceedings Transportation Research Board Annual Meeting 2006*, Washington DC.
- Harvey, J., Roesler, J., Farver, J. and Liang, L. 2000. Preliminary Evaluation of Proposed LLPRS Rigid. Report Prepared for the California Department of Transportation by the University of California Pavement Research Center.
- Kohler, E., Alvarado, R.F. and Jones, D.J. 2007. Measurement and Variability of Coefficient of Thermal Expansion for Concrete Pavements. *Proceedings (CD-ROM) of the 86th annual meeting of the Transportation Research Board*.
- Mallela, J., Abbas, A., Harman, T., Rao, C., Liu, R. and Darter, M.I. 2005. Measurement and Significance of the Coefficient of Thermal Expansion of Concrete in Rigid Pavement Design. In *Transportation Research Record: Journal of the Transportation Research Board*, No. 1919, Transportation Research Board of the National Academies, Washington, D.C., 2005, pp. 38–46.
- NCHRP. 2004. “*Guide for Mechanistic-Empirical Design of New and Rehabilitated Pavement Structures*”. National Cooperative Highway Research Program, Report 1-37A, March 2004.
- Tanesi, J., Kutay, M.E., Abbas, A.R. and Meiningner, R.C. 2007. Effect of Coefficient of Thermal Expansion Variability on Concrete Pavement Performance as Predicted Using Mechanistic-Empirical Pavement Design Guide. *Proceedings Transportation Research Board Annual Meeting*, Washington DC, 2007.
- Tanesi, J., Hossain, M., Khanum, T., Schieber, G. and Montney, R.A. 2006. Portland Cement Concrete Coefficient of Thermal Expansion Input for Mechanistic-Empirical Pavement Design Guide. *Proceedings Transportation Research Board Annual Meeting*, Washington DC, 2006.
- Won, M. Improvements of Testing Procedures for Concrete Coefficient of Thermal Expansion. In *Transportation Research Record: Journal of the Transportation Research Board*, No. 1919, Transportation Research Board of the National Academies, Washington, D.C., 2005, pp. 23–28.

An analytical approach to computing joint opening in concrete pavements

J.R. Roesler & D. Wang

University of Illinois at Urbana-Champaign, Urbana, Illinois USA

ABSTRACT: Satisfactory performance of the transverse joints is crucial for achieving the intended service life of jointed plain concrete pavement. An accurate prediction of joint opening and movement is desired in order to quantify the effects of the environment, base type, concrete material constituents, and slab geometry on the concrete pavement responses. In this paper, an analytical model based on elasticity theory is presented to predict joint opening using a bilinear slab-subbase interfacial constraint assumption. The proposed model predicts the mean joint opening based on uniform temperature change and drying shrinkage through the slab thickness. To account for the temperature curling effect, a “correction” term to the joint opening is proposed using a closed-form solution derived from Westergaard’s temperature curling deflection equation. Initial model calculation using in-situ measured pavement temperature profile suggests that proposed analytical model generates reasonable joint opening during the monitoring period.

1 INTRODUCTION

Performance of the transverse joints is crucial for achieving the intended service life of jointed plain concrete pavement (JPCP). Research results show that most failures in JPCP are caused by failures at the joint rather than inadequate structural bearing capacity (Federal Highway Administration 1990). An accurate prediction of joint opening and movement is necessary in order to assess the effects of the environment, base type, concrete material constituents, and slab geometry on the concrete pavement response. In this study, the primary motivation was to develop a time-dependent, analytical model to predict joint opening and movement that accounts for climatic effects on “young” JPCP. Another motivation is to seek potential refinement of current joint opening prediction algorithm used in AASHTO pavement design guide (AASHTO 1993).

Advancement on a joint opening prediction algorithm will benefit the design of dowelled and non-dowelled JPCPs. For example, the use of dowels is not necessary in lower traffic volume facilities if the joint opening can be kept to a minimum. On airports, it is more common for all contraction joints to be dowelled whereas non-dowelled joints could be used if more consideration was given in designing the maximum joint opening. Furthermore, most transverse joints need sealing in order to minimize the ingress of water and incompressible materials into the joint and pavement structure, which reduces the moisture-related distresses such as pumping and faulting and pressure-related distresses such as spalling and blowups (Federal Highway Administration 1990). One important criterion in selecting and installing appropriate joint sealant is the maximum joint opening over the entire pavement service life (Biel & Lee 1997, Huang 2004). Currently, the joint opening is approximated using Equation 1 from AASHTO pavement design guide (AASHTO 1993)

$$\Delta L = CL(\alpha \cdot \Delta T + \varepsilon) \quad (1)$$

where ΔL = joint opening due to temperature and moisture changes in concrete pavement (mm);
 L = slab length (mm); α = thermal coefficient of expansion/contraction of Portland cement concrete

(PCC) (strain/°C); ΔT = temperature change (°C); ε = PCC coefficient of drying shrinkage (mm/mm); C = adjustment coefficient to account for the slab-base frictional restraint (0.65 for stabilized bases and 0.8 for granular bases).

This equation is intended to give an approximation of the mean joint opening over a daily or yearly time interval, keeping in mind that the adjustment coefficient, C , was derived using limited field testing data (Minkarah et al. 1982). As a result, comparing measured field data with calculated values from Equation 1 can result in significant discrepancy. Morian et al. (1999) came up with the same conclusion based on data collected for the Long-Term Pavement Performance Program.

To capture the “dynamic” feature of joint opening due to temperature and moisture changes in PCC slab and slab-subbase frictional restraint, a mechanistic model is preferred. From a detailed literature review, an existing elasticity-based model was modified and implemented to account for the main contributing factors to the joint opening.

2 MODEL DEVELOPMENT

2.1 Slab-subbase interfacial restraint

To easily present the underlying analytical model, let x be the direction along PCC slab length, z be the direction along PCC slab thickness. z is measured positive downward and $z=0$ is at the mid-depth of slab. The ends of slab are located at $x=0$ and $x=L$. For symmetry of the problem, only half of the slab ($0 \leq x < L/2$) is analyzed. The coordinate system is shown in Figure 1.

Slab-subbase interaction serves as a restraint to joint opening, and proper characterization of this friction is critical for accurately predicting the joint opening in JPCP. A full contact condition between the slab and subbase is assumed in this paper. Field push-off test results suggest that the stress-slippage behavior of a slab-base interface can be satisfactorily approximated by a bilinear function as presented in Equation (2) below (Rasmussen & Rozycki 2001; Wimsatt et al. 1987).

$$\tau(x) = \begin{cases} \frac{\tau_0}{\delta_0} u(x) & \text{if } |u(x)| \leq \delta_0 \\ \tau_0 & \text{if } u(x) > \delta_0 > 0 \\ -\tau_0 & \text{if } u(x) < -\delta_0 < 0 \end{cases} \quad (2)$$

where $\tau(x)$ = slab-subbase interfacial friction at x (MPa), and stress sign convention is applied (Timoshenko & Goodier 1970); τ_0 = steady-state friction (MPa); δ_0 = slippage or displacement (mm) corresponding to the friction of τ_0 ; $u(x)$ = average displacement through PCC slab thickness (mm), $u(x) > 0$ means that slab contracts and $u(x) < 0$ means slab expansion for $0 \leq x < L/2$.

Equation (2) is plotted in Figure 2. Table 1 lists some typical values of τ_0 , δ_0 for different subbase types, and indicates that larger slab-subbase restraint and smaller threshold displacement δ_0 values exist in cement stabilized subbase compared to those in other types of subbase. This is one of the main reasons why JPCP with semi-rigid subbase are susceptible to environment-induced cracking at early ages.

2.2 1-D analytical model to computing the displacement field in PCC slab

Zhang and Li (2001) developed a one-dimensional (1-D) analytical model for predicting the shrinkage-induced stress in PCC slab using Equation 2 to describe slab-subbase restraint. In this paper, this model is modified to predict joint opening based on drying shrinkage and temperature changes (uniform and differential) in the concrete slab. The following summarizes the main results of this analytical model.

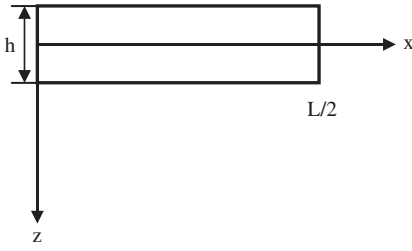


Figure 1. Coordinate system used in this model.

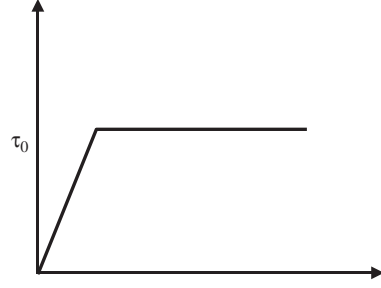


Figure 2. Bilinear Slab-subbase restraint model.

Table 1. Typical slab-subbase frictional restraint values for different types of subbase (after Rasmussen & Rozycki 2001).

Subbase Type	τ_0 (MPa)	δ_0 (mm)
Dense-Graded HMA (Rough)	0.069	0.25
Dense-Graded HMA (Smooth)	0.035	0.51
Cement Stabilized	0.103	0.025
Lime Treated Clay	0.010	0.76
Natural clay	0.007	1.00
Granular	0.014	0.51

The governing equilibrium equation is

$$\frac{d^2u}{dx^2} - \frac{\tau}{Eh} = 0 \quad (3)$$

where $\tau(x)$, $u(x)$ are defined in equation (2); E = elastic modulus of concrete (MPa) and h = the height of slab (mm).

Equation (3) plus appropriate boundary conditions (BCs) constitute a boundary value problem (BVP) for the unknown variable u . Rasmussen & Rozycki (2001) used the same equation along with appropriate BCs to calculate the thermal- and moisture-induced slab stresses using a finite difference scheme. Xin et al. (1992) also used the same equilibrium equation to approximate the structural response of continuously reinforced concrete pavement. Once the displacement field u is determined for the given BCs, the joint opening is simply equal to twice the $u(0)$.

Defining the appropriate BCs for the problem is required to derive the closed-form solution for the displacement u . There are two cases involved and their solutions are given as follows (Zhang & Li 2001).

Case 1: $|u(0)| < \delta_0$

The corresponding BVP for the displacement u is

$$\frac{d^2u}{dx^2} - \frac{\tau_0}{Eh\delta_0} u = 0 \quad (4)$$

subjected to two BCs

$$u\left(\frac{L}{2}\right) = 0, \quad \frac{du}{dx}(0) = \frac{\sigma_0}{E} + \varepsilon_e \quad (5)$$

where σ_0 = average axial stress at $x=0$ (MPa), usually taken to be zero at the joint face; ε_e = environment-induced strain due to uniform temperature and drying shrinkage changes (mm/mm) through the slab thickness.

The final result for u in this case is

$$u(x) = -\frac{1}{\beta} \left(\frac{\sigma_0}{E} + \varepsilon_e \right) \frac{e^{-\beta x} - e^{-\beta(L-x)}}{1 + e^{-\beta L}} \quad (6)$$

where $\beta = \sqrt{\frac{\tau_0}{Eh\delta_0}}$.

Case 2: $u(0) > \delta_0$ and $u(x_0) = \delta_0$ for $x_0 \in (0, L/2)$

In this case, only solutions for the slab contraction (i.e. $\varepsilon_e < 0$) are presented, and similar arguments can be extended for slab expansion.

(1) For $x \in (0, x_0)$

$$\frac{d^2 u_1}{dx^2} - \frac{\tau_0}{Eh} = 0 \quad (7)$$

subjected to two BCs

$$u_1(x_0) = \delta_0, \quad \frac{du_1}{dx}(0) = \frac{\sigma_0}{E} + \varepsilon_e \quad (8)$$

The solution for this BVP is

$$u_1(x) = \delta_0 + \frac{1}{2} \beta^2 \delta_0 (x^2 - x_0^2) + \left(\frac{\sigma_0}{E} + \varepsilon_e \right) (x - x_0) \quad (9)$$

where β is defined in Case 1.

(2) For $x \in (x_0, L/2)$

$$\frac{d^2 u_2}{dx^2} - \frac{\tau_0}{Eh\delta_0} u_2 = 0 \quad (10)$$

subjected to two BCs

$$u_2\left(\frac{L}{2}\right) = 0, \quad \frac{du_2}{dx}(x_0) = \frac{\sigma_{00}}{E} + \varepsilon_e \quad (11)$$

where σ_{00} = average axial stress at x_0 .

The solution for this BVP is

$$u_2(x) = -\frac{1}{\beta} \left(\frac{\sigma_{00}}{E} + \varepsilon_e \right) \frac{e^{-\beta x} - e^{-\beta(L-x)}}{e^{-\beta x_0} + e^{-\beta(L-x_0)}} \quad (12)$$

where β is defined in Case 1.

In order to determine $u(0)$, x_0 must be known, which can be obtained by applying the continuity condition of displacement at x_0 , i.e., $u_1(x_0) = u_2(x_0)$, one obtains

$$\delta_0 = -\frac{1}{\beta} \left[\beta^2 \delta_0 x_0 + \frac{\sigma_0}{E} + \varepsilon_e \right] \frac{e^{-\beta x_0} - e^{-\beta(L-x_0)}}{e^{-\beta x_0} + e^{-\beta(L-x_0)}} \quad (13)$$

x_0 can then be numerically solved by using a nonlinear equation solver, such as Newton-Raphson iterative method (Burden & Faires 2001).

The environment-induced strain, ε_e defined in Equation 5 consists of two components, i.e. $\varepsilon_e(t) = \varepsilon_T(t) + \varepsilon_{dry}(t)$, where ε_T = strain due to uniform temperature change through concrete slab thickness (mm/mm); and ε_{dry} = uniform drying shrinkage strain of concrete slab (mm/mm). The next two subsections focus on methods for predicting the thermal strain, ε_T and drying shrinkage strain, ε_{dry} .

2.3 Thermal strain, $\varepsilon_T(t)$

Thermal strain due to uniform change in temperature through the slab thickness at time t can be calculated using Equation 14

$$\varepsilon_T(t) = \alpha \cdot \Delta T(t) = \alpha \cdot (T_c(t) - T_{ref}) \quad (14)$$

where α is defined in Equation 1; $\Delta T(t)$ = uniform concrete slab temperature change ($^{\circ}\text{C}$); $T_c(t)$ = constant temperature through slab thickness ($^{\circ}\text{C}$); T_{ref} = reference temperature which may be equal to the final set or zero-stress temperature of PCC slab ($^{\circ}\text{C}$). Here, a positive value of $\varepsilon_T(t)$ means expansion while negative means contraction.

The measured and predicted temperature profile data through the slab thickness typically is nonlinear (Liang & Niu 1998, Wang et al. 2007). Any arbitrary nonlinear temperature profile can be decomposed into three components: a constant temperature, an equivalent linear temperature, and a nonlinear temperature component. Since the nonlinear strain causing component “does not precipitate either expansion or bending, but only produces thermal strains, which tend to distort the plate cross section” (Ioannides & Khazanovich, 1998), the effects of nonlinear temperature component on the joint opening is ignored in this paper.

The constant temperature, $T_c(t)$ and equivalent linear temperature component, $T_L(z, t)$ can be extracted from the measured pavement temperature profile, $T(z, t)$ using Equation 15 and 16 respectively, which are derived using the concepts of equivalent resultant force and moment, respectively (Ioannides & Khazanovich, 1998).

$$T_c(t) = \frac{1}{h} \int_{-h/2}^{h/2} T(z, t) dz \quad (15)$$

$$T_L(z, t) = T_{ref} + \frac{12z}{h^3} \int_{-h/2}^{h/2} zT(z, t) dz \quad (16)$$

2.4 Drying shrinkage, $\varepsilon_{dry}(t)$

This type of shrinkage is associated with the hardened concrete. The driving force to cause the drying shrinkage is the loss of water from the hardened concrete. In this paper, uniform drying shrinkage $\varepsilon_{dry}(t)$ through the thickness of the slab is assumed and calculated using Equation 17, which is proposed by American Concrete Institute (ACI) committee 209 (Mindess et al. 2003) for concrete’s free drying shrinkage

$$\varepsilon_{dry}(t) = \frac{t}{35 + t} \varepsilon_u \quad (17)$$

Where t is measured in days; ε_u = ultimate drying shrinkage strain value.

2.5 Effect of temperature curling strain on the joint opening

To calculate the joint opening due to the curling strain caused by the equivalent linear temperature component defined in Equation 16, a formula based on Westergaard’s curling deflection formulation is proposed in this paper.

Referring to Westergaard (1926), let y be the direction along concrete slab width, the deflection $Z(x, y)$ for a rectangular panel due to temperature curling is

$$Z(x, y) = f\left(y - \frac{B}{2}\right) + F\left(x - \frac{L}{2}\right) \quad (18)$$

where f , is the deflection function for the panel with infinite length and finite width B , and F is the deflection function for the panel with infinite width and finite length L . The explicit form for f is given in Equation 18 on page 208 in Westergaard (1926), and F can be analogously expressed as

$$F(x) = -z_0 \frac{2 \cos \lambda \cosh \lambda}{\sin 2\lambda + \sinh 2\lambda} \left[(-\tan \lambda + \tanh \lambda) \cos \frac{x}{l\sqrt{2}} \cosh \frac{x}{l\sqrt{2}} + (\tan \lambda + \tanh \lambda) \sin \frac{x}{l\sqrt{2}} \sinh \frac{x}{l\sqrt{2}} \right] \quad (19)$$

where the radius of relative stiffness, $l = \sqrt[4]{\frac{Eh^3}{12(1-\mu^2)k}}$, μ = Poisson's ratio of concrete, k = the modulus of subgrade reaction; $\lambda = \frac{L}{l\sqrt{8}}$; $z_0 = \frac{(1+\mu)l^2\alpha\Delta T}{h}$, $\Delta T = T_L(-\frac{h}{2}, t) - T_L(\frac{h}{2}, t)$, linear temperature component difference between the top and bottom slab, and $T_L(z, t)$ is given in Equation 16.

The temperature curling along the slab length direction is the main contributor to the joint opening thus the curling along slab width direction is ignored in this paper. The joint opening that is related to temperature curling, CW_{curl} can be approximated as

$$CW_{curl}(t) = \begin{cases} h \left| F' \left(\frac{L}{2} \right) \right| & \text{if } T_L \left(-\frac{h}{2}, t \right) < T_L \left(\frac{h}{2}, t \right) \\ -h \left| F' \left(\frac{L}{2} \right) \right| & \text{if } T_L \left(-\frac{h}{2}, t \right) > T_L \left(\frac{h}{2}, t \right) \end{cases} \quad (20)$$

where $F' \left(\frac{L}{2} \right)$ is the first derivative of F evaluated at $x = L$.

2.6 Steps involved in joint opening prediction

This section summarizes the main steps involved in the proposed analytical model to calculate the time-dependent joint opening.

Step 1: Calculate $T_c(t)$ and $T_L(z, t)$ from Equations 15 and 16 respectively, then calculate $\varepsilon_T(t)$ from Equation 14.

Step 2: Calculate $\varepsilon_{dry}(t)$ from Equation 17.

Step 3: Calculate $u(0)$ from Equation 6 by setting $x = 0$, $\varepsilon_e(t) = \varepsilon_T(t) + \varepsilon_{dry}(t)$ and $\sigma_0 = 0$.

Step 4: If $|u(0)| < \delta_0$, then go to Step 5; if $|u(0)| > \delta_0$, firstly calculate x_0 from Equation 13 by setting $\varepsilon_e(t) = \varepsilon_T(t) + \varepsilon_{dry}(t)$ and $\sigma_0 = 0$, then calculate $u_1(0)$ from Equation 9 by setting $x = 0$.

Step 5: Calculate $CW_{curl}(t)$ from Equation 20.

Step 6: The joint opening, $CW(t)$ can be calculated as

$$CW(t) = \begin{cases} 2u(0) + CW_{curl} & \text{if } |u(0)| < \delta_0 \\ 2u_1(0) + CW_{curl} & \text{if } |u(0)| > \delta_0 \end{cases} \quad (21)$$

3 APPLICATION OF MODEL

In this model calculation, the measured temperature data is taken from a field test section of a 254 mm (10 in.) thick slab with 4.57 m (15 ft) slab length and 3.66 m (12 ft) width, cast on June

Table 2. Material parameters used in the joint opening prediction.

Parameter	Value
Concrete setting temperature, T_{ref} (°C)	45
Coefficient of thermal expansion of concrete, α (1/°C)	10.35×10^{-6}
28-day Elastic modulus of concrete E_{28} (GPa)	25.9
Steady-State slab-subbase friction τ_0 (MPa)	0.052
Slab slippage δ_0 corresponding to τ_0 (mm)	0.38
Poisson's ratio	0.2
Ultimate drying shrinkage strain	7.8×10^{-4}
Composite modulus of subgrade reaction k (pci)	450

22, 2006 in Rantoul, Illinois, USA. The subbase is 406.4 mm (16 in.) thick Hot-Mix Asphalt. The pavement temperatures are measured at different depths of slab, i.e., surface, 1, 3, 5, 7 and 9 inches at 15-minute intervals. The model testing period used in this paper started at 12:08 a.m. on July 01, 2006, ended at 12:38 p.m. on July 13, 2006 (1203 time steps). The slab was constructed on June 22, 2006 and therefore the predicted opening on July 1, 2006 will be greater than zero. The assumed material parameters in the model calculation are given in Table 2.

Also the time-dependent elastic modulus of concrete, E_c is approximated by (Mosley & Bungey 1990)

$$E_c = E_{28} [0.52 + 0.15 \ln t] \quad \text{for } t \leq 28 \quad (22)$$

where E_c is the elastic modulus at time t (in days).

The measured pavement temperature at 25.4 mm (1 in.), 127 mm (5 in.), 228.6 mm (9 in.) and the calculated constant strain causing (mean) temperature are plotted versus time in Figure 3. Figure 4 presents the predicted joint opening values with (red) and without (black) temperature curling correction along with the measured ones (blue), respectively. Figure 3 indicates that the mean temperature varied from 22.5°C to 36°C approximately. Figure 4 shows that the predicted joint opening changed between 1.02 mm (0.04 in.) and 2.29 mm (0.09 in.) approximately under the above-mentioned varying mean temperature and increasing drying shrinkage given in Equation 17, while the measured openings vary between 0.76 mm (0.03 in.) and 1.9 mm (0.075 in.) during the monitoring period.

4 DISCUSSION

There are many factors influencing joint opening prediction, such as the slab's temperature profile, concrete setting temperature, the drying shrinkage over the first few weeks and months, the slab-subbase interfacial restraint and concrete time-dependent material properties (e.g. elastic modulus, creep and stress relaxation). During the first 220 hours of the model calculation (Figure 4), the predicted maximum joint opening matches well with the measured values for each daily cycle. However the measured daily joint movement, i.e. difference between maximum and minimum joint opening, was under-predicted by the model. The main reason for this discrepancy is the drying shrinkage model does not allow for temperature-dependent reversible shrinkage strain. It is the reversible part that tends to decrease joint opening especially during the day. This reversible shrinkage strain has been studied for concrete and is referred to as the hygrothermal strain (Grasley 2006). The current free drying shrinkage model used in this paper does not adequately capture the hygrothermal strain or the concrete's tensile creep, which are both currently under investigation.

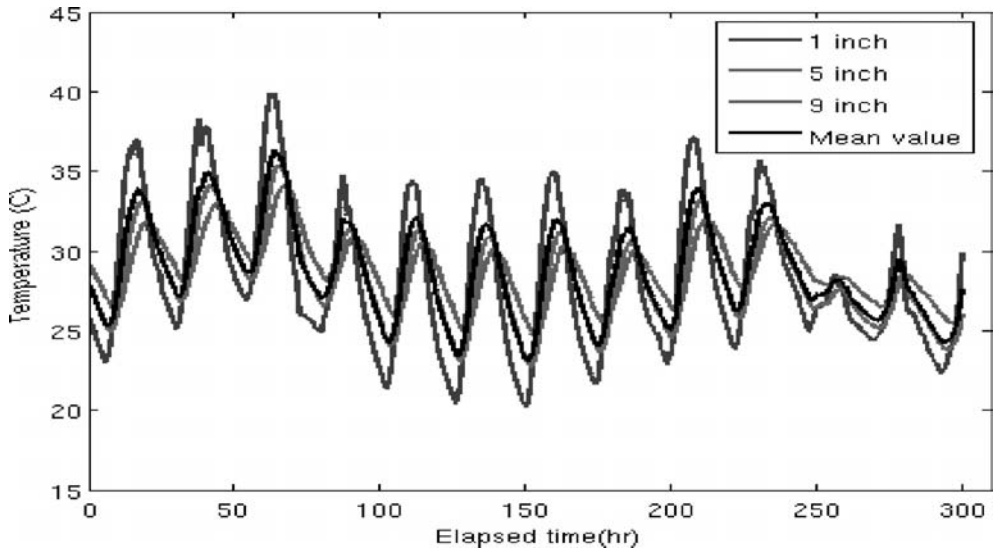


Figure 3. Measured pavement temperature at different slab depths and calculated mean temperature.

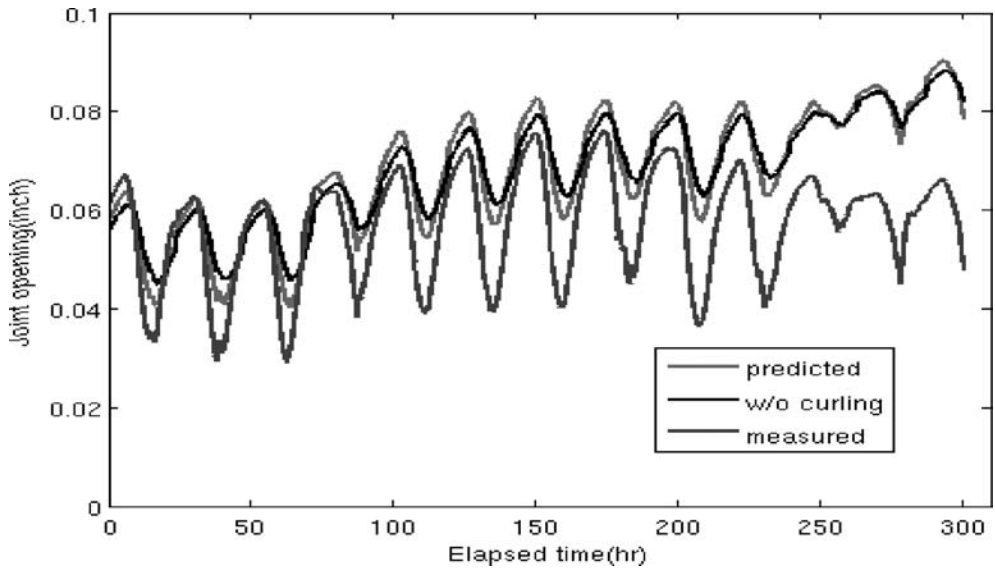


Figure 4. Measured and predicted joint opening values using the proposed model.

5 CONCLUSION

A rational approach to predicting the time-dependent joint opening in JPCP is systematically presented in this paper. The proposed analytical model for joint opening takes the effects of the environment, subbase type, concrete material constituents, and slab geometry into consideration. In particular, a closed-form solution to correct the joint opening value due to temperature curling is also proposed. Initial model calculations using measured slab temperature profiles and assumed material parameters suggest that the proposed analytical model generate reasonable joint opening value for JPCP.

REFERENCES

- Federal Highway Administration. 1990. *Concrete Pavement Joints*, US Department of Transportation Technical Advisory No. T 5040.30.
- AASHTO. 1993. *AASHTO Guide for Design of Pavement Structures*. Washington, D.C., 1993.
- Biel, T.D. & Lee, H. 1997. Performance Study of portland cement concrete pavement joint sealants. *ASCE Journal of Transportation Engineering* 123(5): 398–404.
- Burden, R.L. & Faires, J.D. (Seventh Edition) 2001. *Numerical Analysis*. Brooks/Cole.
- Grasley, Z. 2006. *Measuring and Modeling of Time-Dependent Response of Cementitious Materials to Internal Stress*. Ph.D. thesis, University of Illinois, Urbana, IL.
- Huang, Y.H. (Second Edition) 2004. *Pavement Analysis and Design*. Upper Saddle River: Pearson Education, Inc.
- Ioannides, A.M. & Khazanovich, L. 1998. Nonlinear temperature effects on multilayered concrete pavements. *ASCE Journal of Transportation Engineering* 124(2): 128–136.
- Liang, R.Y. & Niu, Y.Z. 1998. Temperature and curling stress in concrete pavements: analytical solution. *ASCE Journal of Transportation Engineering* 124(1): 91–100.
- Mindess, S., Young, J.F. & Darwin, D. (Second Edition) 2003. *Concrete*. Upper Saddle River: Pearson Education, Inc.
- Minkarah, I.A., Cook, J.P. & McDonough, J.F. 1982. Magnitude of horizontal movement in jointed concrete pavements. In *Transportation Research Record* 821: 61–67. TRB, National Research Council, Washington, D.C.
- Morian, D.A., Suthahar, N. & Stoffels, S.M. 1999. Evaluation of rigid pavement joint seal movement. In *Transportation Research Record* 1684: 25–34. TRB, National Research Council, Washington, D.C.
- Mosley, W.H. & Bungey, J.H. 1990. *Reinforced Concrete Design*. London: Macmillan Press.
- Timoshenko, S.P. & Goodier, J.N. (Third Edition) 1970. *Theory of Elasticity*. McGraw-Hill, Inc., page 4.
- Rasmussen, R.O. & Rozycki, D.K. 2001. Characterization and modeling of axial slab-support restraint. In *Transportation Research Record* 1778: 26–32. TRB, National Research Council, Washington, D.C.
- Wang, D., Roesler, J.R. & Guo, D. 2007. An analytical approach to predicting temperature fields in multi-layered pavement systems, submitted to the *Transportation Research Board 2008 Annual Meeting*.
- Westergaard, H.M. 1926. Analysis of stresses in concrete pavements due to variations of temperature. *Proc. Highway Research Board*, Vol. 6: 201–215.
- Wimsatt, A.W., McCullough, B.F. & Burns, N.H. 1987. *Methods of analyzing and factors influencing frictional effects of subbases*. Center for Transportation Research, University of Texas at Austin, Research Report 495-2F.
- Xin, D., Zollinger, D.G. & Ray, J.W. 1992. One-Dimensional model for analysis of CRC pavement growth. *ASCE Journal of Transportation Engineering* 118(4): 557–575.
- Zhang, J. & Li, V.C. 2001. Influence of supporting base characteristics on shrinkage-induced stresses in concrete pavements. *ASCE Journal of Transportation Engineering* 127(6): 455–462.

Experimental behavior of construction joints in FRC pavements

L. Cominoli

University of Brescia, Italy

A. Meda

University of Bergamo, Italy

G.A. Plizzari

University of Brescia, Italy

ABSTRACT: The behavior of construction joints in Fiber Reinforced Concrete (FRC) pavement is analyzed herein by mean of experimental tests. The joints system is obtained by inserting a dowel connector between two concrete blocks representing a pavement portion. In order to simulate the pavement subgrade, the specimens have been placed on cork bricks that were previously tested for determining their stiffness. Two different pavement thicknesses as well as two different fiber contents have been considered. The results shows the effectiveness of the fiber reinforcement in increasing the bearing capacity of the pavement, particularly when a smaller pavement thickness is adopted.

1 INTRODUCTION

One of the main fields, where Fiber Reinforced Concrete (FRC) has been successfully applied in substitution of conventional reinforcement (welded mesh), concerns slabs on grade (Kukreja, 1987; Falkner et al., 1995; Beckett, 1999; Meda & Plizzari, 2004). In fact, structural fibers (i.e. proper fibers adopted with an adequate dosage) increase mainly concrete toughness that is particularly important in statically indeterminate structures, as slabs on grade, since it facilitates a stress redistribution after the cracking of the concrete matrix (ACI, 1996; Ahmad et al., 2004; di Prisco et al., 2004).

Industrial pavements, roads, parking areas and airport runways are often constituted by slabs on grade under severe conditions with concentrated and dynamic loads. Therefore, pavements should be engineered with a proper attention devoted to subbase preparation, concrete mix design, and a thorough analysis of loading conditions, joint spacing for shrinkage and thermal effects (ACI, 2001; Walker & Holland, 2001).

Since heavy concentrated loads from industrial machinery and shelves cause intensive cracking and excessive deformation of industrial floors, a diffused fiber reinforcement may help the structural behavior. In fact, fibers prevent microcracks from becoming macrocracks and thus protect concrete from aggressive environmental attack. In concrete pavements, some types of (low modulus) fibers are also particularly suitable both for limiting shrinkage effects and for increasing fatigue resistance (Zollo & Hays, 1991; Plizzari et al., 2000).

The substitution of conventional reinforcement with structural fibers allows a reduction of the working time for placing reinforcing bars (rebars) or welded mesh and, as a consequence, a reduction of the construction costs (Meda & Plizzari, 2004). Furthermore, the top layer of conventional reinforcement can hardly remain in the correct position during construction operations (concrete pouring) but this is no longer a problem when fiber reinforcement is adopted.

Many of the problems associated with pavements are related to maintaining joint integrity; in fact the performance of concrete pavements depends to a large extent upon the satisfactory performance of the joints (Concrete Pavement Joints, 1990).

Distresses that may result from joint failure include faulting, punching, spalling, corner breaks, and mid-panel cracking. Characteristics that contribute to satisfactory joint performance, such as adequate load transfer and proper concrete consolidation, have been identified through research and field experience. Loads applied by traffic must be effectively transferred from one slab to the next in order to minimize vertical displacements at the joint. Reduced deflections decrease the potential for pumping of the subbase material and faulting. The principal method adopted for developing load transfer across a joint is the use of a load transfer device, such as a dowel bar (Iowa State University, 2004).

Moreover, the joint stiffness and strength remarkably influence the overall slab behavior in terms of bearing capacity and stiffness (Belletti et al., 2004). A better knowledge of joint behavior is essential for the correct design of such kind of structures.

In order to experimentally investigate the behavior of construction joints with dowel bars, several specimens, representing a portion of pavement across a joint, were tested under a concentrated load. Specimens had two different thicknesses (200 and 350 mm) and were made with different contents of steel fibers. Since designers often consider pavements as slabs on an elastic subgrade (Winkler soil model; Westergaard, 1926), the specimens were placed on elastic supports (cork bricks) reproducing this design assumption. In order to emphasize the role of steel fibers, experimental results show the comparison between the joint behavior of plain and fiber reinforced concrete as well as the effects of the load transfer across the joint. Reference specimens were made of plain concrete (without any welded mesh) in order to better evidence the role of the fibers on the concrete matrix.

2 TESTING SET-UP AND SPECIMEN PREPARATION

The testing set-up adopted for determining the joint behavior is shown in Figure 1: three concrete blocks having a length of 1000 mm, a width of 500 mm and a thickness of 200 or 350 mm, were connected by means of a steel bar (dowel) having a diameter of 20 mm. A point load was applied in the middle of the central block by means of a screw jack. The dowel bar was embedded in the central block and continued with an unbonded length of 500 mm (obtained by means of plastic

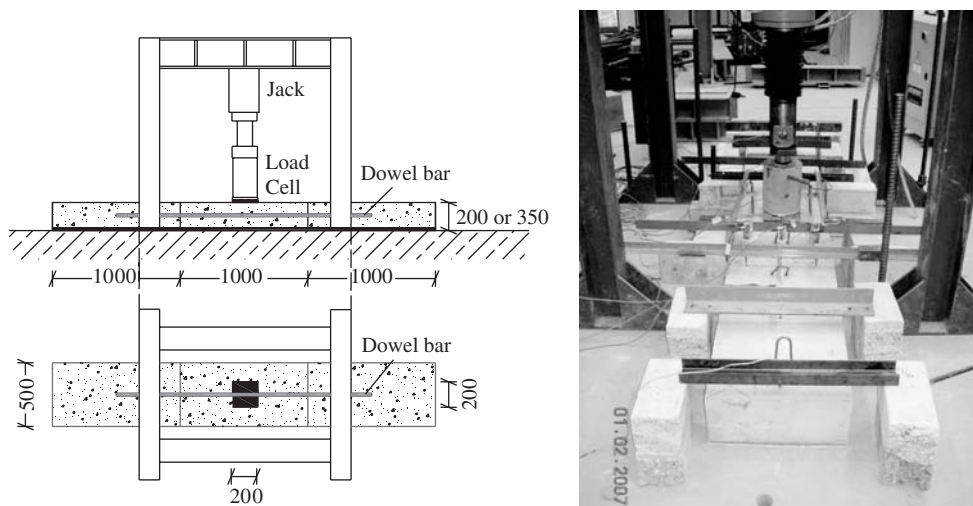


Figure 1. View of the experimental set-up for the tests on construction joints (measures in mm).

tubes) in the lateral blocks. This experimental system aims to represent a portion of pavement with two pavement joints symmetrically placed respect to the applied load (Fig. 2).

The dowel bar is placed in the centroid of the transverse section of the pavement. In order to ensure a correct alignment of the bars, the three concrete blocks were aligned in wooden moulds (Fig. 3). As mentioned above, the specimens were placed on cork bricks in order to simulate a Winkler soil. The bricks layout was determined in order to have a stiffness typical of pavement subgrades (0.076 N/mm^3); the stiffness of the cork bricks was experimentally determined, as described in §3.

Specimens were made of steel fiber reinforced concrete having two fiber contents: 30 kg/m^3 and 60 kg/m^3 , corresponding to a volume percentage (V_f) of 0,38% and 0,76%, respectively. Some specimens made of plain concrete were also tested to obtain reference values. The steel fibers have a hooked geometry, a length (l_f) of 50 mm and a diameter (ϕ_f) of 1.0 mm (aspect ratio $l_f/\phi_f = 50$).

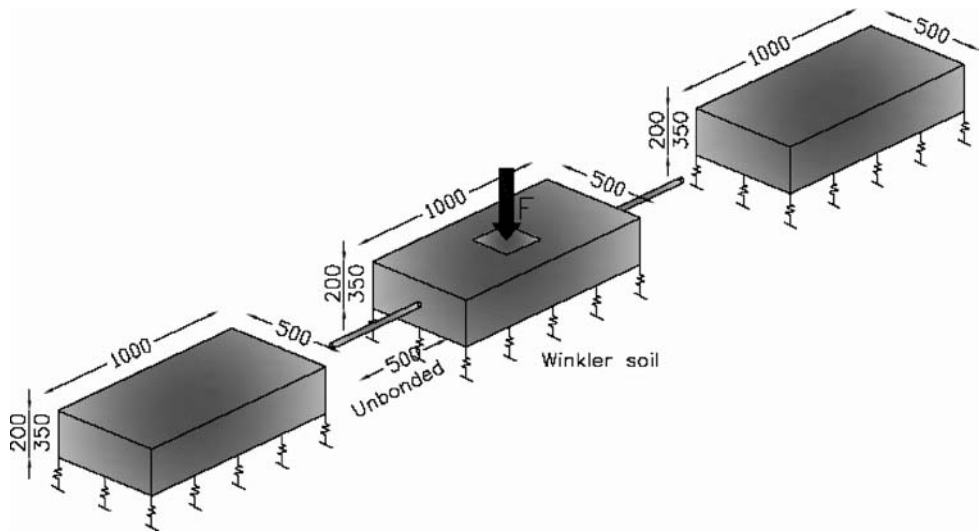


Figure 2. Pavement joints symmetrically placed respect to the applied load (measures in mm).



Figure 3. Wooden moulds with the reinforcing bars.

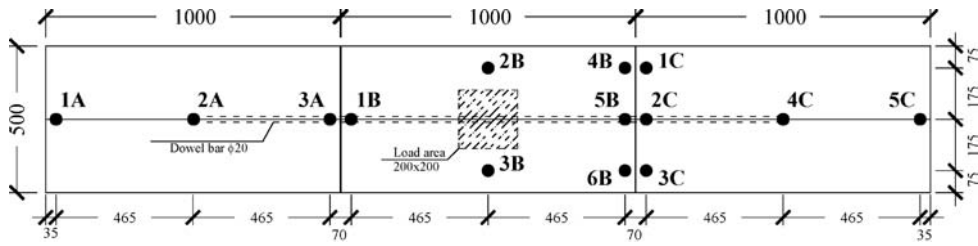


Figure 4. Instrumentation adopted during the tests (top view; measures in mm).

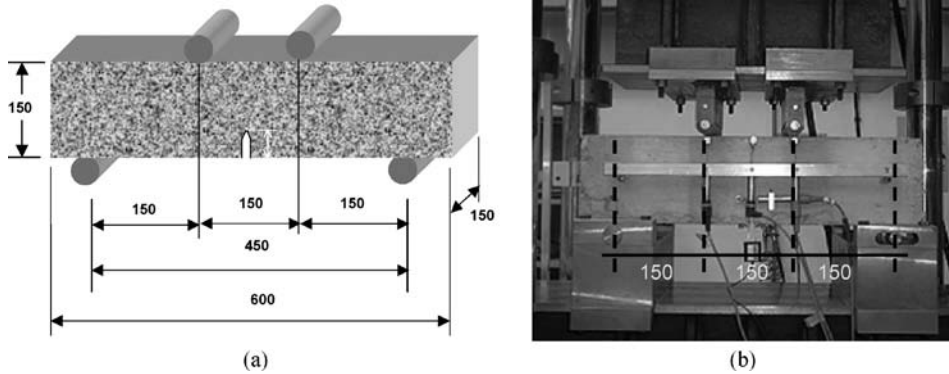


Figure 5. Geometry (a) and instrumentation (b) of the notched specimen for the bending tests, according to UNI 11039 (2003).

The concrete matrix is the same for the three materials, with a cubic compressive strength equal to 41.2 MPa and a Young's modulus equal to 35.2 GPa (mean values).

Figure 4 shows transducers (Linear Variable Differential Transformers, LVDT) position for recording the vertical displacement and determining the deformation of the specimens.

In order to determine the fracture properties of the adopted materials, four notched beams (150 × 150 × 600 mm) for every material were tested under four point bending, according to the Italian Standard (UNI 11039, 2003; Fig. 5) that is very similar to the CEN Standard (2005). A notch with a depth of 45 mm was placed at mid-span (Fig. 5a). Fracture tests were carried out with a servo-hydraulic testing machine by using the Crack Mouth Opening Displacement (CMOD) as a control parameter, which was measured by means of a clip gauge positioned through the notch. Additional LVDTs were used to measure the Crack Tip Opening Displacement (CTOD) and the vertical displacement at the beam mid-span and under the load points (Fig. 5b).

The results of the fracture tests are summarized in Figure 6a: it should be noted that fiber content remarkably influences the concrete toughness (evidenced by the post-peak strength) while the peak stress is not significantly influenced by the presence of fibers (it mainly depends on the tensile strength of the concrete matrix; Fig. 6b).

3 SUBGRADE MODELING

Preliminary experiments on the cork bricks adopted for the subgrade were performed in order to assess their stiffness. All the square bricks, having a side of 100 mm and a thickness of 20 mm, were loaded in compression and their stiffness was measured (Fig. 7). In Figure 8, a typical load-displacement curve is shown: it can be noticed that the behavior is almost linear-elastic; therefore, they could be used successfully to reproduce an elastic subgrade. Since tests were performed on

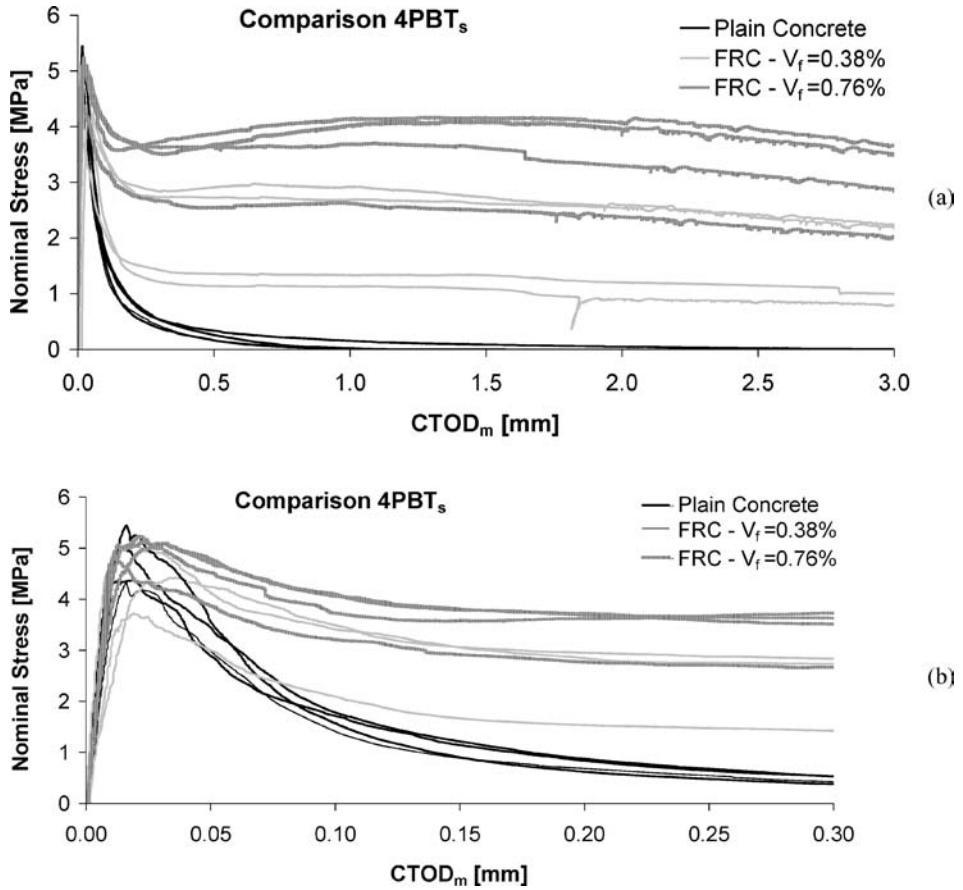


Figure 6. Comparison of the nominal stress versus CTOD_m curves (a) and peak stress versus CTOD_m curves (b) obtained from four point bending tests on plain concrete and FRC specimens.

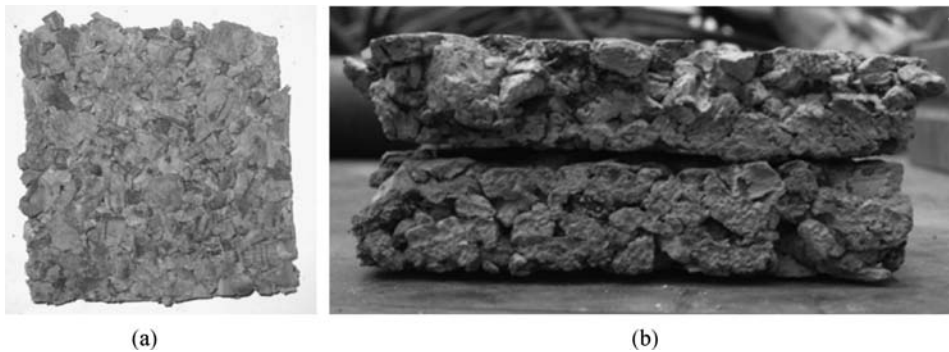


Figure 7. Cork bricks adopted to simulate a Winkler soil: single layer (a) and double layer (b).

all the cork bricks, the ones having a slightly different stiffness have been discarded. The average stiffness of a single brick was equal to 1820 N/mm. The layout was defined as shown in Figure 9a by obtaining a subgrade stiffness equal to 0.076 N/mm³ (similar to that used in previous researches; Sorelli et al. 2006). For the tests on block joints with a thickness of 350 mm, the maximum

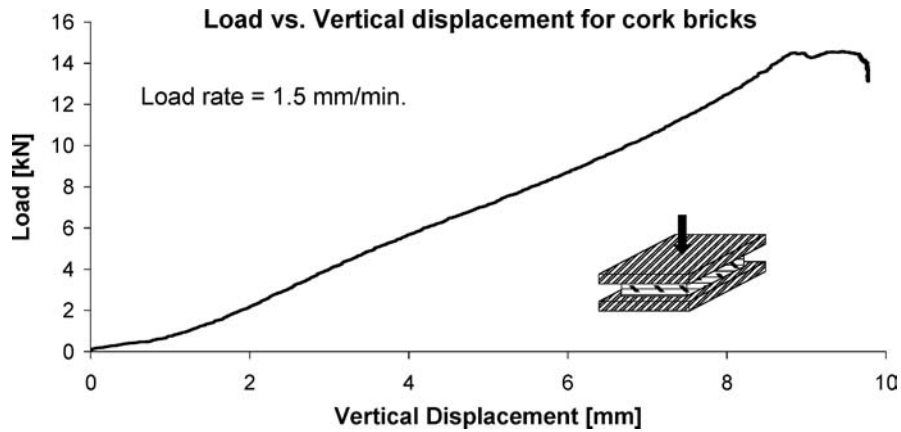


Figure 8. Typical load versus vertical displacement curve obtained from a compressive test on a cork brick.

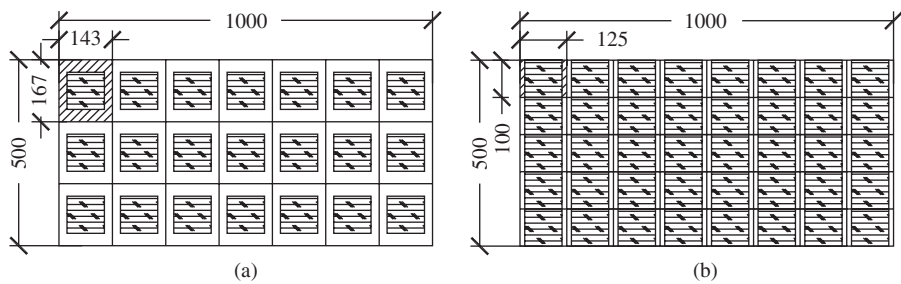


Figure 9. Layout of the cork bricks for the tests on 200 mm (a) and 350 mm thick block (b).

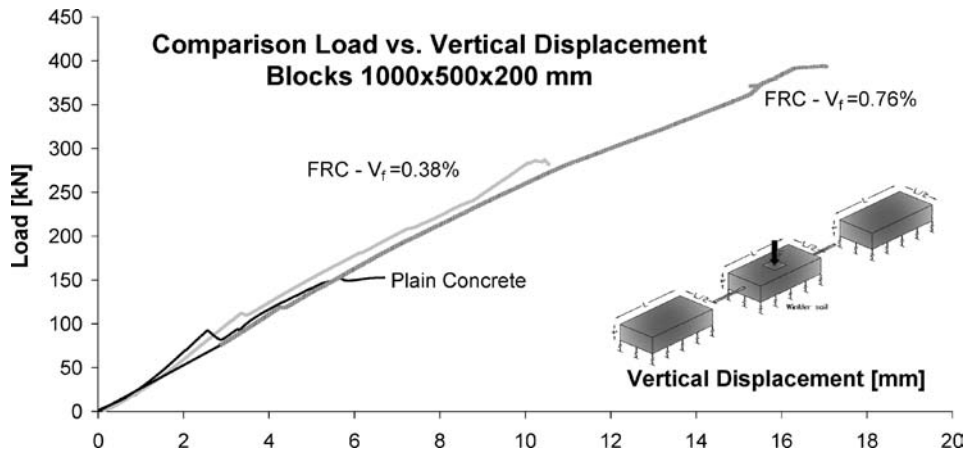


Figure 10. Load vs. vertical displacement curves for the blocks with 200 mm thickness.

displacement of the cork bricks was higher than the linear elastic limit; since this was considered not acceptable, two bricks were superimposed in order to obtain a thickness of 40 mm (Fig. 7b).

For this new subgrade system, the average stiffness, experimentally determined (on a couple of bricks), is equal to 940 N/mm and a new layout was determined (Fig. 9b) in order to obtain a subgrade stiffness similar to previous tests (0.075 N/mm³).

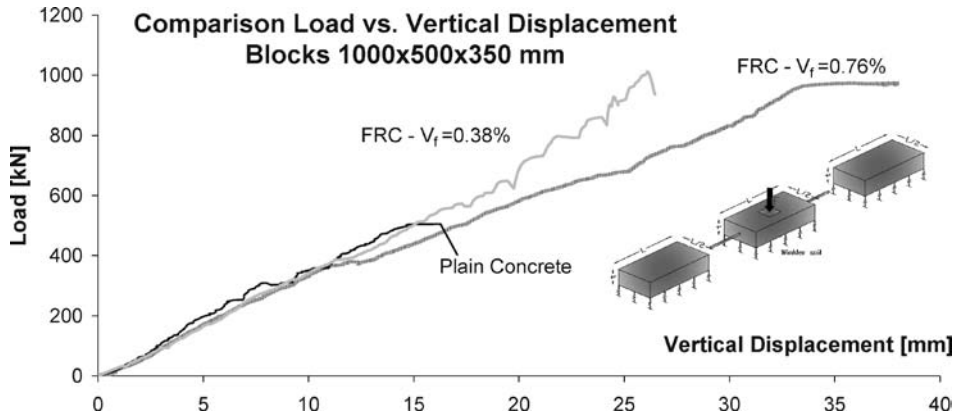


Figure 11. Load vs. vertical displacement curves for the blocks with 350 mm thickness.

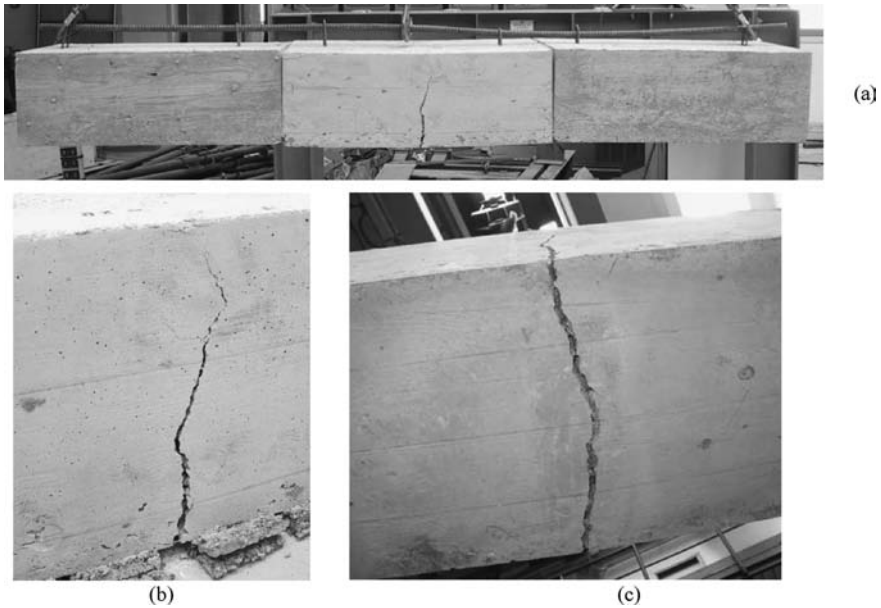


Figure 12. Final crack pattern for FRC elements with a volume fraction of fibers equal to 0,38%: lateral (a, b) and bottom view (c).

4 RESULTS

Experimental results from specimens having a thickness of 200 mm and 350 mm are shown in Figures 10 and 11 respectively, where the load versus displacement curves are plotted. One test for each type of material was performed. The displacement refers to the vertical displacement of the top surface under the point load and it is obtained as the average of the measure in points 2B and 3B of Figure 4.

It can be noticed that, in thinner elements (200 mm), fibers remarkably increase the bearing capacity of the specimen (almost three times, when 60 kg/m^3 are used, with respect to plain concrete; Fig. 10). However, the stiffness is approximately the same for the three materials since it is mainly provided by the uncracked concrete matrix; furthermore, the stiffness remains constant up to failure. Structure's collapse occurs after the propagation of a single flexural crack along the mid section of the central pavement element, as shown in Figure 12.

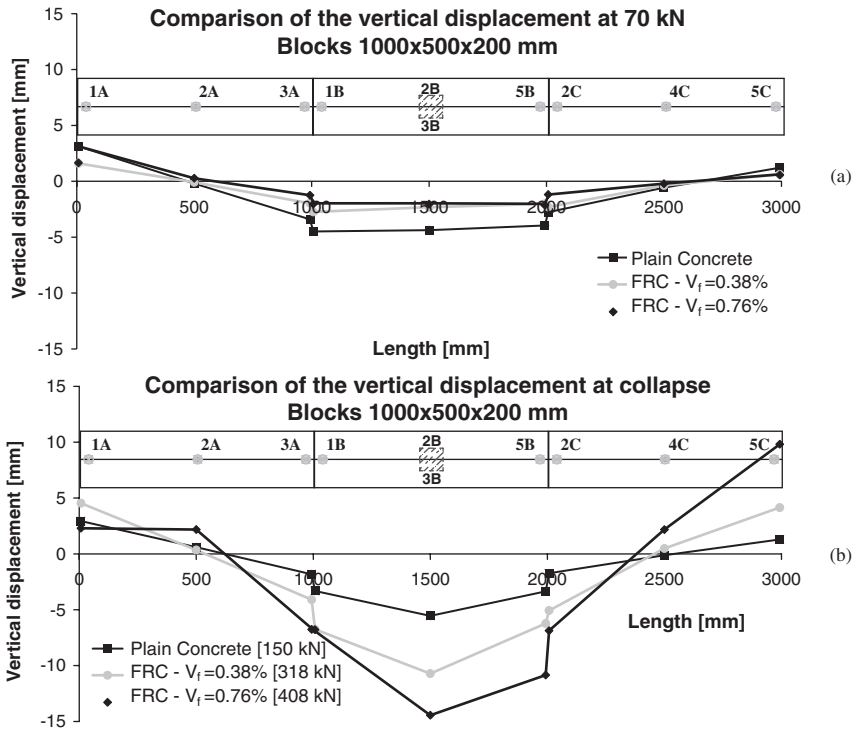


Figure 13. Vertical displacements measured in specimens with a thickness of 200 mm under a load of 70 kN (a) and at collapse (b).

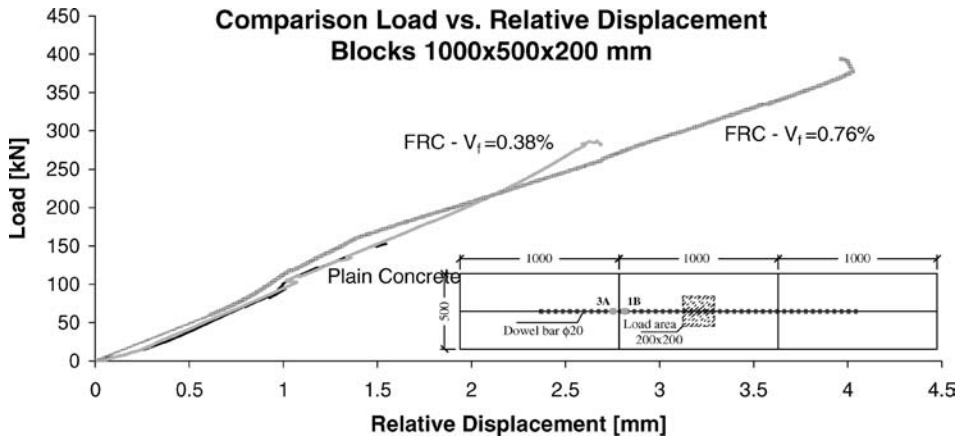


Figure 14. Comparison of the relative vertical displacement across the joint of specimens having a thickness of 200 mm.

In structures with a higher thickness (350 mm), the effect of the fiber content is less important, as shown in Figure 11, even if a remarkable difference is present between plain and FRC specimens.

Figure 13 shows the vertical displacement of the three concrete blocks during the tests; one can notice that, under service conditions, the three concrete blocks move as rigid elements: the central one vertically translates while the lateral ones tend to rotate.

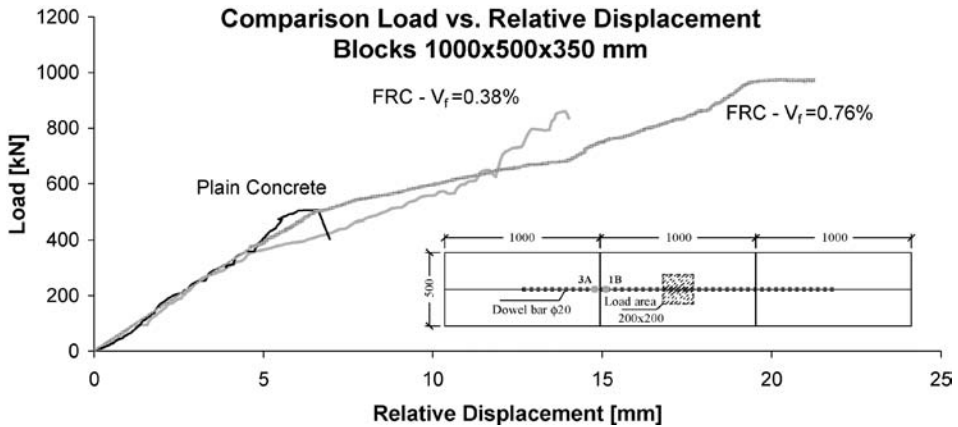


Figure 15. Comparison of the relative vertical displacement for the blocks having a thickness of 350 mm.

In order to evaluate the stiffness of the joint, the load is plotted versus the relative displacement (3A and 1B transducers in Figure 4) across the joint in Figures 14 and 15; it should be mentioned that the plotted displacement includes the deformation of the plastic tube used to make one part of the dowel bar unbonded (Fig. 3). One can notice that, for the pavement having a thickness of 200 mm, the relative displacement is approximately linear up to failure and is very similar for the three different materials (Fig. 14). For the pavement with a thickness of 350 mm, the relative displacement is similar only for lower load levels while it became irregular for higher load levels, where cracking phenomena occur and influence the overall behavior of the specimens (Fig. 15). A similar behavior was obtained for the other joint, where relative displacements were measured between points 4B-1C, 5B-2C and 6B-3C (Fig. 4).

5 CONCLUDING REMARKS

Fiber Reinforced Concrete is now a reality for concrete pavements improvement because of its several advantages in terms of reduced labor time and of durability due to a better crack control. Since cracking phenomena may be presents around a pavement joint, fiber reinforcement may also be helpful in joint behavior.

This paper presents results from an experimental program on pavement blocks with two joints reinforced with a dowel bar. Preliminary tests were performed on specimens with two different fiber contents as well as on plain concrete specimens that are considered as the reference specimens.

A special experimental set-up was prepared and the elastic subgrade was simulated by using cork bricks whose stiffness was experimentally determined. A local load was applied on the pavement by using a screw jack.

The stiffness of the joint with a dowel connector (unbonded at one end), which is useful for a correct pavement design, was experimentally determined. Results also show that fiber reinforcement remarkably increases the bearing capacity of pavements (with respect to plain concrete) while the above mentioned joint stiffness mainly depends on the uncracked concrete matrix.

Further tests will be performed in order in order to verify the bearing capacity of the dowel bar in joints between FRC pavements; joint collapse will be achieved by testing pavement blocks with a smaller thickness or by using a dowel bar with a larger diameter.

ACKNOWLEDGEMENTS

The Authors wish to express their gratitude and sincere appreciation to the Ministry of University and Research (MIUR) for financing this research work with the national project PRIN 2004 “Fiber-Reinforced Concrete for Strong, Durable and Cost-Saving Structures and Infrastructures”.

A special acknowledgement goes to Mr Luca Balestri and Mr. Oluwaseeun Taiwo for their assistance in carrying out the experiments. The Authors would also like to thank the technicians of the Laboratory P. Pisa of the University of Brescia for their help in the experimental work.

REFERENCES

- ACI Committee 544, 1996. *State of the art Report on Fiber Reinforced Concrete*, ACI 544.1R-96, American Concrete Institute, Farmington Hills, Michigan, 66 pp.
- ACI 360R-92, 2001. *Design of Slabs on Grade*, in ACI Manual of Concrete Practice, American Concrete Institute: Farmington Hills, Michigan, 57 pp.
- Ahmad, A., di Prisco, M., Meyer, C., Plizzari, G.A. & Shah, S., Eds., 2004. Proceedings of the International Workshop Fiber Reinforced Concrete: From theory to practice, Bergamo (Italy), 24–25 Sept. 2004, Starrylink, 222 pp.
- Beckett, D. *A comparison of Thickness design methods for concrete industrial ground floors*. 4th International Colloquium on Industrial Floor, January 1999, pp. 12–16.
- Belletti, B., Cerioni, R. & Plizzari, G.A., 2004. *Fracture in SFRC slabs on grade*. Proceedings of BEFIB 2004, the 6th RILEM Symposium on Fibre Reinforced Concretes (FRC), Varenna (Italy), 20–22 Sept., RILEM PRO 39, pp. 723–732.
- CNR – Italian National Research Council, 2006. Guidelines for the design, construction and production control of fiber reinforced concrete structures, 59 pp.
- Concrete Pavement Joints T 5040. 30. Technical advisory, U. S. Department of Transportation, Federal Highway Administration, November 30, 1990.
- Concrete Paving Workforce. Reference n° 3. *Concrete Pavement Joint Sawing, Cleaning, and Sealing*. Center for Portland Cement Concrete Pavement Technology, Iowa State University Eds., November 2004, 6 pp.
- di Prisco, M., Felicetti, R. & Plizzari, G.A. Eds., 2004. Proceedings of the 6th RILEM Symposium on Fibre Reinforced Concretes (FRC), BEFIB 2004, RILEM PRO 39, 1514 pp. 20–22 Sept. 2004, Varenna (Italy).
- CEN (2005). Test method for metallic fibered concrete – Measuring the flexural tensile strength (limit of proportionality (LOP), residual strength. EN 14651. European Committee for Standardization.
- Falkner, H., Huang, Z. & Teutsch, M. 1995. Comparative Study of Plain and Steel Fiber Reinforced Concrete Ground Slabs. *Concrete International*, 17 (1), pp. 45–51.
- Kukreja, C.B. 1987. Ultimate Strength of Fiber Reinforced Concrete Slabs. Proceedings of International Symposium on Fiber Reinforced Concrete, 16–19 December 1987, Madras, pp. 237–255.
- Meda, A. & Plizzari, G.A. 2004. New Design Approach for Steel Fiber-Reinforced Concrete Slabs-on-Ground Based on Fracture Mechanics. *ACI Structural Journal*, 101 (3), pp. 298–303.
- Plizzari, G.A., Cangiano, S. & Cere, N. 2000. Post-peak behavior of fiber reinforced concrete under cyclic tensile loads. *ACI Materials Journal*, 97 (2): pp. 182–192.
- RILEM TC 162 TDF, 2000. Test and Design Method for Steel Fiber Reinforced Concrete – Recommendations, *Materials and Structures*, 33 (225), pp. 3–5.
- RILEM TC 162 TDF, 2000. Sigma-Epsilon design method, *Materials and Structures*, 33 (226), pp. 75–81.
- Sorelli, L., Meda, A., Plizzari, G.A., & Rossi, B. 2004. Experimental investigation on slabs on grade: steel fibers vs. conventional reinforcement, Proceedings of BEFIB 2004, the 6th RILEM symposium on FRC, 20–22 Sept. 2004, Rilem Pro 39, Varenna (Italy), pp. 1083–1093.
- Sorelli, L., Meda, A. & Plizzari, G. A. 2006. Steel fiber concrete slabs on grade: a structural matter. *ACI Structural Journal*, 103 (4): pp. 551–558.
- UNI 11039, 2003. Steel fibre reinforced concrete – Part I: Definitions, classification specification and conformity – Part II: test method for measuring first crack strength and ductility indexes, Italian National Board for Standardization (Italy).
- Walker, W.W. & Holland, J.A. 2001. Design of unreinforced slabs-on-ground: made easy. *Concrete International*, 23 (5), May 2001: pp. 37–42.
- Westergaard, H.M. Stresses in concrete pavements computed by theoretical analysis. *Public Roads*, 7 (2), (1926), pp. 25–35.
- Zollo, R.F. & Hays, C.D. 1991. *Fibers vs. WWF as Non-Structural Slab Reinforcement*. *Concrete International*, 13 (11): pp. 50–55.

Induction of joints in concrete pavements

J.R. Vázquez

A.A. FAROBEL, Madrid, Spain

ABSTRACT: To induce a crack in concrete, a section of pavement must be debilitated. Before the pouring of concrete we lay out the JRI+ device which causes a crack in this section of concrete by shrinkage. The crack's shape will: 1. Transfer the loads and avoid the relative vertical displacements between adjacent slab edges. 2. Have horizontal or close to horizontal plain zones near the middle plane of the slab. These horizontal zones will have enough area to reach small stresses and to guarantee its durability. 3. Have the largest possible support between the slabs. The support surface between slabs will be inclined. The inclination will alternatively vary from one side to the other of the crack's superficial line. In this way, the support will be mutual between adjacent slabs. The crack has to be watertight, avoid the pumping and ground erosion, and the incoming water from above the crack. The application of a rubber joint on the superior portion of the induction device of the crack will supply a permanent watertight seal. The results taken by the Falling Weight Deflectometer (FWD) are shown in a previous test before the execution of the work. A method will be described to reduce the spalling. The top last centimetres of the concrete surface will be separated with a bar. It will cut the fresh concrete.

1 INTRODUCTION

1.1 Background

The joint system (JRI+) presented herein takes advantage of the natural development of shrinkage in concrete to induce the formation of joints along the projections of previously placed system devices.

This system induces in-situ concrete pavement with an efficient interlocking indentation among the slab elements resulting from the shrinkage phenomenon from the vertical loads. These joints have two characteristic missions: to transfer the loads between slabs and to waterproof the pavement. The slabs form a three-dimensional "puzzle" that prevents vertical differential displacements from occurring among their edges. Up to now, this joint system has been used satisfactorily for concrete pavements in urban roads and highways, as well as in tramway tracks and in harbor and airport platforms. Railways, channels, tunnels, dams, culverts and dikes are potential areas of future application.

1.2 What does it involve?

The system involves the development of a hinge between the adjacent sides of a crack induced in-situ in the concrete pavement slab. It is based on the laid out work along the joint lines, of a device that takes advantage of the retraction phenomenon to produce an alternative indentation along the joints.

The procedure complements itself with a rubber band (gum) element that facilitates the formation of the fissure and prevents seepage of water into the sub-grade. This rubber band can be fixed to



Figure 1. Resulting slab with interlocking hinged boundaries.



Figure 2. Core with induced crack by the JRI+ system.

the upper part of the previously mentioned joint device, making the traditional cutting and sealing unnecessary.

This new system induces the crack in the concrete produced by shrinkage, weakens the concrete where it is placed, and controls the crack's shape.

The result is a three-dimensional load transfer system as shown in Figure 1.

The strength to shear of the protuberance has been tested by Laboratory Technology Structures of polytechnic University Cataluña (Spain) "Laboratorio de Tecnología de Estructuras de la Universidad Politécnica de Catalunya" (Universitat Politècnica de Catalunya, 2005). The ratio between the service stress and the breaking stress is approximately 4. This provides a high safety factor and therefore the fatigue life of this transfer device may be considered indefinite. The elements which induce the crack are made of plastic and they are assembled with #3 deformed bars.

Figure 2 demonstrates a crack that has been induced by the JRI+ device. Note that about mid depth the crack has almost a horizontal surface. The load transfer is not only provided by the surface inclination with aggregate interlocking but also by the almost horizontal surface. The intention is to provide load transfer at all times even under very cold temperatures when the joints are at their maximum opening.

Figure 3. In this figure, two edges of adjacent slabs have been displaced horizontally by a machine. In one edge we can see the alternate protuberances which are the support of the adjacent slab. Previously in the lateral edge we can observe that the cracking was already created. Also, you can note the dislocated rebar that is used to assemble the system.

Figure 4. In this figure, the JRI+ joint system is placed and fixed on the ground. One can see the correspondence between the cracks shown in the Figures 2 and 3 with the system.



Figure 3. Crack shape between slabs.



Figure 4. Setting devices prior to pouring concrete in Olean (NY).

2 DESCRIPTION OF THE SYSTEM

2.1 *Figures 5,6,7,8*

As shown in Figure 5, the device 1 for forming contraction joints in PCCP includes three basic components: members formed by equal trays 3, 3', supports 5, 5' and stiff linear members 7, 9, 11. A fourth component of the device 1 (not shown in Figure 5) is a waterproofing joint (Figure 8) situated on the upper portion of the device. The alternating arrangement of trays 3, 3' defines a triangular prismatic shape of the device 1. The Figure 6 show two half-trays 14, 15 that have a broken surface form with an upper portion 17 and a lower portion 19 that are parallel and tilted at an acute angle I with regard to the horizontal plane, and a central, almost horizontal portion 21 (small angle C in Figure 6). The upper portion 17 and lower portion 19 include regularly arranged open areas 22.

On the other hand, the upper edge 27 of the half-tray 15 is configured to facilitate the assembly of a waterproofing joint 40 as demonstrated in Figure 8. The two hooks, 41 and 43, on each side of the cracked concrete slabs, lips 45 and 47, allow for the horizontal separation.

As shown in Figures 7a and 7b, device 1 for forming joints is seen with trays 12, 12' alternately arranged on either side of the superficial crack line 24 coinciding in a same vertical plan with the stiff linear member 11 with gaps 16 in between the plane. The trays 12 and 12' are assembled on stiff linear members 7 and 9 which are made to pass through the orifices 35 and 37 of the supports 30, 31 and through the conduit 25 of the trays 15.

Table 1. Results obtained with the FWD.

P.K.	Deflection (mm/100)	LTE (%)	Difference between slabs (mm/100)	Residual deflection (mm/100)	Holes angle \hat{M} (°)
0.000	16.1	95.27	2.0	1.998	85.047
0.000	14.5	100	0.0	3.446	90.000
0.003	15.8	93.421	1.6	3.084	87.709
0.004	14.9	100	0.5	3.313	88.091
0.007	14.5	94.245	1.4	2.343	87.709
0.007	13.4	100	0.8	1.789	86.947
0.014	17.4	100	2.1	0.576	80.910
0.014	17.3	100	2.5	2.822	80.538
0.021	14.7	97.826	1.2	1.743	86.566
0.021	16.3	95.597	1.1	3.801	85.806
0.028	22.2	100	0.0	1.543	79.796
0.028	27.2	94.313	7.3	0.504	64.049
0.035	15.9	100	1.6	0.916	83.911
0.036	14.7	100	0.1	1.327	89.618
0.042	14.8	92.308	1.6	0.169	88.091
0.043	13.9	100	0.3	0.632	88.854
0.048	16.4	100	2.8	1.689	77.957
0.049	13.7	100	0.7	0.912	87.328
0.054	17.7	100	1.5	2.383	83.911
0.055	17.0	100	1.0	3.783	86.186
0.063	13.7	94.406	0.2	6.034	90.000
0.063	14.9	100	0.9	1.895	86.566
0.071	18.8	99.412	1.9	3.146	83.157
0.072	18.3	100	0.0	4.549	90.000

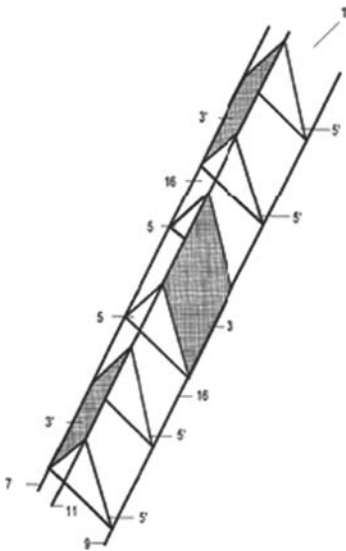


Figure 5.

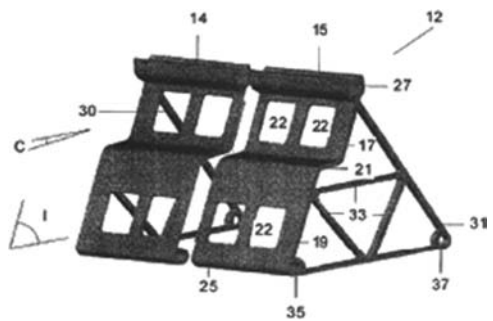


Figure 6.

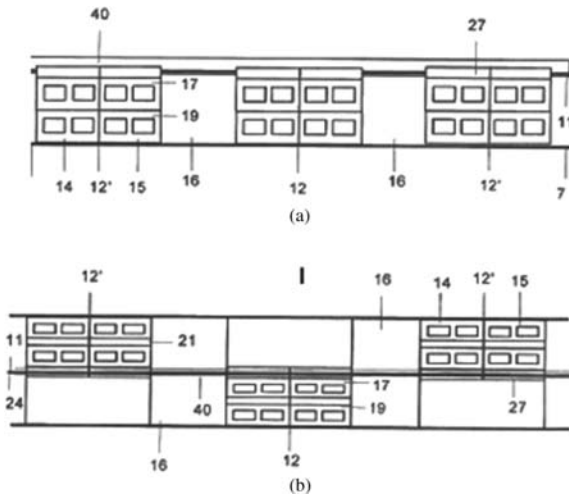


Figure 7.

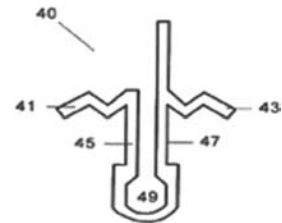


Figure 8.

A third linear member 11 has been added in Figures 7a and 7b which serve to stiffen the waterproofing joint 40, and which is situated in the cavity 49 of its lower portion, which is assembled on the upper edge 27 of the half-trays 14, 15.

The material constituting the trays 3 must be a material suitable for serving as a concrete divider member.

Highly stiff plastic bars or steel bars can be used as stiff linear members 7, 9, 11.

All the components of the device are suitable for prefabrication. Their reduced weight and their shape allow for transporting them in stacks to the work site where they are assembled in the manner indicated and positioned on the ground in the sites provided for the joint. All these characteristics cause that this system is cheaper than the dowel system.

Once assembled, its configuration and particularly the presence of openings in the trays and supports facilitate the positioning of the concrete without moving the device. As a complement, nails for fixing it to the terrain immobilizing the members 7 and 9, and therefore the device 1, are needed.

The device for forming contraction joints includes gaps 16 between alternating trays 3, 3'; 12, 12' so that the crack of the concrete resulting from shrinkage or from the action of a load can easily vary its orientation to either side of the superficial crack line by following the surfaces of said trays 3, 3'; 12, 12'.

2.2 Figure 9

As shown in Figures 9a and 9b, the embedding occurring between the slabs 50 and 52 formed in a pavement, which is facilitated in the event of very wide cracks due to the existence of horizontal flat surfaces 53, 54, 53', 54' corresponding to the areas 21 of the trays 12, 12', is observed.

As concrete cracks, the two slabs 50, 52 are formed with a different configuration in the areas corresponding to the alternating trays 12, 12', respectively.

In the area corresponding to one tray 12 (Figure 9a), the horizontal span 54 of slab 52 is situated above the horizontal span 53 of slab 50, and slab 52 is prevented by slab 50 from moving downwards.

In the tray 12' (Figure 9b), the horizontal span 54' of slab 52 is situated under the horizontal span of 53' of slab 50. Therefore, in this area slab 52 is prevented from moving upwards since the horizontal span of slab 50 is above. Therefore the shear stresses are transmitted among the slabs.

The horizontal portion 21 of the trays 12, 12' always works under compression, therefore its durability is assured. It is recommended that it be thin and/or that its elastic limit be high so

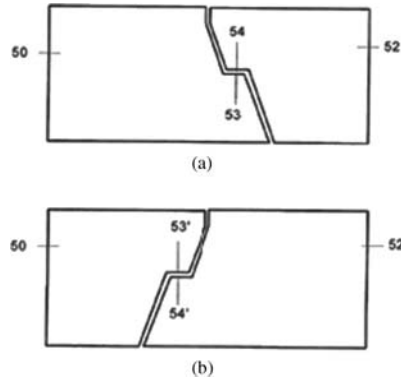


Figure 9.

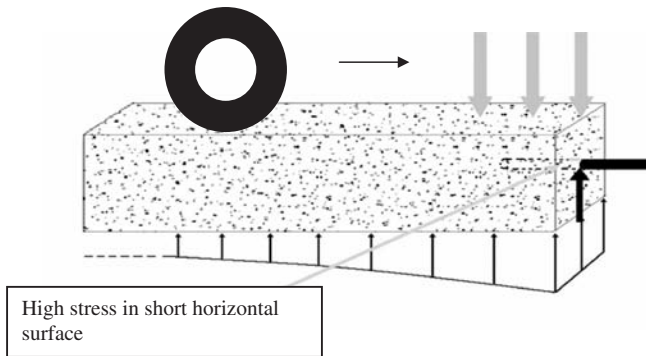


Figure 10. Strengths equilibrium with a dowel bar.

that deformation thereof by compression is small and the transmission of loads is efficient. Any downward movement of a slab must be transmitted to the other one in the same magnitude.

3 FWD RESULTS IN MADRID

3.1 Test and analysis experimental tram in highway M503

Twelve joints were tested in both sides in May, 2006. The results were obtained with a FWD for six loads on each joint. The middle transfer is higher 98%.

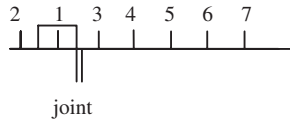
For the determination of Load Transfer Efficiency (LTE) the parameters of the AASHTO GUIDE FOR DESIGN OF PAVEMENT STRUCTURES (AASHTO Guide, 1993) was used and specifically section 3.5 “Non destructive testing deflection measurement” and the method of the Texas University.

Seven geophones were located equidistance from each another. Two of them were located at the same distance from the crack before and after the joint.

The AASHTO’ method (Part III, section 3.5.5: “Use in Slab Void Detection”) was used to calculate the Residual Deflection. One test was performed by three knocks with different charges (8.1, 12.0 and 16.0 ton). Three deflections were used in the analysis. The straight line of these points or the regression line was used to estimate the Residual Deflection as the distance between the origin and the interception with the y-axis.

The method of the University of Texas at Austin to determine the existence of holes below the slab is based in M angle. The M angle is the angle that is formed between the regression line deflection of geophones 1 and 3 with the vertical line.

Location of the geophones



From the above we note that:

$$LTE\% = \left(\frac{d_3}{d_2} \right) * 100 \tag{1}$$

Where LTE% = Load Transfer Efficiency in percent; d_3 = deflection at location 3; and d_2 = deflection at location 2.

The difference between slabs is $d_1 - d_3$

Where d_1 = deflection at location 1; and d_3 = deflection at location 3.

Location of the geophones



From the above we note that:

$$LTE\% = \left(\frac{d_2}{d_3} \right) * 100 \tag{2}$$

Where LTE% = Load Transfer Efficiency in percent; d_3 = deflection at location 3; and d_2 = deflection at location 2.

The difference between slabs is $d_1 - d_2$

Where d_1 = deflection at location 1; and d_2 = deflection at location 2.

4 COMPARISON OF SYSTEMS

4.1 Dowel bar system

$$\text{Ground reaction} + \text{shear} = \text{wheel load}$$

To reduce the contact stresses in the concrete it is necessary to improve load carrying capacity of base and/or sub-grade

4.2 New system

$$\text{Ground reaction} + \text{shear} = \text{wheel load}$$

If ground reaction is low, for equilibrium the shear force will be larger, however the stresses along the horizontal surface are low because there is a larger contact area. Therefore, the load transfer capacity does not depend of the base and sub-grade.

The pavement thickness can be used to check the slab to high stresses. It is possible to calculate with zero ground reaction and to consider that the slab is only supported in their edges. This way is equivalent to assume a high temperature gradient or the existence of voids below the slabs and

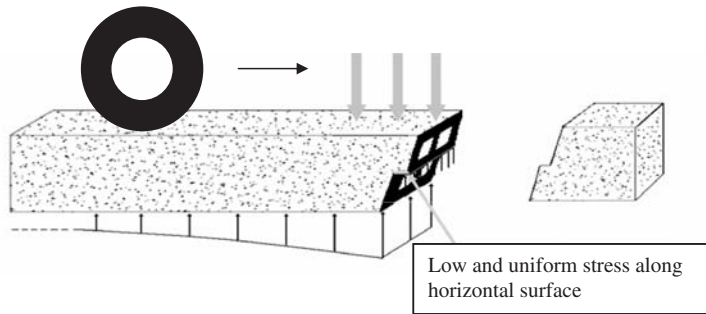


Figure 11. Strengths equilibrium with the new system.

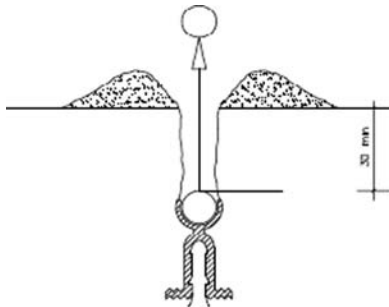


Figure 12. Crack made by pulling the superior bar away.



Figure 13. Vertical crack where the bar was placed.

will allow ensuring long lasting pavement. In this way, the pavement does not require any other layers, at least from the structural point of view.

5 REDUCTION OF THE SPALLING

The Long Term Pavement Performance program (LTPP) defines Spalling of Transverse Joints as cracking, breaking, chipping, or fraying of slab edges within 0.3 m from the face of the transverse joint. Spalling that occurs at transverse joints in Portland Cement Concrete (PCC) pavement with JRI+ joint system is originated by micro-cracks that are produced by the concrete drying after a few hours from pouring the concrete. If a saw cut is not performed or it is performed outside the window of opportunity, this causes the crack to form before we can do the cut. A better approach is to weaken the zone were micro-cracks could be developed. One way to accomplish it is shown in Figure 12, by pulling the superior bar upwards of the fracturing system in fresh concrete. In the fresh concrete the course aggregates are separated from each side of the fracturing system.

When trowelling, one closes the crack, leaving normally the main part of course aggregates at both sides of the same crack and debilitating the concrete in the zone of the crack. This zone only has mortar or concrete that may contain large aggregates. The crack will originate in that place, resulting in a thin crack that is not necessary to waterproof, since it has the rubber band application in place. In Figures 12 and 13 the rubber band has a different shape than Figure 8. Both have lips that connect the rubber band to each side of the crack. This ensures the water seal. With other shapes such as the open tub, the accumulated water in the crack may be drained by the inclined slope of the pavement.

The spalling may also be produced by stones that become embedded in the crack. The method presented in this paper proposes a narrow crack that avoids the introduction of big stones in the crack, therefore reducing spalling by stones.

6 CONCLUSIONS

The JRI+ joint system supports several conditions including the induced formation of joints with a 98% indefinite load transfer efficiency. In addition, JRI+ joint system provides a method of waterproofing of the pavement structure and is a system that does not require additional layers for structural reasons. The system is cheaper than the use of conventional dowel bars.

REFERENCES

- AASHTO Guide for Design of Pavement Structures. 1993. American Association of State Highway and Transportation Official, Washington D.C.
- Technology Transfer News, New York State Department of Transportation. 2005–2006. *New System to induce formation of joints in concrete pavements*. Albany, New York.
- Universitat Politècnica de Catalunya 2005. *Ensayo de determinación de la carga de rotura de probetas de hormigón con aplicación de carga sobre junta JRI+ (TG-LTE/1105-1)*. Barcelona. Universitat Politècnica de Catalunya.
- Vazquez, J.R. 2002. *Hormigón continuo con bordes apoyados y juntas estancas*. Madrid. Colegio de Ingenieros de Caminos Canales y Puertos.
- Vazquez, J.R. 2004. *Pavimentos continuos con juntas tridimensionales*. VI Congreso Nacional de Firms. León. Asociación Española de la Carretera.
- Vazquez, J.R. 2004. *Continuous pavement with three-dimensional joints JRI+*. Istanbul. 9th International Symposium on Concrete Roads.
- Vazquez, J.R. 2006. *Concrete Pavement Without Dowel Bars*. Brussels. 10th International Symposium on Concrete Roads.

Numerical assessment of saw-cutting: The influence on stress development and cracking

K. Raoufi & J. Weiss

Purdue University, West Lafayette, Indiana, USA

T. Nantung

Indiana Department of Transportation, West Lafayette, Indiana, USA

ABSTRACT: Joints are placed in Jointed Plain Concrete Pavements (JPCP) to control random cracking that is caused by the residual stresses that develop due to thermal, hygral, or hydration effects. Although the concept behind the need for saw-cutting is relatively straightforward, determining the time and depth of the saw-cut can be complicated in practice. While saw-cutting is widely done in practice, it is usually based on non-scientific principles. This study used finite element analysis to simulate the effect of saw-cutting on the stress development and cracking behavior of concrete pavements. The interaction between the environmental conditions, properties of the constituent materials, mixture proportions, mechanical properties, and timing of construction operations was assessed in terms of the rate of concrete property development and stress development. This approach presents an exciting step forward that will enable concrete pavement construction practices to be optimized for a given series of construction materials and environmental conditions.

1 INTRODUCTION

Saw-cuts need to be placed within a specific time window in JPCP during construction operations. Placing the saw-cut too early can result in raveling and spalling around the joints, while placing the saw-cut too late can result in random cracking. This time window depends on the constituent materials, the fresh mixture properties, the restraint from subgrade or adjacent pavements, and environmental conditions such as ambient weather conditions. Currently, the guidance from the pavement communities is limited in determining the time at which a saw-cut should be placed. The American Concrete Institute (1995) recommends that “the joints should be sawed as soon as practical wherein the concrete should have hardened enough”, while Indiana Department of Transportation (2005) specifies that saw-cuts should be placed between 2 and 12 hours when the concrete is “sufficiently hardened”.

Not only is the saw-cutting time window difficult to determine, but so is the appropriate depth of the saw-cut. While deeper saw-cuts are better in controlling cracks, shallow saw-cuts may sometimes be preferred since they are introduced at a faster rate and are less demanding on the saw-blade making the saw-cut less expensive. Currently, the determination of the appropriate depth of a saw-cut to insure that random cracking does not occur is not easy. The American Concrete Pavement Association (2002) recommends a saw-cut depth of $D/3$ for longitudinal joints (where D is the pavement depth), $D/4$ for transverse joints in pavements placed on a dense granular subbase, and $D/3$ for transverse joints in pavements placed on a stabilized and open graded subbases (Voigt, 2002). Voigt (2002) reported that 96% of the state agencies require a minimum saw-cut depth of $D/4$. It should be noted that even more complexity arises when the complex interaction between saw-cut depth and the time of saw-cut placement are investigated.

Environmental conditions significantly influence the development of stresses within the pavement at early ages. Weather conditions and fluctuations in weather conditions (relative humidity, temperature, precipitation, wind speed, and wind direction) all play a significant role in early-age stress development, saw-cutting time window, and cracking behavior (Armaghani et al. 1987, Zollinger et al. 1994, Gaedicke et al. 2007). Contractors have begun using hand-held weather monitoring stations which can provide valuable information on current environmental conditions (Thier, 2005); however, little or no guidance is available for the contractor to directly relate their mixture properties with the weather station and the timing of construction operations.

Although many computer programs are available to predict the average section stress development in concrete systems (HIPERPAV, 2007; PLATE, 1999), most of them do not consider the influence of a saw-cut placement on stress development and cracking behavior. Recently, a new feature to include the timing of a saw-cut has been added to the software HIPERPAV (2007). The scientific principles behind the algorithm that should be used to determine time of saw-cutting is not well understood. Detailed information on the stress level surrounding the crack and crack propagation requires further the investigations. As timing of the saw-cut placement and the depth of saw-cutting are two interrelated factors (Raoufi et al. 2008, Gaedicke et al. 2007), further work is still needed to develop a reliable tools to predict the timing of a saw-cut. This paper describes one method which may provide insights into the algorithm that should be used to predict the time of saw-cutting. The model used in this paper considers early age stress development and cracking considering fundamental material properties, environmental conditions, and fundamental mechanics concepts. Emphasis is placed on modeling conventional saw-cutting practices rather than soft early age saw-cutting (when the concrete is green and very early entry saws are used). The approach presented in this paper can provide new insight into how cracks develop and propagate in a concrete pavement such that new algorithms can be used in commercial software.

2 OBJECTIVES

The main objectives of this paper are:

1. To use a finite element method that is based on fundamental mechanics and material properties to assess how the timing of saw-cut placement and ambient conditions influences the stress development, damage development, and random cracking, and
2. To determine the influence of the saw-cut depth on the maturity at which stresses develop and random cracking would be expected to occur in concrete pavements.

3 MODELING APPROACH

Finite element software, FEMMASSE MLS 7.1 (2004), was used to model the influence of saw-cut introduction on stress development and cracking in concrete pavement. A concrete material was used with age-dependent strength, elastic modulus, autogenous shrinkage, and viscoelastic properties. The complex interaction of thermal and moisture gradients with age-dependent property development, viscoelasticity, thermal dilation, and nonlinear fracture mechanics were considered in the analysis. Time-dependent environmental boundary conditions were assigned to the model. In addition, time-dependent saw-cuts with different geometries were modeled. The software provides a detailed analysis of the stresses, displacements, temperature distributions, moisture conditions, and cracking profiles at every point in the concrete pavement at every time during the simulation.

3.1 *An overview of the model*

A two-dimensional concrete pavement section was analyzed (380 mm deep and 5400 mm long). A saw-cut was introduced at the middle of the pavement at different ages as shown in Figure 1.

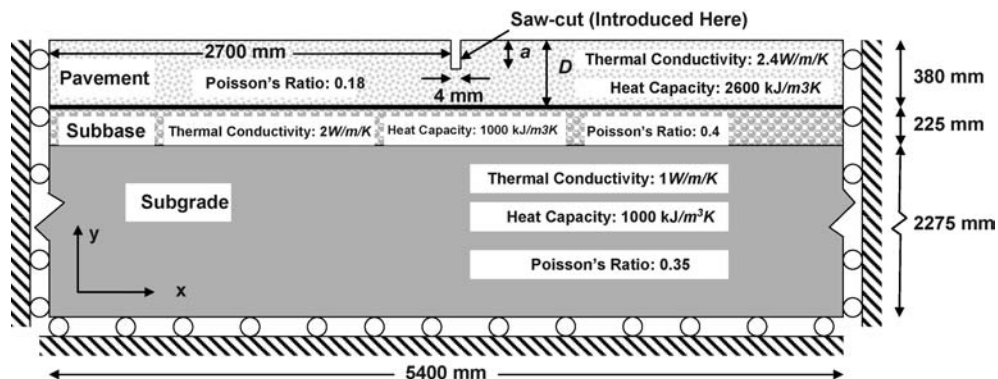


Figure 1. A schematical view of the finite element model.

Table 1. The previously measured age-dependent material inputs at selected times.

Age (hr)	5	12	24	72	168	672
Elastic Modulus (MPa) (Barde, 2004)	500	11500	15242	25000	30000	36000
Tensile Strength (MPa) (Thier, 2005)	0.0	1.9	2.6	2.9	3.0	3.2
Comp. Strength (MPa) (Thier, 2005)	0.0	2.8	14.3	25.2	34.5	40.0
Adiabatic Temp. (°C) (Bentz, 1998)	23.1	44.6	55.1	59.5	60	60
Shrinkage ($\mu\epsilon$) (Pease, 2005)	0	-10	-45	-182	-242	-402

The 5400 mm length of pavement was chosen to mimic the distance between two joints in the field (Thier, 2005, Falker, 2003). The saw-cut width was considered to be 4 mm (Thier, 2005), while the saw-cut depth and the timing of saw-cut were varied. The pavement section was placed over a 225 mm-deep granular base and subbase layer, which was also supported by 2300 mm-deep layer of subgrade in the vertical direction. The subgrade layer was chosen to be large enough to act as a heat sink to eliminate any temperature interference that may arise from the pavement's lower boundary conditions. The initial temperature of the subgrade layer was chosen to be 13°C (Bentz, 2000). A unit thickness of 1000 mm was defined for the model and no variation was considered in the third direction. Quadrilateral elements were used to mesh the model, and the mesh close to the saw-cut location was more refined to enhance the numerical accuracy of the model.

The model was completely sealed from the sides and bottom; however, measured surface evaporation rates of $4.3 \times 10^{-7} \text{ m}^3/\text{m}^2/\text{s}$ for the first 14 hours and $3.4 \times 10^{-8} \text{ m}^3/\text{m}^2/\text{s}$ at later times were used to define the evaporation from the surface. A constant relative humidity of 75% (Barde, 2006) and different ambient temperature functions (i.e., constant or periodical functions) were defined over the surface of the pavement to model the different environmental conditions. A wind speed based heat transfer coefficient of $45 \text{ W}/\text{m}^2\text{K}$ was used to model heat gain and loss of the pavement's surface. As shown in Figure 1, the model sides were restrained from moving in x-direction, but were allowed to move freely in the y-direction.

3.2 Concrete properties

The age-dependent material properties shown in Table 1 were used to model a concrete with a water-to-cement ratio of 0.42 and 70% aggregate by volume. The set time was 5 hours; however,

the computer simulation started at the time of casting. It should be noted that the tensile strength data was fit using Hansen's hydration function (Hansen et al. 1985). A time-dependent Maxwell Chain Model was used to describe the viscoelastic nature of concrete. A bilinear softening model (Hillerborg, 1987) was used to describe the softening behaviors of concrete respectively. Based on the experiments performed by Østergaard (2003), a stress-to-strength ratio and a crack width of 0.2 and 0.8 mm were used to define the knee point of the bilinear softening curve, while a critical crack width of 2.5 mm was used to define a crack width beyond which no stress is transferred across the crack. Further details on all material properties are provided in (Raoufi, 2007).

4 RESULTS AND DISCUSSION

The influence of the timing of saw-cut placement, ambient temperature, and saw-cut depth on the stress development and the time of cracking of pavements are discussed in the following subsections.

4.1 *The timing of saw-cut introduction*

Depending on the time of saw-cut placement in concrete pavements, the placement of saw-cut can lead to either stable or unstable cracking. In stable cracking, crack propagates over time when stress level in pavements is still increasing. In contrast, unstable cracking occurs as soon as the saw-cut is placed.

To assess how the timing of a saw-cut influences the stress development and cracking in concrete pavements, two computer simulations of pavements were performed with the same saw-cut depth of $D/3$. The saw-cuts were placed at 6 hours and 30 hours to illustrate the influence of an early saw-cut and a late saw-cut on the stress development and cracking behavior of pavements, respectively. A constant ambient temperature of 23°C was also defined over the surface of the pavement in this simulation, and the maximum principal stress development and cracking in the pavements were monitored. The placement of a saw-cut creates a weakened plane that reduces the stresses at which a pavement cracks. Further, as the saw-cut depth increases, the stress levels at which pavements crack decreases (Raoufi et al., 2008).

Figure 2 illustrates the maximum principal stress contour plots around the saw-cut location in pavements. Figures 2aI, 2aII, and 2aIII represent the maximum principal stress distributions in the pavement with a saw-cut placed at 6 hours at selected times: 12 hours (the end of stress-free period), 20 hours (2 hours before through cracking occurs), and 22.2 hours (when through cracking occurs). As shown in Figure 2aI, the stress level in the first 12 hours is close to zero; however, crack starts to localize at the tip of the saw-cut at 14 hours. The crack begins to propagate in a stable fashion, and reaches the bottom of the pavement at 22.2 hours.

Figures 2bI, 2bII, and 2bIII illustrate the stress contours at 12 hours (the end of stress-free period), 28 hours (2 hours before through cracking occurs), and 30.2 hours (when through cracking occurs) for the pavement with $D/3$ saw-cut depth, which was placed at 30 hours (when through cracking occurs).

Figure 2c illustrates the average stress (far-field stress, throughout the depth in a standard section of pavements) with different times of saw-cut placement. It is observed that pavements with saw-cuts that are placed at any ages before 18 hours (in this case) have a similar stress development and cracking behavior. The placement of a saw-cut at ages greater than 24 hours (when average stress level in the pavement is higher than the failure stress of the sawed pavement) would result in a brittle unstable instant failure as shown by the vertical lines in Figure 2c.

As shown in Figure 2c and later in Figure 3, when the saw-cut is placed at 6 hours, the crack localizes at 14 hours and through cracking occurs in a stable fashion between 14 and 22 hours as the stress level increases. However, the average section stress of the pavement when sawed at 30 hours rises to a stress level that is significantly higher than the failure stress of the sawed pavement with a saw-cut. Therefore, the crack initiates, localizes and propagates instantly upon the placement of the saw-cut at 30 hours. This would be seen in practice in conditions when saw-cutting crews report

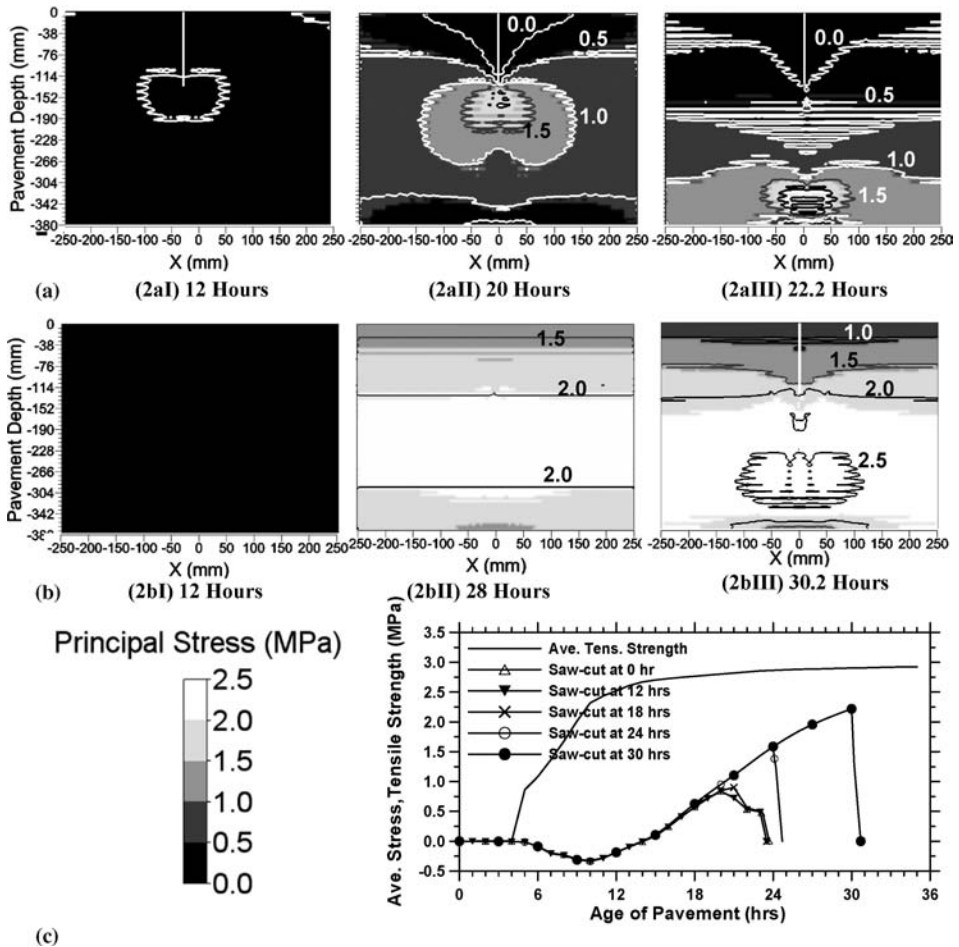


Figure 2. The maximum principal stress (in MPa) contour plots of pavements with: (a) saw-cut placed at 6 hours, and (b) saw-cut placed at 30 hours, and (c) average section stress of pavements with different times of saw-cut placement.

“chasing a crack” across a pavement as the saw-cut is introduced. This shows that the saw-cut does not “control” the cracking properly, rather the saw-cut has been placed too late.

The influence of the timing of the saw-cut on the stress development and cracking behavior of pavements can also be explained by Figure 3. Figure 3 illustrates the age at which tensile stresses develop (average section tensile stress level exceeds zero) in the pavements, the age at which cracking initiates at the tip of the saw-cut (local stress less than 1 mm from the tip of the saw-cut exceeds the tensile strength), the age at which cracking begins to propagate unstably (the crack grows while the average section stress level decreases), and the age at which the crack reaches the bottom of the pavement for pavements sawed at different ages. It is seen that average section stress (i.e., far field stress) develops at the same time irrespective of the timing of saw-cut. The age of crack initiation is independent from the timing of saw-cut until 14 hours (f-or this case). After 14 hours, the crack begins to initiate as soon as the saw-cut is placed. When the saw-cut is placed at ages greater than 22 hours, the crack initiates and propagates instantly. Therefore, a saw-cut needs to be placed before 22 hours, which is the end of saw-cutting time window, to avoid unstable cracking or “chase cracking”. The point identified as no saw-cut in Figure 3 indicates the time at

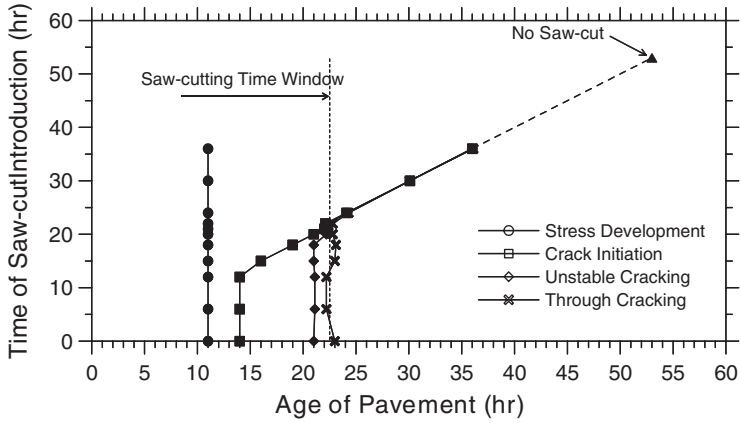


Figure 3. The stress development and cracking behavior of pavements at 23°C with $D/3$ saw-cut depths introduced at different times.

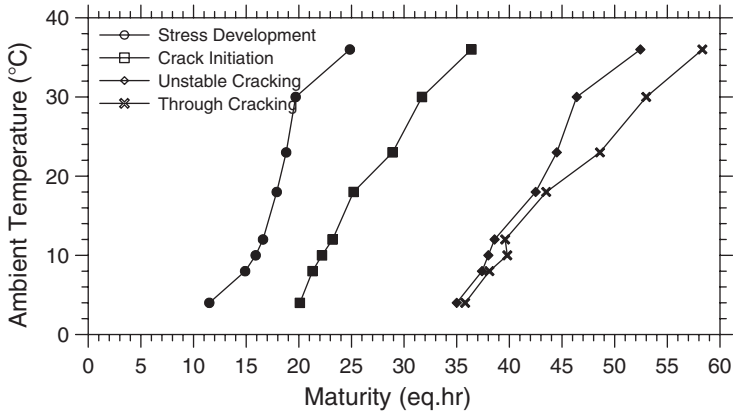


Figure 4. The cracking and stress behavior of pavements with a saw-cut depth of $D/3$ cured at different ambient temperatures.

which a pavement would fail or crack if no saw-cut were applied in the field. It should be noted that depending on the saw-cut depth, the saw-cutting time window can increase or decrease as it will be discussed in more detail in section 4.3.

4.2 The influence of ambient temperature on the time of cracking

Any changes in environmental conditions such as ambient temperature and relative humidity can create a complex stress behavior in concrete pavements especially at early ages (Zollinger et al., 1994). In this discussion, only the effect of constant ambient temperature on the time of stress development and crack development of concrete pavements is discussed. However, other cases including various periodical ambient temperature functions have also been considered (Raoufi, 2007). It should be noted that FEMMASSE can consider any ambient temperature conditions that are of interest.

Figure 4 shows the influence of constant ambient temperature on the maturity at which the stresses begin to build up and cracking occurs in the pavements. All pavements were sawed with a $D/3$ saw-cut depth right after casting. The maturity of pavements was determined based on the

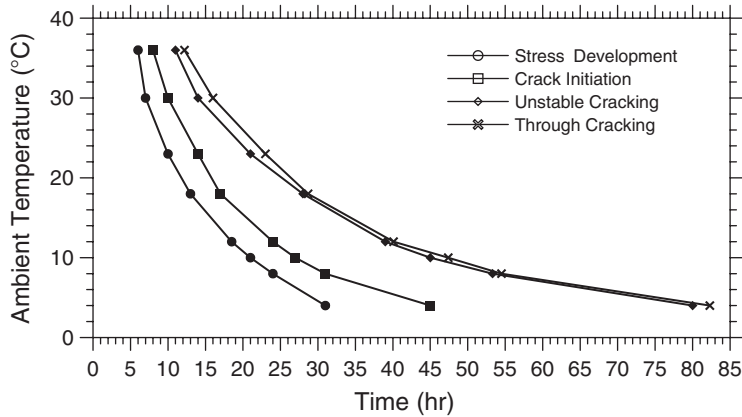


Figure 5. The stress development and cracking behavior of pavements with saw-cut depth of $D/3$.

Arrhenius method at a distance of $D/3$ from the surface of the pavement. It was noticed that at higher ambient temperatures, the rate of heat loss from the pavement decreases considerably at early ages, the concrete matures at higher rates, and pavements experience a greater thermal expansion. The greater thermal expansion tends to compensate for the shrinkage induced stresses to some degree. This reduction in the average section tensile stress development at high temperatures would result in a delay in the cracking of concrete pavements in terms of maturity times. It should, however, be noted that the cracking in fact occurs earlier in real time.

At higher ambient temperatures, cement hydration reactions take place faster, and subsequently the rate of shrinkage in concrete increases. Consequently, a higher rate of shrinkage would result in earlier tensile stress development. This rapid stress development combined with a reduced time for stress relaxation accelerates the stress and cracking development in terms of real time hours. This is more explicitly shown in Figure 5. This figure is similar to Figure 4; however, it shows the real time of stress development and cracking of the same pavements shown in Figure 4. As shown in Figure 5, the real times at which the residual tensile stresses develop, the cracking initiates and unstable cracking and through cracking occur decrease sharply as the ambient temperature increases. Based on the results presented in Figures 4 and 5, it can be concluded that although curing at high ambient temperatures delays cracking of concrete in terms of maturity hours, the real time of stress development and cracking of concrete pavements in fact decreases considerably at high temperatures.

4.3 Depth of saw-cut

To assess how saw-cut depth influences the stress development and cracking behavior of pavements, computer simulations of a pavement with different saw-cut depths were performed. Figure 6 shows the maximum principal stress distributions close to saw-cut locations of pavements with different saw-cut depths at 22 hours. For the purpose of comparison, a stress contour plot of an uncut pavement is also shown. While the maximum stress level in the uncut pavement is about half of the tensile strength of the pavements (i.e., 1.5 MPa) at 22 hours, through cracking has occurred in the pavements with $D/2$ and $D/3$ saw-cut depths, and cracking in the pavement with $D/4$ has just started. The fracture process zone has not yet fully developed in pavements with $D/6$ and $D/8$ saw-cut depths, and higher stress levels are still needed to initiate and grow cracking in pavements with $D/6$ and $D/8$ saw-cut depths. The high stress levels in pavements sawed with shallow saw-cuts would also increase the potential for random cracking and micro-cracking development in pavements, which can reduce the long-term performance of concrete pavements (Yang, 2005, Weiss, 2002).

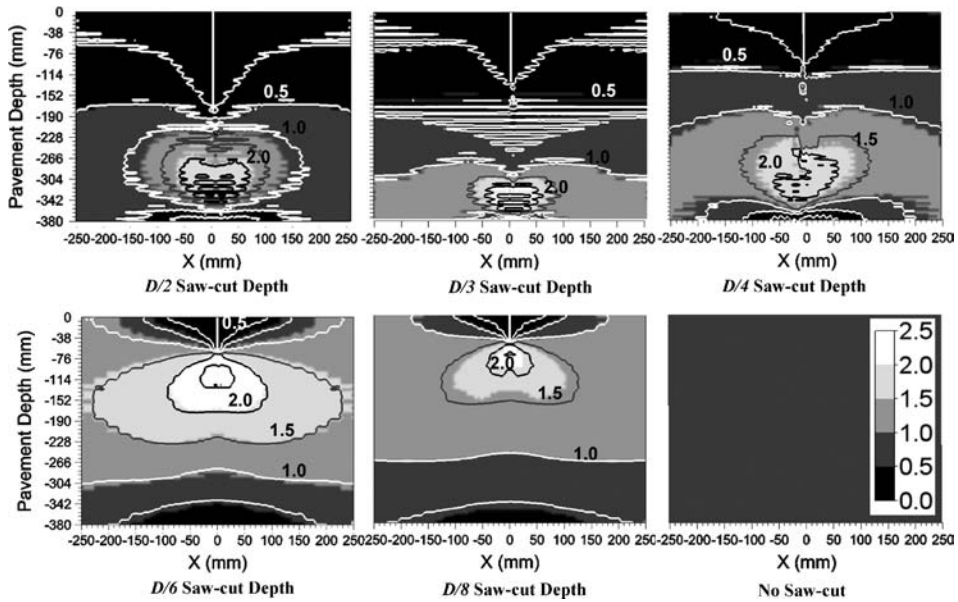


Figure 6. Maximum principal stress (in MPa) distributions in pavements with $D/2$, $D/3$, $D/4$, $D/6$, $D/8$ and no saw-cut shown at 22 hours after the time of casting.

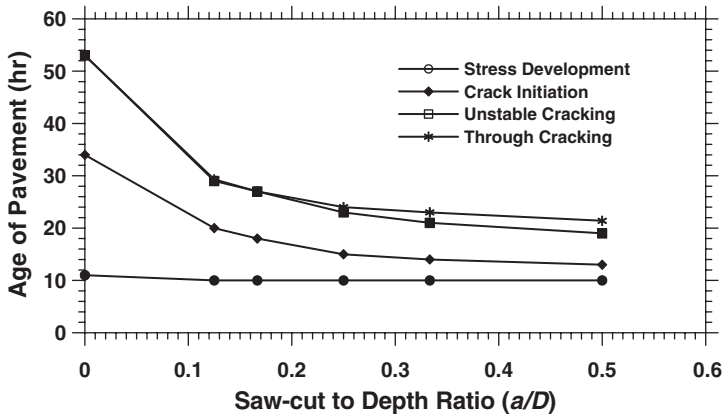


Figure 7. The cracking behavior of pavements with different saw-cut depths at 23°C.

To further quantify the effect of saw-cut depth on the age of stress development and through cracking, a series of similar concrete pavements with various saw-cut depths were modeled. The pavements were cured at 23°C, and the stress development and cracking behavior of pavements were examined as summarized in Figure 8. Figure 8 shows how the depth of saw-cut influences the ages at which residual stresses develop, the ages at which cracking initiates and the ages at which through cracking occurs in PCCP. As one may expect, the age of the average section stress development remains independent of the depth of a saw-cut; however, the age of the crack initiation at the tip of the saw-cut and crack propagation increases as the depth of saw-cut decreases. This implies that deeper saw-cuts have shorter saw-cutting time window in the life of a pavement than shallow ones, and higher levels of average tensile stress (i.e. energy) are needed before cracking can

occur in pavements sawed with shallow saw-cuts. It should be noted, however, that when variability is considered, the impact of saw-cut depth is greatly reduced (Raoufi, 2007, Raoufi et al., 2008).

5 CONCLUSION

This paper introduces the use of finite element software to assess the influence of the timing of saw-cut and saw-cut depth on the cracking behavior of concrete pavements, considering various environmental conditions. The stress development and cracking behavior of pavements cut with saw-cuts at different ages were illustrated and explained. The approach presented in this paper can be used to develop scientifically based algorithms that can be directly implemented into commercial computer programs to predict the time of saw-cutting.

It was shown that the age of cracking of pavements is independent from the timing of saw-cut until a sufficient tensile stress develops in the pavement. An unstable crack can develop on placing a saw-cut well before tensile strength is reached. An algorithm that considers stress development should be used as defined in Raoufi et al. (2008).

Although higher ambient temperatures result in higher thermal expansion, and delays cracking in terms of maturity hours, it leads to shorter saw-cutting time window in terms of real time hours. This is due to higher rates of autogenous shrinkage and less time for stress relaxation at higher temperatures.

Finite element modeling of the concrete pavements sawed with different saw-cut depths shows that the saw-cut depth influences the age of crack initiation and propagation. It was also shown that in cases where the joints are sawed with saw-cuts shallower than $D/4$ saw-cut depths, the average stress levels in pavements can rise to more than 50% of the tensile strength which may lead to micro-cracking development and potential reduction in pavements' long-term performance. It was also shown that the age of cracking also increases as saw-cut depth decreases. This implies that saw-cutting time window is shorter for deeper saw-cuts (e.g. deeper than $D/4$ saw-cut depth), and they need to be placed much earlier in the life of a pavement than shallower saw-cuts.

ACKNOWLEDGEMENTS

This work was supported by the Joint Transportation Research Program administered by the Indiana Department of Transportation and Purdue University (Project SPR 2863). The contents of this paper reflect the views of the authors, who are responsible for the facts and the accuracy of the data presented herein, and do not necessarily reflect the official views or policies of the Federal Highway Administration and the Indiana Department of Transportation, nor do the contents constitute a standard, specification, or regulation. The authors also gratefully acknowledge Dr. Farshad Rajabipour, Dr. Erik Schlangen, Mike Byers, Dick Newell, and Tony Thier for their assistance in this work.

REFERENCES

- American Concrete Institute 1995, Committee 224.3, Joints in Concrete Construction, Farmington Hills, MI.
- American Concrete Pavement Association 2002, Early Cracking of Concrete Pavement – Causes and Repairs, Publication TB016P, Skokie IL.
- Armaghani, J.M., and J.M. Richardson 1987, Stress Caused by Temperature Gradient in Portland Cement Concrete Pavement, In *Transportation Research Record: Journal of the Transportation Research Board, No 1121*, TRB, National Research Council, Washington, D.C., pp. 7–13.
- Barde, A. May 2004, Early-age Flexural Behavior of Cementitious Systems and Factors Affecting Maturity Based Predictions, Master Thesis, Purdue University.
- Barde, V. May 2006, Relating Material Properties to Exposure Conditions for Predicting Service Life of Concrete Bridge Decks in Indiana, Master Thesis, Purdue University.

- Bentz, D. 1998, Prediction of adiabatic temperature rise in conventional and high performance concretes using a 3-D micro-structural model, National Institute of Standards and Technology.
- Bentz, D. August 2000, A computer model to predict the surface temperature and time-of-wetness of concrete pavements and bridge decks, NISTIR 6551, National Institute of Standards and Technology.
- Falker, E. May 2003, Assessing The Impact of Performance-related Specifications on Concrete Pavement Construction, MSCE Thesis, Purdue University, West Lafayette, Indiana.
- Gaeddicke, C., S. Villalobos, J. Roesler and D. Lange 2007, Fracture Mechanics analysis for Saw-cutting Requirements of Concrete Pavements, In *Transportation Research Record: Journal of the Transportation Research Board, No 2020*, TRB, National Research Council, Washington, D.C., pp. 20–29.
- Hansen, F. and E. Pedersen December 1985, Curing of Concrete Structures, Report Prepared for CEB, General Task Group Number 20, Durability and Service Life of Concrete Structures, Danish Concrete and Structural Research Institute, CEB-Guide to Durable Concrete Structures, Lausanne.
- Hillerborg, A. 1978, A Model for Fracture Analysis, Report TVBM-3005, Division of Building Materials, Lund Institute of Technology, Lund, Sweden.
- HIPERPAV II, July 2007, High Performance Concrete Paving Software, Transtec Inc., Austin, TX. www.hiperpav.com
- Indiana Department of Transportation (INDOT) Manual for Concrete Paving, January 2005. <http://www.in.gov/dot/pubs/manuals/pavingConcrete/>
- MLS 7.1 FEMMASSE 2004, Multi Layer System of Finite Element Modules for Materials Science and Structural Engineering, Culemborg, Netherlands.
- Østergaard, Lennart, 2003, Early-Age Fracture Mechanics and Cracking of Concrete Experiments and Modeling, PhD Thesis, Technical University of Denmark.
- Pease, B. May 2005, The Role of Shrinkage Reducing Admixtures on Shrinkage, Stress Development, and Cracking, Master Thesis in Civil Engineering, Purdue University.
- PLATE, 1999, A 3-D Tool to Predict Deformations and Stresses of Concrete Slabs Due to Drying and Thermal Shrinkage, National Science Foundation, Northwestern University.
- Raoufi, K. May 2007, Saw-cutting Guidelines for Concrete Pavements: Examining the Requirements for Time and Depth of Saw-cutting, MSCE Thesis, Purdue University, West Lafayette, Indiana.
- Raoufi, K., A. Radlinska, T. Nantung and J. Weiss. January 2008, A Methodology for Determining the Time of Saw-cutting in Concrete Pavements, 87th Annual Meeting of the Transportation Research Board, National Research Council, Washington D.C.
- Thier, T. May 2005, Examining The Time And Depth Of Saw-Cutting Guidelines For Concrete Pavements, MSCE Thesis, Purdue University, West Lafayette, Indiana.
- Voigt, G.F. 2002, Specification Synthesis and Recommendations for Repairing Uncontrolled Cracks that Occur During Concrete Pavement Construction, ACPA.
- Weiss, W. J. and Chariton, T. 2002, Using Acoustic Emission to Monitor Damage Development in Mortars Restrained from Volumetric Changes, Concrete: Material Science to Application, A Tribute to Surendra P. Shah, ed. P. Balaguru, A. Namaan, W. Weiss, ACI SP-206, pp. 205–218.
- Yang, Z., J. Weiss and J. Olek August 2005, Interaction between Micro-cracking, Cracking, and Reduced Durability of Concrete: Developing Methods for Considering Cumulative Damage in Life-cycle Modeling, Publication FHWA/IN/JTRP-2004/10, Indiana Department of Transportation and Federal Highway Administration, IN.
- Zollinger, D.G., T. Tianxi and D. Xin 1994, Saw-cut depth considerations for jointed Concrete Pavement Based on Fracture Mechanics Analysis, In *Transportation Research Record: Journal of the Transportation Research Board, No 1449*, TRB, National Research Council, Washington, D.C., pp. 91–100.

Moisture warping in slabs on grade

Y. Wei & W. Hansen

University of Michigan, Ann Arbor, Michigan, USA

E. Schlangen

Delft University of Technology, Delft, The Netherlands

ABSTRACT: Curling and warping are slab deformations that cause deviations from its original surface as a result of differences in temperature and moisture, respectively, between slab top and bottom. The upward curled/warped slab condition can change the failure mode from bottom-up to top-down mid-slab cracking. This study is a first step in investigating shrinkage-related slab warping with the presence of drying shrinkage at the top surface combined with wetting at the bottom surface. A laboratory study is currently carried out on concrete beams. The results show that substantial warping develops if slab bottom is in continuous contact with water. Finite Element (FE) analysis suggests that warping is the dominant factor in slab uplift. Internal curing using lightweight fine aggregate (LWFA) is found to be effective in reducing moisture warping.

1 INTRODUCTION

The slab's shape is constantly adapting to the thermal and moisture gradient changes within its cross section. This causes slabs to curl downward when the top surface is warmer than the bottom surface, while an upward curl results when the top of the slab is cooler/drier than the bottom. The upward-curved slab condition will cause significant portions of the slab in the vicinity of joints unsupported. Joint loading under such conditions can increase total stresses in the mid-slab region and adversely affect the long-term service life of a concrete pavement (Poblete et al. 1990, Darter et al. 1995, Khazanovich et al. 2000, Hansen et al. 2002).

The major objective of this paper is to determine if internal curing is effective in reducing uplift from a differential autogenous moisture gradient. New results are presented on autogenous deformation and moisture warping for highway concrete ($w/c > 0.40$) with and without partial replacement of sand by lightweight fine aggregate (LWFA).

2 TOP-DOWN MIDSLAB CRACKING IN TWO JPCP PROJECTS IN MICHIGAN

Premature top-down mid-slab transverse cracking has been found for two highway projects located in southeastern Michigan (Hansen et al. 2002).

The rapid cracking development in this case, as shown in Figure 1, can not be predicted using existing models that are based on bottom-up cracking.

Surface elevation measurements of the uncracked slabs were conducted along the outer edge for west-bound (WB) I-96 on warm sunny days in June and July. Slabs were found to be in a permanent upward-curved condition with joint uplift varying from 2 to 4 mm (0.08 to 0.16 in.) as illustrated in Figure 2. Considering that field measurements were obtained on hot sunny days and this project was constructed during fall temperature conditions, these uplift results preclude daily curl and

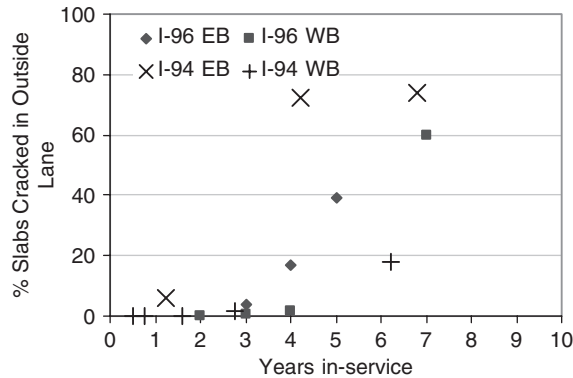


Figure 1. Development of top-down transverse mid-slab cracking for two JPCP projects in Michigan.

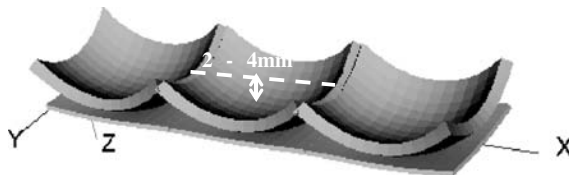


Figure 2. 3-D illustration of mid-slab joint uplift for JPCP project as predicted using EverFE 2.24 (Davids 2003).

built-in curl from a temperature gradient. Thus, the most likely cause for the permanent uplift is moisture warping (Hansen & Wei 2008). Beckemeyer et al. (2002) concluded that premature top-down mid-slab cracking of a JPCP project in Pennsylvania was thermal and shrinkage-related.

A total equivalent linear temperature difference (TELTD) between slab top and bottom was found to range from -28°C to -47°C (-50°F to -85°F). These values were obtained by matching the edge uplift from surface profiles with predicted uplift using ISLAB2000 (Khazanovich et al. 2000). The concept of TELTD is described in detail by Rao & Roesler (2005).

3 AUTOGENOUS DEFORMATION IN HIGHWAY CONCRETE

Autogenous deformation, a uniform volumetric reduction, is a result of cement hydration and self-desiccation of pores within the hydrating cement paste. As long as no external water is added to the system, autogenous shrinkage is a uniform deformation and no moisture gradient results. With the increase of cement hydration, capillary pores depercolate which has been found to affect transport property in concrete (Powers et al. 1959, Bentz 2006). If water is available at one of the free surface, moisture gradient and thus warping can develop in a concrete slab due to the fact that capillary moisture transport is hindered within a certain depth from the moistured surface.

Autogenous shrinkage is well known pronounced in low w/c ratio cementitious system (Jensen & Hansen 1996). However, for highway concrete typically with moderate and high w/c ratio (greater than 0.4) limited data on autogenous shrinkage were found in literature.

In this study, the autogenous shrinkage was conducted on Ordinary Portland cement paste and concrete with w/c ratio of 0.45 using linear measuring equipment (Schleibinger 1999). The specimen, with a cross section of 60 mm by 100 mm and length of 1000 mm, was sealed using a plastic wrap right after casting to prevent external drying. External restraint was overcome by placing

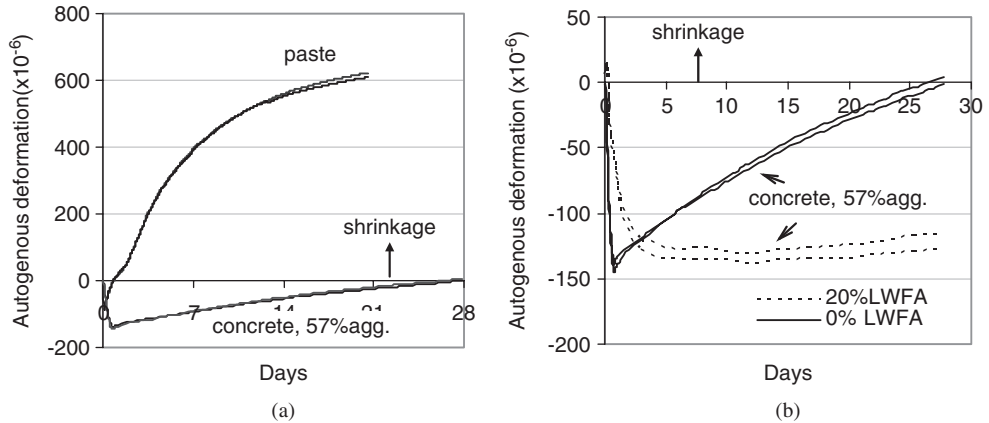


Figure 3. Autogenous deformation for (a) cement paste and concrete, $w/c = 0.45$, and (b) the effect of LWFA on autogenous shrinkage of concrete with 57% aggregate content, $w/c = 0.45$.

a soft, flexible, 2 mm-thick foam rubber between the mold and the sealed specimen. The curing temperature was maintained at 23°C by circulating constant-temperature water through the channels built-into the sides and bottom of the mold. One end of the specimen was fixed to the mold and the other end was free to move horizontally. The free end had an LVDT attached for measuring linear autogenous deformation. This measurement was initiated after final set. Two replicate specimens were tested.

The measured autogenous deformation is shown in Figure 3a. Substantial autogenous shrinkage is observed in cement paste and it decreases with the increase of aggregate content due to the internal restraint from non-shrinking aggregate particles (Pickett 1956). There is expansion followed by shrinkage within the first 1–2 days which has been reported by other investigators (Baroghel-Bouny 1996, Toma et al. 1999). It was suggested that a likely cause for the early expansion is ettringite formation (Bjontegaard 1999).

The pre-soaked LWFA, a type of sand-size expanded shale lightweight aggregate, is found to be effective in eliminating autogenous shrinkage by replacing 20% sand by volume for the $w/c = 0.45$ concrete with 57% aggregate content as shown in Figure 3b. This type of LWFA has a bulk specific gravity of 1.8 and water content of 15% by weight obtained in a 24-hour pre-soaked condition.

4 BEAM UPLIFT FROM MOISTURE WARPING

Since autogenous shrinkage, also known as self-desiccation shrinkage, can develop in $w/c = 0.45$ concrete, it is expected that moisture warping will occur in a concrete slab with w/c of 0.45 if its bottom is exposed to wetting.

To quantify the magnitude of moisture warping, tests were conducted on concrete beams using a modified test procedure based on the work by Springenschmid & Planerer (2001). The test can determine warping of a concrete beam from simultaneous drying at the top and wetting at the bottom. As shown in Figure 4, beam length was 2.3 m (7.5 ft) which is half of the JPCP slab length. The beam cross section was 0.2 m (8 in.) in height and 0.15 m (5.9 in.) in width. One end of the beam was fixed to the supporting steel I-beam and the other end was free to lift up. A dial-gauge was used to record the amount of warping at the free end over time. To facilitate a through-thickness moisture gradient the top surface was exposed to the environment and the bottom surface was either in contact with water or sealed using water-proof paint dependent on the moisture conditions desired. All the other four sides were sealed. A typical highway concrete with $w/c = 0.45$ was used throughout. The entire set up was placed in an environmental chamber maintained at constant

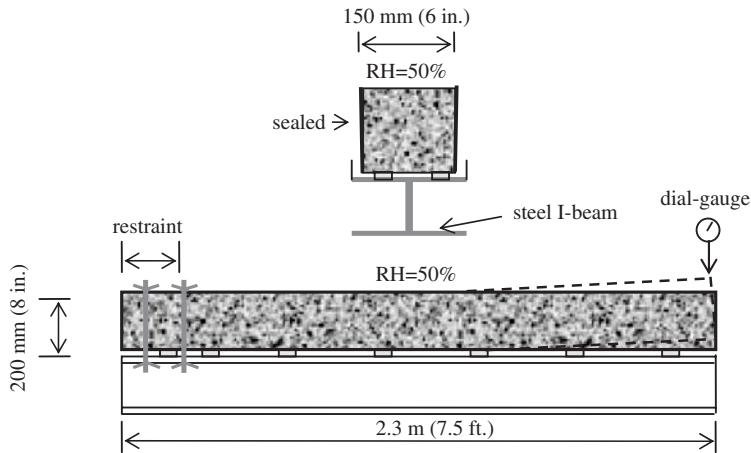


Figure 4. Laboratory moisture warping test.

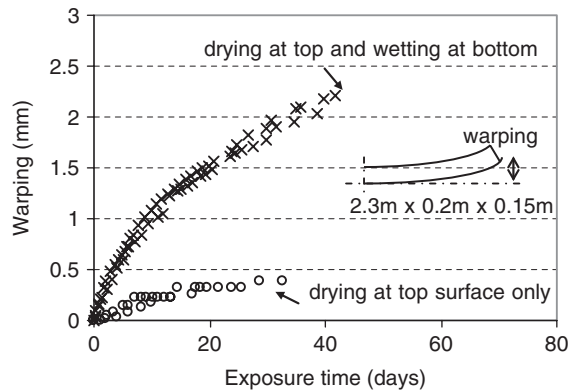


Figure 5. Measured beam warping over time, $w/c = 0.45$.

relative humidity (50%) and temperature (23°C/73°F). Measurements were initiated after 7 days of sealed curing. Two beams were measured for each moisture condition and the amounts of warping over time are plotted in Figure 5.

Results presented in Figure 5 demonstrate that exposure to water at the bottom creates an internal moisture gradient. The moisture gradient at the slab bottom is a result of differential autogenous moisture gradient due to limited moisture transport property within the discontinued pore structure. Moisture gradient at the beam top from drying shrinkage alone is less severe. These results demonstrate that continued moisture contact at the slab bottom is the cause for excessive corner uplift in highway pavements and floors on grade.

It is concluded from the results shown in Figure 6 that 20% sand replacement by volume with LWFA is effective in controlling self-desiccation in sealed concrete with $w/c = 0.45$. A 75% reduction in moisture warping is found after one month exposure to 50% relative humidity at the top and wetting at bottom. According to Weber & Reinhardt (1995), water movement from LWFA to the hydrating cement paste will stop when the relative humidity in the pores of LWFA is equivalent to that in cement paste. This may decrease the effectiveness of LWFA in reducing the moisture gradient associated with drying shrinkage.

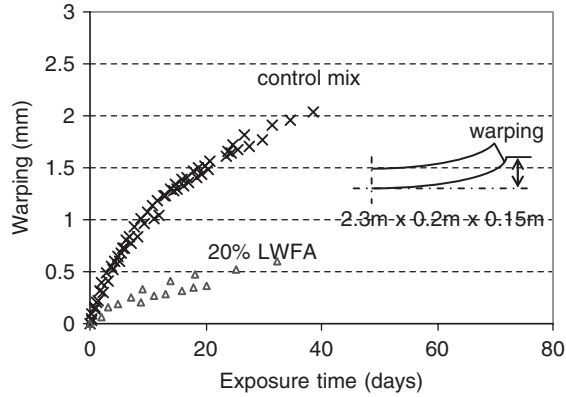


Figure 6. Measured development of beam warping (internal curing with 20% LWFA replacement by volume vs. control mix without internal curing), $w/c = 0.45$.

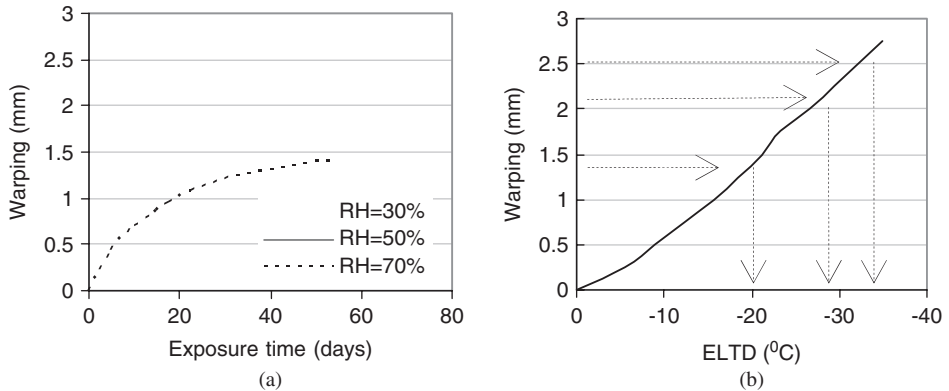


Figure 7. Predicted warping using MLS software for (a) different environmental RH conditions, and (b) the corresponding ELTD predicted using ISLAB software, $w/c = 0.45$.

5 MOISTURE WARPING MODELING

A 2-D FE software MLS, a product of FEMMASSE (MLS 2003), is utilized to model the moisture warping of a 250 mm-thick concrete slab exposed to simultaneous drying at top and wetting at bottom. Details on modeling can be found in Hansen et al. (2008). Moisture warping predictions for three different environmental conditions ($RH = 70\%$, 50% and 30%) in Figure 7a suggest that warping uplift is rapidly developing within 30–60 days of exposure time.

The back-calculated ELTD values using ILSAB 2000 are substantial (Fig 7b).

6 CONCLUSIONS

- Laboratory moisture warping results demonstrate that highway concrete is prone to major moisture warping if exposed to simultaneous wetting at the bottom and drying at the top.
- Internal curing procedure by using pre-soaked lightweight fine aggregate is found to be effective in reducing moisture warping.

ACKNOWLEDGEMENTS

This material is based upon work supported by the Michigan Department of Transportation, Contract No. 2006-0412, and Authorization No. 11 and 11a. The contents of this paper reflect the views of the authors who are responsible for the facts and the accuracy of the data presented herein. The contents do not necessarily reflect the views or policies of the Michigan Department of Transportation or the Federal Highway Administration. This work does not constitute a standard, specification, or regulation.

REFERENCES

- Baroghel-Bouny, V., 1996, Texture and moisture properties of ordinary and high-performance cementitious materials, Proceedings of Séminaire RILEM.
- Beckemeyer, C.A., Khazanovich, L., and Yu, H.T., 2002, Determining amount of built-in curling in Jointed Plain Concrete Pavement: case study of Pennsylvania I-80, Transportation Research Record 1809, 85–92.
- Beddoe, R., and Springenschmid, R., 1999, Moisture transport through concrete structural components, (In German), Beton-und Stahlbetonbau 94 (4), 158–166.
- Bentz, D.P., 2006, Capillary porosity depercolation/repercolation in hydrating cement pastes via low-temperature calorimetry measurements and CEMHYD3D modeling, *J. Am. Ceram. Soc.*, 89 (8), 260–261.
- Bjontegaard, Ø., 1999, Thermal dilation and autogenous deformation as driving forces to self-induced stress in high performance concrete, The Norwegian University of Science and Technology, PhD thesis.
- Darter, M.I., Hall, K.T., and Kuo, C.M., 1995, Support under Portland cement concrete pavements, NCHRP Report 372, 1–50.
- Davids, B., 2003, EverFE theory manual, Univerisy of Maine, Feb., EverFE version 2.24.
- Hansen, W., Smiley, D., Peng, Y., and Jensen, E.A., 2002, Validating top-down premature transverse slab cracking in jointed plain concrete pavement (JPCP), *Transportation Research Record 1809*, Transportation Research Board, Washington, D.C.
- Hansen, W., Wei, Y., and Schlangen, E.H., 2008, Modeling of moisture warping in concrete slabs on grade, *International Conference on Concrete Modeling CONMOD08*, RILEM, in press.
- Hansen, W., and Wei, Y., 2008, PCC pavement acceptance criteria for new construction when built-in curling exists, Michigan Department of Transportation Research Report RC-1481.
- Jensen, O.M., Hansen, P.F., 1996, Autogenous deformation and change of the relative humidity in silica fume-modified cement paste, *ACI Mat. J.*, Nov.–Dec.
- Khazanovich, L., Yu, H. T., and Beckemeyer, C.A., 2000, Application of ISLAB2000 for forensic studies, 2nd Int. Symp., *3D Finite Element for Pavement Analysis*, Design & Research, Charleston, Virginia.
- MLS, 2003, Computer program for the analysis of the thermal and mechanical behavior of hardening concrete, User Manual
- Pickett, G., 1956, Effect of aggregate on shrinkage of concrete and a hypothesis concerning shrinkage, *ACI Journal* 52(5), 1956, 581–590.
- Poblete, M. Garcia, A., David, J., Ceza, P., and Espinosa, R., 1990, Moisture effects on the behavior of PCC pavements, Proceedings, *2nd International Workshop on the Design and the Evaluation of Concrete Pavements*, Siguenza, Spain.
- Powers, T.C., Copeland, L.E., and Mann, H.M., 1959, Capillary continuity or discontinuity in cement paste, *PCA Bull.*, 10, 2–12.
- Rao, S., and Roesler, J.R., 2005, Characterizing effective built-in curling from concrete pavement field measurements, *Journal of Transportation Engineering*, ASCE, April, 320–327.
- Schleibinger, 1999, Manual of autogenous shrinkage deformation measurements
- Springenschmid, R., and Plannerer, M., 2001, Experimental research on the test methods for surface cracking of concrete, Institute for Building Materials, Technical University Munich, Germany.
- Toma, G., Pigeon M., Marchand J., Bissonnette B., and Barcelo L., 1999, Early age restrained shrinkage: stress build up and relaxation, International research seminar: Self-desiccation and Its Importance in Concrete Technology, Lund, Sweden, June 18., 61–71.
- Weber, S., and Reinhardt, H.W., 1995, A blend of aggregates to support curing of concrete, in Proceedings of the International Symposium on Structural Lightweight Aggregate Concrete, Eds. Holand, I., Hammer, T.A., and Fluge, F., Sandefjord, Norway, 662–671.

3. Performance of concrete pavements and white topping

Cracking in concrete pavements – an interaction of various influences

R. Breitenbücher & C. Sievering

Ruhr-Universität Bochum, Bochum, Germany

ABSTRACT: In the last few years cracking in concrete pavements was observed in several highway sections in some regions of Germany. Within the scope of extensive investigations no definite single cause of cracking has been observed in the majority of these cases. Therefore, the presented research program mainly focuses on in-situ experimental studies on selected highway sections in order to reveal which influences and interactions finally are responsible for such cracking.

Besides incremental load-induced stresses by increasing heavy traffic, especially load-independent stresses due to hygral and thermal changes are of relevance within this scope. Several investigations additionally substantiate reaction products of an alkali silica reaction (ASR). Because of this multiplicity of potential causes for cracking it has not been definitely clarified up to now to which extent especially the ASR is relevant for the cracking in concrete pavements. Rather it seems that a superposition and/or interactions of different mechanisms are responsible.

1 INTRODUCTION

In current discussions cracking in concrete pavements often is associated with an alkali silica reaction (ASR). However, even if relevant reaction products were detected in appropriate samples, cracks result only in the rarest cases from an ASR solely. Rather it is assumed, that cracks were caused by a superposition of several stress impacts. Beside restraint stresses due to disabled thermal and hygral self-deformations, concrete pavements are also stressed by traffic loads.

However, the influence of the alkali silica reaction in concrete pavements cannot be neglected. In such constructions especially the infiltration of alkalis from external sources is of a substantial importance. Alkaline de-icing agents applied in the winter months penetrate more or less intensively into the concrete structure, which lead to a continuous increase of the alkali potential. In case of high traffic volume this penetration process is intensified by the following vehicles. The intrusion of the alkalis furthermore is especially forwarded by already existent cracks. Due to these complicated interactions in concrete pavements more extensive measures are necessary to avoid damaging alkali silica reactions than in conventional concrete constructions.

2 CAUSES FOR PAVEMENT CRACKING

2.1 *Impairment of durability due to cracks*

The durability of concrete pavements is strongly impaired by cracks. Therefore a comparatively high flexural strength of at least 5.5 N/mm^2 is generally required in plain concrete slabs to minimize the risk of cracking. Nevertheless cracking in concrete pavements cannot be avoided in general. However, not each crack results in an impairment of the serviceability or a hazard. In this context it should be considered that only 1 to 2 percent of the total 3,600 kilometres concrete pavements are really damaged in Germany nationwide.



Figure 1. Map cracking in a concrete pavement.



Figure 2. Transversal longitudinal cracks in a concrete pavement.

For the characterization of cracks in concrete pavements it must be differentiated between various formations. In particular a differentiation between map cracking (Fig. 1) and clearly recognizable transversal cracks (Fig. 2) is essential.

As long as the crack width remains sufficiently small the serviceability of the pavement is not generally impaired. A critical stage has to be stated, when the edges of the cracks burst, in particular in the surrounding area of joints, due to the over-rolling traffic. In this way the crack widths is expanding continuously by themselves. If larger particles burst out, the following traffic will be seriously endangered, which is absolutely out of question. By this the general conditions of the concrete pavement will be drastically worsened; finally the pavement will be destructed progressively.

In order to be able to define adequate technological measures for avoidance of such critical cracking, the most relevant causes must be identified. In this context it has to be considered that cracks in concrete pavements are raised in the rarest cases only by one cause, in the majority a superposition or interactions between different mechanisms are responsible (Breitenbücher 2006b).

2.2 Restraint stresses

Due to the endless expansion in longitudinal direction, deformations in the pavements are practically completely restrained. In the cases of non-load-induced deformations, e.g. due to thermal or hygral changes, which extent over the complete cross-section, longitudinal restraint stresses are generated. Although in transverse direction a movement is enabled to some extent, restraint stresses also cannot be excluded completely in this case.

If a thermal or a hygral gradient yields over the slab thickness, – which is the standard case – the slab would tend to bend. These deformations are restrained by the tie bars as well as by the dead load of the slab to a large extent. In addition the slabs are pressed down by traffic. In consequence appropriate bending stresses with the tensile zone on the “cold” and/or “dry” side are generated.

In reality a stochastical temperature or moisture distribution will be found in such a slab. So finally between three types of stresses has to be differentiated (Fig. 3) (Springenschmid et al. 1993).

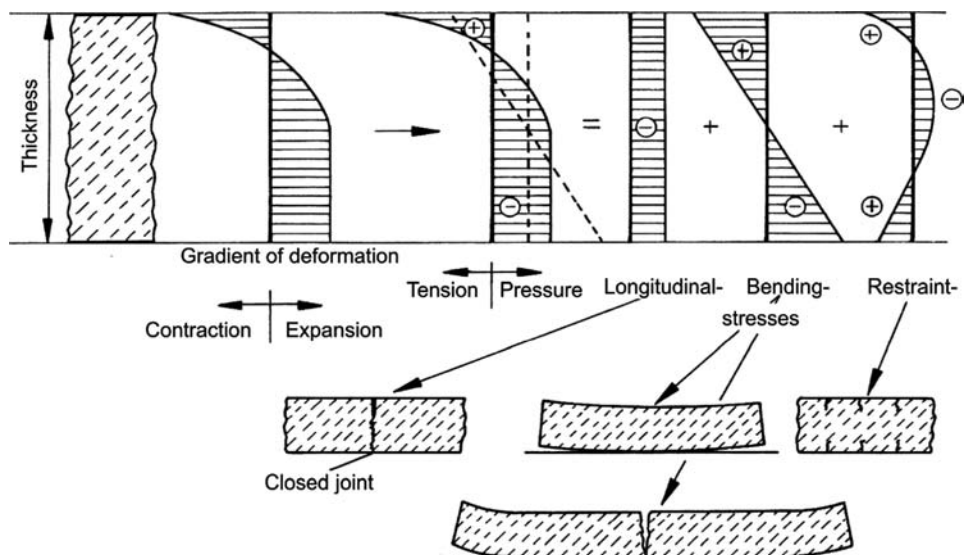


Figure 3. Stresses and cracks in concrete pavements due to negative gradients of deformation (Springenschmid et al. 1993).

While by the longitudinal restraint stresses cracks with approximately constant crack width throughout the complete slab are formed. due to bending stresses cuneiform cracks with the opening on the dry or cold side are raised.

Furthermore residual stresses are generated by a nonlinear deformation part (Fig. 3), which can result in map cracking. Such cracks are formed only in the surface zone, characteristic for them is a depth of only few millimeters.

2.3 Thermal stresses

In pavement slabs with thicknesses between about 25 to 30 cm the concrete can heat up during the hydration within the first few hours already by 15 to 25 K. This temperature raise is unfavorably affected by high temperatures, i.e. in summer, especially by a high fresh concrete temperature and intensive sun exposure. In the following cooling phase already high tensile stresses are generated, which can exceed the tensile strength of the concrete with the consequence of wild cracking (Breitenbücher 2006b).

In order to avoid such an early uncontrolled cracking, early sawing of the joints is indispensable. Nevertheless further bending stresses can be caused by the restraining tie bars.

Such thermal cracking is significantly affected by the fresh concrete temperature as well as by the type and content of cement. Additionally low thermal coefficients of the aggregates are favorable, not only at the early age, but also for the avoidance of cracking due to seasonal temperature changes (Breitenbücher 1990).

2.4 Hygral raised stresses

In the same manner as restrained thermal deformations also restrained hygral deformations result in appropriate restraint stresses (Grasley et al. 2006). Usually moisture changes take place only in the surface zone of a concrete slab (Fleischer 1992). In the case of one-sided drying a stress distribution is generated correlating with the moisture distribution and the hygral deformations resp. (Fig. 4a). These stresses can be essentially divided in constant-, bending- and residual stresses as shown in Figure 3.

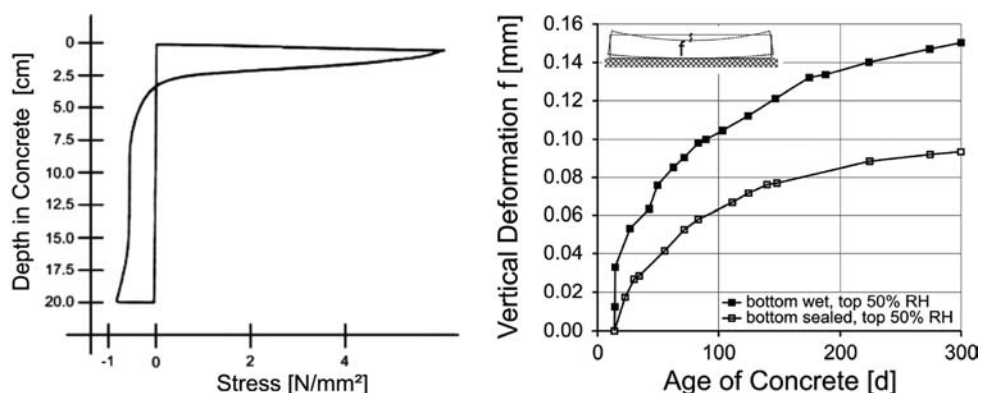


Figure 4. Effect of one sided drying on a) the stress distribution (Janssen 1987) b) the vertical deformation (Foos 2005).

These bending stresses become extreme, if parallel to the drying at the surface a moisturisation from the rear side takes place (Fig. 4b). Due to the collateral swelling at the rear side the warping is increased significantly (Foos 2005). In the case of concrete pavements, where the slabs are connected by dowels, also higher restrained stresses are connected with these effects.

Thus, stresses due to such restrained hygral deformations mainly can be minimized from the constructive part by an effective drainage of the underground (Forsyth et al. 1987). Furthermore shrinking and swelling of the concrete also can be minimized by adequate technological measures. So, cements with low internal surface and low alkali content were found as favorable for prevention of large hygral deformations (Fleischer 1992, Zhen & Zongjin 2005).

Apart from the gradual drying shrinkage cracks can also be generated already by an early drying of the fresh concrete. In this case very fine mapped cracks result within the first few hours. Although these cracks are only a few millimeters in depth, they can favor a later critical cracking as weak points.

2.5 Impact of traffic on microcracking

Within a cause study of cracking in concrete pavements both load-independent influences (thermal and hygral) as well as load-dependent influences (i.e. traffic) have to be considered. Even if the permissible axle loads have not been significantly increased in the past decades in Germany, the volume of the overall traffic and in particular of the heavy traffic has been drastically grown in this period. Between 1970 and 2005 the transported cargo volume increased from 80 billion ton kilometers up to 400 billion ton kilometers, i.e. by five times. Besides the static loads especially the dynamic/cyclic loads can affect the microstructure of the concrete. In appropriate tests, in which the behavior under cyclic loadings was investigated in general, it could be proved by a reduction in the dynamic E-modulus, that already at upper stress levels between about 45 and 70% of the concrete strength degradation processes take place in the microstructure far before fatigue failure is exceeded (Fig. 5) (Breitenbücher et al. 2006a).

Corresponding with the decreasing stiffness an increment in deformations is associated. Such changes in mechanical properties indicate that also in the microstructure alterations have been proceeded. However, such degradations are the basis of microcracking by which the penetration of moisture and other liquids into the concrete structure is improved to a large extent.

2.6 Expansion due to Alkali-Silica-Reaction

In the well-known alkali silica reaction amorphous silica (SiO_2) reacts with alkali hydroxide ions (NaOH , KOH), when simultaneously an appropriate amount of humidity is available. The reaction

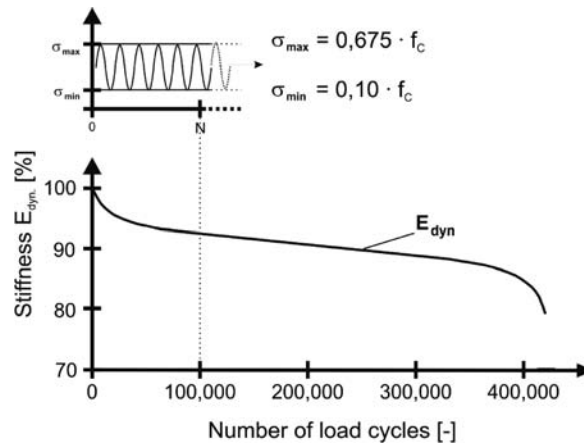


Figure 5. Decreasing stiffness of concrete under cyclic load (Breitenbücher et al. 2006a).

product is an alkali silica gel, which expands significantly due to absorption of water. This expansion is restrained by the surrounding concrete. So an internal pressure is raised, which can amount up to 20 N/mm^2 (Stark et al. 2001), which easily can exceed the tensile strength of the concrete with the consequence of internal cracking. Cracks due to an ASR are usually map distributed and netlike. They are not limited only to the visible surface area but extend over the complete concrete structure.

In the last few years cracking in concrete pavements often is associated with such alkali silica reactions (ASR) (Breitenbücher 2006b). However, even if relevant ASR-products are detected in appropriate samples, cracks result only in the rarest cases from that solely. In this context it has to be considered, that ASR is the only cracking cause, which can be identified later on by their reaction products. Other stresses due to thermal and hygral influences do not leave their marks afterwards. When on thin specimen sections alkali silica reaction products are detected, this proves only, that an ASR has taken place. However, it cannot be quantified up to now, to which extent this ASR has contributed to the crack-generation.

3 INVESTIGATIONS ON CRACKED PAVEMENTS BY ANALYSIS OF CONSTRUCTION DOCUMENTS

Within the scope of extensive investigations highway sections (with and without cracking, map cracking as well as longitudinal and transversal cracks) were selected for studies referring the causes for the cracking. In order to quantify these cracks, typical characteristics, e.g. the average quantity of cracks per slab, the average width of cracks per slab und the average cracking opening area, which is defined by the product of the total crack length and width per slab were determined.

In addition to the evaluation of the crack formation all available construction documents, i.e. daily construction records, reports on initial tests and quality control tests, weather records etc. were compiled and evaluated. In this context also the temperatures at concrete casting were compiled (Table 1).

In these analysis a significant influence of the temperature at concrete casting on the cracking could be proved in general (Fig. 6). Except of two subsections (10-6 and 10-8), which will be discussed below, it can be mentioned, that nearly no cracking was observed, when the temperature at casting was below 15°C to 20°C . Exceeding this temperature range, i.e. concreting in the summer season, cracking increases progressively.

The influence of the temperature at concrete casting becomes also obvious in Figure 7, where the situation in two adjacent sections of another German highway is documented. In section 1,

Table 1. Compilation of crack distribution and temperatures at concrete casting for 9 subsections of two various highways.

Section	Longitudinal und transverse cracking			Map cracking	
	Average quantity of cracks	Average width of cracks	Average area of crack opening	Average width of cracks	Average temperature at concrete casting
	–	mm	mm ²	mm	°C
9-1	5-6	0.40	11,000	0.30	23
9-2	1	0.10	500	0.10	3
9-3	1	0.15	750	0	14
10-2	5-6	0.20	5,650	0.20	26
10-5	4-5	0.20	5,050	0.45	20
10-6	6-9	0.30 – 0.65	14,300	0.55	15
10-8	3-4	0.25	4,500	0.10	10
10-11	0	0	0	0	8
10-12	6	0.20	6,600	0.10	26

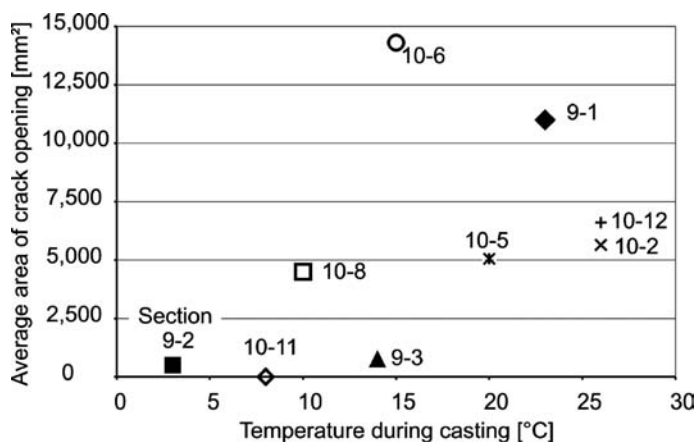


Figure 6. Influence of the temperature at concrete casting on crack opening area.

which was concreted in summer at about 25°C in most of the slabs, cracks have been formed. By contrast in the about 4 km long section 2, in which concrete of the same mix was poured in November/December at only about 5°C to 8°C, no cracks could be detected.

Thus the temperature at concrete casting can be stated as one of the main reasons for the cracking in concrete pavements. However, the scatter in the relations in Fig. 6 also indicates that beside of this thermal influence further parameters from the construction, execution and locality have to be considered.

Beside the thermal influence on concrete cracking in pavements, special hygral conditions may improve cracking as well. In particular one case (section 10-6, which shows a quite differing behaviour in Figure 6) the water drainage/piping system in the surrounding fields was switched off some years before. In consequence the ground water level raised up to the sub-base of the pavement, which became obvious also by the reed growing next to the pavement (Fig. 8). So also the concrete pavement became wet more and more from the bottom side, so that a moisture gradient develops, which could result in more or less additional bending stresses (see 2.4). Furthermore a sub-base

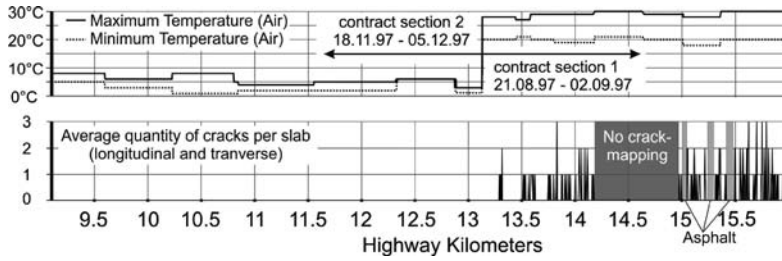


Figure 7. Crack formation and temperatures at concrete casting.



Figure 8. Reed beside the concrete pavement as consequence of ground-water-raising.

Table 2. Concrete mixtures of selected highway sections.

Section	Cement		Alkali-content		Reactive aggregate source
	Grade	Content	Na ₂ O _{eq.}	Total	
	–	kg/m ³	%	kg/m ³	
40-5, cracks observed	PZ 35 F (OPC)	360	0.88	3.17	Greywacke
40-6, no cracks	PZ 35 F (OPC)	340	0.73	2.48	Greywacke
40-7, no cracks	CEM I 32,5 R (OPC)	350	0.78	2.73	Greywacke

breakdown might also be responsible for the very extensive cracking, starting from the rear up to the pavement-surface.

Beside the influence of these boundary conditions within the evaluation also the alkali content of the cement could be proved as a further possible crack-inducing parameter. In three neighbouring sections of a highway in principle the same concrete mixes were used. Only the cement source differed in one case, which was linked with different alkali contents of the cement (Tab. 2).

In the two sections with cement containing only a moderate alkali content (sections 40-6 and 40-7, Tab. 2) no cracking could be observed. In these sections the Na₂O-equivalents of the cements used were below 0.80% by weight and the total alkali supply below 3.0 kg/m³. Because of these low alkali contents both the deformations due to hygral changes as well as the risk of a damaging ASR obviously could be kept below a critical stage.

In order to get more information on already occurred ASR and on further potential for a damaging ASR of the concrete used in the relevant sections cores with 150 mm diameter and full depth over the concrete pavement were taken from selected highway sections. On these cores further laboratory tests were performed.

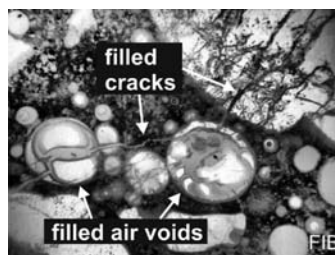


Figure 9. Voids and cracks in the matrix/aggregates filled with ASR products.

4 LABORATORY INVESTGATIONS

4.1 Petrographic scans

In order to identify ASR products, thin sections were taken from the cores for petrographic scans before and after the following appropriate ASR- tests (see 4.2). These thin sections were microscopically investigated at the Finger-Institute for Building Materials Science Weimar and the Research Institute of the German Cement Industry Düsseldorf, both act as partner within this project.

As a result of these scans three types of ASR-situations could be subdivided:

- Already in the sampling stage of the cores ASR products were detected, uniformly distributed all over the complete concrete structure: In the microstructure a lot of cracks could be observed, which were partially very wide. Cracks were observed also in the aggregates, independent whether they were crushed coarse aggregates or naturally rounded sand particles (Fig. 9). Already in this stage cracks and air voids were filled with unambiguous products of an ASR. After the specific ASR-tests a further increase of the reaction products could be ascertained.
- ASR products were detectable only in the surface zone: The concrete structure showed a few cracks in this area, which extended to a depth of about 3 to 4 cm. Small cracks were observed also in the coarse gravel. Cracks and air voids were filled with reaction products in the majority of these cases. Below a depth of approximately 7 cm only microcracks, but no ASR-products could be observed in the sampling stage. However, after the specific ASR-tests reaction products could be detected all over the complete concrete structure of the cores.
- Before as well after the ASR-tests no ASR products were detectable: only in some cases microcracks were observed up to a depth of 5 cm, which were vertically oriented. These cracks were found in the cementitious matrix as well as in the aggregates. Nevertheless, not any reaction products of an ASR could be detected in these cores.

4.2 Specific ASR- Tests on Concrete Cores at 60°C – with and without external alkali impact

To determine the residual potential of ASR within the concrete specimens further ASR-specific tests were performed on them. To obtain information as soon as possible, the tests were performed in special climates at 60°C to accelerate the ASR. In this context also the influence of an external alkali supply was considered. So for this purpose the cores were divided into two parts. One subspecimen was stored constantly at 60°C above water according to the “Alkali-Guideline (2006)” (DAfStB 2006), which is very similar to the “RILEM Recommended Test Method TC 191-ARP AAR-4” (Rilem 2000). The other subspecimen was exposed to following cyclic procedure: 6 days above water at 60°C, 1 day at 20°C, 5 days at 60°C in a dry air and 2 days immersed in a sodium chloride solution with a concentration of 0.6 mol/l. With this procedure the test specimens were loaded for 16 cycles. During the complete test phases the deformations of the specimens under both storing conditions were determined.

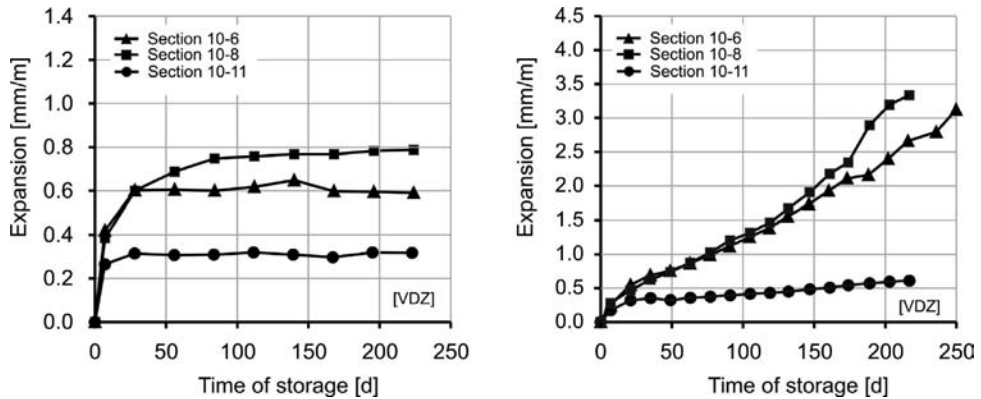


Figure 10. Expansion of drilled cores due to storage at 60°C left: without external alkali supply right: with external alkali supply.

Also when no ASR takes place deformations to some extent will occur in the samples only due to thermal and hygral effects within the test procedure. In the tests without external alkali supply these can lead to an expansion up to about 0.3 to 0.4 mm/m, in case of an external alkali supply they can increase up to 0.5 mm/m. Thus, only deformations exceeding these values may be linked with an ASR and can be considered within the evaluation.

In Figure 10 the results of the deformation measurements with (Fig. 10b) and without (Fig. 10a) external alkali supply are documented.

The comparison of Figure 10a and Figure 10b demonstrates that the expansions increased significantly when external alkali is supplied additionally. This has been known also from other investigations (Stark et al. 2006). Furthermore it could be proved, that the degree of expansion mainly is impacted by the degree of degradation/microcracking within the concrete microstructure. In samples taken from quite intensively cracked sections (sections 10-6 and 10-8, see Fig. 6) the moisture and the external alkalis penetrated much deeper into the concrete and enforced by this way an ASR much more intensive than in an uncracked concrete (section 10-11).

The concretes from the sections 10-6 and 10-11 had been produced with cement from the same plant, i.e. also the same alkali content in the fresh concrete can be assumed as identical. Furthermore also the aggregates derived from the same source, i.e. of the same reactivity (quartz porphyry). In contrary for the production of the concrete in section 10-8 a cement of lower alkali content and also another aggregate (greywacke) had been used. As in the concrete from section 10-8 the largest expansion was determined in the ASR-tests, it can be deduced, that the greywacke-aggregates in the this concrete is of some higher reactivity than the quartz porphyries in the other mix.

5 FINAL DISCUSSION AND CONCLUSION

Because of the multiplicity of potential causes for pavement cracking all possible influences have to be considered in order to reveal the relevant causes. In the minority of the investigated sections only one single reason could be found as responsible for the crack formation.

As presented in Figure 6, the temperature at concrete casting is of significant influence on the initial cracking of concrete pavements. With increasing pouring temperature an increase of the average area of crack opening could be observed in the majority of the investigated highway sections. Additionally, specific hygral circumstances, i.e. a raised level of the ground water can lead to large deformations, which generate primary cracks. As a result of the interpretation of construction documents it can be assumed that the initial cracking in concrete pavements basically is influenced to a larger extent by thermal and hygral circumstances than by ASR.

If in a concrete pavement microcracks have been already formed, moisture as well as external supplied alkalis easily can penetrate deep into the concrete microstructure. As documented in Figure 10 in consequence such pre-existing degradations or damages play a decisive role for the further development of ASR-expansions, provided that simultaneously adequate portions of reactive aggregates are present in the concrete.

If the concrete has not been impaired in any way before, the impact of external alkalis plays only a minor role for the further ASR-expansion. Thus the extent of premature degradations, e.g. raised by thermal/hygral effects or traffic loads, proved to be the most important impact for the formation of an ASR in concrete pavements in cases of external alkali supply. In contrast the alkali content of the cement used seems to be secondary in this case.

ACKNOWLEDGEMENTS

The authors are grateful to the Federal Ministry of Transport, Building and Urban Affairs (Germany) for financial support of this research project. The authors wish to acknowledge the cooperation with the Finger-Institute for Building Materials Science and the Research Institute of the German Cement Industry whose laboratory ASR tests were an important part of this project.

REFERENCES

- Breitenbücher, R. & Ibuk, H. 2006a. Experimentally based investigations on the degradation-process of concrete under cyclic load. *Materials & Structures* 39: 717–724.
- Breitenbücher, R. 2006b: Potentielle Ursachen der Rissbildung in Betonfahrbahndecken. Proceedings of the 16. ibausil, Weimar, Germany, Sept. 20–23 2006, Vol. 1: 1239–1254.
- Breitenbücher, R. 1990. Investigations of thermal cracking with the cracking frame. *Materials and Structures* 23: 172–177.
- DAfStB 2006. Vorbeugende Maßnahmen gegen schädigende Alkali-reaktion im Beton (Alkali-Richtlinie). Deutscher Ausschuss für Stahlbeton (ed.), Berlin: Beuth.
- Fleischer, W. 1992. Einfluß des Zements auf Schwinden und Quellen von Beton. Dissertation (doctoral thesis). In Baustoffinstitut der Technischen Universität München (ed.), *Schriftenreihe Baustoffe*, Vol. 1.
- Forsyth, R. A., Wells, G. K. & Woodstrom, J. H. 1987. Economic Impact of Pavement Subsurface Drainage. Transportation Research Board, Washington D.C., *Transportation Research Record* 1121: 77–85.
- Foos, S. 2005. Unbewehrte Betonfahrbahnplatten unter witterungsbedingten Beanspruchungen. Dissertation (doctoral thesis). In Schriftenreihe des Instituts für Massivbau und Baustofftechnologie (ed.), *Schriftenreihe*, Vol. 56.
- Grasley, Z. C., Lange, D. A. & D'Ambrosia, M. D. 2006. Internal relative humidity and drying stress gradients in concrete. *Materials and Structures* 39: 901–909.
- Janssen, D.J. 1987. Moisture in Portland Cement Concrete., Transportation Research Board, Washington D.C., *Transportation Research Record* 1121: 40–44.
- Rilem 2000. Detection of Potential Alkali-Reactivity– Accelerated method for testing aggregate combinations using concrete prisms. Recommended Test Method TC 191-ARP AAR-4. *Materials and Structures* 33: 290–293.
- Springenschmid, R. & Fleischer, W. 1993. Oberflächenrisse in älteren Betonfahrbahndecken. *Tiefbau-Ingenieurbau-Straßenbau*, Vol. 10: 724–732.
- Stark, J. & Wicht, B. 2001: *Dauerhaftigkeit von Beton*. Basel: Birkhäuser.
- Stark, J., Freyburg, E., Seyfarth, K. & Giebson, C. 2006. AKR-Prüfverfahren zur Beurteilung von Gesteinskörnungen und projektspezifischen Betonen. *Beton* 12: 574–581.
- Zhen, H. & Zongjin, L. 2005. Influence of alkali on restrained shrinkage behavior of cement-based materials. *Cement and Concrete Research* 35: 457–463.

Consequences of fracture mechanics for size effect, crack spacing and crack width in concrete pavements

C.G. Hoover & Z.P. Bažant

Northwestern University, Evanston, Illinois, USA

ABSTRACT: The ASTM standard C 78 for determining the modulus of rupture f_r (or flexural strength) provides a constant value of a measure of tensile strength which is currently used for designing pavements of all thicknesses, as well as concrete structural members, of all sizes. However, accumulated test data on f_r , as well as analytical studies and numerical simulations, clearly indicate that f_r is not constant but significantly decreases as the structure size increases. This evidence of size effect has so far been ignored. The consequence for thick pavements is increased cracking and thus poorer durability and serviceability, and for large structures even a significant increase of failure probability. The size dependence determined from test data follows a simple equation, which represents a gradual transition between a deterministic (energetic) size effect caused by stress redistribution at small sizes, and the power-law size effect of the classical Weibull statistical theory of strength, which is approached for large sizes. The transition is explained and modeled by the non-local Weibull theory. In this paper, modifications to the current standards that incorporate a simple procedure to obtain the size dependence f_r are proposed. Furthermore, the cohesive fracture mechanics, which is a more fundamental way to predict the effect of pavement thickness, resting on a given subsoil, is described. The energy release calculated according to cohesive fracture mechanics is shown to give the initial crack spacing, which may later increase due to instability of interacting parallel cracks. This is an important design consideration, since crack spacing controls the crack opening, and thus the ingress of water and corrosive agents, as well as transmission of shear stresses. Discussion and examples are limited to the formation of secondary cracks in between stress-relieving notches. This summary paper presents a general aperçu of the problem, explains the fracture mechanics approach, and concludes by comparisons with test data.

1 INTRODUCTION

The flexural strength of concrete beams, known also as the modulus of rupture f_r , has long been studied experimentally (Lindner and Sprague 1956; Nielsen 1954; Reigel and Willis 1931; Rocco 1995, 1997; Rokugo et al. 1995; Sabnis and Mirza 1979; Walker and Bloem 1957; Wright 1952; Koide, Akita, and Tomon 1998, 2000), numerically (Hillerborg, Modeer, and Petersson 1976; Petersson 1981) and analytically (Zhu 1990, Bazant and Li 1995; Bazant and Planas 1998). Perhaps the most important results of these studies is the fact that f_r of concrete significantly decreases as the structure size increases. This phenomenon, called the size effect, can compromise the safety of structures designed on the basis f_r . It has been shown that ignorance of size effect must have been one of the factors that led, e.g., to catastrophic collapse of the New York State Thruway Bridge over Schoharie Creek, and the tragic failures of Malpasset arch dam over the Reyran River and of the St. Francis Dam in the Los Angeles aqueduct system. In the case of pavements, it has doubtless increased the frequency of excessive cracking of thick unreinforced pavements, thus reducing their durability. This phenomenon, however, is not reflected in the current ASTM testing standards.

The theoretical basis of the proposed size effect is the energy release aspect of cohesive fracture mechanics. The energy release is what governs the initial crack spacing, which is what governs the crack spacing, which in turn controls the crack opening, and thus the ingress of water and corrosive agents as well as transmission of shear stresses by aggregate interlock. Thus an explanation of how the energy release relates to crack initiation is needed. A brief description is presented.

2 CRACK INITIATION, AS IT RELATED TO CONCRETE PAVEMENTS

According to Hong et al. (1997) the service life of asphalt concrete pavements as well as Portland Cement concrete pavements is often determined by cracking, caused primarily by temperature and humidity changes. In concrete structures, the spacing of parallel cracks is an important factor mainly because it determines the crack width (Bažant and Cedolin 1991). Therefore, it is important to understand the parameters governing crack initiation, as well as how to calculate initial crack spacing. The process of initial crack formation consists of a transition from the pre-initiation state, at which the strength criterion is satisfied, to the post-initiation state, where Griffith's criterion of crack propagation is satisfied. This transition is governed by three main conditions for cohesive crack initiation from smooth surface, as discussed by Li and Bažant (1994), as summarized below.

First, the strength criterion can indicate whether cracks can start at a smooth surface. This is achieved when the tensile stresses that develop in the pavement, most commonly caused by shrinkage and thermal loading, reach the tensile strength of the pavement material. However, neither the strength criterion nor linear elastic fracture mechanics (LEFM) can be used at crack initiation to determine whether or not cracks of finite length can form and what their spacing would be. This is because LEFM considers only the condition of growth of existing cracks, and the energy release rate equals zero for a zero crack length. Therefore, additional conditions for crack initiation are required.

A second condition for crack initiation is that the energy release rate of the structure after the initial cracks form must be equal to the fracture energy of the pavement material in the post-initiation state. The third and final condition states that during the formation of new cracks, the total energy needed to form new crack surfaces, which is αG_f for each crack, must be equal to the energy released by the structure; here α = crack depth, and G_f = fracture energy of the material. This was proposed by Bažant and Ohtsubo (1977), later discussed by Bažant and Cedolin (1991), and used for crack spacing analyzed in a containment vessel by Bažant et al. (2003). Under the assumption that cracks of a certain finite length form suddenly over their entire length, these authors proposed that the total energy release rate from crack initiation, due to drying shrinkage stresses (or cooling stresses) in an isotropic elastic half space, is not zero but finite. By setting this energy equal to the energy required to create cracks, these authors derived the following equation (which was shown to yield realistic predictions of the spacing of thermal cracks in granite):

$$s = \frac{10}{r} \left(\frac{1-\nu}{1+\nu} \right) \left(\frac{G_f}{E} \right) \left(\frac{1+\varphi}{\epsilon_s^0} \right) \left(\frac{a}{\lambda} \right) \quad (1)$$

Here φ = creep coefficient; s = crack spacing; ϵ_s^0 = free shrinkage (or thermal strain) at half-space surface; λ = penetration depth of drying or cooling; ν = Poisson ratio; α = crack length; r = a constant between 0 and 1, probably close to 1; E = Young's modulus.

Equation (1) provides a relationship between the fracture energy and the initial crack spacing. During the subsequent crack growth, some cracks may close and the spacing of open cracks will then change, as decided by stability criteria of the crack system (Bažant and Ohtsubo 1977, Bažant et al. 1979, and Bažant and Cedolin 1991). For simplicity, consider a two-dimensional problem of a homogeneous isotropic elastic half space where a random crack pattern is replaced by a system of parallel cracks, normal to the surface and spaced at a statistically averaged spacing s , caused by cooling or drying shrinkage (see figure 1). Assume also that at an initial state, all crack are equal

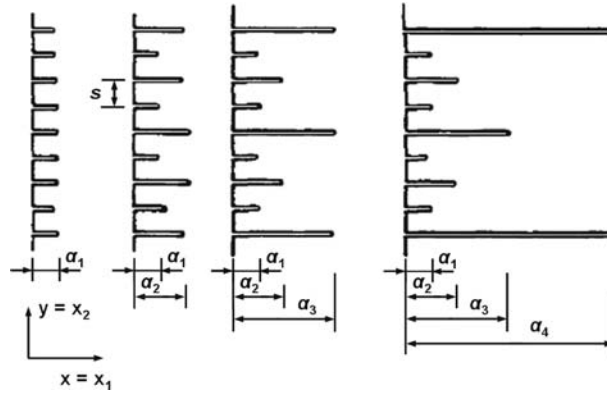


Figure 1. System of Parallel cracks in a half-space. (After Bažant, Ohtsubo, and Aoh, 1979.)

in length ($\alpha_1 = \alpha_2$) and growing, i.e., critical ($K_1 = K_c$), where K_c is fracture toughness and K_i is the mode I stress intensity factor for the i th crack.

Now, consider the possibility that every other crack extends by $\delta\alpha_2$ while the remaining cracks remain stationary ($\delta\alpha_1 = 0$). The instability mode at critical state consists of a sudden advance of every other crack by $\delta\alpha_2 > 0$, occurring at $\delta\alpha_1 = 0$ and at a constant λ , which indicates no change in the distribution of relative humidity in the pores of concrete (or temperature distribution) within the half-space. This represents a critical state, or bifurcation of the equilibrium path. It was discovered, using finite element calculations, that K_1 decreases after the critical state, which indicates that system of equally long parallel cracks is losing its stability, while K_2 remains equal to K_c .

After bifurcation, cracks α_2 grow stably as the cooling front advances, ($K_2 = K_c$), while cracks α_1 are arrested ($\alpha_1 = \text{const.}$) and are closing while their K_1 decreases. Eventually, K_1 becomes zero and, as the cooling front advances further, cracks α_1 begin to close. The solution now becomes equivalent to that at the start—a system of equally long cracks of length α_2 , but the spacing has now doubled to $2s$.

This type of bifurcation will continue to repeat itself, as can be seen in figure 1. The significance of this type of behavior is that the crack opening δ_c at the crack mouth is approximately $\delta_c = \varepsilon^0 s^0$, where s^0 is the spacing of the open cracks. If the relative humidity at halfspace surface is h , the free shrinkage strain is $\varepsilon^0 = k \delta_w$, where $k = \text{constant}$ and δ_w is the specific water loss of concrete corresponding to the relative humidity drop at surface (in the case of cooling at halfspace surface from temperature T_0 to temperature T_1 , the free thermal strain produced is $\varepsilon^0 = \alpha(T_0 - T_1)$, where $\alpha = \text{coefficient of thermal expansion}$).

So, the crack width increases as the crack spacing increases. This is an important design consideration for concrete pavements because, unlike narrow cracks, wide cracks conduct moisture much faster and are not bridged to transmit shear or tensile stresses by aggregate interlock. Wide cracks also allow easier inflow of corrosive agents, which becomes an important consideration for concrete pavements when one considers freeze-thaw damage.

3 SIZE EFFECT PROBLEMS IN CONCRETE PAVEMENTS

The size effect is not negligible. To be specific, see the collection in figure 2 of ten test series by different authors, with a range of specimen sizes commonly used in practice. In this collection, an increase of the beam depth from 75 mm to 1 m, a range that encompasses typical sizes for concrete pavement slabs, causes the flexural strength to drop, on average, by a factor of 1.25. Then, consider the results from specimens tested by Rocco (1995, 1997) and by Lindner and Sprague (1956), figure 3a and 3b. Here the strength drops the factor of 1.33 and 1.58, respectively, for specimens in

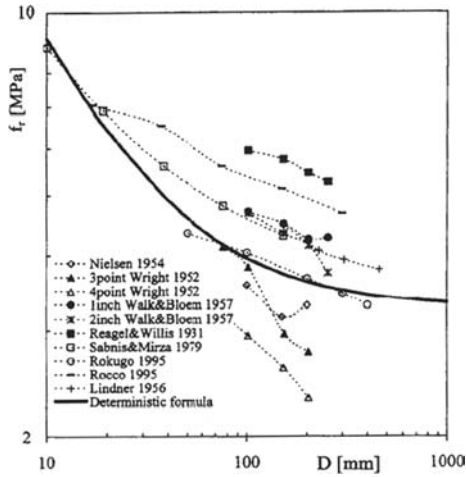


Figure 2. Existing test data from ten investigators on modulus of rupture f_r versus beam size (depth) D .

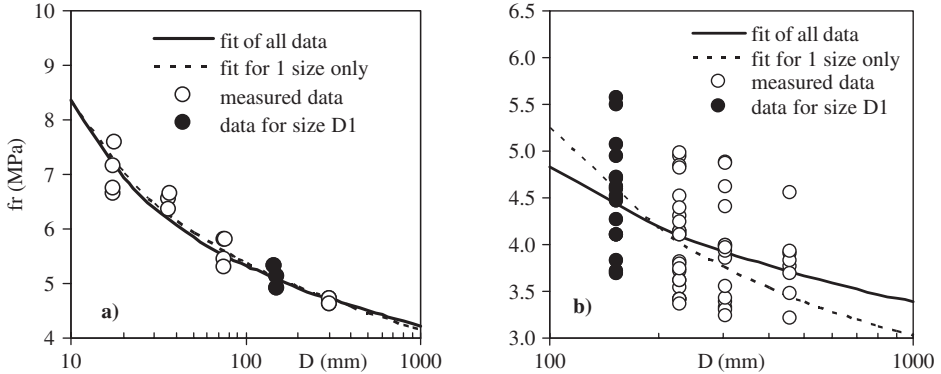


Figure 3. Dependence of modulus of rupture f_r on beam size measured by (a) Rocco, (b) Lindner & Sprague.

the same range. The test methods currently used for determining the modulus of rupture, outlined in standards C 78 – 02 and C 293 – 02, utilize specimens of one size only. They do not provide an experimental basis for determining the dependence of modulus of rupture on the specimen size. Without such a procedure, the size effect cannot be taken into account.

From the viewpoint of design safety and durability, there are only two options. First, insert into the current ASTM standards C78 and C 293 a restriction that the measured value of f_r can be used only for calculating the load capacity of unreinforced beams, slabs or walls whose depth or thickness is close to the specimen depth used in C78 (perhaps 4 to 9 inches). Or, add to C78 and C 293 a section specifying how f_r must be adjusted for size effect if it is used in load capacity calculations of beams, slabs and walls of arbitrary dimensions. Option 1 would reduce the scope of applicability of the current standards, however it acknowledges the existence of size effect, and aims to alleviate misuse of the calculated result. A more useful solution is option two. Bažant and Novák (2000 and 2001) proposed two simple experimental and mathematical procedures for calculating the modulus of rupture for any specimen size. The theory accounts for both the deterministic-energetic size effect and the classical Weibull-type statistical size effect, which is approached for very large structures. An overview of their procedure is presented next.

4 ASTM FORMULA FOR MODULUS OF RUPTURE

The concept of modulus of rupture is based on elastic beam theory. For an unreinforced beam of rectangular cross section, the modulus of rupture is defined to as to coincide with the maximum tensile stress in the beam:

$$f_r = \frac{6M_u}{bD^2} \quad (2)$$

where M_u = ultimate bending moment; D = characteristic size of the specimen, often equal to the depth or height; and b = specimen width. If the concrete would remain linearly elastic up to the peak load, the strength values obtained from flexural tests and direct tensile tests would be equal to each other. However, except for the asymptotic case of an infinitely large beam, the whole section of a concrete beam does not remain elastic up to the maximum load. Thus, f_r represents only the nominal strength σ_N , which is a parameter of the maximum load.

The maximum load of plain concrete beams occurs before a continuous crack localizes, but only after a large boundary layer of distributed cracking of a certain critical thickness develops at the tensile face of the beam. The cracking in the boundary layer, representing the fracture process zone of fixed thickness, causes energy release and stress redistribution throughout the cross section. For beams of different sizes made of the same concrete, the thickness of this layer, governed by the maximum size of aggregates, is independent with specimen size. The formation of this fracture process zone is the main reason why the direct tensile strength differs from the modulus of rupture. Since, in a deeper beam, the cracking layer occupies a smaller percentage of the cross section, there is less stress redistribution. Thus the nominal strength decreases with increasing beam depth.

5 IMPLEMENTATION OF SIZE EFFECT LAW INTO ASTM STANDARDS

The cause of the size effect on the modulus of rupture, and generally the size effect for all failures occurring at crack initiation from a smooth surface, is primarily deterministic. However, for very large size specimens, an additional cause is statistical, stemming from the randomness of local material strength as captured by Weibull's (1939) classical theory. Bažant and Novák (2000c) have shown that the modulus of rupture follows the energetic-statistical size effect trend law:

$$f_r = f_r^0 \left[\left(\frac{D_b}{D} \right)^{\frac{rn}{m}} + \frac{rD_b}{D} \right]^{1/r} \quad (3)$$

where f_r^0 and D_b are constants to be identified, r is a constant, n is the number of dimensions in geometric similarity (either 2 or 3) and m is the Weibull Modulus. Bažant and Novák (2000c) showed that the values $m = 24$, $r = 1.14$ and $n = 2$ are acceptable for all concretes, on the average. Therefore, equation (3) reduces to:

$$f_r = f_r^0 \left[\left(\frac{D_b}{D} \right)^{0.095} + \frac{1.14D_b}{D} \right]^{0.88} \quad (4)$$

Or, approximately:

$$f_r = f_r^0 \left[\left(\frac{D_b}{D} \right)^{0.1} + \frac{1.14D_b}{D} \right] \quad (5)$$

The only two unknown parameters, which need to be identified by tests, are f_r^0 and D_b .

Bažant and Novák (2001) proposed two testing methods to be implemented into the current ASTM Standards for determining the size dependence of f_r . Based on this work, and some valuable comments received from individuals in industry, a simple mathematical procedure is proposed to be included in sub-section 8, "Calculation".

Bažant and Novák (2001) showed that parameter D_b can be approximated as follows:

$$D_b \approx \delta_1 (10)^{0.15+(l_0/l_1)}, \quad \delta_1 = 1 \text{ mm}, \quad l_1 = 53 \text{ mm} \quad (6)$$

Here, l_0 is the characteristic length of concrete. Normally, it is not known. However, l_0 can be roughly taken as

$$l_0 \approx d_a (d_a / d_1)^{1/3}, \quad \delta_1 = 1 \text{ mm} \quad (7)$$

Or approximated as two times the maximum coarse aggregate diameter. Once D_b is known, f_r^0 is then calculated by:

$$f_r^0 = f_r^1 \left[\left(\frac{D_b}{D_1} \right)^{0.1} + \frac{1.14 D_b}{D_1} \right]^{-1} \quad (8)$$

where D_1 = depth of standard test specimen, which is 6 inches; f_r^1 = modulus of rupture, calculated using equations currently in the testing standard. Once D_b and f_r^0 are known, they can be substituted into equation (5) to determine the size dependence on f_r .

6 NUMERICAL EXAMPLES

The specified procedure will now be applied to two sets of published experimental data on three-point bending. The first represents high quality data for beams of five different sizes spanning a wide size range. The first data set reports the specimen dimensions in metric units. For illustrative purposes, the size closest to the standard 6 in. depth will be used. Therefore, assume that the test result for the modulus of rupture for size $D_1 = 148.1$ mm and $d_a = 5$ mm yielded $f_r^1 = 5.12$ MPa. Using the outlined procedure, and equation (7) for l_0 , $f_r^0 = 7.67$ MPa and $D_b = 2.05$ mm. The resulting size dependence of the modulus of rupture according to the size effect law equation (3) is plotted in figure 3a.

The second example uses test data with much greater scatter (figure 3b). For the values $d_a = 25.4$ mm, $D_1 = 152.4$ mm, $f_r^1 = 4.53$ MPa, and using equation (7) for l_0 , the following values are obtained: $f_r^0 = 3.984$ MPa and $D_b = 36.2$ mm. Using these values in the size effect law equation (5) leads to figure 3b. Also shown in both figures is the case where data for all the sizes was used to identify the material parameters. For this purpose, the Levenberg-Marquardt nonlinear optimization algorithm had to be used.

From the diagrams it is clear that the size effect plot obtained from tests of only one size differs little from the plot obtained by nonlinear fitting of equation 3 using all the sizes. Figure 4 shows illustrative figures of these procedures generated using a spread-sheet program.

7 SUMMARY AND CONCLUSIONS

1. The available experimental evidence clearly indicates that the modulus of rupture of unreinforced concrete specimens decreases with increasing specimen depth (size). Ignoring this fact was likely one of the causes of some tragic failures. In pavements resting on the ground, the size effect, of course, does not kill, however it has doubtless increased the frequency of excessive cracking of

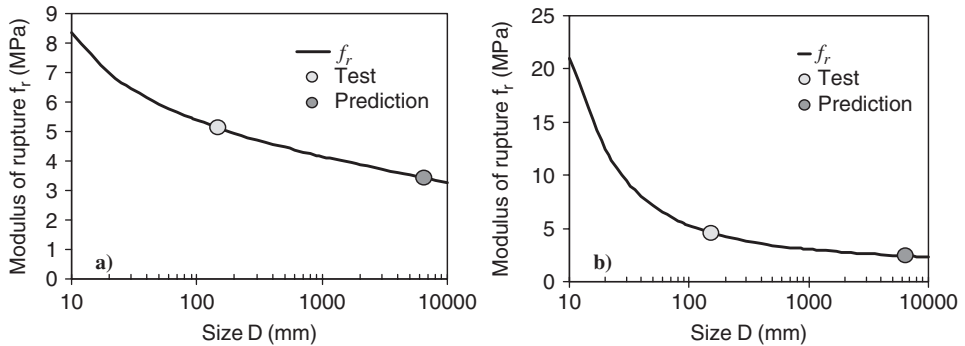


Figure 4. Figures from spreadsheet program using fitted data from a) Rocco, b) Lindner & Sprague.

- unreinforced pavements and thus reduced their durability. The current ASTM standards do not provide an experimental procedure for determining this size dependence of f_r .
2. The theoretical basis of the proposed size effect is the energy release aspect of cohesive fracture mechanics. The energy release is what governs the initial crack spacing, which is what governs the crack spacing, which in turn controls the crack opening. The spacing and opening can then be further influenced by instabilities of a system of parallel cracks caused by drying shrinkage or cooling.
 3. A revised, simplified method for determining the size dependence of f_r is proposed. This method is illustrated by examples from existing published data sets.

REFERENCES

- ASTM, 2006. Designation: C 78 – 02 Standard Test Method for Flexural Strength of Concrete (Using Simple Beam with Third-Point Loading). *Concrete and Concrete Aggregates* 4 (4.02): 39–41.
- ASTM, 2006. Designation: C 293 – 02 Standard Test Method for Flexural Strength of Concrete (Using Simple Beam with Center-Point Loading). *Concrete and Concrete Aggregates* 4 (4.02): 182–184.
- Bažant, Z. P., and Ohtsubo, H. 1977. Stability Conditions for Propagation of a System of Cracks in a Brittle Solid. *Mechanics Research Communications* 4 (5): 353–366.
- Bažant, Z. P. et al. 1979. Stability and Post-Critical Growth of a System of Cooling of Shrinkage Cracks. *Int. J. Fracture* 15 (5): 443–456.
- Bažant, Z. P., and Oh, B. H. 1983. Spacing of Cracks in Reinforced Concrete. *J. of Structural Engineering, ASCE* 109: 2066–2085.
- Bažant, Z. P., and Oh, B. H. 1983. Crack spacing in Reinforced Concrete: Approximate Solution. *J. of Structural Engineering, ASCE* 109: 2207–2212.
- Bažant, Z. P., and Cedolin, L. 1991. *Stability of Structures*. Mineola, New York, Dover Publications, Inc.
- Bažant, Z. P., and Li, Z. 1995. Modulus of Rupture: Size Effect Due to Fracture Initiation in Boundary Layer. *J. of Structural Engineering, ASCE* 121 (No 4): 739–746.
- Bažant, Z. P., and Planas, J. 1998. *Fracture and Size Effect in Concrete and Other Quasi Brittle Materials*. Boca Raton, CRC Press.
- Bažant, Z. P., and Novák, D. 2000a. Probabilistic Nonlocal Theory for Quasibrittle Fracture Initiation and Size Effect. I. Theory. *J. of Engrg. Mech, ASCE* 126 (2): 166–174.
- Bažant, Z. P., and Novák, D. 2000b. Probabilistic Nonlocal Theory for Quasibrittle Fracture Initiation and Size Effect. II. Application. *J. of Engrg. Mech, ASCE* 126 (2): 175–185.
- Bažant, Z. P., and Novák, D. 2000c. Energetic-Statistical Size Effect in Quasi-Brittle Failure at Crack Initiation. *ACI Materials Journal* 97 (No. 3): 381–392.
- Bažant, Z. P., and Novák, D. 2001. Proposal for Standard Test of Modulus of Rupture of Concrete with its Size Dependence. *ACI Materials Journal* 98 (No. 3): 79–87.
- Bažant, Z. P. et al. 2003. Cohesive fracturing and stresses caused by hydration heat in massive concrete wall. *J. of Engrg. Mech. ASCE* 129 (1): 21–30.

- Hillerborg, A. et al. 1976. Analysis of Crack Formulation and Crack Growth in Concrete by Means of Fracture Mechanics and Finite Elements. *Cement and Concrete Research*, 6 (No 6): 773–782.
- Hong, A. P. et al. 1997. Theory of Crack Spacing in Concrete Pavements. *J. of Engrg. Mech, ASCE*, 123 (3): 267–275.
- Koide, H. et al. 1998. Size Effect in Flexural Resistance Due to Bending Span of Concrete Beams. *Fracture Mechanics of Concrete Structures*, Proceedings of the 3rd International Conference, FraMCoS-3, Gifu, Japan, H. Mihashi, and K. Rokugo, eds., Aedification Publishers, Freiburg, Germany: 2121–2130.
- Koide, H. et al. 2000. Probability Model of Flexural Resistance on Different Lengths of Concrete Beams. *Application of Statistics and Probability*, Proceedings of the 8th International Conference, ICASP-8, Sydney, Australia, 1999, R. E. Melchers, and M. G. Stewart, eds., Balkema, Rotterdam, 2: 1053–1057.
- Lindner, C. P. and Sprague, I. C., 1956. Effect of Depth of Beams upon the Modulus of Rupture of Plain Concrete. *ASTM Proceedings*, 15: 1062–1083.
- Li, Y. N., and Bažant, Z. P., 1994. Penetration Fracture of Floating Sea ice-plate: 2D Analysis and Size effect. *J. Engrg. Mech, ASCE* 120 (7): 1481–1498.
- Nielsen, K. E. C., 1954. Effect of Various Factors on the Flexural Strength of Concrete Test Beams. *Magazine of Concrete Research*, 15: 105–114.
- Petersson, P. E., 1981. Crack Growth and Development of Fracture Zone and in Plain Concrete and Similar Materials. *Report No. TVBM-1006*, Division of Building Materials, Lund Institute of Technology, Lund, Sweden.
- Reigel, F. V., and Willis, G. H., 1931. The Effect of Dimensions of Test Specimens on the Flexural Strength of Concrete. *Public Roads*, 12: 37–46.
- Rocco, C. G., 1995. Influencia del Tamano y Mecanismos de Rotura del Ensayo de Compresión Diametral. Doctoral Thesis, Dep. Ciencia de Materiales, Universidad Politecnica de Madrid, ETS de Ingenieros de Caminos, Ciudad Universitaria, 28040 Madrid, Spain. (in Spanish).
- Rocco, C. G., 1997. Private communications by J. Planas on unpublished tests of size effect on modulus of rupture of concrete at Technical University, Madrid.
- Rokugo, K. et al. 1995. Fracture Mechanics Approach to Evaluation of Flexural Strength of Concrete. *ACI Materials Journal* 92 (No. 5): 561–566.
- Sabnis, G. M., and Mirza, S. M., 1979. Size Effect in Model Concretes *ACI Journal of Structural Division* 106: 1007–1020.
- Walker, S., and Bloem, D. L., 1957. Studies of Flexural Strength of Concrete-Part 3: Effects of Variations in Testing Procedures. *ASTM Proceedings* 57: 1122–1139.
- Weibull, W., 1939. The Phenomenon of Rupture in Solids. *Proceedings, Royal Swedish Institute of Engineering Research (Ingenioersvetenskaps Akad. Handl.)* 153: Stockholm, 1–55.
- Wright, P. J. F., 1952. Effect of the Method of Test on the Flexural Strength of Concrete. *Magazine of Concrete Research* 11: 67–76.
- Zhu, Y., 1990. Flexural Strength for Concrete Beams without Initial Cracks. *Proceedings 8th European Congress of Fracture: Fracture Behavior and Design of Materials and Structures (Torino)* 2 D. Firrao, ed., Chameleon Press, Ltd., London: 559–604.

Assessment and mitigation of early-age cracking in concrete pavements due to restrained movement

S.S. Tyson

Federal Highway Administration, Washington D.C., USA

S.D. Tayabji & H.T. Yu

CTL Group, Columbia, Maryland, USA

ABSTRACT: This paper reviews the occurrence of cracking in newly constructed jointed plain concrete pavements (JPCP) in two Midwestern states in the USA during the 2005 construction season. A project in North Dakota and another in Oklahoma developed cracking during construction. In both cases, the cracking was attributed to restrained movement. An immediate assessment was made of the cause of the cracking and remediation measures were recommended. Presented in this paper is a discussion of the factors that can contribute to early age cracking and the cracking mechanism, as well as the steps that can be taken to avoid such cracking.

Various factors can affect the risk of early-age cracking, including material properties of concrete, environmental conditions during construction, pavement design, and slab-base interface conditions. The available methods of evaluating the risk of early-age cracking are discussed. Recognizing the high-risk conditions for early-age cracking is essential to avoid such cracking. The general conditions that present high-risk conditions for early-age cracking are summarized. Also discussed are mitigation and correction of early-age cracking.

1 INTRODUCTION

Uncontrolled, early-age cracking sometimes occurs in jointed plain concrete pavements (JPCP), despite normally adequate design, construction, and jointing practice (1). However, invariably, the cracking is a result of some combination of the risk factors at work, and upon close inspection, the cause of cracking can usually be identified. Various factors can affect the risk of early-age cracking, including paved width, joint spacing, slab thickness, interface friction, modulus of subgrade reaction, temperature and moisture conditions during construction, and concrete modulus of elasticity, as well as strength. Comprehensive analytical procedures are available that are capable of evaluating the interactions of the key factors and assess the risk of cracking. These tools are helpful in identifying the high-risk conditions for early-age cracking. The key to minimizing the occurrences of the undesirable, early-age cracking lies in recognizing and avoiding the high-risk designs and conditions that can lead to cracking.

The cracking is a concern if it has the potential to deteriorate and pose serviceability or structural problem, or both. The impact of cracking depends on the type of cracking, climate, traffic, and pavement design. In some cases, the cracks may have no significant effect, while some cracks are not tolerable on a newly constructed pavement. The treatment selection for early-age cracking should be made with the best long-term pavement performance in mind. This is a separate issue from determining who should pay for the repairs, or whether the contractor deserves a full pay. Ideally, the pavement after the repairs should provide the same level of performance over the design period as the intact pavement. At the very least, the selected treatment should be the best performance option under the circumstances.

This paper focuses on two very specific types of early-age cracking: 1) those related to base restraint and curling/warping stresses, and 2) those caused by edge restraint. A case example of each type of cracking is provided. Presented are discussions on the causes of cracking, evaluation methods, treatment options, and recommendations on how to minimize the occurrence of early-age, random cracking.

2 CAUSES OF EARLY-AGE CRACKING

Concrete pavements crack when the tensile stresses within the concrete exceed the strength. After placement, both strength and restraint stresses develop in concrete. The restraint stresses are a result of volume changes of concrete associated with the hydration process, as well as the changes in the temperature and moisture exposure conditions. The exposure conditions during paving, such as temperature, wind speed, humidity, and sunlight, affect the rate of hydration and amount of moisture loss from concrete, which in turn affects the amount of autogenous shrinkage of concrete. The volume changes corresponding to the changes in concrete temperature since hardening can be significant. The uniform volume change induces direct tensile stresses in the pavement slabs.

Adding to the horizontal restraint stresses are those resulting from the resistance to slab curling and warping. The pavement slabs can be exposed to significant temperature and moisture gradients, depending on the temperature and moisture exposure conditions. Temperature and moisture gradients would cause the slabs to curl or warp, if unrestrained; however, the self-weight of the slab resists the curling and warping to produce bending stresses, which can be very high, depending on the exposure conditions. Whereas the volume changes of concrete is responsible for both types of cracking considered in this paper, the curling and warping stresses only affect the first type, the type related to sawcut timing.

The restraints to concrete volume change and slab curling or warping can cause transverse, longitudinal, or erratic (Figure 1) cracking. The potential for this type of cracking diminishes once the sawcuts are made to relieve the restraint stresses. However, if several adverse factors are at work in concert, it may not be possible to saw early enough to prevent cracking. Figure 2 illustrates the window of opportunity of joint sawing (2). In general, the sawcuts should be made as soon as the concrete can be sawed without raveling. The end of sawing window is when the restraint stresses equal the concrete strength. If the sawcut is not made by the end of sawing window, random cracking will occur. Adverse factors reduce the window of sawing opportunity. In extreme cases, it may not be feasible to accomplish all the sawing before cracking occurs. The factors that affect the available time for joint sawing include the following (3, 4):

- Weather condition – temperature and moisture conditions; night-time temperature drop or temperature drop due to rain or sudden passing of a cold front.
- Construction practice – timing of joint sawing and curing practice.

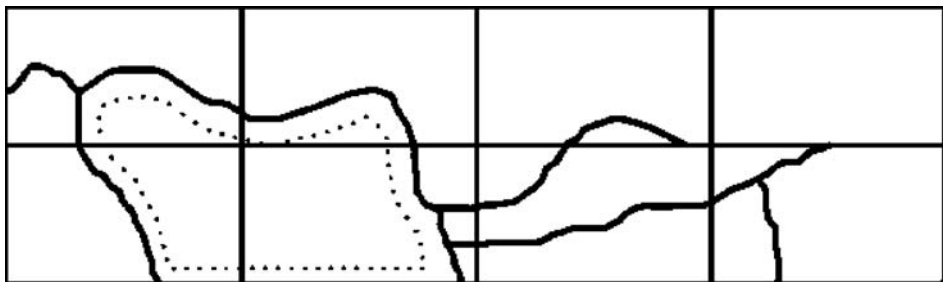


Figure 1. Illustration of erratic cracking (1).

- Structural constraints – interface friction between concrete slab and underlying layer; bonding between a stabilized base and the slab, especially localized bonding; paved width.
- Properties of concrete – PCC modulus and strength gain properties, coefficient of thermal expansion, and shrinkage characteristics.

Figure 3 shows the characteristic pattern of edge-restraint cracking. The principal factor affecting the risk of edge-restraint cracking is the temperature conditions at which the lanes constructed at different times are poured. For highway pavements, this type of cracking can occur if the tied concrete shoulders are paved at a significantly lower temperature than the temperatures at the time of mainline paving.

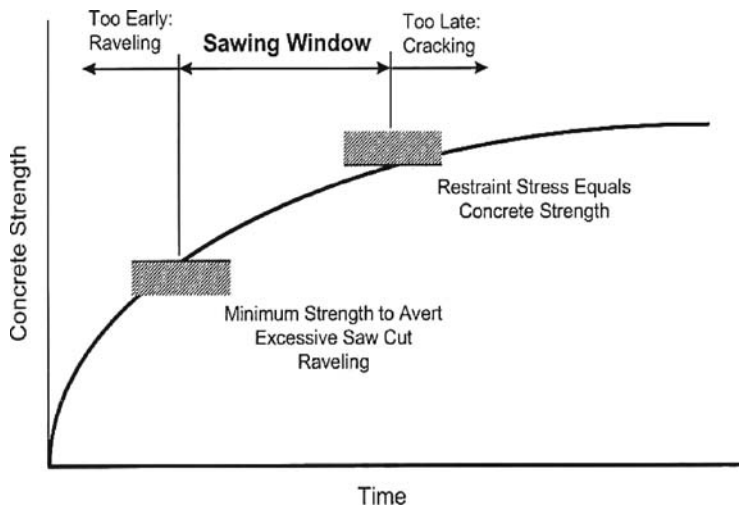


Figure 2. Joint sawing window of opportunity (2).



Figure 3. Characteristic pattern of edge-restraint cracking.

3 ASSESSMENT

3.1 Base-restraint cracking

The risk of cracking due to base-restraint and curling or warping can be evaluated using HIPERPAV (5). HIPERPAV is comprehensive software developed by the Federal Highway Administration (FHWA) for evaluating the risk of early age cracking. The software models the strength and stress development in concrete pavement at early ages (within the first 72 hours) to evaluate the risk of early-age cracking. The program calculates the overall, time-dependent stresses that develop in the pavement and models the PCC strength development, considering pavement design, PCC mix design, environmental, and construction factors. The cracking potential is then checked by comparing the level of total stress and the concrete strength throughout the analysis period. Following a similar approach, Lim and Tayabji (3) developed charts that can be used to evaluate the risk of early-age longitudinal cracking.

The evaluation of the risk of random cracking due to high base-restraint and curling or warping stresses involve assessment of complex interactions of numerous factors that are difficult to predict or quantify. For example, the stresses involved in the development of the cracking, as well as the PCC strength development, are highly sensitive to the temperature and moisture conditions during concrete placement and during the early ages of concrete. For accurate modeling of restraint stress and PCC strength development at early ages, the ability to accurately model heat flow through the pavement structure is needed, in addition to the ability to predict the precise exposure conditions. The pavement structure itself can be highly variable, which is often a significant contributing factor to the restraint cracking. The variability in the pavement structure due to random, localized bonding with a stabilized base, or infiltration of fresh concrete into the base is difficult to predict or quantify. Thus, the best use of the available analysis tools may be for identifying the high-risk conditions, rather than for precise modeling at the individual project level. However, if random cracking does occur during paving, HIPERPAV can be a valuable tool for identifying the cause.

3.2 Edge-restraint cracking

Tayabji and Lotfi (6) showed that the risk of edge-restraint cracking can be evaluated using the structural model shown in figure 4. If the tied concrete shoulders are placed at a much lower temperature than the mainline paving, the shoulder joints close fully well ahead of the mainline joints when exposed to a high temperature. Once the shoulder joints close, any further closing of the mainline joints is restrained by the shoulder. The restraint imposed by the tied shoulders can be modeled by introducing fixed regions over the outer portions of the transverse edges, as shown in figure 4.

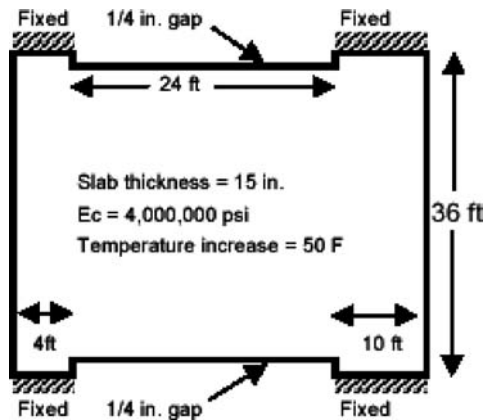


Figure 4. Structural model for analyzing the effects of edge restraint (7).

The effects of constant temperature increase on the structural model shown in figure 4 can be evaluated using a finite element program. The results of such analyses show that significant tensile stresses develop close to the pavement edge at the transverse edges. The stresses are directly proportional to the difference in the temperature at placement of the mainline and shoulder concrete, and if the temperature difference is large enough cracking can result. The risk of this type of cracking can be minimized or eliminated by limiting the allowable difference in ambient temperature at the time of placement of concrete for the tied lanes placed at different times.

4 CASE EXAMPLES

4.1 North Dakota (I-94)

Early-age cracking was experienced during the reconstruction of a section of I-94 in 2005. The cracking was predominantly longitudinal, but transverse cracking and corner breaks also occurred. Typical cracks are shown in figures 5 and 6. The pavement is a 229-mm (9-in) JPCP constructed on a 102-mm (4-in) cement-treated permeable base and 102-mm (4-in) aggregate subbase. Random joint spacing was used with a maximum panel length of 4.6-m (15-ft). The project was 16.1 km (10 mi), but the cracking occurred only on 1 day's paving in 2 areas totaling less than 800 m (0.5 mi).

The cause of cracking was not conclusively determined in this case; however, both the weather conditions at the time of paving and penetration of fresh concrete into the highly permeable, cement-stabilized base were identified as the significant factors. In general, the cracking experienced on I-94 is characteristic of the base-restraint cracking. Given the limited extent of the cracking problem, it is very likely that the weather conditions during paving did play a significant role.

The use of a highly permeable, stabilized base can significantly increase the risk of base-restraint cracking. The penetration of fresh concrete into the base not only has the effect of bonding the PCC surface to the base to restrain the movement of the PCC surface, the incidence also effectively increases the slab thickness, leaving the possibility of the saw-cut depth being inadequate. Localized



Figure 5. Early-age, longitudinal cracking on I-94, North Dakota.



Figure 6. Cracking along a transverse sawcut on I-94, North Dakota.

bonding with the base is always a risk, if no measures are taken to separate a cement-stabilized base and PCC surface. The bonding and penetration of fresh concrete into the base is almost a certainty when a highly permeable base is used. The recommended practice today is to use either an asphalt layer or geotextile as the separator layer, when a cement-stabilized base is used. In Germany, the use of a geotextile interlayer is considered an essential design detail to prevent the bonding between the PCC surface and cement-treated base (8). The risk of base-restraint cracking can be drastically minimized by using a positive measure to separate the PCC surface from a cement-treated base, especially if the base is highly permeable.

The treatment selection for early-age cracking should be made with the best long-term pavement performance in mind. To this end, North Dakota specified the following:

- Cross stitch all longitudinal cracks.
- Retrofit dowel bars on all transverse cracks that have cracked through both lanes and are at least 1.4 m (4.5 ft) away from the sawed joints.
- Full-depth repair transverse cracks that are located within 1.4 m (4.5 ft) of a transverse joint, or the cracks that occurred in only one lane.

The above is a reasonable approach to ensure good long-term pavement performance. Full-depth repairs or slab replacements are not necessarily the best repair alternatives for cracked slabs, because they will not necessarily provide better long-term performance than the less intrusive alternatives the North Dakota DOT implemented.

4.2 Oklahoma (I-35)

The cracking that occurred on I-35 in Oklahoma in 2005 is an example of edge-restraint cracking. The cracking pattern is similar to that shown in figure 3. The pavement was constructed as an overlay over the existing asphalt concrete (AC) pavement. The overlay is 267 mm (10.5 in) thick, and the transverse joints were sawed at 4.6 m (15 ft) spacing. The mainline pavement consisting of two 3.7-m (12-ft) lanes tied at the center was placed first. Later, a 3.0-m (10-ft) outside and

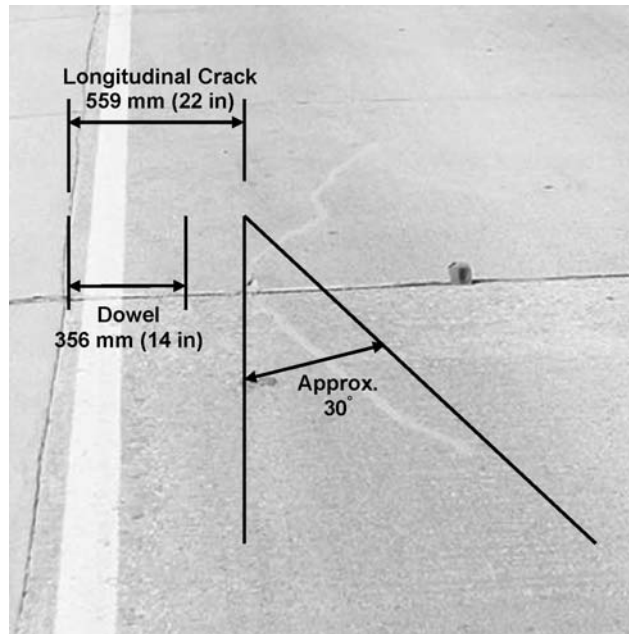


Figure 7. Longitudinal cracking on I-35, Oklahoma.

1.2-m (4-ft) inside tied concrete shoulders were added. The cracking initiated at the transverse joints and propagated diagonally inward at approximately 30 degree angle, as shown in figure 7.

The DOT investigations into the cause of cracking identified the edge-restraint as the most probable cause of the cracking. The analysis results showed that a temperature difference of 11 to 17°C (20 to 30°F) between the temperatures at the time of paving of the mainline and tied concrete shoulders would have been sufficient to initiate cracking in the mainline, if the shoulders were placed at the lower temperature. The cracking mechanism is explained in Section 3.2 above. As a result, Oklahoma DOT placed the following restrictions on the paving temperatures:

- Tied concrete shoulders may be placed at equal or greater ambient air temperature than that at the time of mainline paving.
- The ambient air temperature at the time of tied concrete shoulder placement may be no less than 11°C (20°F) below that at the time of mainline paving.

The cracked slabs were either full-depth repaired or replaced, depending on the extent of cracking. Since the cracking goes across the slab, the removal and replacement of the affected area may be the only feasible repairs. Under heavy traffic, cracks will deteriorate over time, and there are no other effective means of repairing the cracks of this type.

5 MITIGATION OF EARLY-AGE CRACKING

The uncontrolled, early-age cracking is a result of complex interactions of many factors related to the climatic conditions, construction practices, structural constraints, and the properties of concrete. The best way to avoid early-age cracking is to avoid high-risk designs and paving conditions, and following the recommended construction practices. The high-risk conditions include the following:

- High friction base – on a cement-stabilized or lean-concrete base use an AC layer or geotextile to prevent bonding. This is especially important if a cement-treated permeable base is used to prevent penetration of fresh concrete into the base.

- Excessive joint spacing – use a shorter joint spacing (e.g., 4.5 m [15 ft] or less) to minimize the risk of edge-restraint cracking.
- High ambient temperature – the risk of restraint cracking is higher when paving under very hot conditions. Consider night time paving. If paving under very hot conditions cannot be avoided follow the guidelines for hot weather concrete placement, such as those provided in ACI 305 or reference 9.
- Low ambient temperature – make sure the difference in ambient temperature between the time of mainline paving and the shoulder placement is within the allowable range to avoid edge-restraint cracking.

Proper curing is also extremely important to prevent excessive warping and plastic shrinkage cracking, especially in hot, dry areas.

The awareness of the risks is important to avoid early-age cracking, even if the risk is low. If the high-risk conditions cannot be avoided, be sure to identify the risks involved and monitor the critical items, which may include ambient temperature, concrete temperature, and concrete strength. The risk of early-age, restraint cracking can be assessed using HIPERPAVE.

6 REPAIR OPTIONS

As mentioned earlier, the treatment selection for early-age cracking should be made with the best long-term pavement performance in mind. The repair options for cracked slabs include dowel-bar retrofit and full-depth repair for transverse cracks and cross stitching, slot stitching, and full-depth repair for longitudinal cracks. Ideally, the pavement after the repairs should provide the best performance under the circumstances. The repairs implemented by the DOTs in the case examples cited in this paper are reasonable approaches to dealing with cracked slabs. In general, any structural cracks on heavily trafficked roadways will deteriorate over time, and no cracks on new pavements should be left untreated, if it has the potential to deteriorate. The only exception may be transverse cracks on non-dowelled JPCP.

7 CONCLUSIONS

Uncontrolled, early-age cracking sometimes occurs in JPCP, despite normally adequate design, construction, and jointing practice. However, invariably, the cracking is a result of some combination of the risk factors at work, and upon close inspection, the cause of cracking can usually be identified. This paper focused on two very specific types of early-age cracking: (1) those related to base restraint and curling/warping stresses, and (2) those caused by edge restraint. The cause and mitigation of each type of cracking are discussed, and case examples are provided. Comprehensive analytical procedures are available that are capable of evaluating the interactions of the key factors and assess the risk of cracking. However, early-age cracking is a result of complex interactions of numerous factors that are difficult to predict or quantify, and accurate predictions may not always be feasible. The best way to avoid early-age cracking is to avoid high-risk designs and paving conditions, and following the recommended construction practices. If random cracking does occur during paving, HIPERPAV can be a valuable tool for identifying the cause.

REFERENCES

- [1] Voigt, G.F., “Specification Synthesis and Recommendations for Repairing Uncontrolled Cracks that Occur During Concrete Pavement Construction” (American Concrete Pavement Association, Skokie, IL) 2000. <http://www.pavement.com/Downloads/Cracking.pdf>

- [2] Okamoto, P.A., P.J. Nussbaum, K.D. Smith, M.I. Darter, T.P. Wilson, C.L. Wu, and S.D. Tayabji, *Guidelines for Timing Contraction Joint Sawing and Earliest Loading for Concrete Pavements*, Report No. FHWA-RD-91-079 (Federal Highway Administration, McLean, VA, 1994).
- [3] Lim, S. and S.D. Tayabji, "Analytical Technique to Mitigate Early-Age Longitudinal Cracking in Jointed Concrete Pavements," *Proceedings*, 8th International Conference on Concrete Pavements (International Society for Concrete Pavements, Colorado Springs, Colorado, USA, August 14–18, 2005) 1322–1341.
- [4] CTLGroup, *Premature Cracking of Concrete Pavements – Causes and Impact on Performance*, (American Concrete Pavement Association, Skokie, IL 2005).
- [5] Rasmussen, R.O., J.M. Ruiz, D.K. Rozycki, and B.F. McCullough, "Constructing high-performance concrete pavements with FHWA HIPERPAV systems analysis software," *Transportation Research Record 1813*, (Transportation Research Board, Washington, DC, 2002) 11–20.
- [6] Tayabji, S.D. and H. Lotfi, "Pennsylvania I-81 (Franklin County) Pavement Cracking," a report by CTLGroup (Columbia, MD, 2003).
- [7] Tayabji, S.D. and S. Vanikar, "Analysis techniques to investigate early age cracking," *Proceedings of the 5th International CROW Conference*, (Istanbul, Turkey, 2004).
- [8] Hall, K., D. Dawood, S. Vanikar, R. Tally, Jr., T. Cackler, A. Correa, P. Deem, J. Duit, G. Geary, A. Gisi, A. Hanna, S. Kosmatka, R. Rasmussen, S. Tayabji, and G. Voigt, *Long-Life Concrete Pavements: A Scanning Tour of Canada, Germany, Austria, Belgium, The Netherlands, and the United Kingdom*, Final Report, (Federal Highway Administration, Washington, DC) 2007.
- [9] Kohn, S.D. and S.D. Tayabji, *Best Practices for Airport Portland Cement Concrete Pavement Construction*, Report IPRF-01-G-002-1 (Innovative Pavement Research Foundation, Airport Concrete Pavement Technology Program, Washington, DC, 2003).

The effect of different axle configurations on the fatigue life of plain cement concrete

K. Chatti, N.A Brake & S.W. Haider

Michigan State University, East Lansing, Michigan, USA

H. Salama

AlAzhar University, Cairo, Egypt

ABSTRACT: With the adoption of the new mechanistic-empirical pavement design method and the employment of axle load spectra, the question of evaluating the pavement damage resulting from different axle and truck configurations has become more relevant. In particular, the state of Michigan is unique in permitting several heavy truck axle configurations that are composed of up to 11 axles, sometimes with as many as 8 axles within one axle group. Thus, there is a need to identify the relative pavement fatigue damage resulting from these multiple axle trucks.

In this paper, the fatigue life of a typical plain concrete mixture under different truck axle configurations was determined directly from a cyclic four point beam test by using load pulses that are equivalent to the passage of an entire axle group. The S-N curves were determined for each axle configuration from the cyclic beam tests. The laboratory investigation indicates that the fatigue damage due to different axle configurations increases with increasing number of axles within an axle group for a given stress ratio. However, the results also indicate that for the multiple axles, the damage per axle is less than the single axle for the same stress ratio. Additionally, the results show that the axle factors for multiple axles tend to increase as the stress ratio decreases.

1 INTRODUCTION

The most current concrete pavement thickness design is based on mechanistic-empirical procedures (NCHRP 1-37A, 2004). Mechanistic methods are used to compute the primary slab responses such as stress, strain and deflection due to the load induced by the passage of an axle group or a truck. Empirical transfer functions are then used for relating pavement response to the number of allowable load repetitions to failure. Thus, mechanistic models are calibrated with empirical performance data since slab performance over time cannot be modeled accurately using only mechanistic methods. The performance criteria in the case of rigid pavements include fatigue cracking, joint deterioration (pumping or faulting), joint spalling, and serviceability. With the adoption of the new mechanistic-empirical pavement design method and the employment of axle load spectra, the question of evaluating the pavement damage resulting from different axle and truck configurations has become more relevant. In particular, the state of Michigan is unique in permitting several heavy truck axle configurations that are composed of up to 11 axles, sometimes with as many as 8 axles within one axle group. Thus, there is a need to identify the relative pavement fatigue damage resulting from these multiple axle trucks.

Transfer functions are developed in the laboratory under more controlled conditions (materials, environment and loads) in order to study a specific behavior; however, it is essential to calibrate these lab-based models to field conditions. While fatigue cracking phenomenon in rigid pavement slabs has been studied by many researchers in the laboratory, many questions remain unanswered, mainly because of the complex interactions between the factors affecting fatigue cracking. Also, most researchers studying the effect of concrete fatigue have used primarily constant amplitude

pulses in their testing. Many flexural fatigue tests conducted in the laboratory were based on using a sinusoidal or a constant amplitude haversine pulse to simulate a moving wheel load [Hilsdorf and Kesler (1966), Darter (1971), Roesler (1988)]. However, under multiple axle loading, the pulse shapes do not have uniform amplitudes. Thus, in order to accurately assess the damage induced onto the pavement due to these multiple axles, a more thorough investigation of these non-uniform amplitudes is required. Oh (1991) investigated the fatigue behavior of concrete under varying amplitudes of cyclic loading. He found that concrete fatigue failure was greatly affected by the magnitude and sequence of the applied variable load cycles, and Miner's linear theory led to some errors in fatigue failure prediction of concrete materials.

2 MECHANISTIC ANALYSIS

2.1 Finite element modeling

In this study, the DYNASLAB program (Chatti, 1993) was used in the mechanistic analysis to calculate the dynamic longitudinal stress-time response under different axle configurations at mid-slab. The finite element program is similar to ILLI-SLAB (Tabatabaie and Barenberg, 1978), with the main difference being the ability to calculate the dynamic response of different axle configurations under moving loads. The axle spacing was determined from actual traffic data from a Michigan DOT WIM station. A total of 65,535 records were analyzed to determine the most common axle spacing. The results from the WIM data for the eight axle configuration is shown in Figure 1. The most frequent range for the eight axle configuration was between 107 and 112 cm.

A wheel spacing of 107 cm was used to calculate the longitudinal stresses in DYNASLAB for the eight axle as well as for the smaller axle configurations (tandem, tridem, quad, six). This was done to isolate the effects (neglecting possible differences in spacing within different axle groups) caused solely by the addition or subtraction of wheels within an axle group (at that exact spacing) and the subsequent change in interaction. Additionally, each of the axle types was simulated at a speed of 50 kph.

2.2 Critical location within the slab

In the dynamic analysis, a typical 254-mm slab with a joint spacing of 4.6 m and a 3.6 m lane width was used. The foundation was assumed to be a Winkler foundation with a coefficient of subgrade

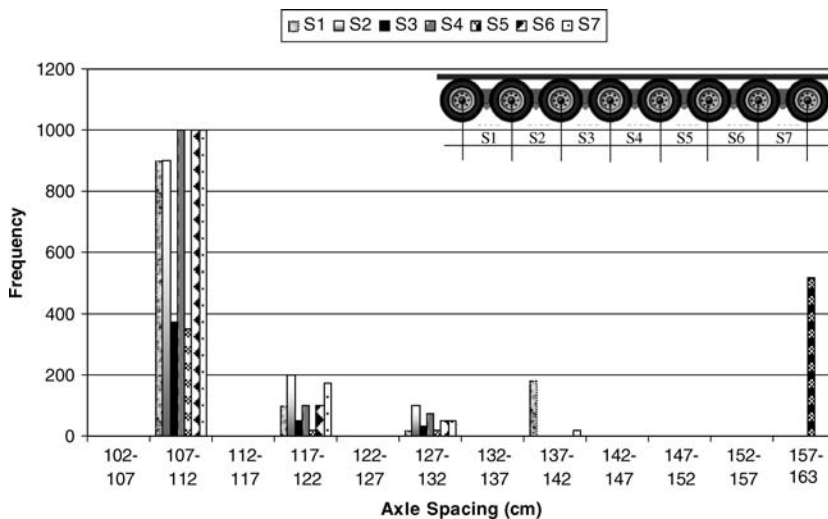















Figure 1. Axle spacing frequency at one WIM station in Michigan.

reaction of $42.86 \times 10^3 \text{ kN/m}^3$. The critical location was located 70 cm from the edge at mid-slab, keeping in consideration the wander effects. The stress histories due to the passage of various axle configurations were determined at the critical location of the slab.

However, it is worth mentioning that the critical location of the slab may change as a result of slab curling induced by a temperature gradient and through a change in axle spacing (Roesler 2005). These effects, however, were not accounted for in the dynamic analysis. They were not considered because focus was placed on the relative effects caused by the interaction within the axle configuration (with equal spacing and equal load), as stated above. Six different axle configurations were considered: single, tandem, tridem, quad, six and eight axles (see Table 1).

Each axle type had an identical load per axle of 58 kN. As shown in Figure 2(a), as the number of axles increases, the overall peak stress within the pulse decreases. This is caused by the compressive stress region. The accumulation of compressive stress due to all the interacting axles within an axle group will decrease the tensile stress and therefore decrease the overall peak stress. Figure 2(b)

Table 1. Axle configurations used in the analysis.

Axle/truck	Example truck configurations	Axle configurations
Single		
Tandem		
Tridem		
Quad		
Five		
Six		
Eight		

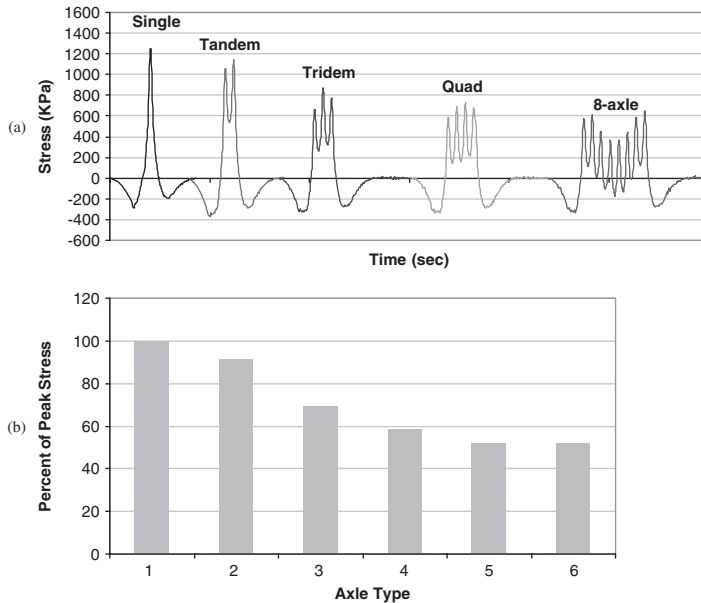


Figure 2. (a) Longitudinal stress pulses under varying axle configurations (DYNASLAB); (b) Peak stress under multiple axles expressed as a percentage of stress caused by a single axle.

illustrates the reduction of peak stress as a result of longitudinal stress interaction under multiple axles.

Under the six and eight axle configurations, the compressive stress is so significant that it causes the stress to fully reverse within the pulse (see Figure 2(a)). Thus, there is a need to not only understand the effects of varying amplitude, but also the effects of stress reversal. Unfortunately, in this research, the focus was placed primarily on the tensile stress region because of difficulty in running cyclic loading with stress-reversal. Given this limitation, it should still be noted that stress reversal does appear to shorten the fatigue life of the concrete (Zhang 1996). Therefore, the results, however beneficial, are not absolute and must not be considered as such.

3 EXPERIMENTAL DESIGN

3.1 *Mix Design*

A typical Michigan DOT concrete mix-Grade P1 was used for the experiment. The mixture consisted of Type IA cement, 2NS fine aggregate and 6AA coarse aggregate. Tables 2, 3, and 4 show the details of the mix design.

3.2 *Flexural Fatigue Testing*

In the laboratory, 150 standard 100 × 100 × 600 mm beams were cast. These specimens were subjected to cyclic loading in uniaxial (flexural) four point bending. The series of cyclic fatigue tests was conducted using different multiple load pulses. The experiment included single, tandem, tridem, quad, six and eight axles. The load pulses were determined by DYNASLAB as stated in section 2.1. Table 5 shows the testing matrix. Beams were kept in a curing room over the entire life (until testing). The flexural strength gain was monitored over time.

Table 2. In-situ properties.

Slump	75 mm
Concrete unit weight	2274.62 kg/m ³
Air content	6.5%

Table 3. PCC mix design.

Material	Class: Source	SSD Weight (kg/m ³)	Yield, m ³
Cement	ASTM C-150 Type I: Essroc	334.61	0.0799
Fine aggregate	2NS: Builders Aggregates (#34–86)	756.43	0.213
Coarse aggregate	6AA: MLO LS(#71-3)	1020.43	0.301
Water		151.87	0.114
Air content		6.5%	0.049
		Total	0.7569

Table 4. Admixtures.

Admixtures added:
ASTM C-494A Water Reducer Type A MB 200 N 0.085 kg/c
ASTM C-260 Air Entrainer MB Microair 0.034 kg/c
Desired Plastic Concrete Properties

The stress ratios were calculated at periodic times throughout the experiment as the ratios of the largest peak within a given pulse over the flexural strength at the time of testing. Modulus of rupture (MOR) tests were conducted at 3, 7, and 28 days. Two additional MOR tests were conducted one day prior to the actual fatigue testing and one day after the fatigue testing had concluded. This was done in order to give the research team an accurate assessment of the concrete strength just prior and immediately after the fatigue testing. This allowed the variation of strength over time to be monitored. Thus, if the strength continued to increase over time, the stress ratios could be adjusted accordingly. Both Table 6 and Figure 3 show the results from the MOR testing. The fatigue testing began 234 days and ended 292 days after casting.

Figure 4 illustrates for a tridem axle the transition from the stress pulse obtained using DYNASLAB (see Figure 2) to the load pulse input into the MTS testing software and the output pulse from the MTS machine. Note that the stress reversal (compression) was not included in the beam load pulse because of difficulty in running cyclic loading with stress-reversal. Additionally, no rest period was prescribed between cycles for two reasons: 1) the elastic behavior of concrete (time independent) and (2) laboratory testing time constraints. Additionally, the literature shows that effect of sustained loading is not significant below a stress ratio of 75% (Zhang 1996). Thus, no rest period was applied.

4 RESULTS

4.1 Univariate regression analysis

All 126 beams were tested and their corresponding test results analyzed. The fatigue test for each axle configuration ran until the complete failure of the beam; i.e., until the middle portion of the

Table 5. Test matrix.

Stress ratio	Number of replicates						
	Axle type						
	Single	Tandem	Tridem	Quad	Six	Eight	Total
0.9	5	–	–	–	–	–	5
0.85	–	5	5	5	6	6	27
0.8	5	7	–	–	–	–	12
0.75	–	–	6	4	6	5	21
0.67	4	4	4	4	4	4	24
0.59	–	5	5	–	–	–	10
0.52	4	–	5	6	4	4	23
0.46	–	–	–	–	–	4	4
Sum	18	21	25	19	20	23	126

Table 6. MOR test results at four different ages after casting.

	3 days	7 days	28 days	234 days	292 days
MOR	Stress (KPa)	Stress (KPa)	Stress (KPa)	Stress (KPa)	Stress (KPa)
	3458	4387	4951	4421	5572
	3693	4728	–	4969	4093
	–	–	–	5631	5574
	–	–	–	5345	5822
	–	–	–	5118	5615
Average	–	–	–	5116	5233
	3575	4558	4951	5100	5318

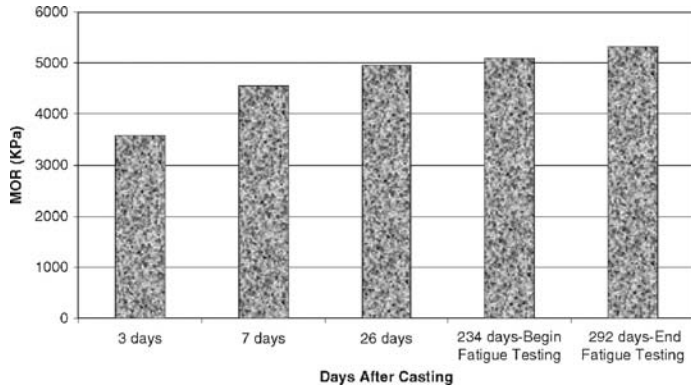


Figure 3. Average MOR at four different ages after casting.

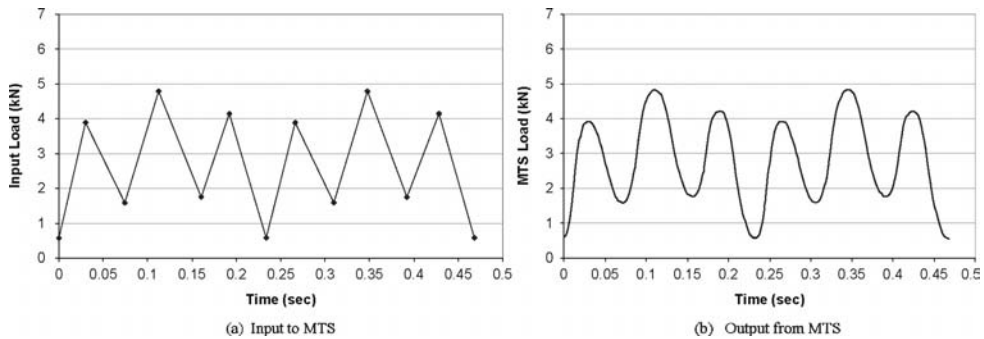


Figure 4. Example for generating an MTS load pulse for tridem axle.

beam is completely fractured. The S-N curves for single, tandem, tridem, quad, six and eight axles are shown in Figure 5. At first glance, the slopes of the S-N curves for each axle type appear to be different from one another, with six and eight axles having the steepest slopes. However, after a statistical analysis of the regression models was completed, it was determined that the slopes for the given axles are not significantly different from each other. This is caused by the large error within each of the models. Table 7 shows the detailed regression analysis for each of the axle types. The last two columns of Table 7 show the upper and lower 95 percent confidence limits of the slope. For each axle type, the upper and lower confidence limits intersect one another, thus making the difference in the slope values statistically insignificant. This means that the slopes for each axle type are essentially the same. Thus, the data from different axle types can be combined and interpreted using a multiple linear regression.

4.1.1 Comparison to previous research

The single axle regression line was compared to the regression lines from previous fatigue experiments to see if similar results were produced. The regression line produced from the current research shows a reasonably similar trend to those from other experiments, as shown in Figure 6.

4.1.2 Axle factors

The number of cycles to failure (N_f) was calculated using the individual regression equation corresponding to each axle configuration. Axle factors (AF) were then calculated for each axle configuration in order to quantify the relative damage between the different configurations. For example, the tandem axle factors were calculated by dividing the number of cycles to failure for

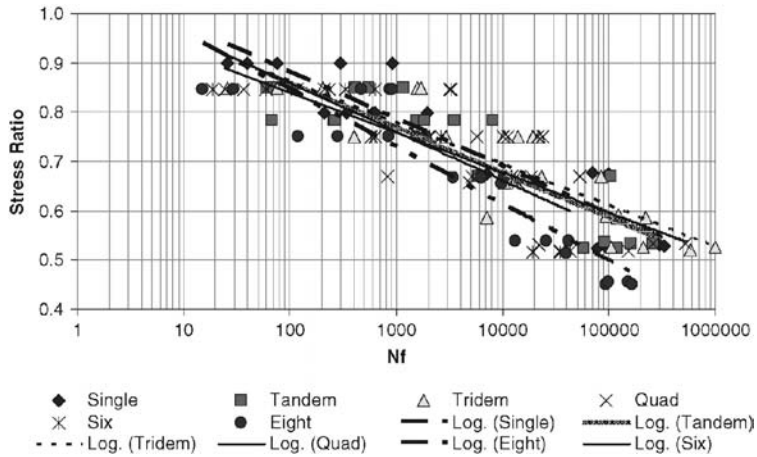


Figure 5. Fatigue curves for various axle configurations.

Table 7. Results from regression analysis.

Axle type	Regression equation	DF	R ²	Type	SE	95% Slope Lower confidence limit	95% Slope Upper confidence limit
Single Axle	SR = -0.0416LogNf + 1.0733	16	0.86	Intercept	0.0370	0.9949	1.1518
				Slope	0.0043	-0.0324	-0.0508
Tandem Axle	SR = -0.0396LogNf + 1.0432	19	0.79	Intercept	0.04222	0.9548	1.1315
				Slope	0.004882	-0.0293	-0.0498
Tridem Axle	SR = -0.0363LogNf + 1.0290	23	0.76	Intercept	0.04343	0.9391	1.1188
				Slope	0.004404	-0.0271	-0.0454
Quad Axle	SR = -0.0353LogNf + 1.0028	17	0.67	Intercept	0.05719	0.8821	1.1234
				Slope	0.006264	-0.0221	-0.0485
Six Axle	SR = -0.0427LogNf + 1.0554	18	0.66	Intercept	0.06002	0.9293	1.1815
				Slope	0.00751	-0.0270	-0.0585
Eight Axle	SR = -0.0500LogNf + 1.0745	22	0.85	Intercept	0.03929	0.9930	1.1560
				Slope	0.004619	-0.0404	-0.0596

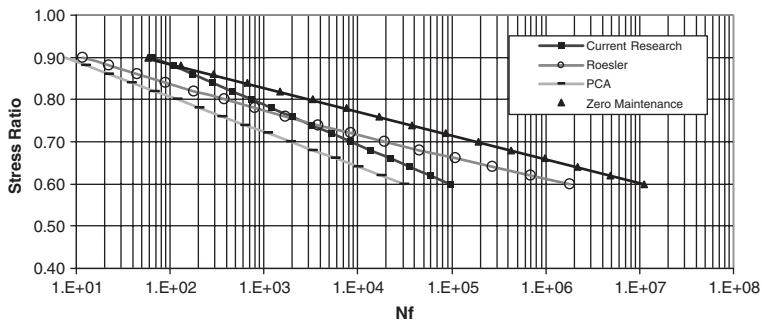


Figure 6. Comparison of S-N curve for single axles to previously published curves.

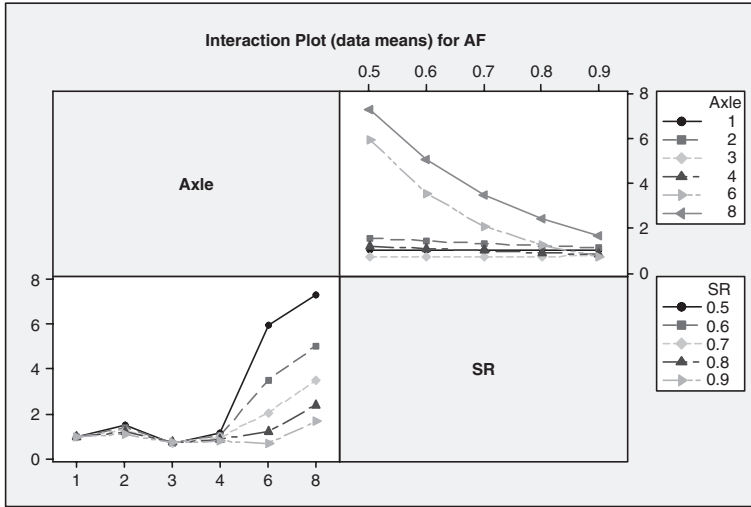


Figure 7. Interaction plot for axle factors with respect to axle configuration and stress ratio.

each single axle over the number of cycles to failure for a tandem axle.

$$AF = \frac{\text{Damage of the axle group}}{\text{Damage of the single axle}} = \frac{\frac{1}{N_f \text{ axle group}}}{\frac{1}{N_f \text{ single axle}}} = \frac{N_f \text{ single axle}}{N_f \text{ axle group}} \quad (2)$$

Figure 7 shows the variation of the AF with respect to stress ratio and axle configuration.

The figure shows that the six- and eight-axle groups are behaving differently from the rest of the axle configurations (The AF's are greater). The preliminary results also show that as the stress ratio increases, the axle factors tend to decrease for the larger axle groups. The effect of time (longevity of the pulse) might have a greater effect on the fatigue life at lower stress levels, thus increasing the axle factors. However, the trend is much weaker for the smaller axle groups, making the observation tentative.

4.2 Multiple linear regression

A multiple linear regression analysis was also conducted to further investigate the behavior between stress ratio and axle types in the hope that the model can provide a more conclusive answer than the individual S-N curves. One of the advantages of using a multiple linear regression equation is that all of the data from the experiments can be used at once, which subsequently increases the degrees of freedom in the model, and ultimately decreases the margin of error.

Since axle type is not a continuous variable, a new variable needed to be created for the regression analysis. A normalized stress impulse, SI, was used for this purpose. SI is a continuous quantity that represents a specific axle type. The equation for SI is the following:

$$SI = \frac{IMPULSE}{PEAKSTRESS} \quad (\text{sec}) \quad (3)$$

The impulse is the area under the stress pulse and the peak stress corresponds to the largest stress within a given pulse. The SI quantity is constant for a given axle type, regardless of the applied stress. Thus, it is a good indicator of axle type. Figure 8 shows the relationship between stress impulse and the number of axles.

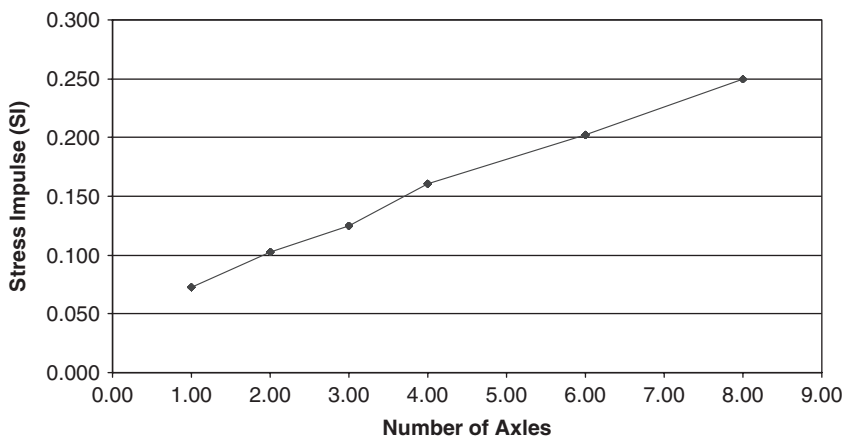


Figure 8. Stress impulse vs. number of axles.

Table 8. Multiple linear regression analysis*.

Predictor	Coefficient	SE	t	p
Constant	21.222	1.112	19.08	0.000
SR	-20.838	1.355	-15.38	0.000
SI	-6.970	1.722	-4.05	0.000
Initial elastic modulus	1.84E-06	9.20E-07	2.01	0.047

* $R^2 = 0.772$, Adjusted $R^2 = 0.766$.

Table 8 shows the output of the multiple linear regression analysis. The variables that were used in the multiple linear regression were elastic modulus (stiffness), stress ratio, and SI.

The analysis shows that SI, SR, and initial elastic modulus are significant variables (p-value is less than 0.05). The initial elastic modulus was calculated through beam theory using the initial measured displacement over the first cycles of the fatigue test. As the stiffness increases, the life of the beam also increases.

The coefficient of the SI variable is also negative. This means that as the number of axles increases, the number of cycles to failure decreases, which is the expected result.

4.2.1 Axle factors

Axle factors were calculated similarly to the previous section although only one equation was used; i.e., the equation obtained from the multiple linear regression (Table 8). Figure 9 shows the relationship between axle factors and axle configuration for the same peak stress value and accounting for the stress reduction caused by interaction within an axle group (Figure 2).

When the peak stress is the same for all axle groups, the axle factors increase as the number of axles increases. The results are similar to that of the individual regression equations. The axle factor for the eight-axle group is approximately 4.5, which suggests that it is 4.5 times as damaging as the single axle. However, the effect of stress reduction is not present within this relationship. If one takes into account the reduction in longitudinal stress caused by stress interaction under multiple axles, as shown in Figure 2, the damage from multiple axles and the corresponding axle factors become much smaller. Next we compare the AF value for tandem and tridem axles with stress reduction from Figure 9 to those obtained from the PCA design manual. From the design example provided in the manual for a 240 mm slab on an untreated base, the allowable number of repetitions for a 232 kN tandem axle is 1.1×10^6 , while that for a 116 kN single axle is 230,000. This leads to an axle factor for the tandem axle of 0.21 compared to 0.28 from Figure 9,

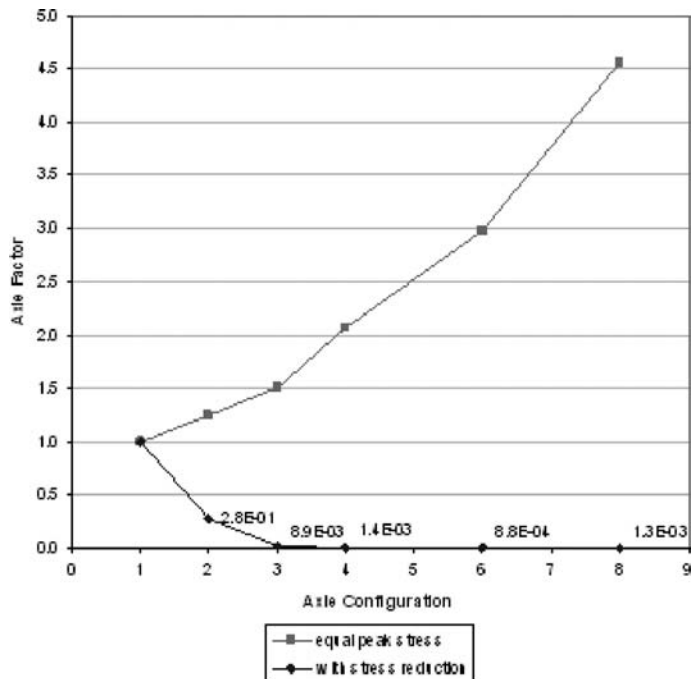


Figure 9. Axle factors versus axle configuration for the same peak stress level.

suggesting that they are reasonably close. For the tridem axle, the example in Appendix C of the PCA manual shows an unlimited number of allowable repetitions of a 240 kN tridem for the same design. This agrees fairly well with the AF value of about 0.01 from Figure 9, which is close to zero.

5 FUTURE RESEARCH

Additional fatigue testing will be conducted to further study the effect of axle configuration. Cylindrical briquettes in split tensile fatigue, rather than concrete beams, will be tested in an attempt to decrease the variability within the data. Over 100 cylinders were cast and will be tested over the next few months. The analysis will also include the effect of slab curling when applying the mechanistic-empirical principles.

6 CONCLUSION

Fatigue testing of plain concrete beams subjected to various types of axle pulses was conducted for the purpose of determining the effect of axle type on concrete fatigue. Despite the variability in the concrete fatigue test results, which is common for plain portland cement concrete, the data analysis showed that for the same peak stress level, multiple axles are more damaging than single axles. However, if one takes into account the longitudinal stress reduction that occurs due to interaction effects within a multiple axle group, the damage from multiple axles and the corresponding axle factors will be much smaller. Further testing is needed to fully assess the damage caused by these multiple axles. Also, the effect that slab curling may have on the stresses caused by multiple axle groups needs to be evaluated.

REFERENCES

- Chatti, K., J. Lysmer and C. L. Monismith, "Dynamic Finite-Element Analysis of Jointed Concrete Pavements"; Transportation Research Record, No. 1449; pp. 79–90, 1994.
- Darter, M.I., Design of Zero-Maintenance Plain Jointed Concrete Pavements, Vol. I – Development of Design Procedures, FHWA-RD-77-111, Federal Highway Research Record No. 370, Highway Research Board, pp. 48–60, Washington D.C., 1971.
- Hilsdorf, H.K. and Kesler, C.E., Fatigue Strength of Concrete Under Varying Flexural Stresses, Journal of the American Concrete Institute, vol. 63, pp. 1059–1075, 1966.
- NCHRP 1-37A, "Guide for Mechanistic-Empirical Design of New and Rehabilitated Pavement Structures," National Cooperative Highway Research Program, Washington, D.C., 2004.
- Oh, B.H., Fatigue Analysis of Plain Concrete in Flexure, Journal of Structural Engineering, ASCE, VS. 112, No. 2, Feb. pp. 273–288, 1986.
- Roesler, J.R., Fatigue of Concrete Beams and Slabs, Ph.D. dissertation, University of Illinois, 1998.
- Tabatabaie, A. M. and E. J. Barenberg, "Finite Element Analysis of Jointed or Cracked Concrete Pavements," Transportation Research Record, No. 671, pp. 11–19, 1978.
- Zhang B., D.V. Phillips and K. Wu, Effect of loading frequency and stress reversal on fatigue life of plain concrete. Magazine of Concrete Research, 48, No. 177, 361–375, 1996.

Evaluation of factors influencing distress development in ultra-thin whitetopping

S.A. Newbolds

Indiana Department of Transportation, West Lafayette, Indiana, USA

J. Olek

Purdue University, West Lafayette, Indiana, USA

ABSTRACT: Ultra-Thin Whitetopping is a pavement rehabilitation technique that involves the placement of a thin Portland Cement Concrete overlay 50 mm to 100 mm thick, over a distressed Hot Mix Asphalt pavement. This study evaluated different factors that influence the distress development in UTW pavements. Three different test areas were constructed in an accelerated pavement testing facility. The results indicated that debonding does occur prior to cracking. The structural properties of the pavement section did have an effect on the observed distresses at the end of the APT loading period. In general, the stiffer sections developed less distress than the more flexible sections. The evaluation of the influence of mixture composition indicated that the mix with fibers may delay cracking even in the presence of debonding. With respect to the interfacial bond, lanes with a lower degree of bonding typically exhibited higher amounts of distress than fully bonded lanes.

1 INTRODUCTION AND PROBLEM STATEMENT

Ultra-thin whitetopping (UTW) is a pavement rehabilitation technique that involves the placement of a thin Portland Cement Concrete (PCC) overlay, 50 mm to 100 mm thick, over a distressed Hot Mixture Asphalt (HMA) pavement. Typically, the HMA pavement is milled and cleaned which helps to create a bond between the existing HMA pavement and the UTW overlay. The bond between the two layers promotes composite action of the pavement section. This composite action allows for the reduced thickness in the UTW layer. Additionally, a short joint spacing is typically used. Previous research on UTW Mack et al. [1998] indicates that the short joint spacing in the UTW causes the slab to deflect rather than bend which reduces the UTW stresses.

Traditionally UTW has been used to rehabilitate full depth HMA pavements. However, research has noted the need to consider the use of UTW over composite pavements, Cable et al. [2001]. Additional research by Rajan and Olek [2001] indicates that performance of UTW may be different when used as a rehabilitation technique for existing composite pavements than when used over an HMA pavement. In the NCHRP report on the state of the practice of UTW, Rasmussen and Rozycki [2004] described the common distresses observed in UTW pavements and proposed mechanisms for their development. It was noted that one major factor influencing distress development was the quality of the underlying layers. Sections constructed with HMA mixes that had a higher quality, mixes that were more rut resistant, performed better. It is thus, hypothesized that the stiffness of all layers underlying the UTW will affect the distress development whether the section is composed of an existing HMA or composite section.

The Portland Cement Concrete Association (PCA) fatigue equations are employed in the PCA UTW design methodology, Wu et al. [1998], to calculate the number of allowable load applications at a given stress level. These equations are based on the stress to strength ratio, which is the ratio

of the applied stress in the concrete to the strength of the concrete. As this ratio increases, the number of load applications that can be applied at this level before failure decreases. However, if the concrete strength is higher, the number of load applications it can withstand before cracking is also high, even at a higher level of applied stress. In general, the concrete used in UTW applications is a higher quality than that used in typical paving applications. Additionally, the addition of fibers to the mix as well as high early strength concrete mixtures has been proposed to improve the performance of the UTW. The literature is mixed as to the benefits of adding fibers. Additionally, there has been little investigation into the use of high early strength mixtures. The effect of the properties of these mixtures on the performance of the UTW is needed.

While it is generally agreed that the deterioration of the bond will cause the pavement to fail, little investigation has been done into how this bond develops and how it degrades under loading. Armaghani and Tu [1997] in their study of Florida UTW sections noted that when debonding of the UTW layer occurs, cracking of the UTW layer soon follows. Addressing the development of cracks in the UTW at MnROAD, Burnham [2005] also indicated that debonding occurred before cracking in the UTW pavement. However, Rasmussen et al. [2002] in their review of the FHWA ALF results proposed that corner cracking was due to the local densification of the HMA at the corner location. The name given to this phenomenon was “virtual void”. As the UTW performance is based on the composite action with the underlying HMA, when debonding of the UTW layer occurs, the strains in the UTW layer would increase. It would thus be expected that the sections with lower bond strengths (partially bonded or debonded conditions) would exhibit greater distress than fully bonded sections.

To address these issues three different UTW pavement sections were constructed in an accelerated pavement testing facility. These sections varied primarily in the design of their underlying pavement layers. The UTW in Test Area 1 (TA1) was constructed over an existing composite pavement section that consisted of HMA over a thick reinforced concrete slab. In Test Area 2 (TA2) the UTW was placed over a more realistic composite section consisting of HMA over a thinner plain concrete slab. Test Area 3 (TA3) was constructed with UTW over an existing HMA pavement (no underlying concrete slab). TA1 had two test lanes while TA2 and TA3 had five test lanes. Individual test lanes within TA2 and TA3 were constructed with one of four different concrete mix designs: MD-1 was a base concrete mix; MD-2 was a high early strength mix; MD-3 was a fiber reinforced mix; and MD-4 was a high early strength mix with fibers. TA2 and TA3 also had test lanes that varied by the bond preparation done in the lanes. An overview of these test areas is contained in Figure 1.

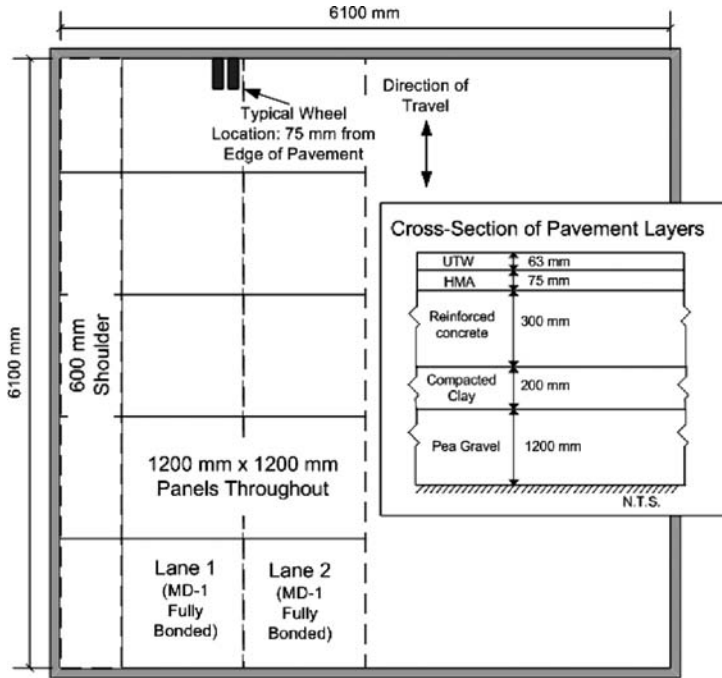
2 ACCELERATED PAVEMENT TESTING FACILITY

Testing was conducted at the Indiana Department of Transportation (INDOT) – Purdue University Accelerated Pavement Testing (APT) Facility located at the INDOT Office of Research and Development in West Lafayette, IN. The APT is housed in approximately 185 m² environmentally controlled building. The APT facility is composed of test pit, a loading mechanism and control and monitoring equipment.

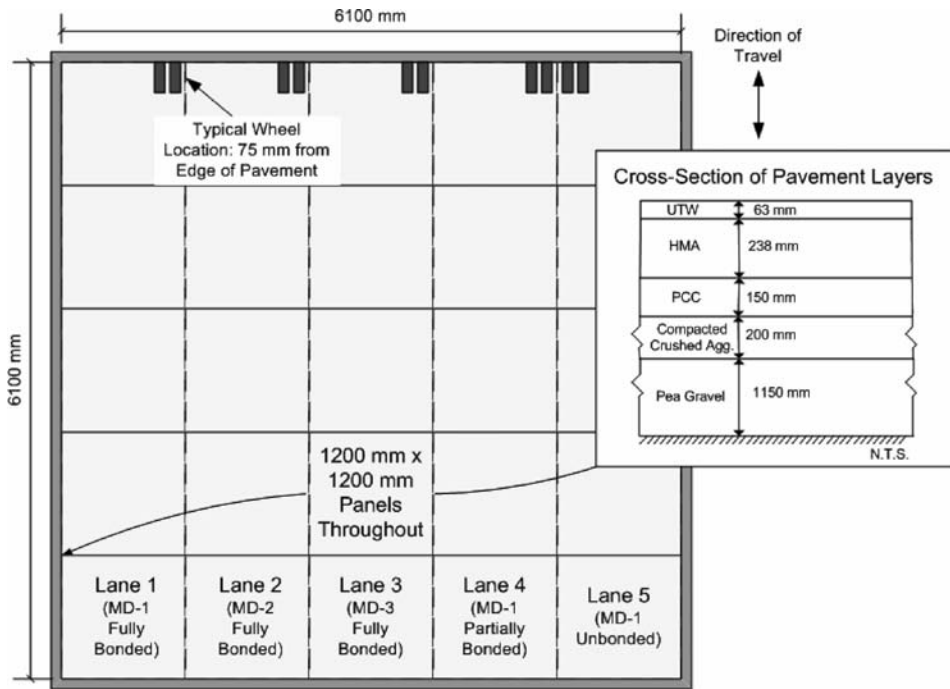
The APT testing area consists of a 6100 mm wide by 6100 mm long by 1800 mm deep test pit. The pit allows the placement of full depth pavements.

The operator control room houses both the software and hardware used to fully control the APT operation. The room is currently equipped with three personal computers networked together. The first computer is used to fully control and operate the APT, the second computer is used for data collection/reduction and the third computer is used for monitoring and diagnoses of the APT hardware.

The APT carriage, which can be equipped with either a full-size, dual-tire truck wheel or a super-single, half-axle assembly, is cable driven by a 22 kW motor and a 37 kW drive. This setup allows speeds up to 8 kph. The APT loading mechanism uses a system of four air pistons that maintain a constant force up to 89 kN. This load can be programmed either in static or dynamic modes. These cylinders also allow the wheels to be raised and returned to the start-up position of the test pad in one direction type of testing.

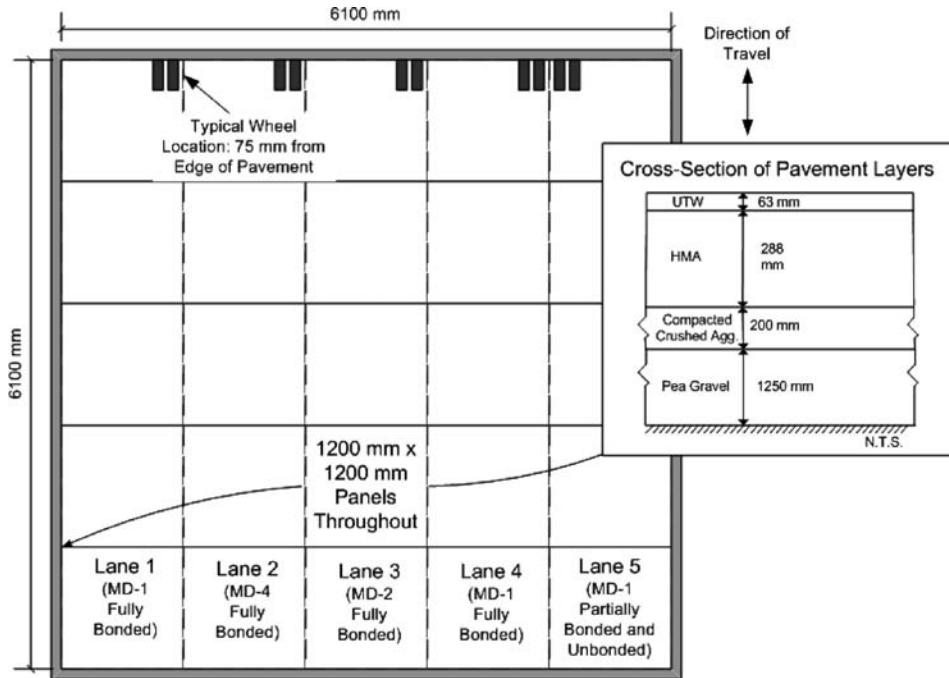


(a)



(b)

Figure 1. Layout of Test Areas (a) TA1 (b) TA2 (c) TA3.



(c)

Figure 1. (Continued).

3 CONSTRUCTION AND EVALUATION OF UTW TEST SECTIONS

Two different composite pavements were constructed as part of the UTW evaluation. TA1 consisted of four, 300 mm thick PCC slabs, each 1550 mm wide on top of 1200 mm of pea gravel. These layers were covered by a 100 mm thick HMA pavement layer that had been tested in the APT as part of a previous investigation. The HMA layer was a Superpave surface mixture with PG 64-28 binder and was subjected to 20,000 APT load passes (single axle, dual tires, and a 40 kN load). One inch of the HMA layer was milled, to completely eliminate the permanent deformation or rutting in the HMA layer due to previous APT loadings, leaving the layer approximately 75 mm thick. Forms were placed around the test pit to allow for construction of a UTW overlay with a 63 mm thickness.

For the construction of the pavement in TA2 and TA3, the APT test pit was completely emptied and cleaned. In both test areas, the test pit was filled with 1150 to 1200 mm of pea gravel and a 200 mm layer of dense graded crushed limestone was placed over the pea gravel. In TA2, a 150 mm thick plain PCC layer was placed over the crushed stone. The PCC layer was then overlaid by four HMA layers totaling 300 mm. The HMA layers were Superpave intermediate and surface mixtures with PG 64-28 binder. 63 mm of the HMA layer were milled to allow the construction of the UTW layer. This left the HMA layer approximately 237 mm thick. In TA3, the six HMA layers (PG 64-28; base, intermediate, and surface mixtures) totaling approximately 350 mm thick were placed over the crushed stone. Again, 63 mm of the HMA layer were milled to allow the construction of the UTW layer. This left the HMA layer approximately 288 mm thick.

3.1 UTW concrete mixtures

Four different UTW concrete mixtures containing Class C fly ash, with a target water-cementitious material ratio of 0.36, were used for the UTW in this experiment. The UTW concrete mixture

Table 1. Mix design proportions.

Material	kg/m ³
Cement	375
(Type I – MD-1 and MD-3; Type III – MD-2 and MD-4)	
Class C Fly Ash	70
Coarse Aggregate (Limestone – INDOT #11)	1000
Fine Aggregate (Natural – INDOT #23)	750
Water	160
HRWR	3–4 l/m ³
Polypropylene Fibers (20 mm monofilament) (MD-2 and MD-4)	1.1

designs are presented in Table 1. Test specimens were cast to evaluate the material properties of the UTW concrete. Specimens made included 100 mm by 200 mm cylinders for compressive strength and modulus of elasticity determination and 150 mm by 525 mm beams for modulus of rupture testing. Testing was performed at 28 days.

3.2 Placement of UTW

The UTW in TA1 was placed at a width of 3050 mm. The UTW was placed and finished by hand. MD-1 was used. After 18 hours the concrete joints were sawed at a spacing of 1200 mm by 1200 mm. This provided for two, 1200 mm wide test lanes and one, 600 mm wide shoulder area. For comparison purposes, one lane was loaded (Lane 1) by the APT and the other lane (Lane 2) was not loaded (Figure 1). The UTW was covered with wet burlap and plastic and cured for 7 days.

In TA2 and TA3, five different UTW test lanes were constructed. Each lane was constructed after the APT loading of the previous lane was completed. In order to evaluate different bond interfaces between the HMA and UTW, three different surface preparation techniques were employed. The surface of the milled HMA was swept and cleaned with a compressed air hose prior to UTW placement in Lanes 1, 2, and 3. In Lane 4, the milled HMA surface was not cleaned prior to placement of the UTW in TA2, but was cleaned as in the other lanes for TA3. A sheet of plastic was placed over the milled HMA layer in Lane 5: full lane in TA2 and half of the lane in TA3. The remaining portion of Lane 5 was not cleaned prior to UTW placement.

In all cases the UTW was placed at a width of 1.2 m. Concrete mixture MD-1 was used in Lanes 1, 4, and 5 in TA2 and TA3. MD-2 was used in Lane 2 and Lane 3 in TA2 and TA3, respectively. MD-3 was used in Lane 3 on TA2. And MD-4 was used on Lane 2 in TA3. The UTW was placed and finished by hand. After 24 hours the concrete joints were sawed at a spacing of 1200 mm by 1200 mm for TA2 using a standard pavement saw. In TA3, an early entry saw was used and the joints were cut (1200 mm by 1200 mm) within 4 hours after the UTW concrete was placed. The concrete was covered with wet burlap and plastic and cured for 3 days.

3.3 Accelerated pavement testing

In the testing of the Lane 1 in TA1, a load of 40 kN was applied after curing for 7 days. The pavement in TA2 and TA3 was tested with a load of 67 kN after the 3-day cure period. For all tests, a single-axle, dual-tire configuration was used and the tire was run bi-directionally over the pavement. Temperature in the APT facility was held relatively constant between 24°C to 29°C during testing. In TA1, over 500,000 load applications were applied to the test section. For TA2 and TA3, approximately 300,000 load applications were applied to each lane except TA2 Lane 5 which only had 180,000 load applications prior to terminating the test.

3.4 Distress evaluation

Distresses in the pavement were recorded periodically during the APT loading. Crack locations, width, and length were charted. Sounding of the UTW was performed to evaluate the bond. Sounding was done with a hammer in a grid pattern to locate the areas of potential debonding. Limits of the debonding were determined with additional sounding of the suspect areas. Limits were marked with paint on the pavement to assess changes in the debonded areas. Finally, faulting of the joints and cracks was also recorded.

3.5 Instrumentation

In order to evaluate the strains throughout the depth of the pavement strain gages were placed in the PCC, HMA, and UTW layers. Three different types of strain gages were used in this experiment. The first gage type, Texas Measurements embedment-type gages (PML-60-2L), was embedded in the UTW and PCC layers at a level of 0.5-inches (12 mm) below the surface and at 0.5-inches (12 mm) from the bottom of the layer. (No gages were placed in the PCC section in TA1 as this layer was placed in the APT under a prior project.) The second gage type, Texas Measurements surface-mount-type gages (WFLM-60-11-2LT), was glued to the surface of the milled HMA. The third type of gage was a CTL (ASG-152) HMA embedment gage that was placed at the bottom of the HMA layer in TA2 and TA3. These gages were connected to a Vishay System 6000 data acquisition system. This system has the ability to take individual strain readings at a very high sampling rate. The high frequency of data sampling enabled the recording of the dynamic strains as the wheel passed over the pavement. Dynamic strain data were collected approximately every 2500 load applications.

4 RESULTS AND DISCUSSION

4.1 Influence of pavement section structural properties

As noted previously, TA1 through TA3 were constructed with different pavement layers. The strains measured at the bottom of the UTW layer were less for test lanes with underlying PCC layers (TA1 and TA2) than in test lanes without PCC layers (TA3) (see Figure 2). The lower strains in pavement sections with the underlying PCC layers are expected to lead to less distress in the test lanes for TA1 and TA2, than in TA3.

TA1 (containing a very stiff underlying concrete layer) had the stiffest pavement section. No formal distress survey was conducted for TA1 as was performed in the other test areas. However, no cracking was noted in the UTW at the end of the APT loading. This result indicates that the strains remained low enough to prevent cracking even after over 550,000, 40 kN load applications.

As noted previously, TA2 (which also contained an underlying PCC layer) was stiffer than TA3 (constructed over an HMA section). A comparison of the distresses observed for all test lanes in these two test areas is presented in Figure 3. These two diagrams illustrate the distresses observed after load testing of the lane was completed. The total number of load applications applied to each lane at the end of testing is included in the figure.

As can be seen in Figure 3, the observed distresses in Lane 1 initially do not match what was expected for the section with an underlying PCC layer. Comparing this lane to Lane 1 in TA3, there is much less distress observed in TA3 than in TA2. However, TA2, Lane 1 debonded as a result of no vibration of the UTW concrete during construction. Therefore, the distresses observed for Lane 1 in TA2 were the result of debonding, not the structural properties of the pavement section. For the other lanes, neglecting the edge effects of the APT test pit (milling was non-uniform in these areas and may have caused uneven bonding and/or stress concentrations to develop in the UTW layer) the results fairly well match what was expected. There is little debonding and very little cracking from the middle of Panel 1 through the middle of Panel 5 for Lanes 2 through 4 in TA2. Additionally, the debonding in Lane 4 is most likely due to partially bonded condition in this

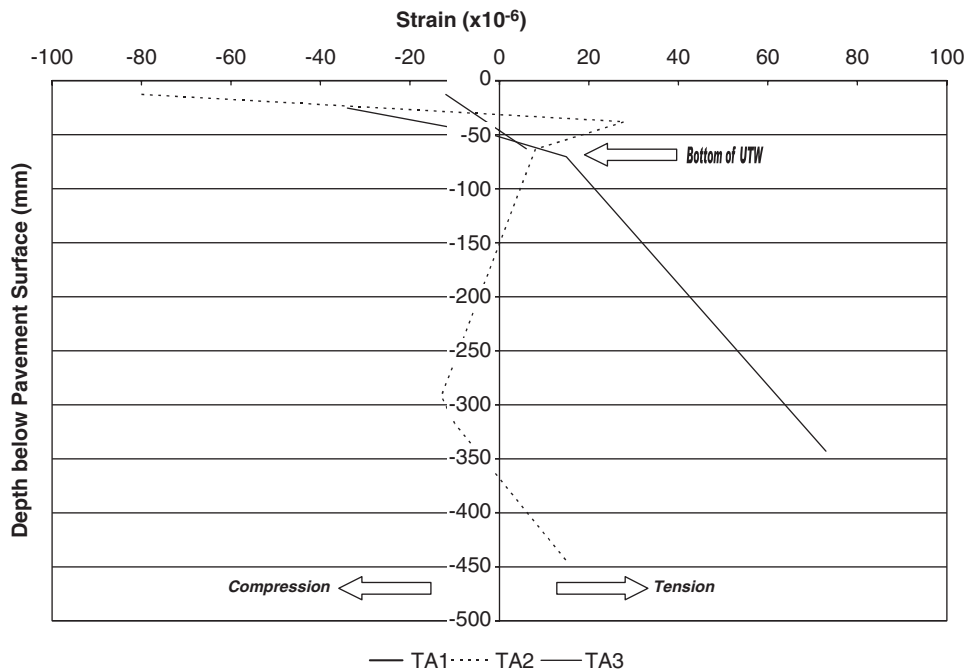


Figure 2. Strain distribution across pavement depths (Lane 1 for All Test Areas; 0 to 20,000 Load Applications).

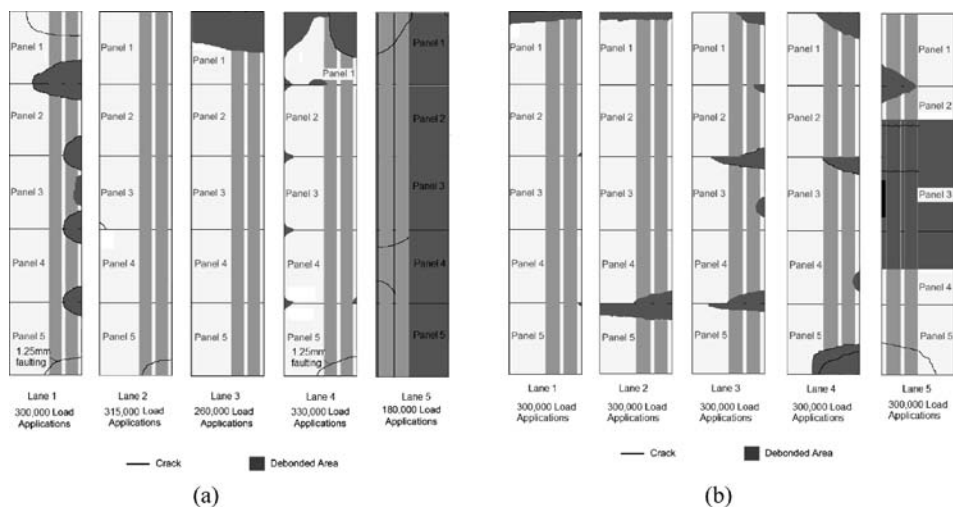


Figure 3. Final distress comparisons (a) Test Area 2 (b) Test Area 3.

lane (bond preparation was eliminated intentionally to evaluate its effects on the performance of the UTW).

In TA3 (Figure 3b), there is some debonding and cracking from the middle of Panel 1 through the middle of Panel 5 for Lanes 2 through 4. In this test area Lanes 2 through 4 lanes were all fully bonded and thus, the results cannot be attributed to the initial bonding condition. In regards to the

distresses observed, these results should be taken in context of the variable mechanical properties of the test lanes. The influence of the concrete mechanical properties is discussed in the next section.

4.2 *Influence of UTW concrete material properties*

To evaluate the effect of the concrete mechanical properties on the distresses a comparison of the test lanes constructed with different mix designs (in TA2 and TA3) is conducted. Concrete mixed using mix designs MD-1 through MD-3 were used to construct Lanes 1 through 3, respectively in TA2. Concrete mixed using MD-1, MD-4, and MD-2 were used to construct Lanes 1 through 3, respectively, in TA3.

The flexural strengths are used as a basis for this comparison as this is the value of the concrete strength that is commonly used in the PCA fatigue equations. The 28 day flexural strengths of the mixes in TA2 were 4.38, 4.17, and 6.52 MPa for MD-1, MD-2, and MD-3, respectively. For TA3, the 28 day flexural strengths for MD-1, MD-4, and MD-2 were 7.31, 6.83 and 7.31 MPa, respectively.

Accordingly, in TA2, the lanes in order of decreasing distress were expected to be Lane 1 (MD-1), Lane 2 (MD-2), and Lane 3 (MD-3). Similarly in TA3, it was expected that Lane 2 (MD-4) would have greater distress than either Lane 1 (MD-1) or Lane 3 (MD-2) which had equivalent strengths.

Figure 3 illustrated the final distresses in TA2 and TA3. In TA2 (Figure 3a), The extent of distresses generally followed the expected trend. Lane 1 (MD-1) had the highest degree of distress. The extent of distress observed in both Lanes 2 (MD-2) and 3 (MD-3) overall was relatively little. The debonding of Panel 1 in Lane 3 and the crack in Panel 5 of Lane 2 are most likely due to the edge conditions in the APT. Disregarding the distresses caused by the edge conditions, there was little difference between the performance of MD-2 (high early strength mix) and MD-3 (fiber mix) in regards to distresses. It should be noted that Lane 3, in which MD-3 was used, debonded only at the outer edge of Panel 1. No cracking was noted in Lane 3 even though debonding had occurred. Thus, the higher flexural strength of MD-3 (which contained fibers) appears to have prevented cracking in the presence of debonding.

In TA3 (Figure 3b), Lanes 1 and 3 constructed with MD-1 and MD-2, respectively, were expected to have a similar degree of distress given that they had equal flexural strengths. However, the lane constructed with MD-2 (high early strength mix) did have more distresses (both debonding and cracking) than the lane constructed with MD-1 (base mix). The lane (Lane 2) constructed using with MD-4 (high early strength and fiber mix), which had a lower flexural strength than in Lanes 1 and 3, did have some distress (debonding only), but not as much as in the lane constructed with MD-2 (Lane 3). Additionally, as noted with the lane constructed with the fiber mix in TA2 (Lane 3) the fibers in the mix may have prevented cracking in the debonded areas of the lane constructed with MD-4 (Lane 2). Overall, however, the flexural strengths among the lanes were fairly close (within 7 percent). As such, this difference may not be significant enough to influence the distress development. This mixed result indicates that there are likely other factors that have a greater influence on the distresses than UTW concrete properties.

Given the greater shrinkage potential of the high early strength mixes, there was a concern that debonding may occur at an early age. This debonding could leave concrete, which would not have gained its full flexural strength, susceptible to early damage. However, debonding evaluations performed after the curing period did not indicate that early-age debonding had occurred for these mixes.

4.3 *Influence of interfacial bond conditions*

Lanes 1, 4, and 5 in test areas TA2 and TA3 were constructed to influence of variable bond conditions. In TA2, Lane 1 behaved as an unbonded or partially bonded section, Lane 4 was partially bonded and Lane 5 was unbonded. In TA3, Lanes 1 and 4 were fully bonded while Lane 5 included panels that were unbonded and partially bonded. These test areas are used in the subsequent discussion to evaluate the influence of bond conditions on the type and severity of distresses.

Figure 3 illustrated the final distresses in TA2 and TA3. In test area TA2 (Figure 3a), while there was a fair amount of overall distress (debonding and cracking) for Lane 4 (partially bonded) it was less than both Lane 1 and Lane 5. The distresses in Lane 4 were mainly debonding at the corners. Lane 1 (partially or unbonded) actually performed worse than Lane 5 (unbonded) which was deliberately debonded. However, this may have been due to the fact that there significantly fewer load applications in Lane 5. Had the same number of load applications been applied to Lane 5 more distresses likely would have been noted.

For TA3, the distress summary presented in Figure 3b indicated that Lane 1 (fully bonded) had very little distress. The debonding noted was likely the result of edge effects of the APT test pit. Lane 4 (fully bonded), neglecting the distresses likely caused by the APT edge effects (in Panels 1 and 5), did have some debonding and one of the debonded areas did crack at the corner. In Lane 5, the degree of distress was greater than in Lane 1 and Lane 4. The UTW in Lane 5 cracked in the unbonded section. Additionally there was debonding noted in the partially bonded areas under Panels 1 and 2 in Lane 5. These results indicate that, as expected the interfacial bond conditions do influence the type and severity of distresses in the UTW layer.

The interfacial bond could provide restraint from shrinkage, thereby causing shrinkage cracks. However, the locations of the cracks are consistent with the high stress areas that result from loading (as discussed in the next section). Additionally, those areas with a higher level of restraint (greater bond) are the areas that would most likely to form shrinkage cracks. However, as noted above this was not the case. The areas with lower restraint had higher distress. Thus, in regards to shrinkage, the curing period appeared to be sufficient for these conditions to prevent any shrinkage related cracking.

4.4 *Influence of mechanical load applications*

TA2, Lane 1 exhibited the most distress (cracking and debonding) as indicated in Figure 3(a). Unfortunately, no sounding to assess the bond condition was performed until after loading was completed. However, the progression of the cracking at the corner is fairly regular such that by the end of the testing all corners in the wheelpath had cracked. The bond evaluation conducted after testing was terminated indicates that all the cracked areas were also debonded. The increasing number of load applications had a large effect on the distress development in this test lane. Figure 3(a) indicates that there were little distresses observed for Lanes 2 and 3 in TA2. While the observations indicated that these observations were made at lower numbers of load applications, these figures are also representative of the distresses observed at the end of the APT evaluations. Thus, the increasing number of load applications had little effect on the distresses in these lanes. For TA2, Lane 4 the figure indicates a debonded area in Panel 1 in the wheel path. This debonded area was noted at 40,000 load application and is most likely due to the edge effects of the APT test pit (Figure 4 and Table 4). That said, further analysis of this progression showed that at 135,000 load applications, the debonded area cracks. This result indicates that debonding does occur prior to cracking in the UTW. For TA2, Lane 5, cracking of the UTW at the corner was noted at 180,000 load applications. This indicates that even though the area was unbonded, the UTW was still able to withstand a significant number of load applications prior to cracking.

The results of the distress mapping for TA3 Lane 1 are presented in Figure 2(b). Other than a debonded area (likely the result of the edge of the APT test pit) there was no distress observed in this lane even after 300,000 load applications. The results from TA3, Lane 2, shown in Figure 3b indicate that even though there was debonding, no cracking developed even after 300,000 load applications. As mentioned previously, the concrete in this lane used fibers and had a very high flexural strength 6.83 MPa. This indicates that even if debonding occurs, the concrete can withstand crack development. TA3 Lane 3 exhibited the same phenomenon as was observed in TA2 Lane 4. Debonding was observed at 135,000 load applications (in Panels 2 and 3) and subsequent cracking of the debonded area was noted at 210,000 load applications. The observation combined with the observation in TA2 indicates that debonding occurs prior to corner cracking supports the findings that were observed at MnROAD, Burnham [2005].

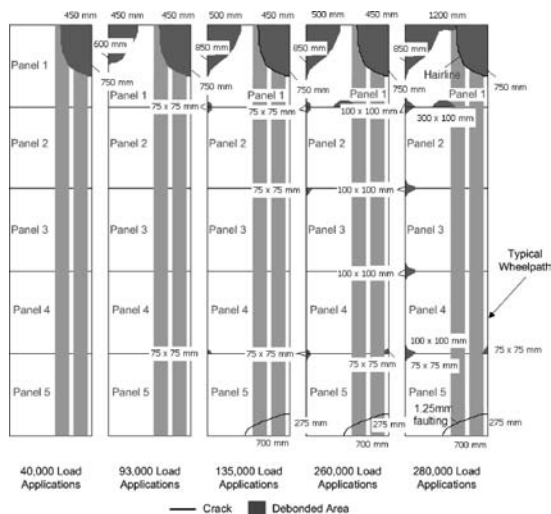


Figure 4. Example distress progression (TA2, Lane 4).

Table 2. Number of load applications to distress.

Lane	Cycles to debonding	Cycles to cracking
2-1	N/A	110,000
2-2	N/A	N/A
2-3	75,000	N/A
2-4	40,000	135,000
2-5	0	180,000
3-1	N/A	N/A
3-2	60,000	N/A
3-3	133,000	210,000
3-4	N/A	N/A
3-5	0	195,000

Neglecting the edge effects of the APT test pit, the results for TA3 Lane 4 indicate that little distress (debonding or cracking) was observed during the first 60,000 load applications. A debonded and cracked area was noted at the corner of Panel 3 after 300,000 load applications. For TA3 Lane 5, cracking of the unbonded sections under Panels 2 and 3 was noted at 195,000 load applications. Additionally, debonding of the corners in Panels 1 and 2 was noted at the same number of load applications. These areas however did not crack even after 300,000 load applications. This was likely due to a high UTW concrete flexural strength in this test lane (1120 psi at 28 days). For all test lanes overall, neglecting the APT edge effects, no debonding was observed until 60,000, 67 kN lb load applications (this converts to approximately 460,000 Equivalent Single Axle Loads (ESALs)). This was observed in TA3, Lane 2. Similarly, no load-induced cracking was observed until 110,000, 67 kN load applications (approximately 840,000 ESALs). This was observed in TA2, Lane 1.

In regards to the debonding patterns, there is a noted difference between the progression observed in TA2 and TA3. The debonding in TA2 appears to be isolated more at the corners, whereas the debonding in TA3 appears to progress along the transverse joints. This phenomenon may have occurred because in most cases in TA2, the debonded areas of the concrete also cracked. The cracking of the concrete may have released the stresses and halted any further progression of the debonding.

5 CONCLUSIONS

The structural properties of the pavement section did have an effect on the observed distresses at the end of the APT loading period. The test areas reflected this affect, as was expected, with the stiffer sections having the less distress than the more flexible sections. However, these results may also be influenced by the mechanical properties of the UTW concrete.

In TA2, the results indicated that the mix with fibers may delay cracking even in the presence of debonding. The fiber mix (MD-3) had the highest flexural strength and performed the best in regards to cracking. Ignoring APT edge effects, both the fiber reinforced concrete and the high early strength concrete performed well in regards to the final distresses. Definite trends were difficult to identify for TA3. The lack of cracking in the lane constructed with MD-4 again indicated that the use of fibers may have delayed cracking of the pavement in the debonded areas. The mixed results

in TA3 may have been due to the fact that flexural strengths were all fairly close to one another and the difference may not have been significant enough to discern a difference amongst them based on the material properties alone.

The amount of distress generally followed the expectations based on the interfacial bond condition. Those lanes having a lower degree of bonding (partially bonded or unbonded conditions) typically exhibited higher amounts of distress. Conversely, the lanes with the highest degree of bonding (fully bonded) typically showed the lowest degree of distress.

The results indicate that debonding does occur prior to cracking. This finding supports the results observed at MnROAD. Additionally, the progression of distress development is such that no debonding was observed before 60,000, 67 kN load applications. No cracking was observed until 110,000, 67 kN load applications.

REFERENCES

- Armaghani, J.M., and Tu, D., "Rehabilitation of Ellaville Weigh Station with Ultrathin Whitetopping," *Transportation Research Record* – 1654, Washington DC, 1999.
- Burnham, T.R., "Forensic Investigation Report for MnROAD Ultrathin Whitetopping Test Cells 93, 94 and 95," Final Report, 2005–45, Minnesota Department of Transportation, St. Paul, Minnesota, September 2005.
- Cable, J.K., Hart, J.M., and Ciha, T.J., "Thin Bonded Overlay Evaluation," Final Report, Iowa State University, June 2001.
- Mack, J.W., Hawbaker, L.D., and Cole, L.W., "Ultrathin Whitetopping – State of the Practice for Thin Concrete Overlays," *Transportation Research Record* – 1610, Transportation Research Board, 1998.
- Rajan, S., and Olek, J., "Concrete Overlays as a Rehabilitation Option for Distressed Asphalt Pavements," Final Report, FHWA/IN/JTRP-2001/6, Joint Transportation Research Program, Purdue University, December 2001.
- Rajan, S., Olek, J., Robertson, T.L., Galal, K., Nantung, T., and Weiss, W.J., "An Analysis of the Performance of Ultra-Thin Whitetopping Subjected to Slow Moving Loads in Accelerated Testing Facility," Conference Proceedings, 7th International Conference on Concrete Pavements, Orlando, FL, September 2001.
- Rasmussen, R.O., McCullough, B.F., Ruiz, J.M., Mack, J., and Sherwood, J., "Identification of Pavement Failure Mechanisms at FHWA Accelerated Loading Facility Ultrathin Whitetopping Project," *Transportation Research Record* – 1816, Transportation Research Board, Washington, DC, 2002.
- Rasmussen, R.O., and Roczycki, D.K., "Thin and Ultra-Thin Whitetopping," National Cooperative Highway Research Program Synthesis 338, Transportation Research Board, Washington, DC, 2004.
- Wu, C.L., Tarr, S.M., Refai, T.M., Nagi, M.A., and Sheehan, M.J., "Development of Ultra-Thin Whitetopping Design Procedure," Portland Cement Association, 1998.

Restrained shrinkage cracking of fiber-reinforced self-consolidating concrete

S.H. Kwon, R.P. Ferron & S.P. Shah

Center for Advanced Cement-Based Materials, Northwestern University, Evanston, Illinois, USA

Y. Akkaya

Istanbul Technical University, Maslak, Istanbul, Turkey

ABSTRACT: Fiber-reinforced self-consolidating concrete (FRSCC) is a new type of concrete mix that can mitigate two opposing weaknesses: poor workability in fiber-reinforced concrete and cracking resistance in plain concrete. This study focused on cracking of FRSCC due to restrained drying shrinkage, one of the most common causes of cracking. In order to investigate the effect of fiber on shrinkage cracking of FRSCC, ring shrinkage tests were performed for polypropylene and steel fiber-reinforced concrete. In addition, a finite element analysis for those specimens was carried out considering drying shrinkage based on moisture diffusion, creep, cracking resistance of concrete, and the effect of fiber. The analysis results were verified via a comparison between the measured and calculated crack width. From the test and analysis results, the effectiveness of fiber with respect to reducing cracking was confirmed and some salient features on the shrinkage cracking of FRSCC were obtained.

1 INSTRUCTIONS


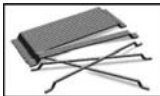
Self consolidating concrete (SCC) offers a number of important advantages. Because of its excellent workability and self-compacting ability, labor for vibration is not needed, and the construction period, which is directly related to construction costs, can be shortened. For this reason, SCC mix is widely used in practice. If fiber is added to SCC mix, many mechanical benefits can be achieved from enhancement of cracking resistance. One difficulty in adding fiber, however, is that it can hinder the flowable rheological property of fresh SCC mix. A few studies have been carried out on optimization of the mix proportion for the addition of steel or polypropylene fibers to SCC (Grünwald & Walraven 2001, Liberato, Park & Shah 2007). Meanwhile, there is a deficit of research on the mechanical properties of fiber-reinforced SCC. In mechanical terms, the greatest disadvantage of cementitious material is vulnerability to cracking. Cracking generally occurs at an early age in concrete structures or members. It may potentially reduce the lifetime of concrete structures and can cause serious durability and serviceability problems. One of the most important causes of early age cracking is drying shrinkage. Numerous experimental works have verified that the addition of fiber is an effective means of reducing the crack width. Furthermore, fiber addition leads to the formation of many dispersed crack rather than a single, large penetration crack (Girzybowski & Shah 1990, Nehdi & Ladanchuk 2004). However, it is still necessary to quantitatively determine the effect of fiber on cracking behavior.

The present study is a part of a project to develop FRSCC. To this end, the project aims to optimize mix proportion and to enhance rheological properties and mechanical properties. The main purpose of this study is to investigate shrinkage cracking behavior of fiber-reinforced SCC both experimentally and analytically. Four fiber-reinforced SCC mixes using polypropylene and

Table 1. Mix proportions.

Specimen	Compressive strength at 28 days	Unit weight (kg/m ³)						
		Binder		Water	Coarse aggregate	Sand	Fiber	Super-plasticizer
		Cement (Type I)	Fly ash (Class F)					
P0.0-G40-W30	66.7 MPa	623	156	234	516	772	0.00	2.6
P1.0-G40-W30	66.7 MPa	623	156	234	504	756	9.10	3.0
P1.0-G50-W30	68.2 MPa	622	156	233	629	629	9.10	3.3
S1.0-G40-W30	51.7 MPa	460	115	173	643	965	78.10	18.1
S1.0-G50-W30	71.5 MPa	461	115	173	801	801	78.10	3.8

Table 2. Fiber properties.

Fiber type	Fiber length (mm)	Aspect ratio (L/D)	Tensile strength (MPa)	Material	Shape
Synthetic 	40	90	620	Polypropylene/polyethylene blend	Fibrillated in thin flat lengths
Steel 	35	65	1050	Cold drawn wire	Round shaft with hooked ends

steel fibers and one plain SCC were produced. Free shrinkage and restrained shrinkage tests using ring type specimens were carried out to examine the cracking behavior due to drying shrinkage. Finite element analyses were performed for the ring shrinkage specimens, considering moisture diffusion, creep, cracking resistance of concrete, and the effect of fiber. From the experiments and analysis, some salient features on early age shrinkage cracking behavior of fiber-reinforced SCC were obtained.

2 EXPERIMENTS

2.1 Materials and mix proportions

Four different fiber-reinforced SCC mixes and one plain SCC mix were designed. Table 1 shows the mix proportions. Polypropylene fiber was added to two mixes (P1.0-G40-W30, P1.0-G50-W30), and steel fiber to the other two mixes (S1.0-G40-W30, S1.0-G50-W30). The plain SCC mix (P0.0-G40-W30) was made for evaluating the difference in cracking resistance between the fiber-reinforced and plain SCC mixes. Details of the fibers are given in Table 2. The binder composition of all mixes was prepared using Type 1 Portland cement with 20% Class F fly ash (substituted by mass), and the paste volume was optimized in order to achieve a good performing SCC. For every mix, the water to binder ratio was 0.3, and the ratio of coarse aggregate to total aggregate was 0.4 or 0.5. Generally, the amount of fiber added to the concrete mix ranges from 0.25% to 1.5% of the total mix volume (Girzybowski & Shah 1990, Nehdi & Ladanchuk 2004). As an average, the volume fraction of fiber was set to 1%.

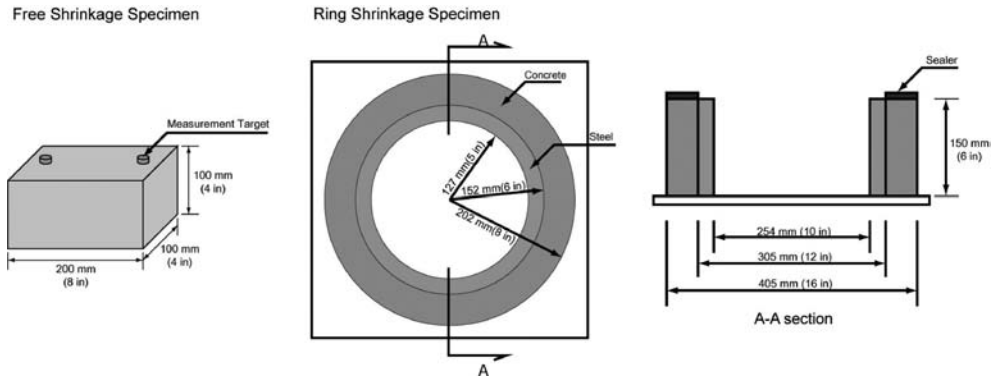


Figure 1. Configuration of specimens.

2.2 Test program

Shrinkage tests were conducted at 40% relative humidity and 22 degrees Celsius using a controlled humidity and temperature chamber. For each mix, three specimens were cast. Free shrinkage tests were conducted using 100 mm × 100 mm × 200 mm prismatic cubes, and restrained shrinkage tests were conducted using rings. Both free and restrained shrinkage specimens were exposed to air 1 day after casting. For the restrained shrinkage test, the concrete was cast around a steel annulus and the top surface of the concrete was coated with a silicon-based caulk while the outer surface was allowed to dry in order to simulate an infinite slab. The inner diameter and the thickness of the steel ring was 254 mm and 25 mm, respectively. The thickness of the outer concrete ring was 50 mm and the height was 150 mm. The outer concrete ring was visually inspected twice a day for cracking, the age at which the concrete cracked was recorded, and the strain of the inner steel ring was also measured over time. After cracking, the width of the crack was measured daily for at least 15 days. In addition, three cylinder specimens of ϕ 100 mm × 200 mm were manufactured for each mix and tested to find their compressive strength at 28 days. Figure 1 shows the configuration of the specimens.

3 FINITE ELEMENT ANALYSIS FOR RESTRAINED SHRINKAGE CRACKING

3.1 General

When concrete is exposed to air of low humidity, the interior moisture is nonlinearly distributed and the internal humidity decreases over time. Because of this differential drying, large tensile stress is induced near the surface while small compressive stress is induced in the inner area at the beginning of drying. In addition to the stress caused by the internal restraint, additional stress can be generated by the external restraints at the boundary, edge or interface of concrete members. The net stresses induced by the internal and the external restraints induce creep deformation, which serves to delay cracking time.

Concrete creep can be divided into basic and drying creep according to the relevant mechanisms. At the positions where the tensile stress exceeds the tensile strength, cracks initiate and propagate. Concrete fracture mechanics indicates that the stress does not suddenly drop to zero after peak stress but instead gradually decreases as the crack opening increases. If fiber is added to the concrete mix, crack widening is reduced. The enhanced cracking resistance loaned by fiber can be explained by the bond characteristics at the interface between the fiber and the matrix.

A prediction model to consider the above shrinkage cracking mechanism was previously established and is applied to FRSCC for analyzing the shrinkage cracking of the ring specimen in the

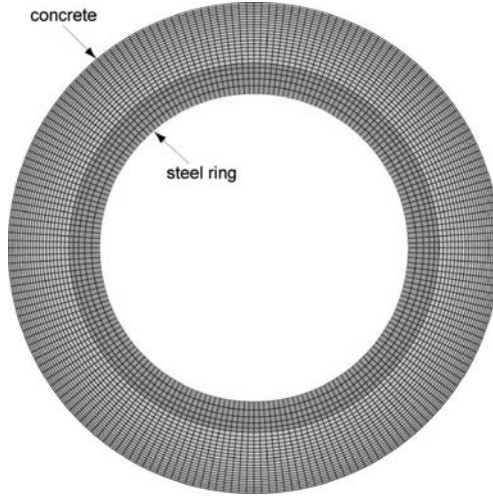


Figure 2. Finite element mesh.

present study. Figure 2 shows the finite element mesh for the test specimen. Two-dimensional plane stress was considered in the analysis. In the process of the analysis, a moisture diffusion analysis was first performed, and then shrinkage strain, creep, and cracking were calculated based on the time-varying internal moisture distribution obtained from the moisture diffusion analysis. The commercial program DIANA Ver. 9.1 was used in the finite element analysis. The material models used in this study are not provided by the program, and specially coded subroutines for the models were incorporated into the program. The modelling procedure for moisture diffusion, shrinkage, creep, and cracking resistance of concrete and fiber, as well as the analysis scheme for the cracking are given below.

3.2 Moisture diffusion and drying shrinkage

In the analysis, a nonlinear moisture diffusion analysis was first performed to determine the internal humidity distribution, which changes over time. The governing equation of the moisture diffusion is as follows.

$$\frac{\partial W}{\partial H} \frac{\partial H}{\partial t} = \text{div}(D_h \text{grad } H) \quad (1)$$

H represents the pore relative humidity, t is time, W is the total water content, D_h is diffusivity, and $(\partial W / \partial H)$ is the moisture capacity. This model of diffusivity and moisture capacity for concrete suggested by Xi, Bazant & Jennings (1994a,b) was employed in this study.

Based on the analysis results for the moisture loss over time due to drying, that is, the solution of Eq. (1), shrinkage strain is calculated by the following equation (Bazant and Xi 1994).

$$\Delta \varepsilon_{sh} = k_{sh} \Delta H, \quad k_{sh} = \varepsilon_s^0 g_s(t) = \varepsilon_s^0 \frac{E(t_0)}{E(t)} \quad (2)$$

$\Delta \varepsilon_{sh}$ is the shrinkage strain increment according to the relative humidity loss H . ε_s is a material constant representing the magnitude of the final shrinkage strain. $E(t_0)$ and $E(t)$ are elastic moduli at time t_0 and t , respectively. The free shrinkage strain is calculated from the final shrinkage strain, ε_s^0 , in the B3 model. The parameter ε_s^0 optimally fitting the measured free shrinkage strain was found for each mix by using the B3 model, as shown in Figure 3.

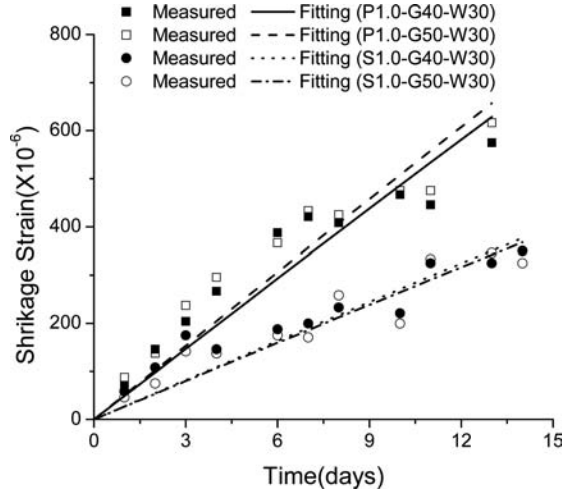


Figure 3. Free shrinkage test results.

3.3 Basic and drying creep

Creep deformation can be divided into two parts: basic creep and drying creep. The former refers to creep deformation under non-drying conditions and can be explained by the solidification theory (Bazant & Baweja 1995). In this study, the BP model (Bazant and Panula 1978) is used as a basic creep model and is expressed as follows.

$$J(t, t') = \frac{1}{E_0} + \frac{\phi}{E_0} (t'^{-m} + \alpha)(t - t')^n \quad (3)$$

$J(t, t')$ is a compliance function including basic creep strain, E_0 is an asymptotic modulus, α , m , and n are parameters determining the shape of creep strain evolution over time, and t' and t are the time at loading and an arbitrary time after loading, respectively. The parameters used in Eq. (3) were determined from the measured compressive strength and the mix proportions shown in Table 1.

Drying creep, known as the Pickett effect (Pickett 1942), refers to the excess of creep at drying over the sum of shrinkage and basic creep. This phenomenon was recently explained in terms of stress-induced shrinkage (Bazant & XI 1994) based on micro-diffusion between micro pores and macro pores. Eq. (2) is modified considering stress-induced shrinkage strain as follows.

$$\Delta \varepsilon_{sh,ij} = k_{ij} \Delta H, \quad k_{ij} = k_{sh} \left[\delta_{ij} + (r \sigma'_{ij} + r' \sigma'_v \delta_{ij}) \frac{\Delta H}{\sqrt{(\Delta H)^2}} \right] \quad (4)$$

The subscripts i and j indicate the direction of strain and stress, respectively, δ_{ij} is the Kronecker delta, and γ and γ' are constants for the stress-induced shrinkage. The two parameters, γ and γ' , are assumed to be the same. According to the literature, the parameter γ ranges from 0.1 to 0.3.

3.4 Cracking resistance of fiber-reinforced concrete

In plain concrete, the stress does not suddenly drop to zero after the peak stress in tension but rather gradually reduces as the crack width increases. The relationship between the post-peak stress and the crack opening displacement, strain softening behaviour, was modelled by the CEB-FIP 1990

model code (1993). The enhanced crack resistance of fiber reinforced concrete is dependent on the interfacial bond between the fiber and matrix. The relationship between the direct pullout force of the fiber that is normally acting on the unit area of the crack surface and the crack width can be obtained from the following equation.

$$\sigma_{\beta} = \frac{4}{\pi} \frac{l}{d} V_f \tau_v \left[\frac{w}{w_s} - \left(\frac{w}{w_s} \right)^2 + \frac{1}{2} \frac{\tau_g}{\tau_v} \left(\frac{w}{w_s} \right)^2 + K' \frac{w}{w_s} \right] \text{ for } w \leq w_s \quad (5)$$

$$\sigma_{\beta} = \frac{2}{\pi} \frac{l}{d} V_f \tau_g \text{ for } w > w_s \quad (6)$$

In Eqs. (5) and (6), l is the length of fiber, d is the diameter of fiber, V_f is the volume fraction of fiber, K is the anchorage force of the end of fiber, w_s is the crack width when the fiber starts to slide at the interface, and τ_v and τ_g are the interfacial shear strength and the frictional shear strength, respectively. The parameters of Eqs. (5) and (6) were determined by referring to a previous study (Girzybowski and Shah 1990).

3.5 Modelling of concrete and steel

In the finite element modelling, concrete cracking was modelled as the crack band model (Bazant & Oh 1983), where the crack opening displacement of the softening curve is transformed into the cracking strain of the continuum body by dividing the displacement by the crack band width. The crack direction is generally determined based on the direction of the principal stresses in the numerical calculation. Differently from the general case, cracks in the ring shrinkage specimen occur and propagate simply in the radial direction perpendicular to the circumferential direction, and the crack band width can be set to be the same as the circumferential length of each element.

In modelling the concrete, the tensile strength of each element was randomly distributed, and was assumed to be more than 95% and less than 105% of the reference strength expressed in Eq. (7) as follows.

$$0.95 f_t \leq f_{t, \text{element}} = 0.95 f_t + 0.1 \text{random}(1,0) f_t \leq 1.05 f_t \quad (7)$$

In Eq. (7), $\text{random}(1,0)$ is a random function that gives a random value between 0 and 1, and f_t is the tensile strength distributed to each element. Therefore, every element will have different tensile strength and also a slightly different softening curve based on the different tensile strength. If every element has the same tensile strength, cracks may initiate in every element at the same time. In reality, a crack begins at the weakest point of concrete. To simulate realistic cracking, this randomly distributed tensile strength was used.

The steel ring was modelled using 1,000 elements, and the outside concrete was modelled using 5,000 elements. The steel was assumed to be an elastic material, of which the elastic modulus and Poisson's ratio used in the analysis were 190 GPa and 0.3, respectively. In the moisture diffusion analysis performed prior to the cracking analysis, the same finite element mesh was used, and it was assumed that moisture diffusion does not take place in the steel.

The steel ring and the outside concrete were modeled as individual bodies. The interface between the steel ring and the concrete was simulated using the Coulomb friction model given by the following equation.

$$\tau_{\text{crit}} = \eta P \quad (8)$$

In this equation, the critical stress τ_{crit} at which sliding between the surfaces starts is defined as the fraction of the contact pressure P that is normally acting on the interface. The constant η is the coefficient of friction. In the analyses, the coefficient of friction of Eq. (8) was set to 0.2 (Baltay &

Gjelsvik 1990, Kwon, Kim & Kim 2005). When the pressure is in tension, brittle gapping occurs between the steel and concrete.

4 DISCUSSION ON TEST AND ANALYSIS RESULTS

4.1 Humidity distribution

Figure 4 shows the internal relative humidity distribution obtained from a nonlinear moisture diffusion analysis of the specimen. The relative humidity was nonlinearly distributed over the thickness of the concrete and becomes flatter over time. Based on this relative humidity distribution, a cracking analysis was performed considering the drying creep and the simultaneous formation of microcracks.

4.2 Cracking

Figure 5 shows the deformed shape of the quarter part of the plain concrete specimen at 2 and 3 days after drying. The deformed shape was highly exaggerated by magnifying the deformation. The arrows in the left part of Fig. 5 indicate microcracks. These microcracks occurred at the beginning of drying. Some of the microcracks continued to open over time with a specific spacing while others stopped opening or started to close. Differently from the direct tension test, fracture is not localized in a single crack, and drying typically induces systems of parallel cracks near the surface exposed to the air (Bazant & Raftshol 1982). As the front of the drying zone moves inside the concrete material, crack propagation and crack opening are concentrated into some of the initial cracks in a systematic manner. The closing and opening of the initial cracks and their spacing were automatically determined in the analyses based on the random distribution of the tensile strength to each element and the compatibility of deformation.

When the concrete is externally restrained, the weakest of the several microcracks on which the crack opening was concentrated develops into a penetration crack. In the plain concrete, only one penetration crack formed, as shown in the right of Figure 5. In contrast with the plain concrete, in the fiber reinforced concrete, a number of penetration cracks formed.

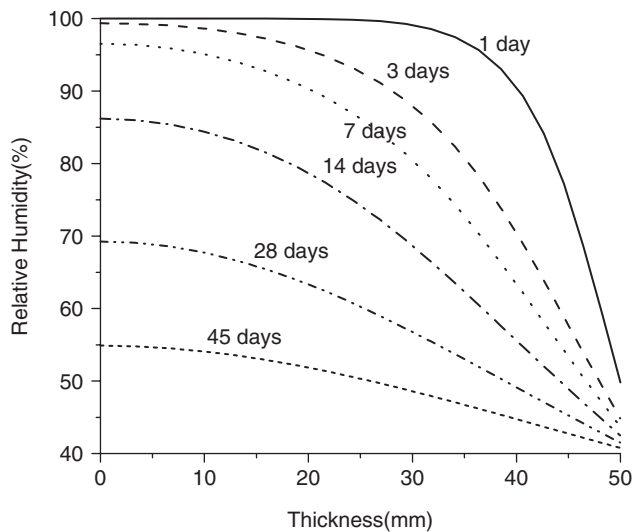


Figure 4. Humidity distribution over time.

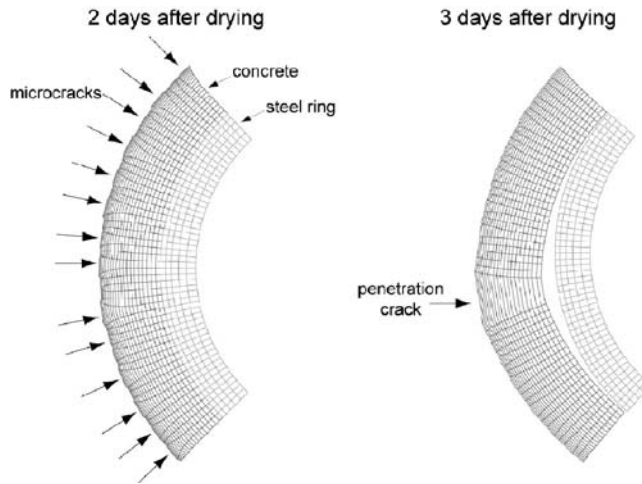


Figure 5. Deformed shape of plain concrete before and after penetration crack.

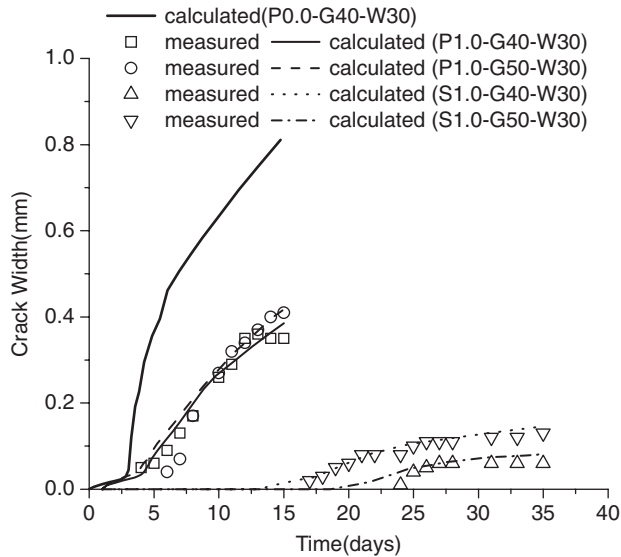


Figure 6. Comparison between the measured and calculated crack width of the first crack.

A comparison between the analysis results and test data for the first penetration crack in each specimen was made, and the results are shown in Figure 6; solid dots denote the measured crack width and the lines represent the analysis results. The analysis results accurately simulate the real cracking behavior of fiber reinforced self-consolidation concrete, and the prediction models used in this study were validated from this comparison. In the case of plain concrete P0.0-G40-W30, a penetration crack occurred at 3 days and its width was 0.8 mm at 15 days after drying. The crack width of P1.0-G40-W30 and P1.0-G50-W30 was about 0.4 mm at 15 days, and the reduced crack width could be attributed to the enhanced cracking resistance due to the added fiber. In the case of the steel fiber reinforced concrete, the crack width was about 0.1 mm 15 days after the penetration crack initiated. The free shrinkage of steel fiber reinforced concrete was almost half that of the polypropylene fiber concrete, as shown in Fig. 3. The delayed cracking and reduced crack width of

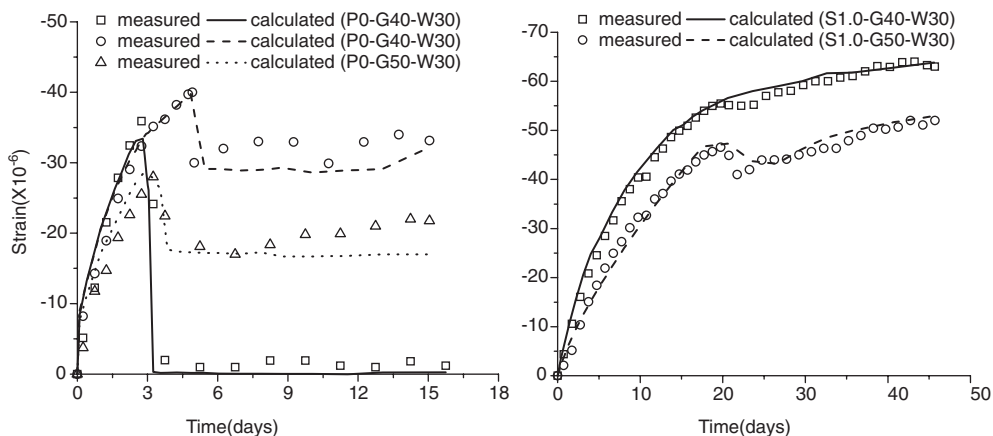


Figure 7. Comparison between the measured and calculated strain of steel ring.

S1.0-G40-W30 and S1.0-G50-W30 appears to be caused by the smaller free shrinkage as well as the greater effectiveness of the steel fiber with respect to enhancing cracking resistance. A significant difference in cracking behaviour was not observed according to the ratio of coarse aggregate to the total aggregate.

4.3 Confinement effect

As the drying shrinkage proceeds, the concrete confines the inner steel ring and the steel ring restrains the deformation due to shrinkage. The confinement effect disappears immediately after formation of the penetration crack in the plain concrete. On the other hand, it remains even after the penetration crack initiates in the fiber-reinforced concrete due to the pullout property of the fiber. The confinement of concrete by the steel ring can be confirmed through the strain variation of the steel ring over time in the experiments and analyses.

Figure 7 shows the strain variation of the inner steel ring over time for the specimens. The strain for P0.0-G40-W30 suddenly drops to zero at the cracking time, while the strains for P1.0-G40-W30 and P1.0-G50-W30 drop to a certain level and then remain constant over time after the penetration crack initiates. Unlike the polypropylene fiber reinforced concrete, the strains for S1.0-G40-W30 and S1.0-G50-W30 continue increasing even after the penetration crack forms. It is apparent that the steel fiber is more effective in reducing the cracking.

5 CONCLUSIONS

Ring shrinkage tests were performed, and numerical analyses for the specimens were carried out to investigate the cracking behavior of polypropylene fiber- and steel fiber-reinforced self-consolidating concrete. From the experimental and analytical investigations, the effectiveness of fiber in terms of reducing cracking can be confirmed, and the following conclusions can be drawn.

1. From the beginning of drying, many microcracks propagate simultaneously. One of these cracks develops into a penetration crack or macro crack. In the case of fiber reinforced concrete, several macro cracks may form after the formation of the first penetration crack as the confinement pressure increases or remains constant over time due to the effect of added fiber.
2. In the case of self-consolidating concrete reinforced with 1% polypropylene fiber, the crack width was reduced to half that of plain SCC.

3. The crack width of steel fiber-reinforced SCC was much smaller than that of polypropylene fiber reinforced SCC. This is due to the larger cracking resistance of the steel fiber as well as the smaller free shrinkage.
4. The calculated crack width and strain of the steel ring accurately simulated the real cracking behavior, and the analytical models used in this study can be used to predict and estimate the cracking of plain and fiber reinforced concrete.

REFERENCES

- Pickett, G. 1942. The effect of change in moisture content on the creep of concrete under a sustained load. *ACI Journal* 38: 333–355.
- Bazant, Z.P. & Osman, E. 1976. Double power law for basic creep of concrete. *Materials and Structures* 9(49): 3–11.
- Bazant, Z.P. & Panular, L. 1978. Practical prediction of creep and shrinkage of concrete. *Materials and Structures* 12(69): 415–434.
- Bazant, Z.P. & Raftshol, W.J. 1982. Effect of cracking in drying and shrinkage specimens. *Cement and Concrete Research* 12(2): 209–226.
- Bazant, Z.P. & Oh, B.H. 1983. Crack band theory for fracture of concrete. *Materials and Structures* 16(93): 155–177.
- Grzybowski, M. & Shah, S.P. 1990. Shrinkage cracking of fiber reinforced concrete. *ACI Materials Journal* 87(2): 138–148.
- Baltay, P. & Gjelsvik, A. 1990. Coefficient of friction for steel on concrete at high normal stress. *Journal of Materials in Civil Engineering* 2(2): 46–49.
- Comite Euro-International Du Beton, “CEB-FIP Model Code 1990,” Thomas Telford, 1993
- Xi, Y., Bazant, Z.P. & Jennings, H.M. 1994a. Moisture diffusion in cementitious materials-adsorption isotherms. *Advanced Cement Based Materials* 1(6): 248–257.
- Xi, Y., Bazant, Z.P. & Jennings, H.M. 1994b. Moisture diffusion in cementitious materials-moisture capacity and diffusivity. *Advanced Cement Based Materials* 1(6): 258–266.
- Bazant, Z.P. & Xi, Y. 1994. Drying creep of concrete: constitutive model and new experiments separating its mechanisms. *Materials and Structures* 27(1): 3–14.
- Bazant, Z. P. & Baweja, S. 1995. Creep and shrinkage prediction model for analysis and design of concrete structures-Model B3. *Materials and Structures* 28: 357–365.
- Shah, S. P., Ouyang, C., Marikunte, S., Yang, W. & Becq-Giraudon, E. 1998. A method to predict shrinkage cracking of concrete. *ACI Materials Journal* 96(4): 339–346.
- Yang, W., Weiss, W.J. & Shah, S.P. 2000. Predicting shrinkage stress field in concrete slab on elastic subgrade. *Journal of Engineering Mechanics* 126(1): 35–42.
- Grünewald, S. & Walraven, J.C. 2001. Parameter-study on the influence of steel fibers and coarse aggregate content on the fresh properties of self-compacting concrete. *Cement and Concrete Research* 31(12): 1793–1798.
- Nehdi, M. & Ladanchuk, J.D. 2004. Fiber synergy in fiber-reinforced self-consolidating concrete. *ACI Material Journal* 101(6): 508–517.
- Kwon, S.H., Kim, Y.Y. & Kim, J.K. 2005. Long-term behaviour under axial service loads of circular columns made from concrete filled steel tubes 57(2): 87–99.
- Ferrara, L., Park, Y.D. & Shah, S.P. 2007. A method for mix-design of fiber-reinforced self-compacting concrete. *Cement and Concrete Research* 37(6): 957–971.

4. Cracking in semi-rigid and stabilized-base pavements

Prediction of fatigue cracking in cement treated base courses

A.A.A. Molenaar & B. Pu

Delft University of Technology, Delft, The Netherlands

ABSTRACT: Stabilizing materials with cement is an attractive option to allow less suitable materials to be used as base-course or subbase. This is especially the case when good quality natural materials are not available or scarce. The problem with cement treated materials however is that they are brittle in nature and are sensitive to overloading. Pavements can only be designed properly when appropriate transfer functions, e.g. fatigue relationships, are available. Unfortunately the amount of information that is available on the fatigue performance of cement treated materials is much less than that is available for asphalt mixtures. Furthermore the information that is available is often not applicable to the specific condition. This paper describes the development of a field fatigue relationship for sand cement treated bases which are often used in the Netherlands. The relationship is based on an extensive analysis of the SHRP-NL data base which contained performance data of a number of pavements with a cement treated base. Furthermore the results will be presented of extensive finite element analyses which have been made to analyze the stress conditions near cracks and to determine the effect of load transfer. Combining all these results, an endurance limit for cement treated bases could be developed that can be used for the design of long life pavements.

1 INTRODUCTION

Stabilizing materials with cement is an attractive option to allow less suitable materials to be used in base-courses and subbases. Because good quality aggregates are not available in the Netherlands, base courses and subbases are made of recycled materials such as mixtures of crushed concrete and crushed masonry but also by stabilizing the available sand with cement or stabilizing recycled materials with cement. The problem with cement treated base courses however, is their cracking behavior. Transverse cracks always occur due to hardening and thermal shrinkage but also traffic may be the cause of extensive cracking. Both types of cracking can result in extensive and costly maintenance.

In the Netherlands, “design and build” contracts are gaining popularity. This implies that the contractor is made responsible for the design and selection of materials and has to guarantee the good performance of the pavement over a 7 years period. For obvious reasons, contractors want to use cost effective materials and stabilization of the existing sand subgrade with cement or using cement stabilized recycled materials as base course materials offer such possibilities. Because of less favorable experiences with cement treated bases, the authorities want solid proof of the contractors that the designs and materials proposed by them guarantee good performance. It is clear that such a proof is hard to give if assumptions have to be made about the mechanical characteristics of these materials because of lack of good quality data.

Although some work on the fatigue resistance of cement treated materials is done in Australia, South Africa, Denmark and France, little of it is applicable for the typical Dutch sand cement base courses and cement treated base courses made of recycled materials. This lack of good quality information on the fatigue performance of cement treated materials is hampering designers to proof that their proposals result in good performing roads. Obtaining fatigue data from laboratory

fatigue tests is not that straight forward as it may seem. First of all, stabilization is mostly done in situ resulting in considerable variation in the characteristics. Secondly, these materials are brittle in nature and the available fatigue relationships (e.g. Theyse e.a., 1996) for these types of material all show a high value of the slope of the relation. This implies that a small change in the applied tensile strain has a very large effect on the number of load repetitions to failure. Both factors imply that quite a number of tests need to be done in order to obtain a reliable fatigue relation. Thirdly, unlike for asphalt mixtures, no nomographs or equations are available to estimate the fatigue characteristics of these materials. Finally, shift factors should be applied to the laboratory derived relationships in order to make them applicable for design purposes. All this implies that fatigue testing of these materials is considered to be cumbersome and questionable and one therefore tries to avoid this type of testing.

In order to be able to arrive at a fatigue relationship that could be used for practical purposes, it was decided to make an analysis of the performance of the pavements with cement treated bases that are part of the SHRP-NL data base. The SHRP-NL data base was developed in the 1990's as a parallel project to the SHRP program in the USA. The data base contains data on the visual condition as well as falling weight deflectometer results, the pavement structures, traffic etc collected over a 10 year period. As will be shown in this paper, a field fatigue relationship could be developed for sand cement base course materials. The analysis of the data base was supported by extensive finite element analyses which were made to determine the stress conditions near cracks and to analyze the effect of load transfer. By combining the field data with the finite element results, an endurance limit for cement treated sand could be developed.

2 SHRP-NL DATA BASE

The SHRP-NL data base contains 15 sections with a cement treated sand base course. Each section was 300 m in length and consisted of 3 subsections of 100 m. Four sections were part of the provincial road network while the remaining 11 were part of the main highway system.

On each section, falling weight deflectometer measurements were performed in and between the wheel paths. These measurements however were taken only a few times during the entire duration of the SHRP-NL project. On some sections, deflection measurements were taken 6 times during the 10 year period the sections were under investigation, while on other sections only one deflection survey was performed.

Furthermore visual condition surveys were available. On some sections the visual condition surveys were performed 8 times during the 10 year period, while on other sections the number of surveys was only 4. Unfortunately the visual condition surveys and deflection measurements were not performed on the same dates making a direct comparison between the measured deflection and the observed damage somewhat complicated.

Also information on the thickness of the pavement layers and the composition of the asphalt layers was available from the cores that were taken in front and behind the 300 m sections (6 cores in total, 3 on either side). Axle load data were not available; the only traffic information available was the average daily traffic on a specific date, traffic growth and percentage of truck traffic.

3 EVALUATION OF THE TYPE OF CRACKING

As mentioned before, the objective of analyzing the performance of the SHRP-NL data was to establish a field fatigue relation. In order to do so, one must be sure that the cracking that is observed is traffic related and is cracking that can be related to deterioration of the cemented base course. In other words one must be sure that the cracks are predominantly bottom-up and not top-down cracking.

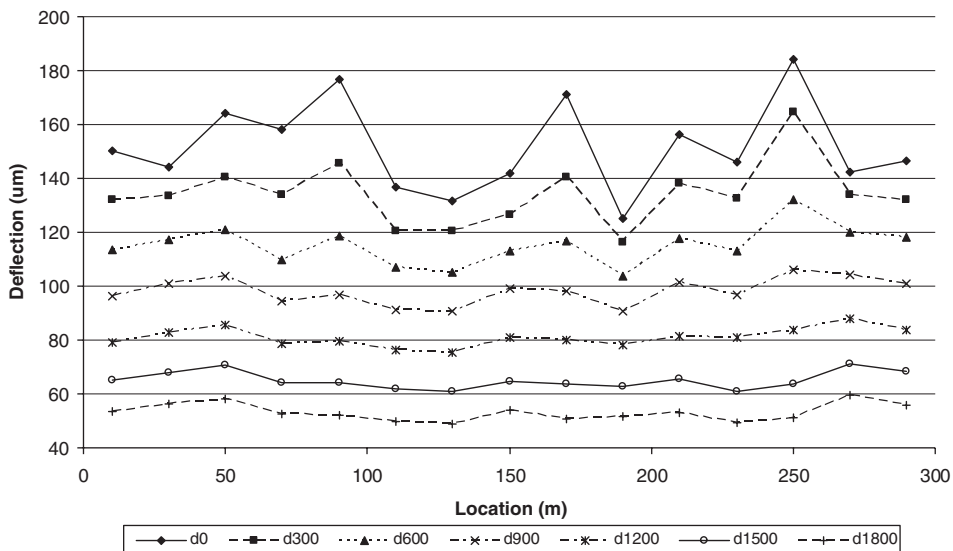


Figure 1a. Deflections measured between the wheel paths on a particular section.

From the detailed crack maps made by the surveyors, the surprising conclusion was that transverse cracking was hardly observed on the sections. Most of the cracks were in the wheel paths.

The small amount of transverse cracks might have to do with the fact that normally rather thick asphalt layers are used in the Netherlands for provincial roads and main highways (> 200 mm asphalt). This combined with the mild winters that occurred during the last decades might be the reason for the limited amount of transverse cracking that is visible at the pavement surface. Most probably there are transverse cracks in the cement treated base but obviously they had not yet propagated through the asphalt top layers.

The question with respect to the longitudinal wheel path cracking that was observed was whether this cracking was top down cracking or bottom up cracking initiating in the cement treated base course. Unfortunately it was not allowed to take any cores and the only way to determine whether cracking had initiated from the bottom of the pavement was by taking deflection measurements in and between the wheel paths. From experience it was known (Groenendijk 1998) that top down cracking hardly results in an increase in deflection level while top down cracking does.

By comparing the deflection measurements taken in and between the wheel paths it was indeed concluded that the observed cracking was bottom-up. This conclusion is based on the fact that at the sections where cracking was observed, the deflections (especially the surface curvature index of the deflection bowl) in the wheel path were larger than those measured between the wheel paths. The deflections measured at a distance of 900 mm and more from the load centre did not increase. An example of this is given in figures 1a and 1b. The higher deflections in the wheel paths indicate a loss of bending stiffness in that area which can be attributed to the damaging effect of traffic. It has been shown in (Molenaar, 2006) and (Molenaar, 2007) that the loss in bending stiffness as observed on the various sections had be due to damage in the asphalt top and cement treated base layer and could not be due to surface cracking that only penetrates to a depth of 40 mm from the surface.

Based on these observations, the conclusion was drawn that the observed cracking was related to traffic and is bottom-up cracking. Therefore it was concluded that the data base could be used to develop an in situ fatigue relation.

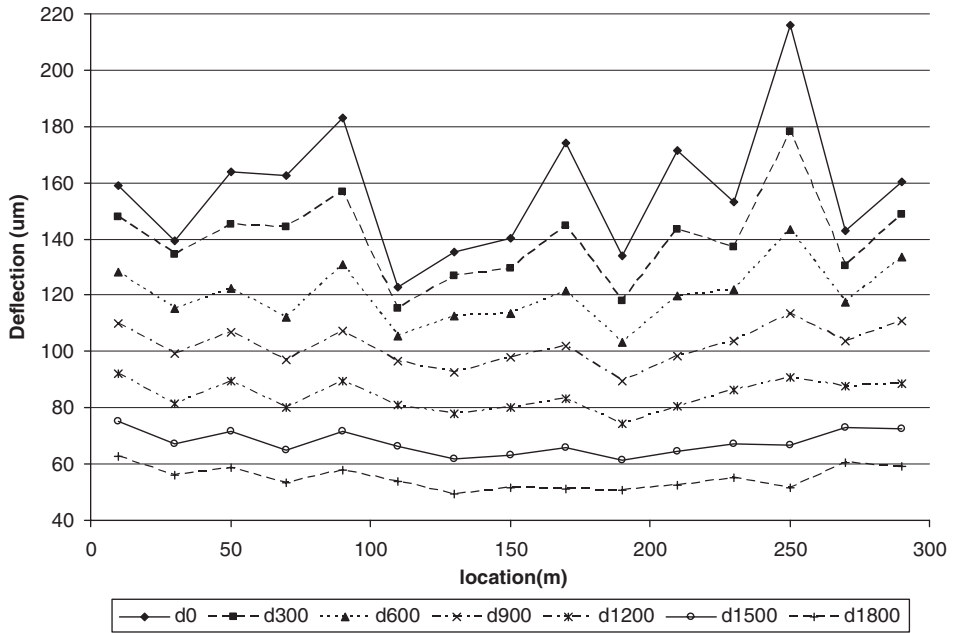


Figure 1b. Deflections measured in the wheel paths on the same section as in figure 1a.

4 DEVELOPMENT OF AN IN SITU FATIGUE RELATION FOR THE CEMENT TREATED BASES

As a first step in the development of the in situ fatigue relationship, the magnitude of the tensile strain at the bottom of the cement treated base in the area between the wheel tracks (this is an area that is not subjected to traffic loads and can therefore be considered as being representative for the original structure) was calculating using equation 1 (Gurp, van, 1996). This equation was developed using the results of a large number of linear elastic multi layer analyses on pavement structures with a cement treated base course.

$$\log \varepsilon = 0.0931 + 0.4011 \log d_0 + 0.3243 \log d_{1800} + 0.4504 \log d_{300} - 0.9958 \log d_{900} + 0.8367 \log BDI \quad (1)$$

where: $BDI = d_{300} - d_{600}$; d_x = deflection at x mm from the load centre [μm]; and ε = tensile strain at the bottom of the cement treated base layer [$\mu\text{m}/\text{m}$].

Next a plot was made of the calculated tensile strain and the observed cracking. This resulted in figure 2 (Pu, 2007). This figure nicely shows that sections where the tensile strain was lower $60 \mu\text{m}/\text{m}$ showed no cracking. A significant amount of cracking was observed on sections where the tensile strain is larger than $80 \mu\text{m}/\text{m}$. It should be noted that the percentage cracking shown in figure 2 is related to the entire pavement surface; 50% cracking implies that both wheelpaths are cracked

The following step was to take into account the traffic volume. Information was only available on the average daily traffic at a given moment in time. This was also the case for the traffic growth and the percentage of truck traffic. Therefore some assumptions had to be made in the calculation of the number of 100 kN equivalent axles that traveled the various sections. Extensive research in the Netherlands (CROW) on axle loads has shown that the number of equivalent 100 kN axles per truck (VSF_{100}) can be related to the truck traffic intensity (table 1). For light truck traffic it was

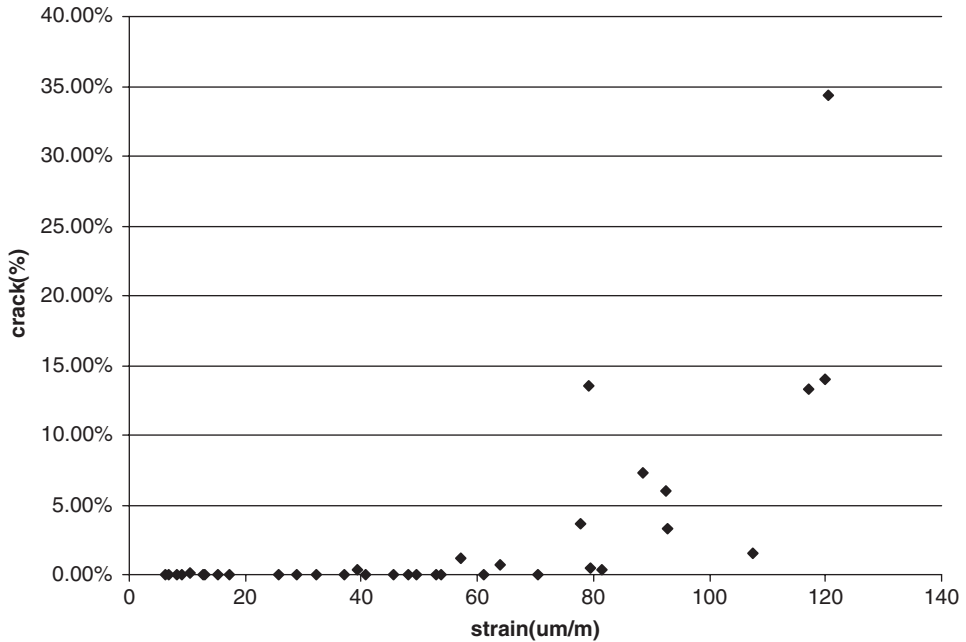


Figure 2. Relationship between the tensile strain at the bottom of the cement treated base measured between the wheel paths and the amount of cracking observed on the pavement surface.

Table 1. Truck damage factor (VSF_{100}) in relation to the truck traffic intensity.

Number of trucks per working day per direction	VSF_{100}
<1000	0.2–0.5
1000–4000	0.5–1.0
>4000	1.0–2.0

Note: the truck damage factor is the number of equivalent 100 kN single axles per truck.

assumed that $VSF_{100} = 0.35$, for medium traffic a value of 0.75 was taken while for heavy traffic a value of 1.5 was assumed.

Combining all information, figure 3 (Pu, 2007) was obtained that shows the relation between the tensile strain at the bottom of the cement treated base, the number of applied 100 kN axle loads and the observed amount of cracking. After careful consideration of all available data, and taking into account the error that could have been made in estimating the applied nr. of load repetitions, the following equation for the prediction of the fatigue life of cement treated base course materials could be developed (equation 2).

$$\log N = 8.5 - 0.034\varepsilon \tag{2}$$

where: N = allowable number of 100 kN equivalent single axles; ε = tensile strain at the bottom of the cement treated base due to a 50 kN falling weight load [$\mu\text{m}/\text{m}$].

Furthermore it appeared that the chance on fatigue failure is very small if the tensile strain level is 60 $\mu\text{m}/\text{m}$ or less.

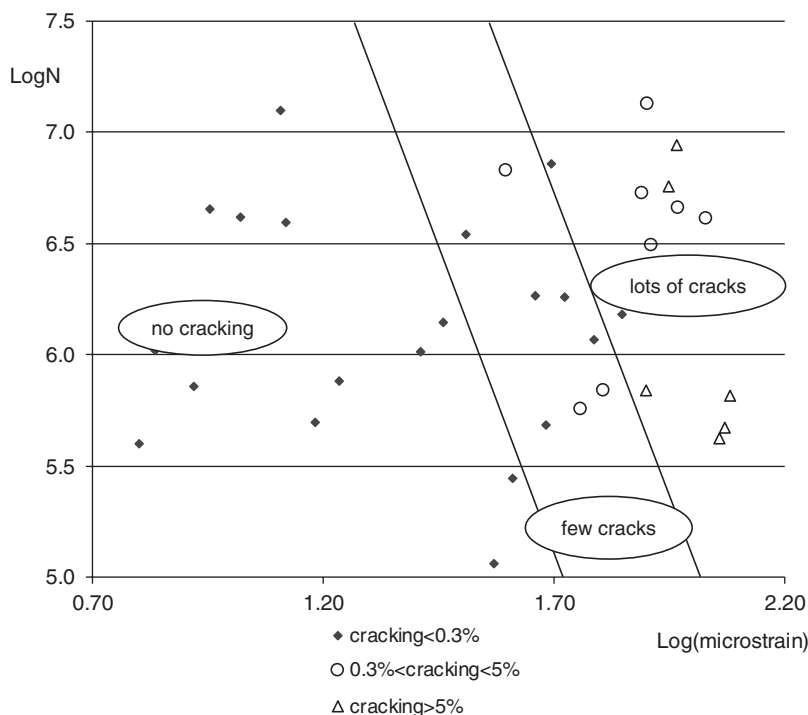


Figure 3. Relationship between tensile strain at the bottom of the cement treated base, the number of 100 kN axles and the amount of observed cracking.

5 SPECIFICATIONS FOR CEMENT TREATED LAYERS

The sections were built in different years. The eldest ones were from the beginning of the 1980's while the youngest ones were from the early 1990's. This implied that they were built under different specification regimes.

Sands in the Netherlands are usually uniformly graded. The average grain size d_{50} is mostly between 146 and 269 μm and the coefficient of uniformity $C_u = d_{60}/d_{10}$ is between 1.55 and 2.45. The CBR values vary between 10 and 15%. Maximum Proctor density is between 1560 and 1830 kg/m^3 and optimum moisture content is between 10 and 17%.

Specifications for cement treated base courses were only limited to the compressive strength of the material. The specifications that were valid before 1985 required for cores taken from the pavement a minimum compressive strength after 90 days of 1.5 MPa. After 1985, this value was required after 28 days. In general this implied that after 1985 a somewhat higher cement content had to be used. In general cement contents varied between 6–8% by mass.

6 LONGITUDINAL CRACKING DUE TO TRANSVERSE CRACKS

It has been mentioned before that it is expected that the pavement sections investigated could certainly have some transverse cracking in the cement treated base which hadn't yet propagated through the covering asphalt layer. It was hypothesized that such transversal cracks, initiated by environmental effects, might very well be the reason for longitudinal, traffic induced wheel path cracks in the cement treated base. The reason for this is schematically shown in figure 4.

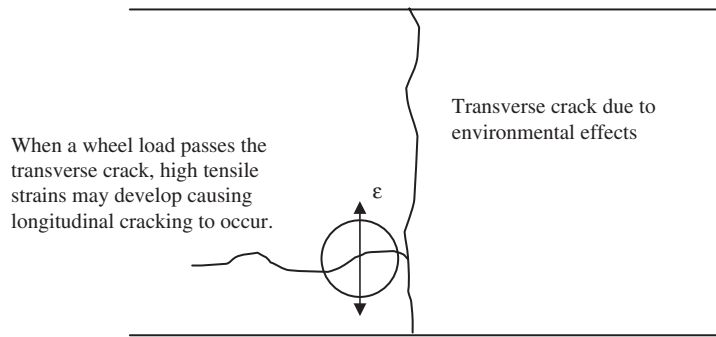


Figure 4. Mechanism causing longitudinal, traffic induced, cracks to occur at a transverse crack in a cement treated base.

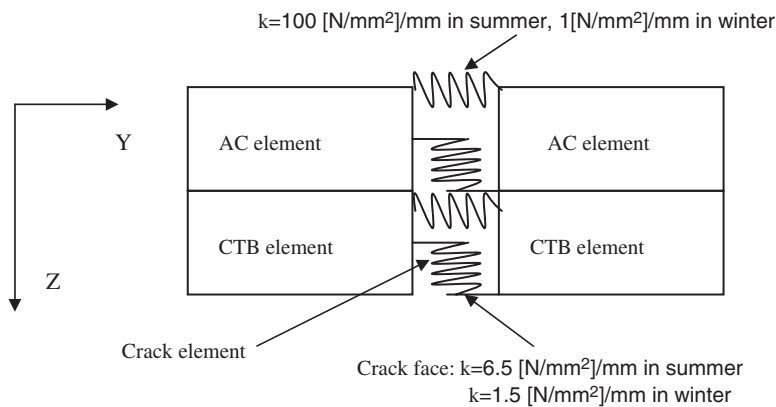


Figure 5. Springs used to characterize load transfer across the transverse crack.

A large number of finite element calculations were made to determine the magnitude of the tensile strains responsible for the development of longitudinal cracks near a transverse crack (Pu, 2007). All structures were three layer structures in which the stiffness of both the asphalt layer ($E_{\text{asphalt}} = 3000, 11000 \text{ MPa}$) and cement treated base ($E_{\text{CTB}} = 3000, 6000, 12000 \text{ MPa}$) was varied. In all cases the subgrade modulus was set at 100 MPa . Furthermore the thickness of both the asphalt and base layer were varied ($h_{\text{asphalt}} = 100, 200, 300 \text{ mm}$; $h_{\text{CTB}} = 150, 300 \text{ mm}$). Summer conditions were simulated by assuming good load transfer across the crack in the cement treated base while winter conditions were simulated by assuming a poor load transfer. The load transfer at the crack was modeled by means of a series of springs (figure 5). Horizontal springs simulated the horizontal stiffness at the crack in case the crack is closed or open. Vertical springs represented the shear stiffness of the crack. Examples of the output of the analysis are given in figures 6a and 6b. The figures show the deflection bowls for a pavement consisting of 100 mm of asphalt on top of a 150 mm thick CTB. The CTB had a modulus of 3000 MPa for both summer and winter conditions. The stiffness modulus for the asphalt layer was set at 3000 MPa for summer conditions and 11000 MPa for winter conditions. In the half cracked pavements, the transverse crack was assumed to be only in the CTB. In the fully cracked pavement, the transverse crack was assumed to have propagated through the CTB and the asphalt layer. The values for the spring stiffness were derived from work done by de Bondt (1999).

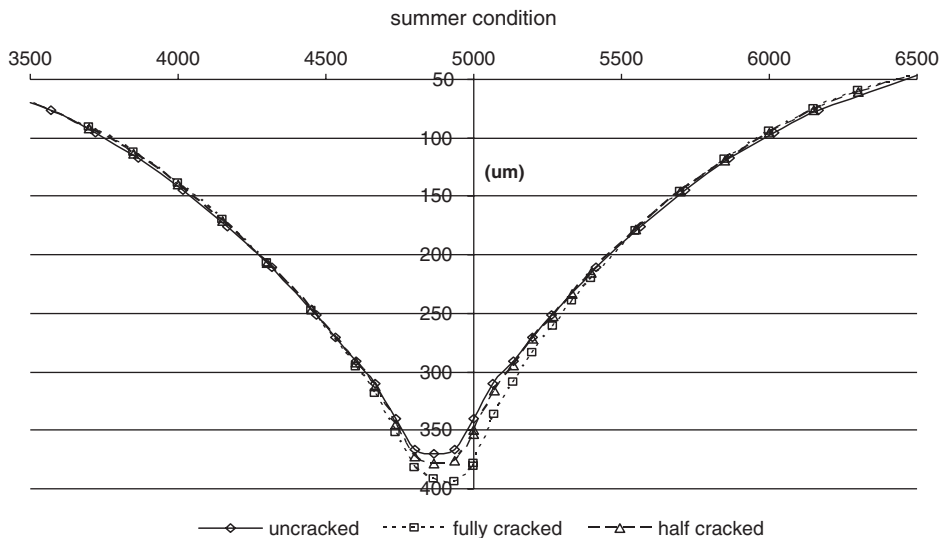


Figure 6a. Deflection bowls of an uncracked and cracked pavement in summer time.

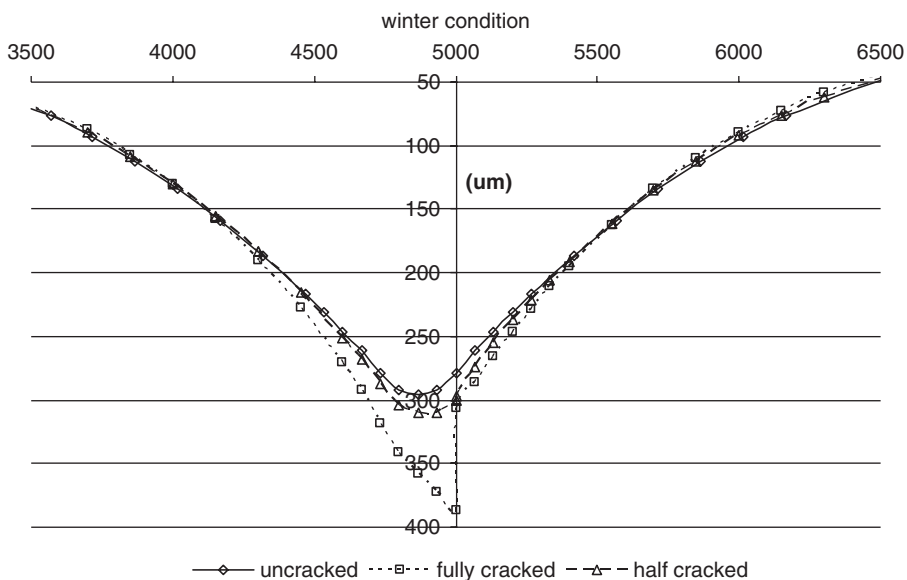


Figure 6b. Deflection bowls of an uncracked and cracked pavement in winter time.

The finite element analyses resulted in the following findings.

- (a) The tensile strain at the bottom of the uncracked CTB as predicted by means of equation 1 agreed very well with the tensile strain as predicted by means of the finite element analyses.
- (b) In summer conditions, when there is a good load transfer across the crack, the tensile strain causing a longitudinal crack to occur at the transverse crack is 1.12 times the tensile strain at the bottom of the uncracked CRTB. This is in case of a half cracked pavement. In case of a fully cracked pavement, the multiplication factor is 1.2.

- (c) In winter conditions when transverse cracks can be assumed to be open resulting in a poor load transfer, the multiplication factors are 1.21 for the half cracked pavement and 1.46 for the fully cracked pavement.

The above findings resulted in the conclusion that traffic induced cracking will not occur in cement treated bases when the strain level remains below $60/1.46 = 41 \mu\text{m/m}$ in cases where the load transfer across transverse cracks is poor. When a good load transfer can be guaranteed, this strain level is $50 \mu\text{m/m}$. These values are proposed to be used as endurance limits for the material investigated.

Although not discussed in this paper, it is believed that climate induced transverse cracking can successfully be controlled by sawing shrinkage cracks in the cement treated base in the same way as this is done in concrete pavements. Experiences on Amsterdam's Schiphol airport technique showed this technique to be very effective in controlling the activity and the width of the transverse cracks in the CTB used under its runways and taxiways.

7 CONCLUSIONS

The following conclusions have been drawn.

1. From the performance data in the SHRP-NL data base, it has been possible to derive a field fatigue relation for sand cement bases.
2. Also an endurance limit for these types of materials was developed. In case good load transfer across transverse cracks is guaranteed, a strain value of $50 \mu\text{m/m}$ can be taken as such a limit.
3. In case the load transfer across transverse cracks must be assumed to be poor, this limit is $41 \mu\text{m/m}$.

REFERENCES

- De Bondt, A.H. 1999. Anti-Reflective Cracking Design of (Reinforced) Asphaltic Overlays. *PhD Thesis*. Delft: Delft University of Technology.
- Groenendijk, J. 1998. Accelerated testing and surface cracking of asphaltic concrete pavements. *PhD Thesis*. Delft. Delft University of Technology.
- Gurp, C.A.P.M. van, & P.M. Wennink. 1996. Rural Road Pavement Design and Evaluation (in Dutch). *Report E96007*. Apeldoorn: KOAC-WMD Consultants.
- Molenaar, A.A.A. 2006. APT as a Tool for the Development of Design and Performance Models. *Proceedings 10th International Conference on Asphalt Pavements*. CD-ROM, Quebec,
- Molenaar, A.A.A. 2007. Prediction of Fatigue Cracking in Asphalt Pavements: Do We Follow the Right Approach. *Paper presented at the 2007 Annual TRB Meeting*. CD-ROM, Washington DC.
- Pu, B. 2007. Analysis of the Performance of Pavements with a Cement Treated Base. *MSc Thesis*. Delft: Delft University of Technology.
- Theyse, H.L., M. de Beer, & F.C. Rust. 1996. Overview of the South African mechanistic pavement design analysis method. *Paper presented at the 1996 Annual TRB Meeting (nr. 961294)*. Washington DC.

Cracking response and service life prediction of flexible and semi-rigid road pavements implementing M-E PDG 2002 code

M. la Agostinacchio
Polytechnic of Milan, Italy

D. Ciampa & S. Olita
University of Basilicata, Italy

ABSTRACT: This study investigates the effectiveness of different construction approaches in relation to the major distress modes affecting flexible and semi-rigid pavement overlay system. Cracking predicting and its control are key components in design of new and exiting pavements. From this point of view the possibility of evaluating the damage by an incremental calculation over the entire target of design life is very interesting. The M-E PDG 2002 (Mechanistic-Empirical Pavement Design Guide v.1.003) software allows to assess the effectiveness of a trial design relating to performance criteria defined by the designer, predicting the service life of the considered pavement system. In particular, it shows the evolvement of structural distresses, as bottom-up fatigue (or alligator) cracking, surface-down fatigue (longitudinal) cracking, permanent deformations (rutting) and thermal cracking, through the design life, evaluating the influence of materials characteristics, thickness of layers, climate and traffic on pavement service life. In this paper the Authors show the results obtained using the above-mentioned software, adopting different pavements typologies (conventional, full-depth, semi-rigid, inverted-section), in order to determinate design solutions which are suitable for inhibiting or limiting the cracking phenomenon and the rutting, evaluating the influence of design parameters. In such way, the study offers useful suggestions that can be used by asphalt pavement designers to reduce in particular the possibility of premature cracking, so as to increase the service life of pavement system.

1 INTRODUCTION

In this paper the Mechanistic-Empirical pavement design method introduced by the “AASHTO Guide 2002” (AASHTO 2004) was applied. The research was focused on two aspects:

- Analysis and optimization of different pavement typologies (conventional, full-depth, semi-rigid, inverted-section) of secondary ordinary extra-urban roads at parity of materials and in standard conditions;
- Evaluation of the effects produced varying the performances of the used materials at parity of design solution and operative conditions (climate, traffic, etc.).

The M-E PDG v 1.003 software (Applied Research Associates – Transportation Arizona State University 2007), developed within the NCHRP 1-37A and 1-40D projects, was used.

The Mechanistic-Empirical methodology implemented by the software implies three different levels of input, according to the criticality of the project, the availability of data and the required level of reliability. Since the numerical comparison analyses among the different structural typologies refer to the same materials in standard conditions, the third level was adopted.

The reference initial Conventional Flexible Section – CFS adopted in this study was selected from the Italian Catalogue of pavements (Consiglio Nazionale Ricerche, 1995), precisely from the

4F card, referring to flexible pavements of secondary ordinary extra-urban roads. This section is defined referring to a number of commercial vehicle transits equal to 4,000,000 on the most loaded lane hypothesizing a service life of twenty years, estimated on the basis of the pavement typology and the traffic spectrum corresponding to the road category. The AADTT (Average Annual Daily Total Traffic) obtained dividing the number of commercial vehicle transits on the most loaded lane (4,000,000) by the days of service life (7300) and multiplying by the lanes number (2) was 1100. The vehicle class distribution was defined both comparing the FHWA Classification used by the M-E PDG software with the Italian Classification, and comparing the Truck Traffic Classification (TTC) groups and the corresponding distribution used by the Design Guide with the CNR Catalogue Traffic Spectra, assessing the TTC 14 group (FHWA 2001) approached better the Italian distribution corresponding to the secondary extra-urban roads.

Since the environmental conditions influence the pavement performance, the flexible especially, all analyses were referred to a same place, the parameters of which are reported in the database of the EICM (Enhanced Integrated Climatic Model) routine, precisely to the “Chicago Midway Intl. Arpt.” (Elevation: 189 m – Latitude: 41.47° – Longitude: –87.45°), which is characterized by a climatic seasonal trend near enough to many areas of the Italian inland.

The particle size distribution of the aggregates, the bitumen percentage, the residual voids and the mechanical characteristics of the bituminous/stabilized cement mixtures were defined according to the CNR Catalogue (Consiglio Nazionale Ricerche, 1995). In particular, the bitumen was characterized by a Conventional Penetration Grade 85–100.

The Conventional Flexible Section adopted in this study consisted of the following layers succession, placed on a natural soil AASHTO Class A-4:

- Compacted Soil AASHTO Class A-3 characterized by a thickness of 40 cm;
- Unbounded Crushed gravel foundation of 15 cm;
- Asphalt concrete base layer characterized by a thickness of 13 cm;
- Asphalt concrete binder of 6 cm;
- Asphalt concrete wearing-course of 5 cm.

Starting from the CFS (Fig. 1a), the following pavements typologies were defined:

- Full Depth Section-FDS (Fig.1b), obtained eliminating the foundation from the CFS;
- Semi-rigid Section-SRS (Fig.1c), obtained replacing the asphalt concrete base with a stabilized cement layer;
- Inverted Section-IS (Fig. 1d), obtained inverting the position of the unbounded layer with the base and modifying the thickness (in particular the thickness of the crushed gravel layer was led to 10 cm). In Figure 1d the AC base is at the bottom of the initial trial section; however in the analyses a stabilized cement base was also adopted.

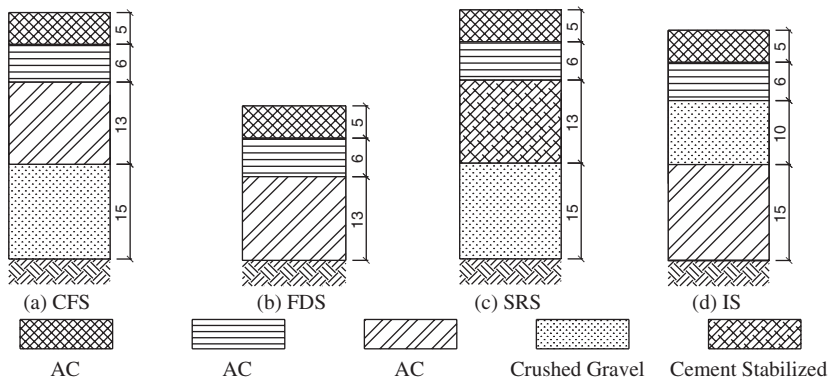


Figure 1. Trial design sections.

2 PERFORMANCE PARAMETERS, LIMITS AND RELIABILITY

In order to investigate the effectiveness of the different construction approaches in relation to the major distress modes, the following performance indexes were assumed:

- IRI (International Roughness Index) – This index depends on the initial pavement profile (roughness) and on the follow development of the distresses during the service life. The IRI model is able to foresee the roughness variation on the basis of the estimated distresses, calculated by specific forecast models, of the initial IRI index and of other parameters referring to the situ. Since for extra-urban roads the IRI is generally in a range from 197.28 cm/km (125 in/mi) to 394.57 cm/km (250 in/mi), a Distress Target of 271.46 cm/km (172 in/mi), with a Reliability Target of 90%, was adopted.
- Longitudinal cracking – Longitudinal cracks can be caused by tensile stresses and strains due to: traffic loads, aging of the asphalt concrete mixture on the top of the pavement or shearing of the Hot Mix Asphalt. The cracks propagation is from the surface to the bottom of pavement. For extra-urban roads the longitudinal cracks index is generally in a range from 100.37 m/km (530 ft/mi) to 501.89 m/km (2650 ft/mi). The adopted Distress Target was equal to 378,79 m/km (2000 ft/mi), with a Reliability Target of 90%.
- Bottom-up fatigue (alligator) cracking – This distress mode starts with longitudinal cracks along the wheel path, which subsequently spread and link up, forming a particular pattern to which the definition of alligator cracking is due. The propagation process starts from the bounded base layer, below the bituminous overlay, because of the repetitiveness of the applied loads. Since for extra-urban roads the admissible damage level is in a range from 10% to 45% of the lane surface, the Distress Target was assumed equal to 25%, with a Reliability Target of 90%.
- Thermal cracking – This phenomenon is due to low temperatures and/or to sudden thermal changes which cause the hardening and the shrinkage of the asphalt concrete. The Distress Target is generally assumed equal to 189.39 m/km (1000 ft/mi), with a Reliability Target of 90%;
- Permanent deformation (rutting) – This distress consists of a superficial depression in the wheel path. It is due to the anelastic or plastic strains of the pavement layers or of the subgrade. The Distress Target is assumed equal to 1.27 cm (0.5 in) for only asphalt concrete and to 1.9 cm (0.75 in) for total pavement, with a Reliability Target of 90%;
- Chemically stabilized layer fatigue fracture – This distress characterized the semi-rigid pavements, precisely the base layers which are chemically stabilized by cement, fly ash or lime-fly ash. Under the repeated load application, microcracks lead to a reduction of the stiffness and so to a decrease of the modulus, which can cause a fatigue breaking. The Distress Target is generally assumed equal to 25%, with a Reliability Target of 90%.

3 SECTIONS OPTIMIZATION

Once defined typologies, sizes and materials characteristics of the trial sections (see Paragraph 1), the optimization was made using the M-E PDG code: the layers thicknesses were set right on the basis of the performance parameters (see Paragraph 2) referring to the different pavement typologies. This stage is described in the following paragraphs.

3.1 *Conventional Flexible Section – CFS*

The analysis of the reference CFS (Fig. 1a) shows all parameters described in Paragraph 2 were verified. In particular, at the end of service life (20 years), the longitudinal cracking trend showed a reliability next to 100% (Fig. 2a), while in the case of rutting for only asphalt concrete (AC) layers the reliability was equal to 94.56%. The optimization process was aimed to reduce the layers thickness in order to obtain a Reliability Target next to 90%. At first, the aim was to balance

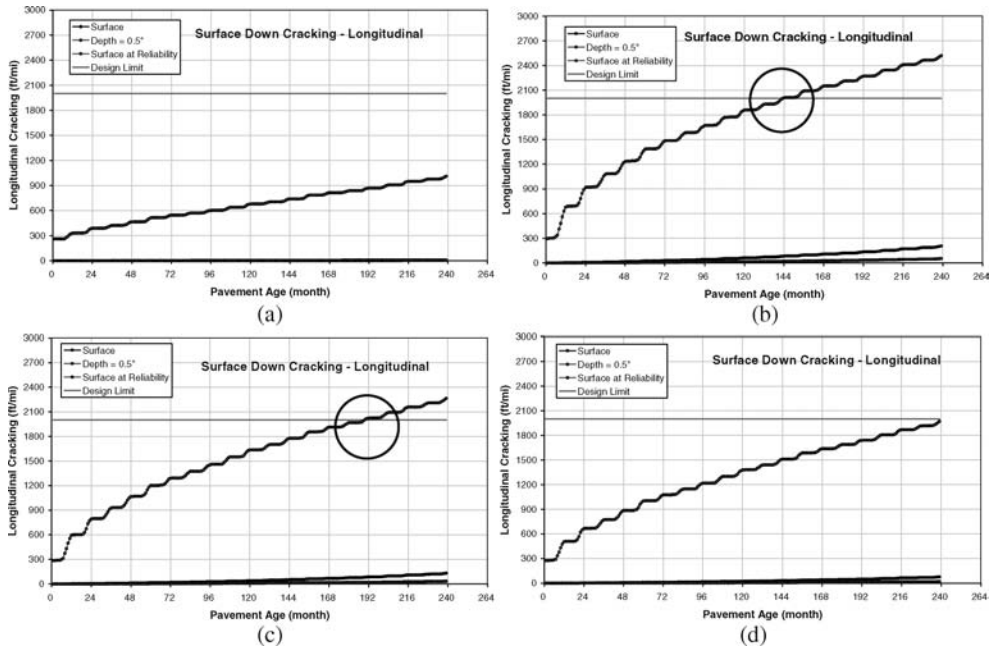


Figure 2. CFS optimization.

the reliability of the above-mentioned parameters, i.e. to increase the reliability in the case of the rutting for only asphalt concrete layers, reducing that one corresponding to the longitudinal cracking. The thickness of the layers on the top (wearing-course and binder) were reduced of 1 cm. In such way, for rutting and longitudinal cracking reliability targets of 98.03% and 96.05% were obtained respectively, while the reliability values of the other parameters were substantially the same. Then, the wearing-course thickness was reduced of 1 cm, achieving reliability values of 98.51% and 93.50% for rutting and longitudinal cracking respectively.

Subsequently, since it wasn't possible reduce further the thickness of the superficial layers, the AC base was considered, making at the beginning a reduction of 3 cm and then limiting this reduction at first to 2 cm and to 1 cm at last, in order to satisfy the longitudinal cracking test.

The Figures below show the longitudinal cracking trend obtained during the optimization process. As it can be seen, the reaching of the reliability limit is at the 12th year (Fig. 2b) adopting a reduction of 3 cm, and at 16th year referring to a reduction of 2 cm (Fig. 2c). Reducing the base layer thickness of 1 cm, all performance parameters are verified, obtaining a reliability of 90.30% in the case of longitudinal cracking test (Fig. 2d).

At the end, the optimized CFS (Fig. 5a) consisted of the following layers succession, placed on a natural soil AASHTO Class A-4:

- Compacted Soil AASHTO Class A-3 characterized by a thickness of 40 cm;
- Unbounded Crushed gravel foundation of 15 cm;
- Asphalt concrete base layer characterized by a thickness of 12 cm;
- Asphalt concrete binder of 5 cm;
- Asphalt concrete wearing-course of 3 cm.

3.2 Full Depth Section – FDS

The FDS optimization process (Fig. 1b) was defined on the basis of the obtained reliability values, which were next to 100% for all performance parameters, with the exception of the value relative

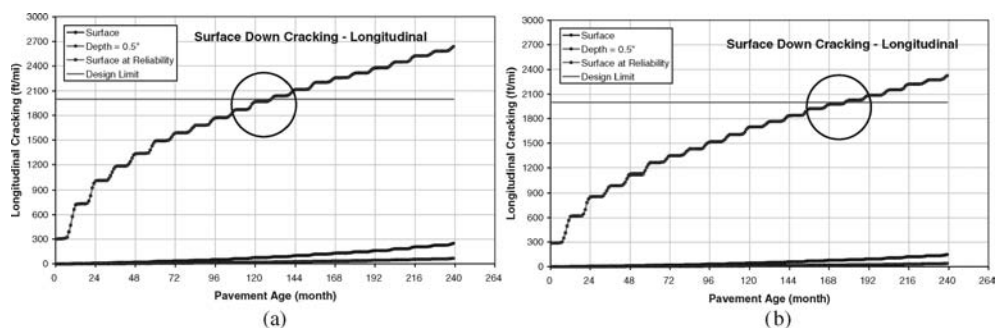


Figure 3. FDS optimization.

to the AC rutting (96.69%), in analogy with the CFS (Fig. 1a), though the FDS was characterized by the absence of foundation.

The same optimization iter developed in Paragraph 3.1 was performed, achieving to a new FDS, characterized by a thickness reduction of 2 cm for the wearing-course, and a reduction of 1 cm both for the binder and base. The same reliability values of the performance parameters estimated in the case of the optimized CFS (see Paragraph 3.1) were obtained, with the exception of the value relative to the AC rutting, which was higher than that one of the FDS (99.46% vs 98.51%), even though the FDS was characterized by the absence of foundation.

The optimized FDS (Fig. 5b) consisted of the following layers succession, placed on a natural soil AASHTO Class A-4:

- Compacted Soil AASHTO Class A-3 characterized by a thickness of 40 cm;
- Asphalt concrete base layer characterized by a thickness of 12 cm;
- Asphalt concrete binder of 5 cm;
- Asphalt concrete wearing-course of 3 cm.

The analysis showed a greater base thickness reduction, for example equal to 3 cm or to 2 cm, leads to a missed verification in terms of reliability referring to the longitudinal cracking. Precisely, the reliability values corresponding to reductions of 3 cm and of 2 cm were 82.57% and 86.13% respectively; the reaching of the admissible damage occurred on the 130th (Fig. 3a) and on 179th month (Fig. 3b).

3.3 Semirigid Section – SRS

The analysis of the SRS (Fig. 1c) put on evidence a reliability deficit referring to AC layers (wearing-course and binder) rutting, showing a corresponding value equal to 64.38% (versus the assumed limit of 90%), which was very low compared with the predicted reliability for the other parameters, values next to 100%. This performance deficit could be overcome modifying the particle size distribution of the aggregates and/or using a bitumen with a lower penetration grade; however, since the considered mix designs of AC layers (wearing-course and binder) were selected in according to the Italian Roads Pavement Catalogue and to the main Italian technique specifications, the problem was resolved by a modify of layers thickness.

The drop of AC rutting reliability of the SRS (64.38%) versus the reliability value corresponding to the CFS (see Paragraph 3.1) was due to the greater stiffness of the base layer, because of the use of different material types (asphalt concrete for the CFS, stabilized cement for the SRS). Tests showed a further stiffening of the layers at the bottom of the pavement section by a thickness increment leads to a worsening: for example increasing of 5 cm the foundation the predicted reliability was 63.7%, while modifying the base thickness from 13 cm to 15 cm the reliability value was equal to 61.04%. Also the thickness increment of the layers at the top of the pavement caused a drop of the

Table 1. Reliability values summary of the optimized SRS.

Performance criteria	Distress target	Reliability target	Distress predicted	Reliability predicted	Acceptable
<i>Reliability summary</i>					
Terminal IRI (in/mi)	172	90	105.2	98.85	Pass
AC Surface Down Cracking (Long. Cracking) ft/mile):	2000	90	3.5	99.98	Pass
AC Bottom Up Cracking (Alligator Cracking) (%):	25	90	0	99.999	Pass
AC Thermal Fracture (Transverse Cracking) (ft/mi):	1000	90	1	99.999	Pass
Chemically Stabilized Layer (Fatigue Fracture)	25	90			N/A
Permanent Deformation (AC Only) (in):	0.25	90	0.13	99.43	Pass
Permanent Deformation (Total Pavement) (in):	0.75	90	0.4	99.999	Pass

reliability index: for example, the reliability values corresponding to a binder thickness of 7 cm and then of 8 cm were 65.66% and 58.09%.

In order to guarantee an AC rutting reliability of 90%, a thickness reduction both of the wearing-course and of the binder was performed. In details: reducing of 1 cm firstly the wearing-course and then also the binder, the predicted reliability values were 78.48% and 89.66% respectively; moreover, a further increment of reliability index (97.77%), corresponding to a thickness decrement equal to 2 cm for the wearing-course and to a 1 cm for the binder in the considered SRS, was obtained.

An improvement of SRS performance was achieved leading to 10 cm the thickness of the base layer, reaching reliability values next to 100% (Tab. 1) for all parameters.

The optimized SRS (Fig. 5c) consisted of the following layers succession, placed on a natural soil AASHTO Class A-4:

- Compacted Soil AASHTO Class A-3 characterized by a thickness of 40 cm;
- Unbounded Crushed gravel foundation of 15 cm;
- Cement stabilized base layer characterized by a thickness of 10 cm;
- Asphalt concrete binder of 5 cm;
- Asphalt concrete wearing-course of 3 cm.

3.4 Inverted Section – IS

The “Inverted Sections” is characterized by the interposition of an unbounded crushed gravel layer between the asphalt layers on the top of the structure (wearing-course and binder) and the AC base. The first experimentations in situ were performed in USA at the beginning of 1970 (Illinois Department of Transportation 1972), with the aim to reduce the cracks propagation in the road pavement structure; then other study were accomplished in order to evaluate its effectiveness (DOTD 2004).

All tests performed considering the IS in Figure 1d were verified, with the exception of rutting the predicted reliability of which was equal to 66%. The following analyses were accomplished firstly modifying the thickness of wearing-course, binder, and AC base. In details: referring to rutting, AC surface down cracking and AC bottom up cracking, the thickness reduction of 2 cm for the wearing-course and of 1 cm for the binder led to reliability values equal to 75.35% (rutting), 79.14% (AC surface down cracking) and 88.37% (AC bottom up cracking), while increasing of 2 cm only the AC base thickness the estimated reliability values were 74.18% (rutting), 86.44% (AC surface down cracking) and 89.10% (AC bottom up cracking).

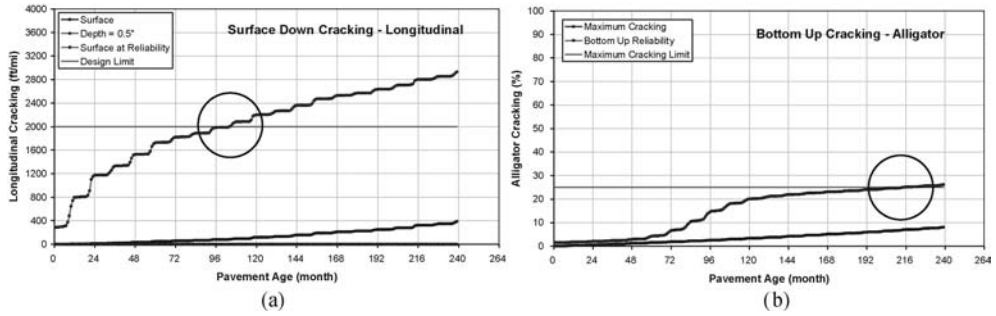


Figure 4. Optimization of the IS.

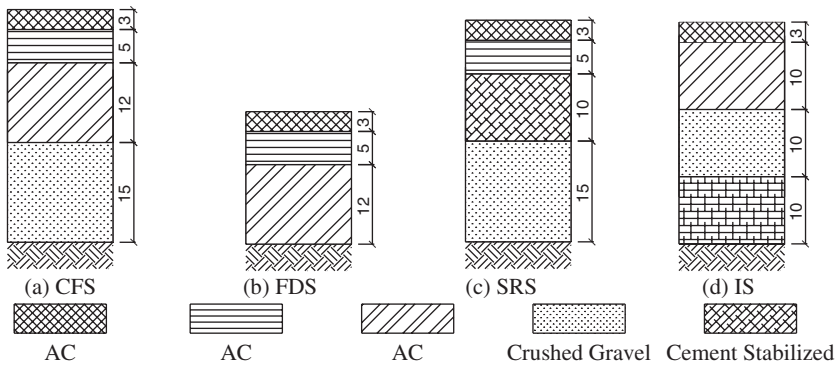


Figure 5. Optimized sections.

On the other hand, thickness increments of wearing-course and binder allowed to verify the tests relative to longitudinal and bottom up cracking, with the exception of rutting: for example, in the case of a section having layers thickness equal to 5 cm for the wearing-course, 6 cm for the binder, 10 cm for the crushed gravel layer and 15 cm for the AC base, the estimated rutting reliability was 79.59%.

The trend of the longitudinal and bottom up cracking indexes, estimated taking into account a thickness reduction of the wearing-course and of the binder, is shown in Figures 4a, b.

Other results were obtained. For example, the introduction of a stabilized cement layer instead of the AC base, in order to give a greater stiffness at the bottom of the section, taking into account a wearing-course thickness of 3 cm and a binder of 5 cm, allowed to verify the AC alligator cracking test, but not the rutting (80.06%) and the AC surface down cracking (80.49%) tests. In particular, different solutions were accomplished introducing, instead of the binder, an AC layer with a greater thickness characterized by a mix design used for base layers, and reducing the thickness of the stabilized cement base.

The obtained optimized IS (Fig. 5d) consisted of the following layers succession, placed on a natural soil AASHTO Class A-4:

- Compacted Soil AASHTO Class A-3 characterized by a thickness of 40 cm;
- Cement stabilized base layer characterized by a thickness of 10 cm;
- Unbounded Crushed gravel interlayer of 10 cm;
- Asphalt concrete layer of 10 cm;
- Asphalt concrete wearing-course of 3 cm.

A reliability values summary is in Table 2.

Table 2. Reliability values summary of the optimized IS.

Performance criteria	Distress target	Reliability target	Distress predicted	Reliability predicted	Acceptable
<i>Reliability summary</i>					
Terminal IRI (in/mi)	172	90	108.7	98.21	Pass
AC Surface Down Cracking (Long. Cracking)(ft/mile):	2000	90	22.1	97.16	Pass
AC Bottom Up Cracking (Alligator Cracking) (%):	25	90	0.1	99.999	Pass
AC Thermal Fracture (Transverse Cracking) (ft/mi):	1000	90	1	99.999	Pass
Chemically Stabilized Layer (Fatigue Fracture)	25	90			N/A
Permanent Deformation (AC Only) (in):	0.25	90	0.17	90.1	Pass
Permanent Deformation (Total Pavement) (in):	0.75	90	0.49	99.81	Pass

4 EVALUATION OF EFFECTS INDUCED BY THE DESIGN PARAMETERS

The optimized sections (Fig. 5), obtained by the iter described in the 3rd Paragraph, are approximately equivalent in terms of reliability referring the considered performance parameters (see Paragraph 2). The second stage of the study consisted of evaluation of the effect produced varying the performance and/or the typologies of the materials, at parity of design solution and operative conditions (clime, traffic, etc.). In particular, the performance characteristics of compacted soil layer and of the natural soil subgrade and the bitumen penetration grade for the AC layers were taken into account. The results are shown in the following paragraphs.

4.1 *Compacted soil layer*

The analysis was performed firstly considering different soil class and then varying only the thickness of the layer, in order to evaluate the sensitivity of performance indexes.

In particular, the assumption of a A-1-a class didn't produce substantial performance variations in the optimized sections, with the exception of the IS, for which the AC rutting reliability index decreased to a lower value than 90% (86.31%), because of the stiffness increment caused by the use of this soil class.

On the other hand, adopting the soil A-2-5 class, in the case of the CFS and the FDS the AC surface down cracking reliability index became 85.44% for the CFS and 79.38% for the FDS, while substantial performance variations were not with regards of the SRS and the IS.

Other results were obtained. In particular, the elimination of the compacted soil layer did not change the performance of the SRS and the IS (the reliability indexes are greater than 90%), but led in the case of the CFS and the FDS to values of AC surface down cracking reliability lesser than 90% (82.85% for CFS and 67.63% for the FDS). The AC surface down cracking reliability index of the FDS decreased also varying the layer thickness. In fact, referring to the soil A-3 class, for layer thicknesses of 30 cm and of 35 cm the reliability index becomes equal to 88.95% and 88.56% respectively; on the contrary the CFS satisfied all tests, even though the estimated AC surface down cracking reliability index is next to the admissible limit.

4.2 *Subgrade*

The study was accomplished taking into account different soil classes.

Results showed only the SRS was not influenced by the class type of soil, because of the stabilized cement base layer, which allows the overlay system is not too influenced by the stiffness of the bearing surface.

A significant reduction of the performance of the CFS, the FDS and the IS, with values of AC surface down cracking reliability equal to 79.69%, 78.19% and 85.14% respectively, occurred selecting the soil A-2-4 class. In particular, the IS got a rutting reliability index equal to 85.57%.

On the contrary, the use of soil A-6 class led to an increment of the AC longitudinal cracking reliability indexes, which were 91.66% for the CFS and 91.44% for FDS. The IS performance was substantially the same obtained selecting the soil A-2-4 class (the rutting reliability index was 90.02%).

4.3 Bitumen penetration grade

Instead of a penetration grade 85-100 were considered penetration grades of 60–70 and of 120–150.

The first case led to the increment of the AC rutting reliability indexes of all sections, with a value equal to 96.75% for the IS and next to 100% for the CFS, the FDS and the SRS. On the contrary, the use of the bitumen Pen. Grade 120–150 did not allow to verify the tests. In particular, the AC surface down cracking reliability index was 87.64% for the CFS and 86.80% for the FDS respectively, while the rutting reliability value was 87.39% for the SRS and 70.95% for and IS.

5 CONCLUSIONS

In this paper the Authors present the results obtained analysing different pavement typologies (CFS, FDS, SRS and IS) at parity of operative conditions (clime, traffic) by the M-E PDG v.1.003 software. Starting from sections defined by the Italian Catalogue, design solutions were developed in order to inhibit the main distress modes (top-down cracking, bottom-up cracking, thermal cracking and rutting). Then, the influence of several parameters (the presence of the compacted soil layer, the use of a different soil class, the variation of layer thickness of the compacted soil layer and the use of different bitumen penetration grade) on the performance of the optimized sections was evaluated, achieving to useful suggests for the design of flexible and semi-rigid pavements. Assessed the substantial equivalency among the optimized sections in terms of performance reliability, results showed:

- The performances of the CFS and the FDS decrease significantly using for the subgrade natural soil with low bearing capacity, for example decreasing the assumed compacted soil layer thickness (40 cm) of the optimized section or eliminating it or using materials of inferior quality;
- The FDS needs a compacted soil layer thickness not lesser than 40 cm;
- The performance of the SRS does not depend on the class type of the compacted soil layer/natural soil subgrade, since the stabilized cement base layer allows that the overlay system is not too influenced by the stiffness of the bearing surface. In particular, the compacted soil layer can be eliminated adopting a subgrade of adequate bearing capacity;
- The IS needs the interposition of a crushed gravel layer between an AC base layer at the top and a stabilized cement base layer at the bottom of the pavement section. The reliability of the IS increases using soil layer with low bearing capacity, i.e. characterized by low thickness. Moreover the IS performance is not influenced by the variation of the characteristics of the soil subgrade;
- The SRS and the IS are more efficient than CFS and the FDS in opposing to the longitudinal cracking.

It means the most reliable is the SRS. The trend of the main performance parameters corresponding to the optimized section (Fig. 5c) is shown in Table 1 and in Figures 6.

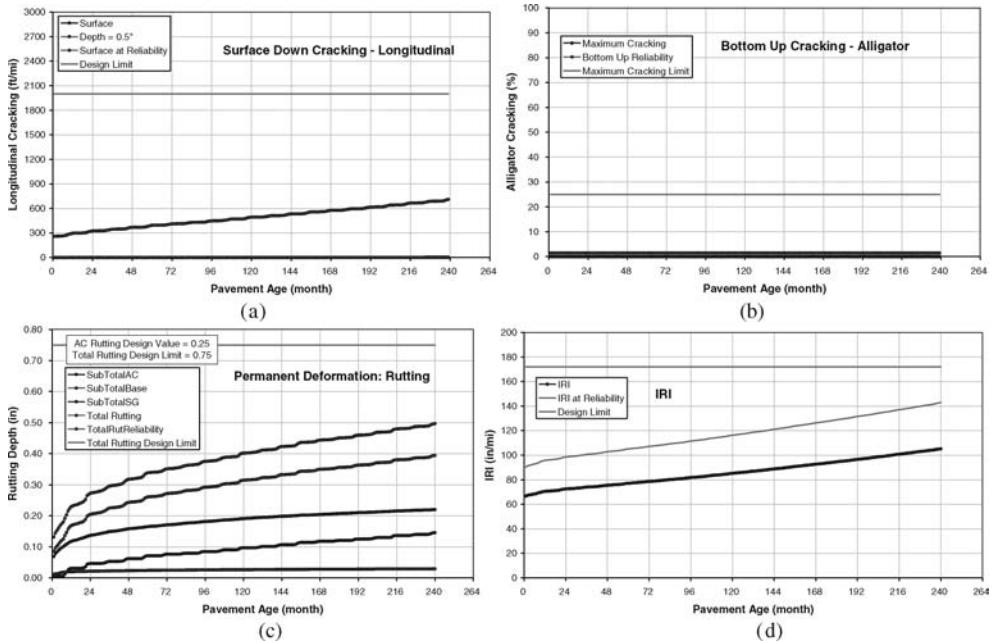


Figure 6. Trend of the main performance indexes of the optimized SRS.

REFERENCES

- AASTHO. 2004. *Guide for Mechanistic-Empirical Design*. NCHRP Project 1-37A. U.S.A.
- Agostinacchio M.la & Olita S. 2007. *Asphalt concrete "inverted section" pavements for long-life roads*. Proceedings of MAIREPAV5 international conference. Park City, Utah, USA, 8–10 August 2007.
- Consiglio Nazionale delle Ricerche CNR. 1995. *Catalogo delle pavimentazioni stradali*. C.N.R.-B.U. n.178/95. Italy.
- FHWA – Federal Highway Administration. 2001. *Guide to LTPP Traffic Data Collection and Processing*. Washington DC. U.S.A.
- Huang, Y.H. 1993. *Pavement analysis and design*. Englewood Cliffs: Prentice Hall.
- Luisiana Department of Transportation and Development DOTD. 2004. *Report about Louisiana Pavement Conference*. October 6&7. Baton Rouge, La Masood Rasoulain, P.E.
- State of Illinois Department of transportation. 1972. *Interim report on the performance of the lake county inverted flexible pavement*. U.S.A.

A prediction procedure of reflective cracking growth life for cement stabilized base asphalt pavement

F.-J. Ni

Southeast University, China

Q. Li

Sejong University, Korea

ABSTRACT: In 2–3 years after completion, reflective cracking is often found in cement stabilized base asphalt pavement in China due to traffic load and environmental factors. The objective of this study is to develop simple models to predict reflective cracking growth life for such pavements. Based on finite element method and fracture mechanics theory, it founded prediction models of cracking spacing and reflective cracking growth life and introduced them to structure design procedure finally. It's observed that using low modulus base is effective in increasing cracking space. Paving asphalt layer at early time has insignificant effect on reducing cracks. It's also found that cracks appearing at the surface of the base extending 10–20 cm downward may make the bottom of asphalt layer crack under traffic loading. The study shows surface modulus, surface thickness and base modulus are the main factors to influence on reflective cracking growth life for such pavements.

1 INTRODUCTION

The typical asphalt pavement in China consists of three layers, a layer of 15 to 18 cm hot mix asphalt mixture, a layer of approximately 40 cm semi-rigid base and lime treated subgrade. The material of cement stabilized macadam with high intensity, good stability and strong anti-erosion is widely used as base or subbase in the high-grade pavements. This kind of structure pattern with strong base and thin surface has good bearing capacity and high economy. However, the project practice indicates that reflective cracking is one of major early distresses in new constructed cement stabilized base asphalt pavement.

Reflective cracking will destroy the continuity and weaken the intensity of pavement structure to some extent, such as increasing deflection and decreasing resilient modulus around the cracks. Especially when the rainwater or snow saturates into the cracks, it will appear relaxation, erosion and slurry in the base under repeated loading and break up asphalt layer of two sides of cracks, consequently influence pavement performance and service life.

Most researches related to shrinkage cracking in cement stabilized base were focused on shrinkage performance of mixture material, microcosmic mechanism and crack resistance measures. Only little theoretical research has been found on shrinkage stress and cracking spacing. For theoretical research on shrinkage cracking for cement stabilized base, dry shrinkage cracking performance and indirect tensile strength of two kinds of semi-rigid base materials were studied from laboratory testing. The performance and space distribution of shrinkage cracking were analyzed during the construction period (Sun et al. 2003). Based on the elastic theory and concrete strength theory, a theoretical model for predict thermal cracking spacing in cement stabilized base was developed. In this study, the compositive effect of dry and thermal shrinkage was considered to predict cracking spacing. Besides, a sensitivity analysis was conducted with several shrinkage related factors (Shi et al. 2004).

In the end of the 70s last century, fracture mechanics principle and method to pavement research field for fracture problem were firstly introduced (Majdzadeh et al. 1980). The fracture mechanics principle to analyze the reflective cracking mechanics of stress and strain relieving interlayer such as SAMI, geotextiles, etc qualitatively was applied (Monismith et al. 1982). In the research on asphalt pavement performance prediction model of SHRP Project, the fracture mechanics to analyze cracking, such as low temperature cracking and fatigue cracking in asphalt pavement was applied (Lytton 1990).

To investigate the cracking mechanism further in cement stabilized base asphalt pavement and inspect their design idea, according to actual pavement diseases, the reflective cracking design indexes for this kind of pavements were determined in this paper. The reflective cracking growth life for cement stabilized base asphalt pavement was predicted based on FEM which makes structure design conform to pavement performance. The final aim of this paper is to optimize the structure design methods for cement stabilized base asphalt pavement.

2 PREDICTION OF SHRINKAGE CRACKING SPACING FOR CEMENT STABILIZED BASE

Shrinkage cracking for cement stabilized bases usually results in transverse cracks in a certain distance along the pavement. In order to determine the standard and criterion of controlling shrinkage cracking, a FEM model was developed to simulate the shrinkage cracking state with different material properties and environment condition factors, such as base modulus, moisture loss ratio, temperature difference, pavement thickness, and etc.

2.1 Basic assumption

- Each layer is composed of homogeneous isotropic linear elastic material, and the influence of stress relaxation is not considered.
- Dry shrinkage strain distribute evenly in the whole base, while thermal shrinkage strain distribute evenly in the horizontal direction. Thus, the model could be simplified as a plane strain problem.

2.2 Interface contact friction

The interface contact friction between the base and the lower layer has a significant effect on shrinkage stress in the base. The Coulomb friction model was introduced to simulate the interface contact between those two layers in this study (Dowson 2003).

2.3 Temperature field model

During the conservation period, the day-night temperature difference results in the temperature gradient through the base depth. The temperature gradient decreases gradually through the base depth. Exponential function as Equations 1–2 was applied to simulate temperature distribution in the base after cooling (Wu et al. 1996).

$$T(x, y) = \begin{cases} P_1 e^{-b_1 y} & 0 \leq y \leq h \\ P_2 e^{-b_2 (y-h)} & h \leq y \leq h+g \\ P_3 e^{-b_3 (y-h-g)} & h+g \leq y < +\infty \end{cases} \quad (1)$$

where P_i = the surface temperature difference of i layer.

$$\begin{cases} P_2 = P_1 e^{-b_1 h} \\ P_3 = P_2 e^{-b_2 g} \end{cases} \quad (2)$$

Table 1. Pavement structure parameters.

Layer	Thickness (cm)	Resilient modulus (MPa)	Poisson ratio	Average temperature shrinkage coefficient ($10^{-6}/^{\circ}\text{C}$)
Base	30	–	0.15	–
Subbase	30	1000	0.20	10
Subgrade	–	60	0.35	20

Table 2. Material parameters of cement stabilized macadam.

Structure	Resilient modulus (MPa)	Splitting strength (MPa)	Average dry shrinkage coefficient ($10^{-6}/\%$)	Average temperature shrinkage coefficient ($10^{-6}/^{\circ}\text{C}$)
1	2000	0.27	70.4	6.7
2	4000	0.45	51.2	7.0
3	6000	0.60	50.4	7.3
4	8000	0.72	60.8	7.6
5	12,000	0.93	115.9	8.2

where b_i = factor related to the temperature difference velocity along with pavement depth. For the three layer structure composed of asphalt surface, semi-rigid base and subbase, it generally thinks that $(b_{sur}, b_{base}, b_{sub}) = (5, 4, 3)$.

2.4 Fracture criterion

The failure stress was adopted in this study as the failure criterion.

2.5 Material properties

Pavement structure and material properties used to calculate shrinkage stresses in cement stabilized base are shown in Table 1–2.

2.6 FEM mesh design

The 8-node plane parametric finite element was used in the FEM model. A contact pair was applied between the base and subbase to simulate constraint effect. The total thickness of model was determined as one meter, since the significant effect of temperature difference on pavement structure is usually less than it. The mesh was designed for half of the structure length with no-rotational constraints at the middle boundary, because of the symmetry of structure and loading. Since maximum shrinkage stress occurs in the middle of structure, the mesh was design from fine at the middle to coarseness at the edge. The size of minimum mesh at the middle of pavement surface was assumed as 5 mm. The friction coefficient was assumed as 0.5, and cohesive sliding resistance was not considered.

2.7 Sensitivity analysis

How pavement modulus affected on shrinkage cracking spacing is shown in Figure 1.

Shrinkage cracking spacing decreases with increasing base modulus, and there is exponential function correlation between them. Thus, it is a disadvantageous way to use cement stabilized base with high strength on account of good correlation between modulus and strength, which may bring harmful effect on pavement performance. Higher pavement strength means shorter cracking spacing and higher density cracks that will aggravate destruction effect of reflective cracking on

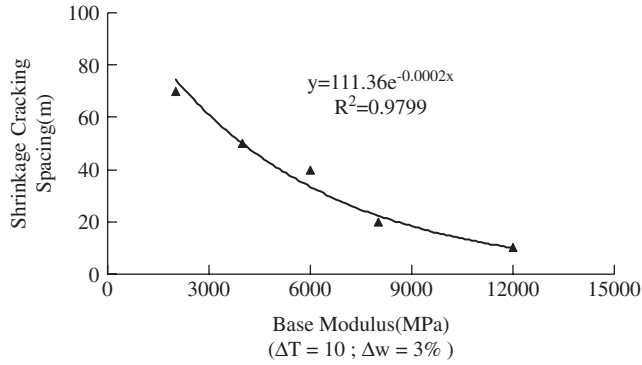


Figure 1. Influence of base modulus on cracking spacing.

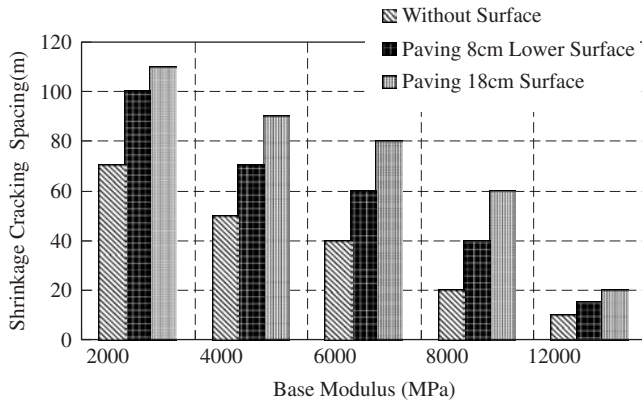


Figure 2. Comparison of cracking spacing in three different models.

pavement. However, for long-term durability, it typically requires higher content cement to coat and protect soil particles. Thus, the optimum cement content and mixture strength will be determined by combination of cracking analysis in this research and the results of durability tests in future.

After paving surface on no-cracking cement stabilized base at early stage, the moisture content in the pavement will lose further while dry shrinkage stress will be accumulated constantly. On account of surface protection, temperature condition in the base will be improved, which causes thermal shrinkage effect alleviating. According to in-situ project, the models of paving 8 cm lower surface and whole 18 cm asphalt surface just before winter were built to predict shrinkage cracking spacing respectively. Elastic modulus and average thermal shrinkage coefficient of asphalt surface were assumed to be 1800 MPa and $2 \times 10^{-5}/^{\circ}\text{C}$ respectively. According to the typical environment condition during construction period of cement stabilized base in Jiangsu Province of China ($\Delta w = 3\%$, $\Delta T = 10^{\circ}\text{C}$), the effect of paving asphalt surface on shrinkage cracking spacing is shown in Figure 2.

Even if paving thicker asphalt surface at early stage, which makes shrinkage cracking alleviating to some extent, using cement stabilized base with higher modulus still tends to have very smaller cracking spacing, particularly under severe dry and thermal shrinkage. It is found that the improvement of paving surface is limited from a large number of former research results. It is proved that adopting geosynthetics to deal with cracks can postpone the appearance and growth of reflective cracking, thus lengthening the service life of asphalt pavement. Thus, to improve pavement performance, it is proposed that shrinkage cracking should be dealt with by geosynthetics such as fiberglass polyester mat in time before paving surface.

Table 3. Fracture parameter C and n of HMA.

Type of HMA	Fracture parameter	
	C	n
Conventional asphalt, AC-20I	1.25×10^{-5}	3.519
SBS modified asphalt, AC-20I	8.64×10^{-6}	3.653
Cement stabilized macadam	3.0×10^{-4}	4

3 PREDICTION OF REFLECTIVE CRACKING GROWTH LIFE FOR CEMENT STABILIZED BASE ASPHALT PAVEMENT

3.1 Paris model

The improved Paris model to calculate growth life of anti-cracking is shown in Equation 3 (Paris 1963).

$$N = \int_0^{a_c} \frac{1}{da/dN} da = \int_{a_1}^{a_c} \frac{1}{C\Delta K^n} da \quad (3)$$

where N = the number of cyclic loading; a = crack length; a_1 = the initial length of crack; a_c = crack length corresponding fracture toughness; ΔK = the increase of K , $\text{MPa} \cdot \text{m}^{1/2}$; C and n = fracture parameter.

In in-situ projects, the stress situation is usually complicated. Especially near crack tips, it is in the compound deformation state mostly. The simple and biased safe criterion to judge instability fracture in project was applied, as Equation 4 showing.

$$K^* = K_I^2 + K_{II}^2 \geq K_{IC}^2 \quad (4)$$

where K_I = stress intensity factor of mode I, $\text{MPa} \cdot \text{m}^{1/2}$; K_{II} = stress intensity factor of mode II, $\text{MPa} \cdot \text{m}^{1/2}$; K^* = compound stress intensity factor, $\text{MPa} \cdot \text{m}^{1/2}$; K_{IC} = fracture toughness, $\text{MPa} \cdot \text{m}^{1/2}$.

In this paper, the initial stress intensity factor was assumed to $0.05 \text{ MPa} \cdot \text{m}^{1/2}$. The fracture toughness of HMA (hot mixture of asphalt) equaled to $0.50 \text{ MPa} \cdot \text{m}^{1/2}$. The initial length of cracking was chosen as 0.5 cm. The fracture parameter C and n of HMA from lab tests are shown in Table 3 (Xu & Wang 2005).

Otherwise, the effect of lower asphalt layer on reflective cracking growth life is far greater than any other layer. So only the difference of whether adopting modified asphalt or not in the over asphalt layer was taken into account.

3.2 FEM model

After completion of cement stabilized base, there are shrinkage cracking inevitably because of moisture loss and temperature difference. At surface the range of their change is generally greater than that at the bottom so that the base surface cracks will appear at first. When shrinkage cracking extends to certain depth, the bottom of thinner asphalt surface will crack. It extends up to the asphalt surface and down to the base bottom at the same time.

Cement stabilized base asphalt pavement was regarded as a four layer system of plane strain problem, in which the contact between layers was thought to be fully continuous. The basic structure parameter is shown in Table 4 and cracking growth models are showed in Figures 3–4. The width of cracks was chosen as 0.5 cm. The load density q and length $2r$ equaled to 0.7 MPa and 30 cm respectively. The singular element was used near the tip. The parametric element was used in the other part of FEM models.

Table 4. The basic structure parameter of pavement.

Layer	Thickness (cm)	Resilient modulus (MPa)	Poisson ratio
Asphalt surface	18	1800	0.30
Cement stabilized base	30	4000	0.15
Subbase	30	1000	0.20
Subgrade	–	60	0.35

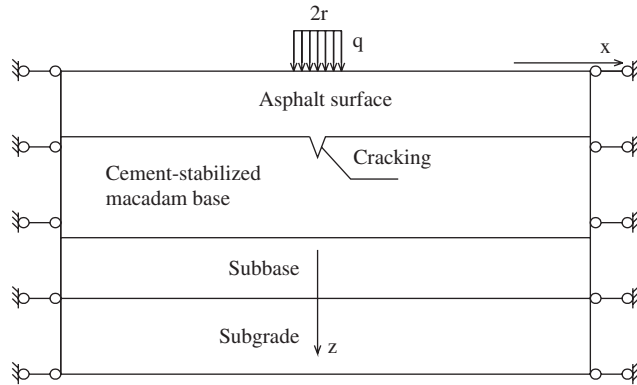


Figure 3. The cracking model for base shrinkage crack.

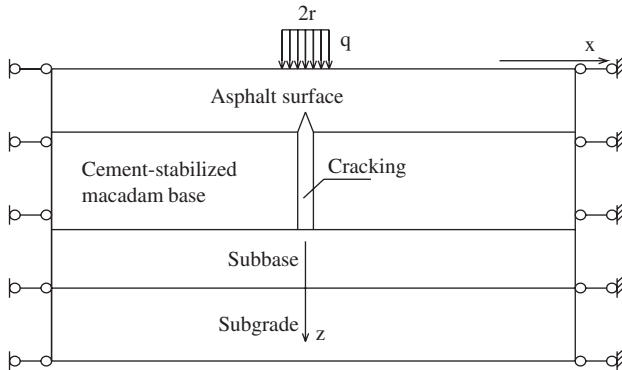


Figure 4. The cracking model for surface reflective crack.

3.3 Effect of base shrinkage cracking on stress at the bottom of asphalt surface

Under traffic loading stress variety at the bottom of asphalt surface during the course of shrinkage cracking growth in cement stabilized base is shown in Figure 5.

Along with base shrinkage cracking extending down, the horizontal stress at the bottom of surface will transfer from compressive stress to tensile stress. Generally, splitting strength used in lower surface is 0.6 ~ 1.0 Mpa. Thus, when shrinkage cracking extending down to 10–20 cm in the base, tensile stress at the bottom of surface will exceed tensile strength and surface will crack at that time, namely reflective cracking occurs. If traffic loading, temperature difference and dry shrinkage that have not completed being considered, it will extend to the top of surface quickly.

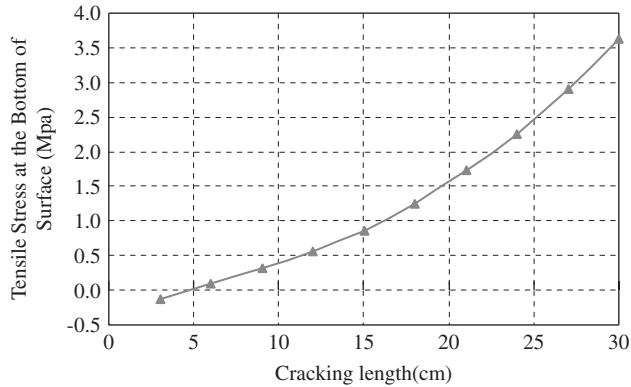


Figure 5. The horizontal stress distribution at the bottom of surface.

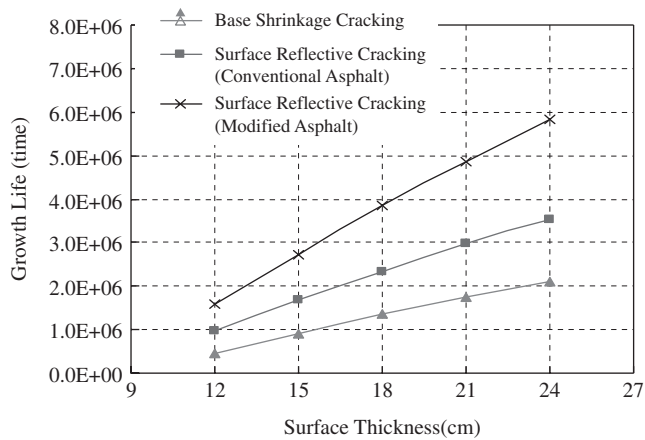


Figure 6. The effect of surface thickness on cracking extending.

3.4 Sensitivity analysis

In Table 4, only surface thickness was changed and other parameters were kept invariable, the effect of surface thickness on growth life in the extending course of base shrinkage cracking and surface reflective cracking is shown in Figure 6. It is found that using thick asphalt surface not only lengthens the growth path of reflective cracking, but also alleviates stress concentration, thus improves the pavement ability to anti- reflective cracking.

Also, only asphalt surface modulus was changed and other parameters were kept invariable, the effect of surface modulus on growth life in the extending course of base shrinkage cracking and surface reflective cracking is shown in Figure 7. The growth life of anti-cracking decreases with increase of HMA modulus, and they are in an approximate exponential correlation, remarkable especially for surface reflective cracking. The surface with higher modulus will bear more loading stress, thus aggravate deformation at cracking tip and cracking extending. In winter, on account of HMA stiffening under low temperature, it is obvious that reflective cracking will occur more easily.

Then, only base modulus was changed and other parameters were kept invariable, the effect of base modulus on growth life in the extending course of base shrinkage cracking and surface reflective cracking is shown in Figure 8. Using higher base will make growth life longer. They are in an approximate logarithmic correlation. Thus, a strong base condition could bear more traffic loading, improve stress concentration at cracking tip, and delay the extending speed.

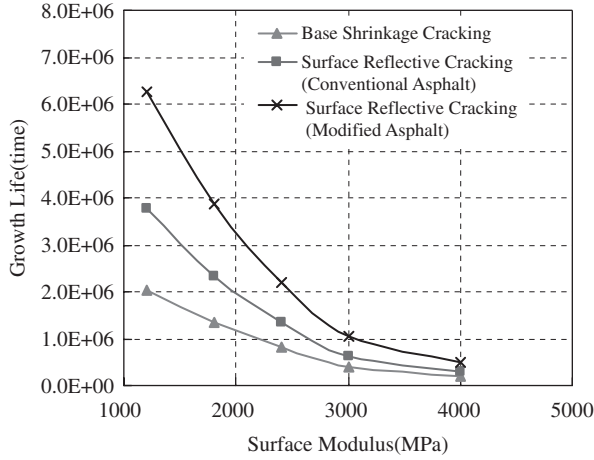


Figure 7. The effect of asphalt surface modulus on cracking extending.

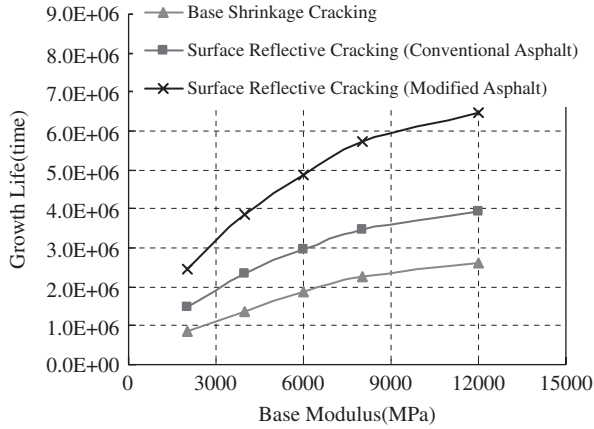


Figure 8. The effect of base modulus on cracking extending.

From the results above, it is found that the major design factors have important influence on the growth life of anti-cracking are surface modulus > surface thickness > base modulus in turn. The other factors have little effect on prediction precision and could be ignored.

4 REGRESSION EQUATIONS

The pavement models with different structure and material parameters were analyzed by orthogonal method. Then, the experiential prediction models of shrinkage cracking spacing and growth life of anti-cracking were founded by regression after parameter normalization.

The regression equation of shrinkage cracking spacing for cement stabilized macadam is showed in Equation 5.

$$\ln L = (a * \frac{\Delta T}{15} + b * \frac{\Delta w}{3} + c) * \frac{E}{12000} + d * \frac{\Delta T}{15} + e * \frac{\Delta w}{3} + f \quad (5)$$

where L = shrinkage cracking spacing, m; ΔT = temperature difference, °C; Δw = moisture loss, %; E = resilient modulus, MPa; a, b, c, d, e, f = regression coefficients, shown in Table 5.

Table 5. Regression coefficients of models.

Structure	Regression coefficients						Tests			
	<i>a</i>	<i>b</i>	<i>c</i>	<i>d</i>	<i>e</i>	<i>f</i>	<i>R</i> ²	<i>RMSE</i>	<i>Chi-Square</i>	<i>F</i>
Without surface	-1.09	2.88	-3.28	-1.72	-5.24	9.63	0.94	0.05	0.52	896
With 8 cm lower surface	-0.84	2.37	-2.92	-1.06	-4.82	9.35	0.95	0.05	0.44	963
With 18 cm surface	-0.51	2.08	-2.66	-0.50	-4.52	9.08	0.93	0.07	0.47	647

The growth life of anti-base shrinkage cracking N_b :

$$\ln N_b = 2.10 * \left(\frac{h_1}{24}\right) + 1.29 * \left(\frac{h_2}{40}\right) - 3.11 * \left(\frac{E_1}{4000}\right) + 1.41 * \left(\frac{E_2}{12000}\right) + 12.49 \quad (6)$$

$(R^2 = 0.84, RMSE = 0.09)$

The growth life of anti-surface reflective cracking N_a :

(1) Conventional asphalt for lower surface

$$\ln N_a = 1.93 * \left(\frac{h_1}{24}\right) - 3.50 * \left(\frac{E_1}{4000}\right) + 0.90 * \left(\frac{E_2}{12000}\right) + 14.47 \quad (7)$$

$(R^2 = 0.93, RMSE = 0.05)$

(2) Modified asphalt for lower surface

$$\ln N_a = 1.95 * \left(\frac{h_1}{24}\right) - 3.53 * \left(\frac{E_1}{4000}\right) + 0.89 * \left(\frac{E_2}{12000}\right) + 14.97 \quad (8)$$

$(R^2 = 0.94, RMSE = 0.05)$

where h_1 = surface thickness, cm; h_2 = base thickness, cm; E_1 = surface modulus, Mpa; h_2 = base modulus, Mpa.

5 DESIGN PROCEDURE

The design procedure to predicting reflective cracking growth life for cement stabilized base asphalt pavement includes three stages, showed in Figure 9.

6 CONCLUSIONS

The forming and extending course of reflective cracking for cement stabilized base asphalt pavement was analyzed systematically in this paper. Based on fracture mechanism, the prediction models of shrinkage cracking spacing and reflective cracking growth life which are the two primary indexes for reflective cracking introduced to the structure design procedure of cement stabilized base asphalt pavement finally were found respectively by using FEM. Moreover, the sensitivity analysis of pavement structure parameters and material parameters was carried on. It is found that using low modulus base is effective in increasing cracking space. Paving asphalt layer at early time has insignificant effect on reducing cracks. It is also suggested that it is more effective to adopt geosynthetics such as fiberglass polyester mat to deal with cracks before paving asphalt, and it will postpone the appearance and growth of reflective cracking, thus lengthening the service life of asphalt pavement. It is observed that cracks appearing at the surface of the base extending 10–20 cm downward will make the bottom of asphalt layer crack under traffic loading. The major

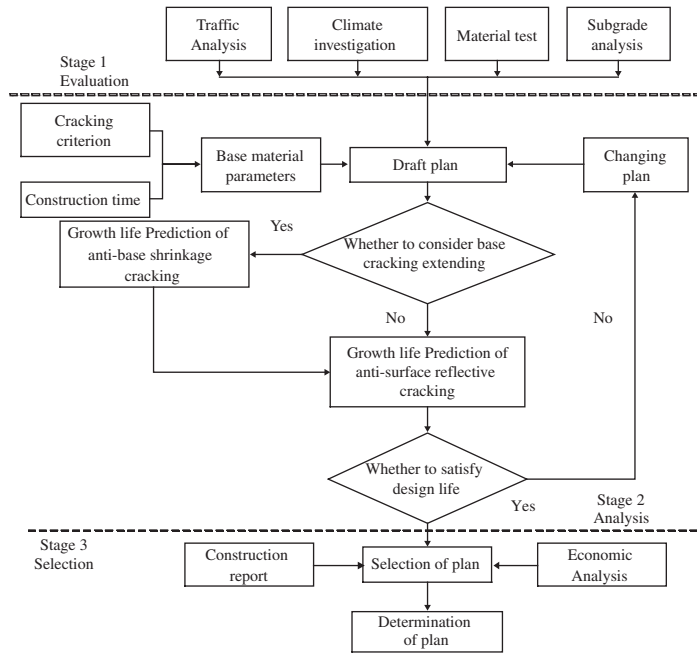


Figure 9. Design Procedure to predicting reflective cracking growth life for cement stabilized base asphalt pavement.

design factors have important influence on the growth life of anti-cracking are surface modulus > surface thickness > base modulus in turn.

REFERENCES

- Dowson, D. 2003. *History of Tribology*. London: Longman Ltd.
- Lytton, R.L. 1990. *An Integrated Model of the Climatic Effects on Pavements*. Austin: Texas Transportation Institute & Texas A & M University.
- Majdzadeh, K. & Ramsamooj, D.V. 1980. Laboratory Studies and design considerations. *Reflection cracking: analysis* 49: 286–313.
- Monismith, C.L. & Coetzee, N.F. 1982. Reflecting cracking: analyses, laboratory studie, and design considerations. *Proceedings of the Association of Asphalt Paving Technologist* 49: 268–313.
- Paris, P.C. & Erdogan, F.A. 1963. Critical analysis of crack propagation laws. *Journal of Basic Engineering* Trans. ASME Series D. 85(3): 528–553.
- Sun, T.B. & Cong, L. 2003. A study on drying shrinkage procedure of semi-rigid base coarse during construction. *Highway* 712(3): 111–115.
- Shi, W.M. & Jiang, Z.S. 2004. Research on the calculation method of temperature stress of cement treated crushed stone base and the method of controlling temperature shrinkage crack. *Journal of Highway and Transportation Research and Development* 21(4): 23–27.
- Wang, H.C. 2005. *Study on two-stage design of semi-rigid base asphalt pavement*. Nanjing: Southeast university.
- Wu, G.C. & Zhang, G.S. 1996. Thermal stress intensity factor analysis for asphalt concrete pavement. *China Journal of Highway and Transport* 9(1): 37–44.
- Xu, H. 2005. *Research on performance and design method of porous asphalt mixture*. Nanjing: Southeast university.

Cracking survey on freeways using asphalt pavement with semi-rigid base in Jiangsu

J. Yang & H. Lu

Southeast University, Nanjing, Jiangsu, China

Y. Yang

Jiangsu Province Freeway Construction Headquarters, Nanjing, Jiangsu, China.

ABSTRACT: In order to identify the situation and causes of crack occurrence in the asphalt pavement with stabilized base constructed in the province of Jiangsu, east of China, a comprehensive survey has been conducted on the five main freeways with different traffic opening time and a wide range of location. On the basis of the gathered information about the pavement structure, geological & climatic condition, construction season, construction technique, proactive crack mitigating countermeasure, latter maintenance strategy and traffic volume, the data on crack type and crack development pattern over time have been recorded in a detailed manner stretching as long as 3–7 years. The influences, base material, traffic volume, and the geo-textile material placed under the pavement may have on the crack occurrence have also been discussed, while it is found that the transverse crack occupies the overwhelming majority of the entire crack occurrence, which exhibits an obvious attribute, that in the initial 3–4 years after opening to traffic, the crack increases at quite a limited rate, however after this stage, the crack will experience a soaring period until a relatively stable stage reappears. Also, it is concluded that the pavement near the structures such as tunnel, bridge and culvert has a much larger crack potential. The summary of the survey results will hopefully join force to provide data and informative reference to the cracking research society, while also some useful clues can be drawn from it in terms of construction technique innovation and improvement.

1 INTRODUCTION

In China, cement stabilized aggregates (CSA) and limestone & fly-ash stabilized aggregates (LFSA), often referred to as semi-rigid base, have been widely used as the material in the base since the start of expressway network program in the early 1990's. Of the current 50,000-kilometer long expressway network, more than 90% of them have been constructed with the semi-rigid base, if the portion used in the total 1,900,000-kilometer long road network is considered, this kind of pavement structure and its material have all the reasons to be paid attention to. As we all know, this kind of base material is often given the credit for its competence of accommodating heavy traffic as well as lower cost as opposed to other materials. However, one problem still exists, more and more complaints have been made by the road community for the susceptibility of the material, when subjected to temperature and moisture variations, which play a crucial role in the process of crack initiation in this layer. With the further traffic load applied, the crack will finally propagate from all through the pavement layer to the surface and that is how a reflection crack is always defined (*Rigo, 1993*). As a prerequisite program of a research project on the reflection crack potential of the asphalt pavement using stabilized base in Jiangsu, an east coastal province in China, an investigation stretching several years' time has been initiated covering five expressway sections, which can

Table 1. Facts of the expressway sections targeted.

Expressway name		NJ airport expressway	LX expressway	FG(lyg) expressway	SX expressway	YJ expressway
Asphalt Pavement	Surface	4.5 cm*	4.0 cm	4.0 cm,	4.0 cm	4.0 cm
		AC-16A**	SMA-13	SMA-13	SMA-13	SMA-13
	Middle	6.0 cm	6.0 cm	6.0 cm	6.0 cm	6.0 cm
Base	Bottom	AC-25I	Sup-20	Sup-20	Sup-20	AC-20I
		6.0 cm	7.0 cm	7.0 cm	8.0 cm	8.0 cm
	AC-25II	Sup25	Sup25	Sup25	AC-25I	
Service since	Upper	17.0 cm	19.0 cm	19.0 cm	19.0 cm	19.0 cm
		LFSA	CSA***	CSA	CSA	CSA
	Bottom	17.0 cm	19.0 cm	19.0 cm	19.0 cm	19.0 cm
Lowest temperature (°)		LFSA	CSA	CSA	CSA	CSA
Construction Sequence		1997	2001	2002	2003	2004
Base crack countermeasure ****		-2~-4	-5~-7	-5~-7	-5~-7	-2~0
		Base + winter + pavement	Base + winter + geogrid + pavement	Base + winter + pavement	Base + winter + pavement	Base + bottom asphalt layer + winter + the rest
Pavement crack countermeasure		seal with HMA	Geogrid covering	Geogrid covering	Geogrid covering	Geogrid covering
		Fill (emulsified asphalt)	Cutting and fill***** (crack glue)	Cutting and fill (emulsified asphalt & asphalt mortar)	Cutting and fill (DEERY- MC180)*****	Fill (emulsified asphalt)

* Thickness of the surface layer of asphalt pavement;

**The constituent of AC-16A, AC-25I, AC-25II, SMA-13, Sup-20, and Sup25 is referred to (Yang et al., 2006);

*** 5% Portland cement is added, so are other CSA listed in the above table;

**** means the crack initiated in the base layer before the asphalt layer is laid down and its countermeasure during the construction process;

*****Before the sealant material is filled, the existing cracking will be cut into some specified profile in order to achieve a better durability and function;

*****A proprietary product whose constituent is not revealed.

serve to represent the main geographical and climatic coverage in Jiangsu. The main focus of the investigation is the developing trend of the cracking number and their length distribution during the developing process.

2 BASIC FACTS OF THE EXPRESSWAY SECTIONS TARGETED

In the following Table 1, the basic facts of the expressway sections investigated are listed, including pavement structure arrangement, base material, construction year and sequence, weather condition and etc.

3 DETAILED SURVEY RESULTS OF EACH SECTION

3.1 NJ airport expressway

This road section was open to traffic in 1997 and the total length the field investigation covered is 28 kilometer; how the crack has developed over years (1998–2004) is shown in the following Table 2. Due to the fact that, blocking crack, fatigue crack and edge crack have been rarely found

Table 2. Crack development over years in NJ airport expressway (1998–2004)*.

Year	1998	1999	2000	2001	2002	2003	2004
Crack number	0	29	539	157	2014	1817	1463

*The crack number listed in Table 2 includes both the new emerging ones and the re-crack after the crack handling carried out, and the minor crack that not observed by naked eye is not recorded. Since 2000, a cracking filling job has been carried out on a yearly basis. Due to the fact of the similar crack handling strategy, material and relatively similar crack fill & seal frequency of each year; the data available is qualified enough to serve to provide a picture of the crack developing trend and pavement deteriorating rate.

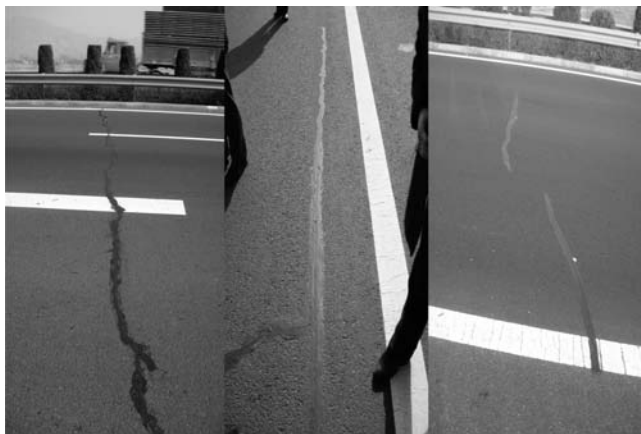


Figure 1. The in-situ longitudinal and transverse crack.

in this road section before 2004 (*Miller & Bellinger, 2003*). Nearly all the cracks taken into count are transverse crack and longitudinal crack. The photos taken from the site are shown in Figure 1.

From Table 2, it is found that in the initial two years after the road is opening to traffic, there are quite limited number of cracks being found from the asphalt pavement surface; since 2000, the crack number has experienced a moderate increase, which leads to a decision of regular cracking filling job on a yearly basis since then. In the year of 2002, which is 5 years after opening to the traffic, the crack number began to be subjected to a rapid increase. Since then, the crack has shift itself back to a “stable” stage, with the crack sealing and filling practice, the crack found was even decreasing, which in fact in some way proves the result of battle between the possibility of new emerging crack and the sustainability and effectiveness of the sealant material.

Since 2004, especially after 2005, the crack number has been recorded in a more detailed and frequent manner, which has listed the crack number in both northbound and southbound direction, as well as the crack type being identified. The following Table 3 lists crack development over years from 2004 to 2006 covering all the section.

During the time covered in Table 3, the fill and seal job has been carried out twice, as marked in the table, it shows clearly that most of the cracks are transverse crack and most of the cracks have developed themselves in the cold season, when the pavement material is subjected to the severe shrinkage induced by the low temperature. In the summer season the crack seldom develops. Also a considerable difference has been found between crack appeared in the northbound and southbound, especially the transverse crack, which will mainly be attributed to the difference of the traffic volume and load spectra in the two directions. The results have also been verified by many other researches and field surveys.

Table 3. Crack number over years in NJ airport expressway (2004–2006).

Survey date		04.2004**	09.2005	12.2005	03.2006**	06.2006	09.2006
Transverse crack	Northbound*	509	284	408	431	15	23
	Southbound*	550	334	531	566	78	89
Longitudinal crack	Northbound	29	25	83	86	3	14
	Southbound	54	46	70	71	7	11

*The northbound is the direction from the airport to the downtown.

The southbound is the direction from the downtown to the airport.

It should be noted that the data in Table 2 for the cracking number of 2004 is recorded in July of that year.

** After which, a fill and seal job has been carried out, before the new round survey. Winter season where the expressway section locates is usually from December to March with the lowest temperature around $-4\sim-2^{\circ}\text{C}$. And the summer season is usually from May to September with the highest temperature around $35\sim38^{\circ}\text{C}$.

Table 4. Number of cracks in different length in LX expressway in 2005 and 2006.

Cracking number		$x > 20\text{ m}$	$20\text{ m} > x > 15\text{ m}$	$15\text{ m} > x > 10\text{ m}$	$10\text{ m} > x > 5\text{ m}$	$5\text{ m} > x > 3\text{ m}$	$3\text{ m} > x$
2005	Eastbound	24	13	77	160	152	55
		5.0%	2.7%	16.0%	33.3%	31.6%	11.4%
	Westbound	20	9	10	84	87	28
		8.4%	3.8%	4.2%	35.2%	36.6%	11.8%
2006	Eastbound	8	11	92	196	159	147
	Westbound	9	3	77	181	220	215

3.2 LX expressway

The section targeted is 236 km and it was open to traffic in 2002. The current annual average daily traffic (AADT) is 12,000. In the first two years after it was open to traffic, quite limited crack was detected, which was mainly developed in the vicinity of the structures (bridges, culvert and etc). Since 2004, the pace of crack occurrence began to increase. Since 2005, two rounds of full range crack investigation have been initiated. By the year of 2005, the crack in length was 7612 meter and the total length in 2006 was 17,518 meter. What is unique about the survey in this section is that the number of cracks in different length is recorded in a detailed manner. The following Table 4 and Figure 2 show the crack in different length detected in 2005 and 2006.

In this expressway section, the fill & seal job was only carried out occasionally before 2005, which can nearly be neglected for the purpose of the cause query of cracking development. Therefore, it is appropriate enough to think in this way that the data of 2005 listed in Table 4 can be used to describe the crack severity of the pavement open to traffic for 3 years influenced only by the structure deterioration, traffic load and weather action. While to the data of 2006, due to a full range fill and seal job, some information was covered especially at a time when the data after 2006 is not available. So the following discussion will mainly be based on the data achieved from the survey carried out in 2005.

It is found from Table 4 and Figure 2 that for the cracks in all length notified in the data, the crack number in the eastbound lane is much larger than that of the westbound lane, which can be explained by the different load magnitude of the traffic in two directions. Because this expressway is a key channel for the shipping of the coal to port lied in the east end of the expressway and there are much more heavy trucks traveling to the eastbound direction. Also it is found that after open to traffic for three years, the length of the cracking found in the pavement surface covers quite a range, still a distribution pattern has been revealed. During the survey, it is found that an overwhelming majority of the cracks in a length more than 15 meter appear to be longitudinal cracks, as a matter

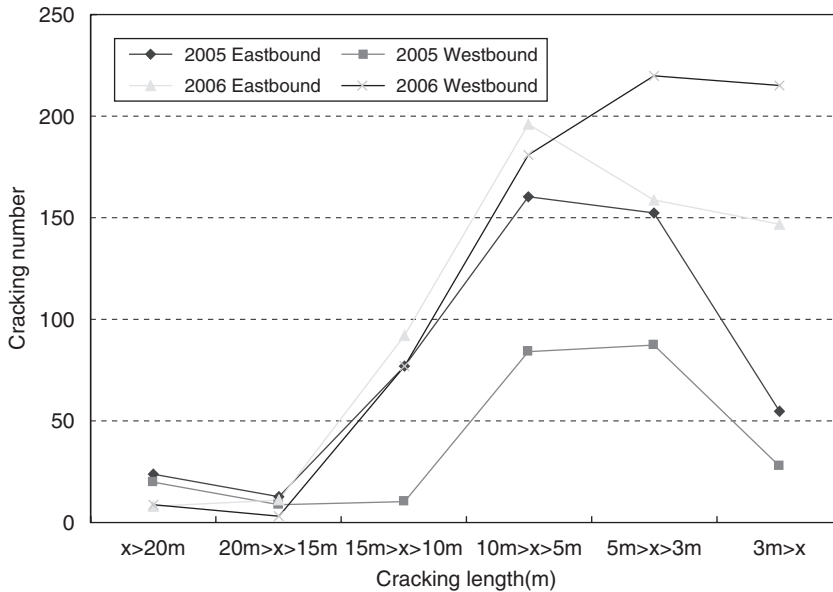


Figure 2. Cracks in LX expressway in 2005 and 2006.

of fact, this number is quite small, while most of cracks in a length below that value turn out to be transverse crack; furthermore, from the data listed in Table 4, it is found that cracks with a length falling into the range of 5–10 m and 3–5 m occupy nearly two thirds of the total cracks, while both of them take a roughly 30% and the cracks in a length below 3 meter occupies a roughly 10% of the total cracks.

3.3 FG (lyg) expressway

The section targeted is 85 km and it was open to traffic in 2002, with a larger traffic volume in the southbound lane as opposed to the northbound lane, the AADT is 8000. The base of this section was constructed at the end of 2001 and experienced a winter before the pavement was laid; during this period of time, crack with a spacing around 20 m has occurred in the base layer. The crack was 1 mm~3 mm in width. Before the pavement layer has been laid, the crack in the base layer has been dealt with the fill of emulsified asphalt, and then a layer of glass-fiber grid, with a width spanning 1.5 m over the crack, was installed right on the underseal layer wherever a crack existed underlying. However, some problems were found right after the construction that the bond between the grid and underseal was too poor to fulfill its function that expected. As a result, some changes were made during the construction that the grid was installed after the bottom layer of pavement had been in place, with the exact installing position point marked beforehand. In March, 2003, a full coverage investigation along the routine was carried out for the first time, and the data of the same scale and pattern in 2004, 2005 and 2006 are also available, shown in the following Table 5.

From Table 5, it is found that, nearly no crack was developed in the first year after its opening to traffic, among which the crack induced near the structures such as bridge, tunnel, and culvert occupies a great majority of them. Still, the pavement kept its stable state in terms of the crack developing in the second year after opening to traffic. In 2006, the number of the crack has encountered a rapid increase; the increasing pace was as large as tenfold compared with that of the first two years. And also a conclusion can be drawn that the crack developed near the structures contributed considerably to the total crack number, though the percentage it has taken exhibit a tendency to drop over the pavement service life. The cause of this kind of crack should be attributed

Table 5. The crack situation in FG (lyg) expressway (2003–2006).

Crack number		2003	2004	2005	2006
Northbound	Total	10	37(27)*	57(20)	341(284)
	Crack near structure **	7	20	35	83
Southbound	Total	9	61(52)	80(19)	354(274)
	Crack near structure	6	36	46	70

* The number in the parentheses denotes the newly emerging crack.

** denotes the crack developed within the range of 10 meters from structures such as bridge, tunnel culvert and etc.

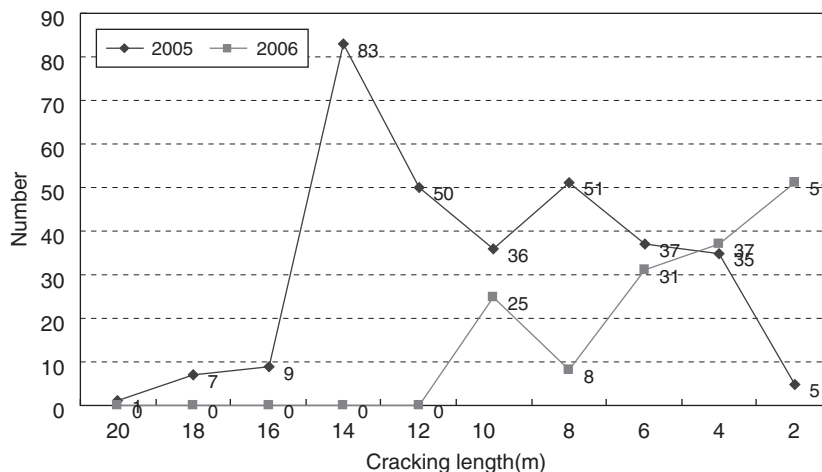


Figure 3. The number of the crack in different length.

to a great reliability of the differential settlement of the sub-grade caused by the structure, therefore, an improved construction technique and design procedure will be highly applauded to combat the crack in the pavement.

3.4 SX expressway

This section targeted is 95 km and it is opening to traffic in September 2003, with an AADT of 1550 in 2006. The construction sequence is the same as that of the aforementioned 3 sections that the base layer had experienced a winter before the pavement was laid. What is unique for this section to be targeted is its recognized well sub-grade support.

After opening to traffic, two full range crack investigations have been initiated in December, 2005 and December, 2006 separately. In 2005, the total length of the crack was 2889.75 m and thereafter a crack fill and seal job was put in place to address the entire crack found, and in 2006 the investigation was carried out at nearly the same period of the last year. In 2006, the total length of the crack found is 543.7 m. In the following Figure 3, the number of the crack in different length is listed.

From Figure 3, it is found that in 2005, the length of the individual crack has covered quite a range, from as large as 20 meter to several centimeters. The majority of the crack falls in the range of 4–14 meters, while that above and below that range are relatively small. However, with regard to the investigation data of 2006, most of the cracks found are below 6 meter in length, and only 14 of them are due to the failure of the fill & seal material and 27 of them due to the propagation

Table 6. The cracks number of YJ expressway in 2004 and 2006.

Location		Crack near structures	Crack over poor sub-grade	Regular crack
Number	2004	56	5	43
	2006	163	5	188
Percent (%)	2004	53.8	4.8	41.4
	2006	45.8	1.4	52.8

of the old crack, which means over 90% of the fill & seal has survived the one year traffic and climatic influence. Something else unique about the pavement was its crack filling material and the installation technique, that the installation of the fill material is divided into two phases. However, till now there is no related research carried out to verify its effectiveness to the crack retarding. Another situation worth paying attention to is the relatively lower AADT compared with other sections mentioned above, such as LX expressway with its AADT of 12,000, in which the one-year surviving rate of the crack filling material is quite small, as it is discussed above.

3.5 YJ expressway

This section targeted was 120 km and it was open to traffic in 2004, with the AADT of 2006 as large as 70,000. What is unique about this section compared with others is that the base has not experienced a winter before the bottom layer is laid down. Right at the end of that year when the road was open to traffic, 104 cracks were found with a total length as large as 1194 meter. In order to distinguish the power of different factors that may lead to cracks, the crack developed was mainly classified into 3 categories based on its location, that is, cracks near the structures (culvert, bridge and special channel etc), cracks in the section with poor sub-grade and other regular cracks. The following Table 6 shows the investigation results following this categorization carried out in 2004 and 2006.

From Table 6, it can be concluded that in the first year, the crack has developed in a much larger number compared with other sections discussed above. Two possible causes may be tracked for its unsatisfied performance early in the first year opened to traffic, the huge traffic volume compared with other sections covered in this survey, and its special construction consequence that prevent the base layer from experiencing a winter season to allow for pre-cracking of the base layer, which could reduce the tensile stress in the asphalt pavement layer dramatically and deter the crack propagation process to a great degree. From the data listed above, it is also found that both the regular crack and crack near the structures occupy a similar percentage of the total cracks, while the number of crack over poor sub-grade is quite small. In 2006, both the regular crack and crack above the structures have experienced a leap increase.

4 CONCLUSIONS

From the survey several conclusions and suggestions can be summarized as follows:

With proper construction, the typical pavement structures with semi-rigid base used in Jiangsu can sustain 3–4 year with only quite few or no cracks found.

An overwhelming majority of the cracks that appear are transverse cracks, most of which are propagated from the base cause. Most of the longitudinal cracks found are due to the poor sub-grade or embankment. Meanwhile, a large number of cracks have developed themselves over or near the structures.

Most of the cracks begin to appear in the pavement surface in winter season, except for the knowledge that the material is more likely to shrink subjected to lower temperature, its potential implication to the cracks propagating process associated with stiffer pavement layer and special

moisture situation under low temperature is also worth further study by means of some controlled tests or theoretical analysis.

Aside from its inherent defect in abrasion stability and durability, LFSA is a qualified base material with regard to its function to be free of crack.

The installation of geo-textile grid is quite effective when dealing with the cracks propagation. However, the suitable construction technique should be in place to secure a desired bond between the grid and the base layer. However, the length of the grid covering the cracks should be determined in a more sophisticated way.

In order to lower the likelihood of reflection cracks, it is necessary and helpful to leave the base layer exposed to a cycle of winter season before the pavement layer is laid.

REFERENCES

- Miller John, S. & Bellinger William, Y. 2003. 6. *Distress Identification Manual for LTTP Report FHWA-RD-03-031*, Federal Highway Administration (FHWA), McLean, Virginia.
- Rigo, J.M. General introduction, main conclusions of the 1989 conference on reflection crack in pavements, and future prospects. *Proceedings of the 2nd international RILEM conference on Reflection Crack in Pavements*, Liege University, Belgium, Edited by Rigo, J. M., et al., 1993, pp. 1–20.
- Yang, M.Y. & Feng, D.C. etc. 2006. *Specifications for Design of Highway Asphalt Pavement JTG D50-2006*, Department of transportation, PR of China, Beijing, China.

Asphalt sand stress absorbing interlayer used in asphalt pavement with semi-rigid base

J. Yang, P. Dai & B. Yu

Southeast University, Nanjing, Jiangsu, China

Y. Yang

Jiangsu Province Freeway Construction Headquarters, Nanjing, Jiangsu, China

ABSTRACT: Due to its high strength and stability, semi-rigid material is widely used as base course of asphalt pavement on expressways in China. However, because of the high shrinkage potential and poor fatigue resistance, the reflection cracking is prone to occur in asphalt pavement with semi-rigid base. In the paper, both mechanics analysis and indoor test were applied to evaluate the effect of the asphalt sand stress absorbing interlayer (ASSAI). Firstly, through three dimensional FEM methods, the technical requirements of ASSAI which meet with the demand of cracking resistance were put forward. According to the analysis results, the anti-fatigue property is ideal when the structural thickness of this layer is between 2cm and 3cm. It is suitable when the modulus of ASSAI materials is between 400MPa and 800MPa. The improved Superpave method was used to design the asphalt sand stress absorbing interlayer, which used rubber asphalt as binder material. Meanwhile, the relative performance of ASSAI mixture, such as cracking resistance, rutting resistance, water susceptibility and permeability, were evaluated in the research. It is proved that ASSAI made with rubber asphalt could meet the demands of these performances according to the design standard.

1 BACKGROUND

At present, there are many ways to prevent reflection cracking occurring in asphalt pavement with semi-rigid base. The concept to reduce reflection crack in semi-rigid base asphalt pavement mainly includes that, (1) using better material of asphalt mat and base; (2) increasing the thickness of surface layer to restrain crack from base course; (3) optimizing pavement structure to solve this problem (Lu 2004). For instance, sand stress absorbing interlayer (SSAI) which has lower modulus of elasticity and higher ductility is applied to slow up the development of reflection crack. The existing experience has proved that the application of ASSAI could mitigate reflection cracks effectively.

Asphalt sand stress absorbing interlayer, which is paved between asphalt course and base course, is a fine graded hot-mix asphalt layer. In order to achieve the aim of decreasing the initiation and propagation of cracking, the aggregate with the size of not exceed 9.5 mm is mixed with modified asphalt to pave ASSAI, and higher amount of bituminous binder is used in this material. As a result of the higher amount of binder and fines, the ASSAI mixture has excellent waterproof performance and fatigue resistance. The elasticity modulus of ASSAI is low. For the higher deformability, it can absorb stress to sustain high strain in pavement structure without breaking and prevent strain from transferring to surface layer. Alleviating the stress concentration of cracking tip on consideration of the structure, ASSAI can prolong the time that cracks reflect from base course to surface layer. Therefore, ASSAI has a notable effect of anti cracking.

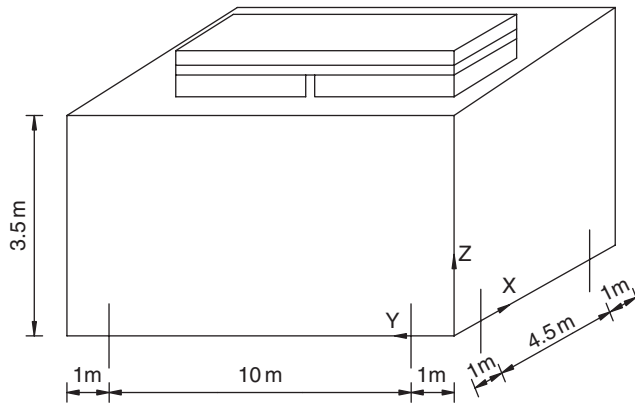


Figure 1. Analysis model using finite element.

Table 1. Parameters of road structure material.

Parameters	Asphalt mat	Base course	Subgrade
Thickness h (cm)	18	40	350
Young modulus E (MPa)	1800	1500	40
Poisson ratio μ	0.25	0.25	0.35

2 MECHANISM ANALYSIS

2.1 Construction of mechanical model

In order to analyze the mechanism of stress absorbing effect of ASSAI, pavement structure on semi-rigid base was taken as linear elastic system of four layers (Wu 2006), including surface layer, interlayer, base course and subgrade. The four layers were assumed as uniform, homogenous and continuous in contact. Surface and base layer are assumed to be 10 m in length while subgrade is to be 12 m. With the two end of the model fixed during calculation, the interlayer is located between semi-rigid base and asphalt surface, considering 1cm crack cutting through the base. The model is shown as Figure 1.

Size of layers and parameters of material are exhibited as Table 1.

2.2 Assumption of load

A BZZ-100 standard load is exerted in the modeling with axle load of 100 kN and tyre pressure of 0.7 MPa while the contact area between tyre and surface is characterized, for simplification, as rectangle of 22.75 cm in length and 15.65 cm in width (Figure 2). According to the study available (Fu 1999), deviating load is the main cause of reflection cracking. Therefore in the analysis, the deviating load is focused while the condition that the load evenly distributes above the crack is ignored. Figure 3 shows the worst load position.

2.3 Analysis of pavement structure

Analyzing by ABAQUS, we select different elasticity modulus and thickness for the interlayer. Accordingly to the output, the optional elastic modulus and thickness for the interlayer are finally identified on control of appropriate indices.

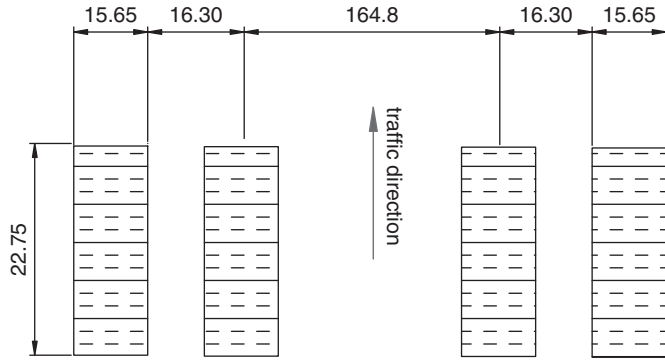


Figure 2. Sketch map of transversal wheel load (Unit: cm).

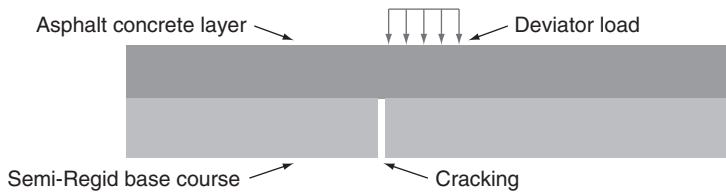


Figure 3. Deviator load at the worst position.

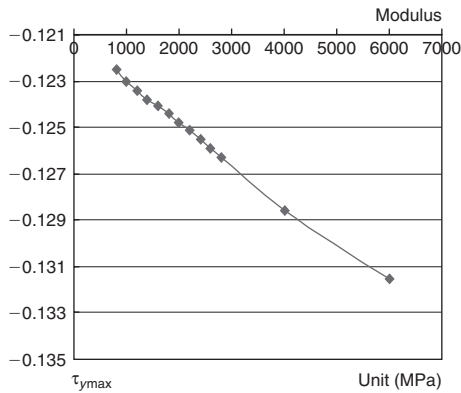


Figure 4. Relation between $\tau_{yz \max}$ and modulus.

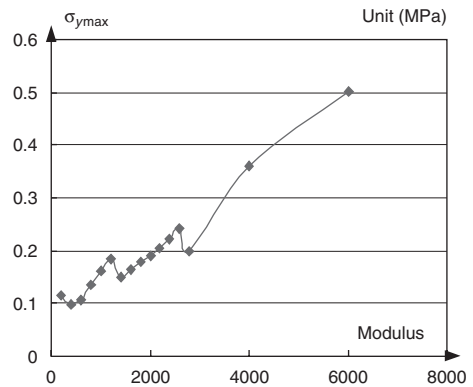


Figure 5. Relation between $\sigma_{y \max}$ and modulus.

2.3.1 Optimal modulus for ASSAI

The results of the calculation is shown in Figure(4–7) with the control indices of maximum tension stress $\sigma_{y \max}$ in the bottom of surface layer and maximum shear stress $\tau_{yz \max}$, maximum nominal stress $\sigma_{1 \max}$ of surface layer, as well as maximum pavement deflection l .

Effective method should be adopted to decrease $\sigma_{y \max}$ and $\tau_{yz \max}$ in order to alleviate the reflection crack caused by loading effect. If the thickness is confined to 2 cm, the interlayer will work best when its modulus is between 400~800 MPa. Meanwhile, $\tau_{yz \max}$ and $\sigma_{1 \max}$ are also at a low level.

2.3.2 Optimal thickness for ASSAI

Based on the conclusion above, optimal modulus for ASSAI is between 400~800 MPa in condition that of the thickness is confined to 2 cm. In the other aspect, it is necessary to determine the optimal

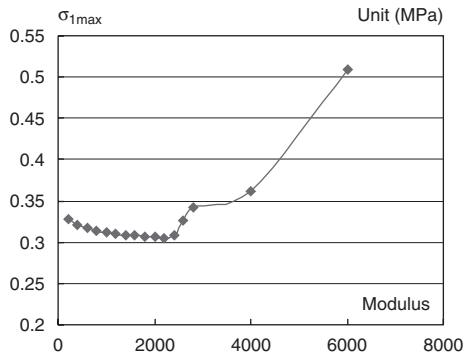


Figure 6. Relation between $\sigma_{1\max}$ and modulus.

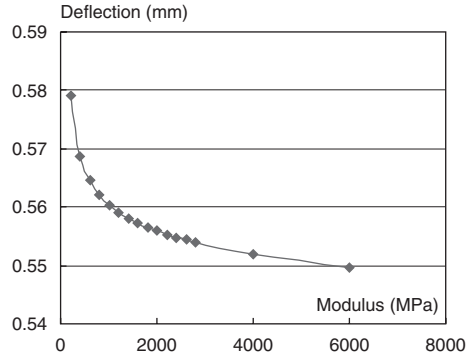


Figure 7. Relation between l and modulus.

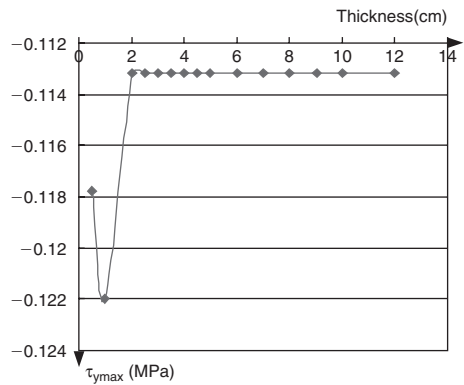


Figure 8. Relation between $\tau_{yz\max}$ and thickness.

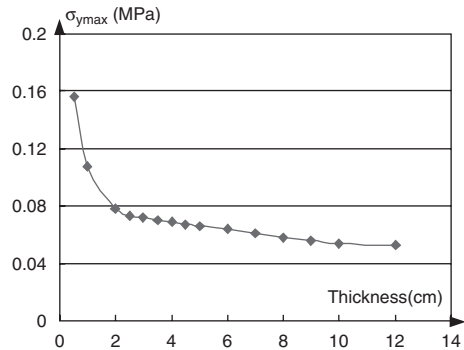


Figure 9. Relation between $\sigma_{y\max}$ and thickness.

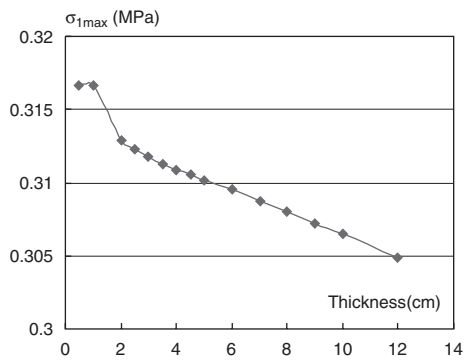


Figure 10. Relation between $\sigma_{1\max}$ and thickness.

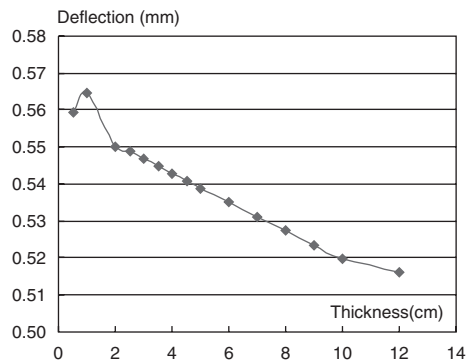


Figure 11. Relation between l and thickness.

thickness for ASSAI when modulus is kept constant, such as 400 MPa, 600 MPa and 800 MPa. The analysis results of SSAI with the modulus 600 MPa are shown in Figures (8–11); and the similar tendency can be drawn while the modulus of ASSAI is 400 and 800 MPa.

From the curve chart under fixed parameters of pavement structure, it is evident that optimal thickness for ASSAI is 2~3 cm while no much decrease of $\sigma_{y\max}$ is observed with the increase of the thickness. Also it is obvious that there will be little influence on $\sigma_{y\max}$, $\sigma_{1\max}$ and l with the

Table 2. Rubber asphalt testing results and specifications.

Testing items	Units	Testing results	Technical requirements	Testing method
Penetration (100 g, 5 s, 25°C)	0.1 mm	67	60–80	T0604-2000
Softening point (Ring and Ball)	°C	62	≥ 60	T0606-2000
Ductility (15°C, 5 cm/min)	cm	31	≥ 30	T0605-1993
Elastic recovery (25°C)	%	70%	≥ 65	T0662-2000
Relative density (25°C)	—	1.023	—	T0603-1993

Table 3. Technical requirements of aggregate quality and testing results in SSAI.

Testing items	Testing results	Technical requirements
Aggregate crushing value (%)	22.9	≤ 24
Los Angeles abrasion value (%)	26.4	≤ 28
Water absorption (%)	0.6	≤ 2.0
Adhesion	4	≥ 4
Soundness (%)	3.6	≤ 12
Flat-elongated particles (%)	5.6	≤ 15

increase of ASSAI thickness. To sum up, 2~3 cm for the thickness of asphalt sand stress absorbing interlayer is recommended.

3 RESEARCH ON ASSAI

3.1 Materials choice

The nature of asphalt may affect the property of the ASSAI to a great extent, such as fatigue cracking resistance and so on. Asphalt should be chosen according to the specific function property of the ASSAI. The ASSAI mixture should have better deformability and fatigue resistance. Therefore, some performance indexes of asphalt are strictly required, such as ductility and elastic recovery, etc (Yang 2005). In the paper, rubber asphalt, which is applied more and more widely in the world, is taken into the study of ASSAI. The performance results of rubber asphalt are as below (Table 2).

The types of aggregate may have great effect on deformability resistance of mixture while it has little effect on fatigue cracking and thermal cracking [Li 2005]. SSAI is mainly used to serve the role of alleviating reflection cracking and waterproof, so the nominal maximum size of aggregates which are mainly machine-made sand should be specified to a limited size, which is usually 4.75 mm. Mine powder adopts limestone powder and the content of mine powder should not exceed 1.2 times than the effective asphalt binder content [Li 2005].

3.2 ASSAI mixture design

The typical characteristics of ASSAI mixture could be summarized as: fine grading, high filler content, high asphalt content, low air void, high VFA and aggregates scattering into the asphalt mastic formed by asphalt and fillers, which enable this interlayer adhering well to the upper layer and base course. Therefore, the ASSAI mixture is different from normal HMA on materials formation

Table 4. The parameter of improved superpave design method for ASSAI.

Testing parameter	Superpave design method	Improved superpave design method
Sample size		
Diameter (mm)	150	100
Height (mm)	95/115/135	63.5
Volume of air voids (%)	4.0	0.5–2.0
Voids in mineral aggregate (%)	≥ 16	≥ 20
Voids filled with asphalt (%)	65–80	85–98
Filler-bitumen Ratio	0.6–1.2	0.5–1.6
Indirect tensile strength (MPa) (15°C)	–	≥ 0.6
Dynamic stability (times/mm) (40°C)	–	≥ 800
Freezing-thawing splitting residual strength ratio (%)	≥ 80	≥ 80

Table 5. The recommended gradation range of SSAI.

	The aggregates passing percentage (square sieve, mm) (%)							
Sieve	9.5	4.75	2.36	1.18	0.6	0.3	0.15	0.075
Upper Limit	100	100	85	70	55	35	20	14
Lower Limit	100	80	60	40	25	15	8	6

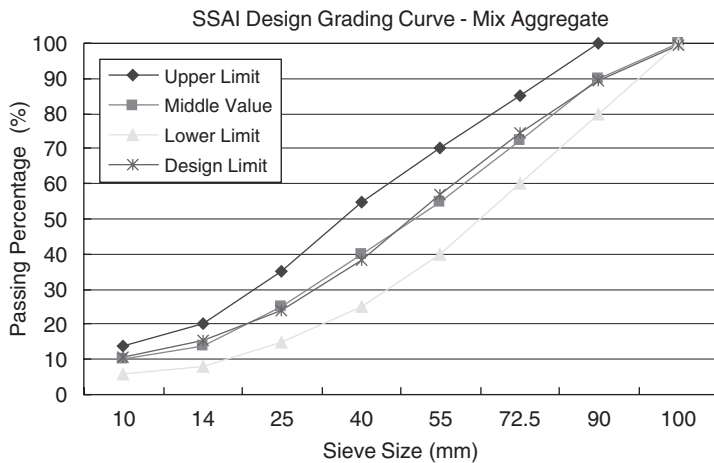


Figure 12. Design grading curve of ASSAI in the study.

and distribution characteristic of mineral grains. Traditional Marshall design method can not reflect the deformation characteristic and fatigue resistance of ASSAI mixture. In the study, Superpave design method that takes the volumetric parameters as its designing standard is improved to design mix ratio of ASSAI mixture. Design parameters are listed in Table 4.

For the specific function and characteristic of ASSAI which is different from normal HMA, the fine aggregates account for high proportion in the ASSAI mixture, and the choice of gradation range should accord with some criterions (Shi 2006). According to the study of sand stress absorbing inter-layer in other countries (Ye 2006), recommended gradation range (Table 5) was selected to ensure the optimum gradation of ASSAI. Figure 12 lists the design grading curve of ASSAI in the study.

As a result of the specific function of SSAI, the asphalt is applied at a high content. According to the practical experience, asphalt binder content should be selected between 7.5%~10.0%. In the

Table 6. Volumetric characteristic of asphalt mixture at different asphalt binder content.

Technical index	Testing results under different asphalt content (%)				
	8.0	8.5	9.0	9.5	10.0
Volume of air voids (%)	1.86	0.92	0.62	0.54	0.55
Voids in mineral aggregate (%)	20.89	21.15	21.90	22.82	23.80
Voids filled with asphalt (%)	91.12	95.63	97.16	97.63	97.71
Filler-bitumen ratio	1.38	1.30	1.23	1.16	1.10

design of ASSAI mixture, 9.0% is chosen as initial asphalt binder content. Volumetric parameters of SGC (Superpave Gyrotory Compact) specimens are listed as follows. In order to achieve the maximum density of mixture, air void is specified to $0.8\% \pm 0.3\%$. Volumetric characteristics of asphalt mixture at different asphalt binder content are shown in Table 6. Based on the improved Superpave design method, the optimum asphalt binder content of ASSAI mixture is 8.8%.

3.3 Test of ASSAI mixture performance

3.3.1 Cracking resistance performance

ASSAI is usually placed between asphalt pavement and base course. The working temperature of ASSAI is mostly between 5° and 25° (Li Z.Z. 2005). Under the effect of traffic load and change of temperature, tension stress would occur in ASSAI. The cracking in base course can also cause tensile stress in ASSAI at the point right above the cracking. The failure in ASSAI is mainly due to tension stress. Therefore, the performance of cracking resistance is very important for ASSAI at normal temperatures. In the study, indirect tension test was performed to evaluate the performance of cracking resistance.

Considering the actual environment of stress absorbing interlayer, the indirect tensile test was performed under the temperature of 15°C , with a loading rate of 50 mm/min. Poisson ratio of asphalt mixture was set as 0.30. The tension strength and stiffness modulus of mixture designed as stress absorbing interlayer, according to test results, were 1.29 MPa and 760 MPa respectively, which indicated that the tension strength was relatively high, and its stiffness modulus was bigger than that of AC-13, indicating a better fatigue resistance [Katy, 1996].

3.3.2 Rutting resistance performance

Rutting resistance is a vital weakness for asphalt sand used as stress absorbing interlayer due to the high content of fine aggregates, filler, and asphalt content. As a result, stability at high temperature must be taken into account. Meanwhile, stress absorbing interlayer lies between surface and base course, so the maximum working temperature in summer is lower than that of surface, which is about 40°C . As a result, stress absorbing interlayer calls for a relatively lower dynamic stability.

Hamburg Wheel tracking test device was employed to evaluate high-temperature rutting resistance of stress absorbing interlayer mixture, under a tyre pressure of 0.707 MPa and 40°C air bath condition. The test results showed that 10 mm rutting depth was induced by 8650 loading passes and its dynamic stability, which means the load passes leading to 1 mm rutting depth in wheel tracking test, was 1040, which met the requirement (more than 800). The rutting development is shown in Figure 13.

3.3.3 Permeability and water susceptibility

(1) Permeability

The test is performed to evaluate the permeability of ASSAI. Firstly fix the permeability tester onto the specimen (size of 30 cm \times 30 cm \times 5 cm) which is ready for the test (Figure 14). And then fill

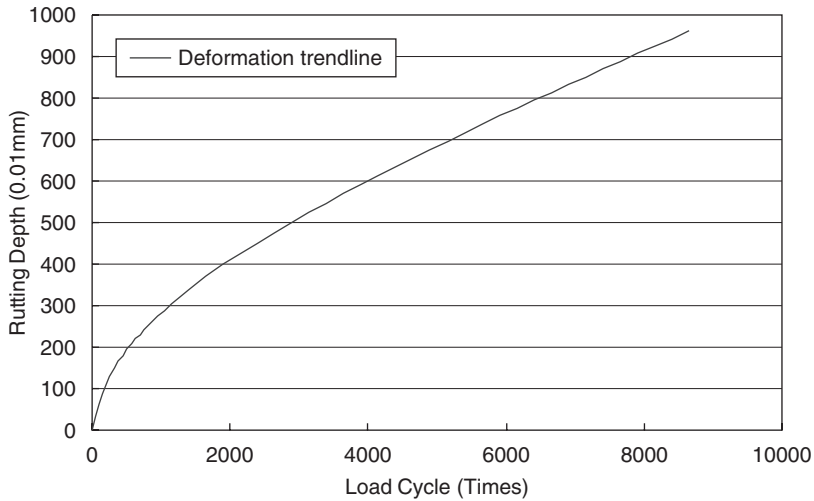


Figure 13. The rutting depth of rubber SSAI.



Figure 14. Permeability tester.

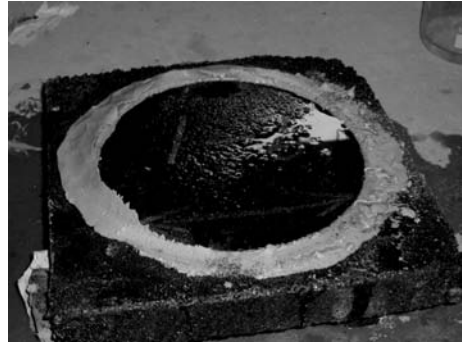


Figure 15. Specimen for permeability test.

the tester with 600 ml red water in order to observe the water position easily. Open the switch of the tester quickly and record the volume of water infiltrating in the specimen at the intervals of 60 s. It is shown in the test that the water level keeps still when dropping to a certain mark (Figure 15). Thus AASAI has been proved to watertight due to its low volume of air voids.

(2) Water susceptibility

There is rarely serious water damage occurring in ASSAI, for the above layers prevent water from penetrating into this layer. However, the water may infiltrate into inner layer detained in rainy seasons and frozen thaw seasons. This results in water erosion to some extent. The water penetrating into the void of ASSAI mixture decreases the binder adhesion to the minerals, and breaks the asphalt membrane away from the surface of minerals, leading to looseness of the mixture and liability to deformation. Therefore, the ASSAI mixture should have adequate water stability and be dense enough to keep water away from base course, which may erode the base.

The test results indicate that the indirect tensile strength ratio of freeze-thaw condition to the control condition of the rubber ASSAI mixture is in excess of 80%, and water damage resistance can meet the requirement. Additionally, due to the dense grading, minor aggregate size, high filler content and low air void, the stress absorbing layers material is completely impermeable according to permeability test.

Table 7. Expense of different reflective crack control measures.

Reflective crack control measures	yuan/m ² (RMB)
Geotextile	6.4
Glass fiber grid	7.6
Stress Absorbing Membranes Interlayer	12
ASSAI	29.5

3.4 Expense of different reflective crack control measures

On account of the expense of different reflective crack control measures as is shown in table 7, ASSAI costs more [Jiangsu, 2004]. However, ASSAI can postpone the occurrence of reflective crack for at least 2 years which will greatly prolong the life of pavement. Meanwhile, ASSAI can prevent the water damage due to its watertight characteristic and easy to be produced and paved by facilities usually used for common hot-mix asphalt. Considering the comprehensive benefit, ASSAI is a method economical for reflective crack control.

4 CONCLUSIONS

Asphalt sand stress absorbing interlayer is a kind of fine concrete structure which has low elasticity modulus, perfect deformability and fine anti-fatigue property. It is used between semi-rigid base course and asphalt surface course in order to delay reflection cracking of semi-rigid base pavement. The conclusion in the research can be drawn as below.

- (1) According to the analysis results, the anti-fatigue property effect is ideal when the structural thickness of stress absorbed layer is between 2 cm and 3 cm. It is suitable when the modulus of ASSAI materials is between 400 MPa to 800 MPa.
- (2) The raw materials of ASSAI should meet strict requirement for the high performance of ASSAI. An improved Superpave design method was well applicable in designing the ASSAI mixture.
- (3) The ASSAI mixture should have strong resistance to cracking, fatigue effect, rutting and water damage. As a result, these performances of mixture material should be evaluated by standard test when designing ASSAI mixture. In the research, it was proved that rubber ASSAI material could meet the demands on these performances according to the design standard.
- (4) Although it costs high, ASSAI can greatly prolong the life of pavement and prevent the water damage, and it is easy to be produced and paved. So, ASSAI is a solution economical for reflective crack prevention.

REFERENCES

- Lu Y. & Li C.L. and etc. 2004, "Application of Interlayer in Overlay of JCP Pavement," *Central South Highway Engineering*, PR of China
- Wu Y.F. 2006, *The Application Study of ISAC on Prevention of Research Cracking on Semi-Rigid Base Bituminous Pavement*, Master Dissertation of School of Transportation of Southeast University
- Fu G.H. & Lu Q. etc. 1999, *Stress Analysis on Interlayer Restraining Reflective Cracks*, Journal of Southeast University, Nanjing, China
- Yang T. 2005, *Forming Mechanism and Prevention Technology of Reflection Cracks in Semi-Rigid Base Asphalt Pavement*, Master Dissertation of Wuhan University of Technology and Science
- Li Z.Z. 2005, *Research on the Pavement Performance of Stress Absorbing Membrane Interlayer*, Master Dissertation of Wuhan University, Wuhan, China
- Shi K.L. 2006, *Research on Preventing Reflection Cracking of Asphalt Pavement with High Viscous Asphalt Stress Absorbing Layer*, Master Dissertation of Harbin Institute of Technology, JiLin province, China

- Ye Z.G. 2006, *Proportioning Design of Stress-absorbing Course Strata Mix against Reflective crack and Its Construction Technology*, Northern Communication
- Katyal N.K. 1996, *Effect of titania on the formation of tricalcumsilicate*. *Cement and Concrete Research*, 29(3):355–359
- Raymond E.Robertson *Chemical Properties of Asphalts and Their Relationship to Pavement Performance* SHRP-A/UWP-91-510
- Jiangsu Province Freeway Construction Headquarters, 2004, *Mechanism of cracks Development in asphalt pavement using cement treated base and Research on Prevention & Cure Measures*, Jiangsu, China

Effectiveness of slab stabilization in mitigating reflective cracking in HMA overlays: A case-history

F.G. Praticò

University of Reggio Calabria, Italy

M. Losa

University of Pisa, Pisa, Italy

ABSTRACT: Slab stabilization is the pressure insertion of a flowable material beneath a concrete slab, in order to restore slab support. The application of such a technique can pose some problems.

Therefore, an experimental study has been performed on the start of the runway (turnaround bay) of an Italian airport in order to assess the real capability of different types of slab stabilization techniques to rehabilitate the needed bearing properties. Crack surveys, deflection tests by the FWD and traditional plate bearing tests on the subgrade have been performed prior and after the four types of interventions in order to evaluate the structural effects at the centre, at joints and corners of slabs. The obtained results are useful in assessing the different capability of such rehabilitation strategies to optimise bearing properties and allow to identify the effect in mitigating reflective cracking in asphalt overlay.

1 INTRODUCTION

HMA (Hot Mix Asphalt) overlays are often applied to an existing rigid pavement when the structural or functional conditions of the pavement have reached an unacceptable level of deterioration. In these cases, rehabilitation strategies can include pre-overlay treatments, such as stabilization, in order to reduce vertical displacement of slabs at joints, therefore delaying cracking occurrence and controlling crack severity.

The aim of this research was to evaluate the effectiveness of slab stabilization in mitigating HMA reflective cracking through an experimental program to check the evolution of structural condition of these slabs.

As above-mentioned, when a given level of deterioration has been reached, prior to selecting pavement MRR (Maintenance, Rehabilitation and Reconstruction) treatments, it is important to establish what are the predominant pavement distresses and their causes. Major distresses include Durability “D” Cracking, Blowups, Corner Breaks, Punchouts, Joint Seal Damage, Transverse Cracking, Scaling, Longitudinal Cracking, Spalling, Faulting, Alkali Silica Reactivity, Pumping. Many factors affect MRR strategy development (Zollinger, 2001): (a) Pavement condition (Distress type, Distress severity, Distress extent); (b) Cause of distress (Structural related, Construction related, Materials related, Functional related); (c) Traffic (Design ESALs (expected traffic volume and axle weights); (d) Climate (temperature, moisture, and free-thaw cycles); (e) Rehabilitation life (Short-term, <5 years; Intermediate-term, 5 to 10 years, Long-term, > 10 years).

In this process, pre-testing and a distress survey are usually required in order to select the most convenient strategy. For example, load transfer inadequacies may be detected through Falling Weight Deflectometer (FWD) testing. These resulting load transfer efficiencies can vary from 30–50% for aggregate bases, to 50–70% for stabilised bases, to 80–95% when using dowel bars.

Preservation can be pursued through maintenance (retrofit edge drains, slab undersealing, resealing joints and cracks, thin asphalt concrete overlay, etc.). Restoration treatments (i.e. Rehabilitation) include dowel bar retrofit, partial depth repair, full depth repair, slab grouting, bonded concrete overlay, unbonded concrete overlay, asphalt concrete overlay, etc. Recycle In-place (RIP) and New Construction (Reconstruction) include remove and replace, remove and recycle, crack and seat, rubblize, etc.

As above-mentioned, pre-overlay treatments and HMA overlay constitute an available alternative (Al-Qadi, 2007). In particular, by referring to overlay systems, improved HMA mixes can be used. Motivations relate to rapid placement, saving, appreciable smoothness, skid resistance, marking contrast. Joint filling or stabilization can be performed and when needed a levelling course is laid. Interlayer systems can be used for reinforcement, for stress relief, or in terms of modified HMA (in order to resist to cracking).

The most important drawback for HMA overlay are reflective cracks. Reflection of cracks in Hot-Mix Asphalt overlays on PCC pavements represents a serious challenge. Three main modes can be considered in Reflective Cracking Mechanisms: Mode I (Opening), Mode II (Sliding) and Mode III (Tearing). Vehicle Loading on PCC can cause Crack opening, Shear failure and Mixed mode. Seasonal variations are usually related to Crack opening (Al-Qadi, 2007). In mode I loading (opening mode), phenomena result from loads that are applied normally to the crack plane (thermal and traffic loading). In mode II loading (sliding mode) phenomena result from in-plane shear loading, which leads to crack faces sliding against each other normal to the leading edge of the crack (traffic loading). Finally, mode III loading (tearing mode) results from out-of-plane shear loading, which causes sliding of the crack faces parallel to the crack leading edge.

As above cited, pre-overlay treatments can help in delaying reflective cracks. The following classes of pre-overlay techniques can be listed:

- a) crack and seat, brake and seat, rubblization;
- b) sawing and sealing joints;
- c) slab stabilization (for example accompanied by load transfer restoration).

As far as the case of slab stabilization is concerned, it is necessary to remark that faulting, pumping, voids beneath the slab can induce to consider as useful this particular treatment. Also called undersealing, subsealing, or pressure grouting, slab stabilization is the pressure insertion of a flowable material beneath a concrete slab, not in order to lift the slab, but rather in order to fill voids beneath the slab so that deflections are reduced and, consequently, deflection-related distresses, such as the above-mentioned pumping or faulting, are prevented or minimized. When slab stabilization is considered, pre-testing, applicability, materials quality, design details, construction procedures and post-testing must be carefully considered.

2 EXPERIMENTAL PLAN

In the light of the above-mentioned facts, a theoretical and experimental study was performed on the start of the runway (turnaround bay) of an Italian airport in order to assess the real capability of different types of slab stabilization techniques to rehabilitate the needed bearing properties. The experimental program was carried out according to the following main steps:

- Slab trenching in order to validate design information on layers typology and thickness;
- Plate bearing tests on the subgrade;
- Cracks survey before the stabilization;
- FWD deflection tests before the stabilization;
- Stabilization according to five different procedures;
- Cracks survey after the stabilization;
- FWD deflection tests after the stabilization (24 and 48 hours after).

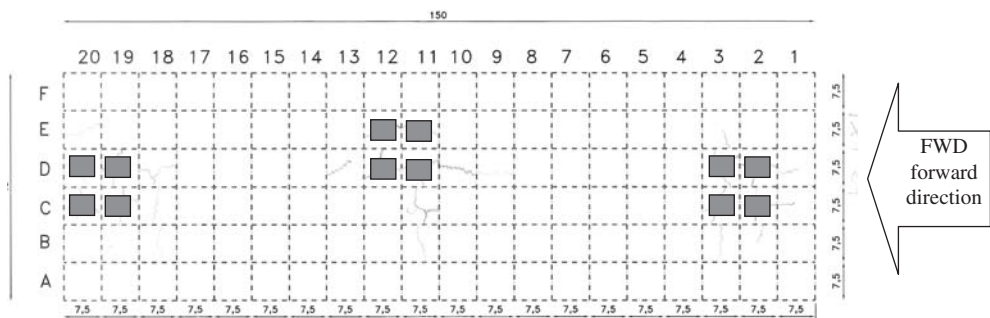


Figure 1. Layout of the experiments (boxes refer to the slabs investigated and stabilized; lengths are in meters).

Table 1. Ranking of investigated slabs in function of distress severity

Slab	Distress severity	Slab	Distress severity
C2	XXXX	D12	XXXX
C3	XXX	C19	XXX
D2	XXX	C20	XXXX
D3	XXX	D19	XXX
C11	XXXX	D20	XX
C12	X	E11	XX
D11	XXX	E12	XX

Legend:

X = Low severity; XX & XXX = Medium severity; XXXX = High severity (FAA AC-150/5380-6, 2007).

Pavement resulted as follows:

- First layer: PCC Slab, thickness: 30 cm;
- Second layer: unbound granular layer, thickness: 30 cm;
- Third layer: subgrade (modulus of subgrade reaction, $k = 40\text{--}115 \text{ MPa/m}$).

The layout of the experiments is shown in figure 1 (visual cracks are there shown). Table 1 summarizes the crack survey: four classes of distress severity have been recorded, depending on cracks wideness.

Stabilization has been carried out according to five different procedures, as shown in table 2.

Stabilization procedures were carried out by taking into account desirable characteristics for materials used for slab stabilization: fluidity (ability to flow into very small voids) and durability (ability to resist traffic and environmental loadings).

Attention was paid to the opportunity to perform slab stabilization especially at joints or cracks where voids were known to exist, on the basis of the presence of certain distresses such as joint and crack faulting, pumping, and corner breaks as indicative that loss of support had occurred or on the basis of falling weight deflectometer (FWD) deflections to help determine whether loss of support had occurred.

First, at appropriate areas identified as needing slab stabilization, holes were drilled through the concrete slab. Attention has been paid in order not to use a too high downward pressure on the drill.

After the hole was drilled, a grout packer was used to inject the material into the hole while preventing material extrusion or backup. Several precautions were taken in order to ensure that the

Table 2. Location and description of stabilization treatments.

Type of procedure	Slab	Description of the treatment
1	C3, D3	Expansive resins (515daN) type H ₂
2	C19, D19, C20, D20	Expansive resins (722 daN) type H ₂ –H ₃
3	D11, E11, D12, E12	Expansive resins (412 daN), type H ₃
4	D2	1 mini-pile
5	C2	4 mini-piles (centre of the slab)

- Notes: 1. In the procedures type 1 to 3, expansive resins have been applied in different weights per single slab: from 412 up to 722 daN per slab. Two qualities of resins has been tested: type H₂ (high density) and type H₃ (very high density). The single mini-pile type 4 has been applied at the center of the slab D2.
2. In the procedure type 1, the length ranged from 0 cm up to 80 cm under the slab. In the procedures 2 and 3, the length ranged from 30 cm up to 50 cm under the slab for the resin type H₂, while from 0 up to 30 cm ca under the slab for the H₃-type resin.

voids were filled and the slab was not lifted (monitoring the elapsed pumping time, monitoring slab pressures, and, above all, monitoring lift).

As above-mentioned, followup deflection testing was conducted 24 to 48 hours after the slab stabilization operation in order to assess its short-term effectiveness in terms of reduced deflections (and therefore in terms of consequences on cracks initiation and propagation in the future HMA overlay). Note that FWD tests were carried out in order to evaluate the structural effects at the centre, at edges and corners of slabs. Measurements were carried out in September in three successive sunny days among which no significant changes in moisture were registered. In order to evaluate the modulus of the concrete slab and the modulus of subgrade reaction, slab centres were tested early in the morning when good contact between the slab center and foundation may be expected. In order to evaluate the foundation support at the joints, measurements at joints were carried out later during the day.

3 DATA ANALYSIS METHODOLOGY

Data recorded during the experimental program were analyzed with the aim to underline the effects produced by the slab stabilization on the bearing capacity of slabs and on the Load Transfer Efficiency (LTE) at joints.

The evaluation of these effects was carried out by three different types of analyses. First of all, pavements data collected at the slab centre, were analyzed by using the theory of a slab on a Winkler foundation to evaluate the elastic modulus of concrete and the modulus of subgrade reaction; successively, data at joints were used to evaluate the LTE, and finally the same data were used to detect voids at joints.

3.1 *Elastic analysis of pavement systems*

Pavements were analysed from a general and a particular point of view.

The load-response data that FWD equipment measures in the field provides valuable information on the strength of the pavement structure. Generally, the initial review of the deflection under the load plate and at the outermost sensor gives information of pavement and subgrade stiffness. Although these data will not provide information about the strength of each pavement layer, they provide a quick assessment of the pavement's overall strength and relative variability of strength within a particular facility. In some cases, the pavement stiffness is evaluated as the dynamic force divided by the pavement deflection at the center of the load plate.

More useful information may be obtained by the modulus of a fictitious half space equivalent to the pavement system, which is calculated by using the Boussinesq equation in the case of uniform distribution of stresses underneath the plate; this equation is valid for central points of slabs when the least slab dimension is more than three times the radius of relative stiffness and the slab center is in good contact with foundation.

The Young's modulus of the concrete slab and of the subgrade, as well as the modulus of subgrade reaction k were calculated by using two different approaches (Ullidtz 1998).

In one case, the modulus of pavement layers was calculated by using the linear elastic theory and by assuming the subgrade as an elastic half space; in this case an approximate value of k may be found from the following equation:

$$k = \frac{0.54 \times E_m}{h_e} \quad (1)$$

where E_m is Young's modulus of the subgrade and h_e is the equivalent thickness of the concrete slab with respect to the subgrade, calculated using Odemark's transformation.

As stated in Ullidtz (1998), Odemark method is based on the assumption that stresses and strains below a layer depend on the stiffness of the layer only, which is proportional to:

$$\frac{h_s^3 E_s}{1 - \nu_s^2} \quad (2)$$

where h_s is the thickness, E_s is the elastic modulus and ν_s is the Poisson's ratio of the slab. This considering, the equivalent thickness of the concrete slab with respect to the subgrade is calculated by the following equation:

$$h_e = f \cdot h_s \sqrt[3]{\frac{E_s}{E_m} \cdot \frac{1 - \nu_m^2}{1 - \nu_s^2}} \quad (3)$$

where:

ν_m is the Poisson's ratio of the subgrade, which has been assumed equal to 0.45 while the Poisson's ratio of the concrete slab has been assumed equal to 0.35;

f is a correction factor introduced to take into account that Odemark's assumption is not mathematically correct; in this paper, in order to obtain results close to the theory of elasticity, the correction factor is equal to 0.9, as stated in Ullidtz (1998) for the first interface of a two-layer system.

In the second case, the modulus of subgrade reaction is calculated by using the theory of a slab on a Winkler foundation; in particular, the relation used to evaluate deflections at the slab interior (the case when the load is at a considerable distance from edges), are those derived by Ioannides, Thompson and Barenberg (1985) using the ILLI-SLAB finite element program. The equations for interior loading are reasonably correct when the least slab dimension is more than three to four times the radius of relative stiffness (Ullidtz 1998). The equation for evaluation of central deflections is function of the plate radius, of the elastic modulus and thickness of the concrete slab and of the modulus of subgrade reaction; this equation is solved with respect to the modulus of subgrade reaction and it is applied iteratively to fit the recorded deflections.

In both the cases, the values of Young's modulus calculated for the concrete slabs refer to an equivalent modulus of concrete which takes into account the cracking of the material; this value would be used successively in the design of pavement overlay.

3.2 Evaluation of Load Transfer Efficiency (LTE)

Traditionally, LTE at joints is evaluated as the ratio of the maximum deflection at the joint of the loaded slab and the deflection at the unloaded slab measured right across the joint. LTE can be calculated according to two different methods. Both methods make use of deflections from the two geophones positioned at each side of the joint, and a bending factor from the centre-slab test using the same geophones. The traditional equation proposed by Westergaard has the following form:

$$LTE = \frac{2d_{ju}}{d_{ju} + d_{jl}} \times \frac{d_{cl}}{d_{cu}} 100 \quad (4)$$

where d refers to deflection, j to joint, c to centre-slab, l and u to the position of the sensors chosen for the LTE calculation, respectively on the loaded and the unloaded slab.

The equation much more widely used has the following form with the same meaning of terms:

$$LTE = \frac{d_{ju}}{d_{jl}} \times \frac{d_{cl}}{d_{cu}} 100 \quad (5)$$

The results reported in this work were calculated by using the second equation. Joint LTE depends on many factors, including the following:

- Joint load transfer mechanism and stiffness;
- Base/subgrade support;
- Temperature.

Load transfer between the slabs occurs through aggregate particles of the fractured surface below the saw cut at a joint, and through the base and subgrade. LTE may vary through the day and the year because of variation in PCC temperature. When temperature decreases, a joint opens wider, which decreases the contact between the two slabs and also LTE may decrease; also PCC slab curling may change the contact between the slab and the underlying layer and affect measured load-induced deflections. For these reasons, LTE data are analyzed on a relative basis by comparing the results of measurements carried out before and after (24 and 48 hours) the slab stabilization with the same positive temperature gradients and moisture conditions.

3.3 Detection of voids

In addition to joint load transfer, another important characteristic of a concrete pavement is the slab support condition. One of the assumption that is made during back-calculation is that the entire slab is in full contact with the foundation. As with a joint condition analysis, the focus of the void analysis is near joints or slab corners. For void analysis, a plot is made of deflections (X-axis μm) versus applied loads (Y-axis daN) for three test drops at three load levels. If the regression line passes through the X-axis near the origin, good support exists beneath the slab. The further the line passes to the right of the origin, the greater the loss of support. The tangent of the regression line is the equivalent stiffness (daN/ μm) of the slab-support system at the joint. In general, a deflection intercept greater than 75 μm (3 miles) indicates the presence of voids (FAA AC 150/5370-11A, 2004). It is important to note that this procedure provides a qualitative indication of the presence of voids rather than an estimate of the void depth, but in any case it doesn't allow to estimate, even in a qualitative manner, the area of the void beneath the slab. Moreover, considering it doesn't allow to differentiate the effects on deflections from voids and from edge curling up, in order to eliminate the last effect, measurements should be carried out with positive temperature gradients.

For these reasons, measurements on joints have been carried out in daytime and the results have been used on a relative basis by comparing deflection intercepts before and after (24 and 48 hours) the slab stabilization.

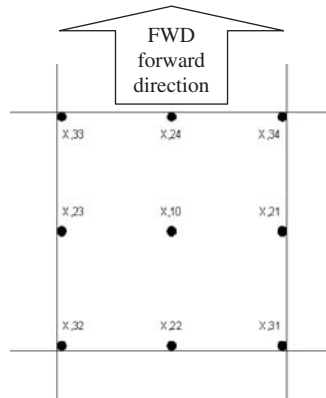


Figure 2. Position of test points.

4 RESULTS

The results obtained by the analysis of collected data, which was carried out by following the procedures described in the previous section, are reported here for each type of intervention considered. It is important to specify that nine different points per slab have been tested (see figure 2). Each point has a code as in the following figure. Note that X stands for the name of the slab (e.g. C2), then slab codes will be C2,33, etc.

In order to allow a better understanding of the results, let us introduce five classes of locations of the FWD load:

- Points at the center-slab (PCS); they are: C2,1; D2,1; C3,1; D3,1; C19,1; C20,1; D19,1; D20,1; C19,1; D11,1; E11,1; E12,1 (note that the zero after 1 is omitted, therefore C2,1 stands for C2,10).
- Type-1 external points (PE-1): this set refers to the points at joints and at the corners, on the boundary of the slabs treated with slab stabilization procedure type 1 or 2 (see table 2); they are: C19,31; C19,22; C19,32; C19,33; C20,32; C20,33; C20,24; C20,34; D20,33; D20,24; D20,34; D20,31; D19,34; D19,31; D19,22; D19,32; C3,31; C3,22; C3,32; C3,33; C3,24; C3,34; D3,33; D3,24; D3,34; D3,31; D3,22; D3,32.
- Type-2 external points (PE-2): these points are always on the boundary of slabs with slab stabilization procedure type 4 or 5 (see table 2); they are: C2,31; C2,22; C2,32; C2,33; C2,24; C2,34; D2,31; D2,22; D2,32; D2,33; D2,24; D2,34.
- Interior points (PI): this set refers to the points at joints and at the corners which are between the slabs stabilized by using the procedure type 1 or 2 (see table 2); they are: C19,34; C20,31; C20,32; D19,33; C19,24; C20,22; D20,22; D19,24.
- Localized points (PL): this set refers to the points at joints and at the corners of the slabs treated with slab stabilization procedure type 3 (see table 2); they are: D11,34; D12,31; E12,32; E11,33; D12,34; E12,33; D11,24; D12,22.

Figure 3 shows the values of the equivalent elastic modulus calculated by using the deflections registered on the slab centre. The results of the backanalysis, which will be described successively, show that the radius of relative stiffness l is lower than 2 m; in this case, considered that slabs are 7.5 m squared, this dimension is more than three times the radius of relative stiffness, and that measurements were carried out early in the morning while the center plate and foundation are in good contact, then the Boussinesq's equation for the evaluation of the equivalent elastic modulus is still valid. This figure shows that an increase of the overall bearing capacity of slabs is obtained

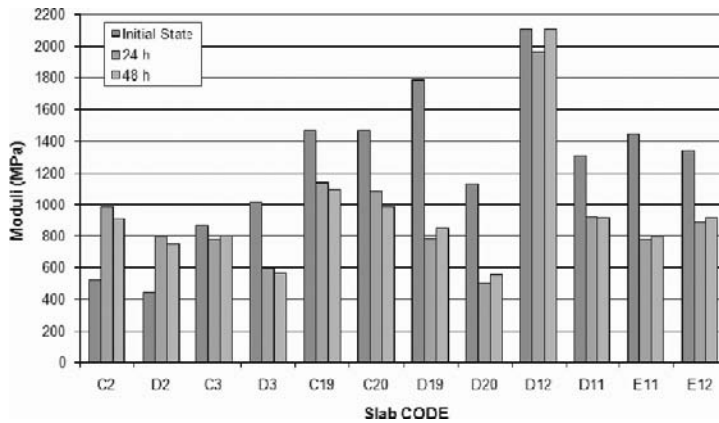


Figure 3. Modulus of the equivalent elastic half-space.

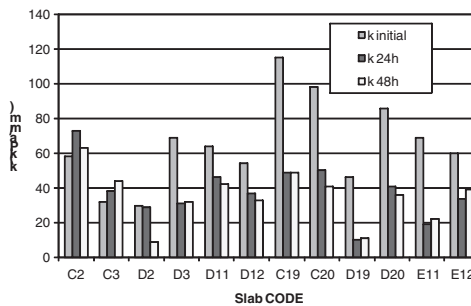


Figure 4. Modulus of subgrade reaction.

only where the interventions types 4 and 5 were realized, while for the other slabs the equivalent elastic modulus reduces or doesn't have appreciable variations.

The values of Young's modulus of the concrete slabs varied between 15000 and 38000 MPa, showing that the cracking state was significantly different among the slabs examined; the modulus of subgrade reaction values, calculated by using equations derived by Ioannides et al (1985), are reported in the Figure 4; this figure shows that in many cases this parameter reduces after the intervention, with the exception of slabs where the procedures types 4 and 5 were applied; in these slabs a slight increase of the subgrade modulus of reaction was registered, which can be due to the support exerted by the mini-piles more than an effective increase of the subgrade strength.

The analysis of data collected on joints appears to be more significant in evaluating the effect of the slab stabilization.

Figures 5 and 6 show the results of tests carried out on the boundary joints of the treatment areas. The LTE calculated by using relations (2) and (3) is improved significantly for slabs C3, D3 where the type 1 intervention was applied, and for slabs C2, D2, where the type 4 and 5 interventions were applied. The mean value of the LTE increases for slabs C3, D3 from 0.41 to 0.61, while for slabs C2, D2 from 0.29 to 0.60. The mean value of the LTE increases slightly, from 0.27 to 0.46, for interior points of slabs C19, C20, D19, D20 (Figure 7), while on all the other slabs no significant beneficial effects or even a decrease of the LTE were registered. The reasons for this reduction is not known, but probably the stabilization determines a beneficial variation of the subgrade support condition which is localized around the treatment point and is detrimental for the outer points on the boundary of the treatment area.

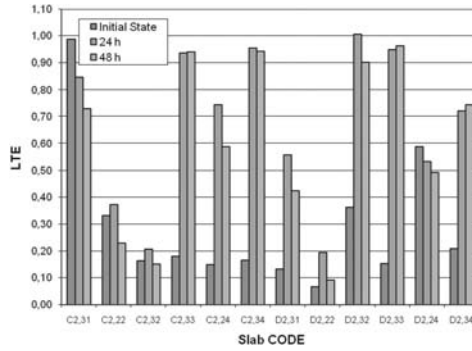


Figure 5. LTE for type 2 external points.

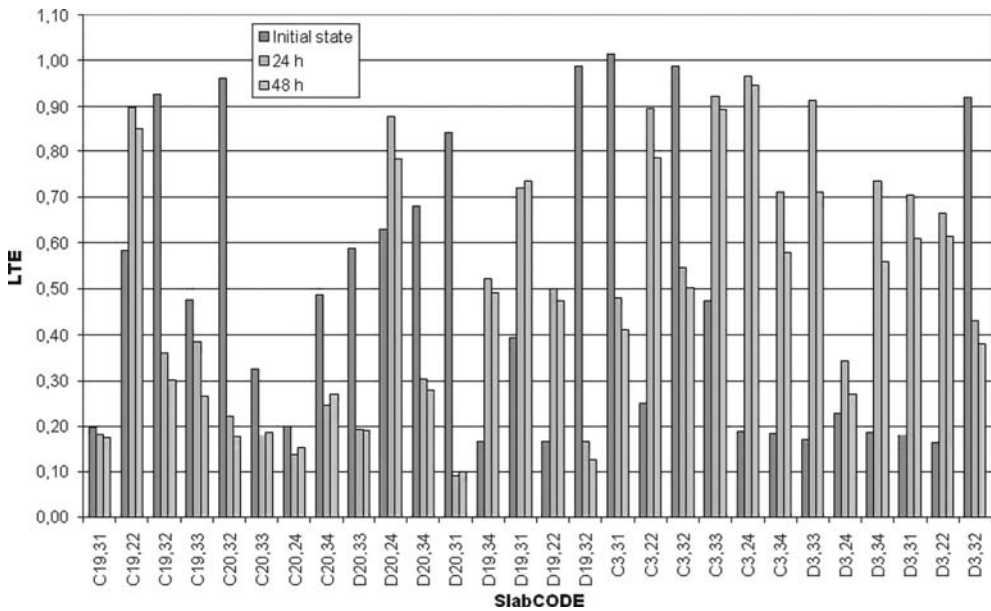


Figure 6. LTE for type 1 external points.

This is confirmed by examining the results reported in Figures 7 and 8, which refer to the values of the LTE calculated on slab joints internal to the treatment area. These figures show a general increase of the LTE for almost all the tested points on slabs C19, D19, D20 and C20, as well as on slabs C11, C12, D11 and D12.

As far as void detection is concerned, the results obtained are not so promising as those of the LTE in evaluating the beneficial effect of slab stabilization in restoring the subgrade support both on joints and slab corners. Figures 9 to 12 show that the intercept reduces significantly on boundary points of slabs C3, D3 (type-1 external points), treated with the type 1 intervention, and on the localized points of slabs D11, D12, E11, E12, treated with the type 3 intervention, for which the intercept after the stabilization is lower than zero; for the other slabs data don't show a clear trend.

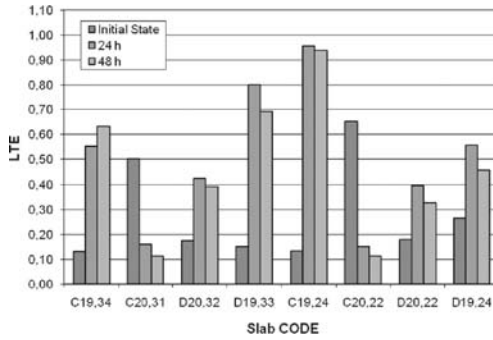


Figure 7. LTE for interior points.

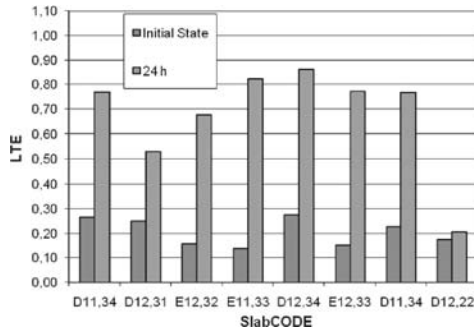


Figure 8. LTE for localized points.

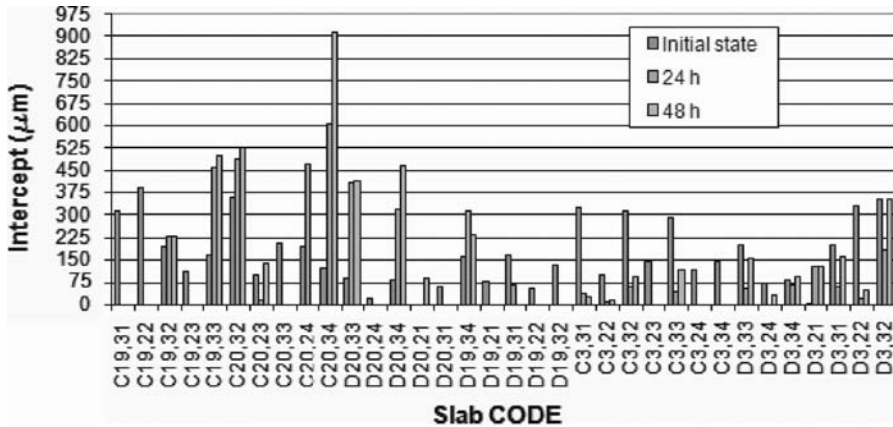


Figure 9. Intercept for type-1 external points.

5 MAIN FINDINGS

As is well known, HMA overlays are often applied to an existing rigid pavement, but drawbacks such as reflective cracking are often detected.

Given that, the aim of the present paper was to evaluate the effectiveness of slab stabilization in mitigating HMA reflective cracking, through an experimental program to check the evolution of structural condition of the slabs. Due to the uncertainties above mentioned, more research is

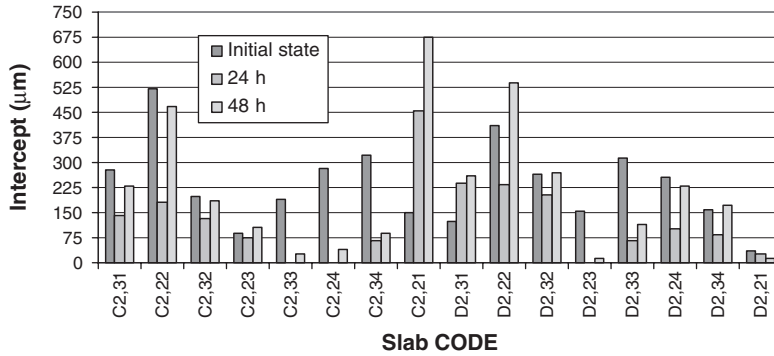


Figure 10. Intercept for type-2 external points.

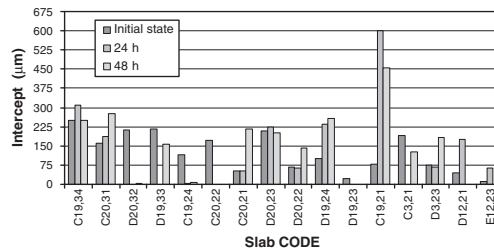


Figure 11. Intercept for interior points.

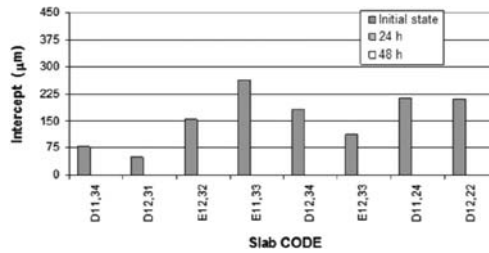


Figure 12. Intercept for localized points.

needed on this topic. However, in the light of the obtained results, the following main findings can be drawn:

1. The typology of slab stabilization greatly affects the obtained results;
2. The effect of such treatments is often strictly localized; in particular, it is important to remark that improvements in load transfer characteristics have been obtained for the so-called localized points;
3. As far as load transfer at joints is concerned, results appear quite encouraging for some of the selected procedures;
4. At the joints between two treated slabs the effectiveness of stabilization increases and LTE results are improved obtaining values that are about 0.60, significantly greater than initial values which range between 0.29 and 0.40. The reduction in void potential is not so encouraging as the LTE, with exception of localized points, for which void potential has been reduced drastically.

REFERENCES

- Al_Qadi, I. L. 2007. *Reflective Cracking: Initiation and Propagation Mechanism*, University of Illinois at Urbana-Champaign, MAIREPAV5, August 07.
- FAA AC 150/5370-11A. 2004. *Use of Nondestructive Testing Devices in the Evaluation of Airport Pavements*.
- FAA AC 150/5380-6B. 2007. *Guidelines and Procedures for Maintenance of Airport Pavements*.
- Ioannides, A.M., Thompson, M.R. and Barenberg, E.J. 1985. *Westergaard Solutions Reconsidered*, Transportation Research Record 1043, Transportation Research Board, National Research Council, Washington, D.C.
- Ullidtz, P. 1998. *Modelling Flexible Pavement Response and Performance*. ISBN-87- 502 0805-5, Polyteknisk Forlag, Copenhagen.
- Zollinger, D.G., Tayabji, S., Smith, Kurt., You, H.T. and Liu, J. 2001. *Repair and Rehabilitation of Concrete Pavement: Preliminary Guidelines Volume II*, Report No. FHWA-01-0080, Texas Transportation Institute, Texas A&M University, College Station, Texas.

Fatigue performance of self cementing base courses

A.A.A. Molenaar

Delft University of Technology, Delft, The Netherlands

ABSTRACT: This paper describes an analysis of the fatigue performance of self cementing base courses. The material investigated consisted of a mixture of crushed concrete and crushed masonry to which 10% of pulverized blast furnace slag was added. These types of base courses are used quite regularly in the Netherlands because they allow re-use of cement concrete and masonry rubble in an effective way. The research showed that these materials show a significant increase in strength and stiffness in time. It also appeared that premature loading or too high stress levels in general disrupt the self cementing process resulting in much lower strength and stiffness values than those of undisturbed samples. Furthermore it appeared that clear cracking patterns develop neither in the samples tested nor in the test section. It seems that the material disintegrates to a real unbound material. A fatigue relation could not be developed for this kind of material. Nevertheless design guidelines with respect to the allowable stresses at the top and tensile strains in the bottom of base courses made of these materials could be derived.

1 INTRODUCTION

In the Netherlands masonry and concrete rubble as well as all kinds of slag are used as base course materials (Schmeitz e.a. 1992, van Niekerk 1996). Quite often such materials are stabilized with a certain amount of cement to prevent leaching of hazardous materials and to give these materials sufficient strength. Several questions however arise when using these materials such as: (a) what is their stiffness and resistance to permanent deformation, (b) what is their fatigue resistance, (c) how are these characteristics changing in time due to progressive hardening, (d) what is the effect of premature loading of such base courses by construction traffic etc. Problems associated with the characterization of these materials are a.o. related to their variability, the required size of the samples (max. grain size is 40 mm) and the difficulty to cut and saw samples. All this implies that there is not too much information available about the characteristics that are needed to perform a ME design analysis of pavements containing base course made of these materials.

This paper presents the results of an investigation that was carried out at the Delft University in order to answer some of the questions raised above (van Niekerk, 2002). The material investigated was a mixture of crushed masonry and crushed concrete which shows some self cementing action. To this material a certain percentage of blast furnace slag was added to stimulate the self cementing of the base course mixture.

First of all some characteristics of the material tested will be presented. After that the results of monotonic and repeated load triaxial tests are discussed. These tests were performed to determine the failure as well as resilient and permanent deformation characteristics. Finally the results obtained on a particular test section are presented. The paper concludes with a discussion on the findings and the results.

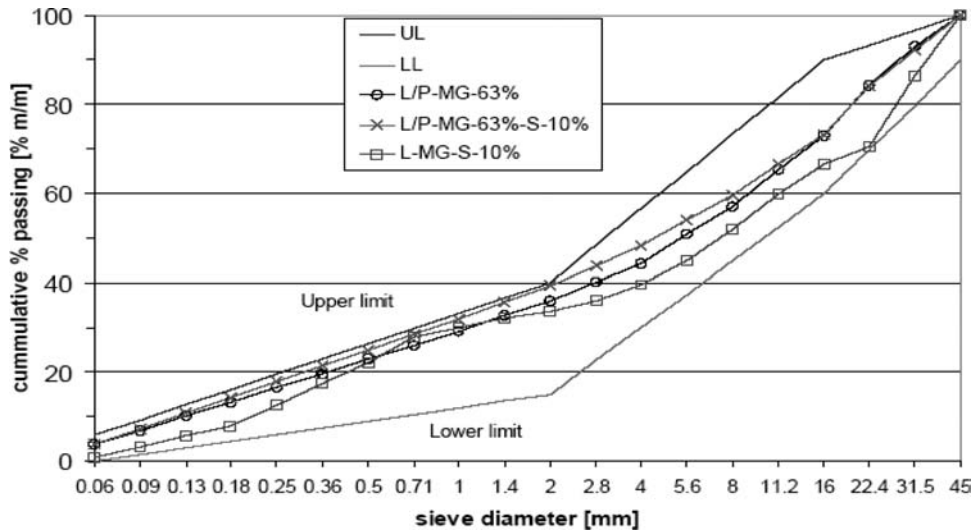


Figure 1. Gradation curves of the materials tested.

2 SOME CHARACTERISTICS OF THE TESTED SELF CEMENTING MATERIALS

The material tested is composed of crushed masonry and crushed concrete mixed at different quantities. To a number of these mixtures, pulverized blast furnace slag has been added. The slags have been pulverized to a kind of sand. Figure 1 shows the gradation of some of the masonry-concrete mixtures tested. The gradation is determined on the grain sizes larger than 8 mm and therefore excludes the blast furnace slag. As shown in figure 1, a special coding system is used to indicate the type of mixture tested. The code L/P-MG-63%-S-10% indicates that laboratory (L) and in situ tests (P) are conducted. The designation MG-63% indicates the mass percentage of crushed concrete used in the mixed granulate (MG). The designation S-10% indicates that 10% by mass (on top of 100% of aggregate) of pulverized blast furnace slag was used in the mixture. Figure 1 also shows the allowable upper (UL) and lower limit (LL) of the gradation curves for base courses as prescribed in the Dutch specifications (CROW, 1995).

According to the Dutch specifications, a base course material is rated as a self cementing material when the initial CBR value is at least 50%. Furthermore, the CBR after 28 days should be a factor 1.5 times higher than the initial CBR value. Figure 2 shows for a number of materials the initial CBR and the increase of the CBR in time.

3 MECHANICAL CHARACTERISTICS OF SELF CEMENTING BASE COURSES

3.1 Failure tests

Triaxial tests were performed on a number of samples having a height of 600 mm and a width of 300 mm. Since confinement is controlled by means of vacuum it was not possible to vary the moisture content; only the degree of compaction could be varied. All samples contained 63% by mass concrete and 10% by mass pulverized blast furnace slag. Confining pressures of 12, 40 and 70 kPa were used. To limit the number of tests, multi stage testing was done implying that by using the same sample, the failure stress was first determined at the lowest confinement level and after that on the higher confinement levels. Some results are shown in table 1.

The results shown in table 1 indicate that after a limited period of curing, the material still behaves like a granular material meaning that failure is dependent on the amount of confinement.

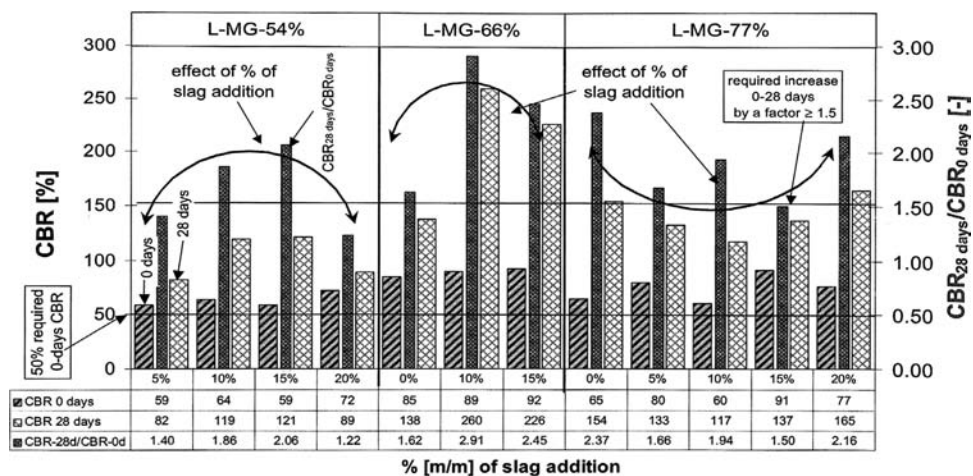


Figure 2. Increase of CBR value in time in relation to composition, degree of compaction and addition of pulverized blast furnace slag.

Table 1. Results of monotonic triaxial tests.

Degree of compaction [%]	Curing time [weeks]	Cohesion [kPa]	Angle of internal friction [$^{\circ}$]
100	4	193	45
99	13	903	0
105	13	1072	0

After a long curing period however, this stress dependency is not visible any more. This might have to do with the fact that the specimen is damaged after the first test which influences the test results obtained in the second and third loading cycle applied at higher confinement levels. In any case these initial cracks do not result in a decrease of the failure stress. It should be noted that clearly defined slip planes did not develop. Furthermore it should be noted that a cohesion of around 1000 kPa implies a compressive strength of around 2 MPa. This is a high value which compares well with values obtained on cores taken from cement stabilized sand base courses (around 7% cement by mass) as have been used often in the Netherlands.

3.2 Resilient modulus testing

Figure 3 shows for a particular material the increase in modulus in relation to the curing time. This figure shows some interesting phenomena. When the material is still fresh (curing time 1 day), it exhibits a stress dependent behavior similar to that of granular materials. This behavior disappears after a certain curing time during which the modulus sharply increases. However the modulus at high values of θ is lower than at lower values of θ indicating that at high stress levels bonds will probably be broken resulting in a lower M_r value.

The modulus values obtained after 13 weeks compare very well to the modulus values that are obtained on samples from sand cement treated base courses.

3.3 Resistance to permanent deformation

A number of repeated load triaxial tests were performed at a fixed confining pressure of 12 kPa. This confinement level was selected because analysis of a number of pavement structures showed

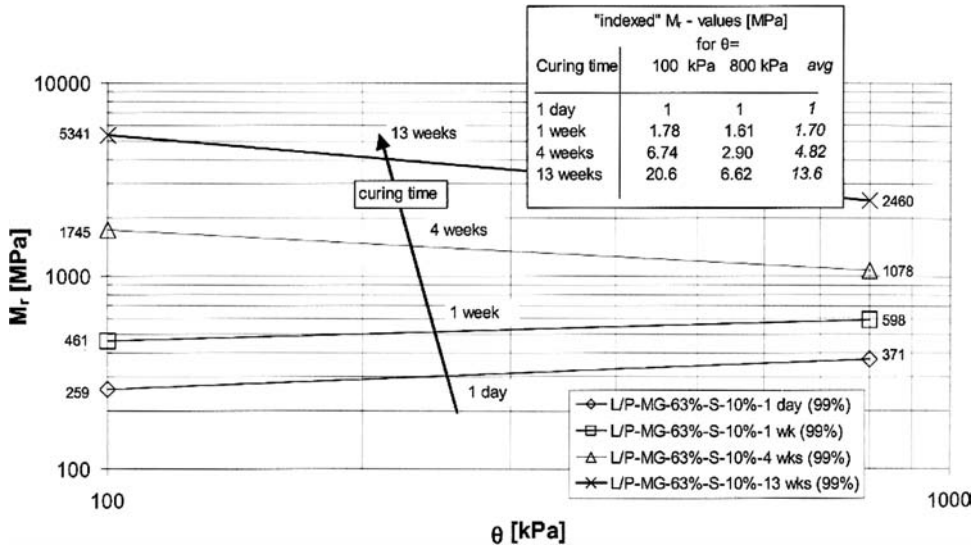


Figure 3. $M_r - \theta$ relationships for L/P-MG-63%-S-10% at 104% degree of compaction.

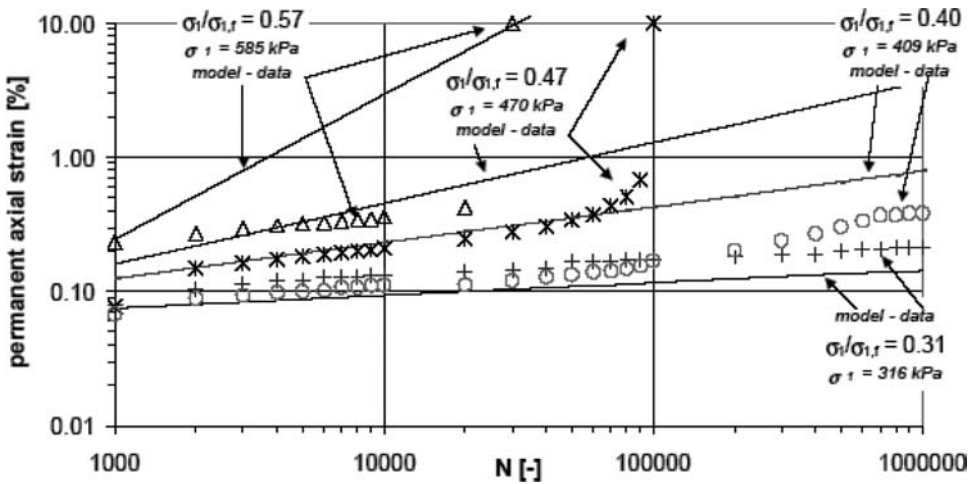


Figure 4. Permanent deformation development in L-MG-S-10% samples after 4 weeks curing.

this value to be fairly representative for the confinement level in base courses of pavements as built in the Netherlands. Some results are shown in Figure 4.

Figure 4 nicely shows the brittle behavior of this type of material. At stress ratios σ_1/σ_{1f} of 0.4 and lower, hardly any permanent deformation develops while at higher stress ratios a sharp increase in permanent deformation develops after a certain number of load repetitions. It should be noted that σ_1 is the applied repeated vertical stress (confinement stress is 12 kPa) while σ_{1f} is the vertical stress at failure at a confinement level of 12 kPa. Figure 4 also shows that this brittle type of behavior was difficult to capture by the permanent deformation model that is commonly used to model the permanent deformation behavior of unbound materials that don't show cementation.

This model is:

$$\epsilon_p = A (N/1000)^B C (e^{DN/1000} - 1)$$



Figure 5. Construction of the base course.

Where: ε_p = permanent strain [%],
 N = number of load repetitions,
 A, B, C and D = material constants depending on the stress conditions,
 A = $x_1(\sigma_1/\sigma_{1,f})^{x_2}$, similar formulations hold for $B, C,$ and D ,
 σ_1 = vertical stress applied during the test,
 $\sigma_{1,f}$ = vertical stress at which failure is reached given the applied confining stress.

3.4 Discussion

From the results obtained so far it appears that the type of base course materials as investigated in this research program develop a high stiffness and high strength when they are allowed to cure for a significant period of time. Furthermore it appears that these materials exhibit a brittle type of behavior. High stiffness values imply that tensile stresses and strains develop at the bottom of base courses made of this type of self cementing materials. The question now is how these materials will perform in practice. Will they be sensitive to shrinkage cracks due to changes in moisture content and temperature, will they show fatigue cracking or will they slowly degrade to a high quality half-bound base? Furthermore the question is what the effects are of heavy construction traffic traveling the freshly placed base course. Will this result in premature damage and if so will self cementation be able to heal the base course after reduction of the tensile stresses and strains due to placement of the asphalt top layer. In order to be able to answer these questions a test section was constructed on which repeated load falling weight deflectometer tests were performed to simulate the effect of traffic. The results obtained on this test section are discussed in the next section.

4 TEST SECTION

4.1 Structure

A test pavement was constructed consisting of a 300 mm thick base course (P-MG-76%-S-10%) on a sand subbase and sand subgrade (van Beers e.a. 1998). A high amount of crushed concrete was used to stimulate self cementation. A double surface treatment was placed on top of the base course. When completed, the base course had a thickness of 304 mm with little variation. The average degree of compaction of the top 100 mm was 105.9% while at a depth of 250 mm the degree of compaction was 104.1% (maximum proctor density was 1748 kg/m^3 , optimum moisture content was 10.7%). Figure 5 shows the placement and compaction of the base course.

The stiffness of the sand substructure is shown in Table 2. These values were determined using a falling weight load of 20 kN.

Table 2. Stiffness of the sand substructure [MPa].

Location number	1	2	3	4	5	6
Left row (see also figure 6)	52	39	73	70	83	90
Right row (see also figure 6)	68	94	86	78	73	87

Table 3. Loading schedule.

Type of load	# of points	Code	Week														
			0	1	2	3	4	5	6	7	8	9	10	11	12	13	
Construction traffic 70 kN	2	CT-70															
Traffic load 70 kN	2	T-70															
Traffic load 50 kN	2	T-50															
Traffic load 30 kN	2	T-30															
Traffic load 10 kN	2	T-10															
Delayed traffic 50 kN	2	DT-50															
Reference point	2	R															
Total	14																

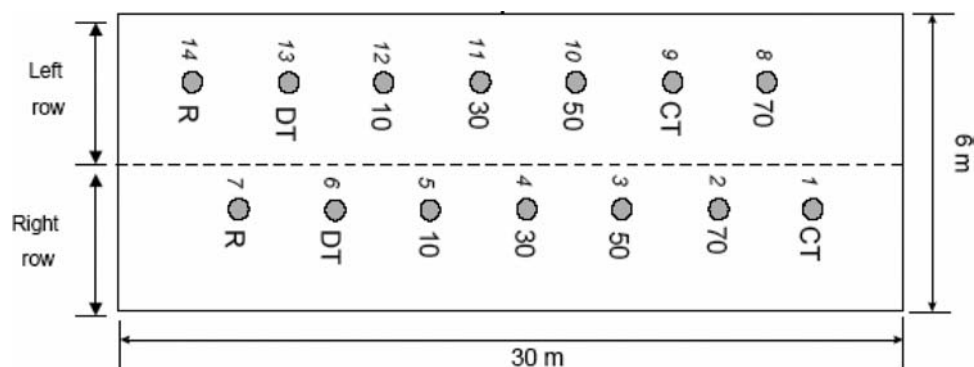


Figure 6. Measurement locations.

4.2 Loading schedule

As mentioned above, repeated load falling weight deflectometer tests were carried out to simulate traffic. The falling weight load was selected such that tensile stresses and strains were generated at the bottom of the base course that could be expected to occur when the base course would be covered by a 60 mm or 150 mm thick asphalt layer or by a bedding layer of sand and a layer of 80 mm thick concrete blocks. Also the effect of construction traffic was simulated. All this meant that repeated falling weight tests were done using load levels of 10, 30, 50 and 70 kN. At each measurement location 100 falling weight loads were applied per day. Table 3 shows the loading schedule applied and Figure 6 shows the measurement locations.

4.3 Results

Figure 7 shows the values for stiffness of the base course as back calculated from the falling weight deflection profiles.

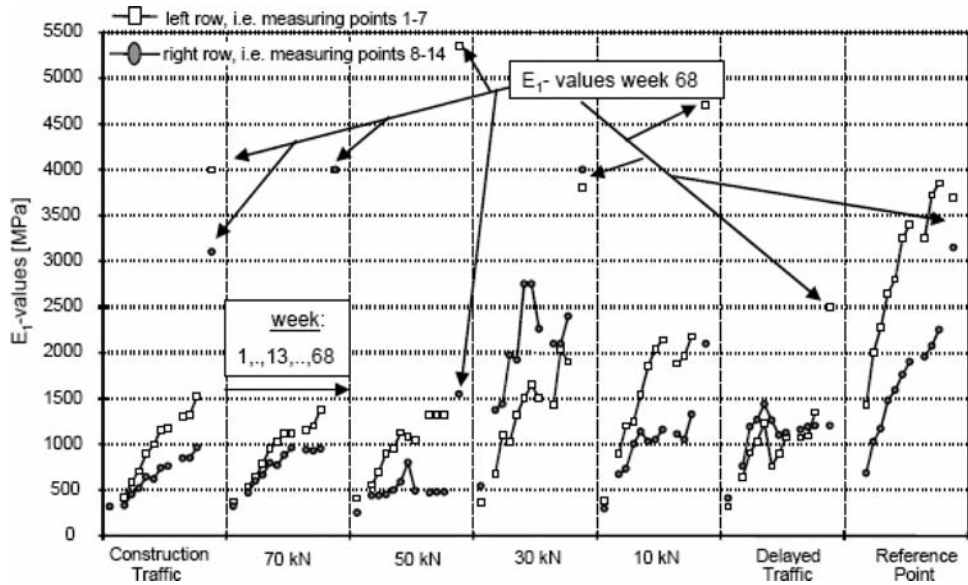


Figure 7. Back calculated stiffness values for the self cementing base course.

When analyzing Figure 7, one should keep in mind that no tests were done between week 13 and week 68. The results obtained in week 68 therefore clearly indicate the effect of healing due to self cementation.

Figure 7 shows a number of things. First of all it shows that there is a distinct difference between the right row and the left row. An explanation for this could not be found but it might have to do with the variability of the material because first the material for the right lane was brought in and after that the material for the left lane. Furthermore the figure clearly shows that the stiffness of the loaded sections is lower than the stiffness of the reference point. This is clearly due to the repeated falling weight loads that were applied each day. In reality however the number of load repetitions per day is usually higher than the number applied on the test section. This could imply that the stiffness development in practice is even less than observed in the test section. It is remarkable however that during the healing period (from week 13 to week 68), the stiffness of the loaded sections recovers to similar values as obtained for the reference locations.

No cracks were observed during the testing period; it is believed that a general disintegration might have occurred which is partly masked by the self cementation of the material.

When analyzing the data obtained from the measurements in week 13 it was concluded that the stiffness modulus of the base course was related to the tensile strain at the bottom of the base course following:

$$E = -3.967 E6 \epsilon + 2455$$

Where: E = stiffness modulus of the base [MPa],

ϵ = tensile strain at the bottom of the base course [m/m].

The tensile strain was calculated using the back calculated stiffness modulus of the base, the stiffness of the sand substructure (table 3), the thickness of the base and the falling weight load as input for a two layer linear elastic analysis. The results show that the initial stiffness of the base course was approximately 500 MPa. Taking into account that an appreciable increase in stiffness only occurred in the 30 kN and 10 kN sections, it was concluded that in spite of repeated loading, self cementation gives the base course stiffness and strength provided that the tensile strain at the

bottom of the base is less than approximately 2.7 E-4 m/m (this value is calculated using a base stiffness of 500 MPa and a falling weight load of 30 kN as input).

From the observations it seems that for design purposes, a stiffness value of approximately 50% of the stiffness of laboratory samples is a realistic value to select provided that the tensile strain stays sufficiently low ($<2.7 \text{ E-4 m/m}$) in the early lifetime of the base course.

5 DISCUSSION

From the results presented in this paper it becomes obvious that the behavior of these materials is rather complex. On the one hand self cementation results in an increase of stiffness and strength in time while on the other hand repeated loading disturbs this self cementation process resulting in a significant lower strength and stiffness when compared to the values obtained on undisturbed samples and sections.

Furthermore neither in the tested samples nor in the test section cracks were observed in spite of the fact that a clear reduction in stiffness was measured. It looks like these materials deteriorate from a bound state to an unbound state without developing clearly visible cracks. The results of the repeated load triaxial tests seem to indicate that the transition from a bound to an unbound state happens quite abruptly. This is typical for a material showing a brittle behavior like cement bound materials.

All in all this implies that unlike for cement treated materials, Portland cement concrete and asphalt concrete, it seems not possible to define a fatigue relation for these types of materials.

Based on the findings from this research the following design guidelines are proposed.

- (a) The ratio σ_1/σ_{1f} (vertical compressive stress: vertical stress at failure at a given level of confinement) at the top of the base course should stay below 0.4.
- (b) The horizontal tensile strain at the bottom of base courses made of self cementing materials should stay below 1 E-4 m/m .

REFERENCES

- Van Niekerk, A.A. 2002. Mechanical Behavior of Granular Bases and Sub-Bases in Pavements. *PhD Dissertation*. Delft: Delft University of Technology.
- CROW. 2000. RAW Standard Conditions of Contract for Works of Civil Engineering (in Dutch). Ede: CROW Information and Technology Centre for Transport and Infrastructure.
- Schmeitz, R.M.H., A.A.A. Molenaar, P.J. Galjaard & L.J.M. Houben. 1992. Determination of the in situ Stiffness of Base Materials used in Test Pavement MEVA 3. *Report 7-92-209-25-M*. Delft: Road and Railway Research Laboratory, Delft University of Technology.
- Van Niekerk, A.A. 1996. Hydraulic Activity in Secondary Base Materials, Literature Survey. *Report 7-95-200-18*. Delft: Road and Railway Research Laboratory, Delft University of Technology.
- Van Beers, P.J.J.M. & A.A. van Niekerk. 1998. The Strength and Stiffness development of Hydraulic Mixed Granulate. *Report 7-98-200-19*. Delft: Road and Railway Research Laboratory, Delft University of Technology.

*5. Fatigue cracking and damage
characterization of HMA*

A five point bending test for asphalt cracking on steel plates

A. Houel & L. Arnaud

Ecole Nationale des Travaux Publics de l'Etat, Vaulx-en-Velin, France

ABSTRACT: The paper deals with the evolving behaviour of asphalt mixture on steel plate. Due to the softness of such a support and the mechanical loads involved, the asphalt pavement is subjected to considerable strain that may generate top-down cracks. The five-point bending fatigue test is the standard device in France for asphalt concrete used on steel orthotropic deck bridges to perform the best asphalt mixture having a strong resistance to cracking. Displacement sensors detect the initiation of cracks where they are most likely to appear. Significant strain increases and decreases are observed when cracks are created. Moreover, a non-destructive measurement technique based on ultrasonic measurements has been developed. From velocities and amplitudes of waves and under the assumption of linear viscoelasticity, complex modulus M^* and the time dependent evolution of damage are followed up. Results from displacement sensors and wave propagation are compared and provide good perspectives. Numerical simulations will also be presented.

1 INTRODUCTION AND CONTEXT

The five-point bending test (bending under negative moment), named FPBT in the following, was developed in France by the *Laboratoire Central des Ponts et Chaussées* (LCPC) in the 1970's (Hameau et al. 1981). This kind of test is essential for the design of the asphalt layer on steel orthotropic decks: essential because the metallic structure is very soft, and as a consequence, the asphalt concrete is submitted to very high levels of strains under traffic load as compared to asphalt on classic roads. It was shown that the results obtained from the FPBT and in situ observations on real steel decks are very consistent. The main damage observed in the asphalt on such bridges is that fatigue cracks are generated in the thickness of the asphalt layer at right angles to the orthotropic plate stiffeners, due to the tensile stress created. These cracks propagate from the road surface through the wearing course and could therefore reach the sealing sheet that protects the steel plate from corrosion. Thus, a special asphalt mixture is needed to obtain better durability of the bridge's structure. This is the case of the Millau viaduct in France.

A new device has been under development since 2003 at the ENTPE laboratory. It enables more accurate measuring of strains in asphalt layers, plus follow-through of damage in the material through a non-destructive test based on compression and shear wave propagation (Laajili 2003, Houel 2004, Arnaud & Houel 2006, 2007b).

In the first part of this paper the experimental device of the FPBT, test conditions and the instrumentation are described. Non-destructive tests, based on P-wave (compression waves) and S-wave (shear waves) propagation, are underlined – with the overcoming of the main difficulties. In the second part, results of two different mixture formulations at two temperatures -10°C and $+10^{\circ}\text{C}$ are exposed. The article shows that the strain measurements allow mechanical evolution of the wearing course analysis, and non-destructive measurements make it possible to monitor the mechanical evolution throughout the fatigue tests and to clearly detect the growing of micro- and macro-cracks. Finally, this test was modeled by means of *Comsol Multiphysics* software based on the finite elements method.

2 DESCRIPTION OF THE FIVE-POINT BENDING TEST

2.1 Specimens

Samples are constituted generally of three main materials:

- a 12 or 14 mm-thick steel plate reinforced at the centre with a welded stiffener,
- a 3 mm-thick sealing sheet.
- the asphalt concrete layer, whose thickness is variable.

The thickness of tested samples is 12 mm for the steel plate and 65 mm for the asphalt layer. The tack coat must have a good adhesion and shear strength to prevent water to penetrate to the steel surface. Two different asphalt concrete formulations are tested: on the one hand, a classic asphalt concrete with 7% pure binder, and on the other hand a special asphalt designed for the Millau viaduct by the Eiffage TP [public works] central laboratory (Héritier et al. 2005). Two samples with the classic asphalt mixture (one at -10°C and one at $+10^{\circ}\text{C}$) and four samples with the Millau asphalt mixture (two at -10°C and two at $+10^{\circ}\text{C}$) were tested.

2.2 Principle (AFNOR 2006)

The FPBT consists in testing a sample reproducing the area located on either side of an orthotropic plate longitudinal stiffener. This is the area where the largest strains are generated because of traffic and therefore where the greatest fatigue damage in the asphalt layer is observed. This is a fatigue test carried out over several million cycles. The regular 2 and 4-point bending tests do not exactly represent the real behaviour of the asphalt laid on an orthotropic steel deck.

The sample is held in its centre on a rigid frame and is loaded using the device as presented in Figure 1. The steel plate is embedded in the centre and its two extremities rest on two simple supports that are adjustable in order to correct any flatness defects of the steel plate. Above the asphalt concrete layer the beam sets to apply the sine compression load.

The load is composed by compression sine cycles at a frequency of 4 Hz. The amplitude of the maximal load is determined during a calibration phase so as to take into account the mechanical role of the steel plate in the sample. This load, applied to the steel plate without any asphalt layer, corresponds to a stress of 120 MPa at right angles to the weld. Of course, the effort depends on

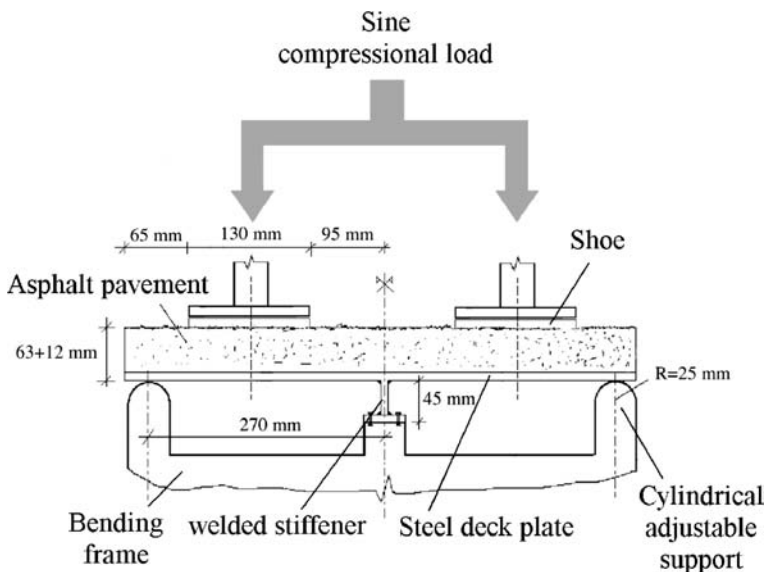


Figure 1. Experimental device of the FPBT (Laajili 2003).

the thickness of the steel plate. For example, for calibrated 12 mm-thick plates, the maximal effort equals the load when a strain of $625 \mu\text{m/m}$ is observed at right angles to the weld, that is to say 32 kN in compression (Fig. 2). Thus, the sine load, applied to the sample with the asphalt layer, ranges between the maximal effort and 10% of this load. A counter measures the number of applied load cycles. For each coating, one sample is tested at -10°C , and another at $+10^\circ\text{C}$ which is very often the critical case, thanks to a heat-regulated chamber. These temperatures are based on the French asphalt mix standardization. Regular tests on asphalt are realized at $+10^\circ\text{C}$, which is an average annual temperature in the country.

According to the requirements, an asphalt mix is considered “good” when no damage can be observed at -10°C after 1 million cycles, and at $+10^\circ\text{C}$ after 2 million cycles. No damage means that no crack was generated and observed with soapy water (Fig. 3). But there is no requirement for the mechanical evolution and the breaking threshold of the material. That is why special instrumentation based on ultrasonic wave propagation is investigated.

2.3 Experimental set up

2.3.1 Instrumentation related to the fatigue test

Two strain gauges are pasted on the two side faces as close to the top face as possible in order to monitor the evolving strains of the asphalt layer where cracks are likely to appear (Fig. 4).

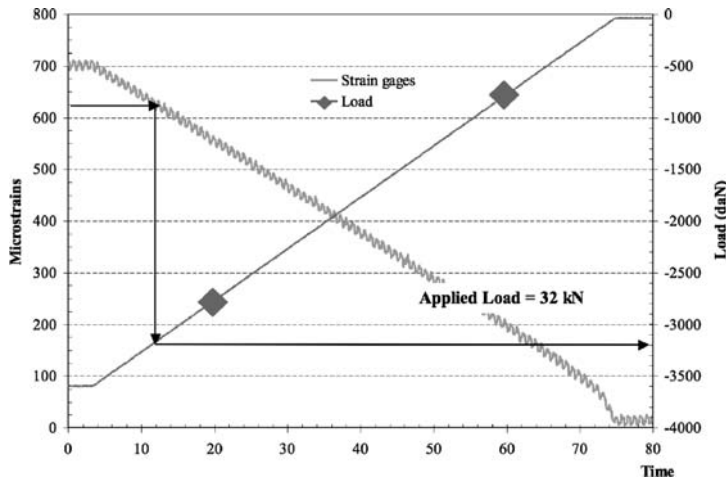


Figure 2. Example of calibration of a 12 mm-thick steel plate. A strain of $625 \mu\text{m/m}$ corresponds to a load of 32 kN.



Figure 3. Soapy water is currently used to detect the appearance of cracks (Somda 2007).

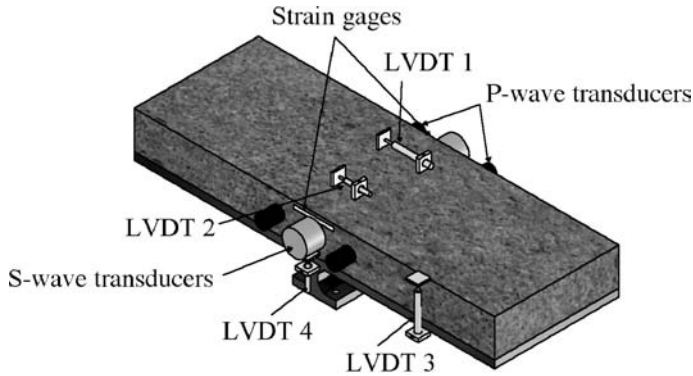


Figure 4. Positions of displacement sensors (LVDT 1 and LVDT 2), strain gages and wave propagation transducers on specimens for the FPBT (Houel 2008).

However, their installation is a delicate and difficult task, and it is possible that because of the glue their breaking does not exactly account for crack appearance. That is why two different displacement sensors of the LVDT (Linear Variable Differential Transformer) type are positioned on the upper face of the sample at the centre (Figs 3, 4). Both accuracy and a large detection area are ensured: the first sensor (LVDT 1: ± 2.5 mm and $\Delta l = 60$ mm) is certain to have a measurement zone where cracks are likely to appear, and the second (LVDT 2: ± 1.0 mm) and $\Delta l = 30$ mm) senses the displacements more precisely.

Moreover several temperature sensors are positioned in the chamber and one at the centre on the upper face of the asphalt concrete.

Load, strains and temperatures are recorded continuously (5 cycles are recorded each hour at a frequency of 100 Hz).

2.3.2 Instrumentation related to the non-destructive test based on ultrasonic wave propagation

The non-destructive test consists in transmitting a wave with the first transducer and receiving this wave that propagates throughout the considered medium. Transducers are placed in the central area on the side faces in order to continuously monitor the asphalt pavement modulus where the material is submitted to tensile stress and thus where cracks are likely to appear. Two kinds of ultrasonic waves are studied: P-waves or compression waves, and S-waves or shear waves. Two pairs of P-wave transducers are used to scan different excitation frequencies, and one pair of S-wave transducers is also positioned and senses the centre part of the asphalt layer. From the recorded signals, the parameters below are followed throughout the fatigue tests (Fig. 5):

- the arrival time, which gives the wave velocity and by an inverse analysis the complex modulus of the asphalt concrete,
- the maximum amplitude of ultrasonic waves, and
- the Fast Fourier Transform of received signal.

A few precautions must be taken into account: an appropriate excitation frequency needs to be chosen carefully in order to avoid diffraction, multiple scattering processes and high attenuation because of the heterogeneity of asphalt concrete and the limited size of specimens. As a consequence, the wavelength should both be smaller than the asphalt layer thickness and larger than the grain size (10 mm) (Hauwaert et al. 1998, Houel 2004, Arnaud & Houel 2007b)

Moreover, wave velocities depend on temperature but not on tested asphalt mixtures (Somda 2007). So, temperature effects must be analysed before choosing adequate excitation frequencies. For example, an increase in temperature of 1°C corresponds to a decrease in modulus of 150 MPa at an approximate frequency of 50 kHz. Characteristics of wave propagation are presented in Table 1. The wavelength of S-waves is of the order of specimen size, but received signals could be analysed.

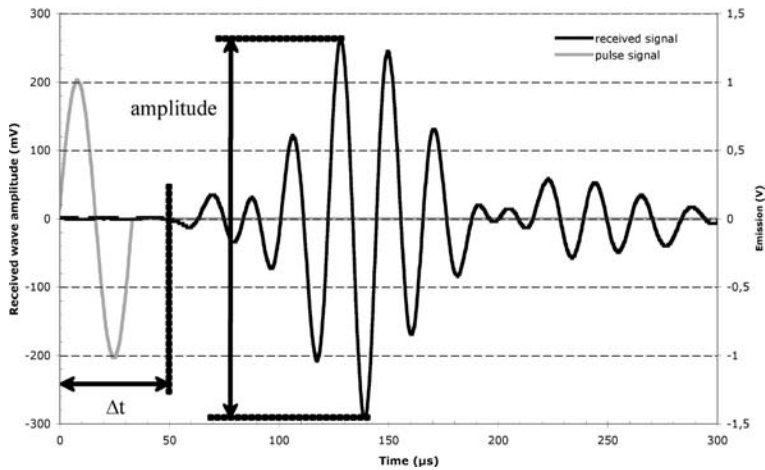


Figure 5. Emitted and received signals of P-wave propagation, determination of time delay and damping (Houel et al. 2007).

Table 1. Wave velocities, frequency excitations of transducers and wavelengths used and measured at the beginning of fatigue tests.

Wave velocity and wavelength		Temperature	
		-10°C	$+10^{\circ}\text{C}$
P-wave (50 kHz)	C_p	4000 m/s	3600 m/s
	λ	7 cm	6 cm
S-wave (10 kHz)	C_s	2100 m/s	1800 m/s
	λ	15 cm	20 cm

3 RESULTS

3.1 Strain results

Maximal and minimal strains were monitored throughout the fatigue test. As expected, both asphalt mixtures showed that strain amplitudes were greater at $+10^{\circ}\text{C}$ than -10°C (Figs 6 and 7). The main differences between the two bituminous mixtures were observed:

- As regards the “classic” asphalt mixture throughout both fatigue tests at -10°C and $+10^{\circ}\text{C}$, amplitudes corresponding to one load cycle increased quickly at the beginning of the test, then a sudden and strong increase appeared, and finally strain amplitudes do not increase any more but are relatively constant (Somda 2007).
- For the Millau viaduct asphalt mixture we firstly observed that amplitudes increased during the test up to about 1,000,000 cycles, then a sudden variation of slopes was recorded from the most accurate sensor. Thus, as regards fatigue behaviour and the appearance of cracks, this special asphalt mixture has a stronger resistance to cracking than the first one.

In each case, variations are determined by linear regression, and the intersection of two straight lines defines the cycle number when cracks appear on the upper side of the asphalt layer. This experimental set up is very sensitive to the appearance of cracks initiated from the top face of the asphalt layer. Table 2 sums up crack detection results from measurements of displacement sensors. Hence, the displacement sensors show a sudden and significant variation of strain amplitudes during the test, proving the appearance of fatigue cracks in the sensed zone in the asphalt concrete. Besides,

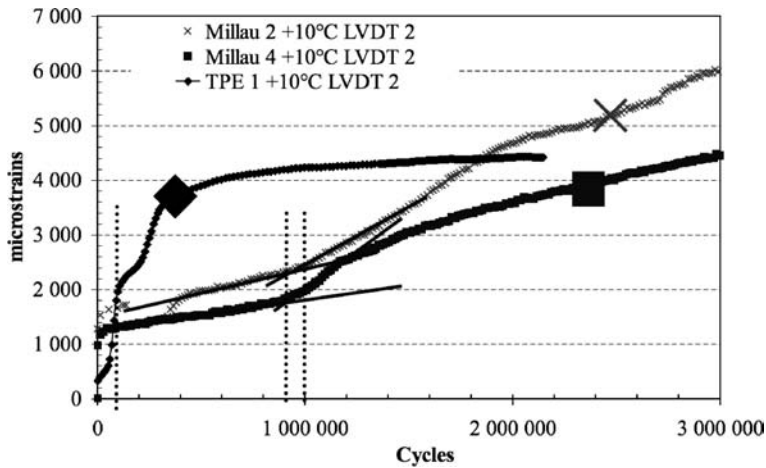


Figure 6. Strain amplitude evolutions throughout the FPBT from LVDT 2 measurements on the upper face of specimens at +10°C.

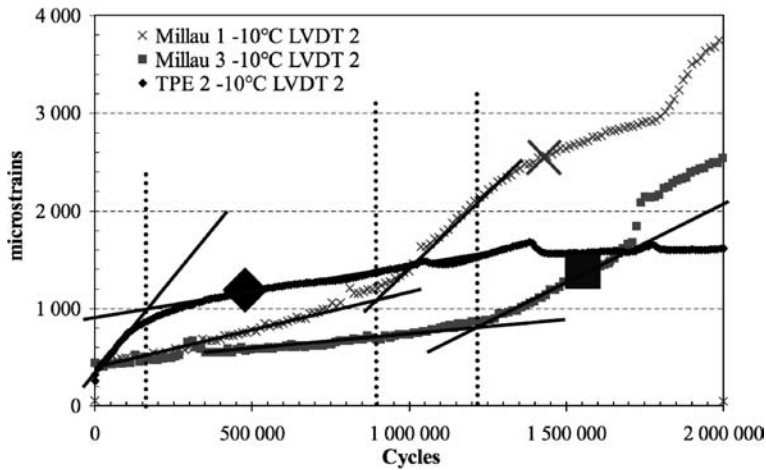


Figure 7. Strain amplitude evolutions throughout the FPBT from LVDT 2 measurements on the upper face of specimens at -10°C.

Table 2. Number of cycles when a sudden variation in strains occurs.

Asphalt mix formulation		Temperature	
		-10°C	+10°C
Millau asphalt:	test 1	900,000	900,000
	test 2	1,200,000	1,000,000
"classic" road asphalt:		200,000	100,000

tests based on ultrasonic wave propagation will confirmed this method. Results are consistent for the same asphalt mixture.

Therefore, for each asphalt layer, cracks appear at an approximate strain of 1500 $\mu\text{m}/\text{m}$ at +10°C and 1000 $\mu\text{m}/\text{m}$ at -10°C. These values could constitute a first step to define a crack criterion, but it will be interesting to test another bituminous mixture to validate this break threshold. This criterion could also depend on bituminous mixture.

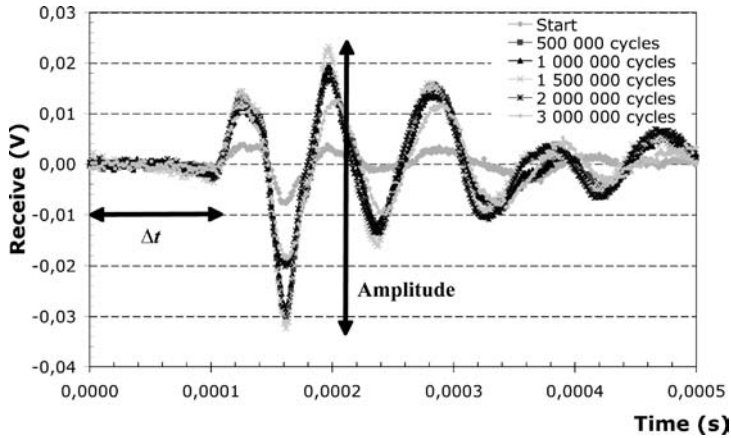


Figure 8. Oscilloscope capture of S-wave propagation throughout the FPBT over 3 million load cycles at +10°C.

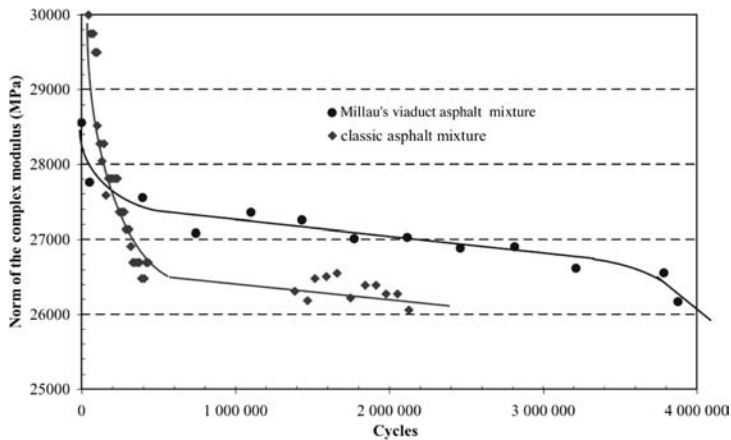


Figure 9. Norm of the complex modulus calculated from P-wave velocities and their damping by inverse analysis throughout the FPBT performed on two asphalt mixtures at +10°C.

3.2 Ultrasonic wave propagation results

From the S-wave propagation results in Figure 8, the signals show a characteristic decrease in amplitude as the number of load cycles increases. Thus attenuation parameters easily provide useful information about the mechanical evolution of the material's characteristics.

An example of such results in Figure 9 shows the mechanical evolution of the asphalt layer through the results of the complex modulus at +10°C from P-wave transducers with the two asphalt concrete mixtures. P-wave and S-wave velocities and their amplitudes decrease clearly as the number of load cycles increases. Then signals stabilize before significant amplitudes decrease.

For the Millau viaduct asphalt mixture, the calculated modulus was about 28,500 MPa at the beginning, and decreased to 27,400 MPa after 800,000 cycles. Then it stabilized up to 3 million cycles before any significant decrease. This last stage revealed the appearance of cracks that were created and propagated as far as the middle of the thickness of the asphalt pavement. In the second case, the decrease appeared throughout the first two hundred thousand cycles as results from LVDT measurements, decreasing from 30,000 MPa to 26,500 MPa.

Wave propagation is therefore an efficient way to compare and to monitor the evolutionary behaviour of different asphalt layers at each instant of the FPBT, and helps damage curve plotting.

4 MODELLING OF THE FIVE-POINT BENDING TEST

A numerical study was initiated to complete the experimental programme. The FPBT was modelled using *COMSOL Multiphysics* software, with 2D structural mechanics and heat transfer models (Comsol 2006).

4.1 The different materials of specimens

The different materials are modelled:

- asphalt concrete: various models exist to describe the viscoelastic behaviour of asphalt concrete. The first step is to define a mechanical modulus that can take account of the fact that the modulus depends on frequency and temperature. So the model called 2S2PID (2 Springs, 2 Parabolics and 1 Dashpot) developed at the ENTPE laboratory is used (Olard 2003). Seven parameters are necessary to correctly describe the complete mechanical behaviour of the material. These parameters are deduced from an experimental complex modulus test on cylindrical specimens. The thermo-physical characteristics such as thermal conductivity λ and heat capacity C_p are determined. The mathematical model for heat transfer by conduction is the heat equation in which a heat source term is integrated that can be linked to the viscous energy dissipated into heat throughout the fatigue test (Comsol 2006, Arnaud & Houel 2007a). Thus, we obtain a thermal and mechanical mathematic model of asphalt concrete. Nevertheless, it had been shown that temperature effects are insufficient to simulate fatigue tests. Modelling must be completed with a damage law that means that the complex modulus decreases slowly in an irreversible way (Piau 1989).
- steel: it is considered as an elastic medium with a Young's modulus of 200,000 MPa.
- sealing sheet: it contains a large percentage of bitumen. So it is the same kind of material as asphalt concrete. The Eiffage TP [public works] central laboratory carried out complex modulus tests on this material (Héritier et al. 2005).

4.2 Geometry and boundary conditions

The geometry of tested specimens with the same thicknesses is implemented in the finite elements software sample (Fig. 10). A 2D plane strain model is used. More information and discussions about the mesh used are given in (Houel 2008). A compression sine load cycle is modelled above the sample as presented in Figure 1. Moreover, each layer is supposed to adhere completely to the adjacent layers.

4.3 Results

Computations presented here were conducted for a fatigue test temperature of $+10^\circ\text{C}$ and show preliminary results. Figure 11 shows horizontal strains in the asphalt layer. It can be seen that strains are generated at the asphalt layer surface over the central web over $130\ \mu\text{m}/\text{m}$ at the beginning of the FPBT. They are more significant than in experimental tests that do not take account of the flexion of the specimen. Moreover, the surface texture of the asphalt layer produces increased

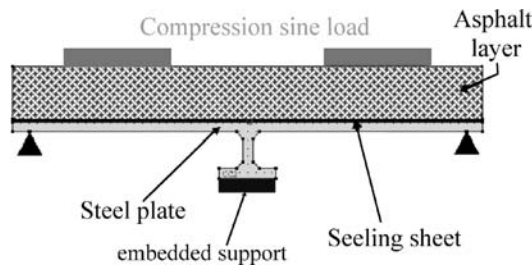


Figure 10. Geometry and boundary conditions of a specimen in COMSOL software.

strain amplitudes. Figure 12 adds that strains are not linear in the thickness of the asphalt layer. As regards these large strains, it will be appropriate to take into account viscous effects of bituminous concrete. Thanks to the heat equation implanted in the model the increase in asphalt temperature reported in Figure 13a can be seen. Actually, in experimental fatigue tests it is difficult to measure an increase in temperature, but it agrees with computations that give an increase in temperature of only 0.05°C in the centre of the layer surface. Moreover the damage law enables the increase in strains at the layer surface to be calculated and as a consequence the decrease in modulus (cf. Figure 13b).

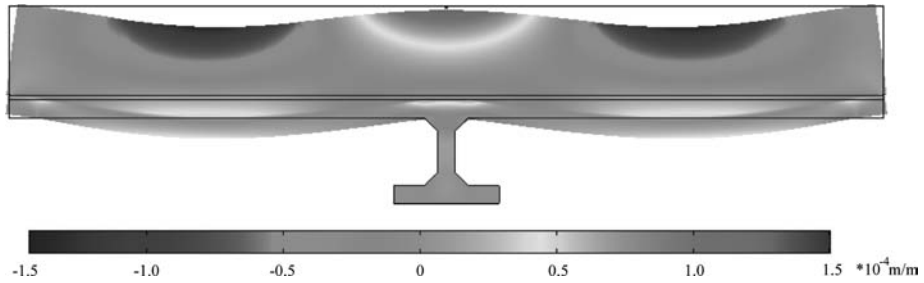


Figure 11. Results of horizontal microstrains in the specimen of the FPBT at +10°C using Comsol software.

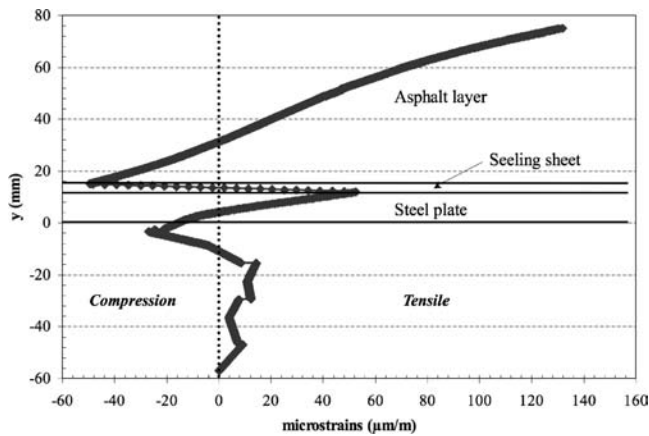


Figure 12. Results of horizontal microstrains in the thickness of the specimens at the beginning of the FPBT at +10°C using Comsol software.

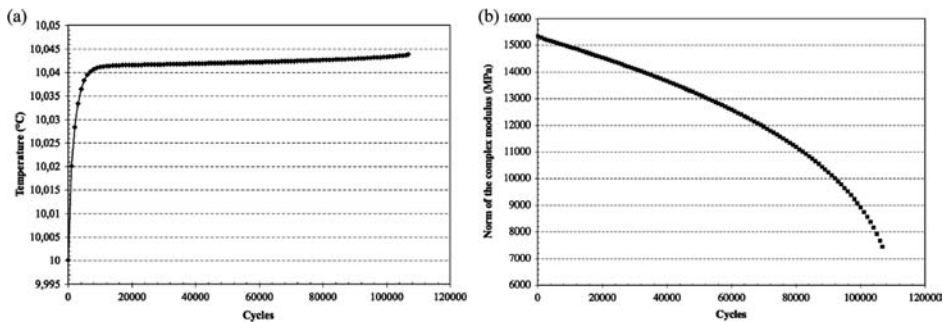


Figure 13. (a) Increase in temperature and (b) decrease in modulus at the centre and at the asphalt layer surface throughout an FPBT at +10°C using Comsol software.

For the moment, values of different parameters of the fatigue law are very sensitive and must be specified with more accuracy. Nevertheless, these preliminary results are very encouraging.

5 CONCLUSIONS

A special design is necessary for asphalt pavements on steel orthotropic decks, because asphalt is subjected to very severe strains due to vehicle traffic and the flexibility of steel structures. The FPBT solves this issue. In this paper, it is shown that:

- Ultrasonic wave propagation can be used to monitor the evolutionary intrinsic mechanical characteristics of the material. From wave velocity measurements and damping coefficients the complex modulus is calculated at each instant during the test and the damage evolution curve can be plotted as a function of the material.
- Strain measurements at the asphalt layer surface by means of displacement sensors make it possible to detect the appearance of fatigue cracks. From these measurements a break threshold is proposed at $+10^{\circ}\text{C}$ and -10°C .
- A preliminary modelling is also proposed and enables the damage area where cracks are likely to appear to be located. It is very encouraging: it takes account of viscoelastic components of asphalt medium, heating in asphalt because of mechanical loads, and a fatigue law.

REFERENCES

- AFNOR 2006. Méthodes d'essai sur banc de fatigue en flexion sous moment négatif. Détermination de la résistance en fatigue d'une étanchéité/roulement sur tôle métallique, Essais relatifs aux chaussées – Produits d'étanchéité pour ouvrages d'art, French standard method (NF P 98–286).
- Arnaud L. & Houel A. 2006. "Fatigue damage and cracking of asphalt pavement on orthotropic steel bridge deck", *Transportation Research Board Annual meeting Compendium of Papers CD-ROM*, Washington D.C.
- Arnaud L. & Houel A. 2007a. Modélisation thermomécanique des enrobés bitumineux lors de l'essai de flexion sous moment négatif, *8ème Colloque National en Calcul des Structures*, vol. 2, pp. 185–191, Giens, France. Hermes Science Publications et Lavoisier. ISBN 978-2-7462-1823-9.
- Arnaud L. & Houel A. 2007b. Fatigue damage of asphalt pavement on an orthotropic bridge deck: mechanical monitoring with ultrasonic wave propagation. *International Journal of Road Materials and Pavement Design*, vol. 8-3.
- Comsol Multiphysics 2006. Comsol Reference manual.
- Hameau G., Puch C. & Ajour A.-M. 1981. Comportement à la fatigue en flexion sous moment négatif, *Bulletin de liaison des Ponts et Chaussées*, no. 111.
- Hauwaert A. V., Thimus J.-F. & Delannay F. 1998. Use of ultrasonics to follow crack growth. *Ultrasonics*, no. 36: 209–217.
- Héritier B., Olard F., Saubot M. & Krafft S. 2005. Design of a specific bituminous surfacing for orthotropic steel bridge decks: application to the Millau viaduct, *7th Symposium on Bearing Capacity of Roads, Railways and Airfields*, Trondheim, Norway.
- Houel A. 2004. Comportement à la fatigue et fissuration mécanique des enrobés bitumineux sur dalle orthotrope, Master recherche génie civil, Ecole doctorale MEGA-ENTPE, France.
- Houel A. & Arnaud L. 2007. Damage characterization of asphalt concrete specimens by ultrasonic P and S-wave propagation in laboratory. *Advanced Characterization of Pavement and Soil Engineering Materials*. Loizos, Scarpas & Al-Qadi eds. Taylor & Francis Group, London, ISBN 978-0-415-44882-6.
- Houel A. 2008. Endommagement et fissuration mécanique des enrobés bitumineux sur dalle orthotrope. Thèse de doctorat. Ecole doctorale MEGA-ENTPE, Lyon, France. To be published.
- Laajili H. 2003. Caractérisation des enrobés bitumineux comme couche de roulement sur tabliers d'ouvrage d'art métallique, Master recherche génie civil, Ecole doctorale MEGA-ENTPE, France.
- Olard F. 2003. Comportement thermomécanique des enrobés bitumineux à basses températures. Relations entre les propriétés du liant et de l'enrobé. Thèse de doctorat. Ecole doctorale MEGA-ENTPE, Lyon, France.
- Piau J.-M. 1989. Modélisation thermomécanique du comportement des enrobés bitumineux. *Bulletin de liaison des Ponts et Chaussées*, no. 163.
- Somda A. R. 2007. Revêtement de tablier de pont métallique: caractérisation et dimensionnement lors d'essai de fatigue, Master génie civil, Ecole doctorale MEGA-ENTPE, France.

FE evaluation of 4-point bending test for fatigue cracking assessment

M. Coni & S. Portas

University of Cagliari, Cagliari, Italy

R. Isola

Nottingham Transportation Engineering Centre, University of Nottingham, Nottingham, UK

J.R.M. Oliveira

University of Minho, Guimarães, Portugal

ABSTRACT: Fatigue lives of asphalt mixtures are, in general, significantly affected by the test method and mode of loading. Previous studies have evaluated the different commonly used test methods on the base of their simplicity, ability to simulate test conditions and applicability of the test results to pavement design against fatigue cracking. From this point of view, the tests based on the principle of simple flexure are commonly preferred. Amongst these, the four-point bending test (also known as third point flexure test) was focused where, unlike other tests, the failure of the specimen occurs in an area of uniform bending moment.

Loading conditions, testing set-up and internal stresses or strains imposed by clamps at the load or reaction points are all factors that are found to influence the specimen response to the test. In this study, a detailed FEM analysis of the structure and geometry of a four-point bending frame, designed at the Nottingham Transportation Engineering Centre (NTEC) of the University of Nottingham, was performed, describing how geometric constraints and dynamic actions can affect the estimation of the fatigue life of asphalt prismatic specimens with various stiffnesses.

In conclusion, the dominating causes of imprecision in the tests results are outlined and the main issues that should be taken into consideration during the design and optimization of this non-standardized equipment are indicated.

1 INTRODUCTION

In a recent interlaboratory campaign organised by RILEM 182-PEB Technical committee “Performance testing and evaluation of bituminous materials”, 11 different test methods, comprising uniaxial tension/compression, 2-, 3- and four-point bending and indirect tension tests, were utilised in order to investigate fatigue characteristics of a dense graded asphalt concrete mixture (Di Benedetto et al., 2003; Di Benedetto et al., 2004). In that study, it was concluded that fatigue lives are significantly affected by the test method. Amongst the test methods studied, the Indirect Tension Test showed the shortest life duration, which, according to the authors, is probably caused by significant accumulation of permanent deformation in addition to fatigue damage. It was also the only test to be carried out in load control, which usually means a shorter fatigue life. Load conditions and testing set-up, together with sample size, were pointed out as the main reasons for the differences in fatigue life obtained for different beam tests.

2 REVIEW OF FATIGUE TEST EQUIPMENT

Rao Tangella et al. (1990) carried out a research programme with the purpose of reviewing various fatigue test methods and recommending the most appropriate method for defining the fatigue

response of asphalt-concrete mixtures. The repeated flexure test received the highest ranking. Several pieces of equipment have been used worldwide to assess the fatigue characteristics of bituminous mixtures, using the simple flexure principle. Most of those recently developed (Tayebali et al., 1994a; Pelgröm, 2000) comprise a four-point bending (4PB) frame (Figure 1).

The results of any fatigue test are influenced by the mode of loading, which can be classified into two different test categories: controlled-stress (or load) and controlled-strain (or displacement). Failure (or the number of cycles to failure) in fatigue testing has been defined in various ways and sometimes arbitrarily, and the value cited depends on the mode of loading (Al-Khateeb and Shenoy, 2004). In controlled-stress tests, some researchers have defined failure as the complete fracture of the specimen at the end of the test (Pell and Cooper, 1975; Tayebali et al., 1992). In order to protect the instrumentation (e.g., LVDTs) a practical limit was suggested by Rowe (1993), which defined failure at 90% reduction of initial stiffness, at which point the specimen displayed large cracks. Regarding controlled-strain tests, failure of the specimens is more difficult to define, since the stresses within the specimen decrease during the test, as the specimens gets progressively weaker due to the accumulation of damage, and total failure of the specimen is unlikely to occur. Several researchers have considered failure of the specimen when its stiffness value has reduced to half of the initial value (Tayebali et al., 1992; Tayebali et al., 1993; Di Benedetto et al., 2004). Van Dijk (1975) and Van Dijk and Visser (1977) have suggested that the dissipated energy approach allows results of different types of tests, carried out under different test conditions with several types of asphalt mixes, to be described by a single mix-specific relationship that relates the number of cycles to failure to the cumulative dissipated energy. Rowe (1993) suggested a new concept related to crack initiation instead of traditional failure of the specimen. Ghuzlan and Carpenter (2000) used a failure criterion based on the change in dissipated energy (ΔDE) between two consecutive cycles. Kim et al. (1997) introduced the 50% reduction in pseudo stiffness as a failure criterion for fatigue testing, which was assumed to be independent of the mode of loading. Al-Khateeb and Shenoy (2004) proposed a new failure criterion based only on the observation of raw data collected during a fatigue test. A fatigue test carried out in controlled-stress can be expressed by a basic relationship between the number of cycles to failure and the stress level used in the test, as presented in Equation 1 (Pell and Taylor, 1969; Tayebali et al., 1994b).

$$N_f = a \left(\frac{1}{\sigma_t} \right)^b \quad (1)$$

where N_f = fatigue life; σ_t = applied tensile stress; a , b = laboratory determined constants. However, according to Rao Tangella et al. (1990), early fatigue research found that fatigue life of bituminous mixtures was often better correlated with tensile strains than with tensile stresses, and that the basic failure relationship could be characterized as in Equation 2. Pell and Taylor (1969) have suggested a similar relationship for the estimation of fatigue in base courses.

$$N_f = c \left(\frac{1}{\varepsilon_t} \right)^d \quad (2)$$

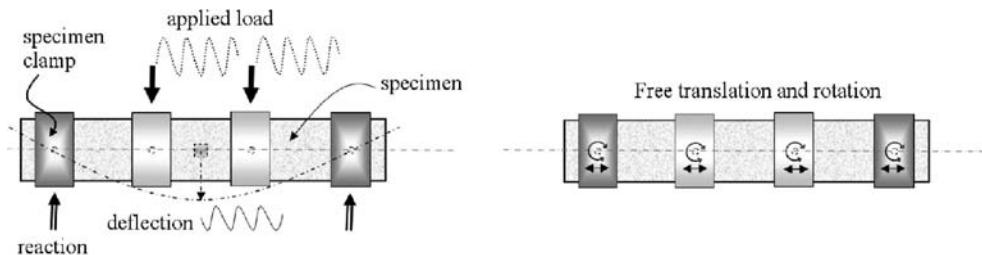


Figure 1. Loading scheme of the specimens in a four-point bending test.

where N_f = fatigue life; ε_t = applied initial tensile strain (in load controlled tests); c, d = constants determined from laboratory testing. In an attempt to account for differences sometimes observed in the fatigue relationship between life and strain, as loading frequency and temperature vary, a mixture stiffness term can be added to Equation 2 as shown in Equation 3 (Monismith et al., 1985).

$$N_f = c \left(\frac{1}{\varepsilon_t} \right)^d \left(\frac{1}{S_0} \right)^e \quad (3)$$

where N_f = number of tensile strain, ε_t , applications to failure; c, d, e = constants determined from laboratory testing; S_0 = initial stiffness modulus of the asphalt mixture. Based on laboratory test data presented in the form of Equation 3, several models have been proposed to predict the fatigue lives (Shell 1978).

3 THE 4PB EQUIPMENT

Taking the aforementioned into consideration, Oliveira (2006) develop a new equipment to study the fatigue response of grouted macadam mixtures using the principle of simple flexure. Among the available methods, the 4PB test was chosen, since the failure of the specimen in this type of test occurs in an area of uniform bending moment. 4PB also avoids the need to glue the specimen to an end plate, as in the cantilever bending test, which can delay the test set up. The dimensions of the specimens to be tested dictated the dimensions of the frame. It was decided to use prismatic specimens (beams) sawn from slabs, which were produced in the laboratory using a roller compactor. The dimensions of the slabs obtained from this process were restricted to 305 mm, which defined, the maximum dimension of the beam. The other dimensions were selected as 50 × 50 (mm). The 4PB rig was then manufactured with 90 mm between each load and reaction point (270 mm total span). This piece of equipment was not designed to allow horizontal movement at the loading and reaction points. However, due to the type of ball bearings chosen, a small amount of lateral movement was detected after construction of the equipment, which was taken into consideration in the calibration process. Lateral movement is necessary to prevent internal stresses developing in the specimen due to end restraints. In order to connect the frame to the testing machine used (Figure 2), special pieces were designed and manufactured to fit the existing actuator and reaction plate. The 4PB rig was also designed taking into account the use of one LVDT, in order to measure the vertical movement at the neutral axis of the specimen and to control the test when using the controlled-strain mode of loading. Figure 2 shows also the 4PB rig obtained from this design process. The bitumen percentage was of 4.1% with the addition of cellulose fibres. The specimens have been prepared with two different types of modified bitumen: SBS and PEN50. Figure 2 reports the grading curves used.

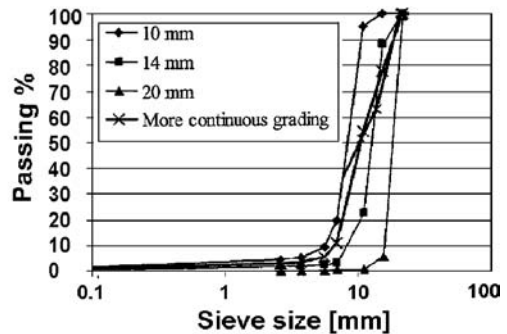
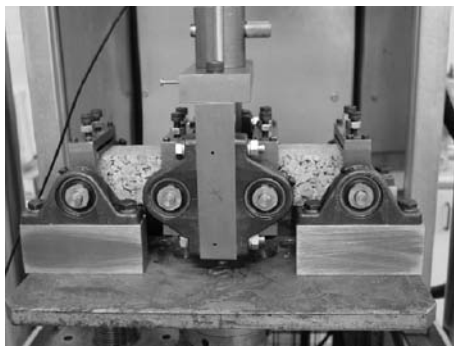


Figure 2. Testing machine to be used in the four-point bending tests and grading curves.

4 TESTS PERFORMED WITH THE EQUIPMENT

Scatter in the results of fatigue tests is unavoidable (Di Benedetto et al., 2004) and it is important to test as many specimens of the same mixture as is practicable. Too few specimens may not represent adequately the mixture behaviour and too many specimens would take too much effort and time to be tested, as well as a large amount of material. According to Ghuzlan and Carpenter (2000), at least four specimens must be tested to establish a representative fatigue curve. In Oliveira's (2006) study, a minimum of five specimens per mixture were used for the stiffness and fatigue tests. 4PB tests were carried out in strain (displacement) control and it was necessary to determine the deflection of the central part of the specimen equivalent to a specific strain level (maximum strain applied at the outer fibre of the beam), which was obtained based on Equations 4 and 5. Both bending and shear deformation of the beam were considered in the calculations.

$$\sigma_t = \frac{P \cdot l}{b \cdot h^2} \quad (4)$$

$$\varepsilon_t = \frac{108 \cdot \delta \cdot h}{23 \cdot l^2 + 36 \cdot h^2 \cdot (l + \nu)} \quad (5)$$

where σ_t = tensile stress (Pa); P = load amplitude applied on specimen (N) = $P/2$ on each loading point; l = beam span (m); b = beam width (m); h = beam height (m); ε_t = applied tensile strain (m/m); δ = beam deflection at neutral axis (m); ν = Poisson's ratio. Based on these relationships, the complex modulus, E (Pa) can be calculated for each cycle of the test, dividing the maximum stress by the maximum strain (Equation 6).

$$E = \frac{\sigma_0}{\varepsilon_0} \quad (6)$$

In the stiffness tests, 100 cycles were used to determine the stiffness modulus of the material, considered as the average of the values obtained for each cycle. The phase angle, ϕ (deg) was obtained based on the dissipated energy, which was computed, for each cycle, as the area within the stress-strain hysteresis loop. The phase angle was, therefore, obtained from the relationship:

$$w_i = 0.25 \cdot \pi \cdot \varepsilon_i^2 \cdot E_i \cdot \sin(\phi_i) \quad (7)$$

where w_i = energy dissipated at cycle i ; ε_i = peak to peak strain at cycle i ; E_i = stiffness modulus at cycle i ; ϕ = phase angle between stress and strain at cycle i . For each specimen, the testing procedure included a stiffness test at 5 Hz, followed by a similar test at 10 Hz and concluded with a fatigue test at the desired strain (displacement) level, also at 10 Hz. The main testing programme was carried out at 20°C, but some tests were also carried out at 0 and 5°C.

5 FINITE ELEMENT ANALYSIS

The FE model (Figure 3) considers, apart from the prismatic specimen, also the loading and constraint system, with the steel in direct contact with the specimen in the upper side.

The FE simulation reproduces the boundary conditions that the specimen is subjected to in the 4PB device. To better simulate these boundary conditions, the presence of a 2 mm lateral gap has been considered in order to allow movement without steel-specimen friction. The mesh used is based on a regular three-dimensional square grid with elements of 5 mm. In total, 7040 3D elements have been used to model the standard specimen, while for the rest of the steel parts 416 elements of the same kind were necessary. Finally, forces and constraints were applied directly on steel chassis. Number of elements could change for different models developed in parametric analysis. The FE package ANSYS was available to perform all FE simulations. The library element SOLID45

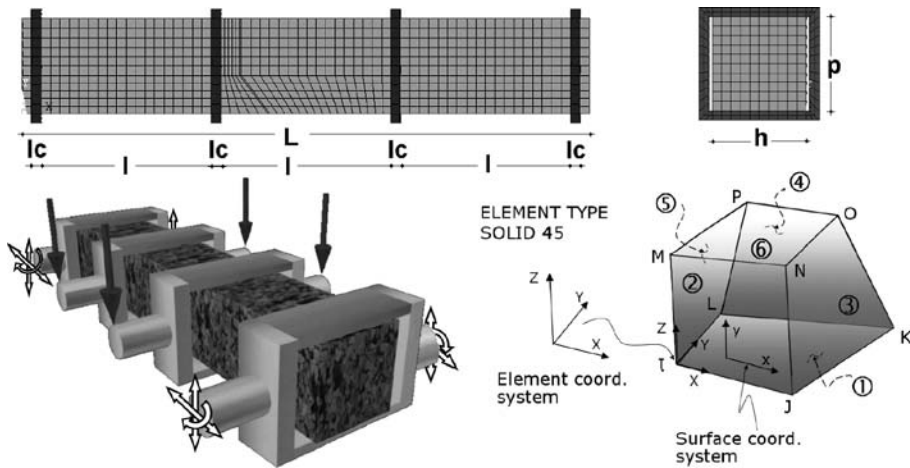


Figure 3. Mesh and type of element used in 4PB test FE model.

was used. It was developed for modelling three-dimensional solid structures, and also allows the input of different material characteristics. After static simulation, modal and harmonic analysis was carried. A constant equivalent viscous damping ratio was introduced in the material during dynamic simulation. In the analyses forced vibration excitation was applied with a sinusoidal forces applied on the model. The system is governed by the expression:

$$[M] \{\ddot{u}\} + [C] \{\dot{u}\} + [K] \{u\} = \{F\} \quad (8)$$

where:

$[M]$ = structure mass matrix	$\{u\}$ = nodal displacement vector
$[C]$ = structure damping matrix	$\{\dot{u}\}$ = nodal velocity vector
$[K]$ = structure stiffness matrix	$\{\ddot{u}\}$ = nodal acceleration vector.
$\{F\}$ = time-dependent forcing function	

Structural damping was included only in harmonic analysis. Modal analysis is used to determine the natural frequency and mode shapes of a structure, with free and undamped vibrations. A modal analysis should precede any other dynamic analysis. The governing equation then is:

$$[M] \{\ddot{u}\} + [K] \{u\} = \{0\} \quad (9)$$

For a linear system, free vibration will be a harmonic of the form, $\{u\} = \{u_0\} \cos \omega t$. For the non-trivial solution, the determinant must be equal zero. This is an eigenvalue problem, whose solutions are the eigenvalues and the corresponding eigenvectors. The eigenvalues represent the natural frequency of the system and the eigenvectors the corresponding mode shapes. Harmonic analysis is used to determine the response of a structure to harmonic sinusoidally varying forces. The function $F(t)$ is a periodic value of known amplitude and frequency. The equation of motion, therefore, can be solved to obtain displacements as a function of frequency. The model calibration has been conducted comparing the results obtained from the simulations with a previous experimental study on the fatigue of grouted macadam mixtures. In the previous study a series of tests were carried out in strain control at 10 and 5 Hz, at the temperature of 20°C. Strain controlled tests are normally stopped after the stiffness modulus of the specimen has been reduced to half of its initial value, but observations made by Oliveira (2006) on the shape of the stiffness reduction curve of grouted macadam suggested non conventional fatigue performance. Figure 4 shows the reduction of the Stiffness Modulus, E , as a function of number of loading cycles and of strain level. To each value of this reduction is also associated the stress level and the value of stiffness modulus.

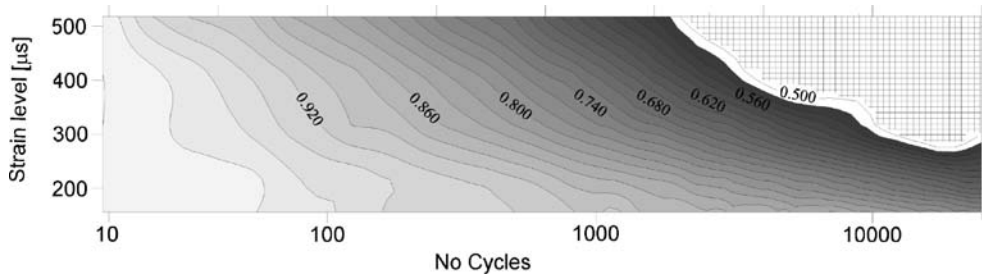


Figure 4. Stiffness modulus reduction obtained in the tests as a function of number of cycles.

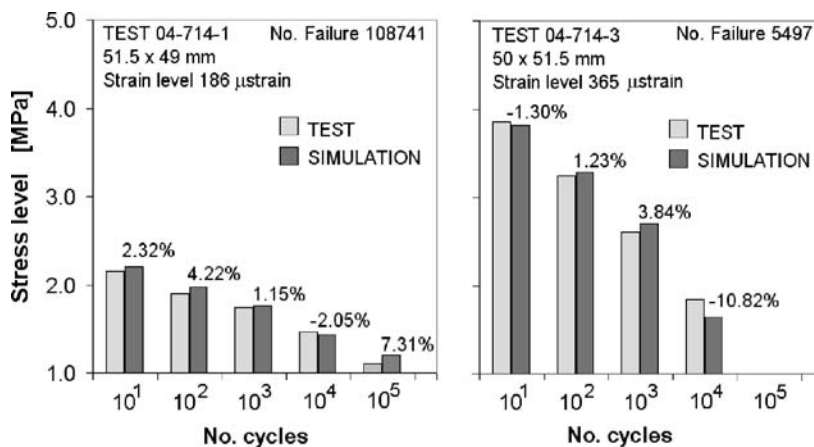


Figure 5. Comparison between experimental and simulated results.

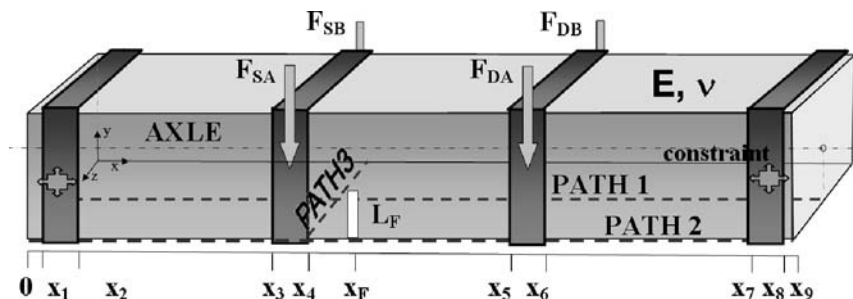


Figure 6. Parameters considered in the FEM model.

On the basis of these tests it has been possible to validate the FE model in every stage of the fatigue test. The calibration phase has been carried out considering the situation of absence of cracks and of linear material behaviour. For each deformation state and cycles number, in the FEM analysis was introduced a value of E derived from Figure 6. The values of s and d obtained in the simulation have been compared to those obtained from equations (4) and (5), therefore within the model was introduced cycle by cycle the experimental evolution of E . This way it has not been necessary to employ complicated constitutive models to describe the damage process. In Figure 5, a comparison between experimental and simulated results for tests performed at two different strain levels is shown.

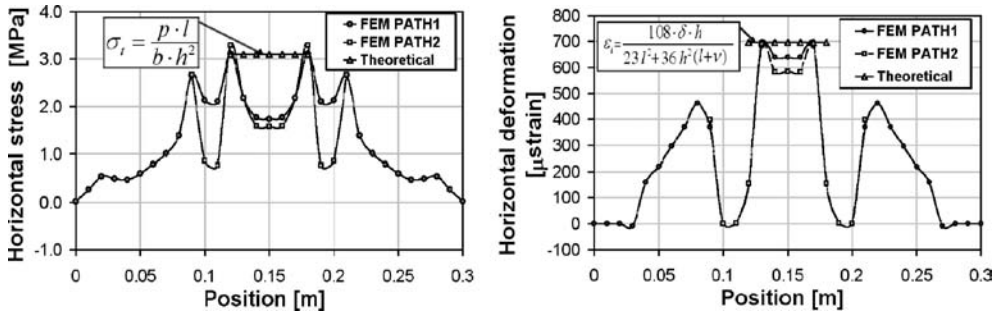


Figure 7. Variation of stress and strain trough the bottom median line of the beam.

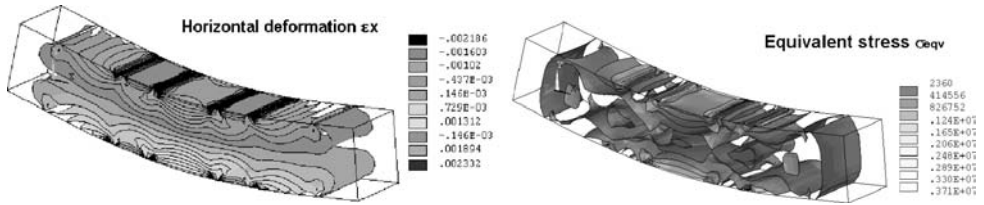


Figure 8. Stress and strain distribution within the beam.

As can be observed, the FE model results are much more accurate in determining stresses at low number of load cycles than high number, when the damage affect linear behaviour of the materials. In this case errors of up to 10% were obtained. After this stage, a parametric analysis of the model has been conducted varying material characteristics, geometry, loads and constraints. Moreover the possible presence of a crack was considered so that it would be able to significantly modify the model's response and its overall symmetry.

6 RESULTS

The results analysis evidences remarkable differences between the FEM results and what was expected from Equations 4 and 5 for the evaluation of stresses and strains within the beam specimen. Figure 7 shows the comparison between horizontal stresses evaluated by Equation 4 and the results of the FE simulation. In the position of the loading points two peaks are evident that define a median sector of the specimen with constant lower stresses. Similar behaviour is observed for the horizontal strains, but with less difference between the values. In the graphs, the peaks were deliberately given the maximum values estimated by Equations 4 and 5. In relation to these values, the reduction of stress and strain in the specimen central part is of 56.0% and 83.5%, respectively.

The FE analysis is evidencing a much more complex stress (strain) distribution than what is traditionally assumed for the 4PB test. Figure 8 shows how in the specimen's initial and final sections this distribution is very heterogeneous, while the central part is subjected to higher stresses and strains distributed more homogeneously.

A detailed analysis of the central sector shows conspicuous differences also in the transversal direction. On the bottom side of this area (PATH2), values 10.3% higher than in the median line (PATH1) take place. Such trend can explain the origin of the cracks observed during the experimental tests. The simplistic hypothesis of constant stress and strain in the bottom face of the central sector would imply an even probability of crack initiation. This is not in accordance with the experimental evidence that reports the formation of cracks mainly at about 5–10 mm from the loading points. While propagating (see Figure 9), these cracks substantially modify the specimen's

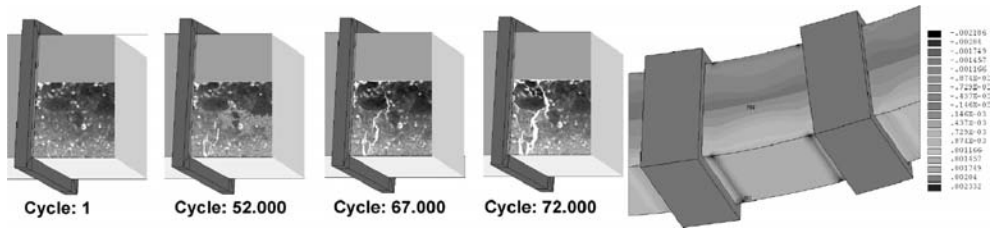


Figure 9. Crack growth and horizontal deformations peak.

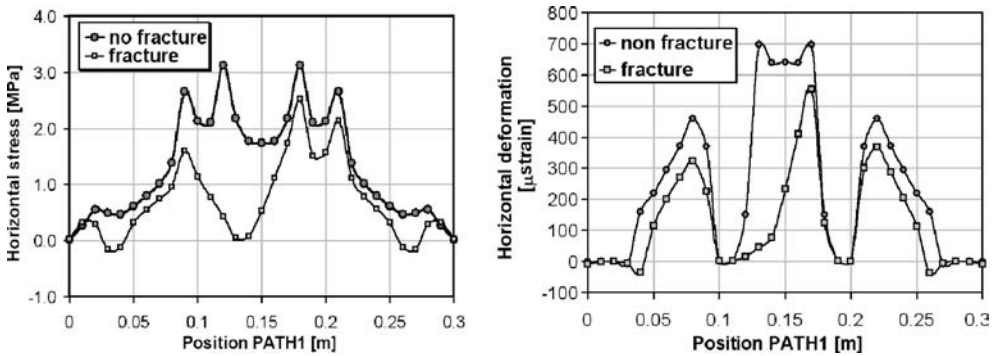


Figure 10. Comparison between an intact and a cracked specimen (PATH1).

geometric configuration and, therefore, the subsequent stress and strain distribution. The evaluation of stresses and strains and of the stiffness modulus has, then, to be reconsidered after the crack initiation as the specimen's reacting section is decreased.

It can be observed (Figure 10) that the specimen's central sector is not anymore characterised by uniform distributions. Strains decrease of 73.8% in the middle of PATH1 with respect to the value without crack. Obviously, the stress state increase dramatically in PATHs different from those considered, particularly in those that pass through the vertex of the crack. The areas adjacent the crack are unloaded but a reduction of 20.4% is noted also close to the loading point. The obvious conclusion is that LVDT measurements taken when a crack occurs induce an artificial evaluation of the strain state in the central sector of the beam, supplying, at most, an estimated average.

The results of the parametric analysis indicate a particularly stable behaviour of the equipment in presence of small imprecision of the lateral constraints placement. For movements of these points of less than 2.0 mm, the maximum central displacement and stress have reported a change less than 3%. When the loading points are not accurately positioned (2 mm of the left) the vertical displacement varies very little and, as a consequence, so does the strain level estimated by Equation 4. On the contrary, the FEM analysis shows that, even if the vertical displacement remains almost unaltered in the middle, the strain peaks on the loading points change. Their trend, now asymmetric, is 19.3% higher in the moved loading point (Figure 11).

A reduced planarity of the specimen's faces determines very little changes in the results. The mechanic parameter that rules the specimen's response is the stiffness modulus E , while the Poisson's ratio is of little importance. Going from $\nu = 0.32$ to $\nu = 0.47$ the strains decrease of less than 3%. It is interesting to observe how the model's response is particularly sensible to the width of the loading points and of the constraints at the end of the beam (Figure 12). When their dimension varies from 30.0 to 10.0 mm the deflections increase of 57.8% while stresses and strains in the middle area change of less than 5%. In the peaks, the stresses increase of 20.1%.

For the same resultant but with forces on the left loading point 15% higher than those on the right loading point the values of deflections, stress and strain remain unaltered. When the unbalance

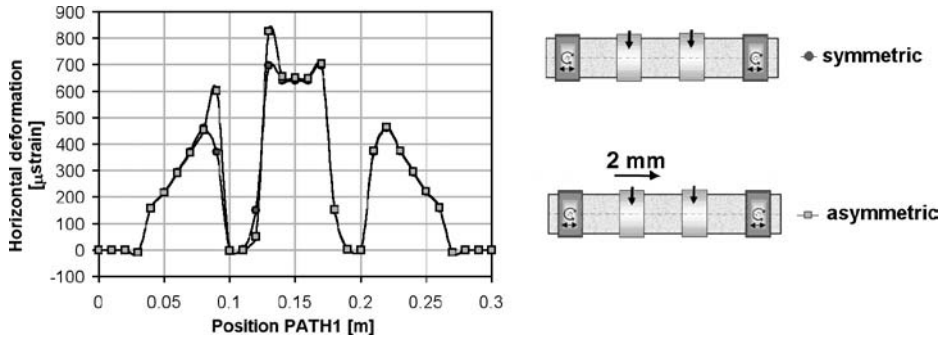


Figure 11. Horizontal deformations under the hypothesis of the movement of the left loading point towards the centre.

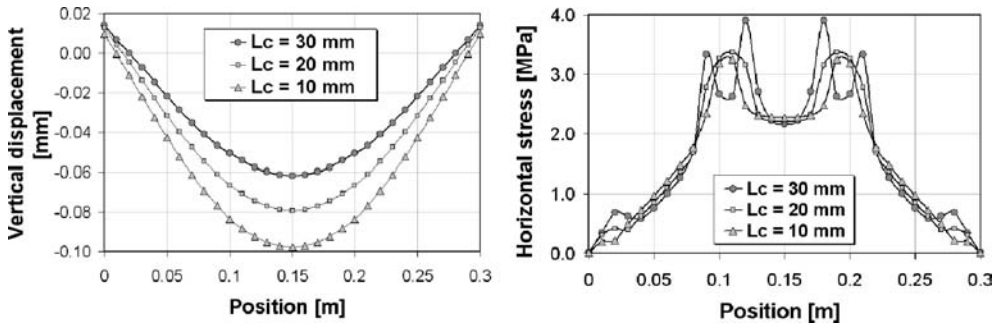


Figure 12. Effects of change of width of loading and constraint points.

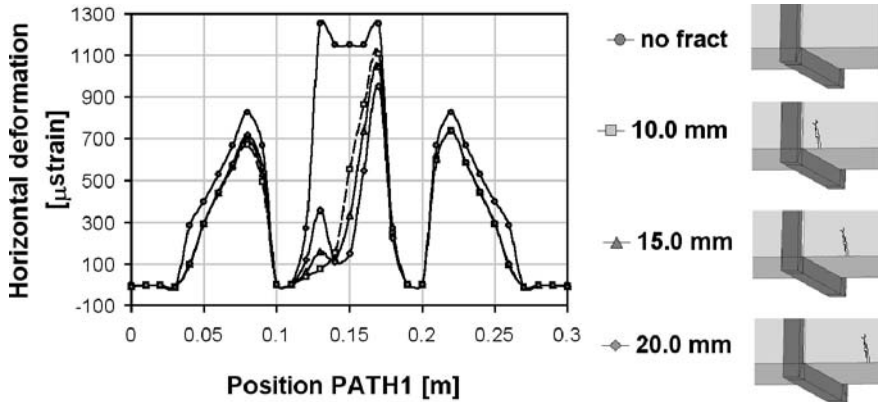


Figure 13. Values of strain for different crack position.

is in the transversal direction, torsion takes place that, in the FE model, does not affect sensibly the tenso-deformative components considered. As for the crack, the deflections increase of 45% independently of its position (5.0, 10.0 and 15.0 mm from the loading point). The stresses in the middle point decrease when the crack initiates far from the loading point. At 20 mm and 10 mm they are reduced by 24.1% and 11.6% respectively (see Figure 13).

The length of the crack also influences the specimen's response. In relation to the FE intact model, it is noted in the middle point the deflections double for a crack length of 25 mm. The

strains reduce their value to 71.7%, 18.3% and 12.6% of the original value respectively for crack length of 5 mm, 15 mm and 25 mm.

7 CONCLUSION

In the UK, the Indirect Tensile Fatigue Test (ITFT) is routinely used to determine the fatigue life of bituminous materials. However, the test does not represent the actual flexure of a pavement layer, under a moving wheel. Therefore, a four-point bending apparatus have been developed, as presented in this paper, in order to carry out a comprehensive study on its fundamental characteristics (i.e., geometry, material, asymmetric condition in loads and constraints, etc.) and consequence on estimated fatigue life. The analysis revealed significant discrepancies between the FEM simulation and the relationships used to calculate stresses and strains within the 4PB beam specimen. The FEM analysis shows much more complex distributions than traditionally accepted. Both stresses and strains in the central part of the specimen are uniformly distributed only in the case of absence of cracks, although even in this situation considerable differences remain in the transversal direction. Moreover, the FE results show peak values of stresses and strains nearby the loading points. This could explain the origin of the cracks observed during the experimental tests. The simplistic hypothesis of constant stress and strain in the bottom face of the central sector, on which Equations 4 and 5 are based, is not in accordance with the experimental evidence. The crack initiation substantially modifies the specimen geometric configuration and, therefore, the consequent stress and strain distribution, therefore their evaluation (and the estimation of E) by Equations 4, 5 and 6 has to be reinterpreted. From what was shown, it appears that the LVDT readings on the beam's neutral axis, especially when a crack occurs, should be reinforced and that they could induce an artificial evaluation of the deformational state in the beam's central part. The parametric analysis demonstrated a stable response of the 4PB to small irregularities in the position of the constraints and in the faces planarity. This also happens for force unbalances not larger than 10–15%. On the other hand, the width of loading and constraint points was found to be important.

On the basis of these, it is clear the need to supply a more robust theoretical background of the real meaning of the test as a function of its geometrical variables, together with its standardisation.

ACKNOWLEDGMENT

A kind thanks goes to Dr Zoorob and Dr Thom of the Nottingham Centre for Transportation Engineering, University of Nottingham, UK, for their availability.

REFERENCES

- Al-Khateeb, G. & Shenoy, A. 2004. A distinctive fatigue failure criterion. *Journal of the Association of Asphalt Paving Technologists* 73: 585–622.
- Di Benedetto, H., De La Roche, C., Baaj, H., Pronk, A. & Lundström, R. 2003. Fatigue bituminous mixture: different approaches and RILEM group contribution, *6th RILEM Symposium on Performance Testing and Evaluation of Bituminous Materials*. Zurich, Switzerland.
- Di Benedetto, H., De La Roche, C., Baaj, H., Pronk, A. & Lundström, R. 2004. Fatigue bituminous mixture: different approaches and RILEM group contribution, *RILEM TC 182-PEB Materials a Structures* 37: 202–216.
- Ghuzlan, K.A. & Carpenter, S. 2000. Energy-derived, damage based failure criterion for fatigue testing. *Transportation Research Record* 1723: 141–149. Washington, DC.
- Kim, Y.R., Lee, H.J. & Little, D.N. 1997. Fatigue characterization of asphalt concrete using viscoelasticity and continuum damage theory. *Journal of the Association of Asphalt Paving Technologists* 66: 520–569.
- Monismith, C. L., Epps, J. A., & Finn, F. N. 1985. Improved asphalt mix design. *Proceedings, Association of Asphalt Paving Technologists*, vol. 54, February.
- Oliveira, J.R.M. 2006. Grouted Macadam: Material characterization for pavement design. *PhD Thesis, University of Nottingham, United Kingdom*.

- Pelgröm, L.J.W. 2000. Engineering mechanical properties Densiasphalt. *Report prepared for Densit a/s by KOAC-WMD*. Aalborg, Denmark.
- Pell, P.S. & Copper, K.E. 1975. The effects of testing and mix variables on the fatigue performance of bituminous materials. *Journal of the Association of Asphalt Paving Technologists* 44: 1–37.
- Pell, P.S. & Taylor, I.F. 1969. Asphaltic road materials in fatigue. *Journal of the Association of Asphalt Paving Technologists* 38: 371–422.
- Rao Tangella, S.C.S., Craus, J., Deacon, J.A. & Monismith, C.L. 1990. Summary report on fatigue response of asphalt mixtures. *Prepared for Strategic Highway Research Program, Project A003-A, Institute of Transportation Studies, University of Carolina*. Berkeley, Carolina.
- Rowe, G.M. 1993. Performance of asphalt mixtures in the trapezoidal fatigue test. *Journal of the Association of Asphalt Paving Technologists* 62: 344–384.
- SHELL 1978. “Shell pavement design manual. Asphalt pavement and overlays for road traffic”. *Shell International Petroleum Company Limited, London*.
- Tayebali, A.A., Rowe, G.M., & Sousa, J.B. 1992. Fatigue response of asphalt-aggregate mixture. *Journal of the Association of Asphalt Paving Technologists* 61: 333–360.
- Tayebali, A.A., Deacon, J.A., Coplantz, J.S., Finn, F.N. & Monismith, C.L. 1993. Modelling fatigue response of asphalt-aggregate mixes. *Journal of the Association of Asphalt Paving Technologists* 62: 385–421.
- Tayebali, A.A., Deacon, J.A., Coplantz, J.S., Finn, F.N. & Monismith, C.L. 1994a. Fatigue response of asphalt-aggregate mixes – Part II – Extended test program. *SHRP-A-404A Strategic Highway Research Program, National Research Council*. Washington, DC.
- Tayebali, A.A., Deacon, J.A., Coplantz, J.S., Finn, F.N. & Monismith, C.L. 1994b. Fatigue response of asphalt-aggregate mixes – Part I – Extended test program. *SHRP-A-404A Strategic Highway Research Program, National Research Council*. Washington, DC.
- Van Dijk, W. 1975. Practical characterization of bituminous mixes. *Journal of the Association of Asphalt Paving Technologists* 44: 38–74.
- Van Dijk, W. & Visser, W. 1977. The energy approach to fatigue for pavement design. *Journal of the Association of Asphalt Paving Technologists* 46: 1–40.

Investigation of cracking in bituminous mixtures with a 4 points bending test

M.L. Nguyen, C. Sauzeat & H. Di Benedetto
ENTPE, Vaulx-en-Velin, France

L. Wendling
CETE Lyon – Laboratoire Régional d'Autun, Autun, France

ABSTRACT: The fracture behavior was investigated for two asphalt mixtures, one with pure bitumen and one with polymer modified bitumen. For this study, a four-point bending notched fracture (FPBNF) test, which has been designed at ENTPE (France), was used. Different displacements were measured on the notched beam specimen (deflection of the beam, crack mouth opening displacement-CMOD, displacements above the supports . . .). The crack length was also determined with crack propagation gauges. Cyclic or monotonic loading paths are applied. Classical analyses are made within the framework of linear elastic fracture mechanics. The fracture toughness is then evaluated with different methods, based on the measurement of the crack length. An improved approach to calculate the crack length is also presented. It relies on inverse analysis with FEM calculation of two displacements recorded during the test: crack mouth opening displacement and deflection of the beam. This new approach allows taking into account the viscoelastic properties of the mixtures.

Keywords: bituminous mixtures, crack propagation, fracture toughness, four-point bending notched fracture test.

1 INTRODUCTION

Cracking is one of the major distresses in asphalt pavements. The main causes of cracking include the road traffic (fatigue cracking . . .), and the climatic conditions (low temperature and temperature cycling). This work deals with the cracking at rather low temperatures.

Fracture mechanics concepts have been applied in recent studies to the fracture behavior of bituminous materials (reviewed in Gauthier & Anderson, 2006). This paper presents part of a study where linear fracture mechanics (LFM) theory is applied to asphalt mixture. A four-point bending notched fracture (FPBNF) test, which has been designed at the ENTPE/DGCB laboratory in Lyon (France), was used. The principle of FPBNF test is presented in Figure 1. It differs from the single edge notched beam (SENB) test (three points bending) which has been widely used in the literature to determine fracture properties of asphalt mixtures (Kim & El Hussein, 1997, Artamendi & Khalid, 2004, Wendling et al., 2004). The main difference between the FPBNF test and the SENB test is that a constant moment field is created in the middle part of the beam. Moreover, in (Artamendi & Khalid, 2006), the authors also presented a comparison between SENB tests and semi-circular bending (SCB) fracture tests for mixtures. The SCB test is also used in other researches (Molenaar & Molenaar, 2000, Marasteanu et al., 2002, Li & Marasteanu, 2005). Another fracture test is the disk-shaped compact tension (DC(T)) test which has been developed as a practical method for obtaining the fracture energy of asphalt concrete (Wagoner et al., 2005). One of the main advantage of the SCB and the DC(T) geometries is that cores obtained directly

from the pavement or gyratory-compacted specimens can be used to make specimens for the tests. However, there has been no major reported work on FPBNF test.

In this paper, the different measurements on the specimen and the description of the FPBNF test are first detailed. Experimental campaign is then presented including tested material, specimen preparation and examples of cyclic loading test results. Analyses are realized on determination of crack length and the fracture toughness parameter which is based on linear elastic fracture mechanics (LEFM) hypothesis. An improved approach to calculate the crack length is also presented. It allows taking into account the viscoelastic properties of the mixtures.

2 PRESENTATION OF THE FOUR POINTS BENDING NOTCHED FRACTURE TEST

Cracking in bituminous mixtures is investigated with a four points bending test which has been designed at ENTPE (Figure 1). Tested specimens are pre-notched prismatic bars 55 cm long, 7 cm high and 6.5 cm wide. A 2 cm high initial notch is made in the middle of the beam. The specimen preparation and the way to create the notch are presented in the next section (3.1).

A servo-hydraulic machine is used to perform the tests. The displacement of the piston (measured by an integrated transducer) is used as the feedback signal, for the considered tests. However any other sensors may be used to monitor the test (crack opening or other). Monotonic tests as well as loading-unloading cycles are applied. A 50 kN load cell equips the press and measures the applied load (P).

In order to control the temperature, a thermal chamber is used. The big size of the specimen imposes to use a specifically designed chamber. The temperature inside the chamber may be regulated from -50°C to 80°C . A thermal gauge is fixed on the specimen to measure its surface temperature.

Three linear variable differential transducers (LVDT) are used to measure displacements on top of the beam: deflection in the centre of the beam, LVDT2, and both displacements at the vertical of the two lower supports, LVDT1 and LVDT3 (see Figure 1). The measurement range of the used LVDTs is 5 cm. Taking into account the punching effect of the lower supports into the beam, the “true” deflection of the beam, called f , is obtained by:

$$f = LVDT2 - \frac{LVDT1 + LVDT3}{2} \quad (1)$$

The displacement of the upper support applying the load is also measured by the LVDT integrated in the piston of the press. An extensometer is used to measure the crack opening displacement (COD) at the notch. It is placed under the beam (see Figure 1).

The most important measurement in such test is certainly the crack length. In order to follow the crack propagation, cracking gauges are also used. These gauges are constituted of 21 parallel wires

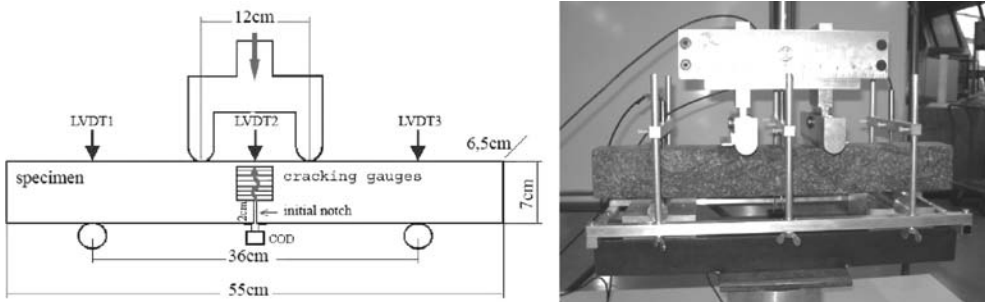


Figure 1. Four points bending notched fracture (FPBNF) test at ENTPE.

separated each other by 2.5 mm, which are supposed to break the ones after the others, in order to indicate the crack propagation. The used gauges are 8 cm long and about 5 cm high. Two gauges are glued on each lateral faces of the specimen, so that the first wire of each is just over the initial notch. The way to obtain the crack length from these gauges is detailed further (see section 4.1).

3 EXPERIMENTAL CAMPAIGN

3.1 Materials and specimen preparation

Two asphalt mixtures were investigated in this study, called “BBC” according to the French classification (NFP98-133, 1991). They have the same type of aggregate (from “La Noubleau” quarry (Maguet, 2005)) and same grading 0/6 mm. The first one is made with pure bitumen (35/50 pen grade) and the second one is made with polymer modified bitumen (Styrelf 13/40). The binder content is the same, 6.85% by dry weight of aggregates.

Tests were carried out on specimens obtained from three slabs: PA and PB (P for pure binder 35/50) and ME (M for binder modified with the polymers Styrelf 13/40), as indicated in Table 1. The specimens were provided by the “Laboratoire Régional des Ponts et Chaussées” of Autun (France). The slabs were compacted with LPC wheel compactor (NFP98-250-2, 1997). The dimensions of each slab are 59.5 × 39.5 × 12 cm. Each slab was sawn to provide 5 specimens of 55 × 6.5 × 7 cm (Figure 2). The edge of the slabs were eliminated to obtain more homogeneous specimens, having well-distributed voids. The tested materials and test conditions are summarized, in Table 1.

As the energy needed to initiate and propagate crack is very dependent on the initial notch, great care was taken to create it. The 2 cm notch was performed in two steps. Firstly, a circular saw was used to obtain a 1.5 cm deep and 5 mm wide notch. Then the notch was ended carefully by hand with a hacksaw. Thus, at the bottom, the notch is about 1 mm wide.

3.2 Experimental campaign and results

Fifteen specimens from three slabs (PA, PB and ME) of two asphalt mixtures were tested (see Table 1). The displacement rate of the piston was fixed at 1 mm/mn for loading or unloading. Temperature remains constant during all tests, at -5°C.

Table 1. Tested materials and test conditions.

Slab	No. of sample	Bitumen	% binder	Material	Temperature test	Displacement rate
PA	1; 2; 3; 4; 5	pure 35/50	6.85	BBC 0/6	-5°C	1 mm/min
PB	1; 2; 3; 4; 5	pure 35/50	6.85	BBC 0/6	-5°C	1 mm/min
ME	1; 2; 3; 4; 5	PMB Styrelf 13/40	6.85	BBC 0/6	-5°C	1 mm/min

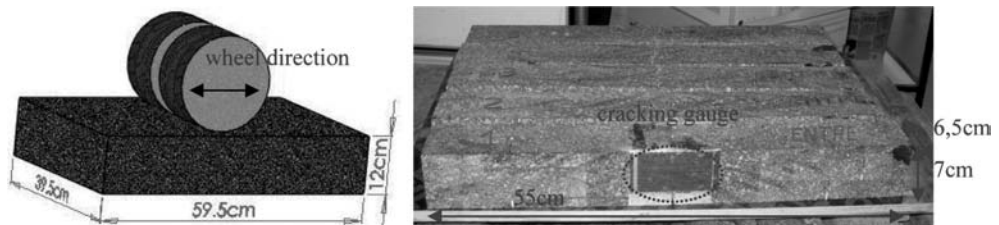


Figure 2. (left): slab from LPC wheel compactor; (right): specimens sawn from the slab (left) (orientation is conserved).

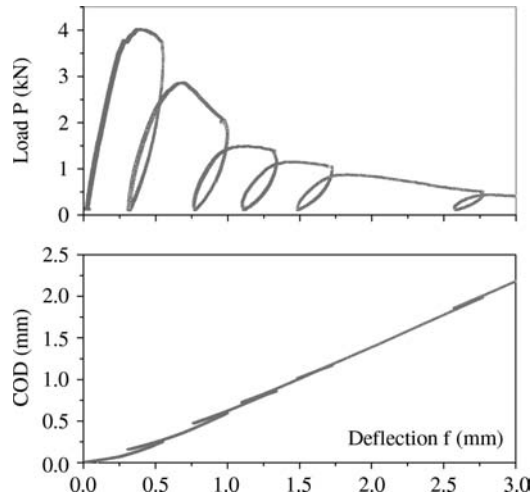


Figure 3. Typical load – deflection curve, and COD – deflection curve of FPBNF test with cyclic loadings (test ME1). Here, deflection f is calculated according to equation (1) (cf. section 2).

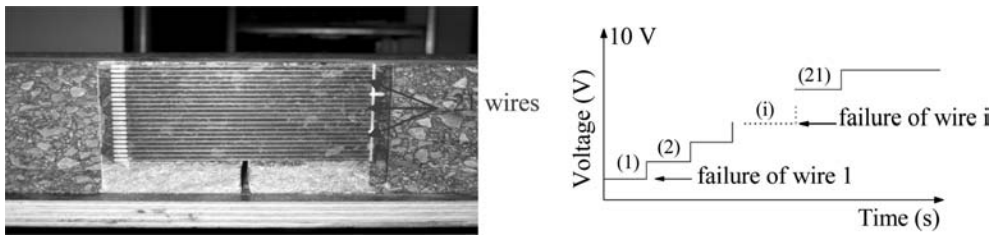


Figure 4. (left): cracking gauges glued on the specimen; and (right): typical measured voltage–time curve.

During the test on specimen PA1, only a monotonic loading was applied until the final failure. For the fourteen other tests, some unloading/reloading cycles were applied. The beam was unloaded down to a load very close to 0 kN then reloaded, both at constant displacement rate.

The results obtained for specimen ME1 (PMB mixture) are presented in Figure 3. Monotonic loading was applied until the peak load, and then some unloading/loading cycles were applied.

In this paper, analyses focus on the methods to determine the crack length. Due to the lack of space, complete analyze of the whole tests campaign is not presented (cf. Sauzéat et al., 2006).

4 DETERMINATION OF CRACK LENGTH

4.1 Measurement of crack length using cracking gauges

Two cracking gauges were glued on lateral faces of the specimen, as shown on Figure 4 (left), to measure crack propagation. This measurement device has been applied in many studies (Lemaistre, 1998, Jiang et al., 2004, Wendling et al., 2004).

As one gauge is used on each side of the specimen, two different crack length values are obtained, noted a_{gauge1} and a_{gauge2} . Results given by the two gauges are plotted in Figure 7, for test ME1 already chosen in Figure 3. As shown in Figure 7, some differences appear between the two values: a_{gauge1} and a_{gauge2} . The crack length is slightly different on each side and may also have a different evolution inside the beam (quicker or slower than on each side).

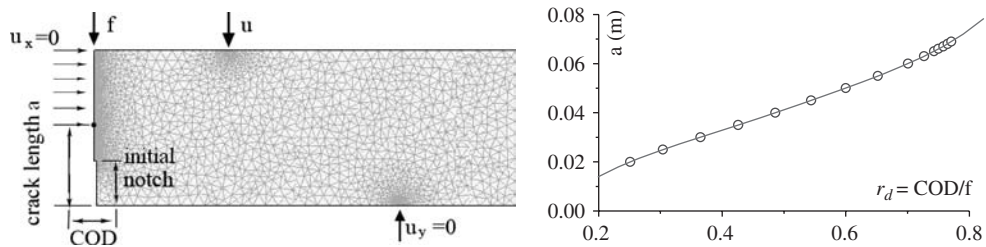


Figure 5. (left): model used in FEM calculation; (right): r_d value calculated by FEM (eq. 2) function of a .

One of the drawback of this method is that the detection of the crack may be delayed due to the strength deformation of the gauge wires. Macro-cracks having a minimal width only may be detected. Figure 7 shows that the detected macro-crack appears after the peak of the load-deflection curve. Damage occurring before the peak load is not observed and needs another method to be detected.

4.2 New proposed approach to estimate crack length

A new approach is presented here to calculate crack length during the test. Our method is based on the relationship between two measured displacements: *COD* and deflection of the beam, f (see section 3). It is named thereafter “Displacement ratio method for predicting crack length” (DRCL) in order to simplify the notation. The ratio between *COD* and deflection f is called r_d :

$$r_d = \frac{COD}{f} \quad (2)$$

This method relies firstly on experimental observation. As shown in Figure 3, the relation between *COD* and f during tests may be analyzed. The reloading part of the unloading/reloading cycles can be assimilated to a line. By extrapolation, the obtained line passes through the origin, as shown in Figure 6. A linear viscoelastic behavior, without propagation of the crack during this reloading period, can then reasonably be assumed for the mixture.

The second part of the method relies on FEM calculation. A calculation is made in order to determine the displacements field in the beam during the test. Considering the boundary conditions imposed on the beam (Figure 5 left), it can be shown that the displacements field is the same for an elastic or a viscoelastic material. It is independent on the modulus of the material.

The code FEMLAB was used for the calculation, which is described in details in (Nguyen, 2005). This calculation is based on the hypothesis of isotropic linear elastic behavior. This calculation is repeated for different values of crack length a , in order to obtain the displacement ratio r_d (eq. 2) as a function of a (Figure 5 right).

The last part of the method consists in linking the ratio r_d determined from measurements with the crack length a , thanks to the calculation. This may be done at the different points where the unloading/reloading cycles are realized.

It has to be underlined that this method can also be applied if no cycle is performed. In that case, a crack length is calculated for all the points of the monotonic curve: *COD* in function of f (Figure 6 right). Then, the crack length evolution is obtained during the whole monotonic loading test.

4.3 Comparison of crack length obtained by the different methods

The different methods to obtain the crack length are exposed in the previous section. The Table 2 presents the notation that will be used to call the different obtained crack length.

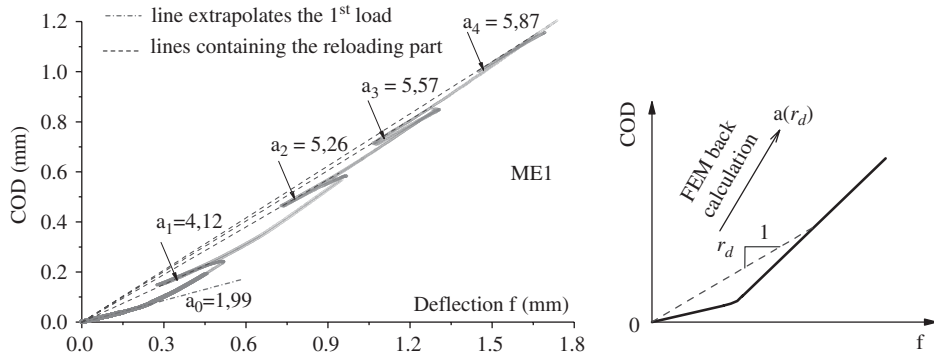


Figure 6. Calculation of the crack lengths “ a_i ” thanks to the displacement ratios r_d determined from the COD-f curve (test ME1). (left): Curve with cyclic loadings; (right): monotonic loading. The values of a_i are in centimeters.

Table 2. Crack length “a” determinations.

a_{gauge}	Obtained from the 2 cracking gauges (failure of different wires) (Figure 4)
$a(r_d)$	Obtained by FEM back calculation from COD-f curve corresponding to the monotonic loading curve (Figure 5, Figure 6)
a_0	Obtained by FEM back calculation from the initial part of the loading curve (Figure 6 left)
a_i	Obtained by FEM back calculation from the reloading part of the cycle n° i (Figure 6 left)

Figure 7 presents a comparison of the crack length obtained by two different methods: $a(r_d)$ and a_{gauge} (see Table 2) for the ME1 test (same test as presented in Figure 3 and in Figure 6). In Figure 7, the evolution of crack length calculated by the DRCL method $a(r_d)$ is rather close to the evolution of crack length obtained experimentally by the cracking gauges system ($a_{\text{gauge}1}$ and $a_{\text{gauge}2}$). A difference can be noted at the beginning of test.

The DRCL method enables to obtain the crack length before propagation, which corresponds to the initial notch length. At the beginning of the curve: the deflection f increases, but the crack length $a(r_d)$ remains constant, equal to a_0 . This first value a_0 is indicated in Figure 6 and its value is 1.99 cm. It corresponds to the length of the initial notch created manually in the beam (see section 3.1). The very good agreement between a_0 (1.99 cm) and initial notch depth (2 cm) proves the relevance of our proposed method.

The main difference between $a(r_d)$ and a_{gauge} is a shift in the initial part. The DRCL method predicts crack existence before the detection by the cracking gauges. The start of calculated $a(r_d)$ propagation (point A in Figure 7) appears clearly before load P reaches its peak value (point B in Figure 7). Furthermore, the cracking gauges detect the propagation start (points C1 and C2 in Figure 7) after this peak value (point B in Figure 7). This phenomenon has already been observed by other authors (Lemaître, 1998), who used the same measurement devices. This delay is due to the possible elongation of the wire before it cracks. A calculation is proposed to investigate this issue in the next section (4.4).

The fact that the calculated crack ($a(r_d)$) propagates before the peak of the load value can be explained when considering the formulated hypothesis: linear material (elastic or viscoelastic) and respect the linear fracture mechanics (LFM). In reality it is well admitted before crack propagation, a phase of initiation (or starting) exists during which no apparent degradation is “visible” (cf. Di Benedetto & Corté, 2005). Only micro-cracks develop. Some studies show that damage occurs before the crack propagation (Simonin, 2000, Wendling et al., 2004). As no damage is considered in our calculation, the calculated crack tip is then situated inside this damage zone.

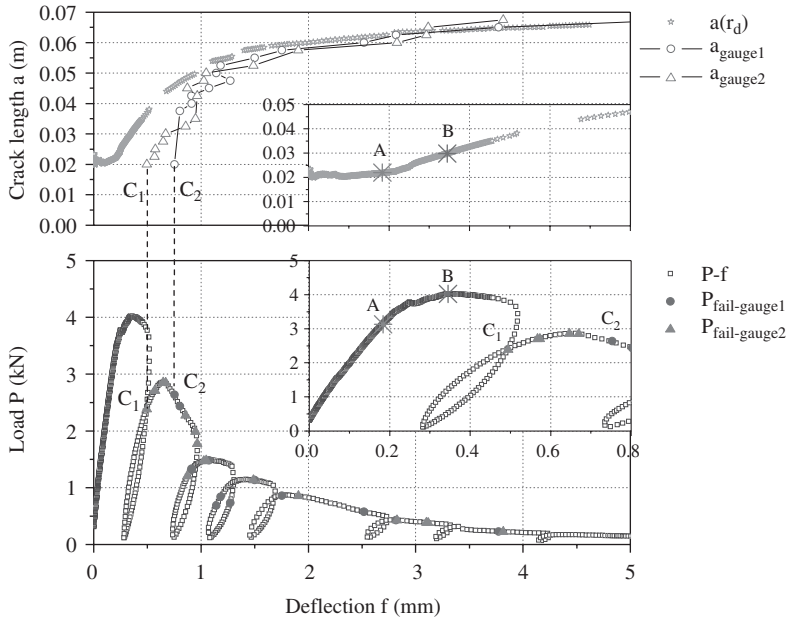


Figure 7. (above): crack length determined by measurement and calculation in function of deflection of the beam [cycles are not considered], and (below): load-deflection curve (test ME1). (above): $a(r_d)$: crack length calculated from the COD- f envelope curve by the DRCL method; a_{gauge1} , a_{gauge2} : crack lengths measured by cracking gauges 1 and 2 respectively; and (below): P-f: experimental load – deflection curve; $P_{\text{fail-gauge1}}$, $P_{\text{fail-gauge2}}$: points located on the load – deflection curve where a wire fails for gauge1 and gauge2 respectively.

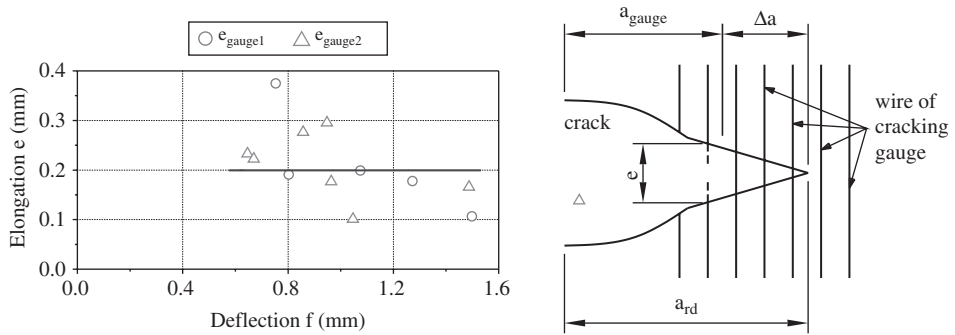


Figure 8. FEM back calculation of elongation of the wires of cracking gauges when they fail (test ME1).

4.4 Calculation of the elongation of the cracking gauge wire when it breaks

In the previous sections, we pointed out an elongation existing before a wire of cracking gauge is cut off. It is possible to estimate this elongation with a FEM calculation. As described in Figure 8, for each measurement of crack length obtained by the gauge, a_{gauge} , it is possible to determine a crack length $a(r_d)$ by the back calculation explained before. Assuming that this crack length defines the bottom of the crack, FEM calculation enables to calculate the crack opening displacement, where the gauge wire is cut off (the distance from the bottom of the crack is given by $a(r_d) - a_{\text{gauge}}$). This displacement corresponds to the elongation of the wire gauge (noted e), when considering the

postulated hypothesis. Figure 8 presents the results of the elongations of cracking gauges wires for test ME1. A value of 0.2 mm could be considered.

5 FRACTURE TOUGHNESS K_{IC}

The fracture toughness is a classical parameter used to evaluate material performance and resistance regarding cracking. It requires the accurate knowledge of crack length.

Considering a linear elastic behavior, the critical stress intensity factor or fracture toughness in mode I is calculated, for the four points bending fracture test, by the formula below:

$$K_{IC} = \frac{3}{2} \frac{P(L-l)}{B.W^2} Y(x) \sqrt{a} \quad (3)$$

where P = fracture load; $Y(x)$ = geometry factor; L = lower span of the beam; l = upper span of the beam; B = width of the beam; W = height of the beam; a = crack length.

The geometry factor $Y(x)$ is calculated, according to the compliance method (Fantozzi et al., 1988), by the formula:

$$Y(x) = \left(\frac{W}{3(L-l)} \right) \sqrt{\frac{2.E'.B}{x} \frac{dC}{dx}} \quad (4)$$

where $x = a/W$ relative depth of the notch; C = compliance of the sample; $E' = E/(1 - \nu^2)$ with E = Young's modulus; ν = Poisson's ratio.

This geometry factor was calculated with a FEM calculation (Nguyen, 2005). It should be underlined that the geometry factor depends only on geometry of the beam and on Poisson's ratio. It is independent on the Young modulus, which can take any value for FEM calculation.

In this paper, different methods are used to calculate this fracture toughness.

The first method is based on the value a of the initial crack (or notch) length and a value P_Q obtained from the load-deflection curve (Figure 9). The ASTM Standard .ASTM-E399, 2005, developed for the determination of the fracture toughness of metals gives the method to obtain

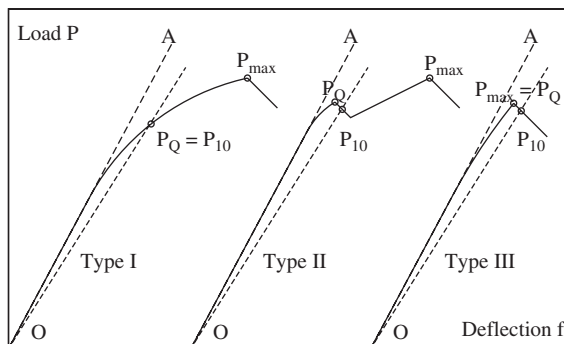


Figure 9. Determination of P_Q according to the slightly modified ASTM standard (ASTM-E399, 2005): First, the secant line OP_{10} is drawn through the origin of the test record with 10% deviation from the initial tangent line OA . If the load at every point on the record which precedes P_{10} is lower than P_{10} , then $P_Q = P_{10}$ (type I); if, however, there is a maximum load preceding P_{10} which exceeds it, then this maximum load is P_Q (type II and III). The following limitation is required to ensure of that the LEFM can be used as a first approximation: $P_{max}/P_Q < 1.10$.

the P_Q . According to Molenaar & Molenaar, 2000, to account for the heterogeneity of asphalt specimens, a slightly more tolerant method based on the ASTM Standard was chosen to obtain the value P_Q . This is explained in Figure 9. The value obtain for fracture toughness is noted $K_{IC}(P_Q)$.

A second method considers each of the re-loading periods. The crack length is calculated by the method presented in section 4.2(cf. also Figure 6 left). The values of crack length are called a_i (cf. Table 2) and the associated load values P_{Qi} are determined in the same way than P_Q when considering each reloading curves. The fracture toughness is noted $K_{IC}(a_i)$.

At last, a third determination of the fracture toughness is considered, in using the crack length values $a(r_d)$ (cf. Table 2 and Figure 6 right) which enables to follow continuously the evolution of crack length during tests. The load values (P of equation 3) are directly obtained on the load-deflection curve.

Before the propagation of the initial crack (point A of Figure 7), the parameter is noted $K_I(a)$. As the crack does not propagate $K_I(a)$ is a stress intensity factor but not the critical stress intensity factor (fracture toughness). After the start of propagation, it is noted $K_{IC}(a)$. The great advantage of the method is that it enables to follow the value of fracture toughness continuously during the test (the cycles periods must be eliminated).

Figure 10 presents the values of fracture toughness (K_{IC}) and stress intensity factors (K_I) obtained from different methods as a function of the crack length, for test ME1 already chosen in Figure 3, Figure 6 and Figure 7. The scatter at the end of the test ($a > 0.055$ m) is explained by the heterogeneity of the material. The evolution of K_{IC} at that moment depends strongly on the size of the ligament.

Figure 10 reveals that fracture toughness increases with the crack length. This result has been observed by other authors using different approaches (Marasteanu et al., 2002). The values of $K_{IC}(a)$ vary from about 1.4 to 4 MPa√m for material ME. These values of $K_{IC}(a)$ are higher than the value calculated from the initial notch length and P_Q ($K_{IC}(P_Q) = 1.21$ MPa√m for the same specimen). It is also slightly higher than the values $K_{IC}(a_i)$ obtained from the cycle periods.

Figure 11 presents the fracture toughness $K_{IC}(a)$ and the stress intensity factor $K_I(a)$ as a function of the crack length of one specimen of each other slab PA and PB. The results show that asphalt mixture with polymer modified bitumen has a slightly better fracture resistance, at the studied experimental conditions ($T = -5^\circ\text{C}$, displacement rate = 1 mm/min). This result is confirmed by the obtained values of $K_{IC}(P_Q)$, presented in Table 3.

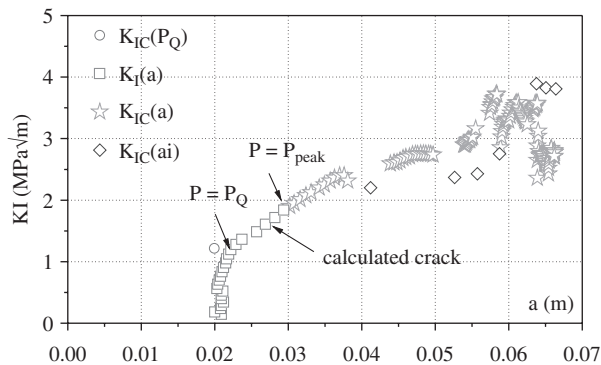


Figure 10. K_{IC} and K_I determined with different approaches (test ME1) : $K_{IC}(P_Q)$: equation (3) with $P = P_Q$ (Figure 9) and $a = a_0 = 1,99$ cm; $K_I(a)$: equation (3) with $P = P_i$ before the peak of the load and $a = a_{rd}$ (Figure 6 right); $K_{IC}(a)$: equation (3) with $P = P_i$ after the peak of the load and $a = a_{rd}$; $K_{IC}(a_i)$: equation (3) with $P = P_{Qi}$ and $a = a_i$ (Figure 6 left).

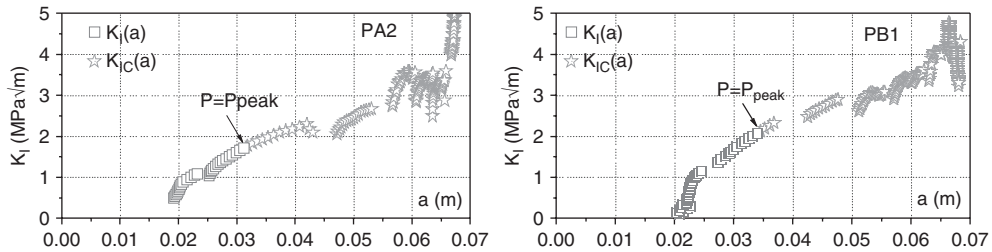


Figure 11. $K_{IC}(a)$ and $K_I(a)$ calculated with the proposed method, of (left): specimen PA2, and (right): specimen PB1.

Table 3. Mean values and standard deviation of $K_{IC}(P_Q)$ of tested asphalt mixtures (Table 1).

No. of slab	PA	PB	ME
$K_{IC}(P_Q)$ (MPa√m)	1.15	1.14	1.23
Standard deviation	0.04	0.08	0.06

6 CONCLUSIONS

The Four Points Bending Notched Fracture Test designed at the ENTPE/DGCB laboratory has been used to study cracking of two bituminous mixtures at low temperature (-5°C).

A new method is used to calculate, from displacement measurements on the beam, the length of the crack in a continuous way during the test. It is compared with direct measurement from cracking gauges. The results show that cracking gauge reacts slightly after the occurrence of the calculated crack considering linear viscoelastic and linear fracture mechanics hypotheses. The elongation of the wire of the crack gauge before failure could be estimated at 0.2 mm.

In fact, the calculated crack length is an equivalent length, which is the sum of the macro-crack and an equivalent crack taking into account the effect of the damaged zone in front of the crack.

Among the 2 tested materials, the mixture composed of polymer modified bitumen has a slightly better resistance than the mixtures made with pure bitumen.

REFERENCES

- Artamendi, I. & H. Khalid. 2004. Fracture characteristics of crumb rubber modified asphalt mixtures. 3rd Eurasphalt & Eurobitume Congress: 1317–1326. Vienna.
- Artamendi, I. & H. Khalid. 2006. A comparison between beam and semi-circular bending fracture tests for asphalt. Road Materials and Pavement Design (EATA 2006): 163–180.
- ASTM Standard E399-05. 2005. Standard Test Method for Linear-Elastic Plane-Strain Fracture Toughness K_{IC} of Metallic Materials. Annual Book of ASTM Standards. Vol. 03.01: 462–495.
- Di Benedetto, H. & J. F. Corté. 2005. Matériaux routiers bitumineux. Vol. 2. Hermes. [in French].
- Fantozzi, G., G. Orange & M. R'Mili. 1988. Rupture des matériaux. Lyon: GEMPPM, INSA. [in French].
- Gauthier, G. & D. A. Anderson. 2006. Fracture mechanics and asphalt binders. Road Materials and Pavement Design (EATA 2006): 9–36.
- Jiang, F., A. Rohatgi, K. S. Vecchio & R. R. Adharapurapu. 2004. Crack length calculation for bend specimens under static and dynamic loading. Engineering Fracture Mechanics, Vol. 71: 1971–1985.
- Kim, K. W. & M. El Hussein. 1997. Variation of fracture toughness of asphalt concrete under low temperatures. Construction and Building Materials, Vol. 11 (Elsevier): 403–411.

- Lemaistre, H. 1998. Etude des propriétés thermomécaniques de divers réfractaires. PhD INSA Lyon. Lyon. 141. [in French]
- Li, X. & M. O. Marasteanu. 2005. The role of temperature and binder type on the fracture resistance of asphalt mixtures at low temperatures. *International Journal of Road Materials and Pavement Design*: 18.
- Maguet, E. 2005. Mélange BBC 0/6 Liants pur, modifié, avec des matériaux de La Noubleau. Rapport LRPC d'Autun. Autun. 53. [in French]
- Marasteanu, M. O., S. Dai, J. F. Labuz & X. Li. 2002. Determining the Low-Temperature Fracture Toughness of Asphalt Mixtures. *Transport Research Record* 1789: 191–199.
- Molenaar, J. M. M. & A. A. A. Molenaar. 2000. Fracture toughness of asphalt in the semi-circular bend test. *Proceedings of the 2nd Eurasphalt & Eurobitume Congress*: 509–517. Barcelona.
- NF P98-133. 1991. Enrobés hydrocarbonés – Couches de roulement : bétons bitumineux cloutés – Définition – Classification – Caractéristiques – Fabrication – Mise en oeuvre. AFNOR Norme française. 13. [in French]
- NF P98-250-2. 1997. Essais relatifs aux chaussées – Préparation des mélanges hydrocarbonés – Partie 2 : compactage des plaques. AFNOR Norme française. 12. [in French]
- Nguyen, M. L. 2005. Etude de la propagation de fissure dans les enrobés bitumineux. Master en Génie Civil ENTPE. Lyon. 140. [in French]
- Sauzéat, C., H. D. Benedetto & M. L. Nguyen. 2006. Etude de la propagation de fissure dans les enrobés bitumineux. Rapport final du contrat : LRPC d'Autun – Laboratoire GéoMatériaux Ecole Nationale des Travaux Publics de l'Etat. 192. [in French]
- Simonin, F. 2000. Comportement thermomécanique de béton réfractaires alumineux contenant du spinelle de magnésium. PhD INSA Lyon. Lyon. 166. [in French]
- Wagoner, M. P., W. G. Buttlar & G. H. Paulino. 2005. Disk-shaped Compact Tension Test for Asphalt Concrete Fracture. *Experimental mechanics*, Vol. 45 (N° 3): 270–277.
- Wendling, L., E. Xolin, D. Gimenez, P. Reynaud, C. De La Roche, J. Chevalier & G. Fantozzi. 2004. Characterisation of crack propagation in butuminous mixtures. Fifth International RILEM Conference on Cracking in Pavements: 639–646. Limoges, FRANCE, RILEM Publications S.A.R.L.

A micromechanics-based computational model and testing protocols to characterize damage-dependent mechanical responses of asphalt mixtures in flexible pavements

Y.-R. Kim

Department of Civil Engineering, University of Nebraska, Lincoln, Nebraska, USA

Felipe, A.C. de Freitas

Stress Engineering Services, Inc., Houston, Texas, USA

D.H. Allen

Department of Engineering Mechanics, University of Nebraska, Lincoln, Nebraska, USA

ABSTRACT: This paper presents a micromechanics-based computational model and testing protocols to characterize damage-associated mechanical responses (such as evolution of microcracks, structural degradation, and fracture failure) of asphalt concrete mixtures in flexible pavements. Based on micromechanics concepts, this approach employs directly-measured material and fracture properties of mixture constituents to predict damage-dependent behaviour of global scale asphalt concrete mixtures. The presented methodology is expected to provide an increase in predictive power and a significant savings in experimental costs and time over traditional phenomenological approaches due to its innovative features including: (1) nonlinear inelastic material behavior, (2) rate-dependent microscale fracture-damage, (3) small-scale material characterization that reduces experimental effort and complexity, and (4) non-destructive image techniques to provide real heterogeneity of asphalt concrete mixtures. Experimental protocols to measure fundamental material properties and fracture-damage characteristics of mixture constituents are introduced, and testing results are presented. Measured mixture constituent properties are then incorporated into constitutive models and micromechanical finite element analyses to ensure that the measured fundamental properties of mixture constituents are key factors controlling overall damage-induced performance of asphaltic composites. The outcomes of this study lead to establishing the linkage between the properties of the mixture constituents, microstructure distribution such as mixture heterogeneity, damage localization, and global structural performance.

1 INTRODUCTION

Fracture damage is a primary cause of failure in asphalt mixtures in flexible pavements. A precise understanding of the fracture damage behavior of asphalt mixtures is required to improve pavement thickness design and hot mix performance evaluation. However, the accurate characterization and evaluation of the fracture damage in asphalt mixtures is challenging because of significant geometric complexity due to aggregates embedded in the mixture and highly nonlinear-inelastic damage evolution phenomena.

Recently, micromechanics-based computational approaches (Buttlar and You 2001; Guddati et al. 2002; Papagiannakis et al. 2002; Birgisson et al. 2004; Dai et al. 2005; Abbas et al. 2007) has been receiving increasing attention from the asphalt materials/mechanics community, because it can separately account for numerous damage modes by considering individual mixture constituents and mixture heterogeneity using microstructural characterization through image analysis techniques.

Even if most computational micromechanics approaches have successfully simulated geometric heterogeneity (i.e., random orientation of irregularly shaped aggregates) and predicted the stiffness reduction due to the damage and fracture of asphalt samples, to the authors' best knowledge, they are somewhat limited to account for damage initiation-evolution due to path- and rate-dependent energy dissipation. In addition, most of the approaches determine damage-dependent properties either by using arbitrary values for simulation purposes only or by *a posteriori* matching of damage evolution characteristics with the laboratory performance testing results from the bulk mixture sample, typically through regression curve fitting. Since the fracture properties are fundamental properties of each mixture constituent, they should be directly identifiable *a priori* by conducting appropriate tests that can characterize constituent-level damage events in asphalt mixtures.

This paper presents a new experimental technique and theoretical modeling concepts based on micromechanics to identify path- and rate-dependent damage evolution characteristics of asphalt mixtures. Successful development of the new testing protocol and the theoretical model is then developed within a fine-mesh finite element model through image analysis techniques to characterize and predict damage dependent material behavior of different asphalt mixtures.

2 MICROMECHANICS-BASED COMPUTATIONAL MODELING

As illustrated in Figure 1, the microstructure of a general asphalt mixture in the pavement surface layer consists of randomly oriented aggregate particles, asphalt binder or mastic surrounding aggregate particles, and entrained air voids. At room temperature or higher, the aggregate particles typically demonstrate linear elastic behavior, while the asphalt binder/mastic phase is subjected to significant damage resulting in nonlinear-inelastic performance of the overall asphalt concrete mixture. Damage exists in the sample in various forms such as cracks and plastic flow, and severity

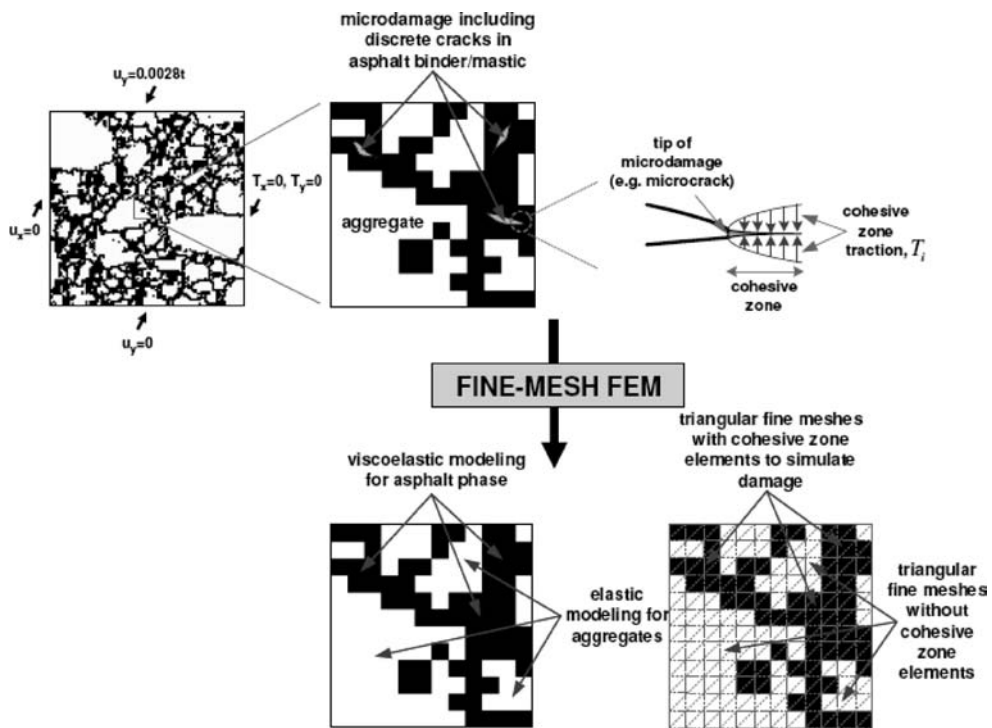


Figure 1. Micromechanics-based computational modeling concept of asphalt concrete mixtures.

and location of the damage depends on stress-strain states developed by applied loading to the sample. Due to the significant geometric complexity and nonlinear-inelastic material response, computational approaches based on the micromechanics concepts have been considered the best option for a realistic simulation of small scale damage and interactions among mixture constituents and their impact on overall structural failure of asphalt concrete mixtures.

2.1 Elastic model for aggregates

The linear elastic constitutive relationship for the aggregate particles can be expressed as:

$$\sigma_{ij}(x_k, t) = C_{ijkl,E} \varepsilon_{kl}(x_k, t) \quad (1)$$

where $\sigma_{ij}(x_k, t)$ = stress as a function of space and time,
 $\varepsilon_{kl}(x_k, t)$ = strain as a function of space and time,
 $C_{ijkl,E}$ = elastic modulus which is not time-dependent,
 x_k = spatial coordinates, and
 t = time of interest.

The time-independent elastic modulus consists of elastic material properties. If the individual particle of aggregates is assumed to follow simply isotropic linear elastic behavior, only two independent material constants among Young's modulus, shear modulus, and Poisson's ratio are required. A Young's modulus of 55.2 GPa and a Poisson's ratio of 0.15 can be reasonably assumed based on a study by Zhou et al. (1995).

2.2 Viscoelastic model for asphalt binder/mastic

The constitutive behavior of the asphalt phase can often be represented by the following linear viscoelastic convolution integral:

$$\sigma_{ij}(x_k, t) = \int_0^t C_{ijkl,VE}(t-\tau) \frac{\partial \varepsilon_{kl}(x_k, \tau)}{\partial \tau} d\tau \quad (2)$$

where $C_{ijkl,VE}(t)$ = linear viscoelastic time-dependent stress relaxation modulus, and
 τ = time-history integration variable.

The linear viscoelastic relaxation modulus of the asphalt phase is determined by performing linear viscoelastic constitutive tests such as static creep/relaxation tests or dynamic frequency sweep tests using the dynamic shear rheometer (DSR). Testing results can be represented by a mathematical form such as a Prony series based on the generalized Maxwell model. The linear viscoelastic stress relaxation modulus by a Prony series can be expressed as

$$C_{ijkl,VE}(t) = C_{ijkl,inf} + \sum_{p=1}^q C_{ijkl,p} \exp\left(-\frac{C_{ijkl,p}}{\eta_{ijkl,p}} t\right) \quad (3)$$

where $C_{ijkl,inf}$ and $C_{ijkl,p}$ = spring constants in the generalized Maxwell model,
 $\eta_{ijkl,p}$ = dashpot constants in the generalized Maxwell model, and
 q = the number of dashpots.

2.3 Nonlinear viscoelastic model for fracture-damage of asphalt phase

Modeling of fracture-damage zone is complex subject particularly for inelastic materials such as asphalt mixtures. The fracture-damage behavior can be modeled in many different ways, and one of the well-known approaches is to implement a cohesive zone as illustrated in Figure 1. The cohesive zone models are well-established tools in classical fracture mechanics developed to remove stress singularities ahead of crack tips. The cohesive zone modeling concept, as implemented and

demonstrated in several recent studies (Souza et al. 2004; Kim and Buttlar 2005; Kim et al. 2005), has been receiving increasing attention from the asphalt mechanics community. The cohesive zone concept is useful and powerful because it can properly model both brittle and ductile failure, which is frequently observed in asphalt mixtures due to their wide range of service temperatures and loading rates.

In 2001, Allen and Searcy proposed a nonlinear viscoelastic cohesive zone model. Since the model developed by Allen and Searcy can appropriately reflect nonlinear viscoelastic damage growth in the asphalt mixtures, the model was selected for this study. The model can predict damage evolution, microcracking, corresponding post-peak material softening, and eventual fracture failure of highly inelastic asphalt mixtures. The two-dimensional traction-displacement relationship for the nonlinear viscoelastic cohesive zone model is as follows (Allen and Searcy 2001):

$$T_i(t) = \frac{u_i(t)}{\lambda(t) \cdot \delta_i} \cdot [1 - \alpha(t)] \cdot \left[\int_0^t E^{CZ}(t - \tau) \frac{\partial \lambda(\tau)}{\partial \tau} d\tau \right] \quad (4)$$

where $T_i(t)$ = cohesive zone traction,
 $u_i(t)$ = cohesive zone displacement,
 δ_i = cohesive zone length parameter,
 $\lambda(t)$ = normalized cohesive zone displacement = $[(u_n(t)/\delta_n)^2 + (u_s(t)/\delta_s)^2]^{0.5}$,
 $\alpha(t)$ = damage evolution function,
 $E^{CZ}(t)$ = linear viscoelastic relaxation modulus of the cohesive zone, and
 $i = n$ (normal direction), or s (tangential direction).

Viscoelastic stress relaxation modulus of the cohesive zone is also determined by performing laboratory constitutive tests, the results of which can also be represented by a Prony series form (in Equation 3) to be implemented into the model.

The cohesive zones are typically implemented by employing interface elements, as shown in Figure 1, to model the growth of new boundary surface (such as cracks). A single interface element consists of two line elements that occupy the same location as the intact state but are separated into two parts when the level of damage at the cohesive zone reaches its critical value. For example, when the damage evolution function $\alpha(t)$ reaches the value of unity in Equation 4, the cohesive zone traction decays to zero, thus resulting in damage growth (e.g., crack extension).

To characterize the cohesive zone model, laboratory testing defining the cohesive zone length parameter, δ_i and the damage evolution function, $\alpha(t)$ needs to be performed. This testing, which can directly determine model parameters of binder/mastic samples, is developed and presented in the later section (Development of a Fracture Testing System). The directly measured damage characteristics can then be incorporated into an analytical equation containing damage evolution parameters (α_1 and m) such as,

$$\frac{d\alpha}{dt} = \begin{cases} \alpha_1 [\lambda(t)]^m, & \frac{d\lambda}{dt} > 0 \text{ and } \alpha < 1 \\ 0, & \frac{d\lambda}{dt} \leq 0 \text{ or } \alpha = 1 \end{cases} \quad (5)$$

The damage evolution is a simple form of power relationship as a function of $\lambda(t)$; therefore, it is appropriate for simulating rate-dependent damage growth which is typical in viscoelastic bodies such as asphaltic composites.

2.4 Fine-mesh finite element method (FEM)

As illustrated in Figure 1, the finite element method based on micromechanics concepts was employed to deal with material characteristics of individual mixture constituents (such as aggregates and asphalt binder/mastic) through microstructure characterization of real asphalt concrete

mixtures. Figure 1 shows a binary digital image, its magnified subsection, and finite element meshes of a real asphalt mixture microstructure consisting of aggregates in white and asphalt binder/mastic in black. The digital image in the figure is the final adjusted image through a sequential image processing of the asphalt mixture microstructure captured from a cross section of a core compacted with a Superpave gyratory compactor.

The cohesive zones which are subjected to initiation of microscale fracture-damage and its propagation have been simulated by employing regularly oriented interface elements based on a pixel grid from the digital image processing. Digital pixel information during image processing has been translated into triangular solid elements and interface elements between solid elements within the binder/mastic to simulate damage within the binder/mastic phase. The binary digital image shown in Figure 1 is 0.028 m by 0.028 m, which has been digitized to 200 by 200 triangular elements. This results in a 280 μm /element, which infers that the finite element analysis can allow one to successfully simulate microscale damage of 280 μm .

3 DEVELOPMENT OF A FRACTURE TESTING SYSTEM

To determine the fracture properties of asphalt binder/mastic, a relatively simple but fundamentally rigorous tensile fracture testing method has been developed. This development was initiated in a previous study performed by Williams (2001). As illustrated in Figure 2, the test setup incorporates the use of digital cameras strategically positioned to capture the geometric variation of the asphalt

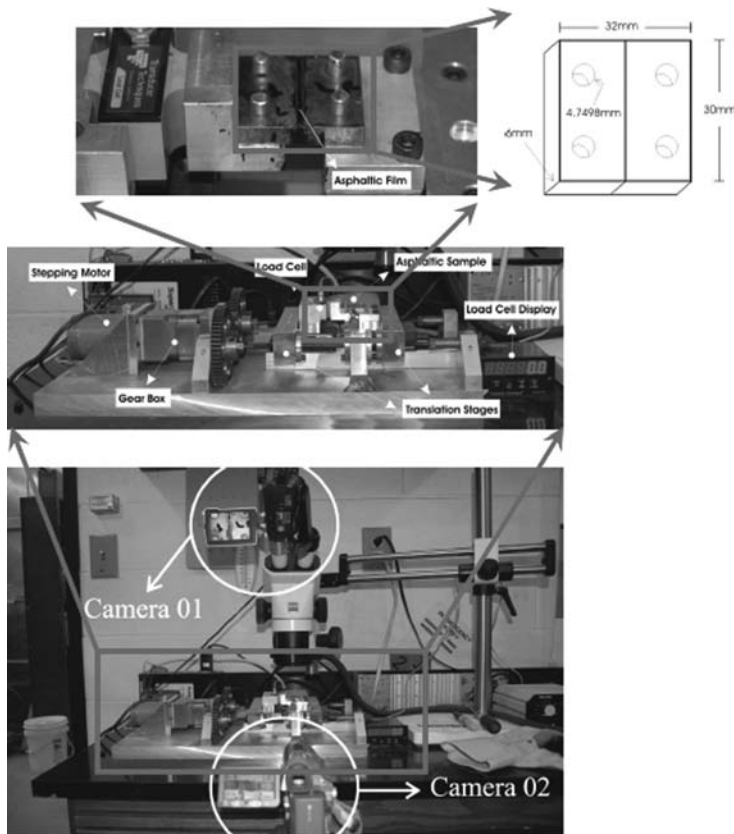


Figure 2. Tensile fracture testing system.

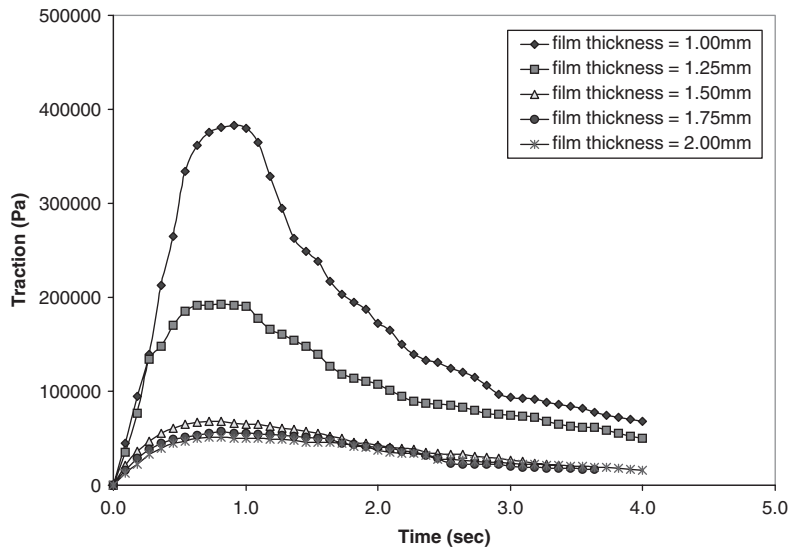


Figure 3. Traction vs. time curves at different film thicknesses.

binder/mastic specimen throughout the test. The test is performed under a displacement-controlled quasi-static monotonic or cyclic mode. The three-dimensional displacements are captured by the cameras at the same time as a load cell, installed in the system, displays the tensile force. The force-displacement data provide the input necessary to characterize the fracture properties.

The testing device is composed of four main parts: (i) a drive system; (ii) a motion system; (iii) a data acquisition system; and (iv) a sample block. A stepping motor connected to a gear box generates a torque to turn the side screws that drive the translation stages in opposite directions. A load cell reads the time-dependent resisting force during the test and sends the electrical signals to a data acquisition system, where these signals are translated into engineering values (e.g., time, displacement, and resisting force). Two digital video cameras are equipped with microscopes to magnify the top and side views of the specimen for further image analyses. The sample blocks have been designed so that a consistent asphaltic film could be formed between them. The fracture testing device can automatically control the film thickness of the specimen.

Figure 3 presents representative test results obtained for a constant displacement rate at the five different asphalt film thicknesses. As the film thickness increases, the tensile strength generally appears to decrease. This is due to the well-known fact that a thinner film induces a more brittle type of failure, and a thicker film is typically subjected to ductile cohesive fracture. However, the tensile strength tends to converge to a constant value that is not influenced by further increases in the film thickness.

As mentioned and shown in Figure 2, two digital video cameras capture the top and side images of the asphalt film as the load cell reads the time-dependent resisting force during the test for increasing opening displacements. The top and side images are then analyzed to calculate the reduction in the cross-sectional area with time. The instantaneous cross-sectional area can then be combined with the measured values of the force to yield tractions. Figure 3 presents the plot of the tractions versus time for the different thicknesses of the asphalt binder. The cohesive zone damage evolution function $\alpha(t)$ can be directly determined by relating test results (such as the results presented in Figure 3) to the cohesive zone model (Equations 4 and 5).

Even if the testing system is still under development for further advancements, the testing results were replicable and demonstrated a substantially sensitive response to the type of materials, testing conditions such as the loading rate, and film thickness as presented in other studies by the authors (Freitas 2007; Kim et al. 2007).

Table 1. Asphalt binder and mastic tested in this study.

Material	Percent of each component (in volume)		
	Neat binder	HL*	LF**
Binder	100	0	0
Binder + LF + HL	70	10	20

*Hydrated lime.

**Limestone filler.

Table 2. Model parameters.

Material properties	Binder	Binder + LF + HL
Linear viscoelastic properties		
E_{inf} (in Pa)	280	780
E_1 (in Pa)	14,600,640	57,771,216
E_2 (in Pa)	2,204,819	11,061,828
E_3 (in Pa)	302,285	1,562,769
E_4 (in Pa)	25,387	175,448
E_5 (in Pa)	1,941	10,531
η_1 (in Pa.sec)	123,655	356,095
η_2 (in Pa.sec)	157,553	657,571
η_3 (in Pa.sec)	192,007	857,526
η_4 (in Pa.sec)	181,682	962,722
η_5 (in Pa.sec)	96,762	653,985
Fracture properties		
δ_n (in m)	0.0020	0.0038
α_1	0.40	0.40
m	0.43	0.56

4 MATERIALS AND MODEL PARAMETERS

Table 1 presents materials tested in this study to ensure that the directly-measured properties of each mixture constituent incorporated with the theoretical model can characterize the nonlinear inelastic fracture-damage behavior of overall asphalt concrete mixtures. A neat asphalt binder, PG 64-22 and two different fillers (hydrated lime and limestone filler) were selected to produce one neat binder and one mastic, as shown in Table 1. The materials were selected with the intention of investigating material-specific fracture-damage characteristics.

The linear viscoelastic constitutive test to characterize the linear viscoelastic material property (i.e., relaxation modulus) and the tensile fracture test to identify fracture characteristics were performed. The tensile fracture test was performed for different film thicknesses of the asphalt specimen (from 1 mm to 2 mm in steps of 0.25 mm) at a constant opening displacement rate (0.00027 m/s) and at 24°C. The results from these two tests (the relaxation modulus and tensile fracture tests) provide the necessary information for determining the linear viscoelastic material properties (such as the Prony series parameters) and fracture properties (δ_n , α_1 , and m) as presented in Table 2.

For a better comparison of the fracture-damage evolution characteristics between materials, the damage evolution coefficient (α_1) was set to a constant value of 0.40, and the best corresponding δ_n and m values to the α_1 value of 0.40 were found by using an optimization technique. The effect of the δ_n and m values on the damage evolution behavior can be seen from Equations 4 and 5. The damage evolution rate ($d\alpha/dt$) decreases as the damage evolution exponent (m value) increases,

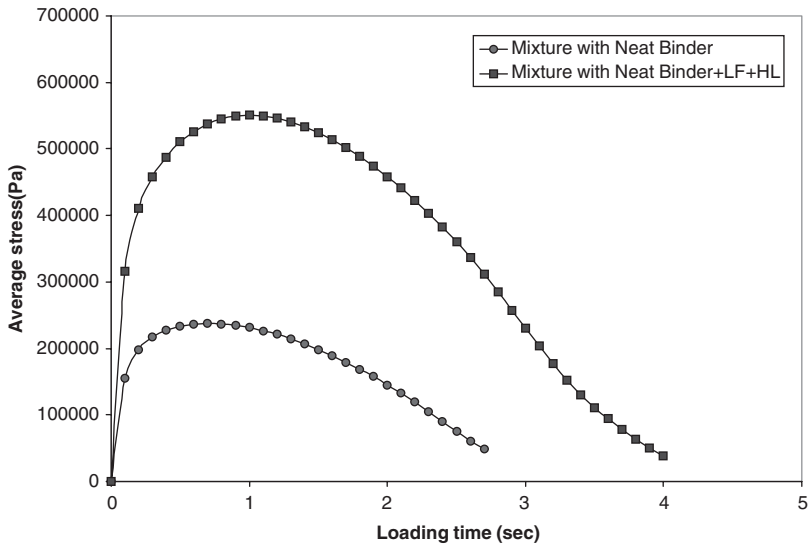


Figure 4. Model simulations of each mixture: average stress vs. loading time.

because the $\lambda(t)$ is typically less than 1.0 before the complete failure of the cohesive zone. As δ_n value decreases, mechanical response is stiffer and the damage growth tends to be faster.

It should be noted that fracture properties for a shearing mode ($i = s$, tangential direction only) can also be obtained by sliding asphalt films. However, the tangential fracture properties for this study have not been directly identified from testing but have been assumed to be identical to the normal direction fracture properties, since sliding mode testing protocols have not been fully developed at this time. Since fracture-damage characteristics are typically mode-dependent (opening vs. shearing), separate testing with shearing mode is under investigation by the authors.

5 MODEL SIMULATIONS AND DISCUSSION

As shown in Figure 1, vertical displacements at the bottom face and horizontal displacements at the left side of the sample were constrained, and uniaxial tensile displacements with a constant rate (0.0028) was applied to the top face for model simulations. The constant 0.0028 is a unit displacement corresponding to a unit strain, 0.1 which is a level of strain mostly (approximately 95%) deriving viscoelastic strain in the sample at the temperature (24°C) according to a study by Chehab et al. (2003).

Computational simulations have been conducted using an in-house finite element program developed by the authors. Figure 4 presents simulation results demonstrating the effect of mixture constituent properties on overall damage performance of asphalt concrete mixtures. As shown in the figure, the asphalt concrete mixture with mastic showed stiffer and better damage-resisting responses than the mixture with neat binder, which is expected from results with constituent property measurements (i.e. viscoelastic properties and the fracture properties in Table 2). Simulation results shown in Figure 4 are generally compatible with laboratory test results available (Si 2001; Kim et al. 2003; Little and Petersen 2005) in that filler-mixed asphalt concrete mixtures are generally capable of resisting to fracture than the mixtures mixed with neat binder under the displacement-controlled tensile test. However, model simulations herein need to be further validated and/or calibrated with more laboratory-field performance results, and this task is under accomplishment by the authors and will be reported in near future papers.

It can be noted that only material properties and damage evolution characteristics of mixture constituents are necessary inputs in order to utilize the micromechanics-based computational model. Furthermore, any arbitrary testing conditions can be easily implemented to simulation by applying appropriate boundary conditions. With given properties of each mixture constituent and known boundary conditions, performance predictions of macroscopic asphalt concrete mixtures can be conducted. Therefore, this approach can save time and cost associated with expensive and repetitive laboratory performance tests that are normally required for each new mixture and/or for each different testing condition.

6 CONCLUDING REMARKS

In this study, a fracture testing system and the experimental procedure were developed and incorporated with computational constitutive damage models including the cohesive zone to characterize the nonlinear viscoelastic damage behavior of asphalt concrete mixtures. The damage evolution and mechanical responses of the asphalt concrete mixture were apparently dependent on the fundamental material properties, which are directly measured. A better understanding of the fracture-damage mechanisms by using this technique will provide guidelines to select mixture constituents in a more appropriate manner and to improve the current design-analysis concepts so that better-performing and longer-lasting asphalt mixtures can be produced.

Even if promising results have been obtained so far, several experimental limitations need to be overcome so that all model inputs addressing fracture and damage of the asphalt sample can be more directly and comprehensively measured from the testing. In addition, a testing method or equivalent techniques to characterize adhesive fracture properties between aggregate particles and asphalt phase need to be developed and implemented into the model. It is well known fact that the adhesive fracture is fundamentally different from the cohesive fracture behavior in its mechanisms involved and an evolving progress associated (Cheng et al. 2003; Bhasin et al. 2006).

ACKNOWLEDGEMENTS

The authors would like to acknowledge the financial support from the Nebraska Department of Roads (NDOR). Special thanks to Dr. Eyad Masad at the Texas A&M University for the asphalt concrete digital image provided.

REFERENCES

- Abbas, A., Masad, E., Papagiannakis, T. and Harman, T. 2007. Micromechanical Modeling of the Viscoelastic Behavior of Asphalt Mixtures Using the Discrete-Element Method. *International Journal of Geomechanics*, 7(2), 131–139.
- Allen, D. H. and Searcy, C. R. 2001. A Micromechanical Model for a Viscoelastic Cohesive Zone. *International Journal of Fracture*, 107, 159–176.
- Bhasin, A., Masad, E., Little, D. N. and Lytton, R. 2006. Limits on Adhesive Bond Energy for Improved Resistance of Hot-Mix Asphalt to Moisture Damage. *Journal of the Transportation Research Board*, 1970, 3–13.
- Birgisson, B., Soranakom, C., Napier, J. A. L. and Roque, R. 2004. Microstructure and Fracture in Asphalt Mixture Using a Boundary Element Approach. *Journal of Materials in Civil Engineering*, 16(2), 116–121.
- Buttlar, W. and You, Z. 2001. Discrete Element Modeling of Asphalt Concrete: Microfabric Approach. *Journal of the Transportation Research Board*, 1757, 111–118.
- Chehab, G., Kim, Y. R., Schapery, R. A., Witzak, M. W. and Bonaquist, R. 2003. Characterization of Asphalt Concrete in Uniaxial Tension under a Viscoelastoplastic Continuum Damage Model. *Journal of the Association of Asphalt Paving Technologists*, 72, 315–355.
- Cheng, D., Little, D. N., Lytton R. L., and Holste J. C. 2003. Moisture Damage Evaluation of Asphalt Mixture by Considering Both Moisture Diffusion and Repeated Load Conditions. *Journal of the Transportation Research Board*, 1832, 42–58.

- Dai, Q., Sadd, M. H., Parameswaran, V., and Shukla, A. 2005. Prediction of Damage Behaviors in Asphalt Materials Using a Micromechanical Finite-Element Model and Image Analysis. *Journal of Engineering Mechanics*, 131(7), 668–677.
- Freitas, A. C. F. 2007. A Theoretical and Experimental Technique to Measure Fracture Properties in Viscoelastic Solids. *Ph.D. Dissertation*, University of Nebraska, Lincoln, Nebraska.
- Guddati, M. N., Feng, Z., and Kim, Y. R. 2002. Towards a Micromechanics-Based Procedure to Characterize Fatigue Performance of Asphalt Concrete. *Journal of the Transportation Research Board*, 1789, 121–128.
- Kim, H. and Buttlar, W. G. 2005. Micromechanical Fracture Modeling of Hot-Mix Asphalt Concrete Based on a Disk-Shaped Compact Tension Test. *Electronic Journal of the Association of Asphalt Paving Technologists*, 74E.
- Kim, Y., Little, D. N., and Song, I. 2003. Effect of Mineral Fillers on Fatigue Resistance and Fundamental Material Characteristics: Mechanistic Evaluation. *Journal of the Transportation Research Board*, 1832, 1–8.
- Kim, Y., Allen, D. H., and Little, D. N. 2005. Damage-Induced Modeling of Asphalt Mixtures Through Computational Micromechanics and Cohesive Zone Fracture. *Journal of Materials in Civil Engineering*, 17(5), 477–484.
- Kim, Y., Freitas, A. C. F., Allen, D. H., and Soares, J. B. 2007. Experimental Characterization of Ductile Fracture-Damage Properties of Asphalt Binders and Mastics. *Journal of the Transportation Research Board*, submitted to TRB.
- Little, D. N. and Petersen, J. C. 2005. Unique Effects of Hydrated Lime Filler on the Performance-Related Properties of Asphalt Cements: Physical and Chemical Interactions Revisited. *Journal of Materials in Civil Engineering*, 17(2), 207–218.
- Papagiannakis, A. T., Abbas, A., and Masad, E. 2002. Micromechanical Analysis of Viscoelastic Properties of Asphalt Concretes. *Journal of the Transportation Research Board*, 1789, 113–120.
- Si, Z. 2001. Characterization of Microdamage and Healing of Asphalt Concrete Mixtures. *Ph.D. Dissertation*, Texas A&M University, College Station, Texas.
- Souza, F. V., Soares, J. B., Allen, D. H., and Evangelista, F. 2004. Model for Predicting Damage Evolution in Heterogeneous Viscoelastic Asphaltic Mixtures. *Journal of the Transportation Research Board*, 1891, 131–139.
- Williams, J. J. 2001. Two Experiments for Measuring Specific Viscoelastic Cohesive Zone Parameters. *Master's Thesis*, Texas A&M University, College Station, Texas.
- Zhou, F. P., Lydon, F. D., and Barr, B. I. G. 1995. Effect of Coarse Aggregate on Elastic Modulus and Compressive Strength of High Performance Concrete. *Cement and Concrete Research*, 20, 177–186.

Use of pseudostress and pseudostrain concepts for characterization of asphalt fatigue tests

M.E. Kutay, N.H. Gibson & J. Youtcheff

Turner-Fairbank Highway Research Center, FHWA, McLean, Virginia, USA

ABSTRACT: Two viscoelastic continuum damage-based models were utilized to better interpret and analyze numerous cyclic tension-compression fatigue tests that were conducted on FHWA's ALF mixtures under both stress and strain controlled test conditions. The models utilize pseudo-variables such as pseudostrain and pseudostress and corresponding continuum damage parameters to model the loss of material integrity during testing of an asphalt specimen. This paper presented derivations of two simplified equations for calculation of damage parameters based on pseudostrain and pseudostress concepts. The equations were derived for a special case of cyclic uniaxial laboratory fatigue tests and use only peak to peak values of stresses and strains. It was observed that when strain controlled cyclic tests were simulated using the VECD parameters of different mixtures, the number of cycles to failure based on the simulations correlated very well with the ALF field fatigue cracking data.

1 INTRODUCTION

Fatigue cracking is one of the principal distresses that affect the design life of asphalt pavements. Fatigue cracking initiates and propagates in areas of the pavement subjected to repeated loading, i.e., along the wheel paths. Initially, fatigue cracking occurs as a series of small isolated microcracks, then with aid of repeated loading, grow and interconnect yielding the characteristic chicken wire or alligator skin cracking patterns. In order to understand fatigue performance of different asphalt/aggregate combinations, typically, cyclic laboratory tests are conducted on the laboratory produced specimens. Traditionally, number of cycles to failure (N_f) has been used as a quantity to describe the fatigue performance of the tested specimen. Depending on the mode of loading (i.e., stress or strain controlled) the ranking of the specimens can be quite different. Kutay et al. (2007a) reported that stress controlled push-pull tests revealed a reverse trend when compared to field fatigue data obtained from FHWA's Accelerated Load Facility (ALF). On the other hand, even though strain controlled tests provided the correct trend, the correlation with the field was poor (Kutay et al. 2007b). Therefore, there is a need for a more advanced method of analysis of laboratory fatigue data to be able to accurately predict the field fatigue performance of asphalt mixtures. Mathematical models such as the viscoelastic continuum damage (VECD) theory offer a great potential for better understanding of fatigue cracking behavior. For the past two decades, numerous researchers have successfully utilized the VECD theory for analysis and modeling of asphalt fatigue behavior (Kim & Little 1990, Kim et al. 1995, Daniel 2001, Chehab 2002, Lundstrom & Isacson 2003, Christensen & Bonaquist 2005, Gibson 2006).

In this study, cyclic uniaxial push-pull (tension-compression) tests were conducted on the mixtures used in FHWA's ALF Transportation Pooled Fund Study TPF-5(019). An alternative test to flexural beam fatigue was investigated because the alternative fatigue characterization (i.e., push-pull test) offered two advantages: (a) Potential to be very compatible with NCHRP 9-29 Simple

Performance Tester equipment, thereby expanding capabilities beyond small strain $[E^*]$ dynamic modulus characterization, and (b) capitalizes on a practical application of continuum damage theories (e.g., VECD theory), which are robust by explaining both stress-control and strain-control phenomena as well as temperature and frequency dependency.

2 DERIVATION OF VISCOELASTIC CONTINUUM DAMAGE PARAMETERS

Viscoelastic continuum damage (VECD) concept has been utilized by numerous researchers to study the fatigue response of asphalt mixtures (Kim & Little 1990, Kim et al. 1995, Daniel 2001, Chehab 2002, Lundstrom & Isacson 2003, Gibson 2006). The concept is based on Shapery's elastic-viscoelastic correspondence principle and the work potential theory (Shapery 1984). According to the theory, one can simplify the time dependent viscoelastic problem into a linearly elastic solution by use of the concepts such as pseudostrain (ε^R) and pseudostress (σ^R), which are defined as follows:

$$\varepsilon^R = \frac{1}{E^R} \int E(t-\tau) \frac{\partial \varepsilon}{\partial \tau} dt \quad \text{and} \quad \sigma^R = E^R \int D(t-\tau) \frac{\partial \sigma}{\partial \tau} dt \quad (1)$$

where E^R is the reference modulus (often taken as unity), $E(t)$ is relaxation modulus, $D(t)$ is creep compliance, t is time, ε is strain and σ is stress. The physical meaning of the pseudostrain (ε^R) corresponds to the linear viscoelastic (LVE) stress for a given strain history. Similarly, pseudostress (σ^R) is the LVE strain for a given stress history. These concepts allow definition of the concept of pseudostiffness (C), which is the loss off stiffness solely due to loss of material integrity caused by damage and defined as follows:

$$\sigma = C \varepsilon^R \quad \text{and} \quad \varepsilon = \frac{\sigma^R}{C} \quad (2)$$

Initially, when the specimen is undamaged, C is equal to unity. As the microdamage develops in the form of microcracks, C decreases and approaches to zero. The development of microcracks are quantified using so-called "damage parameters" which define the damage growth within the specimen (Shapery 1984). In the simplest case of uniaxial tests, a single damage parameter (S) can be used to quantify the damage growth.

Based on the selection of pseudovariabe (i.e., ε^R and σ^R) in the analysis, the formulation and unit of the damage parameter (S) and energy density function (W) are different. In this paper, the damage parameters and energy density functions are denoted as S_ε and W_ε for pseudostrain (ε^R) and S_σ and W_σ for pseudostress (σ^R), respectively. On the other hand, the pseudostiffness (C) is same in both pseudovariabe ε^R and σ^R (Eq. 2). Following set of equations define the uniaxial stress-strain behavior of a viscoelastic solid with a time dependent damage growth. The equations use the simplest form of the energy density function and a single damage parameter (Park et al. 1996):

$$\sigma = \frac{\partial W_\varepsilon}{\partial \varepsilon^R} = I C (S_\varepsilon) \varepsilon^R \quad \text{and} \quad \sigma^R = \frac{\partial W^R}{\partial \varepsilon} = I C (S_\sigma) \frac{\partial W^R}{\partial \sigma^R} \quad (3)$$

$$W_\varepsilon = \frac{I}{2} C (S_\varepsilon) \varepsilon^{R2} \quad \text{and} \quad W_\sigma = \frac{\sigma^{R2}}{2 I C (S_\sigma)} \quad (4)$$

$$\frac{dS_\varepsilon}{dt} = \left[-\frac{\partial W_\varepsilon}{\partial S_\varepsilon} \right]^\alpha \quad \text{and} \quad \frac{dS_\sigma}{dt} = \left[\frac{\partial W_\sigma}{\partial S_\sigma} \right]^\alpha \quad (5)$$

where W_ε is pseudostrain energy density function, W_σ is pseudostress energy density function, S_ε is the damage parameter when ε^R is used in the analysis, and S_σ is the damage parameter when

σ^R is used. $C(S_\varepsilon)$ and $C(S_\sigma)$ are the pseudostiffnesses that are a function of damage parameters S_ε and S_σ , I is an initial stiffness parameter used to eliminate sample to sample variability (usually between 0.9 to 1.1), t is time and α is a material constant related to the rate of damage growth. Theory states that α is dependent on the characteristic of the failure zone. If the material's fracture energy (Γ) and the fracture stress are constant α can be taken as $\alpha = 1 + 1/m$, whereas if Γ and the fracture process zone size are constant, $\alpha = 1/m$ (Park et al. 1996). In both cases m is the max slope of the relaxation modulus versus time graph drawn in log-log scale. This slope indicates the materials propensity to release energy during cracking. Lee and Kim (1998) suggested that former ($\alpha = 1 + 1/m$) is more suitable for strain controlled tests, whereas the latter ($\alpha = 1/m$) is more suitable for the stress controlled tests.

In case of cyclic uniaxial tests with constant frequency, computation of the parameters ε^R , σ^R does not require the solution of computationally expensive hereditary integral given in Equation 1. They can simply be computed using the peak-to-peak values of stress and strain in each loading cycle as follows (Kim et al. 2002, Kutay et al. 2007a, 2007b)

$$\varepsilon_N^R = |E^*|_{LVE} \varepsilon_0^N \quad \text{and} \quad \sigma_N^R = \frac{\sigma_0^N}{|E^*|_{LVE}} \quad (6)$$

where ε_N^R is the peak pseudostrain in N th cycle, $|E^*|_{LVE}$ is the linear viscoelastic (undamaged) dynamic modulus, ε_0^N is the peak strain in N th cycle, σ_N^R is the peak pseudostress, and σ_0^N is the peak stress in N th cycle. It can be seen from Equation 6 that ε_N^R is simply the linear viscoelastic stress and σ_N^R is the linear viscoelastic strain. Plugging Equation 6 into Equation 2 reveals the following for the pseudostiffness in N th cycle (C_N):

$$C_N = \frac{|E^*|_N}{|E^*|_{LVE}} \quad (7)$$

where $|E^*|_N$ is the dynamic modulus in N th cycle (i.e., $|E^*|_N = \sigma_0^N / \varepsilon_0^N$). Plugging Equation 4 into Equation 5 and utilizing the chain rule $\frac{dC}{dS} = \frac{dC}{dt} \frac{dt}{dS}$ in equations that uses ε^R , and $\frac{d}{dS} \left(\frac{1}{C} \right) = \frac{d}{dt} \left(\frac{1}{C} \right) \frac{dt}{dS}$ in equations that uses σ^R , following relations could be obtained for the damage parameter (Kutay et al. 2007a, 2007b):

$$\frac{dS_\varepsilon}{dt} = \left[-I \frac{\varepsilon^{R2}}{2} \frac{dC}{dt} \right]^{1+\alpha} \quad \text{and} \quad \frac{dS_\sigma}{dt} = \left[\frac{\sigma^{R2}}{2I} \frac{d}{dt} \left(\frac{1}{C} \right) \right]^{1+\alpha} \quad (8)$$

Equation 8 can further be simplified for a cyclic uniaxial test with a constant frequency (f) where the following equation holds:

$$N = f t \rightarrow \frac{dN}{dt} = f \quad (9)$$

where N is the cycle number and t is time. Equation 8 can further be simplified using the chain rules $\frac{dC}{dt} = \frac{dC}{dN} \frac{dN}{dt}$, $\frac{dS}{dt} = \frac{dS}{dN} \frac{dN}{dt}$ and given that $\frac{dN}{dt} = f$:

$$\frac{dS_\varepsilon}{dN} f = \left[-I \frac{\varepsilon^{R2}}{2} \frac{dC}{dN} f \right]^{1+\alpha} \quad \text{and} \quad \frac{dS_\sigma}{dN} f = \left[\frac{\sigma^{R2}}{2I} \frac{d(C^{-1})}{dN} f \right]^{1+\alpha} \quad (10)$$

Evolution of the damage parameter at the peak of each cycle can be calculated numerically by rewriting the Equation 10 in a discrete form as follows:

$$S_{\varepsilon}^{N+\Delta N} = S_{\varepsilon}^N + (\Delta N/f)^{\frac{1}{1+\alpha}} \left[-0.5 I \varepsilon_N^{R^2} (C_{N+\Delta N} - C_N) \right]^{\frac{\alpha}{1+\alpha}} \quad (11)$$

$$S_{\sigma}^{N+\Delta N} = S_{\sigma}^N + (\Delta N/f)^{\frac{1}{1+\alpha}} \left[0.5 \frac{1}{I} \sigma_N^{R^2} \left(\frac{1}{C_{N+\Delta N}} - \frac{1}{C_N} \right) \right]^{\frac{\alpha}{1+\alpha}} \quad (12)$$

where superscripts of the damage parameters in Equations 11 & 12 corresponds to the values at different cycles (i.e., N th & $(N + \Delta N)$ th cycles).

3 MATERIALS AND METHODS

As a part of the laboratory fatigue characterization, cyclic uniaxial push-pull (tension-compression) tests were conducted on the mixtures used in FHWA's ALF sections. The tests were run in both stress and strain controlled testing modes. Specimens were prepared in a Superpave gyratory compactor to a height of approximately 180 mm and then cut and cored to a cylindrical sample 71.4 mm in diameter and 150 mm tall. The mix designs of the laboratory specimens were the same as the field ALF sections. Three replicates from each ALF mixture were tested. The mixtures are identified as Control 70-22, an unmodified asphalt; CR-TB, a terminally blended crumb rubber asphalt; SBS-LG a linear grafted SBS modified asphalt; Fiber, the same as the control mixture but containing 0.2% polyester reinforcing fiber by mass of the aggregate; AB, an unmodified asphalt stiffened using the air blowing technique; and a Terpolymer modified asphalt mixture. The air void level was 7.0%, which was approximately same as the field air voids. All mixtures had the same coarse Superpave gradation and 5.3% binder content. All binders have approximately the same high and low temperature grade, which was 70-22.

For both stress and strain controlled tests, the testing frequency and temperature were 10 Hz and 19°C, respectively. For the stress controlled tests, the magnitude of the applied peak stress (in both tension and compression states) was 610 kPa or peak-to-peak 1220 kPa. During strain controlled tests, the strain level at the actuator strain gauge was controlled not on-specimen mounted LVDT strain. However, actuator strains were custom tailored for each mixture such that, the initial LVDT strain on the specimen was 300 microstrains. It should be noted that there are several problems associated with on-specimen mounted LVDT strain controlled tests. For example, if a problem occurs on the LVDT for which closed loop feedback test is controlled, the actuator may easily become unstable and apply a very high load for a fraction of a second damaging the specimen and other LVDTs.

After each test, dynamic modulus ($|E^*|$), and phase angle (ϕ) values were computed for each strain transducer using the procedure given by Bonaquist et al. (2003) for the National Cooperative Highway Research Project 9-29 for the development of the Simple Performance Tester for asphalt concrete. In short, the procedure fits a line through several cycles of strain to approximate creep or drift which is subsequently subtracted. A combination of sinusoid and cosine is fit to both the applied stress and measured strain at each cycle. The amplitudes and phase angles are computed from the sinusoid fit.

4 DAMAGE CHARACTERISTIC CURVES OF ASPHALT MIXTURES

After each cyclic uniaxial tests, pseudostrain, pseudostress and pseudostiffness variables of each mixture were computed using Equations 6 and 7. Then, damage parameters were computed using Equations 11 and 12. According to the VECD theory, a single damage characteristic curve, i.e., pseudostiffness (C) versus damage parameter (S_{ε} or S_{σ}) relationship, exists independent of loading

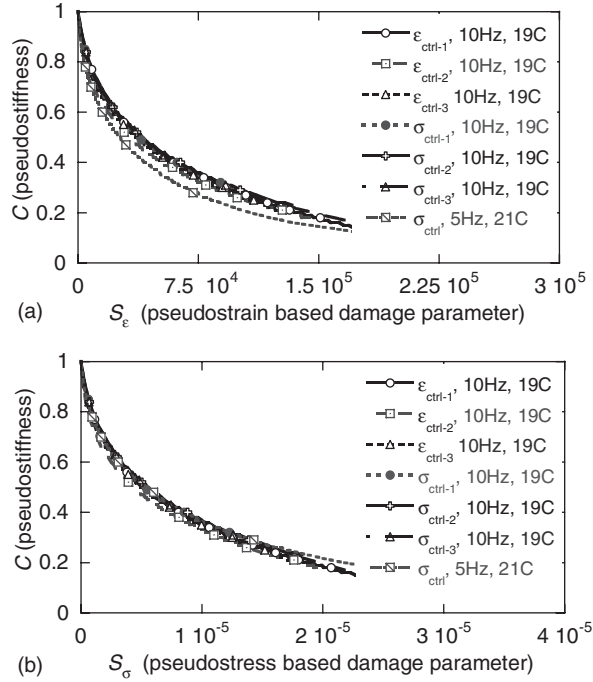


Figure 1. Pseudostiffness versus damage parameter relationships for specimen CR-TB. (a) Damage parameter (S_ϵ) is based on pseudostrain concept (Eq. 11) and (b) damage parameter (S_σ) is based on pseudostress concept (Eq. 12). In legends of the figures, “ ϵ_{ctrl-1} , 10Hz, 19C”: strain controlled test, replicate-1, frequency = 10 Hz and temperature = 19°C.

frequency, temperature and mode of loading. Therefore, C versus S_ϵ or S_σ curves computed after tests conducted at different temperatures, and run at different loading modes should collapse on a single curve. The material parameter α in Equations 11 & 12 can have a significant effect on the calculated damage parameter. Therefore selected α should give same exact curve in both loading modes (stress and strain). It was observed that using $\alpha = 1/m$ (m = the slope of the relaxation modulus versus time graph drawn in log-log scale) in all tests worked out the best to bring all the curves together (Kutay et al. 2007b) in both stress and strain controlled tests. It should be recalled that Lee and Kim (1998) suggested that $\alpha = 1/m$ was more suitable for stress controlled tests. In this study, $\alpha = 1/m$ was suitable for both stress and strain controlled tests. It should be noted that the strain controlled tests run in thus study may not be considered as “truly” strain controlled. As it was discussed previously, the tests were run using the actuator LVDT containing end effect from the glued, restrained ends, not the on-specimen LVDTs. As a result, the strain amplitude measured at the on-specimen LVDTs did not remain constant (in fact increased during the test) while the stress decreased. This might have led to a mode where during the tests, the material’s fracture energy (Γ) and fracture process zone size remained constant (similar to a stress controlled test). It should be noted that the mean drift of the cyclic measured strain was subtracted to remove the viscoplastic strain.

Figures 1a and 1b show the pseudostiffness versus damage parameter relationships for specimen CR-TB where in Figure 1a, x-axis is the damage parameter (S_ϵ) computed using Equation 11 and in Figure 1b, x-axis is the damage parameter (S_σ) computed using Equation 12. It can be observed from Figure 1 that the damage characteristic curves collapse on a single curve regardless of the loading mode, frequency and temperature. This was observed to be true for both damage parameters, S_ϵ (pseudostrain-based) and S_σ (pseudostress-based). It can be concluded that viscoelastic continuum

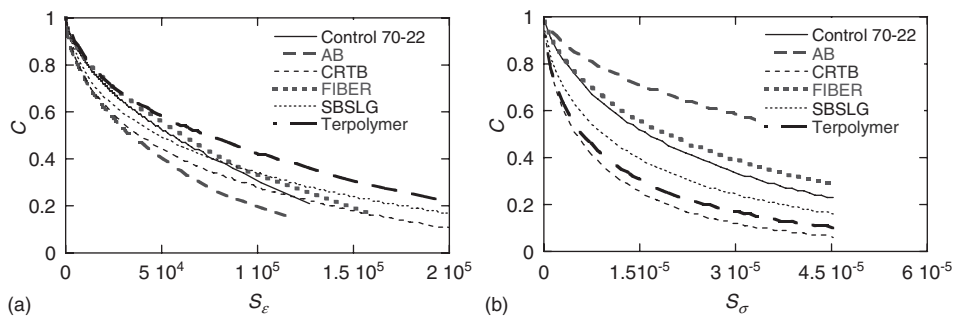


Figure 2. Pseudostiffness versus damage parameter relationships for all specimens. (a) Damage parameter (S_ϵ) is based on pseudostrain concept (Eq. 11) and (b) damage parameter (S_σ) is based on pseudostress concept (Eq. 12).

Table 1. Linear viscoelastic properties ($|E^*|$ and α) and exponential best fit coefficients of damage characteristic curves of asphalt mixtures.

Specimen	$ E^* $ (MPa) at		Pseudostrain-based (S_ϵ)		Pseudostress-based (S_σ)	
	$19^\circ\text{C}, f = 10 \text{ Hz}$	α (1/m)	a	b	a	b
Control 70-22	7847	2.22	-0.000153	0.774	-2318.1	0.736
Air Blown	6561	1.90	-0.000333	0.735	-572.8	0.669
CR-TB	4536	2.86	-0.000337	0.718	-1526.4	0.632
Fiber	7864	2.20	-0.000198	0.740	-1275.1	0.692
SBS-LG	4467	2.70	-0.000358	0.698	-808.9	0.610
Terpolymer	3726	3.00	-0.001250	0.590	-836.7	0.591

damage theory can be implemented by using either of pseudovariables, i.e., pseudostrain (ϵ^R) and pseudostress (σ^R).

Once the damage characteristic curves are obtained, an exponential best fit line in the following form was fitted to the curves:

$$C = \exp(aS^b) \quad (13)$$

where a and b are the constants defining the best fit.

Figures 2a and 2b show the damage characteristic curves of all specimens computed using pseudostrain and pseudostress concepts, respectively. Table 1 shows the exponential best fit coefficients of the mixtures computed for both pseudostrain-based (S_ϵ) and pseudostress-based (S_σ) damage parameters. It may be attractive to rank different asphalt mixtures based on the curves shown in Figure 2 or the coefficients computed in Table 1. However, it should be noted that those parameters along with the equations shown in section 2 are used to facilitate predicting the response of the material to a given loading history. Using only the parameters themselves may not provide an accurate ranking of the mixtures. It is important to compute each material's response under same loading conditions.

5 VECD SIMULATION OF A STRAIN CONTROLLED CYCLIC FATIGUE TEST

In order to compute the reduction in dynamic modulus with different cycles, a 'true' strain controlled cyclic test can be simulated using the parameters shown in Table 1. The ranking of the mixtures

can be accomplished based on the number of cycles to failure. The failure criteria used herein is 50% reduction in $|E^*|$.

The input to the simulation are the parameters in Table 1, cycle (N) and peak strain (ε_0^N) corresponding to each cycle N . From these inputs, the parameters C and S and then the peak stress (σ_0^N) and dynamic modulus ($|E^*|$) in each cycle can be calculated.

Simulation was started with a small value of S and corresponding C was computed. Then damage parameters for the next cycle were computed using Equations 14 and 15. Plugging Equation 4 into Equation 5 and utilizing the chain rule $\frac{dS}{dt} = \frac{dS}{dN} \frac{dN}{dt}$ and given that $\frac{dN}{dt} = f$ reveals the following relations for the damage parameters:

$$S_e^{N+\Delta N} = S_e^N + \Delta N / f \left[-0.5 I \varepsilon_N^{R^2} \frac{dC}{dS} \right]^\alpha \quad (14)$$

$$S_\sigma^{N+\Delta N} = S_\sigma^N + \Delta N / f \left[0.5 \frac{1}{I} \sigma_N^{R^2} \frac{dC^{-1}}{dS} \right]^\alpha \quad (15)$$

where $I = 1$ (since the specimen-to-specimen variability is unknown), $\varepsilon_N^R = \varepsilon_0^N |E^*|_{LVE}$, $\sigma_N^R = \varepsilon_0^N C_N$, $\Delta N = N_{i+1} - N_i$, f is frequency, $\frac{dC}{dS}$ and $\frac{dC^{-1}}{dS}$ are computed by taking the partial derivative of Equation 13:

$$\frac{dC}{dS} = \mathbf{exp}(aS^b) abS^{b-1} \quad \text{and} \quad \frac{dC^{-1}}{dS} = -\mathbf{exp}(-aS^b) abS^{b-1} \quad (16)$$

Once $S_{N+\Delta N}$ is computed, the pseudostiffness ($C_{N+\Delta N}$), dynamic modulus ($|E^*|_{N+\Delta N}$) and the peak stress ($\sigma_0^{N+\Delta N}$) for the next cycle can be computed as follows:

$$C_{N+\Delta N} = \mathbf{exp}(aS_{N+\Delta N}^b) \quad (17)$$

$$|E^*|_{N+\Delta N} = C_{N+\Delta N} |E^*|_{LVE} \quad (18)$$

$$\sigma_0^{N+\Delta N} = \varepsilon_0^{N+\Delta N} |E^*|_{N+\Delta N} \quad (19)$$

In order to validate above formulation, a special cyclic stress controlled test was run on specimen CR-TB at a temperature and frequency of 21°C and 5 Hz. It should be noted that material properties a and b (in Table 1) were computed from tests run at 19°C and 10 Hz. During simulation, the measured strains and the cycle number were input to the model and stresses and dynamic modulus values for each cycle were calculated. Figure 3a shows the predicted versus measured dynamic moduli change over the cycles where a very good agreement is visible. However, ε^R -based predictions were slightly higher, whereas, σ^R -based predictions were slightly lower than the measured values. In Figure 3a, $I = 1$ was used, i.e., the specimen to specimen variability is ignored. In order to investigate if the slight difference is due to the specimen variability, $I = |E^*|_{N=1(measured)} / |E^*|_{LVE}$ was used and simulation was rerun. The results are shown in Figure 3b, where there is an excellent match, indicating that the slight difference between the measured and predicted values in Figure 3a is solely due to the specimen variability.

6 COMPARISON WITH FIELD FATIGUE DATA

Conventional fatigue analysis of mixtures used in this study was presented in Kutay et al. (2007b). It was observed that number of cycles to failure (N_f) based on neither stress nor strain controlled tests correlate well with the ALF field fatigue data. The N_f based on stress controlled laboratory tests provided a reverse trend, i.e., good performing mixtures in the field revealed low N_f in the lab. It was also reported that there was a high correlation between the initial dynamic modulus and the number of cycles to failure at the stress-controlled push-pull tests in the laboratory. This indicated

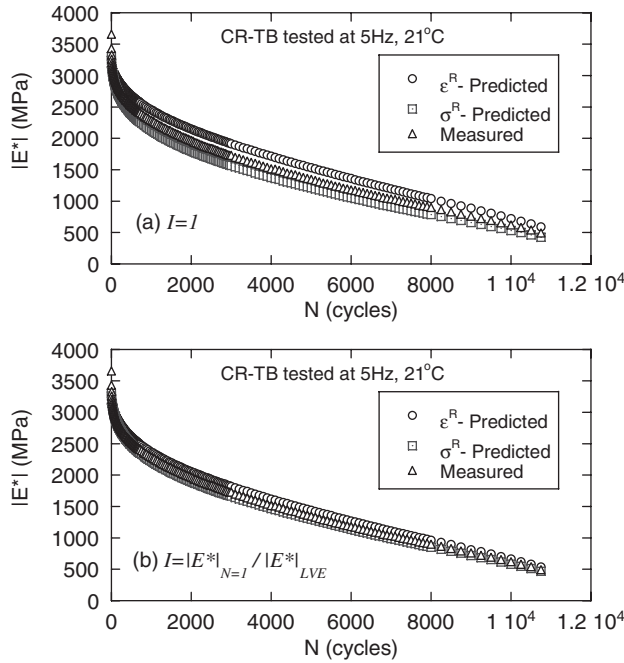


Figure 3. Measured $|E^*|$ versus VECD simulation predictions for specimen CR-TB tested at 5 Hz and 21°C.

that the N_f (under stress controlled test) was actually providing information on the stiffness of the material, not necessarily the fatigue performance of the mixtures in the field (Kutay et al. 2007a). On the other hand, the strain controlled tests were able to capture the general trend of the field; however, the correlation was poor. This was attributed to the fact that the tests were not ‘truly’ strain controlled, where the strain in the actuator was controlled, not the strain at the on-specimen mounted LVDTs.

Simulation of a ‘truly’ strain controlled test is possible once the VECD parameters (in Table 1) are obtained. In order to compare the performance of the different ALF mixtures, a (true) strain-controlled push-pull test at $T = 19^\circ\text{C}$ and $f = 10$ Hz for an applied peak strain of $\epsilon_o = 200 \times 10^{-6}$ was simulated. Figure 4 shows the decrease in dynamic modulus ($|E^*|$) over the cycles for different specimens. Figure 4 indicates that stiff mixtures such as AB and Control 70-22 have a sharper decrease in $|E^*|$ with increasing cycles than soft polymer modified mixtures such as CR-TB, SBS-LG and Terpolymer. This agrees very well with the observations seen at ALF sections and complete opposite of the measured trends observed during the stress controlled tests.

Figure 5 shows a comparison of N_f based on VECD simulation and number of ALF wheel passes to 20% crack length in the field. It can be seen from Figure 5 that the correlation between the VECD-simulated N_f and field data are very high when Fiber and Terpolymer mixtures are excluded. It should be noted that field data for these two particular lanes needs to be interpreted cautiously. First of all, field data in Figure 5 is based on 100 mm thick pavement lanes at ALF where there have been reported problems with the Terpolymer lane. Terpolymer mixture was expected to perform the best based on historical experience and numerous laboratory binder and mixture tests. In fact, Terpolymer mixture performed the best among the 150 mm pavement lanes. During the construction of the ALF lanes, several problems have been reported for the Terpolymer lane with inadequate hydrated lime distribution being the primary culprit. Therefore, slightly worse performance of the Terpolymer (in 100 mm lane) was attributed to construction related reasons.

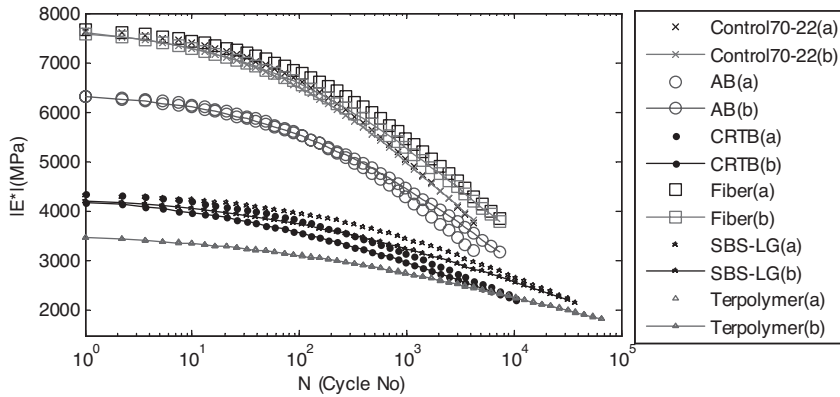


Figure 4. VECD simulated $|E^*|$ versus N graph of all ALF mixtures. In legend, ‘(a)’ and ‘(b)’ correspond to simulations run using pseudostrain and pseudostress concepts, respectively.

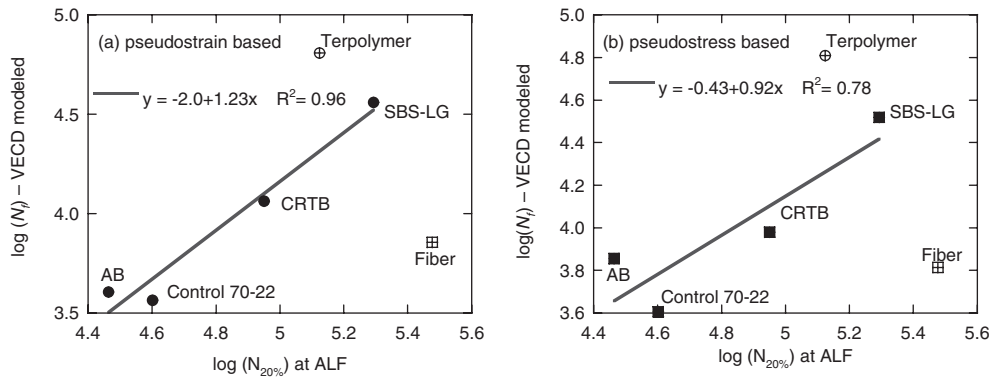


Figure 5. Comparison of N_f based on VECD simulation and number of ALF wheel passes to 20% crack length in the field.

If it had performed the way it was expected, the data point in Figure 5 would shift to right and be close to the trendline.

On the other hand, the apparent good performance of Fiber mixture in the field may be due to its cracking pattern obscuring existing greater damage. It was observed that even though many small (micro) cracks developed on the surface of the Fiber lane, they did not coalesce and lead to a large alligator type cracks which was seen in other lanes. It should be noted that the Fiber mixture is the same as Control 70-22 mixture except that it has 0.2% polyester fiber by mass of the aggregate. Therefore, it was thought that even though the damage occurred earlier in Fiber lane in the form of small cracks, they did not propagate to form large cracks due to the reinforcing effect of the fibers in the mixture. Therefore, crack mapping at the surface of Fiber lane may not be representative of damage occurred within the pavement.

7 CONCLUSIONS

Analysis of laboratory fatigue data using the viscoelastic continuum damage (VECD) theory has the ability to accommodate stress control and strain control laboratory behavior in a single framework and may be very useful to understand field behavior. In this paper, two VECD-based models were

utilized to better interpret and analyze the asphalt laboratory fatigue data. The models utilize pseudo-variables such as pseudostrain and pseudostress and corresponding continuum damage parameters to model the loss of material integrity during testing of an asphalt specimen. These variables may not be representative of directly measured or measurable physical phenomena; however, by means of their mathematical development and derivation, they are related to important processes which are believed to govern material behavior. The damage parameters for each VECD model are intended to quantify the amount of micro crack damage induced in the material which is associated to a specific pseudostiffness, C . This paper presented derivations of two simplified equations for calculation of damage parameters based on pseudostrain and pseudostress concepts. The equations were derived for a special case of cyclic uniaxial laboratory fatigue tests and use only peak to peak values of stresses and strains. The equations were validated using a laboratory test run at a completely different temperature and frequency than those of the tests where material parameters were calibrated. A true strain controlled cyclic tests were simulated using the VECD parameters of different mixtures. The number of cycles to failure based on VECD simulations correlated very well with the ALF field fatigue cracking data. Therefore, instead of directly using the number of cycles to failure at the laboratory tests, it is recommended that laboratory fatigue data should be used to calculate damage characteristic curves. Then different specimens should be compared by performing a simple VECD simulation of a strain controlled fatigue test.

REFERENCES

- Bonaquist, R., Christensen D., and Stump B., NCHRP Report 513 – *simple performance tester for Superpave mix design: first-article development and evaluation*. National Academies Press, Washington D.C., 2003.
- Chehab, G. R. 2002. “Characterization of asphalt concrete in tension using a viscoelastoplastic model.”, PhD dissertation, North Carolina State University, Raleigh, NC.
- Christensen, D. W., and Bonaquist, R. F. 2005. “Practical application of continuum damage theory to fatigue phenomena in asphalt concrete mixtures.” *J. Assn. of Asphalt Paving Technologists*, Vol. 74, pp. 963–1002.
- Daniel, J. S. 2001. “Development of a simplified fatigue test and analysis procedure using a viscoelastic, continuum damage model and its implementation to westrack mixtures.”, Ph.D. Dissertation, North Carolina State University, Raleigh, NC.
- Kim, Y. R., and Little, D. N. 1990. “One-dimensional constitutive modeling of asphalt concrete.” *J. of Eng. Mech.*, ASCE, 116(4).
- Kim, Y. R., Lee, Y., and Lee, H. J. 1995. “Correspondence principle for characterization of asphalt concrete.” *J. Materials in Civil Eng.*, ASCE, 7(1), 59–68.
- Kim, Y. R., Little, D. N., and Lytton, R. L. 2002. “Use of dynamic mechanical analysis (DMA) to evaluate the fatigue and healing potential of asphalt binders in sand asphalt mixtures.” *J. Assn. of Asphalt Paving Technologists*, Vol. 71, pp. 176–206.
- Kutay, M. E., Gibson, N. H., and Youtcheff, J. 2007b. “Conventional and Viscoelastic Continuum Damage (VECD) based Fatigue Analysis of Polymer Modified Asphalt Pavements”, *J. Assn. Asphalt Paving Technologists*, (In review).
- Kutay, M. E., Gibson, N. H., Youtcheff, J., and Qi, X. 2007a. “Fatigue and Healing Analysis of Asphalt Mixtures with Modified Binders used in ALF Pooled Fund Study”, *ASCE Journal of Materials in Civil Engineering*, (In review).
- Lee, H. J., and Kim, Y. R. 1998. “Viscoelastic Continuum Damage Model for Asphalt Concrete Under Cyclic Loading.”, *Journal of Engineering Mechanics*, Vol. 124, No. 1, pp. 32–40.
- Lundstrom, R., and Isacsson, U. 2003. “Asphalt Fatigue Modeling using Viscoelastic Continuum Damage Theory”, *Road Materials and Pavement Design*, Vol. 4, No. 1.
- Park, S. W., Kim, Y. R., and Shapery, R. A. 1996. “A Viscoelastic Continuum Damage Model and its application to Uniaxial Behavior of Asphalt Concrete”, *Mechanics of Materials*, 24, pp. 241–255.
- Schapery, R. A. 1984. “Correspondence principles and a generalized J-integral for large deformation and fracture analysis of viscoelastic media.” *Int. J. Fract.*, 25, pp. 195–223.

Viscoelastic continuum damage model based finite element analysis of fatigue cracking

C. Baek, B.S. Underwood, V. Subramanian, M.N. Guddati & Y.R. Kim
North Carolina State University, Raleigh, North Carolina, USA

K. Lee
Highway Transportation Technology Institute, Korea Expressway Corporation, Korea

ABSTRACT: The Viscoelastic Continuum Damage (VECD) model has been implemented into a finite element package (FEP++), developed at North Carolina State University, to predict the fatigue performance of asphalt concrete (AC) pavements. It is believed that this study is the first application of an integrated structural/material mechanistic model for fatigue performance prediction where damage in asphalt layers is considered for the full time history and the stiffness change due to damage evolution is captured in the subsequent calculation of damage. The VECD model is utilized to account for the material component, whereas other important characteristics, such as temperature, layer thicknesses, stiffness gradients, etc., are taken into account with FEP++. The model is found to effectively capture the influence of changes in pavement characteristics. The need for development of transfer functions for true field performance prediction is also shown and a simple example function is developed as a proof of concept.

1 INTRODUCTION

Recent national efforts towards developing a mechanistic-empirical design methodology have resulted in an increased interest in the full mechanistic modeling of asphalt concrete (AC) pavements. Such interest stems from shortcomings of existing empirical performance prediction methods which become ineffectual because actual conditions in the field differ from those considered in the laboratory. This paper presents results from the mechanistic modeling of AC pavements in terms of fatigue performance. It is important for such efforts to give consideration of both material and structural components and their interaction in an AC pavement. To meet these criteria, the viscoelastic continuum damage (VECD) model has been implemented into a finite element software program (FEP++), developed at North Carolina State University, to predict the fatigue performance of various AC mixtures in the field. This model is referred to as the VECD-FEP++.

For this effort, data from the Federal Highway Administration Accelerated Load Facility (FHWA ALF) and the Korea Expressway Corporation (KEC) test road have been utilized. The goal of the current field study using the ALF is to assess the effects of various asphalt binder modification techniques on mixture performance. To meet this goal a series of pavements, each with similar performance-graded AC mixtures, has been tested until fatigue failure. Load level, temperature, and pavement construction consistency are carefully controlled in these experiments. The KEC test road was constructed in December 2002 to serve as the basis for Korea's new pavement design guide, giving consideration to actual traffic loads and environmental changes. This test road is a 7.7 km two-lane highway consisting of 25 Portland Cement Concrete pavement sections and 15 AC pavement sections as well as 3 bridges and 2 geotechnical structures. The variables considered in this study for AC pavements are surface layer type, base layer type, base layer thickness, and sublayer properties.

2 VECD MODEL BACKGROUND

The VECD model is built on three concepts: (1) the elastic-viscoelastic correspondence principle based on pseudo strain for modeling the viscoelastic behavior of the material; (2) the continuum damage mechanics-based work potential theory for modeling the effects of microcracks on global constitutive behavior; and (3) the time-temperature superposition principle with growing damage to include the joint effects of time/rate and temperature. A full discussion of these concepts is beyond the scope of this paper; however, detailed reviews are available elsewhere (Underwood et al. 2006, Kim & Chehab 2004, Chehab et al. 2002, Daniel et al. 2002, Schapery 1990 & 1984). In short, model characterization requires determination of a material's linear viscoelastic and damage characteristics. For the former, the common temperature-frequency sweep (dynamic modulus via AASHTO TP-62) test is used and for the latter a constant rate tension test is utilized. From these two tests it is possible to compute the damage characteristic, or C vs. S , curve (defining the pseudo secant modulus and the damage respectively) (Underwood et al. 2006), which has been suggested to represent a fundamental material relationship independent of loading mode, loading frequency and temperature (Daniel et al. 2002). This characteristic relationship is shown, along with the dynamic modulus mastercurves for the mixtures in this study in Figure 1.

3 FINITE ELEMENT MODELING

The FEP ++ software used for modeling the asphalt pavement structure utilizes 2-D axisymmetric analysis. Layer thickness, material properties, load conditions and temperature are input by the user. In this study, layer thicknesses are taken from either the as-constructed values (ALF) or, if these are unavailable, from the as-designed values (KEC). In either case, subgrade materials are considered to be semi-infinite. Asphalt layers are modeled using the VECD model (viscoelastic with damage), while unbound materials are assumed linear elastic. In all simulations the pavement temperature is assumed equal to 19°C for all layers, this temperature was used for all tests in the ALF experiment and is representative of the mean average temperature in the KEC test road experiment. A moving load is simulated by applying a 0.1 second (i.e., 10 Hz) haversine loading pulse followed by a 0.9 second rest period to the pavement surface. In all simulations the load level and contact pressure were 73.8 kN (16.6 kip) and 827 kPa (120 psi) respectfully. These conditions were identical to those used in the FHWA ALF experiment.

For ALF pavements the number of simulated cycles ran for each mixture was the same as that applied during the experiment. In the case of the KEC pavements, since no information was available as to the number of load applications, simulations ran for up to one millions cycles. To perform such a long-term simulation in a reasonable amount of time, an extrapolation technique has been developed wherein certain cycles are skipped and the results extrapolated from previous cycles. This approach takes advantage of the fact that damage grows in a generally linear slope with respect to material integrity, C , at higher damage levels. The number of elements used in each simulation changed due to differences in the material structure; however, both the number of elements and number of cycle jumps were set based on thorough sensitivity analyses. Finally, normal finite elements are used for distances up to 1 m from the center of the tire and to the bottom of the aggregate base layer. Special elements are used for longer distances to reproduce the effect of the infinite boundaries and to reduce computational time. Through sensitivity analysis, it is found that the effect of these special elements on the results is negligible.

4 MATERIAL CHARACTERISTICS

The mixtures presented in this paper from the ALF study have been discussed in detail elsewhere (Al-Khateeb et al. 2007, Underwood et al. 2006, Qi et al. 2004), in short each mixture consists of the same Superpave 12.5 mm coarse aggregate gradation, but differing asphalt cements. Three modified

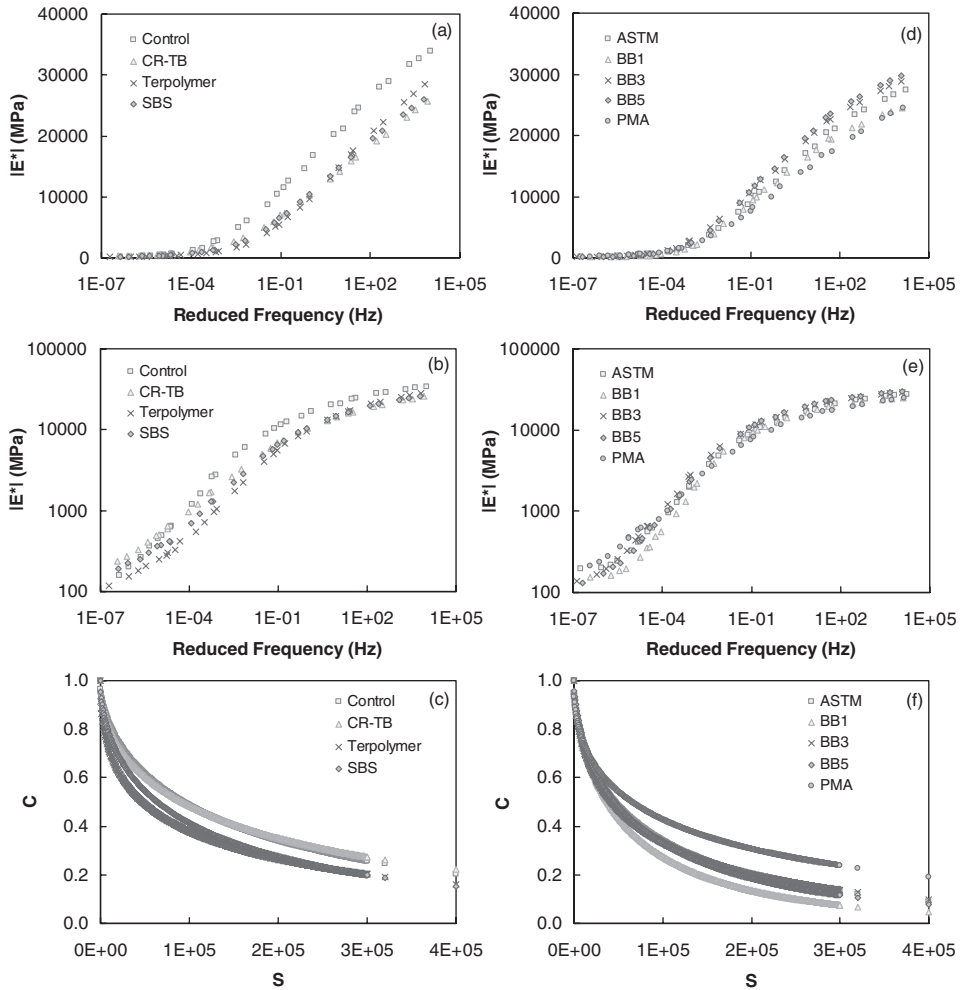


Figure 1. VECD characterization: for ALF mixtures (a) $|E^*|$ in semi-log space, (b) $|E^*|$ in log-log space, and (c) damage characteristic curves; for KEC mixtures (d) $|E^*|$ in semi-log space, (e) $|E^*|$ in log-log space, and (f) damage characteristic curves.

asphalts; SBS, Crumb Rubber-Terminal blended (CR-TB) and Ethylene Terpolymer (Terpolymer) along with a single unmodified PG 70-22 (unmodified) asphalt cement are included. The key properties of the five KEC test road mixtures are summarized in Table 1. These mixtures vary by mixture type (i.e., surface, intermediate or base course), nominal maximum aggregate size, asphalt cement type, asphalt content, and asphalt to filler ratio. Four of the five mixtures use the same unmodified PG 64-22 binder (ASTM, BB1, BB3 and BB5) while one mixture uses a SBS modified binder (PMA). The PMA mixture is also a surface course and is very similar to the ASTM mixture.

5 PERFORMANCE PREDICTION OF ALF PAVEMENTS

5.1 ALF pavement simulation

Due to natural variations in the construction process, certain pavement characteristics are not identical across ALF pavement sections. Table 2 summarizes the as constructed sub-layer moduli

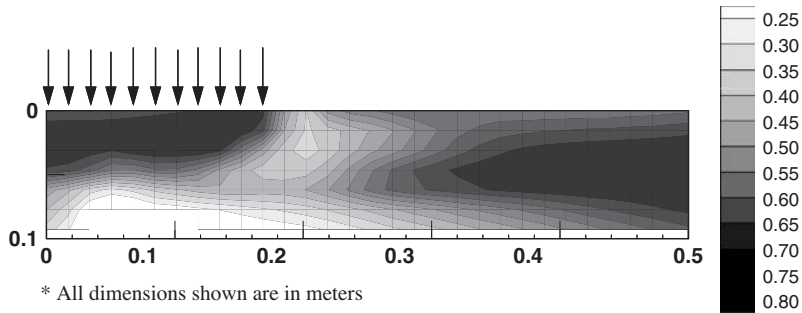
Table 1. Volumetric properties of laboratory mixtures for KEC pavements.

Mixture	Layer type	NMSA* mm	Modifier	Asphalt grade	Asphalt content %	Asphalt-filler ratio
ASTM	Surface	19	N/A	PG 64-22	4.9	1.17
PMA	Surface	19	SBS	PG 76-22	5.0	1.20
BB1	Base	25	N/A	PG 64-22	4.2	1.00
BB3	Base	19	N/A	PG 64-22	4.4	1.10
BB5	Intermediate	19	N/A	PG 64-22	4.3	0.98

*Nominal maximum aggregate size.

Table 2. Base and subgrade moduli and AC layer thicknesses for ALF pavement simulation.

ALF Lane	Mixture	Base modulus MPa (ksi)	Subgrade modulus MPa (ksi)	AC layer thickness mm (in)
2	Control	160(23.2)	46(6.7)	107(4.21)
4	SBS	132(19.1)	42(6.1)	103(4.06)
5	CR-TB	105(15.2)	37(5.4)	93(3.66)
6	Terpolymer	108(15.7)	36(5.2)	105(4.13)



* All dimensions shown are in meters

Figure 2. Typical damage pseudostiffness contour of ALF pavement simulation (CR-TB lane at N = 100,000).

and surface layer thicknesses for each of the test sections. Note that the base and subgrade moduli values are determined via backcalculation from FWD measurements performed at different load levels and locations along the test site. The values shown in Table 2 are used as inputs for developing the finite element structure used in the simulations.

A typical result from the ALF pavement analysis is shown for the CR-TB section at cycle number 100,000 in Figure 2. The contours in Figure 2 represent C values (lower values indicate areas with more severe damage) and the arrows indicate the area where load is being applied. Note that Figure 2 only shows one half of the applied load since FEP++ uses axisymmetric analysis. It is observed for this pavement that damage is concentrated at the bottom of the AC layer. This observation fits the generally accepted failure mechanism for thin asphalt pavements, i.e., bottom-up fatigue cracking.

5.2 ALF field and simulation comparison

To better quantify results such as those shown in Figure 2 an index value, the damage area (%), has been defined. Damage area (%) is calculated by determining the percentage of total nodes, from the load center to 0.5 m in the horizontal direction and from the pavement surface to the

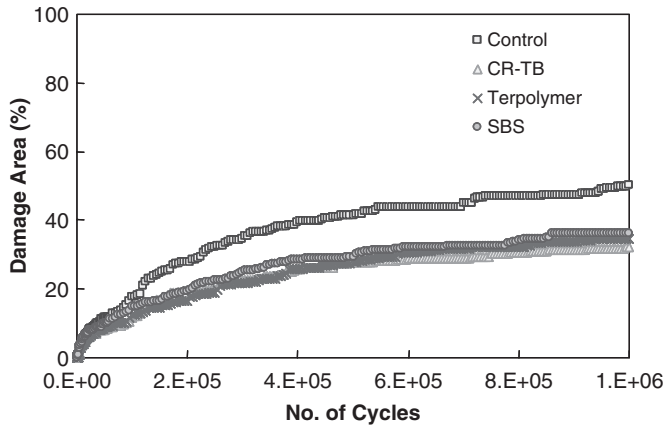


Figure 3. Numerical analysis results of ALF simulation as represented by damage area (%).

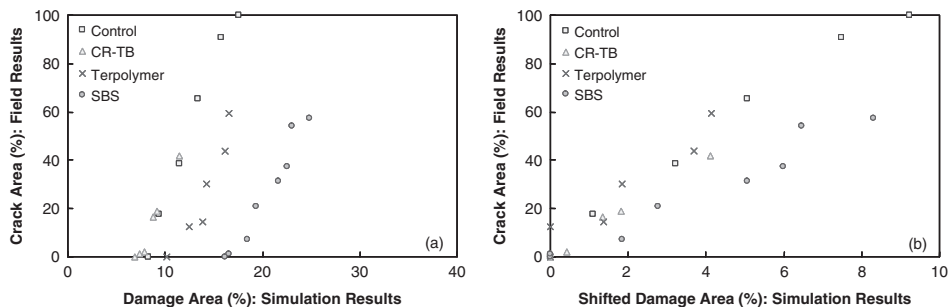


Figure 4. Comparison of ALF field results with: (a) damage area (%) and (b) shifted damage area (%) from simulations.

bottom of the AC layer in the vertical direction, that have C values below 0.25. This value of C generally corresponds to the point at which strains localize and the material fails in the constant rate characterization tests. In light of this definition it should be observed that a lower damage area (%) suggests better fatigue performance. Analysis of the ALF simulations with the damage area (%) index are shown in Figure 3 where it is clearly observed that the control pavement is predicted to have the worst fatigue damage performance and that the modified mixtures are expected to show similar performance. In the ALF experiment the control mixture was observed to display the worst performance followed next by the CR-TB, then the Terpolymer and finally the SBS. However, at the time of this writing no statistical analysis on the field data has been completed to assess the significance of the differences.

Throughout the course of ALF testing, the percentage of cracked lane area was measured as a function of load applications. These results have been plotted against the values obtained from simulations at the same cycle number in Figure 4. The first observation from this figure is that the magnitudes of the damage area (%) index do not directly match with the observed cracking area in the field. This observation suggests the need for developing a simulation to field transfer function. Having such a function is not unexpected given that an index value has been defined from the simulation results, the fact that model characterization was performed on laboratory compacted specimens and a list of other possible minor factors which exist.

From Figure 4 it is also found that a non-unique relationship between the damage area (%) and observed field cracking exists. A possible reason for this non-consistent discrepancy may lie in the

definition of damage area (%). Recall that the field measured values include cracking as visually observed on the pavement surface; whereas, the index value, as a matter of practicality, is defined to represent the damage across the whole pavement cross-section. An examination of the contour plot in Figure 2 shows that damage occurs largely at the bottom of the pavement structure and thus the damage area (%) index is more indicative of what is occurring at the bottom of the pavement layer. As such, the damage area (%) will likely provide a delayed prediction of what is to be expected on the surface. The degree of delay is hypothesized to be a function of the fracture, or macrocrack propagation properties of the mixture. To explore this possibility, the delay between actual observed fatigue cracking and the damage area (%) has been removed by replacing the damage area (%) on the x-axis in Figure 4(a) with the difference between the damage area (%) when field cracks were first observed and the calculated damage area (%) in Figure 4(b). After removing this offset factor it is observed that a more consistent transfer function may be developed, for this particular case it appears that a linear function with a slope of 10 is reasonable. Note however, that in the ALF pavements little field data is available for very low cracking levels.

6 PERFORMANCE PREDICTION OF KEC TEST ROAD PAVEMENTS

6.1 KEC field fatigue performance

The AC pavement structures of the KEC test road are shown schematically in Figure 5. The structural concept; i.e., surface, intermediate, base, subbase, antifrost, and subgrade layers, and thickness ranges represent typically used Korea pavement structures. Note that in Figure 5, the section name is given at the top of the figure (i.e., A1, A2, etc.). Also note that sections with the PMA mixture as the surface layer are denoted as A2-2, A5-2, etc. The different materials are shown with different shades of colors or patterns, and the numbers in each block denote the respective layer thickness in centimeters.

In total, four field performance surveys have been performed since the test road was constructed: 1) August 2005; 2) November 2005; 3) July 2006; and 4) October 2006. The main survey items for fatigue performance include the length of longitudinal and transverse cracking, patching area, and alligator cracking area. Using these measurements, the KEC has adopted Equation (1) to define a representative index of fatigue performance.

$$\text{total crack (m}^2\text{)} = 0.3 * \sum \text{line crack (m)} + \sum \text{alligator crack (m}^2\text{)} + \sum \text{patching (m}^2\text{)} \quad (1)$$

$$\text{Crack Area (\%)} = \frac{\text{total crack (m}^2\text{)}}{\text{section length} \times \text{section width}} * 100 = \frac{\text{total crack (m}^2\text{)}}{\text{section length} \times 7.2} \quad (2)$$

Since each of the test sections differ in the total length, the calculated index values from Equation (1) are normalized by total section area and presented as crack area (%), Equation (2). Figure 6(a) shows the field fatigue performance of the unmodified asphalt pavement sections in the KEC test road. Note that while only the combined index is shown, the sections with high index values are dominated by alligator cracks while sections with lower values are dominated by line cracks.

Although the surveys were conducted at different times, the test road was completely closed to traffic between the first survey and the final survey. In light of this fact, any differences between the survey findings can be attributed to the survey variability and/or deterioration due to environmental factors. It is felt that the latter option is less likely and thus differences are attributed to survey variability. To demonstrate the variability results from all four surveys are shown below; however, note that when comparisons are made with simulation results only the average results from all four surveys are included.

From 6(a) it is observed that the field performance does not show a great deal of deterioration for most sections, but it is clear that the aggregate base sections are (A13–A15) performing the worst of all sections. Among these, the performance of the section with the thinnest base course (A13)

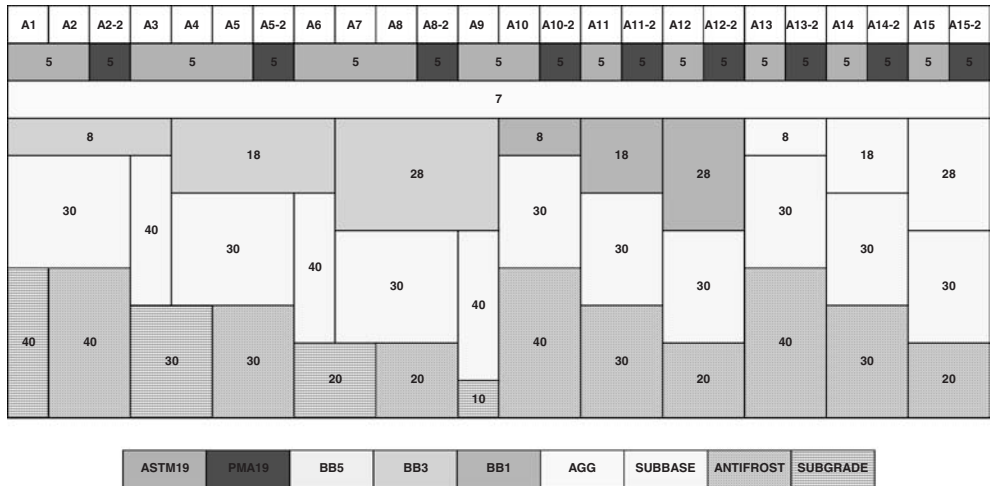


Figure 5. Asphalt concrete pavement structure of KEC test road.

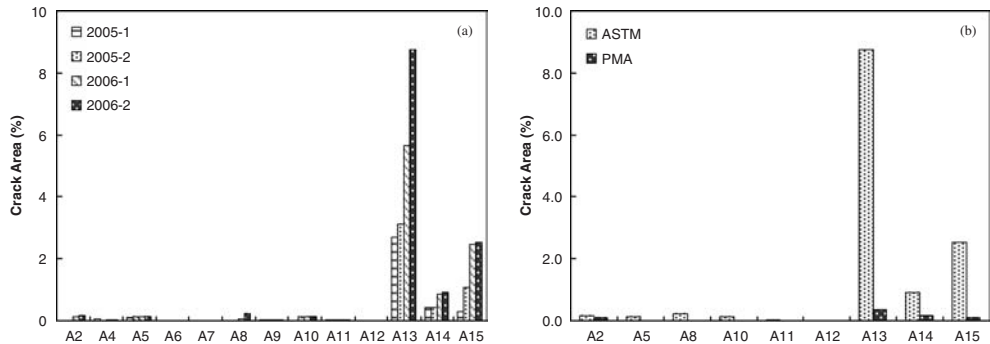


Figure 6. Field fatigue performance of KEC test road sections: (a) crack area (unmodified only), (b) ASTM and PMA comparison (2006-2 only).

is the worst, while sections A14 and A15 do not follow the expected trend, i.e., the section with the thinner base layer (A14) is performing better. This effect is likely due to the natural variability which occurs in the field.

Figure 6(b) shows comparisons between only the sections with PMA and ASTM surface layer. As expected the PMA surface layers are outperforming the pavements with unmodified surface layers. It can also be observed that the same overall trend of poorer performance from the aggregate base pavements is observed.

6.2 KEC test road simulation

Simulations of the 24 different pavement structures shown in Figure 5 were performed using the same loading and temperature conditions used for the FHWA ALF simulations. Note that although the KEC test road is exposed to real traffic and environmental conditions, ALF loading conditions are used for the simulation. ALF conditions are used not only because this study focuses on the effect of the structural variables on fatigue performance rather than making an absolute comparison, but it also focuses on how well the simulation captures those effects in terms of the relative performance of the different sections. The VECD model parameters were obtained from experiment and are shown

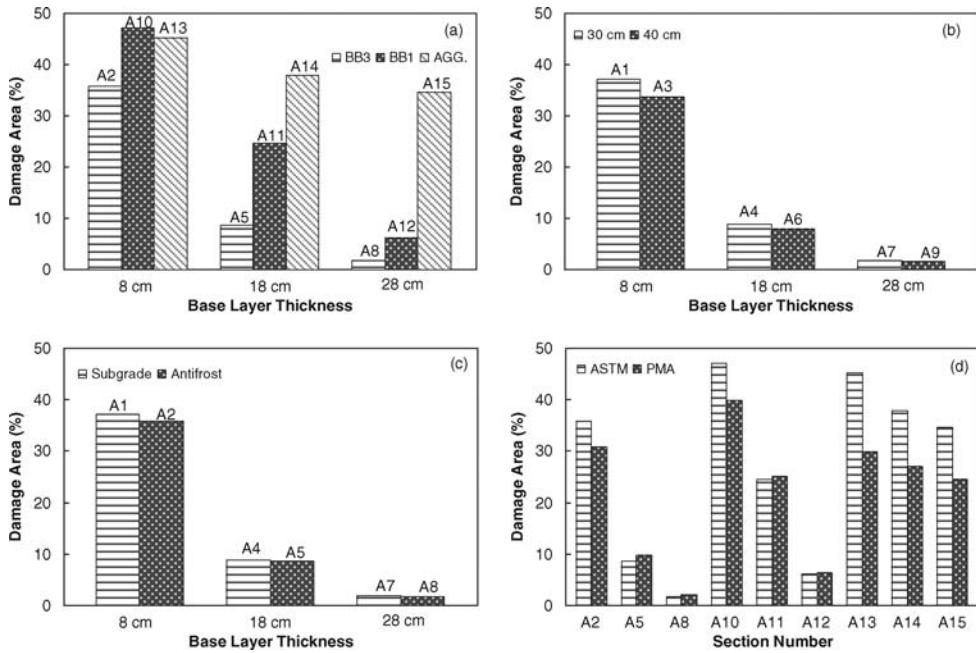


Figure 7. Influence of structural parameters on predicted performance: (a) base type, (b) subbase thickness, and (c) underlying layer type, (d) surface layer type.

in comparison to FHWA ALF materials in Figure 1. Elastic modulus values for unbound layers were assumed based on estimation from the pavement design inputs, as follows: $E_{agg.} = 517$ MPa (75 ksi); $E_{subbase} = 350$ MPa (51 ksi); $E_{antifrost} = 88$ MPa (13 ksi); and $E_{subgrade} = 75$ MPa (11 ksi).

Results from simulations of the 24 pavement sections are summarized, with the damage area (%) index, in Figure 7. Figure 7(a) shows comparisons for the effect of base layer thickness (8, 18, and 28 cm) and type (BB3, BB1 and aggregate). Overall, the expected trends are observed with regards to thickness and material quality. More interesting; however, the interaction between the two factors is also found. For example, in the case of the aggregate base pavements, comparisons between the 8 and 28 cm thicknesses (a 3.5 times increase), show a change in damage area (%) of approximately 10, whereas the same thickness difference in the BB1 case shows an index change of approximately 40.

Comparisons regarding the effect of subbase thickness (30 cm versus 40 cm) as a function of base thickness are shown in Figure 7(b). Comparing this figure with Figure 7(a) it is found that the damage performance is less sensitive to the thickness of the subbase layer than it is to either the base layer type or base layer thickness. Although this result is not surprising, the quantification of expected changes in fatigue performance for such a particular design detail could allow for better optimization of pavement design. With regards to the underlying material influence, Figure 7(c) suggests similar performance can be expected from pavements supported with either the antifrost or subgrade materials. Of course this comparison does not consider any possible benefits of the antifrost layer with regards to frost-heave mitigation.

Finally, the expected effect of surface layer type (ASTM versus PMA) is shown through the comparisons in Figure 7(d). Based on the analysis shown in Figure 7(d), the aggregate base pavements (A13-A15) with the PMA layer are expected to yield a better fatigue performance than those with ASTM. The field observations to date (Fig. 6(b)) support these simulation results. However, in the full-depth pavements (A5-A12), the damage area (%) index suggests that the pavements with a thicker base layer (A5, A8, A11 and A12) would show a slightly better performance with

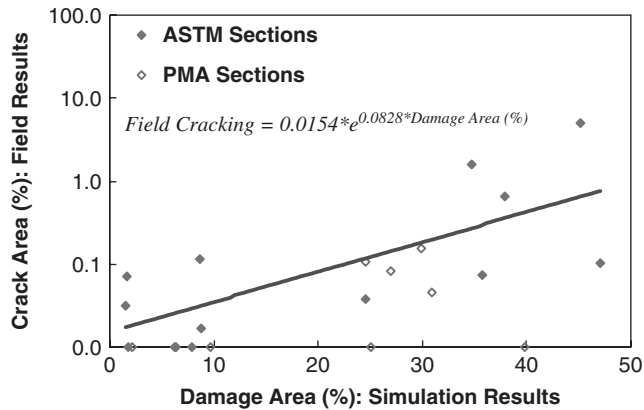


Figure 8. Comparison of observed and simulated fatigue performance for KEC test road pavements.

the ASTM surface layer. Recall, though, that the damage area (%) includes the entire pavement cross-section, i.e., the surface, intermediate and base layers. From a careful examination of the damage contours of these pavement simulations it is found that the extent of damage occurring in the surface layer is reduced in the PMA cases. In short, the particular nature of the PMA causes higher overall damage in the pavement structure but less in the surface layer itself. This is an important distinction to make because, as discussed with the ALF simulations, the damage index (%) value is expected to yield some material dependent delay between the time when it shows a *C* value below 0.25 and visually observed. It is likely that the delay in the PMA mixture would be greater than the ASTM mixture (compare SBS with Control in Figure 4). With this expectation, and the observed reduction in overall surface layer damage, the PMA is expected to yield a better fatigue performance in all cases.

6.3 KEC field and simulation comparison

Direct comparison of KEC simulations and field observations is not as straightforward as similar comparisons from the ALF experiment. The KEC pavements are subjected to variable loading and environmental conditions which are not currently accounted for in the model. Further, as a test road the in place material properties, construction variability and general number of unknowns increases. However, as a proof of the concept for developing a transfer function the results from the average of the four KEC pavement surveys are plotted against the damage area (%) index at one million cycles in Figure 8. Note that a function developed from Figure 8 would include the effect of construction variability, which would change from section to section, and inconsistent loading and environmental factors, which should be the same from section to section. In Figure 8 each data point represents a specific section and it is noted that all 24 sections are included, although the PMA sections are represented with an open symbol. Nevertheless, the data in Figure 8 suggest that a consistent link between simulation and measured in-service field performance can be found. It is finally noted that these field performance observations are part of an ongoing task, and that most of the sections are showing only minor visual cracking at the time of this writing.

7 SUMMARY AND CONCLUSIONS

A mechanistic model of asphalt concrete pavement has been characterized and applied to predict the fatigue performance of AC mixtures tested at the FHWA ALF and the KEC test road project sites. In this mechanistic model, material behavior is considered with the VECD model, whereas

structural influences (e.g., layer thicknesses) are accounted for with the finite element package (FEP++), developed at North Carolina State University. Comparisons between the measured and predicted performance of ALF pavements show that the VECD-FEP++ captures the mixture characteristics with reasonable accuracy. In particular, the model shows the clear differentiation between the unmodified and modified mixtures that was observed in the ALF experiment. The study also reveals that consideration should be given for development of a simulation to field performance transfer function.

The KEC test road project sites were designed to systematically examine the effects of base type, base thickness, sublayer thickness, sublayer type and surface layer type on pavement performance under actual traffic loads and changing environmental conditions. Although the field performance observations for these project sites is an ongoing task, preliminary results clearly show inferior performance from the aggregate base pavements. Predictions made with the VECD-FEP++ for the test road sections demonstrate such a performance trend and also reveal a generally positive relationship between model predictions and field observations for all sections. With such positive relationships, efforts are made to develop a preliminary transfer function for pavement performance predictions. For KEC pavements this transfer function merges factors related to the variable environmental and loading conditions as well as the inherent field variability. This transfer function may be refined with further study and as more field performance information becomes available.

ACKNOWLEDGMENTS

This research is jointly sponsored by the Federal Highway Administration under the project No. DTFH61-05-RA-00108 and by the Korea Expressway Corporation. The authors gratefully acknowledge their support. Special thanks go to Mr. Soon-Min Kwon, Mr. Jae-Hoon Lee, and Dr. Youngguk Seo at the Highway and Transportation Technology Institute at the KEC for their efforts in collecting and sharing the field performance data.

REFERENCES

- Al-Khateeb, G., Gibson, N., & Qi, X. 2007. Mechanistic Analyses of FHWA's Accelerated Loading Facility Pavements: Primary Response. *Transportation Research Record 1990*. National Research Council, Washington, D.C: 150–161.
- Chehab, G.C., Kim, Y.R., Schapery, R. A., Witzack, M., & Bonaquist, R. 2002. Time-Temperature Superposition Principle for Asphalt Concrete Mixtures with Growing Damage in Tension State. *Asphalt Paving Technology*, AAPT V. 71: 559–593.
- Daniel, J.S. & Kim Y.R. 2002. Development of a Simplified Fatigue Test and Analysis Procedure Using a Viscoelastic Continuum Damage Model. *Asphalt Paving Technology*, AAPT V. 71: 619–650.
- Kim, Y.R. & Chehab, G.C. 2004. *Development of a Viscoelastoplastic Continuum Damage Model for Asphalt-Aggregate Mixtures: Final Report as Part of Tasks F and G in the NCHRP 9-19 Project*. National Cooperative Highway Research Program, National Research Council, Washington, D.C.
- Qi, X., Mitchell, T., Stuart, K., Youtcheff, J., Petros, K., Harman, T., & Al-Khateeb, G. 2004. Strain Responses in ALF Modified-Binder Pavement Study. 2nd *International Conference on Accelerated Pavement Testing*, Minneapolis, MN.
- Schapery, R.A. (1984). Correspondence Principles and a Generalized J-integral for Large Deformation and Fracture Analysis of Viscoelastic Media. *Int. Journal of Fracture*, Vol. 25, pp. 195–223.
- Schapery, R.A. (1990). A Theory of Mechanical Behavior of Elastic Media with Growing Damage and Other Changes in Structure. *J. Mech. Phys. Solids*, 38, pp. 215–253.
- Underwood, B.S., Kim, Y.R., & Guddati, M.N. 2006. Characterization and Performance Prediction of ALF Mixtures Using a Viscoelastoplastic Continuum Damage Model. *Asphalt Paving Technology*, AAPT Vol. 75: 577–636.

6. Top-down cracking in flexible pavements

Finite element analysis of top-down cracking in semi-rigid pavement structure

P. Wang & X.-M. Huang

Southeast University, Nanjing, China

Q.-F. Li & Z.-T. Yang

Zhengzhou University, Zhengzhou, China

ABSTRACT: More and more researches indicate many load-related fatigue cracks initiate at the surface and propagate downward through the surface layer. TDC often occurs in the edge of wheel path. The tradition method can't explain the mechanism of this cracking. Because the traditional load is the vertical surface load with average tire pressure and is applied at only one position. No effort is made to distinguish between tire type nor to capture the possible effects of changing load position due to wander in wheel paths. In order to discuss the mechanism of TDC, this paper establish a 3D finite element model of semi-rigid pavement structure and use the large finite element software ABAQUS, The analysis result shows that maximum shear stress is appear in the surface of pavement, and located the edge of wheel path. Maximum shear stress is beyond shear strength of asphalt binder. So the researchers think it is the major reason leading to TDC. It's provide the theory basis on further finding the mechanism of TDC.

Keywords: TDC; Finite element; maximum shear stress.

1 INTRODUCTION

Traditional pavement fatigue cracks are assumed to initiate at the basement and propagate uphill. The research of mechanism of this cracking has gained a lot achievement and many pavement methods are designed based on it. However, recently, longitudinal cracks are often observed to occur in the edge of wheel path and propagate downward through the surface layer, which give rise to more and more attention from pavement experts. Top-down cracking (TDC) of asphalt pavement is defined as fatigue cracks initiate at the surface and propagate downward through the surface layer. Cracking at early stage is also called surface cracking, surface initiated cracking, surface-initiated longitudinal wheel path cracking and longitudinal surface cracking etc. The reason of TDC initiation is discussed through finite element analysis on pavement structure in the paper.

2 THE ESTABLISHMENT OF FINITE ELEMENT MODEL ON PAVEMENT STRUCTURE

2.1 *The selection of wheel-load model*

Wheel load is an external force generating pavement stress, stain and displacement variation and is one of immediate causes inducing pavement destruction. Driving vehicles on pavement can be in different conditions such as stop, braking and turning etc. With movement variation on pavement, the applied direction and force of wheel load are also changed. Therefore, reasonable selection of wheel-load model is the groundwork of correct analysis on pavement response and the reason of

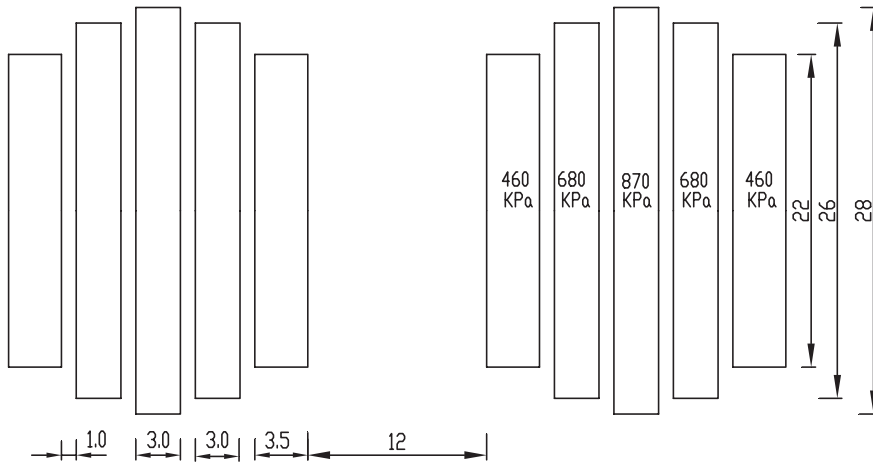


Figure 1. Load model.

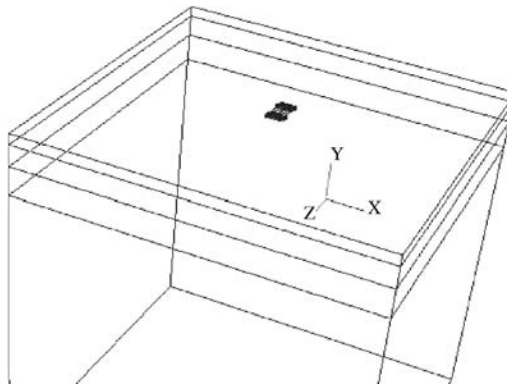


Figure 2. The coordinate of model.

TDC initiation. Systemic research work of wheel-load model has been made [8]. Based on it, the wheel-load model which is selected in the paper is shown as Figure 1 (longitudinal tread contour, 100 KN).

2.2 The selection of finite element model

The selected finite element model is shown as Figure 2: the model dimension is: $5\text{ m} \times 5\text{ m} \times 5\text{ m}$; the boundary condition is fixed support on back surface and slip support on two sides parallel to driving direction; top surface and two sides vertical to driving direction are free; interlamination is continuous; cell is eight-node hexahedron solid mass; grid is divided manually plus automatically; the location applied by wheel-load is divided manually and densely, while others are automatic. The large general software-ABAQUS is applied in computation in the paper.

2.3 Confirmation of pavement structural parameters

Mechanical response is different with the variant pavement structure. Therefore, distinguishing different-type pavement structural parameters are very important. Semi-rigid asphalt pavement specific parameters are shown in Table 1.

Table 1. Pavement structure and parameters for calculation.

Number of layers	Structure layer	Semi-rigid pavement structure			Poisson ratio
		Mixture	Thickness/cm	Modulus/MPa	
1	Surface	Asphalt concrete	15	1200	0.25
2	Base	Cement stabilized macadam	30	1500	0.25
3	Subbase	Lime stabilized soil	40	800	0.30
4	Subgrade			40	0.35

Table 2. The maximum tensile stress, maximum shear stress and locations.

Item	Stress value/Pa	Location/m
Maximum tensile stress	4.128E+04	(0.0, 1.65, 2.5)
Maximum shear stress	3.26E+05	(0.0, 2.5, 2.325)

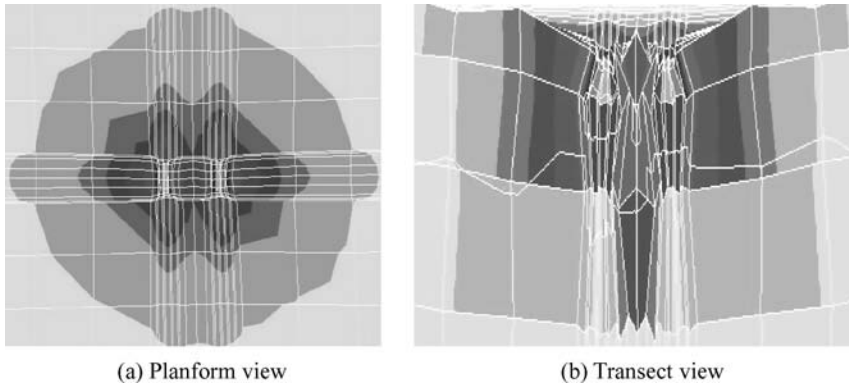


Figure 3. Contour of the maximum shear stress.

3 RESULTS AND ANALYSIS

Input above parameters into finite element model and calculate it. Maximum tensile stress and maximum shear stress obtained are shown in Table 2 and Figure 3.

From studying Table 2, apparently the value of maximum shear stress has of the order of magnitude larger value than maximum tensile stress. Its location is at the bottom of sub-base (the value of y is 1.65, just equal to $(2.5 - 0.85)$). The value of normal tensile strength and shearing strength are of the order of magnitude of 1 MPa^[9] and 0.3 ~ 0.5 MPa^[10]. The value of maximum tensile stress is of the order of magnitude less than tensile strength, while the value of maximum shear stress is in the range of shearing strength. With the consideration of fatigue effect, maximum shear stress is believed to be the direct cause to TDC initiation, which has the same conclusion with literature [11]. To find out maximum shear stress variation rule, the relations of maximum shear stress with $E1/E2$ and with surface thickness are shown in Figure 4 and Table 3.

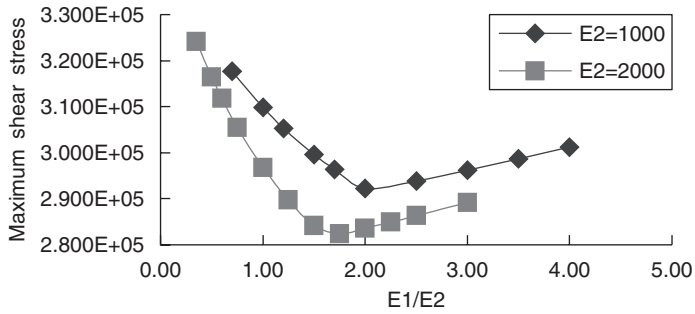


Figure 4. The relation between the maximum shear stress and E1/E2.

Table 3. Effect of surface thickness on stress and deflection.

Thickness/cm	Maximum tensile stress/Pa	Maximum shear stress/Pa	Deflection/m
9	4.129E+04	3.053E+05	-3.851E-04
12	4.019E+04	3.046E+05	-3.771E-04
15	3.901E+04	3.093E+05	-3.696E-04
18	3.782E+04	3.084E+05	-3.626E-04

From Figure 4, when E2- the moduli of basement, is in a larger value, the increment of E1/E2 generates the increment of speed of maximum shear stress decrease. Meanwhile, when the value of E1/E2 is near 2, the value of maximum shear stress is minimal; whereas the value of maximum shear stress is increasing no matter the value of E1/E2 is larger or less than 2; and it is obvious decreasing when less than 2, while obscure decreasing when larger than 2.

From Table 3, the thicker the surface is, the less value of tensile stress and deflection are. But the thickness of pavement has no obvious effect on the maximum shear stress with the maximum error of 2%.

4 CONCLUSIONS

- 1) Maximum shear stress occurs on the surface of pavement and is believed to be the main cause to TDC initiation in semi-rigid pavement;
- 2) Maximum tensile stress occurs at the bottom of sub-base and is believed to be the direct cause to reflected cracking initiation;
- 3) The thickness of pavement has not obvious effect on the maximum shear stress. But the thicker the surface is, the less value of tensile stress and deflection are.
- 4) E1/E2 has certain effect on the maximum shear stress and the value of maximum shear stress is maximal when the ratio is near 2.
- 5) Due to some limitation, the future research work should be kept on.

REFERENCES

- [1] Uhlmeyer J. S., K. Willoughby, L. M. Pierce and J. P. Mahoney. Top-Down Cracking in Washington State Asphalt Concrete Wearing Courses[A]. In *79th Annual Meeting (CD-ROM)*, TRB, National Research Council, Washington, D.C., 2000, Paper No.00-0405

- [2] Svasdisant, T., Schorsch, M. Baladi, G. Y. and Pinyosunun, S. Mechanistic Analysis of Top-Down Cracks in Asphalt Pavements[A]. In *81st Annual Meeting* (CD-ROM), TRB, National Research Council, Washington, D.C., 2002
- [3] Dazats, M. and A. Rampal, Mechanism of Surface Cracking in Wearing Courses[A], *Proceedings, 6th International Conference on the Structural Design of Asphalt Pavements*, The University of Michigan, Ann Arbor, Michigan, July 1987:232–247
- [4] Gerritsen, A. H., van Gorp, C. A. P. M., van der Heide, J. P. J. Molenaar, A. A.A., and A. C. Pronk. Prediction and Prevention of Surface Cracking in Asphaltic Pavement[A]. *Proceedings, 6th International Conference on the Structural Design of Asphalt Pavements*, The University of Michigan, Ann Arbor, Michigan, July 1987:378–391
- [5] Myers, L. A., R. Roque, and B. Birgisson. Propagation Mechanisms for Surface-Initiated Longitudinal Wheel Path Cracks[A]. In *80th Annual Meeting* (CD-ROM), TRB, National Research Council, Washington, D.C., 2001, Paper No.01-0433
- [6] Myers, L., R. Roque, and B. E. Ruth. Mechanisms of Surface-Initiated Longitudinal Wheel Path Cracks in High-Type Bituminous Pavements[J]. *Journal of the Association of Asphalt Paving Technologists*, 1998, 67: 401–432
- [7] Matsuno, S. and Nishizawa, T. Mechanism of Longitudinal Surface Cracking in Asphalt Pavement[A]. *Proceedings, 7th International Conference on Asphalt Pavements*, The University of Nottingham, 1992: 277–291
- [8] Xie shui-you, Effects of Tire Contact Pressure on Asphalt Pavement Structure [D], Xi'an: Master Paper of Chang'an University, 2003, 12–16
- [9] Bi Yu-feng, Sun Li-jun. Research on Test Method of Asphalt Mixture's Shearing Properties, *Journal of Tong Ji University (Natural Science)*, Aug, 2005: 1036–1040
- [10] Li Feng, Sun Li-jun. Finite Element Analysis of Top—Down Cracking in Asphalt Pavement, *Journal of Highway and Transportation Research and Development* 2006, 23(6): 1–4

Investigation of fatigue cracking: Bottom-up or top-down

X. Hu, S. Hu & L.F. Walubita

Texas Transportation Institute, Texas A&M University, College Station, Texas, USA

L. Sun

Tongji University, Shanghai, P.R.China

ABSTRACT: Traditionally, HMA pavement designs and modeling methods have historically been based on the fundamental assumption that fatigue cracking generally initiates at the bottom of the HMA layer due to excessive tensile stresses/strains, and then propagates upwards to the surface. However, fatigue cracking can either be bottom-up or top-down initiated depending on the location of the maximum horizontal tensile stresses and strains in the HMA layer. Various factors such as the pavement structure and wheel/tire loading configurations influence the fatigue crack-related tensile strains that are induced in the HMA layer. In this study, the influence of these factors on the tensile strains responses and potential location of fatigue crack initiation in HMA pavements was investigated. To address the non-uniformity distribution of the tire-pavement contact pressure (TPCP), a three-dimensional finite element (3-D FE) program was utilized for the computational simulations and numerical analyses. Specifically, the actual TPCP of different tire types and tread patterns measured under variable load levels and tire inflation pressures were utilized to evaluate and analyze the potential locations of maximum tensile strains in terms of fatigue crack initiation. The results showed that fatigue cracking, bottom-up or top-down, depended on pavement structure, material parameters, and has little relative with the magnitude and distribution of tire-pavement contact pressure. Finally, the potential locations of fatigue crack initiation in asphalt pavements were recommended.

1 INTRODUCTION

It was generally thought that fatigue cracking generally initiates at the bottom of Hot-mix asphalt (HMA) layer, and then propagates up to the surface of HMA layer. However, many recent studies and field experiences have shown that fatigue cracking can also initiate at the surface of the HMA surfacing/wearing course layer due to high surface tensile stresses/strains and then propagate downwards through that layer. In 1987, Gerritsen et al. (1987) conducted a study of top-down cracking (TDC) on HMA pavements in the Netherlands and confirmed the prevalence of TDC, but that this phenomenon did not extend into the lower bituminous or HMA base layers. Gerritsen et al. (1987) further reported that these surface cracks occurred both inside and outside the wheel path areas, and, in some cases, soon after paving. Dauzats and Rampal (1987) published results that described surface-initiated cracking on HMA pavements in France.

Matsuno and Nishizawa (1992) reported that TDC constitute a major distress in Japan, predominantly occurring near the wheel paths in pavements ranging from 1 to 5 years old and that it is absent in shadowed areas such as under bridges. They conducted that traffic loading cause high tensile strains in hot pavements and that the pavement cross section had little effect on the surface tensile strains. In their study, Meyers et al. (1998) reported that TDC typically occurred outside the wheel paths in Florida; with cracks penetrating to depths ranging from just under the pavement surface to the entire HMA layer depth. They concluded that the main cause of TDC is the increasing use of radial truck tires and that the HMA thickness has little effect on the surface tensile stresses.

Uhlmeier et al. (2000) observed that TDC occurred in and around the wheel paths in pavements that are 3 to 8 years old with HMA thicknesses of more than 160 mm. On this basis, these researchers concluded that pavement thickness has an effect on the initiation of TDC, which contradicts the findings of Matsuno and Nishizawa (1992) and Meyers et al. (1998). In further contrast to Meyers et al.'s (1998) findings, Rogue et al. (2006) found that pavement structure had an effect on the surface-initiated cracking in Florida.

Based on the aforementioned literature review, the following can be inferred: (a) surface-initiated fatigue cracking is widespread in most HMA pavements; (b) it is generally believed that these surface-initiated cracks are caused by some combination of truck tires and thermal stresses; (c) there is no general consensus on the location of the critical surface tensile stresses, however most researchers consider that the critical location is near or at the tire edge; (d) there is no generalized understanding on the effects of the pavement structure variables such as the HMA layer(s) thickness and moduli on the initiation of TDC; (e) some studies based on the actual measured tire-pavement contact pressures and instrumented pavements support the view that truck tires is one of the primary causes of TDC in the HMA surfacing layers.

In general, many influencing factors are considered to affect the tensile stress-strain response and fatigue (cracking) behavior of HMA pavements, when subjected to varying traffic loading and environmental conditions. These factors include the magnitude and distribution of the tire-pavement contact pressure (TCP), pavement structural layer thickness, pavement structural combination, and material properties such as the Poisson's ratio and elastic modulus. All these factors influence the location and mechanism of crack initiation (at the bottom and/or surface of the HMA layer) and need be taken into account when modeling fatigue cracking. To mitigate against this distress, the current mechanistic-empirical (M-E) design concept for the fatigue-resistant perpetual pavements utilizes $70 \mu\epsilon$ as the governing mechanistic response parameter to control bottom-up fatigue cracking in the lowest HMA layer of a flexible HMA pavement structure (APA, 2002; Walubita and Scullion, 2007). According to this criterion, horizontal tensile strains greater than $70 \mu\epsilon$ are indicative of a potential for premature fatigue crack damage and should be minimized.

On the basis of the above discussions, the objective of the work presented in this paper was to computationally investigate the influence of the different combinations of the aforementioned factors on the tensile strains responses and potential locations of fatigue crack initiation in HMA pavements. To address the non-uniformity distribution of the TCP, a three-dimension finite element program (ANSYS) instead of a multi-layer elastic program was used for the computational simulations and numerical analyses. Specifically, the actual contact pressures of different tire types and tread patterns measured under variable load levels and tire inflation pressures in the laboratory were utilized in the tensile strain computations.

2 METHODOLOGICAL APPROACH

This section provides the methodological approach adapted for the study and includes 3D-FE loading configuration, 3D-FE models, and associated boundary conditions.

2.1 3D-FE loading configuration and boundary conditions

Figure 1 shows the 3D-FE loading configuration in terms of the tire contact print area (shaded areas), the X-Y-Z coordinate system, and the pavement structure; simulated as the pavement surface for 3D-FE analysis.

The maximum dimensional lengths adapted for the X, Y, and Z axes were 5.0 m, 5.0 m, and 8.0 m, respectively. The boundary conditions were assumed as follows: 1) no Z-directional displacement on the underside, 2) no X-directional displacements on both the left and right sides of the origin, and 3) no Y-directional displacements on both the front (upper) and back (lower) sides of the origin. All the layers were assumed to be fully-bonded at the interface. The spacing between the tires was taken as 346 mm and 220 mm for the 11.00–20 and 6.5–16 tires, respectively. According to Wang

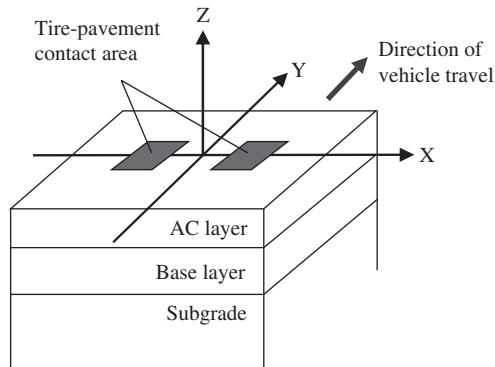


Figure 1. Simulated 3D-FE loading configuration on the pavement surface.

Table 1. Pavement structure and layer material properties.

Material	Thickness (mm)	Modulus (MPa)	Poisson's Ratio
Structure A			
Dense graded HMA	144.8	4878	0.35
Crushed stone base	323.0	389	0.40
Sandy clay subgrade	infinite	100	0.45
Structure B			
Dense graded HMA	51.0	4878	0.35
Crushed stone base	323.0	389	0.40
Sandy clay subgrade	infinite	100	0.45

et al. (2006), the mechanistic response in a HMA layer due to the effect of dual tires on a single axle-wheel configuration is similar to the effect of dual tires on each of the tandem axles. So, only dual tires on a single axle loading configuration were considered in the 3D-FE analysis in this study.

2.2 Validity of 3D-FE model formulation and boundary conditions

It is well known that the appropriateness and accuracy of a 3D-FE analysis model is significantly dependent on the model dimensions and the boundary conditions. As a means to validate the formulated 3D-FE model simulation and associated boundary conditions, a numerical comparison was completed with the multilayer elastic theory (MET). However, because mechanistic response computations under MET are based on a uniform load distribution assumption, a standard axle-wheel load of 80 kN was used in the validation/comparison analyses.

Two typical (simple) pavement structures were arbitrarily utilized; a thick and a thin HMA pavement, differing only in the top HMA layer thickness, see Table 1.

The strains computed at the surface and bottom of HMA layer, located under the center of the tire-pavement contact area, were compared and are shown in Figure 2.

Figure 2 showed a comparative illustration of the result from the computational analyses based on both MET and 3D-FE model simulation, computed at the surface and bottom of the HMA layer. From Figure 2, it is evidently clear that the difference in the computed strain responses between MET and 3D-FE are insignificant. In fact, the strain magnitude do not differ by no more than 3%. These results therefore indicates that the formulated 3D-FE analysis model and the assumed boundary conditions are reasonably feasible and accurate for modeling the mechanistic responses in the HMA pavements considered in this study.

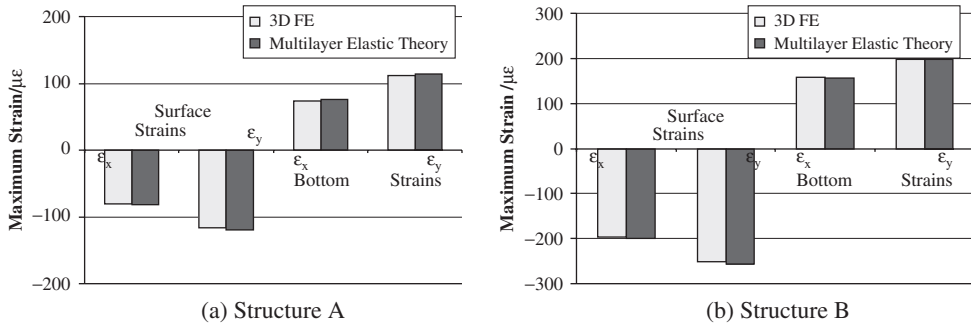


Figure 2. Strain response comparison based on MET and 3D-FE analyses.

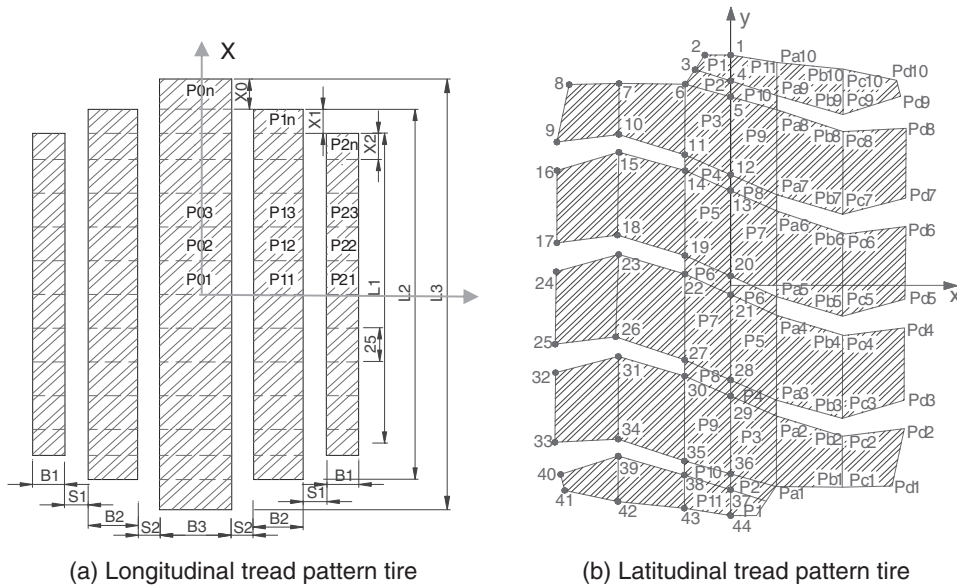


Figure 3. Calculating model of TPCP.

2.3 Tire-pavement contact pressure model in 3D-FE

Based on the actual measured TPCP by Hu (2003), four tire tread patterns were investigated: a 6.5–16 longitudinal, a 6.5–16 latitudinal, an 11.00–20 longitudinal, and an 11.20 latitudinal. All the tires were sourced from the same manufacturer and the rated specifications. The tread pattern and shape of the tire-pavement contact print area of an 11.00–20 longitudinal patterned tire are similar to that of a 6.5–16 longitudinal tread patterned tire, and the tire-pavement contact area was modeled as shown in Figure 3(a) for 3D-FE analysis; a series of interspaced rectangular blocks. However, the width and length of the contact print areas, and subsequently, the magnitude of the contact print areas, are different.

Figure 3(b) shows the tire-pavement contact print area and the 3D-FE simulation of the contact area for a latitudinal tread patterned tire. In Figure 3(b), only the middle blocks denoted as P_i were assumed to have uniform pressure, the rest are not, i.e., were assumed to have non-uniform pressure. For 3D-FE modeling, the load was assumed to be symmetrical about the coordinate origin.

Table 2. TPCP loading parameters.

Tire type and tread pattern	No.	Load (kN)	Inflation pressure (kPa)
A) 11.00–20 bias tire: allowable load levels →		≤ 25.0	460–810
11.00–20 latitudinal tread pattern (heavy-truck tire)	1	25.0	600
	2*	19.0	1050
	3*	25.0	1050
	4*	62.5	1050
11.00–20 longitudinal tread pattern (heavy-truck tire)	5	25.0	460
	6	25.0	600
	7*	19.0	1050
	8*	25.0	1050
	9*	62.5	1050
B) 6.5–16 bias tire: allowable load levels →		≤ 7.15	250–530
6.5–16 latitudinal tread pattern (light-truck tire)	10	7.15	250
	11*	17.88	390
6.5–16 longitudinal tread pattern (light-truck tire)	12	7.15	390
	13*	7.15	700
	14*	17.88	700

*Represents an overload, either the tire inflation pressure and/or the wheel load in *Italics*.

3 TENSILE STRAIN RESPONSES: INFLUENCE OF THE TIRE-PAVEMENT CONTACT PRESSURE

The tire inflation pressure and axle-wheel loading including the pavement structures utilized for the 3D-FE computations are also discussed in this section.

3.1 Tire inflation pressure and axle-wheel load

Based on Hu's (2003) laboratory study of actual TPCP measurements, up to 14 TPCP factor-level combinations including different tire types and tire tread patterns with varied load levels and tire inflation pressures were selected for 3D-FE evaluation in this study. These TPCP factor-level combinations are listed in Table 2.

Based on the rating specifications, 9 of the selected TPCP combinations were overloaded; refer to the numbers with an asterisk (*) in column 2 representing a TPCP combination with tire pressure over-inflation and/or an overload. In Table 2, TPCP Nos. 1~9 are for heavy truck tires and Nos. 10~14 for light truck tires (with a legal single rear axle wheel load of about 30 kN).

3.2 Pavement structures

To evaluate these effects of pavement structure on the magnitude and distribution of the TPCP, 10 thin and thick HMA pavement structures were arbitrarily selected for 3D-FE computational analyses. These pavement structures are listed in Table 3.

In Table 3, PS No's 9 and 10 represent two typical HMA pavement structures mentioned before; PS No's 1 through to 8 have extreme material properties and were incorporated in the analysis to sufficiently illustrate the influence of the moduli/combination on the TPCP. For all the pavement structures, the Poisson's ratio of the HMA and base layers was 0.35, and 0.4 for the subgrade.

3.3 Results and analysis – tensile strain responses due to varying TPCP

Table 4 presents the results of the maximum tensile strains computed in the HMA layer of the different pavement structures listed in Table 3 under the various TPCP combinations listed in Table 2. In Table 4, the column of "TPCP No." corresponds to the TPCP number listed in column 2 of Table 2.

Table 3. Selected HMA pavement structures.

PS No.	HMA layer modulus (MPa)	HMA layer thickness (mm)	Base layer modulus (MPa)	Base layer thickness (mm)	Subgrade modulus (MPa)	Comment
1	1000	50	100	300	50	Thin PS
2	1000	500	100	300	50	Thick PS
3	30000	50	100	300	50	Thin PS
4	30000	500	100	300	50	Thick PS
5	1000	50	15000	300	50	Thin PS
6	1000	500	15000	300	50	Thick PS
7	30000	50	15000	300	50	Thin PS
8	30000	500	15000	300	50	Thick PS
9	4878	144.8	389	323	100	Typical thick PS
10	4878	51	389	323	100	Typical thin PS

*PS = pavement structure.

The column of “ ϵ_{\max} ” refers to the computed maximum tensile strain measured in micro strains ($\mu\epsilon$) and the column of “Direction” refers to the direction of computed maximum tensile strain, X or Y coordinate directions (refer to Figures 1 and 3). The 4th column of “Location” refers to the 3D coordinate location at which the computed maximum tensile strain occurs, e.g., X-Y-Z coordinate location; see Figures 1. The pavement structure number such as “1” or “2” corresponds to the PS No’s in column 1 of Table 3.

Using 70 $\mu\epsilon$ as the reference bench mark, the analysis and findings of the results presented in Table 4 can be summarized as follows:

- (1) For the majority of the pavement structures, the value of ϵ_{\max} in the HMA layer under the different TPCPs is unequal, even under the same wheel load but different tire inflation pressures. However, the location and direction of ϵ_{\max} is seldom influenced by the different TPCPs, e.g., pavement structure 1, and pavement structure 3 ~ 6.
- (2) When the moduli of the HMA layer and base layer are high, e.g., pavement structures 7 and 8, the value of ϵ_{\max} is very small, and mostly occurs at the edge of the simulated 3D-FE model.
- (3) For the pavement structure 2, the ϵ_{\max} is located at the bottom of the HMA layer for the heavy-truck tire loading, where as it is at the surface of the HMA layer under the light-truck tire loading. But to this pavement structure, the modulus of the HMA layer is very low.
- (4) Considering all the 3D-FE input data, the general plane location of ϵ_{\max} is always at the edge or inside of the tire-pavement contact area, except for the cases where both the HMA and base layer moduli are very high. This is so because when both the HMA and base layer moduli are very high, the value of ϵ_{\max} is very small, and may in fact not likely to induce any major fatigue crack initiation in the HMA layer.
- (5) The ϵ_{\max} in pavement structures 1, 2, 3, 5, 6, 9, and 10 are close to or exceed 70 $\mu\epsilon$ under the light-truck tire loading; even under legal loading of 7.15 kN and tire inflation pressure of 250 kPa. This is indicative that depending on the pavement structure and traffic loading conditions, a light truck maybe as fatigue crack damaging as a heavy truck. Note however that due to the possibly high HMA layer moduli, the ϵ_{\max} are substantially less than 70 $\mu\epsilon$ in the pavement structures 4, 7, and 8 under heavy-truck and light-truck tire loading. Theoretically, this means that having the right pavement structure combination in terms of both the layer thicknesses and moduli can significantly reduce the induction of tensile strains in the HMA layer and thus help in minimizing traffic related fatigue cracking.

Table 4. Computed ϵ_{\max} results under varying TPCPs.

TCP No.	ϵ_{\max} ($\mu\epsilon$)	Direction	Location	ϵ_{\max} ($\mu\epsilon$)	Direction	Location
	Pavement	Structure 1	Pavement		Structure 2	
1	893	y	-0.15,0,-0.05	108	y	0,0,-0.5
2	1214	y	-0.14,-0.01,-0.05	86	y	-0.02,0,-0.5
3	1211	y	0.17,0,-0.05	110	y	0,0,-0.5
4	1382	y	-0.14,-0.01,-0.05	268	y	-0.04,0,-0.5
5	806	y	0.15,0,-0.05	110	y	0,0,-0.5
6	907	y	0.17,0,-0.05	110	y	0,0,-0.5
7	1200	y	-0.17,0,-0.05	85	y	0,0,-0.5
8	1303	y	0.17,0,-0.05	111	y	0.02,0,-0.5
9	1359	y	-0.15,0,-0.05	269	y	0,0,-0.5
10	469	y	0.10,-0.01,-0.05	86	x	0,0,0
11	741	y	0.07,0,0,-0.05	151	x	0,-0.02,0
12	519	y	0.1, 0,-0.05	65	x	-0.02,0,0
13	647	y	-0.1,0,-0.05	62	x	0.04,0.03,0
14	964	y	0.09,0,-0.05	128	x	0.01,0,0
	Pavement	Structure 3		Pavement	Structure 4	
1	204	y	-0.10,-0.01,-0.05	5	y	0,0,-0.5
2	199	y	-0.14,0,-0.05	4	y	-0.02,0,-0.5
3	228	y	-0.14,0,-0.05	6	y	0.03,0,-0.5
4	443	y	-0.10,0.03,-0.05	14	y	0,0,-0.5
5	199	y	-0.12,0,-0.05	6	y	0,0,-0.5
6	206	y	0.13,0,-0.05	6	y	0,0,-0.5
7	186	y	0.15,0,-0.05	4	y	0,0,-0.5
8	230	y	0.15,0,-0.05	6	y	0.03,0,-0.5
9	439	y	-0.10,0,-0.05	14	y	0,0,-0.5
10	80	y	0.04,0.01,-0.05	2	y	0,0,-0.5
11	176	y	-0.04,-0.02,-0.05	4	y	0,0,-0.5
12	84	y	0.07,0,-0.05	1	y	-0.01,0,-0.5
13	91	y	-0.09,0,-0.05	1	y	-0.02,0,-0.5
14	193	y	-0.05,0,-0.05	4	y	0,0,-0.5
	Pavement	Structure 5		Pavement	Structure 6	
1	59	x	0.17,0,0	142	x	0,0,0
2	116	x	0.24,-0.07,0	122	x	-0.08,-0.03,0
3	101	x	0.24,0.03,0	134	x	0,-0.03,0
4	74	x	0.17,0,0	303	x	0,0.03,0
5	71	x	0.22,-0.05,0	133	x	-0.03,0,0
6	87	x	0.21,0,0	138	x	-0.03,0,0
7	105	x	0.17,0,0	106	x	-0.09,0,0
8	116	x	0.17,0,0	131	x	-0.03,0,0
9	160	x	0.22,-0.03,0	273	x	0.02,0,0
10	53	x	0,0,0	105	x	0,0,0
11	125	x	0,0.02,0	200	x	0,-0.02,0
12	28	x	-0.2,0,0	84	x	0.02,0,0
13	67	x	-0.15,-0.01,0	82	x	0.04,0.03,0
14	64	x	-0.20,0,0	177	x	0.01,0,0
	Pavement	Structure 7		Pavement	Structure 8	

All strain less than 10 and occur at the edge of the simulated 3D-FE model

(Continued)

Table 4. (Continued).

TPCP No.	$\epsilon_{\max} (\mu\epsilon)$		Location	$\epsilon_{\max} (\mu\epsilon)$	Direction		Location
	Pavement	Structure 9			Pavement	Structure 10	
1	131	y	-0.10,-0.01,-0.1448	224	y	-0.14,0,-0.051	
2	120	y	-0.14,0,-0.1448	288	y	-0.14,0,-0.051	
3	144	y	-0.14,0,-0.1448	295	y	-0.17,0,-0.051	
4	287	y	-0.10,-0.02,-0.1448	363	y	-0.14,0.12,-0.051	
5	130	y	-0.12,0,-0.1448	205	y	0.15,0,-0.051	
6	134	y	-0.14,0,-0.1448	227	y	-0.17,0,-0.051	
7	117	y	-0.15,0,-0.1448	280	y	-0.17,0,-0.051	
8	147	y	-0.14,0,-0.1448	315	y	-0.17,0,-0.051	
9	288	y	-0.10,-0.02,-0.1448	358	y	-0.15,0,-0.051	
10	50	y	0,0,-0.1448	110	y	0.1,-0.01,-0.051	
11	113	y	0,0,-0.1448	181	y	0.07,0.01,-0.051	
12	53	y	0.046,0,-0.1448	124	y	0.01,0,-0.051	
13	56	y	-0.06,0,-0.1448	152	y	0.01,0,-0.051	
14	123	y	0,0,-0.1448	231	y	0.08,0,-0.051	

4 TENSILE STRAIN RESPONSES: INFLUENCE OF THE PAVEMENT STRUCTURE UNDER TIRE LOADING

To further investigate the potential location of crack initiation due to pavement structure when subjected to tire loading, the ϵ_{\max} in the HMA layer under varying HMA moduli and layer thicknesses were computed. To achieve this, the following pavement structural parameters were evaluated: 500, 1000, 2500, 5000, 7000, 15000, 30000 MPa for the HMA layer moduli (i.e., E_{AC}); 25, 50, 100, 150, 200, 300, 400, 500 mm for the HMA layer thickness; and 50, 100, 500, 1000, 2500, 7000, 15000 MPa for the base moduli (i.e., E_{Base}). Together, a total of 392 factorial combinations (i.e., $7 \times 7 \times 8$) were considered. For all the pavement structures evaluated, the Poisson's ratio of HMA and base layers was 0.35, and 0.4 for the subgrade. The base layer thickness was taken as 300 mm through out and the subgrade modulus was taken as 35 MPa. Because TPCP variation under tire loading has little influence on the location and direction of the ϵ_{\max} in the HMA layer, only the TPCP due to 11.00–20 latitudinal tread patterned tire with 25.0 kN wheel loading and 600 kPa tire inflation pressure was considered.

Table 5 provides a list of the 3D-FE computational results. In Table 5, H_{AC} refers to the HMA layer thickness and E_{AC} to the HMA layer modulus. For the computed strains, $\epsilon_{(s,x)}$ stands for maximum tensile strains at the “surface” of the HMA layer in the horizontal “X-coordinate” direction and likewise for $\epsilon_{(s,y)}$. On the same basis, $\epsilon_{(b,x)}$ stands for maximum tensile strains at the “bottom” of the HMA layer in the horizontal “X-coordinate” direction and similarly for $\epsilon_{(b,y)}$. For all the pavement structures evaluated, the computed maximum tensile strain at the surface of the HMA layer was often such that $\epsilon_{(s,x)} > \epsilon_{(s,y)}$, and $\epsilon_{(b,x)} < \epsilon_{(b,y)}$ at the bottom of HMA layer, so only the $\epsilon_{(s,x)}$ and $\epsilon_{(b,y)}$ results were utilized for evaluating the potential location of crack initiation in terms of ϵ_{\max} . Also since all of the computed maximum tensile strains occurred at the edge or inside the tire-pavement contact area, it was deemed unnecessary to list these coordinate locations in the table.

Also using 70 $\mu\epsilon$ as the reference bench mark, then the following observations can be deduced from Table 5:

- (1) When $E_{Base} \leq 500$ MPa and $E_{AC} \leq 1000$ MPa, crack initiation may occur from both the surface and bottom of the HMA layer (in most pavements), irrespective of the HMA layer thickness. That is, it is possible for a pavement structure to simultaneously experience both TDC and

Table 5. Computed ϵ_{\max} results under heavy-truck tire loading.

E _{Base} MPa	H _{AC} mm	E _{AC} = 500 MPa		E _{AC} = 1000 MPa		E _{AC} = 2500 MPa		E _{AC} = 5000 MPa		E _{AC} = 7000 MPa		E _{AC} = 15000 MPa		E _{AC} = 3000 MPa	
		$\epsilon_{(s,x)}$	$\epsilon_{(b,y)}$	$\epsilon_{(s,x)}$	$\epsilon_{(b,y)}$	$\epsilon_{(s,x)}$	$\epsilon_{(b,y)}$	$\epsilon_{(s,x)}$	$\epsilon_{(b,y)}$	$\epsilon_{(s,x)}$	$\epsilon_{(b,y)}$	$\epsilon_{(s,x)}$	$\epsilon_{(b,y)}$	$\epsilon_{(s,x)}$	$\epsilon_{(b,y)}$
		50	25	2048	1326	1654	1393	1654	1393	1088	1250	527	906	239	648
	50	1297	1808	784	1497	784	1497	286	1034	146	603	83	381	50	242
	100	338	1402	226	1011	226	1011	119	599	55	304	27	174	15	102
	150	197	1003	128	688	128	688	65	383	27	181	14	100	8	57
	200	131	743	81	493	81	493	39	264	17	120	10	65	7	35
	300	77	452	41	289	41	289	21	147	11	64	7	32	4	17
	400	144	297	43	186	43	186	16	92	9	38	5	19	2	9
	500	186	206	75	127	75	127	21	61	6	24	3	12	1	6
100	25	1070	504	942	606	942	606	710	672	416	577	228	451	104	336
	50	830	947	582	890	582	890	278	700	109	456	65	306	39	204
	100	267	897	156	715	156	715	90	469	44	259	24	156	13	95
	150	130	693	90	521	90	521	51	319	23	163	13	93	8	54
	200	87	535	60	391	60	391	32	228	15	111	9	61	6	34
	300	125	344	33	241	33	241	19	133	10	60	7	31	4	17
	400	172	234	57	159	57	159	14	84	8	36	4	18	2	9
	500	203	166	83	111	83	111	23	57	6	23	3	11	1	6
500	25	88	48	112	38	112	38	131	38	127	102	103	124	73	120
	50	120	49	121	106	121	106	103	160	57	163	27	137	18	107
	100	150	156	66	182	66	182	24	178	16	135	11	97	7	67
	150	173	153	48	166	48	166	17	147	11	100	8	67	6	43
	200	191	132	53	139	53	139	15	118	10	76	7	48	5	29
	300	217	100	75	101	75	101	13	79	8	46	6	27	3	15
	400	233	76	93	74	93	74	22	54	7	29	4	16	2	9
	500	245	58	106	55	106	55	32	39	7	20	3	10	1	5
1000	25	42	34	37	30	37	30	28	22	49	17	52	46	45	59
	50	41	28	33	22	33	22	36	47	32	79	19	80	10	70
	100	120	36	46	64	46	64	17	88	9	84	7	68	5	51
	150	187	46	63	69	63	69	14	81	9	68	6	51	5	35
	200	220	43	77	62	77	62	13	69	8	55	6	38	4	25
	300	244	35	96	50	96	50	18	50	7	36	5	23	3	14
	400	253	29	108	38	108	38	30	37	6	24	3	14	2	8
	500	259	23	117	30	117	30	37	27	9	16	3	9	1	5
2500	25	69	19	22	18	22	18	19	15	14	11	10	7	15	11
	50	57	18	22	16	22	16	17	12	11	14	8	27	5	31
	100	120	14	40	11	40	11	16	18	9	34	6	34	4	30
	150	214	12	81	9	81	9	14	24	8	32	5	29	4	23
	200	254	9	101	8	101	8	22	23	7	28	5	24	3	18
	300	273	6	117	8	117	8	33	19	6	20	4	16	2	11
	400	274	4	124	8	124	8	40	15	8	15	3	10	2	7
	500	274	2	128	7	128	7	44	12	12	10	4	7	1	4
7000	25	149	11	44	11	44	11	12	10	10	9	9	7	6	0
	50	132	10	36	10	36	10	13	9	10	7	7	5	5	6
	100	144	10	55	9	55	9	13	7	9	4	5	10	3	12
	150	249	9	105	8	105	8	27	5	7	7	4	11	3	11
	200	291	8	127	6	127	6	37	4	6	7	4	10	2	9
	300	302	7	137	4	137	4	45	1	10	7	3	7	2	6
	400	302	6	137	2	137	2	48	2	13	5	4	5	1	4
	500	299	5	137	1	137	1	50	2	15	4	6	4	2	3
15000	25	180	13	73	7	73	7	11	6	7	6	6	5	5	4
	50	163	7	65	7	65	7	8	6	7	5	6	4	4	3
	100	161	6	69	6	69	6	17	5	7	3	5	2	3	4
	150	270	6	122	5	122	5	37	4	6	2	4	3	2	5
	200	312	6	143	5	143	5	46	3	10	1	3	3	2	4
	300	319	5	149	4	149	4	51	2	14	1	4	3	1	3
	400	307	4	146	3	146	3	53	1	16	1	6	2	2	2
	500	298	3	143	2	143	2	53	0	17	1	7	2	3	2

bottom-up cracking (BUC). If this happens, then the ultimate fatigue failure mechanism will be governed by the rate of TDC or BUC propagation, whichever is more rapid.

- (2) When $E_{Base} \leq 500$ MPa and $E_{AC} > 1000$ MPa, the location of crack initiation in the HMA layer is related to the HMA layer thickness as follows:
when

$$H_{AC} \leq a \log^2 E_{AC} + b \log E_{AC} + c \quad (1)$$

both TDC and BUC initiation may potentially occur in the HMA layer;
when

$$a_1 \log^2 E_{AC} + b_1 \log E_{AC} + c_1 \leq H_{AC} \leq a \log^2 E_{AC} + b \log E_{AC} + c \quad (2)$$

only BUC initiation is likely to occur;
when,

$$H_{AC} > a \log^2 E_{AC} + b \log E_{AC} + c \quad (3)$$

no fatigue cracking is likely to occur in the HMA layer; where

$$\begin{aligned} a &= 0.0484 \log^2 E_{Base} - 0.2543 \log E_{Base} + 0.3577 \\ b &= -0.4440 \log^2 E_{Base} + 2.3388 \log E_{Base} - 3.3044 \\ c &= 0.9881 \log^2 E_{Base} - 5.2533 \log E_{Base} + 7.5477 \\ a_1 &= -0.0411 \log^2 E_{Base} + 0.0985 \log E_{Base} + 0.0826 \\ b_1 &= 0.3880 \log^2 E_{Base} - 0.9732 \log E_{Base} - 0.8059 \\ c_1 &= -0.9331 \log^2 E_{Base} + 2.4320 \log E_{Base} + 2.0564 \end{aligned}$$

- (3) When $500 \leq E_{Base} < 2500$ MPa, the location of the crack initiation appears to be related to the HMA layer thickness as follows:
when $E_{AC} \leq 1000$ MPa, only TDC is possible, but with only $HAC > 70$ mm;
when $1000 < E_{AC} \leq 15000$ MPa, only BUC is possible, but only when the HMA layer thickness is in the following span:

$$a_3 \log^2 E_{AC} + b_3 \log E_{AC} + c_3 \leq H_{AC} \leq a_4 \log^2 E_{AC} + b_4 \log E_{AC} + c_4 \quad (4)$$

Where $a_3 = 0.0447$; $b_3 = -0.3721$; $c_3 = 0.8126$; $a_4 = -0.0515$; $b_4 = 0.2562$; $c_4 = -0.0763$.
when $E_{AC} > 15000$ MPa, no fatigue damage is likely to be caused by traffic loading in the HMA pavement.

- (4) When $E_{Base} \geq 2500$ MPa, no BUC is likely to occur irrespective of the HMA layer thickness or TDC when E_{Base} is greater than 2500 MPa. In other words, under these HMA-based moduli combinations, no serious fatigue cracking due to traffic induced tensile strains would theoretically be expected.
(5) When $E_{Base} \geq 2500$ MPa but $E_{AC} < 2500$ MPa, there is a potential for TDC occurrence irrespective of the HMA layer thickness.

5 CONCLUSIONS

In this study, a 3D-FE program ANSYS was utilized to compute the tensile strains in HMA pavements as a means to model the potential location of fatigue crack initiation; bottom-up and/or top-down. Actual measured TPCP were used the analysis and various variables such as pavement structure, heavy-truck tire loading, light-truck tire loading, wheel load, and tire inflation pressure were investigated. On the basis of the computational results presented in this paper, the following conclusions can be drawn:

- (1) The TPCP of a heavy-truck or light-truck tire loading, including different load levels or similar loading under different tire inflation pressures, hardly influence the location of the maximum horizontal tensile strains; but does influence the magnitude of the maximum horizontal tensile strains in the HMA layer.
- (2) The critical location of TDC due to maximum tensile strains appears to be always near (i.e., tire edge) or within the tire-pavement contact area (i.e., wheel path) and that the direction of the maximum tensile strains that induces TDC is always along the Y-direction along the direction of vehicle travel. That is, the top-down cracking that caused by traffic loading occurs near or inside the wheel paths and has the same direction as the direction of vehicle travel.
- (3) The potential location of fatigue crack initiation due to excessive tensile strains caused by tire loading in a given HMA pavement structure are related to the HMA and base layer moduli and the HMA layer thickness:
 - When both the HMA and base layer moduli are low, such as the base modulus less than 500 MPa and HMA modulus less than 1000 MPa, both top-down and bottom-up crack initiation are likely to occur simultaneously, irrespective of the HMA layer thickness;
 - When both the HMA and base layer moduli are high, such as both being more than 2500 MPa, no major fatigue cracking based on the computed lower tensile strains is expected;
 - When the HMA layer modulus is very high, such as more than 15000 MPa, the computed tensile strains are marginally very small and no major fatigue cracking is likely to appear, irrespective of the base layer modulus;
 - When the base layer modulus is lower while the HMA layer modulus is high, such as the base modulus being less than 500 MPa while the HMA modulus is more than 1000 MPa, the magnitude of the computed tensile strains and the potential location of fatigue crack initiation depend on the HMA layer thickness. This is also true for the case where the base layer modulus is higher (i.e., between 500 and 2500 MPa) and the HMA modulus is not very high (i.e., less than 15000 MPa).
 - Regression equations were subsequently developed to estimate and indicate the potential location of fatigue crack initiation based on the maximum tensile strain computations.

REFERENCES

- APA- *Asphalt Pavement Alliance: Perpetual Pavements – A Synthesis, APA 101*. Maryland, US, 2002.
- ANSYS 9.0 User Manual, Ansys Inc., Canonsburg, PA, 2004.
- Dauzats, M., and A. Rampal. Mechanism of Surface Cracking in Wearing Courses. In *Proc., 6th International Conference on Structural Design of Asphalt Pavements*, University of Michigan, Ann Arbor, 1987, pp. 232–247.
- Gerritsen, A. H., C. A. P. M. van Gurp, J. P. J. van der Heide, A. A. A. Molenaar, and A. C. Pronk. Prediction and Prevention of Surface Cracking in Asphaltic Pavements. In *Proc., Sixth International Conference on Structural Design of Asphalt Pavements*, University of Michigan, Ann Arbor, 1987, pp. 378–391.
- Hu, X., Measuring the Distribution of Tire Ground Pressure and Stress Response Analysis of Asphalt Pavement Using Those Results. *The dissertation for doctoral degree at Tongji university*. Shanghai, China 2003.
- Matsuno, S., and T. Nishizawa. Mechanisms of Surface-Initiated Longitudinal Wheel Path Cracks in High-Type Bituminous Pavements. In *Proc., 7th International Conference on Asphalt Pavements*, Vol. 2, University of Nottingham, 1992, pp. 277–291.

- Meyers, L. A., R. Roque, and B. E. Ruth. Mechanisms of Surface-Initiated Longitudinal Wheel Path Cracks in High-Type Bituminous Pavements. *Journal of the Association of Asphalt Paving technologists*, Vol. 67, 1998, pp. 401–432.
- Roque, R., Bjorn Birgisson, Leslie Myers, Zhiwang Zhang, and Christos A. Drakos. Evaluation of Surface-Initiated Longitudinal Wheel Path Cracking: Analytical Evaluation of Surface-Initiated Longitudinal Wheel Path Cracking. Contract No.: C5978. Final Report, Volume 1 of 2. University of Florida, Florida (2006a).
- Roque, R., Bjorn Birgisson, Stephen Sedwick, Oscar Garcia, Adam Jajliardo, Jaeseung Kim, and Christos A. Drakos. Evaluation of Surface-Initiated Longitudinal Wheel Path Cracking: Analytical Evaluation of Surface-Initiated Longitudinal Wheel Path Cracking. Contract No.: C5978. Final Report, Volume 2 of 2. University of Florida, Florida (2006b).
- Uhlmeyer, J. S., K. Willoughby, L. M. Pierce, and J. P. Mahoney. Top-Down Cracking in Washington State Asphalt Concrete Wearing Courses. In *Transportation Research Record: Journal of the Transportation Research Board*, No. 1730, TRB, National Research Council, Washington, D.C., 2000, pp. 110–116.
- Walubita, L. F., and Scullion, S. Walubita, L. F. and Scullion, T. Perpetual Pavements in Texas: The Fort Worth SH 114 Perpetual Pavement in Wise County, *Technical Report FHWA/TX-05/0-4822-2*, TTI, TX, US, 2007.
- Wang, F. and Randy B. Machemehl. Mechanistic–Empirical Study of Effects of Truck Tire Pressure on Pavement. In *Transportation Research Record: Journal of the Transportation Research Board*, No. 1947, TRB, National Research Council, Washington, D.C., 2006, pp. 136–145.

Strength theory, a better explanation for top-down cracking in asphalt pavement

L. Jia & L. Sun

Key Laboratory of Road and Traffic Engineering of MOE, Tongji University, Shanghai, China

X. Hu

Texas Transportation Institute, Texas A&M University, College Station, Texas, USA

X. Hu

Shanghai Municipal Engineering Administration Department, Shanghai, China

ABSTRACT: With fast increasing traffic volume and axle load, a common mode of distress, single or parallel longitudinal cracks, often observed at the surface of asphalt pavement. After taking cores on suspect crackings from sites, it was identified that most of those crackings initiated at pavement surface and propagated downward, therefore they were named Top-Down Cracking (TDC). Because TDC often occur on the heavy-duty pavements, the heavy traffic loads were regarded as the main failure reason for TDC. In fact, there were two different prospectives on cause of TDC. One is high surface horizontal tensile stresses due to non-uniform-distributed tire-pavement contact pressure. The other is high shear stress in wearing course also induced by non-uniform-distributed tire-pavement contact pressure. Before the natural characteristics of TDC been completely understood, it has to be concluded in dilemma that both tensile-type cracking and shear-type cracking could initiate TDC. However in strength theory, both the shear failure and tensile failure are sort of simple yield criterions, reflecting the failure of materials in simple stress states, like the materials in the uniaxial tension test and direct shear test. But they are totally different with the stress response in asphalt pavement caused by complex non-uniform-distributed pressure between tire and pavement. In order to explain the real failure reason for TDC, in this paper the measured tire-pavement contact pressure and 3D finite element method (FEM) were used to analyze the mechanical response of asphalt pavement structures. Comparing with the tensile or shear stress failure theories, the TDC is simulated and explained by either Mohr-Coulomb strength theory or Mises strength theory. The analysis results show that the strength theory of complex stress state can better explain the TDC than the traditional theories, such as maximum tensile stress or maximum share stress.

1 INTRODUCTION

With fast increase in traffic volume and axle load in China, a common mode of distress, single or parallel longitudinal cracks, often appeared at the surface of asphalt pavement. After taking cores on suspect crackings from in-site projects, it was identified that most of those crackings are Top-Down Crackings (TDCs), initiated at pavement surface and propagated downward. Because TDC often occur on the heavy-duty pavements, the heavy traffic loads were regarded as the main reason for TDCs.

What are the causes of TDC in asphalt pavement? Gerritsen et al (1987) (1) and Myer et al (1998) (2) both considered that the effects of non-uniform tire-pavement contact stresses and high surface tensile strains at the edge of the tire are the causation of TDC. Furthermore, Groenendijk (1998) (3) concluded that the aging of the AC at the surface combining with the non-uniform contact

stress could result in critical tensile stress on the surface rather than at the bottom of the AC. A different viewpoint is that TDC is caused by the shear stress/strain in wear course. Bensalem et al (2000) (4) compared the load-induced shear strains at the edge of the wheels on the vertical plane with the tensile strains at the same location on the pavement surface, and concluded that the shear strains on the vertical plane play a dominated role in TDC. In the research report of Michigan State University, Svasdisant T (2003) (5) pointed that the cracks caused by shear failure along a vertical plane should incline at an angle from the vertical plane. Facing those awkward dilemmas, Wang L. B. et al indicated that (2003) (6): (a) top-down cracking may initiate not only at the pavement surface but also at some distance down from the surface; (b) both tensile-type and shear-type cracking could initiate top-down cracking.

However in strength theory, both the shear failure and tensile failure are simple yield criterions, reflecting the failure of materials in simple stress states. Those simple stress states, like uniaxial tension test and direct shear test, are totally different with the stress states in asphalt pavement caused by complex non-uniform-distributed contact pressure between tire and pavement. In this paper, the author tries to introduce the basic principle of strength theory to explain the top-down cracking in asphalt pavement structure, which means the top-down cracking should be explained not only by the maximum tensile stress or the maximum shear stress, but also by the other principal stress or the stresses combination.

2 STRENGTH THEORY

As an interdisciplinary field where the physicist, material scientist, earth scientist, and mechanical and civil engineers interact in a closed loop, strength theory deals with yield and failure of materials under complex stress state. It includes yield criteria and failure criteria, as well as multi axial fatigue criteria, multi axial creep conditions and material models in computational mechanics and computer codes. It is of great significance in theoretical research and engineering application, and is also very important for the effective utilization of materials. Particularly for design purposes, it is important that a reliable strength prediction be available for various combinations of multi axial stresses. In the following chapters, the maximum tensile stress failure and maximum shear stress failure will be re-introduced from perspective of strength theory.

2.1 *Strength theory in 19th century*

The maximum stress failure theory was the first strength theory relating to strength of materials under complex stresses. It considers the maximum or minimum principal stress as the criterion for strength. This criterion was assumed by such scientists as Lamé (1795–1870) and Rankine (1820–1872), and was extended with the well known textbook of Rankine's, *Manual of Applied Mechanics*. (7) Only one principal stress σ_1 of the 3D stresses $\sigma_1, \sigma_2, \sigma_3$ was taken into account.

The second strength theory was the maximum strain theory. Mariotte (1620–1684) made the first statement on the maximum elongation criterion or maximum strain criterion (7). Sometimes, it was called Saint-Venant's criterion or the second strength theory in the Russian and Chinese literature, and the maximum stress criterion was called the first strength theory.

Maximum strain theory was generally accepted, principally under the influence of such authorities as the two French academicians Poncelet (1788–1867) and Saint-Venant (1797–1886) (8). In this theory it is assumed that a material begins to fail when the maximum strain equals the yield point strain in simple tension.

After made a more complete study of the strength of materials, Mohr considered failure can be yielding of the material or fracture. Mohr's criterion may be considered as a generalized version of the Tresca criterion (9). Both criteria were based on the assumption that the maximum shear stress is the only decisive measure of impending failure. However, while the Tresca criterion assumed that the critical value of the shear stress is a constant, Mohr's failure criterion considered the limiting shear stress in a plane to be a function of the stress in the same section at an element point. Mohr

considered only the largest stress circle, named the principal circle, and suggested that such circles should be constructed when experimenting for each stress condition in which failure occurs. The strength of materials under a complex stress state can be determined by the corresponding limiting principal circle.

2.2 Single-shear strength theory (SSS theory)

This series of strength theories considers the maximum shear stress τ_{13} and the influence of stress σ_1, σ_3 acting on the same section. It can be written mathematically as:

$$F(\tau_{13}, \sigma_{13}) = C \quad (1)$$

or

$$f = \sigma_1 - \sigma_3 = \sigma_s \quad (2)$$

2.2.1 Single-shear yield criterion (9)

The expression is:

$$f = \tau_{13} = C \quad (3)$$

It is the one-parameter criterion of the single-shear strength theory. This yield criterion is also referred to as the maximum shear stress criterion or the third strength theory in Russian and in Chinese.

2.2.2 Single-shear strength theory (Mohr-Coulomb 1900)

The expression is

$$F = \tau_{13} + \beta\sigma_{13} = C \quad (4)$$

It is a two-parameter criterion of the single-shear strength theory. It is the famous Mohr-Coulomb theory and is also the most widely used strength theory in engineering. Mohr's theory (Single-shear strength theory) attracted great attention from engineers and physicists. The disadvantage of the Mohr-Coulomb theory is that the intermediate principal stress σ_2 is not taken into account. Substantial departures from the prediction of the Mohr-Coulomb theory were observed by many researchers.

2.2.3 Multi-parameter single-shear criteria

Multi-parameter Single-Shear criteria are nonlinear Mohr-Coulomb criteria used in rock mechanics and rock engineering. Some forms are expressed as follows:

$$F = \tau_{13} + \lambda\sigma_{13}^n = 0 \quad (5)$$

$$F = (\sigma_1 - \sigma_3) + \sqrt{m\sigma_1 - c} = 0 \quad (6)$$

2.3 Octahedral-shear strength theory (OSS theory)

This series of strength theories considers the octahedral shear stress τ_8 and the influence of the octahedral stress σ_8 acting upon the same section. It can be written mathematically as:

$$F(\tau_8, \sigma_8) = C \quad (7)$$

or

$$\tau_8 = f(\sigma_8) \quad (8)$$

2.3.1 Octahedral-shear stress yield criterion (von Mises yield criterion)

It is a one-parameter criterion of the OSS theory:

$$f = \tau_8 = C \quad (9)$$

or

$$\sigma_8 = C \quad (10)$$

$$J_2 = c \quad (11)$$

It is the widely used yield criterion for metallic materials with the same yield stress both in tension and in compression. It is also referred to as the von Mises criterion (10), or octahedral shear stress τ_8 yield criterion by Ros and Eichinger as well as Nadai. Sometimes, it was referred to as the J_2 theory (second invariant of deviatoric stress tensor), shear strain energy theory (energy of distortion), Maxwell, Huber, Hencky, equivalent stress criterion (effect stress or equivalent stress) or mean root square shear stress theory. It was also referred as the mean square shear stress τ_m averaged over all planes by Novozhilov, mean square of principal stress deviations by Paul, tri-shear yield criterion by Shen (11), and the fourth strength theory in Russian, Chinese, etc. All the expressions mentioned above are the same, because of:

$$\tau_8 = \frac{\sqrt{15}}{3} \tau_m = \frac{\sqrt{2}}{3} \sigma_e = \frac{2}{3} \sqrt{\tau_{12}^2 + \tau_{23}^2 + \tau_{13}^2} = \frac{1}{3} \sqrt{(\sigma_1 - \sigma_2)^2 + (\sigma_2 - \sigma_3)^2 + (\sigma_3 - \sigma_1)^2} \quad (12)$$

2.3.2 Octahedral-shear failure criterion (Drucker-Prager criterion)

It is the two-parameter criterion of the OSS (Octahedral shear strength) theory as follows:

$$F = \tau_8 + \beta \sigma_8 = c \quad (13)$$

This criterion is an extension of the von Mises criterion for pressure-dependent materials, and called the Drucker-Prager criterion expressed by Drucker and Prager as a modification of the von Mises yield criterion by adding a hydrostatic stress term σ_m or σ_8 . The Drucker-Prager criterion was used widely in soil mechanics. The extended von Mises criterion, however, gives a very poor approximation to the real failure conditions for rock, soil, and concrete.

2.4 Strength theories in top-down cracking analysis

As introduced above, the regular strength theories, which will be used in TDC analysis, are: (1) maximum stress criterion (the first strength theory), (2) maximum strain criterion (Saint-Venant's criterion or the second Strength Theory), (3) maximum shear stress criterion (Tresca criterion or the third strength theory), (4) Mohr-Coulomb theory, (5) nonlinear Mohr-Coulomb criteria, (6) von Mises criterion (the fourth strength theory) and (7) Drucker-Prager criterion.

According the definition of each strength criterions, the comparison between Tresca criterion and von Mises criterion in 2D space is illustrated in figure 1. And the comparison between Mohr-Coulomb theory and Drucker-Prager criterion in 2D space is illustrated in figure 2.

Form figure 1, it can be concluded, that in the 2D space the von Mises criterion is more conservative than Tresca criterion, which mean for a same stress/strain state, if using the Von Mises criterion found that the material is failure, then using the Tresca criterion this material is definitely failure too. From figure 2, it can also be concluded that the Mohr-Coulomb is more conservative than Drucker-Prager criterion. Therefore, in this paper, only the maximum stress criterion (the first strength theory), maximum shear stress criterion (Tresca criterion or the third strength theory) and the Mohr-Coulomb theory are selected to explain the top-down cracking in asphalt pavement mechanical analysis.

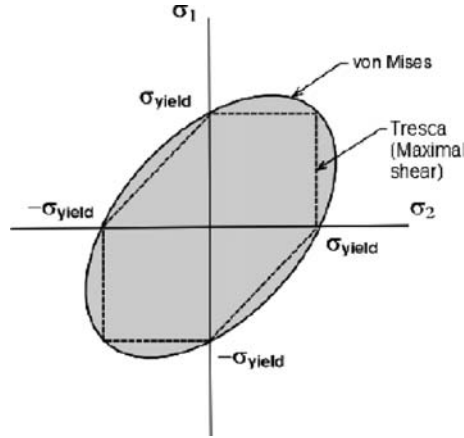


Figure 1. Comparison of Tresca criterion and von Mises criterion in 2D Space.

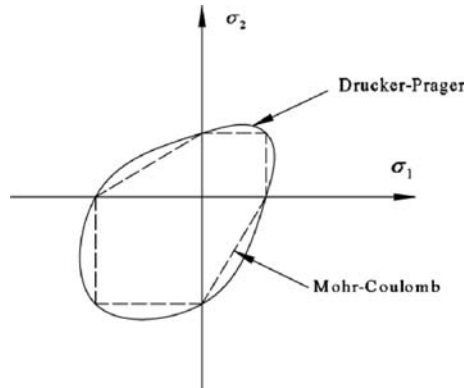


Figure 2. Comparison of Mohr-Coulomb and Drucker-Prager criterion in 2D Space.

In order to detailed explain the differences between those three strength theories, 4 different stress states in 2D space, represented by A, B, C and D, are illustrated in $\sigma - \tau$ coordinate system in figure 3 with three different strength theories, Mohr-Coulomb theory, Tresca Theory and Maximum Tensile stress theory. For all stress states, they satisfied the conditions listed below mathematically:

For the maximum tensile stress of each stress states:

$$\sigma_{2d} > \sigma_{2c} > \sigma_{2b} > \sigma_{2a} \tag{14}$$

For the maximum shear stress for each stress states:

$$\tau_{a \max} = \frac{\sigma_{a2} - \sigma_{a1}}{2} = \frac{\sigma_{d2} - \sigma_{d1}}{2} = \tau_{d \max} \tag{15}$$

$$\tau_{b \max} = \frac{\sigma_{b2} - \sigma_{b1}}{2} = \frac{\sigma_{c2} - \sigma_{c1}}{2} = \tau_{c \max} \tag{16}$$

$$\tau_{b \max} = \tau_{c \max} > \tau_{a \max} = \tau_{d \max} \tag{17}$$

Equation (14) means that the maximum tensile stress in stress state D is the greatest than stress states C, B and A.

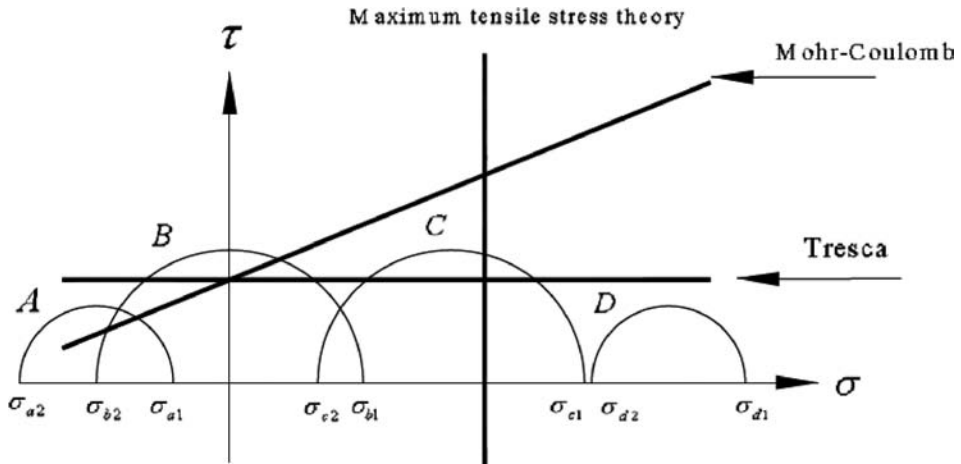


Figure 3. Different stress states and strength theories in $\sigma - \tau$ coordinate system.

Equations (15)~(17) mean that the stress state A and D have same maximum shear stress, stress state B and C have same maximum shear stress, but the maximum shear stress of B and D are greater than the one of A and D.

If the stress circle of certain stress state is below the lines representing Mohr-Coulomb stress theory, it means that at this stress state, the material won't failure. If the parts of the circle is upward the Mohr-Coulomb line, it means the material at this stress state will failure. For the Tresca theory, it is the same thing. If part of stress circle is at right of line representing maximum tensile stress, it means material at this stress state failure.

Depending on those description and illustration in figure 3, it can be found that: (1) When using the maximum tensile stress theory, the C and D will failure; (2) When using the Tresca stress theory (or the maximum shear stress theory), the B and C will failure; (3) When using the Mohr-Coulomb strength theory, the A and B will failure. In one words, when selecting different strength theory, there would be totally different failure results for certain stress state. Furthermore, for the complex stress states in asphalt pavement under non-uniform-distributed tire-pavement contact pressure, using strength theory for complex stress state can get the different analysis results to explain TDC.

3 MECHANICAL ANALYSIS OF ASPHALT PAVEMENT STRUCTURE UNDER MEASURED TIRE-PAVEMENT CONTACT PRESSURE DISTRIBUTION

The traditional explanations about top-down cracking are (1) the high surface tensile strains at the edge of the tire are the causation of TDC, or (2) the shear strains/stress on the vertical plane caused the TDC. Compared with the regular strength theories, the first explanation about TDC, the high tensile stress, is just as same as the maximum stress criterion and the second explanation about TDC, the high shear stress/strain, is just the maximum shear stress criterion (Tresca criterion or the third strength theory).

In strength theory, the maximum stress criterion and the Tresca criterion are all belong to the one-parametric yield criterion. They only reflect the failure of materials in simple stress state. The maximum stress criterion traditional described the failure of materials under the uniaxle tensile stress, and the Tresca criterion traditional described the materials under pure shear stress, The stress/strain distributions for those two strength theories are totally different with the complex stress/strain distributions for asphalt pavement under traffic loads.

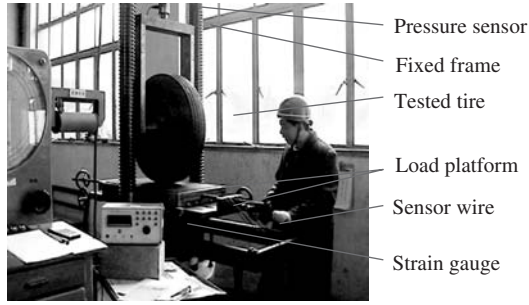


Figure 4. Static measured device for tire-pavement contact pressure.

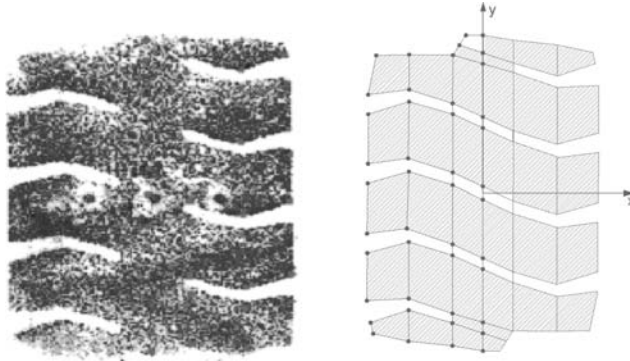


Figure 5. The Loading model of measured tire in FEM analysis.

3.1 *Tire-pavement contact pressure distribution*

Many researchers have adopted various devices to measure the tire-pavement contact pressure and have drawn several important conclusions. But those measurements are all carried out on the rigid platform, which is much different from the flexible structure of asphalt pavement. In order to measure the real tire-pavement contact pressure distribution, a static test device is developed by Xiaodi Hu (2005) (12), as shown in figure 4. In this device a pressure sensor is embedded in the asphalt mixture platform, which simulates the actual interaction between tire and pavement.

3.2 *Mechanical analysis of asphalt pavement structure*

In order to establish a more efficient loading model in FEM, the tire-pavement contact marks have to be simplified, as shown in figure 5. Then employing the measured tire-pavement contact pressure distribution, the mechanical analysis of typical asphalt pavement structure, which is commonly used in China and is shown in table 1, can be performed.

3.3 *Top-down cracking analysis*

3.3.1 *Maximum stress criterion*

In this part the maximum stress criterion was employed to analyze the TDC in asphalt pavement structure. And the σ_x max and σ_y max (maximum value of tensile stress at the direction of x axle and y axle) at asphalt pavement surface are illustrated in figure 6.

It can be concluded from figure 6, that the maximum tensile stress on the pavement surface does not locate under the tire-pavement contact area. And the maximal tensile stresses magnitude

Table 1. Asphalt pavement structural coefficients and mechanical parameters.

Structural layer	Thickness/mm	Modulus/MPa	Poisson's ratio
Wearing course	40	1200	0.35
Binder course	50	1000	0.35
Asphalt stabilized course	60	700	0.35
Lime stabilized course	340	1500	0.20
Lime stabilized soil layer	180	550	0.20
Soil Base	-	35	0.40

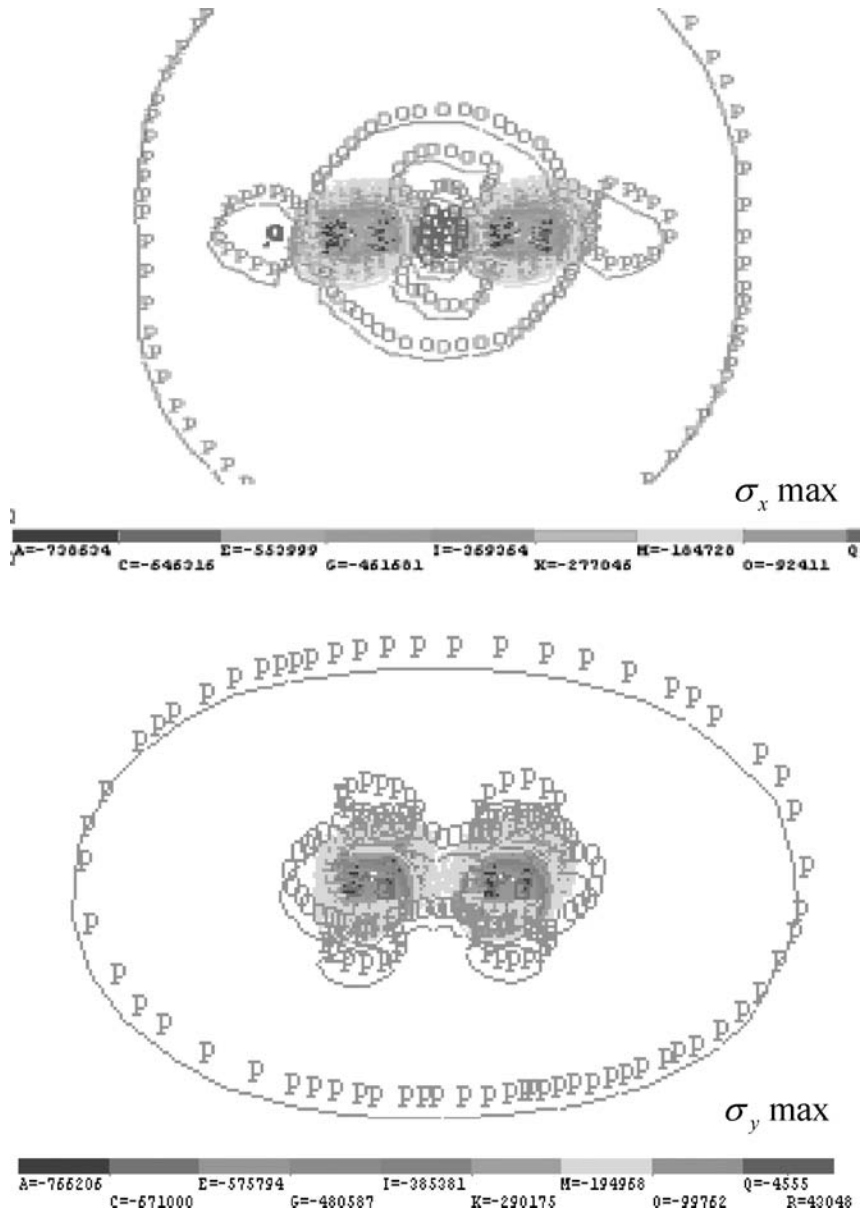


Figure 6. Contour map of maximum tensile stress at X axle and Y axle.

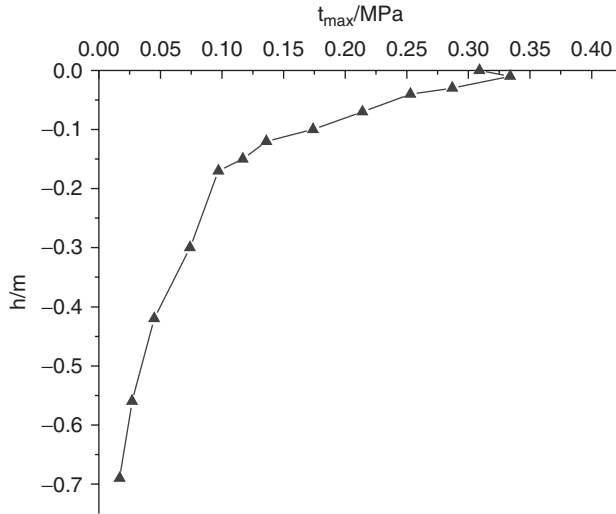


Figure 7. The variation of τ_{\max} with depth.

at X direction and Y direction are very close. If the TDC is determined by the maximum stress criterion and caused by the tensile stress on pavement surface, the crackings should be out of the wheel path and shown as map cracks. But in fact the TDC are generally in the wheel path as parallel cracks, therefore, the maximum stress criterion can not provide the reasonable explanation about TDC.

3.3.2 Tresca criterion (maximum shear stress criterion)

In this part the Tresca criterion (Maximum shear stress criterion) was employed to analysis the TDC in asphalt pavement structure.

The calculated maximum shear stress with depth is illustrated in figure 7.

Form figure 7, it can be concluded that the maximum shear stress does not occur on the pavement surface but in certain depth. In figure 7, the maximum shear stress in asphalt pavement structure is at 1.33 cm deep from pavement surface. The contour map of maximum shear stress at 1.33 cm depth is shown in figure 8.

It can be found that the maximum shear stress area in asphalt pavement structure is under the tire-pavement contact area. The maximum shear stress is in the wheel path as parallel, which is in agreement with the Top-down crackings in direction. It can easily explain why the TDC always are the single or parallel longitudinal cracks. While the maximum shear stress is not located on the pavement surface, it can only be assumed that the TDC firstly initiate at certain depth below the pavement surface, and then propagate to the surface. But until now there is no such cracking samples have been reported or found. Therefore, the Tresca criterion still cannot perfectly explain the TDC in asphalt pavement.

3.3.3 Mohr-Coulomb criterion

According to the Mohr-Coulomb theory, the yield surface can be express as:

$$\sigma_1 = \sigma_3 \cdot \tan^2(45^\circ + \frac{\phi}{2}) + 2c \cdot \tan(45^\circ + \frac{\phi}{2}) \quad (18)$$

Then the failure criterion could be expressed as:

$$F = \tau_{13} - \sigma_{13} \cdot \sin \phi = c \cdot \cos \phi \quad (19)$$

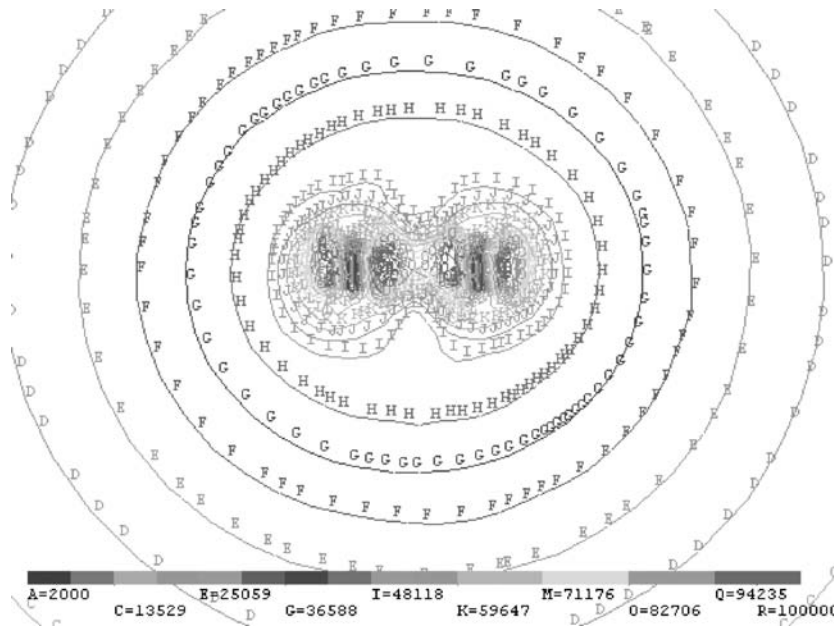


Figure 8. Contour map of maximum shear stress in horizontal plane at 1.33 m depth.

where: ϕ is the internal friction angle and c is the cohesive force, which can be determined by the triaxial test for asphalt mixtures, commonly for HMA the ϕ is varying from 40° to 50° (13).

Without specific value about ϕ and c in this paper, it can be assumed that the maximum value of F is the most dangerous position to have top-down cracking. Depending on the FEM analysis results, the Contour maps of F values on the vertical plane are shown in the figure 9, while the internal friction angle is 40° and 50° .

Form figure 9, it can be concluded that employing the Mohr-Coulomb theory, the most dangerous positions are on the asphalt pavement surface and located at the parallel edge of tires, which is exactly similar with the position of TDC in asphalt pavement structure. At those most dangerous positions, neither the shear stress nor the tensile stress are the maximum value in whole pavement structure. Therefore, those positions are different with the dangerous position depending on the maximum tensile stress or the Tresca criterion. Furthermore, it can be concluded that the top-down cracking is caused by the combination of tensile stress and shear stress.

4 CONCLUSIONS

In this paper, the causes of top-down cracking in asphalt pavement structure are fully investigated using the strength theories. Depending on the measured distribution of the contact pressure between the real tire and pavement and 3D FEM, the stress/strain state of a typical asphalt pavement structural are analyzed. Separately using the maximum stress criterion (the first strength theory), maximum shear stress criterion (Tresca criterion or the third strength theory) and the Mohr-Coulomb theory to find the most disadvantaged positions in whole asphalt pavement and compared with the in-site top down crackings, it was found that:

1. The maximum stress criterion can not explain why the top-down crackings are single or parallel longitudinal cracks;

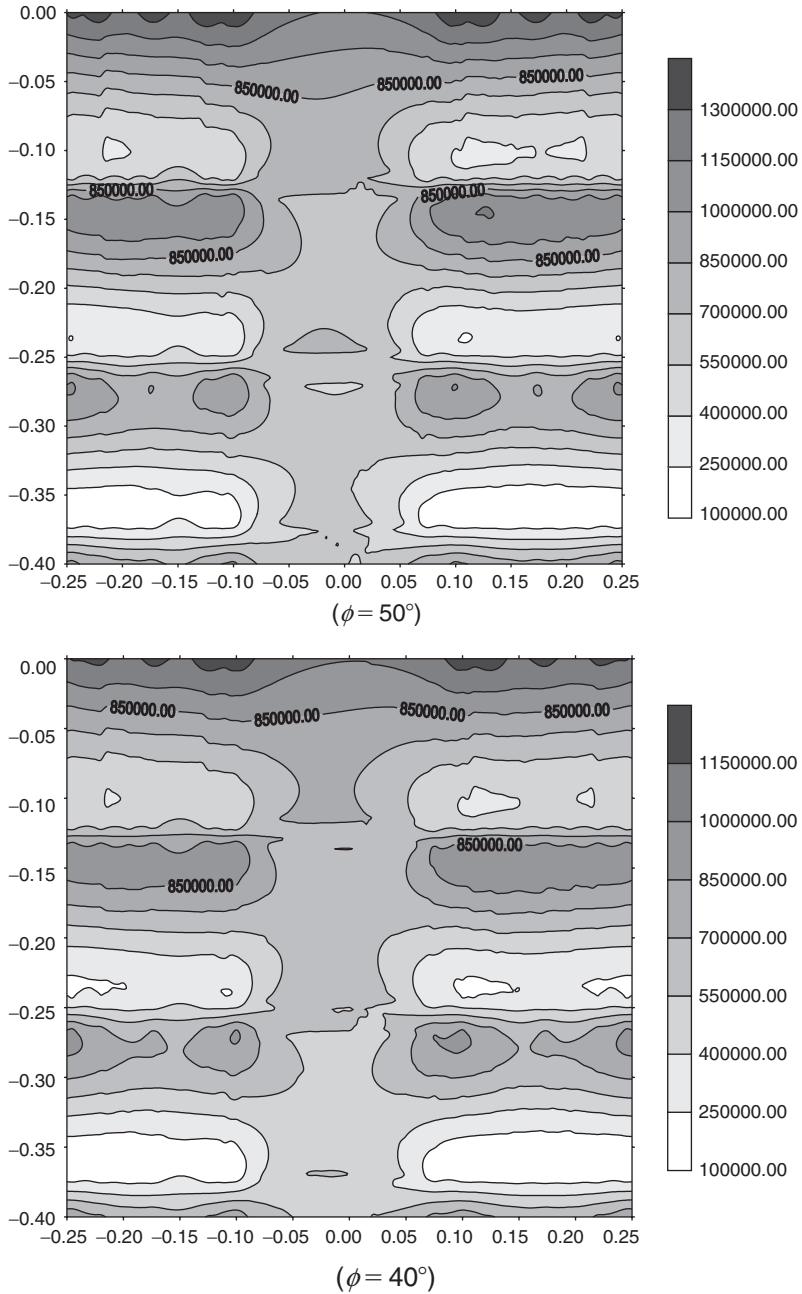


Figure 9. Contour maps of F values in Mohr-Coulomb criterion.

2. The Tresca criterion can not explain why the top-down crackings are initiate at the asphalt pavement surface;
3. On the country, the Mohr-Coulomb theory can reasonable explain the position of TDC in asphalt pavement structure;

4. And it can be also proved that the most dangerous position have not maximum tensile stress or the max shear stress in whole pavement structure, the TDC should be caused by the combination of tensile stress and shear stress.

ACKNOWLEDGEMENT

This project supported by the National Science Found for Distinguished Young Scholars of China (Grant No. 50325825).

REFERENCES

1. Gerritsen, A.H. and van Gurp et al. 1987. *Prediction and Prevention of Surface Cracking in Asphaltic Pavements*. Proceedings of the 6th International Conference on Asphalt Pavements, Ann Arbor.
2. Myers, L.A. and Roque, R. et al, 1998. *Mechanisms of Surface-Initiated Longitudinal Wheel Path Cracks in High-Type Bituminous Pavements*. Proceedings of the A.A.P.T.
3. Groenendijk, J., 1998. *Accelerated testing and Surface Cracking of Asphaltic Concrete Pavements*. Ph.D. Thesis. Department of C.E., Delft University of Technology, Netherlands.
4. Bensalem, A. and Broen A. J. et al, 2000. *Finite Element Modeling of Fully Flexible Pavements: Surface Cracking and Wheel Interaction*. Proceedings of the Second International Symposium on 3D Finite Element for Pavement Analysis, Design, and Research, West Virginia.
5. Svasdisant T. 2003. *Analysis of Top-Down Cracking in Rubblized and Flexible Pavements*. Ph.D. Thesis. Department of Civil and Environmental Engineering, Michigan State University.
6. WANG L. B.; MYERS L. A.; MOHAMMAD L. N., et al., 2003. Micromechanics study on top-down cracking. Transportation research record. Transportation Research Board. 2853. PP:121–131.
7. Rankine WJM (1861), Manual of Applied Mechanics (1st edition, Ref. from Timoshenko, 1953, p. 198; 21st edition, 1921).
8. De Saint-Venant (1870), Memoiresur l'establissement des equations differentielles des mouvements interieurs operas dans les corps solides ductiles au dela des limites ou l'e'lasticite' pourrait les ramener a leur premier e'tat, Comptes Rendus hebdomadaires des Seances de l'Academie des Sciences, 70, 473–480.
9. Tresca H (1864), Sur l'ecoulement des corps solides soumis a defortes pression, Comptes Rendus hebdomadaires des Seances de l'Academie des Sciences, Rend 59,754–758.
10. von Mises R (1913), Mechanik der festen Körper im plastisch deformablen Zustand, *Nachrichten von der Königlichen Gesellschaft der wissenshaften zu Go'ettinger, Mathematisch-physikalische Klasse*, 582–592.
11. Mao-hong Yu, 2002. *Advances in strength theories for materials under complex stress state in the 20th Century*. American Society of Mechanical Engineers.
12. Xiaodi Hu, Lijun Sun, Yufeng Bi, Xiao Hu, Feng Li. 2006 *Top-down Cracking Analysis and Control for Asphalt Pavements*. 10th International Conference on Asphalt Pavements, Canada, Quebec, August.
13. Yuanjun. 2007. *Experimental Research on Influence Factors of Permanent Deformation of Asphalt Mixture*. Ph.D. Thesis. School of Transportation, Tongji University, P.R.China.

Modeling shear properties of airport asphalt mixes using different test methods

A. El-Desouky

M.T.C, Cairo, Egypt

A. Mostafa

Helwan University, Cairo, Egypt

S. Easa

Ryerson University, Toronto, Ontario, Canada

A.O. Abd El Halim

Carleton University, Ottawa, Ontario, Canada

ABSTRACT: Surface deformation or rutting is one of the most serious distresses affecting runway safety. Rutting can restrict the use of runway pavements and cause serious safety problems when exceeds certain limits. Shear properties of asphalt concrete mixes are the most important factor in determining rutting performance of asphalt mixes. The main objective of this paper is to examine the relationships that may exist between shear properties of airfield mixes evaluated using different test methods. Three different asphalt mixes were obtained from the field during the construction of two taxiways at Ottawa International Airport. The experimental investigation included the evaluation of shear properties of the selected airfield mixes using three different test methods; torque machine, triaxial test, and direct shear test. The shear properties were also evaluated under different temperatures. The results were analyzed and used to develop statistical models to predict shear properties of asphalt mixes to with good.

1 INTRODUCTION

Rutting of flexible pavements is defined as “the permanent deformation noticed under the wheel paths” (Sybilski 1994). Surface deformations of asphalt surfaces such as rutting have been observed and reported since the late 1950’s. It was found that rutting of flexible pavements is a common distress type (Deshpande & Cebon 2000, Nikolaidis 2000). Flintsch et al. (2003) suggested that water ponds on the road surface due to rutting could cause deficiency in frictional characteristics of pavement surfaces. If a thin film of water covers the pavement surface, viscous hydroplaning occurs (Moore 1975). In such a case, the channelization or depression caused by the effect of the wheels can represent a serious problem. The Federal Aviation Administration concluded similar finding where it was found that pavement structural failure, such as rutting or raveling, is a contributing factor to airfield friction losses (FAA 1997). Therefore, an important key to improving the air traffic operations and optimizing the use of runways is to reduce rutting of asphalt surfaces without compromising the main mix properties.

Rutting susceptibility of asphalt concrete mixes are usually evaluated in the laboratories. There are three main categories of laboratory tests to measure rutting susceptibility: the wheel track tests, the uniaxial and triaxial tests and the diametrical tests (SHRP 1991). However, many researchers tried to characterize rutting performance utilizing easier tests. Results of research performed as a part of the SHRP project led to the conclusion that shear properties of asphalt concrete, is the

most important factor in characterizing rutting performance (Weissman et al. 1998). If the asphalt mixture has adequate shear strength, rutting will happen after a long time. On the other hand, if the shear strength of asphalt mixture is low, rutting will take place within a short period of time after construction (Nikolaides 2000). In general, increasing the shear strength of the mixture can enhance the rutting resistance of asphalt mixes. The shear strength can be increased by choosing an aggregate gradation that causes particle to particle contact or by using a stiffer binder. Shear properties of asphalt mixes, in terms of shear strength and shear modulus, were usually evaluated using the torque machine (Higdon et al. 1985). To simulate the field condition correctly, triaxial test facility was found to be the best test to evaluate shear properties accurately. Because the test is expensive, complex and time consuming, it was limited to research studies (Brown & Cooper 1984).

This research aims to model the shear properties of airfield asphalt mixes evaluated using different test methods. The experimental program was formulated to evaluate shear properties for airfield asphalt mixes using the torque machine, triaxial test, and direct shear test. In the analytical phase of this study, models concerning with shear properties were developed by relating shear properties evaluated using different test methods. The developed models could be used to evaluate the shear properties with confidence utilizing any available shear test facility.

2 EXPERIMENTAL PROGRAM

The experimental program tested three different airfield asphalt mixes for their shear properties. The field mixes were obtained during the construction of two taxiways at Ottawa International Airport (OIA). These Mixes were referred to as Mix1, Mix2, and Mix3. Mix1 and Mix2 were two different surface courses. However, Mix3 was a base course. The difference between Mix1 and Mix2 was that for Mix2 the limestone aggregates were replaced with dolomite aggregates to enhance the frictional characteristics of the taxiway surface. Table 1 presents aggregate gradations for the studied mixes. Asphalt content was 6% for Mix1 and Mix2 while it was 5% for Mix3. Before performing any test, dimensions and densities were calculated for each core sample to check that density is uniform for each mix under investigation. Different laboratory testing methods have been developed and used by pavement designers and researchers to assess shear properties of asphalt concrete mixes. However, the scope of this paper is limited to three testing methods as follows: shear test using torque machine, triaxial test, and direct shear test.

2.1 Shear test using torque machine

The shear test using the torque machine was performed to determine the shear strength (SSQ). The machine has two jaws to fasten the plates to which the specimen is glued. A scale to measure the angle of twist and a dial gauge to record the maximum torque are attached to the machine.

The dial gauge capacity used in the shear test is 1100Nm with a sensitivity of 2Nm. The specimens were first glued to the steel plates and left in room temperature for 24 hours to dry. Specimens were fastened to the machine jaws using the arms of the steel plated. The dial gauge was set to zero and the torque was applied at constant rate of 18 degrees twist angle per minute till

Table 1. Aggregate gradations for asphalt mixes under investigation.

Sieve size (mm)		26.5	19.0	16.0	13.2	9.5	4.75	2.36	1.18	0.60	0.15	0.075
Passing	Mix1*	100	100	100	96.1	67.4	7.8	2.2	1.9	1.5	1.2	1.1
(%)	Mix3	100	92.5	64.6	31.6	4.4	1.4	1.3	1.2	1.2	1.1	1.1

* For Mix2, HL-1 stone was replaced with dolomite stone.

the failure of specimen. The shear strength was calculated as (Bowes et al. 1990):

$$SSQ = \frac{T R}{J} \quad (1)$$

where T = maximum torque (N.mm), J = polar moment of inertia (mm^4) = $\pi R^4/2$, and R = sample radius (mm).

2.2 Triaxial test

The triaxial compression test is the most commonly used shear strength test for soils (Whitlow 1990). The test can be used to simulate field conditions accurately for asphalt mixes. The apparatus consists of a 4500 kN rock mechanics test system. The system includes load unit control pod and TestStar II digital controller, cascade temperature controller, temperature display, 4500 kN actuator/load frame, and a triaxial chamber. The triaxial chamber has a 2500 kN load cell, three linear variable differential transducers (LVDT), and three circumferential extensometers for load and strain measurements. The system as hole is fully computerized and strain/displacement measurements can be monitored via two strain indicators attached to the system (NRC 2001). The test is carried out by applying different confining pressures (usually three) and increasing the normal load till failure. Then, Mohor circle for each peak stress is plotted. A common tangent to failure circles is then drawn. This tangent represents the failure envelope from which the coefficient of cohesion (C) and angle of internal friction (ϕ) can be determined (Whitlow 1990). Using the shear strength parameters, the shear stress (τ) could be determined for a given normal stress (σ_n) as:

$$\tau = c + \sigma_n \tan \phi \quad (2)$$

The sides of test specimen were encapsulated using heat shrink polyolefin tubing. Then the specimen was sealed by wire wrapping around the polyolefin. Test specimen was placed and centered on the test system load cell and the circumferential extensometer was installed around it at mid height. All LVDT signals were set to zero and the triaxial chamber was closed. Confining pressure was applied by filling the triaxial chamber with a confining fluid. The vertical load was applied till failure of the sample (NRC 2001).

2.3 Direct shear test

The direct shear test facility consists of shear testing machine that has the capability to apply vertical and shear loads on the test specimens. Personal computer and data acquisition system are attached to the machine for data control and collection. Samples are locked in a drill core vise to position the samples before being tested. Load and displacement are measured and recorded by means of load cell and two LVDT. The test is carried out by applying a normal load to the sample and then shearing it with a constant rate till failure. Test procedure is usually repeated for five specimens. The values of normal stresses are plotted versus shear stress values. The line which best fits the plotted stresses is the shear envelope from which C and ϕ can be calculated (Whitlow 1990). First the sample was weighed and placed in the top plate mould. A hydrostone grout was prepared by mixing the hydrostone with water with ratio of 4:1. The grout was poured into the top plate mould and left for one hour to be dried. Then the top plate mould was lowered into position on the direct shear testing machine. Grout was then poured into the bottom plate mould to immerse the lower half of the test specimen. The sample was left for an hour to allow grout to dry and then it was tested for its shear properties. Figure 1 shows the three test methods used in this research to evaluate shear properties of different asphalt mixes.

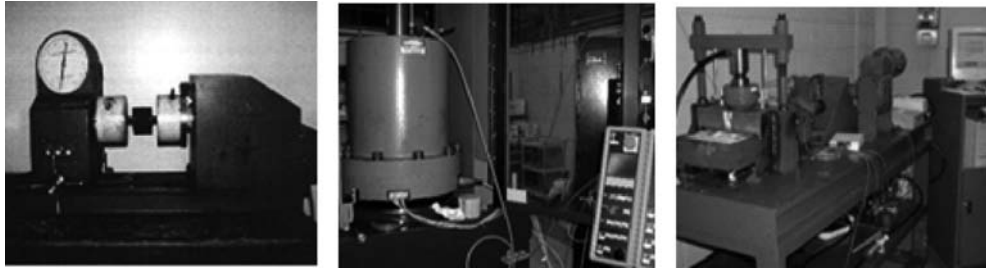


Figure 1. Torque testing machine, triaxial test facility, and direct shear test facility.

Table 2. Shear strength test results for field mixes.

Mix	Temp. (°C)	SSQ (MPa)
1		1.2846
2	25	0.7481
3		0.8385
1		0.8679
2	35	0.5631
3		0.7349
1		0.5095
2	45	0.4442
3		0.5029

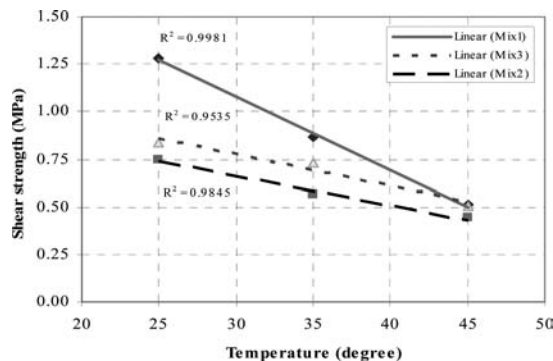


Figure 2. Change of shear strength with temperature, all mixes.

3 EXPERIMENTAL RESULTS

3.1 Shear test results using torque machine

Five core specimens from each mix were prepared, using the Marshall compactor, and tested to evaluate their shear strength using the torque machine. The test was performed at room temperature, 35°C, and 45°C to figure out the effect of temperature on shear properties of the candidate mixes. The test outputs were recorded in torque (T) at failure. Shear strength (SS) was calculated according to Equation 1. The summary of shear test results for all field mixes is shown in Table 2. Based on their mean SSQ values, Mix1 yielded the highest SSQ followed by Mix3 while Mix2 built of dolomite stones resulted in the lowest. This finding was valid for the selected range of temperature of 25°C to 45°C. Figure 2 shows the variation of shear strength with temperature for all mixes.

Table 3. Triaxial test results for field mixes.

Mix	Temp(°C)	No.	σ_3 (MPa)	σ_1 (MPa)	C (MPa)	ϕ (°)			
1	25	1	0.3447	8.6845	1.5143	45			
		2	0.6895	11.1473					
		3	2.7579	22.3081					
		4	0.3447	7.3514					
	35	5	0.6895	9.0649	1.2064	44			
		6	2.7579	20.5115					
		7	0.3447	5.6522					
		45	8	0.6895			8.6601	0.8369	45
			9	2.7579			19.5430		
		2	25	10			0.3447	7.9095	1.2837
11	0.6895			10.4888					
12	2.7579			21.2364					
13	0.3447			8.7123					
3	25	14	0.6895	10.9066	1.3960	44			
		15	2.7579	21.7210					

For Mix1, the mean SSQ was 1.2846 MPa at room temperature. This value decreased to 0.8679 when test was performed at 35°C with percentage decrease of 32.44%.

At 45°C, the mean SSQ was 0.5095 MPa with percentage decrease of 60.34% compared to Mean SSQ value evaluated at room temperature. Same trend was noticed for Mix2 where mean SSQ values were 0.7481 MPa, 0.5631 MPa and 0.4442 MPa at room temperature, 35°C and, 45°C respectively. Compared to Mix1, Mix2 yielded lower mean SSQ values. The percentage decreases were 41.76%, 35.12%, and 12.82% at room temperature, 35°C and 45°C. For Mix3, the mean SSQ value was 0.8385 MPa at room temperature. This value decreased to 0.7349 MPa and 0.5029 MPa as the temperature was increased to 35°C and 45°C respectively.

Generally, SSQ decreased as the temperature increased. Linear models were found to represent these relationships well as indicated by the R² values of 0.9981, 0.9845, and 0.9535 for Mix1, Mix2, and Mix3, respectively. Although Mix1 yielded higher mean SSQ values compared to Mix2, Figure 2 shows that the degradation in SSQ values at higher temperatures is more rapidly for Mix1. This finding can be clearly noticed by comparing the slopes for the two linear models representing Mix1 and Mix2. In other words, Mix1 may yield lower SSQ values at higher in-service pavement temperature. By solving the two equations for Mix1 and Mix2, this temperature is expected to be 48°C. Beyond this degree, Mix1 is expected to yield lower SSQ values compared to Mix2.

3.2 Triaxial test results

For each mix, a set of three core specimens was tested using the triaxial machine at room temperature. The test was performed by applying a pre-load of 150 lb to hold the sample in its position. Confining pressure (σ_3) of 0.3447 MPa (50 psi) was applied to the sample with a loading rate of 0.4137 MPa/min. (60 psi/min.) the loads were held for thirty minutes and then the vertical stress was increased gradually with a rate of 0.1 in/min till failure occurred. The maximum vertical stress at failure (σ_1) was recorded and the test was repeated using confining pressures of 0.6895 MPa and 2.7579 MPa (100 psi and 400 psi). Mohr circles were plotted and the shear strength parameters (C and ϕ) were obtained by drawing the shear envelope as the common tangent for the three circles. The intercept of shear envelope with y-axis determined the coefficient of cohesion (C) while the slope represented the angle of internal friction (ϕ).

To evaluate the sensitivity of triaxial test to temperature variation, two sets of mix1 were tested for their shear parameters at 35°C and 45°C. Table 3 summarizes the triaxial test results for all mixes under investigation. The table shows that ϕ is almost the same for all mixes. The differences

Table 4. Calculated SSQ based on shear stress parameters from triaxial test.

Mix	Temp. (°C)	σ_n (MPa)	τ (MPa)
1	25	0.6895	2.2038
		1.0342	2.5485
		1.3790	2.8932
	35	0.6895	1.8723
		1.0342	2.2052
		1.3790	2.5381
	45	0.6895	1.5264
		1.0342	1.8711
		1.3790	2.2158
2	25	0.6895	1.9496
		1.0342	2.2825
		1.3790	2.6154
3	25	0.6895	2.0619
		1.0342	2.3948
		1.3790	2.7277

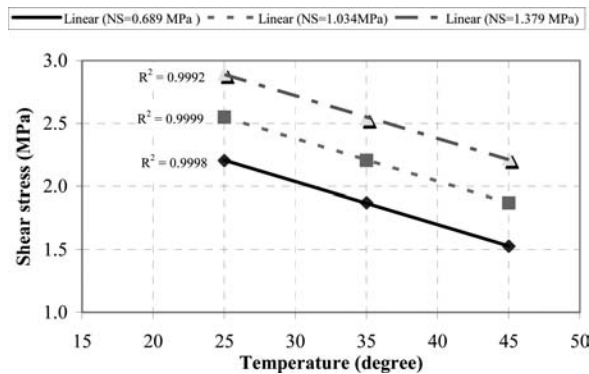


Figure 3. Effect of temperature on shear stresses evaluated by triaxial test, Mix1.

in shear properties were caused by the change in C values. The triaxial test ranked the field mixes in the same order like that obtained by the torque machine. Mix1 resulted in higher shear parameters, in fact C, then Mix3 and finally Mix2. For Mix1, the change of temperature caused the cohesion coefficient C to decrease while ϕ was almost constant. Cohesion value was 1.5143 MPa (219.63 psi) at room temperature, while it decreased to 1.2064 MPa and 0.8369 MPa (174.98 psi and 121.38 psi) as temperature was increased to 35°C and 45°C, respectively. Using the shear strength parameters presented in Table 3, shear stresses were calculated at three different normal stress levels of 0.6895 MPa, 1.0342 MPa, and 1.3790 MPa (100 psi, 150 psi and 200 psi). Table 4 presents the shear stresses (MPa) calculated using Equation 2. The effect of temperature on shear stress evaluated using the triaxial test is shown in Figure 3. The figure shows that the variation of τ at different σ_n levels could be perfectly represented by linear models (for Mix1). In other words, the triaxial test was very sensitive to temperature changes. Reviewing the slopes of linear relationships between τ and temperature, one can see that the variation of τ with temperature was constant and independent of σ_n .

3.3 Direct shear test results

The test was performed at room temperature for all mixes. In addition, for Mix1 only the test was conducted at two higher temperatures (35°C, 45°C). Three different vertical stresses of 0.6895 MPa,

Table 5. Direct shear test results for field mixes.

Mix	Temp. (°C)	No.	σ_n (MPa)	τ (MPa)	C (MPa)	ϕ (°)
1	25	1	0.6895	1.4183	0.8425	40.5
		2	1.0342	1.7503		
		3	1.3790	2.0068		
	35	4	0.6895	0.9763	0.2180	46.5
		5	1.0342	1.2413		
		6	1.3790	1.7019		
	45	7	0.6895	0.9491	0.3599	40.9
		8	1.0342	1.2698		
		9	1.3790	1.5458		
2	25	10	0.6895	1.2720	0.4007	48.6
		11	1.0342	1.3984		
		12	1.3790	2.0550		
3	25	13	0.6895	1.3577	0.8104	36.8
		14	1.0342	1.5199		
		15	1.3790	1.8731		

1.0342 MPa, and 1.3790 MPa were used to determine the shear envelope. First the vertical stress was applied with a loading rate of 0.4137 MPa/min. the stress was held for half an hour and then the shear load was applied with a rate of 1 in/min till failure.

The maximum shear stress at failure (τ) was calculated as the maximum shear load at failure divided by the cross sectional area of core sample. Shear stresses were plotted versus normal stresses and the shear envelope was obtained. The test results are shown in Table 5. For most cases the direct shear test ranked the mixes in the same order as that obtained using the torque machine and triaxial test facility. Mix1 resulted in higher shear properties followed by Mix3 and then Mix2. The only exception was that Mix2 yielded higher shear stress for σ_n of 1.3790 MPa.

For Mix1, the shear stresses decreased for most cases as temperature was increased. However, at 35°C and $\sigma_n = 1.0342$ MPa, the shear stress of 1.2413 MPa was lower than that resulted at 45°C. Reviewing the shear strength parameters of Mix1, at 25°C the cohesion coefficient was 0.8425 MPa and ϕ was 40.5°. As the temperature was increased to 45°C, the cohesion coefficient decreased to 0.3599 MPa while the value of ϕ was approximately constant (40.9°). From these values and the fact that asphalt binders are temperature-dependent, one can expect that when temperature increased, the cohesion would decrease and there was no reason for ϕ to be changed significantly. As a result, it was expected that at 35°C, the value of C would be between 0.8425 MPa and 0.3599 MPa. At the same time it was anticipated that ϕ would range around 40° to 41°. The investigation of results presented in Table 5 suggested that the recorded shear stress value of 1.2413 MPa was not an accurate one.

Similar suggestion can be considered for shear stress of Mix2 at σ_n of 1.3790 MPa. The ϕ value of Mix2 was determined to be 48.6°. As the aggregate gradation of Mix2 was similar to that of Mix1, it was expected that ϕ would be very close to 40.5° (ϕ of Mix1). This may lead to a conclusion that the τ value of 2.0550 MPa was too high.

4 MODEL DEVELOPMENT

Shear strength of asphalt surfaces is an important component that indicates the potential for rutting. While the shear properties of soil are well known, to date the shear properties of asphalt mixtures have not been accurately measured. The shear properties were evaluated in this research using three different methods. Torque machine, direct shear test facility and triaxial test facilities successfully ranked the airfield mixes in similar orders. As was mentioned before in the direct shear test, shear

stresses were determined at normal stresses of 0.6895 MPa, 1.0342 MPa and 1.3790 MPa. To relate shear properties evaluated using different method, shear stresses were calculated using the shear envelopes determined by the triaxial test at the above mentioned normal stresses.

4.1 Shear properties evaluated by triaxial test and direct shear test

The data shown in Tables 4–5 were analyzed using the SPSS software to develop a mathematical model relating the two tests to each other. Independent variable included shear stress evaluated by direct shear test (SSD), test temperature (T), and mix type (M). Normal stress (NS) was excluded as an independent variable as the values of SSD were determined based on the values of NS. First, the analysis was performed considering all independent variable and it was found that T and M were not. Then the stepwise analysis was performed and the following model was developed:

$$SST = 0.735 + 1.024SSD, R^2 = 0.877 \quad (3)$$

where SST, SSD = shear stress evaluated by triaxial test and direct shear test (MPa).

The model of Equation 3 shows that triaxial test yielded higher shear stress values compared to the direct shear test. In addition the relationship between shear properties evaluated by triaxial test and those evaluated by direct shear test did not depend on either mix type nor test temperature.

4.2 Shear properties evaluated by triaxial test and torque machine

Data introduced in Tables 2, 4 were used to develop a model relating SST to SSQ evaluated by the torque machine. The dependent variable was SST while the independent variables were SSQ, NS, T and M. Data were analyzed again by performing the stepwise analysis and mix type was excluded as it caused R^2 to increase by 0.004 only. The new model was developed as:

$$SST = 1.384 + 0.450SS - 0.0167T + 0.979NS, R^2 = 0.996 \quad (4)$$

where SST = shear stress evaluated by triaxial test (MPa), SSQ = shear strength evaluated by torque machine (MPa), T = test temperature ($^{\circ}$ C), NS = normal stress (MPa), M = mix type (M = 0 for Mix1, M = 1.0 for Mix2, and M = 2.0 for Mix3).

5 CONCLUSIONS

Based on the results of this study, the following conclusions can be made:

- Using dolomite stone aggregates instead of limestone aggregates did not enhance the shear properties of asphalt mixes. This conclusion stresses the important role of laboratory mix evaluation prior to construction.
- Models relating shear properties evaluated by different test methods were developed. These models could be used to evaluate shear properties confidently using any available shear test facility.
- The developed model shows that triaxial test yielded higher shear stress values compared to the direct shear test.
- The relationship between the shear properties evaluated by triaxial test and those evaluated by direct shear test did not depend on either mix type nor test temperature.
- Although there were very good relationships between SST and SSD, and between SST and SSQ, no such relationship was found between SSD and SSQ.

REFERENCES

- Bowes, W.H., Russel, L.T., & Suter, G.T. 1990. Mechanics of engineering materials. BRS Publications: 299.
- Brown, S.F. & Cooper K.E. 1984. The Mechanical properties of bituminous materials for road bases and base courses. Asphalt Paving Technology, Proceedings of the Association of Asphalt Paving Technologists, Vol.53: 415–437.
- Deshpande, V.S. & Cebon, D. 2000. Uniaxial experiments on idealized asphalt mixes. Journal of Materials in Civil Engineering, Vol. 12 (3): 262–271.
- Federal Aviation Administration, FAA. 1997. Measurement, construction, and maintenance of skid-resistant airport pavement surfaces. Advisory circular. U.S. Department of Transportation.
- Flintsch, G.W., de Leon, E., McGhee, K.K., & Al-Qadi, I.L. 2003. Pavement surface macrotexture measurement and application. Transportation Research Board Annual Meeting, National Research Council, Washington D.C.
- Higdon, A., Ohlsen, E.H., Stiles, W.B., Weese, J.A., & Riley, W.F.1985. Mechanics of materials. Jhon Wiley & Sons Inc., New York, Fourth Edition.
- Moore, D.F. 1975. Design of texture in standard surfaces: surface texture versus skidding; measurements, frictional aspects, and safety features of tire-pavement interactions. ASTM STP 583, American Society for Testing and Materials, Philadelphia, Pa. 62–74.
- National Research Council, NRC. 2001. Triaxial compressive strength test with servo computer control press. Standard Operating Procedures. National Research Canada.
- Nikolaides, A. 2000. Rutting and volumetric properties of SMA mixtures. Proceedings of the Institution of Civil Engineers–Transport, Vol. 141 (3): 135–141.
- Strategic Highway research program, SHRP, 1991. Summary report on permanent deformation of asphalt concrete. SHRP-A/IR-91-104. Asphalt research program, University of California, Berkeley.
- Sybilski, D. 1994. Relationship between absolute viscosity of polymer-modified bitumens and rutting resistance of pavement. Materials and Structures. Vol. 27 (166): 110–120.
- Weissman, S., Harvey, J., & Long, F. 1998. Asphalt concrete laboratory test and specimen dimensions selection based on mechanical constraints. Proceedings of the 12th Engineering Mechanics Conference, ASCE, La Jolla, California. 1130–1133.
- Whitlow, R. 1990. Basic soil mechanics. Second edition. Longman Group, UK Limited.

7. Low temperature cracking in HMA

Integration of laboratory testing, field performance data and numerical simulations for the study of low-temperature cracking

E.V. Dave, A.F. Braham, W.G. Buttlar & G.H. Paulino
University of Illinois at Urbana-Champaign, USA

A. Zofka
University of Connecticut, Storrs, Connecticut, USA

ABSTRACT: Low temperature cracking remains one of the major pavement distresses in asphalt concrete pavements in cold regions. An integrated laboratory testing, field performance data, and numerical simulation approach was used to study thermal cracking as part of a US National Pooled Fund Study on Low-Temperature Cracking. This paper focuses on testing, analysis, and field data from five controlled test sections at the Minnesota Road Research Program facility (MnROAD).

Low temperature viscoelastic relaxation modulus master curves and tensile strength were obtained from indirect tension testing conducted at three temperatures. Fracture energy of field samples were obtained using the disc-shaped compact tension (DC[T]) test. Temperature-dependent thermal coefficient data was collected by one of the research partners (the University of Wisconsin) for each of the five field mixtures.

A bi-linear cohesive zone model was used in the simulation of thermal cracking in five MnROAD pavement sections. Four custom-designed user subroutines were employed in the commercial finite element program ABAQUS, including: a bi-linear cohesive zone fracture model, a temperature shift factor routine, a time- and depth-dependent temperature profile algorithm, and a bi-linear thermal coefficient routine. The temperature boundary conditions were generated using the Enhanced Integrated Climatic Model (EICM) available in the AASHTO Mechanistic-Empirical Pavement Design Guide (MEPDG) using air temperatures obtained from National Weather Service databases. Detailed field performance crack maps were used to compare actual field cracking against numerical simulation results. This paper describes how this comprehensive, integrated testing and modeling program provided new insights towards the mechanisms of thermal cracking in asphalt pavements.

1 INTRODUCTION

The low temperature cracking of asphalt concrete pavements is a major pavement distress mechanism in cold regions costing millions of dollars in rehabilitation costs to various agencies. The Strategic Highway Research Program (SHRP) conducted during mid-1990s led to development of thermal cracking prediction software TCMModel (Roque et al. [1995]). In recent years sophisticated laboratory tests such as disk-shaped compact tension test (DC[T]) and single edge notch beam (SE[B]) developed by Wagoner et al. [2005a, 2005b] and semi-circular bend test (SC[B]) explored by Molenaar et al. [2002], Li et al. [2006], and Artamendi et al. [2007], have been developed with capability for rigorous fracture characterization of asphalt mixtures. Powerful fracture modeling tools, such as the cohesive zone fracture approach, have increased analysis capabilities through energy based formulations which accurately capture softening (damage) and fracture in quasi-brittle materials such as asphalt concrete. The present study illustrates the integration of recently developed laboratory techniques with computer simulation models utilizing cutting-edge fracture

modeling capabilities for the prediction of thermal cracking in asphalt concrete pavements. This work was conducted as part of US National Pooled Fund Study on Low-Temperature Cracking.

2 INTEGRATED APPROACH

This paper describes a highly integrated laboratory testing and computer simulation approach that was employed in studying thermal cracking which developed at several pavement sections at the Minnesota Road Research facility (MnROAD). Laboratory bulk and fracture characterization of asphalt concrete specimens fabricated from field samples was performed, including:

- Creep compliance/relaxation modulus master-curve using the 1000 second Indirect Tension Test configuration (AASHTO T-332) and time-temperature superposition at three temperatures
- Fracture energy from the Single-Edge Notch Beam, the Semi-Circular Bend, and the Disk-Shaped Compact (ASTM D7313-06) fracture tests
- Tensile strength from indirect tension testing (AASHTO T-332)
- Coefficient of thermal expansion

Multiple properties are required in order to accurately simulate pavement responses and distress development, such as thermal cracking. At the same time, practical considerations of pavement sampling and laboratory testing expense and rigor must be considered in the development of a useful testing and modeling system. A detailed analysis of these tests is beyond the scope of this paper, but can be found in the final project report (Marasteanu et al. [2007]). This work will outline the overall conclusions and findings from the report.

Pavement simulation models were generated using properties obtained from these tests, along with published information on the thickness and mechanical properties of underlying granular and subgrade materials. The temperature boundary conditions for simulation models were generated using the enhanced integrated climatic model, which utilizes climatic information such as air temperature, percent sunshine, latitude, elevation, etc. Additional details concerning laboratory tests and simulation modeling performed are provided in a later section.

The Pooled Fund low temperature cracking study involved the investigation of twelve existing pavement sections, some from the sponsor state, Minnesota (featuring a number of MnROAD) sections, along with sections from other participating states. In this paper, five of the pavement sections from that study are presented to illustrate the integrated testing and simulation approach. Five MnROAD test cells are studied in this paper; namely sections 03, 19, 33, 34, and 35. The pavement layer types (asphalt binder grades, granular base types) and thicknesses for these sections are as illustrated in Figure 2.1.

In order to capture a wide range of properties, three testing temperatures were chosen to encompass the transition from brittle-ductile behavior to brittle behavior. The three temperatures were each 12°C apart, with the middle testing temperature 10°C higher than the low-temperature PG binder grade. This also ensured that asphalt binder and mixture properties were available at one common temperature. Table 2.1 shows the testing temperature used for each mixture. Figure 2.2 presents the creep compliance master curves obtained. There is little difference between Cells 03, 19, 34, and 35, especially at shorter times (also the lower temperatures). Cell 33 appears to have significantly higher compliance at longer loading times, suggesting a more relaxant mixture. This is rather unexpected as it does not have the softest binder (Cell 35 has the softest binder). However, the binder stiffness could be negated based on the testing temperatures relating to the asphalt binder grade.

In addition to creep compliance in the Indirect Tension Test setup, the tensile strength was measured for all five mixtures. Figure 2.3 shows the results of the tensile strength testing. For low temperature testing, it is not uncommon to observe a maximum tensile strength at the intermediate testing temperature selected. This is because although tensile strength in hot-mix asphalt generally increases as temperature is lowered, eventually a point is reached where the brittleness of the binder evidently reduces the tensile strength of the overall composite, possibly aided by the relatively fast testing rate used in the IDT (a loading head velocity of 12.5 mm/minute is used).

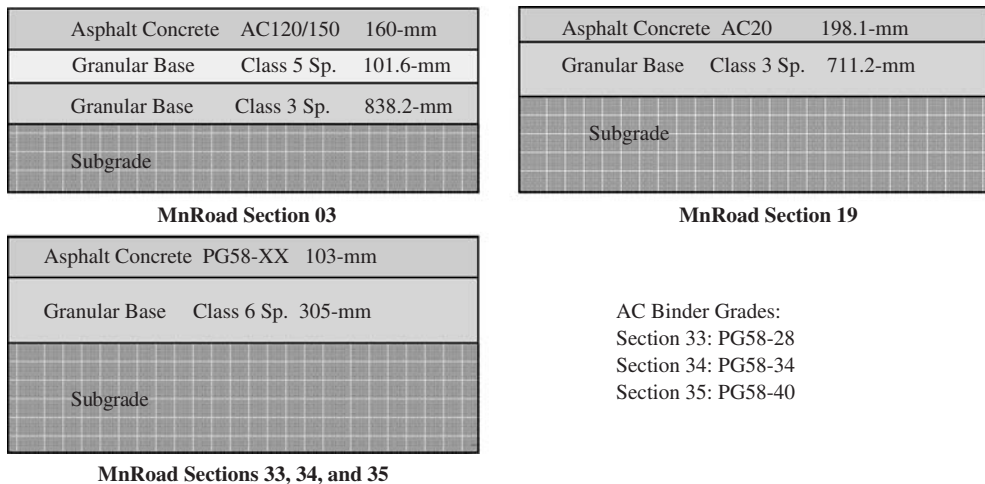


Figure 2.1. Pavement sections studied in this paper.

Table 2.1. Testing temperatures for five mixtures.

	PG binder grade	Testing temperatures (°C)		
		High	Mid	Low
MnROAD 03	PG58-28 (120/150)	-6	-18	-30
MnROAD 19	PG58-34 (AC-20)	-12	-24	-36
MnROAD 33	PG58-28	-6	-18	-30
MnROAD 34	PG58-34	-12	-24	-36
MnROAD 35	PG58-40	-18	-30	-42

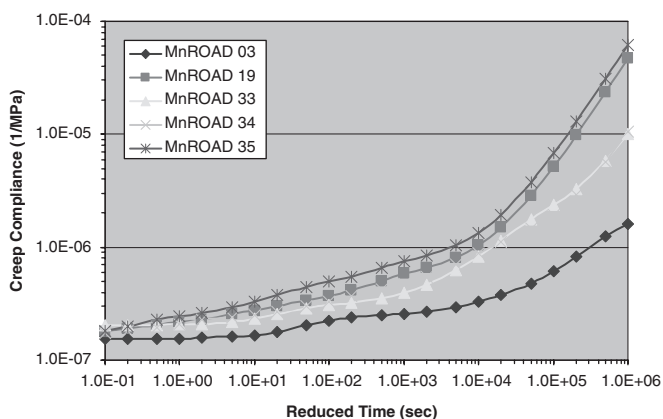


Figure 2.2. Creep compliance mastercurves at reference temperature of -30°C .

Finally, the fracture energy was measured for all five mixtures using the Semi-Circular Bend (SC[B]), the Disk-Shaped Compact Tension (DC[T]), and the Single-Edge Notch Beam (SE[B]). Figures 2.4 show the results at the three testing temperatures selected.

The tests are dissimilar, possess different configurations, and exhibit size effects, which are beyond the scope of this work. While the tests provided similar rankings between mixtures, there

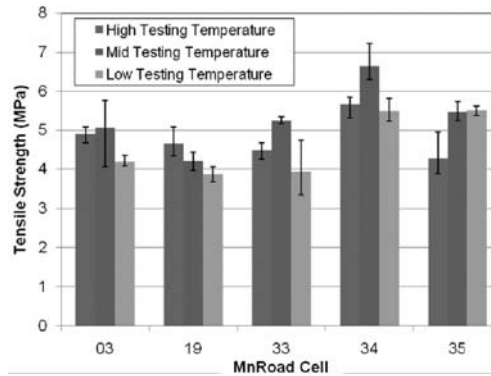


Figure 2.3. Tensile strength summary.

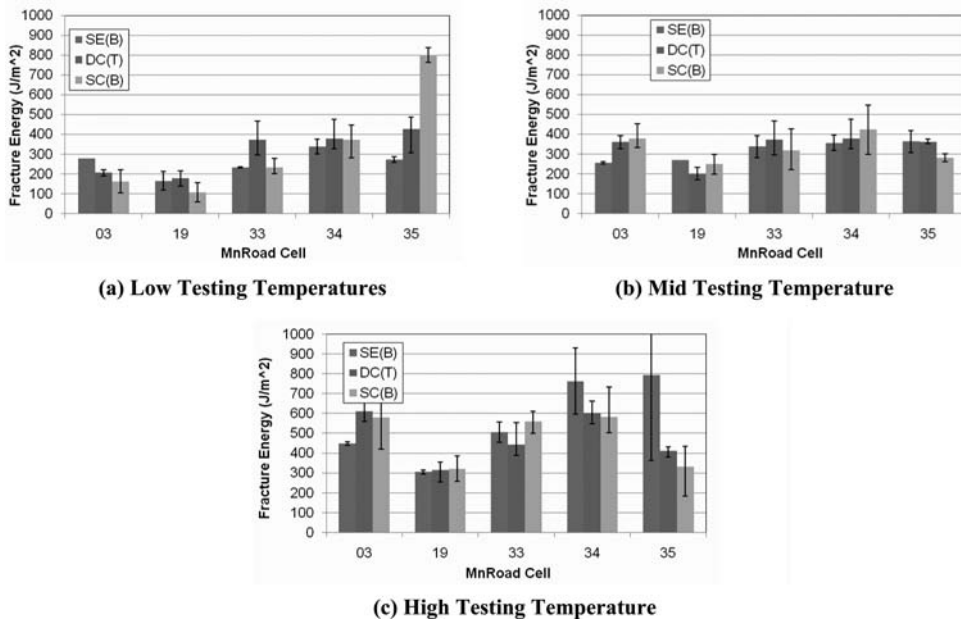


Figure 2.4. Fracture energy results.

were some differences in fracture energy values between the three tests. Given different test geometries used, the different modes of failure, and the different loading rates for each test, the differences were not unexpected. A detailed investigation of these differences can be found in Li et al., 2008. For the numerical simulations presented hereafter, the fracture energy from the DC[T] was used.

3 PAVEMENT SIMULATION MODEL

Numerical simulations were performed using the finite-element (FE) analysis technique with the aid of the commercially available software program ABAQUS. The program was customized by developing and implementing several user-subroutine codes to enable fracture tools to be employed in the simulation of low temperature pavement cracking. The following section is divided into subsections describing various aspects of the simulation model.

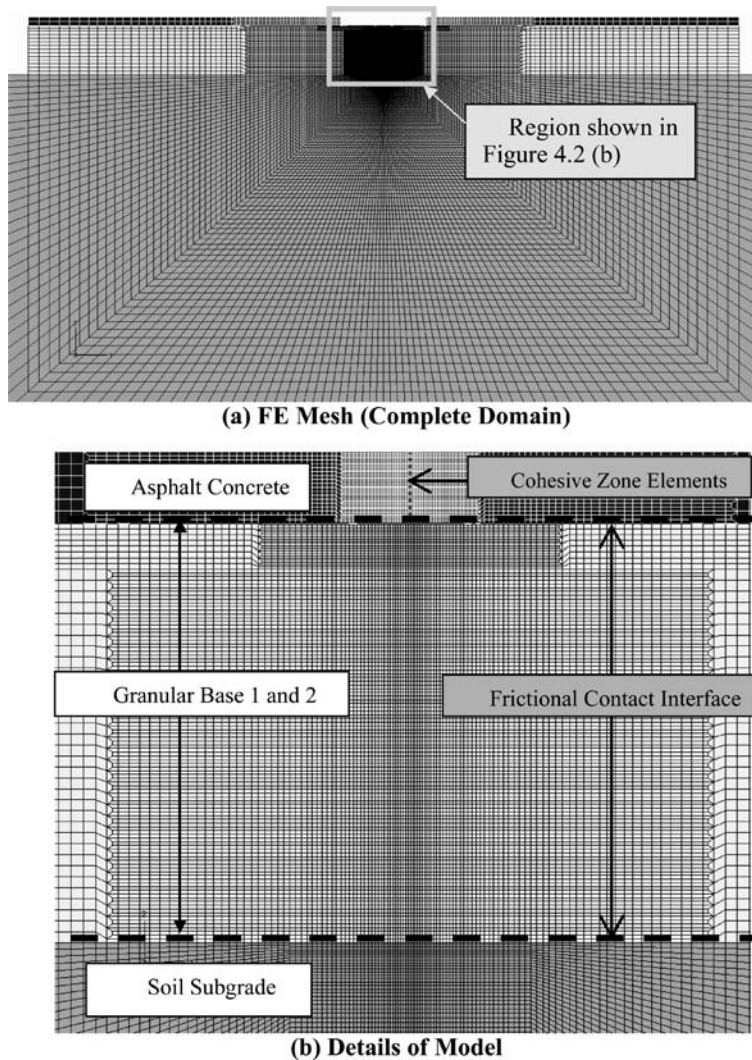


Figure 3.1. Finite element pavement model.

3.1 Finite element model domain and boundaries

The simulations in this study were performed by simplifying the pavement sections under investigation into two-dimensional FE models created along a slice taken in the longitudinal direction (direction of traffic movement). Model boundaries were selected on the basis of previous work by Dave et al. [2007], to ensure that sufficient domain extent was provided to avoid end effects. The FE model was generated using a domain length of 12192-mm (40-ft). The subgrade thickness was selected as 6096-mm (20-ft), beyond which the subgrade was modeled as a semi-infinite boundary by use of special infinite elements to create an infinite half space. Figure 3.1(a) shows a typical mesh used in this study. The FE models for low-temperature cracking simulations were constructed using graded meshes, which are used to significantly reduce the computational requirements. Graded meshes typically have a finer element size close to the areas of high stress variations and potential non-linearity, whereas in the regions of low stress gradients, larger elements are used.

Figure 3.1(b) shows an area in the vicinity of potential crack path. Details of the region where cohesive zone fracture elements are embedded into the mesh to allow for cracking are provided. The mesh in close vicinity to a potential thermal cracking region is constructed with smaller elements (~ 2 mm). Also notice that frictional interfaces between various pavement layers are provided, as indicated in this figure. Multiple, interacting cracks, although possible to simulate with this approach, are not presented herein for brevity. Due to two-dimensional simulation schemes, each crack represents a transverse crack through the width of pavement. The interface between asphalt concrete and granular base and granular base and soil subgrade is especially important because of the potential for relative movement between these layers. In the current project these interfaces were modeled using a small-sliding frictional interface model available in ABAQUS. This model allows for a frictional sliding of the asphalt concrete due to thermal expansion/contraction.

3.2 Bulk material constitutive models

An appropriate bulk material constitutive model is crucial to the accurate simulation of material behavior in the FE modeling technique. Asphalt concrete material is known to have time and temperature dependent behavior across most of the in-service temperature range. Creep tests on asphalt concrete materials have shown linear viscoelastic behavior at low and moderate temperatures. For the numerical simulations, asphalt concrete was modeled using the generalized Maxwell model. The model parameters were determined using the creep compliance data presented in the laboratory testing section. To capture temperature dependent asphalt concrete properties, a customized user-subroutine in ABAQUS was developed using the time-temperature superposition principle. The thermal coefficient of asphalt concrete material was modeled by means of a user subroutine in the form of a nonlinear relationship on the basis of experimental findings. More details on the experimental study of coefficient of thermal expansion are described in the final report of the LTC project [2007]. Granular bases and subgrade materials were modeled using a linear elastic material model. Typical values for elastic modulus and Poisson's ratio of granular base and subgrade were determined based on the information obtained from section profiles and details available through reports published by the Minnesota Road Research Program [2000]. In the case of field section simulations, the use of an elastic model for the granular base and subgrade was deemed adequate due to the relatively low stress levels in the base and subgrade layers, and the relative predominance of thermal stresses relative to traffic induced stresses for the thermal cracking problem.

3.3 Intrinsic cohesive zone fracture model: bi-linear shape

For simulation of crack initiation and propagation, a cohesive zone model was selected because of its accuracy and efficiency in accounting for material response ahead of the crack tip in the nonlinear fracture process zone (region of micro-cracking, crack pinning, branching, material softening, etc.). Wagoner et al. [2006a, 2006b], Li et al. [2006] and other researchers conducting fracture tests of asphalt concrete at low temperatures recognized the influence of the fracture process zone. Among others, Soares et al. [2004], de Souza et al. [2004], Song et al. [2006], Baek and Al-Qadi [2006], and Dave et al. [2007] have applied the cohesive zone model to simulate cracking in asphalt concrete.

The cohesive zone approach readily utilizes experimentally determined fracture energy. In the cohesive fracture approach, the material begins to incur damage (softening) once the stresses exceed the limit stress of material, which in this case is assumed to be the tensile strength. Beyond this peak, the material undergoes a stage of softening (damage) whereby its capacity to transfer load across the potential crack continuously decreases. Once the material dissipates the energy equivalent to its fracture energy, a macro-crack is developed. The region between the point of damage initiation and point of complete failure is often called the fracture process zone. Figure 3.2(a) illustrates the process zone, modeled herein as the region between the cohesive crack tip (where the traction is at a maximum and equivalent to material's tensile strength, (σ_t)) and the material crack tip (where the traction is zero). Figure 3.2(b) shows a schematic illustration of the fracture process zone or cohesive zone (hashed region) with traction forces along the potential crack faces illustrated by a series of arrows.

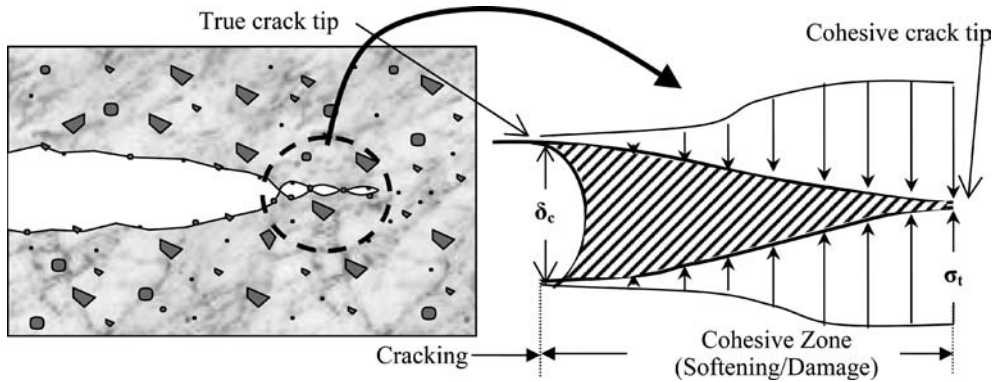


Figure 3.2. Schematic showing of fracture behavior near crack tip and the fracture process zone.

A bilinear model implementation developed by Song et al. [2006] is used in this study. This model allows for minimizing artificially-induced compliance by adjusting the initial slope of the cohesive law. The material parameters used in the cohesive fracture model are: material strength (σ_t) and fracture energy (G_f). These properties for each of the mixtures studied in this project were measured through laboratory testing and are described in the previous section. The bi-linear cohesive zone model was implemented in the commercial finite-element software ABAQUS in the form of a user subroutine.

3.4 Loading conditions

Pavements undergo relatively complicated loading conditions during the course of their service life. Two major load categories imposed on pavements during its course of service include temperature and tire loads. Thermal loads on the pavement structure are transient and depend on factors including air temperature, sunshine, precipitation, etc. The thermal loads for various pavement sections were evaluated using the Enhanced Integrated Climatic Model (EICM) originally proposed by Larson and Dempsey et al. [1999]. The EICM was used to generate the pavement temperature profiles as functions of depth and time. The temperature loads were applied to the model in terms of transient temperature values for each node in the mesh. A user-subroutine was developed to automatically evaluate the nodal temperatures values based on the node location and time in the simulation. A limited number of two-dimensional (2D) simulations were performed with tire loads simultaneously applied to the pavement. It is acknowledged that 2D simulation cannot accurately represent the tire load because of the lack of discretization across the width of the pavement. In the current set of simulations a single 40-KN (9-kip) tire load was modeled in the form of a uniformly loaded strip across the pavement width to evaluate relative trends in thermo mechanical response between test sections.

3.5 Critical conditions approach

By analyzing ambient and pavement temperature profiles throughout the lives of the test sections, the coolest pavement temperatures reached were identified. This approach represents a *critical condition*. In certain simulation cases, additional critical conditions were identified where the highest rates of pavement cooling occurred (in combination with very low temperatures, but perhaps not the coldest absolute temperature reached). The rationale for examining selected critical conditions revolving around low temperature events was as a result of following considerations:

- In general, experimental fracture energies dropped significantly at low temperatures
- The ability of the asphalt concrete to relax stress is greatly reduced at low temperatures
- Most cracking in the field sections was measured to have occurred over the winter months

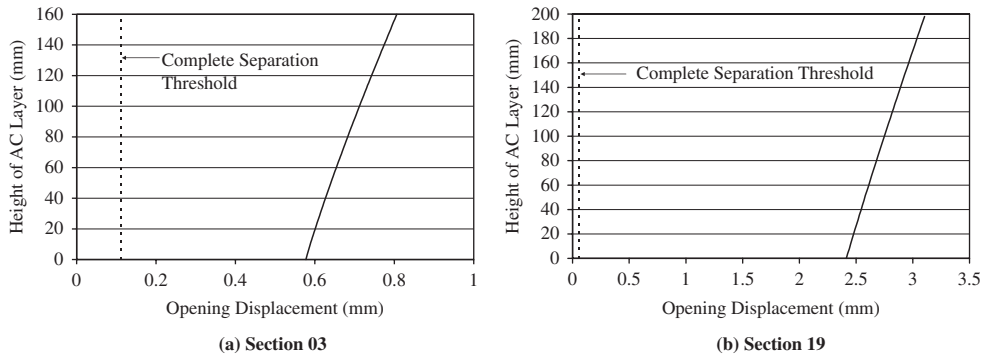


Figure 4.1. Opening displacement plots showing thermal cracking in sections 03 and 19 due to single event cooling.

- The critical conditions approach leads to the most practical simulation times and computational costs when using the FE technique, where model non-linearities (frictional contact interface) and time-dependent material properties are employed. Both of these necessitate an iterative type numerical solution scheme (solver) to be used. Typical simulation times ranged from 1 to 3-hours (not including pre- and post-processing and extracting results) on a workstation PC.

4 SIMULATON RESULTS

The MnROAD sections 03 and 19 are within the high volume traffic sections of MnROAD, located on the mainline of Interstate 94 near St. Cloud, MN and constructed in September 1992 and July 1993 respectively. Sections 33, 34 and 35 are within the low traffic volume test loop, and were constructed in August 1999. Sections 03 and 19 experienced a critical cooling event during 1st–2nd February, 1996. During this event the air temperature cooled to -39.7°C . The pavement surface temperature was predicted to reach a minimum of -33.8°C . The simulation results for thermal loading of sections 03 and 19 are presented in the form of cohesive zone displacement plots, as shown in Figure 4.1. The plot shows the opening displacement for the cohesive elements through the thickness of asphalt concrete layer. The simulation results are plotted with a solid line. The dashed line shows the displacement threshold which can be viewed as the onset of macro cracking. The plots show that for both section 03 and 19 the cohesive displacements are greater than the threshold, indicating that cracking occurred in the pavement due to thermal loading during the aforementioned cooling event. Thus, the FE-based thermal cracking model predicted cracking which occurred during this critical event at MnROAD. Explicit consideration for crack spacing was not pursued with the FE model in the current study. Furthermore, closed form solutions for thermal crack spacing, which were developed in earlier stages of the LTC project, would suggest that a close crack spacing would result from this degree of ‘overstress’ (Yin et al., [2007]).

For sections 33, 34, and 35 the critical coolest event occurred during 30th–31st of January, 2004. During the coolest event, the lowest air temperature reached -31.1°C . The pavement surface temperature was predicted to reach a minimum of -26.2°C . The simulations for this set of sections were performed for thermal loading as well as combined thermo-mechanical loading. For these simulations, a single 40-kN tire load was applied at the coolest pavement surface temperature to study relative thermo-mechanical responses. Sections 33, 34, and 35 showed very limited pavement damage under thermal loading. Under combined thermo-mechanical loading, the sections underwent significant softening (damage). Table 4.1 summarizes the simulation results for sections 33, 34, and 35. For example, under thermo-mechanical loading the simulations for section 33 predicted that a region extending 54-mm from the bottom of the layer (about half of the 103-mm thickness) would be damaged (softened). Interestingly, the section with the softest binder (section 35, with PG

Table 4.1. Extent of softening in sections 33, 34, and 35 under thermo-mechanical loading.

Section (Asphalt Grade)	Length of softened region (mm)
Section 33 (PG58-28)	54-mm from bottom
Section 34 (PG58-34)	24-mm from bottom
Section 35 (PG58-40)	63-mm from bottom

Table 5.1. Amount of cracking in selected MnROAD field sections.

Section	03	19	33	34	35
Observed Cracking (m/100 m)	36.4	109.4	18.2	1.2	149.4

58-40 binder) actually incurred the most cracking in the field. The pattern was that of short, transverse cracks, rather than traditional full-width, full-depth thermal cracks. The simulation model, which accounts for thermo-mechanical loading as well as creep and fracture material properties, did in fact predict the largest extent of bottom-up damage to occur in section 35, which had the largest pavement deflections.

5 DISCUSSION OF SIMULATION RESULTS AND FIELD PERFORMANCE

Table 5.1 shows the pavement cracking data for the five sections, based on field surveys performed in 2006. The data is presented in the form of amount of cracking per 100-m of pavement.

By comparing simulation results with amount of cracking observed in the field, the following observations can be made:

- Simulation results indicate that sections 03 and 19 are susceptible to low temperature thermal cracking during the coolest single event (24-hour) thermal cycle during the Winter of 1995-96. The field observations also indicated significant cracking in both sections.
- Simulations indicate that section 19 has higher thermal cracking potential compared to section 03. The higher thermal cracking potential of section 19 is attributed to an inferior asphalt binder grade for the mixture. Asphalt concrete fracture properties for section 19 are inferior to those of section 03, and the viscoelastic properties indicate that the mixture is less compliant. This prediction agreed with the field observations.
- Simulations of sections 33, 34 and 35 show very limited potential for thermal cracking under the critical cooling event that occurred during the Winter of 2003–04.
- Thermo-mechanical simulations for sections 33, 34 and 35 during the coolest event show that section 35 has the highest amount of potential for damage (softening), followed by section 33, and then section 34. This ranking follows the same order as the cracking observed in the field.
- The prediction of higher extent of softening in section 35 is due to highly compliant asphalt mixture (PG58-40), which causes excessive deformation under the tire load. At the same time, the fracture properties for this mixture are very similar to that of the section 33 (PG58-28) mixture.

6 SUMMARY

The integrated laboratory testing and computer simulation method presented in this paper was utilized in the investigation of low-temperature cracking in five test sections at MnROAD. In

general, the simulation results were found to be in good agreement with field observations. This study demonstrates the importance of integrating both laboratory testing and numerical simulations when investigating a pavement distress mechanism such as low-temperature thermal cracking. The framework of the techniques presented herein has been recommended for phase II of the LTC pooled fund study, and for related airport reflective cracking studies. Planned model extensions include crack spacing prediction, three-dimensional modeling, and comprehensive model validation. The LTC data base will also provide a good opportunity to re-evaluate binder specifications and binder-to-mixture property relations.

ACKNOWLEDGEMENT

We are grateful for the support provided by the sponsors and partners of National Pooled Fund Study 776. Any opinions expressed herein are those of the writers and do not necessarily reflect the views of the sponsors.

REFERENCES

- Artamendi, I., Khalid, H.A. "Effect of Specimen Geometry and Loading Rate on the Fracture Properties of Bituminous Materials," Proceedings of the Advance Characterization of Pavement and Soil Engineering Materials – 2007 (Athens, Greece), pp. 1183–1192 (2007).
- Baek, J., and I. L. Al-Qadi, "Finite Element Method Modeling of Reflective Cracking Initiation and Propagation: Investigation of the Effect of Steel Reinforcement Interlayer on Retarding Reflective Cracking in Hot-Mix Asphalt Overlay," Transportation Research Record, Record Number 1949, pp. 32–42 (2006).
- Dave, E. V., S. H. Song, W. G. Buttlar, and G. H. Paulino, "Reflective and Thermal Cracking Modeling of Asphalt Concrete Overlays," Proceedings of the Advance Characterization of Pavement and Soil Engineering Materials – 2007 (Athens, Greece), pp. 1241–1252 (2007).
- de Souza, F. V., J. B. Soares, D. H. Allen, and F. Evangelista, Jr., "Model for Predicting Damage Evolution in Heterogeneous Viscoelastic Asphaltic Mixtures," Transportation Research Record, Record Number: 1891, pp. 131–139 (2004).
- Larson, G, and B. J. Dempsey, "Enhanced Integrated Climatic Model: Version 2.0", Report number DTFA MN/DOT 72114, Minnesota Road Research Project and Federal Highway Administration (1997).
- Li, X., A. F. Braham, M. O. Marasteanu, W. G. Buttlar, and R. C. Williams, "Effect of Factors Affecting Fracture Energy of Asphalt Concrete at Low Temperature", Accepted to the 3rd European Asphalt Technology Association Conference, Lyon, France, April 14–15th, 2008.
- Molenaar, A. A. A., A. Scarpas, X. Liu, and S.M.J.G. Erkens, "Semi-Circular Bend Test: Simple but Useful?" Proceedings of the Association of Asphalt Paving Technologists, Vol. 71, 2002, pp. 795–815.
- Marasteanu M. O. et al., "Investigation of Low Temperature Cracking in Asphalt Pavements", National Pooled Fund Study 776, Final report, Minnesota Department of Transportation (2007).
- Minnesota Department of Transportation, "MnROAD Aggregate Base Profile," Online Published Report, Office of Materials (2000).
- Roque, R., D. R. Hiltunen, and W. G. Buttlar, "Thermal Cracking Performance and Design of Mixtures Using Superpave(TM)," Journal of the Association of Asphalt Paving Technologists, Vol. 64, pp. 718–735 (1995).
- Soares, J. B., F. A. Colares de Freitas, and D. H. Allen, "Crack Modeling of Asphaltic Mixtures Considering Heterogeneity of the Material," Transportation Research Record, Record Number: 1832, pp. 113–120 (2004).
- Song, S. H., G. H. Paulino, and W.G. Buttlar, "A Bilinear Cohesive Zone Model Tailored for Fracture of Asphalt Concrete considering Rate Effects in Bulk Materials," Engineering Fracture Mechanics, Volume 73, Number 18, pp. 2829–2848 (2006).
- Wagoner, M.P., W.G. Buttlar, and G.H. Paulino, "Disk-Shaped Compact Tension Test for Asphalt Concrete Fracture," Experimental Mechanics, Vol. 45, pp. 270–277 (2005a).
- Wagoner, M. P., W. G. Buttlar, and G. H. Paulino, "Development of a single-edge notched beam test for asphalt concrete mixtures," Journal of Testing and Evaluation, ASTM, Vol. 33, No. 6, pp. 452–460 (2005b).
- Yin, H. M., W. G. Buttlar, and G. H. Paulino, "Simplified solution for periodic thermal discontinuities in asphalt overlays bonded to rigid pavements," Journal of Transportation Engineering, Vol. 133, Issue 1, pp. 39–46 (2007).

Thermal cracking prediction using artificial neural network

M. Zeghal

Institute for Research in Construction, National Research Council, Ottawa, Ontario, Canada

ABSTRACT: Thermal cracking of asphalt concrete is a form of pavement distresses that is of a great importance for northern Canadian jurisdictions where extreme cold conditions and temperature fluctuations are encountered. However, predictions of this distress have not been accurate enough which translated in premature road failures. This is mainly due to the absence of robust mechanistic constitutive models, which translated into reliance on empirical formulations and indicators with inherent limitations. This paper presents a scheme to overcome such shortcomings. It calls for taking advantage of the wealth of field information available from Long Term Pavement Performance (LTPP) sites and using an analytical approach to predict thermal cracking of pavements. This study presents the artificial neural network (ANN) technique as a promising method that can help designers predict thermal cracking based on data accumulated (over the years) from LTPP sites. Several ANN models were trained and tested using simple parameters such as road structure, material properties and environmental conditions as input to predict thermal cracking. Results of ANN simulations showed the potential of the technique to effectively predict low severity thermal cracking of LTPP sites that were not included in the training and testing phases and to delineate the critical factors governing this distress form.

1 INTRODUCTION

Flexible pavements are constructed with asphalt concrete materials that age during all the phases of their production, preparation, transportation and construction. The aging process continues over many years of the pavement in-service life. The aging and hardening increase the stiffness of the material and thus reduces its flexibility, making it vulnerable to different forms of cracking including thermal cracking.

Thermal cracking is a major distress type of conventional (hot mix asphalt concrete) pavements. It has been an important concern for pavement owners, engineers and researchers for the last three decades. It affects many regions in Canada and the United States. These regions are characterized by extreme daily low temperatures during the winter and high temperatures during the summer, which favors hardening of asphalt concrete. Thermal cracking may result from either a single thermal cycle at which the temperature drops below a critical low temperature or from a series of repeated thermal cycles where the temperature fluctuations occurs above the critical temperature. The critical temperature is the fracture temperature of the asphalt concrete mixture. These two modes of thermal cracking are known as low temperature cracking and thermal fatigue, respectively. Vinson et al. (1990) established that low temperature cracking is more likely to develop at temperatures lower than -7°C and /or rapid cooling rate and that thermal fatigue is supposed to occur at milder temperatures in the range of -7°C to 21°C . In 1994, Hiltunen and Roque found that for both types of thermal cracking, crack propagates from top to bottom of the surface layer.

In the last thirty years or so, there were many attempts to delineate the mechanisms of thermal cracking and to predict its development (Haas et al. 1987). In the literature, two types of predictive models are identified; namely empirical and analytical. One of the first attempts of predicting

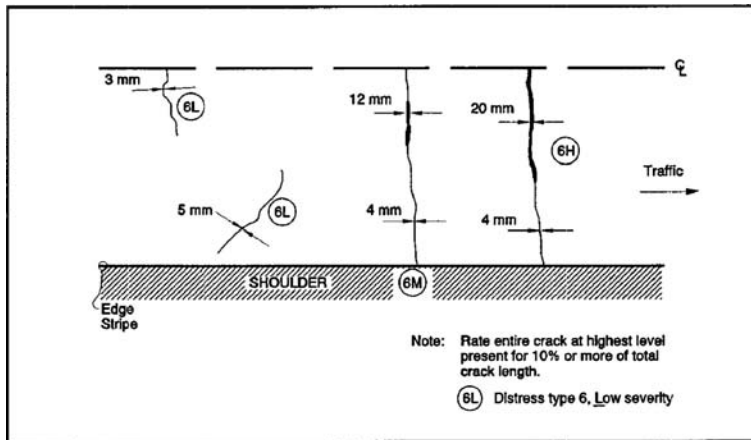


Figure 1. Illustration of the three severity levels of thermal cracking (after Strategic Highway Research Program, 1993).

thermal cracking using the empirical approach was headed by Fromm and Phang (1972). Later, others proposed more models (Chang et al. 1976, Hass et al. 1987). The empirical models mainly correlate cracks spacing to material properties and environmental data based on laboratory tests and field experiments. The analytical models rely on the fracture mechanics to predict the propagation of thermal cracking (Carpenter and Lytton 1975, Lytton et al. 1983, Hiltunen and Roque 1994). Shen et al. (2001) assessed the merit of the two approaches and concluded that they both have drawbacks. They found that empirical predictive models can be used only for limited material properties and environmental conditions. Further, they concluded that fracture mechanics on which analytical models rely cannot explain some important aspects of thermal cracking and is not expected to model the fracture of asphalt concrete in a satisfactory manner. Shen et al. added that analytical models are not capable of simulating the initiation of thermal cracks.

Given the complexity of modeling thermal cracking and the drawbacks of the empirical and analytical approaches discussed above, a study was launched to investigate the merit of using artificial intelligence techniques in predicting thermal cracking. The proposed modeling scheme combines the use of the data from Long Term Pavement Performance (LTPP) sites with the artificial neural network (ANN) technique.

2 THERMAL CRACKING SEVERITY LEVELS

In the distress identification manual for the LTPP Project (Strategic Highway Research Program 1993), thermal cracks are defined as transverse cracks that are predominantly perpendicular to pavement centerline. Further they are classified into the three severity levels described below (Fig. 1).

- Low severity: an unsealed crack with a mean width <6 mm (0.25 in.); or a sealed crack with sealant material in good condition and with a width that cannot be determined.
- Moderate severity: any crack with a mean width >6 mm (0.25 in.) and <19 mm (0.75 in.); or any crack with a mean width <19 mm (0.75 in.) and adjacent to low severity random cracking.
- High severity: any crack with a mean width >19 mm (0.75 in.); or any crack with a mean width <19 mm (0.75 in.) and adjacent to moderate to high severity random cracking.

The scope of the investigation reported in this paper was limited to the low severity level and thus made use of LTPP data related to this type of thermal cracking only.

3 ARTIFICIAL NEURAL NETWORK TECHNIQUE

The ANN technique is a relatively new method of modeling that was originally presented by Ghaboussi et al. (1990 and 1991). Unlike other modeling techniques that rely on mathematical expressions to describe experimental observations, ANN modeling relies on the learning capabilities of its elements.

An ANN model is a collection of interconnected elements (neurons) that are linked together in a way similar to the architecture of the human brain and have the performance characteristics of biological neurons (Fausett 1994). It is capable of recognizing, capturing and mapping features (known as patterns) contained in a set of data mainly due to the high interconnections of neurons that process information in parallel. The learning capabilities allow neural networks to be directly trained with the results of experiments. Once an ANN model has learned the patterns defining the relationship between the input and output of a certain test or process, it can generalize from its training set data to novel cases. Presenting a network with facts for which the input and output are known to delineate the embedded patterns is an integral part of the ANN modeling process.

An ANN model is made up of at least three layers. The first layer contains the input parameters while the last layer contains the output (solution). One or more layers known as hidden layers are usually placed between the input and output layers. The hidden layers constitute the network's means of delineating and learning the patterns governing the data that the network is presented with.

There are many ways a neural network can be trained. The back propagation technique is the most popular process and has been used in many fields of science and engineering such as construction simulation (Flood 1990 and Moselhi et al. 1991), constitutive modeling (Rogers 1994) and structural analysis (Garrett et al. 1992). In a back propagation learning process, training is accomplished by assigning random connection weights to the connections and calculating the output using the present connection weights. At a second stage, the process involves back propagating the error defined as the difference between the actual and computed output through the hidden layer(s). This procedure is repeated for all training facts until the error is within a certain tolerance. The final network with final connection weights is then saved to serve as a prediction model.

4 ANN MODEL BUILDING

The development of an ANN model involves defining the number of nodes in the input, output and one or more hidden layers. The input layer size is generally predetermined based on the parameters known or assumed to affect the targeted output. However, the number of hidden layers as well their nodes is usually determined by a trial-and-error procedure. Determination of the number of hidden layers and their nodes involves training and testing the built network against test sets made of examples with known input and output.

Using a subset of the input data used for the calibration and validation of the 2002 design guide for new constructed pavement sections (NCHRP 2003), an investigation was initiated to examine the effectiveness of the ANN technique in predicting the low severity thermal cracking of conventional pavements. The data used included information related to pavement, climatic information, material characterization data and distress values for flexible pavement sections as shown in Table 1. The data was extracted from the LTPP database.

5 ANN MODEL OPTIMIZATION

In this study, the amount of low severity thermal cracking is the single targeted output. The inputs included all others parameters shown in Table 1 and related to pavement data, climatic information, material characterization data, and pavement age at time of survey to measure the amount of thermal cracking. The number of nodes in the hidden layer(s) was investigated in order to arrive at a robust

Table 1. Information of LTPP sites used in the study.

Pavement data	Climatic data	Aggregates gradation, for asphalt mixture, data	Binder data	Distress data
Section number (A)*	Latitude north (L)	% retained on 3/8" sieve (Q)	Pb (U)	Age at survey (AM)
State code (B)	Longitude west (M)	% retained on 3/8" sieve (R)	Gb (V)	Low severity thermal cracking (AN)
State (C)	Elevation (N)	% retained on #4 sieve (S)	Gmb (W)	
Design period (E)	Water table depth (O)	% passing #200 sieve (T)	Gmm (X)	
Asphalt thickness (P)			Gsb (Y)	
Lane width (F)			Gse (Z)	
Pavement slope (G)			VBE (AA)	
Initial IRI (H)			Original viscosity (AE)	
Thermal conductivity (I)			Viscosity grade (AH)	
Heat capacity (J)			Penetration grade (AI)	
Surface short wave absorption (K)			Penetration at 77°F (AJ)	
Age t (AB)			Viscosity at 140°F (AK)	
Air voids at age = t (AC)			Viscosity at 275°F (AL)	
Original air voids (AF)				
MAAT (AD)				
Total unit weight (AG)				

* The characters given in parentheses after each factor are the symbols used in ANN models

IRI: International roughness index

MAAT: Mean annual average temperature

Pb: Binder content by weight

Gb: Specific gravity of the binder

Gmb: Bulk specific gravity of the mix

Gmm: Maximum theoretical specific gravity of the mix

Gsb: Bulk specific gravity of the aggregate

Gse: Effective specific gravity of the aggregate

VBE: Effective binder content by volume at time of construction

network. The investigation consisted of training ANN models with a varying number of hidden layers and nodes. Ten percent of the data was randomly set aside for testing the trained network and another ten percent of the data was reserved for comparing the predictions of the built network with laboratory obtained data. The effect of the number of hidden nodes on the accuracy of the network was measured by the percentage "Absolute value of the Relative Error" (|ARE|) defined as:

$$|ARE| = \text{abs. } \{(X_{\text{prediction}} - X_{\text{actual}}) / X_{\text{actual}}\} \times 100\% \quad (1)$$

Through trial-and-error, it was found that using more than one hidden layer did not improve the accuracy of the predictions. Consequently, the number of nodes in the single hidden layer was the only parameter left to be determined. The effect of the number of hidden nodes in the single hidden layer on |ARE| is displayed in Figure 2. It shows that the number of nodes in the hidden layer plays a major role in the accuracy of the network. Further, the network consisting of 37 nodes in the

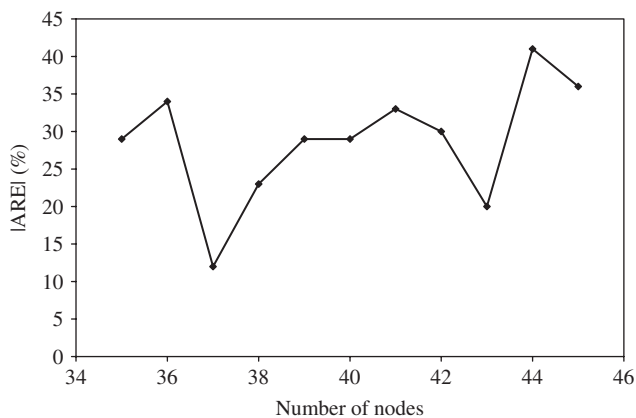


Figure 2. Impact of number of nodes in the hidden layer on the accuracy of predictions.

Table 2. Prediction of thermal cracking of two novel LTPP sections.

State	Years after construction	Measured thermal cracking (m/Km)	Predicted thermal cracking (m/Km)	ARE (%)
Alaska	5.8	12.123	12.244	1
	7.1	15.723	13.180	16
	9.1	18.394	16.629	10
Michigan	9.3	6.156	7.412	20

single hidden layer was found to provide the best accuracy with an |ARE| of about 12%, which was considered acceptable.

6 ANN ABILITY TO PREDICT LOW SEVERITY THERMAL CRACKING

The ability of the ANN technique to predict low severity thermal cracking of roads in a satisfactory manner was determined by comparing ANN predictions and field-measured thermal cracking of several LTPP sections that the model did not see before. A typical comparison done for two LTPP sites is presented in Table 2. It shows that the ANN technique is capable of predicting the low severity thermal cracking with satisfactory accuracy. The |ARE| of predictions were lower than 20%. Further, with the exception of few data points, the predictions of the optimized ANN had an |ARE| consistently lower than 25% when all LTPP sites reserved for validation were considered.

7 FACTORS INFLUENCING LOW SEVERITY THERMAL CRACKING

The complexity of thermal cracking and the multitude of factors known or suspected to influence thermal cracking motivated the use of as much input parameters as possible to make sure not to miss any important factors. In this section, the sensitivity of all these inputs is analyzed. Figure 3 shows an output of the optimized ANN model in which the sensitivity of all input parameters are presented using a bar graph. The sensitivity of a parameter is proportional to the length of the bar. Figure 3 suggests that four parameters have a great impact on low severity thermal cracking. They are, in decreasing order of influence, the binder penetration at 77°F, the age of the pavement, and

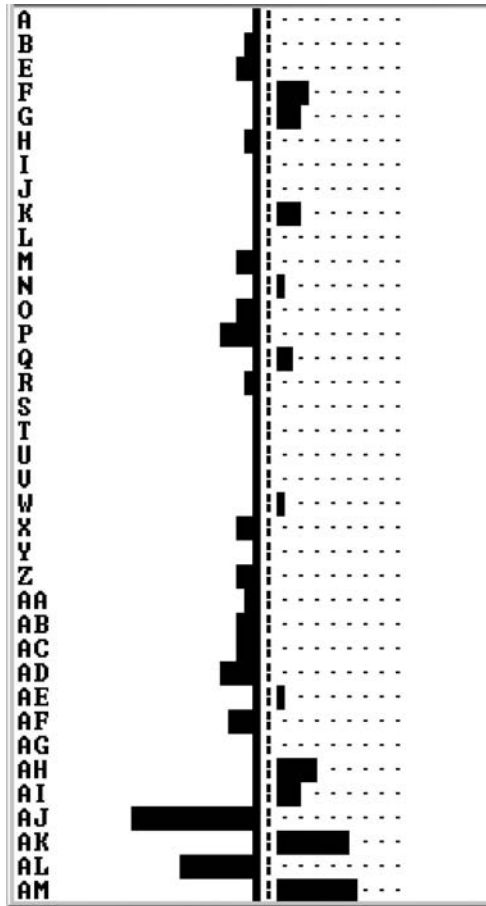


Figure 3. Sensitivity of all inputs used in ANN modeling.

the binder viscosities at 140°F and 270°F. They are represented by the symbols AJ, AM, AK and AL, respectively in the ANN simulations (Fig. 3). The impact of pavement age is further analyzed in Figure 4. It is clear that, in the early years of the pavement age, the rate of development of low severity thermal cracking is low. However this rate becomes more pronounced after 10 years and especially after 15 years.

8 CONCLUSION

Thermal cracking is one of the major forms of road distresses in many jurisdictions in Canada and the United States. The prediction of thermal cracking using empirical and analytical approaches has been faced with many drawbacks mainly due to the complexity of mechanisms governing its development and propagation. This paper presents the artificial neural network as an alternative modeling technique that is capable of considering the wide spectrum of factors that are known to influence thermal cracking and including other factors that are very difficult or tedious to investigate in the field or laboratory and might have an impact. Results obtained from the current study showed that the ANN technique is a valuable tool that has the capability of predicting low severity thermal cracking of pavements with an absolute average error of less than 25%. Further, the ANN has

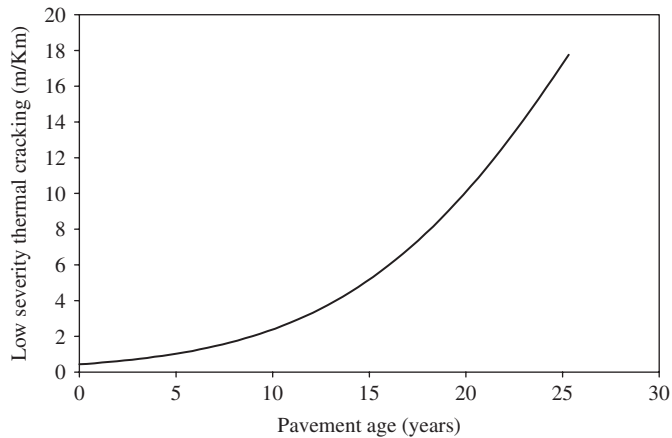


Figure 4. Impact of pavement age on low severity thermal cracking.

the ability to delineate the sensitive factors that influence thermal cracking. The promising results obtained in predicting low severity thermal cracking motivate the move to the next step of the study, which will focus on assessing the ability of the ANN technique in predicting the two other levels of severity of thermal cracking, namely, medium and high.

REFERENCES

- Carpenter, S. H., Epps, J. A., & Lytton, R. L. (1975) "Pavement cracking in West Texas due to freeze-thaw cycling." Transportation Research Record 532, Transportation Research Board, Washington D.C., 1–13.
- Chang, H. S., Lytton, R. L., & Carpenter, H. S. (1976) "Prediction of thermal reflection cracking in West Texas." Report No., TTI-2-8-73-18-3, Texas Transportation Institute, Texas A&M University.
- Fausett, L. (1994) "Fundamentals of neural networks: architectures and applications." Prentice Hall, Upper Saddle River, NJ, USA.
- Flood, I. (1990) "Simulating the construction process using neural networks." Proceedings of the Seventh International Symposium on Automation and Robotics in Construction, ISARC, Bristol Polytechnic, England.
- Fromm, H. J., & Phang., W. A. (1972). "A study of transverse cracking of bituminous pavements." Proceedings, AAPT, Vol. 41, pp. 383–423.
- Garrett, J. H., Ranjitham, S., & Eheartt, J. W. (1992) "Application of neural network to groundwater remediation." In Expert Systems for Civil Engineers: Knowledge Representation, Edited by Allen, R.
- Ghaboussi, J., Garret, J. H. Jr, & Wu, X. (1990) "Material modeling with neural networks." Proceedings of the International Conference on Numerical Methods in Engineering: Theory and Applications, Swansea, UK, pp. 701–717.
- Ghaboussi, J., Garret, J. H. Jr, & Wu, X. (1991) "Knowledge base modeling of material behaviour with neural networks." Journal of Engineering Mechanics Division, ASCE, 117(1), 132–153.
- Haas, R., Meyer, F., Assaf, G. & Lee, H. (1987) "A comprehensive study of cold climate asphalt pavement cracking." Proceedings, AAPT, Vol. 56, pp. 198–245.
- Hiltunen, D. R. & Roque, R. (1994) "A mechanics-based prediction model for thermal cracking of asphaltic concrete pavements." Association of Asphalt Paving Technologists 63: 81–117.
- Lytton, R. L., Shanmugham, U. & Garrett B. (1983) "Design of asphalt pavements thermal fatigue cracking." Report No. FHW-TX-83, Texas Transportation Institute, Texas A&M University.
- Moselhi, O., Hegazi, T. & Fazio, P. (1991) "A hybrid neural network methodology for cost estimation." Proceedings of the Eighth International Symposium on Automation and Robotics in Construction, ISARC, Stuttgart, Germany.
- NCHRP project 1-37A. (2003) "Guide for mechanistic-empirical design of new and rehabilitated pavement structures – Final Report, Appendices EE." TRB, National Research Council, Washington, D.C.

- Rogers, J. L. (1994) "Simulating structural analysis with neural network." *J. Comp. Civ. Engng, ASCE* 8, 80–100.
- Shen, W., & Kirkner, D. J. (2001) "Thermal cracking of viscoelastic asphalt concrete pavement." *Journal of Engineering Mechanics*, 127 (7), 700–709.
- Strategic Highway Research Program (1993) "Distress identification manual for the Long Term Pavement Performance Project." SHRP-P-338, Washington, D.C.
- Vinson, T. S., Janoo, V. C. & Haas, R. C. G. (1990) "Summary report on low temperature and thermal fatigue cracking." SHRP-A/IR-90-001, National Research Council, Washington, D.C.

Effect of aggregate grading on low temperature cracking resistance in asphalt mixtures base on mathematical statistic

Y.-Q. Tan, H.-N. Xu, Z.-J. Dong, & W.-Q. Gong

Harbin Institute of Technology, Harbin, Heilongjiang Province, P.R. China

ABSTRACT: This paper discussed the effect of aggregate grading on the low temperature cracking resistance in asphalt mixtures from the perspective of the degree of aggregate interlock. A total of 9 asphalt mixtures with 9 different aggregate gradations and one asphalt binder content were studied. Volumetric analysis of asphalt mixtures and the coarse portion of the aggregate blend showed aggregate grading had a significant influence on the degree of aggregate interlock in asphalt mixtures. A trend was existed in the low temperature performance changing with the gradation's fluctuation. With the aid of rank sum test, it was indicated the variation of the aggregate grading affected the low temperature performance significantly, and the accepted fluctuating range of gradation was proposed which met low temperature cracking resistance in asphalt pavement. The findings also indicated a positive correlation existed between the degree of aggregate interlock in asphalt mixtures and the low temperature performance.

1 INTRODUCTION

1.1 Background

Low temperature cracking is one of the three major distresses (low temperature cracking, fatigue and rutting) in asphalt pavement (Huang, 2003). Especially in cold region, cracking caused by low temperature is the main distress form.

With the propagation of low temperature cracking through the pavement structure, a conduit is created for the migration of water and fine aggregates into and out of the pavement. During the winter, the intrusion of deicing solutions into the base through the crack can lead to localized thawing of the base and depression at the crack. Pumping of the fine aggregates through the crack produces voids under the pavement and results in a depression at the crack upon loading. All these effects results in poor ride quality and a reduction in service life of the pavement. (Kanerva, 1993)

Researches have been conducted on the factors affecting the low temperature performance in asphalt mixtures. The Strategic Highway Research Program (SHRP) reported that the performance of low temperature attributed more than 80% to asphalt which was the leading factor. Investigation by Shen Ai-qin confirmed this viewpoint. She also reported that it was not rational that the higher the asphalt grade was, the better low temperature performance. In other studies, Per Redelius and Xiaohu Lu observed that using waxy asphalt, the asphalt mixtures tended to have higher fracture temperature. In recent years, it has been reported that other factors, except asphalt binder, were effective in improving the performance of low temperature. Baoshan Huang investigated that the aggregate content made impact on the tensile strength of the asphalt mixtures. Increasing the aggregate content increased the tensile strength of asphalt mixture. Wu Kuang-huai also reported that the coefficient of thermal contraction in dense-graded asphalt mixture is 1.24 times that in gap-graded asphalt mixture at low temperature.

Large numbers of experimental results suggested that the properties of asphalt effectively affected asphalt mixtures low temperature performance. It was also clearly demonstrated that the particle size distribution played an important role in resisting low temperature cracking. Yet, mass researches

Table 1. Physical properties of coarse aggregate.

Sieve size (mm)	16	13.2	9.5	4.75
Bulk specific gravity	2.793	2.795	2.794	2.784
Apparent specific gravity	2.809	2.813	2.814	2.810
Absorption (%)	0.21	0.23	0.24	0.33
Crushed stone value (%)			5.0	
Wear stone value (%)			4.3	

Table 2. Physical properties of fine aggregate.

Sieve size (mm)	2.36	1.18	0.6	0.3	0.15	0.075
Apparent specific gravity FAA	2.815	2.804	2.791	2.805	2.822	2.740
			19(s)			

Table 3. Physical properties of asphalt.

Index	Penetration at 25°C 0.1 mm	Softening point °C	Ductility at 15°C cm	Rotational viscosity at 135°C Pa.s
Test results	106	45.7	> 150	0.275

concentrate on the asphaltic nature and the components of asphalt. There are very limited studies on the correlation between aggregate grading and low temperature cracking resistance.

In this paper, particle is divided into two parts – coarse aggregate and fine aggregate. The effect of gradation on the low temperature performance is conducted by changing the internal particle distribution. With the aid of rank sum test – one of the mathematical statistic methods, the accepted fluctuating range of aggregate grading is proposed which meets low temperature cracking resistance in asphalt pavement.

1.2 Research objectives

The main objectives of this study are to:

- Investigate the trend of the degree of aggregate interlock and low temperature performance of asphalt mixtures changing with the aggregate grading, respectively;
- Evaluate the effect of aggregate grading on asphalt mixtures low temperature cracking resistance;
- Correlate the degree of aggregate interlock with low temperature cracking resistance in asphalt mixtures.

2 MATERIALS AND DESIGN OF AGGREGATE GRADING

2.1 Materials

According to the Technical Specifications for Construction of Highway Asphalt Pavement in China (JTG F40-2004), the properties of coarse aggregate and fine aggregate are listed in Tables 1 and 2. Asphalt propertied is listed in Table 3. Limestone was used as mineral filler.

2.2 Design of aggregate grading

Nominal maximum of asphalt mixture is 16 mm.

Firstly, choose a gradation whose performance is well in practice as standard gradation. It is illustrated in Fig. 1. The optimum asphalt content was selected at 5.2%.

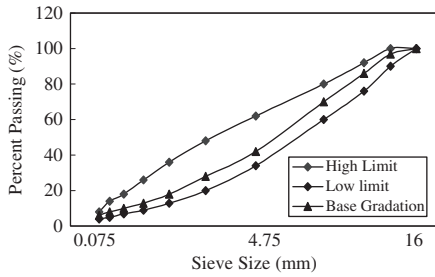


Figure 1. Standard gradation.

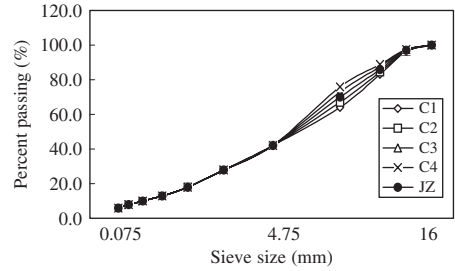


Figure 2. Gradations C1~C4.

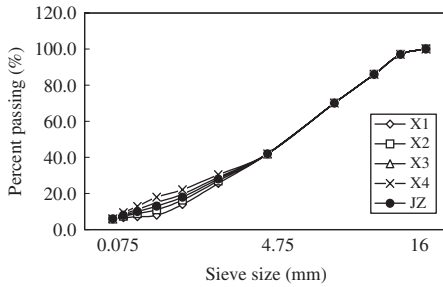


Figure 3. Gradations X1~X4.

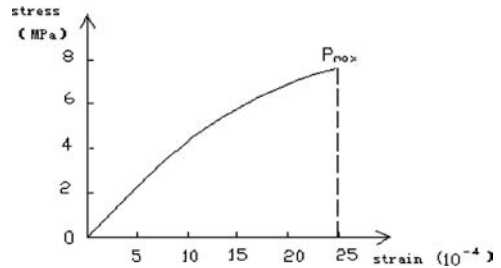


Figure 4. Strain-stress curve.

Secondly, change the coarse aggregate distribution to simulate the fluctuation caused by the variance of coarse aggregate. The gradations C1~C4 are plotted on the curves in Fig. 2.

Thirdly, change the fine aggregate distribution to simulate the fluctuation caused by the variance of fine aggregate. The gradations X1~X4 are plotted on the curves in Fig. 3.

3 TEST METHOD

3.1 VCA testing method

In order to calculate the structure of asphalt mixtures, the loose and rodded unit weights were determined for the coarse portion of the aggregate blend.

This was performed using the aggregate testing apparatus. According to the specifications described in ASTM C1252-93, the coarse portion of the aggregate blend were sampled for testing under the loose condition and 25 rods of compaction in the testing apparatus.

3.2 Asphalt mixture low temperature performance testing method

Low temperature cracking is attributed to tensile stresses induced in the asphalt pavement that develop when the pavement is subjected to a cold temperature. As the pavement is cooled thermal stresses are induced as a result of the asphalt mixture's tendency to contract and deformation. The work done by the stress induces energy accumulated. If the energy accumulated in the pavement is equal to the critical energy of the asphalt mixture at that temperature, a low temperature cracking results. The larger the energy is consumed in failure, the better asphalt mixtures low temperature cracking resistance.

In the present paper, bending strain energy density was adopted as the index to evaluate asphalt mixtures low temperature performance.

Table 4. Volumetric properties of coarse aggregate blend.

Gradation Name	Unit weight (g/cm ³)			VCA(%)	
	Specific gravity	Loose	25 rods	VCA _{DLC}	VCA _{DRC}
JZ	2.789	1.435	1.581	48.5	43.3
C1	2.790	1.426	1.583	48.9	43.3
C2	2.790	1.440	1.582	48.4	43.3
C3	2.789	1.443	1.580	48.3	43.3
C4	2.788	1.443	1.578	48.2	43.4
X1	2.789	1.435	1.581	48.5	43.3
X2	2.789	1.435	1.581	48.5	43.3
X3	2.789	1.435	1.581	48.5	43.3
X4	2.789	1.435	1.581	48.5	43.3

Specimens were fabricated in a steel mold with inside dimensions of 300 × 300 × 50 mm. For each specimen, aggregate and asphalt binder were heated and mixed at a temperature of 155°C. This procedure produced a consistent specimen with the desired dimensions and density.

The test specimen was a beam with the dimension of 35 × 30 × 250 mm. Maximum theoretical specific gravity, bulk specific gravity, and air voids for each test specimen were determined.

The test was performed on a closed-loop controlled servohydraulic MTS810 material test system (−40°C~60°C). In the experiment, test temperature was −10°C; loading speed was at 50 mm/min; loading at one point in the midst of span (200 mm) was adapted as loading mode.

The correlation between stress and strain was approximate a function of a second-degree polynomial:

$$P(\delta) = b_0 + b_1\delta + b_2\delta^2 \quad (1)$$

Where: b_i -Constant, $i = 0, 1, 2$; P -Stress, MPa; δ -Strain.

Failure state was illustrated in Fig. 4. Bending strain energy density in failure state could be calculated as follows:

$$E = \int_0^{\delta_0} P(\delta)d\delta = \int_0^{\delta_0} (b_0 + b_1\delta + b_2\delta^2)\delta d\delta \quad (2)$$

Where: E -Bending strain energy density, KJ/m³ (Hao, 2000; Shen, 2004).

4 RESULTS AND DISCUSSION

4.1 Fluctuation of aggregate grading to the influence on the degree of aggregate interlock

Depending on the degree of aggregate interlock, two structure styles in the asphalt mixtures exist – floating structure and skeleton structure. With gradation changing, the degree of aggregate interlock is altered.

Voids in the coarse aggregate of the mixture (VCA_{mix}) are determined for the coarse portion of the aggregate blend as a property that identifies the existence of a coarse aggregate skeleton with stone-to-stone contact. A coarse aggregate skeleton is developed when the VCA_{mix} is equal to or less than the VCA_{DLC} in dense-graded asphalt mixture.

The volumetric properties of the coarse portion of the aggregate blend and asphalt mixtures are respectively tabulated in Tables 4 and 5.

For ease of comparison, VCA_{mix}, VCA_{DLC} and VCA_{DRC} for various asphalt mixture are shown in Fig. 5. From the figure, one can infer that the change of gradation affected the degree of aggregate interlock in asphalt mixture.

Table 5. Volumetric properties of asphalt mixtures.

Gradation name	ρ_f	VV(%)	VMA(%)	VFA(%)	VCA _{mix}
JZ	2.446	4.1	15.7	73.9	49.1
C1	2.453	5.1	17.5	70.9	48.9
C2	2.424	4.8	17.1	71.7	49.6
C3	2.410	5.2	17.5	70.3	49.9
C4	2.405	5.4	17.7	69.6	50.0
X1	2.328	9.1	20.3	55.5	51.6
X2	2.382	6.9	18.5	62.5	50.5
X3	2.450	3.9	16.2	76.2	49.0
X4	2.484	2.3	15.0	84.4	48.3

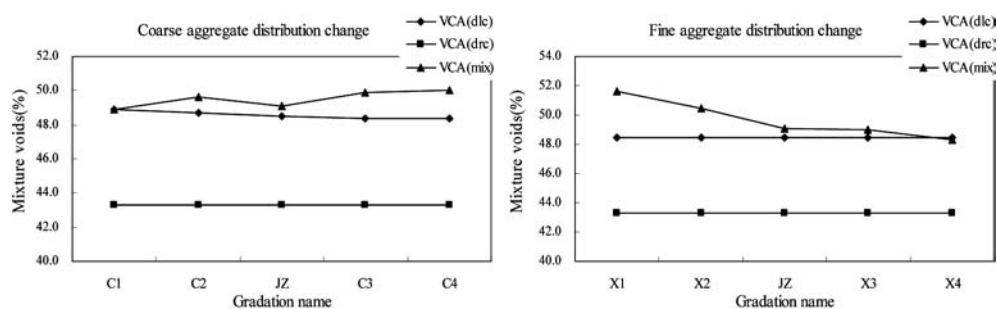


Figure 5. Fluctuation of gradation to the influence on asphalt mixture structure.

Fig. 5-(a) presented that the degree of aggregate interlock weakened with the coarse aggregate distribution fining. The VCA_{mix} value for gradation C1 was equal to the value tested in loose condition. It indicated that the stone-to-stone contact was developed. With the coarse aggregate distribution fining, VCA_{mix} values increased gradually, and they were larger than the values tested in loose condition. In this case, the coarse aggregate was not touching each other and it was “floating” between the fine aggregates. The coarse aggregate distribution fining meant the content of 9.5~16 mm particles increased and the content of 4.75~9.5 mm particles decreased. It can conclude that the more large size particles were, the easier stone-to-stone contact was formed.

Opposite behavior is observed in Fig. 5-(b). The VCA_{mix} value for gradation X1 was larger than VCA_{DLC}. The coarse aggregate particles were spread apart and were not in a uniform stone-to-stone contact condition. With the fine aggregate distribution fining, the VCA_{mix} values decreased. For gradation X4, the coarse aggregate skeleton was developed. One can infer that the fine aggregate distribution fining conduces to the enhance of the degree of aggregate interlock.

4.2 Fluctuation of aggregate grading to the influence on asphalt mixtures low temperature performance

A clear trend was observed with the change of gradation from Fig. 6.

Bending strain energy density decreased with the coarse aggregate distribution fining. It was maximal in gradation C1. After that, with gradation fining, it decreased gradually. However, the difference among gradation C2, JZ, C3, C4 was negligible. The phenomena indicated that the performance of low temperature declined with coarse aggregate distribution fining.

As shown in Fig. 6-(b), with fine aggregate distribution fining, bending strain energy density increased. It was 3.61 KJ/m³ in gradation X1 while it was 7.11 KJ/m³ in gradation X4 which was two times the value of gradation X1. The phenomenon above presented low temperature performance increased with the fine aggregate distribution fining.

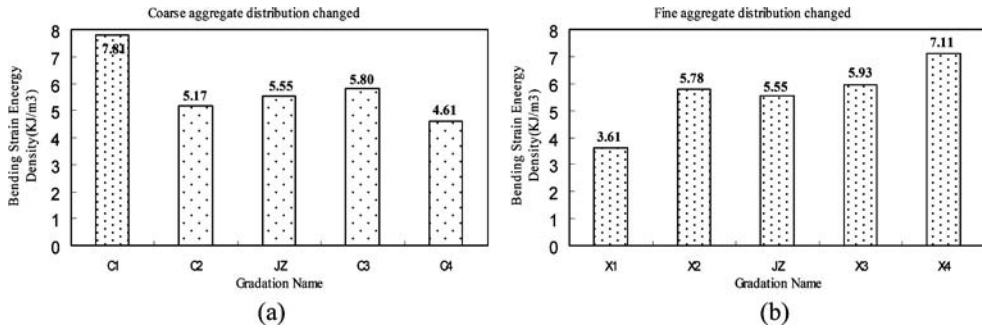


Figure 6. Fluctuation of gradation to the influence on low temperature performance.

Table 6. Rank sum test of coarse aggregate fluctuation to the influence on low temperature performance.

ξ	JZ	T	R_1	T_1	T_2	Change significantly, yes or no ($\alpha = 0.05$)
JZ	C1	JZ	12	14	30	Yes, better
JZ	C2	JZ	24	14	30	No
JZ	C3	JZ	20	14	30	No
JZ	C4	JZ	25	13	27	No

4.3 Research on the fluctuation range of aggregate grading to meet asphalt mixtures low temperature cracking resistance

4.3.1 Fluctuation of aggregate grading to the influence on the low temperature performance based on mathematical statistic

In many applications, the samples are drawn under different conditions, and inferences must be made about possible effect of these conditions. But many experiments are such that if they do little to the samples, the measurements would not be exactly the same. To deal with this problem a mathematical statistic method is often employed. In this work, rank sum test was adapted to analyze the fluctuation of gradation to the influence on low temperature cracking resistance in asphalt pavement.

Table 6 illustrates changing coarse aggregate distribution has an impact on low temperature performance in asphalt pavement. At a 95% confidential level, the performance of low temperature in gradation C1 which became rougher 6% showed preponderance over standard gradation. With the gradation fining, low temperature cracking resistance didn't change significantly compared with standard gradation.

The degree of aggregate interlock in asphalt mixture is a useful parameter in explaining the low temperature cracking resistance changing with aggregate grading's fluctuation. As discussed in part 4.1, a stone-to-stone contact was developed in gradation C1. The coarse aggregate packed closely, and the packing mechanism between stones could provide high resistance to contract and deformation at low temperature. With the degree of interlock weakened, the coarse aggregate was not touching each other as the fine aggregate pushed for more "space" within the asphalt mixtures. In this instance, fine aggregate and asphalt binder mainly played a role in resistance cracking at low temperature. Because the fine aggregate and asphalt mastic were the same in gradation C2, JZ, C3, C4, the low temperature performance was in the same level.

Changing fine aggregate distribution affected the performance of low temperature shown in Table 7. At a 95% confidential level, low temperature performance in gradation X1 was worse, and it was better than standard gradation in gradation X4.

As shown in Fig. 5-(b), with the fine aggregate distribution fining, the degree of aggregate interlock enhances, and stone-to-stone contact is gradually initialed. When the coarse aggregate was not touching each other, fine aggregate and asphalt binder played a role in resisting cracking.

Table 7. Rank sum test of fine aggregate fluctuation to the influence on low temperature performance.

ξ	JZ	T	R ₁	T ₁	T ₂	Change significantly, yes or no ($\alpha = 0.05$)
JZ	X1	X1	3	3	11	Yes, worse
JZ	X2	JZ	19	13	27	No
JZ	X3	JZ	17	14	30	No
JZ	X4	JZ	13	13	27	Yes, better

Table 8. The degree of interlock verse bending strain energy density of asphalt mixtures.

Gradation name	Bending strain energy density (KJ/m ³)	VCA _{DLC} (%)	VCA _{mix} (%)	Skeleton structure yes or no
C1	7.81	48.9	48.9	Yes
X4	7.11	48.5	48.3	Yes
X3	5.93	48.5	49.0	No
C3	5.80	48.3	49.9	No
X2	5.78	48.5	50.5	No
JZ	5.55	48.5	49.1	No
C2	5.17	48.4	49.6	No
C4	4.61	48.2	50.0	No
X1	3.61	48.5	51.6	No

Table 9. Aggregate grading's fluctuating range to meet low temperature cracking resistance.

Component	Fluctuating range to meet low temperature performance (%)
Coarse aggregate	[-6, +6]
Fine aggregate	[-2, +5]

The increase in large size particles within the fine aggregate led to the loss of internal resistance in explaining the decrease of low temperature performance with the fine aggregate roughening. For gradation X4, the skeleton structure was formed. The packing aggregate instead of asphalt played a role in relaxing the stress accumulated in asphalt pavement.

4.4 Aggregate grading's fluctuating range to meet asphalt mixtures low temperature performance

From the perspective of the degree of aggregate interlock in asphalt mixtures, it showed the fluctuation of aggregate grading affected low temperature performance significantly. With the stone-to-stone contact developed, the mixture had a high energy to resist contract and deformation at low temperature. The properties of fine aggregate and asphalt played an important part in resisting low temperature cracking in floating structure. But it provided lower energy to resist low temperature cracking compared to the skeleton structure.

Based on the research above, the gradation's fluctuating range to meet asphalt mixtures low temperature cracking resistance was put forward.

5 CONCLUSIONS

From the perspective of the degree of aggregate interlock in asphalt mixtures, the fluctuation of aggregate grading to the influence on the low temperature performance was evaluated by performing

mechanical tests on the asphalt mixtures and the coarse portion of the aggregate blend. At a 95% confidential level, the accepted fluctuating range of gradation meeting low temperature cracking resistance is proposed. Based on the study, the following conclusions can be drawn:

- Aggregate grading had a significant influence on the degree of aggregate interlock in the asphalt mixtures. The fine aggregate distribution fining cocuded to the enhance of the degree of aggregate interlock. In coarse aggregate, the more large size particles were, the easier stone-to-stone contact was formed.
- A trend was existed in the low temperature performance changing with the gradation's fluctuation. With coarse aggregate distribution fining, bending strain energy density decreased. With fine aggregate distribution fining, bending strain energy density increased.
- The variation of the aggregate grading affected the low temperature performance significantly. This was confirmed by rank sum test results.
- Taken collectively together, there seemed to be a positive correlation between the degree of aggregate interlock in asphalt mixtures and the low temperature performance.

ACKNOWLEDGMENT

The authors are grateful to the reviewers for their helpful comments and suggestions on improving this paper.

REFERENCES

- Easa, S.M., Shalaby, A., Halim, 1996. A.O.A. RELIABILITY-BASED MODEL FOR PREDICTING PAVEMENT THERMAL CRACKING. *JOURNAL OF TRANSPORTATION ENGINEERING* 5: 374–380
- Hao, P.W., Zhang, D.L., Hu, X.N. 2000. Evaluation method for low temperature anti-cracking performance of asphalt mixture. *Journal of Xi'an Highway University* 20: 1–5
- Huang, B., G. Li, L.N. Mohammad 2003. Analytical modeling and experimental study of tensile strength of asphalt concrete composite at low temperatures. *Composites Part B: engineering* 34: 705–714
- Kanerva, H.K. 1993. Prediction of Low Temperature Cracking of Asphalt Concrete Mixture with Thermal Stress Restrained Specimen Test Results. *Dissertation for the Doctor degree in Engineering Oregon State University*: 1–10
- Miller, J.D., Hatsuo, I., Frans, HUM 1989. Interfacial role and properties in model composites: fracture surfaces by scanning electron microscope. *J Mater Sci* 24: 2555–2570
- Mobasher, B., M.S. Mamlouk, Lin, H.M. 1997. EVALUATION OF CRACK PROPAGATION PROPERTIES OF ASPHALT MIXTURES. *JOURNAL OF TRANSPORTATION ENGINEERING* 5: 405–413
- Qiu, Y.F., Lum, K.M. 2006. Design and Performance of Stone Mastic Asphalt. *JOURNAL OF TRANSPORTATION ENGINEERING* 10: 956–963
- Vinson, T.S., Janoo, V.C., Hass, R.C.G. 1989. Low Temperature and Thermal Fatigue Cracking. SHRP-A-306. Washington, DC: National Research Council
- Shen, A.Q., Jiang, Q.H. 2004. Influence factor and appraising on anti-cracking of asphalt mixture at low temperature. *Journal of Chang'an University (Nature Science Edition)* 9: 1–6
- Sun, H. 2006. *Applied mathematical statistics*. Beijing: TSINGHUA UNIVERSITY PRESS.
- Tsangris, G.M. Kouloumbi, N., Kyvelidis, S. 1996. Interfacial relaxation phenomena in particulate composites of epoxy resin with copper or iron particles. *Mater Chem Phys* 44: 245–250
- Vavrik, W.R. 2002. *Bailey Method for Gradation Selection in Hot-Mix Asphalt Mixture Design*. Washington, DC: TRANSPORTATION RESEARCH BOARD OF THE NATIONAL ACADEMIES.
- Vratsanos, L., Farris, R.J. 1993. A predictive model for the mechanical behaviour of particular composites. Part II: Comparison to literature data. *Polym Engng Sci* 33: 1458–1465
- Wu K.H. 1995. Volume Method for Bituminous Mixture Design. *Dissertation for the Master Degree in Engineering. Harbin Institute of Technology*
- Yang, C.C., Hung, R. 1996. A two-phase model for predicting the compressive strength of concrete. *Cem Concr Res* 26: 1567–1577
- Yu, B.X. 2005. *How to build the asphalt pavement*. Beijing: China Communications Press

Discrete element modelling of low temperature monotonic compression tests in an idealised asphalt mixture

J. Wu & A. Collop

Nottingham Transportation Engineering Centre, University of Nottingham, Nottingham, UK

G. McDowell

Nottingham Centre for Geomechanics, University of Nottingham, Nottingham, UK

ABSTRACT: The Discrete Element Method (DEM) has been used to simulate results from monotonic compression tests on an idealised asphalt mixture containing approximately single-sized sand particles conducted in the elastic regime of behaviour. A numerical sample preparation procedure is presented to ensure that the numerical specimen is representative of the physical specimen and bond breakage between adjacent particles has been used to simulate post-peak (softening) behaviour. It has been found that the maximum rate of bond breakage corresponds to the peak stress (compressive strength) and that approximately 6000 particles are required for reasonably accurate estimates of bulk material properties such as compressive strength. A range of simulations has been undertaken using PFC-3D to investigate the effect of random variations in internal sample geometry, the distribution of bond strengths between adjacent particles and the coefficient of friction between particles where the bond has broken on the stress-strain behaviour. It has been found that the random effect of particle position on predicted compressive strength is not significant compared to variability in bond strength and the friction coefficient. For example, a bond strength distribution with a Coefficient of Variation (CoV) of 50% reduces the compressive strength by approximately 30% and increasing the friction coefficient from 0 to 0.5 increases the compressive strength by approximately 25% for simulations containing 6000 particles. Predicted results have been compared to experimental data and qualitatively good agreement has been obtained up to a strain level of approximately 2%.

Keywords: DEM, Idealised Asphalt, Compressive Strength, Bond breakage.

1 INTRODUCTION

Asphalt is a complex multi-phase material comprising bitumen, graded mineral aggregate and air. A range of asphalt types and compositions can be produced depending on the types and proportions of these components, and on the aggregate grading. A typical continuously graded mixture (e.g. asphalt concrete) relies on an interlocking aggregate skeleton for its strength with binder primarily acting as a lubricant to aid compaction and “glue” the mixture together. At the other extreme, a typical gap-graded mixture (e.g. stone mastic asphalt) will have a discontinuous aggregate grading (i.e. some stone sizes will not be present) and relies on a coarse aggregate skeleton bound by a bitumen/filler “mortar” for its strength. It has been shown that for both asphalt mixture types the micromechanical behaviour, at the scale of an aggregate particle, is an important factor in terms of overall material performance (Collop *et al.*, 2006).

The traditional approach to modelling asphaltic materials is to treat them at the macro-scale using continuum-based models (Collop *et al.*, 2004; Blaauwendraad & Scarpas, 2000; Erkens

et al., 2002). This usually involves undertaking careful experiments over a range of conditions (e.g. stress levels, loading rates, temperatures etc), measuring the macroscopic response of the material and fitting continuum-based constitutive models (which can be extremely complex) to the measured behaviour. The micromechanical behaviour of the mixture is not explicitly included in this approach which means that it is not easy to relate observed behaviour to the micromechanics of the material.

In this paper, the Discrete Element Method (DEM) has been utilised to simulate the monotonic compressive behaviour (pre and post-peak) of an idealised asphalt mixture in the elastic regime of behaviour (low temperature, high strain rate).

2 DISCRETE ELEMENT METHOD

The Discrete Element Method (DEM) for modelling movement and interaction of assemblies of rigid particles was originally developed by Cundall & Strack (1979). The computer program, Particle Flow Code in 3D (PFC3D), was used in this paper. This program permits the incorporation of user-defined contact models and bonding of particles. The particles displace independently and only interact at the contacting points through finite contact stiffness. PFC3D uses the so called “soft contact approach” whereby the particles are assumed to be rigid (non-deformable) but can overlap at contact points allowing deformation. The magnitude of overlap is related to the contact force via a force-displacement law. The mechanical behaviour of the system is described in terms of movement of discrete particles and inter-particle forces, which are controlled by Newton’s 2nd law of motion.

The constitutive model used in PFC3D comprises three parts: (i) a linear contact model, (ii) a bonding model and (iii) a friction slip model. The linear contact model is described in terms of a normal secant stiffness (K^n) and a shear tangent contact stiffness (K^s) of the two contacting entities (either wall-particle or particle-particle) acting in series. PFC3D allows particles to be bonded together at contacts. If the magnitude of the tensile normal contact force equals or exceeds the normal contact bond strength, the bond breaks, and both the normal and shear contact forces are set to zero. If the magnitude of the shear contact force equals or exceeds the shear contact bond strength, the bond breaks and the slip model is activated provided the normal force is compressive. The slip model is defined by a friction coefficient at the contact point according to the Coulomb friction law. Elastic shear displacements can be sustained until the shear force is equal to the coefficient of friction times the normal compressive force, at which point slip occurs.

Typical parameters which have to be defined in PFC-3D are the normal and shear particle stiffness K^n , K^s , the normal and shear bond strengths B^n , B^s and the coefficient of friction μ between particles. A full description of PFC3D can be found in (ITASCA 2003) and will not be detailed here for brevity.

Although the DEM has been applied to model the behaviour of soils and granular materials (Cundall & Strack, 1979; Robertson, 2000; McDowell & Harireche, 2002; McDowell & Harireche, 2002b, Ullidtz 2003), it has not been widely used to investigate the mechanical behaviour of asphaltic materials. Rothenburg & Bathurst (1992) modelled asphalt as a set of plane (two-dimensional) elastic angular particles separated by a viscoelastic bitumen. Simulations showed that the peak unconfined compressive strength was obtained when the proportion of cohesive contacts was approximately 60% and the proportion of frictional contacts was approximately 40%. Simulations of creep tests showed that the steady-state properties were largely controlled by the proportion of frictional inter-granular contacts compared to the proportion of cohesive contacts. However, the simulations were two-dimensional and no calibration with laboratory data was given.

Buttlar & You (2000) used DEM to develop a two-dimensional model of an indirect tensile (IDT) test comprising 130 cylindrical stones (12.5 mm in diameter) arranged in a hexagonal packing structure glued together with asphalt mastic. They validated predictions with experimental data (for the same idealised mixture) obtaining good agreement. Buttlar & You (2000) extended this approach to develop a two-dimensional IDT model of Stone Mastic Asphalt (SMA) using a microfabric DEM

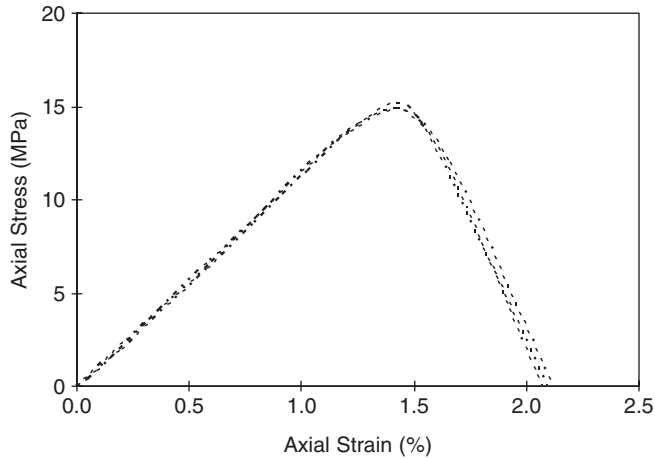


Figure 1. Experimental axial stress-strain results.

approach whereby the various material phases are modelled as clusters of discrete elements. The aggregate structure was captured using a high-resolution optical scanner. Predicted horizontal displacements were approximately 40% greater than measurements which was attributed to the two-dimensional microstructural representation underestimating the actual amount of aggregate interlock.

3 UNIAXIAL COMPRESSION TESTS

3.1 Specimen preparation

A type of idealised asphalt containing approximately single-sized sand mixed with bitumen was chosen because its packing characteristics are well understood (dense random packing) and because the mixture is dominated by the bitumen, whilst the complex aggregate interlock effects are minimised (Deshpande, 1997). It was designed to have the following volumetric proportions; 70% sand, 20% bitumen and 10% air voids and a 40/60 penetration grade bitumen with a softening point of 53.5°C was used. The sand was relatively single-sized with particles between 1.18 mm to 2.36 mm in diameter.

A cylindrical split mould, 75 mm in diameter and 150 mm in height, was used to cast the specimen and a vibrating Kango hammer compactor was used for specimen compaction. The specimen was compacted to an initial height of approximately 120 mm and then trimmed to give a final height of 100 mm. The specimen was compacted from only one side into a single layer and care was taken to insure that the top surface of specimen was flat and smooth. After compaction, the specimen was allowed to cool to room temperature for at least 12 hours. The mould was then opened carefully to avoid any surface damage and the geometry and density of the specimen were measured before being stored in a cold room at 5°C.

A friction reduction system between the specimen ends and the loading platens was used to minimise any end confining effects. This comprised a plastic film, 50 µm in thickness ('Lufflexen') which was coated with a liquid soap ('Zalpon').

3.2 Test protocol & results

Uniaxial compression tests were performed at a constant loading velocity of 0.01 m/s and a test temperature of -20°C. These conditions were chosen to minimise viscoelastic effects so that the response was primarily in the elastic region of behaviour thus simplifying the simulations. In total, three tests were undertaken and the results are shown in Figure 1 where axial stress is plotted against

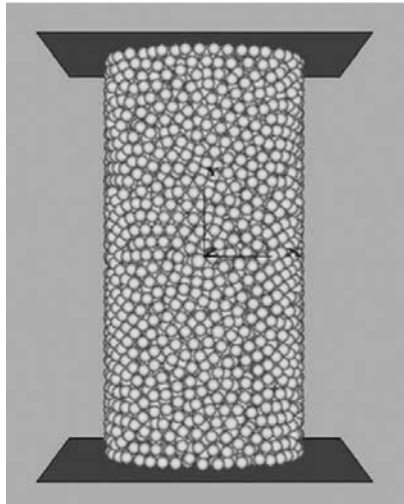


Figure 2. Numerical sample with 6000 particles prepared for uniaxial simulation.

axial strain. It can be seen from this figure that the curves can be divided into three regions. In the early stages of the test, the stress increases approximately in proportion to the strain (i.e. linear behaviour). There is then a small region of hardening where the slope of the stress-strain curve decreases as the peak stress (compressive strength) is approached. After the peak, the material then softens and the stress decreases rapidly as failure occurs. It can also be seen from Figure 1 that repeatability is quite good between the three individual test results.

4 NUMERICAL SAMPLE PREPARATION

Since the objective of this paper was to model results from the uniaxial compression testing, it was necessary to generate an artificial specimen to replicate the idealised asphalt mixture. It was important to ensure that the sample was initially isotropic and densely packed (i.e. similar to the laboratory prepared specimen). Therefore, a numerical sample preparation procedure has been developed to prepare cylindrical samples of known dimensions containing single-sized particles of known radius. The procedure of numerical sample generation is described in the following steps:

- 1) The approximate number of particles required to fill the pre-set volume of sample was calculated.
- 2) The walls (i.e. ‘platen’ or ‘boundary’ in the programme) were generated to enclose a predefined volume and the particles were generated with a small initial radius.
- 3) The radii were then increased and the sample was allowed to “settle” until the stresses within the sample were approximately isotropic.
- 4) The radii of particles were reduced slightly (typically by 3%) to reduce the isotropic stress (i.e. less than 1 kPa).
- 5) Particles with less than four contacts were identified (typically 5% to 8% of the total number of particles) and were expanded slightly (typically by 1%) to create additional contacts with neighbouring particles.
- 6) Normal and shear contact bonds were applied to each contact point.
- 7) The cylindrical confining wall was removed and the sample was ready for uniaxial testing.

Figure 2 shows a sample containing 6000 particles, 1.77 mm in diameter. The numerical sample was densely packed with the particles occupying 63.5% of the total volume with an average 5.8 contacts per particle (co-ordination number).

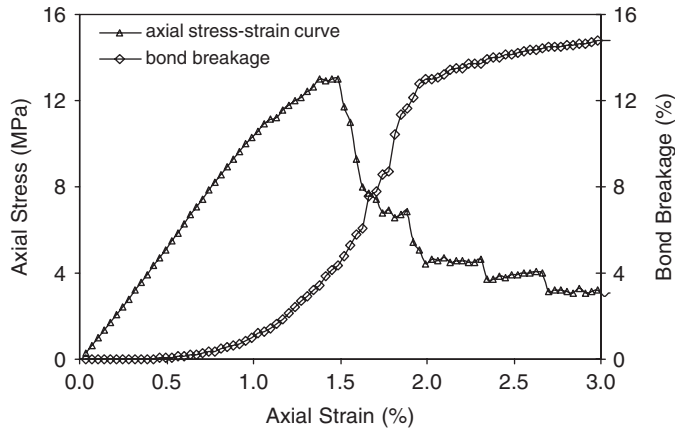


Figure 3. A typical simulation result of axial stress-strain response.

5 BOND BREAKAGE

In the numerical simulations, post-peak (softening) behaviour has been simulated by allowing bond breakage when either normal or shear stress between contacting particles exceeds the normal or shear bond strength. Bond breakage is calculated during each time step of the simulation. A typical simulation result is shown in Figure 3 where axial stress and percentage bonds broken are plotted against axial strain.

In this simulation, the shear and normal contact stiffnesses were taken to be 1.2 MPa and 12 MPa respectively, the normal and shear bond strengths were taken to be 10 MPa and the friction coefficient between contacting particles where the bond has broken was taken to be 0.5. Note that, although these values have been chosen arbitrarily to give sensible predictions, the factor of 10 between the shear and normal contact stiffness was chosen to ensure an appropriate value of Poisson's ratio (see (Collop *et al.*, 2006) for further details). The axial strain was calculated from the displacement of the top loading platen (the bottom platen was fixed) and the axial stress was calculated from the contact forces between the particles in contact with the loading platens. It can be seen from this figure that the general shape of the predicted stress-strain curve (triangle symbols) is qualitatively similar to the experimental results (Figure 1) both in the pre-peak and post-peak regions of behaviour. It can be seen from Figure 3 that bond breakage (diamond symbols) increases progressively from about 0.5% axial strain with the greatest rate of bond breakage coinciding with the peak stress (compressive strength).

6 EFFECT OF NUMBER AND POSITIONS OF PARTICLES

Since the numerical sample was generated by bonding individual particles together to form a pre-defined shape, it was necessary to determine the minimum number of particles (sample size) so that any bulk properties determined from the simulation (e.g. compressive strength) do not depend on the sample size. Therefore, simulations were performed on samples with different numbers of particles. The same values of parameters were used as above and a loading rate of 0.01 m/s was chosen to match the experimental conditions. Note that since the simulations are elastic in nature, a faster loading rate could be used to reduce the run time. However, it was found that loading rates significantly faster than 0.01 m/s resulted in dynamic (wave propagation) effects.

Figure 4 shows the effect of the number of particles on the predicted compressive stress-strain behaviour. It can also be seen from this figure that the curves for 6000 and 12000 particles are

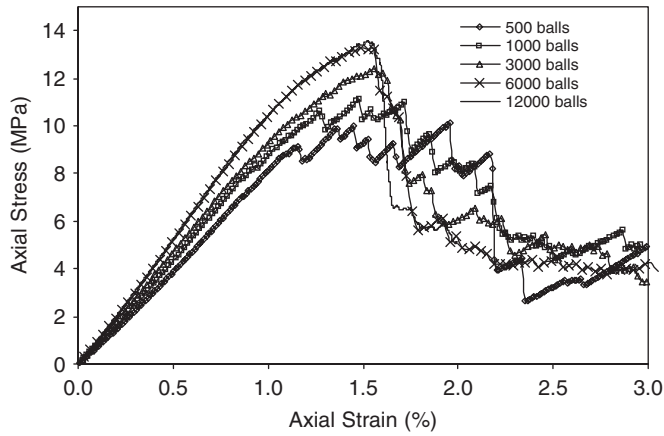


Figure 4. Effect of number of particles on axial stress-strain response.

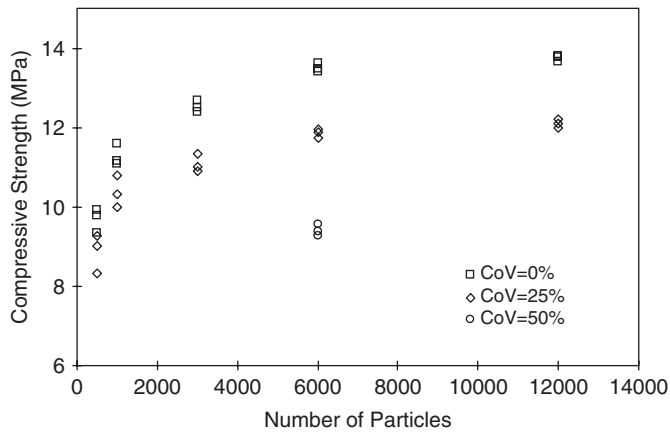


Figure 5. Effect of sample geometry and bond strength variations on compressive strength.

reasonably close together indicating that at least 6000 particles are required in the simulations to obtain reasonable estimates of bulk properties such as compressive strength.

In Figure 5 the compressive strength (peak stress) is plotted as a function of number of particles (square symbols). Since the placement of particles in the numerical specimen is essentially random, for each number of particles, three separate simulations have been performed with the particles in different random positions. It can be seen from Figure 5 that the general trend is for the compressive strength to increase with an increasing number of particles up to approximately 6000 particles. It can also be seen that the variability caused by the random positions of the particles reduces as the number of particles is increased and the effect for 6000 and 12000 particles is small.

7 BOND STRENGTH DISTRIBUTION

In the previous sections, a single value of bond strength has been assumed between contacting particles. However, in reality there is likely to be some variation in bond strength and the objective of this section is to investigate the importance of this variability. The above simulations were repeated

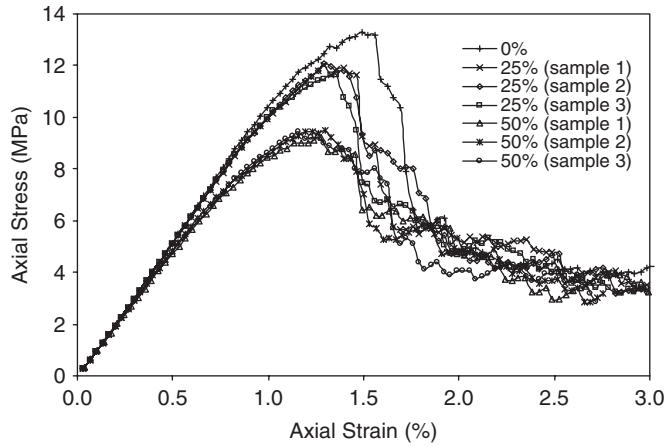


Figure 6. Effect of bond strength distribution on axial stress-strain response.

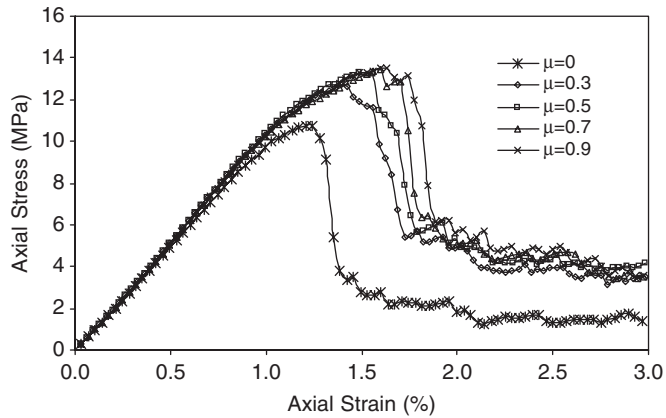


Figure 7. Effect of friction coefficient on axial stress-strain curve.

with identical particle geometries but different Gaussian (normal) bond strength distributions with CoVs of 25% and 50% respectively.

The results have been plotted in Figure 6 where it can be seen that the compressive strength and the strain at the compressive strength reduce as the variability in bond strength increases. This effect can be clearly seen in Figure 5 where the compressive strengths are also plotted versus the number of particles in the specimens. For example, it can be seen that for 6000 particles, increasing the CoV from 0% (single value of bond strength) to 50% reduces the compressive strength by approximately 30%.

8 EFFECT OF INTER-PARTICLE FRICTION

Five numerical samples, each containing 6000 particles, were generated with the same particle geometry and bond strength distributions but different friction coefficients ranging from 0 to 0.9 invoked when the shear contact bond between adjacent particles is broken.

The resulting stress-strain curves are shown in Figure 7 where it can be seen that the compressive strength increases as the friction coefficient is increased up to a value of 0.5 after which it remains

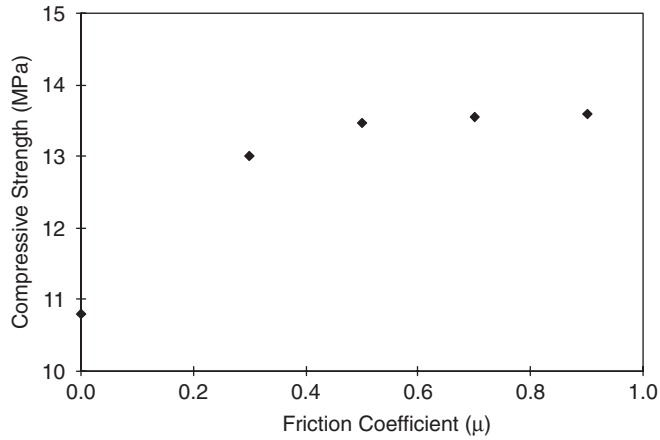


Figure 8. Effect of friction coefficient on compressive strength in axial stress-strain response.

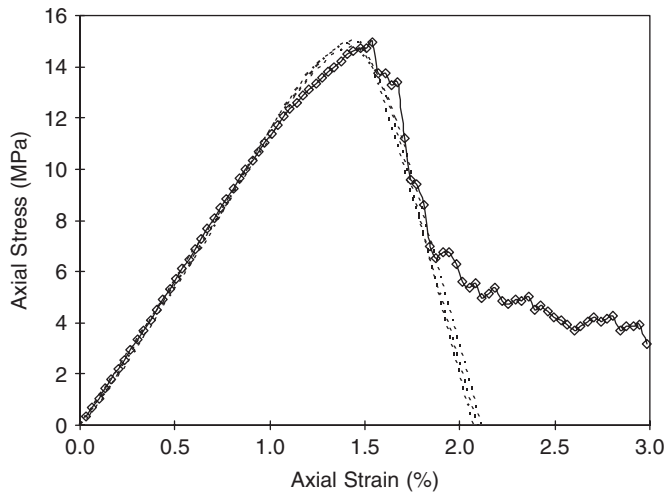


Figure 9. Data comparison between simulation and experiments.

approximately constant. This is shown in Figure 8 where the compressive strength is plotted against the friction coefficient.

9 COMPARISON WITH EXPERIMENTAL RESULTS

Figure 9 shows a comparison between predicted results and experimental results. The simulation contained 6000 particles, the shear and normal contact stiffnesses were taken to be 1.2 MPa and 12 MPa, respectively and the average value of normal and shear bond strengths was taken to be 12 MPa with a CoV of 25% and a friction coefficient of 0.5 between particles where the bond is broken. Note that these properties were chosen arbitrarily so that the predicted stress-strain curve matched the experimental curve. It can be seen from this Figure 9 that the general shape of the predicted curve (diamond symbols) is qualitatively similar to the experimental results up to a strain level of approximately 2% after which the predicted stress-strain curve flattens out significantly.

10 CONCLUSIONS

- 1) DEM has been utilised to simulate the monotonic compressive behaviour of an idealised asphalt mixture in the elastic region of behaviour.
- 2) A sample preparation procedure has been developed to ensure that the numerical sample is initially dense and isotropic.
- 3) Post peak (softening) behaviour was simulated by allowing bond breakage between adjacent particles. Results showed that the maximum rate of bond breakage occurred at the peak stress (compressive strength).
- 4) It was found that approximately 6000 particles are required for reasonably accurate estimates of bulk material properties such as compressive strength.
- 5) It was found that the random effect of particle position on predicted compressive strength is not significant compared to variability in bond strength and the friction coefficient. For example, a bond strength distribution with a Coefficient of Variation (CoV) of 50% reduces the compressive strength by approximately 30% and increasing the friction coefficient from 0 to 0.5 increases the compressive strength by approximately 25% for simulations containing 6000 particles.
- 6) The overall shape of the predicted stress-strain curve from the DEM approach showed a good agreement with the experimental results up to a strain of approximately 2%.

REFERENCES

- Itasca Consulting Group Inc. 2003. *Particle Flow Code in 3 Dimensions- PFC3D Series*. Minnesota, USA.
- Blaauwendraad, J. and Scarpas, A., 2000, '3D Finite element simulation of damage in asphalt concrete pavement' In: MCCI '2000 - International Symposium on Modern Concrete Composites & Infrastructures, Beijing, China, 2000, Vol. I, pp. 11–16.
- Buttlar, W.G. and You, Z., 2000 'Discrete Element Modeling of Asphalt Concrete: A Micro-Fabric Approach,' Transportation Research Record, No. 1757, National Research Council, National Academy Press, Washington, D.C., pp. 111–118.
- Collop, A.C., Scarpas, A., Kasbergen, C. & de Bondt, A. 2004. Development and finite element implementation of a stress dependent elastic-visco-plastic constitutive model with damage for asphalt. *Transportation Research Record* 1832: 96–104.
- Collop, A.C., McDowell, G.R. & Lee, Y. 2006. Modelling dilation in idealised asphalt mixture using discrete element modelling. *Journal of Granular Matter* 8: 3–4.
- Cundall, P. A. & Strack, O. D. L. 1979. A discrete numerical model for granular assemblies. *Géotechnique* 29: 47–65.
- Deshpande, V.S., 1997, 'Steady-state deformation behaviour of bituminous mixes', PhD Thesis, Engineering Department, University of Cambridge.
- Erkens, S.M.J.G., Liu, X., Scarpas, A., Molenaar, A.A.A. and Blaauwendraad, J., 2002, 'Asphalt concrete response: experimental determination and finite element implementation.' Proc. 9th International Conference on Asphalt Pavements, Copenhagen.
- McDowell, G.R. and Harireche, O., 2002a, 'Discrete element modelling of yielding and normal compression of sand.' *Géotechnique* 52, No. 4, 299–304.
- McDowell, G.R. and Harireche, O., 2002b, 'Discrete element modelling of soil particle fracture.' *Géotechnique* 52, No. 2, 131–135.
- Robertson, D., 2000, 'Numerical simulations of crushable aggregates.' Ph.D. dissertation, University of Cambridge.
- Rothernburg, L. and Bathurst, R.J., 1992, 'Micromechanical features of granular assemblies with planar elliptical particles.' *Geotechnique*, 42(1), pp. 79–95.
- Ullidtz, P. 2003, 'Analytical tools for design of flexible pavements.' Keynote Address, Proc. 9th International Conference on Asphalt Pavements, Vol. III, pp. 22–37, Copenhagen, Denmark.

Investigation of low temperature cracking in asphalt mixtures using TSRST

R. Velásquez, M. Turos & M. Marasteanu

University of Minnesota, Minneapolis, Minnesota, USA

N. Gibson

FHWA Turner-Fairbank Highway Research Center, Washington D.C., USA

T. Clyne

Minnesota Department of Transportation, MnROAD, USA

ABSTRACT: In this paper the factors affecting asphalt pavements low temperature cracking are investigated by means of the Thermal Stress Restrained Specimen Test (TSRST). Asphalt mixtures slabs cut from field pavement sections as well as slabs produced in the laboratory, were used to study the influence of binder type, aggregate type, air void content, cooling rate and specimen geometry on the fracture strength and fracture temperature. For the laboratory mixtures, two levels of air void content: 4% and 7%, two levels of binder content: the design value and the design value plus 0.5% and two types of aggregates: limestone and granite were used to prepare the laboratory mixtures. It was found that mixtures with 4% of air void content are less prone to low temperature cracking than mixtures with 7% air void, and that, on average the granite mixtures performed slightly better than the limestone mixtures. A preliminary investigation of the feasibility of using acoustic emission monitoring during TSRST testing was performed including microcracks localization and acoustic events counting.

1 INTRODUCTION

Low temperature cracking is considered to be the critical distress in pavements built in cold climates. The current low temperature specifications rely on mixture properties obtained in the IDT creep and strength tests. However, from a phenomenological point of view, the TSRST method appears to be the closest in simulating single event thermal cracking.

The TSRST system developed under SHRP A-400 contract by Jung and Vinson (1994), is an automated closed loop system which measures the tensile stress in an asphalt concrete specimen as it is cooled at a constant rate. As the temperature drops, the specimen is restrained from contracting thus inducing tensile stresses. The fracture strength and the fracture temperature are measured as part of the TSRST test. This test method has been extensively used in the past to investigate the low temperature properties of asphalt mixtures. Research performed by Monismith *et al* (1965), Arand (1990) and Vinson *et al.* (1994) among others showed that TSRST can be used to evaluate the susceptibility of asphalt mixtures to low temperature cracking.

In this paper twenty eight laboratory prepared mixtures and twenty specimens cut from field sections were tested as part of this comprehensive study on low temperature properties of asphalt materials. For the laboratory mixtures, two levels of air void content, 4% and 7% representing the design value and typical construction values, respectively, were chosen to study the effect of air voids on fracture resistance. Two levels of binder content, the design value and the design value

Table 1. Field samples description.

ID	PG binder	Location
WI US 45	58-34	Wisconsin
MnROAD 03	58-28	MnROAD
MnROAD 19	64-22	MnROAD
MnROAD 33	58-28	MnROAD
MnROAD 34	58-34	MnROAD
MnROAD 35	58-40	MnROAD

plus 0.5%, were used to quantify the effect of asphalt content on the resistance to low temperature cracking. Two types of aggregate with different mechanical and physical properties, limestone and granite, were used to prepare the laboratory mixtures.

2 MATERIALS

A total of 76 specimens were tested in the TSRST system; 20 field specimens and 56 laboratory specimens (two replicates per mixture). The test matrix for this study contains a combination of factors expected to have a significant effect on the low temperature fracture resistance of asphalt concrete. The field specimens were obtained from two different locations: US-45 in Wisconsin and five different cells in MnROAD. The slabs were sawed into prismatic specimens with the following dimensions: 50 ± 5 mm (2.0 ± 0.15 in.) square and 250 ± 5 mm (10.0 ± 0.25 in.) in length. The asphalt binder and location of each slab is presented in Table 1.

Table 2 shows the 28 laboratory mixtures tested. Ten different asphalt binders, both plain and modified that cover six different performance grades were selected. Two aggregates, granite and limestone were selected. Two levels of asphalt binder content, the optimum value and the optimum value plus 0.5% (e.g. bump), were used. Two levels of air void content were select based on typical values for design and construction.

The laboratory prepared slabs were sawed in to prismatic specimens with the following dimensions: 50 ± 5 mm (2.0 ± 0.15 in.) square and 250 ± 5 mm (10.0 ± 0.25 in.) in length. Mixture 58-28:U1:7:LM was not available for testing during the TSRST program and slab 64-22:U1:4:LM was severely cracked before cutting.

3 RESULTS AND DISCUSSION

All tests were performed using a cooling rate of 10°C/hr and following the test procedure described by Jung and Vinson (1994). Additional testing was done to investigate the effect of shape, size and cooling rate on the fracture properties of the mixtures. Figure 1 shows a typical result from TSRST test. As the temperature inside the chamber is dropped at a constant rate, the thermally induced tensile stresses increases until fracture occurs.

The slope of the curve (dS/dT) shown in Figure 1 slowly increases until reaches its maximum value at the transition temperature. After this temperature, dS/dT is constant and the stress temperature curve becomes linear until the specimen fails. The tensile stress and the temperature at the break point are the fracture strength and the fracture temperature, respectively.

3.1 Field specimens

Fracture temperature, fracture strength, transition temperature, dS/dT , specific gravity and absorption of the field specimens are presented in Table 3. Additionally, Figure 2 shows the fracture temperature of the field specimens.

Table 2. Laboratory mixtures description.

ID	PG binder	Description	Aggregate	Binder content	Target Air voids
58-40:M1:4:GR	58-40	SBS	Granite	opt	4%
58-40:M1:4:GR:+0.5AC	58-40	SBS	Granite	bump	4%
58-40:M1:4:LM	58-40	SBS	Limestone	opt	4%
58-34:M1:4:GR	58-34	Elvaloy	Granite	opt	4%
58-34:M1:4:GR:+0.5AC	58-34	Elvaloy	Granite	bump	4%
58-34:M1:4:LM	58-34	Elvaloy	Limestone	opt	4%
58-34:M2:4:GR	58-34	SBS	Granite	opt	4%
58-34:M2:4:LM	58-34	SBS	Limestone	opt	4%
58-28:U1:4:GR	58-28	Unmodified 1	Granite	opt	4%
58-28:U1:4:GR:+0.5AC	58-28	Unmodified 1	Granite	bump	4%
58-28:U1:4:LM	58-28	Unmodified 1	Limestone	opt	4%
58-28:U1:4:LM:+0.5AC	58-28	Unmodified 1	Limestone	bump	4%
58-28:U1:7:GR	58-28	Unmodified 1	Granite	opt	7%
58-28:U1:7:GR:+0.5AC	58-28	Unmodified 1	Granite	bump	7%
58-28:U1:7:LM	58-28	Unmodified 1	Limestone	opt	7%
58-28:U1:7:LM:+0.5AC	58-28	Unmodified 1	Limestone	bump	7%
58-28:U2:4:GR	58-28	Unmodified 2	Granite	opt	4%
58-28:U2:4:LM	58-28	Unmodified 2	Limestone	opt	4%
64-34:M1:4:GR	64-34	Elvaloy	Granite	opt	4%
64-34:M1:4:LM	64-34	Elvaloy	Limestone	opt	4%
64-34:M2:4:GR	64-34	Black Max™	Granite	opt	4%
64-34:M2:4:LM	64-34	Black Max™	Limestone	opt	4%
64-28:U1:4:GR	64-28	Unmodified 1	Granite	opt	4%
64-28:U1:4:LM	64-28	Unmodified 1	Limestone	opt	4%
64-28:M1:4:GR	64-28	SBS	Granite	opt	4%
64-28:M1:4:LM	64-28	SBS	Limestone	opt	4%
64-22:U1:4:GR	64-22	Unmodified 1	Granite	opt	4%
64-22:U1:4:LM	64-22	Unmodified 1	Limestone	opt	4%

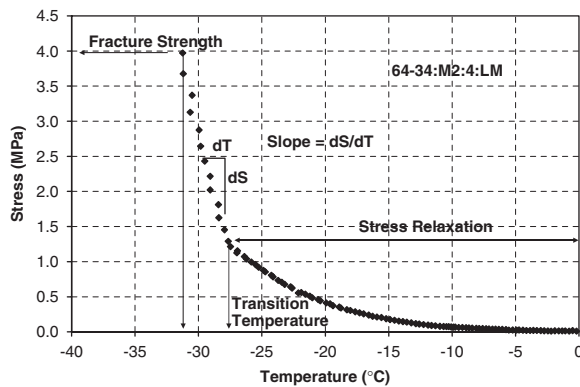


Figure 1. Typical stress-temperature curve from TSRST.

Differences between specimens in the same cell can be seen in Figure 2. For example, for MnROAD 35 there are two different fracture temperatures. The first two specimens have an average fracture temperature of -26°C while the other two (e.g. #3 and #4) have an average fracture temperature of -33.3°C .

Table 3. TSRST results for field specimens.

ID	#	PG binder	Fracture T. (°C)	Fracture Str. (MPa)	dS/dT (MPa/°C)	Trans. T. (°C)	Gs	Abs. (%)
WI US 45	1	58-34	-26.1	3.189	0.137	-10.8	2.37	0.072
WI US 45	2	58-34	-15.4	1.145	0.091	-10.0	2.36	0.086
MnROAD 03	1	58-28	-26.8	3.121	0.213	-16.2	2.39	0.058
MnROAD 03	2	58-28	-27.9	3.128	0.187	-15.6	2.37	0.045
MnROAD 19	1	64-22	-22.3	2.239	0.147	-12.6	2.28	0.048
MnROAD 19	2	64-22	-24.4	2.873	0.159	-10.0	2.29	0.061
MnROAD 19	3	64-22	-25.6	2.158	0.120	-11.0	2.30	0.073
MnROAD 19	4	64-22	-26.9	3.139	0.235	-20.2	2.33	0.060
MnROAD 33	1	58-28	-23.3	2.322	0.153	-14.6	2.35	0.079
MnROAD 33	2	58-28	-25.4	2.255	0.138	-14.8	2.36	0.089
MnROAD 33	3	58-28	-26.6	2.802	0.165	-14.6	2.38	0.087
MnROAD 33	4	58-28	-29.0	3.177	0.219	-22.3	2.36	0.069
MnROAD 34	1	58-34	-32.8	3.750	0.291	-25.9	2.35	0.049
MnROAD 34	2	58-34	-32.9	4.014	0.258	-25.2	2.37	0.078
MnROAD 34	3	58-34	-23.8	1.486	0.101	-13.6	2.38	0.039
MnROAD 34	4	58-34	-33.8	3.731	0.237	-23.9	2.36	0.049
MnROAD 35	1	58-40	-26.5	1.698	0.081	-14.8	2.37	0.083
MnROAD 35	2	58-40	-25.5	1.705	0.096	-19.6	2.37	0.052
MnROAD 35	3	58-40	-34.8	1.101	0.037	-14.8	2.36	0.046
MnROAD 35	4	58-40	-31.8	2.716	0.173	-24.2	2.37	0.071

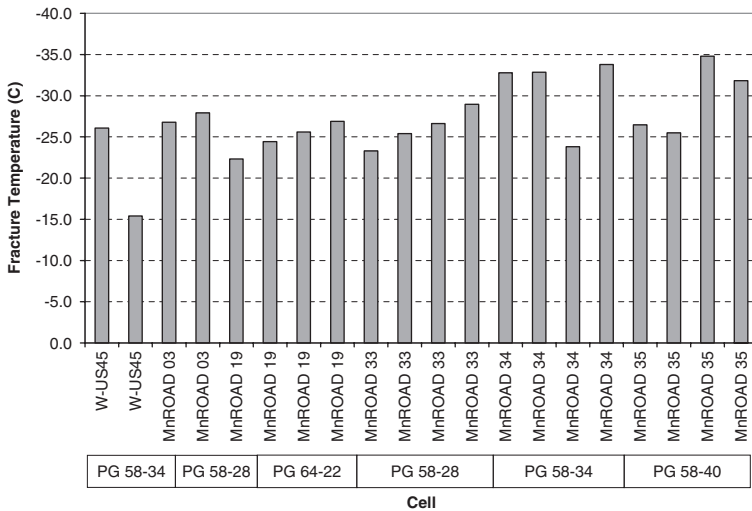


Figure 2. TSRST fracture temperature for field specimens.

The coefficient of variation for the fracture strength measurements (e.g. 33%) is significantly higher compared to the coefficient of variation for the fracture temperature (e.g. 16%). This is one of the reasons fracture temperature instead of fracture strength is used to rank the low temperature resistance of the samples. On average the best performance for low temperature cracking was MnROAD 34 with the PG 58-34 binder. The least resistant to thermal cracking was MnROAD 19 with a PG 64-22 binder as it was expected because it has the highest lower limit grade.

3.2 Laboratory specimens

Table 4 presents the results for the laboratory prepared mixtures. Fracture temperature, fracture strength, dS/dT , transition temperature, specific gravity and absorption for each specimen are shown in Table 4. The average fracture temperature for the laboratory specimens was -30.3°C . The lowest fracture temperature was -38.9°C and the highest was -25.0°C . Again the fracture strength shows more variability than the fracture temperature. The maximum and minimum fracture strength was 6.21 MPa and 1.14 MPa, respectively.

Based on the fracture temperature, on average the laboratory mixture that performed the best was 58-40:M1:4:GR:+0.5AC. The least satisfactory mixture in low temperature resistance was 64-22:U1:4:GR. As expected, the mixture containing binder with the highest lower limit grade (e.g. -22) was ranked as the lowest in thermal cracking resistance. Figure 3 shows the average fracture temperature for each laboratory prepared mixture. There is a high correlation between the lower PG grade of the asphalt binder and the resistance to low temperature of the mixture as it was expected. The best binder was PG 58-40 with the SBS modifier, followed by the PG 64-34 Elvaloy binder. Moreover for these mixtures, 4% of air void are better than 7%. The highest fracture temperatures were obtained for PG 64-22 and PG 58-28 unmodified binders. Additionally, on average the mixtures containing granite as aggregate performed slightly better than the mixture with limestone.

3.3 Statistical analysis

The correlation factors between the parameters obtained during TSRST testing for the laboratory prepared specimens were calculated. Correlation factors more than $2/n^{0.5}$ where n is the number of samples indicates high correlation between the parameters. Table 5 shows the correlation factors for the TSRST test parameters. Factors larger than 0.27 ($n = 54$) are significant and are presented in bold.

Fracture strength has a negative correlation with fracture. The lower PG grade for the binder has a positive correlation with fracture temperature. As it was expected the correlation is significant. Additionally, according to the correlation factors the fracture strength is proportional to dS/dT and the specific gravity. Thus, specimens with a higher density will break at a higher thermally induced tensile load. Moreover, the fracture strength is inversely proportional to the transition temperature, air void content and the PG-lower limit. Thus, it is recommended to use lower air void content and a lower performance grade limit to obtain a better low temperature cracking performance of the mixture. Another important observation from Table 5 is that the slope of the linear part of the stress temperature curve (e.g. dS/dT) becomes steeper as the transition temperature decreases.

4 ACOUSTIC EMISSION MONITORING

Acoustic emission monitoring has been used extensively to characterize the microscopic fracture processes and to evaluate damage growth in materials. In asphalt mixture area AE was used by several researchers to investigate the cracking mechanism: Maji *et al.* (1990), Valkering and Jongeneel (1991), Chang (1994), Wang (1995), Qin (1995), Sinha (1998), Hesp *et al.* (2001), Cordel *et al.* (2003), Li and Marasteanu (2004) and Wendling *et al.* (2004).

Recently, Li and Marasteanu (2006) used eight AE sensors to monitor the failure process during semi circular bend (SCB) testing at low temperature. Sauzéat *et al.* (2007) performed Thermal Stress Restrained Specimen Tests (TSRST) on asphalt mixtures with AE monitoring using two sensors. In this paper a preliminary evaluation of the failure process in TSRST testing was performed using eight AE sensors.

4.1 Materials and test results

Six samples from MnROAD cells 03,19,33,34 and 35 and one sample prepared in the laboratory (58-34:M1:4:LM) were monitored. The AE signals were recorded using four PCI-5112 DAQ

Table 4. TSRST results for laboratory specimens.

ID	#	Fracture T. (°C)	Fracture Str. (MPa)	dS/dT (MPa/°C)	Trans. T. (°C)	Gs	Abs. (%)
58-40:M1:4:GR	1	-31.0	4.049	0.573	-25.2	2.29	0.113
58-40:M1:4:GR	2	-36.8	4.078	0.543	-31.2	2.33	0.062
58-40:M1:4:GR:+0.5AC	1	-38.9	6.207	0.993	-34.5	2.36	0.044
58-40:M1:4:GR:+0.5AC	2	-29.6	3.557	0.829	-26.2	2.36	0.031
58-40:M1:4:LM	1	-34.8	2.959	0.322	-26.3	2.37	0.159
58-40:M1:4:LM	2	-31.7	4.012	0.673	-27.5	2.33	0.117
58-34:M1:4:GR	1	-30.9	3.005	0.393	-27.1	2.32	0.076
58-34:M1:4:GR	2	-27.9	3.200	0.397	-25.1	2.32	0.051
58-34:M1:4:GR	3	-32.8	4.323	0.303	-24.7	2.28	0.097
58-34:M1:4:GR:+0.5AC	1	-31.6	3.279	0.381	-25.1	2.32	0.085
58-34:M1:4:GR:+0.5AC	2	-28.1	2.040	0.828	-27.0	2.34	0.077
58-34:M1:4:LM	1	-31.1	3.834	0.533	-25.5	2.37	0.112
58-34:M1:4:LM	2	-34.1	3.289	0.322	-25.5	2.36	0.111
58-34:M1:4:LM	3	-32.6	2.862	0.259	-26.7	2.36	0.118
58-34:M1:4:LM	4	-26.6	2.531	1.415	-25.5	2.36	0.111
58-34:M2:4:GR	1	-27.0	3.156	1.704	-25.5	2.30	0.077
58-34:M2:4:GR	2	-34.6	2.764	0.496	-32.0	2.28	0.103
58-34:M2:4:LM	1	-32.3	3.167	0.537	-29.3	2.32	0.139
58-34:M2:4:LM	2	-25.6	1.968	0.986	-24.7	2.30	0.115
58-28:U1:4:GR	1	-28.0	2.636	0.509	-25.7	2.31	0.166
58-28:U1:4:GR	2	-31.1	2.585	0.215	-25.2	2.31	0.095
58-28:U1:4:GR:+0.5AC	1	-31.0	3.020	0.228	-23.0	2.32	0.110
58-28:U1:4:GR:+0.5AC	2	-31.8	3.271	0.224	-22.4	2.33	0.059
58-28:U1:4:LM	1	-25.5	1.136	0.410	-24.9	2.37	0.087
58-28:U1:4:LM	2	-27.3	1.818	0.236	-25.2	2.37	0.088
58-28:U1:4:LM:+0.5AC	1	-27.6	2.555	0.503	-25.9	2.38	0.087
58-28:U1:4:LM:+0.5AC	2	-28.5	2.789	0.502	-26.6	2.40	0.150
58-28:U1:7:GR	1	-34.2	2.293	0.342	-29.9	2.16	2.170
58-28:U1:7:GR	2	-31.5	2.156	0.302	-27.0	2.16	2.126
58-28:U1:7:GR:+0.5AC	1	-27.4	2.104	0.160	-20.7	2.26	0.262
58-28:U1:7:GR:+0.5AC	2	-29.4	2.550	0.293	-25.7	2.26	0.254
58-28:U1:7:LM:+0.5AC	1	-30.8	1.990	0.181	-26.0	2.24	0.570
58-28:U1:7:LM:+0.5AC	2	-27.7	1.351	0.114	-20.1	2.27	0.345
58-28:U2:4:GR	1	-32.7	3.012	0.215	-21.6	2.30	0.212
58-28:U2:4:GR	2	-31.8	2.969	0.201	-21.4	2.31	0.135
58-28:U2:4:LM	1	-26.7	1.670	0.182	-22.1	2.33	0.082
58-28:U2:4:LM	2	-26.8	1.859	0.258	-23.6	2.32	0.084
64-34:M1:4:GR	1	-30.8	3.090	0.197	-20.3	2.32	0.120
64-34:M1:4:GR	2	-26.7	3.268	1.263	-25.5	2.31	0.103
64-34:M1:4:LM	1	-32.7	2.934	0.221	-25.5	2.37	0.088
64-34:M1:4:LM	2	-33.8	3.656	0.321	-28.7	2.36	0.108
64-34:M2:4:GR	1	-26.8	3.184	1.126	-25.1	2.32	0.117
64-34:M2:4:GR	2	-34.3	2.669	0.214	-25.3	2.31	0.155
64-34:M2:4:LM	1	-31.3	3.972	0.702	-27.5	2.32	0.121
64-34:M2:4:LM	2	-33.6	2.992	0.343	-29.5	2.33	0.115
64-28:U1:4:GR	1	-31.0	2.958	0.221	-22.1	2.30	0.169
64-28:U1:4:GR	2	-30.7	3.205	0.229	-21.9	2.31	0.078
64-28:U1:4:LM	1	-28.1	2.468	0.185	-22.7	2.33	0.115
64-28:U1:4:LM	2	-27.7	2.331	0.172	-19.6	2.34	0.096
64-28:M1:4:GR	1	-31.0	3.164	0.475	-26.8	2.31	0.351
64-28:M1:4:GR	2	-29.3	3.032	0.689	-26.6	2.29	0.921
64-28:M1:4:LM	1	-28.3	2.629	0.397	-26.4	2.32	0.135
64-22:U1:4:GR	1	-26.8	2.821	0.209	-19.6	2.30	0.247
64-22:U1:4:GR	2	-25.0	3.023	0.206	-18.5	2.32	0.140

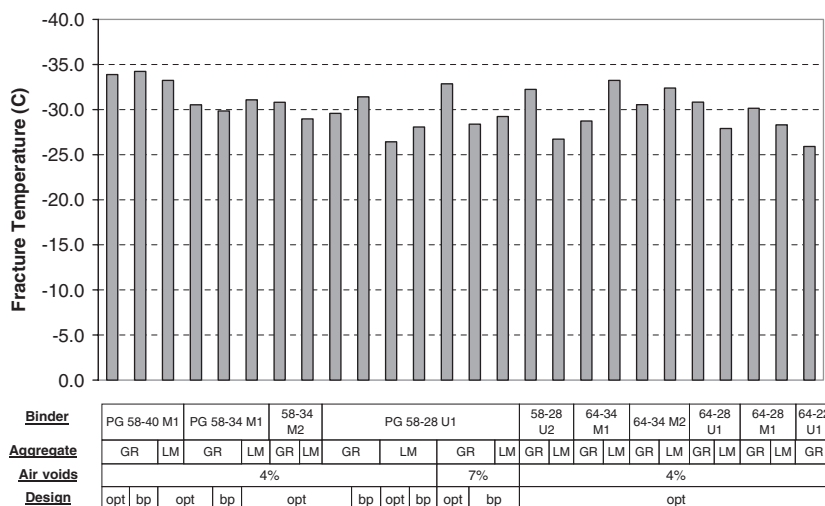


Figure 3. Average fracture temperature for laboratory specimens.

Table 5. Correlation matrix for TSRST test parameters.

Frac_T	1																						
Frac_Str	-0.600	1																					
PG-LL	0.499	-0.580	1																				
Air void	0.015	-0.367	0.276	1																			
Gs	0.050	0.214	-0.283	-0.736	1																		
Abs	-0.130	-0.220	0.254	0.644	-0.763	1																	
dS/dT	0.179	0.290	-0.463	-0.237	0.146	-0.109	1																
Trans_T	0.585	-0.418	0.580	0.039	-0.038	-0.163	-0.383	1															
	Frac_T	Frac_Str	PG-LL	Air void	Gs	Abs	dS/dT	Trans_T															

cards (National Instruments). Each card had two independent channels which acquired AE signals detected by eight piezoelectric S9225 sensors (Physical Acoustics Corporation). Two sensors were mounted on each side of the specimen using M-Bond 200. The preamplification of the AE signals was provided by eight 1220C preamplifiers with a gain of 40 dB. One of the sensors was used as a trigger and the trigger level changed between 10–14 mV for different specimens to investigate the effect of the chamber noise during testing on the acoustic events recorded. The wave velocity of the asphalt mixtures needed for the estimation of the location of the events was determined by generating an elastic wave by pencil lead (0.5 mm diameter) breakage on one of the sides of the specimens. The recorded events number for the seven specimens tested using AE was between 304 and 9650. The recorded event number changed with test sample and trigger level; the lower the trigger level the higher the number of events obtained. Plots of thermal stress and AE event count as a function of the temperature for the field specimens are shown in Figures 4–6.

It is observed that the AE event count curve and the thermal stress curve follow similar trends with respect to temperature. Significant amount of AE events are observed after the transition temperature is reached indicating that no significant damage occurs in the specimen at temperatures higher than the transition temperature. It is also noted that the accumulations of AE events is negligible for stresses lower than 20–30% of the fracture strength. This shows that very little intrinsic damage occurs in this period of loading.

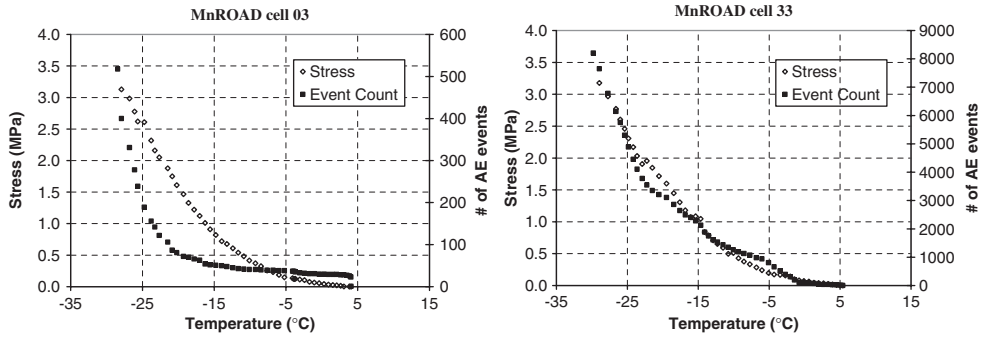


Figure 4. TSRST and acoustic emission monitoring for MnROAD cells 03 and 33.

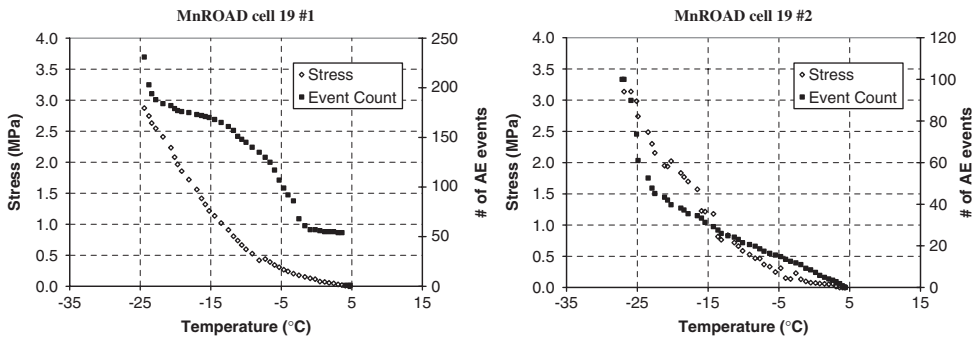


Figure 5. TSRST and acoustic emission monitoring for MnROAD cell 19.

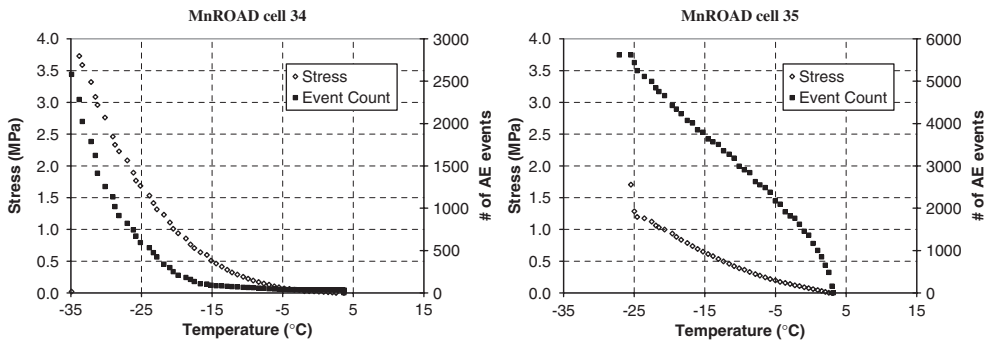


Figure 6. TSRST and acoustic emission monitoring for MnROAD cells 34 and 35.

Figure 7 shows the AE event count and location for the laboratory prepared sample.

The equations and methodology used to estimate the events location is described in detailed by Li and Marasteanu (2006).

It is observed that the AE event count curve mimic the behavior of the thermal stress curve obtained with TSRST. The recorded events are localized around the center of the specimen which corresponds to the location of the distinct fracture plane observed after completion of the test.

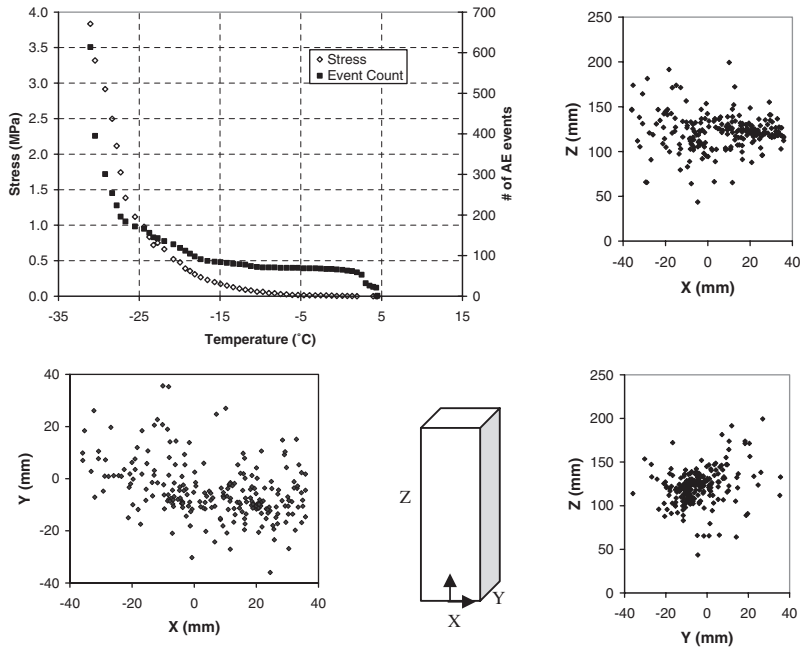


Figure 7. TSRST and acoustic emission monitoring for 58-34:M1:4:LM.

5 CONCLUSIONS AND GENERAL COMMENTS

Based on the experiments performed the following conclusions can be drawn

- As expected, the PG 58-40 mixture performed the best while the PG 58-28 and PG 64-22 mixtures performed the worst in TSRST
- Mixtures with 4% air void content performed better than mixtures with 7% air void.
- On average the granite mixtures performed slightly better than the limestone mixtures.
- For the field samples, the best performance was obtained for MnROAD cell 34 with PG 58-34 binder. MnROAD cell 19 with PG 64-22 binder was the worst performer.
- TSRST results ranking were consistent with the rankings based on asphalt binder performance grade.
- AE event count curve and thermal stress curve follow similar trends. The accumulation of AE events is negligible for stresses lower than 20-30% of the fracture strength.
- The localization of AE events is an important tool in understanding the process of fracture initiation and propagation Interpretation of the localization of AE events should be done with caution because of the limitations and assumptions of the algorithm used to estimate the location of each AE event, problems such as reflection of the stress waves at the edges of the specimens are not taken into account.

ACKNOWLEDGMENTS

This research was sponsored by Federal Highway Administration National Pooled Fund Study 776. This support is gratefully acknowledged. The results and opinions presented are those of the authors and do not necessarily reflect those of the sponsoring agencies.

REFERENCES

- Strategic Highway Research Program. SHRP-A-417. "Accelerated Performance Related Tests for Asphalt-Aggregate Mixes and Their Use in Mix Design and Analysis Systems", Washington DC, 1994.
- Jung, D.H., Vinson, T.S., Strategic Highway Research Program. SHRP A-400. "Low-Temperature Cracking: Test selection", Washington DC, 1994.
- Monismith, C. et al., "Temperature induced stresses and deformations in asphalt concrete", Proceeding of the Association of Asphalt Paving Technologist (AAPT), Vol. 34, 1965.
- Arand, W., "Behaviour of asphalt aggregate mixes at low temperatures", Proc. 4th International RILEM symposium on Mechanical Tests fro Bituminous Mixes Characterisation, Design and Quality Control, pp. 68–84, Budapest, 1990.
- Vinson, T.S., Kanerva, H.K. and Zeng, H., "Low temperature cracking: field validation of the Thermal Stress Restrained Specimen Test (TSRST)", Strategic Highway Research Program SHRP-A-401 contract A-033A, Washington DC, 1994.
- McClave, J. Sincich, Terry. Statistics. Ninth Edition. Prentice Hall. 2003.
- Maji K A., Ouyang C., and Shah P.S., "Fracture Mechanism of Quasi-brittle Materials Based on Acoustic Emission", Journal of Material Research., Vol. 5, No. 1, Jan 1990.
- Valkering, C. P., and Jongeneel, D. J., "Acoustic emission for evaluating the relative performance of asphalt mixes under thermal loading conditions", Journal of the Association of Asphalt Paving Technologists, Vol. 60, 160–187, 1991.
- Chang, W. V., Application of Acoustic Emission to Study the Cohesive and Adhesive Strength of Asphalt. Strategic Highway Research Program, Report No. SHRP-A-682, pp. 81–148, 1994.
- Wang, H.-C., Ultrasonic and acoustic emission in nondestructive evaluation of viscoelastic solids – elastomer, human cornea and asphalt. Ph.D. Thesis, University of Southern California, Chemical Engineering Department, 1995.
- Qin, X., Adhesion properties of polymeric materials. Ph.D. Thesis, University of Southern California, Chemical Engineering Department, 1995.
- Sinha, N. K., Acoustic emission is asphalt subjected to thermal cycling at low temperature. In Acoustic emission/microseismic activity in geologic structures and materials, Proceedings of the Six Conference, by Reginald Hardy, Jr., H., Pennsylvania State University, Vol. 21, pp. 109–120, 1998.
- Hesp, S. A. M., Smith B. J., and Hoare R. T., "The Effect of Filler Particle Size on Low and High Temperature Performance of Asphalt Mastics and Mixtures", Journal of the Association of Asphalt Paving Technologists. Vol. 70, pp. 492–542, 2001.
- Cordel, S., Di Benedetto, H., Malot, M., Chaverot, P., and Perraton, D., "Fissuration à basse température des enrobés bitumineux -essai de retrait thermique empêché et émission acoustique." 6th International RILEM Symposium, Performance Testing & Evaluation of Bituminous Materials (PTEB 03), Editor Partl, M., pp. 465–472, Zurich, 2003.
- Li, X., Marasteanu, M.O., "Evaluation of the Low Temperature Fracture Resistance of Asphalt Mixtures Using the Semi Circular Bend Test", Journal of the Association of Asphalt Paving Technologists, Vol. 73, pp. 401–426, 2004.
- Wendling, L., Xolin, E., Gimenez, D., Reynaud, P., de la Roche, C., Chevalier, J. and Fantozzi, G., "Characterization of Crack Propagation Bituminous Mixtures", Proceedings, the 5th RILEM International Conference: Cracking in Pavements, pp 249-256, University of Limoges, ENSIL France, May 2004.
- Li, X., Marasteanu, M. O., Investigation of Low Temperature Cracking in Asphalt Mixtures by Acoustic Emission, Road Materials and Pavement Design, Vol. 7/4, 2006, pp. 491–512.
- Sauzéat, C., Di Benedetto, H., Chaverot, P. and Gauthier, G., "Low temperature behaviour of bituminous mixes: TSRS tests and acoustic emission". Proceedings, Advanced Characterisation of Pavement and Soil Engineering Materials, pp. 1263–1272, Athens, Greece, 2007.

8. *Binder and HMA laboratory characterization
for cracking potential*

Measurement and effective evaluation of crack growth in asphalt mixtures

H.A. Khalid & I. Artamendi
University of Liverpool, UK

ABSTRACT: A cyclic semi-circular bending beam test was used to study the crack propagation characteristics of two materials: a cold emulsion asphalt and its hot mix equivalent. Linear elastic fracture mechanics principles were used in the analysis which evaluated the materials' stress intensity factor and the Paris Law constants. Two approaches were adopted in interpreting crack growth: a simple straight line method and an effective, more accurate crack path depiction. Results showed that the cold mixture crack growth rate is less sensitive to applied stress than that of the hot asphalt. Although crack growth rate was found higher with the effective interpretation method, the influence of the two methods on the Paris Law parameters for both materials was found insignificant, given the observed data scatter.

1 INTRODUCTION

Fatigue cracking of asphaltic materials is a predominant distress mode that is assessed in the laboratory in a variety of ways. Fracture mechanics tests have been increasingly used to depict crack propagation in asphalt based on linear elastic analysis. Irwin (1957) introduced the stress intensity factor, K , to uniquely define the stress field at the crack tip. In pure tension loading referred to as mode I, Paris & Erdogan (1963) found that the crack growth rate is a function of the stress intensity factor, K_I , of that loading mode. The relationship between K_I and crack growth rate is commonly known as the Paris Law.

Much interest has recently been witnessed in the semi-circular bending (SCB) test as a laboratory tool to study the resistance to crack propagation of asphalt mixtures. A European draft standard (CEN 2005) has been issued that adopts the SCB in a monotonic mode to determine the fracture toughness of notched and un-notched cylindrical specimens. The work reported in this paper aims to use a cyclic SCB test to study crack propagation properties of two materials: a cold asphalt and an equivalent hot applied mixture. It focuses on the evaluation of crack growth in the asphalt mixtures using two approaches and the impact of each approach on the resulting Paris Law parameters. The work forms part of a larger study to investigate the healing characteristics of cold asphalt and compare them to those of a conventional hot mixture.

2 MATERIALS AND SPECIMEN PREPARATION

Two asphalt mixtures were used in the study: a Cold Emulsion Asphalt Mixture (CEAM) and its Hot Mixture Equivalent (HME). A cationic emulsion was used in the CEAM comprising a 160/220 Pen bitumen on an approximately 60/40 binder/water basis and doleritic aggregates from a quarry in Scotland. The HME comprised the same aggregates and a 160/220 Pen bitumen. Furthermore, the same continuously graded, 14 mm maximum nominal size aggregate blend was used.

CEAM specimens were prepared by mixing the aggregates with the emulsion at ambient temperature to give a residual binder content of 4% by weight of the total mixture. The amount of

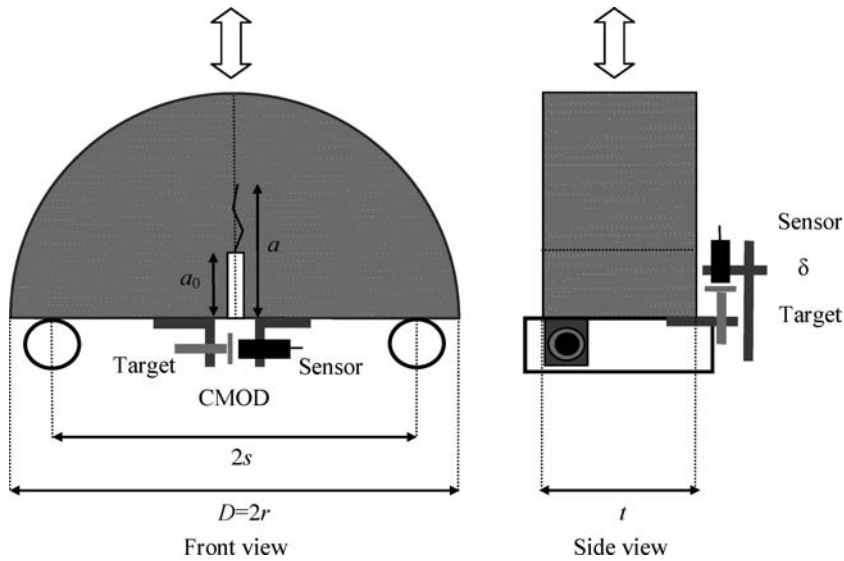


Figure 1. Schematic of the cyclic semi-circular bending beam test.

added water by total weight of mixture was 7% approximately. After mixing, the material was compacted in 153 mm diameter split cylindrical moulds to a thickness of 65 mm using a double plunger static compaction method. The moulds had a perforated base plate to allow water to escape during compaction. After extrusion from the moulds, the specimens were cured in a fan assisted oven at 35°C until no further changes in mass were observed, i.e. fully cured. Volumetric determinations on these specimens gave an average void content of 18.6%.

HME specimens, on the other hand, were prepared by mixing the same aggregates for the CEAM with the bitumen at 155°C at a binder content of 4% by weight of the total mixture. The material was then compacted to 305 × 305 × 65 mm³ slabs using a laboratory-roller compactor. Cylindrical specimens of 153 mm diameter and 65 mm thickness were then cored from the slabs. Volumetric determinations on these specimens gave an average void content of 7.3%.

Cylindrical samples of the two mixtures, of 153 mm diameter, D , and 65 mm thickness, t , were then cut in half to obtain the desired SCB specimens. These were then notched at the mid-point in the direction of the load using a diamond-tip saw tile cutter. Notch length, a_0 , was 15 mm approximately, which gave a notch to radius ratio, a_0/r , of 0.2.

3 CYCLIC SEMI-CIRCULAR BENDING TEST

A Cyclic semi-circular bending (CSCB) test was carried out using a servo-pneumatic loading machine. The machine applied a haversine cyclic load at a selected constant amplitude of 0.5 kN and frequency of 1 Hz to the top of the SCB specimen, which was symmetrically supported by two rollers. The span, $2s$, shown in the CSCB test schematic in Figure 1 was 122 mm, which gave a span to diameter ratio, $2s/2r$, of 0.8. A picture of the test setup is shown in Figure 2.

A load cell was used to measure the load amplitude, ΔP , the maximum load, P_{\max} , and the minimum load, P_{\min} , which is the contact load, during each loading cycle. Figure 3 shows the applied load during a CSCB test on an HME specimen.

The displacement measuring system consisted of two Kaman KD-2300 2S non-contact sensors. The sensors measured the crack mouth opening displacement (CMOD) and the vertical displacement, δ , at the mid-point of the specimen, as shown in Figure 1. These non-contact sensors use

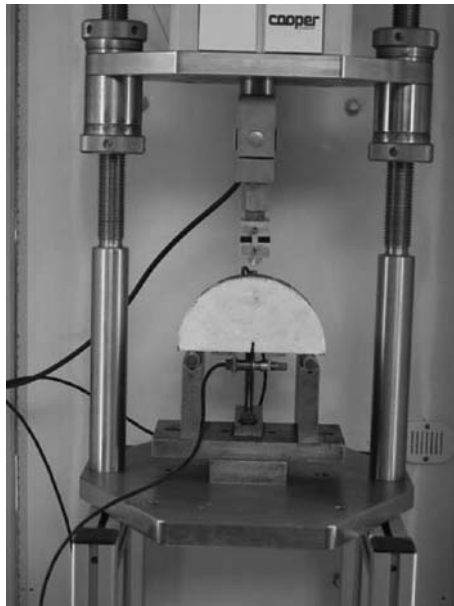


Figure 2. Cyclic semi-circular bending test setup.

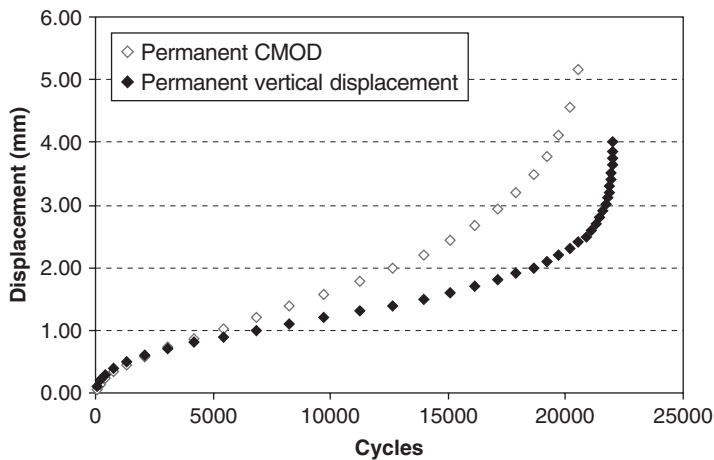


Figure 3. Permanent CMOD and δ for an HME specimen.

inductive, i.e. electromagnetic, technology to determine the position of a target relative to the sensor. They had a range of 0 to 5 mm and a resolution of $0.25 \mu\text{m}$.

For this type of sensors, target material and dimensions are paramount for good performance. The main requirement for a target material is that it be conductive. In addition, non-magnetic materials are recommended. In this work, brass, i.e. non-magnetic, targets of 15 mm diameter and 0.8 mm thickness were used. Furthermore, holders glued to the specimens were used to position the sensors and targets, as seen in Figure 1.

The two sensors measured both permanent and resilient displacements. The permanent, non-recoverable displacement was defined as that accumulated after each load cycle. The resilient displacement, on the other hand, was defined as the difference between the maximum and minimum

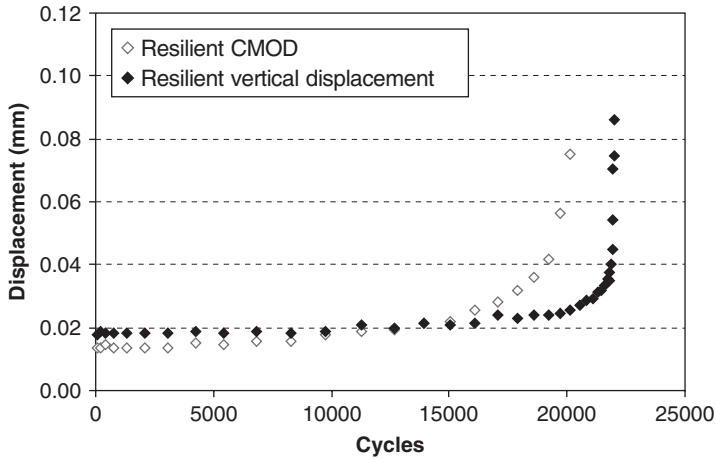


Figure 4. Resilient CMOD and δ for an HME specimen.

displacements in one load cycle, i.e. peak-to-peak displacement. Permanent and resilient CMOD and δ for a CSCB test corresponding to the HME are presented in Figures 3 and 4.

4 CRACK PROPAGATION MEASUREMENT

Crack propagation was monitored by a Marlin F-080B digital camera fitted with a 35 mm lens and capable of operating at 20 fps. The camera was positioned on a tripod 0.5 m away from the specimen, as seen in Figure 2. The specimen and test frame were inside a temperature control cabinet with a double glazed door. The door contained a heating element to avoid condensation. Furthermore, all tests were performed at a temperature of 5°C.

A software program triggered the camera to take a frame as δ , measured by the sensor, increased by 0.1 mm. The same program copied, named and stored the photo files on the hard disc as they were taken. As the sensor range was 5 mm, the maximum number of photos taken during a single test was 50 (5 mm/0.1 mm). It should be noted, however, that for some specimens failure occurred before this displacement level was reached.

An image analysis program was also developed to measure crack length. The procedure adopted in this study was based on the number of pixels from the start to the end of the crack following two methods: a straight line and an effective crack path, i.e. length along the actual crack path. To account for the position of the specimen relative to the camera, a 25 mm marker was stuck to the specimen. The specimens were painted in white using an emulsion-based paint to facilitate the location of the crack. The digital photographs were 1024 × 770 pixels in size.

Figure 5 shows a typical photograph of a cracked SCB specimen taken during a test. It can be seen that the crack started to propagate from the tip of the notch where the concentration of stresses was highest. The crack tended to propagate in the direction of the applied load, thus, perpendicular to the maximum principal tensile stress. Also shown on the figure are the two methods adopted in this paper to monitor crack growth, namely a straight line and an effective crack length measurement.

The evolution of the crack length in both methods with number of cycles during a CSCB test is shown in Figure 6. For both interpretation methods, the HME shows discontinuous, step-wise crack propagation in a manner that is in line with the recommendations made by Zhang et al. (2001). The CEAM, however, shows a continuous crack growth more akin to Paris Law and consistent with results shown in a study by Roque et al. (1999). Differences in crack path for the two materials may be attributed to mixture volumetrics.

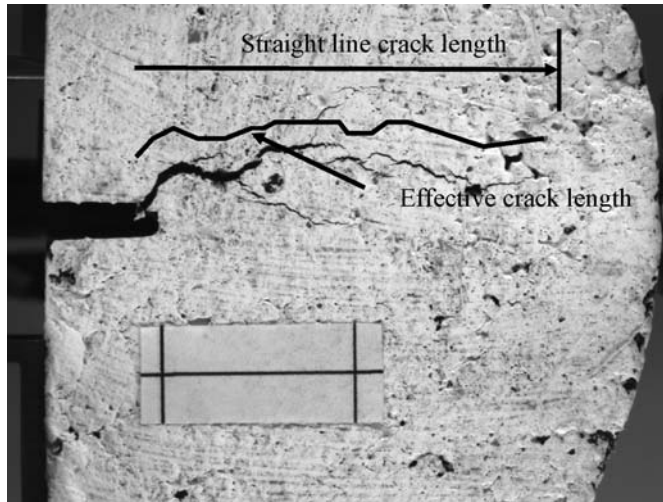


Figure 5. Typical CSCB test photo showing crack growth interpretation.

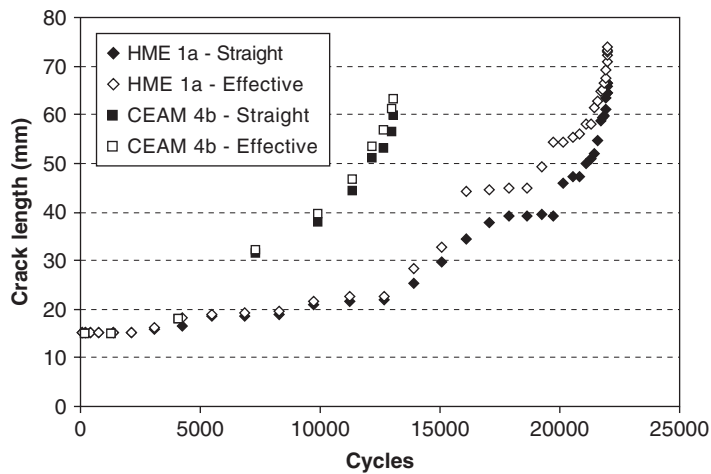


Figure 6. Crack length growth for an HME specimen by the two interpretation methods.

5 THEORY AND ANALYSIS

Linear Elastic Fracture Mechanics (LEFM) analysis has been used to characterise crack growth rate by means of the well known Paris Law (Paris & Erdogan 1963), which is given by the following expression:

$$\frac{da}{dN} = A(\Delta K_I)^n \quad (1)$$

where da/dN = crack growth rate; ΔK_I = mode I stress intensity factor range ($K_{\max} - K_{\min}$); A, n = constants depending on the material and on the test conditions; a = crack length; and N = no. of cycles.

For a SCB specimen, the mode I stress intensity factor range, ΔK_I , is given by (Lim et al. 1993):

$$\Delta K_I = \frac{\Delta P}{2rt} Y_I \sqrt{\pi a} \quad (2)$$

where ΔP = applied load range ($P_{\max} - P_{\min}$); r = specimen radius; t = specimen thickness; and Y_I = normalised mode I stress intensity factor.

Based on finite element analysis, Lim et al. (1993) determined analytical expressions for Y_I for different specimen configurations. For instance, when $s/r = 0.8$, as in the current study, Y_I can be expressed as follows:

$$Y_I = 4.782 - 1.219 \left(\frac{a}{r} \right) + 0.063 \exp \left(7.045 \left(\frac{a}{r} \right) \right) \quad (3)$$

The determination of the Paris Law constants, A and n in Equation (1), involves the calculation of the crack growth rate, da/dN , and the mode I stress intensity factor range, ΔK_I , for the corresponding crack length values. Different techniques have been used to determine crack growth rate. For instance, the British and US standards for metallic materials (BSI 2002, ASTM 2005) suggest using either a secant method, in which da/dN is determined from the slope of a line joining two adjacent points, or an incremental polynomial approach, in which a second order polynomial is fitted to sets of successive data points. For asphalt materials, on the other hand, some researchers (Jacobs et al. 1996, Roque et al. 1999) have fitted a third-order polynomial to the crack growth phase which was then numerically differentiated.

The procedure used in this work was the secant method. In this method, a line is fitted to two adjacent points and the slope of the line is the crack growth rate, da/dN . Furthermore, the average crack length of the interval is used to calculate the corresponding ΔK_I value, which is given by Equation (2). Although this method is very simple, it also exhibits the most scatter in da/dN values. Nevertheless, it is the accurate determination of the crack length and not the method to determine its rate that determines the scatter. The crack growth rate was plotted against ΔK_I on a log-log scale and a straight line was fitted to the data to determine the Paris law constants, A and n . The slope of this line defines n . The constant A is the crack growth rate, da/dN , at a mode I stress intensity factor of $1 \text{ Nmm}^{-3/2}$.

Figures 7–10 show the relationship between the mode I stress intensity factor range, ΔK_I , and crack growth rate, da/dN , for the two materials used following the two interpretation methods for crack growth measurement. From the relationships in these figures, the Paris Law constants, A and n , have been determined based on composite values from replicate tests and are presented in Table 1. Composite values of A and n have been found by the authors and other workers to provide better estimates of the true values than those obtained from single specimens (Artamendi & Khalid 2008, Roque et al. 1999).

Table 1 shows that the two crack growth interpretation methods did not have a significant effect on the Paris Law constants, given the degree of scatter observed. From the lower n values obtained for the CEAM, it may be inferred that its crack growth has a lower sensitivity to applied load than the HME material. A detailed analysis of variance is in order to adjudge the significance of the difference in the obtained n values of the two materials. However, the observed dispersion of the data might suggest that the difference is insignificant. The n values obtained in this study lie between 1 and 2. Although the literature did not reveal any Paris Law parameters for cold asphalt, Sewell et al. (2000) reported n values between 1 and 8 for a High Modulus Base mixture from Compact Tension tests conducted at 10–25°C.

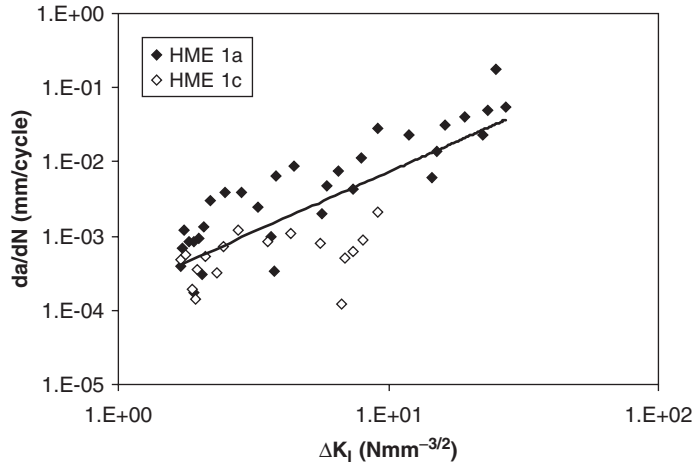


Figure 7. Relation between crack growth rate and stress intensity factor for the HME mixture using the straight line method to evaluate crack length.

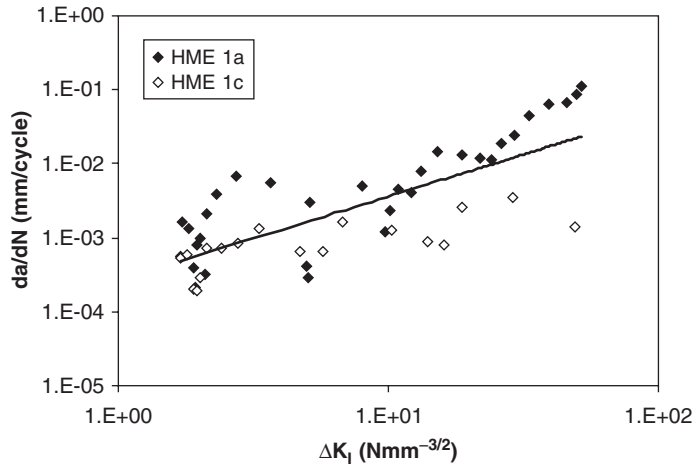


Figure 8. Relation between crack growth rate and stress intensity factor for the HME mixture using the effective method to evaluate crack length.

6 CONCLUSIONS

The cyclic semi-circular bending test developed in this work was found suitable to study the resistance to crack growth of a cold asphalt mixture and its hot mix equivalent using linear fracture mechanics principles. A marked dispersion in the data was observed in the evaluation of the Paris Law constants, A and n , for the two materials studied. Two procedures were adopted to interpret the crack growth: a straight line method and an effective crack growth approach. Despite the lack of statistical analysis of variance, the data scatter for the two approaches did not show a significant difference in the Paris Law parameters of the two materials. Notwithstanding the insignificant difference, the authors believe the effective crack length approach provides a more accurate depiction of crack propagation through the material than the straight line method.

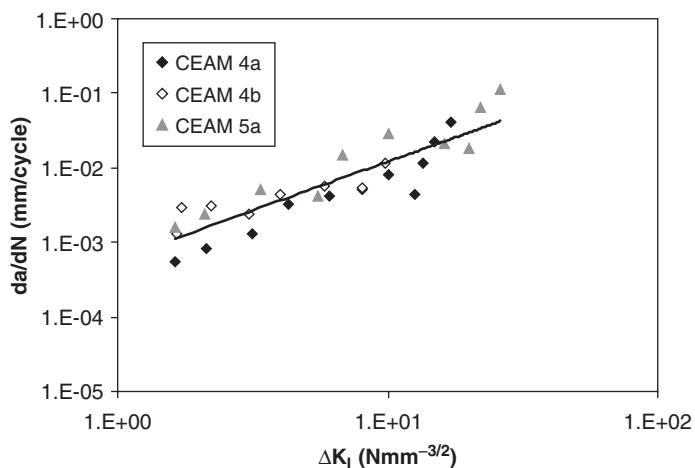


Figure 9. Relation between crack growth rate and stress intensity factor for the CEAM mixture using the straight line method to evaluate crack length.

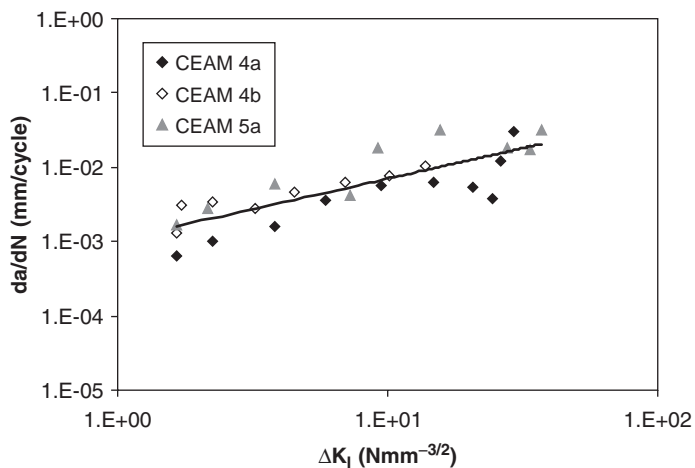


Figure 10. Relation between crack growth rate and stress intensity factor for the CEAM mixture using the effective method to evaluate crack length.

Table 1. Paris law constants for the HME and CEAM materials from the two interpretation methods.

Material	Straight line crack growth			Effective crack growth		
	A	n	R ²	A	n	R ²
HME	0.00017	1.62	0.62	0.00027	1.59	0.60
CEAM	0.00060	1.30	0.80	0.00011	0.82	0.69

ACKNOWLEDGEMENTS

The authors are greatly indebted to Colas Ltd., and especially to Mr John Richardson, for the financial and technical support given to pursue this study. The authors are also grateful for the assistance given by Mr Bassey Okon in interpreting the crack growth photographs.

REFERENCES

- Artamendi, I. & Khalid H.A. 2008. Laboratory assessment of crack growth in cold emulsion asphalt mixtures. *Submitted to the ISAP International Symp. on Asphalt Pavements and Environment, Zurich.*
- ASTM. 2005. Standard test method for measurement of fatigue crack growth rates. ASTM Standard E647-05. *Annual Book of ASTM Standards*, vol. 3.01, American Society for Testing & Materials.
- BSI. 2002. Metallic materials: Fatigue testing; Fatigue crack growth method. BS ISO 12108. *British Standards Institution*, London.
- CEN. 2005. Test methods for hot mix asphalt – Crack Propagation by Semi-Circular Bending Test. prEN 12697-44. *Comité Européen de Normalisation*, Brussels.
- Irwin, G.R. 1957. Analysis of stresses and strains near the end of the crack traversing a plate. *Journal of Applied mechanics* 24: 361–364.
- Jacobs, M.M.J., Hopman, P.C. & Molenaar, A.A.A. 1996. Application of fracture mechanics principles to analyse cracking in asphalt concrete. *Journal of the Association of Asphalt Paving Technologists* 65: 1–39.
- Lim, I.L., Johnson I.W. & Choi S.K. 1993. Stress intensity factors for semi-circular specimens under three-point bending. *Engineering Fracture Mechanics* 44(3): 363–382.
- Paris, P.C. & Erdogan, F.J. 1963. A critical analysis of crack propagation laws. *Transactions of the ASME, Journal of Basic Engineering, Series D*, 85 (3).
- Roque, R., Zhang, Z. & Sankar, B. 1999. Determination of crack growth rate parameters of asphalt mixtures using the superpave IDT. *Journal of the Association of Asphalt Paving Technologists* 68: 404–433.
- Sewell, A.J., Collop, A.C., Thom, N.H. & Brown, S.F. 2000. Assessing crack growth in high modulus base materials. *2nd Eurasphalt & Eurobitume Congress*. Barcelona, Spain: 819–826.
- Zhang, Z., Roque, R., Birgisson, B., & Sangpetngam, B. 2001. Identification and verification of a suitable crack growth law. *Journal of the Association of Asphalt Paving Technologists* 70: 206–236.

Evaluation of fracture properties of hot mix asphalt

L.N. Mohammad & M.D. Kabir

Louisiana State University, Baton Rouge, Louisiana, USA

S. Saadeh

California State University, Long Beach, California, USA

ABSTRACT: One of the major distresses that occur to Hot Mix Asphalt (HMA) is fatigue cracking. It is believed that fatigue cracking occurs due to repeated traffic loading which induce high tensile stresses at the bottom of the asphalt layer. Recently, pavement engineers and researchers have expressed great concern over the cracking of flexible pavements under various traffic loading and environmental conditions.

The fracture properties of three asphalt mixtures containing three binder types will be evaluated in this study. Three binders were used, PG 76-22, PG 70-22 polymer modified asphalt and PG 64-22 unmodified binder. Two tests will be used to characterize the mixtures' fractural properties including Indirect Tensile Strength (ITS) and Semi-Circular Bend (SCB).

The fracture properties in the ITS test are evaluated using the ultimate indirect tensile strength, strain, and the toughness index. The fracture resistance of the mixtures in the SCB test is measured using the J-integral approach. The results from the three tests are analyzed and compared. For both tests ITS and SCB test, aged specimens achieved lower fracture properties than that for the unaged specimens. Good correlation was observed between the Toughness Index (TI) from the ITS test and the J_c from the SCB test.

Keywords: Fracture Energy, Indirect Tensile strength, Semi Circular Bend Test, Hot Mix Asphalt.

1 INTRODUCTION AND BACKGROUND

One of the major distresses that occur to Asphalt Concrete (AC) is fatigue cracking. It is believed that fatigue cracking occurs due to repeated traffic loading which induce high tensile stresses at the bottom of the asphalt layer. Recently, pavement engineers and researchers have expressed great concern over the fracture properties of flexible pavements under various traffic loading and environmental conditions.

The indirect tensile strength test is the most traditional test method used to evaluate the fracture properties of asphalt mixture in laboratory, and has been used in some cracking characteristics study as well [1,2]. During ITS test, the specimen is loaded till failure and the load and deformation is continuously recorded, and then the indirect tensile strength and the corresponding strain can be computed.

Chong and his group proposed to use a semi-circular core specimen with a single edge notch, subjected to three point loading [3]. Recently, this Semi-Circular Bend (SCB) test has been introduced to pavement material area, and many research projects have applied this method to investigate the fracture property of different kind of asphalt mixtures [2, 4, 5, 6, 7]. The SCB can be a potential test to further explore the material fracture properties.

2 OBJECTIVES AND SCOPE

The primary objective of this study is to investigate and compare the fracture properties of asphalt mixtures with different binder types that are commonly used in Louisiana. A polymer modified asphalt cement meeting Louisiana specifications for PG 76-22M, PG 70-22M, and an unmodified PG 64-22 were used. For each binder a 19.0 mm Level 2 HMA mixture was designed and examined. Siliceous limestone aggregates that are commonly used in Louisiana were included in this study. Indirect tensile strength test and Semi-Circular Bend (SCB) test were conducted to define the fracture properties of HMA mixtures. Triplicate samples were used.

3 EXPERIMENTAL DESIGN

3.1 *Asphalt cement*

Table 1 presents the three asphalt cement binders that were used in this study. The first and second binders contain SB polymer modified asphalt cement meeting Louisiana specifications for PG 76-22M and PG 70-22M, where as the third contained an unmodified PG 64-22. It has to be mentioned that Louisiana DOTD specifies higher requirement for the PG 64-22 binder (i.e $G^*/\text{Sin Delta}$ is higher).

3.2 *Mixture design*

Table 2 presents the Job Mix Formula (JMF) for the three 19.0 mm HMA mixtures. A Louisiana Superpave Level 2 design ($N_{\text{initial}} = 8$ -, $N_{\text{design}} = 100$ -, $N_{\text{final}} = 160$ -gyrations) was performed according to AASHTO TP28, “Standard Practice for Designing Superpave HMA” and Section 502 of the 2000 Louisiana Standard Specifications for Roads and Bridges [8]. Specifically, the optimum asphalt cement content was determined based on the following volumetrics (Voids in total mix (VTM) = 2.5–4.5 percent, Voids in Mineral aggregate (VMA) $\geq 12\%$, Voids filled with Asphalt (VFA) = 68%–78%) and densification ($\%G_{\text{mm}}$ at $N_{\text{initial}} \leq 89$, $\%G_{\text{mm}}$ at $N_{\text{final}} \leq 98$) requirements. It is noted that the aggregate structure for all the mixtures considered was similar. Crushed siliceous limestone aggregates were used in this study.

3.3 *Test factorials*

Indirect tensile strength test (ITS) and Semi-Circular Bend Test were conducted in this study. Triplicate samples were used for each test. Table 3 presents the test factorials adopted in this study. Indirect tensile strength test and semi circular bend test were used to examine the fracture properties of asphalt mixtures. The tests were performed on aged and unaged mixtures. Mixture aging was performed according to AASHTO PP2 [9] by placing compacted specimen in forced draft oven for five days at 85°C.

3.4 *Specimen preparation*

Two sizes of specimens were fabricated one for the ITS and the other for SCB. These include 101.6 mm (4 inch) in diameter and about 63.5 mm (2.5 inch) high and 150 mm (5.91 inch) diameter by 57 mm (2.24 inch) high cylindrical specimens. The specimens were compacted with the Superpave Gyrotory Compactor (SGC). The 101.6 mm (4 inch) in diameter and about 63.5 mm (2.5 inch) high cylindrical specimens was prepared for indirect tensile strength. The SCB test specimens were prepared by slicing the 150 mm (5.91 inch) by 57 mm (2.24 inch) high cylindrical specimens along their central axes into two samples. Figure 1 provides the geometry of a SCB specimen used in this study. A vertical notch was then introduced along the symmetrical axis of each SCB specimen in order to study the true fracture properties of asphalt mixtures with regard to the crack propagation.

Table 1. LADOTD asphalt cement specification & test results.

Property	AASHTO test method		PG 76-22M		PG 70-22M		PG 64-22	
	Spec.	Results	Spec.	Results	Spec.	Results	Spec.	Results
<i>Test on Original Binder</i>								
Rotational Viscosity @ 135°C, Pa.s	TP 48	1.7	3.0-	0.9	3.0-	0.9	3.0-	3
Dynamic Shear, 10 rad/s, G*/Sin Delta, KPa	TP 5	1.29	1.00+@82°C	-	1.00+@76°C	-	1.00+@82°C	0.87
Flash Point, °C	T 48	305	232+	1.82	1.00+@70°C	1.64	1.00+@76°C	2.35
Solubility, %	T 44	99.5	99.0+	295	232+	295	232+	305
Force Ductility Ratio (F2/F1, 4°C, 5 cm/min, F2 @ 30 cm elongation)	T 300	0.49	0.30+	99.6	99.0+	99.6	99.0+	99.6
				0.31	0.30+	0.31	0.30+	*
<i>Tests on Rolling Thin Film Oven (RTFO) Residue</i>								
Mass loss, %	T 240	0.08	1.00-	0.03	1.00-	0.03	1.00-	0.1
Dynamic Shear, 10 rad/s, G*/Sin Delta, KPa	TP 5	1.67	2.20+@82°C	1.65	2.20+@76°C	1.65	2.20+@82°C	1.81
Elastic Recovery, 25°C, 10 cm, % elongation, %	T 301	70	60+	2.84	2.20+@70°C	3.14	2.20+@76°C	3.5
<i>Test on Pressure Aging Vessel (PAV) Residue</i>								
Dynamic Shear, @ 25°C, 10 rad/s, G* Sin Delta, KPa	TP 5	2297	5000-	4615	5000-	4615	5000-	6870
Bending Beam Creep Stiffness, S, MPa @ -12°C.	TP1	162	300-	193	300-	193	300-	496 MPa
Bending Beam Creep Slope, m value, @ -12°C	TP1	0.327	0.300+@-12°C	0.315	0.300+@-12°C	0.315	0.300+@-12°C	0.269
		-	0.300+@-6°C	-	0.300+@-6°C	-	0.300+@-6°C	0.35

*Did not meet Force Ductility Ratio Criteria.

Table 2. JMF for the three 19.0 mm HMA mixtures.

Mixture Designation	64CO	M70CO	M76CO
Mix Type	19 mm Superpave		
Binder type	PG 64-22	PG 70-22M	PG 76-22M
% G_{mm} at N_I	87	87	87
% G_{mm} at N_D	96.3	96.3	96.3
% G_{mm} at N_M	97.6	97.6	97.6
Binder content, %	4	4	4
Design air void, %	3.7	3.7	3.7
VMA, %	12	12	12
VFA, %	68	68	68
Metric (U.S.) Sieve	Blend Gradation		
37.5 mm (1 1/2 in)	100	100	100
25 mm (1 in)	100	100	100
19 mm (3/4 in)	98	98	98
12.5 mm (1/2 in)	77	77	77
9.5 mm (3/8 in)	61	61	61
4.75 mm (No.4)	41	41	41
2.36 mm (No.8)	29	29	29
1.18 mm (No.16)	21	21	21
0.6 mm (No.30)	15	15	15
0.3 mm (No.50)	8	8	8
0.075 mm (No.200)	4.6	4.6	4.6

Table 3. Test factorial.

		Laboratory tests					
Mixture type	Asphalt binder	ITS				SCF	
		Unaged		Aged		Unaged	Aged
		25°C	40°C	25°C	40°C		
64CO	PG 64-22	3	3	3	3	3	3
M70CO	PG 70-22	3	3	3	3	3	3
M76CO	PG 76-22M	3	3	3	3	3	3

The notches were cut using a special saw blade of 3.0 mm thickness. Three nominal notch depths: 25.4 mm, 31.8 mm, and 38 mm, were used. The target air void for all specimens characterized in this study was $7.0 \pm 0.5\%$.

3.5 Fundamental/simulate engineering property tests

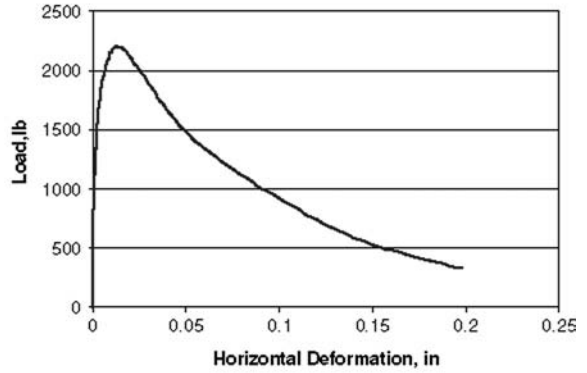
Two fundamental tests were conducted to characterize the three mixtures. A brief review of these tests is given below.

3.5.1 Indirect tensile strength test

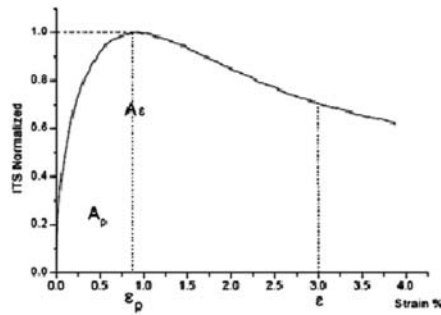
The indirect tensile stress (ITS) and strain test was used to determine the tensile strength and strain of the mixtures, Figure 1a. This test was conducted at 25°C and 40°C. The test specimen was loaded to failure at a 50.8 mm/min (2 in/min) deformation rate. The load and deformations were continuously recorded. Figure 1b shows a typical test output. Indirect tensile strength and strain



(A)



(B)



(C)

Figure 1. (A) Indirect tensile strength test setup, (B) typical results from the indirect tensile strength test, and (C) a typical normalized ITS curve for toughness index calculations.

were computed as follows:

$$ITS = \frac{2P}{\pi DT} \quad (1)$$

$$\epsilon_t = 0.52Ht \quad (2)$$

where,

P = the peak load, lb

D = specimen diameter, in

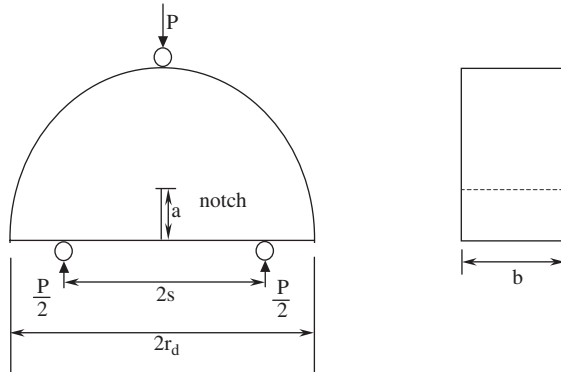
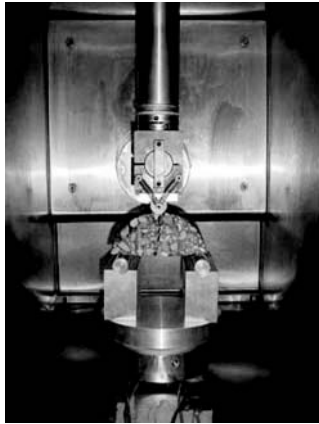
T = specimen thickness, in

Ht = horizontal deformation at peak load, in

The toughness index (TI), a parameter describing the toughening characteristics in the post peak region, was also calculated from the indirect tensile test results. Figure 1c presents a typical normalized indirect tensile stress and strain curve. A dimensionless indirect tensile toughness index, TI is defined as follows:

$$TI = \frac{A_\epsilon - A_p}{\epsilon - \epsilon_p} \quad (3)$$

where,



$2r_d=150\text{mm}, 2s=125\text{mm}, b=57\text{mm}$

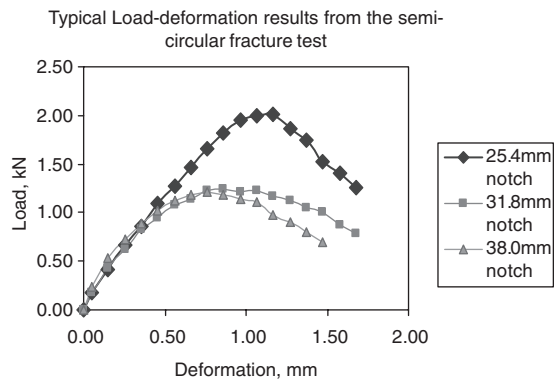
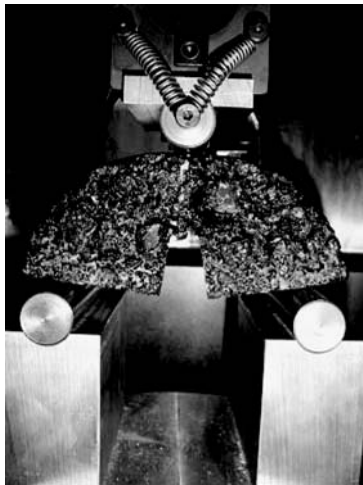


Figure 2. Semi Circular Test Set up and Specimen Configuration.

TI – Toughness index,

A_ε – Area under the normalized stress-strain curve up to strain, ε ,

A_p – Area under the normalized stress-strain curve up to strain, ε_p ,

ε – Strain at the point of interest, and

ε_p – Strain corresponding to the peak stress.

This toughness index compares the performance of a specimen with that of an elastic perfectly plastic reference material, for which the TI remains a constant of one. For an ideal brittle material with no post-peak load carrying capacity, the value of TI equals zero.

3.5.2 Semi-circular bend (SCB) Test

This test characterizes the fracture resistance of HMA mixtures based on fracture mechanics concept, the critical strain energy release rate, also called the critical value of J-integral, or J_c [9]. Figure 2 shows a three-point bend load configuration used in the test and corresponding dimensions.

To determine the critical value of J-integral (J_c), semi-circular specimens with at least two different notch depths need to be tested for each mixture. In this study, three notch depths of 25.4 mm, 31.8 mm and 38 mm were selected based on an a/r_d ratio (the notch depth to the radius

Table 4. Statistical grouping of indirect tensile strength and strain test results.

Property Mix Type	IT strength (psi)				IT strain (%)				TI			
	Un aged		Aged		Un aged		Aged		Un aged		Aged	
	Mean	Group	Mean	Group	Mean	Group	Mean	Group	Mean	Group	Mean	Group
<i>Temperature 25°C</i>												
64CO	177.8	A	206.9	A	0.47	C	0.26	B	0.7	C	0.67	B
M70CO	149.7	C	163.4	C	0.94	B	0.53	A	0.92	B	0.82	A
M76CO	163.5	B	187.4	B	1.3	A	0.63	A	1	A	0.86	A
<i>Temperature 40°C</i>												
64CO	65.2	A/B	82.2	A	0.68	B	0.59	B	0.76	B	0.78	B
M70CO	61.2	B	67.3	B	0.93	A/B	0.75	B	0.95	A	0.87	A
M70CO	71.6	A	76.8	A	1.22	A	0.97	A	0.98	A	0.91	A

of the specimen) of between 0.5 and 0.75 [10]. For each notch depth three duplicates were used. Test temperature was selected to be 25°C. The semi-circular specimen is loaded monotonically till fracture failure under a constant cross-head deformation rate of 0.5 mm/min in a three-point bend load configuration, Figure 2. The load and deformation are continuously recorded, as shown in Figure 2, and the critical value of J-integral (Jc) is determined using the following equation [11] based on the following equation:

$$J_c = - \left(\frac{1}{b} \right) \frac{dU}{da} \quad (4)$$

where b is sample thickness, a is the notch depth and U is the strain energy to failure.

In order to obtain the critical value of fracture resistance, Jc, the area under the loading portion of the load deflection curves, up to the maximum load, was measured for each notch depth and mixture. This area represents the strain energy to failure, U. The average values of U are then plotted versus the different notch depths to compute a slope of a regression line, which is the value of (dU/da) in Equation (4). The critical value of fracture resistance, Jc, is then computed by dividing the dU/da value by the specimen width, b.

4 DISCUSSION OF RESULTS

4.1 Indirect tensile strength test results

The test results were statistically analyzed using the analysis of variance (ANOVA) procedure provided in the Statistical Analysis System (SAS) program from SAS Institute, Inc. A multiple comparison procedure with a risk level of 5 percent was performed on the means. The group column contains the results of the statistical grouping reported with the letters A, B, C, and D. The letter A was assigned to the highest mean followed by the other letters in appropriate order. A double (or more) letter designation, such as A/B (or A/B/C), indicates that in the analysis the difference in the means was not clear-cut, and that the mean was close to either group.

Table 4 presents the mean for the indirect tensile (IT) strength, strain, and toughness index (TI) results along with their statistical grouping for the 25°C and 40°C. In this test, high indirect tensile strength and strain values at failure are desirable properties for stiff mixtures. For the 25°C results, the PG 64-22 binder has the highest IT strength followed by the PG 76-22, then the PG 70-22. This trend is different for than that for IT strain and TI. In general, the PG 76-22 ranked highest followed by the PG 70-22 and then the PG 64-22 for the IT Strain and TI. For all mixtures the fracture

Table 5. SCB test results.

Mix type		J-Value per Notch Depth (mm)			J _c (kJ/m ²)	R ²
		25.4	31.8	38		
64CO	Unaged	0.77	0.45	0.37	0.57	0.9
	Aged	0.69	0.61	0.33	0.5	0.89
M70CO	Unaged	1.02	0.58	0.34	0.96	0.98
	Aged	1.02	0.59	0.36	0.92	0.97
M76CO	Unaged	1.13	0.75	0.45	0.95	1
	Aged	1.11	0.72	0.44	0.93	0.99

properties for the aged specimens were less than that for the unaged specimens. For the 40°C the ranking has a similar trend to the results at 25°C, however, the difference between the parameters was smaller.

4.2 Semi-circular bend test results

Table 5 presents the average semi-circular bend test results for the critical strain energy, J_c, values. It is noted that the aged mixture achieved lower critical strain energy than the unaged mixtures for all mixture. The results also indicate that the critical strain energy for the mixtures containing modified binders is comparable and higher than that for the unmodified mixture.

4.3 Parameters correlations

Figure 3 presents the correlation between the ITS test parameters (IT Strength, IT Strain, and TI) tested at 25 and 40°C and the Semi circular test parameter, J_c. It is noted that the correlation was highest between the TI from the ITS test and the J_c from the SCB test at both temperatures. This is an interesting finding as it proves that the SCB test, which is easier to perform and applies more uniform tensile stress, has a similar trend to the IT toughness index of the traditional ITS test.

5 SUMMARY AND CONCLUSIONS

The fracture properties of three asphalt mixtures containing three binder types were evaluated in this study. Three binders were used, PG 76-22, PG 70-22 polymer modified asphalt and PG 64-22 unmodified binder. Two tests were conducted to characterize the mixtures' fractural properties including Indirect Tensile Strength (ITS) and Semi-Circular Bend (SCB).

The following observations are drawn from this study:

- The IT strength, IT Strain, and TI parameters of the ITS test had ranked the mixtures differently. The TI is the parameter that best represent the material behaviour since it includes the effect of IT strength and IT strain.
- For ITS test, aged specimens achieved lower fracture properties than that for the unaged specimens.
- For the ITS test results, at 40°C the mixtures achieved comparable ranking to the 25°C results, however the difference between the parameters from was smaller.
- For the SCB test the aged mixture achieved lower critical strain energy than the unaged mixtures for all mixture.
- Good correlation was observed between the TI from the ITS test and the J_c from the SCB test. This might be contributed to the fact that both TI and J_c are measured based on the stress and strain responses together.

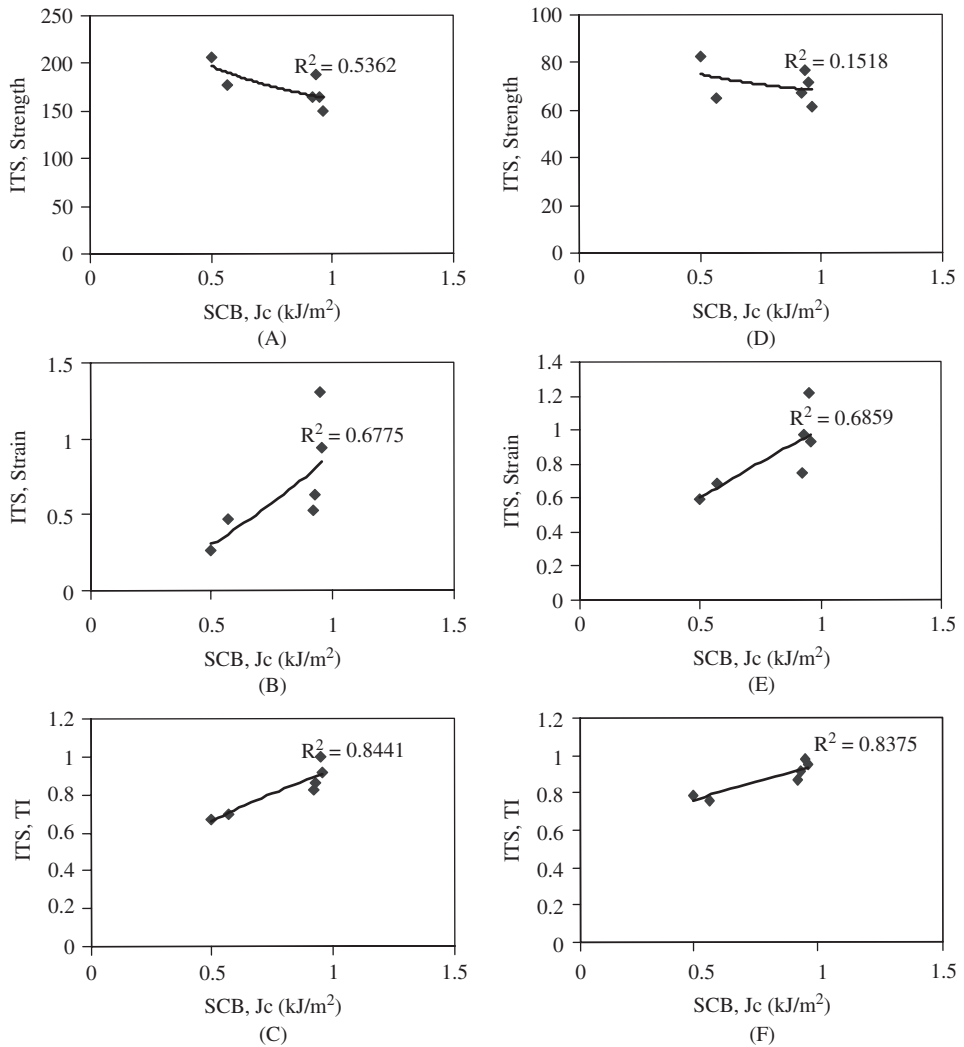


Figure 3. Correlation of the SCB test parameter to the ITS test parameters at (A), (B), and (C) 25°C and (D), (E), and (F) 40°C.

- The SCB test is a simple test that applies more uniform tensile stresses than the ITS and yield good correlation to the ITS parameters.

REFERENCES

- [1] Roque, R., A. Zhang, and B. Sankar, "Determination of Crack Growth Rate Parameters of Asphalt Mixture Using the Superpave IDT", *Journal of the Association of Asphalt Paving Technologists*, Vol. 68, 1999, pp. 404–433.
- [2] Baoshan Huang, Brian K. Egan, William R. Kingery, "Laboratory Study of Fatigue Characteristics of HMA Surface Mixtures Containing RAP" *TRB 2004 Annual Meeting CD-ROM*.
- [3] Chong K. P. and Kuruppu M. D., "New Specimen for Fracture Toughness Determination for Rock and Other Materials", *International Journal of Fracture* Vol. 26, 1984, pp. 59–62.

- [4] Molenaar, A.A.A.; Scarpas, A.; Liu, X.; Erkens, S.M.J.G. "Semi-Circular Bending Test: Simple but Useful?" *Association of Asphalt Paving Technologists Proceedings of the Technical Sessions*, Vol. 71, 2002, pp. 794–815.
- [5] Mull, M. A., Stuart, K. and Yehia, A., "Fracture resistance characterization of chemically modified crumb rubber asphalt pavement," *Journal of Materials Science*, Vol. 37, pp. 557–566, 2002.
- [6] Mohammad, N. L., Wu, Z., Aglan, M., "Characterization of Fracture and Fatigue Resistance on Recycled Polymer-Modified Asphalt Pavements", *The 5th RILEM conference on Pavement Cracking*, France, 2004.
- [7] Mohammad, L. N., Negulescu, I., Wu, Z., Daranga, C., Daly, W.H. and Abadie, C., "Investigation of the Use of Recycled Polymer Modified Asphalt Binder in Asphalt Concrete Pavements", *Asphalt Paving Technology: Association of Asphalt Paving Technologists Proceedings of the Technical Sessions*, Vol. 72, 2003, pp. 551–594.
- [8] Louisiana Standard Specifications for Roads and Bridges, Louisiana Department of Transportation and Development, Baton Rouge, Louisiana, 2000.
- [9] Mohammad, L.N., Wu, Z. and Aglan, M. "Characterization of Fracture and Fatigue Resistance of Recycled Polymer-Modified Asphalt Pavements," *Proceedings of the RILEM: 5th International Conference on Cracking in Pavements Mitigation, Risk Assessment and Prevention*, Eds. Petit, C., Al-Qadui, I., and Millien, A., Limoges, France, May 5–8, 2004, pp. 375–382.
- [10] Rice, J.R., "A path independent integral and the approximate analysis of strain concentration by notches and crack", *Journal of Applied Mechanics*, Vol. 35, 1968, pp. 379–386.
- [11] Wu, Z., Mohammad, L.N., Wang, L.B., Mull, M.A. "Fracture Resistance Characterization of Superpave Mixtures Using the Semi-Circular Bending Test", *Journal of ASTM International*, March 2005, Vol. 2, No. 3. (<http://www.astm.org>).

Crack propagation performance evaluation of asphaltic mixes using a new procedure based on cyclic semi-circular bending tests

R.C. van Rooijen & A.H. de Bondt

Ooms Nederland Holding, Scharwoude, The Netherlands

ABSTRACT: Currently there is no generally accepted procedure to assess the crack propagation performance of asphaltic mixes under traffic loading, which requires test equipment that is available in most (asphalt) laboratories and can be carried out within a relatively short period of time. To fill this gap, a procedure has been developed in the Netherlands which is based on Paris' law. Crack propagation is generated with cyclic semi-circular bending tests performed on notched specimens at a relatively low temperature. Relationships obtained from finite element analyses are used to evaluate the test data.

One (artificially aged) asphalt mixture with five different bituminous binders has been assessed according to the developed procedure. The duration of the crack propagation phase was relatively short for all binders. However, for four binders there was enough data to determine the parameters A and n with good confidence. Although not part of the laboratory testing procedure, it is necessary to also have knowledge about the expected stress intensity factors in the pavement to really enable comparison of the performance of mixes.

The tensile properties of the five types of bitumen are determined with the force-ductility test. Although the influence of the ductility properties of bitumen on (thermally induced) reflective cracking has been demonstrated before, no correlations were found between the parameters from the asphalt mixture and the force-ductility testing.

The procedure and test results are discussed in the paper. They can be used to further improve asphalt and bitumen selection criteria for resistance to traffic induced reflective cracking.

1 INTRODUCTION

The effectiveness of (thin) asphalt overlays as maintenance measure for cracked pavements and the durability of asphalt pavements with stiff, cement treated bases depends amongst others on the resistance to (reflective) cracking.

To assess the performance with respect to reflective cracking, it is necessary to distinguish between temperature and traffic induced cracking. In this paper only reflective cracking due to traffic loading is addressed.

Currently there is no generally accepted procedure to assess the crack propagation performance of asphaltic mixes under traffic loading, which requires test equipment that is available in most (asphalt) laboratories and can be carried out within a relatively short period of time. To fill this gap, a draft procedure has been developed in the Netherlands which is based on Paris' law (CROW, 2006). Crack propagation is generated with cyclic semi-circular bending tests performed on notched specimens at a relatively low temperature, which addresses the West European conditions. Relationships obtained from finite element analyses (Scarpas, 2003) are used to evaluate the test data. Representatives from asphalt testing laboratories, the asphalt industry and the road authorities were all involved in the development of this laboratory testing procedure. The work was part of a national

study about designing and assessing asphaltic mixes on the basis of functional properties instead of the traditional Marshall criteria.

One (artificially aged) asphalt mixture with five different bituminous binders has been assessed according to the developed procedure. Although not part of the laboratory testing procedure, it is necessary to also have knowledge about the expected stress intensity factors in the pavement to really enable comparison of the performance of mixes.

The tensile properties of the five types of bitumen are determined with the force-ductility test. Possible correlations between the parameters from the asphalt mix testing and force-ductility tests are investigated. The influence of the ductility properties of bitumen on (thermally induced) reflective cracking has been demonstrated before, using micro-mechanical modeling (Bijsterveld, 2003).

The experiences with the draft testing procedure, the suggested improvements and the test results are further discussed in this paper.

2 PROCEDURE TO DETERMINE PARIS' LAW MATERIAL PARAMETERS

The proposed procedure is based on Paris' law (Bondt, 1999):

$$\frac{dc}{dN} = A \cdot K_I^n \quad (1)$$

Where c = length of crack [mm]; K_I = stress intensity factor [$\text{MPa} \cdot \sqrt{\text{mm}}$]; N = number of load cycles; and A , n are material parameters.

The material parameters A and n need to be determined. There are many known test geometries to assess crack propagation and determine these material parameters. Each of them has its own advantages and disadvantages. For the method discussed here, crack propagation is assessed on the basis of results from cyclic semi-circular bending (SCB) tests. The main advantages are that sample preparation is relatively simple, the required test equipment is available in many asphalt laboratories and the tests can be completed in a short period of time. One of the main disadvantages is the rather short length (ligament) over which crack propagation can take place.

The whole procedure includes four steps:

- 1) cyclic SCB tests
- 2) calculation of crack length
- 3) calculation of the stress intensity factor K_I
- 4) determination of the material parameters A and n

2.1 Cyclic SCB tests

The cyclic SCB tests are performed on notched specimens. The test conditions are:

- test temperature of 0°C
- haversine loading
- stress controlled
- loading frequency of 30 Hz
- minimum load is 10% of maximum load

For each specimen, the maximum load (F_{\max}) is based on the results of a monotonic SCB test that is carried out on a (notched) specimen from the same set. The monotonic SCB tests are displacement controlled (i.e. 0.85 mm/s). The test temperature is 0°C . The tests are performed according to the European draft test method for the SCB test (CEN, 2006). The parameters that are obtained from the monotonic SCB tests are the maximum load at failure (F_{failure}) and the fracture strength K_{Ic} .

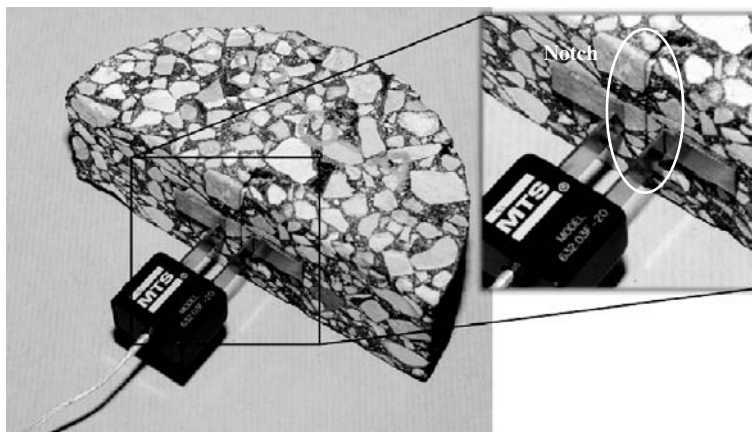


Figure 1. Setup for measurement of horizontal displacement.

During the cyclic SCB tests the horizontal displacement around the notch is measured with a clip-on gage (MTS model 632.03F-20). The gage is placed over the notch between two knife edges, which are glued on the specimen. The distance between them is exactly 12 mm. This is shown in figure 1. The difference between maximum and minimum displacement during one load cycle is defined as the crack opening displacement amplitude (further referred to as COD). The basic result of each test is COD against number of loading cycles.

2.2 Calculation of crack length

The length of the crack is calculated with the following relationship:

$$\left(\frac{c}{h}\right) = 0.1642 \cdot \ln\left(\frac{COD_{N=1}}{COD_N}\right) + 0.1413 \quad (2)$$

Where c = length of the crack [mm]; h = maximum length of the crack (height of the SCB specimen $\approx \frac{1}{2}$ diameter); $COD_{N=1}$ = COD at the beginning of the test and COD_N = COD after N load cycles.

This relationship is obtained from FEM analyses (i.e. CAPA-3D) carried out at Delft University. Using the displacement amplitude as basis for the calculation of the length of the crack instead of cumulative displacements, eliminates creep effects and compensates for differences in mix stiffness. The creep effects are caused by the weight of the specimen, the spring force of the clip-on gage and the minimum applied load (F_{\min}), which is present continuously.

2.3 Calculation of the stress intensity factor K_I

The stress intensity factor K_I is calculated with the following relationship (CROW, 2006):

$$K_I = \sigma_{SCB} \cdot f\left(\frac{c}{h}\right) \quad (3)$$

The stress level σ_{SCB} is calculated with the following relationship (CROW, 2006):

$$\sigma_{SCB} = \frac{4.263 \cdot F_{SCB, N=1}}{l_{SCB} \cdot t_{SCB}} \quad (4)$$

Where $F_{SCB,N=1} = (F_{max} - F_{min})$ at the beginning of the test [N]; l_{SCB} = length of the specimen \approx diameter [mm]; and t_{SCB} = thickness of the specimen [mm].

$f(c/h)$ is a geometry factor and can be determined with FEM analyses. For the SCB test the geometry factor was found to be:

$$f\left(\frac{c}{h}\right) = 1398.6 \cdot \left(\frac{c}{h}\right)^5 - 2709.1 \cdot \left(\frac{c}{h}\right)^4 + 2141.9 \cdot \left(\frac{c}{h}\right)^3 - 799.94 \cdot \left(\frac{c}{h}\right)^2 + 155.58 \cdot \left(\frac{c}{h}\right) - 4.9965 \quad (5)$$

The CAPA-3D analyses carried out at Delft University also showed that neither the Poisson's ratio nor the stiffness modulus of the mix effects the stress intensity factor during the cyclic SCB test.

2.4 Determination of material parameters A and n

To determine the material parameters A and n, dc/dN needs to be plotted against K_I on a log-log scale. A and n are obtained from the power function that fits the part where dc/dN increases linear with K_I (i.e. crack propagation phase).

According to the Dutch draft testing procedure, dc/dN is calculated by first fitting a function through the obtained relationship between crack length and number of loading cycles followed by determining the derivative of this function. The proposed general function for the fit is:

$$c = C_0 + C_1(1 + C_2 \cdot N)^m \quad (6)$$

With C_0 , C_1 , C_2 and m all variables with the restriction that $C_0 + C_1 = 10$ mm (crack length at the beginning of the test). Alternatively, dc/dN can be directly calculated from the test results when there is enough data available (i.e. sampling frequency is high enough).

3 TEST PROGRAM

One asphalt mix with five different bituminous binders is assessed according to the above described procedure. The tested asphalt mixture is an asphalt binder/base course with a maximum nominal aggregate size of 11.2 mm and 5.2% bitumen (of the total mixture). The used binders are two types of standard Penetration Grade bitumen (i.e. Pen 40/60 and Pen 160/220) and three types of polymer modified binder (PMB). PMB1 is a commercial product with SBS polymer. PMB 2 and PMB3 were prepared in the laboratory by mixing 5.0% of polymer (i.e. EVA and PE) with Pen 70/100 till the polymer was homogeneously dispersed.

The asphalt specimens are compacted with a gyratory compactor to a target voids content of 3.5%. For each binder four gyratory samples are prepared. All gyratory samples are artificially aged for 120 hours in a ventilated oven at 85°C. After ageing, four SCB test specimens are sawn out of the middle part of each gyratory sample. The two specimens sawn from one disc make a set. So for each binder 8 sets are prepared. A notch (10 mm deep and 0.35 mm wide) is sawn in the middle of the specimens. Of each set, one specimen is used for the monotonic SCB test and the other for the cyclic SCB test. First the monotonic SCB test is carried out. The load at failure is used to determine the maximum load (F_{max}) for the cyclic SCB test.

The tensile properties of the five binders are determined with the force-ductility test. The test procedure is described in EN 13589 and EN 13703. To address the most critical field conditions the tests are performed at the lowest temperature (i.e. 5°C) and highest strain rate (i.e. 2.8%/s) that was possible with the available equipment. Before testing the virgin binders are artificially aged according to the RTFOT and PAV procedure. This way the binders are tested in a condition that is assumed to represent their physical state at the end of the pavement lifetime, which is considered to be the most critical state with respect to resistance to reflective cracking.

Table 1. Results of monotonic SCB tests (8 tests per case).

	$F_{failure}$ [kN]		$K_{I,c}$ [MPa · $\sqrt{\text{mm}}$]	
	Average	COV	Average	COV
Pen 40/60 bitumen	9.34	5.8%	30.6	5.8%
Pen 160/220 bitumen	8.90	5.7%	29.2	5.6%
PMB 1	10.95	5.4%	35.6	4.9%
PMB 2	11.03	8.0%	35.9	8.0%
PMB 3	9.16	4.5%	29.9	4.4%

Table 2. Loading conditions and some results of cyclic SCB tests (8 tests per case).

	F_{max} [% of $F_{failure}$]		Loading cycles till failure			K_I at failure [MPa · $\sqrt{\text{mm}}$]	
	Range (min-max)		Average	Range (min-max)		Average	COV
Pen 40/60 bitumen	45	55	101,900	28,650	174,150	34.0	6.0%
Pen 160/220 bitumen	40	55	61,950	11,500	93,850	31.6	10.2%
PMB 1	40	55	36,300	5,950	74,950	38.6	7.3%
PMB 2	55	55	20,500	5,300	47,950	38.3	5.0%
PMB 3	50	55	61,750	21,600	106,300	33.5	7.1%

4 RESULTS

From the monotonic SCB test data, load at failure ($F_{failure}$) and fracture strength ($K_{I,c}$) are calculated. The average results are summarized in table 1.

According to the proposed procedure the maximum load for the cyclic SCB tests should be around 60% of $F_{failure}$. However, for all binders a lower load was selected to avoid early failure (i.e. before 10,000 load cycles). Loading conditions and some of the results (i.e. number of load cycles till failure and K_I at failure) are summarized in table 2. The wide range between minimum and maximum cycles till failure can be (at least partly) explained by the different load levels that were applied and the inevitable variations between the test specimens.

Figure 2 gives an example of COD against number of load cycles. For each specimen the crack length was calculated from the COD data and plotted against number of load cycles. Figure 3 shows the calculated crack lengths based on the COD data of figure 2. Also shown in figure 3 is the fit through the obtained relationship between crack length and number of loading cycles. It is obvious that the fit is poor (especially for the steep part at the end of test). This was the case for all specimens and indicates that the proposed general function in combination with the restriction that $C_0 + C_1 = 10$ is not suited to fit these relations. Other general functions used in Excel did not show better fits.

Since it was not possible to find a function that fitted well the relationship between crack length and number of loading cycles, dc/dN could not be calculated correctly as envisaged from the derivative of that function. Therefore, dc/dN was calculated directly from the test data. When plotted against K_I , the picture was more or less the same for all specimens: a fracture initiation phase that varied in duration followed by a relatively short crack propagation phase (1,150–11,500 load cycles). Some specimens showed high dc/dN values at the beginning of the test. As an example the results for a specimen with respectively Pen 160/220 bitumen and PMB1 are shown in figures 4 and 5 (one data point for each 0.5 mm crack length increment). A and n are obtained from fitting a power function through the data during the (assumed) crack propagation phase. The results are

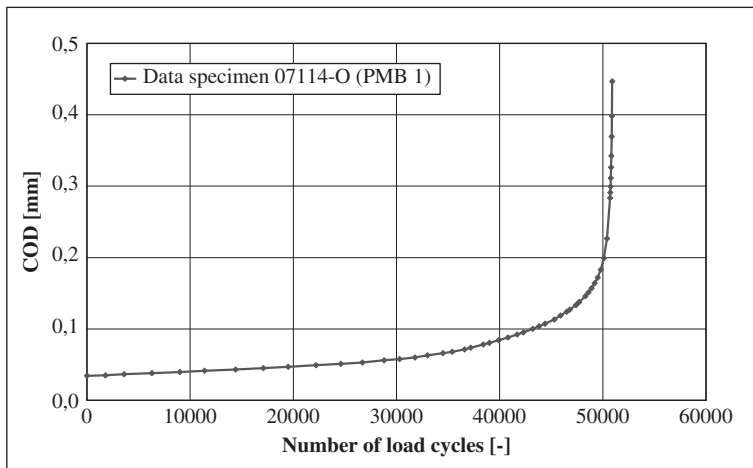


Figure 2. Example of measured COD against number of load cycles.

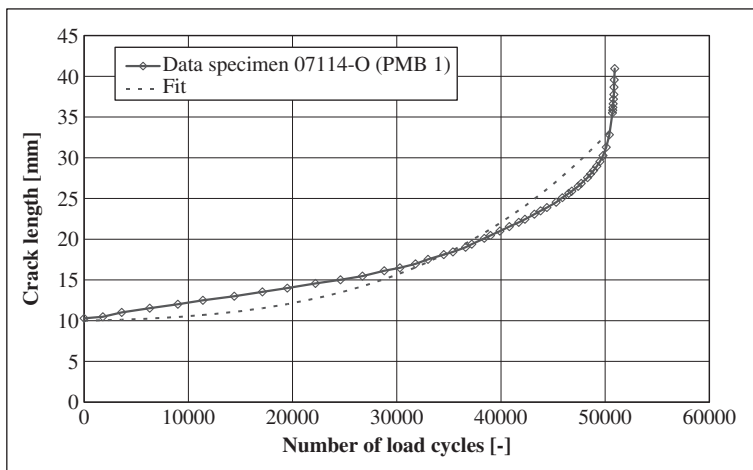


Figure 3. Example of calculated crack length against number of load cycles and curve fit.

summarized in table 3. Data regarding the length and duration of the crack propagation phase is given in table 4.

Four parameters are obtained from the force-ductility tests on the binders: first maximum force level ($F_{\max 1}$), strain at $F_{\max 1}$ (denoted as yield strain $\varepsilon_{\text{yield}}$), strain at failure ($\varepsilon_{\text{break}}$) and the deformation energy till failure (E_{break}). The average results are summarized in table 5.

5 DISCUSSION

Some of the specimens showed high dc/dN values at the beginning of the test. This is normally not observed during the crack initiation phase and may be explained by one or more of the following factors: irregularities (for example air voids) at the tip of the notch, the notch ends in large aggregates which easily break further, damage caused by sawing, etc.

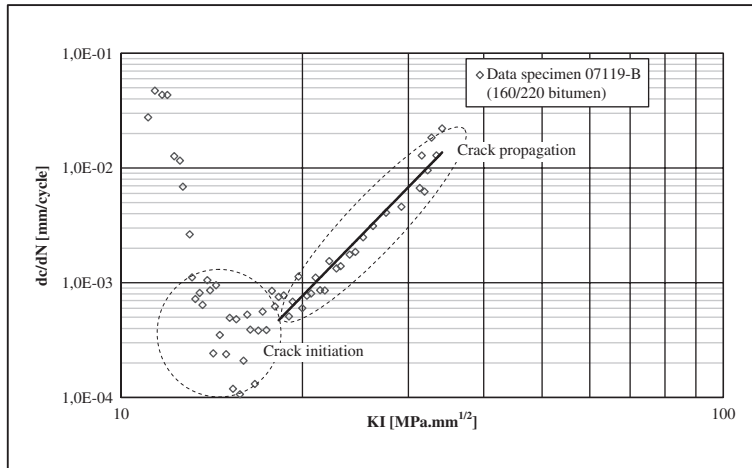


Figure 4. Relation between measured dc/dN and K_I for specimen with Pen 160/220 bitumen.

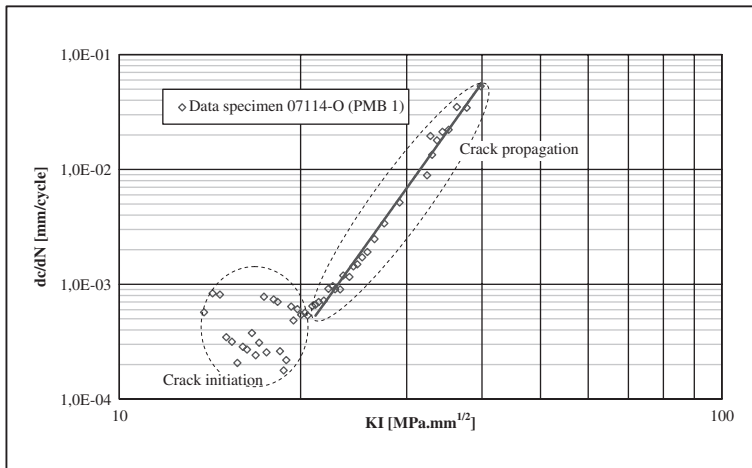


Figure 5. Relation between measured dc/dN and K_I for specimen with PMB1.

The duration of the crack propagation phase was relatively short for all binders. However, for four binders there was enough data to determine the parameters A and n with good confidence. Given existing literature the values for n may be considered a bit high. However, taking into account the high test frequency, the relatively low test temperature, the aged state of the asphalt mix and the type of asphalt mix, they may still agree well with results from other studies.

The results for PMB 2 and PMB 3 show larger variations than those for Pen 160/220 bitumen and PMB 1. A possible explanation for that may be the fact that the polymers that were used for PMB 2 and PMB 3 have a known and observed tendency to separate from bitumen (Wegan, 2000). Consequently, in the mixes these binders may not have been completely homogeneous anymore.

The material parameters found for Pen 40/60 bitumen are not realistic. The crack propagation phase was probably too short (both with respect to crack length and number of load cycles) to be able to determine the parameters correctly. This is also confirmed by the low correlation coefficient of the power function through the data during the (assumed) crack propagation phase. The results for Pen 40/60 bitumen are therefore excluded in the further discussion.

Table 3. Material parameters A and n obtained from results of cyclic SCB tests (8 tests per case).

		A	n	R ²
		[-]	[-]	[-]
Pen 40/60 bitumen	min	9.0E-57	14.4	0.53
	max	5.4E-24	37.9	0.90
	avg	not relevant	22.0	0.76
	COV	not relevant	37.3%	15.1%
	median	6.4E-31	19.9	0.76
Pen 160/220 bitumen	min	3.1E-11	3.93	0.92
	max	1.9E-08	5.62	0.97
	avg	not relevant	5.08	0.94
	COV	not relevant	10.8%	1.8%
	median	2.6E-10	5.20	0.93
PMB 1	min	1.5E-13	5.78	0.95
	max	2.6E-11	7.40	0.99
	avg	not relevant	6.85	0.98
	COV	not relevant	8.8%	1.6%
	median	3.6E-13	7.14	0.98
PMB 2	min	2.7E-24	4.82	0.92
	max	3.3E-10	14.2	0.97
	avg	not relevant	8.31	0.95
	COV	not relevant	35.4%	1.9%
	median	1.2E-14	7.66	0.95
PMB 3	min	7.1E-21	3.78	0.76
	max	8.1E-09	11.9	0.94
	avg	not relevant	6.85	0.89
	COV	not relevant	35.6%	6.6%
	median	3.4E-12	6.30	0.90

Table 4. Length and duration of the crack propagation phase.

	Start [c/h]		Length [$\Delta c/h$]		Cycles [-]	
	Avg	COV	Avg	COV	Avg	COV
Pen 40/60 bitumen	0.36	7.2%	0.12	25.2%	4,450	65.1%
Pen 160/220 bitumen	0.33	25.8%	0.21	22.1%	8,350	22.6%
PMB 1	0.28	22.7%	0.26	11.7%	6,000	23.1%
PMB 2	0.26	22.0%	0.19	31.1%	5,300	48.4%
PMB 3	0.32	11.9%	0.15	20.7%	8,750	27.3%

Table 5. Results of the force-ductility tests on the binders.

	F _{max1} [N]	ϵ_{yield} [%]	ϵ_{break} [%]	E _{break} [J]
Pen 40/60 bitumen	153	13	13	0.2
Pen 160/220 bitumen	88	43	412	5.1
PMB 1	169	40	584	18.8
PMB 2	307	37	110	7.2
PMB 3	207	14	14	0.2

Table 6. Crack propagation performance for two loading conditions (Pen 160/220 as reference).

	Stiffness modulus		Loading condition I		Loading condition II	
	[MPa]	[%]	K_I [MPa · √mm]	dc/dN [mm/cycle]	K_I [MPa · √mm]	dc/dN [mm/cycle]
Pen 160/220 bitumen	5,230	100	15.0	3.43E-04	25.0	4.88E-03
PMB 1	4,040	77	11.6	1.42E-05	19.3	5.45E-04
PMB 2	4,580	88	13.2	4.26E-06	22.0	2.13E-04
PMB 3	5,390	103	15.5	1.07E-04	25.8	2.67E-03

When of all tested specimens the obtained values for n are plotted against $\log A$ the following relationship between the two parameters is found ($R^2 = 1.00$):

$$\log(A) = -1.4397 \cdot n - 2.5273 \quad (7)$$

Although not part of the laboratory testing procedure, it is necessary to also have knowledge about the expected stress intensity factors in the pavement to enable comparison of the expected performance of the mixes. The stress intensity factors depend amongst others on the stiffness of the asphalt mix and the displacements around the crack (Ingraffea, 1980), which in turn also depend on the stiffness of the asphalt mix. However, for overlays the displacements are more controlled by the (deflection) of the underlying existing pavement layers than by the stiffness of the overlay mix. So, for that particular situation comparison is possible when the stiffness of the mixes is known. From the results of the FEM analyses mentioned before, the following correlation between mix stiffness and the COD amplitude at the beginning of the test can be obtained:

$$E_{mix} = 16.342 \cdot \left(\frac{500}{F_{SCB,N=1}} \cdot COD_{N=1} \right)^{-0.9972} \quad (8)$$

Where E_{mix} = stiffness of the asphalt mix [MPa], $F_{SCB,N=1} = (F_{max} - F_{min})$ at the beginning of the test [N] and $COD_{N=1}$ = COD at the beginning of the test [mm].

With this correlation the stiffness of the mixes is calculated. Using the obtained stiffness values the performance of the three PMBs is compared with Pen 160/220 bitumen for two loading conditions (note that the median values for A and n are used for this). The results are shown in table 6. In this table the K_I values for the PMBs are based on the chosen K_I values for the Pen 160/220 bitumen (Bondt, 1999), but corrected for the difference in stiffness modulus. It is clear that under these conditions PMB 1 and PMB 2 have the best performance (i.e. lowest rate of crack propagation); PMB 3 performs only slightly better than the Pen 160/220 bitumen. This result does not fully agree with field experience. Factors like healing (not included in the testing procedure but occurring in practice) and creep (taking place during the tests but little to none in reality) probably cause this discrepancy. For example, the difference in cumulative COD displacements for PMB 1 and PMB 2 is higher than expected on the basis of the determined crack propagation rates. This indicates that the mix with PMB 1 has had more creep deformation than the mix with PMB 2.

Possible correlations between the parameters obtained from the force-ductility tests and the results of the cyclic SCB tests have been assessed during the data analysis phase. It appears that a low value for the ductility parameters strain at failure (ϵ_{break}) and deformation energy till failure (E_{break}) is an indicator for poor performance. However, high values for these parameters do not seem a guarantee for good performance.

6 CONCLUSIONS AND RECOMMENDATIONS

A new testing procedure to assess crack propagation performance of asphaltic mixes has been developed in the Netherlands. Crack propagation is generated with cyclic semi-circular bending tests performed on notched specimens. The procedure has been completed successfully for one asphalt mix with different binders, but for the data analysis some modifications were necessary.

The duration of the crack propagation phase was relatively short for all binders. This may be improved with a shorter notch length (for example 5 mm).

The results do not fully agree with field experience. Creep occurring during the tests may (partly) cause this discrepancy and should be studied further. Also the effect of healing needs further attention.

No correlations were found between the parameters from the asphalt mixture testing and the force-ductility testing. It is recommended to assess correlations with parameters from relevant cyclic binder tests.

For comparison of binder performance it is probably advisable to use a finer and more binder rich asphalt mixture.

ACKNOWLEDGEMENT

The authors wish to thank the working group CROW-FEA for their efforts in developing the (initial) Dutch draft testing procedure used for the study that is presented in this paper, especially dr. ir. M.J.J. Jacobs, ir. F. Tolman and dr. ir. A.H. de Bondt.

REFERENCES

- Bijsterveld, W.T. van & Bondt, A.H. de. 2003. Bitumen specification for thermal reflective cracking applications. Eurasphalt & Eurobitume congress, Vienna, 12–14 May 2003.
- Bondt, A.H. de. 1999. Anti-reflective cracking design of (reinforced) asphaltic overlays. Ph.D – Thesis. Delft University of Technology. May 1999.
- CEN. 2006. prEN 12697-44. Test methods for hot mix asphalt – part 44: crack propagation by semi-circular bending test. October 2006.
- CROW. 2006. COMPASS⁺. The next step in specifying asphalt mixes. Final report of CROW task group FEA (in Dutch).
- Ingraffea, A.R. & Manu, C. 1980. Stress-intensity factor computation in three dimensions with quarter-point elements. International journal for numerical methods in engineering, Vol. 15, pp. 1427–1445.
- Scarpas, A. & Kringos, N. 2003. CAPA-3D Finite element analyses for the SCB test (in Dutch).
- Wegan, V. 2000. Microstructure of polymer modified binders in bituminous mixtures. Eurasphalt & Eurobitume congress, Barcelona, 20–22 September 2000.

A new laboratory test for reflective cracking in mode I and/or mode II

D. Perraton & G. Guissi

École de technologie supérieure, Quebec, Canada

P. Pierre & G. Doré

Université Laval, Quebec, Canada

ABSTRACT: Even though the overlay method results in reflective cracking due to thermal (mode I) and to load effects generated by truck traffic (modes I and II), it is nonetheless still the most important technique for rehabilitation; in fact, it is complemented by several systems that have been developed to prevent reflective cracking. Laboratory tools used to evaluate their performances and quantify their differences have thus far not proven to be useful, which is why a test has been developed at the École de technologie supérieure in Montréal to evaluate overlay systems used to prevent such cracking and to quantify their performance. Testing can be performed on laboratory samples or on sections collected from a pavement. The test simulates reflective cracking in an overlay subjected to a stretching cyclic displacement (mode I) combined with a vertical cyclic displacement (mode II). Asphalt concrete overlay samples mixed in the laboratory are compacted over substrate elements with a wheel track compactor, which is generally used to compact rutting specimens for the French Wheel Tracking Tester (FWTT). For asphalt concrete overlay samples collected from a pavement, specimens are glued directly to aluminium substrate plates using an epoxy material. This test allows mode I and/or mode II simulations at various frequencies and temperatures, and its preliminary results clearly show the difference between the performance of a Stress Absorbing Membrane Interlayer (SAMI) system and a conventional overlay system.

1 INTRODUCTION

Even though significant advances have been made in asphalt pavement rehabilitation, the overlay method still remains the most important technique in the domain. Several systems have been developed to prevent reflective cracking (Colombier, 1989 and 1991; Goacolou, 1982), but laboratory tools used to evaluate their performances and quantify their differences have thus far not proven to be useful, which is why a test has been developed at Montreal's École de technologie supérieure for use in evaluating the performance of overlay systems. The test simulates reflective cracking in overlays subjected to a stretching cyclic displacement (mode I), combined with a vertical cyclic displacement (mode II). This paper describes this new testing device and presents the results of a testing program used to evaluate the behaviour of three different overlay systems.

2 GENERAL DESCRIPTION

A laboratory test method has been developed at the École de technologie supérieure in Montreal (QC, Canada) for use in evaluating overlay systems used to prevent reflective cracking. Testing can be performed on laboratory samples or on sections collected from a pavement. The test simulates reflective cracking in an overlay subjected to a stretching cyclic displacement (mode I), combined

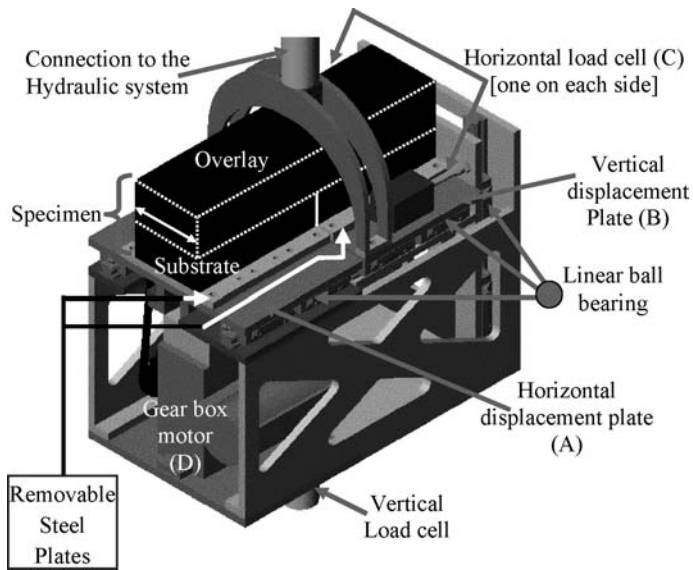


Figure 1. Overview of apparatus used to simulate reflective cracking of overlay systems.

with a vertical cyclic displacement (mode II), and is performed at a constant temperature, using the apparatus designed to be kept in a thermal control chamber. Figure 1 presents a schematic description of the apparatus.

The specimen is glued to two moveable plates, one of which can move in the horizontal plane (Fig. 1- plate A), and the other, freely in the vertical plane (Fig. 1 - plate B). The moveable plates (A and B) are set on linear bearings on parallel rails. The horizontal motion of plate B is restrained by two load cells placed on either side of the plate. These load cells give the strength passing through the overlay system right over the substrate notched section. The evolution of the horizontal strength is directly related to the overlay system degradation. The horizontal displacement is driven by a mechanical system, and the vertical one, by a hydraulic system.

Extensometers are used to measure the vertical and horizontal displacements of the sample. One set is attached to the surface of the overlay as shown in Figure 2, and another beside the sample, directly glued to 50 mm from the top surface of the overlay system, over the notch.

3 SPECIMEN SIZES

Asphalt concrete overlay samples mixed in the laboratory are compacted directly over asphalt concrete substrates glued to steel plates, using a wheel track compactor, which is generally used to compact rutting specimens for the French Wheel Tracking Tester (FWTT). For asphalt concrete overlay samples collected from a pavement, the cut samples are glued with an epoxy material directly to asphalt concrete substrates, which are also glued to removable steel plates with an epoxy material. The specimen sizes for testing are shown in Table 1.

4 TESTING CONDITIONS

Testing is done at constant temperatures under different solicitations: mode I, mode II, and modes I and II simultaneously. The possible ranges of testing conditions are shown in Table 2.

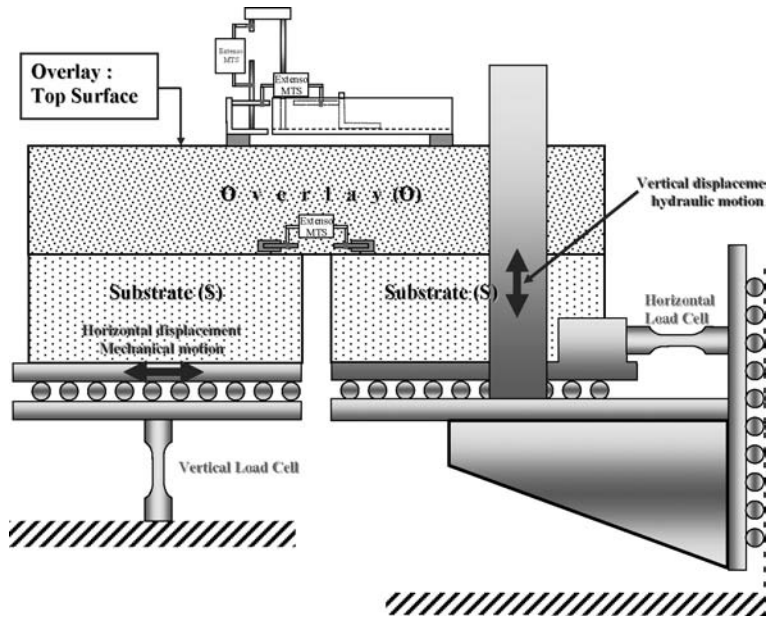


Figure 2. Sketch to illustrate the test and measurement setup.

Table 1. Specimen sizes for testing.

Layer	Material	Width mm	Thickness mm	Length mm	Connection between the upper layer to the underlayer material
Overlay	Asphalt concrete (lab or in situ)	120	25 to 80	440	• Interface material ⁽²⁾
Substrate ⁽¹⁾	Asphalt concrete (Lab or in situ)	120	10 to 50	220	• Epoxy glue on removable steel plates
	Concrete	120	10 to 50	220	• Screwed directly to removable steel plates
	Aluminium	120	30	220	• Screwed directly to removable steel plates
Notch		120	10 to 50	3 to 10	

⁽¹⁾ Two per overlay system to be tested.

⁽²⁾ The type of connection to the substrate will depend on the overlay system to be tested and on the substrate used. For an asphalt bituminous substrate, the simple method involves using a bitumen material.

Table 2. Ranges of testing conditions.

Testing temperature	Horizontal displacement (Δx)	Vertical displacement (Δy)
Isotherm condition Range: -20°C to +50°C	Sinusoidal motion Amplitude: Displacement is controlled at the base of the substrate in the 0 to 3 mm range Frequency of 0.0003 Hz	Sinusoidal motion Amplitude: Displacement is controlled in reference to the vertical displacement on the top surface of the overlay in the 0 to 80 μm range Frequency of 1 Hz

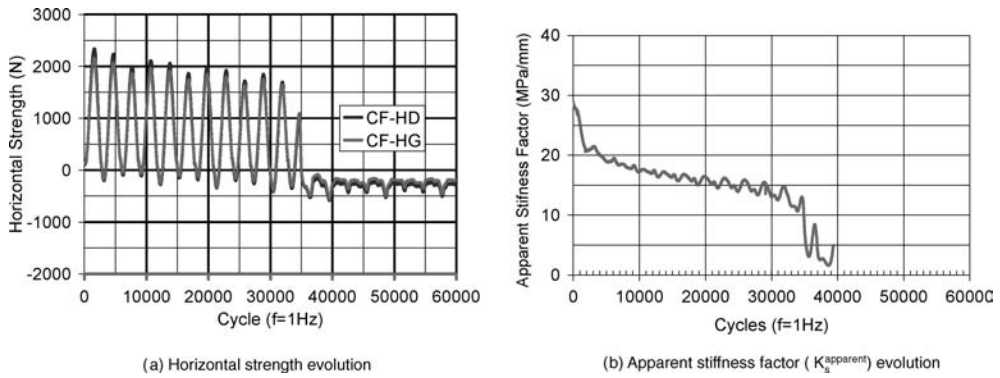


Figure 3. Typical test result.

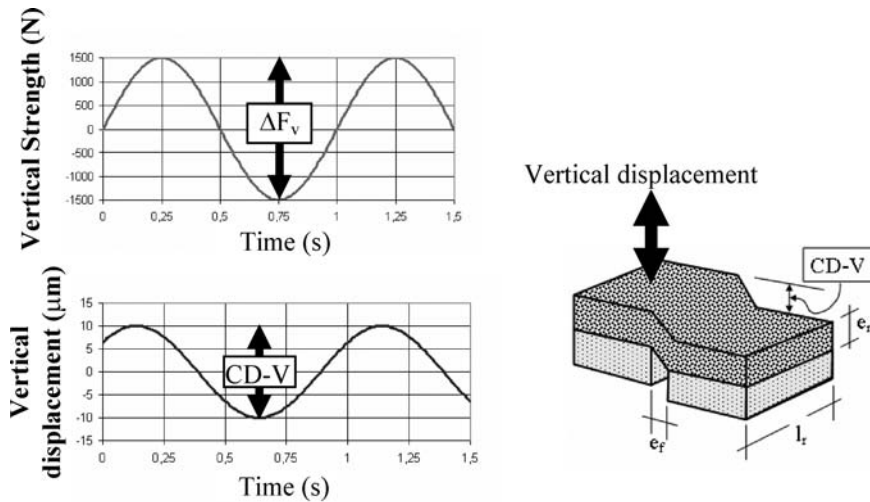


Figure 4. Sketch to illustrate the evolution of the vertical parameters used to calculate the $K_s^{apparent}$ values.

5 PARAMETERS USED TO FOLLOW UP THE OVERLAY SYSTEM DEGRADATION

The overlay system degradation is evaluated under a cycling process by monitoring the evolution of the horizontal strength and by calculating the system's apparent stiffness factor ($K_s^{apparent}$).

The two load cells placed behind the testing sample, and which work in the horizontal plane, give the strength passing through the overlay system under solicitation. Figure 3a shows a typical result of the horizontal force evolution under testing.

Depending on the vertical monitored displacement measured on the top surface of the overlay and the associated vertical strength, a part of the damage evolution of the overlay can be followed by the ratio between the amplitude of the apparent shear stress and the amplitude of the corresponding vertical displacement, which is also known as the apparent stiffness factor ($K_s^{apparent}$). Since the test is not homogeneous, the shear stress cannot be directly known. By assuming a shear mean value in the overlay, the $K_s^{apparent}$ value can be calculated according to the following relationship (Figure 4):

$$K_s^{apparent} = \frac{\Delta F_v * 1000}{e_r * l_r * \Delta(CD - V)} \quad (1)$$

Figure 3b shows typical variations in the apparent stiffness factor ($K_s^{apparent}$) under testing conditions.

5.1 Life span of the overlay system

The failure of the overlay system under solicitation is determined according to the strength measured by the horizontal load cells (Figs. 1 and 2). As a crack progresses up to the surface of the overlay system, the strength decreases until it eventually reaches zero at the failure point. The life span of the sample is then expressed as the number of vertical cycles ($f = 1$ Hz) needed to reach the failure point ($N_f^{VC} : f$ for failure and VC for vertical cracking propagation). Nevertheless, cracks will sometimes propagate in the direction parallel to the interface before shooting all the way up to the top surface. In such cases, the apparent stiffness factor of the overlay system ($K_s^{apparent}$) will be used to establish the life span of the overlay system, which will correspond to the number of vertical cycles needed to achieve a 50% reduction in the initial $K_s^{apparent}$ value ($N_f^{HC} : HC$ for horizontal cracking propagation).

6 EXPERIMENTAL PROGRAM

Three different overlay systems commonly used for road rehabilitation were tested. For the substrate layer, a classical HMA, known as **EB14**, was used, and the **ESG10** asphalt concrete mix, typically used in Quebec for top surface layers, was used as the top layer in the overlay system. Three different interfaces between the overlay and the substrate were tested: 1) emulsion (REF: 0.25 kg/m²), 2) asphalt sand mix (CH10), and 3) a Stress Absorbing Membrane Interlayer (SAMI). The SAMI system consists in covering the substrate with a 3 mm thick elastomer bitumen membrane, itself covered with a cold mix asphalt (~15 mm) prior to the top layer being compacted with the ESG10 asphalt mix. The cold mix asphalt acts as a thermal barrier to the membrane, protecting it during the top layer material (ESG10) compaction process.

6.1 Testing conditions




In Nordic countries, seasonal temperature variations initiate transversal cracking in the pavement and thus constitute a significant factor in the reflective cracking that occurs during overlay rehabilitation, as they create the opening-stretching cyclic motion of cracks (mode I mechanism) (Colombier, 1989). To avoid mechanical testing problems due to temperature cycles, we decided to simulate the thermal effect using a mechanical motion, imposed on the horizontal plane of the overlay system, under an isotherm condition. To estimate the magnitude of the motion and the appropriate testing temperature, we referred to specific conditions in the eastern Canadian environment. For the Montreal region in Quebec, the annual mean winter temperature is nearly -5°C . Assuming that the spacing length between transversal cracks in a damaged pavement in Quebec often measure approximately 3 to 4 meters, the magnitude of the opening-stretching motion of a transversal crack with a temperature variation of between -5 and -30°C will be about 1 millimeter. A recent road investigation of the opening-stretching motion of transversal crack tips by Transports Quebec revealed variations of less than 3 mm between the summer and winter seasons in over 80% of all instrumented cracks (more than 320 transversal cracks were instrumented) (St-Laurent and Bergeron 2000). Table 3 shows the testing conditions used in the experimental program.

7 TEST RESULTS

Figure 5 and Table 4 present the evolution of both the horizontal strength and the $K_s^{apparent}$ values for the three overlay systems tested.

As we can see, the new testing device is useful in highlighting the differences in the ability of the overlay systems to delay reflective cracking. The life span of the reference overlay system (emulsion interface) is less than those of the two other systems, and it was observed that the system with the SAMI interface did not manifest any reflective cracking at all under testing. The test was

Table 3. Testing conditions used in experimental program.

Sample number	Asphalt concrete substrate	Interface material overlay-substrate	Asphalt concrete overlay	Testing conditions	Sample
A	EB14 (55 mm)	Emulsion REF	ESG10 (55 mm)	$T = -5^{\circ}\text{C}$ $\Delta x = 1 \text{ mm}$ $\Delta y = 20 \mu\text{m}$	
B	EB14 (55 mm)	Asphalt sand mix CH10 (15 mm)	ESG10 (55 mm)	$T = -5^{\circ}\text{C}$ $\Delta x = 1 \text{ mm}$ $\Delta y = 20 \mu\text{m}$	
C	EB14 (55 mm)	Elastomer membrane SAMI (14 mm)	ESG10 (55 mm)	$T = -5^{\circ}\text{C}$ $\Delta x = 1 \text{ mm}$ $\Delta y = 20 \mu\text{m}$	

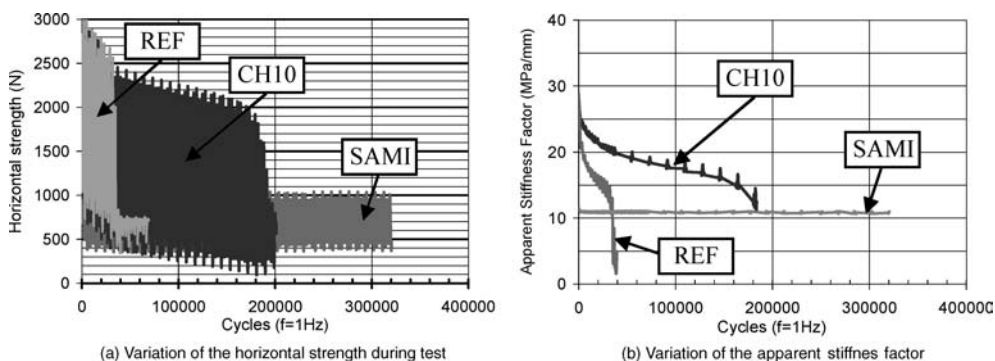


Figure 5. Test results for the three different overlay systems tested with the new device.

stopped after a period of over 3.5 days. Overlay failure was observed at about 35,000 cycles for the reference overlay system, and at more than 180,000 cycles for the overlay system with a sand mix asphalt interface (CH10).

Figure 6 shows the typical cracking observed post failure for the reference overlay (emulsion) and for the overlay system with a sand mix asphalt interface.

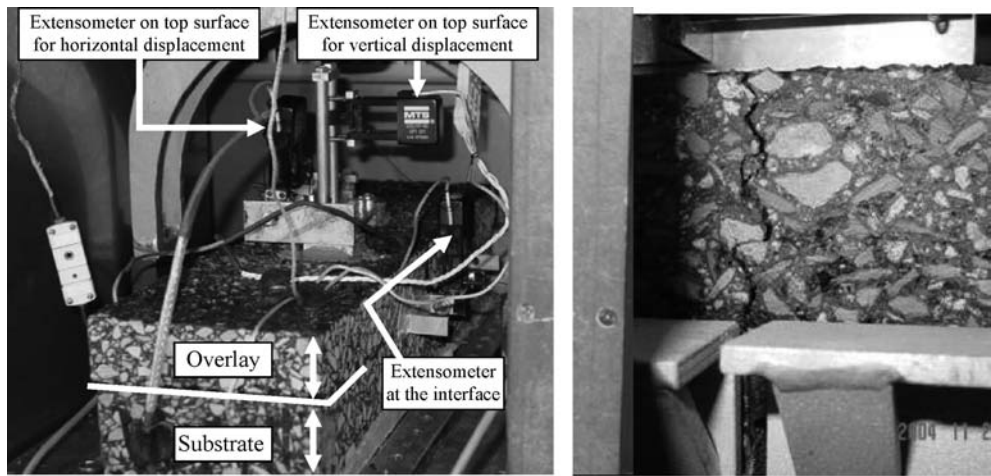
Figure 5a shows the differential strength level induced in the top layer material under cycling solicitations. The SAMI interface significantly affects the horizontal strength passing through the top layer (ESG10) of the overlay system, and the elastomer membrane directly affects the level of stress on the top layer of the overlay. The new testing device clearly shows the distinctive behavior of the SAMI interface as compared to those of the two other overlay systems tested. It is clear that the SAMI interface reduces the level of the strength transit on the top layer of the overlay system by dissipating part of the mechanical energy applied to the sample.

Measurements in the vertical direction indicate a slower damage evolution in the top layer material in the SAMI overlay system. Figure 5b shows the evolution of the apparent stiffness factor under loading cycles for the three overlay systems tested. The slope of the “ $K_s^{\text{apparent}}-N$ ” relationship is related to the damage rate per cycle of loading. For each loading cycle, micro cracks and heat dissipation in the overlay materials will cause a significant drop in the apparent stiffness factor of the overlay system, and the rate of that drop is an indicator of the damage progression in the system.

Table 4. Compilation (Substrate: EB14; testing temperature: -5°C).

Overlay (ESG10)	Displacement												
	Interface	N_f cycles	Δx 1st cycle		Δx Prior failure		Δy 1st cycle On top ² μm	1st cycle		Prior failure			
			Bottom ¹ μm	On Top ² μm	Bottom ¹ μm	On top ² μm		ΔF_H (Right) N	ΔF_H (Left) N	ΔF_H (Right) N	ΔF_H (Left) N		
55	Emulsion	$\sim 35,000$	72	110	154	76	18.6	2544	2346	2114	1974	$K_s = 29 \text{ MPa/mm}$	$K_s = 7 \text{ MPa/mm}$
74	CH10	$\sim 180,000$	110	126	280	74	17.4	2170	1990	1754	1898	$K_s = 28 \text{ MPa/mm}$	$K_s = 13 \text{ MPa/mm}$
67	SAMI	$\sim 320,000$	30	32	24	24	18.6	680	676	522	496	$K_s = 12 \text{ MPa/mm}$	$K_s = 11 \text{ MPa/mm}$

- (1) Displacement measured at the bottom of the overlay material with an extensometer glued to 50 mm from the top surface of the overlay system. The length of the measurement is set at 55 mm (details on Fig. 2)
 (2) Displacement measured directly on the top surface of the overlay (details on Fig. 2)



a) Overview of the sample with extensometers b) Typical failure crack observed for the reference and asphalt sand mix overlay systems

Figure 6. Reflective cracking in the overlay at the failure point.

For the first 40,000 loading cycles, Figure 7 highlights the damage progression of each overlay system tested, and Table 5 indicates the slope in the linear part of the “ $K_s^{apparent}-N$ ” relationship for each one. Based on the reference overlay system (emulsion interface), we estimate that the relative rate of damage of the overlay system with an asphalt sand mix interface is reduced by 41%, and that for the SAMI interface, this reduction is over 98%. That means the damage progression of the SAMI overlay system is 75 times slower than that of the reference overlay system (emulsion

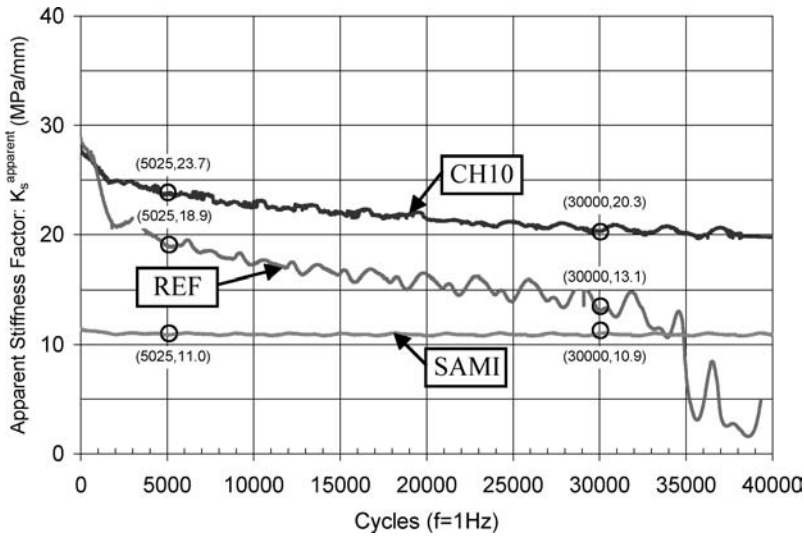


Figure 7. Relation of the apparent stiffness factor ($K_s^{apparent}$) based on the number of cycles for the first 40,000 loading cycles of the three different overlay systems tested ($T_{testing} = -5^{\circ}C$; $\Delta x = 1$ mm; $e_r = 55$ mm; Substrate = EB14).

Table 5. Slope of the linear part of the relationship between $K_s^{apparent}$ and the number of cycles.

Overlay system	Stiffness rate decreasing in the first 30,000 cycles ($K_s^{apparent}$ vs. N)		Life span	
	Slope ($\times 10^5$) MPa/mm/cycle	Relatively ⁽¹⁾ %	N_f^{VC} Cycles	Relatively ⁽¹⁾
Emulsion – REF	-23.2	100	~35,000	1.0
Asphalt sand mix – CH10	-13.6	59	~180,000	5.1
Elastomer membrane – SAMI	-0.4	<2	>320,000	>9.1

(1) Ratio of calculated slope of an overlay system with respect to the reference system, expressed in %

(2) Ratio of the measured N_f^{VC} of an overlay system with respect to the reference system

interface). From the life span values, we see that the overlay system with an asphalt sand mix interface and that with a SAMI interface are respectively about 5 and 10 times more durable than the reference interface. For the SAMI interface, this value is conservative, given that the failure point was not reached under testing conditions.

7.1 Horizontal strain and horizontal strain rate under testing

Because of the viscous elastic behavior of the bituminous material, the horizontal strain rate applied to the sample, $\dot{\epsilon}$, and the level of the strain itself, ϵ , will both affect the life span of the overlay system. However, since the test is not homogeneous, only an estimated value of these values can be determined.

We can assume that the interface zone will drive the reflective process in the overlay. To estimate the level of horizontal strain applied to the overlay, we will refer to the displacement measurement with the extensometer glued to 50 mm from the top surface of the overlay system, over the notch

Table 6. Horizontal strains and strain rates under testing conditions for the three overlay systems tested ($T_{\text{Testing}}: -5^{\circ}\text{C}$; Substrate: EB14; Top layer: ESG10; $f_t: 320 \times 10^{-6}$ Hz).

Overlay interface	$\Delta x^{(1)}$ μm	$\varepsilon^{(2)}$ μs	$\bar{\varepsilon}^{(3)}$ $\mu\text{s/h}$	N_f Cycles	ΔF_H N
Emulsion – REF	72	1309	3020	35,000	5890
Asphalt sand mix – CH10	110	2000	4615	180,000	4160
Elastomer membrane – SAMI	30	545	1258	320,000	1356

(1) Horizontal displacement measured at the bottom of the overlay material (refer to Table 4)

(2) ε is calculated based on the interface extensometer length measurement of 55 mm

(3) $\bar{\varepsilon}$ ($\mu\text{s/hr}$) = $7200 * f_t * \varepsilon$ (μs)

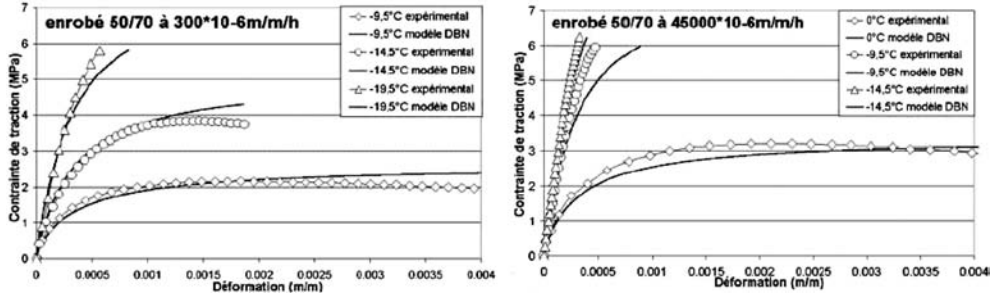


Figure 8. Typical stress-strain relationships of an asphalt concrete mix (bitumen 50–70) tested under direct traction test on cylindrical specimen ($\phi 80 \times 120 \text{ mm}^2$) for various testing temperature and strain rate solicitations (Olard, 2003).

(Fig. 2), and to the imposed horizontal displacement evolution under testing, when calculating the horizontal strain rate. As we note in Table 2, the imposed horizontal displacement evolution is sinusoidal, and we will refer to a mean value for the horizontal strain rate, $\bar{\varepsilon}$, by assuming a linear displacement variation for each cycle. The horizontal strains (ε) and the mean value of the horizontal strain rates ($\bar{\varepsilon}$) for the three overlay systems tested are presented in Table 6.

Table 6 shows that the level of the strain and the rate of the strain applied to the overlay vary with the system tested. The level of strain applied to the overlay system during testing is relatively high, with a magnitude almost equivalent to the critical strain level observed for direct traction tests, as is shown in Figure 8.

For a strain rate of $300 \mu\text{s/h}$, Figure 8 shows that the admissible stress at -9.5°C is low, less than 2.2 MPa , and drops for a strain higher than 0.15% (0.0015). Based on the results presented in Table 6, the estimated level of the horizontal strain applied to the overlay system under testing conditions is very severe for the overlay systems with an emulsion interface and with an asphalt sand mix interface (0.13% and 0.20% , respectively) and lower for the SAMI interface (0.06%).

7.1.1 Relationship between the horizontal strength (F_H) and the imposed strain rate

Figure 9 shows the relationship between the horizontal strength passing through the overlay system measured after the first horizontal loading cycle ($\sim 3,125$ seconds) and the corresponding estimated strain rate. The measured horizontal strength is induced by the horizontal and vertical displacements. We found that the life span is correlated to the horizontal strain rate imposed on the overlay system.

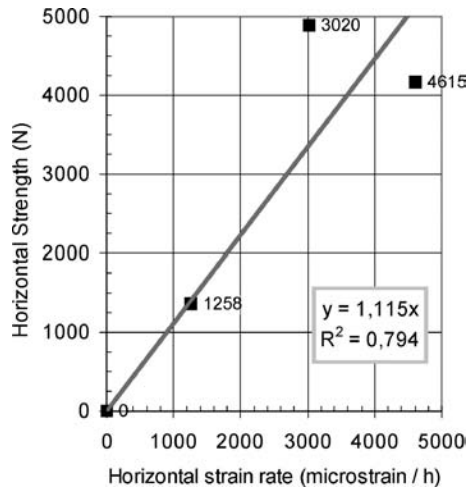


Figure 9. Relationship between the horizontal strength and the horizontal strain rate applied to the sample for all overlay systems tested ($T_{\text{Testing}} = -5^{\circ}\text{C}$; $e_r = 55 \text{ mm}$; Top layer: ESG10).

8 CONCLUSION

The new testing device is useful for highlighting the differences between overlay systems in terms of their respective abilities to delay reflective cracking. The life span of the reference overlay system (emulsion interface) is lower than that of the SAMI overlay system. The SAMI interface has a considerable impact on the horizontal strength passing through the top layer (ESG10) of the overlay system: the elastomer membrane directly affects the level of stress in the top layer of the overlay. Based on the reference overlay system (emulsion interface), we estimate that the relative rate of damage of the overlay system with an asphalt sand mix interface is reduced by 41%, and for the SAMI interface, this reduction is more than 98%, which means that the damage progression of the SAMI overlay system is 75 times slower than that of the reference overlay system (emulsion interface). In terms of life span values, the overlay system with the asphalt sand mix interface and that with the SAMI interface are respectively about 5 and 10 times more durable than the reference interface.

The new testing device will allow the optimization of overlay systems and top layer materials in order to minimize reflective cracking after overlay rehabilitation. Different asphalt mixes incorporating different types of materials (rubber and shingle particles, additives, etc.) could be investigated and optimized in the laboratory prior to being validated on actual roads.

REFERENCES

- Olard, F., 2003, Comportement thermomécanique des enrobés bitumineux à basses températures. Relations entre les propriétés du liant et de l'enrobé". Ph.D. Thesis, *ENTPE*.
- Colombier, G., 1989, Fissuration des chaussées – nature et origine des fissures – Moyens pour maîtriser leur remontée. *LCPC*, France, 22p.
- Colombier, G., 1991, Fissuration des chaussées – nature et origine des fissures, moyens pour maîtriser leur remontée. Journée: "La lutte contre les fissures", *ENPC*.
- Goacolou, H., Marchand, JP., 1982, Fissuration des couches de roulement, 5^{ème} Conférence Internationale sur les chaussées bitumineuses, *DELFA*.
- Lefort, M., Sicard, D., Merrien, P., 1999, Techniques anti-remontée des fissures: Guide d'emploi en chaussées aéronautiques. Bonneuil-sur-Marne, France: *Service technique des bases aériennes*.
- St-Laurent, D., Bergeron, G., 2000, Interventions pour réduire la fissuration des chaussées, 4th *International RILEM Conference on Reflective Cracking in Pavements: Research and Practice*, Ottawa, Canada.

New procedure to evaluate fatigue of bituminous mastics using an annular shear rheometer prototype

B. Delaporte

SETEC – groupe Roger Martin, Diors; Formerly ENTPE & TOTAL, France

J. Van Rompu

ENTPE, France

H. Di Benedetto, P. Chaverot & G. Gauthier

TOTAL France, Centre de Recherche de Solaize, France

ABSTRACT: An experimental campaign has been performed at ENTPE/DGCB laboratory in order to measure fatigue properties of bituminous mastics with a specifically developed experimental device, the annular shear rheometer (ASR). This apparatus allows measuring the linear viscoelastic (LVE) shear complex modulus ($G^* = G^*LVE$) of bituminous materials for small strain amplitudes, and the pseudo complex modulus G^*NL in the non linear domain for higher strain levels applied during fatigue tests.

Fatigue tests were performed using sinusoidal shear loadings at 10°C and 10 Hz, with different strain amplitudes ranging from 0.125% to 0.5%. A specific experimental protocol was used in order to measure the evolution of the LVE properties (at low strain level and at different frequencies) of the materials during the fatigue test. In the first phase of the test (phase 1), LVE complex moduli measured within the linear domain are very close to the LVE G^* master curve of the mastic. The decrease of G^* in this phase can be explained by an “equivalent” heating of the material. It has been compared to the “real” heating measured by a temperature sensor in contact with the mastic. It seems that heating does not entirely account for the modulus decrease observed in phase 1. Then, the stiffness decrease at the beginning of the fatigue test could be explained by both heating and another phenomenon such as thixotropy.

1 INTRODUCTION

In pavement structure, fatigue is one of the main failure mode for bituminous materials. It results from repeated applications of loading cycles, which can damage the materials until macro-cracking. Binder plays an important role in the failure mechanism induced by fatigue in the bituminous mixture (Bahia, Zhai et al., 1999). Then, the fatigue properties of bituminous binders have been evaluated by different authors, using oscillation testing with a DSR (Dynamic Shear Rheometer) (Soenen, De La Roche et al., 2003; Bodin, Soenen et al., 2004; Soenen, De La Roche et al., 2004; Bocci, Cerni et al., 2006). The fatigue life of binder is sensitive to the applied initial load. It was also confirmed that the fatigue behaviour of binders is a significant phenomenon at low temperature. “True” fatigue, as associated with internal micro-damage, occurs actually at temperatures in which the modulus is “high” (low temperature), whereas in the low-modulus region (high temperature) edge buckling or instability flow dominates (Anderson, Le Hir et al., 2001; Planche, Anderson et al., 2003). Fatigue of binder has also been studied in previous works in order to find correlation between the fatigue behaviour of binder and the one the mixture (Baaj, 2002; Soenen, De La Roche et al., 2003; Soenen, De La Roche et al., 2004).

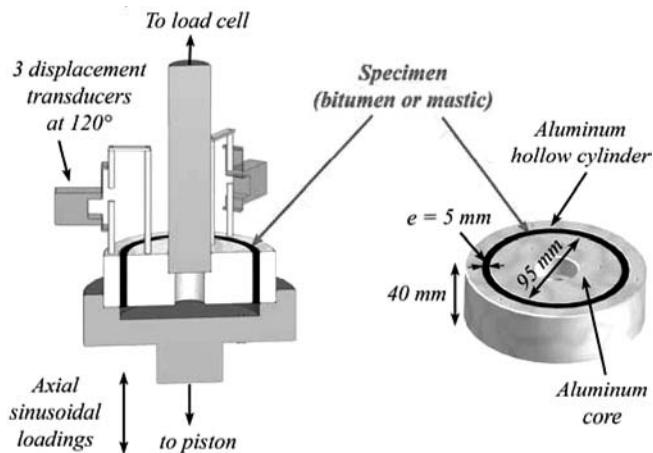


Figure 1. Schematic view of the annular shear rheometer (ASR) for bitumen and mastic.

It is generally admitted that the mastic, composed of bitumen and filler, is the “real” binder in the bituminous mixture. It is known to play an important role in the performance of bituminous mixtures. Consequently, studies on mastics, rather than on pure bitumen, may be more appropriate to investigate correlations between fatigue behaviour of binders and asphalt mixtures. Recent studies showed that there is a significant difference between the fatigue results for pure bitumen and those associated mastics. Fatigue life was significantly affected by the filler concentration (Airey, Thom et al., 2004; Airey, Liao et al., 2006; Thom, Osman et al., 2006). In addition, it was observed that the temperature effect was similar on the fatigue behaviour of bitumen and mastic.

A general research topic aimed at analyzing and modelling fatigue behaviour of mastics, for different types of fillers and bitumens, is currently being conducted at the ENTPE/DGCB laboratory in cooperation with Total Company. The fatigue study of mastics treated in this paper presents two interests. On the one hand, the experimental device (the annular shear rheometer) allows performing homogeneous tests, which is generally not the case for classical apparatuses (Di Benedetto, De La Roche et al., 2004). On the other hand, the linear viscoelastic properties in the small strain domain of the tested materials are measured during fatigue tests, at different frequencies (from 0.03 Hz to 10 Hz). Results allow analyzing the change of the LVE complex modulus (G^*_{LVE}) during fatigue test.

The experimental campaign is presented, including the description of the annular shear rheometer, tested material and loading protocol. Typical results are detailed by plotting different measured parameters as a function of the cycle numbers, such as complex modulus during fatigue (G^*_{NL}), shear strain, temperature of the specimen and linear viscoelastic modulus G^*_{LVE} . Interpretation of the parameters evolution is proposed. The influence of temperature and thixotropy is underlined.

2 EXPERIMENTAL CAMPAIGN

2.1 Presentation of the annular shear rheometer

The principle of the annular shear rheometer (ASR) consists in applying sinusoidal shear stress or sinusoidal shear strain (distortion) on a hollow cylinder of bitumen or mastic, at different temperatures and frequencies. The hollow cylinder has a rather large size: 5 mm thickness, 105 mm outer diameter and 40 mm height. With these geometrical features, the test is homogenous as a first approximation even with aggregate sizes up to 1 millimetre. A schematic view of the apparatus is presented in figure 1 (Delaporte, Di Benedetto et al., 2005; Delaporte, Di Benedetto et al., 2007).

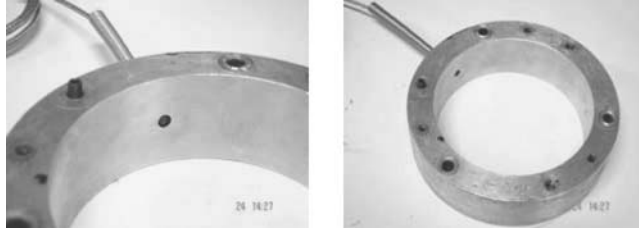


Figure 2. Pictures of the temperature sensor inserted into the external aluminium mold.

A sinusoidal cyclic excitation is applied in stress or strain mode using the control system of a 50 kN capacity hydraulic press on which the ASR is fixed. Strain is measured by three displacement transducers placed at 120° around the sample. The control strain is made with the mean value of the three displacement measurements. The transducers measure the displacement between outer lateral surface and inner lateral surface of the bituminous hollow cylinder. The outer surface sticks to the aluminium hollow cylinder linked to the mobile piston of the press. The inner surface of the sample adheres to the aluminium core, which is linked to the load cell. The apparatus allows measuring the linear viscoelastic (LVE) shear complex modulus of bituminous materials for small strain amplitudes called G^*_{LVE} , and the non linear modulus (G^*_{NL}) for higher strain levels applied during fatigue tests. In the following G^*_{NL} is noted G^* otherwise specified.

The complex shear modulus (G^*) of the material can be obtained from the data. Expression of the complex shear modulus G^* is given in equation (1):

$$G^* = |G^*| e^{i\phi} = G_1 + iG_2 \quad (1)$$

$|G^*|$ is the norm of the complex shear modulus, ϕ is its the phase angle, G_1 is the storage modulus and G_2 is the loss modulus. G^* can be measured at different temperatures from about -25°C to 80°C and different frequencies (f_r) from 0.03 Hz to 10 Hz. $|G^*|$ is the ratio between the amplitude of distortion γ_0 with $\gamma(t) = \gamma_0 \sin(\omega t - \phi)$, and the amplitude of shear stress τ_0 with $\tau(t) = \tau_0 \sin(\omega t)$, where $\omega = 2\pi f_r$. Phase angle ϕ is calculated by measuring the phase lag between load and displacement signals.

As the material is non linear, G^* is a function of strain amplitude. In the small strain domain, the behaviour is linear viscoelastic (LVE) and the constant value of G^* (independent of strain amplitude) is noted G^*_{LVE} (Olard, Di Benedetto et al., 2003; Airey and Behzad, 2004; Delaporte, 2007). Two sensors are used for the temperature measurements. One is fixed in the thermal chamber. The other one is inserted in the aluminium mould and is in contact with the material as shown in figure 2. It allows assessing the heating of the material during fatigue tests.

2.2 Testing procedures

Fatigue tests consist in applying shear strain at a frequency of 10 Hz and a temperature of 10°C . The study is realized on a unique mastic composed of a 50/70 penetration grade pure bitumen associated to a limestone filler proportioned at 30% in volume ($V_{\text{filler}}/(V_{\text{bitumen}} + V_{\text{filler}}) = 30\%$). Six tests have been performed in strain control mode, including four different strain levels and two duplicates. The selected strain levels, reported in table 1, are not within the small strain domain (linear domain). Then, the fatigue complex modulus is a non-linear complex modulus. It depends on strain amplitude and is different of G^*_{LVE} at 10 Hz. Shear stress values measured at the first loading cycles of the test are also reported in table 1. Test name is chosen as follow: in M30D1250, M stands for “mastic”, “30” for the percentage of filler in volume, “D” means deformation mode and “1250” is the strain amplitude in 10^{-6} m/m (μdef).

Table 1. Characteristics of the fatigue tests.

Test name	Control mode	Strain amplitude ε_{rz} (%)	Stress amplitude τ (Shante and Kirkpatrick) at the first cycle of the test
M30D1250	strain	0.125	351
M30D1250R01	strain	0.125	378
M30D1800	strain	0.180	507
M30D2500	strain	0.250	676
M30D2500R01	strain	0.250	685
M30D5000	strain	0.500	1042

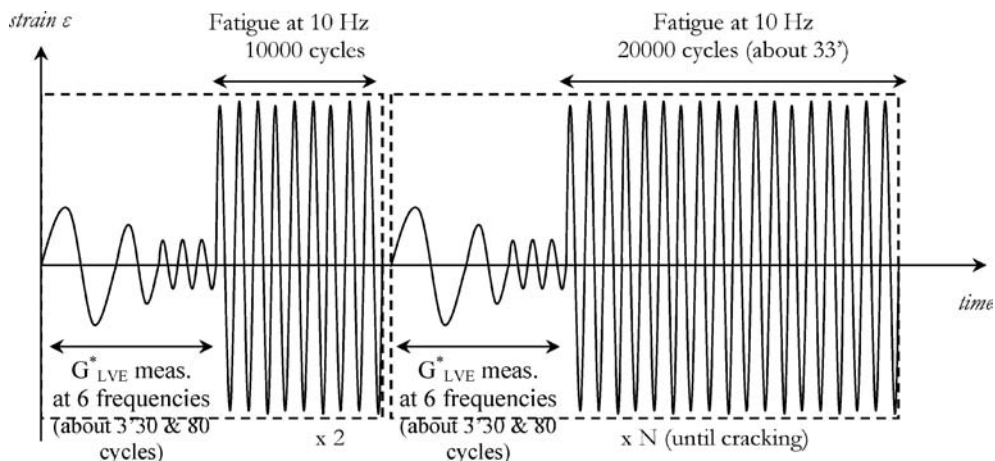


Figure 3. Fatigue testing protocol in strain control: G^*_{LVE} is measured from 0.03 to 10 Hz.

The great originality and improvement of the test is that, at chosen intervals, complex modulus measurements in the linear domain are inserted during fatigue tests. The specimen is loaded at lower strain levels. These measurements are performed for 6 frequencies, from 0.03 Hz to 10 Hz (0.03, 0.1, 0.3, 1, 3 and 10 Hz) every step of 20000 fatigue cycles. Additional measurements are performed before starting the fatigue cycles and 10000 cycles after the test has started. The LVE G^* determined at the frequency f_r and at the step i is denoted as $G^{*i}_{f_r}$. It has to be underlined that LVE G^* measurements period (about 218 seconds or 3.6 minutes) is “short” in comparison to fatigue period (about 33 minutes for 20000 cycles). For the material, this period can probably be considered as a quasi rest period. Transition between, i) fatigue loading and LVE G^* measurements, as well as, ii) LVE G^* measurements and fatigue loading is instantaneous. The general testing protocol is presented in Figure 3. The interest of this protocol is to allow analysing the LVE G^* change during fatigue test.

The use of different frequencies allows characterizing the LVE properties not only at 10 Hz (frequency of the fatigue test) but on a range of frequencies. The evolution of the global LVE law during fatigue test can then be determined.

3 TYPICAL RESULTS

3.1 Fatigue complex modulus

Results of fatigue test M30D1250 are considered, as example. Fatigue complex modulus G^* , in norm, is plotted as a function of the number of cycles in figure 4. Phase angle change is presented in figure 5 and G^* is plotted in Black space in figure 6. As suggested in previous works (Di Benedetto

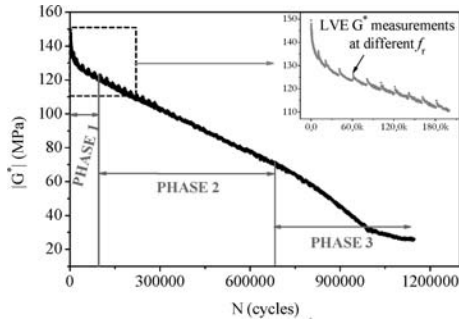


Figure 4. Complex modulus $|G^*|$ as a function of the number of cycles during fatigue test M30D1250.

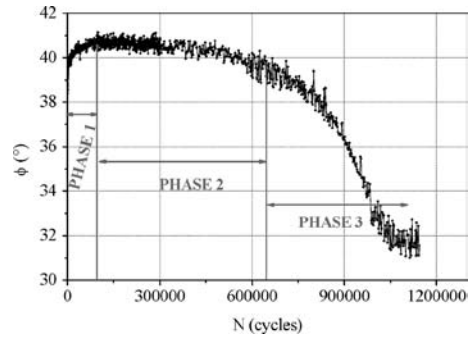


Figure 5. Phase angle ϕ as a function of the number of cycles during fatigue test M30D1250.

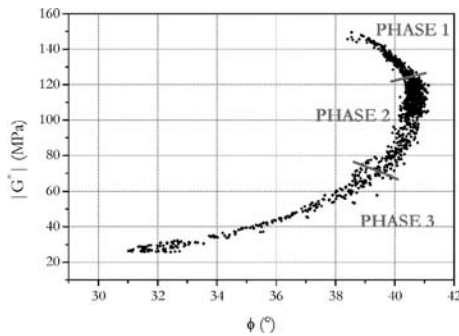


Figure 6. Representation of G^* in Black space during fatigue test M30D1250.

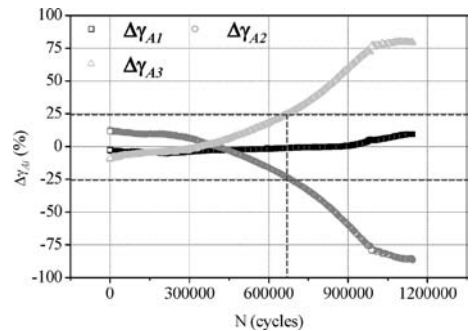


Figure 7. Amplitude differences of strain measured by the displacement transducers as a function of the number of cycles. Test M30D1250.

and Ashayer Soltani, 1996; Baaj, 2002; Di Benedetto, De La Roche et al., 2004; Baaj, Di Benedetto et al., 2005), three phases appearing successively during a fatigue test can be identified:

- Phase 1 (or adaptation phase) characterized by a rapid decrease of the modulus. The decrease is not only explained by fatigue damage. Heating and a third phenomenon such as thixotropy probably play important role.
- Phase 2 (or quasi-stationary phase) where $|G^*|$ decrease is quasi-linear as a function of the number of cycles. In this phase, the role of fatigue by micro-cracks is predominant. Beginning of phase 2 is chosen when $|G^*|$ decrease becomes quasi-linear and when the phase angle is maximum.
- Phase 3 (or failure phase) this corresponds to the macro crack-propagation, where the test can't be considered as homogenous anymore. In this paper, fatigue failure is defined as an arbitrary 50% reduction in initial stiffness. It could be defined by the cycle when the non-homogeneity of the shear strain reaches 25% (cf. figure 7), which has more a physical meaning.

The $|G^*|$ discontinuities, observed on figure 4, correspond to the LVE G^* measurements, in the linear domain, at different frequencies. For the material, these periods are probably close to rest periods. Then, during these measurements, the stiffness of the material increases. When fatigue loadings restart, a decrease of the modulus is observed again.

Phase angle ϕ quickly increases (few degrees) at the beginning of the test (phase 1). At the beginning of phase 2, ϕ slightly decreases (less than 1 degree). The end of the test (phase 3) is

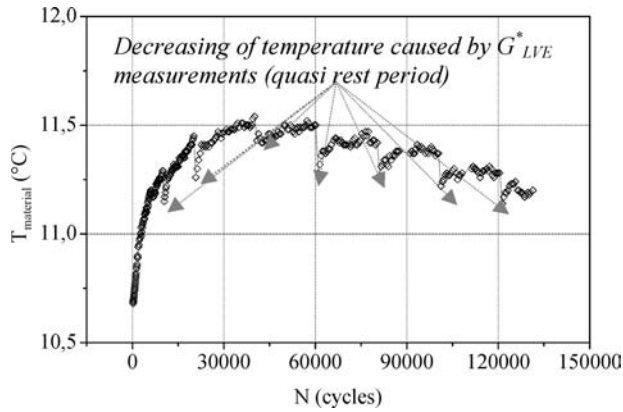


Figure 8. Evolution of the temperature during fatigue test M30D2500.

characterized by a quick decrease of the phase angle corresponding to the crack-propagation in the material.

3.2 Shear strain

For each material, three shear strain amplitudes $\gamma_{Ai} = 2\varepsilon_{rAi}$ ($i = 1, 2$ and 3) are measured, corresponding to the three displacement transducers (Figure 1). These values are compared to the average γ_A of the three amplitudes by plotting the difference $\Delta\gamma_{Ai}$ between γ_{Ai} and γ_A (equation (2)). It allows analyzing the homogeneity of the test (γ_A values are used to calculate G^*).

$$\Delta\gamma_i = \gamma_{Ai} - \gamma_A \quad (2)$$

$\Delta\gamma_{Ai}$ has been plotted for the fatigue test M30D1250 in figure 7. This figure reveals that at the beginning of the test, amplitudes of the signals are close for the three displacement transducers. Then, shear stress and shear strain are nearly the same in the whole volume of the specimen. When number of cycle increases, differences between strain amplitudes increase, which highlights that strain field is becoming less homogeneous. When the difference between strain values of a displacement transducers reaches a value fixed at 25%, the test is considered as not interpretable anymore. It may indicate the appearance of macro-cracks in the material, and then corresponds to a definition of fatigue life (figure 7) (Van Rompu, 2006; Delaporte, 2007).

3.3 Heating

During fatigue tests, temperature is measured in the thermal chamber and at the surface of the material, as explained in section 2.1. The sensor which is in contact with the material directly allows determining heating of the material, created by dissipation during repeated loadings. As the temperature probe only touches the surface of the specimen, it is suspected that the measured temperature change is lower than the real one. This point will be checked in future work.

The measured temperature of the material is plotted as a function of the cycle numbers in figure 8, for 0.25% strain amplitude (test M30D2500). A quick increase of the temperature is observed at the beginning of the test, where heating reaches about 0.8°C. Then, heating slowly decrease until the end of the test. In addition, figure 8 reveals that, during the linear viscoelastic G^*_{LVE} measurements, temperature of the material decreases. When restarting the loading cycles of fatigue test, temperature re-joined the previous global evolution curve.

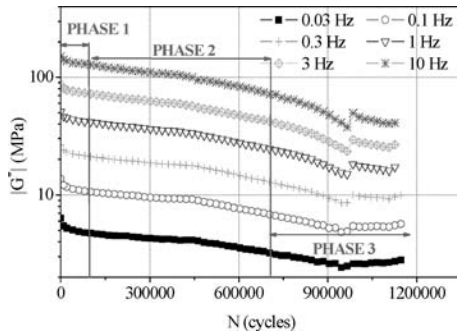


Figure 9. LVE complex modulus $|G_{fr}^{*i}|$ as a function of the cycle number during fatigue test, at 6 frequencies. Test M30D1250.

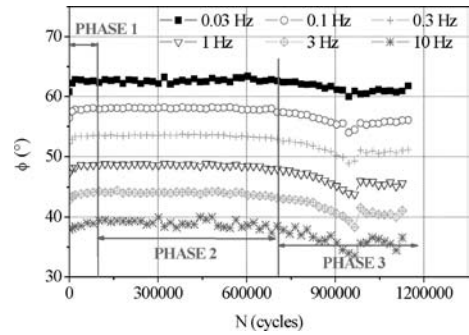


Figure 10. Phase angles of the LVE complex modulus G_{fr}^{*i} as a function of the cycle number during fatigue test, at 6 frequencies. Test M30D1250.

3.4 LVE complex modulus

As explained before (section 2.2), LVE complex modulus (G_{fr}^{*i}) is measured at 6 frequencies f_r (0.03, 0.1, 0.3, 1, 3 and 10 Hz), before the test and at every step i , after 20000 fatigue cycles period. An additional measure is performed 10000 cycles after the test has started. Fatigue effect on the LVE complex modulus is analyzed by plotting the G_{fr}^{*i} (in norm and in phase angle) as a function of cycle numbers. Results for the test M30D1250 are presented in figure 9 (norm $|G^*|$) and figure 10 (phase angle ϕ).

During fatigue test the stiffness (in the non linear range) of bituminous materials decreases because of different phenomena such as fatigue, heating or thixotropy as explained in section 3.1. A decrease of the LVE G^* for the 6 tested frequencies in figure 9 is also observed. As concern the phase angle ϕ , figure 10 reveals that, as observed for the non-linear modulus phase angle, it increases at the beginning of the test. Then it slowly decreases with the number of cycles, for the 6 selected frequencies.

4 RESULTS AND DISCUSSION

4.1 Fatigue life of mastic

Several definitions of fatigue failure can be considered for sinusoidal strain or stress controlled fatigue test. In this study 2 fatigue failure criteria are considered to obtain the fatigue life, for the controlled strain tests:

- i) the traditional one corresponding to an arbitrary 50% reduction in initial stiffness (“classical criterion: $Nf_{50\%}$ ”) of the sample,
- ii) a difference of 25% in the shear strain measurement as presented in section 3.2. It is noted “shear strain criterion: $Nf_{25\%}$ ”.

Strain amplitudes are plotted in figure 11 as a function of fatigue life for the six tests and the 2 criteria. Data are approached by a power law (equation 3), where N is the cycle number at failure for a strain amplitude ε . ε_6 is the strain amplitude which corresponds to a fatigue life of 10^6 cycles and b the fatigue slope:

$$\varepsilon = \varepsilon_6 \left(N / 10^6 \right)^{-b} \quad (3)$$

The classical criterion: $Nf_{50\%}$ results in figure 11 obtained with the ASR can be compared to the fatigue life given by DSR. For the mastic tested in this study, composed of a 50/70 pen grade

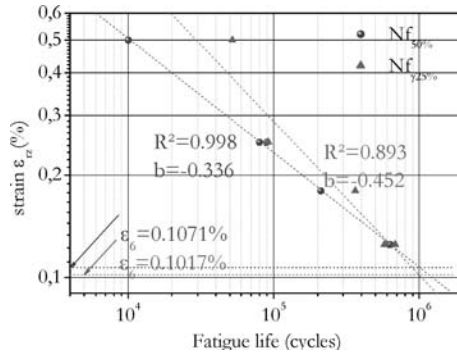


Figure 11. Fatigue life of mastic M30: classical criterion $Nf_{50\%}$ and shear strain criterion $Nf_{25\%}$.

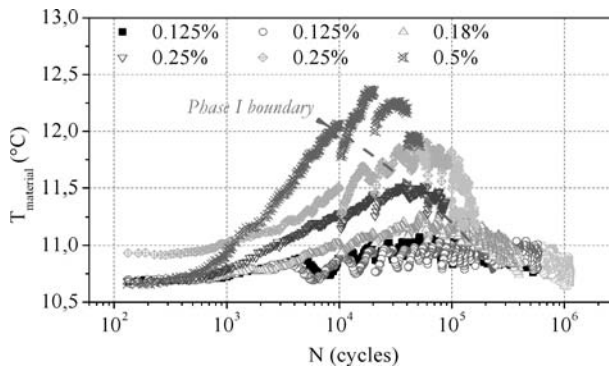


Figure 12. Temperature vs. cycle numbers (in log scale) for the 6 fatigue tests.

bitumen and 30% filler in volume, fatigue life at $\varepsilon = 0.5\%$ is close to 6000 cycles. A stiffer mastic composed of a 40/60 pen bitumen associated with 40% filler in volume has been tested with a DSR (Airey, Liao et al., 2006). The fatigue life obtained for the same strain level ($\varepsilon = 0.5\%$) was found at about 300000 cycles. In strain control, it is admitted that when increasing modulus, fatigue life decreases (Di Benedetto and Corté, 2005). As a consequence, it seems that the two different apparatuses give significantly different results in terms of fatigue performance, which can be explained by the non-uniformity of the stress-strain fields for DSR test. It has been showed (Di Benedetto, De La Roche et al., 2004; Di Benedetto and Corté, 2005) that rational interpretation of a non homogenous fatigue tests (such as DSR) is very complex and generally not proposed.

4.2 Heating

Figure 12 shows that the temperature of the material highly increases at the beginning of the test, which approximately corresponds to the phase 1. Then, it slowly decreases until the end of the test. During the LVE G_{fr}^{*i} measurements, temperatures drops because the dissipated energy becomes low. When fatigue restarts, temperature increases again and rejoins the previous fatigue curve.

The maximum values of heating (denoted as ΔT_{max}) significantly depend on the strain amplitudes which is applied. ΔT_{max} is very low for the small strain amplitude (less than 0.5°C). It reaches 2°C for $\varepsilon = 0.5\%$.

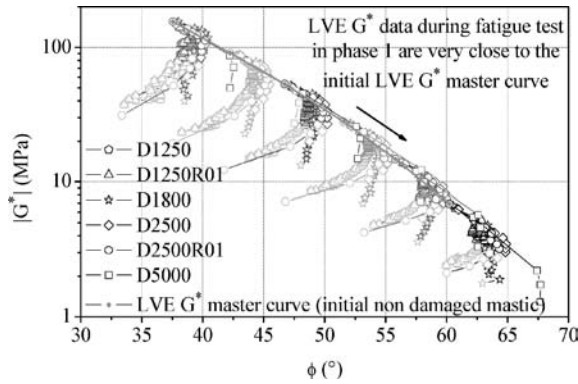


Figure 13. G^*_{LVE} measured during fatigue test and G^*_{LVE} master curve obtained with a complex modulus test.

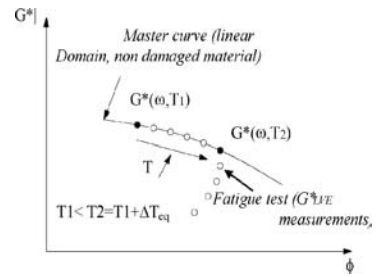


Figure 14. Schematic interpretation of the LVE G^* decrease: master curve in Black space as a function of the temperature (T) ($\omega = fr/2\pi$).

4.3 Linear viscoelastic properties of mastics during fatigue test

Measurements of the linear complex modulus during the 6 fatigue tests, plotted in Black space, are presented in figure 13. It reveals that, in the first phase of the tests (phase 1), G^{*i}_{fr} moduli are very close to the LVE G^* master curve of the initial mastic (without fatigue damage). In addition, this result is validated for the 4 different strain levels (ϵ_{rz}), from 0.125% to 0.5%. During phase 2, data points do not lay on the master curve of the non damaged material because of the decrease of both the norm and the phase angle.

Following interpretations can be pointed out:

- While the test is in phase 1, linear viscoelastic properties of material are very few affected by fatigue loadings. Complex modulus measurements remain on the G^* master curve of the material in the linear domain. The stiffness decrease is indeed probably mainly explained by heating and/or thixotropy.
- After phase 1, the LVE G^{*i}_{fr} values are different to the ones of the G^*_{LVE} master curve of the non damaged mastic. Then, the linear viscoelastic properties of mastic, which become gradually rather different from the initial one, reveal the existence of damage created by cyclic loading. Thanks to this approach, this damage can be rationally quantified. Fatigue by micro-cracks may actually be predominant after phase 1 in the decrease of $|G^*_{LVE}|$.

In Black space, decrease of G^{*i}_{fr} along the G^*_{LVE} master curve of the non damaged material (as observed in phase 1 of fatigue test) is obtained when heating the material, as explained in figure 14. This Temperature increase is denoted as ΔT_{eq} . It can be determined using the Time Temperature Superposition Principle (TTSP) and a linear viscoelastic model. The TTSP holds for the considered mastic which has been tested in the small strain domain. The shift factors used for the construction of the master curve are fitted by the WLF law (see equation (4)) calibrated at the reference temperature $T_{ref} = 10^\circ\text{C}$ with $C_1 = 21.5$ and $C_2 = 153.2$.

$$\log(a_T) = -C_1(T - T_{ref}) / [C_2 + T - T_{ref}] \quad (4)$$

The ΔT_{eq} are reported in table 2. They are compared to the heating of the material measured by the temperature sensor in contact with the material. Table 2 reveals that equivalent heatings ΔT_{eq} are few dependant of the frequency, which confirms the proposed explanation. In addition, these values are greater than the one corresponding to measurements. It seems that heating may not entirely account for the modulus decrease observed in phase 1. The stiffness decrease at the beginning of the fatigue test could be explained by both heating and another phenomenon such as thixotropy, having a similar influence than heating. Meanwhile this conclusion should be checked

Table 2. Comparison between equivalent heating (calculated from 2S2PID linear viscoelastic model (Delaporte, Di Benedetto et al., 2007) and time-temperature superposition principle using WLF law (equation (4))) and measured heating (M30D1250_R01).

Test	Equivalent heating ΔT_{eq} (°C)						Measured heating (°C)
	0.03 Hz	0.1 Hz	0.3 Hz	1 Hz	3 Hz	10 Hz	
M30D1250_R01	1.41	1.44	1.54	1.54	1.49	1.42	0.37

using better temperature measurement, as mentioned section 3.3. New obtained results seem to indicate that temperature increase is the main phenomenon which explains modulus decrease.

5 CONCLUSION

The test protocol developed at ENTPE/DGCB, using the ASR, opens a new way to study fatigue of bituminous binders and mastics. In addition to the intrinsic qualities of the experimental device (homogenous test, large size of the samples), it is the originality of the test protocol (measures of the evolution of the LVE properties during fatigue test) that needs to be underlined. Indeed, measures of mechanical characteristics in the small strain domain at different frequencies, allow better understanding of fatigue phenomenon.

It is for example shown that the decrease of modulus during the first phase of fatigue test can be explained by an equivalent (or real?) increase of temperature (ΔT_{eq}). More accurate temperature measurements still need to be performed to confirm this important conclusion. In addition, thanks to the proposed procedure reversible and irreversible damages can be clearly identified.

This work is associated with rheological modelling developments, which are not presented.

REFERENCES

- Airey, G. D. and R. Behzad (2004). "Combined bituminous binder and mixture linear rheological properties." *Construction and Building Materials* **Vol. 18**: pp. 535–548.
- Airey, G. D., M.-C. Liao and N. H. Thom (2006). *Fatigue Behaviour of Bitumen-Filler Mastics*. ISAP 2006–10th International Conference on Asphalt Pavements, Québec.
- Airey, G. D., N. H. Thom, S. Osman, H. Huang and A. Collop (2004). *A comparison of Bitumen/Mastic Fatigue Data From Different Test Methods*. Eurobitume Workshop 2004.
- Anderson, D. A., Y. M. Le Hir, M. Marasteanu, J.-P. Planche, D. Martin and G. Gauthier (2001). "Evaluation of Fatigue Criteria for Asphalt Binders." *Transportation Research Record* **1766**: pp. 48–56.
- Baaj, H. (2002). *Comportement des matériaux granulaires traités aux liants hydrocarbonés*. Mécanique, Energétique, Acoustique et Génie Civil. Lyon, PhD ENTPE - INSA Lyon: 247 p. [French].
- Baaj, H., H. Di Benedetto and P. Chaverot (2005). "Effect of Binder Characteristics on Fatigue of Asphalt Pavement Using an Intrinsic Damage Approach" **Vol. 6**(Issue 2): pp. 147–174.
- Bahia, H. U., H. Zhai, K. Bonetti and S. Kose (1999). "Non-Linear Viscoelastic and Fatigue Properties of Asphalt Binders." *Association of Asphalt Pavement Technology (75th)* **Vol. 68**: pp. 1–35.
- Bocci, M., G. Cerni and E. Santagata (2006). *Rheological Characterization of the Fatigue Resistance of Asphalt Binders*. ISAP 2006–10th International Conference on Asphalt Pavements, Québec.
- Bodin, D., H. Soenen and C. De La Roche (2004). *Temperature Effects in Binder Fatigue and Healing Tests*. 3rd Euraspahl & Eurobitume Congress, Vienna.
- Delaporte, B. (2007). *Etude de la rhéologie des mastics bitumineux à l'aide d'un rhéomètre à cisaillement annulaire*. Mécanique, Energétique, Acoustique et Génie Civil. Lyon, PhD ENTPE – INSA Lyon: 248 p. [in french].
- Delaporte, B., H. Di Benedetto, P. Chaverot and G. Gauthier (2007). "Linear Viscoelastic Properties of Bituminous Materials: from Binders to Mastics." *Journal of the Association of Asphalt Paving Technologists* **Vol. 76**.

- Delaporte, B., H. Di Benedetto, C. Sauzéat and P. Chaverot (2005). Linear viscoelastic properties of mastics: results from a new annular shear rheometer, and modelling. Bearing Capacity of Roads, Railways and Airfields (CD-Rom), Trondheim.
- Di Benedetto, H. and M. A. Ashayer Soltani (1996). "Fatigue damage for bituminous mixtures: a pertinent approach." *Journal of the Association of Asphalt Paving Technologists* **65**.
- Di Benedetto, H. and J.-F. Corté (2005). *Matériaux routiers bitumineux 2*, Hermes.
- Di Benedetto, H., C. De La Roche, H. Baaj, A. Pronk and R. Lundström (2004). "Fatigue of bituminous mixtures." *Materials and Structures* **Vol. 37**: pp. 202–216.
- Olard, F., H. Di Benedetto, B. Eckmann and J.-P. Triquigneaux (2003). "Linear viscoelastic properties of bituminous binders and mixtures at low and intermediate temperatures." *Road Materials and Pavement Design* **Vol. 4**(Issue 2): pp. 185–224.
- Planche, J.-P., D. A. Anderson, G. Gauthier, Y. M. Le Hir and D. Martin (2003). Evaluation of Fatigue Properties of Bituminous Binders. 6th RILEM Symposium PTEBM'03, Zurich.
- Soenen, H., C. De La Roche and P. Redelius (2003). "Fatigue Behaviour of Bituminous Materials: From Binders to Mixes." *Road Materials and Pavement Design* **Vol. 4**(Issue 1): pp. 7–27.
- Soenen, H., C. De La Roche and P. Redelius (2004). Predict Mix Fatigue Tests from Binder Fatigue Properties, measured with DSR. 3rd Eurasphalt & Eurobitume Congress, Vienna.
- Thom, N. H., S. Osman, A. C. Collop and G. D. Airey (2006). Fracture and Fatigue of Binder and Binder/filler Mortar. ISAP 2006 – 10th International Conference on Asphalt Pavements, Québec.
- Van Rompu, J. (2006). "Etude du comportement mécanique des mastics bitumineux à l'aide d'un rhéomètre à cisaillement annulaire (mémoire de master recherche)." 171 p. [French].

Thermo-volumetric properties of asphalt binders and mixtures

J.O. Ojo, D. Fratta, H.U. Bahia, & C. Daranga
University of Wisconsin, Madison, Wisconsin, USA

M. Marasteanu
University of Minnesota, Minneapolis, Minnesota, USA

ABSTRACT: The glass transition temperature of asphalt binders and mixtures is an essential component for the prediction of thermal cracking of pavements. For many decades this subject has been studied but published results are very limited. Measuring thermo-volumetric properties of asphalt paving materials is not simple and there are no standard methods for conducting such measurements. In this study, a dilatometric system for measuring binder properties was used to study the glass transition of ten binders and a length change measuring system was used to measure the glass transition of asphalt mixtures. Results show a variation in glass transition behavior as function of the binder grade and modification. Furthermore, the glass transition of the mixtures does not correlate with binder glass transition properties, which highlights the importance of aggregate characteristics and mixture compaction in defining mixture thermo-volumetric properties. It is also found that the contraction and dilation behavior of mixtures shows a hysteretic response. These findings hint at a need for fundamental understanding of the effect of aggregate interaction in the thermal behavior of asphalt mixtures and they also shed some light on the important aspect of thermal cracking of pavements and the measurements needed for better modeling.

1 INTRODUCTION

Engineers have long been challenged to link binder and mixture physical properties to field distresses and thermal cracking in asphalt pavements. Thermal cracking is caused by volumetric changes in asphalt mixtures that put it in tension until the binder fails. The binder is not only the weakest link in the failure mechanisms but it is considered to be a key component in the volumetric change behavior of asphalt mixtures. As a result, efforts have been geared toward linking binder thermal properties with pavement thermal cracking. The most immediate consequence of the binder-mixture thermal properties link is the use of higher penetration grade binders in cold climates. In the AC grading system, temperature susceptibility is controlled by specifying binder physical properties at three broadly spaced test temperatures, namely 135, 60, and 25°C. In the Superpave system, a bending beam rheometer is used to control low-temperature binder properties. The goal of these methods is to link low temperature mixture properties to thermal cracking resistance of the pavement. Researchers have attempted to measure the true values of the volumetric change both in binders and mixtures, but the published results are limited.

This paper presents the thermo-volumetric properties of ten asphalt binders commonly used in the Midwestern region of North America, by using the dilatometric system along with thermal length changes in laboratory asphalt mixtures. These experimental results show that not only the binder influences the thermo-volumetric behavior of mixtures but also aggregate type, film thickness, and void ratio are controlling factors and must be accounted for in the evaluation of field responses of asphalt pavements.

Table 1. Experimental layout: Evaluation of binder type on the thermal behavior of mixes.

Binder type										
Aggregate	PG58-28, plain 1	PG58-28, plain 2	PG58-34, modifier 1	PG58-34, modifier 2	PG58-40, modifier 1	PG64-22, plain	PG64-28, plain 1	PG64-28, modifier 1	PG64-34, modifier 1	PG64-34, modifier 2
Granite (4% air void)	✓	✓	✓	✓	✓	✓	✓	✓	✓	✓
Limestone (4% air void)	✓	✓	✓	✓	✓		✓	✓	✓	✓

Table 2. Experimental layout: Evaluation of mix design parameters on the thermal behavior of mixes

Aggregate	Granite		Limestone		Granite		Limestone	
	4% air void		4% air void		7% air void		7% air void	
Binder Type	Design	Film thickness	Design	Film thickness	Design	Film thickness	Design	Film thickness
PG58-28, plain 1	✓	✓	✓	✓	✓	✓	✓	✓
PG58-40, modifier 1	✓	✓	✓		✓		✓	✓

2 EXPERIMENTAL DESIGN

The experimental design was developed to evaluate the correlation between binder properties and mixtures thermo-volumetric behavior, and to establish the main interactions between the thermo-volumetric properties of the asphalt mixture's components. To achieve these goals, a parametric experimental study was developed as shown in Tables 1 and 2. Ten different binders (plain and modified) along with granite and limestone aggregates were used in several mix designs. The void content in the compacted mixtures was either 4% or 7% by volume. The asphalt binder contents were set to 6.0% or 6.5% for the granite mixes and 6.9% or 7.4% for the limestone mixes. Tables 1 and 2 summarize the control variables included in the study. There were two replicates for each of the samples. The response variables were used to determine the following parameters: glass transition temperature (T_g), thermal expansion coefficient in the glassy state (α_g – testing temperature $T < T_g$), and thermal expansion coefficient in the liquid state (α_l – testing temperature $T > T_g$).

3 EXPERIMENTAL PROCEDURES

3.1 Binder thermal characterization

The binders used for this study were the same binders used in the Low-Temperature Cracking in Asphalt Pavements Investigation project under National Pooled Fund Study 776. Both plain (unmodified) and modified binders were included in the study. The grade and the type of asphalt cements used are shown in Table 1. These binders were tested to evaluate their glass transition temperatures (T_g) using the thermal dilatometric method.

Samples Preparation: The binders were aged using a Pressure Aging Vessel (PAV) in accordance with the AASHTO PPI standard. The preparation of the sample included heating the PAV aged binder until it was sufficiently fluid to pour into two clean silicon rubber molds. It was then allowed to cool in the mold at ambient temperature for 60 minutes before the binder sample was trimmed and dressed to achieve a shiny surface. After cooling at ambient temperature for another

15 minutes, the sample was demolded. If there was any suspicion of air bubble inclusion, the sample was discarded; otherwise the sample weight was recorded before testing.

Dilatometer Apparatus: The Glass Transition Test (GTT) system consists of a *dilatometer* where the 10-ml binder sample is placed and its volume change is measured by reading the level on a alcohol filled precision-bore capillary tube, an *insulated chamber* for heating and cooling the dilatometer and sample using a heating element and liquid nitrogen, and *thermocouples* and *data acquisition system* to measure and collect temperature readings during testing. This technique provides a direct way for measuring dimensional changes with temperature.

Test Procedure: The test starts by assembling the dilatometer cells and filling the capillary tubes with air-free ethyl alcohol (medium for reading thermal volume changes). The dilatometer is then mounted inside the environmental chamber and all supporting sensors, data acquisition, and temperature control systems are connected and initiated.

Testing starts at 40°C and remains at this temperature for 10 minutes to allow for the thermal equilibration of the sample. The system is then cooled to -76°C with a rate of 1°C/min. This cooling rate was selected using the experience obtained from previous studies (Nam and Bahia, 2004). The volume and temperature change are recorded every 2 minutes.

Calibrations (Nam 2005): To account for the change in the capillary height due to changes in the temperature and shrinkage of the dilatometric cell, each cell was calibrated using an aluminum sample identical in volume to the asphalt sample (The thermal contraction/expansion coefficient of aluminum is known). Then, the obtained thermal response of the aluminum sample was used to adjust the capillary height recorded for binders in the glass transition temperature T_g calculation. Finally, in order to account for the temperature differences between the cells' interior and the insulated chamber, the dilatometric cell temperature was measured in relation with the cooling chamber. A correction correlation was derived and used in the glass transition temperature T_g calculation.

Computation: Data collected were analyzed using a regression analysis method and curve fitting for each tested binder sample. The following equation was used to fit the data (modified after Bahia and Anderson, 1993):

$$\frac{v}{v_o} = \frac{v_c}{v_o} + \alpha_g(T - T_g) + R(\alpha_l - \alpha_g) \ln \left[1 + \exp\left(\frac{T - T_g}{R}\right) \right] \quad (1)$$

where v is the specific volume in ml/g at temperature T in °C, v_o is the initial specific volume ml/g, v_c is the specific volume in ml/g at the glass transition temperature T_g in °C, R represents the curvature in °C at the glass transition temperature, α_g is the thermal expansion coefficient 1/°C defined for $T < T_g$, and α_l is liquid thermal expansion coefficient in 1/°C defined for $T > T_g$. Figure 1 shows an example test results and data interpretation.

Binder Test Results: The summary of the binder test results is presented in Table 3. To measure the reproducibility of the measurements as determined using independent samples, three of the binders were tested at a different time using different samples. There is a relatively good agreement for the coefficients of thermal contractions above and below T_g for both binders. However, the range of the obtained T_g values show a relatively high variability, particularly for the PG 64-34 binder. Table 3 summarizes the averaged thermo-volumetric properties of the binders. The measurements include the glass transition temperature (T_g), the thermal coefficient of contraction above T_g (liquid state α_l), and the thermal coefficient of contraction below T_g (glassy state α_g).

3.2 Thermal properties of asphalt mixtures material

Samples used for this testing program were prepared from mix samples obtained from Iowa State University as part of the Low Temperature Cracking in Asphalt Pavements Investigation project under the National Pooled Fund Study 776. A total of 11 combinations of mixtures were prepared using the binders presented in Table 1. Every mixture sample was used to prepare two samples for testing. The supplied mixture samples were approximately 200 mm wide by 380 mm long by

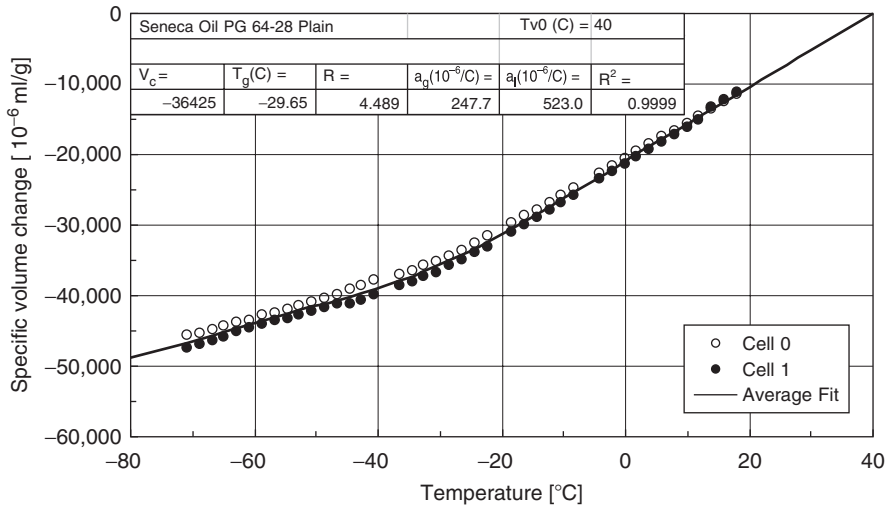


Figure 1. Typical specific volume versus temperature response. The data and associated fitting equation analysis allow determining the parameters α_1 , α_g , and T_g of the tested binder sample.

Table 3. Summary of binder thermal properties.

Binders PG grade	Thermal properties			
	$T_g(^{\circ}\text{C})$	$\alpha_g (10^{-6}/^{\circ}\text{C})$	$\alpha_l (10^{-6}/^{\circ}\text{C})$	R^2
PG58-28, plain 1	-20.14	202.7	477.3	0.9994
PG58-28, plain 2	-26.42	350.6	578.4	0.9998
PG58-34, modifier 1	-37.15	143.1	463.4	0.9998
PG58-34, modifier 2	-29.64	195.9	583.3	0.9997
PG58-40, modifier 1	-24.98	333.4	538.3	0.9989
PG64-22, plain	-31.87	308.9	513.7	0.9995
PG64-28, modifier 1	-24.26	262.7	456.2	0.9997
PG64-28, plain 1	-31.03	224.5	545.4	0.9997
PG64-34, modifier 1	-34.41	214.6	458.9	0.9998
PG64-34, modifier 2	-47.98	240.4	569.2	0.9994
Mean	-30.79	247.7	518.4	
Maximum	-20.14	350.6	583.3	
Minimum	-47.98	143.1	456.2	

65 mm high. These samples were cut with a masonry saw to create two 65 mm wide, 50 mm high, and 380 mm long beam samples. The two replicate beams for each mixture type were tested to evaluate the repeatability of the results. All the mixture samples were tested in cooling and heating cycles. Figure 2 shows a cut beam ready for testing.

Sample Preparation: Prior to testing, end caps and connecting rods were mounted to both ends of the mixture beams using a thin layer of epoxy adhesive. The rods are made of the special G7 polymer (a glass-silicon laminate used for its excellent heating insulation properties). The G7 polymer thermal expansion coefficient is $1.29 \times 10^{-5} 1/^{\circ}\text{C}$ along the longitudinal direction of the rods (Boedeker Plastics, 2007).

Test Procedure: Testing starts by placing the sample on a frictionless Teflon base in the insulating chamber as shown in Figure 3. Two linear variable displacement transducers (LVDT) were connected to the ends of the G7 polymer rods. The heating element installed inside of the chamber

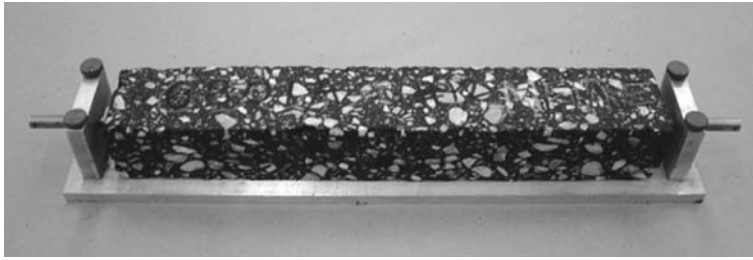


Figure 2. Mixture beam prepared for thermal testing.

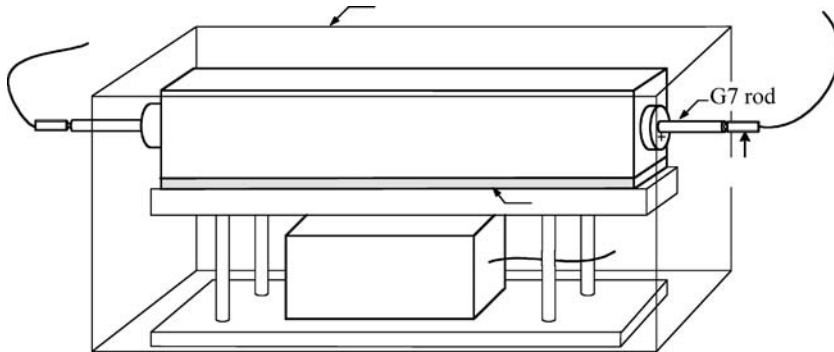


Figure 3. Schematic of the cooling and heating setup (after Nam, 2005).

increased the temperature of the chamber and cooling was achieved by injecting nitrogen gas from a liquid nitrogen tank. The temperature measurements were made using calibrated T-type thermocouples. A dummy asphalt mix beam was placed at the bottom of the insulated chamber for estimating interior temperatures of the mixture samples during the thermal testing. The two thermocouples were placed on the surface of the test beam and in the center of the dummy mix beam.

Samples were held at 40°C for 10 minutes before cooling them at the rate of $-1^{\circ}\text{C}/\text{min}$ to -80°C . After reaching -80°C , the mixture beams were held at this constant temperature for 10 minutes before the heating to 40°C starts. The rate of heating used was $1^{\circ}\text{C}/\text{min}$. The rate of temperature change corresponded to typical temperature rates used in previous studies (Nam and Bahia, 2004). Figure 4 depicts an example of the results of the temperatures measured on the surface and in the center of the dummy sample. As the temperature changed, the two LVDTs placed at the end of G7 polymer rods monitored the changes in length of the sample during cooling and heating cycles. Temperature and LVDT readings were collected every 5 seconds. A LabView virtual instrument program was used to control the temperature in the testing chamber via the heating elements and the inflow of nitrogen gas. The LabView virtual instrument program was also used to capture the thermocouple and LVDT readings.

Computation: Equation 1 was also used to evaluate the thermal response of the mixture by replacing specific volumes by the length of the sample at temperature T , the initial length of the sample L_0 , and the length of the sample at the glass transition temperature L_c . Figure 4 shows a temperature lag between the interior and exterior of dummy sample. The lag is caused by the slow heat transfer from the sample surface to its center. It was presumed that the internal dummy sample better represented the temperature of mixture sample (The dummy sample has the same cross-sectional dimensions and thermal conductivity as the mixture samples). The dummy sample temperature was therefore used in the data interpretation. Figure 5 shows a typical thermal deformation (note the hysteretic response) during a cooling and heating cycle. Table 4 and 5 summarizes all the thermal results for the asphalt mixture samples.

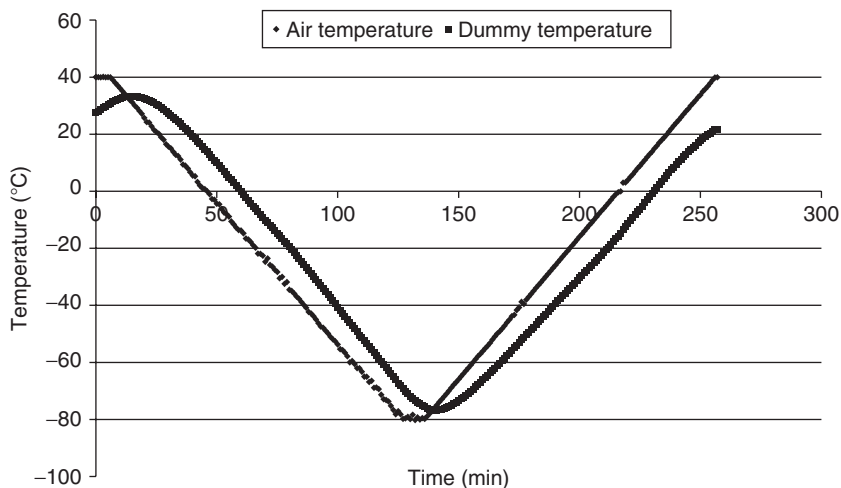


Figure 4. Temperature profile in the testing chamber and dummy sample during the test (cooling and heating cycles).

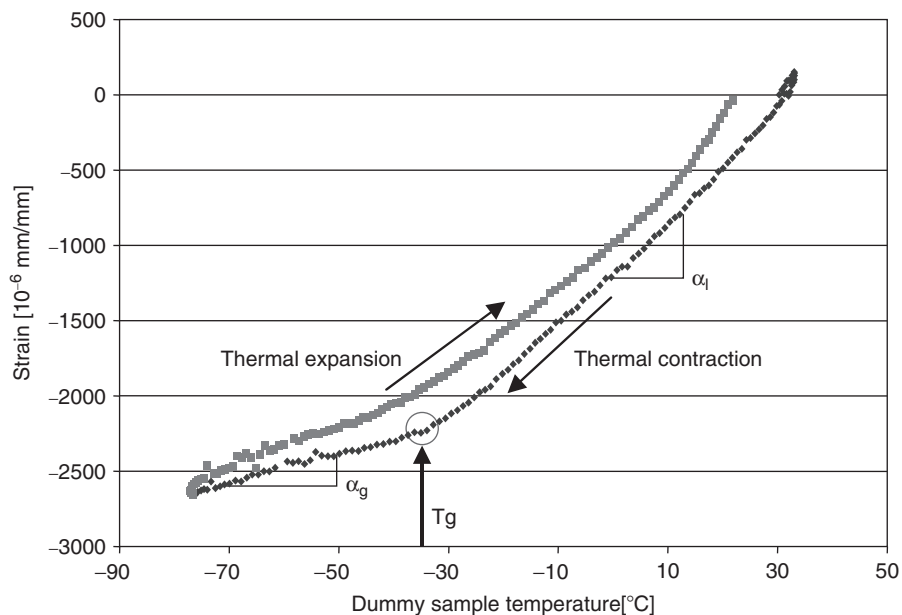


Figure 5. Typical results of the thermal response of mixture samples.

4 FINDINGS

As depicted in Table 3, the binder thermo-volumetric results show a wide range of glass transition temperature T_g values: minimum -48°C and maximum -21.1°C . The results also show a wide range of thermal coefficient values ($143.1 - 350.6 \times 10^{-6} \text{ 1/}^\circ\text{C}$) for contraction below the glass transition temperature T_g (glassy state α_g) with standard deviation of $66 \times 10^{-6} \text{ 1/}^\circ\text{C}$. The coefficients of thermal contraction above the glass transition temperature T_g (liquid state α_l) ranged from 456.2 to $583.3 \times 10^{-6} \text{ 1/}^\circ\text{C}$ which is narrower than the range found for α_g . As expected, the

Table 4. Experimental results: Evaluation of binder type on the thermal behavior of mixtures (Symbols: G-granite, LS-limestone).

Aggregate (Air void: 4%)	Binder type	Result cooling				Result heating			
		T_g (C)	α_g ($10^{-6} 1/^\circ\text{C}$)	α_1 ($10^{-6} 1/^\circ\text{C}$)	R^2	T_g (C)	α_g ($10^{-6} 1/^\circ\text{C}$)	α_1 ($10^{-6} 1/^\circ\text{C}$)	R^2
G	58-28, Plain 1	-29.7	11.6	32.0	0.9970	-29.6	16.7	30.6	0.9985
G	58-28, Plain 1	-27.9	9.4	36.7	0.9994	-23.7	14.6	35.6	0.9994
G	58-28, Plain 2	-38.8	16.4	37.6	0.9892	-10.9	25.4	58.6	0.9993
G	58-28, Plain 2	-44.7	12.1	30.6	0.9983	-40.4	14.6	36.4	0.9995
G	58-34, Modifier 1	-38.9	10.8	30.6	0.9984	-33.3	15.1	30.5	0.9988
G	58-34, Modifier 1	-36.3	9.6	31.9	0.9974	-24.9	15.0	34.0	0.9988
G	58-34, Modifier 2	-30.8	10.8	34.8	0.9984	-26.7	15.6	33.3	0.9972
G	58-34, Modifier 2	-32.9	11.6	32.2	0.9996	-26.7	15.6	33.3	0.9972
G	58-40, Modifier 1	-46.3	13.1	29.2	0.9993	-24.2	16.5	37.8	0.9986
G	58-40, Modifier 1	-48.2	15.5	31.8	0.9928	-24.2	16.5	37.8	0.9986
G	64-22, Plain 1	-28.6	9.1	33.5	0.9995	-29.8	11.7	32.2	0.9991
G	64-22, Plain 1	-27.3	12.9	32.9	0.9997	-27.2	15.0	33.0	0.9986
G	64-28, Plain 1	-34.4	10.4	33.3	0.9957	-18.2	15.3	40.7	0.9991
G	64-28, Plain 1	-31.5	9.4	33.7	0.9986	-30.6	14.9	32.0	0.9978
G	64-28, Modifier 1	-29.0	13.8	33.1	0.9996	-23.6	17.0	33.2	0.9973
G	64-28, Modifier 1	-37.9	9.5	33.5	0.9943	-16.9	16.8	32.9	0.9991
G	64-34, Modifier 1	-34.7	8.7	33.3	0.9941	-29.6	15.1	32.0	0.9997
G	64-34, Modifier 1	-38.2	12.9	33.5	0.9963	-26.6	11.9	42.6	0.9970
G	64-34, Modifier 2	-39.9	9.7	32.8	0.9980	-23.7	15.5	36.8	0.9981
G	64-34, Modifier 2	-40.8	10.6	31.4	0.9986	-26.1	12.8	41.1	0.9983
LS	58-28, Plain 1	-34.3	10.2	35.3	0.9973	-18.7	16.1	42.1	0.9996
LS	58-28, Plain 1	-32.0	10.6	35.8	0.9980	-18.0	15.5	45.2	0.9982
LS	58-28, Plain 2	-26.4	10.1	40.5	0.9871	-15.9	13.9	45.8	0.9963
LS	58-28, Plain 2	-32.0	7.0	38.1	0.9998	-21.7	13.1	41.6	0.9989
LS	58-34, Modifier 1	-32.4	9.4	36.2	0.9967	-26.8	16.0	35.4	0.9989
LS	58-34, Modifier 1	-32.8	10.1	32.5	0.9892	-25.2	12.4	36.2	0.9970
LS	58-34, Modifier 2	-32.6	9.4	32.9	0.9994	-21.1	13.6	34.3	0.9973
LS	58-34, Modifier 2	-36.8	9.4	28.9	0.9965	-35.4	11.3	29.8	0.9973
LS	58-40, Modifier 1	-36.7	12.5	32.7	0.9960	-12.7	15.1	49.9	0.9983
LS	58-40, Modifier 1	-45.8	10.4	31.1	0.9996	-29.2	15.6	32.1	0.9980
LS	64-28, Plain 1	-31.0	8.3	35.9	0.9998	-20.4	14.7	37.0	0.9977
LS	64-28, Plain 1	-30.7	9.1	37.0	0.9991	-35.2	11.3	34.3	0.9989
LS	64-28, Modifier 1	-34.4	7.3	39.7	0.9994	-29.2	15.4	37.0	0.9969
LS	64-28, Modifier 1	-27.7	10.8	38.6	0.9995	-26.2	13.0	38.7	0.9985
LS	64-34, Modifier 1	-37.6	11.1	35.5	0.9997	-25.0	12.2	42.3	0.9993
LS	64-34, Modifier 1	-39.2	12.1	37.0	0.9993	-25.4	19.5	36.0	0.9981
LS	64-34, Modifier 2	-38.0	5.0	32.7	0.9974	-31.5	11.8	33.4	0.9978
LS	64-34, Modifier 2	-36.4	9.4	31.3	0.9998	-29.3	12.6	34.1	0.9990
Mean		-35.1	10.5	34.0		-25.4	14.9	37.1	
Maximum value		-26.4	16.4	40.5		-10.9	25.4	58.6	
Minimum value		-48.2	5.0	28.9		-40.4	11.3	29.8	

values of α_g are always smaller than α_1 (30% to 60% of the α_1 values). A general trend for the thermal properties revealed that low-grade temperature binders show lower glass transition temperatures and higher thermal coefficients of contraction than high-grade temperature binders. This trend indicates that low-grade temperature binders have positive effects on the low temperature

Table 5. Experimental results: Evaluation of mixture design parameters on the thermal behavior of mixtures.

Binder type	Aggregate	Air voids	Film thickness	Result cooling				Result heating			
				$T_g(^{\circ}\text{C})$	α_g ($10^{-6} 1/^{\circ}\text{C}$)	α_1 ($10^{-6} 1/^{\circ}\text{C}$)	R^2	$T_g(^{\circ}\text{C})$	α_g ($10^{-6} 1/^{\circ}\text{C}$)	α_1 ($10^{-6} 1/^{\circ}\text{C}$)	R^2
PG 58-28, plain 1	G	4%	OPT	-38.8	16.4	37.6	0.9892	-10.9	25.4	58.6	0.9993
PG 58-28, plain 1	G	4%	OPT	-44.7	12.1	30.6	0.9983	-40.4	14.6	36.4	0.9995
PG 58-28, plain 1	G	4%	OPT	-29.7	11.6	32.0	0.9970	-29.6	16.7	30.6	0.9985
PG 58-28, plain 1	G	4%	OPT	-27.9	9.4	36.7	0.9994	-23.7	14.6	35.6	0.9994
PG 58-28, plain 1	G	4%	BUMP	-43.3	13.3	35.8	0.9942	-32.7	17.7	39.3	0.9990
PG 58-28, plain 1	G	4%	BUMP	-41.8	12.2	37.8	0.9968	-26.1	18.7	43.1	0.9993
PG 58-28, plain 1	G	7%	OPT	-35.0	10.2	32.9	0.9936	-12.1	13.4	47.7	0.9995
PG 58-28, plain 1	G	7%	OPT	-34.2	8.2	33.1	0.9886	-12.1	13.4	47.7	0.9995
PG 58-28, plain 1	G	7%	BUMP	-31.0	6.6	38.4	0.9995	-18.0	16.3	38.8	0.9968
PG 58-28, plain 1	G	7%	BUMP	-30.7	12.5	35.5	0.9992	-19.2	17.5	39.3	0.9984
PG 58-28, plain 1	LS	4%	OPT	-26.4	10.1	40.5	0.9871	-15.9	13.9	45.8	0.9963
PG 58-28, plain 1	LS	4%	OPT	-32.0	7.0	38.1	0.9998	-21.7	13.1	41.6	0.9989
PG 58-28, plain 1	LS	4%	OPT	-34.3	10.2	35.3	0.9973	-18.7	16.1	42.1	0.9996
PG 58-28, plain 1	LS	4%	OPT	-32.0	10.6	35.8	0.9980	-18.0	15.5	45.2	0.9982
PG 58-28, plain 1	LS	4%	BUMP	-29.9	10.9	39.6	0.9997	-19.3	13.7	42.2	0.9975
PG 58-28, plain 1	LS	4%	BUMP	-29.7	9.6	40.4	0.9998	-19.0	13.8	42.0	0.9981
PG 58-28, plain 1	LS	7%	OPT	-33.3	11.3	35.7	0.9994	-28.6	15.4	31.6	0.9927
PG 58-28, plain 1	LS	7%	OPT	-31.0	13.5	36.8	0.9996	-29.0	15.9	33.2	0.9975
PG 58-28, plain 1	LS	7%	BUMP	-30.8	9.9	41.7	0.9999	-22.4	14.4	42.9	0.9979
PG 58-28, plain 1	LS	7%	BUMP	-28.9	9.5	39.8	0.9827	-17.2	15.3	45.8	0.9981
PG 58-40, modifier 1	G	4%	OPT	-46.3	13.1	29.2	0.9993	-24.2	16.5	37.8	0.9986
PG 58-40, modifier 1	G	4%	OPT	-48.2	15.5	31.8	0.9928	-24.2	16.5	37.8	0.9986
PG 58-40, modifier 1	G	4%	BUMP	-46.3	12.6	35.2	0.9988	-30.4	12.2	46.9	0.9984
PG 58-40, modifier 1	G	4%	BUMP	-49.7	11.4	30.4	0.9947	-34.7	12.9	38.2	0.9985
PG 58-40, modifier 1	LS	4%	OPT	-36.7	12.5	32.7	0.9960	-12.7	15.1	49.9	0.9983
PG 58-40, modifier 1	LS	4%	OPT	-45.8	10.4	31.1	0.9996	-29.2	15.6	32.1	0.9980
Mean				-36.1	11.2	35.6		-22.7	15.6	41.2	
Maximum value				-26.4	16.4	41.7		-10.9	25.4	58.6	
Minimum value				-49.7	6.6	29.2		-40.4	12.2	30.6	

Symbols: G-granite, LS-limestone, OPT-Optimum asphalt content corresponds to 6.0% and 6.9% for granite and limestone mixes respectively. BUMP is 0.5% higher asphalt content than OPT.

properties of binders. The results also indicate that the level of the effect depends on the type of modifier.

Asphalt mixture testing results presented in Tables 4 and 5 indicate that mixture glass transition temperature values during cooling range between -47.98°C and -27.94°C with a standard deviation of 5.46°C . Thermal coefficients of contraction α_g below the glass transition temperature T_g range between 7.18 and $14.30 \times 10^{-6} 1/^{\circ}\text{C}$. The thermal coefficients of contraction above T_g (α_1) vary between 10.26 and $30.48 \times 10^{-6} 1/^{\circ}\text{C}$.

Cooling and heating testing yielded different parameters. Thermal properties in the heating cycle were systematically higher than in the cooling cycle. Glass transition temperature T_g values ranged between -32.56°C and -12.12°C . The range for thermal expansion coefficients below the glass transition temperature T_g (α_g) was between 12.21 to $20.02 \times 10^{-6} 1/^{\circ}\text{C}$ and the range for the coefficients of expansion above the glass transition temperature T_g (α_1) ranged between 32.08 and $47.66 \times 10^{-6} 1/^{\circ}\text{C}$.

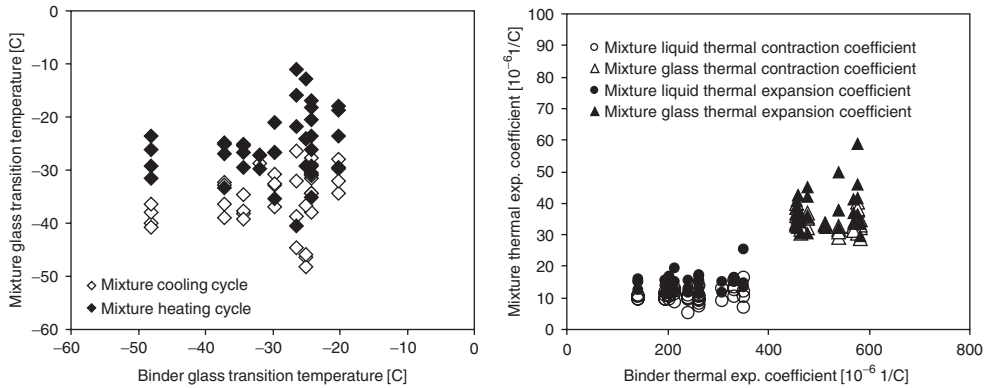


Figure 6. Binder versus mixture thermo-volumetric properties: there is little to no correlation between binder and mixtures.

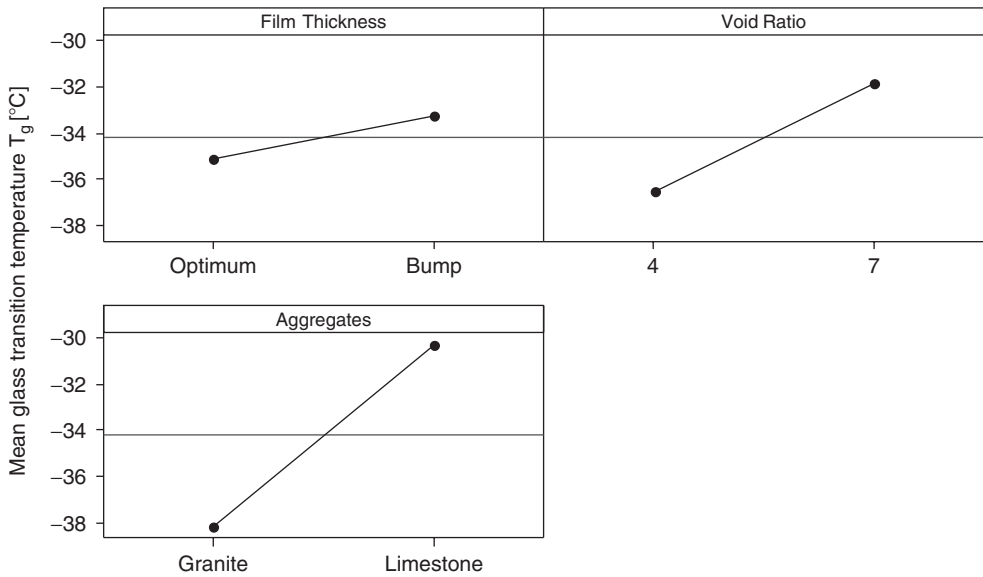


Figure 7. The effect of mixture parameters on thermo-volumetric properties: mixture glass transition temperature T_g versus film thickness, void ratio and aggregate type.

The differences in the thermal parameters between cooling and heating cycles could be caused by several phenomena including issues related to the material behavior, for example:

- thermal hysteresis caused by uneven temperature in the mixture sample (the research team is evaluating thermal diffusion effects both numerically and experimentally and the proper use of different temperatures in the plotting and interpretation of the data)
- thermal instabilities in the binders (this phenomenon is being studied by reducing temperature rates and increasing temperature equilibration times)

Regardless of the true causes for the cooling and heating differences, the above results seem to indicate the presence of cyclic thermal loading effects on the thermo-volumetric properties of mixtures. These observations require further research.

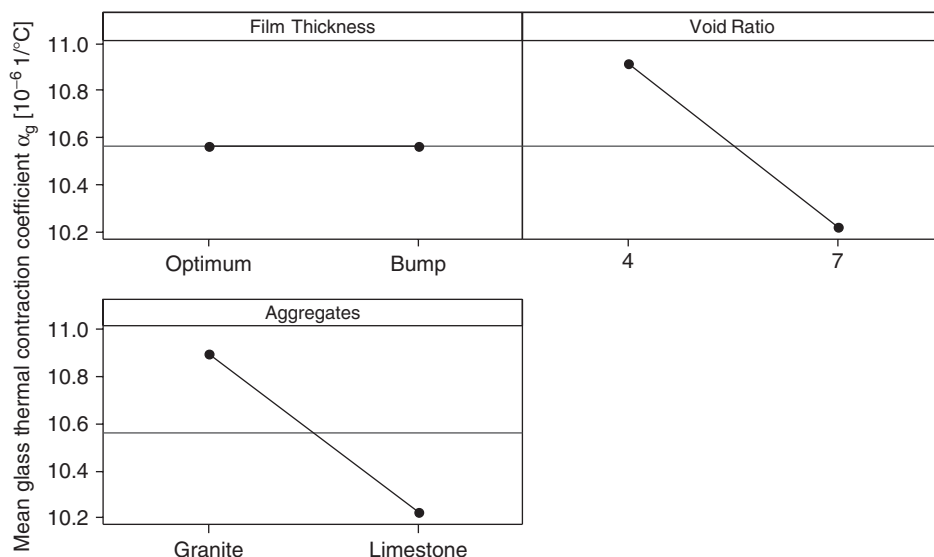


Figure 8. The effect of mixture parameters on thermo-volumetric properties: thermal contraction coefficient α_g in the glassy state (cooling cycle) versus film thickness, void ratio and aggregate type.

An attempt was also made to evaluate the effect of different mixture variables on the thermo-volumetric properties of asphalt mixes. Figures 6 to 9 give summary analyses for T_g , α_g and α_l for both cooling and heating conditions versus binder properties and a number of the mixture parameters. Figure 6 shows very low correlation between binder and mixture thermo-volumetric properties. These results demonstrate that both aggregates and percent air voids together have a significant effect on the mixture glass transition temperature (T_g) and thermal coefficients of contraction in the glassy state (α_g) during cooling on mixture samples. Furthermore, binder film thickness and aggregate types have a strong influence on the values of the thermal contraction coefficient in the liquid state (α_l). During the heating cycle, film thickness and aggregate types together with their interactions are significant in the determination of T_g , α_g and α_l while the void ratio only affects the glass transition temperature. During cooling cycles, void ratio affects the thermal contraction coefficient in the glassy state.

These results suggest that the thermo-volumetric behavior of the asphalt mix is not solely controlled by the thermo-volumetric properties of the binder but other mixture parameters are important as well. This observation should not come as a surprise as aggregates make up to 90% of the asphalt mixtures' volume. This experimental evidence challenges the importance of the binder properties as the key component in the thermo-volumetric behavior of asphalt mixes.

5 CONCLUSIONS

In this study, a dilatometric system for measuring binder properties was used to evaluate the glass transition of ten binders and a length change measuring system was used to measure the glass transition of asphalt mixtures. Thermo-volumetric testing results show a variation in glass transition behavior as function of the binder grade and modification. Furthermore, the mixture thermo-volumetric properties do not correlate well with binder properties highlighting the importance of aggregate characteristics and mixture compaction in defining mixture thermo-volumetric properties.

The experimental study also showed that: (a) the glass transition temperatures of asphalt mixtures were in general lower than that of the corresponding asphalt binders, (b) the thermal expansion

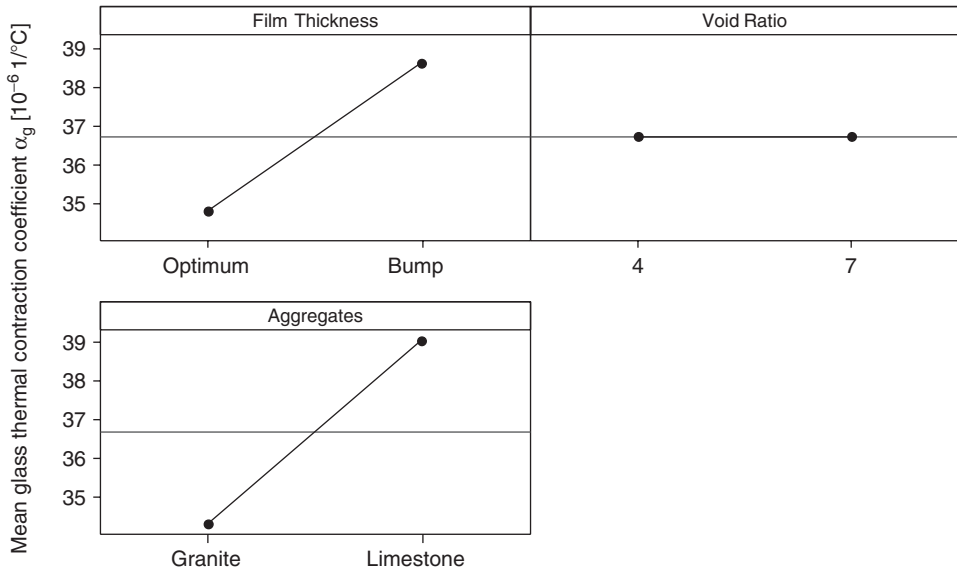


Figure 9. The effect of mixture parameters on thermo-volumetric properties: thermal contraction coefficient α_l in the liquid state (cooling cycle) versus film thickness, void ratio and aggregate type.

coefficient of asphalt mixtures was larger than the thermal contraction coefficient, and (c) both granite and limestone aggregates showed a significant effect on the thermal properties of the mixtures (Figures 7 to 9). Contrary to intuition, film thickness did not seem to have a significant effect on the thermal properties of the mixture during the glassy state of the mix (Figure 8). Finally, it is also found that for the contraction and dilation behavior of mixtures shows a hysteretic response during cooling and heating cycles. These findings hint at a need for more fundamental understanding of the effect of aggregate interaction and thermal heating/cooling rate in the thermal behavior of asphalt mixtures as they may shed some light on the important aspect of thermal cracking of pavements and the measurements needed for better modeling.

REFERENCES

- Bahia H.U. and Anderson D.A., 1993, "Glass Transition Behavior and Physical Hardening of Asphalt Binders." *Proceedings of the Association of Asphalt Paving Technologists*, Vol. 62, pp. 93–129.
- Bahia, H.U., Zeng, M. and Nam, K., 2000, "Consideration of Strain at Failure and Strength in Prediction of Pavement Thermal Cracking," *Proceedings of the Association of Asphalt Paving Technologists*, Vol. 69, pp. 455–498.
- Boedeker Plastics, Inc., 2007, *Company Web Site*. URL: <http://www.boedeker.com/>.
- Nam, K. and Bahia, H.U., 2004, "Effect of Binder and Mixture Variables on Glass Transition Behavior of Asphalt Mixtures," *Proceedings of the Association of Asphalt Paving Technologists*, Vol. 73.
- Nam, K., 2005, "Effects of Thermo-Volumetric Properties of Modified Asphalt Mixtures on Low-Temperature Cracking," Ph. D. thesis, Department of Civil and Environmental Engineering, University of Wisconsin, Madison.
- Zeng, H. and Vinson, T.S., 1998, "Thermal Contraction of Asphalt Concrete Mixture" Conference Proceedings, *Ninth International Conference on Cold Region Engineering*, Duluth, Minnesota, Newcomb D.E. Editor, ASCE. pp. 20–33.
- Zeng, M. and Shields, D.H., 1999, "Nonlinear Thermal Expansion and Contraction of Asphalt Concrete," *Canadian Journal of Civil Engineering*, Vol. 26, pp. 26–34.

Low temperature behavior of very hard bituminous binder material for road applications

R.N. Khedoe, A.A.A. Molenaar, & M.F.C. v.d. Ven
Delft University of Technology, Delft, The Netherlands

ABSTRACT: Very hard bituminous binders are becoming popular in pavement design. Mixtures with very high stiffness are used already for a number of years in the Netherlands as base course materials. Asphalt mixtures containing these hard bituminous binders are very stable but at lower temperatures the material can become very brittle. This brittle behavior can result in premature cracking during early service life.

At the laboratory of Road and Railway Engineering of Delft University of Technology a special very hard binder called C-fix was investigated. Different low temperature tests were performed on this hard binder as well as the mixture containing this material. The relaxation behavior of the material provides insight into the low temperature behavior of hard binder material. First frequency sweeps were done with the dynamic shear rheometer (DSR) at a range of temperatures. The tests were performed to determine the stiffness and phase angle of the material. With the dynamic mechanical analysis (DMA) on beams of both binder and mastic (bitumen and filler) glass transition temperatures were determined. The filler influenced the results considerably. Direct tensile tests were performed on samples of bitumen and mastic. Both failure tests and relaxation tests were done. The results showed that the filler type could influence the behavior considerably. Finally relaxation tests were performed on a porous asphalt mixture in a specially designed tension test set-up. From the results it became clear that already at 0°C the relaxation capacity of the porous mixture with C-fix binder was strongly reduced. In all cases the C-fix binder was compared with a 70–100 pen grade bitumen.

1 INTRODUCTION

Hard bituminous binder materials are gaining popularity in road applications in the Netherlands. Asphalt mixtures containing hard bituminous binder material are already used in the asphaltic base layer. IN this paper the use of hard binders in surface layers is considered. One of the most common used asphalt mixtures used as surface layer on the Dutch motorways is Porous Asphalt Concrete (PAC). The main problem in PAC is its service life. Its ravelling resistance mainly determines the durability of a PAC wearing course. Ravelling or loss of aggregate from the wearing course is a form of “fatigue” that occurs in the surface layer of the pavement structure. Due to the open structure of PAC, oxygen, water and salt can easily penetrate into the asphalt layer resulting in a rapid ageing of the binder. The combined effects can lead to deterioration of the properties of the bitumen and break up the bond between bitumen and the aggregate structure. This results in loss of surfacing material. Improvement has to be found in improving size, shape and properties of the bituminous “contact bridges” between the aggregate particles. In this paper the possibility of using a hard binder like C-fix in PAC is discussed.

C-fix is a special binder with a low temperature susceptibility, a high resistance to ageing and it has environmental benefits. At the same temperature and loading condition the material has a much

higher strength and stiffness than normal pen grade binders. The name C-fix is an abbreviation for Carbon Fixation. The binder is the ultimate hard residue of crude oil. In the refinery process the crude oil is separated into two streams: heavy, carbon rich, fractions to create bituminous binders and light, hydrogen rich fractions for high-energy fuel. The heavy fractions from the conventional refinery processes are used as heavy fuels but can also be used for the production of C-fix. Using C-fix as a construction material, rather than having the carbon burnt in heavy fuel streams, results in significant carbon dioxide reductions. The used hard binder material in this paper is denoted as C9. This binder has a penetration of 9 [0.1 mm] at 25°C.

The binder, mastic and mixture were tested. The hard bituminous binder material is compared with conventional pen grade bitumen, in this case with 70/100 pen grade bitumen, which is normally used in single layer PAC mixture in the Netherlands. [1] The mastic was composed of the binder material and a filler Wigro 60k, which contains hydrated lime. The mastics had different filler-binder ratio by mass. The mixture, which was tested, is a standard Porous Asphalt Concrete according to the Dutch specification (RAW). [2]

In this paper the low temperature behavior of the binder and mastic will be discussed in chapter 2. In Chapter 3 relaxation tests on a Porous Asphalt Concrete mixture are reported. The paper ends with conclusions.

2 TESTS ON THE BINDERS AND MASTICS

2.1 *Test program*

The hard binder becomes brittle at low temperatures. The brittle behavior of the material can cause thermal cracking even at relatively high temperatures. Tests were performed to get insight into the low temperature behavior of this material. First rheological tests including frequency sweeps at a range of temperatures were done with the dynamic shear rheometer (DSR). The Glass Transition Temperature was determined with the Dynamic Mechanical Analyzer and the relaxation behavior of the binder and mastic was obtained from the Direct Tension Test.

2.2 *Dynamic Shear Rheometer*

With the Dynamic Shear Rheometer (DSR) frequency sweeps are performed at different temperatures on the binders. [3] Comparison of the master curves for complex modulus G^* of 70/100 pen grade bitumen and C9 (Figure 1) shows that at very high frequencies the slope approaches to zero and the values do not differ a lot, but when the frequency decreases the slope of the 70/100 bitumen increases much faster than for the C9. The values of the Complex Modulus G^* for the C-fix are higher than for the pen grade bitumen. For the C9 binder the stiffness at low frequencies is less sensitive to the change in the loading time compared to 70/100 bitumen.

The master curve for the phase angle shows that 70/100 bitumen is viscous at long loading times because the phase angle becomes 90° but the C9 still has an elastic component at the same loading time. So, the permanent deformation of 70/100 bitumen will be much higher when compared to C9 at the same temperature and frequency. Both materials get more elastic when the frequency increases. Overall it can be concluded that C9 is a very stiff binder compared to 70/100 bitumen over the whole range and specially at normal service temperatures.

2.3 *Glass transition temperature*

Viscoelastic materials such as bitumen or polymers typically exist in two distinct states. They exhibit the properties of a glass (higher modulus and brittle behavior) at very low temperatures and those of a rubber (lower modulus) at higher temperatures. The temperature at which a polymer undergoes the transformation from rubbery to a glassy state at a frequency rate of 1 Hertz is known as the glass transition temperature, T_g . There is a dramatic change in the properties of a polymer at the

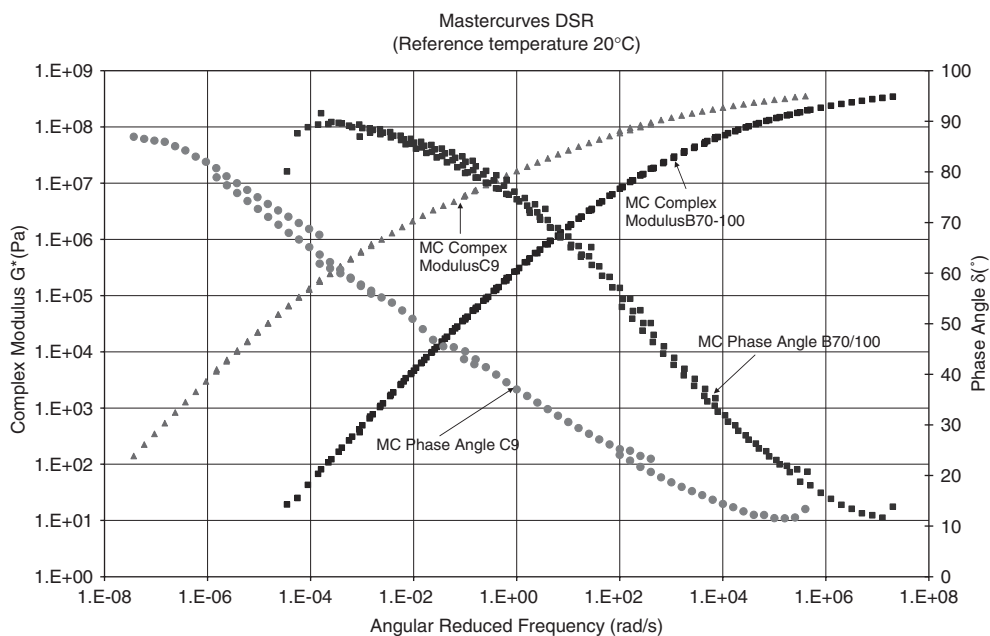


Figure 1. Complex modulus and phase angle master curves at 20°C of C9 binder and 70/100 bitumen.

Table 1. Glass temperature for different binders and mastics from the DMA in dual cantilever (1 Hz).

Type	# Samples tested	Average glass temperature [°C]	Standard deviation
B70-100	3	-29.4	0.82
B70-100 Mastic	3	-24.0	1.12
C9	3	-18.0	1.05
C9 Mastic (f/b:1)	3	-23.1	0.59
C9 Mastic (f/b:1.2)	3	-23.0	0.83
C9 Mastic (f/b:0.5)	3	-23.6	0.22

glass transition temperature. By scanning the temperature during a DMA experiment the change of state can be observed. Bitumen becomes totally brittle at lower temperatures, the glassy state. The glass transition temperature of the different binders and mastics was determined to compare the extent of brittleness. [4]

The set up used in the DMA was the dual cantilever test. In this test a rectangular specimen with dimensions 3.5 mm × 13 mm × 60 mm is clamped in the dual cantilever. A sinusoidal deformation is induced in the middle of the rectangular specimen. The results of this test are displayed in Table 1.

As expected, the glass transition temperature of the 70/100 pen grade bitumen is much lower than the C-fix binders. The difference is 10 to 15°C. The higher glass temperature can be explained by the length and shape of the carbon chains molecules. The larger chains can not move and slide in the way as the molecules and chains of the 70/100 pen grade bitumen can. Remarkably, the glass temperature of all the mastics is around -24°C. The effect of this filler for the bitumen and the C9 binder is very different. Filler lowers the glass transition temperature of the C-fix binder, whereas for the bitumen it increases the glass transition temperature. Adding this filler into the C9 binder seems to make it less brittle.

Table 2. Average failure stress and strain of C9 binder and mastic and B70-100 binder and mastic with DTT displacement rate 1 mm/min.

Type	Temperature [°C]	# tests	σ_f Mean [MPa]	σ_f Standard deviation [MPa]	ε_f Mean [%]	ε_f Standard deviation [%]
B70-100	-10	6	2,35	0,57	6,54	0,43
B70-100 Mastic	-10	6	4,95	1,08	4,26	0,67
C9	8,5	9	0,98	0,05	1,31	0,13
C9 Mastic (f/b:1)	8,5	12	3,59	0,13	4,27	0,44
C9 Mastic (f/b:1.2)	8,5	6	3,73	0,30	2,27	0,06
C9 Mastic (f/b:0.5)	8,5	6	1,86	0,21	1,76	0,59
C9 Mastic (f/b:1)	0	16	3,58	0,74	0,58	0,12
C9 Mastic (f/b:1)	-10	6	2,88	0,97	0,32	0,14

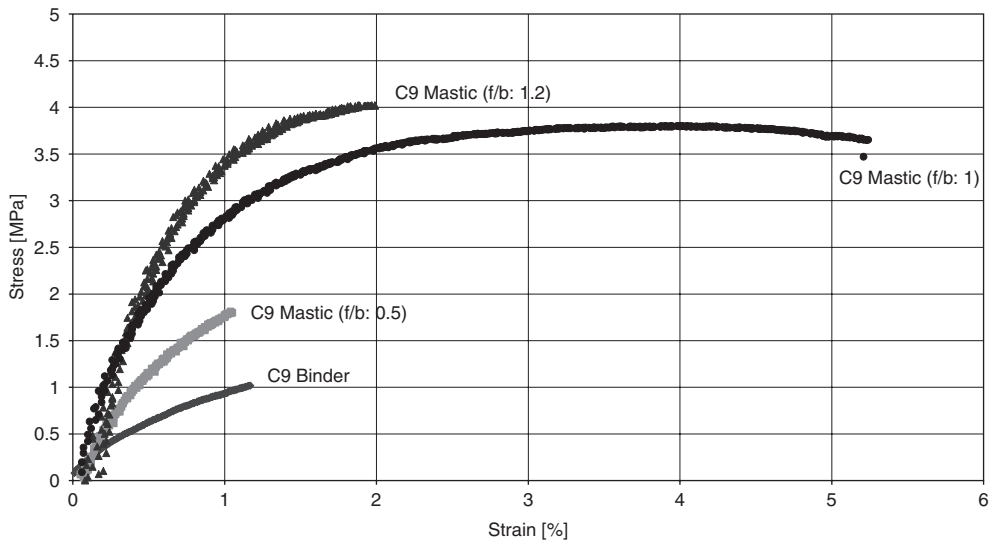


Figure 2. Representative result stress-strain for C9 binder and mastics at 8.5°C with displacement rate 1 mm/min.

2.4 The Direct Tension Test

The Direct Tension Test or DTT was performed to determine the tensile strength and the strain at failure of the different C-fix-filler combinations and to compare with the standard 70–100 mastic. [5] Test temperatures and test results are shown in Table 2. All tests were performed at a displacement rate of 1 mm/min.

The C9 mastics with a binder-filler-ratio of 1 shows to perform the best at 8.5°C, considering the failure stress and strain. This binder-filler-ratio is the same as used in PAC mixtures. It is more ductile at this temperature than all the other C9 mastics. The C9 binder is more brittle than the C9 mastics. The strain at break for the mastic with a filler-binder ratio 1 is much higher than for the binder. Adding filler to the binder seems to make the material tougher. An optimum can be seen in the test results at a filler-binder ratio of 1, adding more filler reduces the toughness. Above the ratio of 1 the strain at break reduces again.

Table 3. Relaxation with the DTT for different binders and mastics at -10°C .

Material	f/b	Displacement rate* [mm/min]	Displacement [mm]	Strain [%]	Area [mm ²]	Max. stress [MPa]	Relaxation (t = 600 s) [%]
B70/100	0	3	0,127	0,38	36,0	0,76	100,0
B70/100	1	3	0,127	0,38	36,0	2,04	100,0
C9	0	0,3	0,073	0,22	37,0	1,05	55,7
C9	0,5	0,3	0,054	0,16	39,3	1,05	34,8
C9	1	0,3	0,063	0,19	38,4	1,29	25,4
C9	1,2	0,3	0,059	0,17	41,0	1,46	22,4

*In order to get reliable results, a higher displacement rate had to be used for the B70/100 specimens.

2.5 Relaxation in binder and mastic

The relaxation of the binders and mastics at low temperature is important because if reduction of stress occurs, the material has the ability to overcome or minimize cracking due to the combined effect of traffic and thermal load.

Relaxation of the binder and mastics was measured in the Direct Tension Tester. The sample was subjected to a small displacement, which resulted in a tensile stress in the sample. The reduction of the stress was measured. In order to compare the relaxation of the different binders and mastics, the relaxation is displayed as a percentage of the maximum stress measured.

The response can be divided in three parts, elastic, visco elastic and viscous. The amount of the relaxation of the stress depends on the loading speed. Applying the defined displacement faster will result in a higher load. For the displacement controlled tests relatively short loading times were initiated. The second part of the response, the viscoelastic response, or the relaxation will start after that. If a specimen is monitored for a very long time the viscous part will be visible and even all the stress can decay. The samples were monitored for 600 seconds. An example of results from the relaxation tests is given in Table 3.

The relaxation of B70/100 binder and mastic was 100 percent after five minutes, whereas the relaxation in C9 mastics was less than 50 percent for the mastics. The binder has a relaxation of 56 percent of the maximum stress after ten minutes. The pure binder relaxes more than the mastics. But after 10 minutes the residual tensile stress in the C-fix specimens is still between 0.5 and 1.15 MPa. Its is also clear that adding filler considerably reduces the relaxation of the C9.

3 TEST ON A POROUS ASPHALT CONCRETE MIXTURE

Pavement surface layers are always subjected to a combination of thermal and traffic induced stresses. From cement concrete technology it is well known that in order to get the same number of load repetitions, the repeated traffic reduced stress should be much lower when a thermal induced stress is present than when such a stress is not present. The effect of the thermal stress however is significantly reduced when the material exhibits a significant stress relaxation behavior. Since the C-fix binder appears to be a stiff material and shows only limited relaxation behavior it was expected that asphalt mixtures with a C-fix binder also show a limited relaxation behavior, indicating that they might be sensitive to a combination of thermal and traffic induced stresses.

In order to determine the stress relaxation of a mixture, tests were performed on a PAC mixture (see Table 4 for the mixture composition) using a Uniaxial Tension Tester (UTT). [6] From gyrotary compacted specimen cylinders were sawn with a height of 130 mm and a diameter of 65 mm.

3.1 Relaxation in displacement controlled tests

A small displacement was imposed on the specimen in the longitudinal direction and held at the specific strain level of 1.25×10^{-4} . The longitudinal strain rate $\dot{\epsilon}$ was 0.25×10^{-4} implying that

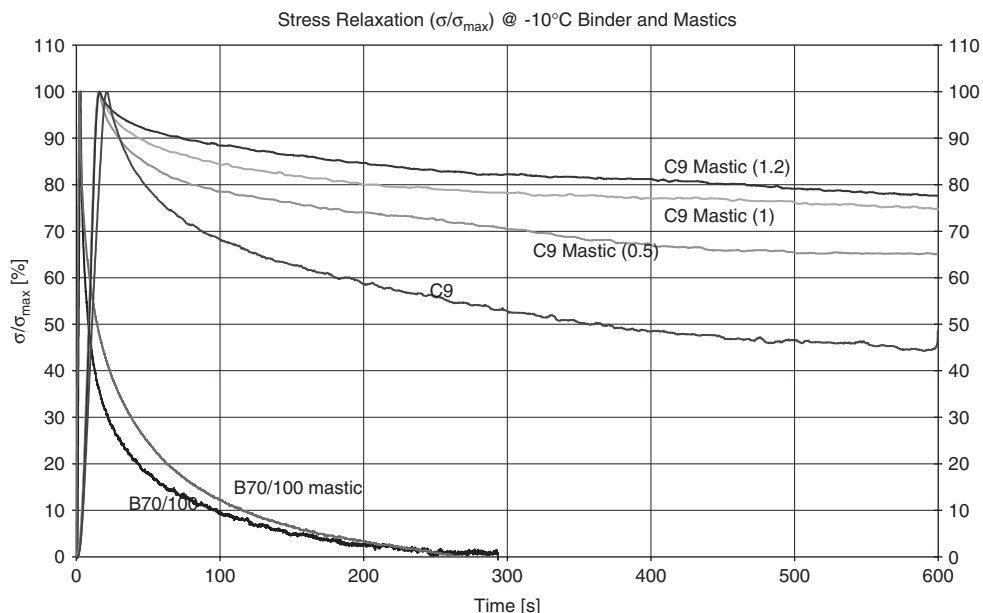


Figure 3. Relaxation of stress displayed as percentage of maximum stress. (note that the loading speed was different for C9 compared to B70/100).

Table 4. Composition of porous asphalt concrete 0/16 [% (m/m)].

Gradation	Composition [% (m/m)]
16–11.2	30.0
11.2–8	35.0
8–5.6	20.0
5.6–2	0.0
2–0.063 (sand)	10.5
>0.063 (filler)	4.5
Content of bitumen	4.5

it took 5 seconds to obtain the desired deformation. The load and its reduction were measured for 600 seconds. The displacements were kept small to ensure that they were in the linear viscoelastic range. Figure 4 shows the test setup, while Table 5 shows some of the results obtained. The results are also illustrated in Figure 5.

Relaxation in the C9 mixture at -10°C is still present, although just 35 percent of the maximum stress dissipated. At higher temperatures the maximum stress reduces considerably and more relaxation occurs in the C9 specimens. At $+10^{\circ}\text{C}$ 77 percent of the maximum stress of 0.76 MPa, was dissipated after 10 minutes. The relaxation of the B70/100 mixture at 0°C is almost 100 percent after 6 minutes. The maximum initiated stress at the beginning of the test with the same elongation and elongation rate $\dot{\epsilon}$ is also very low. The relaxation of the PAC with B70/100 at -10°C is almost the same as PAC with C9 binder at $+10^{\circ}\text{C}$, both in terms of the maximum stress developing in the specimen as well as the shape of relaxation curve (Figure 5). So it seems that a shift of 20°C can be observed for a PAC mixture.



Figure 4. Uniaxial tension test setup.

Table 5. Relaxation of PAC mixture at different temperatures after loading till a strain level of approximately 1.25×10^{-4} and strain rate 0.25×10^{-4} .

Material	Temperature [°C]	Maximum stress [MPa]	Stress relaxation after 600 s [%]	Displacement [mm]	$\varepsilon(\text{long})_{\text{max}}$
C9	-10	1,64	35,1	0,016	1,22E-04
	0	1,37	51,3	0,016	1,24E-04
	+10	0,76	77,1	0,016	1,26E-04
B70/100	-10	0,94	85,1	0,016	1,26E-04
	0	0,35	100,0	0,016	1,25E-04

3.2 Relaxation in temperature controlled tests

Tensile stresses will develop in asphalt concrete mixtures in a pavement structure due to a decrease in temperature. In order to get an idea of the tensile stresses that develop and the relaxation of those stresses the following test was performed. The asphalt specimen was fastened in a uniaxial tension test setup. The temperature was decreased with a constant temperature rate. Stress will build up in the specimen due to the temperature change. After the desired temperature was reached, the temperature was kept constant for a certain amount of time. During the temperature decrease and after reaching the desired temperature some stress relaxation occurred.

The temperature in the temperature chamber was decreased from $+10^{\circ}\text{C}$ to -10°C with a cooling rate of 2 and 5°C per hour. The increasing stress and its relaxation due to the temperature decrease are illustrated in Figure 6.

As shown in Table 6, the maximum induced tensile stress in the C9 mixture seemed to be independent from the cooling rate. This was not the case for the B70/100 mixtures, but the stress build up was very low as can be seen in Table 6. Furthermore it appeared that much higher stresses were generated in the C9 mixtures. It also appeared that the relaxation in the B70/100 mixtures was much more pronounced than in the C9 mixture. This became already clear during the cooling period the maximum stress for the B70/100 was much lower than for the C9. The B70/100 mixture already relaxed during the cooling period.

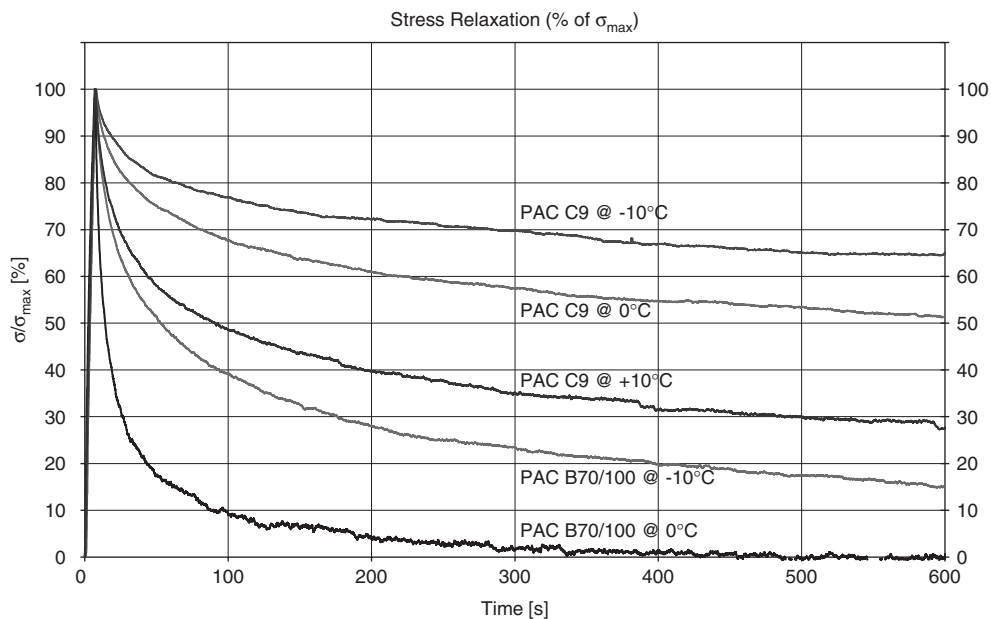


Figure 5. Relaxation of PAC with B70/100 and C9 binder at different temperatures.

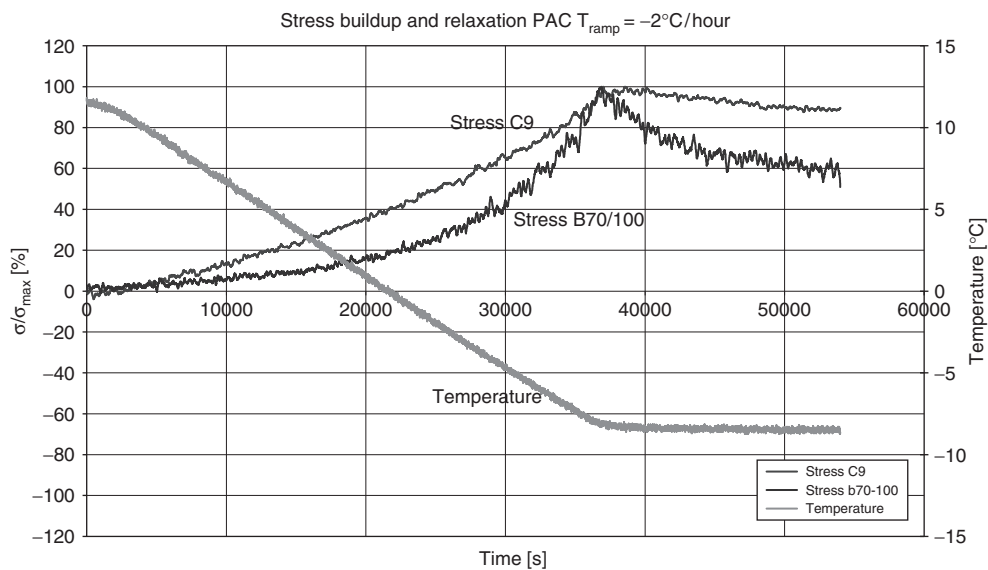


Figure 6. Comparison of the stress build up and relaxation of the two PAC mixtures with temperature decrease of $2^\circ\text{C}/\text{hour}$.

3.3 Tensile strength

In the previous section attention is paid to tensile stresses that develop due to temperature and the relaxation behavior of both the C9 and B70/100 mixtures. It is shown that the tensile stress in the C9 is much higher than in B70/100, but the tensile strength of the materials at the given conditions

Table 6. Relaxation compared after 5 hours relaxation time.

Mixture	T_{ramp} [°C/hour]	σ_{max} [MPa]	Relaxation [%] (after 5 hours)
C9	-2	0,81	10,3
C9	-5	0,84	12,8
B70/100	-2	0,08	38,2
B70/100	-5	0,12	57,8

Table 7. Results of tensile strength [MPa] for the different PAC mixtures and temperatures.

Temperature [°C]	Tensile strength C9 PAC [MPa]	Tensile strength B70/100 PAC [MPa]
+10	1.72	-
0	1.78	0.77
-10	1.89	1.90

are also important to know. The results of the tensile strength, which were measured in the UTT, are shown in Table 7.

The strength of the PAC with C9 does not differ much with temperature change, whereas in the PAC with B70/100 a significant decrease in strength can be noticed. Comparing the tensile stress developed in the previous tests and the tensile strength, shows that the stresses for the PAC with C9 at -10°C are quite near the strength of the material.

4 CONCLUSIONS

Adding filler to the C-fix binder material has besides a stiffening effect also a toughening effect, which can be derived from the results of the Direct Tension Test of the binders and mastics. This toughening effect for the hard bituminous binder can also be observed in the shift of Glass Transition Temperature.

From the results of the short term relaxation with the displacement controlled test it becomes clear that already at 0°C the relaxation capacity of the porous mixture with C9 is strongly reduced, indicating high tensile stresses. After 10 minutes the initial stress of 1.37 MPa was only reduced to half of its value. At -10°C the stress in the PAC with C9 reaches almost 85% of its strength. A shift of approximately 20°C between standard PAC (70/100) and C9 PAC is noticed. At $+10^{\circ}\text{C}$ the C9 PAC shows the same short term relaxation behavior as PAC with 70/100 bitumen at -10°C .

Building up of temperature induced stresses was investigated with a long term cooling test with fixed specimen length. The used cooling rates from $+10^{\circ}\text{C}$ to -10°C hardly results in stresses in the standard PAC, but in stresses above 0.8 MPa in C9 PAC. Even after 5 hours at -10°C still tensile stress levels of 0.7 MPa in the C9 PAC mixture are measured.

Comparison of the mastic behavior with the PAC mixture behavior (Figure 3 and 5 at -10°C) gives a similar picture, indicating that mastic behavior is the driving force for relaxation.

REFERENCES

Khedoe R.N. 2006. *Possible use of C-Fix in Porous Asphalt*. M. Sc. Thesis Delft: Delft University of Technology 2005. *RAW Standard Conditions of Contract for Works of Civil Engineering Construction*. Ede: CROW (in Dutch)

2003. *EN 14770: 2003, Bitumen and bituminous binders – Determination of complex shear modulus and phase angle – Dynamic Shear Rheometer (DSR)*. Brussels
2004. *ASTM E 1640 – 04: Standard Test Method for Assignment of the Glass Transition Temperature by Dynamic Mechanical Analysis*. West Conshohoken, PA, USA
2002. *ASTM D6723-02, Standard Test Method for Determining the Fracture Properties of Asphalt Binder in Direct Tension*. West Conshohoken, PA, USA
- Erkens S.M.J.G. 2002. *Asphalt Concrete Response (ACRe) – Determination, Modelling and Prediction*. dissertation Delft: Delft University of Technology

Comparison of the modulus of high-modulus asphalt mixtures – experimental determination and calculation

F. Vervaecke, J. Maeck & A. Vanelstraete
Belgian Road Research Centre, Sterrebeek, Belgium

ABSTRACT: The correlation between the stiffness moduli of a bituminous binder and an asphalt mixture was intensively investigated by BRRC in earlier research. It was found that the complex modulus of an asphalt mixture can be calculated using a function that includes the ratio of the volume of dry aggregates to the volume of binder, air voids content, and the complex modulus of the bituminous binder (Francken, 1996).

In this paper the validity of this correlation is verified for the special case of high-modulus asphalt concrete. This asphalt type is characterized by a high-modulus bitumen and a higher binder content. The experimentally determined complex modulus of a series of high-modulus mixtures is compared with calculations based on Francken's method. Different calculations are made with different estimations of the stiffness of the bituminous binder (i.e. Van der Poel's method, and DSR measurements combined with the Arrhenius equation) and different approximations of the pure elastic modulus of the bituminous binder (i.e. asymptotically approximated from DSR measurements, an average value of 3000 MPa often used for traditional pen. binders, and a new averaged value of 3640 MPa). Francken's method combined with the different estimations of binder stiffness makes it possible to estimate the stiffness modulus of a high-modulus asphalt mixture at different temperatures and frequencies with an accuracy of approximately 10–20%.

Furthermore, the reliability of this stiffness estimation for use in structural design is investigated with design software used in Belgium (DimMET, 2006). The findings show that Francken's prediction method as investigated in this paper, with an accuracy of 10–20% in estimating stiffness, is good for use in the design of a road structure.

1 INTRODUCTION

Recently, there has been an increasing growth in traffic volume and loading. New road designs and materials are introduced in response to this changing reality. One possible alternative is the introduction of high-modulus asphalt. This type of bituminous mixture is characterized by a high-modulus bitumen and a higher binder content. These mixtures have a higher stiffness and, as such, a higher bearing capacity. They also perform better in fatigue, owing to the higher binder content (BRRC, 2008).

The structural design of a road is based on the stiffness and fatigue properties of the bituminous mixtures. Both parameters have an impact on the length of life of the road structure. Therefore, it is important to accurately estimate the stiffness of a bituminous mixture from the various mixture parameters. It was demonstrated in the past that there is a good correlation between the stiffness of a bituminous mixture and three parameters: the volume ratio of dry aggregates and binder, voids content, and the stiffness of the bituminous binder (Francken, 1996). This was demonstrated for traditional asphalt concrete, porous asphalt, and stone mastic asphalt. In this paper, the validity of this correlation is investigated for the case of high-modulus asphalt. This is done by comparing the

experimentally determined stiffness of a series of high-modulus asphalt mixtures with calculated values. Different calculations are made with different approaches to estimate the stiffness of the bituminous binder (i.e. Van der Poel's method, and DSR measurements combined with the Arrhenius equation) and different approximations of the pure elastic modulus of the bituminous binder (i.e. asymptotically approximated from DSR measurements, an average value of 3000 MPa often used for pure binders, and an new averaged value of 3640 MPa).

In a final section, the impact of variations in stiffness, of the order of 10–20%, on the structural design of a road is investigated. This is done in order to verify the impact of the accuracy of Francken's calculation – combined with the different methods to estimate binder stiffness and the pure elastic modulus – on the design of a road structure.

2 MODEL TO ESTIMATE THE STIFFNESS OF BITUMINOUS MIXTURES

The stiffness of a bituminous mixture can be estimated with a series of empirical relations as presented below, in which mix composition and the complex modulus of the bituminous binder are considered (Francken, 1996):

$$|E^*(T, f)| = E_\infty \cdot R^*(T, f); \quad (1)$$

where E_∞ is the pure elastic modulus, which is constant for a given mixture, and R^* the reduced modulus ($0 < R^* < 1$), which describes the shape of the master curve of the modulus.

For these parameters the following relations are valid:

$$E_\infty = 14360 \cdot \left(\frac{V_a}{V_l}\right)^{0.55} \cdot \exp(-0.0584 \cdot \nu); \quad (2)$$

$$\log(R^*) = \log(B^*) \cdot \left[1 - 1.35 \cdot F\left(\frac{V_a}{V_l}\right) \cdot G(B^*)\right]; \quad (3)$$

$$B^* = \frac{E_{bit}^*}{E_{\infty, bit}^*}; \quad (4)$$

$$G(B^*) = 1 + 0.11 \cdot \log(B^*); \quad (5)$$

$$F\left(\frac{V_a}{V_l}\right) = 1 - \exp\left(-0.13 \cdot \frac{V_a}{V_l}\right); \quad (6)$$

where

- E_{bit}^* is the complex modulus of the bituminous binder at a given temperature T and frequency f ;
- $E_{\infty, bit}^*$ represents the pure elastic modulus of the bitumen. For traditional binders (with a normal pen. value and no polymer modification) the pure elastic modulus can be approximated by 3000 MPa (Francken, 1996). Alternatively, parameter $E_{\infty, bit}^*$ can be determined from DSR measurement (dynamic shear rheometer) at low temperatures;
- V_a is the volume percentage of dry aggregates in the mixture;
- V_l the volume percentage of binder in the mixture;
- ν the percentage of voids in the mixture. The voids content is determined by hydrostatic weighing of the sample according to EN 12697-5.

Different methods exist to estimate the stiffness of the binder. Stiffness can be estimated from its conventional properties by means of Van der Poel's nomogram (VDP). Alternatively, it can be determined with (DSR) measurements. A master curve, giving binder stiffness as a function of temperature and loading frequency, is experimentally determined. Different methods are available to describe temperature dependency, such as the WLF method and the Arrhenius relation. The latter is used in this paper.

2.1 Van der Poel's nomogram

This nomogram was developed decades ago (Van der Poel, 1954) to estimate the stiffness modulus of pure bituminous binders from their conventional properties: the ring-and-ball temperature $T_{R\&B}$, the penetration index (PI), the frequency f of loading (in Hz), and temperature T . Note that Van der Poel's monogram is not valid for polymer-modified binders.

2.2 Master curve based on the rheological properties of a bitumen

With the dynamic shear rheometer (DSR), the stiffness modulus of a bitumen can be measured for a wide range of temperature and frequency combinations. The results can be plotted into a master curve giving the modulus as a function of a reduced parameter X , which is determined by temperature and frequency – as follows:

$$X = \log \alpha_T + \log f. \quad (7)$$

The relation between temperature T and α_T can be represented by the equation of Arrhenius:

$$\log \alpha_T = 0.4343 \cdot \frac{\delta H}{R} \cdot \left(\frac{1}{T} - \frac{1}{T_{ref}} \right); \quad (8)$$

where δH is the activation energy (cal/mol); R , is the universal gas constant (cal/mol.K); and T_{ref} , is the reference temperature (in K). Moreover, it is known that E_{bit}^* asymptotically approximates the pure elastic modulus $E_{\infty,bit}^*$ for high X values (that is, for low temperatures and high loading frequencies).

3 STIFFNESS MEASUREMENTS ON HIGH-MODULUS ASPHALT

For this study, a series of fifteen high-modulus asphalt mixtures was investigated. Within this series several mixture parameters were varied:

- 4 bituminous binders: Bit 1, Bit 2, Bit 3 and Bit 4;
- 2 types of skeleton: 3 mixtures with a sandy skeleton, and 12 with a stony skeleton;
- reclaimed asphalt (% RA): 6 mixtures with different percentages of RA (25% and 40%), and 9 mixtures without RA;
- binder content (% b);
- voids content (% of voids).

The fifteen mixtures and their respective parameters are presented in table 1. More details on mix composition and other properties can be found in (BRRC, 2008; De Visscher et al., 2008).

The different binders were characterized and their properties are presented in table 1. Ring-and-ball temperature, $T_{R\&B}$, was determined according to EN 1427:2000-(01/2000); penetration, $pen.$, according to EN 1426:2000-(01/2000). For the mixtures with RA, $T_{R\&B}$ and $pen.$ of the total binder were, therefore, determined by applying the mixing rules (Read et al., 2003):

$$\log(pen(blend)) = v_o \cdot \log(pen(o)) + v_n \cdot \log(pen(n)); \quad (9)$$

$$T_{R\&K}(blend) = v_o \cdot T_{R\&K}(o) + v_n \cdot T_{R\&K}(n); \quad (10)$$

where v_o and v_n are the percentages of RA and new bitumen, respectively, and o , n , and $blend$ represent the RA and the new, and the blended binder, respectively.

Dynamic shear rheometer (DSR) measurements were performed on the bituminous binders according to EN 14770:2005-(10/2005). The pure elastic modulus of the bitumen, $E_{\infty,bit}^*$, was

Table 1. Overview of the bituminous mixtures.

Mix	Skeleton	Bitumen	% b	% RA	Voids (%)	$T_{R\&B}$ (°C)	Pen. (1/10 mm)	$E_{\infty,bit}^*$ (MPa)	E^* (MPa) 15°C, 10 Hz
1	stony	2	5.5	0	1.5	66.4	23.0	4357	12381
2	sandy	2	5.4	0	2.4	66.4	23.0	4357	12722
3	stony	1	5.5	0	2.6	69.8	17.0	4557	14556
4	stony	3	5.5	0	2.5	66.0	18.0	2729	14608
5	stony	4	5.5	0	1.7	68.6	23.0	2929	14272
6	stony	1	5.5	0	2.4	70.2	16.0	4557	12740
7	stony	1	5.3	0	2.3	70.2	16.0	4557	11859
8	stony	1	5.5	40	2.3	69.0	16.4	4557	12839
9	sandy	2	5.3	25	3.1	67.2	23.0	4357	11989
10	stony	1	5.8	0	1.2	70.2	16.0	4557	13900
11	stony	1	5.8	40	3.9	65.9	21.1	4557	10581
12	stony	1	5.7	25	2.1	67.5	19.0	4557	12461
13	stony	1	5.6	40	2.7	65.9	21.1	4557	10579
14	sandy	2	4.9	0	3.6	66.4	23.0	4357	13492
15	stony	1	5.8	40	1.4	65.9	21.1	4557	12048

determined as the asymptotic value of E_{bit}^* towards low X values (low temperatures, high frequencies) in a DSR measurement. Note that DSR measurements are performed on new binders only and not on binders which are a blend of a new and an old binder (from RA). Consequently, the $E_{\infty,bit}^*$ values reported for the bituminous mixtures containing RA only represent the new binder. This is a good approximation, since the new binder is the largest fraction in the blend of binders; moreover, in the case of high-modulus asphalt, in which hard binders are used, the stiffness of the RA binder is generally comparable to the stiffness of the new binder (BRRC, 2008).

The stiffness modulus E^* of the bituminous mixtures was measured with the two-point bending test according to EN 12697-26 (Annex A). This test was performed at various temperatures between -20°C and 30°C and different loading frequencies between 1 Hz and 30 Hz. The stiffness moduli of the different mixtures at 15°C and 10 Hz are given in the last column of table 1.

4 COMPARISON BETWEEN STIFFNESS MEASUREMENTS AND ESTIMATIONS

Following the model presented in section 2, four different methods were used to estimate the stiffness modulus of the various bituminous mixtures. All of them are based on Francken's method to estimate the stiffness modulus from the stiffness of the binder.

A first method makes use of Van der Poel's nomogram to estimate the stiffness of a bitumen from its conventional properties. This method is referred to as Van der Poel-Francken method. Three different values of $E_{\infty,bit}^*$ were tried:

1. the experimentally estimated $E_{\infty,bit}^*$ (asymptotically determined from DSR measurements at low temperatures and high frequencies);
2. $E_{\infty,bit}^*$ was approximated by 3000 MPa, as it is done for traditional pen. binders;
3. $E_{\infty,bit}^*$ was approximated by 3640 MPa, the averaged value of the asymptotically determined $E_{\infty,bit}^*$ -values of the 4 high-modulus binders investigated in this study.

Note that $E_{\infty,bit}^*$ was determined by extrapolation from the DSR measurements, but that the limits of the DSR measurement are lower for high-modulus bitumens than for traditional pen. binders.

Another method makes use of the Arrhenius relation to determine a master curve from DSR measurements performed on the bituminous binder. The combination with Francken's method is called the Arrhenius-Francken method. Details of the calculations can be found in (BRRC, 2006).

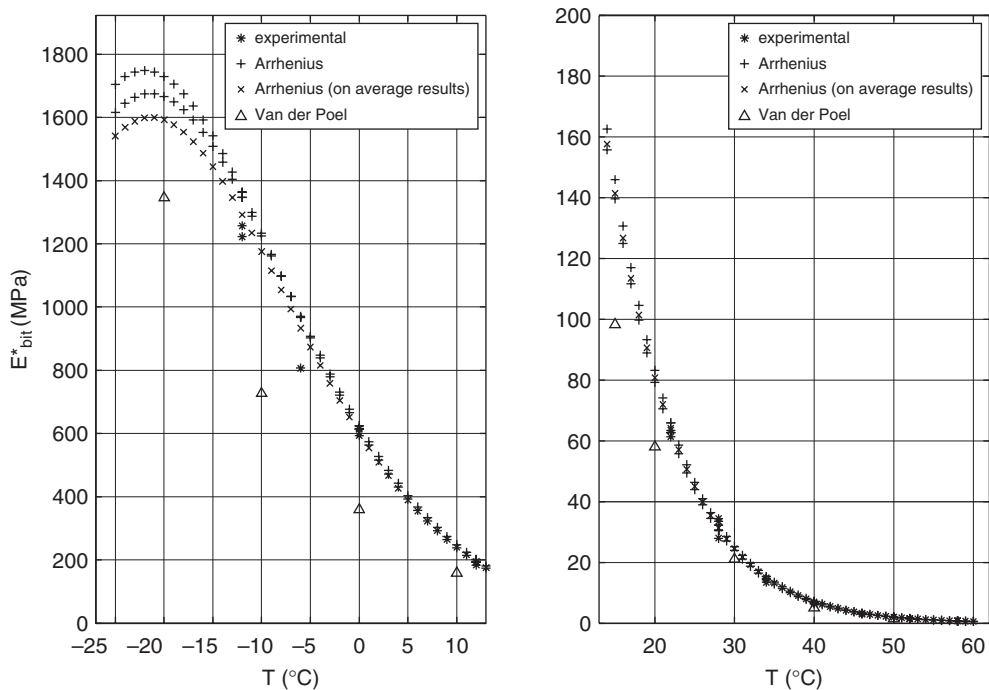


Figure 1. Stiffness of bitumen 4 versus temperature T, at a frequency of 10 Hz.

Figure 1 shows the stiffness modulus of bitumen 4 as a function of temperature. This graph contains the experimentally determined stiffness (represented by black circles), the Van der Poel simulation with $E_{\infty,bit}^*$ estimated from DSR measurements (represented by white triangles), and the Arrhenius approximation (represented by crosses). Figure 2 shows the stiffness of asphalt mixture 5 versus temperature. This graph represents the experimentally determined stiffness (represented by black circles) as well as the estimations by the Van der Poel-Francken method (with $E_{\infty,bit}^*$ asymptotically estimated from DSR measurements) (represented by white triangles) and the Arrhenius-Francken method (represented by crosses).

In figure 3, the relative differences between the estimated and the experimentally determined stiffnesses are represented per mixture. The black, dark grey, light grey, and white bars respectively represent the estimations by the Van der Poel-Francken method with $E_{\infty,bit}^*$ = asymptotically determined from DSR measurements, with $E_{\infty,bit}^* = 3000$ MPa and with $E_{\infty,bit}^* = 3640$ MPa, and the estimation by the Arrhenius-Francken method. The various plots (a), (b), (c), and (d) respectively represent the differences in stiffness at -10°C , 0°C , 15°C , and 30°C , for a frequency of 10 Hz.

In order to compare the different estimation methods, the average value of the relative difference between estimated and experimental values is presented in table 2. The largest differences are obtained for the estimation by the Van der Poel-Francken method with $E_{\infty,bit}^* = 3000$ MPa. This method overestimates the stiffness modulus by more than 20% over all temperatures investigated. At high temperatures very large overestimates are found. For the other methods, it is hard to assess from the available data which method gives the best estimation of stiffness, as the results are very similar. Hence, it can be concluded that the various methods are capable of predicting the stiffness of a high-modulus asphalt mixture with an accuracy of 15 to 20%, except the Van der Poel-Francken method with $E_{\infty,bit}^* = 3000$ MPa.

The influence of the skeleton of the asphalt mixture on the accuracy of the stiffness estimation was investigated. No correlation between the skeleton and the accuracy of the stiffness estimation

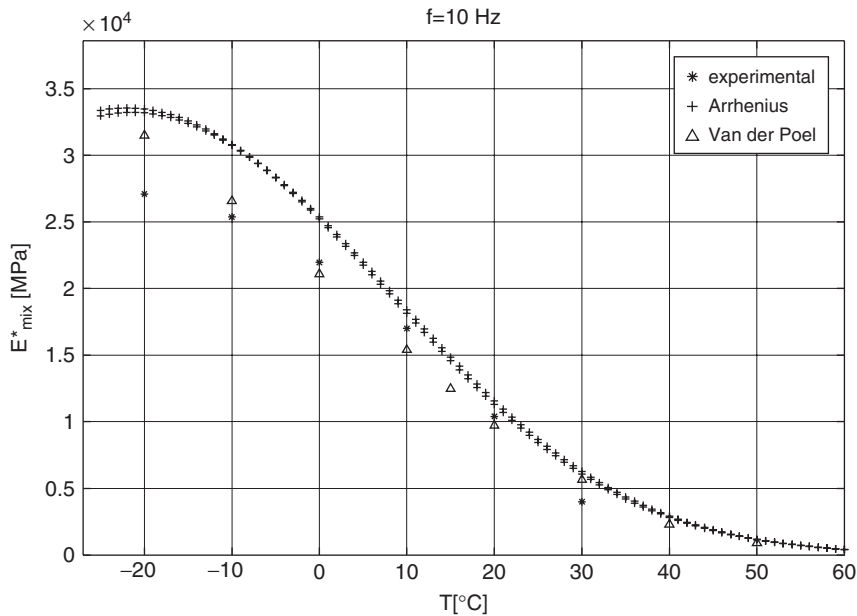


Figure 2. Stiffness of bituminous mixture 5 versus temperature.

Table 2. Average value and standard deviation of the relative differences between estimated and experimentally determined stiffness moduli (in %).

	-10°C	0°C	15°C	30°C
VDP-Francken	6 ± 10	1.5 ± 12	-7 ± 11	4 ± 15
<i>E_{∞,bit} DSR-estimated</i>				
VDP-Francken	15 ± 12	12 ± 12	9 ± 13	26 ± 20
<i>E_{∞,bit} = 3000 MPa</i>				
VDP-Francken	11 ± 11	5 ± 11	1 ± 12	14 ± 19
<i>E_{∞,bit} = 3640 MPa</i>				
Arrhenius-Francken	11 ± 12	3 ± 12	-9 ± 14	-8 ± 14

was found (BRRC, 2006). Also investigated was the influence of the use of RA in the asphalt mixture. The average difference between simulation and experimental stiffness modulus is presented in table 3. The Arrhenius-Francken method was not used in this case, because no rheological measurements are performed on blends of new and aged (RA) bituminous binders. In spite of the limited amount of available data, there is a clear tendency for the three methods to lead to larger deviations when RA has been used. This may be caused by the mixing rules used to estimate $T_{R\&B}$ and $pen.$ of the blends, and will be studied in more detail in the future.

5 INFLUENCE OF THE STIFFNESS OF THE BITUMINOUS MIXTURE ON STRUCTURAL DESIGN

In this section, the influence of variations in stiffness on the structural design of a road is investigated. One of the aims of the particular study is to determine the impact of a difference of 10–20% in

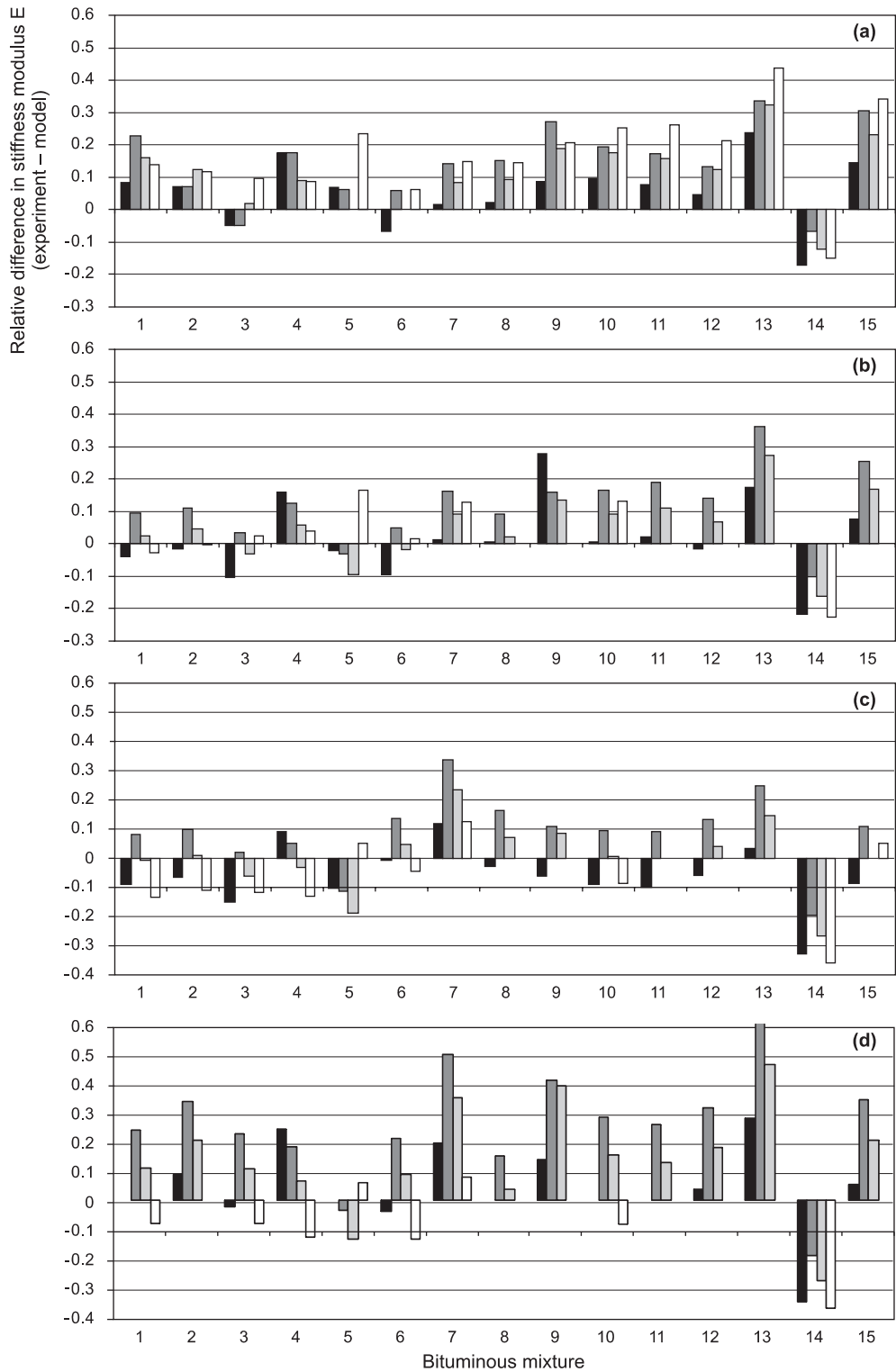


Figure 3. Relative differences between measured and estimated stiffness modulus, for the various estimation methods used.

Table 3. Average value and standard deviation of the relative differences between estimated and experimentally determined stiffness moduli (in %).

	-10°C		0°C		15°C		30°C	
	RA	RA	RA	RA	RA	RA	RA	
VDP-Francken $E_{\infty,bit}$ DSR-estimated	3 ± 11	10 ± 7	-4 ± 10	9 ± 12	-7 ± 13	-5 ± 5	1.5 ± 17	9 ± 11
VDP-Francken $E_{\infty,bit} = 3000$ MPa	9 ± 10	23 ± 8	7 ± 9	20 ± 10	6 ± 15	-14 ± 6	20 ± 20	36 ± 16
VDP-Francken $E_{\infty,bit} = 3640$ MPa	6 ± 10	19 ± 8	0 ± 9	13 ± 9	-3 ± 14	-6 ± 5	8 ± 19	24 ± 16
Arrhenius-Francken	11 ± 12	/	3 ± 12	/	-9 ± 14	/	-8 ± 14	/

stiffness (which is a realistic variation in stiffness between experimental and calculated value, as it was found in the previous section) on the structural design of a road.

Structural design was studied with the software DimMET jointly developed by BRRC and Febelcem on the request of MET (the Walloon Road Administration) (DimMET, 2006). This design software makes use of the multilayer model of elastic materials for the structural design of semi-rigid and flexible road pavements with a bituminous surface layer.

The example considered is the following: a standard Belgian traffic histogram in which only single axles are considered; an average of 5000 heavy vehicles per day; 300 working days per year; and an average of 3.6 axles per vehicle. The road structure used for this simulation consisted of a bituminous surface layer of 50 mm in AC-1B, a bituminous binder course of 100 mm in high-modulus asphalt (mixture 10 from table 1), an unbound base layer of 215 mm in crushed stone ($E = 650$ MPa), a subbase layer of 400 mm in sand ($E = 500$ MPa), and a subgrade soil with a CBR of 4.

For the simplicity of the simulation, a fixed temperature of 15°C during the entire year was considered instead of seasonal temperature changes. The loading frequency was 30 Hz, corresponding with a vehicle speed of approximately 60 km/h. Under those conditions, the stiffness modulus of the AC-1B surface layer is approximately 9900 MPa, while the stiffness modulus of high-modulus asphalt mixture 10 is 15900 MPa. The stiffness of the HMA was reduced by approximately 10, 20 and 30%, respectively, in order to investigate its effect on the structural design. The influence of the reduction in stiffness on the structural design is represented in table 4. In this table, the first column gives the HMA's stiffness used for the structural design, while the second column indicates the relative deviation of the stiffness modulus used from the original value of 15900 MPa. The 3rd column indicates the design life of the road structure, and the 4th column the failure probability after a period of 30 years. The last column gives a compensation in thickness of HMA needed to maintain the design life of 30 years of the original structure (with $E = 15900$ MPa).

From these results, it can be inferred that a difference of 30% in stiffness only has a minor influence on the design life of the road structure. In that case, the life decreases from 30 to 27 years, i.e., by approximately 10%. This reduction in life can be compensated by an increase in layer thickness of 8 mm, or approximately 8%. For smaller deviations in stiffness, the decrease in life is even smaller. A reduction of approximately 10% in stiffness shortens the design life by only 3 to 4% and requires an increase in layer thickness of only 2 to 3% for equal life.

6 CONCLUSIONS

Complex moduli of a series of high-modulus mixtures were experimentally determined and compared with values predicted from Francken's method, in which the influence of mix composition and binder properties are considered.

Table 4. Results of the structural design simulations performed in DimMET as a function of the stiffness of the HMA.

$E_{\text{Mix } 10}^*$ (MPa)	Relative difference (%)	Design life (years)	Failure probability (%)	Extra thickness for equal life (mm)
15900	0	30	47.6	
14700	10	29	50.7	2
13300	20	28	53.8	4
11100	30	27	58.8	8

It can be concluded that for asphalt mixtures with high-modulus bitumen, the stiffness modulus of the mix can be very well predicted with both the Van der Poel-Francken method with the pure elastic modulus, $E_{\infty, \text{bit}}^*$, determined from the DSR measurements or approximated by 3640 MPa, and the Arrhenius-Francken method. Both methods give an estimate of the stiffness modulus accurate to within 10–20%. A slightly worse estimate of the stiffness modulus, with an accuracy of more than 20%, is obtained with the Van der Poel-Francken method when an approximated pure elastic modulus, $E_{\infty, \text{bit}}^*$, of 3000 MPa is used for the bitumen.

In order to decide if such models are acceptable for use in structural design calculations, the impact of various variations in stiffness modulus on structural design was evaluated. It can be concluded that such variations in stiffness only have a limited impact on structural design. A difference of 10% in stiffness gives rise to a change of 3–4% in design life and 2–3% in thickness. From this we can conclude that prediction models, based on the mix composition and the binder properties, are indeed interesting means for use in structural design calculations.

REFERENCES

- BRRC, 2006, “*Prestatie-indicatoren voor bitumieuzen bindmiddelen en mengsels*”, final research report, Sterrebeek, 2006.
- BRRC, 2007, “*Asfalt met verhoogde stijfheid*”, final IWT research report, Sterrebeek, to be published in March 2008.
- Devisscher, J., Vansteenkiste, S., Vanelstraete, A., 2008, “*Test sections in high modulus asphalt: mix design and performance tests*”, submitted for publication to Eurasphalt & Eurobitume Congress, Copenhagen, 2008.
- DimMET, 2006, “*Logiciel pour le Dimensionnement des Chaussées*”, jointly developed by BRRC and Febelcem for MET, 2001–2006.
- Francken L. & Vanelstraete A., 1996, “*Complex moduli of bituminous binders and mixtures. Interpretation and evaluation*”, Eurasphalt & Eurobitume Congress, Strassbourg, 1996, paper 4.047.
- Van der Poel, C., 1954, “*A general system describing the viscoelastic properties of bitumen and its relation to routine test data*”, Journal of Applied chemistry, 1954, 4, 22.
- Read, J., Whiteoak, D., “*The Shell Bitumen Handbook*”, London, Telford Books.

Acoustic emission in asphalt mixture IDT creep and strength tests

X. Li

Iowa State University, Ames, USA

M.O. Marasteanu & J.F. Labuz

University of Minnesota, Minneapolis, Minnesota, USA

ABSTRACT: The objective of the research was to investigate the use of acoustic emission to analyze the microstructural phenomena of damage and the corresponding macroscopic behavior in asphalt mixtures tested at low temperature. An acoustic emission system with eight channels of recording was used to monitor the specimens tested in creep and in strength testing. The source location and the AE event count were used to illustrate the relationship between the micro damage and macroscopic behavior for the two different test conditions. The analysis indicates that a damage zone develops in both the creep and the strength tests. The damage zone changes with the test temperature and the loading level applied during the creep test.

1 INTRODUCTION

It is well recognized that asphalt mixtures have complex temperature-sensitive behaviors. The response to a given loading is strongly dependent on temperature and loading path. A change of a few degrees in temperature induces dramatic changes in behavior of the asphalt mixture. The behavior can vary from relatively ductile at higher temperature to brittle at lower temperature.

Low temperature cracking is the most significant distresses in asphalt pavements built in cold climates. Low temperature cracking is attributed to tensile stresses induced in the asphalt pavement as the temperature drops to extremely low values. The accumulation of tensile stress to a certain level is associated with the formation of microcracks, which release energy in the form of elastic waves called acoustic emission (AE). The current AASHTO specification for asphalt mixture low temperature characterization consists of two tests: the indirect tensile creep test (ITC) and the indirect tensile strength test (ITS). For both tests, cylindrical specimens of 150 mm diameter \times 50 mm thickness are loaded in compression across the diametral plane.

This paper investigates the use of AE to analyze the microstructural phenomena and the corresponding macroscopic behavior in asphalt mixtures tested at three low temperatures. For each test temperature, two different loading levels were used in the creep test and one constant stroke rate of 1 mm/min was employed in the strength tests. This was done to identify the damage development with loading levels and to compare the damage zone in creep and failure tests.

This research is important because it provides physical evidence of damage and its development in asphalt mixtures subjected to constant loading at low temperatures. This raises the important question of the validity of linear assumptions in the IDT creep test and data analysis and of how representative of true pavement conditions are the creep load level and the strength displacement rate recommended by AASHTO. In addition, this research sheds more light into the failure mechanism at low temperature and provides information that can be used to design better fracture resistant asphalt pavements.

2 BACKGROUND

AE methods represent a well-documented and widely used tool to characterize microscopic fracture processes and therefore to evaluate damage growth in brittle materials. An acoustic emission is defined as a transient elastic wave generated by the sudden release of energy from localized damage processes within the stressed material. This energy release causes the propagation of stress waves that can be detected at the surface of the material. Acoustic emissions result from microcracking, dislocation movement, phase transformation, and other irreversible changes in the material.

Due to its capability of detecting internal damage, AE has been used for many years to study the behavior of materials such as rock and concrete. By studying the occurrence of AE events, the investigations are generally focused on the cumulative number of AE events, the rate of occurrence, amplitude distribution, energy and frequency distribution.

Compared to the vast number of studies performed on Portland cement concrete and rocks, a literature search on the use of AE in asphalt materials results in a very limited number of references. This is due to the fact that for most service temperatures asphalt mixtures display viscous and ductile behavior and the development of defects is gradual and does not produce emissions that can be detected.

In one of the first efforts to document the use of AE to characterize the fracture of asphalt mixtures under thermal loading conditions at low temperatures, Valkering & Jongeneel (1991) used a single piezoelectric transducer mounted on the surface of the specimen. The cumulative event counting was analyzed to determine how damage accumulates during loading. Their work was followed by a small number of studies performed by different authors who also limited their analyses to counting of AE events.

AE techniques were also investigated during the Strategic Highway Research Program (SHRP) in an effort to better characterize the cohesive, adhesive and thermal properties of asphalt binders (Chang, 1994; Wang, 1995; Qin, 1995). However, this work was performed at higher temperatures that considerably limited the analysis of the AE results. Sinha (1998) reported on the AE activity in unrestrained asphalt mixture samples exposed to thermal cycling at low temperatures to show that micro cracking occurs in asphalt mixtures due to the difference between the thermal contraction coefficients of the aggregate and of the asphalt binder. Hesp et al. (2001) investigated AE activity in restrained asphalt mixture samples undergoing various temperature cycles and Cordel et al. (2003) used two transducers to detect the AE events in asphalt mixture direct tension tests performed at low temperatures.

In a recent study by Li & Marasteanu (2006), the accumulated AE events obtained from an AE system with eight channels of recording were analyzed to illustrate the relationship between the micro damage and macroscopic behavior of the asphalt mixtures at different loading levels. In addition, the initiation and propagation of the cracking were observed using the localization of the event source and the fracture process zone in the asphalt mixtures was measured by observing the distribution of microcracks with different energy levels.

3 EXPERIMENTAL PROCEDURE

The asphalt mixture used in this study was prepared using the Superpave design procedure outlined in SP-2. One asphalt binder with performance grade (PG) 58-34 and modified by styrene-butadiene-styrene (SBS) was used. Granite aggregate was selected to prepare the mixture. Cylindrical specimens 150 mm by 170 mm were compacted using the Brovold gyratory compactor. A 4% target air voids was achieved after compaction. The compacted samples were then cut into 3 slices with 50 mm in thickness.

The indirect tensile test set-up is shown in Figure 1. A sample with dimensions of 150 mm diameter by 50 mm height was loaded in static compression across its diametral plane. Different load levels were applied in the creep test to investigate the effect of load levels on the development of the micro damage during the creep test. A constant loading rate of 10 kN/s was used at the

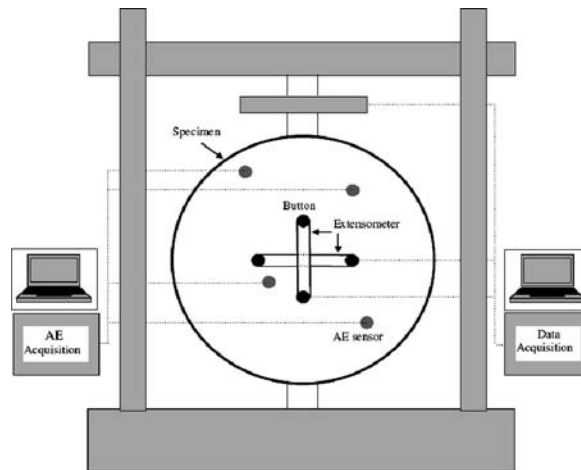


Figure 1. Schematic of experimental setup.

beginning of the creep test. Following the creep test, indirect tensile strength test was performed at the same temperature. A constant stroke rate of 1 mm/min was applied during the strength test until failure.

An AE system with eight channels of recording was used to monitor the asphalt mixture specimens tested in creep and strength tests. The AE event signals were recorded using four DAQ cards (Model PCI-5112, National Instruments). Each card had two independent channels which acquired AE signals detected by eight piezoelectric sensors (Model S9225, Physical Acoustics Corporation). Four sensors were mounted on each side of the specimen using M-Bond 200, a modified alkyl cyanoacrylate. The preamplification of the AE signals was provided by eight preamplifiers (Model 1220C, PAC) with a gain set to 40 dB. One of the sensors was used as a trigger, which was often the one closest to the tip of the initial notch. Trigger level was set at 10 mV in this research. Once the recording was triggered, signals were band-pass filtered (0.1–1.2 MHz) and sampled at 20 MHz over 200 microseconds.

Considering the ringing of the resonant sensor, a sleep time of 9 milliseconds between two consecutive events was prescribed during which the system could not be triggered. The velocity of propagation of the longitudinal waves was determined by generating an elastic wave by pencil lead (0.5 mm diameter) breakage on the opposite side of the specimens.

Tests were performed in a MTS servo-hydraulic testing system. The TestStar IIs control system was used to set up and perform the tests and to collect the data. The software package Multi Purpose TestWare was used to custom-design the tests and collect the data. All tests were performed inside an environmental chamber. Liquid nitrogen tanks were used to obtain the required low temperature. The temperature was controlled by MTS temperature controller and verified using an independent platinum RTD thermometer.

Three test temperatures, -12°C , -24°C and -36°C were selected based on the PG lower limit of the asphalt binder. Two specimens, one replicate for two different loading levels, were fabricated for the creep testing at each temperature. The specimen used for the creep test at the lower loading level was also used for the strength test, 30 minutes after the creep test.

4 DISCUSSION OF RESULTS

The mechanical response for all three temperatures during the strength tests are shown in Figure 2. At the highest temperature (-12°C), the asphalt mixture is more ductile and it has lower peak load and larger displacements. At the lowest temperature (-36°C), the material is brittle. At -24°C temperature, the mixture exhibits an intermediate behavior.

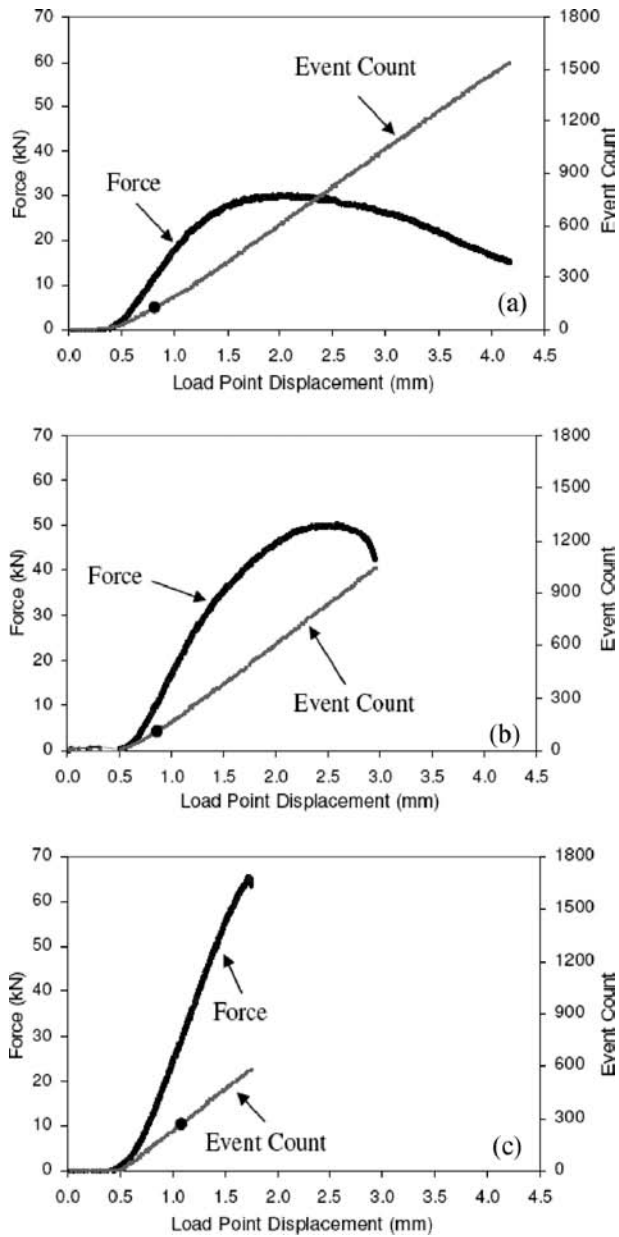


Figure 2. Load and AE count versus displacement from strength test: (a) -12°C ; (b) -24°C ; (c) -36°C .

4.1 AE event counting

The event count curves under different temperatures follow a similar pattern. Very few AE events were detected at the beginning of the test but soon after the AE rate was constant at 7 to 8 events per second. The black circle on the event count curve shows the loading level in the creep test performed before the strength test. For all strength plots under different temperatures, more than 100 events were recorded before the loading level applied in the creep test was reached. This appears to indicate that the Kaiser effect, which describes the phenomenon that a material under load emits acoustic

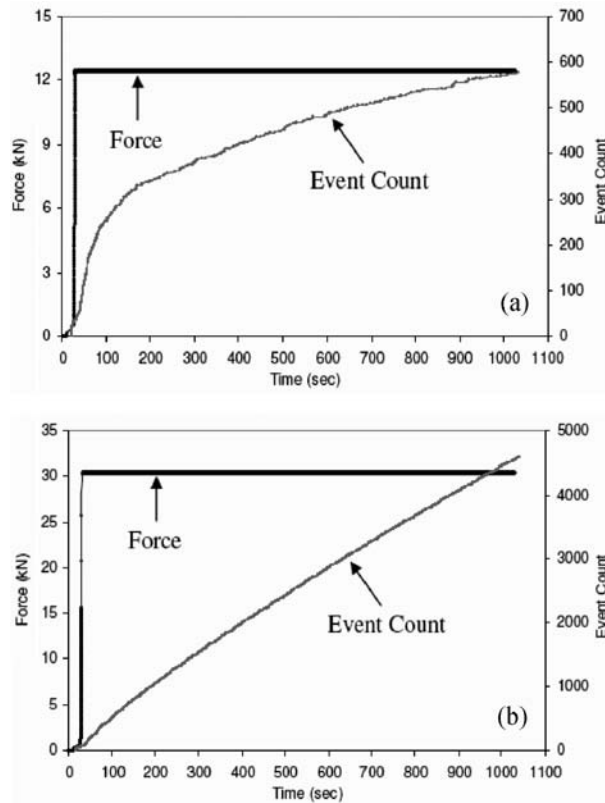


Figure 3. Typical plot for load and AE count versus time from creep test: (a) 12.5 kN at -24°C ; (b) 30 kN at -24°C .

waves only after a primary load level is exceeded, is not applicable to the material investigated in this study.

A typical plot of loading and AE event count versus time for the creep test is shown in Figure 3. The two creep tests with different load level under the same temperature show a similar trend with time. AE events were recorded with a fast event rate immediately after the creep load level was applied in a short time and the event rate decreased with time. It was found that more events were recorded in the creep test with higher loading level.

4.2 AE source location

The source location of the AE events can be inferred by investigating the differences of the first time of arrival among the transducers placed at different locations on the specimen. Therefore, it is necessary to determine the arrival time of the elastic waves for each sensor from the recorded AE event. The correct picking of the first arrival strongly affects the accuracy of the source location (Labuz et al., 1997). The mean amplitude and standard deviation of the noise during the pre-trigger period was calculated and a threshold was set at three times the standard deviation from the mean. By measuring the time at which the signal passes this threshold value for each sensor, the relative arrival time can be obtained.

Once the arrival times of the event were determined from the sensor records, the location of the AE event source can be estimated. It should be noted that not all events can be located. It was found that only 143 events were located with 10 mm error for the creep test under the lower loading level

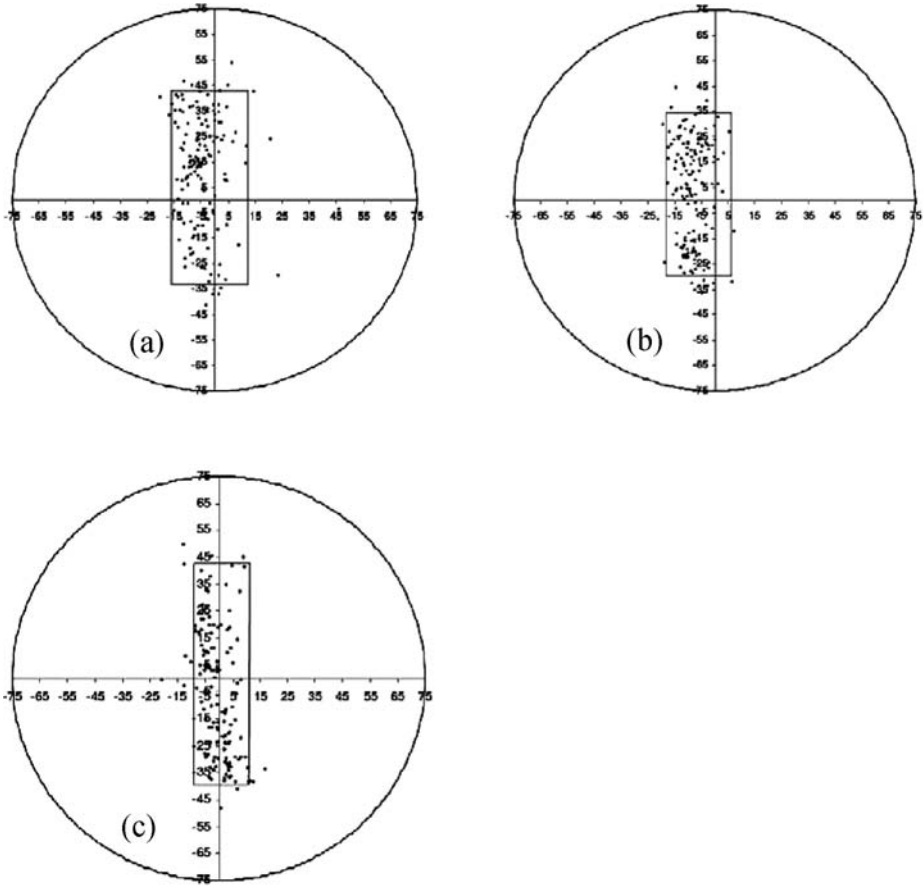


Figure 4. Event locations and damage zone for strength test: (a) -12°C ; (b) -24°C ; (c) -36°C .

at -24°C . Therefore, event locations with 143 events are selected and plotted for the comparison. A rectangle was drawn to contain 90% of these 143 events. Figure 4 shows the first 143 AE locations obtained from the strength test under different temperatures. It can be seen that the AE events in Figure 4(a) and (c) are evenly distributed along the symmetric axis of the specimen, whereas the AE events in Figure 4(c) is skewed to the left side of the specimen. This may be explained by the fact the asphalt mixture is not perfectly homogenous and its properties can be affect by the air voids and aggregate distribution inside the material. It is found that the size of the damage zone, which is defined here as the area with microcracking inside the rectangle, changes with temperature for the strength test. The width of this zone decreases with the decrease in test temperature. While no clear difference is found for the length of the damage zone for the two higher temperatures, the damage zone at the lowest temperature is obviously longer than the damage zones at the two higher temperatures.

Figures 5, 6 and 7 show the locations for the last 143 events during the creep test for all temperatures. It should be noted that the damage zone in most specimens is skewed to the left side; this is most likely due to the non-homogeneity of the test specimens, although substantially more testing is required to validate this statement. It is observed that for all temperatures the damage zone obtained at the higher load was significantly larger in width than the zone obtained from the lower load creep test. For example, the damage zone obtained from the lower load level creep test

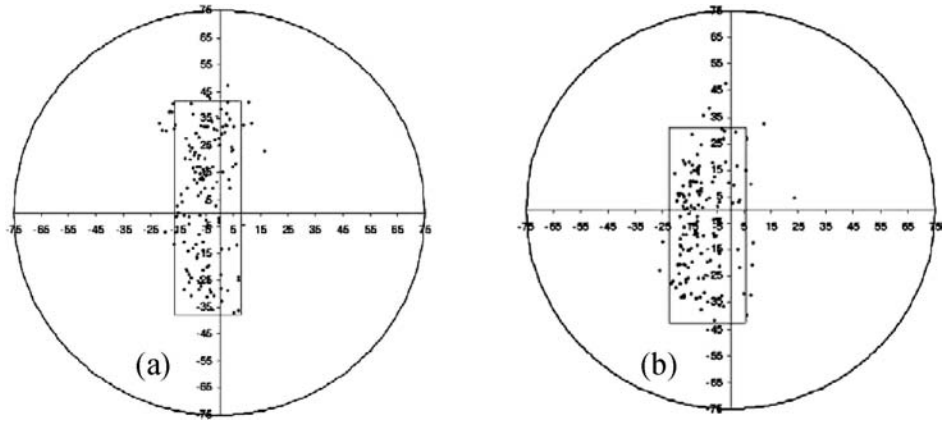


Figure 5. Event locations and damage zone for creep test at -12°C : (a) 10 kN (33% of strength); (b) 15 kN (50% of strength).

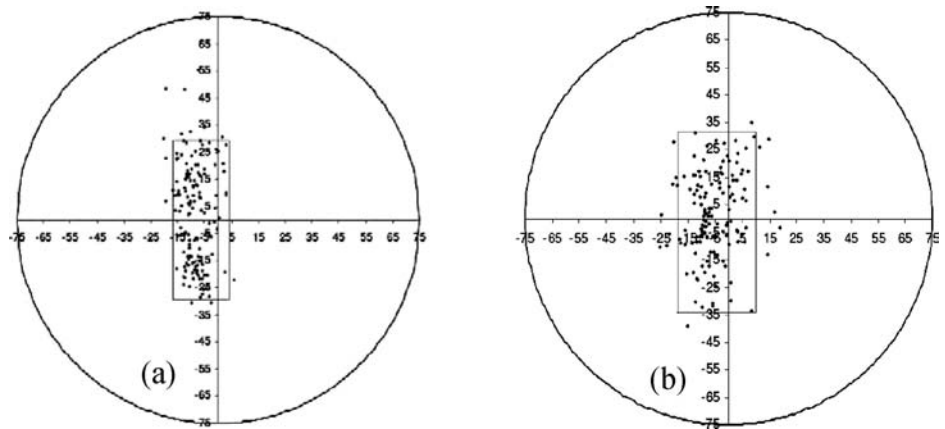


Figure 6. Event locations and damage zone for creep test at -24°C : (a) 12.5 kN (25% of strength); (b) 30 kN (60% of strength).

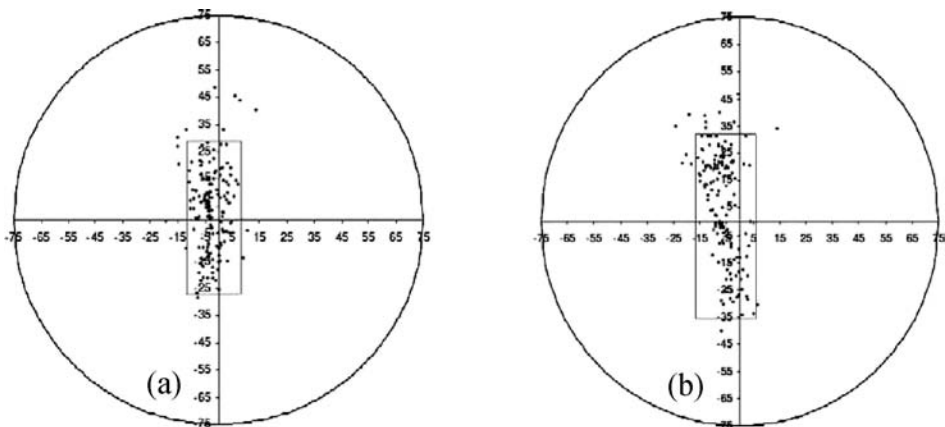


Figure 7. Event locations and damage zone for creep test at -36°C : (a) 25 kN (38% of strength); (b) 40 kN (61% of strength).

at -12°C is 24 mm in width, while the damage zone from the higher load level creep at the same temperature is 29 mm wide. For the creep tests with relatively lower load level, both the width and length of the damage zone decreased with the decrease of test temperature (Figs 5a, 6a, 7a). For example, the damage zone obtained from the lower load level creep at -24°C is 21 mm by 60 mm, while the size of damage zone from the higher load level creep at -36°C is 18 mm by 55 mm.

5 CONCLUSIONS

Indirect tensile creep tests at two different loading levels and strength tests were performed at three different test temperatures for one asphalt mixture. An acoustic emission system with eight channels of recording was used to monitor the development of microcracking in the specimens for both tests.

The experimental data show that the asphalt mixture presented more brittle behavior with decrease in test temperature, as expected. Few events were recorded at the beginning of the strength test but the AE rate was constant at 7 to 8 events per second above a certain loading level. However, a similar event rate was found immediately after the creep load was applied, but the event rate decreased with time. Creep tests at higher load levels were found to produce more events than the tests with lower load levels for all test temperatures. This information suggests that micro damage occurs during creep tests, which has not been previously reported. This investigation appears to indicate that linear viscoelastic conditions are not always present during IDT testing and raises the question of how representative of field conditions are the loading parameters recommended in the AASHTO specification.

REFERENCES

- Chang W. V. 1994. Application of Acoustic Emission to Study the Cohesive and Adhesive Strength of Asphalt. Strategic Highway Research Program, SHRP-A-682, pp. 81–148.
- Cordel S., Benedetto H. Di., Malot M., Chaverot P., and Perraton D. 2003. Fissuration à basse température des enrobés bitumineux-essai de retrait thermique empêché et émission acoustique. 6th International RILEM Symposium, Performance Testing & Evaluation of Bituminous Materials (PTEB 03), Editor Partl, M., pp. 465–472, Zurich, 2003.
- Hesp S.A.M., Smith B.J. 2001. The Effect of Filler Particle Size on Low and High Temperature Performance of Asphalt Mastics and Mixtures. *Journal of the Association of Asphalt Paving Technologists*, Vol. 70, pp. 492–542.
- Labuz J.F., Dai S.-T., and Shah K.R. 1997. Identifying Failure Through Location of Acoustic Emission. *Transportation Research Record 1526*, TRB, National Research Council, Washington, D.C., pp. 104–111.
- Li X., and Marasteanu M.O. 2006. Investigation of Low Temperature Cracking in Asphalt Mixtures by Acoustic Emission. *International Journal of Road Material and Pavement Design*, Vol. 7, No. 4/2006, pp. 491–512.
- Qin X. 1995. Adhesion properties of polymeric materials. Ph.D. thesis, University of Southern California, Chemical Engineering.
- Sinha N.K. 1998. Acoustic emission in asphalt subjected to thermal cycling at low temperature. In *Acoustic emission/microseismic activity in geologic structures and materials*, Proceedings of the Six Conference, by Reginald Hardy, Jr., H., Pennsylvania State University, Vol. 21, 109–120.
- Valkering C.P. and Jongeneel D.J. (1991). Acoustic emission for evaluating the relative performance of asphalt mixes under thermal loading conditions. *Journal of the Association of Asphalt Paving Technologists*, Vol. 60, 160–187.
- Wang H.-C. 1995. Ultrasonic and acoustic emission in nondestructive evaluation of viscoelastic solids – elastomer, human cornea and asphalt. Ph.D. thesis, University of Southern California, Chemical Engineering.

The effects of different waveforms and rest period in cyclic loading on the fatigue behavior of the asphalt mixtures

K. Kogo & K. Himeno
Chuo University, Tokyo, Japan

ABSTRACT: The four point bending fatigue tests were carried out for dense graded asphalt mixtures under various wave patterns in repeated loading: sinusoidal, triangular, twin peaks, sinusoidal with one second rest period, sinusoidal with ten second rest period. Analyzing the results using classical fatigue analysis, energy approach and ENTPE fatigue damage approach, it was found 1) that the fatigue damage subjected in asphalt mixtures differs significantly depending on the wave patterns of repeated loading, giving much difference in the number of load applications to failure, 2) that the number of load applications to failure is depending considerably on the rest period 3) that there are linear relations between the rate of dissipated energy change and the number of load applications to failure without the rest period, showing approximately constant relations even if loading wave pattern is different, 4) that there are linear relations between the rate of stiffness change and the number of load applications to failure, showing approximately constant relations even if loading wave pattern and rest period are different.

Keywords: fatigue, crack, asphalt mixture, dissipated energy, damage approach.

1 INTRODUCTION

1.1 *Background*

Fatigue cracking due to repeated traffic loading is one of the major distresses in asphalt pavements. Resistance against fatigue cracking is therefore an essential property to be considered in the design of asphalt pavement [1].

The factors that affect the fatigue of an asphalt mixture include those related to load, environment, and the mixture. The load factors include load level, loading wave pattern, loading time (frequency and presence/absence of rest period); the environmental factors include temperature, water, and changes in the materials during the use of the mixture; and the mixture factors include mixture formula and the properties of binder and aggregate [2].

As regards loading wave pattern and rest period, which are addressed in this study, many of the past studies based on laboratory experiment adopted sinusoidal waves and continuous loading. Actual traffic loads, however, are not continuous sinusoidal waves but are rather complicated wave patterns that occur discontinuously and irregularly. It is therefore considered meaningful to investigate the effect of wave pattern and rest period on the fatigue behavior of asphalt mixtures with the aim of understanding the fatigue behavior of asphalt mixtures on real roads and developing measures to improve the crack resistance of asphalt pavement.

1.2 *Objective*

The effect of the wave pattern and rest period of loading on the fatigue behavior of an asphalt mixture was investigated in this study through laboratory fatigue testing. The experimental results

Table 1. Asphalt mixture formula and grading.

Proportion of aggregate %	13–5 mm	37.5
	5–2.5 mm	20.0
	Coarse Sand	32.7
	Fine Sand	6.5
	Filler	3.3
Mass, percent passing %	13.2 mm	100
	4.75	62.5
	2.36	42.5
	600 μm	24.1
	300	15.1
	150	9.3
	75	6.0
Straight Asphalt 60–80%		5.8

were then analyzed with the aim of finding an index of the fatigue damage of asphalt mixtures that can be used universally regardless of loading conditions.

1.3 Outline of this study

Fatigue tests with different loading wave patterns and rest periods were carried out by using four-point bending fatigue test equipment.

From the experimental results, dissipated energy for each wave pattern was determined, and total dissipated energy to failure and the rate of dissipated energy change were investigated in relation to the number of load applications to failure. The relationship between the rate of stiffness change and the number of load applications to failure was also investigated by using the fatigue analysis method developed by Ecole Nationale des Travaux Publics de l'Etat (ENTPE) in France [3, 4]. Here, the rate of stiffness change is an index of fatigue damage corrected for the effect of specimen temperature change due to dissipated energy change and the effect of binder thixotropy.

2 EXPERIMENTAL METHOD

2.1 Mixture formula

The mixture formula and grading of the dense graded asphalt mixture (13) used in this study are shown in Table 1. Straight asphalt 60–80 was selected as a binder, and the binder content was set to 5.8% (optimum asphalt content).

2.2 Test methods

a) Four-point bending fatigue test

The conditions of the four-point bending fatigue test are listed in Table 2, and the loading wave patterns used are shown in Figure 1.

Dense graded asphalt mixture (13), with the prescribed density, was formed into a platy shape of $40 \times 300 \times 400$ mm and then cut into five specimens of $40 \times 40 \times 400$ mm in shape.

Four different wave patterns (triangular wave, twin-peaks wave, sinusoidal wave with 1s rest period, and sinusoidal wave with 10s rest period) were prepared by using the 0105 Arbitrary Wave Pattern Editor software of NF Corporation. The data generated was then input to the fatigue test equipment through the WF1943A Multifunction Synthesizer of NF Corporation. The test was controlled with regard to displacement, so that strain amplitude generated on the top and bottom faces of the specimen would be within the range between 200 and 400 $\mu\text{m}/\text{m}$.

Table 2. Test conditions.

Dimension of specimen	40 × 40 × 400 mm
Span	300 mm
Type of loading	4 point bending
Mode of loading	Strain controlled
Wave pattern	Sinusoidal, Triangular, Twin peaks Sinusoidal + Rest1s Sinusoidal + Rest10s
Frequency	Sinusoidal, Triangular → 5 Hz Twin peaks → 2.5 Hz Sinusoidal + Rest1s → Loading0.2s + Rest1s Sinusoidal + Rest10s → Loading0.2s + Rest10s
Test Temperature	10°C

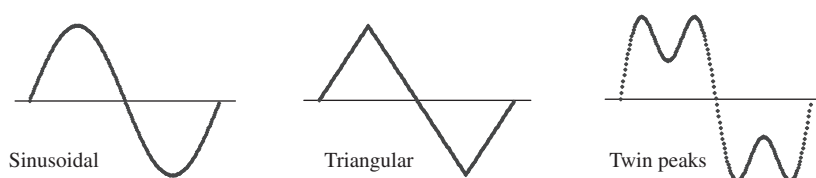


Figure 1. Loading wave patterns.



Figure 2. Uniaxial fatigue test equipment.

The number of load applications to failure corresponds to a sudden decrease observed in stress amplitude.

b) Phase angle measurement in uniaxial fatigue test

Because it was difficult to measure phase angle precisely with the four-point bending fatigue test equipment used in this study, the phase angle used for calculating dissipated energy was inferred from the relationship between stiffness and phase angle (see section 4.1) measured by using uniaxial fatigue test equipment (Figure 2) [5].

To prepare specimens for the uniaxial fatigue test, an asphalt mixture of the prescribed density was formed into a rectangular piece of 300 × 300 × 100 mm. Then, the central part of the rectangular piece was cut and shaped into three cylinders of 75 mm in diameter and 120 mm in height, and the top and bottom faces of each cylinder were polished to make them parallel to each other. Phase angle was measured by means of displacement control; displacement amplitude was controlled so that strain amplitude generated in the specimen would be 50 μm/m. Test temperature was varied within the range between -10 and 50°C.

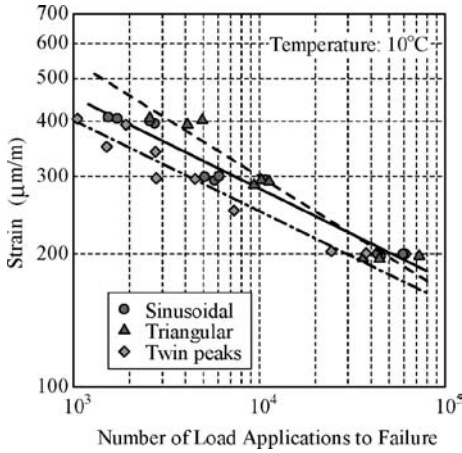


Figure 3. Fatigue test result (Effect of wave pattern).

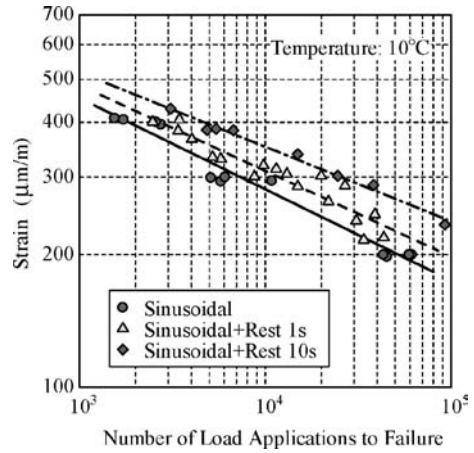


Figure 4. Fatigue test result (Effect of rest period).

3 EXPERIMENTAL RESULTS

3.1 Effect of loading wave pattern

The results of the four-point bending fatigue test for different wave patterns are summarized in Figure 3.

The number of load applications to failure varies with the wave pattern of load. Regardless of strain, the number of load applications to failure in the twin peaks wave was about one half that in the sinusoidal wave. The number of load applications to failure in the triangular wave is greater than that in the sinusoidal wave when strain is high (about 400 $\mu\text{m/m}$), but they are about the same when strain is low (about 200 $\mu\text{m/m}$).

3.2 Effect of rest period

The results of the four-point bending fatigue test for different rest periods are summarized in Figure 4.

For the same strain level, the number of load applications to failure was greater in the wave patterns having rest period than in the continuous sinusoidal wave pattern. The longer the rest period, the greater the number of load applications to failure.

4 DISSIPATED ENERGY AND FATIGUE FAILURE CHARACTERISTICS

4.1 Phase angle measurement

When an external cyclic load is applied to a viscoelastic substance such as an asphalt mixture, the observed stress wave pattern becomes advanced in phase than the strain wave pattern. When strain is plotted against stress, a hysteresis loop is drawn as shown in Figure 5. Stress and strain measurements were carried out at intervals of 0.002 s in the present study. Phase angle ϕ was calculated from equation (1), where L_1 and L_2 were read from Figure 5.

$$\sin \phi = L_2 / L_1 \quad (1)$$

The relationship between stiffness and phase angle measured with the uniaxial fatigue test equipment is shown in Figure 6.

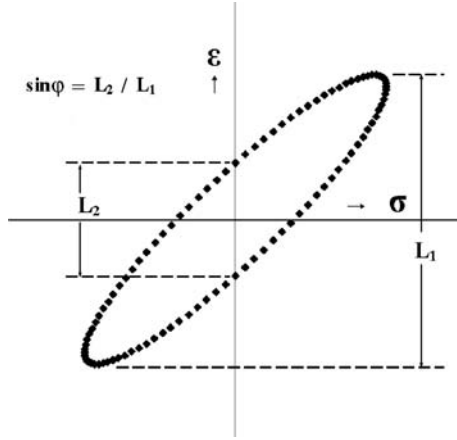


Figure 5. Calculation of phase angle.

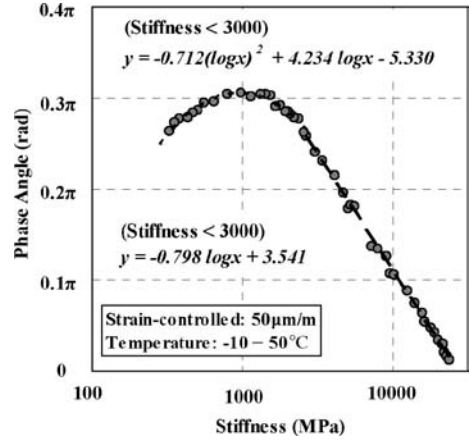


Figure 6. Relationship between stiffness and phase angle.

4.2 Dissipated energy and fatigue failure characteristics

Because it was difficult to measure phase angle precisely with the four-point bending fatigue test equipment used in this study, dissipated energy was determined by using phase angle estimated from Figure 6, where stiffness values were obtained by the four-point bending fatigue test.

With an external load of sinusoidal wave pattern applied to the specimen, stress given by equation (2) and strain given by equation (3) with phase angle lag ϕ are generated in the specimen. Then dissipated energy per volume per load cycle is given by equation (4) on the basis of viscous elements in the specimen.

$$\sigma(t) = \sigma_0 \sin \omega t \quad (2)$$

$$\varepsilon(t) = \varepsilon_0 \sin(\omega t - \phi) \quad (3)$$

$$\begin{aligned} w_0 &= \int \sigma d\varepsilon = \int_0^{2\pi} \sigma \frac{d\varepsilon}{dt} dt = \sigma_0 \varepsilon_0 \int_0^{2\pi} (\sin \omega t)(\cos \omega t - \phi) dt \\ &= \pi \sigma_0 \varepsilon_0 \sin \phi \end{aligned} \quad (4)$$

Here, σ_0 and ε_0 are stress amplitude and strain amplitude, respectively.

For the triangular wave, stress is given by a function obtained by extending equation (5) cyclically with $\sigma(t + 2\pi/\omega) = \sigma(t)$, and the Fourier series expansion of this function results in equation (6). Then, strain with phase angle lag ϕ is given by equation (7). Similar to the case of sinusoidal wave, dissipated energy per volume per load cycle for the triangular wave is given by equation (8), which can be solved by numerical integration.

$$\sigma(t) = \sigma_0 \left(\frac{2}{\pi} |\omega t| - 1 \right) \quad \left(-\frac{\pi}{\omega} \leq t \leq \frac{\pi}{\omega} \right) \quad (5)$$

$$\sigma(t) = -\frac{8\sigma_0}{\pi^2} \sum_{n=0}^{\infty} \frac{\cos((2n+1)\omega t)}{(2n+1)^2} \quad (6)$$

$$\varepsilon(t) = -\frac{8\varepsilon_0}{\pi^2} \sum_{n=0}^{\infty} \frac{\cos((2n+1)\omega t - \phi)}{(2n+1)^2} \quad (7)$$

$$w_0 = -\frac{64}{\pi^4} \sigma_0 \varepsilon_0 \omega \int_0^{2\pi} \sum_{n=0}^{\infty} \frac{\cos((2n+1)\omega t)}{(2n+1)^2} \sum_{n=0}^{\infty} \frac{\sin((2n+1)\omega t - \phi)}{2n+1} dt \quad (8)$$

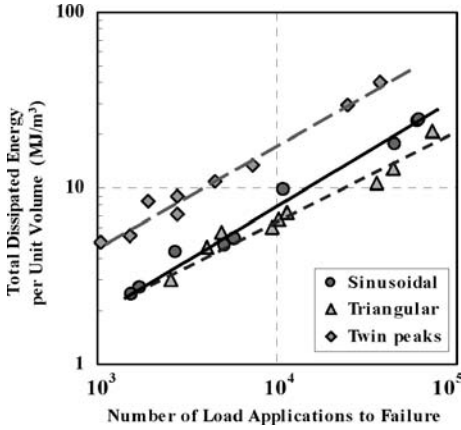


Figure 7. Relationship between total dissipated energy and the number of load applications to failure.

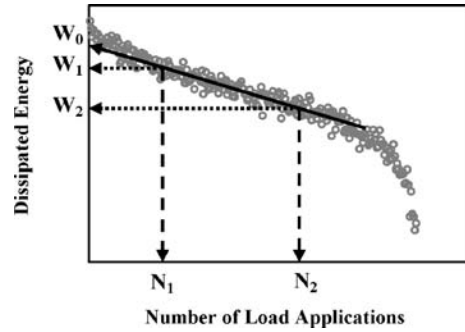


Figure 8. Rate of dissipated energy change.

Similarly, dissipated energy for the twin peaks wave is given by equation (11).

$$\sigma(t) = \sigma_0 \left(\sin \omega t + \frac{\sin 3\omega t}{2} \right) \quad (9)$$

$$\varepsilon(t) = \varepsilon_0 \left(\sin(\omega t - \phi) + \frac{\sin(3\omega t - \phi)}{2} \right) \quad (10)$$

$$w_0 = \sigma_0 \varepsilon_0 \omega \int_0^{2\pi} \left(\sin \omega t + \frac{\sin 3\omega t}{2} \right) \left(\cos(\omega t - \phi) + \frac{3 \cos(3\omega t - \phi)}{2} \right) dt \quad (11)$$

Figure 7 shows the relationship between total dissipated energy and the number of load applications to failure. Although these values are plotted linearly on a double logarithmic chart as found in past studies [6, 7], the position of the plot varies with loading wave pattern (e.g., a difference is seen between the sinusoidal and twin peaks wave). Although the reason for this difference is not clear, it is suggested by Kim et al. [8] that not all dissipated energy contributes to fatigue damage. Therefore, the percentage of the total dissipated energy that contributes to fatigue damage may vary with loading wave pattern. It is inferred that the percentage is smaller in the twin peaks wave than the sinusoidal and triangular waves and that the percentage is about the same in the latter two waves.

Making reference to the dissipated energy ratio (DER) proposed as an index of fatigue damage by Ghuzlan, Carpenter, and others [9, 10, 11], the rate of dissipated energy change was deduced as described below to investigate its relation to the number of load applications to failure.

In the displacement-controlled fatigue test, dissipated energy decreased gradually as the number of load applications increased and dropped sharply when the number approached the state of failure (Figure 8). The rate of dissipated energy change was obtained from equation (12), which describes the slope of the plot within the range where dissipated energy changes linearly with the number of applications in Figure 8.

$$\text{Rate of Dissipated Energy Change} = \frac{|W_2 - W_1|}{(N_2 - N_1)W_0} \quad (12)$$

Figure 9(a) shows the relationship between the rate of dissipated energy and the number of load applications to failure. Figure 9(b) shows the results of a uniaxial fatigue test conducted in a previous study [5] in addition to the results obtained in the present study. For the same continuous

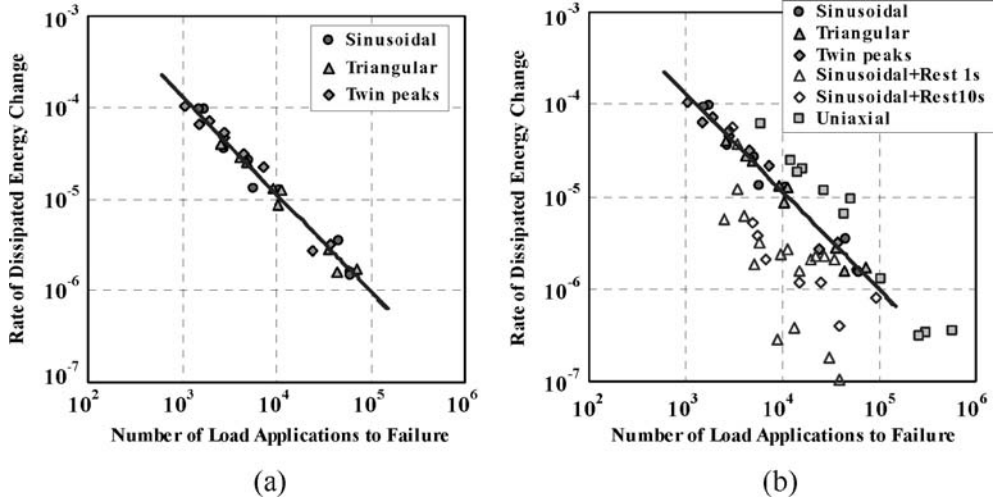


Figure 9. Relationship between the rate of dissipated energy and the number of load applications to failure.

loading (four-point bending), there is a nearly-constant, linear relationship between the rate of dissipated energy and the number of load applications to failure regardless of the wave patterns (Figure 9(a)). A different relationship is observed, however, when rest period is introduced or a different type of loading (uniaxial fatigue test) is used (Figure 9(b)).

5 ENTPE'S APPROACH TO FATIGUE DAMAGE [3, 4]

The relationship between the rate of stiffness change and the number of load applications to failure was investigated by using the method of fatigue damage analysis developed by ENTPE.

Three phases of stiffness decrease were observed in the displacement-controlled fatigue test (Figure 10).

- Phase I: Stiffness decreases sharply because of the development of microcracks as a kind of fatigue damage, the increase of specimen temperature associated with dissipated energy, and the thixotropy of binder.
- Phase II: Stiffness decreases gradually mainly by fatigue damage, while the effects of dissipated energy and thixotropy are diminished.
- Phase III: Stiffness decreases sharply because of the local crack propagation (the macrocrack begins to develop) until the failure of the specimen.

While there are some definitions of thixotropy, we adopt the definition given by Bauer et al. [12]: *When a reduction in magnitude of rheological properties of a system such as elastic modulus, yield stress, and viscosity, for example, occurs reversibly and isothermally with a distinct time dependence, the system is described as thixotropic.*

In the ENTPE's method, the rate of stiffness change, an index of fatigue damage, is given by equation (13), which consists of the rate of stiffness change and the rate of dissipated energy change at any interval in phase II (between N_1 and N_2), during which damage prevails.

$$\text{Rate of Stiffness Change, } S_r = \frac{|E_2 - E_1|}{(N_2 - N_1)E_{0i}} + \frac{|W_2 - W_1|}{(N_2 - N_1)W_0} \cdot \frac{C_i(E_0 - E_{0i})}{E_{0i}} \quad (13)$$

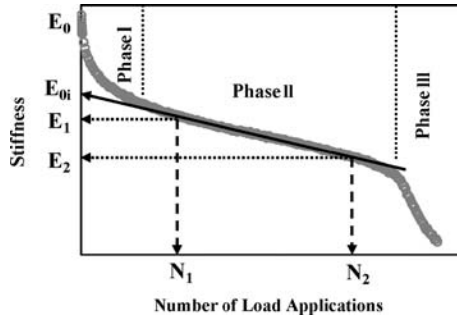


Figure 10. Rate of stiffness change.

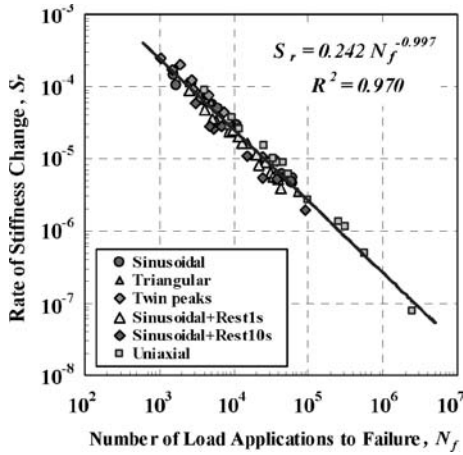


Figure 11. Relationship between the rate of stiffness change and the number of load applications to failure.

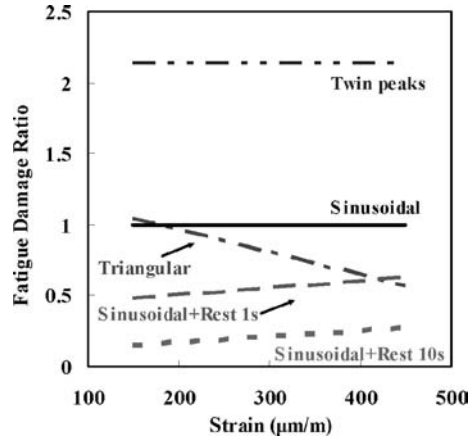


Figure 12. Fatigue damage per load application.

Here, the second term on the right-hand side corrects for the effect of specimen temperature change due to dissipated energy change as well as the effect of binder thixotropy. The coefficient C_i varies between $2/3$ and $5/6$ according to the number of load applications for the interval between N_1 and N_2 .

Figure 11 shows the relationship between the rate of stiffness change and the number of load applications to failure. The linear relationship is almost the same regardless of loading wave pattern, presence/absence of rest period, and type of loading. It is assumed that the exponent of N_f in the regression line is about -1 and $N_f S_r \approx 0.24$. Then, under the present test conditions (dense graded asphalt mixture (13), 10°C), the specimen fails when the decreasing rate of stiffness caused by fatigue damage reaches about 24% regardless of loading wave pattern, rest period, and type of loading.

Figure 12 shows the relative rate of stiffness change, as an index of fatigue damage per load application, for different wave patterns normalized to the rate of stiffness change for the continuous sinusoidal wave. There are differences in fatigue damage per load application between the wave patterns; the twin peaks wave is about twice effective as the sinusoidal wave in causing damage. Moreover, fatigue damage recovers during rest period. It is considered that, under the present test conditions, 40% to 50% of the fatigue damage per sinusoidal wave load application is recovered by introducing a rest period of 1 s, and 70% to 80% of the damage is recovered by a rest period of 10 s.

6 CONCLUSIONS

The main findings of this study are summarized as follows.

- 1) The fatigue damage of an asphalt mixture depends on the wave pattern of loading; therefore the number of load applications to failure depends on the wave pattern.
- 2) The number of load applications to failure is greatly affected by the rest period of loading; rest period has a healing effect.
- 3) There is a linear relationship between the total dissipated energy and the number of load applications to failure, and the position of the linear plot varies with loading wave pattern.
- 4) Under continuous loading, there is a nearly-constant, linear relationship between the rate of dissipated energy change and the number of load applications to failure regardless of loading wave pattern. A different relationship is observed, however, when rest period is introduced or a different type of loading is used.
- 5) There is a nearly-constant, linear relationship between the rate of stiffness change obtained by the ENTPE's method and the number of load applications to failure regardless of loading wave pattern, rest period, and type of loading.

REFERENCES

- [1] Japan Road Association: Handbook for Pavement Design and Constuction, 2006.
- [2] Deacon J.A. and Monismith C.L.: Laboratory Flexural-Fatigue Testing of Asphalt-Concrete with Emphasis on Compound-Loading Tests, Highway Research Record, No. 158, pp. 1–31, 1967.
- [3] Di Benedetto H., de La Roche C., Baaj H., Pronk A., and Lundström R.: Fatigue of Bituminous Mixtures, RILEM TC 182-PEB 'Performance Tsetting and Evaluation of Bituminous Materials', Materials and Structures, Vol. 37, pp. 202–216, Apr., 2004.
- [4] Baaj H., Di Benedetto H., Chaverot P.: Effect of Binder Characteristics on Fatigue of Asphalt Pavement Using an Intrinsic Damage Approach, International Journal of Road Materials and Pavement Design, Hermes Lavoisier, Paris, France, Vol. 6, No. 2, pp. 147–174, 2005.
- [5] Kogo K., Himeno K.: Uniaxial Fatigue Test of Asphalt Mixtures, Proceeding of the 62nd JSCE Annual Meeting, V-292, 2007.
- [6] Van Dijk W.: Practical Fatigue Characterization of Bituminous Mixes, Proceedings of the Association of Asphalt Paving Technologists, Vol. 44, pp. 38–74, 1975.
- [7] Himeno K., Watanabe T., Maruyama T.: Fatigue Failure Characteristics of Asphalt Mixes at Low Stiffness Modulus, Proceedings of the Japan Society of Civil Engineers, No. 366/V-4, pp. 143–151, 1986.
- [8] Kim J., Roque R. and Birgisson B.: Interpreting Dissipated Energy from Complex Modulus Data, International Journal of Road Materials and Pavement Design, Hermes Lavoisier, Paris, France, Vol. 7, No. 2, pp. 223–245, 2006.
- [9] Ghuzlan K. A. and Carpenter S.H.: Energy-Derived, Damage Failure Criterion for Fatigue Testing, Journal of Transportation Research Record, No. 1723, pp. 141–149, 2000.
- [10] Carpenter S.H. and Ghuzlan K. A.: Fatigue Endurance Limit for Highway and Airport Pavements, Journal of Transportation Research Record, No. 1832, pp. 131–138, 2003.
- [11] Shen S, Airey G.D. and Carpenter S.H.: A Dissipated Energy Approach to Fatigue Evaluation, International Journal of Road Materials and Pavement Design, Hermes Lavoisier, Paris, France, Vol. 7, No. 1, pp. 47–69, 2006.
- [12] Bauer W.H. and Collins E.A.: Thixotropy and Dilatancy, Ch. 8 in Rheology: Theory and Applications, Eirich F.R., Vol. 4, Academic Press, New York, 1967.

Evaluation of cracking in recycled pavements with foamed asphalt and cement stabilization

A. Loizos & V. Papavasiliou

National Technical University of Athens (NTUA), Athens, Greece

ABSTRACT: The cold in place recycling (CIPR) technique using foamed asphalt and cement as stabilizers was applied for the rehabilitation of a severely cracked originally asphalt pavement with cement treated base (CTB), which was considered as a test section. Three years after construction of the test section, a limited number of transverse cracks were observed on the asphalt pavement surface. In order to investigate the severity and the origin of the cracking, several cores were taken along the location of the cracks. In-situ non-destructive tests (NDTs) using the FWD were also performed 4 times within a two year period after the observation of the cracks. Intensive coring investigation has shown that the transverse cracks were all the way through the asphaltic overlay and the recycled layers as well. According to the deflection analysis no significant reduction of the load transfer efficiency was observed during the measurements along the location of the transverse crack. Backcalculated moduli of the recycled material did not show reduction during the two years of pavement performance after the appearance of the crack. Strain response analysis has shown no increase of the critical strains in the body of the recycled material during this period of monitoring.

1 INTRODUCTION

Cold in-place recycling (CIPR) of distressed pavements using foamed asphalt and cement as stabilization agents is a treatment that has, over the past years, witnessed a sharp increase in its usage. The asphalt is foamed in a specially designed expansion chamber. A carefully metered quantity of water is mixed with air and hot asphalt, forming foam of much higher volume and lower viscosity than the asphalt component. This allows the asphalt to disperse through the recycled material. Additional water is sprayed into the mixing chamber to achieve the optimal moisture content for compaction (Chen 2006).

The foaming procedures in the laboratory, as well as related construction aspects, although not standardized, are satisfactorily documented in current international literature. However, not enough information is available concerning the condition and field performance of foamed treated recycled materials and when published it has been limited to low or medium volume roads.

For this purpose of the experiment, the CIPR technique using foamed asphalt and cement was applied for the rehabilitation of a severely cracked heavy-duty (approximately 10^6 equivalent axle loads of 13 tons per year) pavement test section. The pavement before rehabilitation comprised of a cement treated base (CTB), overlaid with asphalt concrete layer material and referred to as a “semi-rigid” pavement (FEHRL, 2004). In order to investigate the performance of the abovementioned CIPR technique, an annual comprehensive monitoring is performed, concentrating on the Falling Weight Deflectometer (FWD) as a major tool for the in-situ evaluation (Loizos & Papavasiliou 2006).

Three years after construction of the test section a limited number of transverse cracks were observed through visual inspection on the asphalt pavement surface. In order to investigate the

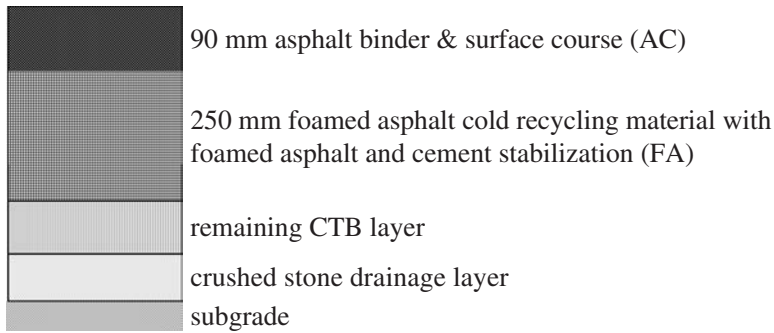


Figure 1. Recycled pavement structure.

severity and the origin of the cracking, several cores were taken at the location of the cracks. In-situ non-destructive tests (NDTs) using the FWD were also performed 4 times within a two year period after the observation of the cracks. During this period air temperature ranged between 0°C and 40°C and the rainfall was approximately 450 mm per year. In order to study the influence of traffic loads on the condition of the recycled pavement near the crack, no crack-sealing or other maintenance means was undertaken. In the present paper a representative example of a transverse crack study is presented. It must be noted, that similar results were derived from the analysis of other cracks as well. The major findings of the analysis are presented and discussed in the following.

2 PAVEMENT AND MIX DESIGN

Foamed asphalt (FA) mix design was undertaken to establish the application rates for foamed asphalt and cement to achieve optimal strength and to determine the strength characteristics for use in the structural design exercise. Several different blends of material were treated with foamed asphalt using the appropriate laboratory unit and several briquettes were manufactured for the testing purpose in terms of the indirect tensile strength (ITS), the unconfined compressive strength (UCS), the cohesion (c) and the angle of internal friction (Φ), as well as the determination of the indirect tensile stiffness modulus (ITSM). According to the mix design, 2.5% foamed asphalt and 1% cement was used in the recycled material. The decision to introduce 1% cement was based on the improvement in the achieved soaked strengths. Further, details on the mix design blends can be found in reference (Loizos et al. 2004).

An analytical design approach was used for the estimation of the structural capacity of the pavement. Taking into account traffic volume history, a structural capacity requirement of more than 10×10^6 equivalent 13 tons axle loads was anticipated for any work to be undertaken on this test section. According to the analytical design, a pavement structure consisting of a 90 mm asphalt concrete (AC) layer overlaying the layer of recycled material was assumed. An iterative process was applied to adjust the thickness of the in depth recycled layer (base layer) until structural capacity requirements were met. A uniform thickness of 250 mm was adopted over which two asphalt layers were laid. First, a leveling dense binder course with a nominal thickness of 50 mm, overlayed by a 40 mm surface course of 40 mm semi-open graded asphalt mix modified by polymer. The final pavement design of the test section is presented in Figure 1.

3 IN-SITU DATA COLLECTION

Several cores were taken along the location of the cracks, which were observed for the first time three years after construction of the test section. In-situ non-destructive tests (NDTs) using the

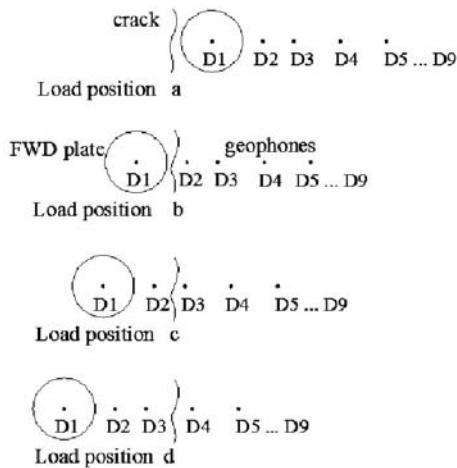


Figure 2. FWD measurements: Load position with respect to the crack position.

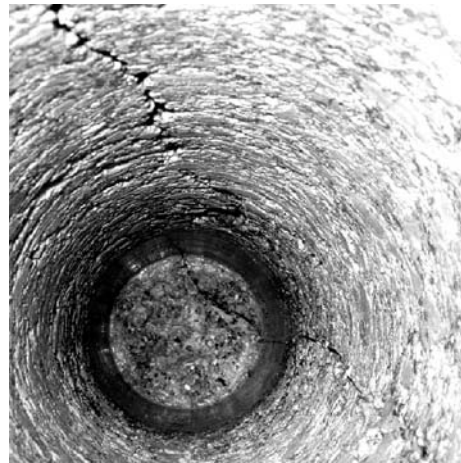


Figure 3. Crack along wall and bottom section of the hole left from the extracted core.

FWD were also performed. The monitoring levels were comprised of measurements 3, 3.5, 4 and 5 years after construction, i.e. all monitoring levels were performed after the appearance of the crack. The FWD measurements were conducted with the loading plate located at several positions in respect to the crack as indicated graphically in Figure 2. In this way, the FWD was used to give a measure of the load transfer and hence of the crack severity (De Bondt & Saathof 1993). The geophones are referred to hereafter as D_i ($i = 1 \dots 9$) and the deflections as d_i ($i = 1 \dots 9$)

4 VISUAL INSPECTION

Transverse cracks were present not only on the heavy trafficked lane, but in some cases they were extended to the middle and the inside and emergency lanes. The crack width was 2–3 mm. Further investigation of the cores has shown that the cracks were all the way through the asphaltic overlay and the recycled layer as well. The crack was also visible on the upper surface of the remaining CTB layer in the hole after coring, as shown in Figure 3.

An interesting observation was that in short time (less than a year) the crack has passed through a previously extracted core that was filled with asphalt material to a thickness of about 35 cm (see Figure 4), a fact not typical for top-down cracking. According to this observation, the appearance of thermal cracking due to the FA recycled material can also be excluded

The above mentioned observations from the visual inspection of the transverse cracks are indicative of reflective cracking from the remaining CTB layer. Further analysis of the in-situ collected data was performed, in order to investigate the rate of deterioration of the structural condition of the pavement due to the impact of the crack appearance.

5 ANALYSIS OF THE IN-SITU COLLECTED DATA

5.1 Deflection analysis

The center deflection d_1 measured with the plate of the FWD near the crack (see Figure 2: load position b, crack between geophones D_1 and D_2) is presented in Figure 5. The in-situ collected values were properly corrected to the reference temperature of 20°C (Van Gurp 1995). Measured temperatures at the mid-depth of the asphalt layers were 21°C, 19°C, 29°C and 27°C respectively

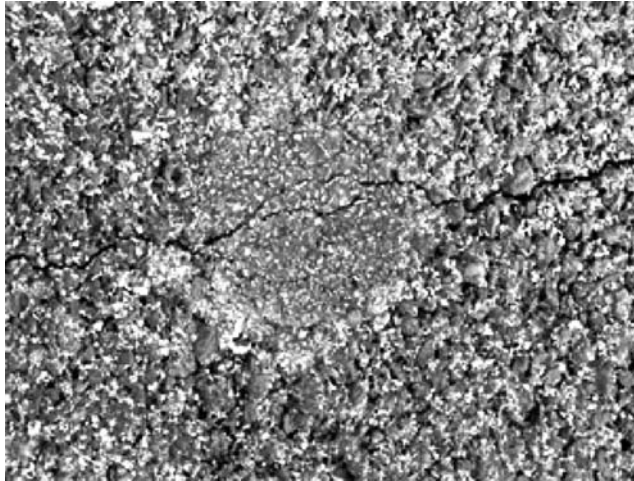


Figure 4. Crack through previously extracted core.

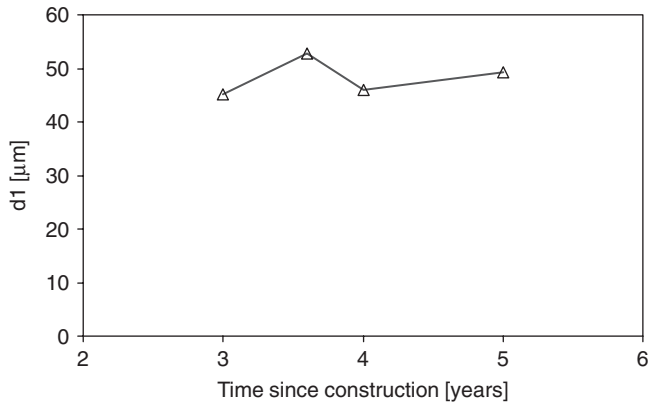


Figure 5. Center deflection near the crack.

for the measurements 3, 3.5, 4 and 5 years since construction. The center (maximum) deflection is an indication of the overall pavement condition (Hakim et al. 2002) at the location of the crack at the time of the investigation. No significant center deflection values differences were observed, a fact indicating no changes in the overall pavement condition, at least during the first two years of the crack appearance under traffic loads.

Criteria of the load transfer efficiency are the load transfer ratio (d_U/d_L) (De Bondt & Saathof 1993) and the differential deflection ($d_L - d_U$) (Shahid & Thom 1996), where d_L and d_U represent the deflection of the loaded and unloaded side of the crack respectively.

For the purpose of the present investigation, two different load transfer approaches were taking into account. According to the above mentioned procedure, the deflections d_{1L} and d_{2U} were measured and corrected to a reference temperature of 20°C (Van Gurp 1995), for load position b (see Figure 2: crack between geophones D1 and D2). The load transfer ratio (d_{2U}/d_{1L}) was ranged between 58% and 67%. Results are presented in Figure 6. No significant reduction of the load transfer efficiency was observed during two years of FWD measurements near the crack. It can be concluded that the amount of the aggregate interlock in the AC and the recycled layers has not been changed during this period.

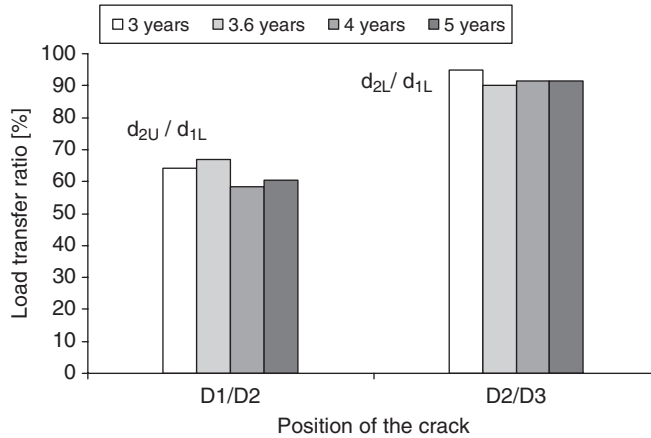


Figure 6. Load transfer ratio.

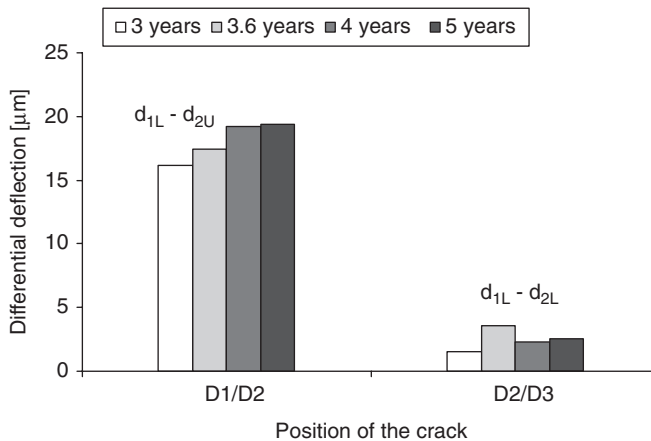


Figure 7. Differential deflection.

The same procedure was used in order to calculate the load transfer between two adjacent geophones in the loaded side of the crack. In this case, the deflections d_{1L} and d_{2L} were measured and corrected to a reference temperature of 20°C, for load position c (see Figure 2: crack between geophones D2 and D3). According to these calculations, the load transfer ratio (d_{2L}/d_{1L}) was as expected higher (above 90%) than in the previous case (see Figure 6).

The differential deflection ($d_{1L} - d_{2U}$) for load position b (see Figure 2) ranged between 16.2 and 19.4 μm , showing an increase during the first year of crack measurements and a tendency towards stabilization thereafter, while ($d_{1L} - d_{2L}$) for load position c (see Figure 2) was up to 3.5 μm . Results are presented graphically in Figure 7.

It can be seen, that no significant reduction of the load transfer efficiency was observed and consequently no indication of an increase in crack severity was observed during the first two years monitoring of the crack.

In order to estimate the influence of the recycled layer (FA) temperature to load transfer efficiency, the difference of the average load transfer ratio for a load position with the crack not between two adjusted geophones (d_{i+1L}/d_{iL}) and the average load transfer ratio for load position with the crack between two adjusted geophones (d_{i+1L}/d_{iU}) was calculated. This difference is referred hereafter to as $\Delta(d_{i+1}/d_i)$. The temperature at the mid depth of the recycled (FA) layer was estimated using

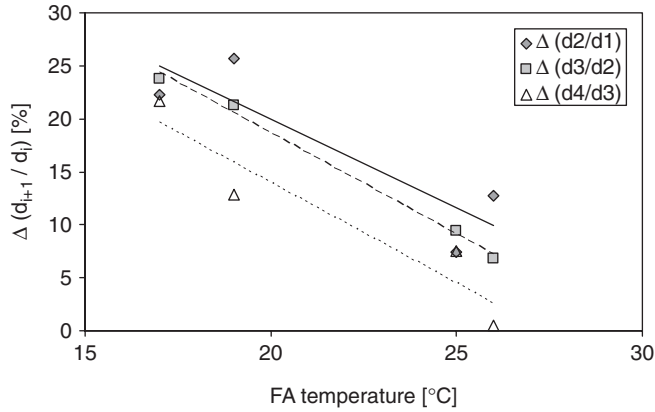


Figure 8. Load transfer ratio differences between loaded and unloaded geophones [$\Delta(d_{i+1}/d_i)$].

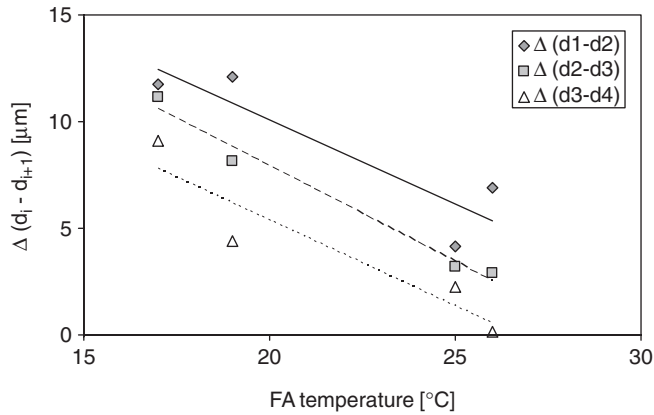


Figure 9. Differential deflection differences between loaded and unloaded geophones $\Delta(d_i - d_{i+1})$.

the BELLS2 equation (Baltzer et al. 1994). Results of the above mentioned calculations $\Delta(d_{i+1}/d_i)$ for $i = 1, 2$ and 3 (see Figure 2: load positions b, c and d) in respect to the recycled layer (FA) temperature are presented in Figure 8. It can be seen, that for higher FA temperatures the $\Delta(d_{i+1}/d_i)$ decreases, indicating improved load transfer efficiency.

Similar results were derived for the differences of the differential deflection ($d_{iL} - d_{i+1U}$) with the crack between two adjusted geophones and ($d_{iL} - d_{i+1L}$) with the crack not between two adjusted geophones, referred to as $\Delta(d_i - d_{i+1})$. Results of the $\Delta(d_i - d_{i+1})$ in respect to FA temperature are presented graphically in Figure 9.

5.2 Backanalysis results

Measured deflections near the crack (see Figure 2, load position a) were used in order to estimate the modulus of the asphalt layers (AC) and the recycled material (FA). The backanalysis was undertaken using ELMOD software (Dynatest 2001). Considering the level of the subgrade, not at the bottom of the drainage layer (Figure 1), but at the bottom of the CTB layer, the backanalysis model consisted of four layers. As far as the thickness input is concerned, backanalysis was conducted using core thickness measurements. For the evaluation of the structural condition of the rehabilitated pavement layers, a simplified approach which takes into account the influence of both the asphalt and the recycled

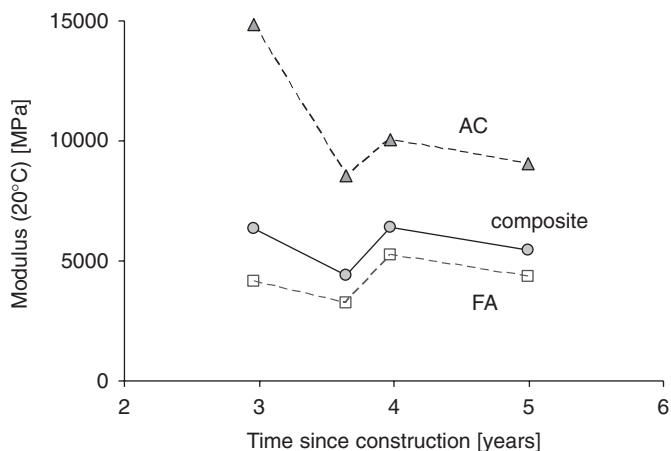


Figure 10. Backanalysis results.

layers was used. This is the estimation of the composite modulus (Milton & Earland 1999) i.e. the combined asphalt layers and recycled layer modulus (Loizos & Papavasiliou 2006). Backcalculated moduli values were corrected to the reference temperature of 20°C (Baltzer & Jansen 1994) and the results are presented in Figure 10. A reduction of the modulus during the two years of measurements is apparent only in the AC layer, which was very stiff during the monitoring 3 years after construction. It should also be noted, that the backcalculated modulus of the remaining CTB layer was very high (about 20000–25000 MPa), indicating that the structural condition is good and the layer is stiff. Backcalculated moduli of the recycled material and the composite moduli did not show any significant reduction during the two years of the presence of the crack under traffic loads. Consequently, the presence of the crack did not influence negatively the structural condition of the pavement.

5.3 Strain response analysis

Maximum tensile strain ($\max \varepsilon_{xx}$) in the body of the recycled layer is an important factor for the evaluation of the structural condition of the pavement. Based on the data collected after the appearance of crack, the in-situ $\max \varepsilon_{xx}$ was calculated using finite element (FE) linear analysis with ABAQUS software (Hibbitt et al. 2000). However, it should be mentioned that pavement systems often exhibit stress-dependent behavior. Advanced models may help to explain the discrepancies between the theoretical analysis and the observed pavement behavior and pavement responses, an issue that merits further investigation beyond the limits of the present research study. The load used for the calculations was a 65 kN single wheel with 15 cm radius, in accordance with the maximum allowed axle load in Greece (13 tons).

Figure 11 presents the strains of the recycled pavement, as it is modeled in Figure 1. The $\max \varepsilon_{xx}$ has been located in most cases in the upper part of the recycled layer. Figure 12 shows the maximum calculated tensile strain ($\max \varepsilon_{xx}$) in the body of the recycled material. It can be seen, that the values are low, while no significant variation of the $\max \varepsilon_{xx}$ was observed. This fact indicates that during the two years of presence of the crack under traffic loads, no increase of the critical strains has been observed in the body of the recycled material and consequently the “damage” did not increase. These results can be considered as expected taking into account the results of backanalysis.

6 CONCLUSIONS

The present research study has attempted to contribute towards the evaluation of cracking in recycled pavements with foamed asphalt and cement stabilization. In order to study the influence of

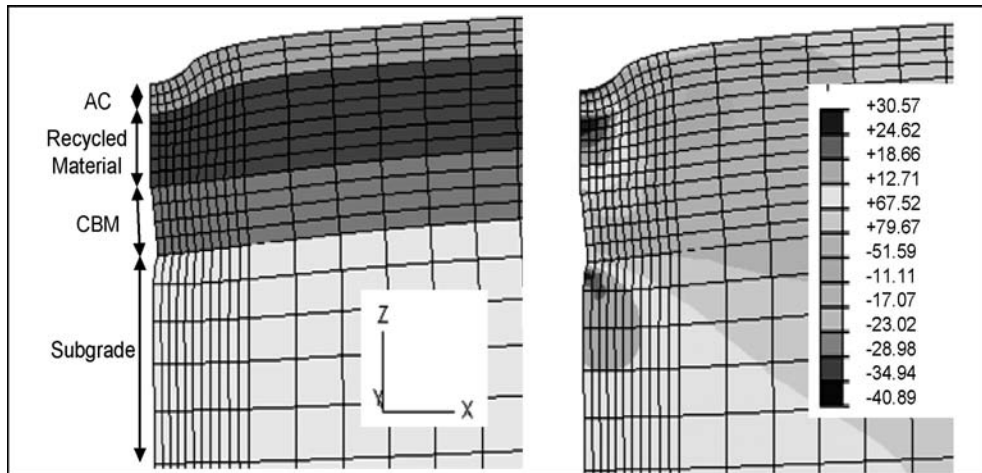


Figure 11. FE analysis (horizontal tensile strain).

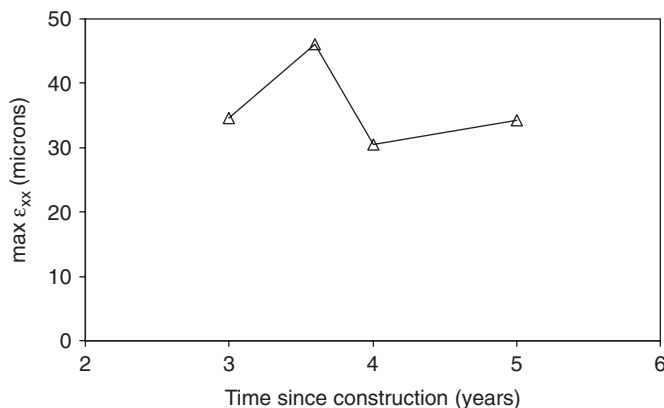


Figure 12. Maximum horizontal tensile strain ($\max \epsilon_{xx}$) in the body of the recycled material.

traffic loads on the condition of the recycled pavement near the crack, no crack-sealing or other maintenance means were undertaken. The field investigation was based on coring, as well as on non-destructive tests (NDT) using FWD along a trial section of a rehabilitated heavy-duty originally asphalt pavement with cement treated base (CTB). The main findings and discussion points are as follows:

From the visual inspection and the related extracted cores it was found that the transverse cracks penetrated through both the asphaltic and recycled layers. Observations from the visual inspection of the transverse cracks are indicative of reflective cracking from the remaining CTB layer.

According to the NDT analysis using FWD loading near the transverse crack, no significant difference of the center deflection values was observed, a fact indicating no changes of the overall pavement condition, at least during the first two years of presence of the crack under traffic loads.

No significant reduction of the load transfer efficiency was observed during two years of FWD measurements near the crack. It can be concluded that the amount of the aggregate interlock in the AC and the recycled layers did not change during this period. For higher recycled layer temperatures there is an indication of improved load transfer efficiency.

Backcalculated moduli of the asphaltic and the recycled material layers did not show any significant reduction during the two years of monitoring of the crack, indicating that the presence of the crack did not influence negatively the structural condition of the pavement.

Strain response analysis has shown, that during the two years of presence of the crack under traffic loads, no increase of the critical strains has been observed in the body of the recycled material and consequently the “damage” has not been increased.

The remaining CTB layer underneath the recycled layer seems to be responsible for the appearance and the propagation of the cracking on the surface of the recycled pavement. For technical, as well as financial reasons, it is not always possible to remove the entire CTB layer, especially if the level of the lower surface of this layer is significantly deeper than the anticipated depth of the recycling. Nevertheless, after two years of presence of the cracking under heavy traffic loads the structural condition of the recycled pavement near the crack was adequate indicating that in such cases, simple maintenance techniques i.e. crack-sealing may have been efficient.

The NTUA Laboratory of Highway Engineering continues to undertake further re-research on the subject, including continuous monitoring of the pavement performance through detailed analysis. Due to the importance of the Trans European Highway under rehabilitation, the investigated trial section is considered, both for the National and the European database, as a Long Term Pavement Performance (LTPP) site.

REFERENCES

- Baltzer, S., Ertman-Larson, H. J., Lukanen E. O. & Stubstad, R. N. 1994. Prediction of AC Mat. Temperature for routine load/deflection measurements. *in Fourth International Conference on Bearing Capacity of Roads and Airfields*. Vol. 1: 401–412.
- Baltzer, S. & Jansen, J. M. 1994. Temperature Correction of Asphalt-Moduli for FWD-Measurements. *In Fourth International Conference on Bearing Capacity of Roads and Airfields*. Vol. 1: 401–412.
- Chen, D.-H., Bilyeu, J., Scullion, T., Nazarian, S. & Chiu, C.-T. 2006. Failure Investigation of a Foamed-Asphalt Highway Project. *Journal of Infrastructure Systems*. Vol. 12, No. 1: 33–40.
- De Bondt, A. H. & Saathof, L. E. B. 1993. Movements of a Cracked Semi-rigid Pavement Structures. *In Proceedings of 2nd International RILEM Conference*. Liege, Belgium: 449–457.
- Dynatest. 2001. ELMOD : Pavement Evaluation Manual.
- FEHRL. 2004. A guide to the use of long-life fully-flexible pavements. *FEHRL Report 2004/1*. Brussels.
- Hakim, B. A., Brown, S. F. & Armitage, R. J. 2002. Pavement Evaluation and Strengthening Design: Sixteen Years Experience. In Carlo Viggiani (ed.), *in Proceedings of 9th International Conference on Asphalt Pavements. ISAP*. Copenhagen 3:1–12.
- Hibbitt, Karlsson & Sorensen Inc. 2000. 1. ABAQUS User's Manual. USA.
- Loizos, A., Collins, D. & Jenkins, K. 2004. Rehabilitation of a Major Greek Highway by Recycling/Stabilizing with Foamed Bitumen. *Presented at 8th Conference on Asphalt Pavements for Southern Africa (CAPSA)*. Sun City, South Africa: 119–126.
- Loizos, A. & Papavasiliou, V. 2006. Evaluation of Foamed Asphalt Cold in-place Pavement Recycling Using Nondestructive Techniques. *Journal of Transportation Engineering*. Vol. 132, No. 12: 970–978.
- Milton, L. J. & Earland, M. G. 1999. Design Guide and Specification for Structural Maintenance of Highway Pavements by Cold In-Situ Recycling, *Transportation Research Laboratory (TRL)*. Report 386.
- Shahid, M. A. & Thom, N. H. 1996. Performance of Cement Bound bases with Controlled cracking, *In Proceedings of 3rd International RILEM Conference*. Maastricht, The Netherlands: 55–64.
- Van Gurp, C. 1995. Seasonal Influence on Asphalt Pavements with the Use of Falling Weight Deflectometers. *Phd Thesis*. Delft, The Netherlands.

The effects of cracking type and location on the choice of asphalt pavement recycling method

S.W. Haider & G.Y. Baladi

Michigan State University, East Lansing, Michigan, USA

T. Akram & A. Hussain

National Institute of Transportation, National University of Science & Technology, Risalpur, Pakistan

ABSTRACT: Funding for preventive maintenance, preservation, rehabilitation, and reconstruction of roadways will have to compete with other demands on the limited public funds. Hence, innovation is required in order to do more with less. Asphalt pavement recycling is one way to stretch existing budgets to maintain, preserve, rehabilitate and reconstruct more kilometers of roadways. This paper presents a pavement evaluation process for the selection of an appropriate asphalt pavement recycling methodology in Pakistan. The process includes non-destructive data collection scheme (surface distresses, ride quality and surface deflections) and destructive sampling (coring) to determine the extent of cracking along the asphalt concrete layer thickness. The paper shows that such data are sufficient to conduct proper evaluation of pavement structures and to select the appropriate asphalt pavement recycling methodology including hot in-place (HIR), cold in-place (CIR) and hot in-plant (HIPR) asphalt recycling. It is shown that such pavement evaluation process would yield information relative to the structural capacity of the lower pavement layers and the extent of cracking. The role of pavement cracking type, causes and propagation in the selection of asphalt recycling methodology is also addressed in the paper.

1 INTRODUCTION

Road networks in developing countries are experiencing high rates of deterioration due to tremendous traffic growth. Although funds to expand or reconstruct the roadway network are appropriated, the funding level for pavement maintenance and preservation is very poor. For example, relative to asphalt pavements, the practice in Pakistan for the last fifty years can be summarized in few words “break-up the deteriorated pavement sections pile the materials on the side of the road and use fresh aggregate and asphalt mix.” Pavement recycling as a rehabilitation alternative was not considered by the road authorities in Pakistan.

It is well known that various rehabilitation alternatives including recycling can be used to rehabilitate asphalt pavements. Each alternative is applicable to certain pavement conditions having its advantages and disadvantages, which must be evaluated prior to selecting the preferred alternative. For example, the advantages of asphalt pavement surface recycling methods (hot or cold in-place and in-plant recycling) include (Epps et al. 1980; Kandhal and Mallick 1997):

1. Conservation of natural resources.
2. Better pavement performance, for example, HMA overlay over recycled HMA base has better performance than HMA overlay on the existing pavement surface.
3. Reduced traffic disruption and maintained pavement geometry and thicknesses.

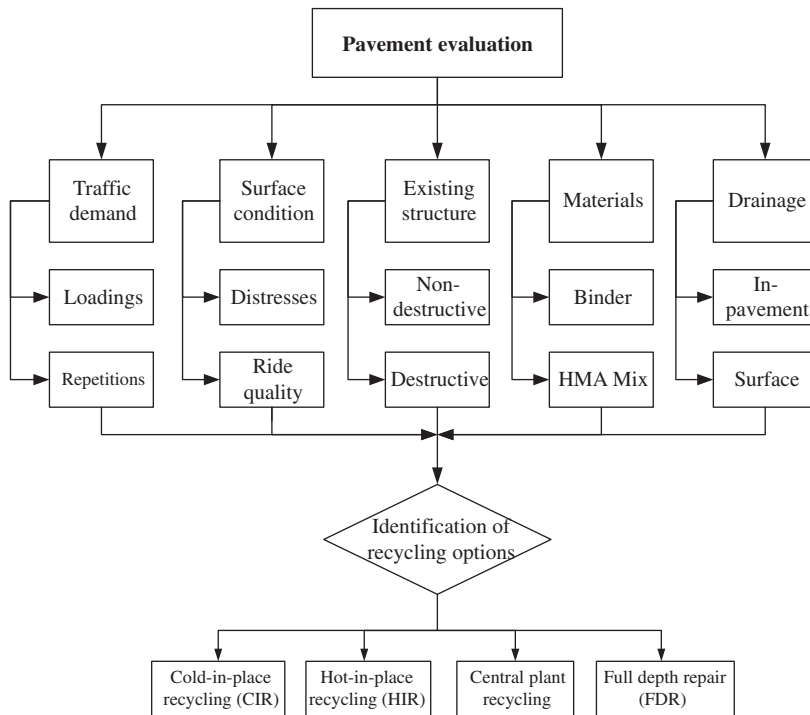


Figure 1. Pavement evaluation process for the selection of asphalt recycling method.

In the United States, the experiences of different state highway agencies indicate that in most cases the performance of recycled asphalt pavements is better than or at least is comparable to conventional asphalt pavements (ARRA 2001; Kandhal and Mallick 1997; McDaniel and Anderson 2001). The performance of recycled asphalt pavements is a function of the project selection process, proper design of the recycled materials, and construction practices. Hence, the first step in any pavement preservation project is the evaluation of the existing conditions of the pavement surface and the pavement structural capacity (AASHTO 1993; FHWA 1998; Hall et al. 2001). Pavement deterioration accelerates with increasing age and traffic. Therefore, if no pavement preservation is undertaken at appropriate times, the roadway condition will quickly decline to the point where expensive reconstruction will be the only option. An extension in the pavement service life can be achieved if the pavement is preserved in a timely manner using the appropriate action. For a given pavement section, the most appropriate pavement preservation action can be determined through a comprehensive and well designed pavement evaluation process. Such process entails some or all the activities shown in Figure 1. This paper describes the type of data needed to conduct the proper pavement evaluation, and subsequently demonstrates that how this evaluation can be utilized to select the appropriate asphalt pavement recycling methodology. The asphalt recycling strategies include: hot in-place (HIR), cold in-place (CIR) and hot in-plant (HIPR) asphalt recycling. The roles of the pavement cracking types, their causes and propagation in the selection of asphalt recycling methodology are also demonstrated in the paper.

2 RECYCLING STRATEGIES BASED ON PAVEMENT CONDITION

The pavement surface conditions reflect both the structural and functional integrity of the pavement. Some distress types (e.g. cracking and rutting) reflect the structural adequacy of the pavement

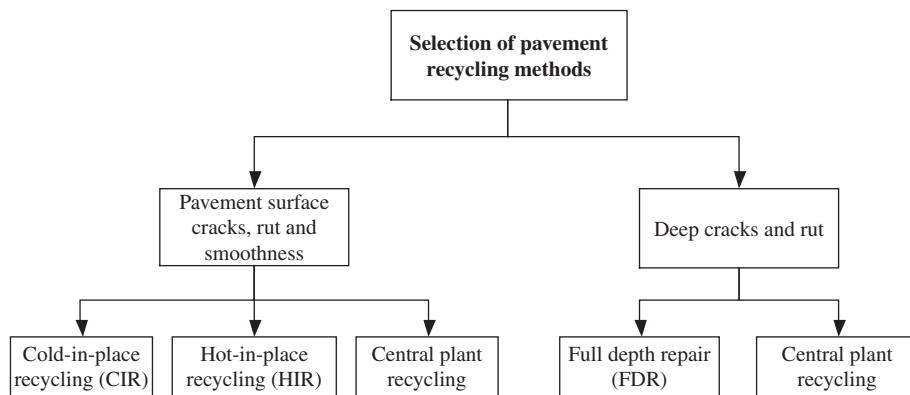


Figure 2. Selection of pavement recycling methods based on crack severity and extent.

structure whereas ride quality reveals the functional sufficiency of the pavement surface. During the pavement evaluation and project selection process, all distress types, their severity and extents should be documented (Miller and Bellinger 2003) along with the mechanism and causes of the distresses. The information facilitate the selection of an appropriate preservation option for a given pavement project. Figure 2 presents a general strategy for the selection of the appropriate asphalt recycling method based on the depths of the various distresses. For example, if the distress is confined to the upper portion of the asphalt layer, in-place recycling is an option. For any pavement section where the distresses have penetrated throughout the asphalt layer, the asphalt recycling option depends upon the total thickness of the asphalt layer. If the asphalt layer is less than 6-inch thick, in-place recycling is an option. For thicker pavements, the upper portion of the asphalt layer should be subjected to milling where the milled materials can be subjected to in-plant recycling and the remaining part of the asphalt layer can be subjected to in-place recycling. For pavement sections where the causes of the pavement surface distress can be traced to the granular base, full depth repair is required and the asphalt materials can be subjected to in-plant recycling only. Ride quality, in general, is a surface distress and is an important indicator of user comfort and vehicle operating costs (VOC). Figure 2 also illustrates that pavement sections having poor ride quality can be rehabilitated with in-place surface recycling techniques. In general, asphalt recycling options that address pavement structural inadequacy are more expensive than those that attend to functional inadequacy.

In-situ structural evaluation of various pavement layers is essential to substantiate the causes and effects of distresses and to determine the seat (depth) of the distresses and their causes. Deflection testing is an extremely valuable engineering tool in assessing; the engineering properties of the various pavement layers, the uniformity of the pavement section and structural adequacy, and in identifying weak pavement layers. The information are vital to the selection of the appropriate asphalt recycling technique. As stated earlier, for a weak upper pavement layer, in-place recycling can be used whereas poor base/subbase and/or subgrade materials require full depth repair and perhaps, in-plant recycling.

The above scenario implies that the proper pavement evaluation process must include the appropriate technique such as pavement coring to identify the depth of cracking. There are two categories of cracks; load and non-load related. Load related cracks tend to initiate in or in the vicinity of the wheel paths (Matsuno and Nishizawa 1992; Myers et al. 1998; Svasdisant et al. 2002). These include top-down cracking due to tire-pavement interaction and bottom-up cracks due to fatigue in the asphalt layer. Non-load related cracks such as temperature and block cracking are typically top-down cracks. They initiate at the pavement surface and propagate downward. It should be noted that bottom-up cracks (or fatigue cracks) initiate several years before they are observed on the pavement surface. A core taken over such cracks will show wider crack at the bottom of the

Table 1. Pavement cross-section details.

Pavement section	Asphalt thickness (mm)	Base/subbase thickness (mm)	Embankment height (m)
N5S-4	165	508	1.2
N5S-6	203	356	1.2

asphalt layer and the cracks have propagated throughout the asphalt layer. Pavement cores taken over top-down cracks, on the other hand, show wider cracks at the top of the asphalt layer and the cracks have propagated partially or fully throughout the thickness of the asphalt layer. The point here is that the depth of the cracks dictates the asphalt recycling methodology to be employed, thus, as a part of the pavement evaluation process, pavement cores should be obtained to determine the depth of the cracks.

Non-load related cracks—temperature and block cracks, are not concentrated or initiated in the wheel path. Both types of cracks are related to the hardening and oxidation of the asphalt binder. Since the surface of the asphalt layer is exposed to the atmosphere, the hardening and oxidation at the surface is more pronounced. Pavement surface showing early sign of temperature cracks can be cheaply rehabilitated by milling and filling the top one or two inches of the asphalt layer. The remaining depth of the asphalt layer will still be intact and may have minor or no hardening or oxidation problem. The milled material can be transported to an asphalt mixing plant where it will be sorted and rejuvenated and can be used on the same road or on lower class roads (farm to market roads). The percent of reclaimed asphalt pavement (RAP) and asphalt binder to be combined with virgin aggregate materials depends on the type of the road. For interstate and primary highways, the percent RAP could vary from 10 to 30 percent maximum, whereas for low volume roads, 70 to 90 percent RAP could be used. It should be noted that RAP materials containing high percent of soft aggregate should not be used on high class roads; they can be used on low class roads.

In summary, crack type, depth, extent and severity levels and structural capacity of the lower pavement layers are crucial information that are needed to make sound and cost-effective decision regarding pavement recycling. The selection of an appropriate pavement recycling strategy based on such information would lead to a better pavement performance. The applicability of best recycling strategies for existing pavement sections is demonstrated below.

3 PAVEMENT EVALUATION CASE STUDIES

Two 150 m long pavement sections along the National Highway in Pakistan (N5S-4 and N5S-6) were in urgent need of rehabilitation due to severe cracking. Section N5S-4 is close to the city of Mandra while section N5S-6 is in the vicinity of Wazirabad city. Both pavement sections consist of two-lanes in each direction. The asphalt layer on the sections contains crushed river run gravel and quartzite rock, respectively. The 20 years design traffic for both sections is 40 million ESALs. Table 1 summarizes the existing pavement cross-section for both sections.

Both sections were subjected to a systematic pavement evaluation process that included distress survey, deflection testing and pavement coring. Results of the evaluation are presented in the next subsections.

3.1 Distress survey

For both pavement sections, detailed distress maps were prepared in accordance with the long-term pavement performance (LTPP) distress manual (Miller and Bellinger 2003). The maps included the types of distress and their severity and extent. Pavement section N5S-4 showed both longitudinal cracks in the vicinity of the wheel paths and block cracking across the asphalt mat as shown in

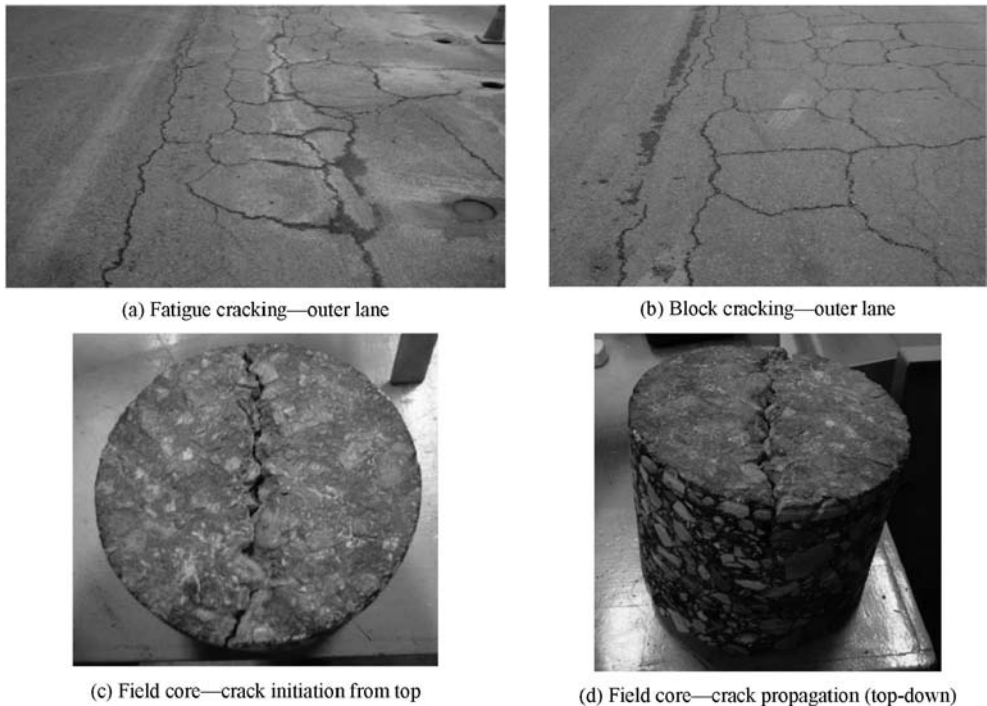


Figure 3. Pavement surface conditions and crack propagation at site N5S-4 (Mandra section).

Figures 3a & 3b. The cracks were mostly located in the outer lane (the traffic or slow lane) and they were more severe in the left wheel-path. Several pavement cores were taken over the cracks. Examination of the cores indicates that all cracks were top-down cracks and have not propagated throughout the entire asphalt layer as shown in Figures 3c & 3d.

Pavement section N5S-6 near the city of Wazirabad exhibited high severity fatigue cracks extending along and across the outer lane as shown in Figures 4a & 4b. Examination of the two figures suggests that the cracks are conventional bottom-up fatigue or alligator cracks. Several cores that were extracted over cracked areas showed that the cracks are top-down cracks and have propagated through the upper portion of the asphalt layer only (see Figures 5a and 5b). This finding support an earlier statement that pavement coring must be included in the pavement evaluation process prior to making decision regarding the selection of pavement rehabilitation option.

3.2 Deflection testing

Deflection tests were conducted on both pavement projects using a KUAB Falling Weight Deflectometer (FWD). The KUAB FWD sensors were spaced as shown in Table 2 and the deflection data were recorded by an on-board computer to an accuracy of 0.254 microns. For each pavement section, 11 FWD deflection test locations were marked on the pavement surface at 15 m spacing. Extreme care was taken to mark the test location as far from cracks as possible. At each test location, three FWD tests were conducted; one at each of the left wheel-path, the middle of the lane and the right wheel-path. Each test consisted of 9 drops; three drops at each of the following loads; 2800 kg, 4100 kg and 7000 kg. After checking the quality and integrity of all deflection data, the data along with the pavement cross-section information were analyzed to determine:

- The variability of the deflection data along and across the pavement.
- The nature or linearity of the material response to loads.

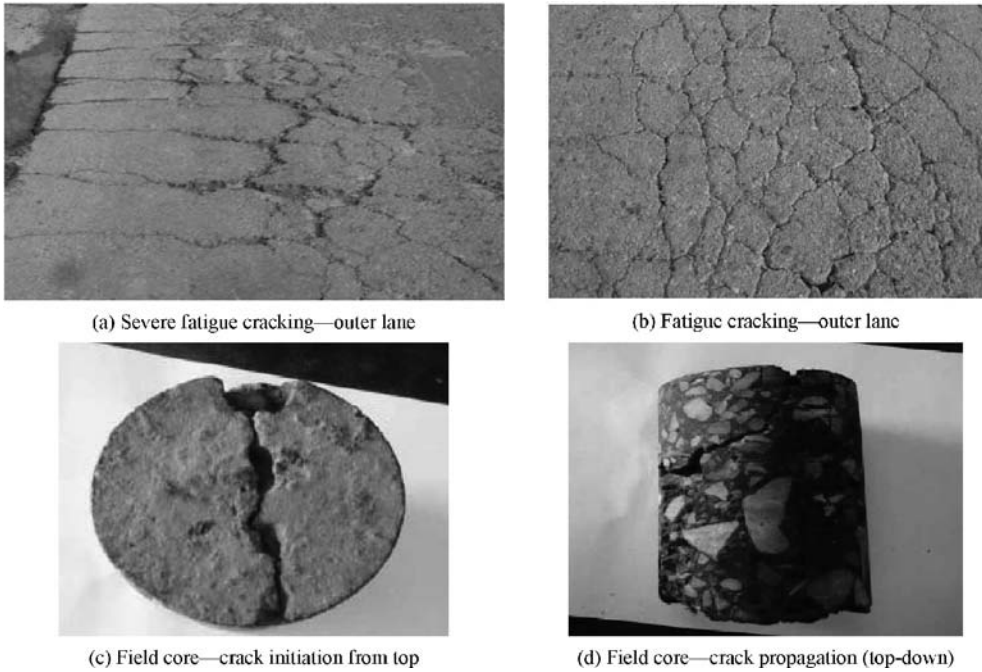
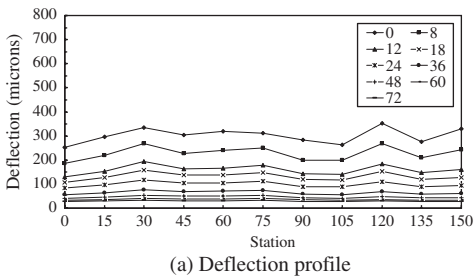
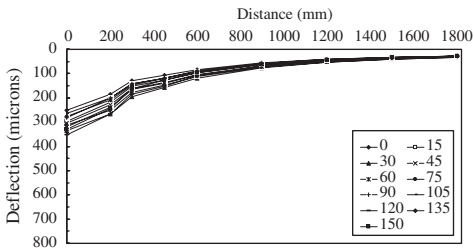


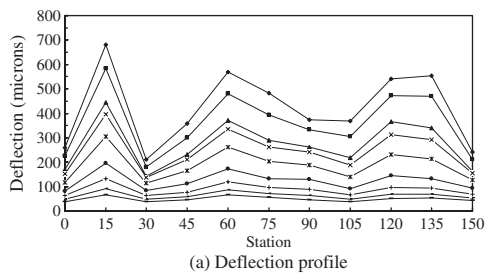
Figure 4. Pavement surface conditions and crack propagation at site N5S-6 (Wazirabad section).



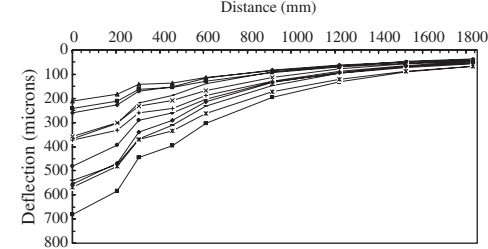
(a) Deflection profile



(b) Deflection basins



(a) Deflection profile



(b) Deflection basins

Figure 5. Deflection data along the N5S-4 section. Figure 6. Deflection data along the N5S-6 section.

- The in-situ modulus of each pavement layer using the 4100 kg load deflection data.
- The overall structural capacity of each pavement section.

Figures 5 and 6 show the variations of the deflection data collected by the various deflection sensors along the two pavement sections due to the 4100 kg load level. The figures also show the

Table 2. Spacing of the FWD sensors.

Load levels (kg)	Spacing of the FWD deflection sensors (mm)								
	0	203	305	457	610	914	1219	1524	1829
2800, 4100, 7000	0	203	305	457	610	914	1219	1524	1829
4100*	0	203	305	457	610	914		1524	1829

* SHRP sensor spacing and load level used for backcalculation of layer moduli

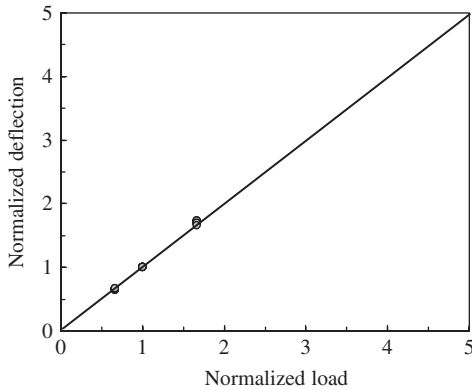


Figure 7. Linearity check (N5S-4 section).

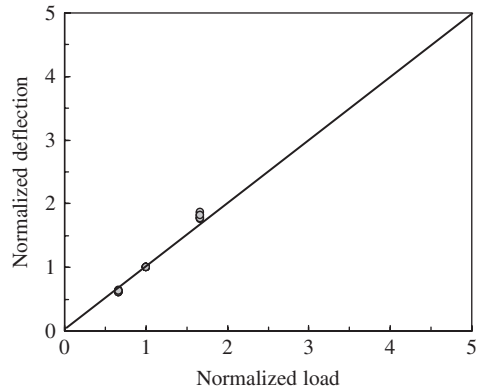
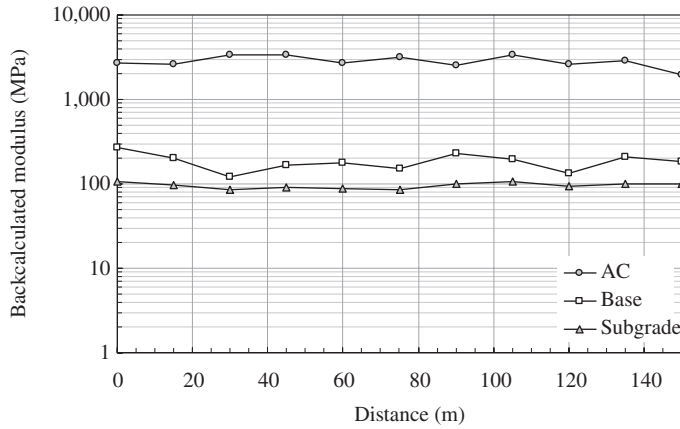


Figure 8. Linearity check (N5S-6 section).

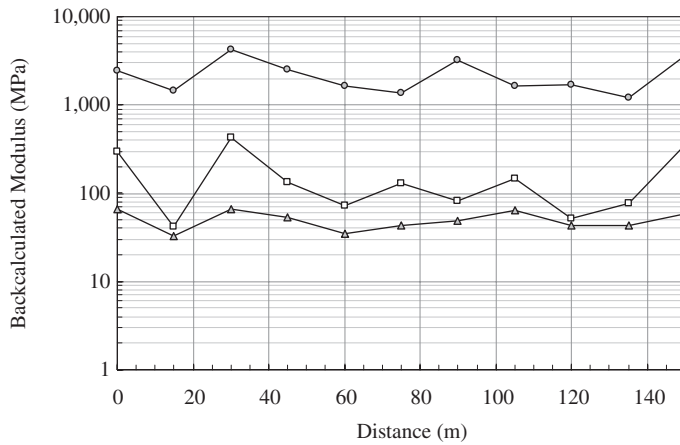
deflection basins at 11 test locations. The data indicated that the variability of the deflections along the N5S-4 section is moderate (see Figure 5a), while much higher variability was observed on N5S-6 section (see Figure 6a). For both pavement sections, the peak pavement deflection (D_0 , under the center of the load) shows the highest variation whereas the deflection recorded at sensor 8 (D_8 , located at 1829 mm from the center of the load) show minor to very low variation. The variability in the deflection data indicates that the roadbed soil along the 150 m long pavement sections has, more or less, similar physical and engineering properties whereas the properties of the upper pavement layers are highly variable. This implies that the structural capacity of the pavement section varies from one point to another which was expected due to pavement cracking. Finally, for both pavement sections, variation in the deflection data due to the other three load levels showed similar patterns as those shown in Figures 5 and 6.

The linearity of the pavement response to load was examined by studying the deflection data collected at three load levels. First, the peak deflection measured at each load level was normalized relative to the peak deflection measured at the 4100 kg load level. Results of the normalized deflections are shown in Figures 7 and 8. It can be seen that, the materials in both pavement sections show linear response between 2800 kg and 4100 kg load levels, and slight but insignificant non-linearity at the 7000 kg level. Based on this finding, linear elastic layered analysis was employed in the backcalculation of layer moduli.

Before the initiation of backcalculation, each deflection basin was examined using Boussinesq equivalent modulus procedure (Ullidtz 1987; Ullidtz 1998) to determine the presence and to estimate the depth to stiff layer. Later, MICHBACK and MODULUS computer programs were used to backcalculate the layer moduli. Results of the backcalculation are shown in Figure 9. As expected, the degree of variability of the backcalculated layer moduli is parallel to the degree of variability of the deflection data. That is, the moduli along the N5S-4 (Mandra section) are much higher than that of the N5S-6 (Wazirabad section). Table 3 presents representative values of the backcalculated moduli for each pavement layer in both sections.



(a) Site N5S-4 (Mandra section)



(b) Site N5S-6 (Wazirabad section)

Figure 9. Variation in the backcalculated layer moduli.

Table 3. Representative back-calculated layer moduli.

Pavement section	Representative layer modulus (MPa)		
	Asphalt*	Subbase/base	Subgrade
N5S-4 (Mandra)	4,212	158	79
N5S-6 (Wazirabad)	2,580	110	43

Note: * Temperature corrected moduli. The asphalt moduli were corrected at a reference temperature of 20°C using equations developed for the FHWA report (Baladi 1988).

Considering the high spatial variability, especially for section N5S-6, the representative moduli were determined (after deleting few outliers) at the 85 percentile level (only 15% of the values are less than the selected value).

Considering the backcalculated layer moduli for both sections, it is evident that section N5S-4 can be a candidate for in-place asphalt recycling while section N5S-6 needs more detailed recycling

strategy. The most cost effective and feasible recycling alternative for a pavement section depends on several activities as mentioned above. The specific recycling strategy selection for these two pavement sections is presented later in the paper.

3.3 *Laboratory investigations*

During the field evaluation of the pavement sections cores were taken along the length of both sections. Also, granular material and subgrade soil samples were acquired by excavating a pit in both sections. Asphalt cores were used in the laboratory to determine: (1) aggregate gradation for surface and base layers, (2) binder hardening for extracted asphalt. The aggregate gradation will be used for the asphalt mixture design with RAP material while the binder aging results will assist in determining the asphalt content and binder rejuvenation need. The conventional asphalt binder tests (penetration and viscosity) on the extracted binder for both sections have indicated significant binder aging.

4 PAVEMENT RECYCLING STRATEGY SELECTION

Having completed the pavement evaluation process, the proper asphalt recycling strategy can be selected for both pavement sections. Such strategy must be based on the results of the pavement evaluation (ground realities), sound engineering judgments, economics and available technology.

For section N5S-4, the following data were available:

- Distress data showed presence of severe fatigue and block cracks.
- Cores indicated that most of these cracks are top-down cracks that have penetrated 50 to 75 mm in depth.
- Deflection testing and subsequent analysis have indicated that the lower pavement layers (subbase/base and subgrade) have adequate residual strengths.
- Laboratory testing on extracted binder showed that it was considerably aged and hardened.

Based on the above information, hot in-place asphalt recycling of the top 75 mm (partial asphalt thickness) of the asphalt mat is feasible and cost-effective option for section N5S-4.

For section N5S-6, the following data were available:

- Distress data showed presence of severe fatigue cracks.
- Cores indicated that most of these cracks are top-down and cracks have penetrated 75 to 127 mm in depth.
- Deflection testing and subsequent analysis have indicated that the lower pavement layers (subbase/base and subgrade) have relatively adequate layer moduli.
- Laboratory testing on extracted binder showed that it was significantly aged and hardened.

Based on the above information, this section should be subjected to milling the top 75 mm of the asphalt mat, transport the milled material to an asphalt mixing plant for potential recycling as RAP material. The remaining 127 mm of the asphalt mat should be subjected to cold in-place recycling.

After the recycling job is completed, a 50 mm thick capping layer of virgin asphalt mixture should be placed on both sections to improve the ride quality.

For the pavement structural design, the expected life of the rehabilitated sections can be predicted using mechanistic-empirical analysis considering the in-situ material properties and future traffic. If recycling of the top surface layer is not sufficient to cater to future traffic demand, one can design an additional asphalt overlay over the recycled layer(s).

5 CONCLUSIONS AND RECOMMENDATIONS

This paper summarizes the role of a systematic pavement evaluation procedure for the selection of asphalt pavement recycling strategy. The effects of crack types, crack depth and initiation, and

propagation on the adoption of asphalt recycling strategies are demonstrated with the help of case studies involving two in-service pavement sections.

The methodology described in the paper highlights the need for a systematic pavement investigation that includes pavement surface condition, non-destructive testing, cores and material testing that is needed for the selection of a cost-effective pavement recycling strategy. In addition, crack types (load-related versus non-load-related), crack depths, initiation and propagation information (bottom-up and top-down) play major roles in the selection of a cost-effective asphalt pavement recycling options.

For the pavement section showing top-down cracks (medium severity and high extent) to a depth of 75 mm, partial depth in-place asphalt recycling strategy is recommended. Whereas, for the pavement section exhibiting top-down cracks (high severity and extent) to a depth of 127 mm, a combination of in-place and in-plant asphalt recycling strategies is recommended.

ACKNOWLEDGEMENT

The authors acknowledge the Pakistan-United States Science and Technology Cooperative Program for funding this research. The opinions and conclusions expressed or implied in the paper are those of the authors. They are not necessarily those of the Pakistan-United States Science and Technology Cooperative Program.

REFERENCES

- AASHTO. (1993). *AAHTO Guide for Design of Pavement Structures (1993)*, American Association of State Highway and Transportation Officials, Washington, D. C.
- ARRA. (2001). *Basic Asphalt Recycling Manual*, Asphalt Recycling and Reclaiming Association, U.S. Department of Transportation.
- Baladi, G. Y. (1988). "Integrated Material and Structural Design Method for Flexible Pavements: Volume I – Technical Report." *FHWA-RD-88-109*, Federal Highway Administration, Washington D.C.
- Epps, J. A., Little, D. N., Holmgreen, R. J., and Terrel, R. L. (1980). "Guidelines for Recycling Pavement Materials." *NCHRP Report 224*, Transportation Research Board, National Research Council, Washington, D.C.
- FHWA. (1998). "Techniques for Pavement Rehabilitation (Reference Manual), 6th Edition." *FHWA HI-98-033, Course Number 13108*, Federal Highway Administration, National Highway Institute, Washington D.C.
- Hall, K. T., Correa, C. E., Carpenter, S. H., and Elliot, R. P. (2001). "Rehabilitation Strategies for Highway Pavements." *NCHRP Web Document 35 (Project C1-38)*, NCHRP, Washington D.C.
- Kandhal, P. S., and Mallick, R. B. (1997). "Pavement Recycling Guidelines for State and Local Governments." *FHWA-SA-98-042*, FHWA, Washington, DC.
- Matsuno, S., and Nishizawa, T. "Mechanism of Longitudinal Surface Cracking in Asphalt Pavement." *7th International Conference on the Structural Design of Asphalt Pavements*, Ann Arbor.
- McDaniel, R., and Anderson, R. M. (2001). "Recommended Use of Reclaimed Asphalt Pavement in the Superpave Mix Design Method: Technician's Manual." *NCHRP Report 452*, Washington, D.C.
- Miller, J. S., and Bellinger, W. Y. (2003). "Distress Identification Manual." *FHWA-RD-03-031*.
- Myers, L. A., Roque, R., and Ruth, B. E. (1998). "Mechanisms of Surface Initiated Longitudinal Wheel Path Cracks in High-Type Bituminous Pavements." *Association of Asphalt Paving Technologists*, 67, 401–432.
- Svasdisant, T., Schorsch, M., Baladi, G. Y., and Pinyosunun, S. (2002). "Mechanistic Analysis of Top-down Cracks in Asphalt Pavement." *Transportation Research Board*, 1809, 126–136.
- Ullidtz, P. (1987). *Pavement Analysis*, Elsevier Science Publisher B.V., Amsterdam, Netherlands.
- Ullidtz, P. (1998). *Modeling Flexible Pavement Response and Performance*, Narayana Press, Gylling, Denmark.

Cracks in porous European mixes: A theoretical and experimental study

F. G. Praticò, R. Ammendola & A. Moro

Mediterranean University of Reggio Calabria, Italy

ABSTRACT: As is well known, cracking in pavements occurs when a stress is built up in a surface layer that exceeds the tensile or shear strength of the pavement and may be associated with various distress mechanisms.

In the case of fatigue cracking, phenomena can be the result of repetitive traffic loads or high deflections, for example, due to the underlying layers defects.

On the other hand, it is well known that Porous European Mixes (PEMs) do not seal the underlying pavement against moisture intrusion and this fact can increase the potential for stripping of both the surface and underlying layers (especially when the underlying binder course, BIC, has high void contents).

In the light of the above-mentioned facts, the purpose of this study is the analysis of the bottom-up cracking associated with stripping in underlying layers and the evaluation of the effectiveness of laboratory testing in predicting premature failure. A case-history is described. Analyses show the synergetic importance of the system BIC & PEM. Recommendations are proposed in order to minimize the risk of such premature failures in Porous European Mixes.

1 LITERATURE REVIEW

As is well known, surface cracking can result from the overall performance of the multilayer system (pavement) and may be associated with various distress mechanisms (Al Qadi, 2007).

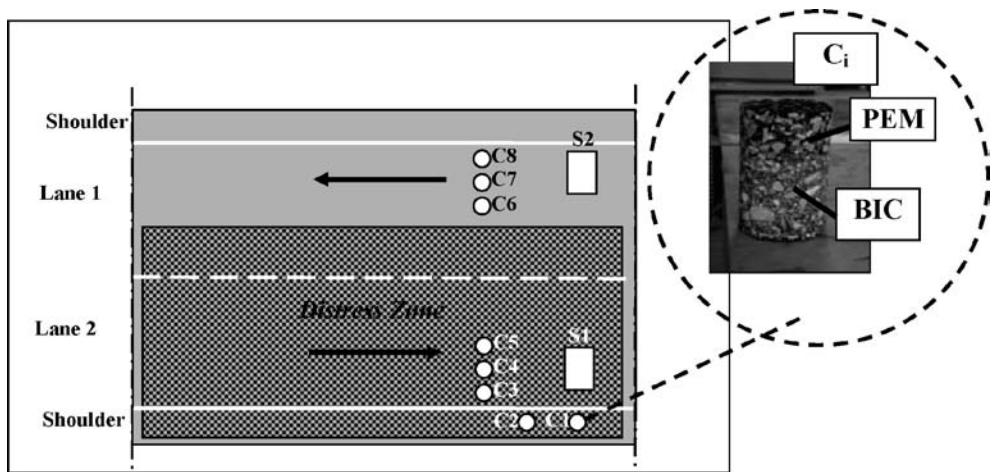
The balance among the mechanical properties of the different layers rules (under given load conditions) where and when cracks will appear and how they will propagate thorough the multilayered pavement system. So there is the possibility to detect surface distress substantially related to the failure of inside layers.

A class of typical premature, impulsive degradation phenomena originates from the breakage of the link between asphalt binder and aggregates. Separation or removal of asphalt binder from aggregate surface due primarily to the action of moisture and/or moisture vapour is generally termed stripping.

The following factors can be useful in analyzing such phenomena (Watson et al., 1998; Kandhal and Richards, 2001; Lavin, 2002; AA.VV., 2004; Long and Ioannides, 2007):

- Physio-chemical incompatibility of the asphalt system;
- Interaction between different HMA (Hot Mix Asphalt) courses;
- air void content (Turochy and Parker, 2007), presence of water, high stress, high temperature range, dusty or dirty aggregates.

Given that, the purpose of this study was the analysis of the bottom-up cracking associated with stripping in underlying layers and the evaluation of the effectiveness of laboratory testing in predicting premature failure. A particular case history has been analysed thorough a wide experimental campaign (§2 and §3). Following the obtained results, the present research aimed to provide insight into establishing criteria for more durable porous asphalt concretes (§4 and §5).



Symbols

C_i = i -th core; C1, C2 = Cores in the shoulder of lane 2; Distress Zone, DZ; C3, C4, C5 = Cores in lane 2 (DZ); S1 = Slab in lane 2 (DZ); C6, C7, C8 = Cores in lane 1 (Non Distress Zone); S2 = Slab in lane 1 (Non Distress Zone); BIC = Binder Course; PEM = Porous European Mix.

Figure 1. Cores and slabs location.

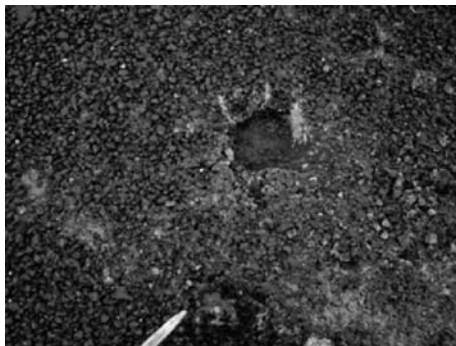


Figure 2. Distress zone: rutting, cracks, water and fines bleeding.

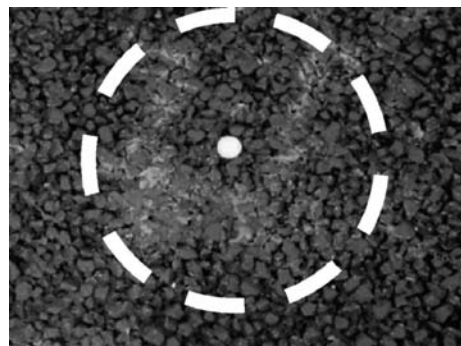


Figure 3. Fines bleeding.

2 CASE-HISTORY

A premature failure of a Porous European Mix (PEM) has been detected on a motorway in southern Italy.

Pavement surface condition was assessed through the following procedure:

- visual surface inspection;
- visual inspection after coring and trenching;
- in-lab testing;
- data analysis.

Four sections have been investigated. In each section, eight cores (C1 to C8) and two slabs (S1 and S2) have been extracted (figure 1).

Figures 2 to 9 illustrate in-site investigations.

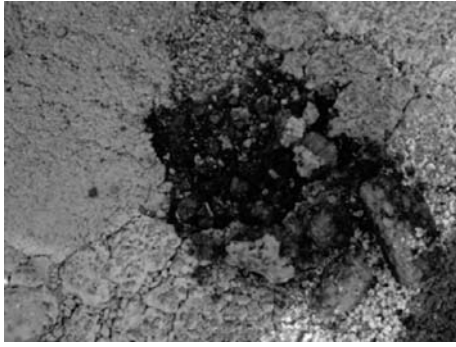


Figure 4. Distress zone.



Figure 5. Visual inspection.

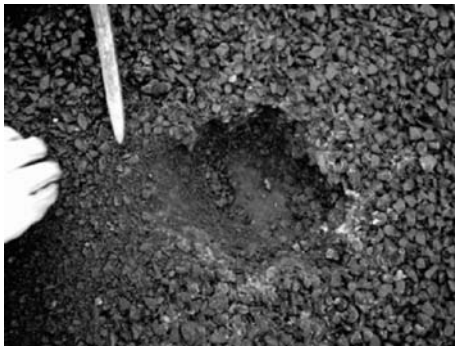


Figure 6. Development of potholes.



Figure 7. Dimension of pavement distress.



Figure 8. Water presence.

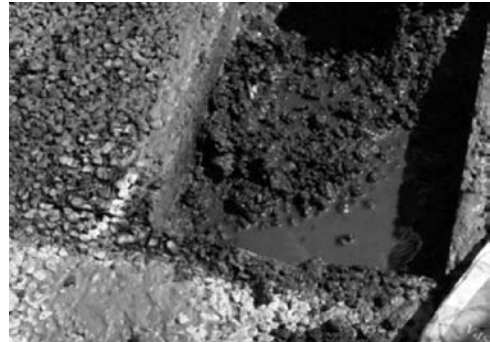


Figure 9. Slab extraction.

The following pavement structure has been detected:

1. first layer: PEM;
2. second layer: HMA binder course, BIC, (where HMA stands for Hot Mix Asphalt);
3. third layer: HMA base course; condition: good;
4. fourth layer: granular base; condition: good;
5. fifth layer: subgrade; condition: good.

The slabs (1st + 2nd layer) extracted from the wheel path resulted significantly defective (both for PEM and BIC).

The cores (1st + 2nd layer) extracted from outside the trafficked area (shoulders) resulted in good conditions; on the contrary, the cores extracted in “wheel path” locations resulted significantly damaged (both for PEM and BIC).

According to the analysis above performed, in order to scan the possible causes the following main factors have been considered:

- a) Surface water drainage (it resulted to need improvements).
- b) Binder course and tack coat between binder course and PEM.
Binder course revealed to be strongly stripped. Tack coat has not been clearly detected.
- c) Friction course (PEM).
Rutting has been monitored (about 1 cm on wheel path); the friction course appeared cracked (only) in the wheel path. Water seepage out of cracks (water bleeding) has been detected and water and fine material appeared ejected from underlying layers through cracks in the HMA layer under moving loads (water pumping). According to the investigation above performed, water bleeding and pumping have been associated to a decreased skid resistance and structural support. Among the possible causes, several including poor drainage, underlaying failure and fines excess and dusty aggregates have been hypothesized. Though the presence, only in the wheel paths, of bleeding of fines and water and cracks, tests on the friction course (PEM) resulted always conforming to the specifications set out in the contract (and following European recommendation).
- d) Anomalies in load conditions.
Operational speeds and load spectrum have been surveyed and resulted conforming to the road class and to the design hypotheses.
- e) Weather conditions during construction.
Agency engineer didn't report rain after the construction of the binder course and before the construction of the friction course.

3 EXPERIMENTS AND RESULTS

In-lab experiments have been planned according to the following standards (figure 10):

- a) Volumetric tests
The following parameters have been determined: b (%) = asphalt binder content as a percentage of aggregate weight (EN 12697 – 1:2002; ASTM 6307); G = aggregate gradation (UNI EN 933–1:1999); NMA = Nominal Maximum Aggregate Size; f (%) = filler content ($d \leq 0.075$ mm); s (%) = sand content (0.075 mm $\leq d \leq 2$ mm); γ_g = aggregate apparent specific gravity (UNI EN 1097/3:1999); G_{mb} = mix bulk specific gravity (ASTM D6752; ASTM D6857); G_{mbAO} = mix bulk specific gravity after opening (ASTM D6752; ASTM D6857); n_{eff} = mix effective porosity (ASTM D6752; ASTM D6857). The effective porosity (n_{eff}) has been calculated from G_{mb} and G_{mbAO} : $n_{eff} = (G_{mbAO} \cdot \gamma_w - G_{mb} \cdot \gamma_w) \cdot (G_{mbAO} \cdot \gamma_w)^{-1}$, γ_w = water density.
- b) Permeability tests
 K_{cv} , the coefficient of water permeability, has been calculated, using a Flexible Wall Permeameter – FWP (ASTM PS 129-01), according to the formula: $K_{cv} = R_T \cdot a_{cs} \cdot l \cdot A_{cs}^{-1} \cdot t^{-1} \cdot \ln(h_1/h_2)$, where a_{cs} is the inside cross-sectional area of inlet standpipe (cm²); l is the thickness of test specimen (cm); A_{cs} is the cross-sectional area of test specimen (cm²); t is the average elapsed time of water flow between timing marks (s); h_1 is the initial hydraulic head on specimen (cm); h_2 is the final hydraulic head on specimen (cm); R_T is a coefficient that corrects the calculated K at given temperature to that for 20°C.
- c) Asphalt binder tests
Penetration test (Pen (dmm)) according to CNR BU N.24-1971 (Norme per l'accettazione dei

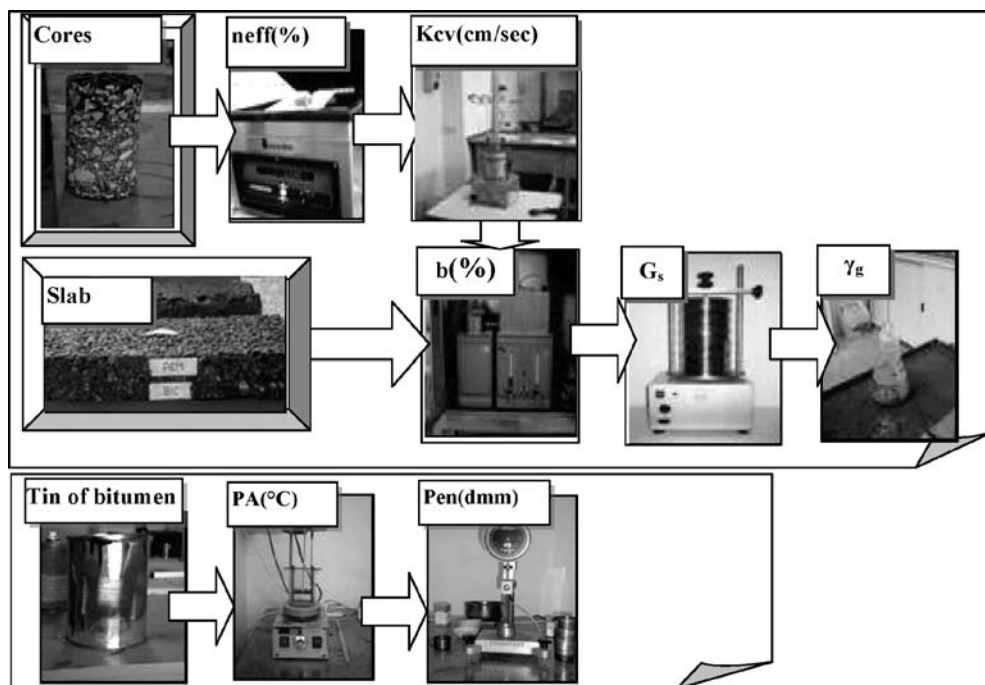


Figure 10. Main tests.

Table 1. Main composition parameters of the two mixes.

ϕ (mm) Sieve Size	Percent Passing (%)	
	BIC	PEM
40	100.00	100.00
30	100.00	100.00
25	99.34	100.00
15	90.52	85.69
10	66.11	29.90
5	47.65	12.91
2	37.11	11.13
0.4	16.56	8.40
0.18	7.98	6.81
0.075	5.54	5.53
b %	4.4–5.2	4.5–5.3
n_{eff} (%)	8.1–14.5	16.3–21.2

Symbols

Mix 1 = Binder Course (BIC), Mix 2 = Porous European Mix (PEM), b(%) = asphalt binder content as a percentage of aggregates, n_{eff} (%) = mix effective porosity.

bitumi per usi Stradali; EN 1426:2007: Bitumen and bituminous binders – Determination of needle penetration); Softening point (PA °C) (Ball and ring) according to CNR BU N.35-1973; EN 1427: 2007: Bitumen and bituminous binders – Determination of the softening point – Ring and Ball method).

Tables 1 to 3 and figures 11 to 15 summarize the obtained results.

Table 2. Asphalt binder main properties.

Asphalt Binder	PA(°C)	Pen (dmm)	η (Pas) (135°C)	η (Pas) (150°C)	η (Pas) (170°C)
Modified (PEM)	73	53	1.1	0.7	0.4
Non modified (BIC)	47	66	0.4	0.2	0.1

Table 3. Effective porosity and hydraulic conductivity for BICs and PEMs (mean values).

Cores (C)/ Slabs (S)	BIC		PEM	
	n_{eff} (%)	Kcv (cm/sec)	n_{eff} (%)	Kcv (cm/sec)
C1	14.50	0.0360	18.10	0.1479
C2	14.13	0.0350	18.80	0.1554
C3	11.90	0.0110	16.26	0.0942
C6	8.06	0.0010	21.19	0.2591
C7	9.39	0.0060	19.96	0.2579
S2	13.21	nd	–	–

Legend nd = Not available.

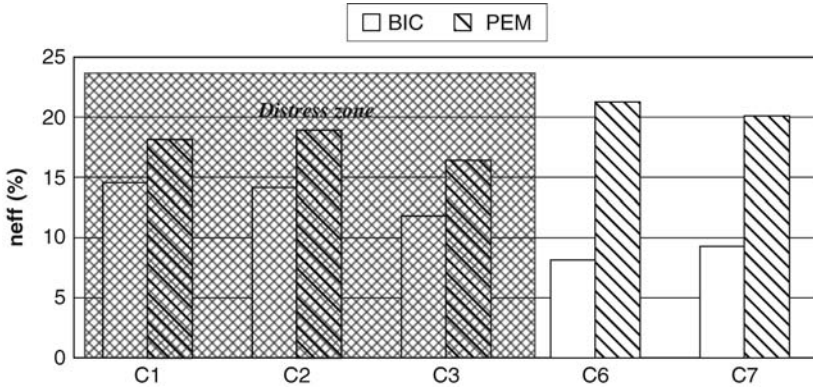


Figure 11. Effective porosity as a function of core location (average values).

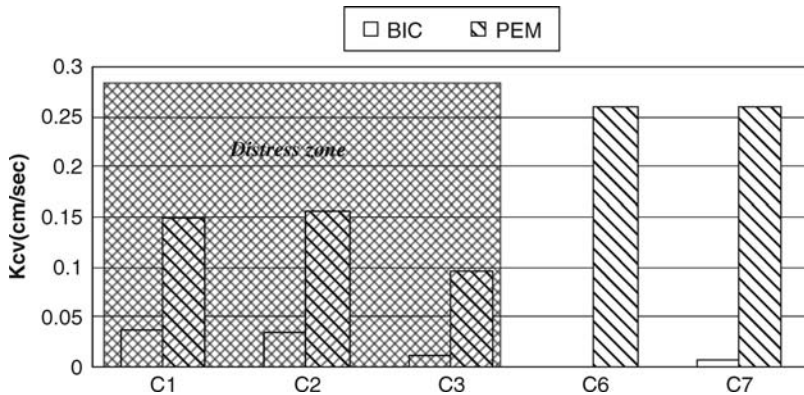


Figure 12. Permeability as a function of core location (average values).

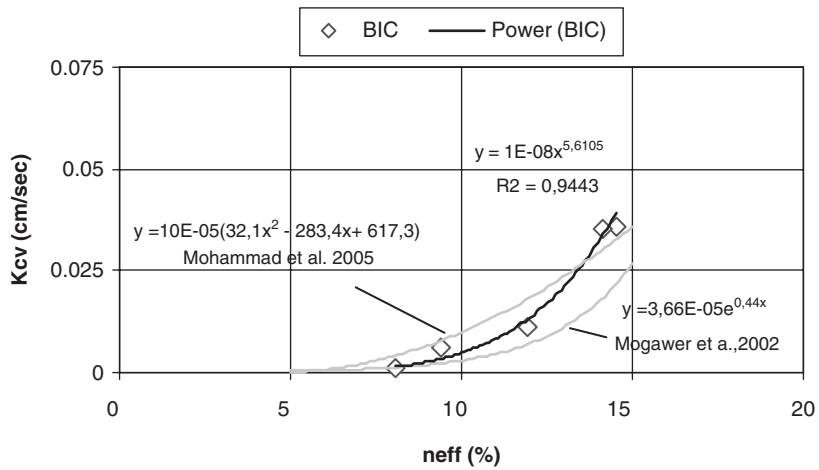


Figure 13. Kcv vs. neff (BIC).

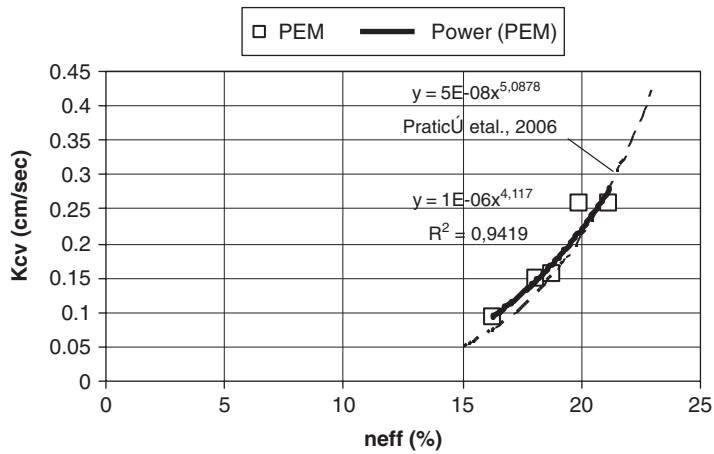


Figure 14. Kcv vs neff (PEM).

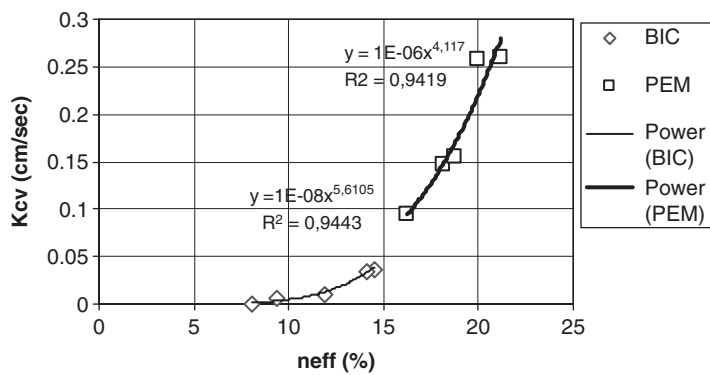


Figure 15. Kcv vs. neff (BIC and PEM).

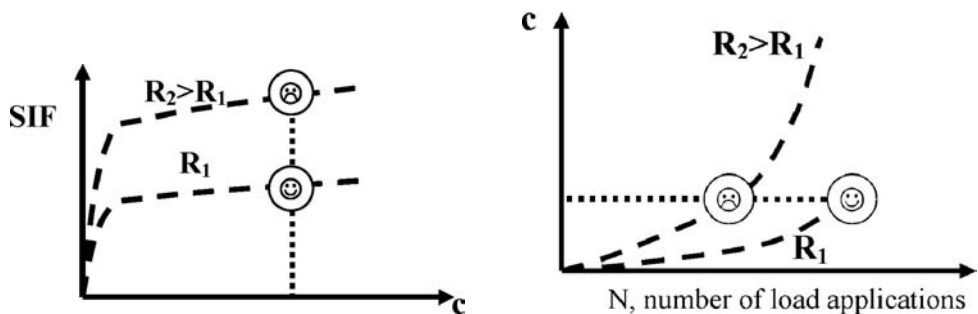


Figure 16. Stress Intensity Factor vs. crack length. Figure 17. Crack length vs. N.

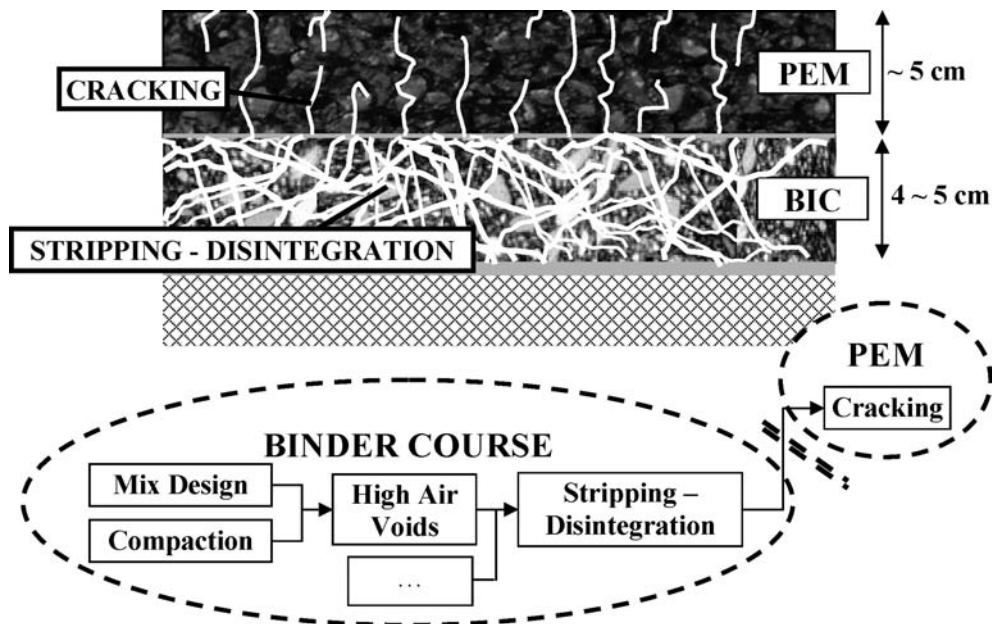


Figure 18. Lesson learned.

The specifications set out in the contract (substantially in accordance with European recommendations) required an air voids content of the BIC in the range 4% ~ 8%, a quantity of tack coat in the PEM-BIC interface of at least 1000 g/m², and a permeability of the BIC lower than 10⁻⁶ cm/s.

The analysis of aggregate grading, asphalt binder content and characteristics didn't reveal any particular issue. On the contrary, BIC effective porosity and permeability resulted out of range.

On the basis of the collected data, plots 11 to 15 have been derived. Figures 11 and 12 show a strong relationship between BIC high effective porosity and high permeability in the distress zones.

Figures 13 to 15 show how permeability depends on the effective porosity for the selected sections. Some known fitting curves are referenced.

4 FINAL DISCUSSION AND LESSON LEARNED

In the light of data analysis it is possible to suppose that the following primary chain of factors (figures 16 to 18) has been involved in the premature failure:

- percolation of water through the PEM in the direction of the binder course;
- high air void content of the binder course;

- related processes of stripping and therefore progressive disintegration of the binder course with consequences for the PEM.
- reduction of the modulus of the binder course, due to the high void content (as is well known, when air voids increase from 5% to 11%, then relative modulus can decrease, e.g., from 1 to 0.6 circa);
- effect of the BIC stripping on the stress intensity factor. The higher the ratio $R = E_{PEM}/E_{BIC}$ between the effective moduli (Cebon, 2000, see qualitative estimate in figure 16), the higher the stress intensity factor (SIF), for a given crack length (c);
- effect of the BIC stripping on the number of load applications (N) to have a given crack length (c). The higher the E_{PEM}/E_{BIC} ratio (R), the steeper the curve, the quicker the cracks growth (see qualitative estimate in figure 17).

Figure 18 summarizes the lesson learned through the analyses for the given case-history.

5 MAIN FINDINGS

It is well known that Porous European Mixes do not seal the underlying pavement against moisture intrusion and this fact can increase the potential for stripping of both the surface and underlying layers (especially when the underlying binder courses have high air void contents). A case history has been analysed through a wide experimental campaign.

Specifications set out in the contract didn't appear to be the main cause of the premature failure of the PEM. More precisely, the key-factors appeared Quality Assurance and Controls (QA/QC procedures). Laboratory testing resulted useful to appropriately understand premature failure of PEMs due to the underlying layers.

In the light of the above facts, the following possible additional criteria for delaying and controlling crack initiation and propagation in PEMs can be considered:

- introducing more precise QC/QA specifications on tack coats in the boundary binder course-PEM;
- introducing QC/QA specifications on transverse and longitudinal slope for the drainage of water over the binder course;
- introducing more precise QC/QA specifications on BIC permeability;
- lowering stripping risk in BICs which underlie PEMs through the use of anti-stripping agents and a lower air void content.

ACKNOWLEDGEMENTS

Authors would like to express appreciation to Alessandro Bellantonio for the contributions he made during the preparation of this paper.

REFERENCES

- AA.VV. 2004. *Cracking in Pavements: Mitigation, Risk Assessment and Prevention* C. Petit, I.L. Al-Qadi and A. Millien.
- Al_Qadi, I. L. 2007. *Reflective Cracking: Initiation and Propagation Mechanism*, University of Illinois at Urbana-Champaign, MAIREPAV5, August 07.
- Cebon, D. 2000. *Handbook of vehicle-road interaction*, Swets & Zeitlinger B.V., the Netherlands.
- Kandhal, P.S. & Richards, I.J. 2001. *Premature Failure of Asphalt overlays from stripping: case histories*, Annual meeting of the association of asphalt technologists, Clear Water, Florida.
- Lavin, P. 2002. *The effects of dusty aggregates towards stripping in asphalt pavement*, the asphalt institute Spring meeting, the Woodlands, Texas, US, April 14.
- Long, A. & Ioannides, A. 2007. *Performance of Permeable Bases*, 86th Transportation Research Board Annual Meeting, Washington, D.C., USA, January 21–25.

- Mogawer, W.S., Mallick, R.B., Teto, M. & Crockford, W.C. 2002. *Evaluation of Permeability of Superpave Mixes*, Project No. NETC 00-2.
- Mohammad, L.N., Hetath, A., Wu, Z. & Cooper, S. 2005. *Factors Influencing the Permeability of Hot-Mix Asphalt Mixtures*. Louisiana Asphalt Technology Conference, Shreveport, Louisiana.
- Praticò, F.G. & Moro, A. 2006. *Hot Mix Asphalts Drainability and Permeability: a Theoretical and Experimental Investigation on four different Devices*, 10th International Conference on Asphalt Pavements, ICAP Québec, Canada.
- Turochy, R. & Parker, F. 2007. *Comparison of Contractor and State Transportation Agency Quality Assurance Test Results on Mat Properties of Hot-Mix Asphalt Concrete: Findings of a Multistate Analysis*, 86th TRB Annual Meeting, Washington, D.C., USA, January 21–25.
- Watson, D., Johnson, A., Jared, D. 1998. *Georgia Department of Transportation's Progress in Open-Graded Friction Course Development*, Journal Transportation Research Record, Transportation Research Board of the National Academies, ISSN 0361-1981, Issue Volume 1616.

9. Pavement modeling-response, crack analysis, and damage prediction

Reflective cracking behavior for traffic and temperature effects

M.J.C. Minhoto

Bragança Polytechnic Institute, Bragança, Portugal

J.C. Pais & P.A.A. Pereira

University of Minho, Guimarães, Portugal

ABSTRACT: This paper presents a study on the influence of the effects of temperature variations, in comparison with traffic effects, on the reflective cracking overlay behavior. It is intended to contribute to the improvement of the pavement overlay design methods which consider reflective cracking as one among distress criteria. The development of this study was based on the numerical simulation of the overlay behavior, through the implementation of numerical thermal and mechanical models based on the finite element, considering the simultaneous action of traffic and temperature variations and their influence on reflective cracking.

1 INTRODUCTION

The aim of the paper is to present a study on the influence of temperature variations on the reflective cracking overlay. With the obtained knowledge, emphasis will be placed on the improvement of the pavement overlay design methods, by demonstrating the possibility to develop relationships that consider temperature variation effects in relation to the reflective cracking phenomena in the pavement overlay design methodologies. The developments of this study were supported on the numerical simulation of the overlay behavior, based on the finite element methodology and considering the simultaneous loading of traffic and temperature variations on a conventional asphalt overlay.

This study also involves an evaluation of the hourly stresses and strains, generated by traffic and thermal loading characterized through temperature variation in the full-depth of the pavement during a year. That temperature distribution throughout the pavement structure was obtained by field measurements in a pavement section located along IP4 main road, near Bragança (northeast of Portugal), for a period of a year, using a temperature-recording equipment. Traffic data were obtained in field near the temperature measurements location.

The 3D finite element methodology was used to model the reflective cracking phenomena, in order to calculate the stresses and strains associated to each single case of loading: traffic (130 kN axle load) and observed full-depth pavement temperatures. Based on those strains results, the strain state of the combination of both cases was evaluated.

In the case of thermal loading strain evaluation, the bituminous material behavior was considered as viscoelastic, characterized by the relaxation modulus, as the overall state of tension in the overlay caused by the temperature variation is time-dependent and thus function of the viscoelastic response of the bituminous materials. In the case of traffic loading the bituminous material behavior was considered as “elastic” material, characterized by the stiffness modulus.

Those computed stresses and strains became concentrated above the existing cracks, creating an active zone of pavement overlay failure or crack propagation. The traffic and thermal stresses and strains, calculated for each case of loading, were used to verify the influence of the thermal loading in the overlay behavior through the evaluation of the hourly damage associated to each type of load.

The overlay damage evaluation was made hourly along the year was made through the ratio between the hourly observed traffic and the hourly predictive overlay life. The overlay life evaluation was made using the mechanistic-empirical methodology proposed by Sousa et al (2005).

This methodology is capable of assembling Modes I and II deflection patterns simultaneously on asphalt concrete specimens into a coherent procedure. The influence of pavement characteristics on state of stress and strain was considered by applying the Von Mises strain deviator, expressed by Equation 1.

$$\varepsilon_{VM} = \frac{1}{1+\nu} \sqrt{\frac{1}{2}((\varepsilon_1 - \varepsilon_2)^2 + (\varepsilon_1 - \varepsilon_3)^2 + (\varepsilon_2 - \varepsilon_3)^2)} \quad (1)$$

where ε_{VM} is the Von Mises strain and $\varepsilon_1, \varepsilon_2, \varepsilon_3$ are the principal strains.

This mechanistic-empirical methodology is based on the results of flexural fatigue tests, in controlled strain, based on the Von Mises strain as the “controller” parameter of the phenomenon. For beam fatigue test conditions subjected to four-point bending, ε_{VM} can also be written as:

$$\varepsilon_{VM} = \varepsilon_{fat} (1 + \nu) \quad (2)$$

where ε_{fat} is the fatigue strain for beam fatigue test conditions subjected to four-point bending.

2 THERMAL LOADING

The full-depth pavement structure temperature distribution was obtained through field measurements, using temperature-recording equipment – a Datalogger associated with thermocouples – because, by this means, actual temperature can be reliably measured. However, this method is relatively slow and it only provides information about temperature in the measurement period (Minhoto et al, 2005). During twelve months (January 2004 to December 2004) pavement temperatures were measured at a new pavement section, located at IP4 main road, near Bragança (north of Portugal). At that location, seven thermocouples were installed in the pavement at seven different depths: at surface, 0.028 m, 0.055 m, 0.125 m, 0.165 m 0.220 m and 0.340 m.

The depths were chosen to offer a proper representation of the whole asphalt concrete layers (0.340 m). The temperatures were recorded at every hour, every day, allowing to produce the visualization of the annual temperature evolution, such as the observed temperatures at the bottom of the overlay, as presented in Figure 1. In that figure the typical temperature variations of summer and winter periods are clearly identified.

3 PAVEMENT MODELLING

The pavement structure was modeled as presented in Figure 2. For crack reflection analysis the top layer represents the bituminous overlay and the subjacent layer represents the old cracked bituminous layer, where a crack is modeled by elements without stiffness.

The finite element model used in three-dimensional numerical analysis was developed by using a general finite elements code, ANSYS 7.0. The design of a mechanical model is based on a finite element mesh definition, oriented to mechanical analysis, considering a finer element mesh closer to the pavement surface, nearer the wheel load point and in the overlay above the crack. An eight-node structural solid element was used assuming linear approximation of the displacement field and three degrees of freedom per node.

The model is 4.63 m long, 7.45 m wide and 2.24 m thick. The model total thickness is the result of all pavement layers thicknesses: 0.125 m overlay, 0.215 m cracked layer, 0.30 m aggregate base layer and 1.6 m subgrade. A longitudinal crack was modeled on the layer which is just below the

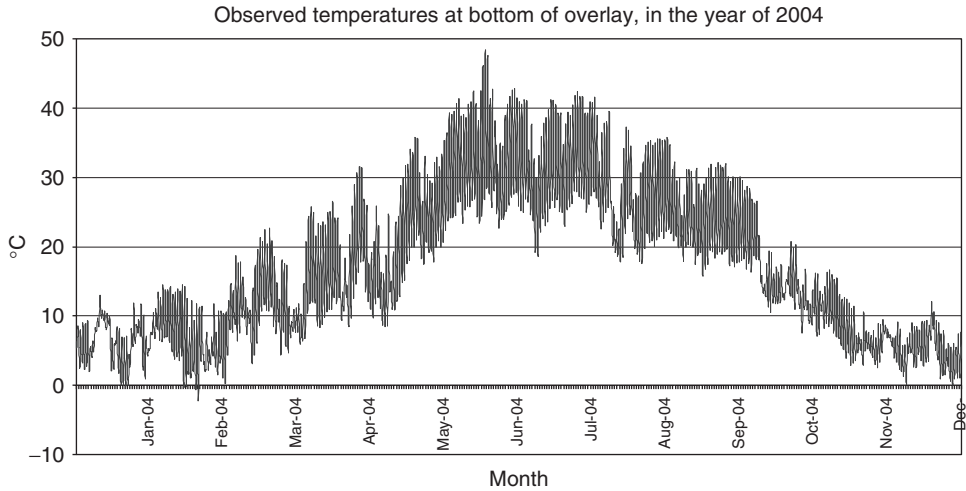


Figure 1. Observed temperatures at overlay bottom.

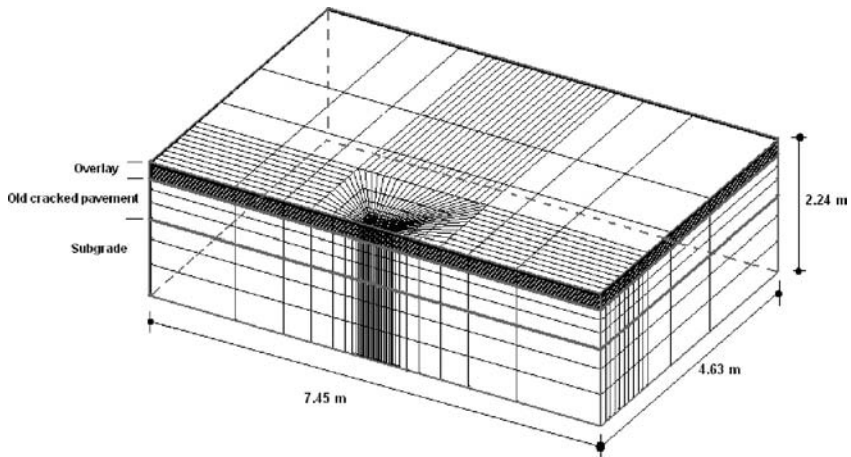


Figure 2. Structural model configuration used in numerical simulation.

overlay with 10 mm width. The resulting number of elements was 13538, in both traffic and thermal cases.

The first effort in order to verify and calibrate the purely FEM mechanical analysis of a cracked pavement before and after the overlay was accomplished by comparing the vertical crack activity measured in the model with the one measured in the pavement using a crack activity meter, according to the model developed by Pais et al (2002). The calibration was accomplished by comparing the crack movements in a pavement and in the FEM model for two different conditions: before and after the pavement overlay.

Once the type of processing depends on the loading case considered, for thermal loading, the model processing was carried out as a transient process (time-rate dependent), because that load type is a long term load, and the material properties are time-rate dependent. For the traffic loading case, the model processing was based on a steady-state process, as that load is considered to be a short-term load, and the material properties were defined as elastic material, or non-time-dependent.

Table 1. Elastic properties of the bituminous mixture used in this study.

Temperature (°C)	Stiffness (MPa)
-5	16157
5	13563
15	9304
25	478

4 MECHANICAL PROPERTIES

The stiffness modulus for modeling was obtained from flexural fatigue tests, conducted according to the AASHTO TP 8-94, performed for 4 different temperatures: -5°C ; 5°C , 15°C and 25°C . The stiffness modulus values obtained for the conventional mix used in this work are presented in Table 1.

The fatigue behavior considered for the studied mixtures was evaluated after the stiffness modulus tests for the same test temperatures. For each test temperature (-5°C ; 5°C , 15°C and 25°C) a fatigue life law was achieved and fitted in the following model:

$$N_f = \left(\frac{\varepsilon_t}{(aV_b + b)E^{-c}} \right)^{-d} \quad (3)$$

where N_f is the fatigue resistance, ε_t is the strain level, E is the stiffness modulus, V_b is the volume of the binder in the mixture, $a = 1.009$; $b = 0.9283$, $c = -0.3772$ and $d = 3.961$

For the temperature variation modeling, it was considered that the bituminous material shows a linear viscoelastic behavior, time-and-temperature dependent, modeled through thermal-reological simplicity principle. With this principle, the relaxation curve for high temperatures is identical to the low temperature relaxation curve, when loading time is scaled.

Relaxation tests were also performed at -5°C , 5°C , 15°C and 25°C , using bituminous samples of the conventional mix. Tests results were fitted in kernel functions and considering the thermal-reological simplicity principle, elastic shear modulus, G_i , elastic volumetric modulus, K_i , relaxation modulus, τ_i , and C_1 and C_2 for WLF function were obtained and presented in Table 2.

Thermal contraction tests were performed and the coefficient of thermal contraction, constant and independent from temperature, obtained for this study was $3.54 \times 10^{-5}/^{\circ}\text{C}$. The Poisson's ratio was assumed to be constant and the value adopted was 0.35 for bituminous layers and subgrade and 0.30 for granular layers.

5 SIMULATION PROCEDURES

The simulation procedures to achieve the purposes of this study involved a multiple 3-D finite-element runs considering the pavement structure referred above. Each solution was obtained for each hour and for each loading case (traffic, temperature variation and both superimposed). The main analysis procedure involved in the present study is schematized in Figure 3.

In the first stage, for each hour of the day along a year, all nodal pavement temperatures of the finite element model were calculated by using the thermal model, a steady-state thermal analysis based, and applied in all nodes of traffic and temperature variation models. The input data of the thermal model were the field pavement temperatures obtained in the seven points of the pavement.

Table 2. Prony parameters of the bituminous mixture used in this study.

Parameters	Value
Shear Parameters	
K_{∞}	2.81E + 01
K_1	7.85E + 02
K_2	2.60E + 02
K_3	3.07E + 01
τ_1^K	5.85E - 01
τ_2^K	9.16E + 00
τ_3^K	9.92E + 03
Volumetric Parameters	
G_{∞}	1.04E + 01
G_1	2.89E + 02
G_2	9.45E + 01
G_3	1.13E + 01
τ_1^G	5.99E - 01
τ_2^G	9.49E + 00
τ_3^G	1.00E + 04
WLF	
T_r	1.31E + 01
C_1	2.56E + 07
C_2	1.39E + 08

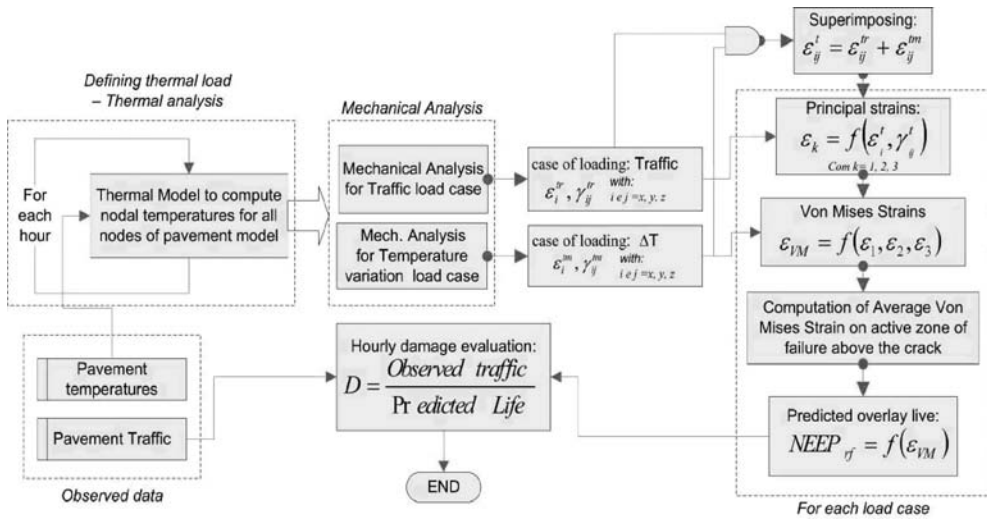


Figure 3. Procedures involved in the study.

The computed pavement temperatures were applied in all nodes of the traffic model to set the elements stiffness for stress and strain calculation for 130 kN traffic loading case. The computed pavement temperatures were also applied in all nodes of thermal mechanical model.

The strain and stress states obtained for traffic loading and temperature variations were superimposed to obtain the stress and strain states for resulted loading. After that, the average Von Mises strains in the finite element nodes above the crack zone were computed for each case. This Von Mises strains were used to estimate the overlay life of each studied case.

Equation 2 was used to relate the average Von Mises strain with a fatigue strain concept used on flexural fatigue laws, obtained from four-point flexural fatigue tests, normally used to evaluate the prediction of pavement life. In this way, fatigue life was estimated considering the Von Mises strain of the overlay. The four-point flexural fatigue tests performed to obtain the fatigue laws to be used in this study were carried out at different temperatures. Those fatigue laws were developed in terms of temperature-dependency.

The overlay life was obtained from nodal temperature occurred in the zone above the crack at every hour. After that, the hourly damage was evaluated.

6 VON MISES STRAIN AND OVERLAY LIFE RESULTS

In one-year time-period the main results obtained from this simulation were: i) the Von Mises strains; ii) predicted overlay life; iii) overlay damage. These calculations were performed for traffic loading, temperature variations and the combination of both, traffic and temperature. In Figure 4, the hourly means Von Mises strain evolution along the year is plotted against the time.

The Von Mises strain for each loading case was used to predict the pavement life after overlying. Figure 5 shows the hourly predictive overlay life resulting from traffic and traffic + ΔT loading cases.

The results show that the overlay life obtained from traffic loading is higher than the overlay life obtained from traffic + ΔT loading, mainly in winter season, when low temperatures occur. In summer, the predicted overlay life is inferior to that of winter. Thus, the effect of traffic + ΔT may have a significant influence on the overlay life, which will justify a special attention.

7 DAMAGE RESULTS

Knowing the predicted overlay life and the number of axles distribution during the year allows to perform an annual damage evolution estimation. The damage evaluation is made in terms of damage distribution and in terms of accumulated damage evolution, measured hourly and monthly.

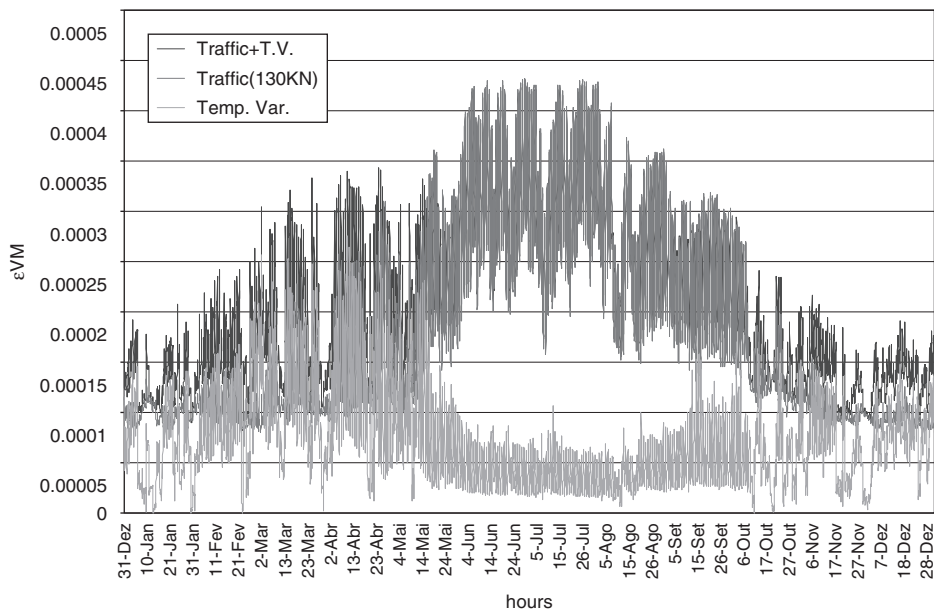


Figure 4. Von Mises strain for all loading cases.

Figure 6 shows the accumulated monthly damage occurred in a conventional mix overlay for traffic and traffic + ΔT . In this figure the accumulated monthly damage occurred in relation to traffic loading is lower than the damage observed for traffic + ΔT . Thus, the traffic + ΔT effect in the overlay damage may have a significant influence when compared with traffic effects that should be considered in a design process..

Monthly and annual damage for the real loading conditions (traffic and temperature variations) was obtained from the previously presented results, as shown in Table 3.

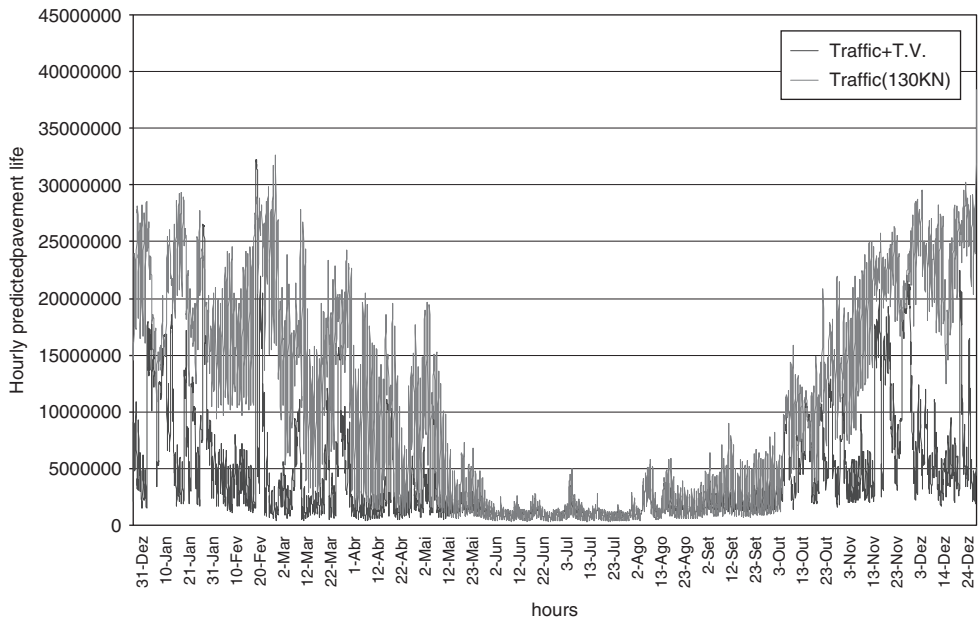


Figure 5. Predicted overlay life for traffic + temperature variations.

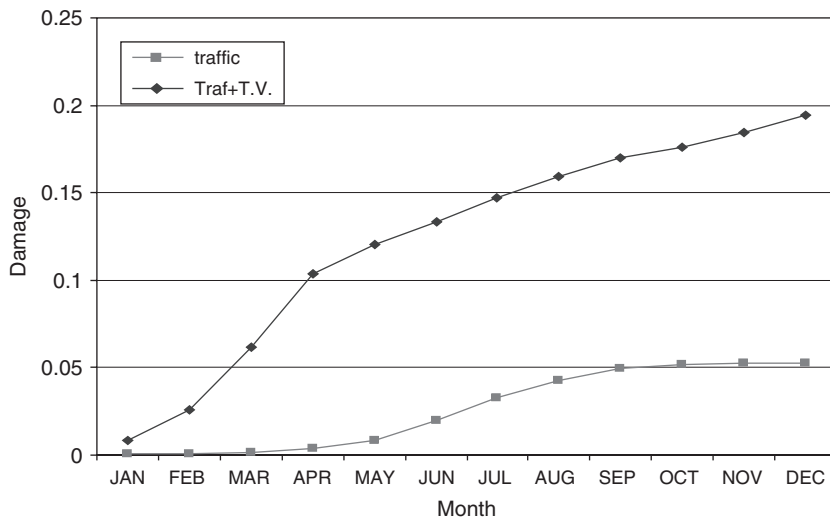


Figure 6. Accumulated monthly damage occurred in a conventional mix overlay.

Table 3. Real monthly and annually damage for real loading conditions.

Period	Air temperature				Real damage
	T_{ref}	ΔT	T_{min}	T_{mean}	
January-04	10.14	8.06	2.08	5.96	0.008340
February-04	11.02	10.67	0.36	5.06	0.017382
March-04	11.69	9.95	1.73	6.65	0.036154
April-04	15.69	13.13	2.56	9.41	0.041459
May-04	19.68	12.29	7.39	13.68	0.017202
June-04	28.13	15.22	12.91	20.99	0.012995
July-04	27.68	15.17	12.51	20.58	0.013910
August-04	25.78	11.49	14.29	20.30	0.011692
September-04	25.16	16.46	8.70	16.62	0.010663
October-04	16.75	9.12	7.63	11.98	0.006598
November-04	10.09	9.13	0.97	4.95	0.008147
December-04	9.08	9.45	-0.37	3.81	0.010155
Annual	20.80	13.15	7.65	14.27	0.194697

8 THEORETICAL SIMULATION

The reflective cracking evaluation presented needs time investment in terms of computing processes and does not provide immediate results. Thus, the development of procedures that allow a rapid evaluation of the damage associated to each loading condition is important for this study, mainly for the development or improvement of the pavement overlay design methodologies in order to consider the temperature variations effect in the reflective cracking phenomena.

Thus, the development of relationships between the thermal loading parameters and the corresponding pavement damage and the development of shift factors between that theoretical damage and the damage for real loading conditions are some of the purposes of the present research.

For a large number of “theoretical standard situations” of temperature variations loading, the hourly damage was calculated in order to establish a direct relationship between those two variables (loading conditions and associated damage). The standard situations of temperature variations are characterized, for a period of twenty four hours, by means of two parameters: reference temperature, T_{ref} (the maximum daily air temperature), and the maximum daily temperature variation, ΔT . Those situations were considered theoretical and it was assumed that these conditions happened during the analysis period. The theoretical damage was calculated for the observed traffic.

First, for each theoretical loading situation, an hourly distribution was adopted, for twenty-four hours, for the main atmospheric parameters that influence the pavement thermal state, specifically the air temperature evolution, the solar radiation evolution, the mean wind speed and the full-depth pavement temperature distribution for the initial thermal state. Those parameters were established through an exhaustive analysis of temperature measurements.

After that, the evaluation of the theoretical stress/strain states in the pavement overlay associated to each standard situation was carried out. This procedure involved the use of simulation thermal models for full-depth pavement temperature determination. Considering these temperatures, mechanical models were applied to determinate the stress/strain states in the pavement overlay.

A set of damage curves between (T_{ref} , ΔT) and the obtained damage were deduced. Each damage curve represents the variation of the damage during any period, as a function of the temperature variation, ΔT , for a specific reference temperature, T_{ref} . Figure 7 presents the curves of the annual damage for a reference temperature, T_{ref} , respectively.

The establishment of a reasonable number of damage curves allowed developing a statistical study for fitting the results within a generalized law. These results provide evidence that monthly

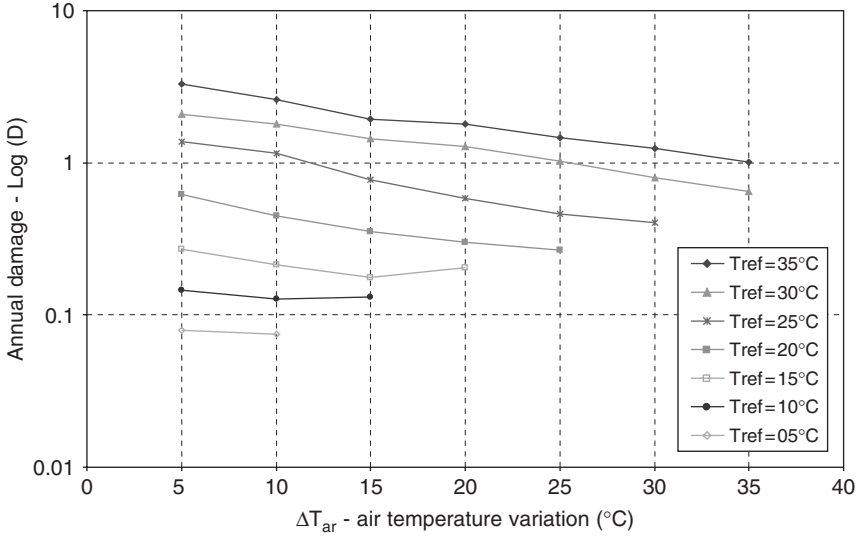


Figure 7. Overlay damage for theoretical simulations.

Table 4. Generalized constant values for monthly damage evaluation.

Validation range	Constant values			R ²
	a	b	c	
35°C < T _{ref} < 15°C	1.770E - 06	2.617E + 00	-5.653E - 02	8.618E - 01
15°C < T _{ref} < 5°C	8.388E - 04	1.199E + 00	-1.598E - 02	7.814E - 01

damage variation against reference temperature, T_{ref}, and temperature variations, ΔT, for each month, show an exponential trend, and the best-fit relationship obtained follows Equation 4.

$$damage = a \times T_{ref}^b \times e^{c \times \Delta T} \quad (4)$$

where: a, b and c = monthly damage fitting constants, for each month; T_{ref} = reference temperature; ΔT = temperature variation.

The a, b and c generalized constants were obtained statistically for each month, through the monthly damage evolution analysis, by fitting Equation 4 to damage values associated to the (T_{ref}, ΔT) standard cases. The constants obtained for the statistical analysis are presented in Table 4 and are function of the reference temperature.

With the real and theoretical damage values, obtained for each considered period, a representative factor between the theoretical damage and the real damage can be established for each standard situation. This factor, called “damage shift factor”, is expressed by Equation 4.

$$r = \frac{D_{monthly}^{real}}{D_{monthly}^{theoretical}} \quad (5)$$

where r = damage shift factor between theoretical and real damage; D_{real} = total monthly damage resulting from real traffic and temperature variations; D_{theoretical} = total monthly damage resulting from theoretical situations of traffic and temperature variations.

Table 5. Real damage, theoretical damage and damage shift factor.

Period	Air temperature				Real damage	Theoretical damage	Shift factor (Dr/Dt)
	T _{ref}	ΔT	T _{min}	T _{mean}			
January-04	10.14	8.06	2.08	5.96	0.008340	0.011862	0.703097
February-04	11.02	10.67	0.36	5.06	0.017382	0.012580	1.381666
March-04	11.69	9.95	1.73	6.65	0.036154	0.013649	2.648738
April-04	15.69	13.13	2.56	9.41	0.041459	0.018468	2.244931
May-04	19.68	12.29	7.39	13.68	0.017202	0.002151	7.995755
June-04	28.13	15.22	12.91	20.99	0.012995	0.004643	2.798691
July-04	27.68	15.17	12.51	20.58	0.013910	0.004463	3.116920
August-04	25.78	11.49	14.29	20.30	0.011692	0.004562	2.563000
September-04	25.16	16.46	8.70	16.62	0.010663	0.003232	3.298987
October-04	16.75	9.12	7.63	11.98	0.006598	0.001688	3.907951
November-04	10.09	9.13	0.97	4.95	0.008147	0.011599	0.702369
December-04	9.08	9.45	-0.37	3.81	0.010155	0.010169	0.998642
Annual	20.80	13.15	7.65	14.27	0.194697	0.524624	0.371117

Table 5 shows the “damage shift factor” values for each analysis period. The fitting statistical study for obtaining *a*, *b* and *c* constants was carried out monthly and during the global analysis period.

The analysis of Table 5 allows concluding that, during cold months, the values of the damage shift factor are values near 1. During warm months that parameter presents dispersion and, in the majority of cases, shows values higher than 1.

9 DESIGN PROCEDURES

The purpose of the present study is to develop a generalized overlay design methodology. It three phases: a) data definition; b) daily damage evaluation and c) performance evaluation.

Data definition and damage evaluation phases must have the same treatment as the procedure for the establishment of damage relationships previously presented.

In the future the proposed methodology must develop the process of evaluation of the hourly damage for 24 hours, which will consist in the application of relationships that produce the results obtained for traffic and thermal effects observed during the year. The establishment of relationships to obtain these objectives will have to observe the following aspects:

- the relationships for standard (theoretical) loading situations must be established with basis on the acceptance of two values of air temperature (T_{ref}, ΔT) as adopted in the second part of this paper.
- the relationships will have to be developed for several overlay structure types, characterized for diverse thicknesses of the pavement and several values of the stiffness of the existing layers, including that of the subgrade foundation.

The process of development of the relationship proposed must generally follow the procedures adopted in this paper. The resulting relationships will have to allow:

- the establishment of a pair of values (T_{ref}, ΔT) which must guarantee the calculation of a daily profile of Von Mises strains associated to the combination of traffic and variations of temperature loading;
- the establishment of a pair of values (T_{ref}, ΔT) which must allow the calculation of a daily profile that makes possible to obtain a permissible hourly traffic, as an alternative to the profile considered in the previous point;

- the establishment of a pair of values (T_{ref} , ΔT) which must guarantee the calculation of a daily profile of hourly damages associated to the combination of traffic loading and temperature variation.

10 CONCLUSIONS

The finite-element analysis was used to simulate the reflective cracking performance of bituminous mixture overlays throughout a year, considering the temperature variations as the main cause for reflective cracking. A thermal response of the pavement structure, made by a thermal analysis, was performed before a mechanical analysis. In the mechanical analysis the transient effect of relaxation was considered, once the overall state of tension in the overlay caused by the temperature variation is also a function of the viscoelastic response of the bituminous materials.

Temperature variations in bituminous layers (overlay and cracked layers) which cause a state of tension in the overlay are particularly important for estimating the overlay life. The effect of accumulated restrained thermal stresses, as a result of the effect of temperature variations shrinkage, added to the traffic loading effect, will reduce the overlay life. Thus, the effect of temperature variation will support the need for a special attention towards overlay design procedures.

This study has demonstrated that it is possible to include the effects of temperature variations in a design process of pavement overlays. For that, it is necessary to develop a methodology that includes relationships, such as the ones presented in this paper, for evaluating damage and shift factors to adjust the results to the real behavior of overlays.

REFERENCES

- Sousa, J.B., Pais, J.C., Saim, R., Way, G. & Stubstad, R.N. 2002. Development of a Mechanistic-Empirical Based Overlay Design Method for Reflective Cracking, Journal of the Transportation Research Board.
- Minhoto, M.J.C., Pais, J.C., Pereira, P.A.A. & Picado-Santos, L.G. 2005. "Predicting Asphalt Pavement Temperature with a Three-Dimensional Finite Element Model". Transportation Research Record: Journal of the Transportation Research Board n° 1919 – Rigid and Flexible Pavement Design 2005. pp. 96–110. TRB. Washington DC.
- Pais, J.C., Pereira, P.A.A., Sousa, J.B. & Capitão, S. 2002. "Evaluation of the load associated cracking in flexible pavements", Sixth International Conference on the Bearing Capacity of Roads, Railways and Airfields, Lisboa, Portugal, pp. 585–594.

Mechanism of overlay reinforcement to retard reflective cracking under moving vehicular loading

J. Baek & I.L. Al-Qadi

University of Illinois at Urbana-Champaign, Urbana, Illinois, USA

ABSTRACT: Interlayer systems have been incorporated into hot-mix asphalt (HMA) overlays to reduce reflective cracking development. This paper describes an investigation of the reflective cracking mechanism and the ability of steel reinforcement netting interlayer to retard reflective cracking due to vehicular loading utilizing three-dimensional finite element method and the ABAQUS cohesive zone model. For HMA overlay that consists of wearing surface and leveling binder, it was found that reflective cracking occurs under the wheel path and at the lower one third of the leveling binder layer and propagates transversely. The study found that steel reinforcement netting placed between the HMA overlay and existing PCC pavement delays reflective crack initiation time by seven folds. Also, the rate of fractured area by reflective cracking in the reinforced overlay is 4.7 times lower than that of the unreinforced overlay. This study concludes that steel reinforcement netting is an efficient interlayer system to delay the initiation and propagation of reflective cracking given that it is properly installed.

1 INTRODUCTION

Several rehabilitation methods have been commonly used to alleviate reflective cracking in hot-mix asphalt (HMA) overlays. These methods include increasing overlay thickness, cracking-and-sealing, sawing-and-sealing joints in overlay, adding a crack-arresting granular layer, and installing interlayer systems (Mukhtar 1994, Cleveland *et al.* 2002). However, no ideal solution has yet been found to prevent reflective cracking (Button and Lytton 2007). Interlayer systems have worked effectively to reduce the occurrence of reflective cracking as a relatively efficient technique in terms of cost as well as performance (Button and Lytton 1987, Buttlar *et al.* 2000). The interlayer system, a layer made of a material depending on its functions, is laid down either between an overlay and an existing pavement or within the pavement system. However, some of the interlayer systems used in the past have shown minimal benefits in retarding reflective cracking due to the lack of understanding of the interlayer systems mechanism and/or inappropriate installation of the interlayer system (Peredoehl 1989). Based on field experiences of glass-grid interlayer, for example, Steinberg (1992) noticed that the benefit of glass-grid interlayer was questionable due to improper installation. The installation of the interlayer system and its interaction with the surrounding layers is important to ensure its effectiveness.

2 BACKGROUND

2.1 *Steel reinforcement netting interlayer*

An interlayer system that is stiffer than HMA overlay has been typically used as reinforcement to compensate the lack of HMA's tensile strength; this includes steel reinforcement. A new class of steel reinforcement netting interlayer, hexagonal opening shape, coated against rusting has been successfully reutilized to retard reflective cracking (Vanelstraete and Francken 1993, BRRC 1998,

Al-Qadi 2003). Vanelstraete and Francken (1993) showed results of two-dimensional (2D) numerical analysis where an interlayer of metallic grid alone or with slurry seal reduced tensile strain at the bottom of the overlay when induced by thermal loading. This results in delayed crack initiation time. The Belgian Road Research Centre reported (1998) that steel mesh led to deflection reduction at the vicinity of crack tip induced by shear strain. Based on two criteria of tensile strain by thermal and shear strain by traffic, a relative gain factor (RGF) was calculated. The RGF represents the ratio of number of cracks of reinforced overlay to that of the unreinforced section. The RGF for thermal loading was 3.2–5.0 for glass-fiber and 6.4–8.8 for steel netting. For traffic loading, the steel netting was also more efficient than glass-fiber due to higher steel stiffness. The first successful application in the USA was conducted at the Virginia Smart Road by Al-Qadi *et al.* (2003). Al-Qadi and his coworkers evaluated the benefits of the steel reinforcement by field observations and FE analyses (Hughes and Al-Qadi 2001, Al-Qadi 2003, Elseifi and Al-Qadi 2005). They reported that steel reinforcement netting increased the service life of overlays by a factor of 50% to 90%. Steel reinforcement netting was found to reduce maximum transverse strain at the bottom of 100 mm HMA overlay by 15% due to vehicular loading and by 20% due to one cycle of daily temperature variation of 22°C–51°C. Baek and Al-Qadi (2006) used numerical analysis to investigate the role of single steel reinforcement wire, in a two-layered beam specimen, on delaying crack development at –10°C. Crack initiation time was delayed, and growth rate was reduced. Steel reinforcement redistributed concentrated stresses around crack tips. The researchers commented that steel reinforcement effectiveness was affected by interface conditions, HMA material characteristics, and temperature. The behavior of reflective cracking in full-scaled pavement model, however, has not been addressed explicitly.

2.2 HMA crack modeling

Since Dugdale and Barenblatt introduced the concept of the cohesive zone model (CZM) in the early 1960's, many researches have developed various types of the CZM to describe fracture behavior ahead of the crack. The CZM represents an inelastic, especially softening, behavior at a fracture process zone (FPZ). The FPZ is assumed to have a thin yet negligible width; hence, the FPZ is a localized strain field tangential to an existing crack trajectory. The original existing crack is extended artificially into a FPZ at which a non-zero traction force, t corresponding to separation, Δ is specified on both sides of the cracked surfaces as a closure force by the traction-separation law (TSL). Geubelle and Baylor (1998) utilized a bilinear CZM to alleviate compliance problems due to an initial hardening part by adjusting the slope of the initial curve. Song *et al.* (2004) adapted an intrinsic bilinear CZM in simulating mode I and mixed mode cracks after resolving the compliance problem.

For HMA, Jenq and Perng (1991) applied the CZM with various combinations of nonlinear spring and dashpot units to represent the HMA viscous behavior. Soares *et al.* (2003) extended the CZM to characterize HMA heterogeneity by applying the CZM into interface between aggregate grains and asphalt mastic. Paulino *et al.* (2004) implemented an intrinsic CZM in FEM for HMA and validated the resulting model with the indirect tension (IDT) test using calibrated cohesive parameters obtained from single edge notched beam (SENB) tests. After that, Song *et al.* (2004) showed another successful application to HMA with the bilinear CZM. Baek and Al-Qadi (2006) simulated a modified SENB test that consisted of two HMA layers reinforced with a steel wire utilizing cohesive elements provided by a commercial FEM code, ABAQUS. They adapted time-dependent viscoelastic material properties for HMA bulk elements, while time-independent fracture properties were used for the cohesive elements. Currently, more applications of the CZM are conducted in pavement analysis because of the efficiency of FEM implementation and the versatility of the TSL.

3 NUMERICAL MODELING OF HMA OVERLAYS

3.1 Geometry and boundary conditions

A 57-mm HMA overlay (38-mm wearing surface and 19-mm leveling binder) is placed on a 200-mm jointed Portland cement concrete (PCC) pavement. The PCC pavement consists of a

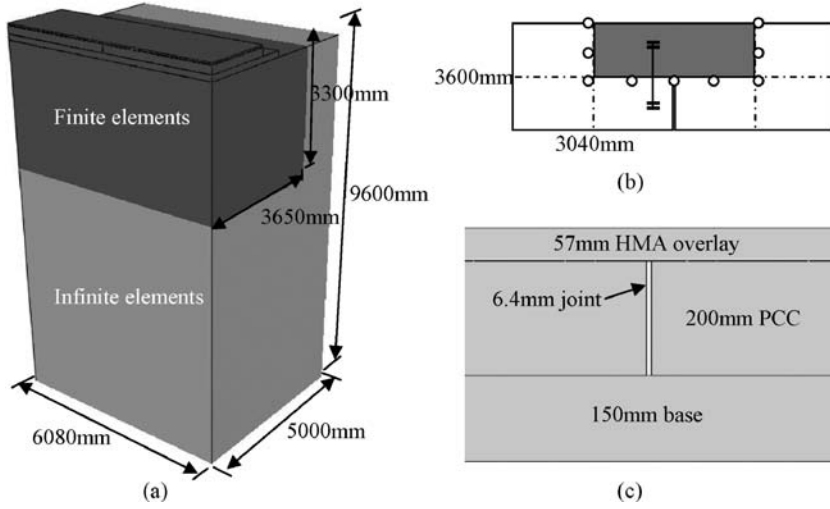


Figure 1. (a) Geometry of HMA overlaid pavement model; (b) geometrical symmetry; and (c) pavement profile.

150-mm base and a 9600-mm subgrade; the PCC joint width is 6.4 mm (Figure 1). Since a PCC slab is geometrically symmetric, one quarter of the slab was modeled. A symmetric boundary condition was applied to the three sides surrounding the considered PCC slab (o symbols in Figure 1(b)). Infinite elements are used at a far-field zone (light grey color in Figure 1(a)) to ensure zero deformation and to minimize the stress wave reflection, “quite” boundary condition for dynamic analysis. Based on mesh sensitivity analysis, critical responses at the bottom of HMA overlay were converged at this domain size.

3.2 Material properties

In general, a HMA material exhibits time-temperature dependent characteristics. At low and intermediate temperatures and/or under a short loading period, a linear viscoelastic constitutive model has been shown to be a valid representation of HMA behavior. For the linear viscoelastic material, time-dependent stress is formulated with the integration of shear and bulk parts as follows (ABAQUS 2007):

$$\sigma(t) = \int_0^t 2G(\tau - \tau') \dot{\epsilon} d\tau' + I \int_0^t K(\tau - \tau') \dot{\phi} d\tau' \quad (1)$$

where G , K = shear and bulk moduli and function of reduced time τ ; and $\dot{\epsilon}$, $\dot{\phi}$ = deviatoric and volumetric strains.

The generalized Maxwell solid model, which consists of parallelized single Maxwell units and an isolated spring, is a mechanical model to define the relaxation of material in a time domain. The Prony series expansion is used to formulate the relaxation function of G and K with respect to the reduced time in the generalized Maxwell model as follows:

$$G_R(t) = G_0 \left[1 - \sum_{i=1}^N g_i \left(1 - e^{-\tau/\tau_i} \right) \right] \quad (2)$$

$$K_R(t) = K_0 \left[1 - \sum_{i=1}^N k_i \left(1 - e^{-\tau/\tau_i} \right) \right] \quad (3)$$

where $G_R(\tau)$, $K_R(\tau)$ = shear and bulk relaxation moduli at a reduced time τ ; G_0 , K_0 = instantaneous shear and bulk relaxation moduli, $G_R(0)$ and $K_R(0)$, respectively; g_i , k_i = dimensionless shear and bulk Prony series parameters; τ_i = relaxation time; and N = number of the parameters.

The Prony parameters and instantaneous moduli were determined from dynamic (complex) modulus tests. The dynamic modulus, $|E^*|$ obtained from an indirect tension (IDT) test device (AASHTO T322) at -20°C , -10°C , and 0°C were converted into shear dynamic modulus at a constant Poisson's ratio and decomposed into storage, $G'(\omega_r) = |G^*(\omega_r)|\cos\phi(\omega_r)$ and loss part, $G''(\omega_r) = |G^*(\omega_r)|\sin\phi(\omega_r)$ with respect to reduced angular frequency, $\omega_r = 2\pi f_r$ at a reference temperature of -10°C . On the other hand, using the Fourier transformation, the shear relaxation modulus is converted into the same two parts as follows:

$$G'(\omega_r) = G_0 \left(1 - \sum_{i=1}^N g_i \right) + G_0 \sum_{i=1}^N \frac{g_i \tau_i^2 \omega_r^2}{1 + \tau_i^2 \omega_r^2} \quad (4)$$

$$G''(\omega_r) = G_0 \sum_{i=1}^N \frac{g_i \tau_i \omega_r}{1 + \tau_i^2 \omega_r^2} \quad (5)$$

where $G'(\omega_r)$, $G''(\omega_r)$ = storage and loss part of shear modulus at ω_r .

The Prony parameters are determined by the nonlinear least square fit of both components. Then, the bulk parameters are assumed to be the same as the shear parameters. Table 1 shows the determined Prony parameters for HMA shear relaxation and instantaneous moduli. Other materials are assumed simply as isotropic linear elastic materials in a typical elastic range (Huang, 1993). Table 2 shows the other materials' properties.

3.3 Steel reinforcement netting modeling

Steel reinforcement netting with hexagonal openings, which consists of single and double twisted wires and reinforcing bars, is modeled with beam elements, since it is able to resist bending as well as axial tensioning (Figure 2). Before HMA overlay placement in the field, slurry seals are usually applied for better fixation to existing PCC surface and bonding to HMA. In addition, they provide a strain tolerant layer. In order to reproduce the installation procedure of steel mesh on PCC, a thin layer is added between PCC slabs and the HMA overlay by means of membrane elements, which carry only in-plane force. By sharing nodes of the membrane layer, steel mesh is embedded in the slurry seal identically; hence, no relative displacements exist between the steel mesh and slurry seal. Interface bonding conditions between steel mesh and HMA and PCC layers are controlled

Table 1. Prony series parameters, g and τ and shear instantaneous modulus, G_0 .

N	1	2	3	4	5	6	7	8	9	10	G_0
g_i	0.070	0.096	0.114	0.136	0.119	0.110	0.100	0.083	0.060	0.030	7.0
τ_i	10^{-4}	10^{-3}	10^{-2}	10^{-1}	10^0	10^1	10^2	10^3	10^4	10^5	GPa

Table 2. Material properties of HMA overlaid pavement model.

Material	Elastic modulus (GPa)	Poisson's ratio	Density (tonne/m ³)
HMA	17.2*	0.22	2.3
PCC	27.5	0.20	2.4
Base	0.3	0.35	1.9
Subgrade	0.14	0.40	1.9

*Instantaneous modulus.

by friction. In general, relatively better bonding exists between interlayer and HMA than between interlayer and PCC. So, it is rational to assume that friction between the HMA overlay and slurry seal layer including steel mesh is infinite, a perfect bonded condition. This case was verified by field cores. On the other hand, the interfacial behavior between the PCC slabs and slurry seal layer is governed by the Coulomb friction model. In this case, a friction coefficient indicates the degree of bonding. Material properties for the slurry seal and steel reinforcement are presented in Table 3. The slurry seal is assumed low stiffness mastic at -10°C .

3.4 Crack modeling

To model reflective cracking, cohesive elements are assigned at a region over a joint where a reflective crack will potentially develop (Figure 3(a)). The zero-thickness feature of the cohesive element is capable of satisfying a geometrical equivalency of a body. Numerically, however, unit thickness is assigned to the cohesive elements to avoid numerical singularity so the strain in the elements is the same as displacement. During fracture, they hold the surfaces of the crack by means of traction assigned in the cohesive elements. Relative displacement at two crack surfaces, namely separation, is treated as a crack when the separation is greater than a critical value. As the separation increases, traction increases up to the cohesive strength, t^o ; then decreases gradually, and vanishes at the critical separation, Δ^{cr} . In order to define a bilinear TSL curve, at least two out of three parameters are needed: cohesive strength, critical separation, and fracture energy, G^c (Rahulkumar *et al.* 2000). Using the disk-shape compact tension (DCT) test (ASTM D7317-07), the fracture parameters were obtained for HMA at -10°C . The fracture energy was calculated with the area

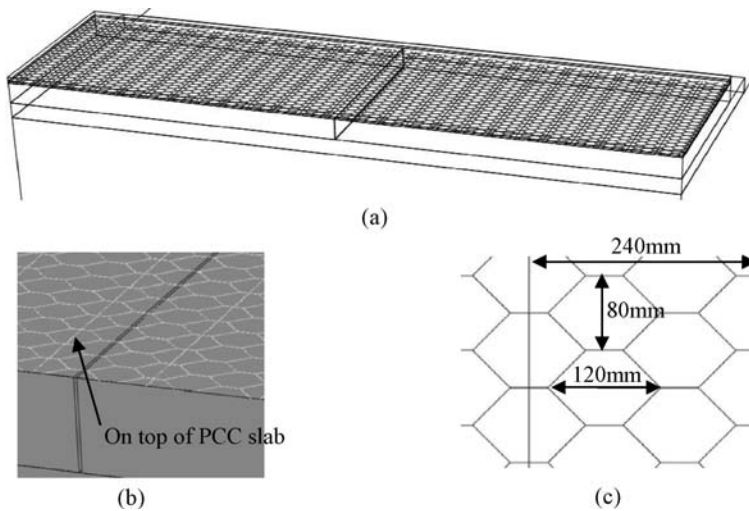


Figure 2. (a) Overall placement of steel reinforcement netting between overlay and PCC slabs; (b) detail view on the PCC slabs; and (c) mesh configurations.

Table 3. Material properties of membrane and steel reinforcement.

Material	Elastic modulus (GPa)	Poisson's ratio	Density (tonne/m ³)
Slurry seal	1.0	0.35	2.0
Steel	200.0	0.28	7.8
Diameter (mm)	Single wire 2.7	Double wire 5.4	Reinforcing bar 4.9

under the force-crack mouth opening displacement (CMOD) curve and the cohesive strength was calculated from a peak load divided by the ligament (fractured) area of the specimen. For mode I, fracture energy and cohesive strength achieved from nine-year-old overlay field specimens are 274 J/m^2 and 0.58 MPa , respectively. Critical separation, Δ^{cr} , and separation corresponding to the cohesive strength, Δ^0 , are computed 0.95 mm ($= 2G^c/t^0$) and $3.4 \times 10^{-5} \text{ mm}$, respectively, using bilinear TSL. Crack initiation and evolution are governed by quadratic nominal stress and fracture energy criterion, respectively, in a mixed mode.

$$\left\{ \frac{t_n}{t_n^0} \right\}^2 + \left\{ \frac{t_s}{t_s^0} \right\}^2 + \left\{ \frac{t_l}{t_l^0} \right\}^2 = 1 \quad (6)$$

$$\left\{ \frac{G_n}{G_n^c} \right\}^2 + \left\{ \frac{G_s}{G_s^c} \right\}^2 + \left\{ \frac{G_l}{G_l^c} \right\}^2 = 1 \quad (7)$$

where t_n, t_s, t_l = traction in normal and shear (vertical and lateral) directions, respectively; G_n, G_s, G_l = traction in normal and shear (vertical and lateral) directions, respectively; and 0 denotes maximum value.

4 REFLECTIVE CRACKING INITIATION AND PROPAGATION

In order to analyze reflective cracking development, cohesive elements were inserted into a potential crack location above a joint (Figure 3(a)). The cohesive elements were inserted only into the leveling binder level layer to minimize the compliance problem by the existence of the cohesive elements. The study focuses on the early stage of reflective cracking.

4.1 Reflective cracking initiation

A scalar of degradation, D , is utilized to investigate the initiation of reflective cracking, ranging from 0.0 to 1.0 (Baek and Al-Qadi 2006). Until the damage initiation criterion (Eq. 6) is satisfied, D remains 0.0 and it begins to increase as a fracture is progressed to crack evolution. When the

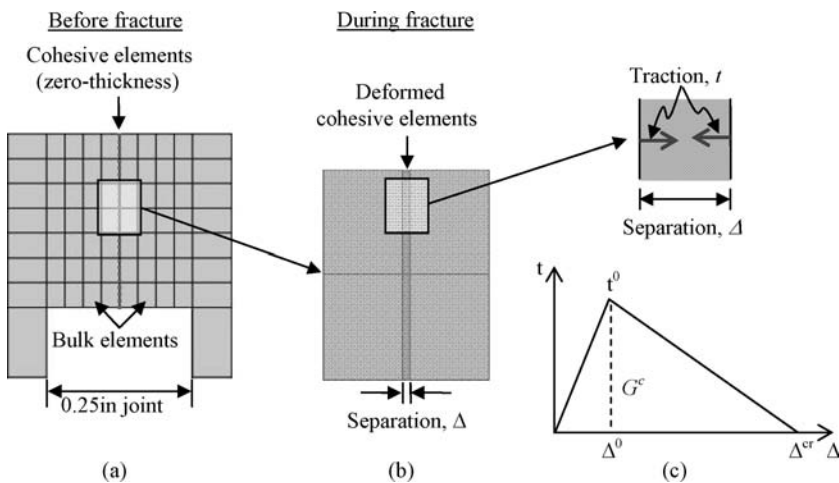


Figure 3. Schematic of a cracked body with cohesive elements: (a) cohesive elements in a potential crack location before fracture; (b) deformed cohesive element during fracture; and (c) bilinear traction separation law utilized in the cohesive elements.

fracture energy criterion for crack initiation is satisfied (Eq. 7), D is equal to 1.0. Figure 4 presents the degradation scalar, D , at two locations, under a tire and between dual-tire assembly, as a function of distance from a joint. Regardless of the tire locations, the peak D of 0.65 occurs in $0.25 h/h_{LB}$ to $0.36 h/h_{LB}$ at a loading time of 0.009 sec; where h is a vertical distance from the bottom of the leveling binder and h_{LB} is the lift thickness of the leveling binder. The locations are coincided with the region where maximum shear stress occurs. At this moment, the upper parts ($h/h_{LB} > 0.4$) of the peak location have greater D values than the lower parts ($h/h_{LB} < 0.2$); especially when D_s are still 0.0 at the bottom of the leveling binder (the last two cohesive elements). Thus, reflective cracking is expected to occur at the middle of the leveling binder, not at the bottom. As loading time increases, D_s increase up to 0.94 at 0.0018 sec and 0.97 at 0.0027 sec; but do not reach 1.0 at any locations. This suggests that due to one passing of vehicular loading, micro-cracks or damages are considerably progressed in the fracture process zone; but reflective cracking explicitly is not initiated yet. In this study, as an alternative way of saving excessive computational cost to apply numerous loads, potential fracture behavior of reflective cracking is analyzed by adapting lower fracture criterion, i.e., reflective crack initiation at $D = 0.5$ instead of $D = 1.0$.

4.2 Reflective cracking propagation

Under the assumption that a crack initiates when $D = 0.5$, reflective crack initiation locations are investigated (Figure 5). Reflective cracking initiates at 0.007 sec under the center of the dual-tire assembly at one third of the leveling binder thickness, not at the bottom of the leveling binder. Then, reflective cracking propagates upward and downward and reaches the leveling binder surface and bottom at 0.013 sec and 0.016 sec, respectively. The main driving force of the crack propagation is shear stress at the beginning and then tensile stresses. If more loading is applied, the reflective cracking propagating to the leveling binder surface will propagate further through the wearing surface. Thus, reflective cracking due to vehicular loading can be classified as a bottom-up crack.

The fractured area in the leveling binder layer by reflective cracking is plotted over loading time as a function of D in Figure 6. While no fractured area at $D = 1.0$ exists over the whole loading time, the potential fractured area increases with the decrease of D . This means that the potential fractured area will be fractured when more loading is applied. For $D = 0.50$ to 0.95, the fractured area rapidly increases at a loading time of 0.027 sec when a front edge of the tire is located 126.8 mm away from a joint. During the rapid increase in the fracture area, reflective cracking occurs under the tires and reaches on top of the leveling binder layer. Then, the fractured area increases gradually. As shown

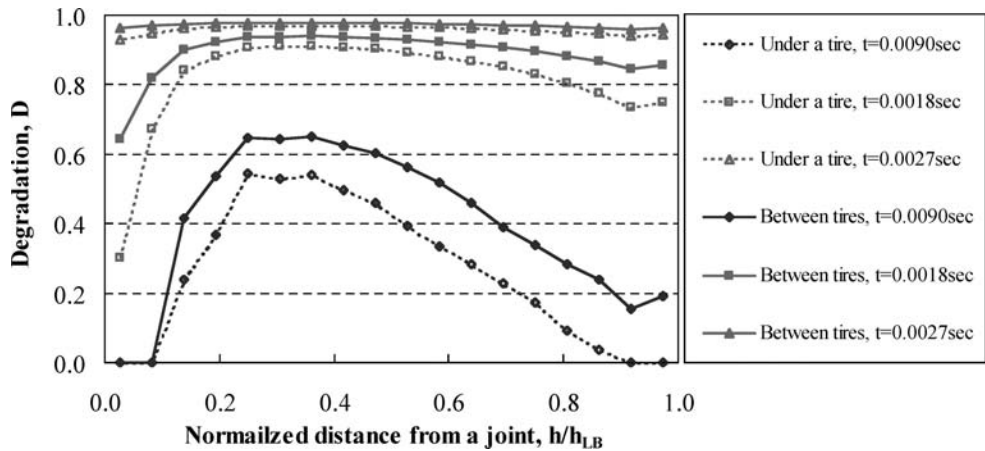


Figure 4. Comparison of reflective crack evolution under a tire and between two tires as a function of distance from the joint.

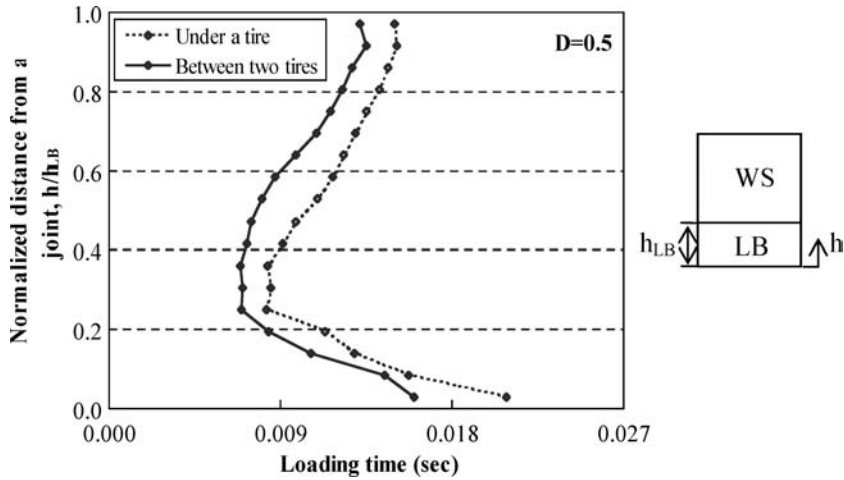


Figure 5. Crack initiation locations under a single tire and dual-tire assembly over loading time.

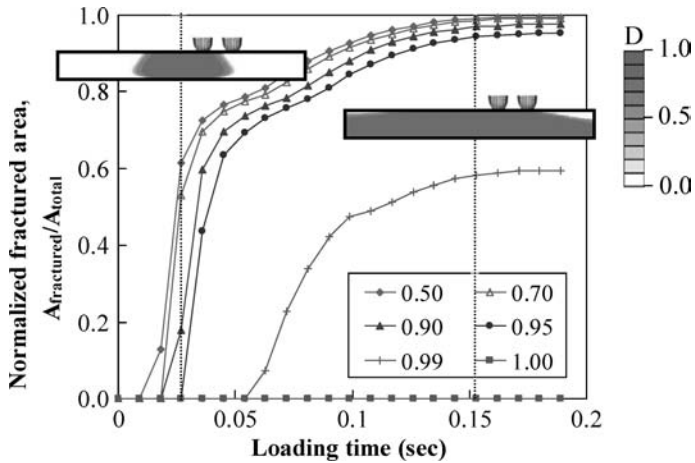


Figure 6. Variation of fractured area in the leveling binder layer over time as a function of D .

in Figures 6 and 7(a), it is evident that reflective cracking initiates at one third of the leveling binder layer under the wheel path and it propagates upward and downward under the wheel path prior to transverse propagating.

5 EFFECTIVENESS OF STEEL REINFORCEMENT NETTING

The contour of the degradation scalar, D for unreinforced and reinforced overlays, exposed to the same conditions, is shown in Figure 7(a). From the contours, the fractured area of the reinforced overlays is significantly less than that of the unreinforced overlay. Also, the fractured area of the reinforced overlay occurs at the bottom of the leveling binder layer, not within the layer. This explains the reinforcement mechanism to retard reflective cracking. Very strong steel netting stiffness supports relatively weak HMA overlay to avoid uneven vertical deformation over a joint, i.e., decreasing vertical shear deformation. Consequently, it can prevent reflective crack initiation

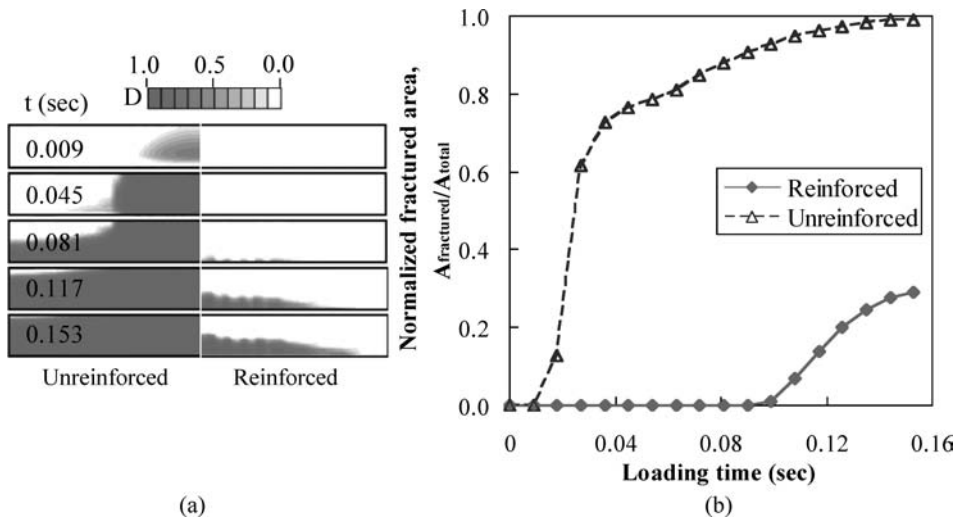


Figure 7. Comparison of fractured area in the leveling binder between unreinforced and reinforced overlays: (a) reflective crack evolution in leveling binder layer over loading time (not to scale) and (b) normalized fractured area variation at $D = 0.5$.

due to shear failure. In addition, tensile strain at the region that steel netting is embedded is locally restricted. Therefore, reflective cracking in reinforced overlay occurs at the bottom of the leveling binder layer and propagates upward. It has to be noted that debonding could occur if the vertical movement at the joint is high.

The effectiveness of steel reinforcement netting on retarding reflective cracking is evaluated through the overall performance of overlay using fractured area. In this approach, the location of reflective cracking is ignored. As shown in Figure 7(b), the fractured area in the unreinforced overlay increases abruptly after the loading application; the rate of fractured area increases gradually after 70% of the area is fractured. When the normalized fractured area becomes 0.1, it is defined as reflective crack initiation time, and the propagation rate is calculated as the slope of the fractured area curve from 0.1 to 0.7 of the normalized fractured area. Thus, the reflective crack initiation time is 0.016 sec and 0.112 sec for the unreinforced and reinforced overlay. Thus, the steel reinforcement netting delays reflective crack initiation about seven times. The rate of fractured area for the unreinforced overlay is $1.2 \text{ m}^2/\text{sec}$ which is 4.7 times faster than $0.26 \text{ m}^2/\text{sec}$ for the reinforced overlay.

6 SUMMARY

In this paper, a full-scale three-dimensional finite element model was built for HMA overlay placed on existing joint PCC pavements. In order to analyze the behavior of reflective cracking, interface elements governed by the cohesive zone model, cohesive elements were inserted at a potential location. A degradation scalar, D , was used to determine crack initiation. Due to one pass of a moving vehicular loading, micro-cracks or damages are initiated right over the joint at one third of leveling binder thickness from the bottom. Using lower fracture criterion, $D = 0.5$, the initiation of reflective cracking was determined. The fractured area in the leveling binder shows that reflective cracking occurs under a wheel path and propagates transversely over a joint.

A hexagonal opening steel reinforcement netting interlayer was inserted between the HMA overlay and PCC pavement surface to evaluate its effectiveness of retarding reflective cracking. When reinforcement is present, a reflective crack initiates at the bottom of the leveling binder and

propagates upward. Compared to unreinforced overlay, the initiation time of reflective cracking is 7 times slower, and the rate of fractured area is 4.7 times lower. Hence, it is evident that the steel reinforcement netting is an efficient method to retard reflective cracking if properly installed.

ACKNOWLEDGMENTS

The authors greatly appreciated the support of our colleagues at the Advanced Transportation Research and Engineering Laboratory (ATREL) and the Illinois Center for Transportation (ICT) at UIUC. In addition, this work was partially supported by the National Center for Supercomputing Applications under project #DMS050004N and utilized the IBM p690 Copper machine.

REFERENCES

- AASHTO, Determining the Creep Compliance and Strength of Hot-Mix Asphalt (HMA) Using the Indirect Tensile Strength Device, AASHTO T322.
- ASTM, Standard Test Method for Determining Fracture Energy of Asphalt-Aggregate Mixtures Using the Disk-Shaped Compact Tension Geometry, ASTM D7317-07.
- Al-Qadi, I. L., M. Elseifi, and D. Leonard. 2003. Steel Reinforcing Nettings Mechanism to Delay Reflective Cracking in Asphalt Concrete Overlays. *Journal of the Association of Asphalt Paving Technologists*, Vol. 82, pp. 388–423.
- Baek, J., and I. L. Al-Qadi. 2006. Finite Element Method Modeling of Reflective Cracking Initiation and Propagation: Investigation of the Effect of Steel Reinforcement Interlayer on Retarding Reflective Cracking in Hot-Mix Asphalt Overlay. *Transportation Research Record 1949*, Transportation Research Board, Washington, D.C., pp. 32–42.
- Belgian Road Research Centre. 1998. Design of Overlaid Cement Concrete Pavements Reinforced with Bitufo®Traffic Loading. *Research Report EP5035/3544*, BRCC, Brussels, Belgium.
- Buttlar, W. G., D. Bozkurt, and B. J. Dempsey. 2000. Cost-Effectiveness of Paving Fabrics Used to Control Reflective Cracking. *Transportation Research Record 1117*, Transportation Research Board, Washington, D.C., pp. 139–149.
- Button, J. W., and R. L. Lytton. 1987. Evaluation of Fabrics, Fibers, and Grids in Overlays. *Proceedings of the 6th International Conference on Structural Design of Asphalt Pavements*, Ann Arbor, MI, Vol.1, pp. 925–934.
- Button, J. W., and R. L. Lytton. 2007. Guidelines for Using Geosynthetics with Hot Mix Asphalt Overlays to Reduce Reflective Cracking. *Presented at the 86th Annual Meeting of the Transportation Research Board*, CD-ROM, Transportation Research Board, Washington, D. C.
- Cleveland, G. S., J. W. Button, and R. L. Lytton. 2002. Geosynthetics in Flexible and Rigid Pavement Overlay Systems to Reduce Reflection Cracking. *Research Report 0-177701*, Texas Transportation Institute, College Station, TX.
- Elseifi, M. and I. L. Al-Qadi. 2005. Effectiveness of Steel Reinforcing Netting in Combating Fatigue Cracking in New Flexible Pavement Systems. *Journal of Transportation Engineering*, ASCE, Vol. 131, No. 1, 2005, pp. 37–45.
- Geubelle, P. H., and J. Baylor. 1998. The Impact-Induced Delamination of Laminated Composite: A 2D Simulation, *Composites*, Part B, Vol. 29B, pp. 589–602.
- Hughes, J. J., and I. L. Al-Qadi. 2001. Evaluation of Steel Paving Mesh, *Construction Report FHWA-PA-2002-001+2000-058*. Pennsylvania Department of Transportation, Harrisburg, PA.
- Jenq, Y.-S., and J.-D. Perng. 1991. Analysis of Crack Propagation in Asphalt Concrete Using Cohesive Crack Model. *Transportation Research Record 1317*, Transportation Research Board, Washington, D.C., pp. 90–99.
- Mukhtar, M. T. 1994. Interlayer Stress Absorbing Composite (ISAC) for Mitigating Reflection Cracking in Asphalt Concrete Overlays. *Dissertation*. University of Illinois at Urbana-Champaign, Urbana, IL.
- Paulino, G. H., S. H. Song, and W.G. Buttlar. 2004. Cohesive Zone Modeling of Fracture in Asphalt Concrete, *Proceedings of the International RILEM Conference, No. 37, Cracking in Pavements – Mitigation, Risk Assessment, and Prevention*, C. Petit, I. L. Al-Qadi, and A. Millien, Eds., Limoges, France.
- Predoehl, N. H. 1989. Evaluation of Paving Fabric Test Installation in California, *Final Report*, Draft Report, California Department of Transportation, Translab.

- Rahulkumar, P. A. Jagota, S. J. Bennison, and S. Saigal. 2000. Cohesive Element Modeling of Viscoelastic Fracture: Application to Peel Testing of Polymers, *International Journal of Solids Structures*, Vol. 37, pp. 1873–1897.
- Soares, J. B., F. A. C. de Freitas, and D. H. Allen. 2003. Crack Modeling of Asphalt Mixtures Considering Heterogeneity of the Material, *Presented at the 82nd Transportation Research Board Annual Meeting*, CD-ROM, Transportation Research Board, Washington D.C.
- Song, S. H., G. H. Paulino, and W. G. Buttlar. 2004. Simulation of Mode I and Mixed-Mode Crack propagation in Asphalt Concrete Using a Bilinear Cohesive Zone Model, *Presented at 84th Annual Meeting of the Transportation Research Board*, CD-ROM, Transportation Research Board, Washington, D.C.
- Steinberg, M. L. 1992. Geogrid as a Rehabilitation Remedy for Asphaltic Concrete Pavements. *Transportation Research Record 1369*, Transportation Research Board, Washington, D.C., pp. 54–62.
- Vanelstraete, A., and L. Francken. 1993. Numerical Modeling of Crack Initiation under Thermal Stresses and Traffic Loads. *Proc., 2nd International RILEM Conference – Reflective Cracking in Pavements*, E & FN Spon, Liege, Belgium, pp. 136–145.

Virtual testing procedure for cracking performance prediction of HMA

Z. Feng

Huntley, Nyce & Associates, LTD., Ashburn, Virginia, USA

P. Zhang

Tierra, Inc., Raleigh, North Carolina, USA

M.N. Guddati & Y.R. Kim

North Carolina State University, Raleigh, North Carolina, USA

D.N. Little

Texas A&M University, College Station, Texas, USA

ABSTRACT: A multiscale virtual-testing methodology is developed and evaluated with the goal of linking the binder and aggregate properties to the cracking performance of asphalt concrete. The main ingredients of the proposed methodology are (a) a virtual fabrication technique that generates the microstructure of asphalt concrete specimens without the need for physical fabrication, (b) a lattice modeling approach that simulates the micromechanical behavior of cracked asphalt concrete specimens, and (c) a multiscale methodology that incorporates the effects of aggregates of widely varying sizes. The resulting methodology is utilized to simulate the load-deformation behavior of real uniaxial tension test specimens. A comparison of the predicted response to the measured response indicates that the proposed method shows promise, but requires further work aimed at the fundamental understanding of the micromechanical behavior of the binder.

1 INTRODUCTION

Fatigue cracking is one of the major distresses in asphalt pavements. Numerous field and laboratory studies that have been conducted on the Superpave PG binder specification clearly indicate that the fatigue cracking performance of hot mix asphalt (HMA) is dependent on the interaction of the aggregate and asphalt binder. This fact makes it difficult to develop a reliable component material specification for fatigue cracking by testing only one component. On the other hand, it is impossible to test asphalt-aggregate mixtures for the binder specification because asphalt binders are normally purchased long before the aggregate sources are determined. Although some locally representative combinations of aggregate and binder may be identified, the large experimental cost involved in the mixture testing makes the testing of HMA an improbable alternative for the binder specification. In an attempt to reduce the cost of better understanding and characterizing the cracking performance of HMA, and to produce an enhanced component material specification, a micromechanics-based virtual testing procedure is developed in this study. It is important to note that this study attempts to predict the mixture properties from the component material properties, which is in contrast to other HMA micromechanical modeling studies that use the mixture and/or mastic properties to simulate the cracking of asphalt concrete (Birgisson et al. 2004, Song et al. 2005).

Average micromechanical modeling, as the name implies, provides an efficient way to approximate micromechanical simulation to predict macro-mechanical behavior. Discrete element modeling techniques have been successfully used in modeling other granular materials and rock

masses (Cundall 1971, Zubelewicz & Bazant 1987, Ricardo & Tang-Tat 1992). Although discrete particle modeling has been used to simulate HMA (Meegoda & Chang 1994), an alternative technique based on lattice modeling may be more effective due to the bond-dominant nature of the material. Succinctly put, lattice modeling involves approximating the continuum using a lattice, with each element representing an intact bond that can be broken at any time to create a microcrack.

In this study, a lattice modeling methodology that incorporates a fracture energy-based failure criterion is developed as the numerical analysis tool to predict the mechanical behavior of HMA. Complementary to the lattice model, a stand-alone virtual microstructure fabrication approach is developed that automatically attains the two-dimensional (2D) internal structure of HMA which is derived from the job mix formula. To improve computational efficiency, these two approaches are integrated through the multiscale modeling method to perform a seamless microstructural analysis of actual HMA specimens with the ultimate aim of performance evaluation and mix design optimization.

The resulting multiscale virtual testing procedure is applied to simulate the uniaxial tension test, and the predictions are compared with the experimental observations. This comparison indicates that a comprehensive understanding of the behavior of the asphalt binder at a microscopic scale is required. With the help of a calibration process, this study attempts to identify the critical areas that need further investigation.

2 VIRTUAL TESTING

In this section, a virtual fabrication technique that generates the microstructure of a virtual specimen is first developed and tested. A mesh generation procedure is then developed to represent the virtual specimen with a discrete random truss network, which is then analyzed using a lattice modeling approach.

2.1 *Virtual fabrication technique*

The study of the complex constitutive behavior of HMA requires capturing its microstructure for subsequent modeling of the complex interaction among its constituents. Digital imaging techniques have been widely used to quantify the aggregate configurations, but it requires the fabrication of specimens. In order to reduce, and possibly eliminate, the need for the physical fabrication of specimens, an alternative to digital imaging, namely virtual fabrication, is introduced in this study. Virtual fabrication refers to utilizing the mix properties to virtually fabricate a 2D microstructure of a specimen for the 2D lattice analysis. The fabricated microstructure is expected to mimic the microstructure of the actual specimen and, more importantly, the mechanical behavior of the specimen.

Such an approach starts with inverse stereology that converts the volumetric aggregate gradation into a 2D apparent area gradation. Stereology (Underwood 1970) is the process of predicting the three-dimensional (3D) geometrical structure from 2D information, that is, the geometry of cross-sections on several parallel planes. One of the most commonly used approaches to stereological problems is the so-called statistical-geometrical approach, which measures and classifies a large number of 2D figures or images to build an actual picture of the average 3D structure (Fig. 1(a)). In an analogous manner, inverse stereology, as the name implies, reconstructs the 2D cross-sections based on given 3D information. In this study, an inverse stereology-based method is developed to convert the 3D volumetric aggregate gradation into the 2D apparent area gradation in a cut surface (Fig. 1(b)).

A particle generation program is then employed to represent an aggregate particle by a polygon. First, a polygon with an arbitrary shape is generated within the area between two serial sieves. Its geometrical shape and size and spatial position are, in turn, randomly adjusted according to the aspect ratio and orientation distribution functions, which are obtained from a previously generated database of the images of actual cut surfaces. The resulting aggregate particle is then randomly placed into an area of the specimen. A check for possible overlaps of the particles is made, and the

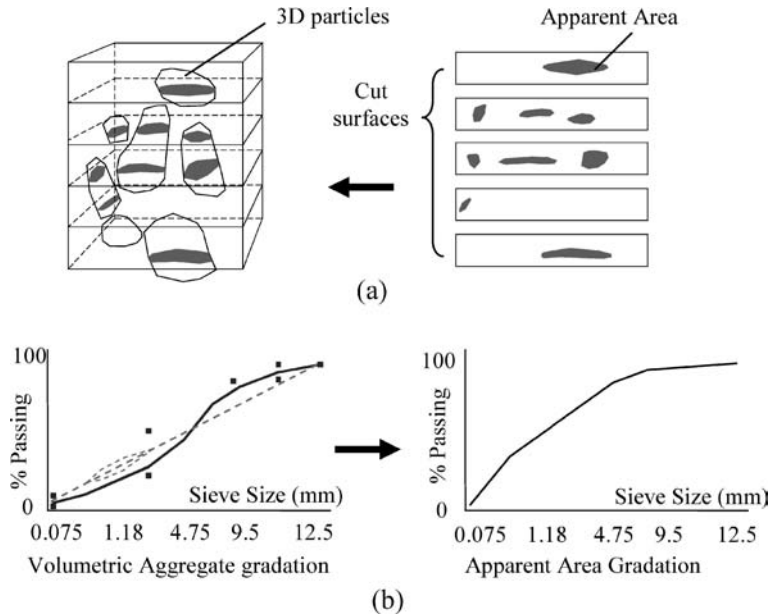


Figure 1. Conversion between 3D and 2D structural information using (a) stereology, and (b) inverse stereology.

generated particle is accepted only if there are no overlaps with other previously generated particles inside the specimen. Starting with the largest aggregate, the above procedure is applied recursively until the area is populated with all the aggregates.

The effectiveness of the above procedure is evaluated by comparing the virtual microstructures with microstructures obtained from digital imaging. The comparison is performed with respect to geometry as well as the mechanical properties. It was found (Kim et al. 2005) that the two microstructures appear similar visually. Quantitatively, there are 281 and 284 particles in the actual and virtual cut faces, respectively, and the difference between them of the total aggregate areas is about 9%. More importantly, the mechanical properties of the two microstructures, namely their stiffness and strength, are found to be very similar (Kim et al. 2005).

2.2 Numerical lattice modeling

A lattice modeling methodology is adopted in this study to analyze the virtually fabricated HMA specimens and capture the effects of the component materials' mechanical and geometric properties. The lattice modeling approach starts with lattice mesh generation that discretizes the continuum microstructure into a network of truss elements, which is then analyzed using standard matrix structural analysis. These steps are described in the following sections.

2.2.1 Lattice mesh generation

HMA is modeled as a two-phase system, i.e., as a homogeneous binder with rigid aggregate particles that do not deform or crack. A random truss lattice, which has been proved to be statistically homogeneous and isotropic (Guddati et al. 2002), is used for the mastic to eliminate any computational anisotropies that are characteristic of regular lattice networks. As shown in Figure 2, the generation of such a lattice begins with a regular square mesh called the base mesh. Each cell of the base mesh contains a single node whose exact location (that is, deviation from the center) is determined based on a uniform probability distribution function. Once the nodes are generated,

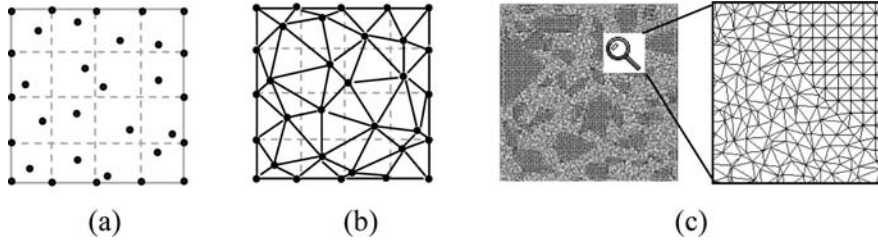


Figure 2. Lattice representation of Hot Mix Asphalt (HMA): (a) random nodes inside base mesh; (b) lattice network formed by Delaunay triangulation; and (c) lattice mesh for HMA.

the lattice network is constructed by linking the nodes using Delaunay's triangulation (Fig. 2(b)) (Christ et al. 1982, Moukarzel & Herrmann 1992). The basic idea of Delaunay's triangulation is to take three points and check if their circumscribing circle contains no other points inside. If it does not, these three points are connected to form a triangle. Different from the mastic, the aggregate is represented by a lattice mesh with regularly distributed nodes and random connections that illustrate its configuration. In particular, its boundary is captured and represented by a group of regularly spaced lattice nodes (Fig. 2(c)).

2.2.2 Stiffness properties of the lattice links

The lattice link size is determined primarily by the minimum aggregate size and the computational cost requirements. The mechanical properties of each link are chosen based on the component material(s) over which the link lies. The geometrical properties, however, are mainly dependent on mesh density and usually can be used to adjust the global behavior of the lattice network to match the actual mechanical response of the material being simulated. In this study, the aggregate particles are modeled as rigid inclusions, and deformation and cracks occur only inside the binder, or mastic. Thus, only the binder (mastic) link properties are needed in the numerical analysis. Specifically, considering the linear stress-strain relationship of lattice links, one may define the relationship between the cross-sectional area of the binder link (A_l) and the lattice characteristic length (L_c), as shown in the following equation, so that the macroscopic Young's modulus of the lattice network matches the actual binder modulus:

$$A_l = C \cdot L_c \cdot t. \quad (1)$$

In the above equation, t is the thickness of the specimen, which is the unit length in the 2D analysis. Constant C (≈ 1.031) is obtained by simulating the uniaxial tension test on a binder patch represented by a network of lattice links with an identical link modulus but with varying A_l and L_c . Once the link properties are determined, the material stiffness is predicted by analyzing the resulting lattice system using standard matrix analysis techniques.

Note that the above procedure is for elastic deformation only. Since asphalt concrete is viscoelastic, whenever such behavior needs to be simulated, the links are replaced by generalized Maxwell elements represented by the Prony coefficients of the binder.

2.2.3 Lattice modeling of progressive crack growth

The lattice approach simulates damage in bond-dominant materials by the successive removal of failed links, representing microcracks. Thus, in addition to the parameters required for linear deformation analysis (the cross-sectional area and the link modulus), a failure criterion is required to trigger the creation of microcracks. Noting that the breakage of a failed lattice link can be viewed as the creation of a microcrack in the continuum representation, it is reasonable to assume that the failure criterion is related to the energy needed to create the associated microcrack. Based on classical fracture mechanics, the required energy to create the crack is a multiple of the crack area and the specific fracture energy associated with the broken bond (Gdoutos 1990, Ewalds & Wanhill 1984).

The lattice link used in this study is idealized as linear elastic-brittle, with failure occurring when the energy stored in the link exceeds the fracture energy of the associated microcrack. Thus, the link is removed when the linear elastic strain energy (U_i^e) exceeds the multiple of the microcrack surface area (i.e., the cross-sectional area, A_i) and the specific fracture energy (γ_i); that is, the link cracks when

$$U_i^e \geq \gamma_i \cdot A_i. \quad (2)$$

In Equation (2), the fracture energy, γ_i , is actually representing the interface fracture energy in the lattice system. For a binder-to-binder link, γ_i is the fracture energy of cohesion – the energy required to create a unit area crack within the binder, which is twice the specific fracture energy of the asphalt binder (γ_b),

$$\gamma_i = 2\gamma_b. \quad (3)$$

For a binder-to-aggregate link, γ_i is the fracture energy of adhesion – the energy required to create a unit crack area between the binder and aggregate, which can be calculated using the following equation:

$$\gamma_i = \gamma_a + \gamma_b - \gamma_{ab}, \quad (4)$$

where γ_a is the aggregate surface energy, and γ_{ab} is derived from the interface effects between the aggregate and binder (Cheng et al. 2002). Noting that:

$$U_i^e = \frac{1}{2} E_i \cdot A_i \cdot L_i \cdot \varepsilon_i^2, \quad (5)$$

where E_i , A_i , and ε_i are Young's modulus, cross-sectional area, and axial strain of the link, respectively; the fracture energy-based failure criterion immediately translates into the following strain-based criterion:

$$\varepsilon_i < \varepsilon_i^f = \sqrt{\frac{2\gamma_i}{E_i L_i}}. \quad (6)$$

Thus, any link subjected to a tensile force that has strain exceeding its specified failure strain threshold in Equation (6) is removed to represent microcracks. Note that the above failure criterion applies only to links in tension, and there is no compressive failure of the links in the current lattice model. Presently, the analysis is quasistatic, and inertial effects are ignored.

3 MULTISCALE ANALYSIS APPROACH

The virtual testing procedure (virtual fabrication followed by lattice modeling), although appearing straightforward at the outset, has significant practical limitations due to its computational cost. In this study, the multiscale modeling approach is employed to handle the computationally intensive aspect of the lattice modeling. Essentially, the multiscale approach considers the effect of different-sized aggregates at different scales. Such an approach reduces the computational cost significantly while capturing the mechanical phenomena at various scale lengths. The virtual testing procedure integrated by the multiscale analysis approach is illustrated in Figure 3. As shown in the figure, given the mixture aggregate gradation, inverse stereology is applied to obtain the aggregate gradation in terms of the apparent aggregate area percentage. Then, the resulting 2D apparent aggregate gradation may be divided into a series of subregions based on different scales of observation.

The analysis starts with the virtual fabrication of a group of representative volume elements (RVEs) at the smallest scale (scale n). Noting that the heterogeneity at scale n can be averaged

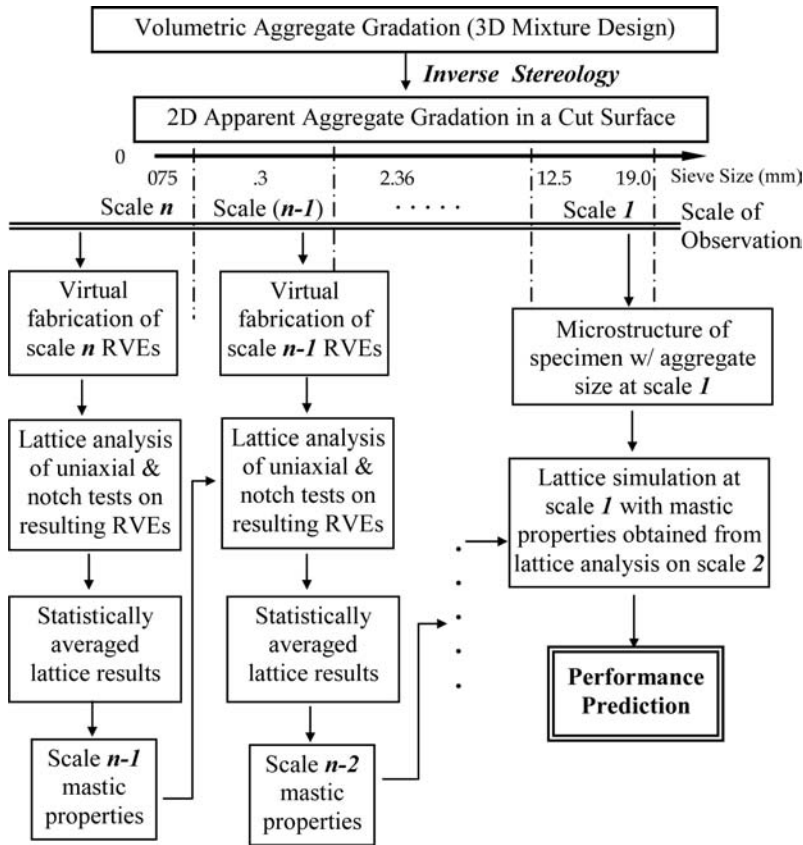


Figure 3. Multiscale virtual testing procedure.

at the larger scale (scale $n-1$), scale n RVE can be regarded as homogeneous mastic in the analysis performed at scale $n-1$. The RVEs at various scales are analyzed using the lattice modeling. The lattice analysis takes the fracture energy of the binder, surface energy of aggregates and modulus of the binder, and calculates the effective stiffness and fracture energies of RVEs at scale n . This is accomplished by simulating the SEN test for fracture energies and the uniaxial test for the effective stiffness of RVEs. The resulting stiffness and fracture energies from all the RVEs are statistically averaged to eliminate the RVE-to-RVE variation due to the random nature of microstructure generation. The processed mastic properties are, in turn, used in the larger scale (scale $n-1$) lattice modeling. This procedure is recursively applied until all subregions of the gradation are considered. In particular, the microstructure of the specimen being simulated is created and analyzed at scale 1 to predict its mechanical response and, eventually, the mixture's cracking performance.

An important point to note is that in the multiscale analysis, the heterogeneities observed at the smaller scale and their effects on microcracking are considered in an average sense by using homogenized (averaged) mechanical properties. Given that the main objective is to characterize the cracking behavior at a macroscopic level, as previously mentioned, it is unnecessary to precisely simulate the micromechanical phenomena, such as stress singularity and the propagation of individual microcracks. Thus, in the current research, the multiscale approach is sufficient and, due to its efficiency, appropriate and desirable.

4 EVALUATION OF THE MULTISCALE VIRTUAL TESTING PROCEDURE

In order to test its predictive abilities, the virtual testing procedure is utilized to simulate the uniaxial tension test, and the resulting load-displacement curves are compared with those obtained from the physical tests.

4.1 *Physical testing*

The asphalt mixture used in this study is a 12.5 mm Maryland State Highway Administration Superpave mix design. Cylindrical specimens of 150 mm diameter and 170 mm height are fabricated using the Australian gyratory compactor, ServoPac. Cores of 75 mm diameter and 150 mm height are taken from the middle of the specimen. Four LVDTs set 90° apart are installed in the middle of the specimen with a gauge length of 100 mm. Constant crosshead rate tests are performed at -10°C with the constant crosshead rates that correspond to strain rates of 806, 43.8, and 2.48 microstrains/second. Low temperature was selected to ensure that the nature of the fracture is mainly elastic. This condition is necessary because the viscoelastic fracture has not been incorporated into the current lattice model (note that only fracturing is considered elastic, but the deformation includes viscoelastic effects).

4.2 *Virtual testing*

Based on the aggregate gradation, it is determined that virtual testing for the current case is best performed by using a four-scale approach: scale 1 for coarse aggregates between 2.36 and 19 mm, scale 2 for aggregates between 0.6 and 2.36 mm, scale 3 for aggregates between 0.15 and 0.6 mm, and scale 4 for fine aggregates below 0.15 mm. For the smaller three scales, an elastic analysis is conducted to up-scale the binder elastic modulus and the fracture energy. The up-scaled elastic modulus for scale 1 mastic is multiplied by the time-dependence of the binder stiffness to obtain the mastic relaxation modulus at scale 1. The relaxation modulus and fracture energies of scale 1 mastic are then used to perform the analysis on a 75 mm \times 150 mm rectangle to obtain the final load-deflection curves. The fundamental inputs for this procedure are, therefore, the binder relaxation modulus and the binder/aggregate fracture energies.

The asphalt binder used in this study is an unmodified PG 64-22 obtained from the Paulsboro, New Jersey terminal of the Citgo Asphalt Refining Company, which is the AAK binder designated by the SHRP. In this study, the Dynamic Shear Rheometer (DSR) and the Bending Beam Rheometer (BBR) data are utilized to derive the relaxation modulus. However, note that the binder in the asphalt concrete is in a thin-film form and is significantly stiffer than that measured by the DSR and BBR tests. This phenomenon was quantified by Huang et al. (1998), who presented the viscosity values for films of various thicknesses. This data indicates that a 10-micron film is 1.91 times more viscous than a 150-micron film. Assuming that the average film thickness is 10 microns, and the viscosity of 150-micron film is the same as the viscosity measured by DSR and BBR, the binder modulus is scaled by 1.91 to account for the stiffening effect in thin films. The final scaled binder modulus is plotted in Figure 4 (referred to as the original modulus).

The binder and aggregate surface energies used in this study are obtained from the extensive experimentation conducted by the Texas A&M research team (Cheng et al. 2002) and are shown in Table 1. Once the component material properties are obtained, the next step is to up-scale the stiffness properties and fracture energies for scale 1 mastic. As mentioned earlier, this is performed through elastic lattice modeling at scales 4 through 2. At scale 4, lattice modeling is performed on six virtually fabricated uniaxial tension test specimens. The binder elastic modulus is taken as 209 MPa, and the stiffness of the uniaxial tension test specimens is computed; these stiffness results are then averaged to obtain the stiffness of scale 3 mastic. This procedure is repeated at scales 3 and 2 to eventually obtain the elastic modulus of scale 1 mastic. Similarly, the fracture energy for each scale is obtained by simulating SEN tests on three realizations of microstructures. The averaged mastic fracture energy for a given scale is used in the lattice modeling of the material RVEs at the upper

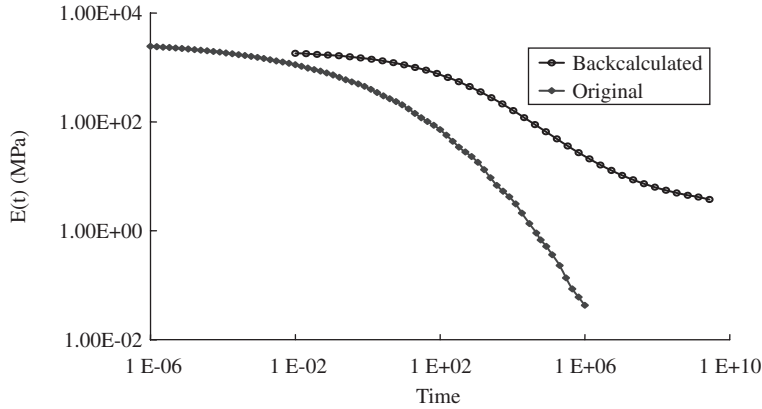


Figure 4. Comparison between original and back-calculated binder relaxation modulus.

Table 1. Mechanical properties of mastics at various scales.

Scale	Scale 3	Scale 2	Scale 1
Elastic Modulus (MPa)	470.0	755.0	1516.0
Surface Energy of Binder (ergs/cm ²)	27.4	27.4	27.4
Surface Energy of Aggregate (ergs/cm ²)	206.5	206.5	206.5
Fracture Energy of Mastic (ergs/cm ²)	223.0	1760.0	11900.0
Interfacial Surface Energy between Mastic-Aggregate (ergs/cm ²)	102.6	102.6	102.6
Mastic-to-Mastic Fracture Energy (ergs/cm ²)	446.0	3520.0	23800.0
Mastic-to-Binder Fracture Energy (ergs/cm ²)	326.0	1862.0	11980.0

scale until the fracture energy of scale 1 mastic is obtained. Table 1 lists the mechanical properties of each scale obtained using the process described above. Note that the interfacial surface energy between mastic and aggregate is assumed to be the same as the interfacial surface energy between the binder and aggregate, which is determined by the Lifshitz–van der Waals component and the Acid-Base component of the surface energies of both aggregate and binder (Cheng et al. 2002).

Since the goal of the largest scale analysis is to predict the load-deflection response, and not further up-scaling, it is important to incorporate the effect of binder viscoelasticity at this stage (scale 1). The viscoelastic stiffness of the binder is obtained from the up-scaled elastic modulus, based on the simple observation that, since the aggregate particles are rigid, the time-dependency of the mixture will be the same as the time-dependency of the binder. Thus, the relaxation modulus of scale 1 mastic is obtained by multiplying the binder relaxation modulus by the factor 7.25 (=1516/209), which is the ratio of the elastic modulus of scale 1 mastic to that of the binder. The resulting relaxation modulus and fracture energy of scale 1 mastic, obtained from the last column of Table 1, are utilized to obtain the load-deflection curves at the three strain rates of interest. Figure 5 compares the predicted and measured load-deflection curves.

Clearly, the comparison in Figure 5 is far from satisfactory. Focusing first on the stiffness prediction, note that the prediction is fairly accurate for the fastest strain rate, but unsatisfactory for slower rates. This leads to the belief that the film thickness may have a different effect on the stiffness at different rates. Similarly, the failure load of the lattice simulation is higher than the experimentally observed values. Since the failure criterion is based solely on the fracture energies, the input fracture energies may also need to be corrected. In fact, from Table 1, note that the effective fracture energy could be significantly different at different scales, which implies that special care needs to be exercised in using this quantity. Another possibly important factor that has not been considered heretofore is the air void content. Careful investigation of these three phenomena is

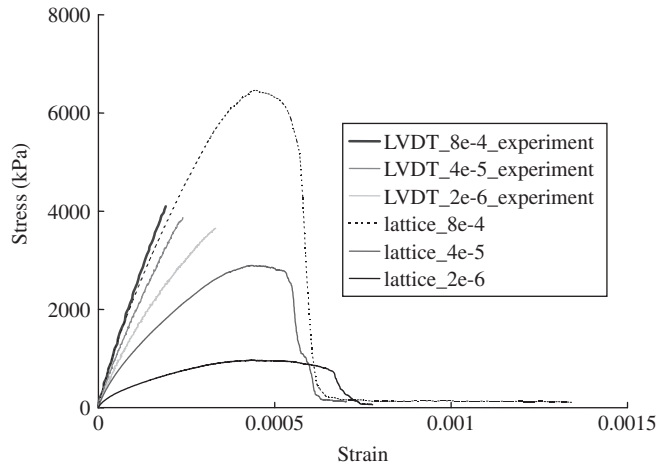


Figure 5. Lattice simulations versus experimental strain-stress curves.

necessary before the proposed technique can be used with confidence. The rest of the section attempts to verify the hypothesis, through calibration, that the proper treatment of thin-film effects and the scale-dependency of fracture energy can lead to accurate predictions.

Thin-film effects: The main idea behind the proposed approach is based on the observation that the time-dependent behavior of asphalt concrete differs from that of the binder. Yet, based on the linear viscoelastic behavior of the binder and infinite rigidity of the aggregate particles, the time-dependence of the binder and the mixture must be the same. It is hypothesized that this difference is because of the complex behavior of asphalt in thin films which leads to altered time-dependency in the deformation of the binder. This complex behavior needs careful investigation and is a subject for future study. This paper, however, attempts to back-calculate the binder modulus from the mixture modulus. This is performed by simply scaling the mixture modulus so that the back-calculated and the input binder moduli match at the fastest rate (because the elastic modulus is assumed to be accurate). The comparison between the back-calculated and the original relaxation moduli is given in Figure 4. When this back-calculated relaxation modulus is used in the lattice modeling the initial portion of the load-deflection curves match with the experimentally observed curves (Fig. 6(a)). However, the strength predictions are still not accurate; this may be attributed to the lack of air-voids in the model and/or scale dependency of fracture energy. In this effort, we focus on scale-dependency of fracture energy.

Scale-dependency of fracture energy: Noting that fracture energy can vary significantly with the scale of observation, a significant error could occur in the input fracture energy. Again, the proper use of measured fracture energy requires careful and fundamental investigations related to the scale-dependency of fracture energy; such investigation is left for future work. This study attempts to scale the fracture energy to match the experimental results – it is important to note that, if this hypothesis is correct, the scaling factor should not depend on the rate of loading, but only on the scale of the fracture energy tests. The fracture energies are measured by examining the cohesion on a 20 mm × 10 mm × 1.6 mm plate, which is at a much larger scale than the length scale associated with scale 4 analysis. Noting that the fracture energy increases with the observation scale, the experimentally measured fracture energy must be scaled by a factor less than unity to obtain the scale 4 fracture energy. Based on a trial-and-error procedure, it is determined that a factor of 1/7 works best. Figure 6(b) contains the load-deflection curves obtained when the fracture energies are scaled by 1/7; clearly, a very good match is seen between the predicted and measured load-deflection curves. It should be cautioned, however, that this scaling factor is not universal and depends on the exact way the fracture energy is measured.

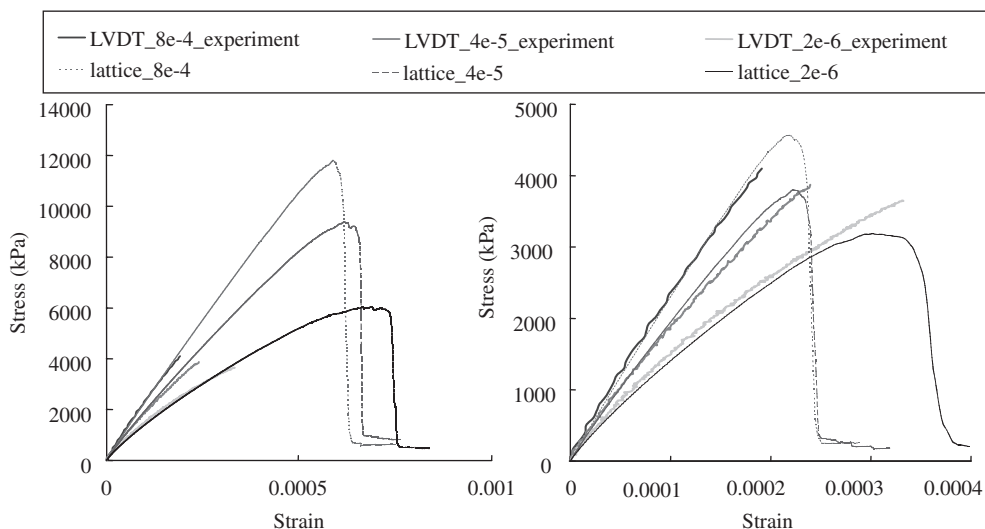


Figure 6. (a) Lattice simulation by back-calculated binder relaxation modulus; (b) Lattice simulation by back-calculated binder relaxation modulus and adjusted fracture energy.

5 CONCLUSIONS AND RECOMMENDATIONS FOR FUTURE RESEARCH

In this paper, a virtual testing procedure for the characterization of cracking in HMA is presented. Its two major components, a virtual fabrication technique and numerical lattice modeling tool coupled with a fracture energy-based failure criterion, are systematically developed and tested. Due to the disparate scale lengths associated with microcracking and specimen size, virtual testing demands an unrealistic computational cost for modeling even laboratory-scale HMA specimens. In order to make the procedure more practical, a multiscale approach is implemented to consider the effect of different-sized aggregates at different scale lengths. Such an approach reduces the computational cost significantly, while capturing the mechanical phenomena at various scale lengths.

The predictive capability of the resulting multiscale virtual testing procedure is evaluated by simulating the uniaxial tension test. Based on a comparison of load-deflection curves, it appears that two important phenomena need to be carefully studied: the stiffening of the binder in thin-films due to the complex behavior of asphalt and the scale dependency of fracture energy.

Other areas needing further research include the modeling of the air voids and viscoelastic fracture. While a systematic calibration is successful in matching the simulated and experimental results, the authors feel that it is important to study these physical phenomena carefully before placing confidence in such calibration. Nevertheless, the proposed procedure shows promise in realistic virtual testing for the cracking performance of asphalt concrete.

ACKNOWLEDGMENTS

This material is based upon work supported by the National Science Foundation under Grant No. 9812741 and the Texas A&M Research Foundation/Western Research Institute.

REFERENCES

Birgisson, B., Soranakom, C., Napier, J.A.L., and Roque, R. 2004. Microstructure and fracture in asphalt mixtures using a boundary element approach. *Journal of Materials in Civil Engineering*, Vol. 16: 116–121.

- Cheng, D., Little, D.N., Lytton, R.L., and Holste, J.C. 2002. Use of surface free energy of asphalt-aggregate system to predict moisture damage potential. *Journal of the Association of Asphalt Paving Technologists*, Vol. 71: 59–88.
- Christ, N.H., Friedberg, R., and Lee, T.D. 1982. Random lattice field theory: General formulation. *Nuclear Physics B: Particle Physics*, Vol. B202: 89–125.
- Cundall, P.A. 1971. A computer model for simulating progressive large scale movements in blocky rock systems. *Proceedings of the International Symposium on Rock Fracture*, ISRM, Nancy, France.
- Ewalds, H.L. and Wanhill, R.J.H. 1984. *Fracture mechanics*: Edward Arnold Ltd.
- Gdoutos, E.E. 1990. *Failure mechanics criteria and applications*: Kluwer Academic Publishers.
- Guddati, M.N., Feng, Z., and Kim, Y.R. 2002. Toward a micromechanics-based procedure to characterize fatigue performance of asphalt concrete. *Journal of the Transportation Research Board*, No. 1789, TRB, National Research Council, Washington, D.C.: 121–128.
- Huang, S.C., Branthaver, J.F., Robertson, R.E., and Kim, S.S. 1998. Effect of film thickness on the rheological properties of asphalts in contact with aggregate surface. *Transportation Research Record: Journal of the Transportation Research Board*, No. 1638, TRB, National Research Council, Washington, D.C.: 31–39.
- Kim, Y.R., Guddati, M.N., Feng, Z., Zhang, P., and Subramainian, V. 2005. *A micromechanics-based methodology for the study of cracking in asphalt concrete*. Research Report, Department of Civil Engineering, North Carolina State University, Raleigh, NC.
- Meegoda, J.N. and Chang, K.G. 1994. Modeling of viscoelastic behavior of hot mix asphalt (HMA) using discrete element methods. *Proceedings of the third ASCE Materials Engineering Conference-Infrastructure: New Materials and Methods of Repair*, San Diego, CA.
- Moukarzel, C. and Herrmann, H.J. 1992. A vectorizable random lattice. *Journal of Statistical Physics*, Vol. 68: 911–923.
- Ricardo, D. and Tang-Tat, N.G. 1992. Discrete modeling of stress-strain behavior of granular media at small and large strains. *Engineering Computations*, Vol. 9: 129–43.
- Song, S.H., Paulino, G.H., Buttlar, W.G. 2005. Cohesive zone simulation of mode I and mixed-mode crack propagation in asphalt concrete. *Proceedings of the Geo-Frontiers 2005 Congress*, Austin, TX.
- Underwood, E.E. 1970. *Quantitative stereology*: Addison-Wesley Publishing Company.
- Zubelewicz, A. and Bazant, Z.P. 1987. Interface element modeling of fracture in aggregate composites. *Journal of Engineering Mechanics*, Vol. 113: 1619–1630.

Structural impact and dynamics response in brittle materials

M. Buonsanti, G. Leonardi & F. Scopelliti

University of Reggio Calabria, Reggio Calabria, Italy

ABSTRACT: Impact events occur in a wide variety of circumstances, from everyday occurrence as the striking of a nail with a hammer, to the protection of spacecraft against meteoroid impact. In the present paper, we restricted our attention on a small scale event of the problem, which namely is the impact on heterogeneous materials, as the runway pavement, during an aircraft landing. We propose a theoretical model based on shock wave-induced phase transformations after the impact due to the landing of the aircraft, considering the contact phenomena produced by the impact. We investigated a small scale model of the fragmentation phenomena which simulates the concrete asphalt behavior at macro scale. This phenomenon is strictly linked with material degradation associated with damage evolution. The problem is developed by energetic approach on an elasto-plastic element by utilizing the functional energy containing two contributions, bulk and surface. The model simulates the behavior of flexible runway pavements during the landing phase.

1 INTRODUCTION

In recent years several studies analyse the behaviour of flexible pavements developing three-dimensional (3D) finite element models [1][2] that are capable of accurately determining stresses in flexible pavements caused by aircraft with multiple-wheel landing gear configurations.

Flexible pavements can often be idealized as closed system consisting of several linear elastic layers, with each layer both uniform in thickness and infinite in horizontal extent. This layered elastic approach to pavement modeling is no longer acceptable in pavement analysis and the need for consideration of non-linear material behavior becomes increasingly important (Sukumaran et al. [3]). The stress state dependency of granular materials, and strain based sub-grade soil models must be considered for an accurate estimation of true pavement response (Nazarian and Boddspati [4]). However, many methods for the analysis of pavements employ the liner elastic theory as a first approximation for the evaluation of the materials response.

The model used in the study conducted by Zaghoul and White [5] incorporated an elasto-plastic model for the base, sub-base and sub-grade and a visco-elastic model for the asphalt layer. Zaghoul and White researched the ability of three-dimensional dynamic finite element programs to predict the response of pavement structures under moving loads. In their study, the granular material was modeled using the Drucker-Prager model.

This assigns elastic properties to materials at low stress levels and plastic properties when the stress level reaches the yield stress. The clay sub-grade was modeled using the Cam-Clay model. The validation of their model was accomplished by testing the model's ability to predict deformations under static and dynamic load conditions. The final results show that their model was capable of simulating truckloads and realistic deformation predictions were obtained.

This paper covers the theoretical study of the problem, the development and the implementation of a three-dimensional finite element model for flexible pavements; in particular the paper is organized as follows: the second paragraph illustrates the theoretical aspects of pavements behavior in the runway during the landing phase. Particularly, we focused our attention on the physics of the impact since the phenomenon is characterized by an abrupt change in the values of the system variables, most commonly discontinuities in the stress and strain. Other effects directly related to the

phenomenon are those of vibration propagation through the solid, local elastic/plastic deformations at the contact zone and frictional energy dissipation.

The third paragraph covers the development of a preliminary numerical model and describes the various components that are included in the final model.

The fourth paragraph describes the gear characteristics of the considered aircraft (B737), the landing load conditions and shows the results of the FEA simulation. In the fifth paragraph we discuss the micro-macro transition scale, formulating the *RVE* (representative volume element) concept and putting a possible modelization of the *RVE* asphalt concrete. In the *RVE* model hypothesis we formulate the equilibrium conditions and joint it to the fracture phenomenon as well as generative of the asphalt mixture fragmentation.

2 THE MACRO-SCALE CLASSICAL APPROACH

When we restrict attention on macro-scale then continuum hypothesis can be used and so a regular multi-layer plane solid can be considered. For this model type, when one layer is considered, a classical reference is Timoshenko & Woinowsky-Krieger [6] theory.

We assume that the intensity of the reaction of the sub-grade is proportional to the displacement of the solid plane.

This intensity is then given by the expression kw where the constant k is called modulus of the sub-grade and its value depends largely on the properties of the sub-grade.

2.1 Plane solids on elastic medium

When a rectangular sub-part is considered, we schematize a plate resting on elastic sub-grade. In accordance with the classical assumption the differential equation written in rectangular coordinates becomes

$$w_{xxxx} + 2w_{xyxy} + w_{yyyy} = q/D - kw/D \quad (1)$$

with q acting load and D the plate stiffness. Assuming the boundary conditions type with the Cartesian reference system (x, y) of the form

$$(w)_{x=0, x=a} = 0 \quad (w_{xx})_{x=0, x=a} = 0 \quad (2)$$

$$(w)_{y=b/2} = 0 \quad (w_y)_{y=b/2} = 0 \quad (3)$$

the displacements field can be taken in the series form

$$w = \frac{4kw^o}{D\pi} \sum_{m=1,3,5} \frac{\sin \frac{m\pi x}{a}}{m \left(\frac{m^4 \pi^4}{a^4} + \frac{k}{D} \right)} + \sum_{m=1,3,5} Y_m \sin \frac{m\pi x}{a} \quad (4)$$

The first series on the right hand side is a particular solution of the equation (1) while the second series is solution of the associate homogeneous equation. Now let us consider a plate, which rests on an elastic sub-grade, loaded at equidistant point along one reference axis (example x -axis). Then a possible solution as the form

$$w = w^o + \sum_{m=2,4,6} Y_m \cos \frac{m\pi x}{a} \quad (5)$$

where the first term represents the displacement field of an infinitely long strip of unit width parallel to the y -axis loaded at $y=0$ by the load P/a . After the constants calculation we have the final form for the displacement field

$$w = w^o + \frac{P\lambda^2}{ak} \sum_{m=2,4,6} \frac{(-1)^{m/2}}{\sqrt{\lambda^4 + \mu_m^4}} \cos \frac{m\pi x}{a} e^{-\beta y} (\gamma_m \cos \gamma_m y + \beta_m \sin \gamma_m y) \quad (6)$$

2.2 Plate undergoing carrying loads

Let us consider an infinite plate resting on elastic sub-grade and carrying equidistant and equal loads, each load being distributed uniformly over a prescribed rectangular area ($u \times v$).

A possible treatment of this case can be regarded by means of a simple series of Westergaard's solution, however other simple adequate solutions can be sided by means the double series of the Navier's method.

Representing the lateral load due to the columns in form of a cosine series, the intensity of the given load P , is put as P/uv on the inside of the rectangular area, we obtain the final results as the form

$$w = \frac{4P}{\pi^2 uv} \sum_{n=0}^{\infty} \sum_{m=0}^{\infty} \frac{\varepsilon \sin \frac{m\pi u}{a} \sin \frac{n\pi v}{b} \cos \alpha x \cos \beta y}{mn(D\gamma^4 + k)} \quad (7)$$

If we perform an energetic approach, taking a circular portion of radius a , the strain deformation energy of the plate as the form (A and B are constants to be determined from the boundary condition, assuming that the stable equilibrium appears as consequence of the energy minimum)

$$E^P = 4B^2 D \pi a^2 (1+\nu) \quad (8)$$

while the strain energy of the sub-grade is

$$E^S = \int_0^{2\pi} \int_0^a \frac{k w^2}{2} r dr d\theta = \pi k \left(\frac{1}{2} A^2 a^2 + \frac{1}{2} A B a^4 + \frac{1}{6} B^2 a^6 \right) \quad (9)$$

The total functional energy, when the load is applied in the center, takes the final form as

$$E^T = 4B^2 D \pi a^2 (1+\nu) + \pi k \left(\frac{1}{2} A^2 a^2 + \frac{1}{2} A B a^4 + \frac{1}{6} B^2 a^6 \right) - P A \quad (10)$$

Consequently the variational problem can be formulated as $\min E^T$, respecting boundary conditions and then finding the stress and strain fields at macroscale.

A closed form solution for standard variational approach presents computational difficulty, then a numerical solution can be carried out by finite element approach, as shown in the third paragraph.

2.3 Plate under load impact

This aspect can be regarded as the realistic situation of the question. For the general aspect to the solid impact problem we follow Goldsmith [7] and Jones [8].

This approach implies that the transverse dimension of the plate is small compared to its lateral dimensions.

Let u_c be the displacement of the plate at the impact point (c) due to concentrated force $F(t)$, then in the load density surface case $W(x, y, t)$ the differential relationship becomes

$$W = D \nabla^4 u + 2\rho h \frac{\partial^2 u}{\partial t^2} \quad (11)$$

If a solution of (10) is sought in the form of the normal harmonic of vibration, or shock wave, a simple integral expression may be obtained and the displacement field, under impact is given by

$$u(x, y, t) = \frac{1}{2b\rho} \sum_{n=1}^{\infty} \sum_{m=1}^{\infty} \frac{\mathfrak{I}_{i,m}(x, y)_t}{\omega_{i,m}} \int_0^t \mathfrak{I}_{i,m} W(\tau) \sin \omega_{i,m} (t - \tau) \quad (12)$$

We can observe that over classical solutions of stress and strain fields, an other aspect of the material response appears, namely induced vibration and consequently travelling shock wave, such that stress and strain fields are increasing.

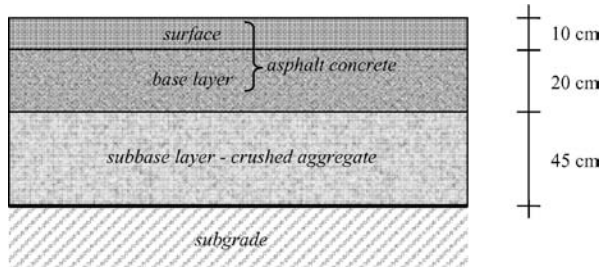


Figure 1. Pavement section.

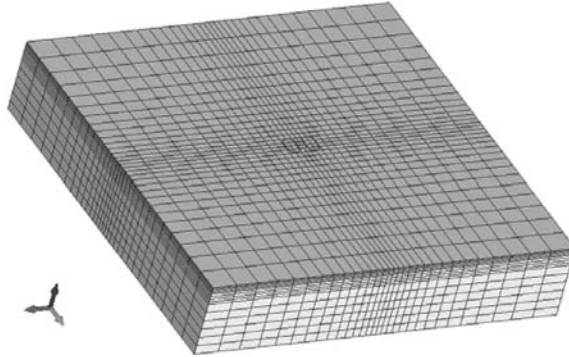


Figure 2. Finite element mesh.

3 FINITE ELEMENT MODEL

Flexible pavements can often be idealized as closed systems consisting of several layers; so it was decided to model the surface, base, sub-base and sub-grade material using three-dimensional finite elements. The pavement section is comprised of asphalt concrete and crushed aggregate, as shown in Figure 1.

The finite element mesh developed has the following dimensions: 15 m in x and y directions and 3 m in the z-direction (Figure 2). The degree of mesh refinement is the most important factor in estimating an accurate stress field in the pavement: the finest mesh is required near the loads to capture the stress and strain gradients. The mesh presented has 18331 nodes and 13564 elements (brick8).

3.1 Material models for the finite element analyses

The pavement materials are divided in three groups: asphalt mixtures, granular materials and cohesive soils.

Asphalt mixtures were modelled as visco-elastic materials, in particular to characterize the permanent deformation properties of the asphalt mixtures can be used the creep model:

$$\dot{\bar{\epsilon}}^{cr} = A \cdot (\bar{\sigma}^{cr})^n \cdot t^m \quad (13)$$

where $\dot{\bar{\epsilon}}^{cr}$ is the equivalent creep rate; $\bar{\sigma}^{cr}$ is the equivalent Mises stress; t is the total creep time; and A , m , and n are material parameters (NX Nastran [9]). Granular material (sub-base) was modelled using a von-Mises model. The sub-grade layer was modelled using the Mohr-Coulomb material model. This is an elasto-plastic model in which granular materials are assumed to behave as elastic materials for low stress levels. When the stress level reaches a certain yield stress, the material will start to behave as a plastic material. The yield surface is specified using a friction

Table 1. Estimated temperatures of the three considered seasons.

Season	Summer	Spring-autumn	Winter
Temperature [°C]	40	20	5

Table 2. Material properties for the asphalt mixtures used in the 3D FEM model ($t = 20^{\circ}\text{C}$).

Material	Surface	Base
Thickness [mm]	100	200
E [MPa]	2490	4000
μ	0.35	0.30
Damping coeff. [%]	5	5

Table 3. Material properties for the sub-base and sub-grade layers used in the 3D FEM model.

Material	Sub-base	Sub-grade
Thickness [mm]	450	>2000
E [MPa]	350	100
μ	0.40	0.45
Angle of internal friction [°]	45	10
Cohesion [MPa]	0	0.08
Yield stress [MPa]	0.55	0.12
Damping coefficient [%]	5	5

Table 4. B737/200 characteristics (VNG = maximum vertical nose gear ground load at most forward center of gravity – VMG = maximum vertical main gear ground load at most aft center of gravity – H = maximum horizontal ground load from braking).

Maximum design taxi weight [N]	Main gear tire pressure [MPa]	V_{MG} vertical load [N]	H horizontal load [N]	
			Steady braking	Instantaneous braking
462619	1.007	213520	71611	170812

angle (Sukumaran et al. [3]). When the temperatures of the pavement were estimated Table 1, we calculated the modulus and the Poisson coefficient of asphalt mixtures in the three climate seasons: summer, spring-autumn and winter [10].

The material properties used in the analysis are given in Tables 2 and 3.

4 MODEL ANALYSIS

In the proposed model we consider an aircraft for civil aviation: B737-200 with the characteristics shown in the following [11]:

The most common way of applying wheel loads in a finite element analysis is to apply pressure loads to a circular or rectangular equivalent contact area with uniform tire pressure (Huang [12]). The loads (vertical and horizontal – Table 4) were applied to the element, which was created to be the same size as the wheel imprint of a B737 (Figure 3).

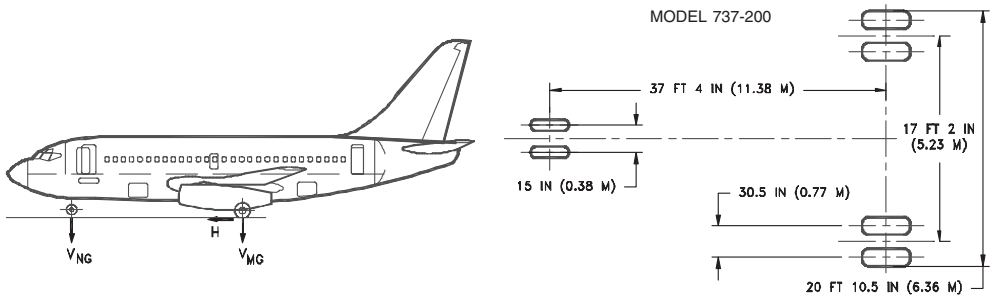


Figure 3. B-737 layout.

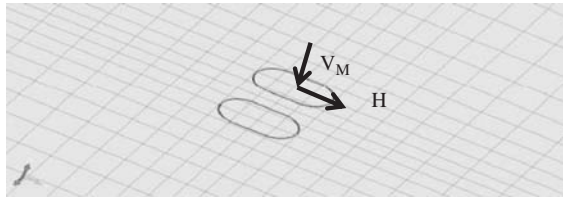


Figure 4. Pavement loads.

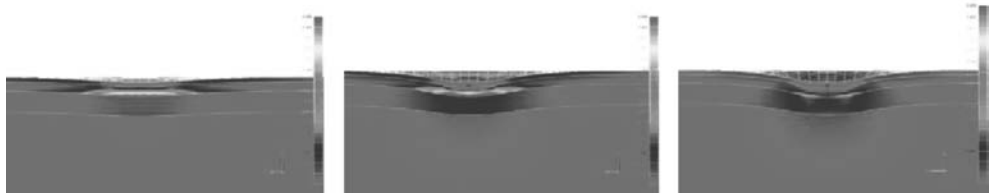


Figure 5. Solid stress and deflection (winter – spring/autumn – summer).

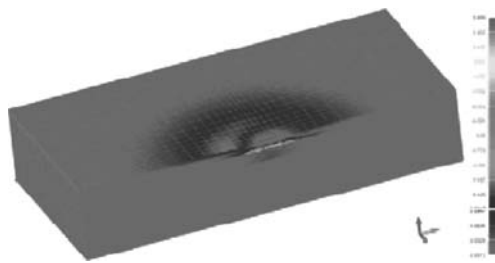


Figure 6. Solid stress and longitudinal deflection (winter).

Since the boundary conditions have a significant influence in predicting the response of the model, the model was constrained at the bottom and on the sides.

The results of the non-linear FE analysis [9] are illustrated in the following figures; in particular, Figure 5 shows, for the three considered seasons, the predicted layers deflection along transverse center line of the two contact areas.

Figure 6 presents the results of pavement surface deflection along longitudinal direction in winter season.

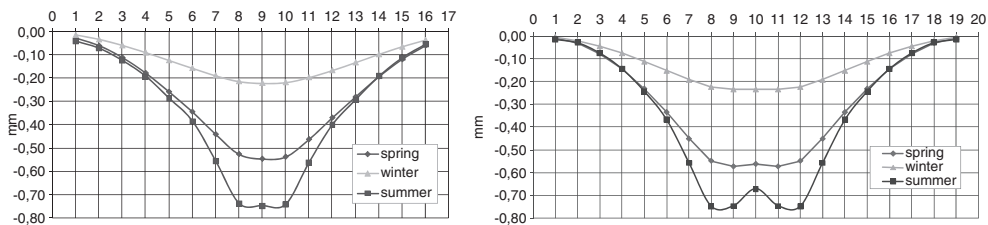


Figure 7. Surface deflection profiles along longitudinal and transverse directions.

The same results are plotted in Figure 7, where the pavement deflection profiles along the x and y axes are illustrated.

The two graphs are shown with the same y axis scale to facilitate visual comparison of deflection magnitude in the different seasons.

5 THE MICROSACLE APPROACH

In this paragraph is presented the link among microscale effects and material behaviors at macroscale. Particularly our attention is focalized on the micromechanics of the damage processes because; the non linear response of typical engineering materials is almost entirely dependent on the primary change in the concentration, distribution, orientation and defects in its structural composition.

According with Krajcinovic and Lemaitre [13], this particular study will be restricted to micro-cracks being only one of the many classes of micro-defects influencing the mechanical macro response.

The relation between the continuum damage mechanics and the fracture mechanics is of more insidious nature is, in essence, a question of scale. The important role of scale can be clarified by the discussion of the energies needed to propagate crack in an elastic solid. Then, a crack nucleated in an elastic solid could be stopped only if the level of the external load is increased ever so slightly.

Back to the general aspects, we will specify that all analytical models used in engineering describe the events either in micro or macro scale. In view of the simplicity of the continuum theories and the physical foundation of micromechanical models, a promising strategy would consist of combining the best features of both models. In this approach we consider only the first layer of the pavement package because, at micro-scale, damage distribution at the edge of the body, where surface degradation is of importance, is expected to be significantly different from the damage distribution far from the edge in the body. According with Frantziskonis [14] we consider that damage at the edge due to surface effects is additive to the damage accumulation as if no surface effects were present.

5.1 Homogenization

We follow the volume element theory *RVE*, and so it's possible to represent a non homogeneous solid with periodic microstructure. Particularly in the transition toward the micro-scale our *RVE* can be represented by more granular elements joint by means of an asphalt mixture, so considerations are applied on the contact area among two granular elements.

According to classical scale effects models, the equivalent deformation conditions are given by the link among engineering deformation gradient and deformation gradient at micro-scale. Choosing an appropriate *RVE* for a given irregular mixture, we assume a solid with spatial periodic microstructure.

Thus, consider a *RVE* with given microstructure and a corresponding *RVE** of the homogenized body under equivalent deformation conditions. Both volume elements are assumed to be mechanically equivalent on the macroscopic level, when the stored energy is equal.

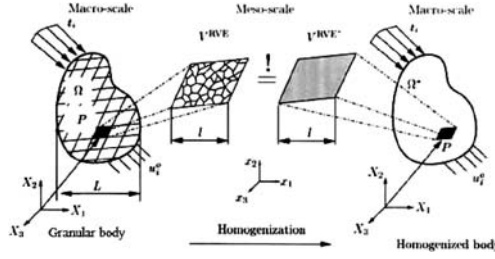


Figure 8. RVE homogenization.

5.2 Modeling the micro-scale behaviors

Besides the constitutive parameters a solid has a surface energy form. This one characterizes the nature of bounds ensuring the cohesion of the solid through an imaginary plane of unit area where 2ϕ represents the work needed to cut the microstructure's internal links.

The first coupled surface energy-elasticity was performed by Griffith in what was the fracture mechanics birth. Successively (Irwin) has introduced the strain energy released Γ by means of the relation $\Gamma = 2\phi$. The singularity of stresses near a crack tip was introduced by means of the stress intensity factor, controlling the intensity of the stress fields in the relation between energy approach and stress field terms. Now let us schematize the micro model (or RVE) as a Boussinesq problem with surface energy, namely a classical unilateral problem, and for this we refer to Del Piero and Maceri [15].

Modeling the physics of impact (landing-gear/ground) by means of a rigid frictionless asymmetric punch, with generic concave profile described by the function $f(r)$, in contact with an elastic half-space over an area of radius a . Following Sneddon's solution type we find respectively, the σ_z pressure distribution under the punch, the surface displacement u_z . In order to determine the penetration depth, the load P which must be applied is given by

$$P = \frac{\pi a E}{1 - \nu^2} \int_0^1 \rho(x) dx \quad (14)$$

$$\sigma_z = -\frac{E}{2(1 - \nu^2)a} \left[\frac{\chi(1)}{(1 - k^2)^{1/2}} - \int_0^1 \frac{\chi'(x)}{(t^2 - k^2)^{1/2}} \right] \quad (15)$$

$$u_z = \int_0^1 \frac{\chi(x)}{(k^2 - x^2)} dx \quad (16)$$

$$\delta = \int_0^1 \frac{f'(k)}{(1 - k^2)^{1/2}} + \frac{\pi}{2} \chi(1) \quad (17)$$

where $k = r/a$ and $\chi(t)$ describe the mutual action of micro-forces and give rise to singular tensile stress and to a displacement continuity at the edge of the contact area. When we consider the flat punch type, the given relationship in the compressive load case follow

$$\delta = \frac{1 - \nu^2}{E} \frac{P}{2a} \quad (18)$$

Imposing energy balance among elastic, potential and surface energy ($-\pi a^2 w$, where w represents the Dupre's adhesion energy) we find the adherence force P^E as

$$P^E = - \left(\frac{8\pi E}{1 - \nu^2} a^3 w \right)^{1/2} \quad (19)$$

Using the polar coordinates, the stress tensor for a flat punch with surface energy, namely is

$$\begin{aligned}
 \sigma_r &= \frac{K_I}{\sqrt{2\pi k}} \cos \vartheta/2 (1 - \sin \vartheta/2 \sin 3\vartheta/2) \\
 \sigma_\theta &= \frac{K_I}{\sqrt{2\pi k}} 2\nu \cos \vartheta/2 \\
 \sigma_z &= \frac{K_I}{\sqrt{2\pi k}} \cos \vartheta/2 (1 + \sin \vartheta/2 \sin 3\vartheta/2) \\
 \tau_{rz} &= \frac{K_I}{\sqrt{2\pi k}} \cos \vartheta/2 (\sin \vartheta/2 \cos 3\vartheta/2)
 \end{aligned} \tag{20}$$

At edge of the contact area displacement field the form similarly as in the fracture mechanics, namely is

$$u_z - \delta = \frac{K_I}{2\mu} \sqrt{\frac{k}{2\kappa}} \sin \vartheta/2 (3 - 4\nu - \cos \vartheta) \tag{21}$$

The difference from the corresponding classical expression in fracture mechanics can be, probably, arising from the hypothesis of frictionless contact which implies a radial displacement under the impact.

6 A MICROSCALE FEM RESULTS

In this paragraph we model the unilateral contact among granular elements and asphalt mixture when macro action, with reduced scale effect, is present. Starting with a simplified approach to determine *RVE* property, we assume that each constituent material is homogeneous and isotropic.

In according with Cambou [16] and Bardet [17], here we utilize a modified cylinder model as well as spherical model. Particularly, our attention focalized on the *RVE* considering three distinct parts, namely granular, asphalt and voids. On this *RVE*, five different sizes of granular elements are considered joint with asphalt. Finally, void ratio completes the elementary volume.

The basic hypothesis, in this case, is to consider that the medium may be considered by a periodic (micro) structure, namely the *unit cell* and so *RVE* coincide whit the *unit cell*. These deterministic models are able to account exact local information, perhaps shape, dimension and orientation of the heterogeneous components

To build the micromechanical finite element model we refer to Sadd [18], adopting the concept that the aggregate material is normally much stiffer than the binder, and thus the aggregate is taken as *quasi-rigid*. On the other hand, the bituminous mastic is a compliant material with elastic, inelastic and time-dependent behaviour.

Here we consider an elastic-perfectly plastic joint among two aggregate particles. About the modelization of this contact, the relationship is activated when traction stress operate on two aggregate (unilateral restraint). Let us k_n an k_t , respectively normal and tangential stiffness, Δn and Δt the normal and tangential displacement component of the contact, then the value of the, normal N and tangential T , contact force follow as

$$N(t+\Delta t) = N(t) + k_n \Delta n \tag{22}$$

$$T(t+\Delta t) = T(t) + k_t \Delta t \tag{23}$$

The stress-strain evolution analysis is performed by applying Newmark integration scheme and by *Mathematica Code* the upper map results (see Figure 9). Finally the transition micro-macro is formulated by averaging operations, where V is the macro-scale volume in which σ_{ij} and E_{ij} are

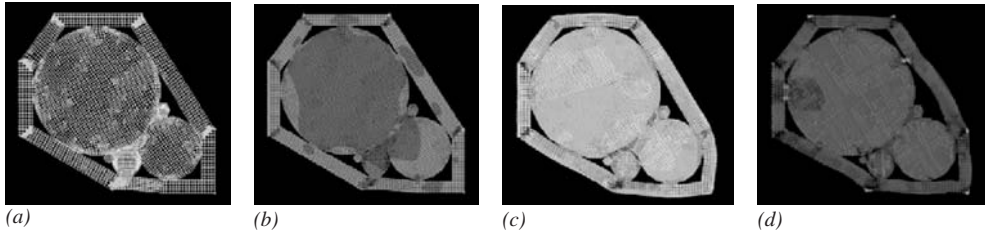


Figure 9. (a) RVE-mesh; (b) Pressure stress-max; (c) Temperature stress-max; (d) Von Mises stress and final deformation.

defined and $W(E_{ij})$ represent the stored deformation energy functional

$$\sigma_{ij} = \frac{1}{V} \int_V \sigma_{ij}^* dV = \langle \sigma_{ij}^* \rangle ; E_{ij} = \frac{1}{V} \int_V E_{ij}^* dV ; W(E_{ij}) = \frac{1}{W} \int_V \sigma_{ij}^* E_{ij}^* dV \quad (24)$$

7 CONCLUSION

A complete analysis, for a complex problem is proposed starting of the macro-scale with transition at microscale. Stress-strain fields in elastic and plastic range (phase coexistence) and stress concentration represent the macro-scale results in the complete pavement package, while the transition at microscale point-out the initial damage. Regarding the external hand of the pavement, the surface effects roles play a basic aspect in the constitutive degradation of the layer.

The latter should be regarded as the initial process towards the global damage with the other layer. Consequently, when damage processes grow, the fragmentation states visually appear.

Particularly any aspects of surface damage in flexible pavements can be sided as scale effects over non homogeneous materials. In fact, the micromechanics of the problem can be utilized for maintenance models refinement.

REFERENCES

- [1] Chen D. H., Zaman M., Laguros J., Soltani, A., "Assessment of computer programs for analysis of flexible pavement structure", Transportation Research Record 1482, TRB, National Research Council, Washington, D.C., 1995, 123–133.
- [2] Cho Y.-H., McCullough B. F. and Weissman J., "Considerations on finite element method application in pavement structural analysis", Transportation Research Record 1539, TRB, National Research Council, Washington, D.C., 1996, 96–101.
- [3] Sukumaran B., Chamala N., Willis M., Davis J., Jurewicz S. and Kyatham V., "Three dimensional finite element modeling of flexible pavements", FAA Worldwide Airport Technology Transfer Conference, Atlantic City, New Jersey, USA, 2004.
- [4] Nazarian S. and K. M. Boddspati, "Pavement-Falling Weight Deflection Interaction Using Dynamic Finite Element Analysis," In Transportation Research Record 1449, TRB, National Research Council, Washington, D.C., 1995, 123–133.
- [5] Zaghoul S. M. and White T. D., "Use of a Three-Dimensional, Dynamic Finite Element Program for Analysis of Flexible Pavement," In Transportation Research Record 1388, TRB, National Research Council, Washington, D.C., 1993, 60–69.
- [6] Timoschenko, S. and Woinowsky-Krieger S., Theory of Plate and Shell, McGraw-Hill 2nd Ed. Singapore, 1976.
- [7] Goldsmith, W., Impact, Dover Pb. 2nd Ed., Toronto, 2001.

- [8] Jones, N., *Structural Impact*, Cambridge University Press, Cambridge, 1997.
- [9] UGS Corp., “NX Nastran - Quick Reference Guide”, UGS Corp, 2007.
- [10] Verstraeten J., “Moduli and Critical Strains in Repeated Bending of Bituminous Mixes. Application to Pavement Design” Proceedings, International Conference on the Structural Design of Asphalt Pavements, London 1972.
- [11] Boeing, “737 Airplane Characteristics for Airport Planning”, October 2005.
- [12] Huang Y.H., *Pavement Analysis and Design*, Prentice Hall, Englewood Cliffs, New Jersey, 1993.
- [13] Krajcinovic D. and Lemaitre J., *Continuum Damage Mechanics*, CISM n° 295, Springer, Wien, 1987.
- [14] Frantziskonis, G., Surface effects in Brittle Materials and Internal Length Estimation, *Appl. Mechanics Review*, 45, 3, 2, 1992.
- [15] Del Piero, G. and Maceri, F., *Unilateral Problems in Structural Analysis*, CISM n° 285, Springer – Verlag, Wien, 1985.
- [16] Cambou, B., *Micromechanical Approach in Granular Materials*, in *Behaviour Granular Materials*, CISM Course and Lecture n° 385, Springer-Verlag, New York, 1998.
- [17] Bardet, J.P., *Introduction to Computational Granular Materials*, in *Behaviour Granular Materials*, CISM Course and Lecture n° 385, Springer-Verlag, New York, 1998.
- [18] Sadd, M.H., et al., *Simulation of Asphalt Materials Using a Finite Element Micromechanical Model with Damage Mechanics*, TRB Annual Meeting TRB2003 publ. Transportation Research Record.

Multiscale computational modeling for predicting evolution of damage in asphaltic pavements

R.F. Soares, Y.-R. Kim, D.H. Allen

University of Nebraska, Lincoln, Nebraska, USA

ABSTRACT: Heavy-load vehicles significantly influence pavement distresses and failure. As a primary variable of pavement design, accurate investigation of damage associated with the impact of heavy traffics on pavement performance is an important issue and a big challenge that pavement engineers face. To this end, this study presents a multiscale computational model for predicting evolution of damage in asphaltic pavements. The model developed herein is based on continuum mechanics and is expected to increase the ability for predicting damage-dependent behavior and the service life of pavement systems while minimizing testing effort and producing more accurate simulations than traditional experience-based phenomenological approaches. Global and local scales are systemically included in the model, represented by a whole pavement structure and a representative volume element (RVE) of the heterogeneous asphalt concrete mixture in the pavement structure, respectively. With the unique multiscale (global-local) computational analysis it is possible to take into account the effect of materials heterogeneity and damage-dependent behaviour of each mixture constituent on overall pavement performance by simply linking the properties of mixture constituents (local-scale) and pavement structural performance (global-scale). As a preliminary modeling stage, computational results depending on loading conditions are investigated herein to monitor the impact of vehicular loading conditions on pavement failure and fracture behavior. It can be concluded that the successfully developed techniques in this paper might be useful as a predictive tool for selecting better mixture components and for designing pavement structure with improved performance.

1 INTRODUCTION

Pavement engineers have traditionally relied on empirical methods for the design and analysis of pavements. However, as illustrated in many studies including a study by Al-Qadi et al. (2005), the empirical approach has been proven to be limited in its use and somewhat inaccurate and unreliable, since it only works for a certain set of loading conditions, materials, and pavement structures. To overcome limitations found from the empirical approach, the new pavement design guide (so-called Mechanistic-Empirical Pavement Design Guide (NCHRP 2004) has been developed. The new design guide incorporates mechanistic relations in the form of loading time (or frequency)-dependent viscoelastic dynamic modulus as the primary material property for asphalt concrete layer, but performance analysis is based on layered elastic theories, and design life of pavements is determined by incorporating mechanistic pavement responses with empirical transfer functions.

Consequently, it is clear that a realistic characterization of the variables involved in pavement design is a key to predict pavement distresses and failure and thus a successful design. One of these variables is damage associated with the impact of heavy traffics on pavement performance. This is an important issue and a big challenge that pavement engineers face today.

This study presents a multiscale computational model for predicting evolution of damage and overall performance of asphalt pavements. The model is in its early stage and has been developed

based on continuum mechanics. The model herein is expected to increase the ability for predicting damage-dependent behavior and the service life of pavement systems while minimizing modeling effort and producing more mechanics-based simulations than traditional approaches, with significant savings in experimental costs and time.

2 MULTISCALE MODELING CONCEPTS

Numerous experimental observations have demonstrated that many cracks develop in a solid object in small scale, and those small scale cracks can coalesce into macrocracks to cause structural failure. The current state of the art of fracture mechanics cannot yet accurately predict when multiple cracks in an object will grow, while several attempts (Needleman 1987; Camacho and Ortiz 1996; Espinosa et al. 1998; Ghosh et al. 2001; Song et al. 2006; Molinari et al. 2007) have been made to investigate crack initiation/propagation and fragmentation phenomena under static/dynamic loading in conjunction with cohesive zone modeling approaches. When the cracks are developed in a widely separated length scale, the concept of multiscale modeling as shown in Figure 1 can be used. This concept by itself is not new but is based on the necessary condition that the object is “statistically homogeneous”. This means that spatial variations on stresses and strains of the object are small compared to the mean stresses and strains. Therefore, the constituents should be several orders of magnitude smaller than the object itself. By assuming that statistical homogeneity is present, the smaller scale (or local scale) can be solved independently from the larger scale (or global scale).

2.1 Local scale modeling

Consider a global scale solid object (length scale $l^{\mu+1}$ in Figure 1) with a region wherein microcracks are evolving on the local scale (length scale, l^μ in Figure 1) representative volume element (RVE). The RVE is a sample size that is sufficiently large so that the estimation of the effective properties is independent of the sample size.

Suppose that the local scale RVE can be treated as viscoelastic, so that the following initial boundary value problem (IBVP) can be posed:

$$\frac{\partial \sigma_{ji}^\mu}{\partial x_j^\mu} = 0 \quad \text{on } V^\mu + \partial V_E^\mu \quad (1)$$

$$\sigma_{ji}^\mu = \sigma_{ij}^\mu \quad \text{on } V^\mu + \partial V_E^\mu \quad (2)$$

$$\varepsilon_{ij}^\mu = \frac{1}{2} \left(\frac{\partial u_i^\mu}{\partial x_j^\mu} + \frac{\partial u_j^\mu}{\partial x_i^\mu} \right) \quad \text{on } V^\mu + \partial V_E^\mu \quad (3)$$

$$\sigma_{ij}^\mu = \Omega_{r=-\infty}^{r=t} \{ \varepsilon_{kl}^\mu \} \quad \text{on } V^\mu + \partial V_E^\mu \quad (4)$$

where σ_{ij}^μ is the Cauchy stress tensor defined on length scale μ (i.e., local scale), ε_{ij}^μ is the strain tensor on the length scale μ , u_i^μ is the displacement vector on the length scale μ , x_i^μ is the coordinate location in the object on the length scale μ , which has interior V^μ and boundary ∂V_E^μ . Note that inertial effects and body force have been neglected, and the linearized form of the strain tensor has been taken for simplicity.

The equation (4) implies that the entire history of strain at any point in the local scale body is mapped into the current stress, which is the definition of a viscoelastic material model. Equations (1) through (4) must apply in the body, together with appropriate initial and boundary conditions. These are then adjoined with a fracture criterion that is capable of predicting the growth of new or existing microcracks anywhere in the body.

There are multiple possibilities to represent the growth of new or existing microcracks, and one of the first approaches is by Griffith (1920), where he proposed that a crack in an elastic body

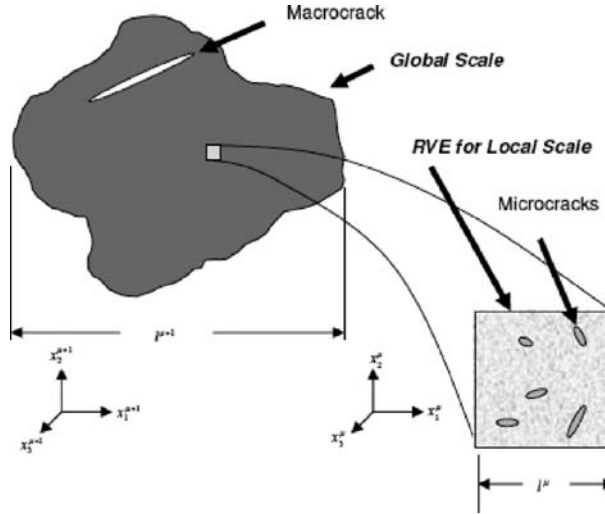


Figure 1. Two scale problem with cracks on both length scales.

would extend whenever the energy released per unit area of crack created exceeded the critical energy release rate. However, this criterion is often found to be inaccurate for viscoelastic media. For this reason, a different approach using a viscoelastic cohesive zone model (Allen and Searcy 2001) is taken herein for simulating crack growth. This model has been shown to be consistent with advanced fracture mechanics, in that the cohesive zone requires a non-stationary critical energy release rate in order for a crack to propagate (Costanzo and Allen 1993, 1996).

The traction-displacement relationship for a nonlinear viscoelastic cohesive zone can be written as follows (Allen and Searcy 2001):

$$T_i^\mu(t) = \frac{u_i^\mu(t)}{\lambda^\mu(t) \cdot \delta_i^\mu} [1 - \alpha^\mu(t)] \cdot \left[\int_0^t C^\mu(t - \tau) \frac{\partial \lambda^\mu(\tau)}{\partial \tau} d\tau \right] \quad \text{on } \partial V_i^\mu \quad (5)$$

where T_i^μ = cohesive zone traction (local scale), u_i^μ = cohesive zone displacement (local scale), λ^μ = normalized cohesive zone displacement (local scale), δ_i^μ = cohesive zone material length parameter (local scale), $\alpha^\mu(t)$ = cohesive zone damage evolution function (local scale), $C^\mu(t)$ = cohesive zone viscoelastic relaxation modulus, ∂V_i^μ = internal boundary representing cracks, and $i = n$ (normal direction), r (radial direction), or s (tangential direction). It can be seen that when the damage evolution function, $\alpha^\mu(t)$ goes to unity, the cohesive zone traction in equation (5) becomes zero, thereby inducing crack propagation.

The damage evolution function can be determined by performing fracture tests as presented in several studies (Williams 2001; Freitas 2007). The measured damage characteristics can then be incorporated into an equation containing damage evolution parameters (α_1 and m) such as,

$$\frac{d\alpha^\mu}{dt} = \begin{cases} \alpha_1 [\lambda^\mu(t)]^m, & \frac{d\lambda^\mu}{dt} > 0 \text{ and } \alpha^\mu < 1 \\ 0, & \frac{d\lambda^\mu}{dt} \leq 0 \text{ or } \alpha^\mu = 1 \end{cases} \quad (6)$$

The damage evolution is a simple form of power relationship as a function of the $\lambda^\mu(t)$; thus, it is appropriate for simulating rate-dependent damage growth which is typical in viscoelastic bodies such as asphalt mixtures.

Recently, the cohesive zone modeling approach, as implemented and demonstrated in several studies (Souza et al. 2004; Kim and Buttlar 2005; Kim et al. 2005), has been receiving increasing attention from the asphalt pavement mechanics community; this is because it is useful and powerful, in particular for modeling both brittle and ductile fracture, which is frequently observed in asphalt mixtures due to their wide range of service temperatures and loading rates.

2.2 Homogenization for scale-linking between local and global

Accumulated damage and structural degradation resulting from local scale analysis influence constitutive behavior at the next larger scale (i.e., global scale). The results from the local scale analysis are homogenized and linked to the global scale problem. The concept of homogenization (Christensen 1979; Mura 1987; Nemat-Nasser and Hori 1993; Allen and Searcy 2006), replacement of a heterogeneous medium with a macroscopically equivalent homogeneous one, is applicable whenever the heterogeneous medium satisfies statistical homogeneity. Homogenization is central to the idea of multiscale and is typically through the averaging process of local fields within the heterogeneous medium. A finally derived form of the homogenized global scale modulus due to local scale damage effects can be written as:

$$C_{ijkl}^{\mu+1}(t) = \frac{1}{V^{\mu}} \int_{V^{\mu}} C_{ijkl}^{\mu}(t - \tau) dV \quad (7)$$

where $C_{ijkl}^{\mu+1}$ = averaged global scale modulus, and $\mu + 1$ indicates the next larger length scale, that is the global scale.

2.3 Global scale modeling

Upon completing the homogenization process at the local scale, a global scale initial boundary value problem can be posed. Similar to the local scale problem, general forms of equations at global scale can be established. In the absence of body forces, inertial effects, and large deformations again for simplicity, the equations at global scale can be written as follows:

$$\frac{\partial \sigma_{ji}^{\mu+1}}{\partial x_j^{\mu+1}} = 0 \quad \text{on } V^{\mu+1} + \partial V_E^{\mu+1} \quad (8)$$

$$\sigma_{ji}^{\mu+1} = \sigma_{ij}^{\mu+1} \quad \text{on } V^{\mu+1} + \partial V_E^{\mu+1} \quad (9)$$

$$\varepsilon_{ij}^{\mu+1} = \frac{1}{2} \left(\frac{\partial u_i^{\mu+1}}{\partial x_j^{\mu+1}} + \frac{\partial u_j^{\mu+1}}{\partial x_i^{\mu+1}} \right) \quad \text{on } V^{\mu+1} + \partial V_E^{\mu+1} \quad (10)$$

$$\sigma_{ij}^{\mu+1} = \Omega_{\tau=-\infty}^{\tau=t} \{ \varepsilon_{kl}^{\mu+1} \} \quad \text{on } V^{\mu+1} + \partial V_E^{\mu+1} \quad (11)$$

where $\sigma_{ij}^{\mu+1}$ = stress tensor (global scale), $\varepsilon_{ij}^{\mu+1}$ = strain tensor (global scale), $u_i^{\mu+1}$ = displacement vector (global scale), $x_i^{\mu+1}$ = spatial coordinates (global scale), $V^{\mu+1}$ = volume of the global scale object, and $\partial V_E^{\mu+1}$ = external boundary of the global scale object.

It is apparent that global scale equations (8)–(11) correspond to local scale equations (1)–(4), so that a similar algorithm may be utilized for the analysis on both scales. The significant difference is that the introduction of cracks (or damage) at the local scale results in a more complex and inherently nonlinear formulation of the constitutive equations at the global scale. A more detailed description of the homogenization process, modeling of each scale, and their linking can be given by other literature (Yoon and Allen 1999; Allen and Searcy 2001; Allen and Soares 2007).

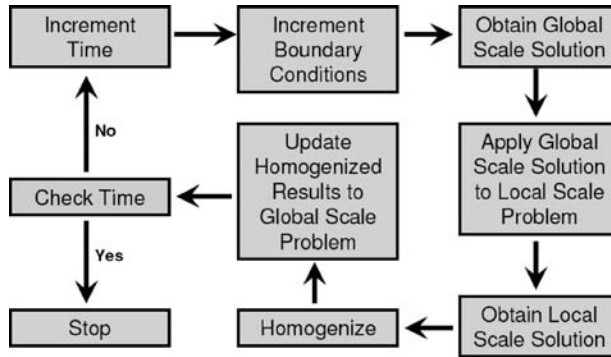


Figure 2. Flowchart showing multiscale computational algorithm.

2.4 Formation of a multiscale algorithm

The approach detailed above may be used to develop a multiscale computational algorithm (such as the finite element method) for obtaining approximate solutions to problems containing multiple cracks growing simultaneously on widely differing length scales. This is accomplished by constructing a time stepping process in which the global solution is first obtained for a small time step, as shown in Figure 2. The global solution for this time step is then utilized to obtain solutions for integration points at the local scale RVE, using the state variables obtained as output from the global analysis to obtain the solution at the local scale. During this process, nodal forces resulting from the global scale finite element analysis are applied to the local RVE as boundary conditions. The results for each integration point are then homogenized to produce the global constitutive equations to be used on the next time step at the global scale. Sufficient accuracy can usually be obtained by this method if successively smaller time steps are employed until convergence is obtained.

3 MULTISCALE MODELING OF ASPHALT PAVEMENTS

In this section, an example problem is presented in order to demonstrate the technique of multiscale modeling with damage applied to asphaltic pavements. The results obtained from this study are not yet complete, but they provide an overall idea with the purpose of comparing damage-dependent performance of asphaltic pavements in different loading configurations.

Consider a typical two-lane asphaltic roadway as shown in Figure 3. All layers are modeled as isotropic elastic media. The global and local scale objects are discretized and the finite element meshes are constructed as shown in Figure 3. The multiscale modeling should be applied to all global scale elements for the best results, however only four global scale elements located under the tire load have been chosen for this particular study to reduce considerable computing time but still to demonstrate how this modeling approach is accomplished.

For the local scale, both asphalt phase and aggregates are modeled as linear elastic, however fracture in the form of discrete cracks is introduced at the local scale by including viscoelastic cohesive zone elements. Each cohesive zone element is incorporated with the damage evolution function ($\alpha(t)$ in equation (5)) to predict the evolution of new boundary surfaces (i.e., cracks). Cohesive zone elements are located within the asphalt phase and along the interfaces between aggregates and asphalt phase. Tables 1 and 2 present global and local scale material properties as model inputs. Again, the properties used for this study are arbitrarily assumed for simulation purposes only, even if they can be directly measured by performing constitutive tests (Kim et al. 2005, 2007)

For the multiscale analysis, we seek the response of a load applied by a truck on the pavement. The response is considered in the form of damage caused by two different types of tire configurations: the conventional dual tires (two 29.5-cm tires in dual mode) and the wide-base single tire (44.5-cm

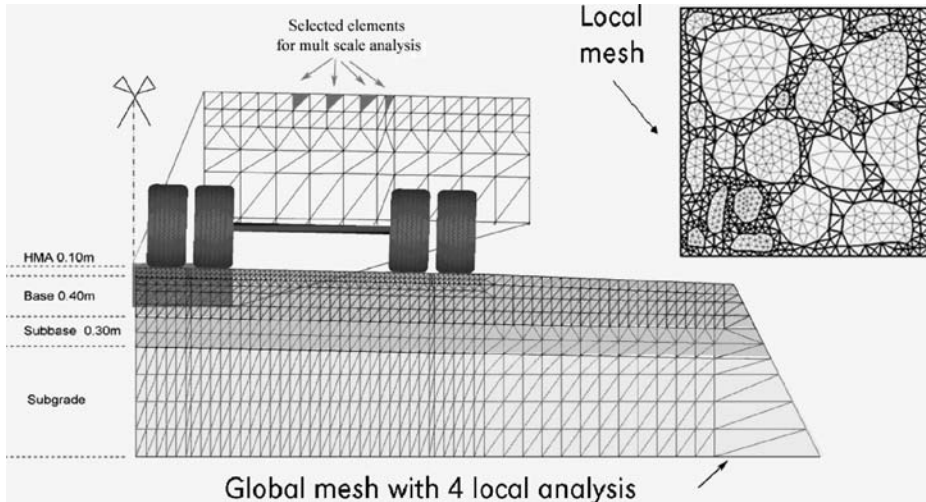


Figure 3. Global and local scale objects and their finite element meshes.

Table 1. Material properties for global scale.

Pavement layer	Elastic properties	
	Young's modulus (MPa)	Poisson's ratio
Asphalt Surface	2047	0.40
Base	1200	0.35
Subbase	800	0.35
Subgrade	200	0.35

Table 2. Material properties for local scale.

Local scale elements			
Bulk properties		Cohesive zone properties	
Asphalt Phase		E_{∞} (Pa)	7.69E03
E (Pa)	1.38E06	E_I (Pa)	6.13E04
ν	0.35	η_I (Pa-s)	2.72E04
Aggregates		ν	0.40
E (Pa)	5.52E10	δ_n (m)	7.00E-03
ν	0.15	δ_s (m)	7.00E-03
		α_I	0.19
		m	0.67

wide). The wide-base tires are currently being used to replace a set of dual tires in trucks as depicted in Figure 4. They are more commonly used in Europe and Canada; however these configurations are slowly appearing in the U.S. market. This study complements the research done by Soares (2005), where he proposed a pavement service life comparison by using these two types of tires. In that study, viscoelasticity was the only form of energy dissipation and damage was not included.

Even if a truck applies a cyclic load to the pavement, a more simplistic load was considered for this study with the purpose of illustrating the technique, since this multiscale modeling is still in its

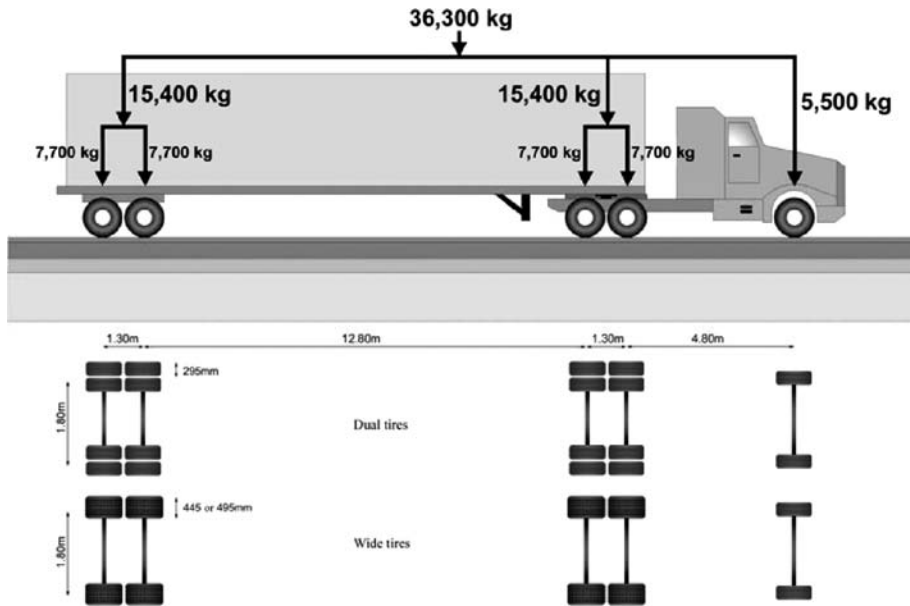


Figure 4. A truck with dual tires or wide-base single tire configuration and weight distribution.

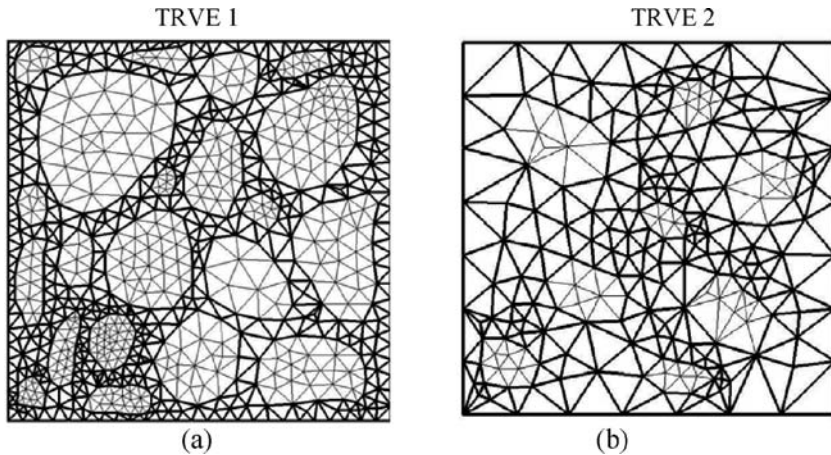


Figure 5. Local scale trial representative volume elements (TRVEs).

early stage. A tandem axle with a constant load (15,400 kg: 151 kN) was applied to the pavement surface as shown in Figure 4.

In addition to the different tire configurations, two different trial representative volume elements (TRVE 1 and TRVE 2 shown in Figure 5) with different aggregate volume fractions were also considered in this study. Each TRVE is 0.025 m × 0.025 m which is arbitrarily chosen. A study to find a proper size of the RVE is necessary and currently under accomplishment by the authors.

4 MODELING RESULTS

Figure 6 presents the accumulation of damage (α value) in TRVE 1 subjected to different tire load configurations (dual tires vs. wide-base tires). It can be seen that the dual tire case performs better

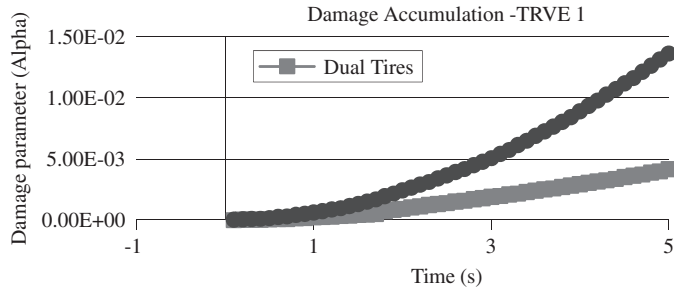


Figure 6. Damage evolution (dual tires vs. wide-base tires).

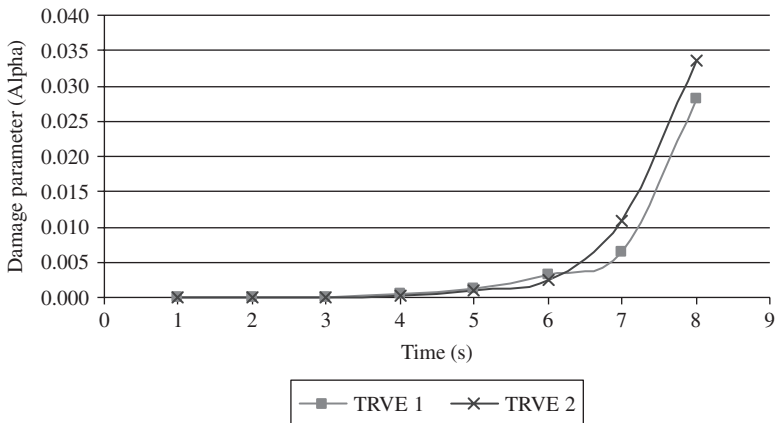


Figure 7. Damage evolution (TRVE 1 vs. TRVE 2).

than the wide-base single tires. This result indicates that a truck with 29.5-cm dual tires gives a pavement performance life longer than the wide-base tire case.

The effect of mixture constituents' volume fraction in the local scale object (i.e., asphalt concrete mixture) on overall pavement performance is illustrated in Figure 7. The wide-base tires was equally applied to the pavement by merely varying TRVEs, and simulation results shown in Figure 7 indicate that volume fraction of mixture constituents play an important role to damage evolution and consequent pavement performance. As expected, the TRVE 1 was better resistant to damage, since the volume fraction of aggregates, which are not subjected to damage, in the TRVE 1 was greater than the volume fraction of aggregates in TRVE 2.

5 CONCLUSIONS

A multiscale approach for modeling asphalt pavements, including the heterogeneity and material viscoelasticity, described herein, appears to be within reach of the design community. Even though the model is still in its early stage, it shows a great potential as a promising tool for the next generation pavement design and analysis.

The multiscale method has been developed for analysis of asphalt pavements that exhibit two length scales. While the model described can apply to more than two length scales, at this point it fully works for two scales. This approach has the capability of predicting the evolution of damage in the global scale structure by simply identifying material properties and fracture-damage characteristics of mixture constituents in the local scale RVE. Furthermore, any arbitrary traffic

loading conditions can be implemented to pavement structure by applying appropriate boundary conditions to the finite element analysis of the pavement structure. Despite a great deal of computing effort expected due to the realistic simulation of mixture heterogeneity and nonlinear-inelastic damage-dependent material behavior within the entire pavement structure, computational results of a simple roadway problem presented herein imply that the successfully developed techniques such as this might be useful as a purely mechanistic predictive tool for selecting better mixture constituents and for designing pavement structure with improved performance.

REFERENCES

- Allen, D.H. and Searcy, C.R. 2001. A Micromechanical Model for a Viscoelastic Cohesive Zone. *International Journal of Fracture* 107:159–176.
- Allen, D.H. and Searcy, C.R. 2006. A Model for Predicting the Evolution of Multiple Cracks on Multiple Length Scales in Viscoelastic Composites. *Journal of Materials Science* 41(20): 6510–6519.
- Allen, D.H. and Soares, R.F. 2007. Multiscale Modeling of the Evolution of Damage in Heterogeneous Viscoelastic Solids. In Y. W. Kwon, D. H. Allen, and R. R. Talreja. *Multiscale Modeling and Simulation of Composite Materials and Structures*: 513–545. Springer (In Press).
- Allen, D.H. and Yoon, C. 1998. Homogenization Techniques for Thermoviscoelastic Solids Containing Cracks. *International Journal of Solids and Structures* 35: 4035–4054.
- Al-Qadi, I.L., Yoo, P. J. and Elseifi, M. A. 2005. Characterization of Pavement Damage Due to Different Tire Configurations. *Journal of the Association of Asphalt Paving Technologists* 74:921–962.
- Barenblatt, G.I. 1962. The Mathematical Theory of Equilibrium Cracks in Brittle Fracture. *Advances in Applied Mechanics* 7:55–129.
- Camacho, G. T. and Ortiz, M. 1996. Computational Modelling of Impact Damage in Brittle Materials. *International Journal of Solids and Structures*, 33: 2899–2938.
- Christensen R.M. (1) 1979. *Mechanics of composite materials*. New York: John Wiley & Sons.
- Costanzo, F. and Allen, D.H. 1993. A Continuum Mechanics Approach to Some Problems in Subcritical Crack Propagation. *International Journal of Fracture* 63(1):27–57.
- Costanzo, F. and Allen, D.H. 1996. A Continuum Thermodynamic Analysis of Cohesive Zone Models,” *International Journal of Engineering Science* 33(15): 2197–2219.
- Dugdale D.S. 1960. Yielding of Steel Sheets Containing Slits. *Journal of Mechanics and Physics of Solids* 8(2):100–104.
- Espinosa, H. D., Zavattieri, P. D., and Dwivedi, S. K. 1998. A Finite Deformation Continuum/Discrete Model for the Description of Fragmentation and Damage in Brittle Materials. *Journal of the Mechanics and Physics of Solids*, 46: 1909–1942.
- Freitas, A. C. F. 2007. A Theoretical and Experimental Technique to Measure Fracture Properties in Viscoelastic Solids. *Ph.D. Dissertation*, University of Nebraska, Lincoln, Nebraska.
- Ghosh, S., Lee, K., and Raghavan, P. 2001. A Multi-Level Computational Model for Multiscale Damage Analysis in Composite and Porous Materials. *International Journal of Solids and Structures*, 38: 2335–2385.
- Griffith, A.A. 1920. The Phenomena of Rupture and Flow in Solids. *Philosophical Transactions of the Royal Society of London A*221:163–197.
- Kim, H. and Buttlar, W. G. 2005. Micromechanical Fracture Modeling of Hot-Mix Asphalt Concrete Based on a Disk-Shaped Compact Tension Test. *Electronic Journal of the Association of Asphalt Paving Technologists*, 74E.
- Kim, Y., Allen, D. H., and Little, D. N. 2005. Damage-Induced Modeling of Asphalt Mixtures Through Computational Micromechanics and Cohesive Zone Fracture. *Journal of Materials in Civil Engineering*, 17(5):477–484.
- Kim, Y., Freitas, A. C. F., Allen, D. H., and Soares, J. B. 2007. Experimental Characterization of Ductile Fracture-Damage Properties of Asphalt Binders and Mastics. *Journal of the Transportation Research Board*, submitted to TRB.
- Molinari, J. F., Gazonas, G. A., Raghupathy, R., Rusinek, A., and Zhou, F. 2007. The Cohesive Element Approach to Dynamic Fragmentation: The Question of Energy Convergence. *International Journal for Numerical Methods in Engineering*, 69(3):484–503.
- Mura, T. (2) 1987. *Micromechanics of Defects in Solids*. Boston: Kluwer Academic Publishers.
- NCHRP 1-37A. 2004. Guide for Mechanistic-Empirical Design of new and rehabilitated pavement structures, *Final Report, Part 1. Introduction, Chapter 1. Background, Scope and Overview*.

- Needleman, A., 1987. A Continuum Model for Void Nucleation by Inclusion Debonding. *Journal of Applied Mechanics*, 54:525–531.
- Nemat-Nasser S. and Hori M. (2) 1993. *Micromechanics: Overall Properties of Heterogeneous Solids*. The Netherlands: Elsevier Science Publishers.
- Soares, R.F. 2005. Finite Element Analysis of the Mechanics of Viscoelastic Asphaltic Pavements Subjected to Varying Tire Configurations. MsC Thesis. University of Nebraska – Lincoln.
- Song, S. H., Paulino, G. H., and Buttlar, W. G. 2006. A Bilinear Cohesive Zone Model Tailored for Fracture of Asphalt Concrete Considering Viscoelastic Bulk Material. *Engineering Fracture Mechanics*, 73(18): 2829–2848.
- Souza, F. V., Soares, J. B., Allen, D. H., and Evangelista, F. 2004. Model for Predicting Damage Evolution in Heterogeneous Viscoelastic Asphaltic Mixtures. *Journal of the Transportation Research Board*, 1891:131–139.
- Yoon, C. and Allen, D.H. 1999. Damage dependent constitutive behavior and energy release rate for a cohesive zone in a thermoviscoelastic solid. *International Journal of Fracture* 96:56–74.
- Williams, J. J. 2001. Two Experiments for Measuring Specific Viscoelastic Cohesive Zone Parameters. *Master's Thesis*, Texas A&M University, College Station, Texas.

Finite element modeling of fatigue shear tests: Contribution to pavement lifetime design under traffic loading

F. Bouhas, A. Millien & C. Petit

University of Limoges, GEMH Laboratory, Egletons, France

ABSTRACT: Pavement overlaying is a repair technique mainly used for road network maintenance. Durability of pavement depend strongly on reflective cracking phenomenon. A pavement structure is submitted to thermal variations and traffic loading. All design methods assume opening mode and neglect shearing mode when trucks axles are closed to pre-existing cracks. Assuming an uncoupled approach, we limit ourselves to traffic loading and shear fatigue model is proposed. With taking into account of a localized degradation scheme, both crack initiation and crack propagation are considered. The damage law proposed is stemming of experimental data. This fatigue model is integrated in a finite element code (CAST3M). The principal objective of this study is the development of a model based on an overall resistant cord. The suggested modeling of the bituminous mixtures behavior above cracks would contribute to improve pavement repair design. In this way a numerical study has been carried out to quantify the effect of mesh refinement and loading conditions.

Keywords: shear fatigue, damage, finite element modeling, reflective cracking, pavement.

1 INTRODUCTION

Pavement overlaying is a repair technique usually used for maintenance actions on the road network. These paper deal with fatigue cracking in asphaltic overlays. Here we propose a damage and cracking model in overlays for pavement lifetime design. Indeed, traffic loading lead to fatigue cracking in overlays. These crack initiation are close to transverse crack in damaged old pavement. In a lot of pavement structures, traffic induce mainly shear loading mode for cracking in new overlays. Most of current studies for such problems assume opening mode associated to fatigue cracking test. Opening mode is verified in flexible pavement, shearing mode become important for semi-rigid and rigid pavements. Shearing effect is also greater for thin overlays. According (Vergne et al 1989 & De bondt 1999), The traffic loading which is mainly shear stress contribute in the final phase of propagation, while the thermal effects (in opening mode) act in the initiation phase of crack. Assuming an uncoupled approach, we limit ourselves in this paper to traffic loading. Many laboratory tests were developed in order to simulate reflective cracking and to qualify the efficiency of possible anti reflective crack systems. Fatigue cracking experimental results due to shear loading can be given with the Mefisto test (Wendling 1997), ETS test (High School of technology, University of Quebec) (Guissi 2005) and our test developed in GEMH laboratory (Petit 2002). DST test is a Double Shear Test for bituminous material. The experimental results lead to initiation and crack propagation modeling across asphalt overlays.

The background of the model is a damage localization on a band. A joint finite element has been developed for that.

The presented work present finite element simulations of reflective cracking in overlays. Two experimental test have been simulated the ETS test and the DST test for which some experimental results are available.

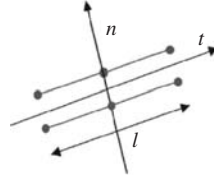


Figure 1. An isoparametric finite element joint.

2 MODELING OF THE SHEARING FATIGUE LOCALIZED ON A BAND

The damage model enable to describe the crack initiation and the crack propagation (Petit 2002). Assuming a damage localization on a band with low thickness, we can then associate a joint finite element (fig. 1).

For the element joint, the displacement field W is defined by both components u and v such as:

$$W = \begin{Bmatrix} u \\ v \end{Bmatrix} \quad (1)$$

where \vec{l} and \vec{n} are respectively the relative displacement vectors.

It does not exist coupling between the normal force and shearing, thus:

$$\begin{Bmatrix} \tau \\ \sigma \end{Bmatrix} = \begin{bmatrix} K_s & 0 \\ 0 & K_n \end{bmatrix} \begin{Bmatrix} u \\ v \end{Bmatrix} \quad (2)$$

The linear behavior of plane isoparametric joint finite elements are defined by K_s and K_0 .

K_n is very high and constant, and the evolution law $K_s = K_s(E)$ is defined by the experimental results in previous study (Petit, 2002) such us :

$$\frac{K_s}{K_0} = \frac{K_{si}}{K_0} - \alpha \cdot E_{tot} \quad \text{with} \quad E_{tot} = \sum_{i=1}^N \overline{\Delta\tau_i \cdot \Delta u_i} \quad (3)$$

where K_0 = the initial stiffness of material not damaged; K_s = the stiffness at considered time; α = the parameter of the model and will be function of the level of shearing; E_{tot} = the total deformation energy density (J/m²).

The cyclic shearing fatigue test showed, as in the case of flexion or traction-compression fatigue tests (De la roche 1996 & Di Benedetto 1997), that in the first loading cycles, the stiffness of the resistant cord drop quickly then the variation becomes quasi linear.

We thus have took into account this abrupt drop at beginning of the test by introducing a bituminous concrete shearing stiffness K_s below which the damage is a linear function of the total energy accumulated per unit of surface. The model considers a micro-cracking appearance for a damage threshold D_c .

The numerical behavior of finite element modeling was carried out by considering a 2D plane strain analysis and an elastic linear isotropic behavior of material. The bituminous mixtures viscoelastic properties were introduced with taking in to account for the bituminous material of an elasticity modulus and a shearing stiffness equivalents (Huet 1963) (deducted from the main curves at temperature and frequency test and/or the obtained experimental results).

Figures 2 and 3 presents the mesh specimen and the limiting conditions.

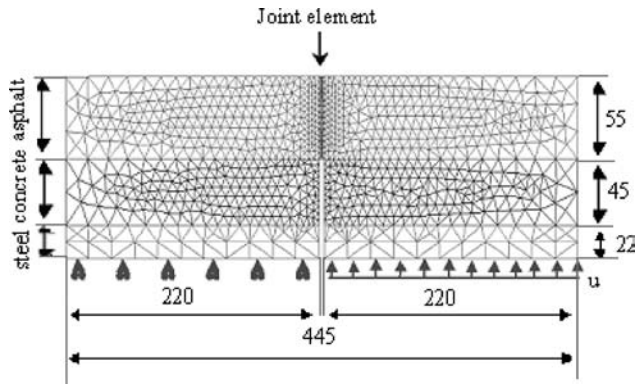


Figure 2. Mesh of ETS test.

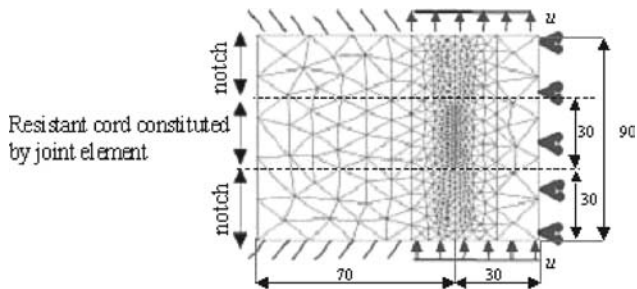


Figure 3. Mesh of DST test.

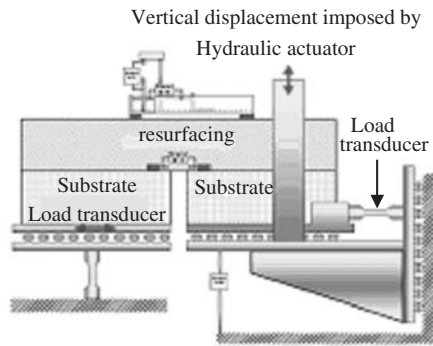


Figure 4. ETS test (Guissi, 2005).

3 PARAMETRIC STUDY: CRITERIA OF CONVERGENCE

The test selected for this analysis is the shearing fatigue test E.T.S used to study the reflective cracks in the resurfacing systems. It is constituted by two horizontal plates supporting the specimen, one is mobile in the horizontal plan and the other is mobile in the vertical plan (fig. 4).

The vertical movement serves for feigning the vehicles passage action on the place of cracks, and the horizontal movement to feign the thermal effects. For this study only the tests under vertical alternate load reproducing the mode II were retained.

This parametric analysis was carried out in two stages in order to analyze the necessary criteria of convergence:

- A spatial discretization to determine the joints finite element size or the number of elements constituting the resistant cord (fig. 5),
- A temporal discretization to determine the number of the step calculation increments (fig. 6).

The mechanical properties of the materials constituting the specimen for the E.T.S test are summarized in the following table 1.

The initial shearing stiffness influence of the resistant cord was studied. For the presented calculations, it is fixed at 130 MPa/mm, value resulting from experimental results of (Laveissiere 2002). The damage threshold taken into account for the passage between damage and macro-cracking is conventionally fixed at a reduction of 50% of the initial stiffness (Doan 1977).

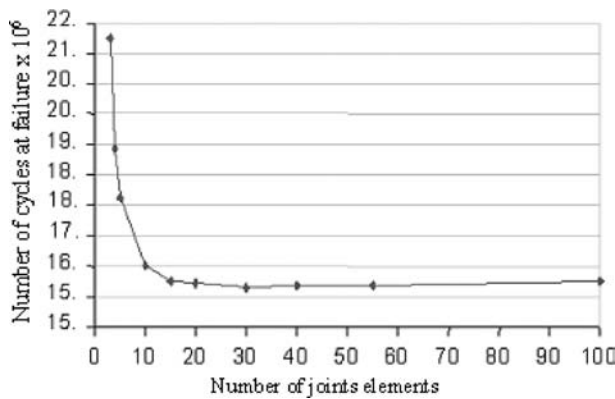


Figure 5. Influence of spatial discretization.

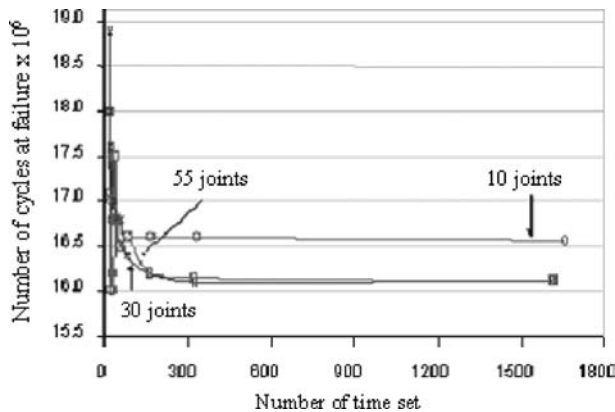


Figure 6. Influence of time discretization.

Table 1. Material properties.

Material	E (MPa)	ν
Bituminous mixture	5900	0.35
Concrete	39000	0.30
Steel	210000	0.30

The applied load corresponds to an imposed vertical displacement of 0.020 mm (Fig. 2), applied to one of the mobile plates in the vertical direction (Guissi 2005). This model considers at the first cycles, 10% of shearing stiffness initial fall, then the damage is a linear function of the total cumulated energy per unity of surface.

We carried out the numerical simulation by considering that specimen resistant cord is constituted of n joint elements with identical dimensions. At considered threshold damage, the joint's stiffness is cancelled and the joint element becomes a crack.

The load applied to specimen bottom induce a stresses concentration at point of crack and during the calculation, the crack propagates then from down to top.

The number of cycles at specimen's failure depends strongly of the joint elements size (Fig. 5). More the number of elements increases (their size decreases), more the number of cycles at failure decreases, until the number $n_{min} = 20$ elements from which the number of cycles at the failure is almost constant. This allows us to conclude that the convergence criterion is verified if the joint elements size does not exceed 5% of the cord height.

Figure 6 shows us the influence of the time step on the number of cycles at failure. More the number of time steps increases, more the number of cycles at failure decrease. In the same way we can say that the convergence is reached starting 300 time steps (checking carried out for joints elements that the size does not exceed 5% of the cord height).

Tests are at present in progress at Montreal High School of Technology. A validation is necessary at the reception of the results.

4 EXPERIMENTAL VALIDATION

For validation, we compared the model results with those of the cyclic shearing tests on notched specimens, of CS modified type (Compact Shearing). The experimental device is that of the Civil engineering laboratory of University of Limoges (fig. 7 and fig. 8). The side supports are embedded and the central part is maintained in a rigid frame interdependent of the electromechanical testing machine mobile axis. The symmetry of the specimen induces us to choice an cyclic and symmetric shearing load.

The specimen geometry is given on figure 7.

Testing conditions are a constant temperature $T = 5^{\circ}\text{C}$ and a loading frequency $f = 1\text{ Hz}$. The bituminous concrete is a French standard semicoarse bituminous concrete 0/10, with 5.8% of 35–50 pen grade bitumen by weight of aggregate.

The convergence criteria previously validated were verified on specimen used for this test.

The results comparison is carried out with the results obtained on two specimens subjected to 1.25 MPa of average shearing stress level in the cord. The damage intervenes quickly in first joints on both sides of the specimen. A shear stresses redistribution is followed from there on all the cord height through each joint elements. The cracking propagates from both edges to finish at central part by successive and symmetric joints failure.

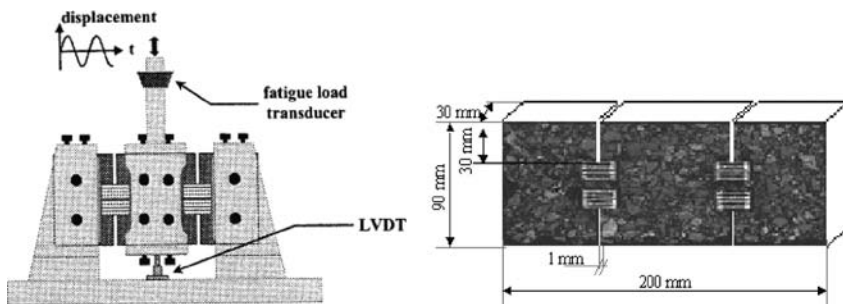


Figure 7. Schematic view of the modified shearing test and the specimen geometry.

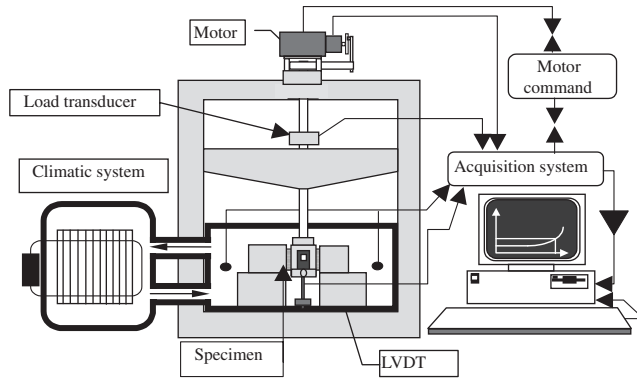


Figure 8. Diagram of experimental device.

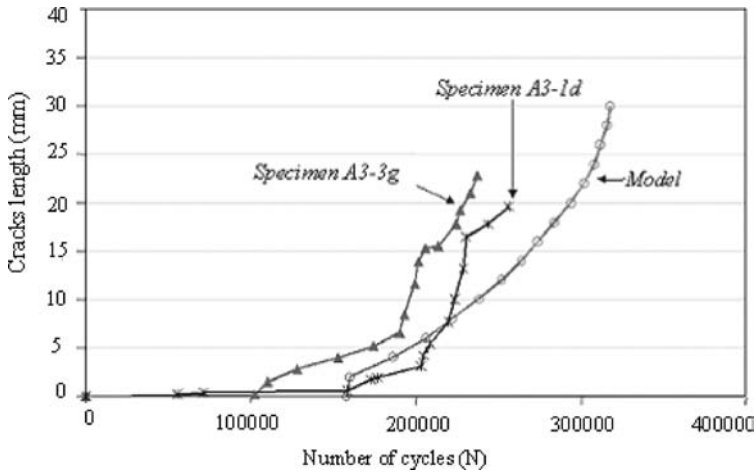


Figure 9. Evolution of crack length.

The results obtained from our model concern in particular the duration of the crack initiation phase and the propagation modeling.

As showed on the Figure 9, the numerical results obtained for these parameters are close to the experimental observations.

The mechanical response (force) is represented on Figure 10. During the starting phase of cracks, the force amplitudes decrease weakly as the damage progresses. From 150000 cycles the force falls sharply according to crack propagation . The calculated forces with the model are in adequacy with measurements.

5 CONCLUSION

The suggested modeling of the bituminous mixtures behavior at the place of cracks is based on an overall resistant cord degradation. The presented numerical tool is from a simplified approach allowing the pavement overlay design. The parametric analysis lead to give some numerical parameters in order to define both main numerical parameters (size of the joint finite elements and the time step).

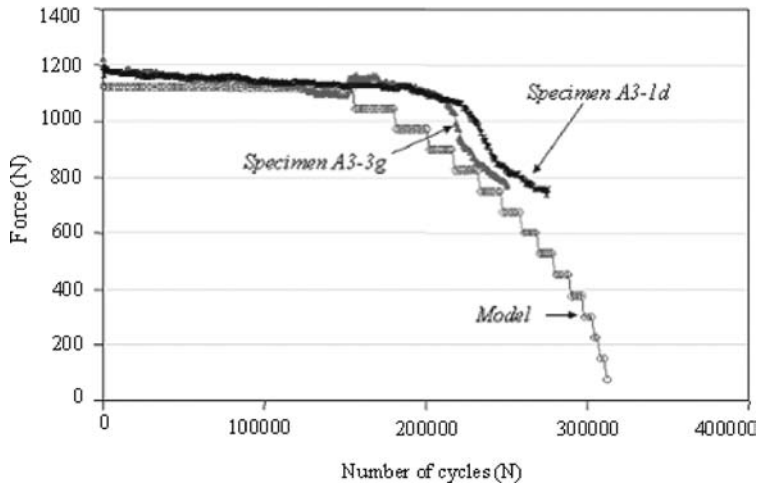


Figure 10. Evolution of vertical force.

The numerical results of simulations are interesting and allows to represent the initiation and propagation phases of crack. The numerical simulations results are rather close to experiment results about the initiation and propagation phases.

ACKNOWLEDGMENTS

Authors would like to thank Daniel Perraton and Guillaume Guissi for collaboration with datas and experimental results relative to ETS specimen (Montreal High School of Technology).

REFERENCES

- De Bondt A.H. 1999. Anti-reflective cracking design of reinforced asphaltic overlays. Ph.D. thesis, Faculty of Civil Engineering, Delft University of Technology.
- De la Roche C., Marsac P. 1996. Caractérisation expérimentale de la dissipation thermique dans un enrobé bitumineux sollicité en fatigue. 1st Int. Eurobitume and Eurasphalt Congress.
- Di Benedetto H & Soltani M.A. A. & Chaverot P.1997. Fatigue damage for bituminous mixtures. Mechanical Tests for Bituminous Materials, Essais Mécaniques pour les Matériaux Bitumineux, pp. 263–270, RILEM.
- Doan T.H. 1977. Les études de fatigue des enrobés bitumineux. Bulletin de liaison du Laboratoire des Ponts et Chaussées, n° spécial V.
- Guissi G. 2005. La remontée des fissures dans les re-surfaçages: Développement d'une méthodologie de conception des re-surfaçages. rapport de synthèse, École de Technologie Supérieure, Montréal.
- Huet C. 1963. Étude par une méthode d'impédance du comportement viscoélastique des matériaux hydrocarbonés. Thèse de docteur-Ingénieur, Faculté des sciences de Paris.
- Laveissiere D. 2002. Modélisation de la remontée de fissure en fatigue dans les structures routières par endommagement et macro-fissuration – de l'expérimentation à l'outil de dimensionnement pour l'estimation de la durée de vie. Thèse de doctorat, Faculté des sciences -Université de LIMOGES.
- Petit C. & Laveissière D. & Millien A. avril 2002. Modeling of Reflective Cracking in Pavements : Fatigue under shear stresses. pp. 111–124, Third int. Symp. on 3D Finite Element for Pavement Analysis, Design and Research, Amsterdam.
- Vergne A., Petit C., Zhang X., Capper S. & Faure B. 1989. simulation numérique de la remontée de fissure dans une structure routière. 1st Rilem conf. Reflective cracking in pavements, Ed. E & FN Spon, pp. 182–189.
- Wendling L. & Piau J.M. 1997. MEFISTO un nouveau banc de fissuration pour l'étude de la fissuration en mode mixte des enrobés bitumineux. 4^{ème} réunion annuelle GEO-Aussois.

Shift factor model evaluations using tested data from PMA at low temperatures and data reduction methods for IDT and HT-BBR testing

B.-Q. Bai

Camosun College, Victoria, British Columbia, Canada

ABSTRACT: Using the data tested from polymer modified asphalt (PMA) binders and mixes at low temperatures, this paper evaluates three different models describing the relationship between the shift factor and temperature ($\log a_T$ vs. T), which include the WLF equation, the Arrhenius Function, and the linear model. The testing methods are the Bending Beam Rheometer test using Hyper Terminal control (HT-BBR) for the binders and the indirect tensile test (IDT) for the mixes. SBS with concentrations of 2, 4, and 6% and EVA with 2 and 4% are used for the polymer modification. The HT-BBR can be used to extend the testing capacity of the standard Bending Beam Rheometer (BBR) based on AASHTO TP1.

This paper also describes the data reduction procedures for the HT-BBR and the IDT from the raw data acquisition to the plotting of creep stiffness master curves at low temperatures. Currently, among the researchers in this area, there is no generally agreed software available for the data reduction of both testing procedures.

1 INTRODUCTION

1.1 *Stiffness master curve and time–temperature superposition*

In thermal cracking prediction of asphalt pavement, a wide range of loading time from a split second to many hours is involved, which is out of the ordinary lab testing capacity or convenience. However, under the assumption that asphalt is thermo-rheologically simple linear viscoelastic material, time-temperature superposition technique can be used. The creep tests are usually carried out under a wide range of temperatures. With respect to a reference temperature (T_{ref}), the test results at lower temperatures are equivalent to those at the T_{ref} but with shorter loading times, and vice versa. In this way, a master curve of stiffness modulus can be built covering a wide range of loading time regarding the T_{ref} .

At very low temperature and/or at very short loading time, the stiffness approaches an elastic limit. On the other hand, at very high temperature and/or at very long loading time, the asphalt material behaves as a Newtonian fluid, which means that the master curve of log stiffness versus log loading time approaches a straight line with a slope of “–1”.

Two well-known functions were developed for the relationship of $\log a_T$ vs. T . One is the Arrhenius function (AF) [1] that can be expressed as

$$\log a_T = a_1 \left(\frac{1}{T} - \frac{1}{T_{ref}} \right) \quad (1)$$

where

$\log a_T$ = time temperature shift factor;

a_1 = Arrhenius constant,

T and T_{ref} = the temperature and the reference temperature.

The other is the William-Landel-Ferry equation (WLF) [2].

$$\log a_T = -\frac{C_1(T - T_{Ref})}{C_2 + T - T_{Ref}} \quad (2)$$

where C_1 and C_2 are empirically determined constants.

At low temperatures, WLF and AF may not hold valid. Thus, some researchers [3] [4] used a linear relationship, $\log a_T = b(T - T_{Ref})$. This paper tries to evaluate the three models, using the data tested from both conventional and PMA binders and mixes at low temperatures.

1.2 Data reduction for HT-BBR and IDT testing

The standard Bending Beam Rheometer (BBR) used in this study, based on AASHTO TP1 [5], can measure the binder creep stiffness from 8 to 240 seconds (a very short time range). But the software is not able to produce the stiffness master curves. Furthermore, this equipment has a maximum deflection of about 5 mm. It aborts the test if the deflection is over this limit, and then all the data before the limit is also lost. The authors [6] [7] described a HT-BBR procedure to extend the standard BBR's capacity using hyper terminal (HT) control for data acquisition. However, a systematic method is needed to treat the test data.

The IDT creep test data reduction method from some previous researchers [8] [9] were found various errors [10] and was only applicable for temperatures of 0 to -20°C . Christensen's method [10] used a linear relationship for $\log a_T$ vs. T also ranged from 0 to -20°C . Thus, a systematic data reduction method for IDT test must also be developed. This paper describes the procedures for the data reduction of both the HT-BBR and the IDT creep testing.

2 RELATIONSHIP OF SHIFT FACTOR VERSUS TEMPERATURE

The fitting results of the three models are presented in Table 1. All the models go through a fixed point at $\log a_T = 0$ while $T = T_{Ref}$. The WLF fitting is based on the following transformation from Equation (2):

$$-\frac{T - T_{Ref}}{\log a_T} = \frac{1}{C_1}(T - T_{Ref}) + \frac{C_2}{C_1} \quad (3)$$

In Equation (3), when $T = T_{Ref}$, the left side of the equation becomes an indeterminate form, 0/0. In this analysis, the L'Hospital rule is used, i.e.

$$\frac{T - T_{Ref}}{\log a_T} = \frac{d(T - T_{Ref})}{d(\log a_T)} = \frac{1}{d(\log a_T)/d(T)} \quad (4)$$

The values of $d(\log a_T)/dT$ are directly read as the slopes of the tested curves of $\log a_T$ vs. T at $T = T_{Ref}$, from the graphs given in Appendix A. The standard deviation, defined as

$$\sigma = [\sum(\log a_{Ti} - \log a_T)^2 / (N - 1)]^{0.5} \quad (5)$$

is used in Table 1 as the criterion for the model evaluation, where $\log a_{Ti}$ is the shift factor from the tests, $\log a_T$ is that from the models, and N is the number of data.

From Table 1, it is apparent that for the mixes, with the exception for 4%SBS and 6%SBS, the linear model fits the best since it has the lowest values of " σ ". In most cases, the tested data fit similarly to WLF and AF. For 4%SBS mix, WLF fits better than AF that, in turn, is better than the linear model. For 6%SBS mix, the three models are not much different, with AF fitting the best, and WLF the worst.

For the binders, except for 2%EVA, WLF fits the best, and AF fits better than the linear model. For 2%EVA mix, AF fits the best, followed by WLF.

Table 1. Fitting results for the test data.

	Models	Fitted parameters			Standard deviation σ	
			Binder	Mix	Binder	Mix
Husky 150-200A	WLF	C₁/C₂	24.8/131	-5.74/-57.4	0.042	0.836
	AF	a₁	12,000	9,960	0.066	0.837
	Linear	b	-0.187	-0.159	0.140	0.672
Husky 200-300A	WLF	C₁/C₂	16.4/94.0	-28.4/-167	0.041	0.599
	AF	a₁	11,100	10,900	0.112	0.505
	Linear	slope b	-0.173	-0.173	0.180	0.379
2% EVA	WLF	C₁/C₂	42.7/244	-13.0/-94.3	0.023	0.610
	AF	a₁	11,100	10,400	0.002	0.647
	Linear	slope b	-0.173	-0.165	0.070	0.490
4% EVA	WLF	C₁/C₂	68.4/391	602/3,880	0.004	0.111
	AF	a₁	11,200	9,490	0.024	0.189
	Linear	slope b	-0.176	-0.150	0.045	0.074
2% SBS	WLF	C₁/C₂	26.3/150	-1,270/-7470	0.022	0.381
	AF	a₁	11,400	9,860	0.050	0.319
	Linear	b	-0.178	-0.156	0.120	0.261
4% SBS	WLF	C₁/C₂	30.9/176	9.62/46.9	0.004	0.346
	AF	a₁	11,300	10,200	0.030	0.826
	Linear	slope b	-0.176	-0.158	0.100	1.02
6% SBS	WLF	C₁/C₂	5.42/31.0	25.4/156	0.194	0.470
	AF	a₁	11,500	8,250	0.464	0.356
	Linear	slope b	-0.179	-0.129	0.535	0.427

It should be mentioned that the mix testing was conducted under five temperatures, and the binders were tested only in three temperatures. Therefore, the analysis for the mixes is more creditable than that for the binders. The properties of the binders are summarized in Appendix B, and the details of the tests used in this research can be found in references [6] and [7].

3 HT-BBR DATA REDUCTION

The HT-BBR can measure stiffness in “any” time and load ranges, subject to researchers’ discretion based on the specific binder and test temperature. The raw data obtained from the HT-BBR are in hex-decimals as shown in Figure 1, which is a part of an example of raw data in terms of “bits”. The first column is the load, the second records the deflection, the third presents the bath temperature, and the last represents the test status. The HT-BBR still follows the SHRP standard procedure. From the first “OK”, the test starts with one second loading followed by 30 seconds rest without loading. The second “OK” starts the real loading. The Hyper Terminal collects the data for every half second, so one test produces about 3600 sets of data for a half-hour loading time, which is saved in a text file as shown in Figure 1.

A computer program is created using Visual Basic in Microsoft Excel for the data reduction. It contains five modules: Module 1 – Input; Module 2 – Calibration of HT-BBR; Module 3 – Creep Stiffness Calculation for Each Temperature; Module 4 – Generation of Stiffness Isothermal Curves; Module 5 – Generation of Stiffness Master Curves.

3.1 Module 1 – Input

The primary input data for the data reduction include calibration file names, asphalt binder names, creep test file names, temperatures and loading times for the creep tests.

OK 3EF4 8378 B5D2 RLB 40E9 9CBE B5D2 RLB	OK 3F0D 8374 B5E2 RLB 4100 9CC1 B5E2 RLB
---	---

Figure 1. Part of an example of HT-BBR raw data.

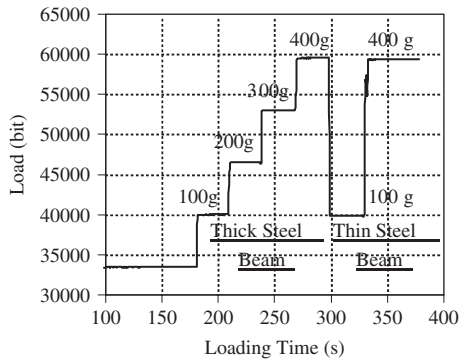


Figure 2. Load Calibration procedure (Husky 200-300A at -20°C).

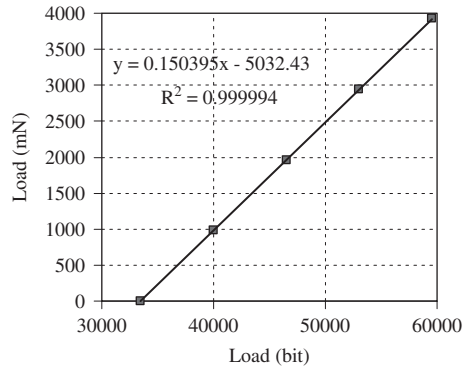


Figure 3. Load calibration result (Husky 200-300A at -20°C).

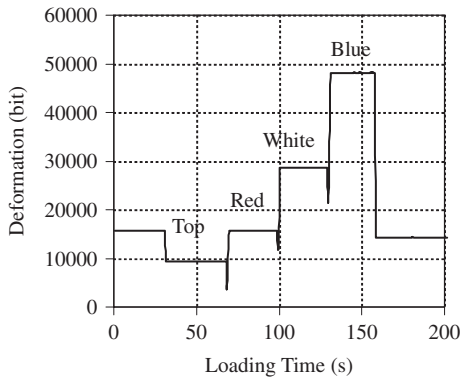


Figure 4. Deflection calibration procedure (Husky 200-300A at -20°C).

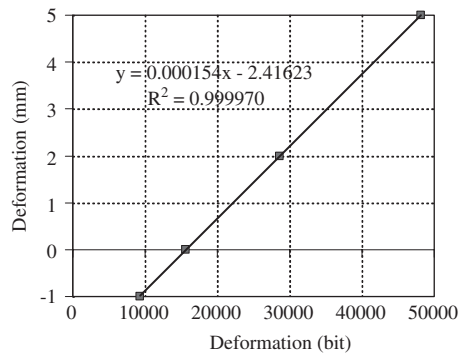


Figure 5. Deflection calibration result (Husky 200-300A at -20°C).

3.2 Module 2 – Calibration of HT-BBR

The HT-BBR calibration procedure is similar to that in a standard BBR test. But the calibration data is saved in a text file similar to Figure 1, and the data reduction process is needed for the calibration results. Module 2 primarily contains the following sub-procedures:

- Open a calibration text file and transform it into an Excel file.
- Transform the hexadecimal to decimal data (in terms of “bits”).
- Calibrate load (in terms of N/bit) and deflection (in terms of mm/bit).
- Plot calibration results (examples from Figure 2 to Figure 5). In Figure 4, the top gage corresponds to -1 mm; the red gage, 0 mm; the white gage, $+2$ mm; the blue gage, $+5$ mm.

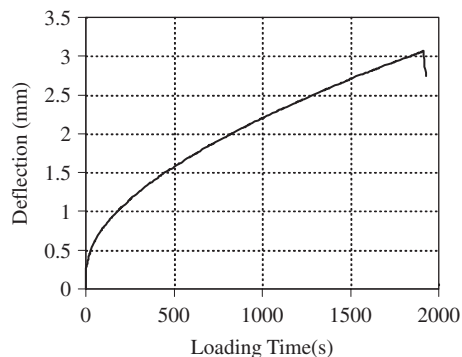


Figure 6. Plot from Module 3 (Husky 200-300A Specimen 2 at -20°C).

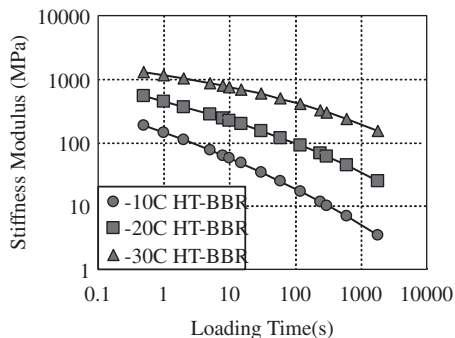


Figure 7. Stiffness isothermal curves (Husky 200-300A).

3.3 Module 3 – Calculation of creep stiffness for each temperature

This module primarily contains the following sub-procedures:

- Open a creep test data file and transform it into an Excel file.
- Change hexadecimal to decimal data (in terms of “bits”).
- Change decimal data in bits to data in engineering units: “N” for load and “mm” for deflection using the calibration results obtained in Module 2.
- Plot deflection vs. loading time (an example in Figure 6).
- Calculate stiffness modulus.

3.4 Module 4 – Generation of stiffness isothermal curves

This module collects the stiffness data from the Module 3 for all temperatures and then plots them into the isothermal curves as shown in Figure 7.

3.5 Module 5 – Generation of stiffness master curves

Module 5 uses the data from Module 4 and builds the master curves of the stiffness modulus. The following sub-procedures are created in this module: a) Open a file saved in Module 4; b) Calculate and plot shift factor $\log a_T$ vs. temperature; c) Generate and plot a master curve for each binder.

From Section 2, we found that each of the studied models of $\log a_T$ vs. T has its limitations in describing the tested relationship. Thus in this paper, a multi-branch linear regression (MBLR) is used to establish the relationship to more closely represent the testing result. This method assumes a linear relationship of $\log a_T$ vs. T within any two successive test temperatures. An example is given in Figure 8. An example master curve is shown in Figure 9.

4 IDT TEST DATA REDUCTION

The IDT creep test generated 15 text data files per mix in this study for 5 temperatures and 3 parallel specimens. Five modules were developed for the data reduction: Module 1 – Input; Module 2 – Plot of Raw Data; Module 3 – Compliance Calculation; Module 4 – Plots of Compliance Isothermal Curves and $\log a_T$ vs. T; Module 5 – Generation of Master Curves of Creep Compliance and Relaxation Modulus.

4.1 Module 1 – Input

The primary input includes raw data file names; binder names used in the mixes; IDT specimen thickness; temperatures; and loading times.

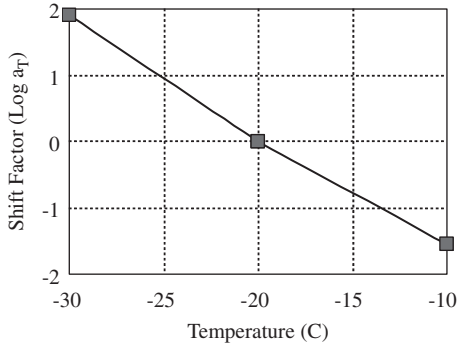


Figure 8. Multi-branch linear regression (Husky 200-300A, $T_{Ref} = -20^{\circ}\text{C}$).

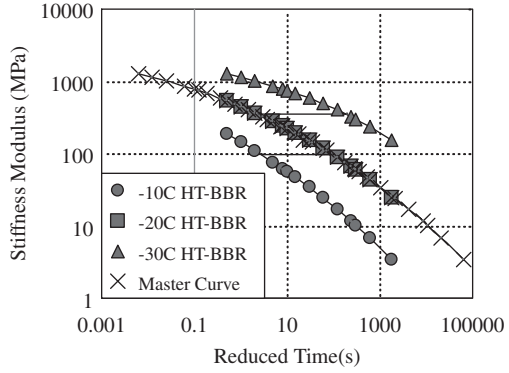


Figure 9. Stiffness master curve (Husky 200-300A, $T_{Ref} = -20^{\circ}\text{C}$).

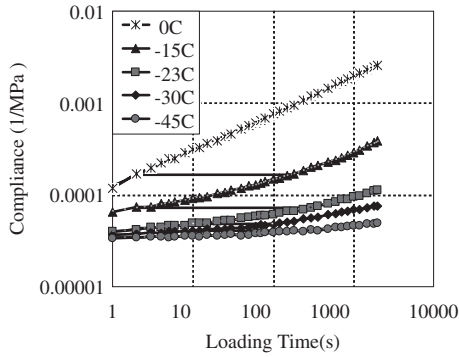


Figure 10. Isothermal curves (Husky 150-200A).

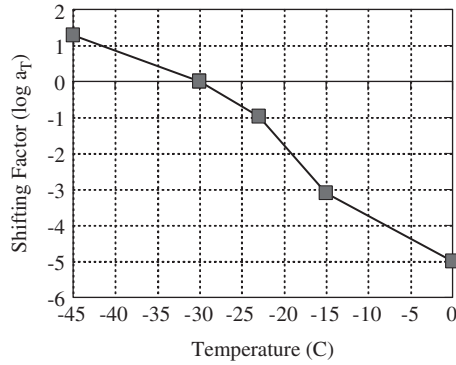


Figure 11. Multi-branch linear regression (Husky 150-200A, $T_{Ref} = -30^{\circ}\text{C}$).

4.2 Module 2 – Plot of raw data

This module transforms the raw data in text format into Excel format and plots the raw data for a preliminary examination. Each data file contains the following measurements: Load (kN), Stroke (mm), Vertical Deformation (VD) 1 (μm), VD 2 (μm), Horizontal Deformation (HD) 1 (μm), and HD 2 (μm). Here “1” and “2” represent the two faces of the IDT specimens.

4.3 Module 3 – Compliance calculation

This module calculates the normalized, the average and the trimmed means of deformations, the Poisson’s ratio (PR), and the creep compliance based on the AASHTO TP9 [11]. Compliance values were calculated with three considerations of PR: a constant at a time corresponding to one half (1000 seconds here) of the total loading time [11], varied values as tested, and a constant averaged through the whole logarithm loading time scale. It is found that the varied PR is more reasonable than the other two constant PRs. Thus, this study uses the varied PR for the compliance calculation.

4.4 Module 4 – Plot of compliance isothermal curves and shift factors

The isothermal curves of compliance are plotted in this module for each mix. An example is shown in Figure 10, in which the distances measured along the “log t” scale between the isothermal curves are also plotted. “log a_T vs. T” is then plotted as shown in Figure 11.

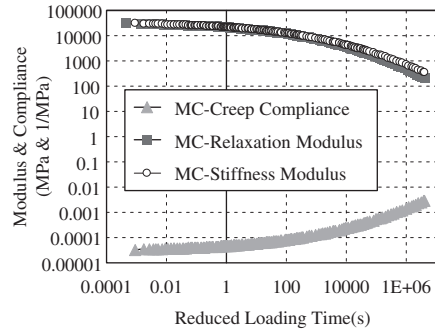


Figure 12. IDT master curves (Husky 150-200A at $T_{Ref} = -20^{\circ}\text{C}$).

The MBLR method as used for the binders is applied to establish the relationship of $\log a_T$ vs. T of the mixes. This means that the graph of $\log a_T$ vs. T is composed of line segments. Here $T_{Ref} = -30^{\circ}\text{C}$ because -20°C was not used in the IDT testing.

4.5 Module 5 – Master curves of compliance and of relaxation modulus

Since the stiffness master curves of the binders were created with $T_{Ref} = -20^{\circ}\text{C}$, the master curves (Figure 12) of the IDT compliance and the relaxation modulus of the mixes are also plotted at $T_{Ref} = -20^{\circ}$ for consistence. The relaxation modulus is calculated by the method described by Hopkins and Hamming [11]. In Figure 12, the stiffness, which is the reciprocal of the compliance, is also plotted for comparison. We can see that in short loading time region, the relaxation modulus is almost the same as the stiffness. As the loading time gets longer, the difference increases, but the stiffness is always larger than the relaxation modulus.

5 CONCLUSIONS

From this study, it is found that for the mixes, with the exception for 4%SBS and 6%SBS, the linear model has the best fit. For the binders, except for 2%EVA, the WLF equation fits the best. However, the multi-branch linear regression method can be used to best satisfy the test data. The developed data reduction methods in this paper can be used to systematically treat test data from HT-BBR and IDT testing for asphalt binders and mixes.

ACKNOWLEDGEMENTS

The testing was conducted in the University of Calgary under the guidance of Dr. Ludo Zanzotto and Dr. Jiri Stastna. Their comments and suggestions on the paper are highly appreciated. The author would also like to acknowledge the financial supports from the National Science and Engineering Research Council of Canada and from Husky Energy Ltd.

REFERENCES

- [1] McCrum, N.G., Buckley, C.P., and Bucknall, C.B. (1997), *Principles of Polymer Engineering*, 2nd Edition, Oxford Science Publications, Oxford University Press, New York.
- [2] Ferry, J.D. (1980), *Viscoelastic Properties of Polymers*, 3rd Edition, Wiley, New York.
- [3] Bahia, H.U., Anderson, D.A., and Christensen, D.W. (1992), "The Bending Beam Rheometer: A Simple Device for Measuring Low-Temperature Rheology of Asphalt Binders," *Journal of the Association of Asphalt Paving Technologists*, Vol. 61, pp. 117–153.

- [4] Bahia, H.U., Zeng, M., and Nam, K. (2000), "Consideration of Strain at Failure and Strength in Prediction of Pavement Thermal Cracking," *Journal of the Association of Asphalt Paving Technologists*, Vol. 69, pp. 497–539.
- [5] AASHTO, "Method for Determining the Flexural Creep Stiffness of Asphalt Binder Using the Bending Beam Rheometer", AASHTO TP1-93.
- [6] Bai, B.Q., Zanzotto, L., Stastna, J. "Low Temperature Testing on Some PMA Binders and Mixes and Predictions of Stiffness and Failure Stress of Asphalt Mixes", *Road Materials and Pavement Design – an International Journal*, 5/SI, 227–258 (2004).
- [7] Bai, B.Q. "Low Temperature Properties of PMA Binders and Mixes and Thermal Cracking Prediction of Asphalt Pavement", Ph.D. Dissertation, University of Calgary, Alberta (2005).
- [8] Roque, R., Hiltunen, D.H., Buttlar, W.G., Farwana, T. "Development of the SHRP Superpave Mixture Specification Test Method to Control Thermal Cracking Performance of Pavements", ASTM Special Technical Publication, 1265, 55–73 (1994).
- [9] Buttlar, W.G., Roque, R., Reid, B. "Automated Procedure for Generation of Creep Compliance Master Curve for Asphalt Mixtures", *Transportation Research Record*, No. 1630, 28–36 (1998).
- [10] Christensen, D. "Analysis of Creep Data from Indirect Tension Test on Asphalt Concrete", *Journal, Association of Asphalt Paving Technologists*, 67, 458–489 (1998).
- [11] AASHTO, "Test Method for Determining the Creep Compliance and Strength of Hot Mix Asphalt (HMA) Using the Indirect Tensile Test Device", AASHTO TP9-96.
- [12] Hopkins, I.L., Hamming, R.W. "On Creep and Relaxation", *Journal, Applied Physics*, 28, (8), 906–909 (1957).

APPENDIX A. GRAPHS OF $\log a_T$ vs. T FOR MIXES ($T_{REF} = -30^{\circ}C$)

The binder's graphs and all the linear model's fitting graphs are not provided here due to the limited number of pages.

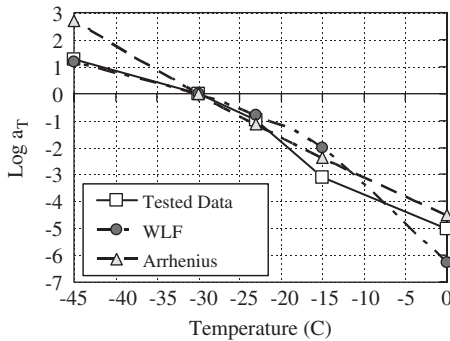


Figure A1. Husky 150-200A Mix.

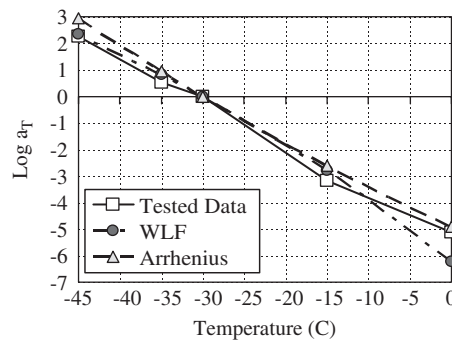


Figure A2. Husky 200-300A Mix.

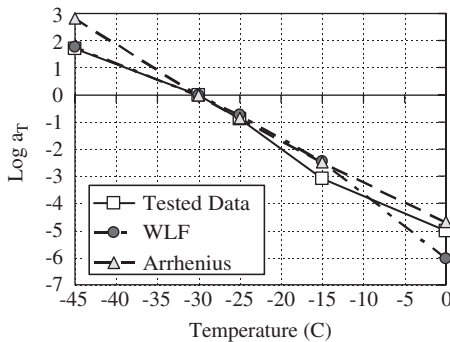


Figure A3. 2%EVA Mix.

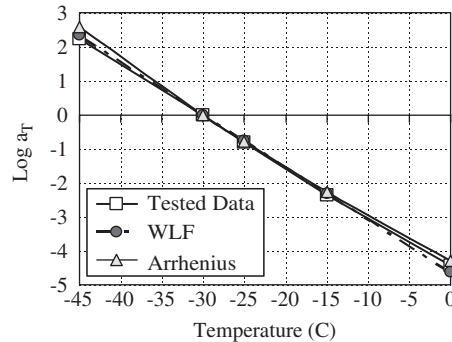


Figure A4. 4%EVA Mix.

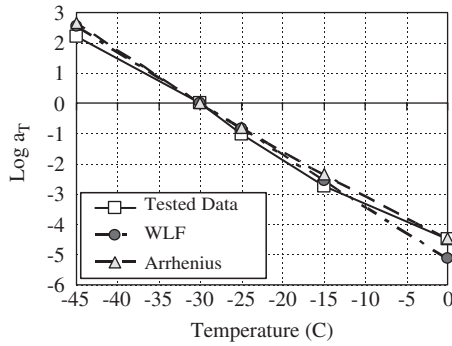


Figure A5. 2% SBS Mix.

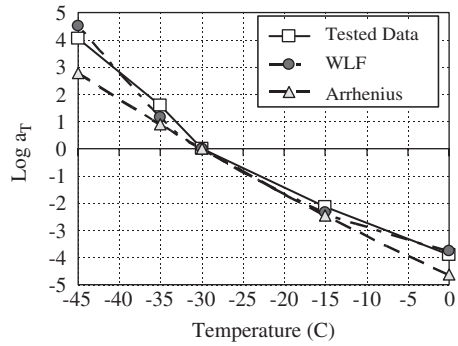


Figure A6. 4% SBS Mix.

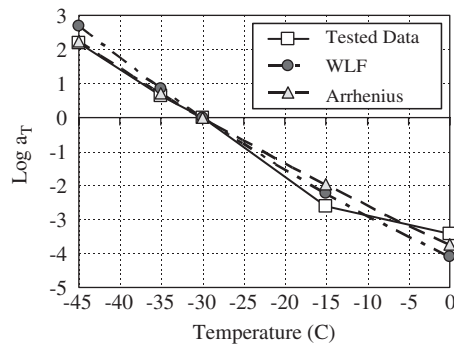


Figure A7. 6% SBS Mix.

APPENDIX B. SUMMARY OF THE PROPERTIES OF THE ASPHALT BINDERS

Properties	Husky ¹ 150-200A	Husky 200-300A	2%EVA ⁽²⁾	4%EVA
Original Binder				
Dynamic shear ($G^*/\sin\delta$ @ Temp) (kPa @ °C, 10 rad/s)	1.05@58	1.02@52	1.59@52 1.01@57 0.96@58	1.03@61
After RTFO⁽³⁾				
Dynamic shear ($G^*/\sin\delta$ @ Temp) (kPa @ °C, 10 rad/s)	1.94@60 2.18@59	2.47@52	4.22@52 2.31@57	2.08@64 2.43@63
After PAV⁽⁴⁾				
Temperature (°C)	100	90	90	100
Dynamic shear ($G^*/\sin\delta$ @ Temp) (kPa @ °C, 10 rad/s)	3870@16	2545@13	4794@10	4051@10
Creep Stiffness (MPa, 60s)	292	197 265	224	248 228 243
m-Value (60s)	0.32	0.36 0.32	0.34	0.31 0.30 0.30
Temp(°C) for creep	-22	-24 -26	-24	-26 -24 -25
SHRP Grading (MP1)	PG 58-28	PG 52-34	PG 52-34	PG 58-34
Actual Grading	PG 58-32	PG 52-36	PG 57-36	PG 61-34

Properties	2%SBS ⁽⁵⁾			4%SBS		6%SBS	
Original Binder							
Dynamic shear	1.2@58			1.71@64		2.04@70	
(G*/sinδ @ Temp), (kPa @ °C, 10 rad/s)	1.08@59			1.05@69		1.03@78	
After RTFO							
Dynamic shear	3.14@58			3.14@64		2.97@70	
(G*/sinδ @ Temp) (kPa @ °C, 10 rad/s)	2.53@60 2.18@61			2.32@67		2.43@72	
After PAV							
Temperature (°C)	100			100		100	
Dynamic shear (G*/sinδ @ Temp) (kPa @ °C, 10 rad/s)	3601@13			1360@19		722@25	
Creep Stiffness (MPa, 60s)	202	258	303	154	244	168	288
m-Value (60s)	0.33	0.33	0.31	0.35	0.32	0.34	0.29
Temp(°C) for creep	-24	-26	-27	-24	-27	-24	-27
SHRP Grading (MP1)	PG 58-34			PG 64-34		PG 70-34	
Actual Grading	PG 59-36			PG 67-37		PG 72-36	

(1) "Husky 200-300A" and "Husky 150-200A" are based on the CGSB binder specification.

(2) "2%EVA" = Ethylene Vinyl Acetate, 2% weight concentration over the base binder Husky 200-300A.

(3) SBS = Styrene Butadiene Styrene tri-block copolymer.

(4) RTFO = Rolling Thin Film Oven test.

(5) PAV = Pressure Aging Vessel.

For polymer modification of asphalt (PMA), only Husky 200-300A was used as the base binder. For the IDT testing, only one asphalt mix design is applied for all the asphalt binders using the same aggregate type, gradation, and binder content. This mix design was based on the asphalt binder Husky 150-200A. The details of the testing and research are presented in Reference [7].

An experimental investigation of the fracture mechanics of bitumen and asphalt

O. Portillo & D. Cebon

Cambridge University, Cambridge, UK

ABSTRACT: Systematic 3-point bend tests were conducted on bitumen and idealised asphalt mix specimens in order to develop fracture mechanism maps classifying the brittle, ductile and transition response of the materials as a function of temperature and load rate. Analysis of experimental data was carried out in terms of the stress intensity factor, K_{IC} , fracture energy, G_{IC} , and J -integral, J_{IC} . Fracture characterization parameters obtained from this experimental program showed good agreement with other test data reported in the literature. Three different failure regimes were identified for both bitumen and asphalt mixtures.

1 INTRODUCTION

Fracture cracking is an important failure mechanism in roads designed for lower traffic volumes. Cyclic thermal and traffic loads are the principal sources of pavement stress which contribute to crack formation and crack growth. In order to improve the serviceability and design methods of pavements, the nature of the process of crack initiation and growth must be better understood. Therefore, the overall objective of this paper is to investigate the fracture mechanics of bitumen and asphalt mixes.

Bituminous mixes are used extensively in surface layers of pavements. It is believed that the loading conditions that contribute to crack initiation and propagation in asphalt pavements are a combination of repetitive wheel loads and thermal cycling effects. A key barrier to improving the durability of asphaltic materials used in roads and predicting road lives accurately is the current lack of fundamental understanding of the micromechanics of crack initiation and growth in asphalts.

In order to understand fatigue cracking of asphalt mixes, a useful first step is to study the fracture processes in pure bitumen and 'idealised' asphalt mixes during monotonic loading. Idealised asphalt mixes contain pure bitumen mixed with carefully controlled distributions of aggregate particle sizes and shapes. Once the monotonic behaviour has been characterised, understanding the cyclic (fatigue) behaviour of realistic mixes becomes more tractable.

Genin & Cebon (2000) conducted a series of experiments to characterize the fracture behaviour of a stressed, confined pre-crack in a layer of bitumen over a range of temperatures. The specimens were designed to study the crack growing in bitumen that is positioned between two rocks and to investigate the fracture mechanism in the neighbouring rocks as the crack grows. The confined-crack specimens were stressed in Mode I by pulling the central piston from the cup-like cylinder, this type of loading is analogous to that a crack-like flaw would be stressed by the separation of rocks situated above and below the crack. Confined-crack specimens of 50 pen bitumen were tested at temperatures ranging from -20°C to 30°C under a nominal strain rate of 0.1 sec^{-1} . This strain rate is representative of the loading rate that asphalt pavement undergoes during service. Load-line deflection curves were recorded. The researchers found that void coalescence and/or void growth were the mechanism of failure for specimens tested at high temperatures. However,

at low temperatures the mechanism of failure was a combination of brittle fracture in the bitumen and fracture along the interface between the bitumen and the cup-like aluminium cylinder.

Harvey & Cebon (2003; 2005) adapted testing methods commonly used for adhesives to investigate the fracture properties of pure bitumens. They conducted an extensive tensile testing program on bitumen films to map out the fracture behaviour. The test temperature ranged from -30°C to 30°C and nominal strain rates in the range 0.03 to 100 s^{-1} . Two types of specimen configuration that simulate Mode I cracking in bitumen films were used: double cantilever beam specimens (DCB) and butt joints. Load-displacement curves were measured. The fracture mechanisms in bitumen films were summarized in a plot of normalized toughness $G/2h$ (fracture energy per unit volume) against temperature-compensated strain rate, over 14 decades. Three main regimes of behaviour were observed: ductile, brittle and transition. In the ductile regime, $G/2h$ was found to have a power-law dependence on the strain rate, whereas in the brittle regime, $G/2h$ was found to be independent of strain rate.

Some authors such as Li & Marasteanu (2006), Kim & Hussein (1997) and Sulaiman & Stock (1995) also reported the change in fracture toughness as temperature changes. For instance, Kim & Hussein (1997) performed tests on asphalt mixes consisting of an asphalt binder graded with penetration as 85/100 at temperatures ranging from -5°C to -30°C at intervals of 5°C . They found that the fracture toughness increased from -5°C to -15°C and decreased thereafter. They stated that the evolution of fracture toughness with temperature was the result of the balance between two factors: the strengthening grip of the asphalt matrix and the micro damage due to the differential shrinkages of asphalt matrix and aggregates.

Most of the research found in the literature about fracture of asphaltic materials is concerned with fracture at low service temperatures, where brittle failure prevails. The aim of this experimental investigation is to study the fracture behaviour of bitumen and bituminous mixes subjected to a wide range of temperatures and load rates, and to develop a failure mechanism map to characterize the response of the materials similar to the failure mechanism map for bitumen films reported by Harvey & Cebon (2003).

2 FRACTURE CHARACTERIZATION PARAMETERS

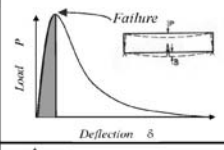
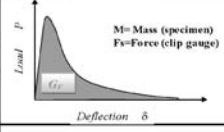
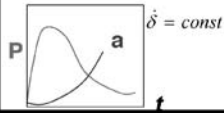
Cracking in flexible asphalt pavements has received considerable attention for many years and fracture mechanics concepts have been introduced to investigate the fracture behaviour. Several parameters have been proposed for characterizing the fracture behaviour of asphalt materials (Table 1). These include: the stress intensity factor, K , fracture energy, G , contour integral, J , and energy rate line integral, C^* . The range of material behaviours applicability to these fracture parameters is listed in Table 1.

For the case of a three-point single edge notched bend specimen (SE(B)), see Figure 1, the stress intensity factor K can be calculated using the relationship derived by Srawley (1976) which is based on the boundary collocation method and has an accuracy of $\pm 0.5\%$. This relationship is also recommended by the ASTM E399 standard (2005). The maximum load on the load-deflection curve is used to compute the critical stress intensity factor, K_{IC} , as shown in Table 1.

The strain energy release rate, G (or “crack driving force”) is defined as the rate of change of potential energy with respect to the crack area in a linear elastic material, Irwin (1948). For a three-point bend specimen, SE(B), the total energy required to fracture the beam is equal to the area under the load versus load-line deflection response plus the work done by the self-weight of the beam and by the clip gauge, see Figure 1. The appropriate expression of the specific fracture energy G_{IC} (fracture energy divided by the projected area of uncracked ligament) is given in Table 1.

Rice (1968) and Begley & Landes (Begley 1972; Landes 1972) showed that the J line integral is equivalent to the potential energy change with crack growth. Rice et al. (1973) developed a simple method for estimating J as a function of displacement for a single specimen. Later, Sumpter & Turner (1976) suggested an alternative method for evaluating J , which requires only one specimen and one crack length. Table 1 shows the expression to calculate the J-integral for a SE(B) specimen,

Table 1. Fracture characterization parameters and formulas for the single edge notch SE(B) specimen.

PARAMETER	APPLIES TO	FORMULA	NOTES
Stress Intensity Factor K_{IC}	Linear Elastic Materials	$K_{IC} = \frac{PS}{BW^{3/2}} Y(a/W)$ $Y(a/W) = \frac{3\left(\frac{a}{W}\right)^{3/2} \left[1.99 - \frac{a}{W} \left(1 - \frac{a}{W} \right) \left(2.15 - 3.93 \frac{a}{W} + 2.7 \left(\frac{a}{W} \right)^2 \right) \right]}{2 \left(1 + 2 \frac{a}{W} \right) \left(1 - \frac{a}{W} \right)^{3/2}}$	 <p>Failure</p> <p>Load P</p> <p>Deflection δ</p>
Fracture Energy G_{IC}	Linear Elastic Materials	$G_{IC} = \frac{\int_0^{\delta_{max}} P(\delta) d\delta + \frac{1}{2} Mg \delta_{max} + \int_0^{\Delta_{max}} F_s d\Delta}{B(W-a)}$	 <p>Load P</p> <p>Deflection δ</p> <p>M = Mass (specimen) F_s = Force (clip gauge)</p>
J_{IC}-Integral	Elastic-Plastic Materials	$J_{IC} = \frac{2(U_e + U_p)}{B(W-a)} = \frac{2U_e}{B(W-a)}$	<p>U_c = Total critical potential energy</p> <p>3-Point SE(B) $S = 4W$ and $0.45 \leq a/W \leq 0.65$</p>
C^*-Integral	Time-Dependent (Viscoplastic) Materials	$C^* = -\frac{1}{B} \left(\frac{\partial}{\partial a} \int_0^{\delta} P d\dot{\delta} \right)_{\dot{\delta}}$	 <p>$\dot{\delta} = const.$</p> <p>P</p> <p>a</p> <p>t</p>

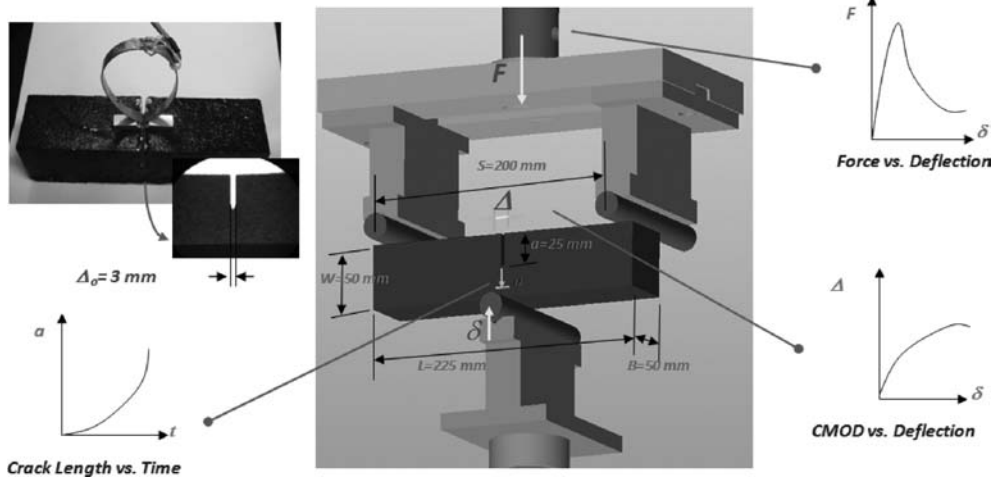


Figure 1. 3-Point bend experimental set up. Specimen dimensions meet the requirements of the ASTM E399 standard (2005).

tested over a span S of $4W$ and has $0.45 \leq a/W \leq 0.65$. The potential energy U_c is computed until the measured peak load in the load-line deflection curve. The standard test procedure, ASTM E813, recommends that the equation given in Table 1 can be used to calculate the J -values for a SE(B) configuration.

Landes & Begley (1976), Ohji et al. (1976), and Nikbin et al. (1976) independently suggested what became known as the path-independent energy rate C^* -integral, to correlate crack growth rate behaviour for materials undergoing steady-state creep fracture. The parameter estimation methods used to calculate the J -integral for elastic-plastic bodies can also be extended to define the C^* -integral from measured P vs. load-line displacement rate curves. Therefore, C^* can be established in terms of a power release rate, see Table 1. In this work, crack length was measured as a function of time, which enables the C^* -integral to be evaluated.

3 EXPERIMENTAL TESTING

3.1 *Material specification*

Pure Bitumen: A 50 pen pure bitumen (penetration grade: 53 dmm, softening point: 53.5°C) was used to prepare the SE(B) specimens.

Bitumen Mix: The same 50 pen bitumen was used for the mix preparation. The mix consisted of pure bitumen and 64% volume fraction of subspherical sand particles between 150 and 300 μm in size.

3.2 *Specimen preparation*

A rectangular mould was manufactured and used to cast and compact the specimens, the mould was designed to manufacture three point bend specimens with geometric dimensions given by the ASTM E399 standard test method. A lubricant made of natural soap and glycerine was applied to the inside surface of the mould to prevent sticking of the asphalt mixture samples, and a Teflon film was attached on the walls of the mould to prevent the pure bitumen specimen from adhering to the mould. In addition, the bottom plate of the mould was covered with aluminium foil which helped to release the specimen from the crack initiator.

For asphalt specimen manufacture, the mix of bitumen and aggregate was heated to melt the bitumen at a temperature of 160°C for 45 minutes. The mix was then well stirred and poured into the mould. A hydraulic press was used to compact the specimen in one layer by single plunger compression at a pressure of 10 MPa. After the mix was compacted, it was allowed to cool down to room temperature for 2 hours. The specimen was then slowly pushed out of the mould and stored in a freezer at subzero temperature, the specimen was kept inside the freezer until it was tested. Similarly, pure bitumen was melted and poured into the mould. Once the mould was filled with the right amount of bitumen, it was placed into the freezer to reach subzero temperature for 3 hours. After that, the specimen was removed from the mould and stored in the freezer. X-Ray pictures were taken to verify the crack profile of the specimens and their density, see Figure 1. Two aluminium holders were glued on the surface of the specimen for the purpose of attaching the crack mouth opening clip gauge.

3.3 *Testing procedure*

A 3-point bend fixture was designed in order to carry out fracture tests on pure bitumen and bituminous mixes, see Figure 1. An environmental chamber fitted to the testing machine was used to control the test temperature. The environmental chamber had a resolution of $\pm 0.5^\circ\text{C}$, and testing temperatures ranged from -30°C to room temperature. A 2 kN load cell was used to measure force-time and force-displacement histories. The specimens were brought to the desired temperature by keeping them inside the chamber for sufficient time to reach equilibrium prior to the test.

A spring steel chip gauge was manufactured to measure the crack mouth opening displacement of the 3-point bend specimens, see Figure 1. This novel clip-gauge was designed for measuring large displacements that are beyond the measurement range of commercial clip gauges. The clip gauge displayed a linear relationship between the voltage and displacement for a range of temperatures and over the desired range of crack mouth opening measurements.

Two props were used to support the ends of the specimen when it was placed in the 3-point bend fixture and they were removed just before the start of the test. This prevented distortion of the beams as a result of creep due to self-weight. All tests were conducted under axial constant displacement rate control.

Crack length analysis was conducted by using an optical system. The system comprised an analogue video camera located outside the environmental chamber which photographed the test specimen through a window. A flashing LED light signal was used to synchronize the time signals recorded on the video and the servo-hydraulic testing machine. Care was taken to illuminate the

surface of the specimen using a photographic light located inside the environmental chamber. A “frame grabber” adapter converted the analog video signal from the camera to a digital video in a personal computer. A commercial movie maker program was utilized to extract frames from the test video, the images were then stored and crack propagation profile and crack length measurements for each frame were carried out by an image digitization program written in MATLAB. All test data crack images and pedigree information were stored in a single integrated material data management system, Portillo et al. (2007).

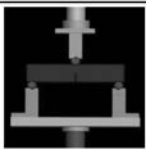
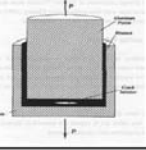
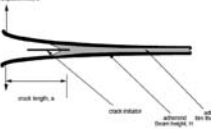
4 EXPERIMENTAL RESULTS FOR PURE BITUMEN

Fracture 3-point bend tests on pure bitumen specimens were conducted at temperatures ranging from -30°C to 0°C . It was not possible to perform tests at higher temperatures because bitumen beams exhibited excessive creep deformation due to self-weight. It was found that the fracture energy G_{IC} of pure bitumen lay in the range of $2\text{--}13\text{ J/m}^2$ at a temperature of -20°C and $5\text{--}11\text{ J/m}^2$ at a test temperature of -30°C , whereas the critical stress intensity factor K_{IC} ranged from $0.01\text{--}0.05\text{ MPa m}^{1/2}$ at a temperature of -20°C and $0.02\text{--}0.1\text{ MPa m}^{1/2}$ at -30°C . These results correlate well with the Mode I fracture toughness range reported by Genin & Cebon (2000) in the confined crack configuration test (K_{IC} was found to be $0.02\text{--}0.05\text{ MPa m}^{1/2}$ at a test temperature of -20°C), and the toughness range found by Harvey & Cebon (2003) in double cantilever beams and butt joints (G_{IC} was found to be $5\text{--}10\text{ J/m}^2$ at -30°C). Table 2 summarizes these results. It should be pointed out that different specimen test configurations (3-point bend, double cantilever beam and confined-crack specimens) give equivalent values of K_{IC} and G_{IC} .

Crack arrest was observed in some bitumen specimens, Figure 2a shows a typical force-displacement curve exhibiting crack arrest. It was observed the crack propagated as the load increased and eventually stopped growing as result of a reduction in the applied load in a displacement rate control test. The crack propagated again once the load reached a sufficient level. Crack arrest was also reported by Harvey & Cebon (2005) in double cantilever beams, Figure 2b. Further analysis of the fracture behaviour at the arrest points is needed.

In order to compare experimental results from tests at different temperatures and load rates, a temperature-compensated crack mouth opening strain rate \dot{E}_T is defined in similar

Table 2. Comparison of test results for bitumen specimens.

Author	Test	Test Temperature	K_{IC} (MPa m ^{1/2})	G_{IC} (J/m ²)
<i>Portillo and Cebon</i>	3Point Bend SE(B) 	-20 °C	0.01 - 0.04	2 - 13
		-30 °C	0.06 - 0.1	5 - 11
<i>Genin and Cebon (2000)</i>	Plug Pull-Out 	-20 °C	0.02 - 0.05	
<i>Harvey and Cebon (2005)</i>	DCB 	-30 °C		5 - 10

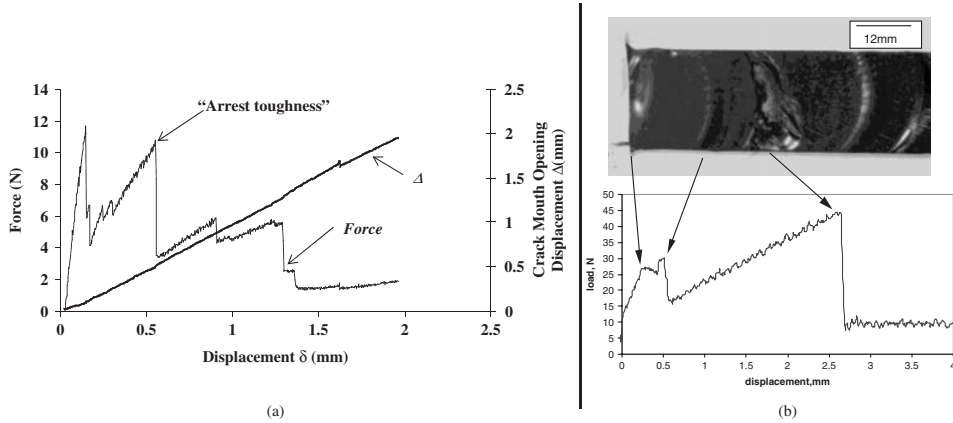


Figure 2. (a) 3-point bend SE(B) specimen, test temperature: -20°C , displacement rate: 0.01 mm/s . (b) DCB specimen, (Harvey & Cebon, 2005).

manner to the temperature-compensated strain rate proposed by Harvey & Cebon (2005). \dot{E}_T is expressed as:

$$\dot{E}_T = \frac{\dot{\Delta}}{\Delta_0} \exp \left[\frac{-Q}{R} \left(\frac{1}{T_0} - \frac{1}{T_1} \right) \right] \quad (1)$$

where $\dot{\Delta}$ is the crack mouth opening displacement rate and Δ_0 is the initial notch width, Q represents the thermal activation energy, R is the universal gas constant, T_0 and T_1 stand for the reference temperature and test temperature respectively.

In this study the $\dot{\Delta}$ was computed from the Δ vs. *time* test characteristic curve, specimens were manufactured with a Δ_0 of 3 mm (see Figure 1), Q is $228 \times 10^3\text{ J mol}^{-1}$ as per Cheung & Cebon (1997) for 50 pen bitumen, R is equal to $8.314\text{ Jmol}^{-1}\text{K}^{-1}$ and the reference temperature was chosen to be 273 K.

Fracture energy results for the tests on pure bitumen are presented in the form of a failure mechanism map similar to the failure mechanism maps in viscoelastic films reported by Harvey & Cebon (2003, 2005). Ductile, brittle and transition regimes of behaviour are observed in the map, Figure 3. The failure mechanisms are dependent on temperature and crack mouth opening rate. In the ductile region, the fracture energy increases with in a power law relationship until a critical value. It then decreases rapidly through the transition region for temperature compensated crack mouth opening rates ranging from 0.03 s^{-1} to 0.35 s^{-1} . In the brittle region, the fracture energy is largely independent of and is considerable lower than in the ductile region, indicating that the energy needed to initiate fracture is less at high displacement rates and lower temperatures, as expected.

A more comprehensive matrix of tests is planned in future to corroborate this behaviour.

5 EXPERIMENTAL RESULTS FOR IDEALIZED ASPHALT MIXES

An experimental program of 3-point bend testing on idealized asphalt mixes was conducted to map out the fracture behaviour over a temperature range from -30°C to 30°C . Typical force vs. deflection curves for 4 specimens tested at different temperatures and the same displacement rate of 0.01 mm/s are shown in Figure 4a. The plots illustrate the temperature dependence of the asphalt mix samples (temperature range from -30°C to 0°C). It is observed that the peak force increases with temperature. The load-line displacement curve of the specimen tested at 0°C in Figure 4a shows crack arrest in the vicinity of the peak load. At lower temperatures, crack growth develops

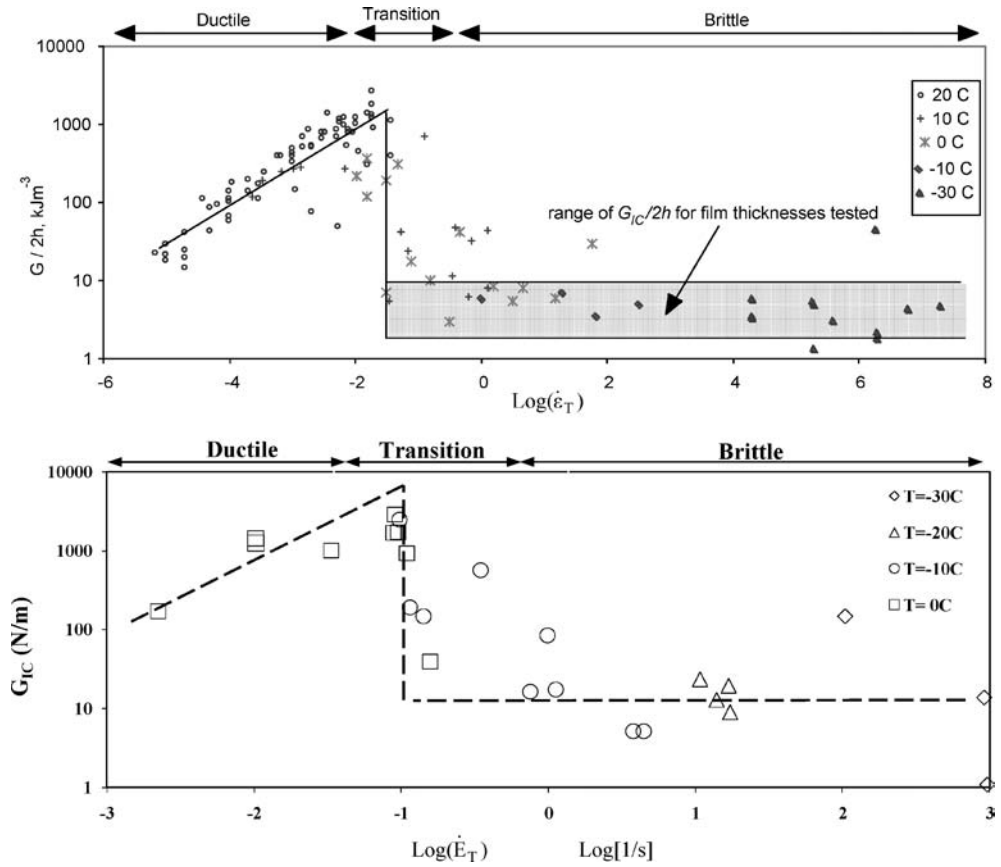


Figure 3. Mechanism map for pure bitumen.

(a) Fracture energy per unit volume $G/2h$ of DCB bitumen specimens, Harvey & Cebon (2005).

(b) Specific fracture energy of SE(B) bitumen specimens.

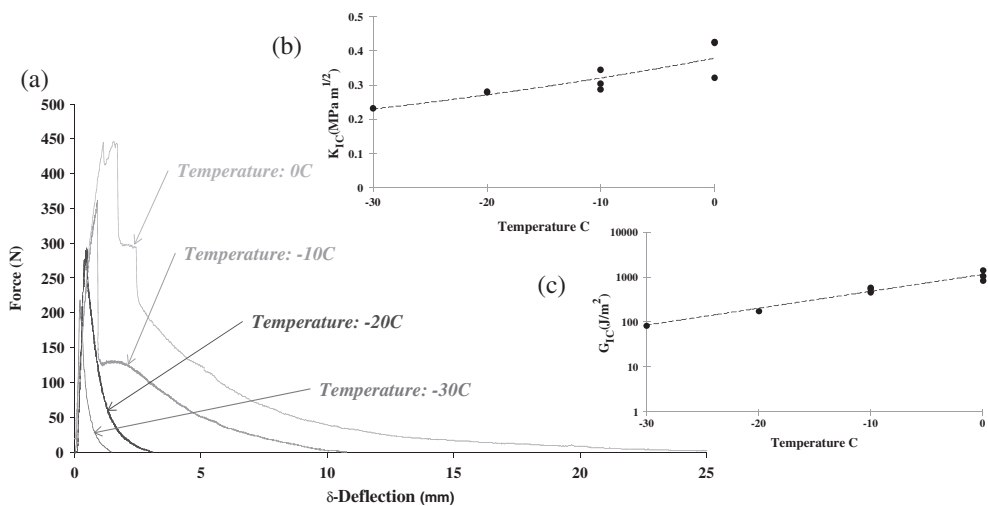


Figure 4. (a) Force vs. deflection plots for asphalt specimens tested at a displacement rate of 0.01 mm/s, showing the effects of Temperature. (b) Fracture toughness vs. Temperature. (c) G_{IC} vs. Temperature.

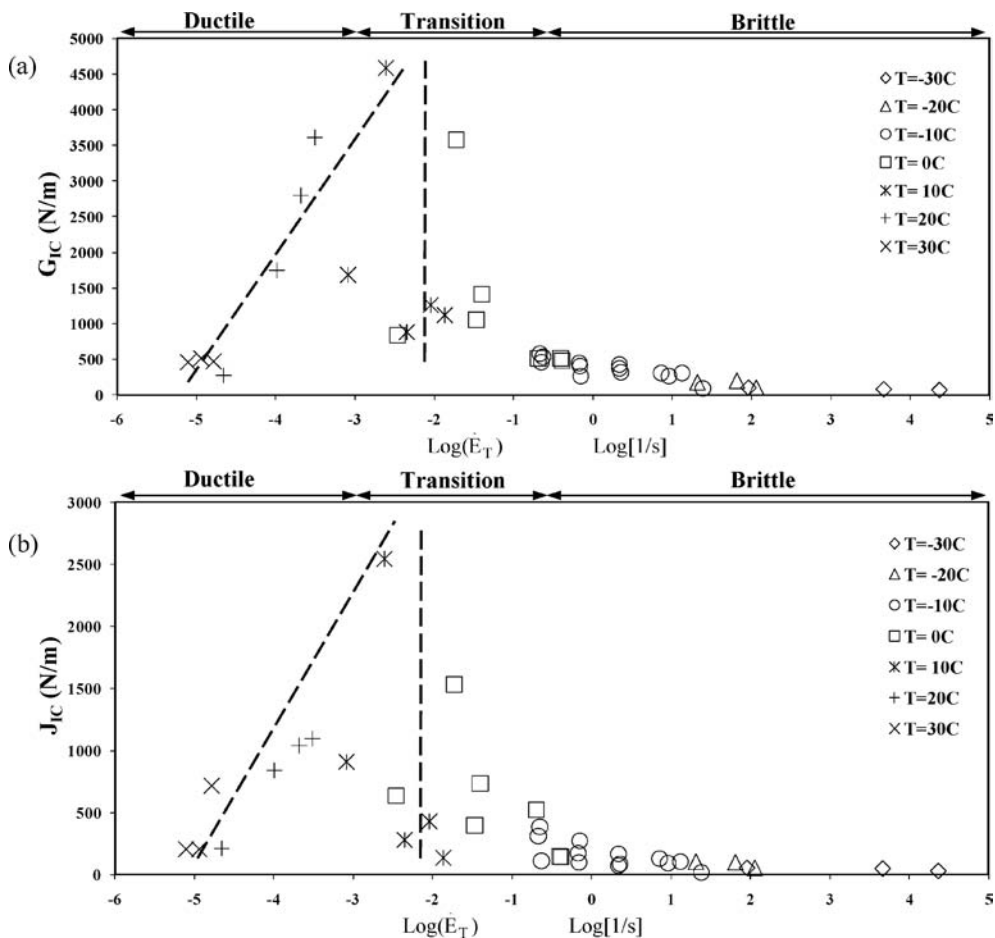


Figure 5. Mechanism map for asphalt mix specimens. (a) G_{IC} vs. $\text{Log}(\dot{\epsilon}_T)$. (b) J_{IC} vs. $\text{Log}(\dot{\epsilon}_T)$.

in a smooth fashion showing more brittle behaviour and less energy is required to propagate the crack. A crack arrest mechanism was also reported by Genin & Cebon (2000) at low temperatures in asphalt concrete. More analysis is needed to better understand the arrest behaviour of bituminous mixes.

Values of the critical stress intensity factor K_{IC} correlate the increase of peak force with temperature as depicted in the K_{IC} vs. *Temperature* plot for these tests, Figure 4b. It can also be seen that the area under load-deflection response increases with temperature, therefore fracture energy G_{IC} increases as well with test temperature for the same displacement rate condition, the plot G_{IC} vs. *Temperature* in Figure 4c illustrates this relationship. Similar findings can be drawn from the J -integral, indicating that less potential fracture energy is needed to propagate the crack at lower temperatures for the same rate of load application of 0.01 mm/s.

A failure mechanism map plotting strain energy release rate as a function of the temperature-compensated crack mouth opening strain rate (Eq. 1) in asphalt mix specimens is presented in Figure 5. It again displays three main regimes of failure behaviour: ductile, brittle and transition. In the ductile regime, the fracture energy increases as the temperature decreases from 30°C to 0°C. Conversely, the fracture energy of the mix decreased as the temperature decreases from -10°C to -30°C in the brittle region, a softening mechanism can also be observed. The ductile to brittle transition is located at temperatures between 10°C and 0°C or $0.002 \text{ s}^{-1} < \dot{\epsilon}_T < 0.04 \text{ s}^{-1}$, although there is some evidence of strain rate sensitivity up to $\dot{\epsilon}_T = 1 \text{ s}^{-1}$. A similar description of the failure

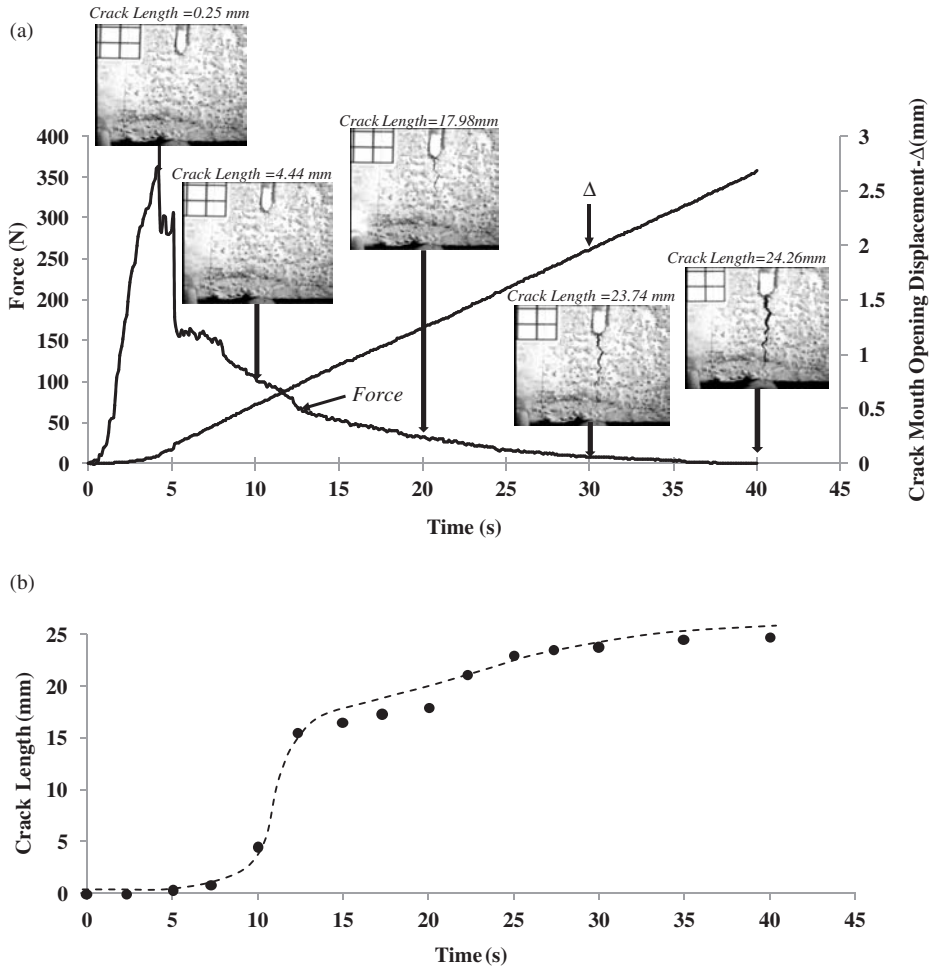


Figure 6. Behaviour of an asphalt SE(B) specimen, the sample was tested at a temperature of -20°C and displacement rate of 0.05 mm/s . (a) Force and Δ vs. Time with superimposed photographs of the specimen. (b) Crack length vs. Time for the same test.

behaviour in asphalt was found using the J-integral as a fracture characterization parameter. It was also observed that the J-integral decreases as the temperature decreases from -10°C to -30°C (brittle regime) indicating that resistance to crack growth is lower at lower temperatures. J_{IC} and G_{IC} are very similar at high values of \dot{E}_T , as expected.

Crack length measurements were conducted using the optical system described in the previous section. Details of the process of image acquisition, length analysis and data storage can be found in Portillo et al. (2007). Figure 6 depicts some images of the crack growth as a function of time superimposed in a typical Force and Δ vs. time curve for an asphalt specimen. It is interesting to observe that the strains are small at the peak load when fracture occurs ($t \sim 4\text{ s}$) and the crack is not visible until the deformation is larger and the force is low ($t \sim 10\text{ s}$).

6 CONCLUSIONS

1. 3-point bend tests were performed on pure bitumen and asphalt mix to characterize the fracture behaviour over a wide range of temperatures and loading rates. Evaluation of fracture toughness

of test specimens was conducted in terms of the stress intensity factor, K_{IC} , fracture energy, G_{IC} , and J-integral, J_{IC} .

2. Fracture characterization parameters obtained from this test program correlated favourably other experimental data reported in the literature.
3. A wide range of crack behaviour was observed including brittle, ductile, transition and crack arrest. These regimes can be seen clearly on the failure mechanism maps for both pure bitumen and asphalt materials.
4. Crack length has been measured as a function of time. On-going work will evaluate the C*-integral parameter to determine the best fracture modelling approach in each regime of behaviour.
5. Further laboratory work of fracture tests at more temperatures and loading rates is planned to add more points to the failure mechanism maps.

REFERENCES

- ASTM Standard E 399. 2005. Standard Test Method for Plane-Strain Fracture Toughness of Metallic Materials.
- Begley, J.A. & Landes, J.D. 1972. The J-Integral as a Fracture Criterion. *ASTM, STP 514, American Society for Testing and Materials* 1–20.
- Genin, G.M. & Cebon, D. 2000. Fracture Mechanics in Asphalt Concrete. *Road Materials and Pavement Design* 1(4): 419–450.
- Harvey, J.A.F. & Cebon, D. 2003. Failure Mechanism in Viscoelastic Films. *Journal of Materials Science* 38: 1021–1032.
- Harvey, J.A.F. & Cebon, D. 2005. Fracture Tests on Bitumen Films. *Journal of Materials in Civil Engineering* 17(1): 99–106.
- Irwin, G.R. 1948. Fracture Dynamics, Fracturing of Metals. A. S. f. Metals. Cleveland, Ohio: 147–166.
- Kim, K.W., & Hussein, M.El. 1997. Variation of Fracture toughness of Asphalt concrete under Low Temperatures. *Construction and Building Materials* 11: 403–411.
- Landes, J.D. & Begley, J.A. 1972. The Effect of Specimen Geometry on Jic. *ASTM, STP 514, American Society for Testing and Materials*. Philadelphia, PA.: 24–29.
- Landes, J.D. & Begley, J.A. 1976. A Fracture Mechanics Approach to Creep Crack Growth. *Mechanics of Crack Growth, ASTM STP 590, American Society for Testing Materials*: 128–148.
- Li, X. & Marasteanu, M.O. 2006. The Role of Temperature and Binder Type on the Fracture Resistance of Asphalt Mixtures at Low Temperatures. *Road Materials and Pavement Design* 3: 331–348.
- Nikbin, K.M., Webster, G.A. & Turner, C.E. 1976. Relevance of Nonlinear Fracture Mechanics to Creep Crack Growth. *ASTM, STP 601, American Society for Testing Materials*: 47–62.
- Ohji, K., Ogura, K. & Kubo, S. 1976. Creep Crack Growth Propagation Rate in SUS 304 Stainless Steel and Interpretation in Terms of Modified J-Integral. *Transactions, Japanese Society of Mechanical Engineers* 42: 350–358.
- Portillo, O., Johnson, G., Lam, W. & Cebon, D. 2007. Automated Analysis and Data Handling for Asphalt Fracture Experiments. Cambridge, UK., CUED/C-MATS/TR.262.
- Rice, J.R. 1968. A Path Independent Integral and the Approximate Analysis of Strain Concentration by Notches and Cracks. *Journal of Applied Mechanics* 35: 379–386.
- Rice, J.R., Paris, P.C. & Merkle, J.C. 1973. Some Further Results of J-Integral Analysis and Estimates. *ASTM, STP 536, American Society for Testing and Materials* 231–245.
- Srawley, J. E. 1976. *International Journal of Fracture Mechanics* 12(3): 205–213.
- Sulaiman, S.J. & Stock, A.F. 1995. The Use of Fracture Mechanics for the Evaluation of Asphalt Mixes. *AAPT Association of Asphalt Paving Technologist*: 500–531.
- Sumpter, J.D.G. & Turner, C.E. 1976. Method for Laboratory Determination of Jic. *Cracks and Fracture, ASTM STP 601, American Society for Testing and Materials*: 3–18.

Using semi-analytical finite element method to evaluate stress intensity factors in pavement structure

S. Hu, X. Hu & F. Zhou

Texas Transportation Institute, Texas A&M University, College Station, Texas, USA

ABSTRACT: The stress intensity factor is a very important fracture mechanics parameter for the analysis of cracked bodies such as cracking in pavement structure. It provides the basis for crack propagation, fatigue life prediction, and consequently for pavement design. Although three-dimensional finite element methods are able to determine these values correctly, the cost of solutions in terms of computation time and complexity increases significantly compared with two-dimensional method and, on occasion, overtaxes the available computer capability when the pavement structure is too complicated.

To address the aforementioned problem, a specific stress intensity factor calculating program named *SA-CrackPro* was developed for pavement structures and discussed. It is essentially a two-dimensional FE program which incorporated the semi-analytical method. Theoretically it has comparable accuracy of three-dimensional result but much faster speed and much less computer resource requirement. Based on the typical pavement structure and the standard single axle load, the accuracy of program was verified by comparing with ANSYS software.

1 INTRODUCTION

It has long been accepted that cracking is one of the major distress modes observed in hot-mix asphalt (HMA) concrete pavement. To analyze the crack propagation problem, one of the most important fracture mechanics parameter used for this purpose is the stress intensity factor (SIF) value. It is well known that SIF is not simply a material problem, but also is highly related to pavement structure, traffic loading and environmental conditions. Therefore, the determination of SIF values for generalized pavement loading and environmental and geometric configurations requires numerical solutions, such as finite element (FE) method.

In general, there are two categories of FE tools available to compute the SIF values. First is the general purpose FE package such as ANSYS. It is no doubt about the capability of these FE packages. However, the complexity of these FE programs and consequently the time-consuming user training process often prevent pavement engineers from using them. The other category FE tools are those specifically developed for pavement analysis. For example, CRACKTIP was developed for thermal cracking by Lytton and his associates (Chang et al. 1976) at the Texas Transportation Institute. The CRACKTIP is a two-dimensional (2D) FE program, and has been successfully used to develop the SIF model and predict the cracking propagation (Lytton et al. 1993). However, it is well known that, the difference between 2D plane strain conditions and the three-dimensional (3D) nature of a cracked geometry and loading, leads to a gross overestimation. Another pavement SIF computing program named CAPA (Computer Aided Pavement Analysis) was developed by Delft University of Technology in 1990s (Scarpas et al. 1993, Scarpas et al. 1996). The CAPA-3D program has some special functions that were created to specifically address the reflective cracking issue, such as special elements for simulating interface and interlayer, automatic finite element re-meshing technique to simulate crack propagation, etc. All of these functions make the CAPA-3D

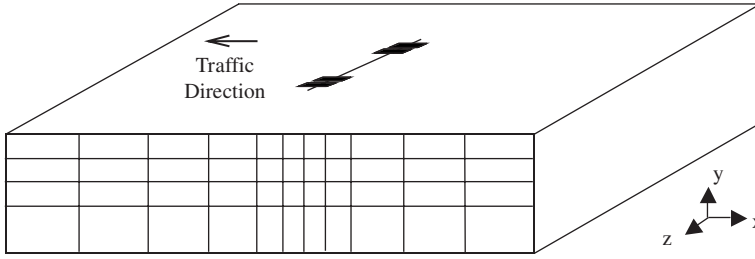


Figure 1. Pavement structure geometry and load mode.

a good option for reflective cracking analysis and prediction. Unfortunately, due to 3D character, its high hardware and execution time demands render it suitable primarily for research purposes.

Thus it's in great need to find means to both improve the calculating speed and reduce the resource requirement without the loss of accuracy. One of the methods that seem most promising for this purpose is the method known as the Semi-Analytical FE method (Zienkiewicz 1977). For a cracked pavement structure problem (see Figure 1), the geometry and material properties of structure layers do not vary along z-direction, only the load terms exhibit a variation in that direction, preventing the use of such simplifying assumptions as a 2D plane strain case. However, by making use of orthogonal functions and Fourier series, problem of such class can be simplified as a series of 2D plane strain cases. This is what called the semi-analytical method. Built on this method, a new program named *SA-CrackPro* was specifically developed for pavement SIF evaluation.

In the following sections, this paper first presents two key components of the *SA-CrackPro*: the semi-analytical FE method and SIF evaluation method. Then a typical pavement structure under a standard single axle load was used to verify the accuracy of the *SA-CrackPro* by comparing with the ANSYS (ANSYS 2004) software. Finally, a brief summary and conclusion is provided at end of this paper.

2 DESCRIPTION OF SEMI-ANALYTICAL FINITE ELEMENT METHOD

The basic procedure in the FE formulation is to express the element coordinates and element displacements in the form of interpolations using the natural coordinate system of the element. So is Semi-analytical FE method.

In *SA-CrackPro*, the 8-node isoparametric elements (in XY plane, see Figure 2) are used, and the displacement functions are as following:

$$\begin{aligned}
 u(x, y, z) &= \sum_{l=1}^L \sum_{k=1}^8 N_K u_{kl} Z_{1l}(z) \\
 v(x, y, z) &= \sum_{l=1}^L \sum_{k=1}^8 N_K v_{kl} Z_{2l}(z) \\
 w(x, y, z) &= \sum_{l=1}^L \sum_{k=1}^8 N_K w_{kl} Z_{3l}(z)
 \end{aligned} \tag{1}$$

where l identifies the l^{th} term of the Fourier series and L is the number of terms considered; $Z_{1l}(z)$, $Z_{2l}(z)$, $Z_{3l}(z)$ are 3 analytical function along z direction, in *SA-CrackPro*, they are:

$$Z_{1l}(z) = Z_{2l}(z) = \text{Sin} \frac{l\pi z}{a} \quad Z_{3l}(z) = \text{Cos} \frac{l\pi z}{a} \quad 0 \leq z \leq a \tag{2}$$

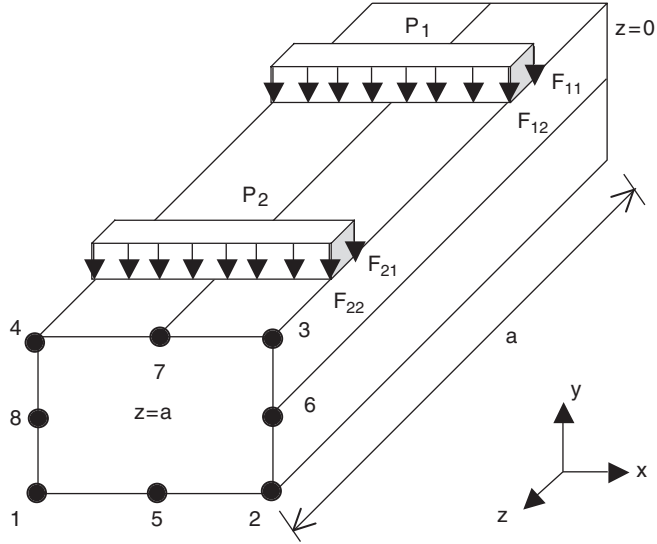


Figure 2. 8-node isoparametric element in XY plane and tire load sketch.

N_k is the same interpolation function used to express displacement for the two-dimensional problem in XY plane; u_{kl}, v_{kl}, w_{kl} are the k^{th} nodes displacements along x, y, z direction respectively in the l^{th} terms.

To determine the element contribution to the equation minimizing the potential energy, a typical sub-matrix of the element stiffness matrix $[k]^e$ is:

$$[k^{lm}]^e = \iiint_{vol} [B^l]^T [D] [B^m] dx dy dz \quad (3)$$

A typical term for the force vector becomes:

$$[F^l]^e = \iiint_{vol} [N^l]^T \{p\}^l dx dy dz \quad (4)$$

where l, m identify the l^{th} and m^{th} terms of Fourier series respectively; $[B]$ is strain-displacement matrix. N^l and $\{p\}^l$ are l^{th} interpolation function and l^{th} load function respectively.

As pointed out by Zienkiewicz (1977), the matrix given in Equation 3 will contain the following integrals:

$$\begin{aligned} I_1 &= \int_0^a \sin \frac{l\pi z}{a} \cos \frac{m\pi z}{a} dz \\ I_2 &= \int_0^a \sin \frac{l\pi z}{a} \sin \frac{m\pi z}{a} dz \\ I_3 &= \int_0^a \cos \frac{l\pi z}{a} \cos \frac{m\pi z}{a} dz \end{aligned} \quad (5)$$

The integrals exhibit the orthogonal property which ensures that:

$$I_2 = I_3 = 0 \quad \text{for } l \neq m \quad (6)$$

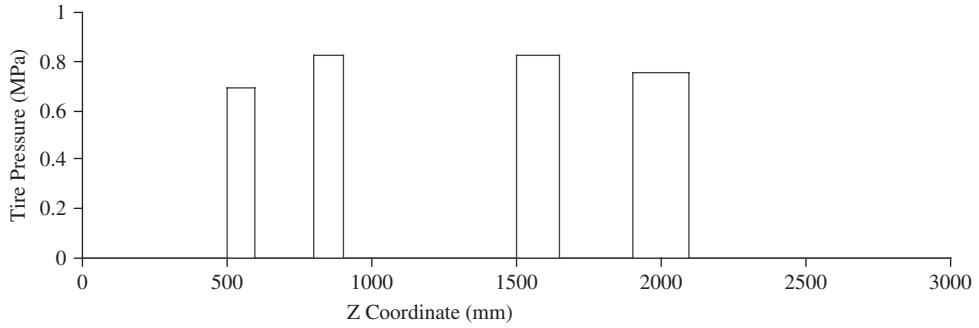


Figure 3. Assumed 4 tires load shape and location.

The orthogonal property causes the matrix $[k]^e$ to become diagonal. The final assembled equations for the problem have the form:

$$\begin{bmatrix} [K^{11}] & & & \\ & [K^{22}] & & \\ & & \dots & \\ & & & [K^{LL}] \end{bmatrix} \begin{Bmatrix} \delta^1 \\ \delta^2 \\ \dots \\ \delta^L \end{Bmatrix} + \begin{Bmatrix} F^1 \\ F^2 \\ \dots \\ F^L \end{Bmatrix} = 0 \quad (7)$$

Equation 7 shows that the large system of equations splits into L separate problems. Zienkiewicz (1977) points out that this property is of extreme importance, because, if the expansion of the loading factors involves only one term for a particular harmonic, then only one set of simultaneous equations need to be solved. Thus, what was originally a three-dimensional problem now has been reduced to a two-dimensional one with consequent reduction of computational effort.

Another important aspect of the semi-analytical FE method is to select appropriate load terms to ensure that the applied load shape is correctly simulated in the z domain. For example, in pavement analysis applications with a single axle with dual tires, the load terms can be represented by the following expansion:

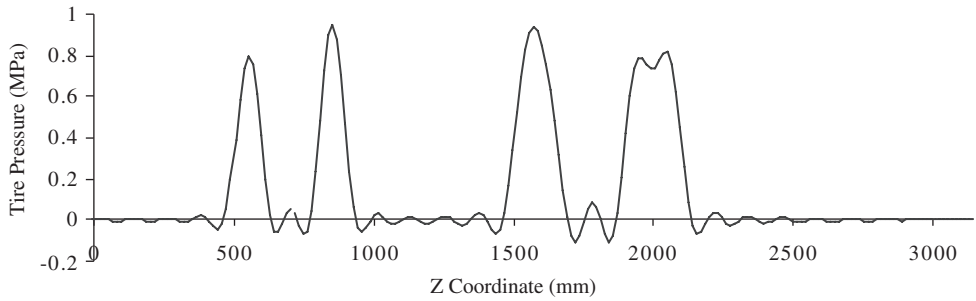
$$F(z) = \sum_{i=1}^L b_n \text{Sin}\left(\frac{l\pi z}{a}\right) \quad (8)$$

with:

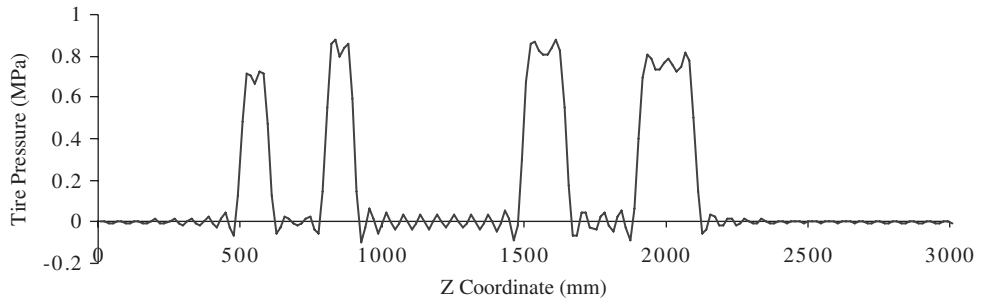
$$b_n = \sum_{i=1}^4 \left(\frac{2P_i}{l\pi} \right) \left[\text{Cos}\left(\frac{l\pi F_{i1}}{a}\right) - \text{Cos}\left(\frac{l\pi F_{i2}}{a}\right) \right] \quad (9)$$

where P_i is the i^{th} tire load pressure; F_{i1} is the z coordinates where the i^{th} tire load starts; F_{i2} is z coordinate where the i^{th} tire load ends. Figure 2 showed the load sketch, for clarity, only 2 tires were displayed.

To demonstrate the Fourier expansion effect under different terms, Figure 3 showed assumed 4 tires with different tire pressure values and locations. Then based on the calculation results using Equation 8 and Equation 9, Figure 4a and 4b showed the 50 terms and 100 terms Fourier series expansion effect respectively. Theoretically, more terms, more exact simulation effect can be obtained. In *SA-CrackPro*, the 70 terms were adopted because the determined SIF values change very little after 70 terms, see Figure 5.



(a) Load shape after 50 terms Fourier series expansion.



(b) Load shape after 100 terms Fourier series expansion.

Figure 4. Fourier series expansion results of 50 terms (a) and 100 terms (b).

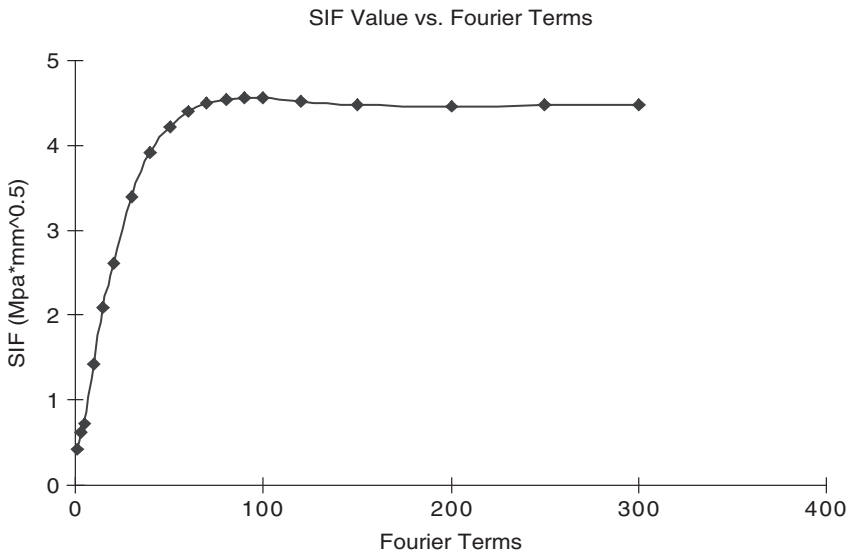


Figure 5. SIF values vs. Fourier Terms.

3 DESCRIPTION OF SIF EVALUATION METHOD

To determine SIF value, a fundamental difficulty is that the polynomial basis functions used for most conventional elements cannot represent the singular crack-tip stress and strain fields predicted by the fracture mechanics theory. So a number of researchers investigated special finite element

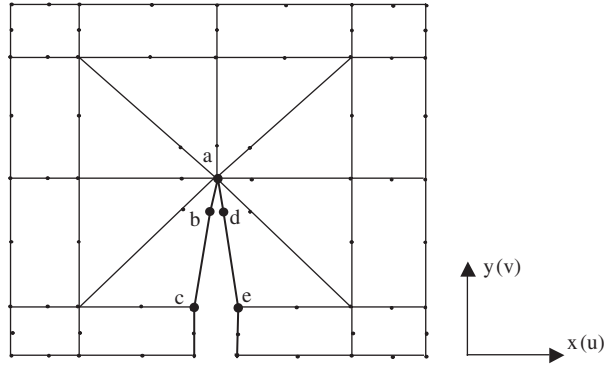


Figure 6. Finite elements meshing around crack tip.

formulations that incorporate singular basis functions or stress intensity factors as nodal variables, while successful, these special purpose elements are not available in most general-purpose FE programs and thus are used very infrequently.

A significant milestone in this area was the “quarter-point” elements discovered by Henshell and Shaw (1975) and Barsoum (1976). These researchers showed that the proper crack-tip displacement, stress, and strain fields can be modeled by standard quadratic order isoparametric finite elements if one simply moves the element’s mid-side node to the position one quarter of the way from the crack tip to the far end of the element. With these elements standard and widely available, FE programs can be used to model crack tip fields accurately with only minimal preprocessing required. The same approach was implemented in the program *SA-CrackPro*.

The expressions for the SIF’s using 2D plane strain assumptions are as following (Ingraffea et al. 2003). The finite elements meshing around crack tip was showed in Figure 6.

$$K_I = \frac{G\sqrt{2\pi}}{\sqrt{r_{a-b-c}}(4-4\mu)} [4(u_d - u_b) + (u_c - u_e)] \quad (10)$$

$$K_{II} = \frac{G\sqrt{2\pi}}{\sqrt{r_{a-b-c}}(4-4\mu)} [4(v_d - v_b) + (v_c - v_e)] \quad (11)$$

where r_{a-b-c} = distance from crack tip point a to point c; K_I, K_{II} = SIF value for Mode I (opening crack mode) and Mode II (shearing crack mode) respectively; G = shearing modulus; μ = Poisson’s ratio; and u_i, v_i = the x, y displacements at point i .

Since *SA-CrackPro* used analytical FE method, it means under the given Fourier term and given analysis XY plane in the pavement structure, the response is subject to two-dimensional plane strain law. So the equation 10 and 11 can be directly used after determine the displacements of related points. This method is simple and clearly related to the typical loading mode such as bending load (related with opening cracking mode) and shearing load (related with shearing cracking mode). Also it shows pretty stable and reliable ability when adopting different mesh size.

4 PROGRAM VERIFICATION

As discussed before, due to the reduction in dimensional analysis compared to 3D FE method, the Semi-analytical method has much less nodes and smaller number of equations and matrix with much narrower bandwidth. Also, it has quite small amount of input data and output data because of the smaller number of mesh lines. Consequently not only does it need much shorter computing time for solution, but also it is much easier to prepare input data file and to clean up the output result file. All these advantages have been confirmed both theoretically and practically by many

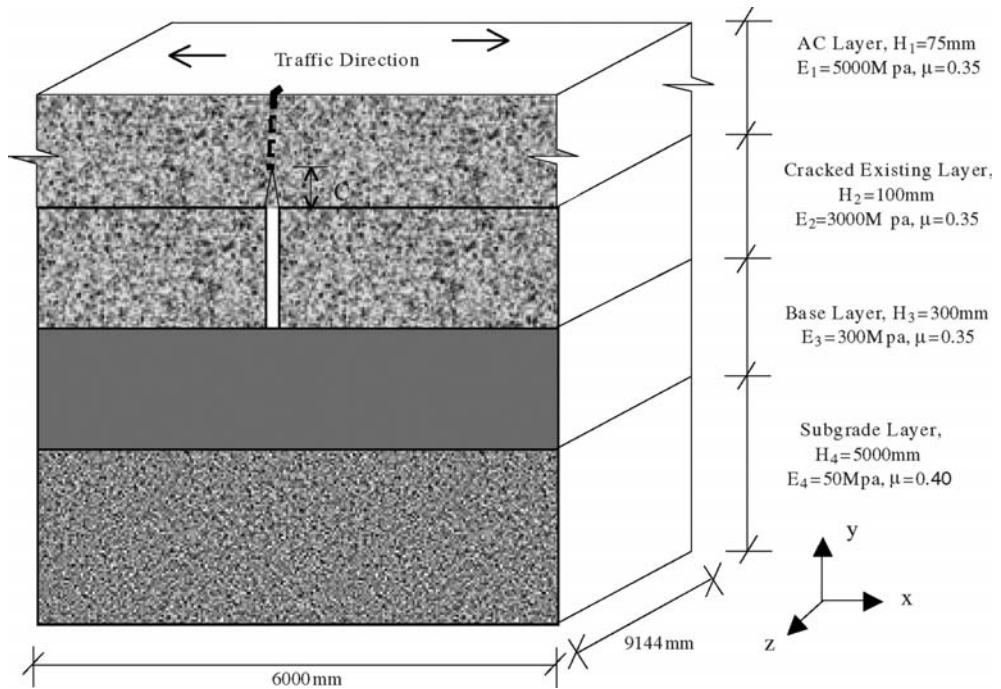


Figure 7. Typical pavement structure and parameters for verification study.

researchers (Zienkiewicz 1977, Cheung & Tham 1998, Fritz 2002). So in this paper, the major concern for the program verification is the accuracy of the results of *SA-CrackPro* compared with a 3D FE program.

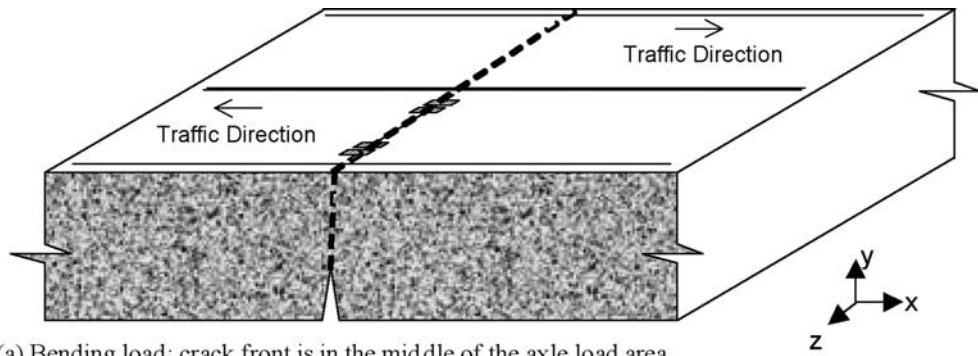
4.1 Typical pavement structure for verification

Figure 7 shows the typical two-lane with shoulder pavement structure for verification study. There are totally 4 layers, Asphalt Concrete Overlay (AC layer), Cracked Existing layer with 2mm width joint, Base layer and Subgrade. The material property and thickness of each layer are also noted in the figure. There are five different crack length values (C), which are 7.5 mm, 22.5 mm, 37.5 mm, 52.5 mm and 67.5 mm respectively.

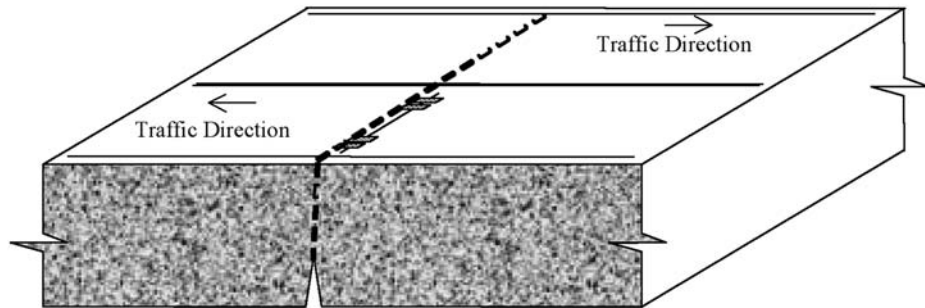
To verify the accuracy of *SA-CrackPro*, studies were conducted on two type cases: one is comparison of ANSYS 3D results with semi-analytical results under exactly the same 3D load form; the other is comparison of ANSYS 2D plain strain results under 2D load form with *SA-CrackPro* semi-analytical results under equivalent 3D load form (the load that covered the full pavement width with the same tire pressure as 2D load pressure value). Both cases will consider the bending and shearing load with different crack length values. The load form is a standard 18-kip(80KN)single axle dual tires load, and the tire pressure is 0.689 MPa (100 PSI).

4.2 Case 1: Comparison of SA-CrackPro results with ANSYS 3D results

Figure 8 showed bending and shearing load form used both in ANSYS 3D software and *SA-CrackPro*. Figure 8a is the bending mode which means this load only will cause the mode I cracking (opening cracking mode), so only the K_I values exist and K_{II} values equal to zero. Figure 8b is the shearing load mode which will potentially both cause the mode I and Mode II cracking, but the mode II cracking is dominant, mode I cracking is not as critical as compared with



(a) Bending load: crack front is in the middle of the axle load area.



(b) Shearing load: crack front is at the edge of the axle load area.

Figure 8. Typical load form of bending (a) and shearing (b).

Table 1. SIF value comparison results between SA-CrackPro and ANSYS-3D.

Crack Length (mm)	K_I (MPa* mm ^{0.5})			K_{II} (MPa* mm ^{0.5})		
	SA-CrackPro	ANSYS 3D	Error (%)	SA-CrackPro	ANSYS 3D	Error (%)
7.5	1.724	1.641	4.8	2.560	2.694	5.3
22.5	0.280	0.278	0.7	3.482	3.658	5.1
37.5	-2.115	-1.959	7.4	4.512	4.569	1.3
52.5	-5.786	-5.401	6.7	5.736	5.796	1.0
67.5	-13.652	-12.446	8.8	8.485	8.191	-3.5

the bending load mode. So in this paper, for bending load mode, the K_I values were compared, and for shearing load mode, the K_{II} values were compared.

The comparison results were showed in Table 1.

4.3 Case 2: Comparison of two-dimensional plain strain and semi-analytical result

Figure 9 showed load mode used in ANSYS 2D calculation (Figure 9a and 9b) and in SA-CrackPro calculation (Figure 9c and 9d). It is obviously that under such load form, theoretically the 3D results should be equal to the 2D results, because in this situation, 3D cases are qualified for the simplification as 2D plain strain cases. For the same reason as case 1, only the K_I values were compared for the bending load mode, and only the K_{II} values were compared for the shearing load mode. The comparison results were showed in Table 2.

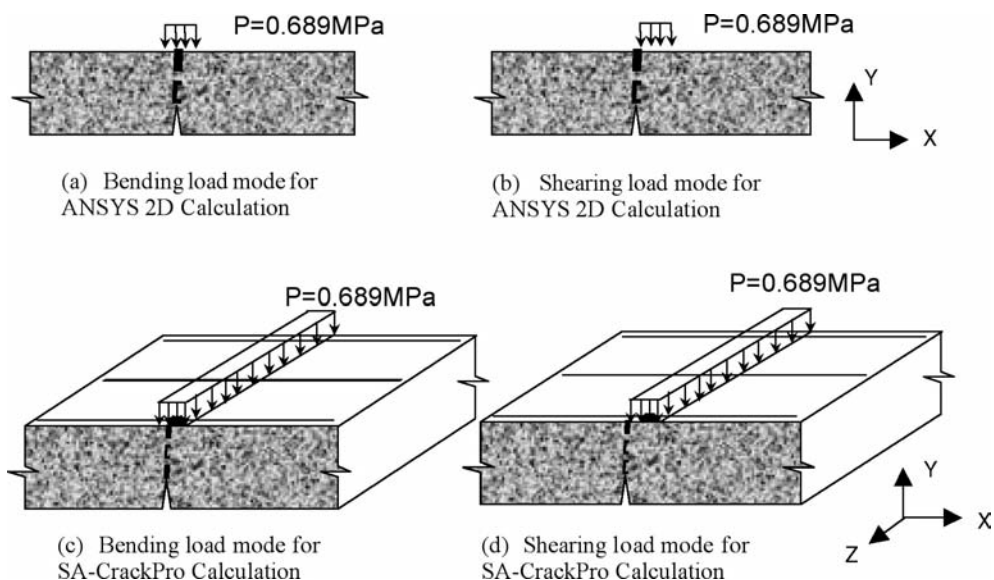


Figure 9. 2D plain strain cases of bending load (a) and shearing load (b) vs. equivalent 3D bending load (c) and shearing load (d).

Table 2. SIF value comparison results between SA-CrackPro and ANSYS-2D.

Crack Length (mm)	K_I (MPa* mm ^{0.5})			K_{II} (MPa* mm ^{0.5})		
	<i>SA-CrackPro</i>	ANSYS 2D	Error (%)	<i>SA-CrackPro</i>	ANSYS 2D	Error (%)
7.5	4.271	3.917	-8.3	4.632	4.821	4.1
22.5	0.217	0.197	-9.4	6.030	6.068	0.6
37.5	-6.055	-6.068	0.2	7.581	7.624	0.6
52.5	-15.782	-15.458	-2.1	9.532	9.751	2.3
67.5	-38.344	-36.854	-3.9	14.304	15.233	6.5

From the study of the two cases, it can be concluded that:

- Both cases indicate that the SIF values calculated by *SA-CrackPro* conformed to the calculation of ANSYS results. The average errors are less than 5%.
- The theoretical relationship between 3D and 2D plain strain simplification for Case 2 further confirmed the correctness of the *SA-CrackPro* results.
- The big difference between Case 1 and Case 2 (see Table 1 and Table 2) showed that when consider normal vehicle load, 3D results can not be substituted by 2D results. This explained the necessity of 3D analysis and also highlighted the value of *SA-CrackPro*.

5 SUMMARY AND CONCLUSIONS

This paper proposed using Semi-analytical method to evaluate SIF values in cracked pavement structures. The specific program *SA-CrackPro* was developed and discussed. The accuracy of the program was verified by comparison with the ANSYS software. Two cases were conducted for the verification. One is comparison of ANSYS 3D results with *SA-CrackPro* results under the real

vehicle load form; the other is comparison of ANSYS 2D plain strain results under 2D load form with *SA-CrackPro* results under equivalent 3D load form (the load that covered the full pavement width with the same tire pressure as 2D load pressure value). Both cases indicated that the SIF values calculated by *SA-CrackPro* conformed to the calculation of ANSYS results. Also, the big difference between the two cases showed that when consider real vehicle load, 3D results can not be substituted by 2D results during SIF calculation. This explained the necessity of 3D analysis and also highlighted the value of *SA-CrackPro*. With this verified *SA-CrackPro* program, SIF under various traffic loading conditions and pavement structures can be easily evaluated. As one of the potential applications, the *SA-CrackPro* program has been used to perform large scale pavement SIF calculations and then to develop SIF regression models for different research projects including the TxDOT project 0-5123 “Integrated Asphalt (Overlay) Mixture Design, Balancing Rutting and Cracking Requirement”, and the NCHRP project 1-41 “Models for Predicting Reflection Cracking of Hot-Mix Asphalt Overlays”.

REFERENCES

- ANSYS 9.0. 2004. User Manual.
- Barsoum, R.S. On the Use of Isoparametric Elements in Linear Fracture Mechanics. *International Journal Numerical Methods in Engineering*, Vol. 10, 1976, pp. 25–37.
- Chang, H. S., Lytton, R. L. & Carpenter, S. H. 1976. *Prediction of Thermal Reflection Cracking in West Texas*, Texas Transportation Institute. Research Report 18-3, Study 2-8-73-18.
- Cheung, Y. K. & Tham, L. G. 1998. *The Finite Strip Method*, CRC Press, Boca Raton, FL.
- Henshell, R.D. & Shaw, K.G. 1975. Crack tip elements are unnecessary. *International Journal for Numerical Methods in Engineering*, Vol. 9, pp. 495–507.
- Fritz J. Jooste. 2002. Flexible Pavement Response Evaluation Using the Semi-Analytical Finite Element Method, *International Journal of Materials and Pavement Design*, Vol. 3, No.2, pp. 211–225.
- Ingraffea, A. R. & Wawrzynek, P. A. 2003. *Finite Element Methods for Linear Elastic Fracture Mechanics*, Elsevier Science Ltd., Oxford, England.
- Lytton, R. L., Uzan J., Fernando E. G., Roque R., Hiltumen D. & Stoffels, S. M. 1993. *Development and Validation of Performance Prediction Models and Specifications for Asphalt Binders and Paving Mixes*. SHRP A-357, TRB, National Research Council, Washington, D. C.
- Scarpas, A., J. Blaauwendraad, de Bondt, A. H. & Molenaar, A. A. A. 1993. CAPA: A Modern Tool for the Analysis and Design of Pavements, *Proceedings of the 2nd International Conference on Reflective Cracking in Pavements*, pp. 121–128.
- Scarpas, A., de Bondt, A. H. & Gaarkeuken, 1996. G. Reflective Cracking Control via Reinforcing System: FE Modelling of Reinforced Overlays, *Proceedings of the 3rd International RILEM Conference*, Maastricht, the Netherlands, October, pp. 344–353.
- Zienkiewicz, O.C. 1977. *The finite element method for engineers*, Mc. Graw-Hill, London.

10. Pavement interface testing and modeling

Interface fatigue cracking in multilayered pavements: Experimental analysis

M. Diakhaté, Christophe Petit, A. Millien & A. Phelipot-Mardelé
University of Limoges, Egletons, France

B. Pouteau & H. Goacolou
EUROVIA, Centre de Recherche de Mérignac, Mérignac, France

ABSTRACT: This paper deals with interface shear durability in a multi-layered pavement. A test, named DST, has been performed in order to characterize monotonic and fatigue shear behavior of the interface. Tested specimens and the experimental device are described. Two types of interface are tested for 10°C and 20°C temperature conditions. So fatigue laws are presented and compared to interface shear monotonic strength (vs loading rate). This approach enables us to find a relationship between monotonic and cyclic experiments. The main practical objective of pavements companies is to get fatigue parameters of tack coat from short time consuming and easy tests. So pavements companies will be able to introduce lifetime of tack coat in pavement design. Practically speaking, this experimental work connected to pavement simulation (Diakhaté, 2007) shows that the shortest lifetime in pavement is classically at the bottom of the multi-layered pavement except in curves, roundabouts and if the surface layer is thin.

1 INTRODUCTION

More and more pavement constructors have troubles in predicting debonding at the interfaces of a multilayered pavement. This interface distress may be due, on the one hand, to the construction method (layers insufficiently bonded, no tack coat, water infiltration at the interfaces, etc.), and on the other hand, to the traffic load which becomes more and more high, with horizontal component (braking, turn, etc.), over thin wearing courses. In a mechanistic analysis, interface debonding can be due to cyclic tensile or shear loading (Granju et al. 2004), (Tran et al. 2005). Some studies have been performed in tension and are limited to pavements where interface is subjected to tensile stresses (sometimes, viscoelastic effect can generate tension at the interface). In other studies, shear loadings are applied to investigate the interface shear behavior (Partl et al. 2006), (Canestrari et al. 2005), (Diakhaté et al. 2007). However, results from these studies are restricted to monotonic shear behavior. Very few studies have been carried out to investigate the interface behavior under shear fatigue loadings.

Finite element simulations (Diakhaté, 2007) have shown that maximum shear stresses are close to the tire edge (the normal stresses are negligible at this position) and the maximum normal stresses are in the center of the tire(s) (no shear stresses at this point). This simulation enable us to justify cyclic pure shear testing.

This paper deals with the interface shear fatigue. French pavement design is based on criteria of fatigue behavior of bituminous materials, and on criteria of unbound layer rutting. It also assumes that layers are either perfectly bonded or debonded. So results from this work will enable the pavement designer to assess the interface bonding lifetime as well as the pavement lifetime. For the purpose of this work, a specific double shear test device has been designed and manufactured. Viscoelastic and fatigue results of the interface between two AC layers will be discussed.

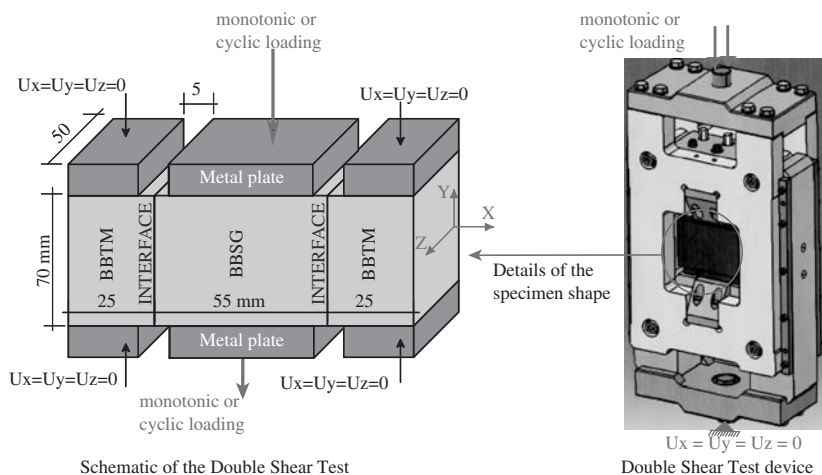


Figure 1. Schematic of the Double Shear Test: specimen and device.

2 EXPERIMENTAL TEST

2.1 Presentation

In this work, the specific test device developed is based on the double shear test (DST) principle. This testing method have been successfully used in a former study to investigate the shear damage behavior and mode II fatigue crack propagation of AC mixes (Petit et al. 2002).

As depicted in figure 1, the DST is performed on a sample which is made of three layers, bonded in two. The two side layers are fixed during the test, and the central layer is subjected to the load (monotonic or cyclic). A numerical optimization of the specimen and device geometries was performed, in order to obtain a quite pure shearing load at the interfaces. Experimental validations by the mean of image analysis confirmed this fact (Diakhaté, 2007).

The DST device is mounted on a servo-hydraulic frame. The upper part of the device is connected to the jack, and the lower part is connected to the load cell.

2.2 Asphalt material

Two types of interface are studied: one with tack coat (TC-70/100), and one without tack coat (WTC). The tack coat used in this study is a conventional rapid-set cationic emulsion. This emulsion contains approximately 65 percent bitumen (Pen 70/100), and a 300 g/m² application rate of residual bitumen is done.

Two types of asphalt concrete mix are selected to manufacture the composite laboratory slab. Both mixes contain the same pure bitumen as the one used to formulate the tack coat but have different design characteristics (Tab. 1).

2.3 Fabrication of samples

In laboratory, two methods (Fig. 2) can be followed to manufacture a sample which consists of three layers of AC.

As depicted in figure 2, method (A) leads to a sample where layers are successively compacted. Then, the interface 1 will be more compacted than the interface 2. Same thing when comparing layer 1 and layer 3. So, this method (A) leads to case where interfaces of the same sample have different characteristics in term, among others, of roughness.

Table 1. Asphalt concrete mixes: design characteristics.

	Mix type	Aggregates nominal size	Geological nature	Binder content mass %	Mean thickness	Air void content
Upper Layer AC	very thin layer (BBTM)	0/10 mm	grey diorite, from Mazières-en-Gâtine (Fr)	5.6	30 mm	12%
Lower Layer AC	thick layer (BBSG)	0/10 mm	pink quartzite sandstone from Munneville (Fr)	6.0	50 mm	7%

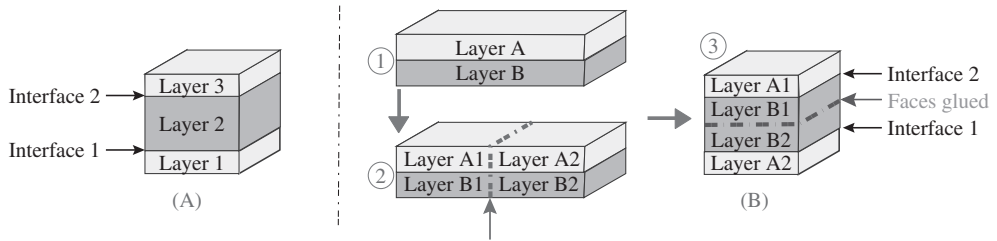


Figure 2. Fabrication of a specimen consisted of three layers of AC.



Figure 3. Preparation of the slab and the sample in laboratory, and photograph of obtained sample.

To obtain a sample by following the method (B) (Fig. 2), a double layered slab is firstly manufactured (phase 1). After sawing the slab (phase 2), the two resulting parts are glued together (phase 3) to obtain the desired shape of the sample. An epoxy is used to glue both faces of layer B.

The process used to prepare slabs needs the French rolling wheel compactor. Each layer of the slab (600 mm in length, 400 mm in width, and 80 mm in thickness) is compacted according to the European standard NF EN 12697-33 (Fig. 3).

The hot mix asphalt (160°C) is poured in the mold, and the lower layer is compacted to 50 mm thickness. After 2 hours of cooling, temperature of the lower layer is about 40/45°C, and the emulsion is uniformly applied. Once the emulsion is applied, a rest time of 2 hours is considered enough for ensuring its breaking process. Afterwards, the compaction process is repeated to manufacture the upper layer to a thickness of 30 mm. 12 samples (dimensions 70 × 105 × 50 mm³) are extracted from a molded specimen, after sawing and gluing.

3 FATIGUE LOADING

3.1 Cyclic loading

48 fatigue tests have been performed, and carried out under force control, and at 10 Hz. The force values is measured by a cell force (± 100 kN), and the tangential relative displacement, which

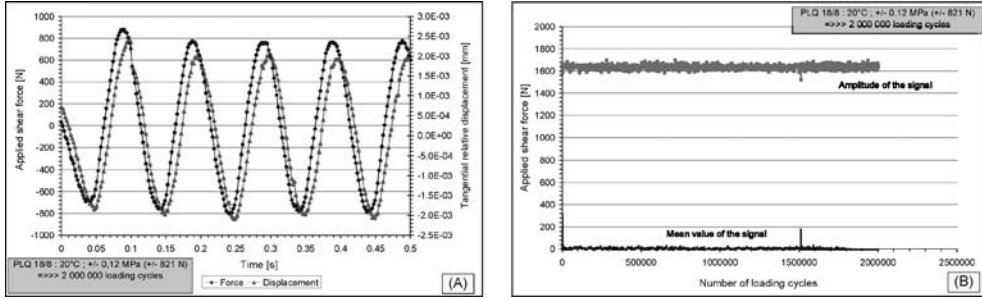


Figure 4. (A) First cycles of the test, (B) Applied shear force (amplitude and mean values).

represents the displacement between the central layer and the side layers of the sample, is measured by a displacement sensor (extensometer technology, ± 1 mm). Figure 4 shows the first five cycles of applied shear force and tangential relative displacement on a sample, subjected to two million of loading cycles. In this figure, it can be noticed that the force amplitude is constant during the test and the force mean value is null.

3.2 Damage behavior

The damage behavior of the interface between AC layers is analyzed from the evolution of the shear stiffness modulus (ΔK_s) during test. For each fatigue test, the interface shear stiffness can be expressed as a dynamic value $K_{s,k}^*$ (Eq. 1).

$$\begin{cases} K_{s,k}^* (i\omega) = \frac{\Delta F_k}{S \cdot \Delta u_k} \cdot e^{i\varphi_k} \\ \Delta K_s = \left| K_{s,k}^* (i\omega) \right| = \frac{\Delta F_k}{S \cdot \Delta u_k} \end{cases} \quad (1)$$

where ΔF_k = amplitude of the shear force at cycle $n^\circ k$; Δu_k = amplitude of the displacement at the same cycle; S = sheared area at both interfaces; and φ_k = phase angle between the shear force and the displacement signals.

In figure 5, one can see a representative result of a fatigue test. The shear stiffness modulus of the interface, ΔK_s , (normalized value) decreases during test. This decrease may be divided into two main stages. In the first one, the damage grows, as microcracking occurs and ΔK_s decreases slowly. In the second stage, ΔK_s decreases quickly, meaning a coalescence and fast propagation of macroscopic cracks at the interfaces.

3.3 Fatigue law in a Whöler analysis

The shear fatigue tests are analyzed to identify the fatigue laws of the two types of interface studied (with tack coat “TC-70/100”, and without tack coat “WTC”). Each fatigue law links the amplitude of the applied shear stress with the number of loading cycles to failure. Results from oligocyclic tests and fatigue are well described through a same power law.

This last parameter is assessed by means of a failure criterion. When one refers to fatigue tests performed on bituminous materials, the number of loading cycles to failure is defined conventionally as a drop by half of the initial specimen stiffness. In this paper, the fatigue failure criterion is based on a drop percentage of the initial value of the shear stiffness modulus (ΔK_s). For instance, the interface shear fatigue law is analyzed for a drop of 10%, 20%, 50%, and 70% of ΔK_s .

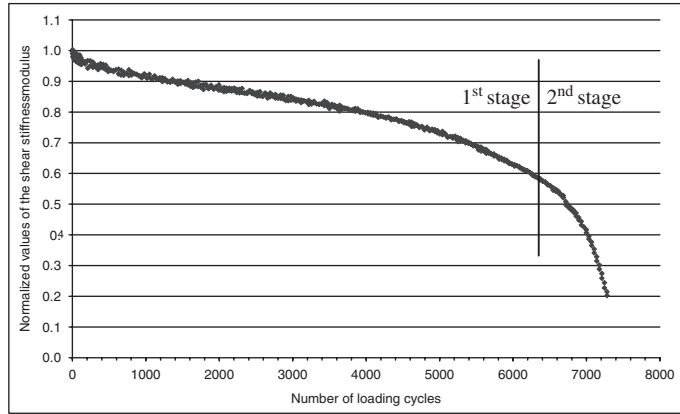


Figure 5. Evolution of the interface shear stiffness modulus versus the number of loading cycles.

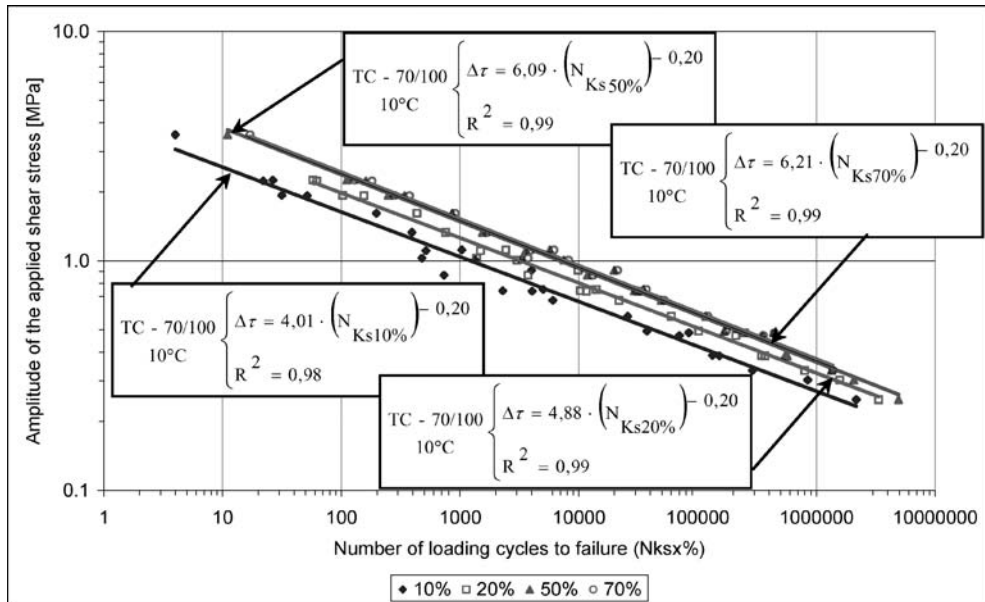


Figure 6. Fatigue laws for different failure criteria (tests performed at 10°C with tack coat 70/100).

In a log-log scale, for each drop percentage, the amplitude of the applied shear stress is plotted with the number of loading cycles equivalent to x% of ΔK_s drop (Fig. 6). From this figure, one can notice that there is a very good correlation between the amplitude of the shear stress and the number of cycles to x% of ΔK_s drop. Results are better when we consider a drop percentage greater than 10.

It can also be noticed from figure 6 that, for drop percentage greater than 50, the obtained shear fatigue laws are similar. In fact, at these drop percentages, the interface fails quickly, and then the equivalent numbers of cycles to failure are quite equal.

Referring to previous analysis (Fig. 6), the picked criterion for the number of loading cycles to failure is defined as a drop by half (50%) of initial value of the interface shear stiffness modulus.

Figure 7 presents, for each type of interface studied at 10 and 20°C, the obtained fatigue laws.

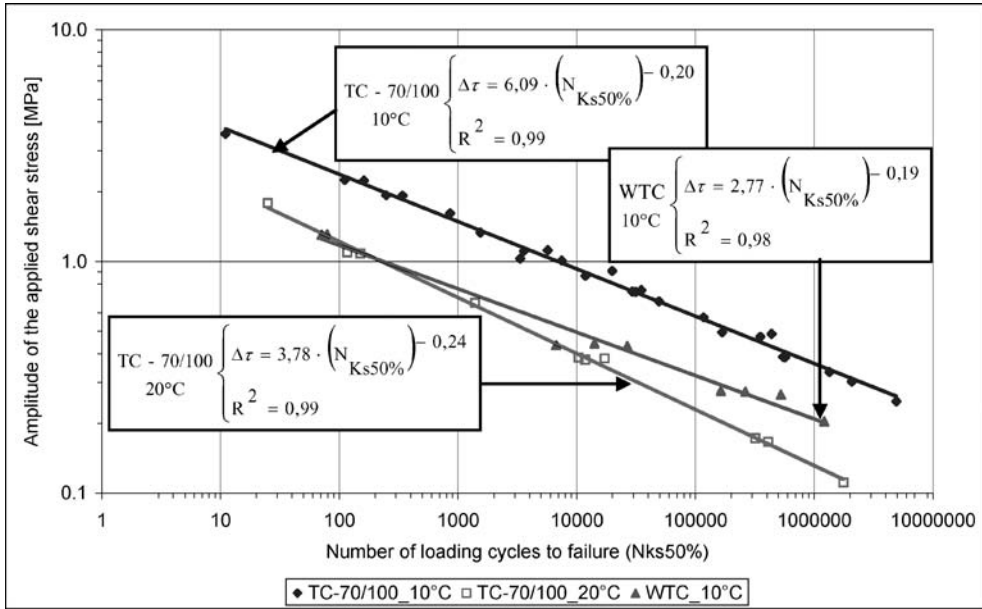


Figure 7. Fatigue laws of the studied types of interface.

In case of interface with tack coat (TC-70/100), the power laws, which are proposed to describe the interface fatigue behavior at 10 and 20°C, are similar.

When comparing the effect of tack coat on the interface fatigue performance, results show that, at 10°C, the interface without tack coat has lower performance than the one with tack coat. This finding shows the importance of applying, at 10°C, a tack coat between AC layers to provide a greater fatigue performance. However, at this temperature, the slope of the fatigue law seems to be not affected by the type of interface. Hence, one can assume that, at 10°C, the slope of the fatigue law is about -0.20 .

The French fatigue cracking model (LCPC-SETRA, 1994), is derived from bending tests (NF P 98-261-1) performed on laboratory AC mix specimens. This model is presented hereafter (Eq. 2):

$$\varepsilon_t = \varepsilon_6 \cdot \left(\frac{N_F}{10^6} \right)^b \quad (2)$$

where ε_t = applied tensile strain which leads to a number of cycles to failure N_F ; ε_6 = applied tensile strain which leads to a number of cycles to bending failure (at 10°C and 25 Hz) equal to one million; b = slope of the fatigue law (conventionally $b = -0.20$).

If we compare the fatigue law equation of bituminous materials (Eq. 2) with the interface fatigue law (Fig. 7), we can write this latter as follows (Eq. 3).

$$\Delta \tau = \Delta \tau_6 \cdot \left(\frac{N_{Ks50\%}}{10^6} \right)^b \quad (3)$$

where $\Delta \tau_6$ = amplitude of the applied shear stress which leads to a number of cycles to failure equal to one million; b = slope of the fatigue law.

For the case of interface with tack coat (TC-70/100), the value of $\Delta \tau_6$ is 0.36 MPa at 10°C, and 0.13 MPa at 20°C. The value of the slope b is -0.20 at 10°C, and -0.24 at 20°C.

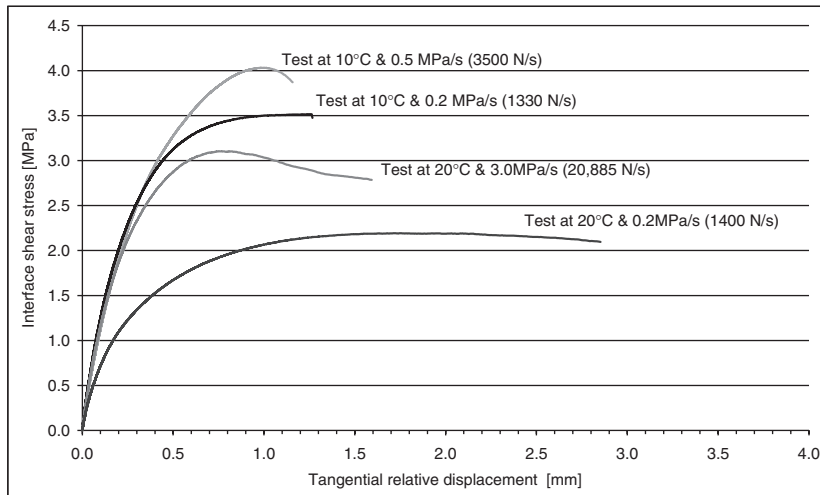


Figure 8. Evolution of the interface shear stress versus tangential relative displacement (TC-70/100).

4 MONOTONIC LOADING

21 monotonic Double Shear Tests have been carried out under force control, with the device described Figure 1. The shear force values is measured by a cell force (± 100 kN), and the tangential relative displacement, which represents the displacement between the central layer and the side layers of the sample, is measured by a LVDT (± 75 mm). The nominal shear stress, applied at the interfaces, is computed by dividing the measured shear force by the sheared section at the interfaces. For four tests carried out at 10 and 20°C, and at several loading velocities, Figure 8 shows the evolution of the nominal interface shear stress versus the tangential relative displacement.

From the curves presented in figure 8, the maximum value of the shear stress corresponds to the interface shear strength. This parameter is generally used to compare the monotonic performance of different tack coats.

4.1 Interface shear strength

In this part of the work, the effect of loading velocity on the interface shear strength is analyzed. In a log-log scale, the interface shear strength is plotted with the loading velocity (Fig. 9). It can be noticed that, at 10 and 20°C, results are well described through a power law with a slope which is similar and about 0.17 for those materials. When comparing results obtained, it can be concluded that, for a temperature between 10 and 20°C, the interface shear strength value can be evaluated.

5 FROM MONOTONIC RESULTS TO FATIGUE LAW

In this part of the paper, we are interesting in predicting the interface fatigue law from the monotonic tests results.

Firstly, monotonic tests results are analyzed in frequency. For each monotonic test, the shear strength value corresponds to a failure time (T_R , see Fig. 10). When one compares monotonic loading with fatigue loading, it can be assume that the interface shear strength that corresponds to a failure within T_R seconds would be equal to the amplitude of the shear stress that leads to a failure within $\frac{1}{4}$ cycle of loading.

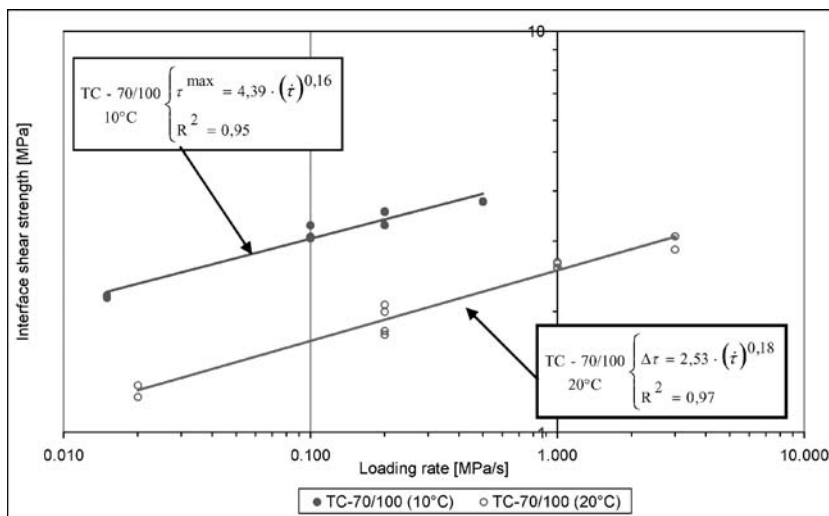


Figure 9. Interface shear strength versus loading rate.

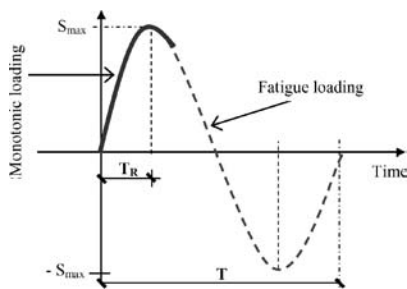


Figure 10. Comparison between monotonic loading and fatigue loading.

Fatigue tests are carried out at 10 Hz. For each monotonic test, the loading frequency (f_{eq}) equivalent to the failure time T_R can be assessed as follows (4):

$$f_{eq} = \frac{1}{4 \cdot T_R} \quad (4)$$

In a first method, the predictable fatigue law could be written as follows (5):

$$\text{Fatigue laws (simulation)} \begin{cases} 10^\circ\text{C} - 10 \text{ Hz}: \Delta\tau = \tau^{\max}(f_{eq}) \cdot (N_{Ks50\%})^{-0.20} \\ 20^\circ\text{C} - 10 \text{ Hz}: \Delta\tau = \tau^{\max}(f_{eq}) \cdot (N_{Ks50\%})^{-0.24} \\ \text{with } \tau^{\max}(f_{eq}) = \Delta\tau(N_{Ks50\%} = 1) \end{cases} \quad (5)$$

In Figure 11, the interface shear strength values are plotted with the equivalent frequency. Since fatigue tests are carried out at 10 Hz, the value τ^{\max} (for $f_{eq} = 10$ Hz) is compared with $\Delta\tau$ (for $N_{Ks50\%} = 1$ cycle). It can be seen from Figure 10 that these values are different.

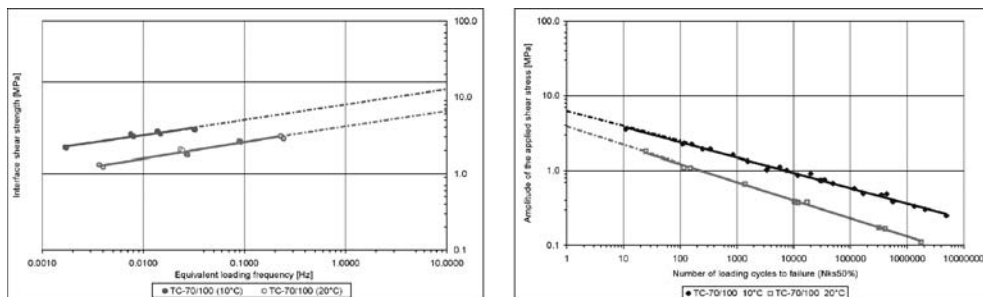


Figure 11. Comparison between monotonic law and fatigue law (TC-70/100, tests at 10 and 20°C).

In a second method, the predictable fatigue law could be written as follows (6):

$$\text{Fatigue laws (simulation)} \left\{ \begin{array}{l} 10^{\circ}\text{C} - 10 \text{ Hz}: \Delta\tau = \tau^{\max}(\dot{\tau}) \cdot \left(\frac{N_{Ks50\%}}{10}\right)^{-0.20} \\ 20^{\circ}\text{C} - 10 \text{ Hz}: \Delta\tau = \tau^{\max}(\dot{\tau}) \cdot \left(\frac{N_{Ks50\%}}{10}\right)^{-0.24} \\ \text{with } \tau^{\max}(\dot{\tau}) = \Delta\tau(N_{Ks50\%} = 10) \end{array} \right. \quad (6)$$

From the former equation, the objective is to evaluate the loading rate. From Figure 11, for $N_{Ks50\%} = 10$ cycles, $\Delta\tau = 3.80$ MPa at 10°C. From figure 9, at the same temperature, for $\tau^{\max} = 3.80$ MPa, $\dot{\tau} = 0.41$ MPa/s. This process is followed to evaluate the corresponding loading rate at 20°C ($\dot{\tau} = 0.38$ MPa/s).

Finally, at 10°C, a monotonic test carried out at 0.41 MPa/s leads to a shear strength value which is equal to the amplitude of the shear stress that leads to 10 loading cycles to failure.

In Figure 12, a comparison between the fatigue law obtained from laboratory tests and the one predictable is presented. It can be seen that the predictable fatigue laws describe, at 10 and 20°C, the fatigue behaviors of the interface TC-70/100.

6 CONCLUSION AND PERSPECTIVES

This paper deals with the characterization of the interface shear behavior under monotonic loading and fatigue loading. This is one of the first works about investigation of the interface shear fatigue behavior. The studied interface is the one between a very thin asphalt concrete layer and a thick asphalt concrete layer. Two types of interface are tested: with and without tack coat.

For the purpose of this study, a specific double shear test device has been designed and manufactured. The sample tested is consisted of three layers bonded in two with or without tack coat. With the test device developed, the interfaces of the sample are subjected to a quite pure shear stress.

Oligocyclic and fatigue tests were carried out under force control, at 10 and 20°C, and at 10 Hz. Several failure criteria are analyzed to derive the interface fatigue law. In a log-log scale, the amplitude of the applied shear stress is plotted with the number of loading cycles to failure. This number is defined as a drop by half of the initial value of the shear stiffness modulus. There is a very low scattering of fatigue results. At each testing temperature, a power law leads to a very good correlation between the applied shear stress and the number of loading cycles to failure. This is

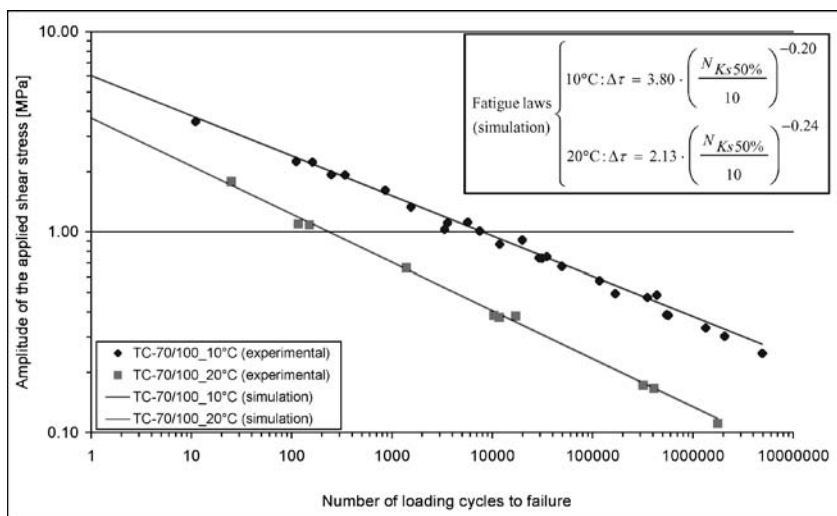


Figure 12. Comparison between fatigue laws: simulation and experimental.

a very interesting finding, since oligocyclic and fatigue results can be plotted in a same diagram, and correlated together through a power law.

Another finding from fatigue tests results is, at 10°C, the fatigue performance of the interface without tack coat is lower than the one of the interface with tack coat. This means that, at this temperature, the application of tack coat improves the fatigue performance of the interface.

At 10°C, the slope of the fatigue seems to be not affected by the type of the interface (with or without tack coat). It's is about -0.20 , so, the same as the obtained from fatigue tests carried out on bituminous materials. However, this slope of the fatigue law is related by the testing temperature. At 20°C, the slope is about -0.24 .

The monotonic shear tests were carried out at 10 and 20°C, and at several loading velocities. In the analysis of the results, we are interesting in evaluating the interface shear strength value. In the literature, this value is usually used to compare monotonic performance of tack coat. In a log-log scale, the interface shear strength values are plotted with the loading velocity. Power laws lead to very correlation of these data.

An advanced analysis of the experimental results obtained has been conduction to find a relationship between the monotonic tests results and the fatigue law. Since monotonic tests are simple and quick to carry out, this relationship would be very useful to predict the fatigue performance of tack coats. The finding of this analysis is, at each testing temperature, a monotonic test is to be carried out a specific loading rate (0.41 MPa/s at 10°C or 0.38 MPa/s at 20°C) to obtain a couple of values (shear stress and number of cycles to failure) of the fatigue law. Then, the fatigue law is completed since its slope is known at each testing temperature (-0.20 at 10°C, and -0.24 at 20°C).

The interface fatigue laws obtained from these laboratory tests allows the designer to take into account the interface fatigue behavior for the pavement design. The effect of taking into account this interface fatigue behavior on the pavement response is analyzed in finite elements. Results show that, for the case with horizontal efforts acting at the surface of the pavement, the lifetime of the bonding at the uppermost interface is lower than the one of the bituminous layers (Diakhaté, 2007). Effectively, we can easily show that in a pavement curve by assuming cyclic horizontal effects at each standard axle, fatigue of tack coat can be the first damage, so in this case the pavement design has to include fatigue of interface.

In perspective, the effect of water infiltration at the interface on fatigue behavior will be analyzed. The relationship which allows the designer to get fatigue properties from monotonic results will be validated with other materials.

REFERENCES

- Canestrari, F., Ferrotti, G., Partl, M.N. & Santagata, E. 2005. Advanced testing and characterization of interlayer shear resistance. *In 84th TRB annual meeting, 9–13 January 2005*: 1–26.
- Diakhaté, 2007. Fatigue et comportement des couches d'accrochage dans les structures de chaussées, *Ph-D thesis, University of Limoges, October*.
- Diakhaté, M., Petit, C., Millien, A., Phelipot-Mardelé, A., Pouteau, B. & Goacolou, H. 2007. Comparison of direct shear and torque tests for determining viscoelastic shear behaviour of tack coats. *Proceedings of the International Conference on advanced characterization of pavement and soil engineering materials, 20–22 June 2007, Athens (Greece)*.
- Granju, J.-L., Sabathier, V., Turatsinze, A., Toumi, A. 2004. Interface between an old concrete and a bonded overlay: debonding mechanism. *Interface science, 12*: 381–388.
- Partl, M.N., Canestrari, F., Ferrotti, G. & Santagata, F.A. 2006. Influence of contact surface roughness on interlayer shear resistance. *In 10th International Conference on Asphalt Pavements, ISAP, Quebec, August 2006*.
- Tran, Q. T., Toumi, A., Granju, J.-L. 2005. Experimental and numerical investigation of the debonding interface between an old concrete and an overlay. *Materials and Structures*.

A fracture-based constitutive model for pavement interface characterization

H. Ozer, I.L. Al-Qadi & Z. Leng

University of Illinois at Urbana-Champaign, Urbana, Illinois, USA

ABSTRACT: This paper presents a new fracture-based constitutive model to characterize pavement interfaces. The constitutive model captures the entire range of interface responses from fully bonded (initial elastic) to fully debonded. Failure (debonding) mechanisms can occur in the following states which the model also captures: pure shear, pure tensile, shear with compression, and shear with tension. Additionally, the developed model shows promise for characterizing cracking problems.

In this model, an interface constitutive relationship has been implemented with a frictional Mohr-Coulomb plasticity model. The constitutive model and interface elements were implemented by means of the user element (UEL) of ABAQUS finite element (FE) software. An algorithmically consistent tangent operator for the interface elasto-plastic modulus was used to facilitate convergence. Non-associative plasticity was implemented to have a better control of volumetric expansion (dilation) at the interface element. Debonding was formulated by a nonlinear softening model integrated into an elasto-plastic constitutive model. The model addresses frictional properties, including pressure dependency of the interface shear strength and dilation due to roughness of interfaces.

This paper provides numerical examples and discusses the experiments conducted for characterization of hot-mix asphalt (HMA) overlay and Portland cement concrete (PCC) interfaces, including tests on direct shear at various temperatures, tack coat materials, tack coat application rates, and concrete surface texture. As part of the experiments, three-dimensional interface elements were inserted on a predefined failure plane. Load displacement responses obtained from direct shear tests were in agreement with the finite element simulations. The developed model with its inherent frictional nature is ideal for use with interface problems especially under various loading conditions (pure tensile, pure shear, shear with compression, and shear with tension). The model can also be further advanced to be used in the finite element analysis of pavement cracking problems under mixed-mode loading.

Keywords: pavement interface, plasticity, friction, dilation

1 INTRODUCTION

Interface elements within the concept of finite element (FE) theory have been commonly used to address geometrical discontinuities occurring as cracks, dissimilar material interfaces, joints, etc. The concept of using interface elements was implemented by Mahtab and Goodman (1970) and Zienkiewicz and Pande (1977) to describe load transfer through rock joint interfaces with a Mohr-Coulomb friction model. Desai et al. (1984) used similar interface elements and improved the interface constitutive model with a visco-plastic constitutive model, focusing on soil-structure interactions and sand-concrete interfaces. Non-associated plasticity was also used to control dilation. Beer (1985) introduced a general framework for isoparametric interface elements. Hohberg

(1992) used interface elements in seismic analysis of arch dams. One of the enhanced features of Hohberg's study was to use multi-surface plasticity. This allowed decoupling of interface degradation in the different modes of loading. Similar interface elements and constitutive models are also used in micromechanical problems to explain cracking in quasi-brittle materials (Carol et al., 2001).

Within the scope of this current study, interface element formulations are adopted for pavement interfaces between hot-mix asphalt (HMA) overlays and concrete pavements. The primary objective is to develop a rigorous interface model to characterize the response of pavement layer interfaces under various loading conditions focusing on frictional sliding. These loading combinations can generate the following four stress states at the interface: pure tension, pure shear (sliding), shear with compression, and shear with tension. The well-established theory of plasticity can be utilized to better model interface problems involving frictional sliding. Therefore, the Mohr-Coulomb friction model was considered as the basis and tailored accordingly to the needs of the current problem at hand. This model allows consideration of surface roughness, which could result in volumetric deformations and determination of normal pressure dependency of the interfaces. Another feature of the model developed herein was based on robust integration algorithm techniques developed in the mid 1980's by Simo and Taylor (1985). The contribution of these algorithms manifested as fast convergence, which could be a quite complicated issue in problems with softening response. The developed algorithms are integrated into ABAQUS as user elements (UEL).

This paper introduces the theoretical formulations for interface elements and plasticity constitutive models. A numerical example is presented to demonstrate some important features of the developed model. Experimental validation of the model is described. Additionally, the paper explains how the model parameters were determined and compares the load displacements between the model and experiments.

The developed model is general and can be applied to different interface problems with suitable parameters. A promising potential for this interface model application is that with further modifications, it can be used for various modes of cracking in pavements.

2 INTERFACE ELEMENTS AND CONSTITUTIVE MODEL

2.1 Interface element technology

Two and three-dimensional zero thickness interface elements are formulated within the concept of the FE theory. Linear shape functions are used to approximate relative interface displacement fields. Interface elements and relative displacements in two dimensions are shown in Figure 1.

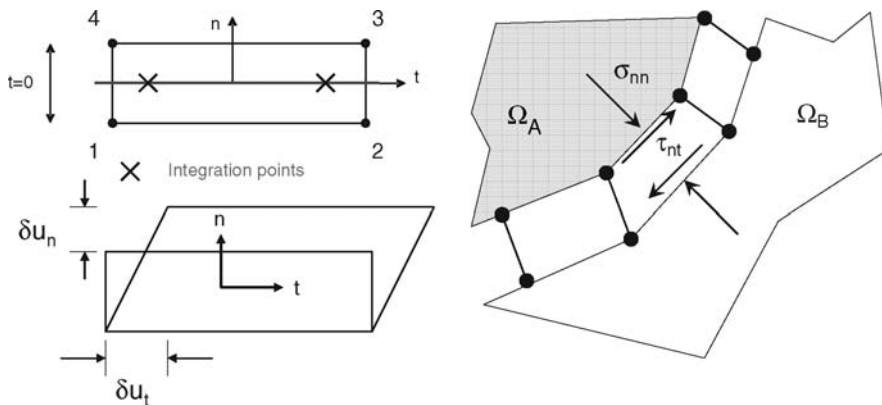


Figure 1. Two dimensional interface elements inserted between two deformable bodies.

Traction-relative displacement relationships in the perfectly bonded case reduce to the following constitutive equations. These equations show the linear relationship between tractions and relative interface displacements.

$$\begin{Bmatrix} \sigma_{nn} \\ \tau_{nt} \end{Bmatrix} = \begin{bmatrix} k_{nn} & 0 \\ 0 & k_{nt} \end{bmatrix} * \begin{Bmatrix} \delta u_n \\ \delta u_t \end{Bmatrix} \quad (1)$$

$$\begin{Bmatrix} \sigma_{nn} \\ \tau_{ns} \\ \tau_{nt} \end{Bmatrix} = \begin{bmatrix} k_{nn} & 0 & 0 \\ 0 & k_{ns} & 0 \\ 0 & 0 & k_{nt} \end{bmatrix} * \begin{Bmatrix} \delta u_n \\ \delta u_s \\ \delta u_t \end{Bmatrix} \quad (2)$$

where, σ_{nn} is normal traction; τ_{ns} and τ_{nt} are tangential tractions; k_{nn} , k_{ns} , and k_{nt} are normal and tangential stiffnesses; and δu_n , δu_s and δu_t are displacement jumps at the interface.

Interface elements are embedded as user elements (UEL) in the nonlinear solution framework of ABAQUS. This requires calculation of the tangent stiffness matrix and finding the contribution of internal force vector to the global force vector. The tangent stiffness and internal force vector are shown in equation (3). One of the main contributions of this study to the current interface models is the implementation of consistent tangent operators as described in Simo and Taylor (1985) and Belytschko et al. (2000). A consistent tangent operator is used to calculate the algorithmic modulus of interface element, which enhances the convergence of the nonlinear set of system of equations.

$$\mathbf{K}_{n+1}^{(i)} = \sum_{nel=1}^{nnel} \left[\int_{\Gamma_c} \mathbf{B}^T \left(\frac{\partial \mathbf{t}}{\partial \boldsymbol{\varepsilon}} \right)_{n+1}^{(i)} \mathbf{B} d\Gamma \right] \text{ and } \mathbf{f}_{n+1}^{\text{int}(i)} = \sum_{nel=1}^{nnel} \left[\int_{\Gamma_c} \mathbf{B}^T \mathbf{t}_{n+1}^{(i)} d\Gamma \right] \quad (3)$$

where $\left(\frac{\partial \mathbf{t}}{\partial \boldsymbol{\varepsilon}} \right)_{n+1}^{(i)} = C^{a/g}$ (algorithmic modulus); \mathbf{B} is the strain-displacement matrix; \mathbf{t} is the tractions at the interface; $\mathbf{K}_{n+1}^{(i)}$ is the interface element stiffness matrix calculated at load increment $n + 1$ and iteration (i); and $\mathbf{f}_{n+1}^{\text{int}(i)}$ is the internal force vector calculated at load increment $n + 1$ and iteration (i).

These equations, which show nonlinear relationships and bring a consistent tangent operator, were essential during this study to investigate the debonding process at the interface level. Consistent tangent operator facilitated convergence in finite element simulations, which is a challenging issue in such highly nonlinear problems.

2.2 Interface constitutive model

2.2.1 Yield surface

In this study, an interface constitutive relationship has been implemented with a frictional Mohr-Coulomb plasticity model. Non-associated plasticity and nonlinear work softening rules have been implemented to describe an entire range of interface responses from fully bonded to debonded cases. The model is capable of capturing initial elastic response followed by nonlinear post peak softening tail, which is commonly observed at cohesive interfaces under shear loading.

The Hyperbolic Mohr-Coulomb friction model, as defined by Zienkiewicz and Pande (1977) and Carol et al. (2001), was implemented as the interface constitutive model. This relationship is shown in equation (4). The hyperbolic yield surface was chosen because of its suitability to plasticity equations where gradients of yield surface need to be calculated. Smooth yield curves are always desirable in plasticity gradient calculations. The shape of the yield curve and also the potential surface are shown in Figure 2.

$$F = \tau_{eq}^2 - (c - \sigma_{nn} * \tan \phi)^2 + (c - s * \tan \phi)^2 \quad (4)$$

where $\tau_{eq} = \sqrt{\sigma_{ns}^2 + \sigma_m^2}$ is equivalent tangential tractions; σ_{nn} is normal traction; s is tensile strength; c is cohesion; and ϕ is friction angle.

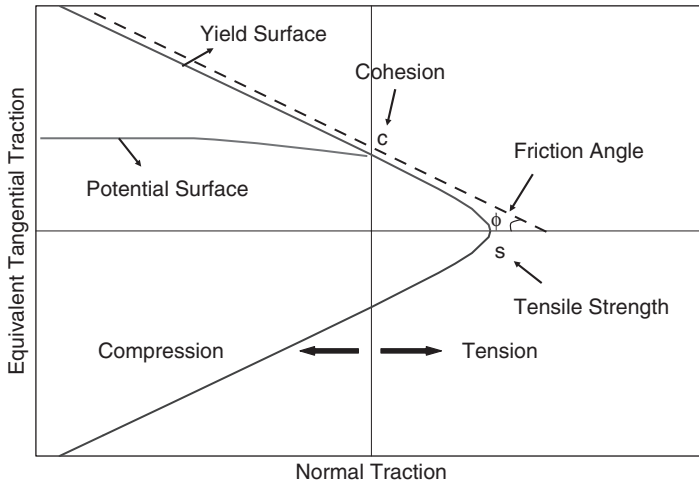


Figure 2. Yield and potential curves (after Carol et al., 2001).

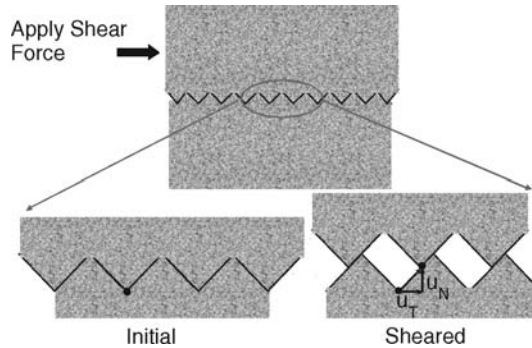


Figure 3. Illustration of interface dilation with a saw-tooth idealization.

As mentioned earlier, non-associated and associated flow rules were implemented together to better control dilation, which can be crucial in understanding interface behavior under shear loading. Prior to presenting that non-associated plasticity is related to the dilation response of the interfaces, it is important to describe the dilation phenomena. Dilatancy is best described as the change in volume associated with the distortion of granular materials. In this case, dilation is limited to the interface, and it occurs when asperities on contacting surfaces override each other. In this particular case, aggregate to aggregate contact generates a rough surface at the interface and as the upper layer starts to shear on top of the bottom layer. The movement occurs horizontally as well as normally on the interface plane. This causes normal expansion to the interface plane in addition to shearing. This phenomenon is illustrated in Figure 3. Roughness at the contacting surfaces is idealized with this saw-tooth type of model.

The non-associated flow rule relates the gradients of potential surface to the plastic interface displacement through plasticity parameter as shown in equation (5). When the interface is under compression only, non-associated plasticity becomes active as given by equation (7).

$$\delta \dot{u}_i^{pl} = \dot{\lambda}^* r_i \quad (5)$$

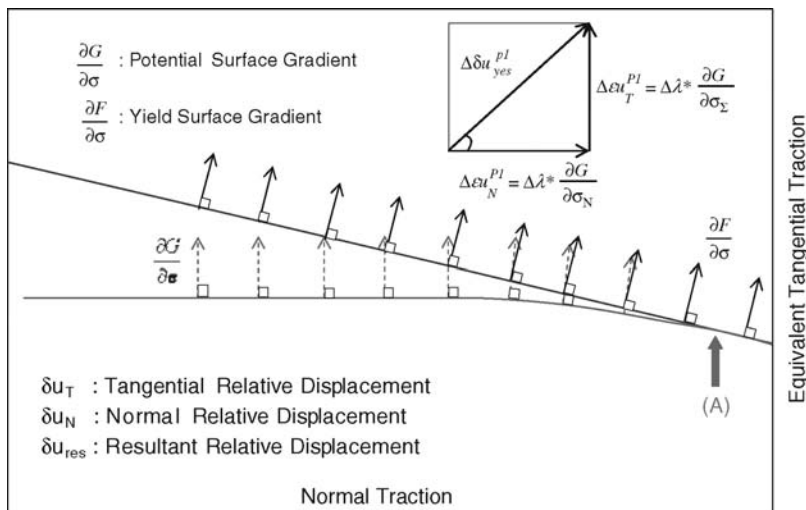


Figure 4. Close-up view at the yield and potential curves with gradient illustrations.

$$\text{where } \delta \mathbf{u} = \begin{bmatrix} \delta u_N \\ \delta u_T \end{bmatrix} \text{ in 2D } \delta \mathbf{u} = \begin{bmatrix} \delta u_N \\ \delta u_T \\ \delta u_S \end{bmatrix} \text{ in 3D} \quad (6)$$

$$r = \begin{cases} \frac{\partial F}{\partial \sigma_i} & \sigma_N > 0 \\ \frac{\partial G}{\partial \sigma_i} & \sigma_T < 0 \end{cases} \quad (7)$$

Figure 4 illustrates the significance of using the non-associated flow rule; and the gradients at yield and potential curves are graphically illustrated. As seen in the figure, yield surface gradients produce approximately similar magnitudes of horizontal vectors at each point representing the relative displacements in the positive normal dilation. On the other hand, potential surface gradients vary from low to high normal pressures. For example, potential surface gradients deviate from yield surface gradients as normal pressure increases. After a predefined point illustrated by (A), potential surface gradient dives towards the positive y-axis, which makes the horizontal component of the gradients zero; hence the normal component of relative displacement. This method provides flexibility to describe various levels of dilation depending on the interface roughness.

2.2.2 Softening rules and interface debonding mechanism

Strength degradation at the interface level is implemented with the nonlinear softening rules as described by Carol et al. (2001). These functions, as given by equations (8) and (9), show how strength parameters degrade as a function of plastic work. Nonlinearity in the post-peak softening region provides better agreement with the experimental results.

$$\tan \phi = \tan \phi_0 - (\tan \phi_0 - \tan \phi_r) * S_\phi \left(\frac{W}{G_f} \right) \quad (8)$$

$$c = c_0 [1 - S_c \left(\frac{W}{G_f} \right)] \text{ and } s = s_0 [1 - S_s \left(\frac{W}{G_f} \right)] \quad (9)$$

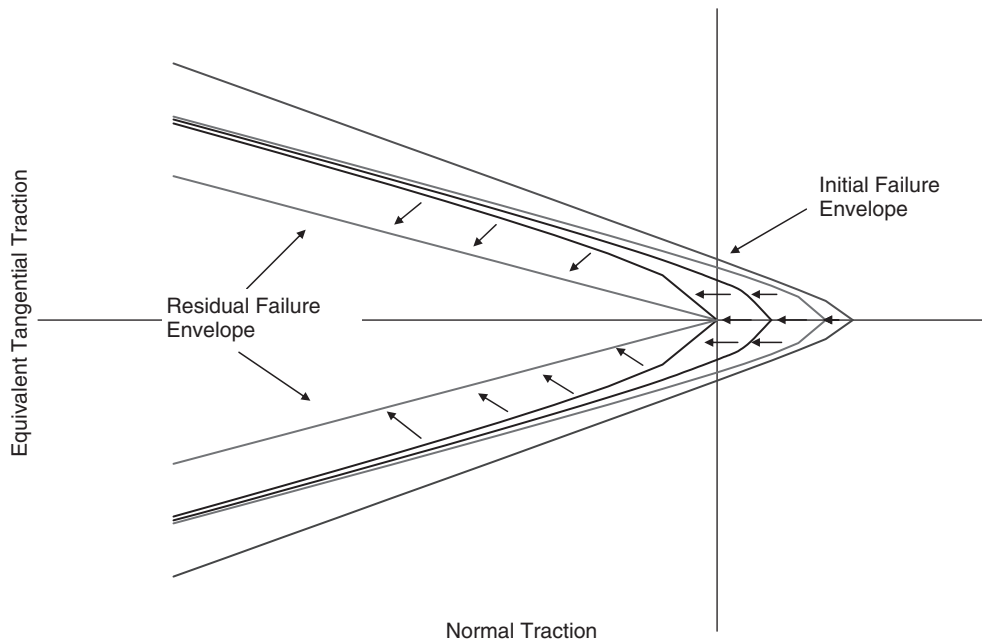


Figure 5. Evolution of yield surface (Carol et al., 2001).

where the scale parameter is given as follows:

$$S_i(\xi_i) = \frac{e^{-\alpha} * \xi_i}{1 + (e^{-\alpha} - 1) * \xi_i} = \begin{cases} 1 & \xi = 1 \\ 0 & \xi = 0 \end{cases} \quad (10)$$

where, G_f^I and G_f^{II} are the failure energies in mode-I and mode-II; ϕ_0 is initial friction angle; ϕ_r is residual friction angle; c_0 is initial cohesion; s_0 is initial tensile strength; and W is the plastic work done at the interface.

According to this, yield surface evolves from its original position to a residual surface where only simple friction is left. This evolution is presented in Figure 5. As shown, the yield surface first translates to the origin until tensile strength is fully degraded. Tensile strength is fully consumed when plastic work (W) becomes equal to G_f^I . Following that, it shrinks to a residual surface where the cohesive strength is degraded fully. This happens when plastic work (W) is equal to G_f^{II} . This mechanism is consistent with cracking in mode-I (tensile separation) and mode-II (shear sliding). Therefore, this type of interface model has also been used in cracking problems; especially for brittle materials. Yield surface defined for interface failure in this case can also be considered as cracking potential as defined by Carol et al. (2001). The advantage of this developed model is the inherent frictional feature which can be crucial in mixed mode cracking cases.

3 NUMERICAL EXAMPLES AND APPLICATIONS OF THE INTERFACE MODEL

3.1 Mixed mode loading conditions

A numerical example illustrates some of the important features of the developed model. Three dimensional interface elements are inserted in between two deformable elastic bodies as shown in Figure 6. Various combinations of loading are applied to generate a variety of traction states at the interface level. Loading states (a) to (c) are combinations of shear and compression whereas

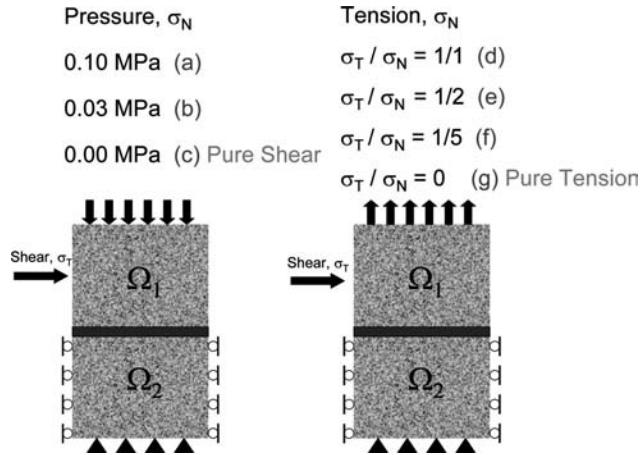


Figure 6. Interface loading conditions in a numerical example.

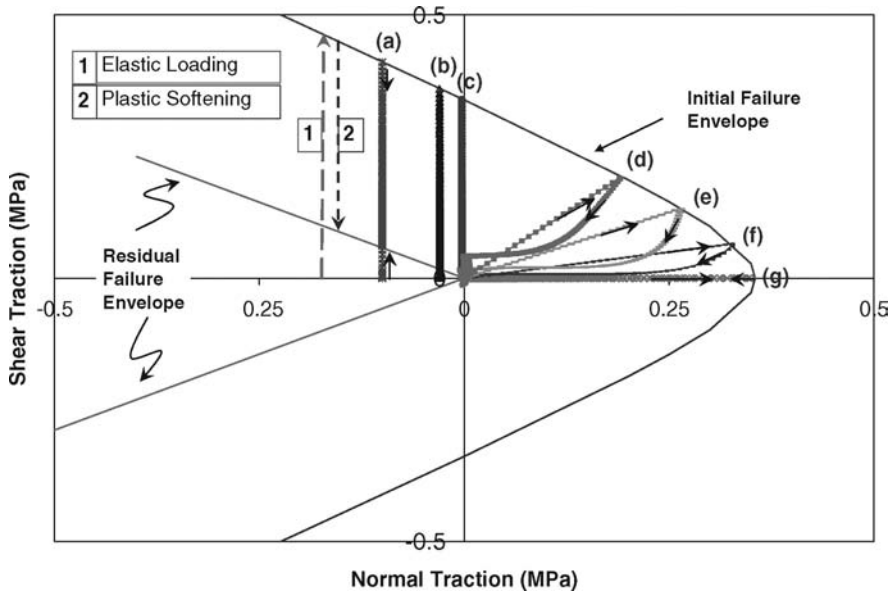


Figure 7. Loading history in the traction space.

(d) to (g) are combinations of shear and tension. Therefore, this test generates almost an entire range of loading conditions including pure shear and pure tension. Interface parameters for this example are the following:

- Tensile strength and cohesion = 0.355 MPa
- Normal and tangential stiffness = 0.15 MPa/mm
- Friction angle = 30°
- Fracture energies G_I and G_{II} = 1.05 and 1.40 N/mm

These loading states are also shown in the form of a loading path in the traction space. Figure 7 presents the loading paths associated with each loading state. The loading path basically shows the history of loading or traction levels at a material point until it approximates to the yield surface

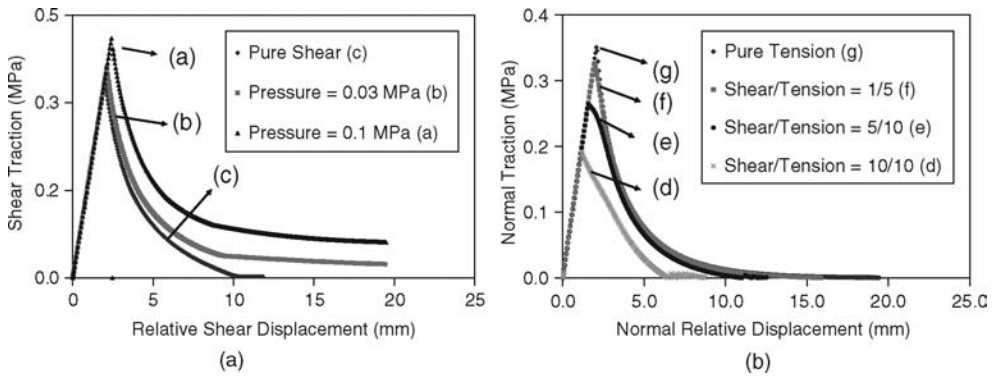


Figure 8. A material point traction displacement response at various loading conditions.

(elastic state) and beyond the yield surface (plastic state). Once the traction levels at this material point hit the yield surface, the interface starts softening until it reaches a residual level as shown by the arrows in Figure 7. Each point in the plastic state, therefore, represents a point on the evolving yield surface.

In addition to the history of loading, it is also important to show the traction-displacement response at the same material point. Figure 8 shows the traction-displacement curves for each loading combination. The normal compression effect on shear traction and the effect of shear traction on tensile strength are shown in Figure 8(a) and (b), respectively. It is evident from a frictional model that as normal compression increases from 0 to 0.1 MPa, shear resistance also increases depending on the friction angle. Increasing maximum shear strength and also residual shear strength is clearly shown in Figure 8(a). On the other hand, existence of shear tractions when interface is subjected to tensile separation significantly decreases the maximum tensile tractions as shown in (b). This numerical example illustrates the effect of various mixed combinations of loading conditions.

3.2 Comparison with direct shear experimental data

The developed interface model is also used to simulate the direct shear experiment conducted as a part of tack coat effectiveness study (Leng et al., 2008). The objective of the experimental study is to investigate bonding conditions between hot-mix asphalt (HMA) and Portland cement concrete (PCC) layers. Several parameters were investigated including various tack coat materials, tack coat application rate, temperature, and surface texture. The tests were conducted at zero normal pressure. Test results provided a wide range of data to test the accuracy and robustness of the model.

Maximum shear tractions obtained from the tests at three various temperatures (10°C, 20°C, and 30°C) for three replicates are presented in Figure 9. Analytical yield surface given by equation (4) is also presented. In the absence of tensile strength data, the tensile strength is simply assumed to be equal to cohesion. A limited number of tests also indicate that normal pressure dependency is insignificant. Therefore, the friction angle is taken at 3°.

Once yield surface is obtained utilizing the testing results; finite element simulations were conducted for each set of input parameters at three various temperatures. Figure 10 shows the comparisons between testing results and model output. Results show that interface strength, when tack coat is incorporated, is temperature dependent. After the interface reaches a maximum value of shear traction, debonding occurs gradually until it reaches a residual state. The developed model successfully captures the testing results in the entire range of response. The results are obtained without any calibration, as shown with yield surface derivations, which suggests the suitability of the model for this application.

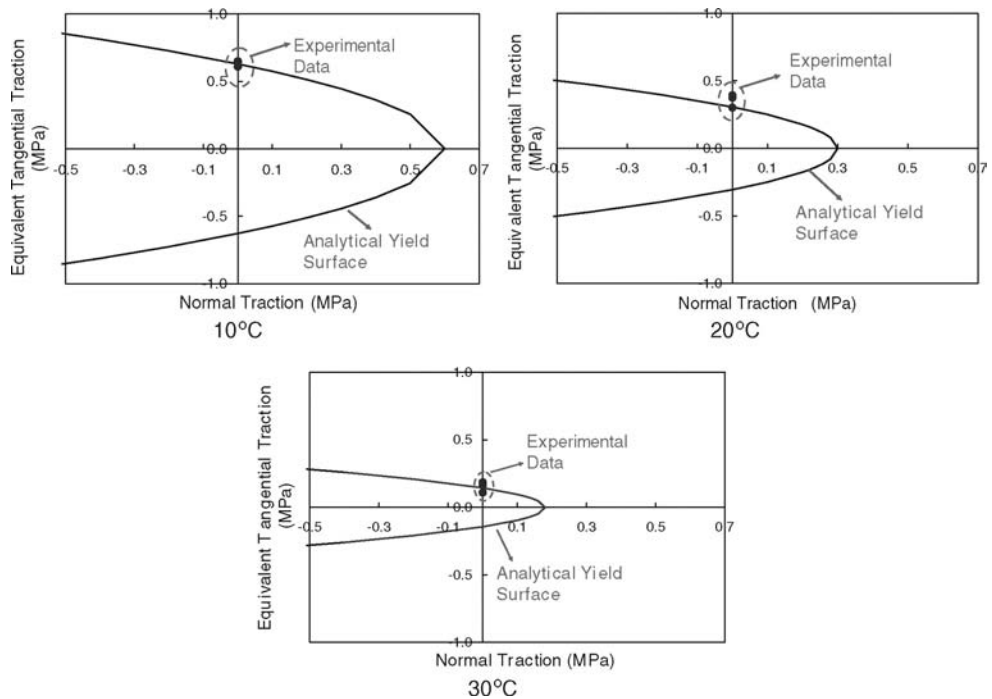


Figure 9. Model yield surface with experimental data.

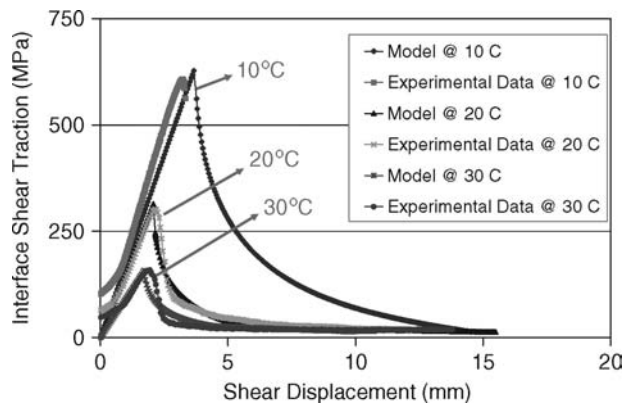


Figure 10. Model results with experimental comparisons.

4 CONCLUSIONS

In conclusion, this paper presents a frictional interface model developed in a plasticity framework. The researchers implemented non-associated plasticity with nonlinear softening rules to capture the responses of interfaces and to simulate dilation at the interface level. The developed model with its inherent frictional nature is ideal for use with interface problems especially under various loading conditions (pure tensile, pure shear, shear with compression, and shear with tension). Dilation, also known as volumetric expansion due to surface roughness, can play a significant role in interface response especially at rough interfaces under shear loading. Although dilation is usually neglected

in most interface models due to its complexity, this model's approach is very well suited to handle dilation phenomena with sufficient accuracy. In addition, nonlinear softening rules add another sophistication level to the plasticity formulations but at the same time provide extensive flexibility to capture debonding at the interfaces. Interface elements and constitutive models were generated using ABAQUS user elements.

One of the main contributions of this study is the implementation of algorithmically consistent tangent operator to an interface debonding model. The consistent tangent operator was derived and implemented in the UEL algorithm. This resulted in faster convergence in the finite element simulations.

Mixed-mode loading conditions were investigated to demonstrate the versatility and robustness of the model. In addition, laboratory test results were used to validate the model. Good agreement was obtained between the model and laboratory testing results at various temperatures. With further modifications, this model has the potential to be implemented for use in characterizing cracking problems. The frictional feature and dilation control of the model can be especially useful for modeling cracks in mixed mode.

REFERENCES

- Beer, G. An Isoparametric Joint/Interface Element for Finite Element Analysis. *International Journal for Numerical Methods in Engineering*, Vol. 21, 1985: 585–600.
- Belytschko, T., W. K. Liu, and B. Moran. *Nonlinear Finite Elements for Continua and Structures*. 2000. New York: John Wiley and Sons, Inc.
- Carol, I., M. L. Carlos, and O. Roa. Micromechanical Analysis of Quasi-Brittle Materials Using Fracture Based Interface Elements. *International Journal for Numerical Methods in Engineering*, Vol. 52, 2001: 193–215.
- Desai, C. S., M. M. Zaman, J. G. Lightner, and H. J. Siriwardane, Thin-Layer Element for Interfaces and Joints. *International Journal for Numerical and Analytical Methods in Geomechanics*, Vol. 8, 1984: 19–43.
- Hohberg, J-M. PhD Dissertation: A Joint Element for the Nonlinear Dynamic Analysis of Arch Dams. Swiss Federal Institute of Technology, Zurich, 1992.
- Leng, Z., H. Ozer, I. L. Al-Qadi, and S. H. Carpenter. Interface Bonding between HMA and Various PCC Surfaces: Laboratory Assessment. Submitted for Publication at TRB, 2008.
- Mahtab, M. A., and R. E. Goodman. Three Dimensional Finite Element Analysis of Jointed Rock Slopes, Belgrade. *Proceedings of 2nd International Conference of Rock Mechanics*, Vol. 3, 1970: 353–360.
- Simo. J. C., and R. L. Taylor. Consistent Tangent Operators for Rate-Independent Elastoplasticity. *Computer Methods in Applied Mechanics and Engineering*, Vol. 48, 1985: 101–118.
- Zienkiewicz, O. C., and G. N. Pande. *Some Useful Forms of Isotropic Yield Surfaces for Soil and Rock Mechanics*. FEs in Geomechanics, 1977, London: J. Wiley. 179–190.

FABAC accelerated loading test of bond between cement overlay and asphalt layers

A. Chabot & J.M. Balay

Division Matériaux et Structures de Chaussées – LCPC, Bouguenais, France

B. Pouteau

Eurovia Management, Merignac, France

F. de Larrard

Direction Scientifique-LCPC, Bouguenais, France

ABSTRACT: This paper focuses on an experimental mechanical study of the bond fatigue life of composite (concrete over asphalt) pavements. This in-situ experiment is based on the use of an accelerated pavement testing facility (FABAC fatigue device). With the support of the French cement industry, a pavement section similar to an Ultra Thin White-topping structure has been realized at the LCPC-Nantes Center. Vertical joints of plain concrete have been loaded up to one million cycles. A non destructive seismic method, COLIBRI device, has been used to follow the interface debonding. Combined with core observations, it is possible to propose the accelerated fatigue damage scenario of such a composite pavement. The bond as well as the layers has been damaged by fatigue. These damages depend on temperature conditions wheel positions and interface treatments. Specific modeling and laboratory fatigue tests are proposed to be developed to deepen the knowledge of these deteriorations.

1 INTRODUCTION

Since 1990's, composite pavement structures have been raising a significant interest. Among these structures, those based on the association of a concrete overlay bonded to an existing asphalt sub-base are studying in this paper. Assuming a long lasting bond between these layers allows a reduction of layer thickness and therefore a reduction of construction costs (Cole et al., 1998). However, due to a lack of feedback, the durability of this bond under traffic condition is not granted. Previous studies have concluded that the weakness of the bond is located in the vicinity of vertical shrinkage cracks of cement concrete overlay (Pouteau et al., 2002). It is well known that the different elastic properties of the two media combined to the vertical crack down to the interface leads to theoretical stress singularities (Chabot et al., 2005). In practice, stress concentrations are expected and need to be studied in these zones (Fig. 1).

In 2001, due to a lack of long-lasting bond life data, the French government and the cementer industry proposed to launch a study aiming to a better prediction of lifetime of these composite pavement structures. This paper gives an overview of the in-situ accelerated loading pavement study that has been carried on during 2003 in relation to the PhD CIFRE ATILH Pouteau thesis (Pouteau, 2004) (Pouteau et al., 2004b) on composite pavements similar to Ultra-Thin White-topping (UTW) ones (CIMbéton, 2004) (Qi et al., 2004).

First the experimental study is presented. Then, results coming from non-destructive and destructive investigations are given. They lead to propose the damage scenario that has been probably occurred. Finally, specific modeling considerations are noticed before conclude.

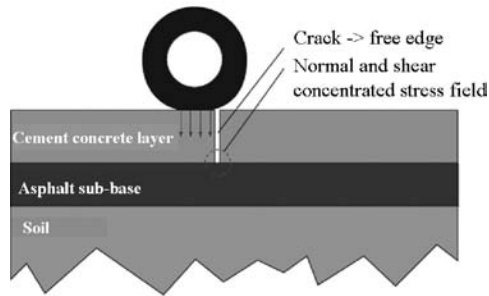


Figure 1. Location of stress singularities at the interface near a crack on a loaded composite pavement structure.

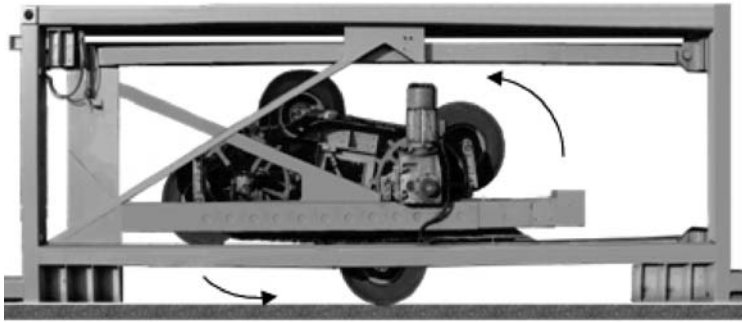


Figure 2. The FABAC machine, general view.

2 ACCELERATED LOADING PAVEMENT STUDY

At LCPC – Nantes Centre, the large circular Accelerated Loading Facilities (ALF), “Manège de fatigue” (Autret et al., 1987), can produce interesting fatigue pavement results (Hornych et al., 2008) but these tests are relatively expensive. For such an in-situ bond fatigue life study, the two linear ALF, called FABAC (Aunis & Balay 1998), offer an alternative solution at lower cost.

First, the FABAC machines are described. Then the composite pavement test section and its instrumentation are given before presenting the accelerated loading tests conditions.

2.1 FABAC Accelerated Loading Facility (ALF)

The two FABAC ALF are small heavy traffic simulators built in 1995. The two machines are similar enough, making it possible to test simultaneously two experimental pavement structures or surface layer under quite identical loading and environmental conditions. Each machine has four load modules. They are carried by a chain to apply the load along 2 m of the test track without lateral wandering (Fig. 2). The weight applied to each load module (twinned or single wheel) varies from 30 to 75 kN. The wheel speed varies from 0.5 to 7 km/h and the maximal load frequency is 50 loads per minute. The cumulated traffic is between 200 000 and 320 000 loadings weekly (http://www.lcpc.fr/fr/presentation/organigramme/div_msc/equip/fabac.php).

FABAC machine main characteristics are: overall length 11.20 m; overall width 2.50 m; total weight 173 kN; electrical power 50 kVA; complementary equipment: halogen heating system (25 kVA) for temperature control in the tested pavement (maximal temperature 70°C).



Figure 3. The composite pavement test section and the two FABAC machines (Pouteau, 2004a).

Table 1. Materials characteristic of the test pavement section.

Material	Theoretical mixes	In-situ control
Sand cement		Density: 94.7% (OPM)
Asphalt material (GB3)	Particle size distribution : 0/14 Pure bitumen grade: 35/50 Binder content: 4.3% Fatigue 1 million strain value: $\epsilon_6 = 91.10^{-6}$	Average thickness: 9.6 cm Void content: 7%
Cement concrete (BC)	Particle size distribution: 0/14 Type I Portland (CEM I 52.5): 255 kg/m ³ Filler: 55 kg/m ³ ; Water: 156 kg/m ³ 28 days slitting tension strength: 3.3 MPa 28 days compression strength: 32.6 MPa 28 days splitting tension strength: 4 MPa	Average thickness: 8 cm air content: 4,8% Slump: 3.5 cm

2.2 Composite pavement test section and instrumentation of the accelerated loading test

The pavement test section has been first designed with the help of the French ALIZE software and standard materials of its library. This calculus gives rather good global elastic pavement response although it uses the axisymmetric elastic Burmister modelling (1943) that can not take into account pavement discontinuities and the visco-elastic behaviour of asphalt material either. This pavement test section has been designed to get the greater interface shear rate between twin wheels. According to the French design method (LCPC-SETRA, 1994) and to bonding or not assumptions, the pavement test section was expected to resist to more than 1 million cycles of loadings for a 10 cm asphalt layer thickness (Pouteau, 2004a) (Pouteau et al., 2006a).

The composite pavement test section has been built on a 27.5 m long and 2 m width track. 9 joints (0.5 mm width) have been realized through the middle of the thickness of the cement concrete overlay. It produced 10 slabs with 2.75 m long and 1.95 m width (Fig. 3). This test section is composed of three kinds of joints: (i) shot blasted interface, (ii) no specific interface treatment, (iii) delaminated interface. This last type of joint has been obtained by using a plastic membrane interposed between the two layers to provide a slippery interface. Standard French twinned wheels have been used (0.662 MPa per wheel separated from 0.375 m each other). Experimental measurements gave an average $0.18 \times 0.28 \text{ m}^2$ contact area for each.

Similar to UTW structures, this pavement test section was built with a 0.08 m cement concrete (BC) thickness overlay ($E = 32600 \text{ MPa}$; $\nu = 0.35$) on a new 0.95 m asphalt material (GB3) thickness sub-base. This composite structure lays on a 0.15 m sand cement thickness capping layer so that this bi-material structure is assumed to be supported by an equivalent soil with a 120 MPa modulus and a $\nu = 0.35$ Poisson ratio. Table 1 details the material characteristics and in situ control procedures.

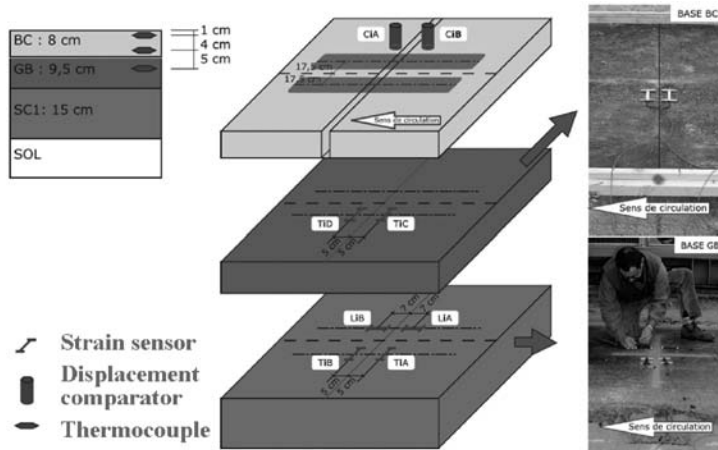


Figure 4. Instrumentation of the “i” joint of the composite pavement test section (Pouteau, 2004a).

For the asphalt material modulus characterization, Huet-Sayegh model (1963) fits rather good visco-elastic behavior predictions of experimental data. Equation 1 summarizes its complex modulus that depends on the frequency ω and the temperature θ :

$$E^*(\omega, \theta) = E_0 + \frac{E_\infty - E_0}{1 + \delta(j\omega\tau(\theta))^{-k} + (j\omega\tau(\theta))^{-h}} \quad (1)$$

with $\tau(\theta) = \exp(A_0 + A_1\theta + A_2\theta^2)$ a function of the temperature and three scalar parameters A_0 , A_1 and A_2 ; parameter E_∞ the instantaneous elastic modulus; E_0 the static elastic modulus; k and h are the exponents of the parabolic dampers ($1 > h > k > 0$) and δ a positive a dimensional coefficient balancing the contribution of the first damper in the global behavior. In that pavement section, the GB3 Huet Sayegh Poisson ratio used is $\nu = 0.35$ and the modulus coefficients fitted are: $E_0 = 40$ MPa, $E_\infty = 32800$ Mpa, $h = 0.71$, $k = 0.213$, $\delta = 2.2$, $A_0 = 3.62941$, $A_1 = -0.39557$, $A_2 = 0.00205$. At the French average speed (72 km/h) and the French average temperature (15°C), the time-frequency equivalence assumption gives an asphalt equivalent modulus (15°C–10 Hz) equal to 13000 MPa. With FABAC devices the speed is 7 km/h, that is to say 10 times less than the French average speed. As the ratio between the speed of the load and the frequency is also supposed to be constant (Peyronne & Caroff, 1984), in a first approximation, the frequency taken into account for the E modulus determination is 1 Hz. Therefore, for pavement elastic calculus, the equivalent GB3 modulus value at 15°C is assumed to be $E(15^\circ\text{C} - 1 \text{ Hz}) = 8500$ MPa and, for a greater temperature, $E(30^\circ\text{C} - 1 \text{ HZ}) = 1100$ MPa.

To get mechanical informations near each joint, several sensors have been introduced.

On Figure 4, one can see that three thermal gages have been used for the measurement of cement and asphalt material temperatures. CiA and CiB are supposed to give informations on possible relative displacements between the BC layer and the GB layer. LiA, LiB, TiA and TiB denote respectively the two longitudinal and transversal strain sensors that have been put on the bottom of the GB3 at 5 cm both side of the joint number “i”. TiC and TiD denote the two longitudinal strain sensors that have been put at the bottom of the BC at 5 cm both side of the joint.

To test the effect of a shot basting interface treatment with the help of the two FABAC machines, two similar environmental tests have been performed on two different types of interface (shot basted or not) between cement overlay and the asphalt layer. Only joints initially perfectly bonded have been loaded. The first test has been done during summer, loading joints number 3 and 7. The second test have been done during winter, loading joints number 2 and 6 (Fig. 3).

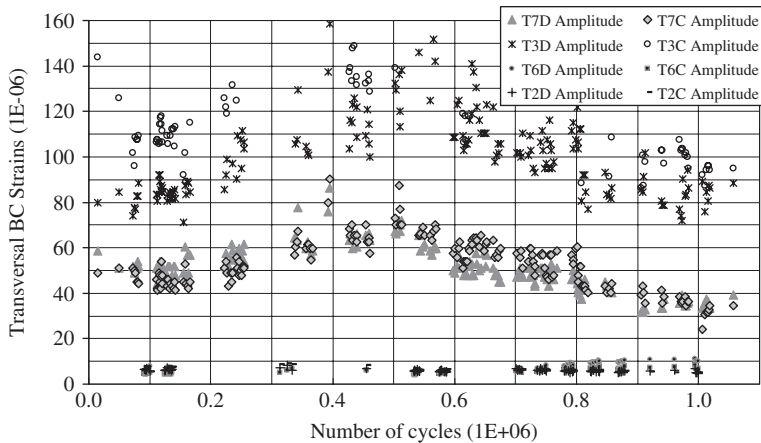


Figure 5. Transversal strains at the bottom of the concrete cement layer for joints 2,3,6,7 (Pouteau, 2004a).

3 INVESTIGATION TOOLS AND RESULTS

In that section, gage results for the 4 joints tested (J2, J6 and J3, J6) (Fig. 3) are first presented. Then a non destructive method and its results are given. The experiment ends with a coring campaign which gives the opportunity to analyze the last phase of life of this pavement section.

3.1 Gage results and interpretation

The thermal gages indicated that the winter test of joint 2 and 6 has been made at a temperature contained between 5 to 15°C. The summer test of joints number 3 and 7 have been tested at 16 to 30°C before and after the heat wave of summer 2003 (Fig. 3).

Relative displacement measurements between cement and asphalt layers (CiA and CiB) gave values in the range of the gage resolution. Unfortunately, these sensors were not well located to be sensible to the delamination process and no useful data provided by them (Pouteau, 2004a). Thus, during the pavement building and the tests a lot of strain gages at the bottom of asphalt layers have been unfortunately disabled. Here-under only results on TiC and TiD transversal strain measurements at the bottom of the BC layers can be used (Fig. 5).

Figure 5 shows that there is a sharp difference between winter tests (joints number 2 and 6) and summer tests (joints number 3 and 7) in terms of transversal strain at the bottom of the BC layer. These experimental strain results have been compared to calculation without any discontinuity assumption (that is to say bounding hypothesis and no joint or crack modelling). Viscoelastic calculus made with ViscoRoute software that integrates Huet Sayegh law (equation1) (Duhamel et al., 2005) shows that the viscoelasticity of the asphalt material layer does not affect so much the structure behavior for the speed and the different temperature values that have been measured during the tests. Both elastic and viscoelastic calculus made for the asphalt material at 15°C and 30°C give higher transversal strain values than longitudinal ones at the bottom of the BC layer. For winter tests at 15°C, pavement calculus, under only one load, give strain transversal value around $10 \cdot 10^{-6}$, while at 30°C for summer tests, they give $50 \cdot 10^{-6}$ to $60 \cdot 10^{-6}$ values depending on the elastic or viscoelastic calculus assumptions (§2.2). These values are in same range of values than those obtained on (Fig. 5) at the initial state of joints number 2, 6 and 7.

In addition, for summer tests, the transversal strains at the bottom of the BC layer of the joint 3 (not shot basted) have greater values compared to those obtained for the joint 7 (shot basted). All these transversal strain values increase until 0.45 million cycle loadings before decreasing. Increase of strain fits with a growing of debonding interface. Strain decreasing can be explained

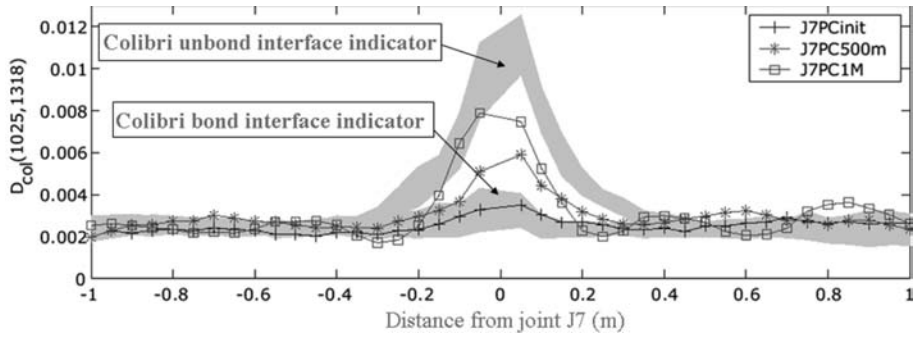


Figure 6. Evolution of the bond interface indicator of joint 7 (shot blasted – hot T°C) (Pouteau, 2004a).

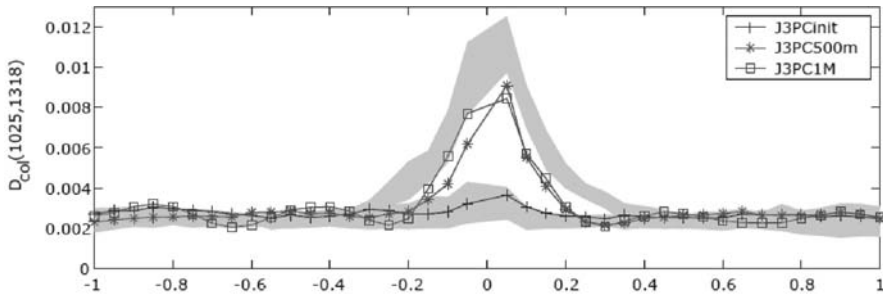


Figure 7. Evolution of the bond interface indicator of joint 3 (not shot blasted – hot T°C) (Pouteau, 2004a).

by a vertical crack initiation at the bottom of the BC layer, under the wheel path. On the contrary, during the winter environmental conditions, no great strain differences can be founded between joint 2 (not shot basted) and joint 6 (shot basted). The only difference observed is that the strain field of joint 6 seems to increase a little until the end of the test.

3.2 Non destructive “Colibri” results

To investigate on the evolution of the pavement test section and the durability of the bond of its interface layers, a non destructive method has been used with the help of the seismic Colibri device. This method consists on beating the structure with a hammer. Then the seismic pavement response by means of an accelerometer is measured. Different investigations have been made to find a UTW Colibri bounding indicator. All details can be found in (Pouteau, 2004a) (Pouteau et al., 2006b). To summarize, the best UTW Colibri bounding indicator was found for the 1025 Hz to 1318 Hz range of frequencies. It has been denote $D_{col}(1025, 1318)$. That method was used on initial bounding joint 2, 3, 6, 7, 8, 9 and initial delaminated joint 1, 4 and 5 (Fig. 3). It has been possible to give typical bounding or delaminated signal envelopes (Fig. 6). With that reference signals, the four joints tested have been investigated at different loading states among two positions of the wheel path. Here under, Colibri indicator curves between the two wheel paths (JiPC, i number of the joint) are presented for joint 7, 3, 6 and 2 on Figures 6 to 9 at different positions from the joint. JiPCinit indicates the initial state of the joint. JiPC250m, JiPC500m and JiPC1M indicate respectively the 0.25, 0.5 and 1 million of cycle loadings. They are quite similar to those obtained under the wheel path (Pouteau, 2004a).

From these non destructive results (Figs 6 to 9), it is clear that failure mechanisms have been located around the joint. On these signals, it was difficult to really notice at the end of the million cycles of loadings the benefit of the shot blasting interface treatment on bounding conditions.

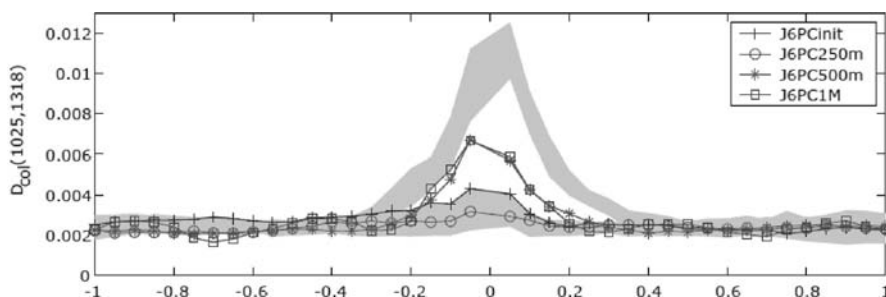


Figure 8. Evolution of the bond interface indicator of joint 6 (shot blasted – low T°C) (Pouteau, 2004a).

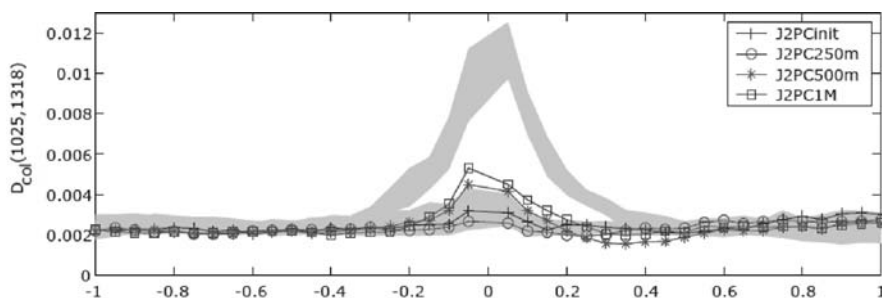


Figure 9. Evolution of the bond interface indicator of joint2 (not shot blasted – low T°C) (Pouteau, 2004a).

Nerveless it might be observed that the summer conditions have been the worst conditions for the long lasting composite pavement life (Fig. 6) (Fig. 7). For those high temperatures, the shot blasting interface treatment (Fig. 6) seems to delay the failure debonding process between the BC and the GB3 layers. Laboratory fatigue test data have confirmed that the shot blasting treatment of interface between cement and asphalt is important for the long lasting bond life (Pouteau et al., 2004b). But in relation to Colibri measurements that have been made on a real experimental pavement of the French national road number 4 (RN4) (Pouteau et al., 2006b), at this state of this study, it is hard to conclude that the Colibri signal evolution represents precisely delamination phenomenon or more generally failures among the material layers.

3.3 Core results

To add more information about failure, a core sample campaign has been finally made to link Colibri results with bounding core states. For each joint, 8 cores have been extracted at several positions of the wheel path and distance from the joint (Fig. 10). Interface cracking propagation informations and failure mechanisms had to be found out. On Figure 10 are only presented core sample photos that have been taken under the wheel path and on the joint (I), between the two twin wheel path (II) and under the wheel path at 15 cm before the joint position (D index for joint 2, C index for joint 6, 3 and 7).

First, according to the first assumptions written in the introduction of this paper, Figure 10 shows that the loads of the FABAC devices propagated the crack vertically from the joint to the interface between BC and GB3 layers. This is true for all the type of joints. These vertical cracks located near the two different material layers produce stress singularities (Fig. 1).

Concerning joint 7 and 3, it can be noticed that hot temperature conditions of loading (from 15°C to 30°C) lead to damage easily the interface between layers near the joint (Fig. 10). For joint 3 which its interface is not shot blasted, it seems that the bonding conditions have not been realized at all. No damages can be seen in its asphalt layer. Under the wheel path, the cement concrete layer

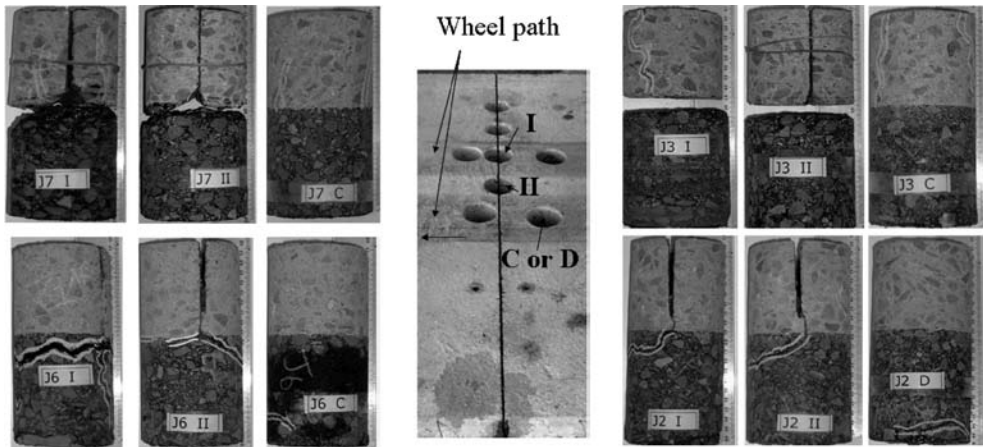


Figure 10. Core sample campaign after 1million loadings for joints number 7, 3, 6 and 3 (Pouteau, 2004a).

has been hardly damaged by vertical cracks coming from the interface even if, far from the joint, there is no delamination observed. These observations can explain the high level of transversal strain measurements at the bottom of the BC layer (Fig. 5). For joint 7 which its interface is shot blasted, the top of its GB3 layer have been hardly damaged. It seems that these damages have occurred before the delamination and the propagation of the vertical crack along the BC layer under the wheel path. In these two cases, the great difference of modulus value between these two material layers associated to a thin overlay is an enemy to a long lasting interface bond between these layers near the joint. In that case, the shot blasted interface treatment between BC and GB3 layers is important to ameliorate the long lasting bond life.

On Figure 10, related to joint 6 and 2, it can be observed that the low temperature conditions of loading (from 5°C to 15°C) lead to damage the asphalt layer. The bond between the two layers seems to resist. No damages, as vertical cracks, have been observed at the bottom of the BC slayers. The vertical crack coming from the joint propagated in the GB3 layer in a parallel way to the interface between layers. High level of shear stresses is supposed to be found. In that case, the effect of the different interface treatments (shot blasted or not) did not count so much on the conditions of the long lasting bond life compared to the shear mechanical performance of the GB3 layer.

These fatigue tests and this study have to be linked to more data before conclude.

3.4 Damage scenario

From all of these experiment observations, temperature effects on the ratio of modulus between the cement and asphalt material and the load positions from the joint seem to be the more damageable effects of the long lasting bond life of such a composite pavement. These first conclusions lead to propose a damage scenario of this composite pavement test section (Fig. 11) (Pouteau, 2004a).

From the core campaign and Colibri measurements, it has been confirmed that the first failures appear upon the joint between the two wheel paths. Then, depending of the temperature, cracks propagate along the joint under the wheel path. They generate a delamination between the BC and the GB3 layers or cracks parallel to the interface in the GB3 layer. Finally, when a delamination between layers exists vertical cracks appear at the bottom of the BC layer.

4 PAVEMENT MODELING CONSIDERATIONS

To add more information on that deterioration process and to get finally failure criteria of such a pavement structure, it is necessary to link these experimental results to careful analyses of the 3D stress field state. Due to existing singular stress fields located near the vertical crack of the

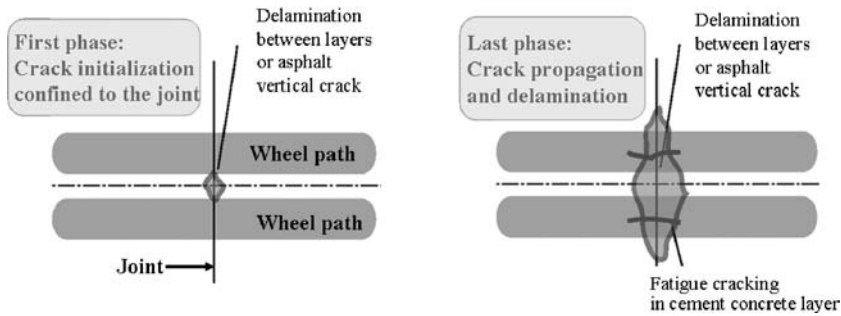


Figure 11. Damage scenario.

cement concrete overlay and the interface of these two different material media (Fig. 1), it is hard to analyze easily these 3D stress fields with classical modelling and FEM 3D.

Since 2001, it is proposed at LCPC to develop and make a proper analysis of crack initiation and propagation in such a cracked pavement structures. This approach is destined to be used by engineers. A 3D simplified model (named the Multi-particle Model of Multi-layer Materials, M4) linked to the Boussinesq model for the soil (M4-5nB) has been developed (Tran et al., 2004). It has the advantage of reducing the real 3D problem to the determination of regular plane fields (x, y) per layer and interfaces. M4-5n modelling approach makes possible simple determinations of delamination criteria (Caron et al., 2006). M4-5nB computations are in good accordance compared to 3D FEM results and need less time consuming (Chabot et al., 2005). Several inelastic fields can be introduced as data for the modelling of shrinkage, thermal conditions and debonding effects (Chabot et al., 2007). A software tool is under development.

With that so-called M4-Boussinesq model, it has been proposed to analyze the initial mechanical fields of that in-situ experiment (Chabot et al., 2004). This modelling shows in simplified modelling conditions that, when the load is located at the edge of the joint, the interface pavement composite system is loaded in mixed mode conditions. In fact, it gives maximum shear and normal stress fields at the edge of the crack at the interface between the concrete and the asphalt layers. These results needs to be examined in greater details under real experimental conditions (free edges along the transversal-axis; inclusion of thermal gradient effects in the thin bonded cement concrete layer; real distribution of tire/pavement contact; comparison with instrumentation-based measurements; analysis of visco-elastic effects from asphalt material, etc.) (Chabot et al., 2007). Nevertheless, this modeling finds that the normal interface stress is highly in compression underneath the load and remains significant in tension on the unloaded side. These interface stress fields produce debonding.

To help engineer to find the best realistic and resistant bi-material couple, it is necessary to deepen this work with the help of bi-material specimens controlled with mixed mode laboratory fatigue tests. A first tentative approach has been made for the BC and GB3 materials of this study (Pouteau et al., 2002) (Pouteau, 2004). M4-5n approach help to design the lab specimens for optimizing the delamination of the interface. These lab experiments shown that a shot blasted interface could stop and delay the debonding. But in such a bi-material couple, due to the parasite effect of the visco-elastic behavior of the asphalt material, another specific flexural laboratory tests have to be developed. Those produced by the so-called "Mefisto" device (Vecoven, 1990) or by the new laboratory test proposed at ENPC by (Florence et al., 2004) should be better candidates to these experimental studies.

5 CONCLUSIONS

This study deals with an experimental in-situ performance of a pavement bound interface between a thin cement concrete layer and an asphalt one (Pouteau, 2004). The traffic loading is simulated by means of two LCPC linear Accelerated Loading Facilities, call FABAC devices. These FABAC

devices simulate heavy traffic by applying the passage of 6.5 tonne twin axle repeatedly loads. After a million passages of this reference axle on different pavement joints, fatigue damage have been observed. It has occurred as well at the interface between layers as in the concrete and the asphalt materials. Transversal strain measurements at the bottom of the BC layer, non-destructive Colibri measurements combined with core sampling after the tests, make it possible to reconstitute a structural deterioration scenario. These tests had shown that the temperature and the position of the load near the joint are the most damageable factors. Especially for hot temperature environmental conditions, it also has being shown that a shot blasting interface treatment delay the delamination between the cement overlay and the asphalt layer. During lab test on bi-material specimen, the effect has been also observed for low temperature.

To find a simple delamination criteria to use and design recommendations, it is proposed to deep the mechanical understandings of this deterioration with the help of a specific modeling and laboratory fatigue bi-material tests. Connected to reflective cracking ALT-APT experience done by (Pérez et al., 2007), these studies help to develop of a laboratory equipment to evaluate the crack propagation of such a cracked pavements. These investigations are proposed to be continuing in relation to a LCPC research program called Fondephy (<http://or.lcpc.fr/fondephy>).

ACKNOWLEDGEMENT

Authors acknowledge the financial and technical supports of ATILH (Association Technique de l'Industrie des Liants Hydrauliques) and thank SPECBEA and CIMBETON for their contribution to this study. Authors also acknowledge Gilles Coirier, Thierry Gouy, Jean-Pierre Kerzreho, Patrick Maisonnœuvre, Gérard Leroy, Jean-Paul Nerfie and Jean-Michel Simonin from LCPC for their experimental technical support.

REFERENCES

- Autret, P., de Boissoudy, A. B. & Gramsammer, J. C. 1987. The circular test track of the Laboratoire Central des Ponts et Chaussées – First Results. *Proc. 6th Intern. Conf. on Structural Design of Asphalt Pavements*, Ann Arbor, June 13–17 1997, 1: 550–561.
- Aunis, J. & Balay, J. M. 1998. An applied research programme on continuous reinforced concrete pavements: the FABAC project. *Proceedings of the 8th International Symposium on Concrete Roads*, Lisbon September 13–16 1998.
- Caron, J. F., Diaz Diaz, A., Carreira, R. P., Chabot, A. & Ehrlacher, A. 2006. Multi-particle modelling for the prediction of delamination in multi-layered materials. *Composites Sciences and Technology*, **66**(6), 755–765.
- Chabot, A., Tran, Q. D. & Pouteau, B. 2004. Simplified modelling of a cracked composite pavement, *First International Elsevier Conference on Failure Analysis*, Lisbon July 12–14 2004.
- Chabot, A., Tran, Q. D. & Ehrlacher, A. 2005. A simplified modeling for cracked pavements - Modèle simplifié pour le calcul des chaussées, *Bulletin des Laboratoires des Ponts et chaussées* (258–259): 105–120.
- Chabot, A., Tran Q. D. & Ehrlacher, A. 2007. A modeling to understand where a vertical crack can propagate in pavements. In Taylor & Francis Group Proceedings, *International Conference on Advanced Characterization of Pavement and Soil Engineering Materials*, Athens June 20–22 2007, 1: 431–440.
- CIMbéton, 2004. Le Béton de Ciment Mince Collé “BCMC”. *Collection Technique CIMbeton T60*, 2nd edition.
- Cole, L. W., Mack, J. W. & Packard, R. G. 1998. Whitetopping and ultra-thin whitetopping the US experience. *8th International Symposium on Concrete Roads*, 1998.
- Duhamel, D., Chabot, A., Tamagny, P. & Harfouche, L. 2005. Viscoroute: Visco-elastic modeling for asphalt pavements – Viscoroute: Modélisation des chaussées bitumineuses. *Bulletin des Laboratoires des Ponts et chaussées* (258–259): 89–103.
- Florence, C., Foret, G., Tamagny, P., Sener, J.Y. & Ehrlacher, A. 2004. Design of a new laboratory test simulating the reflective cracking in Pavements with cement treated bases. In RILEM Proceedings PRO 37, *Fifth Internat.l RILEM Conf. Cracking in Pavements*, Limoges May 5–8 2004, 147–154.
- Hornych, P., Kerzreho, J. P., Chabot, A., Bodin, D. & Balay, J. M. 2008. The LCPC's ALT facility contribution to pavement cracking knowledge. Proposed to the *Sixth International RILEM Conference Cracking in Pavements*, Chicago June 16–18.

- LCPC-SETRA (décembre) 1994. Conception et dimensionnement des structures de chaussée. *Guide Technique LCPC- SETRA*.
- Peyronne, C. & Caroff, G. 1984. *Cours des routes – Dimensionnement des chaussées*. Paris: Presses de l'École Nationale des Ponts et Chaussées (ISBN 2-85978-066-1).
- Pérez, S. A., Balay, J. M., Tamagny, P. & Petit, Ch. 2007. Accelerated pavement testing and modeling of reflective cracking in pavements. *Engineering Failure Analysis*, 14 (8): 1526–1537.
- Pouteau, B., Chabot, A. & De Larrard, F. 2002. Etude en laboratoire du collage béton/ matériaux bitumineux. *Matériaux 2002*, 21–25 octobre, Tours.
- Pouteau, B. 2004a. *Durabilité mécanique du collage blanc sur noir dans les chaussées*. PhD thesis of the Ecole Centrale de Nantes (<http://www.lcpc.fr/msc>).
- Pouteau, B., Balay, J.-M., Chabot, A. & De Larrard, F. 2004b. Fatigue test and mechanical study of adhesion between concrete and asphalt. *9th International Symposium on Concrete Roads*, Istanbul 3–6 April 2004.
- Pouteau, B., Chabot, A., De Larrard, F. & Balay, J. M. 2006a. Mécanique des chaussées Béton sur grave-bitume, Etude de la tenue du collage entre béton et enrobé sur chaussée expérimentale (1^{re} partie). *Revue Générale des Routes et des Aérodrômes (RGRA)* (847): 85–90.
- Pouteau, B., Simonin, J. M. & De Larrard, F. 2006b. Mécanique des chaussées Béton sur grave-bitume, Suivi du chantier expérimental RN4 de chaussée composite (2^{ème} partie). *Revue Générale des Routes et des Aérodrômes (RGRA)* (848): 62–66.
- Qi, X., Mitchell, T. & Sherwood, J. A. 2004. Evaluation of UTW fatigue cracking using FHWA's Accelerated Loading Facility. In RILEM Proceedings PRO 37, *Fifth International RILEM Conference Cracking in Pavements*, Limoges May 5–8 2004: 37–44.
- Tran, Q. D., Chabot, A., Ehrlacher, A. & Tamagny, P. 2004. A simplified modelling for cracking in pavements. In RILEM Proceedings PRO 37, *Fifth International RILEM Conference Cracking in Pavements*, Limoges May 5–8 2004: 299–306.
- Vecoven 1990. Crack reflection treatment testing machine for hydraulic treated pavement. *Revue Générale des Routes et des Aérodrômes (RGRA)* (680): 19–21.

Low temperature cracking in asphalt overlays bonded to rigid pavements

H.M. Yin

Transportation Laboratory, California Department of Transportation, Sacramento, California, USA

W.G. Buttlar & G.H. Paulino

University of Illinois at Urbana-Champaign, USA

ABSTRACT: The elastic fields in an overlay bonded to a stiffer substrate are investigated, when the system is subjected to thermally induced stress. A two-dimensional solution of the displacement field is derived for periodic discontinuities distributed in a hot mix asphalt overlay bonded to a Portland Cement Concrete pavement, where the length of the pavement before cracking develops is much larger than its layer thickness. Energy release rates are calculated from the model for three-dimensional channeling. By comparing the energy release rates with the fracture toughness of the overlay, crack initiation and crack spacing for a given temperature change can be estimated. The solutions are valuable to the pavement analyst who seeks to understand the general mechanisms of thermally induced pavement deterioration and for the researcher wishing to perform early stage verification of more complex pavement models.

Keywords: Thermal stresses; Fracture mechanics; Asphalt overlay; Rigid pavements; Cracking.

1 INTRODUCTION

Hot Mix Asphalt (HMA) pavements are typically overlay/substrate systems with one or more asphalt concrete layers constructed upon either: granular aggregate layers; compacted soil layers (sometimes cement- or pozzolanically-stabilized), or, in case of pavement rehabilitation; existing Portland Cement concrete slabs. When an asphalt pavement is subjected to a thermal loading due to the ambient temperature change, thermal cracking can form across the width of the pavement [1]. Thermal cracking is one of the most devastating distresses that can occur in asphalt pavements in cold climates. Various empirical and “mechanistic-empirical” models [1–3] have been proposed, in which various field observations and laboratory experiments were conducted to predict crack spacing in asphalt pavements.

The aforementioned empirical models have provided good insight towards the factors underlying crack development and crack spacing in asphalt pavements. However, the thermal stress distribution in pavements, a dominant factor controlling thermal crack development, has not been directly investigated in those models. To analyze the elastic fields of pavements, finite element method has been widely used to calculate the local stress and strain [4–6]. Since the quality of numerical simulations depends on the quality of meshing (e.g. discretization aspects), it is not straightforward to extend the results to general cases. Thus, analytical solutions are a valuable tool for researchers for model verification, and ultimately, to gain a better insight into mechanical responses and damage mechanisms in pavements.

One-dimensional (1D) models [7–9] have been developed to predict tensile stress distribution in a pavement with frictional constraint. The frictional force from the substrate is balanced by a uniform tensile stress along the thickness of the overlay. Because the frictional shear forces reside at the

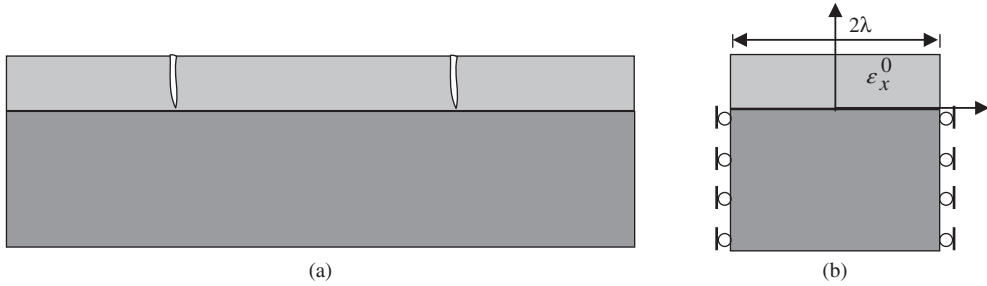


Figure 1. An asphalt overlay fully bonded to a thick base-layer: (a) the lateral view of the cracks, and; (b) one section between two cracks with a fully-bonded interface.

bottom of the pavement, considerable shear stress will be induced along the bottom of the overlay but vanishes at the unrestrained upper surface of the pavement. Since a 1D model can neither solve the shear stress distribution in the overlay nor consider the temperature field along the thickness, a two-dimensional (2D) model is necessary to accurately describe the thermal stress distribution.

Beuth [10] presented solutions for fully and partially cracked film problems for elastic films bonded to elastic substrates with one crack. Hong et al. [11] developed a model to predict the crack spacing and crack depth in highway pavements assuming that the effect of a crack in the overlay could be described by an increase in effective compliance. Xia and Hutchinson [12] and Shenoy et al. [13], respectively, investigated the crack patterns in the overlay and proposed an elastic solution in the integral form using dislocations as the kernel functions. Due to the diversity of pavement design and construction procedure, thermal cracking may develop within asphalt pavement in various forms, which depend on the corresponding loading conditions and boundary conditions.

Yin et al. [14] presented an explicit elastic solution for an overlay resting on a granular base considering frictional boundary condition and fully thermal discontinuities. Recently, a series form solution was obtained for partial-depth cracks within asphalt overlay rested on rigid pavements, in which the stiffness of rigid pavements are assumed to be infinite [15]. This paper investigates the elastic fields due to low temperature cracking in a HMA overlay bonded to a Portland Cement Concrete (PCC) pavement as seen in Fig. 1, where the stiffness of the PCC is typically higher than that of the asphalt layer, and the joint spacing of the PCC pavement is much higher than the thermal crack spacing of the asphalt overlay. Therefore, the effect of reflective cracking of the base layer is not investigated in this study.

A two dimensional elastic solution is derived for a section of pavement surface between two discontinuities within the overlay. From this solution, the energy release rate of the three-dimensional channeling cracks is calculated. Using Beuth's exact solution [10] of energy release rate for one crack occurring in an infinitely long section, the closed-form solution for a finite width pavement section between cracks is derived. Comparisons to FEM simulations are then provided to verify the accuracy and applicability of the proposed solution.

2 FORMULATIONS

Consider a long asphalt pavement (thickness h , Young's modulus E , Poisson's ratio ν , thermal expansion coefficient α) resting upon a base-layer (see Fig. 1). With a drop in ambient temperature, the asphalt overlay is subjected to a larger contractive deformation than that in the base-layer. When the thermal stress reaches a certain value, uniformly spaced thermal cracks may initiate. Because the width of pavements is much larger than their depth, the stress gradient in the width direction is small. Based upon a periodic boundary condition, two-dimensional stress/strain distributions in a section between two neighboring cracks can be analyzed, which describe the mechanical fields in the overall pavement.

Because the pavement is fully bonded with the base-layer, the bottom of the pavement can be assumed to remain in plane (i.e., in a horizontal plane). Because the thickness of the pavement is much smaller than its length and the top surface is free, generally the top surface of the pavement remains approximately in plane during the temperature change if a negligible amount of uplift due to curling occurs. Thus, we assume that all points of a plane normal to the y direction is still in the same plane after deformation, i.e.,

$$u_y(x, y) = u_y(y). \quad (1)$$

For this two-dimensional elastic problem, the constitutive law reads

$$\sigma_x = E(\varepsilon_x - \bar{\alpha}T), \quad \tau_{xy} = \mu\gamma_{xy}, \quad (2)$$

where $\bar{\alpha}$ denotes the difference between the coefficients of thermal expansion for the asphalt overlay and the base-layer. Considering the equilibrium condition in x direction, we can write

$$Eu_{x,xx} + \mu u_{x,yy} = 0. \quad (3)$$

Using the method of separation of variables, we can find the general solution as

$$u_x(x, y) = (A_1 e^{cx/h} + A_2 e^{-cx/h}) [B_1 \sin(dy/h) + B_2 \cos(dy/h)], \quad (4)$$

where A_1, A_2, B_1 and B_2 are constants to be determined via boundary conditions, and where

$$d = \sqrt{E/\mu c}.$$

From the symmetry of the geometry and the free upper surface, we can write

$$u_x(0, y) = 0; \quad u_{x,y}(x, h) = 0. \quad (5)$$

Using the above boundary conditions, we simplify Eq. (4) as follow:

$$u_x(x, y) = B \sinh(cx/h) \cos d(1 - y/h). \quad (6)$$

Due to the temperature change, there exists a contractive mismatch thermal strain in the overlay, written as ε_x^0 . Because the overlay is fully bonded to the thick base-layer, thermal stress will be induced and cracks may form when the stress is beyond the strength of the asphalt materials. To solve the stress distribution in the asphalt overlay, a 2D Cartesian coordinate system is setup with the origin at the central bottom of the section. The plane strain problem is considered.

The displacement field in the asphalt overlay in Fig. 1(b) can be obtained by superposition of the following two problems: First, the asphalt overlay is subjected to both the thermal strain and an imaginary tensile stress (see Fig. 2(b)), and the final displacement is zero. Second, the asphalt overlay is subjected to the corresponding compressive stress, but no thermal strain exists in the overlay (see Fig. 2(b)). The displacement field can be obtained by the general displacement solution in Eq (6), in which two parameters are to be determined as B and c .

At both ends, stress $\sigma_x = -\bar{E}_1 \varepsilon_x^0$. Due to assumptions of Eq. (1), this boundary condition cannot be rigorously satisfied at every point. However, the total normal force should be zero, namely

$$\frac{1}{h} \int_{y=0}^h \sigma_x(\lambda, y) dy = -\bar{E}_1 \varepsilon_x^0. \quad (7)$$

The substitution of Eq (6) into Eq (2), and Eq (2) into Eq (7) yields

$$B = -\frac{\bar{E}_1}{\mu_1} \frac{h \varepsilon_x^0}{\cosh(c\lambda/h) \sin d}. \quad (8)$$

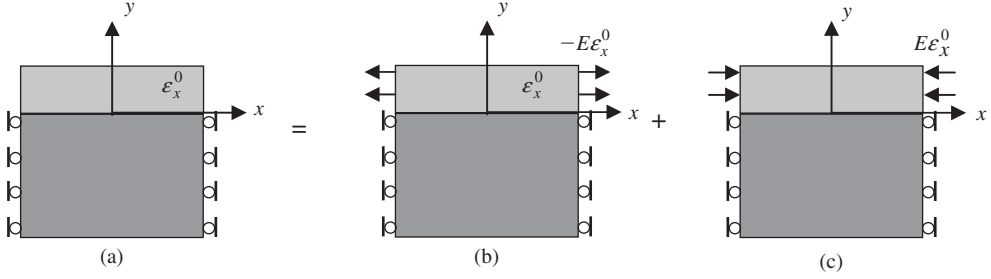


Figure 2. Schematic illustration for solving the elastic field in one section: (a) the overlay subjected to a mismatch contractive thermal strain; (b) the overlay subjected to the thermal strain and an imaginary tensile stress, and; (c) the overlay subjected to the imaginary compressive stress.

To obtain the parameter c , Xia and Hutchinson's method [12] is used, in which comparison of the energy release rate with the exact solution provides

$$c = \frac{2}{\pi g(\alpha, \beta)}; \quad d = \sqrt{\frac{\bar{E}_1}{\mu_1}} c. \quad (9)$$

The detailed derivation of the above equation is given later. Here the function $g(\alpha, \beta)$ is illustrated in Fig. 3. It depends on Dundur's parameters, α and β , namely,

$$\alpha = \frac{\bar{E}_1 - \bar{E}_0}{\bar{E}_1 + \bar{E}_0}, \quad \beta = \frac{\mu_1(1-2\nu_0) - \mu_0(1-2\nu_1)}{2\mu_1(1-\nu_0) + 2\mu_0(1-\nu_1)}, \quad (10)$$

with $\bar{E}_0 = E_0/(1-\nu_0^2)$ and $\mu_0 = E_0/[2(1-\nu_0)]$. Fig. 3 shows the function $g(\alpha, \beta)$ for $\beta=0$ and $\beta=\alpha/4$ [10], respectively. For convenience of the later simulation, $g(\alpha, \beta)$ is fitted by a function (see Fig. 3) as:

$$g(\alpha, \beta) \approx \frac{1.258 - 0.40\alpha - 0.26\alpha^3 - 0.30\alpha^4}{1-\alpha}. \quad (11)$$

Fig. 3 shows that the dependence of $g(\alpha, \beta)$ on β is weak except when α close to -1 [12]. Thus, the fitted function in Eq (11) will be used to approximate $g(\alpha, \beta)$ in the following simulations.

The combination of Eqs. (6), (8), and (9) provides a closed-form elastic solution for the reduced problem. Then, the total displacement and stress fields in Fig. 1(b) are:

$$u_x(x, y) = B \sinh(cx/h) \cos d(1-y/h), \quad (12)$$

$$\sigma_x = \bar{E}_1 \left(\varepsilon_x^0 + Bc/h \cosh(cx/h) \cos[d(1-y/h)] \right), \quad (13)$$

and

$$\tau_{xy} = \mu_1 B d / h \sinh(cx/h) \sin d(1-y/h) \quad (14)$$

with B in Eq (8), d and c in Eq (9).

Eq. (9) is derived by comparison of the energy release rate of the crack in this solution with the exact solution provided by Beuth [10]. Consider the section in Fig. 1(b) with two discontinuities at the both ends and with a large width compared to the thickness. When the external mechanical loading in the substrate increases, a straight, steady-state channeling crack will initiate at the middle edge of the section and propagate in the $-z$ direction as seen in Fig. 4. Far ahead of the crack front, the elastic fields are not influenced by the crack and are written in Eqs. (12)–(14). Thus the tensile

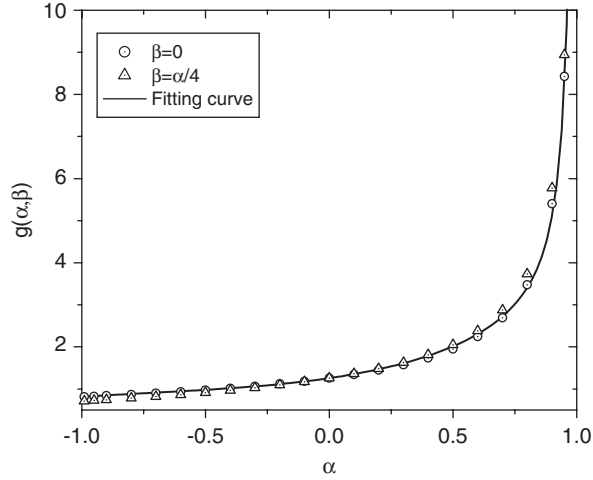


Figure 3. The function of $g(\alpha, \beta)$ vs. α for $\beta=0$, $\beta = \alpha/4$ and the fitting curve.

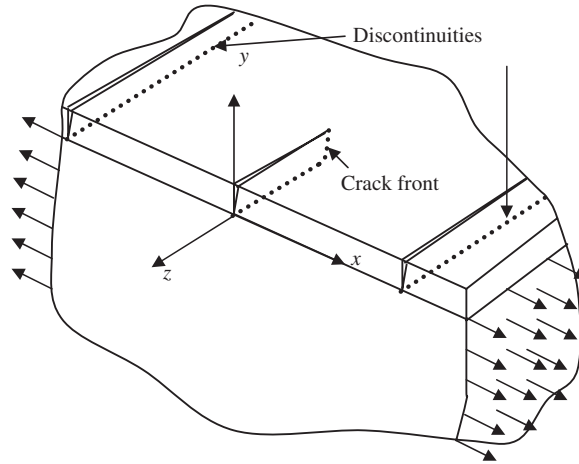


Figure 4. Schematic illustration of three-dimensional channeling.

stress at the symmetric plane is

$$\sigma_x(0, y) = \left(1 - \frac{d \cos[d(1-y/h)]}{\cosh(c\lambda/h) \sin d} \right) \sigma_x^0, \quad (15)$$

with $\sigma_x^0 = \bar{E}_1 \varepsilon_x^0$, and the shear stress is zero.

Far behind the crack front, the pavement is cracked into two sections, and the elastic fields in each section can also be obtained by Eq. (12) by replacing λ by $\lambda/2$ in the new local coordinate system. Then we can solve the crack opening displacement as:

$$\delta(0, y) = 2 \sqrt{\frac{\bar{E}_1}{\mu_1}} h \varepsilon_x^0 \frac{\tanh\left(\frac{c\lambda}{2h}\right)}{\sin d} \cos[d(1-y/h)], \quad (16)$$

To recover this crack opening displacement, the stress in Eq. (15) has to be applied along the cracking surface. Thus, the energy release rate of the crack front can be obtained as the work done to close the crack opening displacement [10], namely,

$$G = \frac{1}{2h} \int_0^h \sigma_x(0, y) \delta(0, y) dy. \quad (17)$$

Because the free boundary condition in Eq. (7) cannot rigorously be satisfied at every point along the crack surface, we used the averaged stress along the thickness to represent the local stress. Here we also use the averaged stress in Eq. (17), such that the energy release rate can be explicitly written as

$$G = \frac{(\sigma_x^0)^2}{E_1} \frac{h}{c} \left[2 \tanh\left(\frac{c\lambda}{2h}\right) - \tanh(c\lambda/h) \right], \quad (18)$$

which provides the same form as Xia and Hutchinson's results [12] (Eq (30) of the Ref.) by setting $l = h/c$.

When the section is infinite long, i.e. $\lambda \rightarrow \infty$, Eq (17) is reduced to

$$G = \frac{(\sigma_x^0)^2}{E_1} \frac{h}{c}. \quad (19)$$

Beuth [10] also proposed the energy release rate averaged over the front of a semi-infinite isolated crack as

$$G = \frac{(\sigma_x^0)^2}{E_1} \frac{h}{2} \pi g(\alpha, \beta), \quad (20)$$

where $g(\alpha, \beta)$ can be further approximated by Eq (11) as a function of α . These two cases should be equivalent [12], so that the following is obtained

$$c = \frac{2}{\pi g(\alpha, \beta)}. \quad (21)$$

This equation has been used to calibrate the constants c and d in Eq (9).

3 COMPARISON WITH FEM SIMULATION

If this periodic section is extended to the total surface layer, the geometry and the loading at a crack surface is the same as the fully cracked problem of Beuth [10] except that the former considers the periodically distributed discontinuities but the latter considers only a single crack. From Eqs. (6) and (8), we can solve the work done by the external loading as

$$W = \frac{(\sigma_x^0)^2}{E_1 c} h^2 \tanh(c\lambda/h). \quad (22)$$

To verify the integrity of the proposed analytical model, comparisons are made with the FEM simulation by ABAQUS. Due to the symmetry of the problem, only half of the section is modeled by 240×40 four-node quadrilateral elements with equal size under plane strain. Because a singular point exists at the edge of the interface, the FEM mesh shown in Fig. 5 includes refined elements in the vicinity of that point. The x -directional displacement along the symmetric plane and the end of the substrate is constrained. Here the thickness of the substrate is 20 times that of the surface layer, and 11260 four-node quadrilateral elements are used. To simulate variable section length, transformation of the mesh in the x -direction was employed.

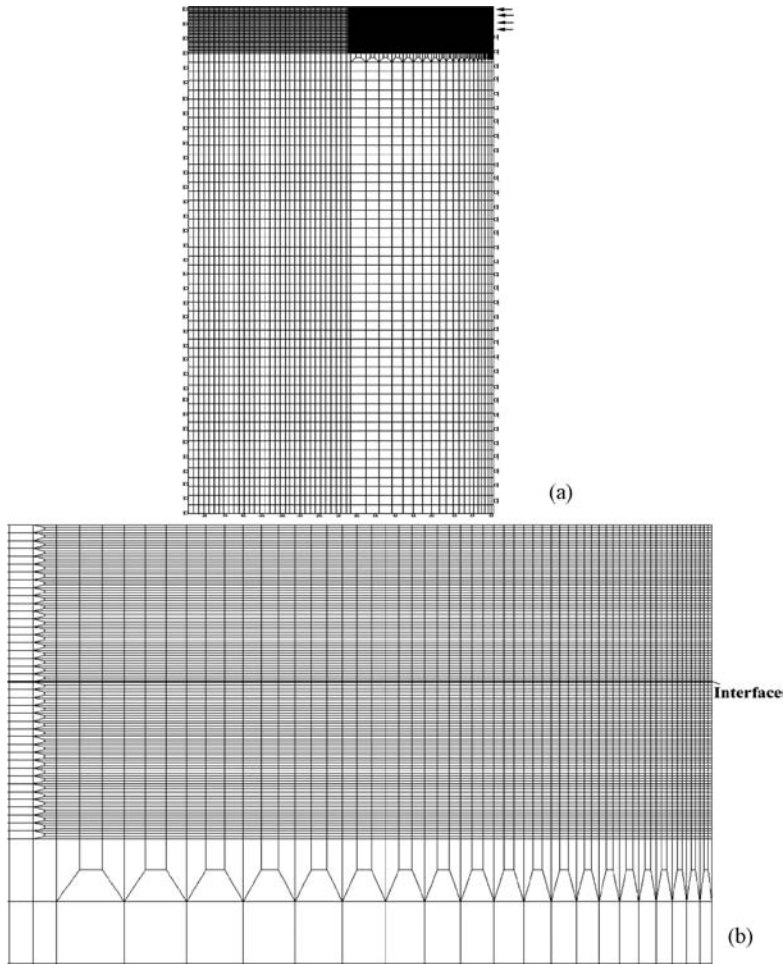


Figure 5. Finite element mesh used to model half of the geometry of the reduced problem. (a) Total mesh and (b) refined mesh at the vicinity of the singular point.

Figure 6 shows the external work calculated by Eq (22) with comparisons to FEM simulations. With the Young's modulus of the substrate E_0 , the external work reduces and is finally convergent to a constant. When the interface or substrate is stiff, namely, $E_0/E_1 > 1$, the cases of $\lambda = 12$ and $\lambda = 6$ provide the same result. Thus, the edge effect can be disregarded. However, when the interface or substrate is compliant, the case of $\lambda = 6$ gives a considerably lower result than that of $\lambda = 12$. As for asphalt overlay bonded to PCC pavements, typically the PCC is considerably stiffer than the asphalt materials. In this case, the solution produces a very estimate of the fracture energy consumed by low temperature cracking.

Figure 7 illustrates the comparison of the solution with the FEM simulation for the shear stress and displacement distributions. To show the effect of the stiffness of the substrate, two cases of $E_0/E_1 = 100$ and $E_0/E_1 = 1$ are considered. For a stiffer substrate, i.e. $E_0/E_1 = 100$, the proposed solution provided an excellent prediction for both the shear stress and displacement distribution. However, when $E_0/E_1 = 1$, the difference between the proposed solution and the FEM results is still considerable. The reason is that the assumption of a plane surface in Eq. (1) is not accurate due to the weaker constraint from the substrate during cracking. Therefore, the accuracy of the proposed solution is not good when the stiffness of two layers is very close.

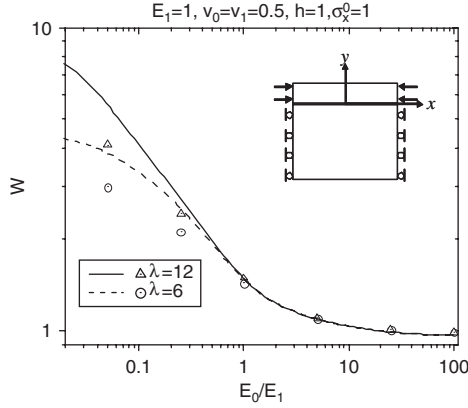


Figure 6. The work done by the force along the ends of the surface layer. Curves denote the theoretical predications; symbols the FEM results.

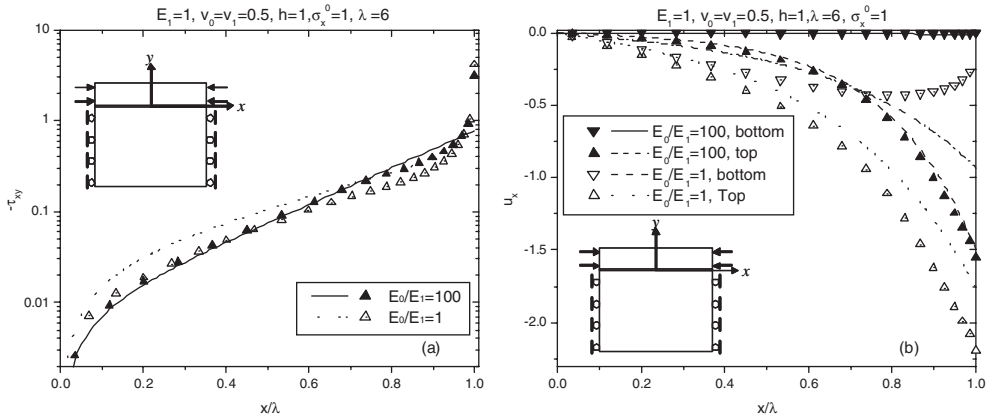


Figure 7. Comparison of the proposed solution with the FEM simulation: (a) the shear stress distribution along the bottom of overlay and (b) the displacement distribution along the top and bottom of overlay. Curves denote the theoretical predications; symbols used for FEM results.

4 APPLICATION TO FRACTURE ANALYSIS

From the above verification, we find that the proposed solution provides a very good prediction for a compliant overlay bonded to a stiffer substrate, so it can be applied to asphalt overlays placed on PCC pavement. The interfacial shear stress distribution is very important for evaluation of the interfacial shear strength [14, 15]. Combining Eqs. (8) and (14), we obtain an explicit solution of the interfacial shear stress as

$$\tau_{xy} = -c\sigma_x^0 \frac{\sinh(cx/h)}{\cosh(c\lambda/h)}, \quad (23)$$

from which the interfacial shear stress can be solved with c defined by Eq. (9). Obviously, it is different from Agrwal and Raj's assumption [14] where they used a sine wave function to approximate the interfacial shear stress. In Fig. 8, we can find that at the singular point ($x/\lambda = 1$), the shear stress

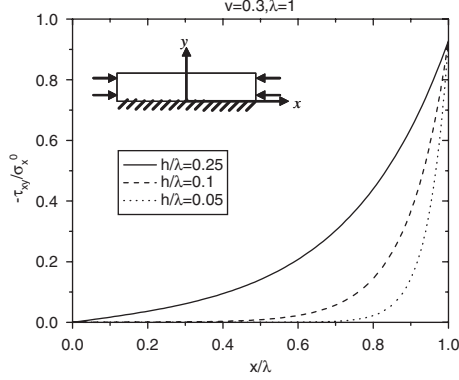


Figure 8. Interfacial shear stress distribution for the thin film fully bonded to a rigid substrate with the thickness $h/\lambda = 0.25, 0.1, \text{ and } 0.05$.

is almost same for each the ratio of h/λ because the thickness h is typically much smaller than the crack spacing and then $\tan h(c\lambda/h)$ is convergent to 1. The shear stress exponentially decreases from the singular point and finally reaches zero at the symmetric point. The smaller the ratio of h/λ , the higher the rate of decay. Thus, for a very thin surface layer, the interfacial shear stress is only concentrated in the neighborhood of the singular point. When the shear strength along the interface is given, comparing the maximum shear stress and the shear strength, we can determine whether curling will occur in an asphalt overlay subjected a low temperature load.

When the fracture energy of the asphalt material is provided, we can also predict the crack spacing under a certain temperature change for an asphalt overlay placed on a PCC pavement. Because the proposed model uses elastic material properties and corresponding experimental data for asphalt pavements is limited, here we compare with the experimental data conducted by Thouless et al. [16] with metallic materials. $\text{PrBa}_2\text{Cu}_3\text{O}_{7-x}$ overlays bonded to SrTiO_3 substrates were tested to observe the relation between the crack spacing and overlay thickness under a temperature loading. Elastic constants for SrTiO_3 were given as $E_0 = 267 \text{ Gpa}$ and $\nu_0 = 0.24$. The Young's modulus of $\text{PrBa}_2\text{Cu}_3\text{O}_{7-x}$ and tensile strain were $E_1 = 102 \text{ Gpa}$ and $\varepsilon_x^0 = 0.02$ respectively. In our numerical simulations, both the Poisson's ratio of the overlay was taken as $\nu_1 = 0.32$. Using Eq.(9), we can determine that $c = 0.631$.

Figure 9 shows a comparison with the experimental data [16] for crack spacing as a function of overlay thickness with the proposed prediction for the fracture toughness of the overlay as $\Gamma_{cr} = 5.5, 6.5, \text{ and } 7.5 \text{ Jm}^{-2}$, respectively. We see that the curve for $\Gamma_{cr} = 5.5 \text{ Jm}^{-2}$ fits the experimental data very well. With the increased overlay thickness, the crack spacing becomes larger. However, a critical thickness exists for each curve of the fracture toughness, below which the crack spacing quickly increases to be infinite. Thus, the crack spacing does not monotonically increase with the overlay thickness. The critical thickness increases with the fracture toughness of the overlay and the quantity of c . Although asphalt pavement materials are not purely elastic materials, this analysis shows that a critical thickness of the asphalt overlay exists, below which the low temperature cracking might be eliminated or significantly reduced.

5 CONCLUSIONS

An analytical model is presented to investigate thermal cracking in asphalt pavements. Using the boundary and loading conditions, we obtain the solution for an asphalt overlay fully bonded to a thick PCC base-layer. Comparisons of the solution with the FEM simulations show that the proposed model provides accurate predictions of the elastic fields. Using this solution, the energy release

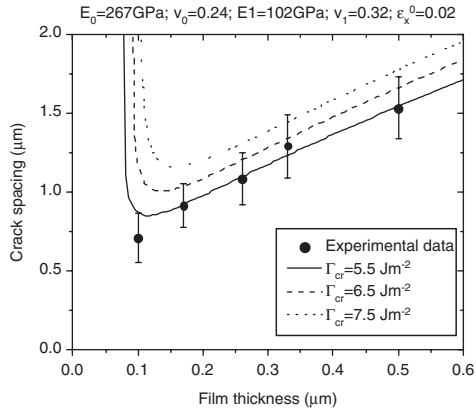


Figure 9. A comparison of the experimental data for crack spacing as a function of overlay thickness with the proposed predictions for different fracture toughness of the overlay.

rates can be calculated for 3D channeling. Fracture analysis of asphalt pavements is conducted based on strength and energy criteria. Potential benefits in using thin asphalt overlays over PCC are suggested by the model.

REFERENCES

- Roque R., Hiltunen D.R., and Buttlar W.G. (1995). Thermal cracking performance and design of mixtures using superpaveTM. *J. Assoc. Asphalt Paving Technol.*, 64, 718–733.
- Fromm, H.F., and Phang, W.A. (1972). A study of transverse cracking of bituminous pavements. *Proc. Assoc. Asphalt Paving Technol.*, 41, 383–423.
- Haas, R., Meyer, F., Assaf, G., and Lee, H. (1987). A comprehensive study of cold climate airport pavement cracking. *Proc. Assoc. Asphalt Paving Technol.*, 56, 198–245.
- Yang, Y.B., and Lin, B.H. (1995). Vehicle-bridge interaction analysis by dynamic condensation method. *J. Struct. Eng.*, 121, 1636–1643.
- Shalaby, A., Abd. E.I., Halim, A.O., and Easa, S.M. (1996). Low-temperature stresses and fracture analysis of asphalt overlays. *Transp. Res. Rec.*, 1539, 132–139.
- Waldhoff A.S., Buttlar W.G., Kim J. (2000). Investigation of thermal cracking at Mn/ROAD using the Superpave IDT. *Proc. Assoc. Asphalt Paving Technol.*, 45, 228–259.
- Shen W., Kirkner D.J. (1999). Distributed thermal cracking of AC pavement with frictional constraint. *J. Eng. Mech.*, 125(5), 554–560.
- Timm, D.H., Guzina, B.B., and Voller, V.R. (2003). Prediction of thermal crack spacing. *Int. J. Solids Struct.*, 40, 125–142.
- Chen, G., and Baker, G. (2004). Analytical model for predication of crack spacing due to shrinkage in concrete pavements. *J. Struct. Eng.*, 130, 1529–1533.
- Beuth, J.L. (1992). Cracking of thin bonded films in residual tension. *Int. J. Solids Struct.*, 29, 1657–1675.
- Hong, A.P., Li, Y.N., and Bažant, Z.P. (1997). Theory of crack spacing in concrete pavements. *J. Eng. Mech.*, 123, 267–275.
- Xia, Z.C., and Hutchinson, J.W. (2000). Crack patterns in thin films. *J. Mech. Phys. Solids.*, 48, 1107–1131.
- Shenoy, V.B., Schwartzman, A.F., and Freund, L.B. (2001). Crack patterns in brittle thin films. *Int. J. Fract.*, 109, 29–45.
- Yin, H.M., Buttlar, W.G., and Paulino, G.H. (2005). A two-dimensional elastic model of pavements with thermal failure discontinuities, 3rd MIT Conf. Comput. Fluid Solid Mech., pp. 539–542, Boston, MA.
- Yin, H.M., Buttlar, W.G., and Paulino, G.H. (2007). A simplified solution for periodic thermal discontinuities in asphalt overlays bonded to rigid pavements. *J. Trans. Eng.*, 133, 39–46.
- Thouless, M.D., Olsson, E., Gupta, A. (1992). Cracking of brittle films on elastic substrates. *Acta Metall. Mater.*, 40, 1287–1292.

*11. Interlayer system effectiveness in reducing
reflective cracking in pavements*

Techniques to mitigate reflective cracking in asphalt overlay

H. Wen

University of Wisconsin, Madison, Wisconsin, USA

W. Shitangkoon

National Technology Development, LLC, Horseheads, New York, USA

ABSTRACT: Asphalt overlay has been largely the pavement rehabilitation method for both asphalt and concrete pavements. However, asphalt overlay is susceptible to the deterioration due to the distresses in underlying pavements. Therefore, proper selection of pre-overlay repair and overlay construction method is critical to overlay pavement performance. This study addresses a statistical analysis of overlay performance to identify factors that could mitigate reflective cracking in overlay. Data related to previous overlay design, materials, and construction was reviewed and analyzed, such as as-built plan, pre-overlay condition, overlay materials, overlay thickness, pre-overlay repair, maintenance history, and overlay performance. A concept of distress development rate, as opposed to overlay pavement condition rating, was defined as the overlay performance to characterize overlay performance. It was found that for existing concrete pavement, full-depth doweled concrete repair is needed to control reflective cracking in asphalt overlay. It was also found, the amount of pre-overlay repair greatly affects the overlay performance. Increasing the ratio of overlay thickness to milling depth could effectively mitigate the reflective cracking in overlay on existing asphalt pavement.

1 INTRODUCTION

A large percentage of the asphaltic paving projects performed in Wisconsin are asphalt overlays of existing asphaltic or concrete pavements. The conditions and distresses in these pavements vary considerably when they are chosen for overlay, and the amount and methods of pre-overlay repairs also vary widely. This lack of consistency in the pre-overlay repair leads to large variations in the performance of these asphaltic overlays. Hall et al. (2002) studied the effects of rehabilitation methods on performance of asphalt overlay, using Long Term Performance Program (LTPP) data in National Cooperative Highway Research Program (NCHRP) project 20–50. For flexible pavement rehabilitation, the data from LTPP SPS-5 and GPS-6B sections indicated that no significant mean differences were detected in long-term rutting between virgin versus recycled mixes, minimal versus intensive preparation, or thin versus thick overlays. For asphalt overlay of concrete pavement, it was reported that no significant differences in the annual rate of change of rutting was detected among the various groups of asphalt overlays of intact slabs, nor between 101.6 mm (four-inch) versus 203.2 mm overlays of cracked/broken and seated slabs. Harvey et al. (2001) used a heavy vehicle simulator to study the asphalt overlay performance on existing asphalt pavement. It was found by Harvey et al. (2001) that the asphalt overlay failed by reflection cracking, instead of fatigue cracking or rutting. The failure due to reflection cracking was verified by mapping the cracks in the existing asphalt pavements and overlays.

However, the pre-overlay repair methods have been empirical in Wisconsin and the United States. A standard method of surface preparation would make the performance of these overlays

more consistent and thus easier to determine more accurate life cycle costs. The amount of surface preparation is also determined largely in the field during construction and this leads to increased project costs or an understanding that the proper amount of work is not done to the existing pavement in order to maintain the project budget. A standard set of guidelines to determine the amount of surface preparation or rehabilitation prior to asphaltic overlay that would address concerns during design and construction would provide this consistency along with more accurate and stable project budgets for this type of work.

The performance of overlay using different pre-overlay repair methods was evaluated in this study. Factors affecting the overlay performance were also investigated. The objective of this study is to identify the best practices for overlay performance by retrieving and analyzing the performance overlays in Wisconsin, USA.

2 DATA ANALYSIS

Asphalt overlay could be the rehabilitation method for both asphalt and concrete pavements. Prior to the asphalt overlay, the major distresses in an existing asphalt pavement may include block cracking, alligator cracking, transverse cracking, longitudinal cracking, raveling, rutting, and distortion, according to the Wisconsin Department of Transportation (WisDOT) *Pavement Surface Distresses Manual*. The major distresses in an existing concrete pavement may include slab breakup, distressed joint/cracks, surface distresses, longitudinal joint distress, and transverse faulting. Additional distresses for continuous reinforced concrete pavement could be wide cracks, punch outs, diagonal cracking, pavement deterioration, and delamination.

2.1 *Current pre-overlay repair methods*

The severe distresses in existing pavements need to be repaired prior to the asphalt overlay to provide a uniform support to the overlay. For existing asphalt pavements, milling and overlay is often used. The milling depth depends on the conditions of existing pavements and other constraints. The milled asphalt materials could be disposed or re-laid underneath the asphalt overlay, namely mill and relay. When the existing asphalt pavements are severely deteriorated, pulverization could be used prior to the asphalt overlay. The pulverization depth is down to either the bottom of asphalt layer or sometime partial or full-depth into the base course, namely full-depth reclamation (FDR). Occasionally, asphaltic base patching is used to repair the localized distresses.

For the existing concrete pavements, the distressed transverse/longitudinal joints and transverse cracks are generally repaired prior to the asphalt overlay. Severely cracked slabs are also replaced. The pre-overlay repairs of distressed joints/cracks in the concrete pavement often consist of two methods: full-depth repair and partial-depth repair. Full-depth repair is often referred to base patching. Three base patching methods are often used in WisDOT projects: asphaltic base patching; non-doweled concrete base patching; and doweled concrete base patching. For non-doweled concrete base patching, the sawcutting could be full-depth or partial-depth followed by full depth removal of concrete. The partial-depth sawcutting is intended to increase the load transfer by concrete aggregate interlocking. For concrete base patching, the PCC concrete could be regular, high-early strength concrete, or special high-early strength concrete, depending on the time needed to open the road to traffic.

2.2 *Analysis approach*

To evaluate the effectiveness of pre-overlay repair, the overlay performance has to be evaluated. Except for IRI and the rut depth, other distresses are surveyed manually and the extent and severity of the distresses are classified. Every 161-meter segment is surveyed for a 1.6 km section. WisDOT assigned a weight factor matrix to each distress taking into account of combination of severity and extent. These coefficients are used to represent the effect of a specific distress in calculating the

Table 1. Example of weight factor matrix for alligator cracking.

Weight factor Extent, % of area	Severity		
	1	2	3
10–24%	0.658	0.559	0.415
25–49%	0.577	0.469	0.316
50–74%	0.505	0.388	0.190
>75%	0.370	0.253	0.100

pavement distress index (PDI). When the extent or severity level becomes higher, a smaller value is given, indicating a deterioration of the pavement condition. When there is no distresses observed, a weight factor of “1” is given. An example of weight factor for the alligator cracking is given in Table 1, as follows:

WisDOT has been using the PDI as an indicator of the pavement performance. PDI is a mathematical expression for the pavement condition rating. The State Trunk Highway (STH) and Interstate Highways (IH) were surveyed by the WisDOT pavement unit every other year to obtain PDI and international roughness index (IRI), following the WisDOT *Pavement Distress Survey Manual* (1993). The PDI is expressed in the following formulas:

For asphalt pavement:

$$PDI = 100 \times [1 - (\text{Alligator_Cracking} / \text{Block_Cracking} \times \text{Longitudinal_Cracking} \times \text{Transverse_Cracking} \times \text{Patching} \times \text{Flushing} \times \text{Edge_Raveling} \times \text{Surface_Raveling} \times \text{Rutting} \times \text{Longitudinal_Distortion} \times \text{Transverse_Distortion} \times \text{Segregation} \times \text{Seal Coating} \times \text{Cracking_Filling})] \quad (1)$$

For concrete pavement:

$$PDI = 100 \times [1 - (\text{Slab_Breakup} \times \text{Distressed_Joint/Cracks} \times \text{Patching} \times \text{Surface_Distress} \times \text{Longitudinal_Joint_Distress} \times \text{Transverse_Faulting})] \quad (2)$$

In addition to the PDI, several major distresses, such as transverse cracking or rutting, were analyzed individually. Therefore, a set of distress indices were given for each individual distress using the following equation:

$$\text{Distress Indicator} = 100 \times (1 - \text{individual distress weight factor}) \quad (3)$$

Equation (3) is analogous to PDI expression when only one type of distress is analyzed. For an individual distress, a higher value of a distress indicator means that a more severe distress is present.

The overlay condition fluctuates significantly, largely due to maintenance, especially at later stage of overlay life. Simply using the latest overlay conditions could be misleading. Therefore, the first peak distress conditions prior to the maintenance activity were used to evaluate overlay performance, as shown in Figure 1. Since the peak distress conditions might not happen at the same age among the overlays, a concept of distress development rate was used. The distress development rate was calculated by averaging the slope rates of lines from the origin of coordinate to the PDI or individual distress indicator in a certain year, as illustrated in Figure 1. The distress development rate was used as the overlay performance for the purpose of comparison.

The distress development rate is calculated using Equation (4):

$$\text{Distress Development Rate} = \frac{\sum_{i=1}^n \frac{PDI_i}{i}}{n} \quad (4)$$

where n is the overlay service years.

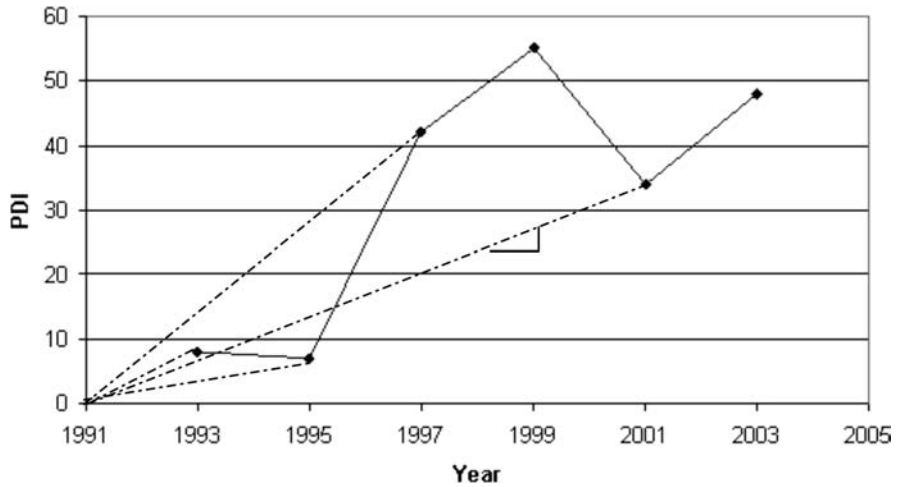


Figure 1. Fluctuation of overlay conditions.

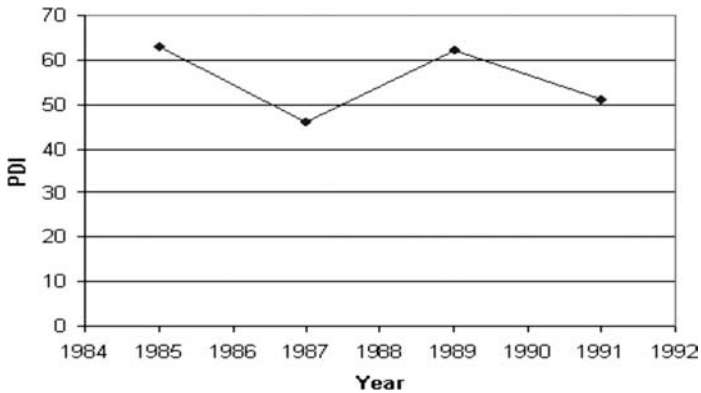


Figure 2. Fluctuation of existing pavement condition.

For the pre-overlay conditions of the existing pavement, PDI and individual distress indicator also fluctuate significantly due to maintenance, as shown in Figure 2. The pre-overlay condition immediately before overlay construction does not necessarily reflect the true condition of a pavement. Therefore, a strategy adopted in the previous study was “worse case history forward”. The highest history PDI and distress indicators were used as the pre-overlay conditions. This based on the fact that maintenance provides functional repair, instead of structural repair. In Figure 2, for example, a PDI of 63 in 1985 was used as the pre-overlay condition, instead of a PDI of 51 in 1991.

3 STATISTICAL ANALYSIS

A statistical analysis of the asphalt overlay performance was conducted. The parameters that were investigated in this study included pre-overlay conditions, pre-overlay repair method, overlay performance. Some findings are reported in the following sections.

3.1 *Effects of base patching on overlay on concrete pavement*

Prior to the asphalt overlay, the distressed joints or cracks in concrete pavements are usually removed and patched. Three pre-overlay repair methods have been used to patch the existing

Table 2. t-test of transverse cracking development rates.

t-Test: Two-sample assuming unequal variances

	HMA vs. Doweled concrete		Non-doweled vs. Doweled concrete		HMA vs. Non-doweled concrete	
	HMA	Doweled concrete	Non-Doweled concrete	Doweled concrete	HMA	Non-doweled concrete
Mean	3.35	2.54	2.99	2.54	3.36	2.99
Variance	3.10	1.11	2.90	1.11	3.10	2.90
Observations	43	36	13	36	43	13
Hypothesized Mean Difference	0.81		0.45		0.37	
df	70		15		20	
t Stat	-0.011		0.0068		-0.013	
P(T <= t) one-tail	0.495		0.497		0.495	
t Critical one-tail	1.667		1.753		1.725	
P(T <= t) two-tail	0.991		0.995		0.990	
t Critical two-tail	1.994		2.131		2.086	

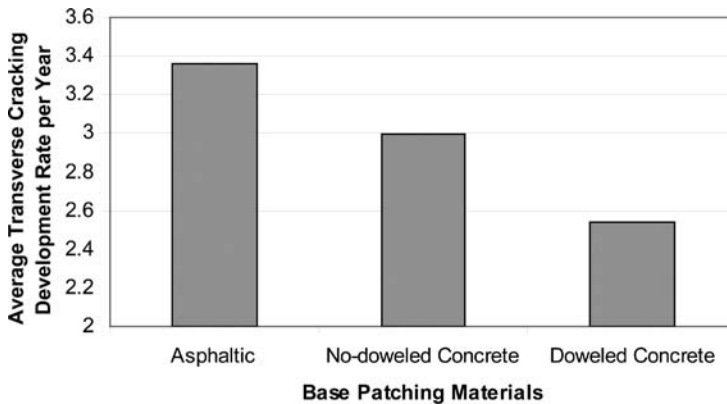


Figure 3. Effects of patching material/method on transverse cracking development.

concrete pavements in Wisconsin: asphaltic patching, non-doweled concrete patching, and doweled concrete patching. In this study, the average transverse cracking development rates in overlays using doweled concrete, non-doweled, and asphaltic patching were found to be 2.54, 2.99, and 3.36/year, respectively.

A t-test was performed to evaluate the difference between the development rates of three repair methods, as shown in Table 2. The differences between average transverse cracking development rates in overlays using the three methods are found to be statistically significant. The effect of base patching methods on overlay performance is presented in Figure 3. Overlays using non-doweled concrete or asphaltic patching deteriorated faster than those using doweled concrete base patching. This finding agrees with that by Hall et al. in another study (1991).

3.2 Effects of overlay thickness on transverse cracking in overlay on concrete pavement

The effect of the overlay thickness on transverse cracking was also investigated. Figure 4 shows the relationship between the overlay thickness and the transverse cracking development rate. It

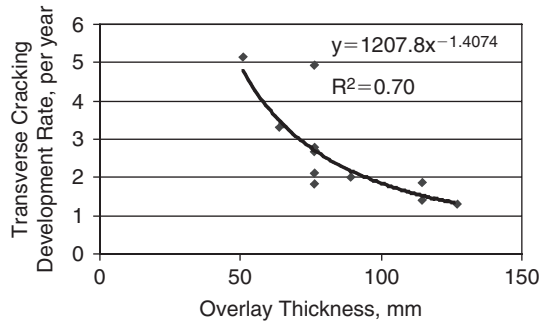


Figure 4. Overlay thickness vs. transverse cracking development rate.

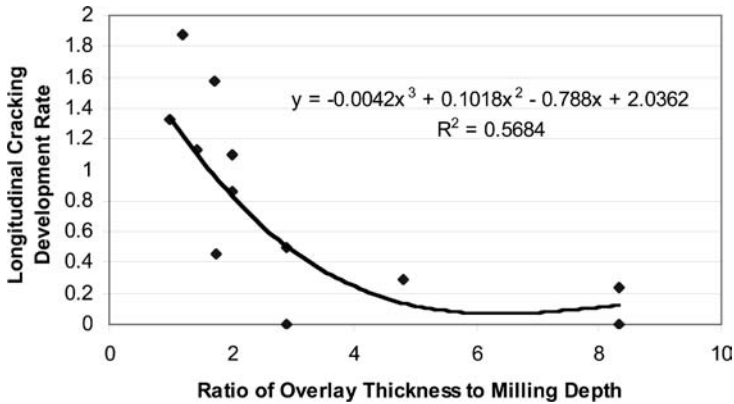


Figure 5. Effect of the ratio of overlay thickness to milling depth on longitudinal cracking.

could be seen that with the increase of overlay thickness, the transverse cracking development rate decreases. When overlay thickness is less than 76.2 mm, the curve in Figure 4 is steep. A slight increase of the overlay thickness could effectively reduce the transverse cracking development rate. However, beyond the thickness of 76.2 mm, the relationship curve between the overlay thickness and the transverse cracking development rate tends to be flat, indicating that simply increasing the thickness might not be as effective.

3.3 Longitudinal cracking in asphalt overlay of asphalt pavement

In this study, it was found that when the ratio of the overlay thickness to the milling depth increases, the longitudinal cracking development rate decreases, as shown in Figure 5. The ratio of overlay thickness to milling depth could be up to 8, as shown in Figure 5. This is because some overlay projects only milled the very top of the existing asphalt pavement surface. It could be seen from Figure 5 that when the ratio of overlay thickness to milling depth increases from one to three, longitudinal cracking development rate drops sharply. It seems that a ratio of three is a critical threshold. Therefore, it is suggested that the ratio of overlay thickness to milling depth be a minimum of three. When the ratio is more than three, the relationship curve in Figure 5 tends to be flat, indicating that simply increasing the ratio is not as effective.

It should be noted that meeting the ratio of three does not automatically yield a good overlay performance. The practitioner should not try to reduce the milling depth so as to get the ratio of three with a thin overlay. Sufficient milling depth is important to provide a smooth and consistent foundation for a structural overlay.

4 SUMMARY AND CONCLUSIONS

Asphalt overlay on existing asphalt and concrete pavements is one of common pavement rehabilitation methods. The performance of asphalt overlay is affected by many factors and varies significantly. This study investigated the factors influencing the performance of overlay. Performance of overlays on existing asphaltic and concrete pavements was reviewed and analyzed. For asphalt overlay of existing concrete pavements, it was found that overlays using doweled concrete to patch the existing concrete pavement performed best, followed by those using non-doweled concrete patching and then asphaltic patching. The transverse cracking development rate in asphalt overlay decreases with the increase of overlay thickness. For asphalt overlay on existing asphalt pavements, the longitudinal cracking development rate decreases when the ratio of overlay thickness to milling depth increases. Further study is needed to mitigate reflective cracking as a result of other distresses in existing pavements.

REFERENCES

- Hall K.T., Correa C.E., and Simpson A.L. (2002), *LTPP Data Analysis: Effectiveness of Maintenance and Rehabilitation Option*, Prepared for: National Cooperative Highway Research Program (NCHRP) Project 20-50, Transportation Research Board, National Research Council.
- Hall K., Darter M., and Hall J. (1991), "Performance of Asphalt Concrete Resurfacing of Jointed Reinforced Concrete Pavement on the Illinois Interstate Highway System", TRR 1307, pp. 180-187.
- Harvey J., and Bejarano M.O. (2001), "Performance of Two Overlay Strategies Under HVS Trafficking", 80th Transportation Research Board Annual Meeting, Washington DC.
- Wisconsin Department of Transportation (1993), *Pavement Surface Distress Manual*, Madison, Wisconsin.

Proper installation of paving fabric interlayers when placed prior to chip sealing

L. Davis

Federal Highway Administration, Expert Task Group on Pavement Preservation, California, USA

J. Dendurant

TenCate Geosynthetics, Kansas, USA

ABSTRACT: The problem facing the pavement owner today is how to obtain or exceed a pavement's design life, while working with shrinking budgets and increasing repair needs.

All levels of government are searching for better preventive maintenance strategies. One strategy is placing an asphalt-saturated paving fabric interlayer underneath a chip seal to extend the life of an asphalt pavement, retard reflective cracking, prevent surface water infiltration, and decrease road maintenance costs. Placing a paving fabric interlayer prior to chip sealing is similar, but does differ, when placed prior to an asphalt concrete overlay. The user who wishes to use this strategy needs to be aware of the placement differences in order to realize its benefits.

This paper will discuss the proper placement of paving fabric interlayers on asphalt concrete pavements, when used in conjunction with chip seals, and the common problems that can be encountered and addressed during the construction process.

1 INTRODUCTION

This paper provides guidelines on the proper installation of paving fabric interlayers (paving fabric) when placed immediately prior to chip sealing an asphalt concrete pavement (pavement). Placing paving fabric interlayers prior to chip sealing a roadway is a cost-effective maintenance solution for pavements exposed to extreme ambient temperatures (extreme daytime heat and freezing evening temperatures) and surface water infiltration.

Many have experience placing paving fabric prior to an asphalt concrete overlay, which is similar but not identical when placing paving fabric prior to a chip seal. Reason being, chip seals do not have the heat or weight that an asphalt concrete overlay does. Saturation of the paving fabric is essential with both applications. Less paving grade asphalt is required when placing fabric prior to an asphalt concrete overlay because the heat and weight of asphalt concrete overlays draw the underlying paving grade asphalt through the paving fabric to obtain the necessary saturation. Because chip seals do not have the heat and weight that asphalt concrete overlays do, modifications must be made to the placement of the paving fabric to insure the same level of success.

The paving grade asphalt bonds the paving fabric to the pavement. When these two products (paving fabric system) are placed together on a pavement, they form an asphalt membrane interlayer which reduces reflective cracking and acts as a barrier to surface water infiltration which limits softening of the subgrade.

The key to receiving these benefits is the proper installation of the paving grade asphalt and the paving fabric.

This paper will serve as a guide for the various steps involved in placing paving fabric interlayers, including:

- Site Selection
- Materials

- Equipment
- Weather
- Surface Preparation
- Applying Paving Grade Asphalt
- Installing Paving Fabric
- Sanding and Rolling
- Preparing the Paving Fabric Surface for Chip Sealing

2 SITE SELECTION

Chip sealing over paving fabric is designed for specific conditions and is a cost effective pavement preservation treatment when you are considering the various strategies in your pavement preservation toolbox. This pavement preservation treatment has great benefits if applied on the right road at the right time.

Generally, chip seals can be placed on winding curves and steep grades; however, these areas may have to be evaluated when placing a chip seal in conjunction with a paving fabric.

Paving fabrics can be placed on vertical grades of ten (10) percent or less. Paving fabrics can be placed on vertical grades greater than 10 percent, but require additional consideration in the design phase. Paving fabrics can also be placed on straight sections of pavement as well as on gradual horizontal curves.

There are some areas that should be avoided to prevent paving fabric slippage such as:

- Intersection radius,
- Traffic circles
- Horizontal curves with a radius of 200 feet or less,
- Bubble portion of a cul-de-sac
- Areas of hard starting, stopping or turning and include intersections where high wheel loads are expected, and
- Subgrade water penetration from high water tables.

3 MATERIALS

3.1 *Paving grade asphalt*

The paving fabric system consists of a paving fabric interlayer placed on top of binder. The grade of the binder should be an aged residue (AR), asphalt cement (AC) or performance grade (PG) of uncut asphalt cement based on local availability of binder resources. For the purpose of this paper, the binder is referred to as paving grade asphalt.

The paving grade asphalt should be selected based on the maximum and minimum ambient temperatures experienced at the job site throughout the year, not just at the time of placement. Reason being, the paving grade asphalt should be flexible so that it hardens, not brittle, when exposed to cold temperatures. The paving grade asphalt should soften, not liquefy, when exposed to hot ambient or pavement temperatures.

Asphalt emulsions have been used but are not recommended as a binder for the fabric. Reason being, the emulsion's application rate must be increased to allow for complete evaporation of the water and additives present in the emulsified asphalt. If an emulsion must be used, it is important that a sufficient amount of time be allowed for the emulsion to completely cure before placing the paving fabric; the time required typically is not available during the construction process when one is also trying to accomplish production. The length of time required for all the water and additives to evaporate from the emulsion is dependent on the type of emulsion used and weather conditions. If emulsions are used, expertise in the selection of the emulsion, rate of application, cure time and the chip seal aggregate to be used should be considered.

Table 1. Mechanical and physical properties.

Mechanical properties	Test method	Unit	Minimum average roll value
Grab Tensile Strength Machine and Cross Direction	ASTM D 4632	Lbs (kN)	101 (0.45)
Grab Tensile Elongation Machine and Cross Direction	ASTM D 4632	%	> 50
Grab Tensile Asphalt Saturated	ASTM D 4632 ¹	Lbs (kN)	200 (0.90)
Grab Tensile Elongation Asphalt Saturated	ASTM D 4632 ¹	%	40–70
Mullen Burst Strength	ASTM D 3786	psi (kPa)	200 (1378)
Asphalt Retention	ASTM D 6140	Gal/sy (oz/sf) (l/sm)	0.25 (3.6) (1.13)
Change in Area Asphalt Saturated	TX DOT 3099	%	+/-15
Melting Point	ASTM D 276	°F (°C)	325 (163)
Mass per Unit Area	ASTM D 5261	oz/sy (g/sm)	4.1 (139)
UV Resistance after 500 Hours	ASTM D 4365	% Strength Retained	70
shshs			
Physical properties	Unit	Typical value	
Roll Width	ft (m)	10.5 (3.2)	12.5 (3.8) 14.5 (4.4)
Roll Length	ft (m)	360 (110)	360 (110)
Roll Area	sy (sm)	420 (351)	500 (418) 580 (484)
Estimated Roll Weight	lbs (kg)	115 (52)	137 (62) 159 (72)

¹Modification to procedure: Sample is saturated with Asphalt.

A “Certificate of Compliance”, that provides the information required by the project’s specifications, should be furnished from the manufacturer of the paving grade asphalt to the project engineer for each shipment (truck load) delivered to the job site.

3.2 Paving fabric

The paving fabric is typically a nonwoven, needle-punched paving fabric which absorbs and holds the asphalt cement binder to provide a durable, stable, waterproofing membrane designed for use in pavement preservation.

One side of the fabric is heat-set and appears as a smooth surface; the other side is not heat-set and appears fuzzy. The fuzzy side of the paving fabric comes in contact with the asphalt cement binder. The heat-set side helps reduce bleed-through of the asphalt cement and helps prevent pick-up by traffic during warm or hot weather installation. The heat-set side is not placed against the asphalt cement binder.

The paving fabric is wound on a high strength thick walled composite tube or core commonly referred to as fabric rolls. The fabric rolls come in various widths to match most roadway requirements, such as the width of a travel lane or shoulder. The length and weight of a paving fabric roll is dependent on the width of the fabric roll. The mechanical and physical properties of fabric rolls are as follows:

A “Certificate of Compliance”, that provides the information required by the projects specifications, should be furnished from the manufacturer to the project engineer for each shipment (truck load) delivered to the job site.

3.3 Sand

Sand should be uniform, clean and free from deleterious matter and organic contaminants and should conform to the following gradation:

Sieve Size	Percent Passing
3/8-inch	100
No. 4	90-100
No. 200	0-5

4 EQUIPMENT

4.1 Distributor truck

The distributor truck provides a uniform application rate of the binder which is critical to ensure the paving fabric is saturated with paving grade asphalt in order to provide its full waterproofing benefit. It is common to see distributor trucks equipment with computerized rate controls for controlling and adjusting the application rate.

Prior to applying the paving grade asphalt, check that the proper size spray nozzles are installed; this is critical in providing a uniform application. The height of the spray bar and spray nozzles should be adjusted to attain the correct spray height and width in order to provide uniform volume and uniform horizontal distribution; this is discussed further under “Applying Paving Grade Asphalt” in this paper.

4.2 Paving fabric installation equipment

Installers typically use a tractor, front-end loader or a distributor truck that is specially designed to hold and place the fabric roll. Each of these has attachments to lay down the paving fabric, provide uniform tension, and broom the paving fabric smooth during placement.

The lay down equipment consists of a roll brake at each end of the fabric boom to prevent uncontrolled rolling of the paving fabric, adjustable brake tension to limit wrinkling, and brooms to smooth out the paving fabric as it is placed. The tension bar is also adjustable to smooth out the paving fabric; best results are obtained if the tension bar is bowed out. A pipe can be inserted in the core of the roll to prevent unwanted sagging which can cause wrinkling of the paving fabric.

If a distributor truck is used, the distributor truck will have the hydraulic lay down apparatus mounted on the rear of the truck. However, the ability to monitor the nozzles on the spray bar is limited due to the location of the lay down equipment with the spray bar. This can be addressed by an employee assigned to the rear of the truck to monitor both the nozzles on the spray bar and the fabric lay down equipment during fabric placement operations.

During cool or warm ambient temperatures, all three pieces of equipment are successful in placing the paving fabric immediately behind binder application. However, during warm or hot ambient temperatures, it is recommended that either a tractor or front-end loader be used to place the fabric. Reason being, fabric placement can be delayed to allow the binder to cool and prevent premature saturation of the paving fabric.

4.3 Sand distributor truck

A mechanical spreader, capable of spreading sand uniformly, is used to spread sand on the paving fabric. The spreader should be equipped with a mechanism for adjusting the spread rate.

Typically a sand truck is used for spreading the sand over the paving fabric. However, any means of spreading the sand uniformly is acceptable.

Sanding may be avoided if the pneumatic-tired rollers are equipped with a spray system, including check valves on nozzles, to apply a release agent to the roller tires. Release agents may be used if they are compatible with paving grade asphalt and polypropylene.

4.4 *Pneumatic-tired rollers*

Pneumatic-tired rollers are used to embed the paving fabric into the underlying paving fabric binder. An adequate number of rollers should be used on the job site to immediately embed the full width and length of the paving fabric. Pneumatic-tired rollers used for asphalt concrete overlay projects meet the same requirements for rollers for this process.

To avoid the need for sanding, pneumatic-tired rollers should be equipped with a spray system, including check valves on the nozzles, to apply a release agent to the roller tires. Release agents may be used if they are compatible with paving grade asphalt and polypropylene.

4.5 *Miscellaneous equipment*

There are other tools that should be available on the job site to assist in the professional installation of the paving fabric, which have not been addressed thus far, these are:

- Utility knife or scissors for removing longitudinal overlaps or trimming excess folds.
- Stiff bristle push brooms to help embed the fabric into the binder or address folds.
- Pipe to insert inside the fabric roll core to prevent unwanted sagging which can cause wrinkling of the paving fabric.
- Hand wand on the distributor truck to spray paving grade asphalt in areas that cannot be reached by the distributor truck's spray bar.

5 WEATHER

Typically, the minimum ambient and pavement temperature requirements for placing paving grade asphalt are similar for placing hot mix overlays; typically 50°F (10°C). This is beneficial because placement of the hot mix overlay can begin immediately after the placement of the paving fabric.

However, the ambient and pavement temperature requirements for placing chip seal emulsion are higher than what is required for paving grade asphalt; typically 65°F to 110°F (20°C to 40°C) ambient and minimum of 80°F (25°C) pavement. It is then recommended that placement of the paving grade asphalt does not begin until the required temperatures for placing the chip seal emulsion have been reached. By following this recommendation, chip seal operations can begin once paving fabric embedment is completed.

6 SURFACE PREPARATION

6.1 *Addressing isolated pavement distress*

The existing pavement surface should be reviewed to determine if there are any signs of structural or subgrade distress, such as severe alligator cracking or pavement deformation. The chip seal over paving fabric is a surface treatment and will not address, correct or improve deficiencies in the pavement's structural section. However, it may strengthen the pavement support systems by lowering the moisture content to the base and subgrade.

The pavement surface should also be evaluated to determine what surface preparation is required, such as wide surface cracks. Cracks that range from 1/8-inch to 3/8-inch (3.175 mm to 9.525 mm) can be filled with a crack sealant to prevent the fabric's binder from flowing down into the crack and not being able to saturate the paving fabric. Cracks that are greater than 3/8-inch (9.525 mm) require a crack filler such as an asphalt leveling course, slurry emulsion, or commercial crack filler. Crack filler should be flush with, or slightly below, the surrounding pavement. If the crack filler is higher than the surrounding pavement, a bump will be noticeable physically and visually after the chip seal is placed. Wide cracks that are not addressed could cause chip loss which may be an aesthetic issue for the agency.

After the isolated distress areas and surface cracks are addressed the grade of the pavement surface should prevent ponding of water. The pavement surface should be free of dirt, dust, debris,

water, oil or any other foreign matter to provide a clean surface for the fabric binder to bond to the pavement. If properly prepared, the fabric binder and paving fabric should be able to cover the entire pavement surface.

6.2 *Protect utilities*

Temporary covers should be placed to protect items located within the pavement surface such as survey monument covers, utility access covers, valve covers, and portland cement concrete pads surrounding these items. Pavement markers (e.g. ceramic and reflective) and delineators should be removed in order to provide a flat, uniform pavement surface.

6.3 *Prevent exposure to water*

Placement of the paving fabric system should not occur on wet pavement because this will affect the bonding of the paving fabric to the underlying binder. Also, the paving fabric system is designed for pavements whose grade allows the water to flow off the surface of the pavement. The paving fabric system is not designed for pavements that have water entering the pavement surface via the road's subgrade.

If rain occurs prior to placement of the chip seal, it will not hurt the fabric system because it is saturated with paving grade asphalt which protects the paving fabric and seals the pavement. If the paving fabric surface is exposed to moisture or ponding water, the skid resistance may be reduced. Areas exposed to moisture may require additional sand, and warning signs should be placed until the area is dry and chip sealing is completed.

Protective measures should also be taken to prevent the fabric binder or chip seal emulsion from entering any water conveyance system (e.g., cross gutter, storm drain inlet, curb inlet, channel, etc.) Protective measures should also be taken from water entering or ponding on the roadway surface; moisture will affect the bonding of the paving grade asphalt and the chip seal.

6.4 *Construction warning signs*

Before spreading the paving grade asphalt, construction warning signs should be placed in advance and throughout the project site. The warning signs should include FRESH OIL and LOOSE GRAVEL to warn motorists about exposure to the fabric binder and sand cover. SLIPPERY WHEN WET signs should be placed if the fabric may be exposed to moisture before the chip seal is placed. Signage requirements are normally specified by the agency.

All traffic (construction and public) should be maintained at speeds of 25 miles per hour (40 kilometers per hour) or less to prevent damage to the paving fabric.

7 APPLYING PAVING GRADE ASPHALT

The success of placing a chip seal over paving fabric is insuring the paving fabric is saturated with the correct grade and quantity of paving grade asphalt. As stated earlier, the binder recommended for paving fabric is AR, AC or PG grade of uncut asphalt cement (paving grade asphalt); asphalt emulsion is not recommended. Suitable binders are listed in Table 2.

7.1 *Distributor truck operation*

Before the work begins, each distributor truck should be calibrated to confirm it is applying the desired quantity of paving grade asphalt to the pavement surface. The distributor truck driver should have paperwork certifying calibration has been done within four weeks prior to the start of work; calibration can be done in the field if the agency desires. Proper application of the paving grade asphalt is critical to the successful placement of paving fabric and subsequent chip seal.

The distributor truck applies the paving grade asphalt in a uniform spray, free of streaks or gaps. The height of the spray bar and size of spray nozzles can be adjusted to obtain the correct spray

Table 2. General guide lines for asphalt binders.

Penetration grade	AC grades	AR grades	PG grades	Modified
50			PG 70-22	SBSPG 76-22
60	AC 20	AR 8000	PG 67-22 PG 64-22	SBSPG 70-22
70-85	AC 10	AR 4000	PG 58-10	
100			PG 48-28	
120	AC 5	AR 2000		HPSPG 76-10

width and overlap. The spray bars and nozzles should be clean and adjusted to the proper height and angle to provide uniform application.

Frequent starting and stopping of the distributor truck should be avoided to prevent non-uniform spread rates and overlaps which result in double applications.

7.2 Binder temperature

The paving grade asphalt (binder) must remain liquid long enough to saturate the paving fabric and should be high enough in temperature to allow uniform application. While in the distributor truck, the allowable temperature range for uncut paving grade asphalt is 290°F to 325°F (143°C to 163°C). The proper amount of binder will saturate the paving fabric as well as bond the paving fabric to the pavement surface.

7.3 Binder application

The temperature of the paving grade asphalt (binder) is generally 290°F to 325°F (143°C to 163°C) at the time of application. If the binder exceeds 325°F (163°C), it is important that the binder be allowed to cool before placing the paving fabric to prevent fabric shrinkage.

Agency requirements differ as to how much paving grade asphalt (binder) should be applied to saturate the paving fabric. In general, binder application rates range between 0.22 to 0.30-gallons per square yard (0.90 to 1.35 liter per square meter) to achieve optimum saturation and ease of construction.

The spray bar should be at a height that provides triple spray bar patten overlap. Also, the binder should extend two to four inches (50 to 100 mm) beyond all edges of the paving fabric, including overlaps, to insure the paving fabric edges are saturated and bonded to the pavement surface. Failing to saturate the paving fabric along the longitudinal and transverse edges will guarantee subsequent chip loss.

The condition of the existing pavement surface is one of the determining factors for determining the proper binder application rate; onsite weather conditions is another factor (ambient and wind).

The length of time the binder is able to stay in its liquid state is impacted when it comes in contact with cool or hot pavement temperatures, for example:

- When binder is applied to a cool pavement, it can stiffen within seconds. Depending on field conditions, the binder may remain tacky long enough to hold the paving fabric in place. To be on the safe side, paving fabric should be placed on the binder immediately before the binder loses its tackiness.
- When the binder is applied during hot ambient temperatures or to a hot pavement, the binder normally stays liquid long enough to saturate the paving fabric. However, care should be taken not to over saturate the fabric as this can cause fabric slippage when hot ambient temperatures are present.

Too little or too much binder application can cause slippage. The selection of the proper binder can reduce slippage as well.

A good indicator that you have an adequate amount of binder is if you notice binder in the wheel tracks of the fabric applicator if a tractor or front-end loader is used, or from the pneumatic-tired roller or construction vehicles that drive on the fabric.

Should the job site experience a broad range of temperatures throughout the day, such as cool pavement in the morning and hot pavement temperatures in the afternoon, it is important to insure proper saturation (and not over saturation) of the fabric is consistently obtained in the field.

Being aware of how temperatures affect the materials in this construction process is consistent with placing materials for other construction processes. Understanding the concept of a material should perform in the field, and recognizing when an adjustment needs to be made due to changing field conditions, is important to the successful placement of any material used during construction.

8 INSTALLING PAVING FABRIC

The temperature of the paving grade asphalt (binder) is generally 290°F to 325°F (143°C to 163°C) at the time of application. If the binder exceeds 325°F (163°C), it is important that the binder be allowed to cool before placing the paving fabric to prevent fabric shrinkage.

The temperature of the binder drops very quickly after application, especially during cooler ambient temperatures. During cool temperatures it is important that the paving fabric be placed immediately after binder application in order to achieve proper fabric saturation. Should hot ambient temperatures be present, greater than 100°F (38°C), you may observe premature saturation of the paving fabric. Should premature saturation occur, consider placing the materials during morning hours before the onset of the hot ambient temperatures.

If a distributor truck is used to lay down the paving fabric, the distributor truck will have the hydraulic lay down apparatus mounted on the rear of the truck. However, the ability to monitor the nozzles on the spray bar is limited due to the location of the lay down equipment with the spray bar. Fabric placement can still be done successfully by having an employee assigned to the rear of the distributor truck to monitor both the nozzles on the spray bar and the fabric lay down equipment during fabric placement operations.

The fabric is unrolled so that the fuzzy side comes in contact with the binder; this provides optimum bonding to the binder.

As mentioned earlier, the binder should extend two to four inches beyond all edges of the paving fabric.

Similar to hot mix overlay projects, longitudinal joints of the paving fabric should be overlapped approximately two to four inches (50 to 100 mm). However, transverse joints should not be overlapped as they are on hot mix overlay projects. When paving fabric is being placed prior to a chip seal operation, it is important transverse joints be placed adjacent to each other without overlapping; this is referred to as a butt joint. If transverse joints are left overlapped, a bump will be noticeable audibly in the car ride after the chip seal is placed.

Folds that result in three layers of fabric must be removed since there is no binder between the layers. These excess layers of fabric can be removed by with the use of a utility knife. The use of a propane torch is not recommended because surrounding fabric can be damaged; as such, propane torches are not recommended unless it is done by a skilled fabric installer.

9 SANDING AND ROLLING

On asphalt concrete overlay projects it is not necessary to sand and embed the paving fabric with pneumatic-tired rollers. The heat and weight of the asphalt concrete overlay provides fabric saturation by drawing the paving grade asphalt (binder) to the surface of the paving fabric.

However, when a paving fabric is placed in conjunction with a chip seal, this fabric saturation process will not occur unless the paving fabric is embedded into the underlying fabric binder with the use of pneumatic-tired rollers. Conventional chip seal emulsions do not have the heat or weight that an asphalt concrete overlay does. At the time of application, chip seal emulsion temperatures range from 130°F to 180°F (55°C to 80°C); asphalt concrete overlays range from 250°F (120°C)

or higher. Therefore, modifications must be made to the construction process to obtain fabric saturation with the underlying binder.

To avoid the need for sanding, pneumatic-tired rollers equipped with a spray system, including check valves on the nozzles, to apply a parting agent to the roller tires. The parting agent helps prevent the roller tires from bonding to the fabric binder during the embedment process. If the rollers do not come equipped with such a system, then sanding may be necessary to prevent the tires from bonding to the fabric binder.

9.1 *Applying sand*

After the paving fabric is placed, dry sand may be placed over paving fabric. The sand acts as a bond breaker and prevents the binder from coming in contact with tires from vehicular traffic, or from the pneumatic-tired rollers when seating the paving fabric into the underlying binder.

The sand remains in place until the road is ready for chip sealing. Depending on the agency requirements, chip sealing may or may not occur the same day the fabric is placed. If the chip seal is scheduled for a later date, it is important that the fabric surface is monitored to insure adequate sand is present to address any bleed through or exposure to surface moisture.

Sand should be dry in order to provide uniform coverage during application. If the sand is damp or wet, it may spread in clumps and will not provide uniform coverage to the paving fabric surface.

9.2 *Rolling operation*

The pneumatic-tired rollers should make a minimum number of three passes on the paving fabric to insure the paving fabric is completely saturated by the underlying paving grade asphalt. However, more than three passes may be required.

What is important is the rolling operations should continue until the texture of the pavement surface is visible on the surface of the paving fabric. When this occurs, it is a sign that the paving fabric is properly saturated by the underlying paving grade asphalt.

10 DRIVING ON PAVING FABRIC

Generally traffic should not be allowed on the paving fabric. However, if it is necessary, precautions can be taken to prevent damage. All traffic (public and construction) should travel at low speeds (25 MPH or less). If the roadway is normally traveled at speeds greater than 25 MPH, a pilot car should be used to control traffic speeds on the fabric.

Installed fabric may have less skid resistance than dry pavement. Exposure to the binder, rainfall or moisture may further reduce the skid resistance. For these reasons, public traffic should not be permitted directly on the fabric until the fabric has been sanded because the sanding will help increase the skid resistance.

Should it be necessary for traffic to travel on the paving fabric prior to placing the hot mix overlay, this can occur by first broadcasting asphalt concrete on the fabric surface. The broadcast asphalt concrete will serve as a bond-breaker between the tires and the fabric binder.

Should it be necessary for traffic to travel on the paving fabric prior to chip sealing, this can occur by first broadcasting sand on the fabric surface. The broadcast sand will serve as a bond-breaker between the tires and the fabric binder.

11 PREPARING THE PAVING FABRIC SURFACE FOR CHIP SEALING

Once fabric embedment is completed, the roadway is ready for chip sealing. The fabric surface should be swept to remove any excess sand and provide a clean surface for the chip seal emulsion. Sweeping can be done by mechanical means, such as mobile pick-up brooms or kick brooms. After sweeping is completed, review the fabric surface to determine if there are any fabric defects such as folds or frayed fabric. These minor defects must be addressed before the chip seal emulsion is applied.

If proper fabric saturation is obtained, standard application rates for the chip seal emulsion can be applied. However, if there is concern that fabric saturation was not obtained, it is then necessary to complete the fabric saturation process by increasing the application rate of the chip seal emulsion. This will insure the fabric saturation was completed and there is a sufficient amount of emulsion on the fabric surface to retain the chips. Failing to increase the chip seal emulsion on a porous paving fabric may result in subsequent chip loss.

12 SUMMARY

It is common knowledge that asphalt pavements require maintenance to obtain or extend its design life. The problem facing the pavement owner today is how to obtain or exceed that pavement's design life, while working with shrinking budgets and increasing repair needs and costs.

There is a push for better preventive maintenance strategies at all levels of government. A growing number of cities, counties and states are now using this preventive maintenance strategy of placing an asphalt-saturated paving fabric interlayer immediately prior to a chip seal operation to prolong the life of an asphalt pavement, retard reflective cracking, prevent surface water infiltration, and decrease road maintenance costs.

Those agencies that have tried this process are finding that when the right road is selected for this process and proper preparation and construction occur, subsequent road maintenance is drastically reduced.

Agencies that have tried this strategy, placing a chip seal over fabric, are reporting there is no need for subsequent crack sealing for 10 to 20 years after placing the paving fabric. This can be attributed to proper road selection, road preparation, material selection and construction operations; each of which are important to make this preventive maintenance treatment successful.

REFERENCES

- National Cooperative Highway Research Program, 2006. *Chip Seal Best Practices*, Synthesis 342.
- Davis, 2004. *Chip Sealing over Fabric in Borrego Springs*, Fifth RILEM International Conference.
- Davis, 2003. *Protecting Roads in the Desert: Chip Sealing over Fabric Retards Reflective Surface Cracks*, TR News, Number 228.
- Davis, 2003. *Chip Sealing over Fabric, Paving Fabric Halts Reflective Surface Cracks*, GFR Magazine.
- Asphalt Interlayer Association, 1994. *Sacramento County Chip Seal over Paving Fabric*.
- Miner, Spaulding & Donahue, 1990. *The Use of Saturated Textiles with Chip Seals*, Paper presented to National Pavement Exposition.
- Sanders, South Carolina Department of Highways, 1990. *Evaluation of Petromat When Used with Bituminous Surface Treatments*.



The use of geogrids to retard reflective cracking on airport runways, taxiways and aprons

J. Penman

Tensar International Corporation, Atlanta, Georgia, USA

K.D. Hook

Saint-Gobain Technical Fabrics, Worcester, Massachusetts, USA

ABSTRACT: Reflective cracking in composite or flexible asphalt pavements is typically caused by traffic loading, age hardening or temperature cycling. The onset of such cracking generally signals the start of rapid pavement deterioration and a need for rehabilitation. Failure to act on the surface cracking in a timely manner will result in permanent damage to the lower layers within the road and in time, the need for a more costly replacement of the entire pavement structure. This problem is particularly troublesome in airport runways and aprons where loadings from aircraft landing gear can be significantly higher than those experienced on traditional road pavements.

Pavement engineers have used interlayers to help retard reflective cracking for many years. By placing an interlayer within a new lift of asphalt, the time taken for reflective cracks to reach the surface can be extended significantly. This can be particularly important in an airport environment where there is a need to meet stringent safety regulations; this is balanced with the fact that airport authorities cannot afford to have these pavements shut down for any significant period of time.

This paper describes how glass-fiber based geogrids have successfully been used as interlayers over the last 20 years to extend the design life of asphalt pavements on airport runways, taxiways and aprons. The pavement life extension is quantified through reference to the results from a number of research studies and performance data from project sites constructed throughout the world during the last 20 years.

1 INTRODUCTION

Reflective cracking is the process by which an existing crack, joint or other discontinuity propagates towards the surface through an overlying layer of asphalt cement concrete. The rate of crack propagation varies significantly based on various environmental and trafficking factors. However, a general “rule of thumb” commonly used by pavement engineers, states that under typical conditions, a reflective crack will propagate upwards towards the surface at a rate of approximately one inch per year of service.

Once a reflective crack reaches the surface, an open path exists for the flow of surface water into the lower layers of the pavement. Left untreated, this situation will lead to deterioration of the pavement structure and a reduction in overall serviceability. Breakdown of the pavement is particularly rapid in areas where the annual precipitation is higher, or where the applied loads are greater in magnitude – pavements associated with aircraft loads (runways, aprons, taxiways, etc.) are therefore of particular concern.

The use of geosynthetic or steel interlayer products within an asphalt overlay has gained widespread acceptance since their introduction more than 50 years ago. Products of varying types have been used to either reinforce the asphalt or provide a relatively impermeable layer within it, thereby improving the long-term performance of the pavement. This paper will focus on one particular type of geosynthetic, a geogrid consisting mostly of glass-fibers. Evidence will be presented

from various laboratory studies in order to define the performance benefits yielded through the use of this type of product. Reference will be made to a number of airport projects where a glass-fiber geogrid was used to reinforce the pavement structure.

2 THE DEVELOPMENT OF INTERLAYER PRODUCTS

Beck (1999) describes how as early as the 1930's, road builders in South Carolina were attempting to improve the performance of their pavements by inserting woven cotton sheets between layers of liquid asphalt. By the 1950's, engineers in the United States, Canada and Great Britain had developed wire mesh products for inclusion within asphalt layers. Although there was compelling data to demonstrate that these products could reduce rutting and cracking within the asphalt, they proved very difficult to install due to their rigid nature. They also complicated the milling and recycling process (Brown et al, 1985).

The next significant development in interlayer technology occurred in the 1960's and involved the incorporation of geotextiles (manmade fabric products) within the asphalt layers of a pavement structure. Unlike the earlier cotton fabrics, these materials did not deteriorate when exposed to water or the chemicals present within the asphalt. However, most research determined that although non-woven geotextiles were beneficial to pavements in terms of stress relief and waterproofing, they were unable to arrest crack development (Carver and Sprague, 2000).

The first use of geogrids as interlayer products dates back to the early 1980's. Stiff, punched and drawn, polypropylene, biaxial geogrids developed in the United Kingdom were tested extensively at various sites and at the University of Nottingham (Brown et al, 1985). It was demonstrated that geogrids were able to reduce deformation by up to 70% and significantly retard the development of reflective cracks.

One of the more popular developments in pavement interlayer technology to occur during the last 25 years involves the use of glass fibers for the main component of the geogrid ribs. Glass fibers provide very high stiffness at low strain along with excellent creep resistance; the latter is important when attempting to combat the sustained loads imposed during the thermal expansion of a pavement. The fact that glass fibers easily break down during the milling process provides an added benefit ensuring that pavements containing these geogrids can easily be recycled. The flexible nature of a glass-fiber geogrid lends itself particularly well to the installation process, leading to expedited construction. For example, an experienced team of installers would expect to place of the order of 25,000 square yards (21,000 square metres) of product per day.

3 REINFORCEMENT MECHANISM

Conventional rehabilitation procedures involve the placement of an asphalt overlay on top of an existing cracked pavement. This provides some additional road life, but the existing reflective cracks continue to propagate uninhibited toward the surface, as shown in Figure 1a.

When used to reinforce asphalt concrete, a glass-fiber geogrid helps to create a composite material combining the compressive strength of the asphalt mix with the tensile strength of the glass fibers. By introducing a stiff tensile element at the base of an overlay, cracks propagating toward the surface are intercepted and prevented from migrating further. Instead, the crack is redirected horizontally, as shown in Figure 1b.

Research has clearly demonstrated that the bond between the asphalt layers above and below the geogrid is critical to the performance benefits yielded by an interlayer product. At the University of Nottingham in the United Kingdom for example, Brown et al (1985) demonstrated that there is a significant reduction in the interface shear stiffness when an interlayer product prevents direct bonding of the asphalt layers. This study further demonstrated that for maximum performance, an interlayer needs to promote "through-hole bonding" between asphalt layers. This can be achieved only when an open aperture grid structure is used for the reinforcement.

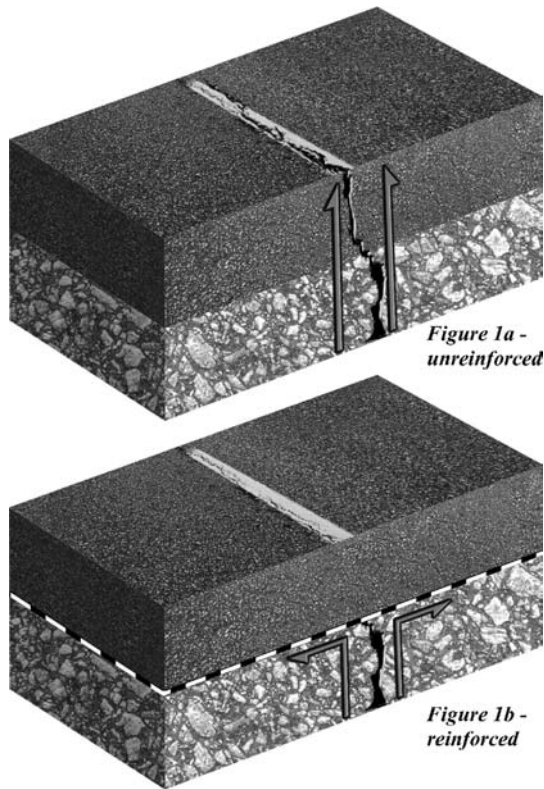


Figure 1. Direction of crack propagation in asphalt pavements.

In Figure 1b, the geogrid-reinforced overlay will itself start to crack in time, but at a much-reduced rate, thereby significantly extending the life of the pavement.

4 RESEARCH AND DEVELOPMENT STUDIES

4.1 *The University of Nottingham, UK*

Brown et al. (2001) reported on a series of semi-continuously supported beam tests (Figure 2) undertaken in the laboratory. This equipment determines the ability of an interlayer material to resist crack propagation in a beam constructed of asphalt cement. A notch is placed at the bottom of the beam to help facilitate crack propagation.

Tests were undertaken on control samples (i.e. no reinforcement) and a range of geosynthetic products. The results indicated that an open-aperture glass-fiber geogrid performed significantly better than any other type of geosynthetic product and that when compared with an unreinforced (control) section of the same thickness, it was able to reduce the rate of crack propagation by a factor of 2 to 3 times.

4.2 *Texas A&M University, College Station, Texas, USA*

Lytton et al (1986) and Lytton (1988) reported on a series of tests undertaken at Texas A&M University. The results from a series of beam fatigue tests (similar to those undertaken at Nottingham University) are presented in Figure 3. These show that the number of cycles to reach a particular target strain within the asphalt is more than 10 times greater for a 3 inch thick reinforced beam, than for a 4 inch thick unreinforced beam.

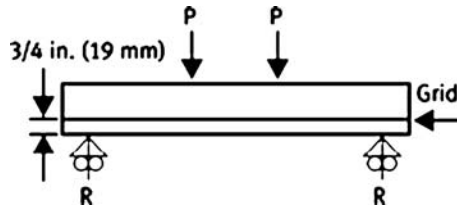


Figure 2. Semi-continuously supported beam test at Nottingham University.

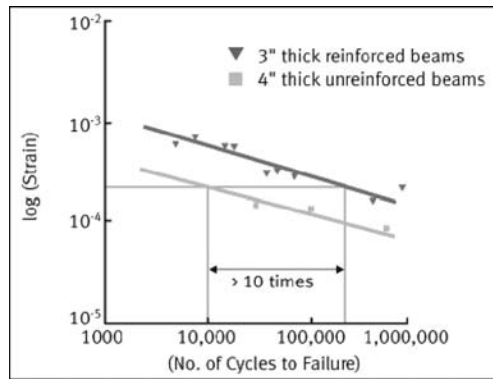


Figure 3. Results from the beam tests undertaken at Texas A&M University.

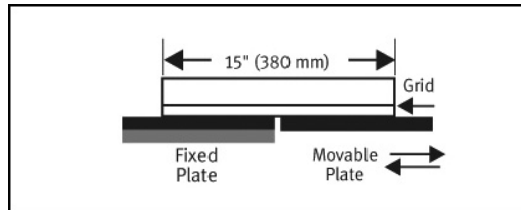


Figure 4. Overlay test machine used at Texas A&M University.

In addition to the main laboratory testing undertaken at Texas A&M University, a performance prediction model was developed using data obtained from an overlay test machine (Figure 4). This apparatus essentially uses a fixed plate and a movable plate both bonded to an asphalt beam. As the two plates move apart, this imparts a tensile force into the asphalt and simulates the sort of behavior that occurs during the thermal expansion and contraction of an asphalt pavement.

Using traffic, temperature and pavement geometry variables, comparisons were made of the predicted performance for unreinforced and glass-fiber geogrid-reinforced overlays. For the example shown in Figure 5, the predicted performance benefit of an overlay reinforced with a glass-fiber geogrid is 1.5 to 2 times that for an unreinforced overlay of the same thickness.

4.3 Delft University, the Netherlands

An extensive field performance evaluation study and comprehensive laboratory testing program were undertaken at Delft University in the Netherlands. The results of the study are reported in De Bondt (1999). An extension of the practical work undertaken for this study involved the development of a performance prediction model for pavement overlays subject to reflective cracking caused by thermally induced stresses.

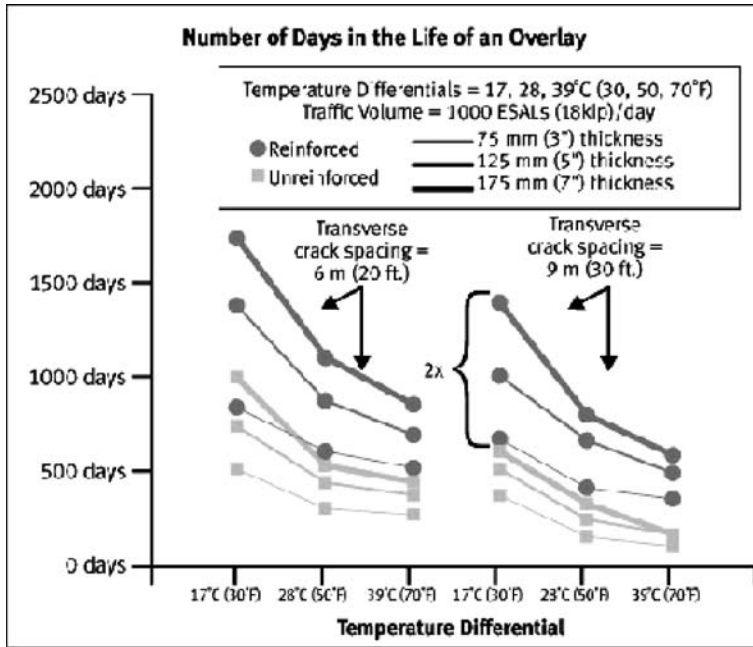


Figure 5. Results from the testing undertaken at Texas A&M University.

The model demonstrated that for a range of input parameters, the design life of an asphalt overlay reinforced with a glass-fiber geogrid, is likely to be double that for an unreinforced overlay of the same thickness and composition. Subsequently this model was used to develop the industry leading Anti-Reflective Cracking Design Software (ARCDISO®).

4.4 National Center for Asphalt Testing (NCAT), Opelika, Alabama, USA

The pavement test facility at NCAT constitutes the premier full-scale asphalt pavement testing center in the United States. The oval shaped test track at the facility is 1.7 miles in length and is divided into a series of forty-five 200-foot long sections. Trafficking is carried out using a set of heavily loaded trucks that are able to apply the equivalent of several years' worth of vehicle loads during a much shorter period of time.

During the main construction phase of the project in June 2000, a glass-fiber geogrid was installed towards the top of the 20 inch thick hot mix asphalt pavement layer, in one half of a 200-foot long test section. The remaining length of the test section was left unreinforced to act as a control section. Since the initial construction, the test section has been subjected to more than 20 million ESALs (equivalent single axle loads) of traffic loading; this would be comparable to the trafficking experienced by an average interstate highway over a period of 20 years.

At the end of the trafficking, the area containing the glass-fiber geogrid remained crack free. In contrast, a large longitudinal crack was observed along the centerline joint between the inside and outside lanes of the unreinforced section. The crack disappears completely at the interface between the reinforced and unreinforced areas of the pavement.

5 CASE STUDIES

5.1 Inyokern Airport, California, USA

In 1995, The Indian Wells Valley District Airport Authority decided to undertake the rehabilitation of Runway 15-33. The airport is located in a remote corner of the Mojave High Desert where

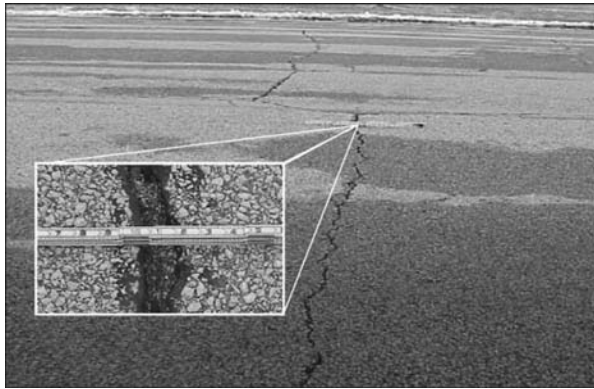


Figure 6. Thermal crack in existing pavement at Peoria Airport prior to placement of overlay.

average monthly temperatures range from 103°F in July down to 30°F in January. High thermal stresses resulting from this wide range in temperature had resulted in serious cracking and general degradation of the runway. Prior to undertaking the rehabilitation, the runway had become extremely oxidized and brittle due to the harsh climate. The surface exhibited alligator, transverse and longitudinal cracking, with many of the transverse cracks up to 1 inch in width. The airport authority considered adding a thicker overlay to the runway, but this approach would have proven to be very expensive. Experience also suggested that this approach would provide only a temporary solution, since the large temperature variation and subsequent stresses induced, were likely to cause thermal cracks to reflect back through to the surface at an approximate rate of 1" per year.

During the replacement of the surface materials, a glass-fiber geogrid was installed between a fresh binder course and the new two inch thick wearing course. While undertaking a site visit in January 2007, it was observed that the reinforced pavement had suffered only minor hairline cracking after more than 11 years of service and thermal exposure. The geogrid had therefore been successful in significantly delaying the propagation of the underlying cracks. In contrast, in areas where the geogrid had not been used, numerous cracks up to 1 inch in width had reflected through to the surface mainly years earlier. Since the reinforced pavement was performing so well, only an inexpensive, thin surface dressing was required to once again bring the runway back up to a top quality condition.

5.2 Greater Peoria Regional Airport, Illinois, USA

Since there are no other key airports within a two hour driving distance, the Greater Peoria Regional Airport is a connecting hub for major airports throughout the Midwest and the South. In 2000, the airport authority began investigating options for rehabilitating the facility's Echo taxiway using interlayer products. The combination of inclement weather and commercial traffic had led to significant degradation of the airport's taxiways and earlier attempts to rehabilitate the problem areas with routine asphalt overlays had proved unsuccessful. Extensive thermal cracking generally restricted the standard pavement life to approximately 7 years.

Peoria's highest recorded average monthly temperature is 86°F while the lowest is 16°F. Prior to their rehabilitation in 2000, the airport's taxiways suffered from block cracks, high severity thermal cracks (Figure 6) and construction related longitudinal cracks.

Rehabilitation of the Echo taxiway began by cold planing the entire pavement area by 2 inches. This was followed by additional localized 2 inch deep and 4 foot wide transverse planing over the areas exhibiting major distress. These areas were then filled with a specialized "SAMI" type mix containing fine aggregate and 0.83% polymer-modified asphalt cement. A glass-fiber geogrid was placed between this layer and the main asphalt that consisted of a 4.5 inch (114 mm) thick layer of P401 ACC mix.

The “SAMI” mix acts principally as a strain based distress control mechanism within the pavement structure. Essentially, its main function is to reduce the amount of spalling that takes place around existing reflective cracks. However, the product itself does not help in reducing the formation or the propagation rate of reflective cracks, hence the requirement for the glass-fiber geogrid component within the overlay.

To evaluate the performance of this unique treatment, the FAA funded the installation of a series of instruments that were subsequently monitored by the University of Illinois at Urbana-Champaign. Analysis of the data and a follow-up field survey in 2007 indicated that the pavement had performed particularly well. Specifically, following 6 years of service, less than 10% of the severe transverse cracks had reflected back through to the surface.

5.3 *Hector International Airport, Fargo, North Dakota, USA*

This Municipal airport acts as a connecting hub for flights throughout the Midwest, West and South. In 1996, the airport authority investigated options for using a high strength interlayer to prolong the pavement life of its main runway.

Runway 13–31 is exposed to harsh climatic conditions on a year-round basis. Average temperatures range from 82°F in July to 16°F in January. Wide temperature fluctuations, severe general weather conditions and heavy aircraft loadings were taking their toll on the runway. The existing asphalt had become brittle with surface distress types including a combination of thermal, alligator, block, transverse and longitudinal cracks.

The airport management considered adopting a routine rehabilitation program involving the installation of an asphalt overlay. However, previous experience suggested that the extreme thermal stresses that would be induced in the pavement, would likely result in the cracks reflecting through to the surface within just a few years. Instead, it was decided to adopt an alternative strategy involving the use of glass-fiber geogrids.

The rehabilitation began by performing crack repairs and some localized milling of the existing surface, followed by the placement of a thin, 0.5 to 0.75 inch (13 to 19 mm) thick leveling course. The treated area was 50 feet (15 m) wide and ran down the center of the runway. A glass-fiber geogrid was placed over the surface of the leveling course, before installing a 1.75 inch (44.5 mm) thick wearing course. The work was completed within only two days and therefore had only minimal impact on the normal airport operations.

A recent follow-up distress survey carried out at the site indicated that the geogrid system is performing very well with only minor cracking observed after more than 10 years of service.

6 CONCLUSIONS

Glass-fiber geogrids have been used successfully for more than 25 years in order to retard the propagation of reflective cracks in asphalt pavements. In addition to their general use, there are more than 100 examples of projects where this type of product has been used to reinforce overlays for airfield runways, taxiways and aprons.

Based on extensive laboratory testing and surveys conducted on many project sites, it has been shown that the inclusion of a glass-fiber geogrid within a pavement overlay will reduce the rate of reflective crack propagation by a factor of 2 to 3 times. This leads to an extension of the pavement service life and reduced maintenance costs. In a typical airport pavement, these benefits are likely to yield life cycle cost savings of between 20% and 30%.

REFERENCES

- Beck, D.E. (1999) The Emerging Role of Geosynthetics for Pavement Rehabilitation CE News, November 1999, pp. 46–52.
- Brown, S.F., Brunton, M., Hughes, D.A.B. and Brodrick, B.V. (1985) Polymer Grid Reinforcement of Asphalt Proceedings of The Association of Asphalt Paving Technologists, Vol 54, pp. 18–44.

- Brown, S.F., Thom, N.H. and Sanders, P.J. (2001) A Study of Grid Reinforced Asphalt To Combat Reflective Cracking AAPT Annual Meeting.
- Carver, C. and Sprague, C.J. (2000) Asphalt Overlay Reinforcement: The State of the Practice Summarized Geotechnical Fabrics Report, March 2000, pp. 30–33.
- De Bondt, A.H. (1999) Anti-reflective Cracking Design of (Reinforced).
- Lytton, R.L. and Jayawickrama, P. (1986) Reinforcing Fiberglass Grids for Asphalt Overlays Texas Transportation Institute Report for Bay Mills Limited, Texas A&M University, College Station, Texas.
- Lytton, R.L. (1988) Reinforcing Fiberglass Grids for Asphalt Overlays Texas Transportation Institute Report for Bay Mills Limited, Texas A&M University, College Station, Texas.

Evaluation of fiber reinforced bituminous interlayers for pavement preservation

C. Palacios & G.R. Chehab

The Pennsylvania State University, University Park, Pennsylvania, USA

F. Chaignon

Colas Inc., Morristown, New Jersey, USA

M. Thompson

Midland Asphalt Materials Inc, Tonawanda, New York, USA

ABSTRACT: The objective of this paper is to evaluate a fiber-reinforced asphalt treatment used as a stress absorbing membrane interlayer (SAMI) to mitigate reflective cracking. To evaluate the SAMI, experimental and control field sections were constructed at the Pennsylvania Transportation Institute (PTI) test track. The control section consists of a 2" HMA overlay on top of existing asphalt pavement, while the experimental section additionally contained the SAMI between the old and new HMA overlay. The sections experienced both controlled bus traffic and 1,000,000 loading cycles using the Mobile Model Load Simulator 1/3 scale (MMLS3). Effectiveness of the SAMI is assessed through distress surveys using visual inspection and high resolution imaging. Additionally, a Portable Seismic Pavement Analyzer (PSPA) was used to detect and compare any decrease in the modulus of the overlay due to microcrack development. Finally, cores were removed to observe existence and crack growth in both control and experimental sections. The results obtained reveal partial improvement in reflective cracking resistance due to the incorporation of the fiber-reinforced interlayer.

1 INTRODUCTION

Pavement preservation is a vital tool for highway agencies to manage its roadway assets by mitigating early pavement distresses and extending the service life of the roadways (Wittwer, Bittner et al. 2003). In the latter periods of their design service life, pavements exhibit cracking distresses: fatigue and thermal cracking in Asphalt Concrete (AC) pavements and faulting and mid-slab cracking in the case of Portland Cement Concrete (PCC) pavements (Hein and Croteau 2004). When cracks start to appear on the surface they are sealed with asphalt bitumen as a first remedy. However, as the cracks develop further, propagate and widen it is often the case that an AC overlay or a bituminous surface treatment becomes warranted. While the overlay is a relatively low-cost rehabilitation technique, it is, however, considered a short-term fix because in most cases the existent cracks in the underlying layers eventually propagate upwards into the overlay and reappear at the surface, hence forming what is referred to as reflective cracks. It is well documented that cracks propagate to new overlays due to vertical movement of the underlying pavement layers which may be due to traffic loading, frost heave and consolidation of subgrade soils, and/or to the horizontal movement of the pavement upper layers due to temperature changes. These movements create shear or tensile stresses, respectively, in the new overlay. When the stresses exceed the material strength, cracks initiate and further develop substantially reducing the new overlay's service life (Lytton 1989).

Stress absorbent membrane interlayer (SAMI), is one of the available remedies directed at inhibiting the propagation of reflective cracks. The interlayer systems, with high tensile strength in addition to high ductility act as a crack-inhibitor layer when placed between the old surface and the new overlay. This paper presents techniques to evaluate a SAMI on an experimental AC pavement section constructed at the Pennsylvania Transportation Institute Test Track, being part of a larger study conducted by the authors at the Pennsylvania State University to evaluate the performance of such a SAMI for low volume roads in Pennsylvania. The study addresses interlayer systems on existent AC pavements only.

2 MECHANISMS OF REFLECTIVE CRACKING

When the new overlay is perfectly bonded to the old distressed pavement, cracks from the old pavement propagate likely within one to five years at an average rate of 25 mm-year (Chen and Frederick 1992). There are cases, however, where the cracks propagate as early as a few months after application (Elseifi 2003).

Application of wheel loads over a crack create three critical load pulses (one maximum bending and two maximum shear stresses) at frequencies where the thin overlay, being viscoelastic, is stiff. The bending stresses are likely to create a crack at the bottom of the overlay at the location of an existent fatigue, or other longitudinal crack, due to the stress concentration at the crack tip. Eventually, the existent crack will propagate upwards reaching the surface.

Temperature can also contribute to the development of reflective cracking. The overlay presents a main constraint for the old pavement to freely expand or contract due to thermal changes if the layers are properly bonded. This phenomenon concentrates tensile stresses exactly on top of old thermal cracks. When the stresses induced exceed the material's strength, a crack initiates on the top of the old crack that eventually propagates upwards and manifests itself as a reflective crack. It is worthy to note however that thermal cracks also occur at the top of the pavement. At cold temperatures, the overlay has the tendency to contract. Because it is constrained in the longitudinal direction, thermal stresses develop and lead to a thermal crack in the transverse direction when those stresses exceed the material's strength. This thermal crack starts at the surface and propagates downwards. Both top down thermal cracking and reflective cracking can happen at the same time given the right conditions.

3 STRESS ABSORBENT INTERLAYER

A way to delay or mitigate the problem of reflective cracking is the use of interlayer systems between the old pavement surface and the overlay. The interlayer can have a reinforcing function or a strain relief function. Reinforcement occurs when the interlayer has a higher modulus than the top and bottom pavements layers; whereas, strain relief occurs when the interlayer modulus is lower (Lytton 1989). The interlayer should reduce longitudinal (horizontal) tensile stresses in the overlay caused by loading and thermal cycling (Kim and Buttlar 2002). If the interlayer is too soft, it may induce more horizontal movement at the bottom of the overlay, creating more susceptibility to fatigue cracks. When strain-relief mode interlayer systems are used, the crack normally begins at the crack on the old pavement and stops for some time at the interlayer.

The SAMI under study, previously evaluated by Yeates (1994), Michaut (1996), and CFTR (2007), consists of two layers of bituminous emulsion and a layer of sliced glass fiber strands sandwiched between the two emulsion layers. On top of the two emulsion layers 6.35 mm to 9.5 mm aggregate is spread and rolled. At this stage the interlayer acts as a stress absorbent membrane (SAM) or as a reinforced surface treatment. The application of an overlay on top turns the SAM into a SAMI (Figure 1). This dual function is one of the main advantages of this treatment. The application rate of fibers, emulsion and aggregates are specified in Table 1. The thickness of the treatment would depend on the size of the aggregate.

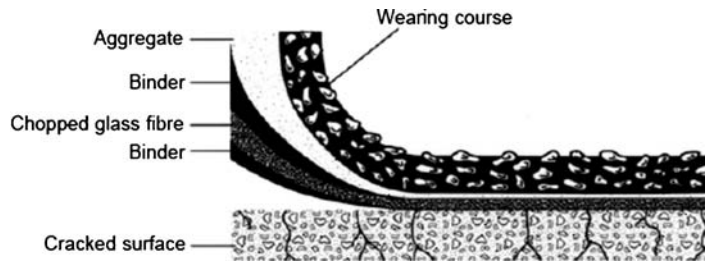


Figure 1. Schematic of SAMI (Courtesy of Midland Asphalt).

Table 1. Application rates.

SAMI type	Emulsion (liter/m ²)	Fiber (grams/m ²)	Aggregate (kg/m ²)
FiberMat B [®]	1.81–2.26	101–136	13



Figure 2. PTI test track.

4 EVALUATION PROCESS AND FINDINGS

This study focuses on the field evaluation of a fiber reinforced stress absorbing interlayer as a mitigating remedy for reflective cracking for asphalt low volume roads in Pennsylvania. The study involves comparison of overlays with an interlayer, and those without the interlayer (Control) on pavement test sections at the Pennsylvania Transportation Institute's (PTI) test track (Figure 2). Studies on complementary field sites and results from laboratory tests are published elsewhere (Chehab and Palacios 2007). The field evaluation process of the new treatment comprises of: observation of construction process, accelerated trafficking, periodic distress and image surveys, in addition to non-destructive and destructive structural evaluation.

4.1 Observation of construction process

In June 2005, two 30 meter long sections were constructed, one with the SAMI and an overlay and the other with only an overlay, over a 22 year old heavily distressed HMA pavement structure (Table 2). The old pavement surface presented medium-severity alligator cracking, low-severity block cracking, high-severity joint reflection cracking, medium-severity longitudinal and transverse cracking, medium-severity polished aggregate and medium-severity raveling. It should be noted that some of the non-wheel longitudinal cracks (joint reflection cracking) and transverse cracks on

Table 2. Old AC pavement structure; source: (Anderson, Kilareski et al. 1984).

Layer	Material	Thickness (cm)
Wearing Course	ID-2 (HMA)	3.8
Base Course	BCBC	15
Permeable Sub-base	HP crushed stone	10
Compacted Subgrade	2A compacted crushed stone	5
Subgrade	Clayey soil	–

the old pavement had a crack opening of 6.5 mm. A portion of the longitudinal cracks were sealed with AC 20 binder to study the advantage of crack sealing before the application of the SAMI.

4.2 Observation of construction process

In June 2005, two 30 meter long sections were constructed, one with the SAMI and an overlay and the other with only an overlay, over a 22 year old heavily distressed HMA pavement structure (Table 2). The old pavement surface presented medium-severity alligator cracking, low-severity block cracking, high-severity joint reflection cracking, medium-severity longitudinal and transverse cracking, medium-severity polished aggregate and medium-severity raveling. It should be noted that some of the non-wheel longitudinal cracks (joint reflection cracking) and transverse cracks on the old pavement had a crack opening of 6.5 mm. A portion of the longitudinal cracks were sealed with AC 20 binder to study the advantage of crack sealing before the application of the SAMI.

The construction of the SAMI involves application of the two emulsion layers and a fiber layer simultaneously using a truck with nozzles arranged in three rows. The first row of nozzles sprays the emulsion; the second row spreads the sliced glass fiber strands at the specified rate, and the third row of nozzles again sprays the emulsion forming a film of emulsion-fiber-emulsion over the old pavement. A special truck is used that has an attachment to suitably place the three layers. As the truck sprays the three layers, it moves forward and tracing the section equal to its width. The whole area is continuously covered with the emulsion-fiber-emulsion layer. Over the emulsion-fiber-emulsion film, 6.3 mm size aggregates are spread and then compacted with a pneumatic-tire roller. The emulsion used is polymer modified with a PG 64-22 asphalt binder base. A day after the SAMI was constructed, a 32 mm thick 9.5-mm Superpave overlay was placed. For the control section, a tack coat was applied to improve bonding between the layers.

4.3 Distress monitoring

Both SAMI and control sections were constantly monitored from the day of construction in June 2005 until July of 2007. A pre-construction distress survey was done for the SAMI section according to the LTPP Distress Identification Manual (Miller and Bellinger 2003). Both sections were divided into a grid of 1.8 by 1.8 meter parcels. Photographs and documentation of the distresses were recorded for each of the parcels in a database developed for that specific purpose during the period of the project (Figure 3).

A summary of the crack reappearance after two years on the SAMI section is given in Table 3. After two years of monitoring, no significant difference was observed between the SAMI section and the control section from the surface distress surveys. The monitoring period is yet short for any fatigue induced crack to reflect; however, it was observed after the two harsh winters that the pre-existing transverse cracks were beginning to slightly reflect on the surface of the control and SAMI sections. As mentioned before, some of those reflective cracks had an opening of 6.5 mm and were not sealed. It is most likely that the binder/emulsion placed during construction seeped into the cracks; thus preventing the fibers to properly bridge the crack opening (Figure 4). A similar behavior is observed with the overlay in the control section. No reflective cracks were observed where AC 20 sealant was applied.



Figure 3. Sample of 1.8 by 1.8 meter parcel on SAMI section a) parcel 3A before treatment b) parcel 3A after treatment.

Table 3. Summary of surface cracks from surveys of SAMI section.

	Time	Fatigue (m ²)	Wheel path longitudinal (m)	Non-wheel longitudinal (m)	Transverse (m)
SAMI	Before Construction	5.8	14.6	32.4	10.8
	2 years after	0	0	1.8	4
	% crack propagation	0%	0%	6%	37%
Control Section	Before Construction	5.6	13.2	30	10.8
	2 years after	0	0	2	4
	% crack propagation	0%	0%	7%	37%

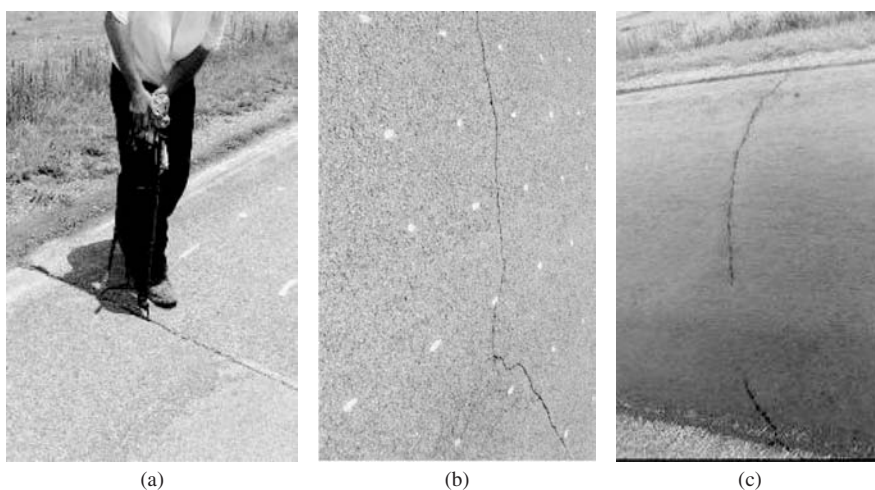


Figure 4. a) Sealing of crack; b) unsealed crack; c) fiber-emulsion layer on the unsealed crack (emulsion was absorbed into the crack that remained unsealed).

4.4 Bus trafficking

Throughout the project, roughly 15,000 bus passes were applied on the sections with an average daily traffic of 21 measured with a Hi-Star NC-200 digital traffic counter. The 2-axle buses consisted of 22 different types with an average weight of 110 kN with a standard deviation of 77 kN (PTI 2007).

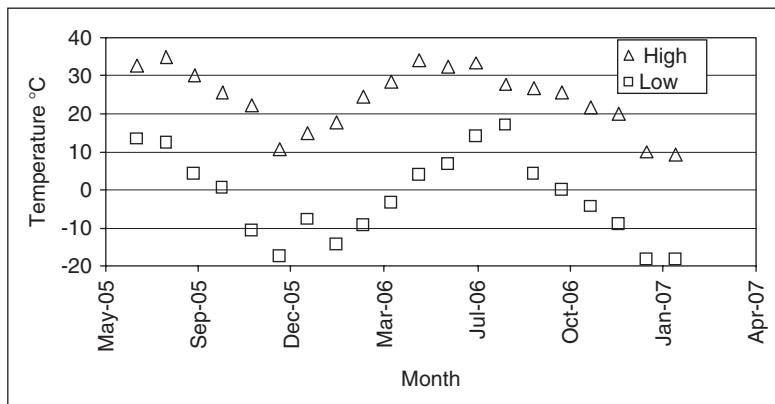


Figure 5. Maximum and minimum air temperatures.

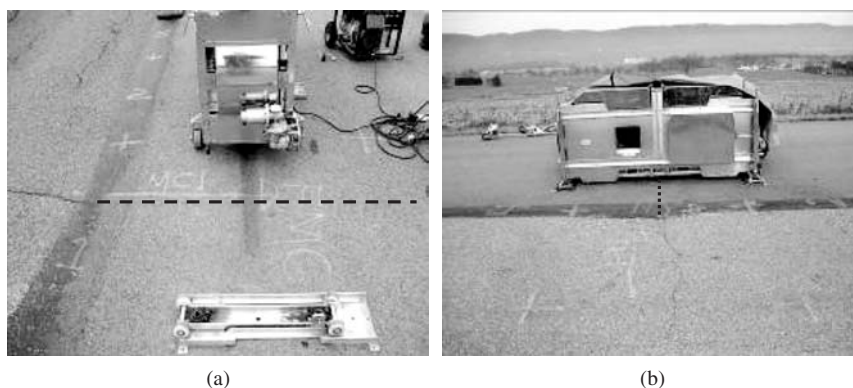


Figure 6. a) MMLS and its wheel path after loading at control section b) MMLS trafficking at SAMI section. Dashed lines show locations of underlying transverse cracks that did not propagate after loading.

This amount of traffic is low even for a low volume road. However, the loads are significantly high. Neither fatigue cracks nor permanent deformation were observed due to these loads after 2 years of monitoring.

4.5 Environmental conditions

As mentioned in section 4.2, transverse cracks were observed after the second winter. The environmental conditions at this location can be described as severe. The geographic location of the test site experiences freezing temperatures and is exposed to wind-chill factors that cause the actual temperatures to be lower than the reported air temperatures (Figure 5). These conditions are propitious for phenomena explained in Section 2.

4.6 MMLS3 loading

To expedite the evaluation of the effectiveness of SAMI on delaying reflective cracking, accelerated pavement testing was performed on sections at locations where underlying cracks pre-exist (Figure 6). One million wheel applications were applied at a speed of 2.5 m/sec on top of pre-existent transverse cracks of similar size at both SAMI and control sections. The wheel load exerted by the MMLS3 is 2.7 kN, with a contact pressure of 700 kPa (De Vos, Hugo et al. 2006). The load creates

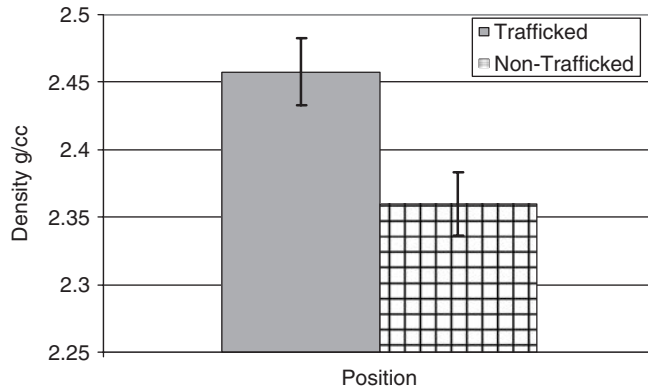


Figure 7. Densification of the surface layer under the MMLS3 wheel path.

an approximate vertical stress of 500 kPa at the interlayer interface. The wheel loads were applied at very low temperatures, and thus no rutting was observed. For better comparison, the sections trafficked were scanned with a digital image scanner before and after trafficking. After one million cycles of MMLS3 traffic loading, no cracks were observed under the MMLS3 wheel path for both sections. However densification was found under the wheel path measured by a pavement quality indicator (PQI) (ASTM D 7113-05) (see Figure 7).

4.7 Non destructive testing

After applying one million cycles on top of pre-existing cracks on both SAMI and the control sections, no visible reflective cracks appeared. To further evaluate the two sections, a Portable Seismic Property Analyzer (PSPA) was used on the surface of both sections. The Portable Seismic Pavement Analyzer (PSPA) is an instrument designed to determine the variation in modulus with depth of exposed layer being concrete or asphalt (De Vos, Hugo et al. 2006). The operating principle of the PSPA is based on generating and detecting stress waves in a medium (Nazarian, Yuan et al. 1999). The PSPA was used to determine the modulus of SAMI and the control section. Stiffness of the top 50 mm was measured at locations where a crack was known to exist and at locations with no preexistent cracks, for both SAMI and control sections.

Average stiffness from five readings of each section was measured at -7°C and at 7°C . In addition, a variability study on stiffness readings was performed at 7°C on the SAMI section. Three readings every two meters were measured along the 30 m section, totaling 45 readings. An average stiffness of 14,000 MPa was recorded with a standard deviation of 2,500 MPa. The standard deviation between every three readings was 80 MPa. This suggests that due to variability of stiffness along the same section, any comparison between SAMI and control sections would not be able to statistically detect the treatment effects on stiffness. A similar measurement was done with the PQI. Results showed significant variability of density along and across the pavement.

4.8 Field cores

Field cores were taken from the SAMI and control sections. Three cores were taken from locations that did not originally exhibit any cracks. The cores removed were 150mm in diameter and covered the full depth of the pavement. A set of two cores were extracted on top of similar cracks in the pre-existing pavement. No reflective cracks were observed on the core removed from the SAMI section (Figure 8). However, an existing crack was observed propagating towards the surface of the new layer at the control section (Figure 8). In addition, the cores removed were sawed in slices and

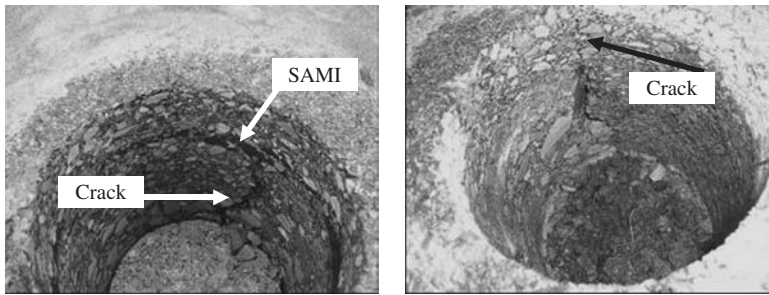


Figure 8. a) Hole from core with SAMI, crack stopping at SAMI layer b) Hole from control section, crack propagating towards surface.

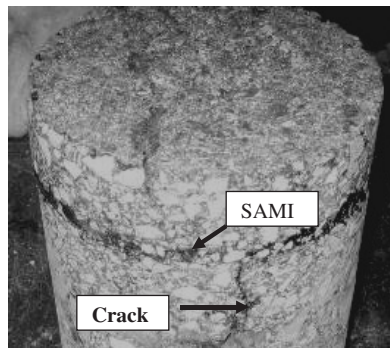


Figure 9. Crack stopped at the SAMI.

the interlayer was found to be highly impermeable. Variability of overlay depth also was an issue. Values measured from the cores were in the range of 25 mm to 50 mm.

From one of the cores removed from top of a transverse crack one can see the fact that the fibers are deflecting the crack path. This makes the water path not straight which helps to keep the water out (Figure 9).

5 CONCLUSIONS AND RECOMMENDATIONS

The study evaluated the effectiveness of a stress absorbing membrane interlayer from inhibiting reflective cracking. The field study was conducted on constructed sections at the Pennsylvania Transportation Institute (PTI) test track. During the two year period of loading and environmental exposure, few reflective cracks were observed that mainly propagated from wide cracks that were left unsealed. This agrees with findings from (Buttler, Bozkurt et al. 2000) and (Lytton 1989). The overall surface condition after two years is rated as very good for both sections.

One million cycles of MMLS3 on top of pre-existing cracks did not induce any visible cracks neither on the treated nor the control sections. Measurements of modulus for both sections made using a Portable Seismic Property Analyzer do not offer conclusive evidence that the modulus of the control section was decreasing with time and loading.

Cores removed from both sections at locations with pre-existing cracks show that reflective cracks occur only in the control section. In sample cores, it was observed that upward propagating cracks stopped at the SAMI interlayer; whereas they continued their propagation in the control sections. However it should be noted that variability of construction could have been a factor in promoting such cracks. The thin layer of overlay had variability in depth, stiffness, and density.

The following recommendations should be considered for future work:

1. Cracks relatively severe should be sealed before laying the treatment.
2. For sites experiencing low temperature conditions, a lower low temperature PG grade binder could be beneficial to prevent top down cracking and prevent mix mode cracking.
3. Laboratory tests should be performed to characterize the mechanical properties of the interlayer, such as low temperature creep compliance, fracture properties of the interlayer, and fatigue failure susceptibility.

REFERENCES

- Anderson, D., Kilaeski, W. P., and Bonaquist, R. F. 1984. Fourth Cycle of Pavement Research at the Pennsylvania Transportation Research Facility, Vol. 1, Construction and Operation of the Pavement Durability Research Facility.
- ASTM. 2005b. Standard Test Method for Density of Bituminous Paving Mixtures in Place by the Electromagnetic Surface Contact Methods.
- Buttler, W. and Bozkurt, D. 2000. Cost-Effectiveness of Paving Fabrics Used to Control Reflective Cracking. Transportation Research Record. Washington, D.C., Transportation Research Board. No. 1730, pp. 139–149.
- CFTR 2007. Avis Technique Colfibre®. Chausees 146. C. F. p. I. T. Routières.
- Chehab, G. R. and Palacios, C. 2007. Evaluation Study of FiberMat B® Interlayer System for Roadway Pavement Rehabilitation. Low Volume Roads Product Evaluation Division of Municipal Services Pennsylvania Department of Transportation Final Report.
- Chehab, G., Seo, Y., and Kim, R. 2006. Viscoelastoplastic Damage Characterization of Asphalt Concrete Using Digital Image Correlation. *International Journal of Geomechanics ASCE Vol. 7 (Issue 2)*.
- Chen, H. J. and Frederick, D. A. 1992. Interlayer on flexible pavements. Transportation Research Record Washington D.C., Transportation Research Board. 1374 pp. 90–94.
- De Vos, E. R., Hugo, F., Strauss, P., Prozzi, J. A., Fults, K. W., and Tayob, H. 2007. Comparative Scaled MMLS3 tests vs. full-scale MLS10 tests in Mozambique. Conference Proceeding, Transportation Research Board 86th Annual Meeting, Washington, D.C.
- Elseifi, M. 2003. Performance Quantification of Interlayer Systems in Flexible Pavements using Finite Element Analysis, Instrument Response, and Non Destructive Testing. The Via Department of Civil and Environmental Engineering. Blacksbourg, VA, Virginia Polytechnic Institute and State University. Ph.D.
- Elseifi, M. and Al-Qadi, I. 2005. Modeling of Strain Energy Absorbers for Rehabilitated Cracked Flexible Pavements. *Journal of Transportation Engineering: pp. 653–661*.
- Hein, D. and Croteau, J. 2004. The Impact of Preventive Maintenance Programs on the Condition of Roadway Networks. Annual Conference of the Transportation Association of Canada. Québec City, Québec.
- Kim, J. and Buttler, W. 2002. Analysis of Reflective Crack Control System Involving Reinforcing Grid over Base-Isolating Interlayer Mixture. *Journal of Transportation Engineering July/August: pp. 375–384*.
- Lytton, R. L. 1989. Use of geotextiles for reinforcement and strain relief in asphalt concrete. *Geotextiles and Geomembranes 8: pp. 217–237*.
- Michaut, J. P. 1996. Enduit superficiel aux fibres: Colfibre. Third international RILEM conference. Maastricht, The Netherlands, E & FN Spon an imprint of Chapman & Hall, London. 33: pp. 176–182.
- Miller, J. S. and Bellinger, W. Y. 2003. Distress Identification Manual for the Long-Term Pavement Performance Program (Fourth Revised Edition). FHWA-RD-03-031.
- Nazarian, S. & Yuan, D. 1999. Structural Field Testing of Flexible Pavements Layers with Seismic Methods for Quality Control. Transportation Research Record Vol. 1654/1999: pp. 50–60.
- PTI. 2007. The Altoona Bus Research and Testing Center. Retrieved 8/30/07, from <http://146.186.225.57/pti/busdata/>.
- Wittwer, E. & Bittner, J. 2003. Asset Management and City Government. Mid-Continent Transportation Research Symposium.
- Yeates, C. 1994. Evaluation of fibre-reinforced membranes. Performance and Durability of Bituminous Materials. J. Cabrera and J. Dixon, Taylor & Francis, London.

Installation and performance of a fiberglass geogrid interlayer on the NCAT Pavement Test Track

R.B. Powell

National Center for Asphalt Technology, Auburn, Alabama, USA

ABSTRACT: The Pavement Test Track is a full-scale, accelerated performance test facility for flexible pavements managed by the National Center for Asphalt Technology (NCAT) at Auburn University. Forty-six unique 60-m test sections are installed around a 2.8-km oval and subjected to accelerated damage via a fleet of tractors pulling heavy triple trailers. Methods and materials that produce better performance for research sponsors are identified so that future pavements can be selected based on objective life cycle comparisons. Within one section, NCAT was asked by the research sponsor to evaluate the installation and performance of a fiberglass geogrid interlayer. Half of the selected test section was constructed with a fiberglass geogrid interlayer and the other half without. Initial observations were made for the section sponsor regarding ease of construction, and weekly pavement management data collected throughout the section facilitated a field performance comparison with and without the product. Construction documentation and performance data relating to potential differences in smoothness, rutting, and cracking are presented. No problems were reported during the installation of the geogrid interlayer, which was completed just before the placement of surface mix. Pavement performance was comparable for the portion of the test section with the geogrid interlayer and the portion without, with the exception of longitudinal cracking along the centerline joint. Extensive centerline cracking was noted without the geogrid interlayer, but no centerline cracking was noted with the geogrid interlayer.

1 INTRODUCTION

1.1 *Background*

The Pavement Test Track (referred to hereafter as simply the Track) is a full-scale accelerated performance test (APT) facility managed by the National Center for Asphalt Technology (NCAT) at Auburn University. The project is funded and directed by a multi-state research co-op in which sponsors ship in hot-mix asphalt materials and methods that are local to their jurisdictions for placement on the Track. Forty-six different 60-m sections have been built around the 2.8-km oval to facilitate field performance comparisons in an identical climate where traffic conditions are precisely monitored. The primary objective of the project is to identify pavements with superior field performance and lower life cycle costs through the application of a design lifetime of truck traffic (10 million equivalent single axle loadings, or ESALs, over 2.6M km) in 2 years. Within one section, NCAT was asked by the research sponsor to evaluate the installation and performance of a fiberglass geogrid interlayer.

1.2 *Scope*

The Track was originally constructed in the summer of 2000. The extra effort required to install the fiberglass geogrid interlayer was provided by the manufacturer, who also selected the test section for the installation under the direction of the state sponsor. The second half of the selected test section was constructed with the interlayer and the other half without. The geogrid mesh was sandwiched

between two 50 mm lifts of granite stone matrix asphalt (SMA). The study test section (both with and without the geogrid) survived the original 10 million ESAL loading and remained in service for another round of truck traffic on the 2003 Track. Construction documentation and performance data relating to potential differences in smoothness, rutting, and cracking were included in this research. The analysis period began with the construction of the test section in June of 2000 and ended after the completion of the second round of truck traffic in December of 2005. Forensic testing was conducted in January of 2006.

2 CONSTRUCTION

2.1 *Track foundation*

In order to isolate distresses to experimental surface mixes, the foundation for the 2000 Track was designed for perpetual performance. The total thickness of all hot-mix asphalt layers was approximately 600 mm in order to produce underlying strains so low that the structure would not fail from the bottom up. A permeable base layer was also included to remove water from underneath the pavement structure via edgerains on both sides of the roadway. This approach provided a stable platform on which the performance of the upper 100 mm of surface mixes could be studied.

2.2 *Experimental mix*

The 50 mm lifts placed above and below the fiberglass geogrid interlayer consisted of SMA mix blended with granite coarse and fine aggregates, flyash filler, SBR-modified PG76-22 binder and mineral fibers. A Marshall hammer was used to apply the 50 blow compactive effort for the mixture, and asphalt content was adjusted to target 4 percent air voids (as a percentage of the laboratory maximum). Properties of the plant produced mix are presented in Table 1.

Table 1. Mix properties.

Design Method	SMA
Compactive Effort:	50 blows
Binder Performance Grade	76–22
Modifier Type:	SBR
Aggregate Type:	Granite
Gradation Type:	SMA
Avg. Lab Properties of Plant Produced Mix	
Sieve Size:	% Passing:
1"	100
3/4"	100
1/2"	95
3/8"	68
No. 4	28
No. 8	20
No. 16	18
No. 30	16
No. 50	14
No. 100	12
No. 200	9.7
Asphalt Binder Content:	6.1%
Compacted Pill Bulk Gravity:	2.337
Theoretical Maximum Gravity:	2.422
Computed Air Voids:	3.5%



Figure 1. Application of fiberglass geogrid interlayer.

2.3 Grid installation

Trial mix was produced and placed in an off-Track location prior to placement on the actual test section in order to ensure the mix met the sponsor's expectations. The lower lift was placed on Friday, June 9, 2000 with in-place air voids of 3.5 percent (of the laboratory maximum). The compactive effort applied to the mat consisted of four coverages with a 105 kN pound vibratory roller set on a frequency of 3800 vibrations per minute at an amplitude of 0.75 mm, followed by two coverages set on a frequency of 3400 vibrations per minute at an amplitude of 0.50 mm, then finish rolled with one static pass using the same unit. The temperature of the mat cooled from approximately 150°C at the beginning of breakdown rolling to approximately 90°C at the end of finish rolling.

On Tuesday, June 13, 2000 the lower lift was prepared for the placement of the upper lift. An emulsified CQS-1h asphalt tack coat was applied at a rate of 0.14 liters per square meter on the lower layer after it had been swept. The geogrid interlayer was rolled out onto the tacked mat as seen in Figure 1 using a tractor equipped with an application attachment. Because the lower lift had been in place for several days, there was no problem staying within the 5°C to 60°C surface temperature requirement. Longitudinal joints were overlapped 25 to 50 mm, as specified by the manufacturer. Figure 2 shows the verification process for adhesion between the geogrid and the lower lift of SMA, where a 5 kg pull on the mesh cannot result in movement. Because the product is manufactured with a pressure-sensitive adhesive backing and the lower lift had been thoroughly tacked beforehand, as seen in Figure 3 and 4 there was no indication of geogrid slippage of any type during construction of the upper lift.

The upper layer was placed at an average temperature behind the paver of approximately 165°C. Because the lower layer was slightly over compacted, the effort was reduced for the upper layer. Here, rolling was reduced to three coverages set on a frequency of 3800 vibrations per minute at an amplitude of 0.75 mm, then finished with one static coverage. The temperature of the mat again cooled from approximately 150°C at the beginning of breakdown rolling to approximately 90°C at the end of finish rolling. Average air voids in the finished upper layer were 6.5 percent of the laboratory maximum.



Figure 2. Bond strength verification.



Figure 3. Material transfer device traveling on geogrid surface.

3 LABORATORY PERFORMANCE

3.1 *Mix properties*

Plant settings for the produced mix are included in Table 2. In junction with the volumetric information provided earlier in Table 1, it was found that the voids in the mineral aggregates of the plant produced mix averaged 17 percent (expected in a mix with a design value of 17½ percent). Average air voids of the laboratory quality control (QC) specimens were determined to be 3.5 percent. These same QC specimens were subjected to loaded wheel testing with an Asphalt Pavement Analyzer (applying a 445N load via 690 kPa contact pressure on specimens conditioned to 64°C), which induced 2.0 mm of average rutting after 8,000 load cycles (16,000 wheel loadings). Because of the use of mineral fibers at a rate of 0.4 percent, only 0.02 percent draindown was measured in the QC laboratory. The thickness of the completed mat in the field averaged 99 mm with a standard



Figure 4. Paving train on geogrid surface.

Table 2. Mix properties.

Completion date	Tuesday, June 13, 2000
24 Hour High Temperature (F):	92
24 Hour Low Temperature (F):	73
24 Hour Rainfall (in):	0.00
Lift Tupe:	dual
Design Thickness of Test Mix (in):	4.0
Plant Configuration and Placement Details	
Component:	% Setting:
Liquid Binder Setting	6.2%
Granite 7	73.0%
Granite 89	11.0%
Granite M10	10.0%
Stabilizer Mineral Fiber	0.4%
Filier Fly Ash	6.0%
Approximate Length (ft):	202
Surveyed Thickness of Section (in):	3.9
Std Dev of Section Thickness (in):	0.1
Type of Tack Coat Utilized:	CQS-1h
Target Tack Application Rate:	0.03 gl/sy
Avg Mat Temperature Behind Paver (F):	328
Average Section Compaction:	95.0%

deviation of 2.5 mm, which was very close to the design target. The overall quality of the placed mix was generally very positive in both the laboratory and the field.

3.2 Grid properties

The product utilized for this study is known commercially as GlasGrid@8501. Developed in the late 1980s, it consists of a stiff fiberglass material coated with an elastomeric polymer. It is advertised to have a 69 million kPa elastic modulus and a tensile strength of 100 kN/m (in both directions); however, no laboratory testing was done in this study to verify these claims. The underside of the mesh is coated with a pressure-sensitive adhesive that is activated by the act of rolling. This

feature is intended to stabilize the product on the mat and prevent slippage during construction. This particular product was specified by the sponsor of the test section; therefore, no effort was invested in comparing advertised properties to other products that may be available in the marketplace. This was possible because the vendor provided both the product and the installation at no cost to the project or the sponsor.

4 FIELD PERFORMANCE

4.1 *Truck traffic*

Trucking operations began at the Track in the fall of 2000 utilizing conventional tractors driven by live operators pulling heavy triple trailer trains. Each axle in the optimized configuration was loaded to approximately the federal legal bridge limit of 89 kN, which produced a gross vehicle weight for the entire triple trailer train of approximately 676 kN. Truck computers were set such that cruise speed was held constant at 72 km/hr, which is the design speed of the test oval. Generally, trucking operations ran from 5:00 AM to approximately 11:00 PM, with about an hour of down time midday to accommodate refueling and driver shift changes. The fleet was idle on Sunday to provide for a day of rest and again on Monday to accommodate pavement condition testing while preventive and corrective maintenance was completed on the trucks. In each research cycle, 10 million ESALs were applied to the surface of experimental pavements, which means that 20 million ESALs had been applied to the geogrid section by the end of the second research cycle in December of 2005.

4.2 *Roughness*

A high-speed laser profiler with an inertial compensation system was utilized to produce profile-based roughness measurements for each section on the Track. Output data were summarized in 8 m measurement segments such that the middle 46 m of each section could be examined without the influence of adjacent transverse joints (affecting approximately 8 m on either end of each section). Roughness was reported in m/km in accordance with the International Roughness Index (IRI) approach, which is a mathematical assessment of amplified profile wavelengths tuned specifically to quantify the feel of the roadway for a traveler in a passenger car. Roughness measurements before the application of any traffic, after the application of 10 million ESALs, and after the application of 20 million ESALs are provided in Figure 5. Here it is seen that generally the test section gets smoother the farther you travel from the near transverse joint. This was also observed for other sections on the Track.

4.3 *Rutting*

Elevations were measured weekly along transverse profiles at random test locations so that rutting performance for each test section could also be characterized. The 6-point algorithm standardized in AASHTO PP 38-00 (“Determining Maximum Rut Depth in Asphalt Pavements”) was used to compute rut depths that considered the effect of heave on the outside of each wheelpath. In this approach, the 3 elevations that define the peaks and valley of the left wheelpath are used to compute a maximum trough depth. The same procedure is used to produce a maximum trough depth for the right wheelpath, which is then used to compute a single average rut depth for the entire transverse profile. Average rut depth measurements after the application of 10 million ESALs and after the application of 20 million ESALs are provided in Figure 6.

4.4 *Cracking*

Test sections were also inspected on a weekly basis for evidence of cracking. When cracking was found on the Track, it was characterized in terms of the defining coordinate geometry within each test section. Due to the perpetual nature of the geogrid test section, it was not expected that cracking

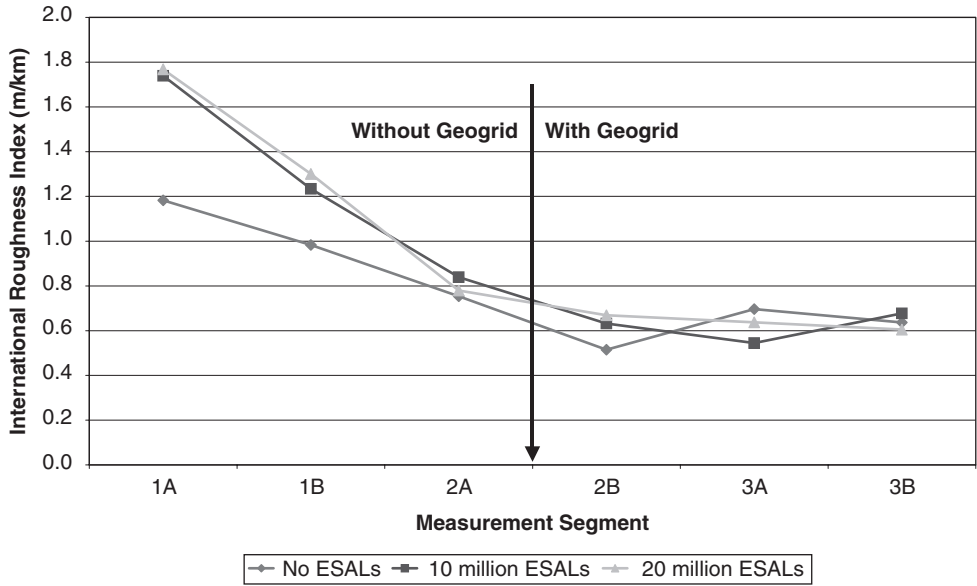


Figure 5. Roughness measurements as a function of traffic on section containing geogrid.

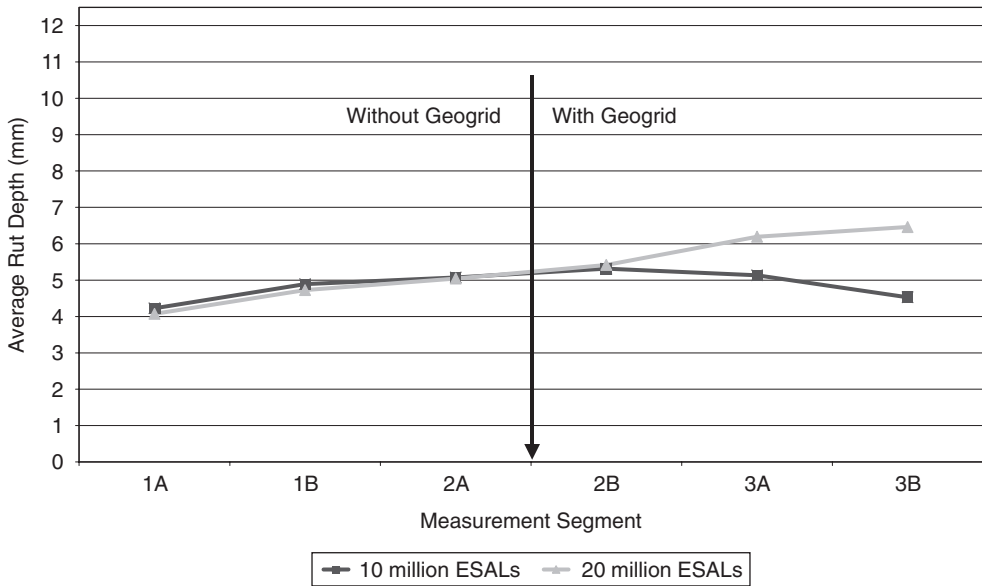


Figure 6. Rutting measurements as a function of traffic on test section containing geogrid.

would be a significant distress. During both periods of fleet operation, this was observed to be the case; however, longitudinal cracking along the centerline joint between the inside and outside lanes was noted in January of 2006 approximately one month after the completion of 20 million ESALs. No cracking was found in the half of the section that contained the geogrid interlayer; however, cracking was observed along the entire unreinforced length of centerline. A picture of cracking in the unreinforced length of the test section is included as Figure 7. In this picture, traffic runs right to left and the white line is a transverse test location.

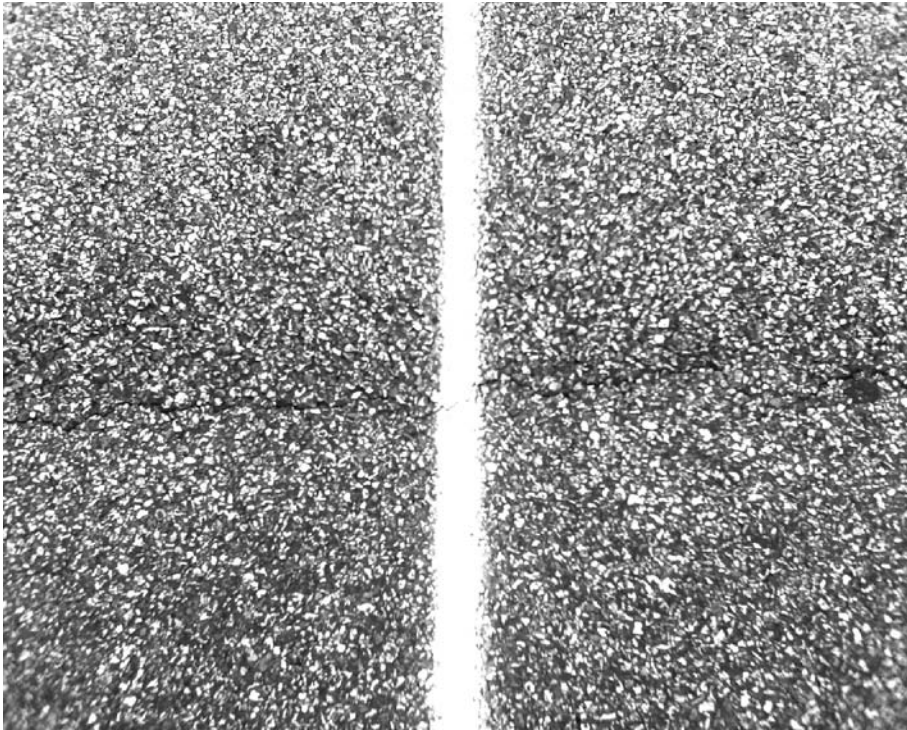


Figure 7. Longitudinal centerline cracking without interlayer (traffic runs right to left).

4.5 Forensics

Cores were cut from each test section on a quarterly basis. It was noted that in warmer months the bond between the upper and lower lifts in the reinforced part of the geogrid test section seemed to be comparable to other unreinforced sections; however, in colder months the upper lift would become detached from the lower lift before the core could be fully extracted during the drilling process. Inspection of the cores revealed the geogrid appeared to be in good condition, and it was deduced the bond failure was the result of increased stiffness of the asphalt mix and/or increased brittleness of the tack between the layers. No laboratory bond strength testing was run at these times because it was not possible to remove specimens without failing the bond in the field.

A forensic study was conducted on January 20, 2006 approximately 1 month after the completion of 20 million ESALs. As seen in Figure 8, a slab was carefully removed from the outside edge of the pavement in order to recover and visually inspect a section of geogrid mesh. A concrete masonry saw, a hammer chisel, a skid steer with a forklift attachment and an assortment of hand tools were used to remove the upper layer. The block was flipped over and the geogrid was then peeled off the underside of the upper layer. This process was difficult but it was accomplished without visually damaging the mesh. As a result of this exercise, it was found that after 5½ years the grid still appeared to be in good condition and well-bonded to both the lower and upper hot-mix asphalt sandwiching layers. Because of minor damage that occurred to the mesh during removal, it was not possible to test the specimen in the laboratory to determine an aged tensile strength.

5 CONCLUSIONS

Several important conclusions can be drawn from this study. Based on the author's personal experience during the installation of the fiberglass geogrid interlayer reported herein, the product can



Figure 8. Geogrid sample recovery during forensic study.

be installed without significantly hindering the overall construction process or compromising construction quality. No change to the standard construction methodology was necessary aside from allowing a tractor to apply the geogrid immediately before paving began. There was no creasing or folding, even though the test section was only 60 meters long and sharp turning of the heavy construction equipment (including a material transfer device) was necessary. No adjustment was made to production and placement temperatures, and forensics would later reveal that the fiberglass mesh appeared to be in excellent condition 5½ years after it was installed.

Pavement performance was quantified after 10 million ESALs and again after 20 million ESALs. The latter part of the test section in which the geogrid was installed was initially smoother than the first part of the section in which it was not installed; however, this effect was observed in many other test sections and is likely not the result of any effect of the interlayer. Roughness as a result of truck traffic increased in the unreinforced length, but no increase was observed in the reinforced length. This has not generally been observed in other sections and could conceivably be a result of the effect of the interlayer.

A very minor amount of rutting was induced by the truck traffic. The unreinforced length did not change at all between 10 million and 20 million ESALs; however, the length containing the geogrid did rut slightly more as a result of the additional traffic. The section containing the fiberglass geogrid interlayer was left in place for the 2006 research cycle, and will continue to be monitored for any sign of performance differences that may be the result of geogrid reinforcement. When the section is ultimately taken out of service, possibly during the construction of the research cycle that will begin in 2009, trenching may reveal whether the geogrid played a role (possibly through decreased bond strength) in the additional rutting that was observed in the reinforced length. At that time, milling for section replacement will also allow researchers to evaluate the effect of the interlayer on reclamation and recycling.

A forensic study was conducted outside of the wheelpath along the edge of the shoulder. The careful removal of a section of mesh revealed the fiberglass geogrid interlayer still appears to be in good condition 5½ years after it was installed.

Evaluation of reflective cracking performance of AC mixes with asphalt rubber binder using HVS tests and recursive mechanistic-empirical analysis

P. Ullidtz

Dynatest International

J. Harvey & D. Jones

University of California Pavement Research Center, Davis, California, USA

B.-W. Tsai

University of California Pavement Research Center, Berkeley, California, USA

ABSTRACT: A major research project has been conducted at the University of California Pavement Research Center (UCPRC) to evaluate the performances of several AC overlays that contained asphalt rubber binder. This paper presents the analysis with respect to reflection cracking using a recursive mechanistic-empirical analysis procedure, known as *CalME*. For reflection cracking a simple model for calculating the strain in the overlay over an existing crack is presented. The fatigue properties required by the procedure for different AC mixes were determined from laboratory test data. The analysis procedure was validated by simulating full-scale pavement testing using the Heavy Vehicle Simulator (HVS). The results of the HVS tests were imported to the *CalME* database and the simulations were done in increments of one hour. Most HVS tests show a considerable increase in deflections during the test, due to damage of the pavement layers. This implies that other response parameters, such as stresses and strains, also change considerably during the test. As these response parameters are used in the empirical relationships to predict pavement performance, it is very important that correct values are used at any point in time during the simulation. Care was taken to ensure that the simulations with *CalME* would produce response values (deflections in this case) that were reasonably close to the measured responses. The predicted changes in the moduli of the overlays and the relationship between predicted damage and observed cracking indicate that recursive mechanistic-empirical approach with the reflection cracking model worked satisfactory.

1 INTRODUCTION

The goal of this study was to evaluate the reflection cracking performance of asphalt mixes used in overlays for rehabilitating cracked asphalt concrete pavement in California. The main objective was to compare the performance of three overlays with mixes containing binders using Caltrans' MB specification (binders including recycled tire rubber and polymers blended at the refinery) against two control overlay mixes [dense-graded asphalt concrete (DGAC) and gap-graded rubberized asphalt concrete (RAC-G)]. These control overlays represent typical pavement structures currently used throughout California.

The project was divided into two phases. In the first phase, the uniform test pavement, which consisted of six test sections, was trafficked with the HVS to induce fatigue cracking on the asphalt concrete layer. The original pavement consisted of 77 to 88 mm of DGAC on a design thickness of 410 mm of aggregate base (AB) on a clay subgrade. The AB consisted of 100% recycled building

waste material with a high percentage of crushed concrete. Reactive cement was found in the AB. In the second phase, selected overlay mixes were placed to evaluate:

- Reflection cracking (expected failure mode) under HVS trafficking at moderate temperatures, and
- Rutting performance under HVS loading at high temperature.

Only the reflection cracking tests are included in this paper. They were performed by applying HVS trafficking directly over the previously cracked Phase I test sections. A laboratory study, primarily investigating the shear and fatigue properties of the mixes, was undertaken in parallel with the HVS study.

The six reflection cracking test sections, constructed as part of the second phase of the study, were as follows:

1. Half-thickness (45 mm) MB4 gap-graded overlay with minimum 15 percent recycled tire rubber (referred to as “MB15” in this paper)
2. Half-thickness rubberized asphalt concrete gap-graded (RAC-G) overlay
3. Full-thickness (90 mm) DGAC overlay (split into two subsections in the analysis)
4. Half-thickness MB4 gap-graded overlay
5. Full-thickness MB4 gap-graded overlay
6. Half-thickness MAC15TR gap-graded overlay with minimum 15 percent recycled tire rubber.

The test sections were instrumented with Multi Depth Deflectometers (MDDs) and thermocouples. At regular intervals during the HVS tests the resilient deflections were recorded at several depths using the MDDs and at the pavement surface using a Road Surface Deflectometer (RSD, similar to a Benkelman beam). The permanent deformations were also recorded by the MDDs and the pavement profile was measured using a laser profilometer. Any distress at the surface of the pavement was recorded. During HVS testing the temperature was controlled using a climate chamber. Falling Weight Deflectometer (FWD) tests were carried out before and after the HVS tests. Details on the HVS and the instrumentation can be found in Harvey et al., 1998 and on the overall study in Jones et al, 2007.

2 SIMULATION OF HVS TESTS USING CalME

The HVS tests were simulated using an incremental-recursive program known as *CalME* (Ullidtz et al., 2007). Data from each HVS test were imported into a *CalME* database. The data comprised information on loads (time of application and load level), temperatures at different levels, RSD results, MDD resilient and permanent deformations and pavement profiles.

The backcalculated layer moduli from the last FWD test before commencement of the HVS loading were used as the initial layer moduli (for asphalt layers at the reference temperature of 20°C). Layer moduli were backcalculated using *CalBack*. For asphalt layers the master curve was obtained from frequency sweep tests on beams in the laboratory, with the exception of the original DGAC layer where the master curve was based on FWD backcalculated moduli. For the subgrade the change in stiffness with changing stiffness of the pavement layers and with changing load level was obtained from FWD backcalculated values. These parameters were used with the response model (*LEAP*, Symplectic Engineering Corporation, 2004) to calculate stresses, strains and deflections in the pavement structure. The strain in the overlay over an existing cracked asphalt layer was calculated using the reflection cracking model described below.

To predict the pavement performance, in terms of cracking and permanent deformation, a number of models were used. Parameters for prediction of asphalt damage were obtained from controlled strain fatigue tests on beams. Repeated Simple Shear Tests at Constant Height (RSST-CH) were used to determine the parameters for predicting permanent deformation in the asphalt layers. A crushing model was developed for the self-cementing base layer, consisting of recycled building

waste material with a high content of crushed concrete. Cracking at the pavement surface was calculated from the reflection damage to the surface layer, using a model developed based on previous simulations of HVS tests and the WesTrack experiment, with coefficients modified based on the results of the present experiment.

An incremental-recursive process was used to simulate the performance of the test sections. The time increment used was one hour. For the first hour of the simulation the program would read the temperatures from the database and calculate the moduli, for a constant wheel speed of 9.6 km/h, the approximate speed of the HVS wheel. The number of loads during the first hour, as well as the load level and the tire pressure, were also read from the database. The modulus of the subgrade would be adjusted to the stiffness of the pavement layers and to the load level. If the test had wheel wander, five different positions of the wheel would be considered. For the first wheel position the stresses and strains at the center line of the test section were calculated and used to determine the decrease in moduli and the increase in permanent deformation of each of the pavement layers. The output from these calculations were used, recursively, as input to the calculation for the next wheel position. Because of the changes to moduli, response, damage, and permanent deformation the “time hardening” procedure was used (Deacon et al. 2002).

The first step in the simulation is to make sure that the calculated pavement response is reasonably close to the actual pavement response during the test. The calculated pavement response is used to predict the pavement performance (damage and permanent deformation). Therefore, if the calculated response is not reasonably correct it would be futile to try to use it for calibration of the performance models. For the HVS tests used for this paper, response measurements were available in the form of resilient MDD deflections and/or RSD deflections.

Once the resilient deflections are predicted reasonably well during the simulations, it is possible to calibrate the performance models so that the permanent deformation of each layer, the decrease in layer moduli and the observed surface cracking, are reasonably well predicted.

3 REFLECTION CRACKING MODEL

Reflection cracking damage was calculated using the method developed by Wu (2005). In this method the tensile strain at the bottom of the overlay is estimated using a regression equation. The calculated tensile strain at the bottom of the overlay is used with the fatigue equation described in the next section to calculate damage in the asphalt layers.

The regression equation for tensile strain at the bottom of the overlay is based on many 2D and 3D finite element calculations, and assumes a dual wheel on a single axle:

$$\varepsilon = \alpha \times E_{an}^{\beta_1} \times E_{bn}^{\beta_2} \times (a_1 + b_1 \times \ln(LS_n)) \times \exp(b_2 \times H_{an}) \times (1 + b_3 \times H_{un}) \times (1 + b_4 \times E_{un}) \times \sigma_n$$

$$E_{an} = E_a / E_s, E_{bn} = E_b / E_s, E_{un} = E_u / E_s, \sigma_n = \sigma_o / E_s,$$

$$LS_n = LS / a, H_{an} = H_a / a, H_{un} = H_u / a$$

Equation 1 Strain, in μ strain, over existing crack

where E_a is the modulus of the overlay,

H_a is the thickness of the overlay,

E_u is the modulus of the underlayer,

H_u is the thickness of the underlayer,

E_b is the modulus of the base/sub-base,

E_s is the modulus of the subgrade,

LS is the crack spacing,

σ_o is the tire pressure, and

a is the radius of the loaded area for one wheel.

The following constants were used:

$$\alpha = 342650, \beta_1 = -0.73722, \beta_2 = -0.2645, \beta_3 = -1.16472, a_1 = 0.88432, b_1 = 0.15272, \\ b_2 = -0.21632, b_3 = -0.061, b_4 = 0.018752.$$

To predict reflection cracking, the resulting strain was used with the model for the master curve of the damaged asphalt, which has the format:

$$\log(E) = \delta + \frac{\alpha \times (1 - \omega)}{1 + \exp(\beta + \gamma \log(tr))}$$

Equation 2 Modulus of damaged asphalt.

where δ , α , β , and γ are constants, tr is reduced time in sec and the damage, ω , is calculated from:

$$\omega = \left(\frac{MN}{MNP} \right)^\alpha \\ MNP = A \times \left(\frac{\mu\varepsilon}{\mu\varepsilon_{ref}} \right)^\beta \times \left(\frac{E}{E_{ref}} \right)^{\beta/2} = A \times \left(\frac{SE}{SE_{ref}} \right)^{\beta/2}$$

Equation 3 Damage as a function of number of loads, strain, and modulus.

where E is the modulus of damaged material,

E_i is the modulus of intact material,

MN is the number of load repetitions in millions ($N/10^6$),

$\mu\varepsilon$ is the strain at the bottom of the asphalt layer in μ strain,

SE is the strain energy, and

$A, A', \alpha, \beta, \mu\varepsilon_{ref}, E_{ref}$, and SE_{ref} are constants

The initial (intact) modulus, E_i , corresponds to a damage, ω , of 0 and the minimum modulus, $E_{min} = 10^8$, to a damage of 1.

From previous calibration studies on cracking of new pavements it has been found that the damage at crack initiation may be determined from:

$$\omega_{initiation} = \frac{1}{1 + \left(\frac{h_{AC}}{250 \text{ mm}} \right)^{-2}}$$

Equation 4 Damage at crack initiation.

where h_{AC} is the combined thickness of the asphalt layers.

From a calibration study using WesTrack data it was found that the propagation of cracking could be approximated by:

$$Cr\% = \frac{100\%}{1 + \left(\frac{\omega}{\omega_o} \right)^{-8}}$$

Equation 5 Cracking in percent as a function of damage.

where $Cr\%$ is the cracking in percent of wheelpaths,

ω is the calculated damage, and

ω_o , is a constant determined by assuming 5% cracking at crack initiation.

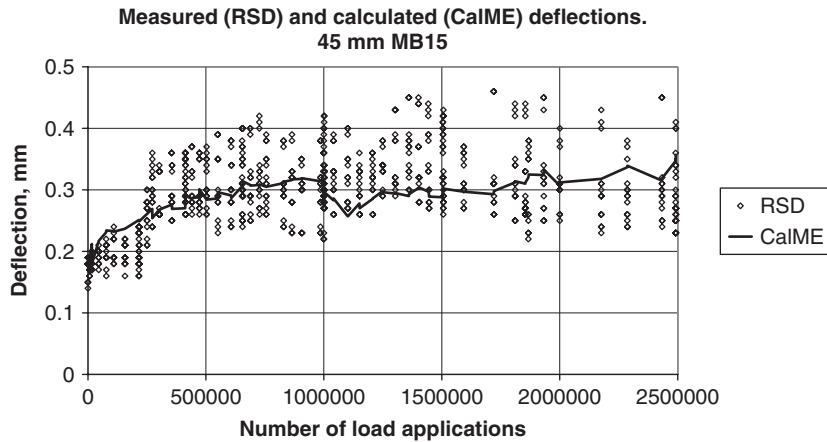


Figure 1. Example of deflections calculated by *CalME* compared to measured surface deflections.

During HVS testing cracking was measured in m/m^2 , so the equation was changed to:

$$Cr \text{ m / m}^2 = \frac{A}{1 + \left(\frac{\omega}{\omega_o}\right)^\alpha}$$

Equation 6 Cracking in m/m^2 as a function of damage.

The maximum recorded cracking during the HVS experiments was about 8–9 m/m^2 . It is reasonable to assume that about 10 m/m^2 would correspond to 100% cracking.

4 SIMULATION OF PAVEMENT RESPONSE

As mentioned previously, the deflections normally increase considerable during an HVS test, as a result of damage to the bound layers (asphalt and self-cementing AB in this case). This means that the stresses and strains in the pavement layers, which are used in calculation of the pavement performance, also change during the test. To ensure that the pavement response calculated by *CalME* was reasonably correct for the duration of the test, the surface deflections and the deflections at the depths of the MDD modules were calculated by *CalME* and compared to the RSD and MDD measurements.

Figure 1 shows a comparison for the test section with a 45 mm MB15 overlay. Even though the test section is only 6 m long the surface deflections vary considerably over the area of the test section. The coefficient of variation on the RSD measurements varies from less than 10% to more than 20%. It may be noticed that the deflection increases by more than 50% within the first one million load applications. The drop in deflection after one million load applications is due to the temperature being reduced from 20°C to 15°C.

The three MDDs shown in Figure 2 measured the deflection at (approximately) the top of the aggregate base. They also indicate a considerable variation within the test section, and show the same trend as the RSD deflections. The deflections calculated by *CalME* are seen to be in good agreement with the measured deflections.

Figure 3 compares all of the deflections measured by the MDD modules nearest the pavement surface, for all of the HVS tests, to the deflections calculated by *CalME*.

The section with 90 mm DGAC overlay was split into two sections in the analysis, approximately at the middle of the section, because the behavior of the two sections were distinctly different.

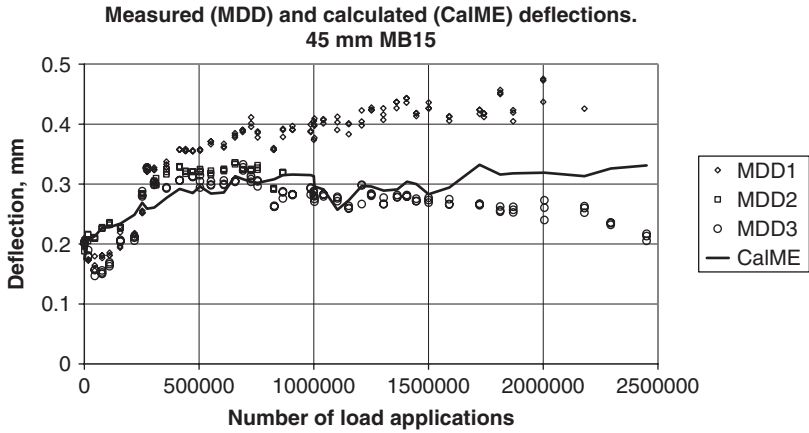


Figure 2. Example of deflections calculated by *CalME* compared to measured deflections at top of base.

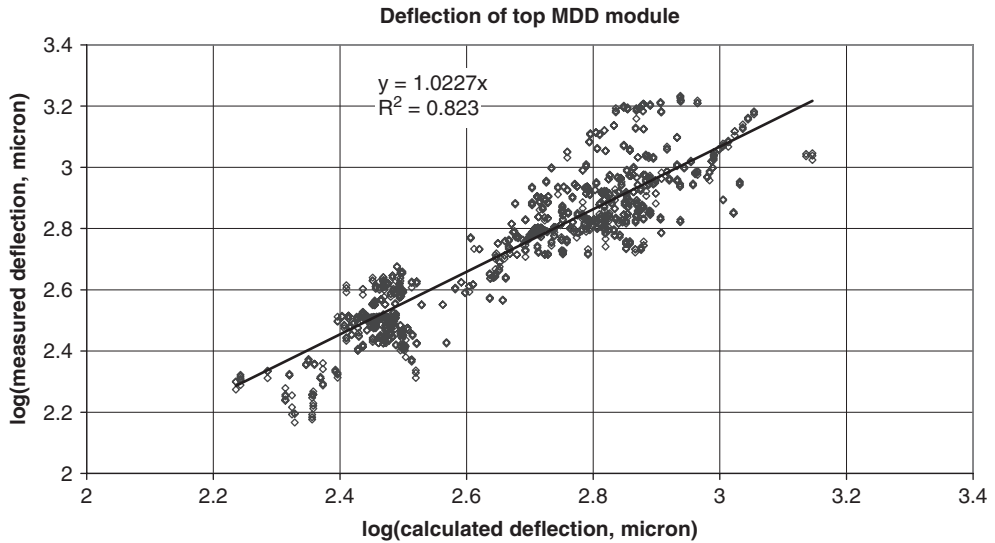


Figure 3. Comparison of deflections measured by all top MDD modules to *CalME* deflections.

5 DAMAGE AND CRACKING

The terminal moduli predicted by *CalME* should be similar to the moduli backcalculated from FWD tests following the HVS experiment if the damage to the pavement layers has been correctly calculated. For the present tests there was a decrease in the moduli of the asphalt layers and of the self-cementing AB. The modulus of the subgrade also decreased with the decrease in the stiffness of the pavement layers.

In Figure 4 the moduli backcalculated from the first FWD test series after the completion of each HVS experiment are compared to the terminal moduli from the simulation with *CalME*. To show the full range of moduli for all of the pavement layers, the logarithm of the moduli, in MPa, are shown.

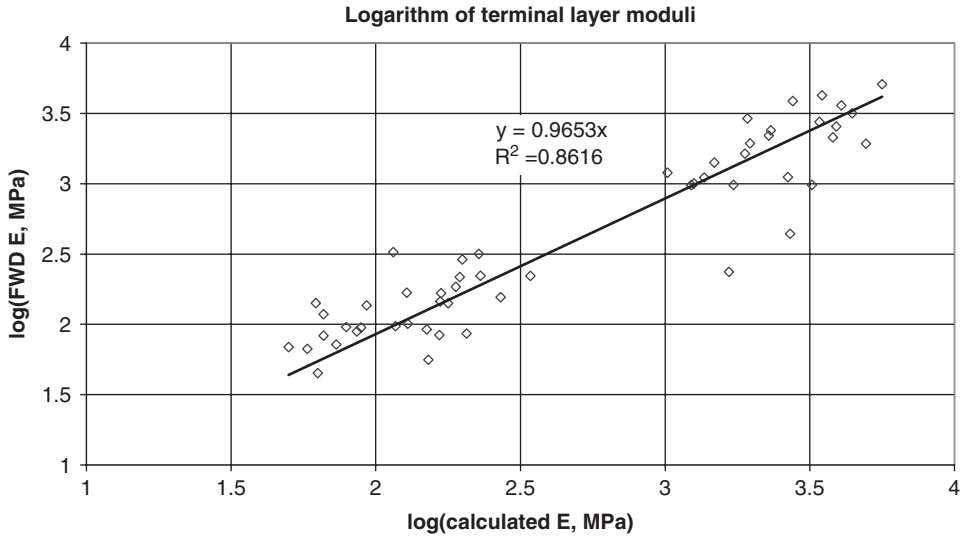


Figure 4. Logarithm of terminal moduli, FWD tests versus simulation with *CalME*.

For prediction of reflection cracking the coefficients of Equation 4 and Equation 6 were modified to the values shown in Equation 7 and Equation 8.

$$\omega_{initiation} = \frac{1}{1 + \left(\frac{h_{AC}}{390\text{mm}} \right)^{-1}}$$

Equation 7 Coefficients for crack initiation model.

$$Cr\ m/m^2 = \frac{10}{1 + \left(\frac{\omega}{\omega_0} \right)^{-3.5}}$$

Equation 8 Coefficients for crack propagation model.

Figure 5 shows the observed reflection cracking (Obs), in m/m^2 , versus the reflection damage, ω , calculated by *CalME* for the surface layer. Also shown is the cracking as calculated from Equation 7 and Equation 8 (Calc), with the assumptions that crack initiation corresponds to $0.5\ m/m^2$ of cracking. The calculated cracking is shown for layer thicknesses of 125 and 170 mm, which correspond roughly to the combined AC thickness for the sections with thin and thick overlays, respectively.

The figure illustrates that the visible cracking follows the development of damage.

In Figure 6 the reflection cracking predicted using Equation 7 and Equation 8 is shown as a function of the observed reflection cracking.

6 CONCLUSIONS

The main conclusion of the analysis was that it was possible to simulate the pavement response and performance using *CalME*. The resilient pavement deflections, at the surface and at different

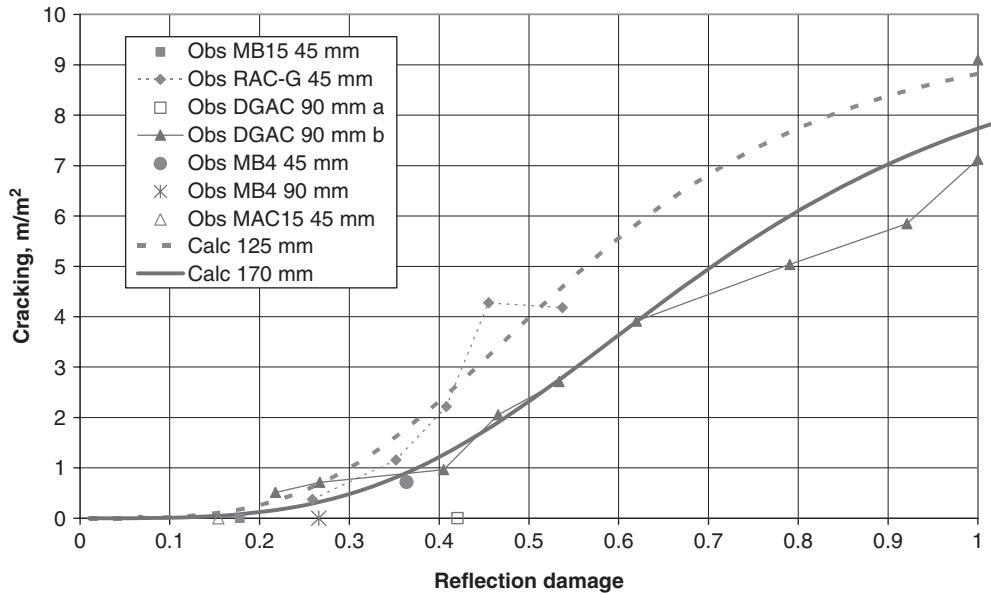


Figure 5. Observed and calculated cracking versus damage from *CalME*.

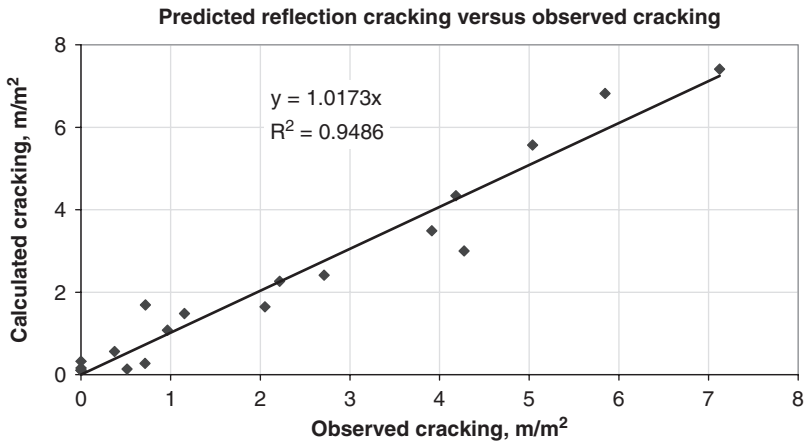


Figure 6. Predicted versus observed reflection cracking.

depths, were predicted reasonably well for the whole duration of the HVS tests. The empirical relationships derived from laboratory experiments, to determine permanent deformation and damage, also predicted the pavement performance reasonably well for the duration of the experiment, when appropriate shift factors were applied to allow for the difference between the laboratory experiments and the HVS loading. The simple reflection cracking model appeared to work correctly with respect to the development of reflection damage and cracking.

Another important conclusion of the experiment was that a recursive mechanistic-empirical method is needed to interpret the results of HVS (or other full scale) testing. This is exemplified by the test section with 90 mm DGAC overlay. Although the original pavement was constructed to be uniform over all six test sections it was found that it had quite large variations, both spatially and with respect to time. The two subsections of the 90 mm DGAC overlay section showed very different

performances. This difference was predicted reasonably well using the recursive mechanistic-empirical approach, but would hardly have been possible to consider in a purely empirical analysis.

Once the models of the recursive mechanistic-empirical method have been calibrated the different overlay materials may be compared through simulations, where the underlying pavement, the loading, and the climatic conditions are exactly the same for each material. The sensitivity to the condition of the underlying pavement, the loading, and the climate can likewise be studied. Such studies are presently being carried out.

ACKNOWLEDGEMENT

This paper describes research activities requested and sponsored by the California Department of Transportation (Caltrans), Division of Research and Innovation. Caltrans sponsorship is gratefully acknowledged. The contents of this paper reflect the views of the authors and do not reflect the official views or policies of the State of California or the Federal Highway Administration. The authors would also like to thank Jeremy Lea and Lorina Popescu of the UCPRC and CSIR for their work in preparing the HVS database for *CalME* calibration.

REFERENCES

- Deacon, J.A., Harvey, J.T., Guada, I., Popescu, L., and Monismith, C.L. 2002. *Analytically based approach to rutting prediction*. Transportation Research Record 1806. Washington D.C.
- Harvey, J.T., Hoover, T., Coetzee, N.F., Nokes, W.A., and Rust, F.C. *Caltrans Accelerated Pavement Test (CAL/APT) Program—Test Results: 1994–1997*. AAPT Symposium on Accelerated Pavement Testing, Boston, MA, March 16–18, 1998.
- Jones, D., J. Harvey, T. Bressette. 2007. *An Accelerated Pavement Testing Experiment to Assess the Use of Modified Binders to Limit Reflective Cracking in Thin Asphalt Concrete Overlays*. Paper submitted to 6th RILEM International Conference on Cracking in Pavements, Chicago, 2007.
- Symplectic Engineering Corporation, Leap2.0 a layer elastic analysis program, Release 2.0, March 2004. Berkeley, California.
- Ullidtz, P., Harvey, J.T., Tsai, B.-W. and Monismith, C.L. *Calibration of Incremental-Recursive Flexible Damage Models in CalME Using HVS Experiments*. Report prepared for the California Department of Transportation (Caltrans) Division of Research and Innovation by the University of California Pavement Research Center, Davis and Berkeley. UCPRC-RR-2005-06. This and several related reports may be downloaded from <http://www.its.berkeley.edu/pavementresearch/>.
- Wu, R.-Z. *Finite Element Analyses of Reflective Cracking in Asphalt Concrete Overlays*. Doctoral dissertation. Department of Civil and Environmental Engineering, University of California, Berkeley, 2005.

Fatigue investigations of asphalt concrete beams reinforced with geosynthetics interlayer

P. Zieliński

Institute of Road and Railway Engineering, Cracow University of Technology, Poland

ABSTRACT: The paper presents the results of extensive fatigue investigations on asphalt concrete beams reinforced with the geosynthetics interlayer. The objective of this research is an evaluation of the influence of geosynthetics on interlayer bonding and fatigue life of beams reinforced with geosynthetics. Interlayer bonding is expressed by the interface shear strength and shear stiffness. Fatigue life is characterized by the initial strain ε_0 and the number of load application needed to reduce stiffness by half. As independent variables the following were taken: the type of mix (asphalt concrete and SMA) and the type of geosynthetics (polyester nonwoven, polyester geocomposite, composite: glass grid with polyester nonwoven, as well as for comparative purposes, specimens without geosynthetics). It was found, that the shear strength at the geosynthetics interlayer contact area with asphalt layers, even in the optimal bonding conditions, is lower than inside the layer, so applying geosynthetics in asphalt pavement worsens interlayer bonding in comparison with the pavement without geosynthetics. For both test temperatures, statistically significant positive correlation between fatigue and parameters of interlayer bonding (shear strength, shear stiffness) was proven in statistical analysis, so regressive equations for bituminous pavement characteristics and their fatigue life were formulated. The paper presents final conclusions and also suggests directions for the future research.

1 INTRODUCTION

The paper presents selected results of fatigue investigations of asphalt concrete beams with the geosynthetics interlayer [1], [2]. That problem was the subject of number of papers referred to in [3], [4], [5], [6], [7], [8], [9], [10]. The aim of investigations is an evaluation of influence of a type and amount of bitumen as well as a type of geosynthetics on fatigue durability of samples. In the case of application of geosynthetics in asphalt pavement, fatigue durability primarily depends on interlayer bonding. In this paper the interlayer bonding is represented by shear strength, while the fatigue durability is expressed by the number of the load applications needed to reduce the stiffness by half.

2 THE TEST METHODS

In laboratory tests, interlayer bonding was represented by shear strength between layers and shear stiffness, which were examined with the prototype apparatus (Fig. 1). Maximum shearing force P_s [kN] was calculated according to the formula (1), whereas shear strength R_s [MPa] was given by the formula (2). Then, value of tangent modulus T [N/mm] was fixed from graph force-displacement

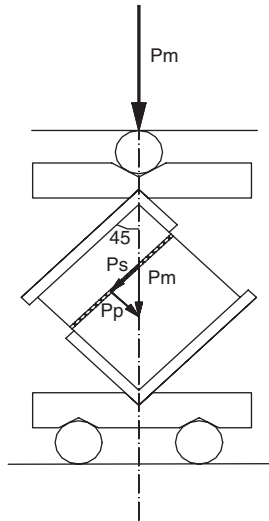


Figure 1. Shearing of sample of asphalt concrete with geosynthetic interlayer.

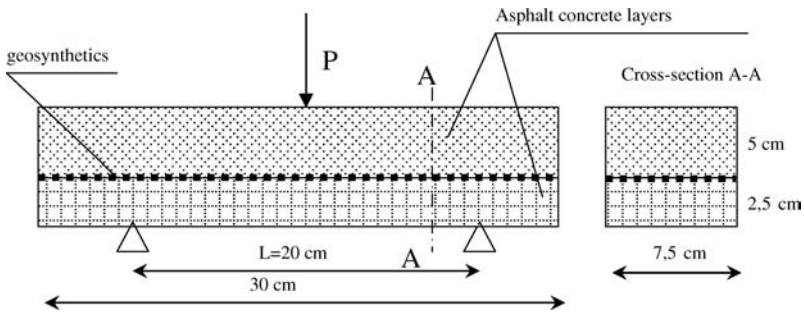


Figure 2. Scheme of cyclic bending test on asphalt concrete samples reinforced with geosynthetics interlayer.

and shear stiffness S_s [N/mm/mm²] was established according to the formula (3).

$$P_s = \frac{P_m}{\sqrt{2}} \quad (1)$$

$$R_s = \frac{P_s}{F} \quad (2)$$

where F is a area of shearing.

$$S_s = \frac{T}{F} \quad (3)$$

Fatigue tests were performed on 3-point bending beam samples, under constant load frequency (10 Hz), for two temperatures: -2°C and $+18^\circ\text{C}$ (Fig. 2). The temperature -2°C was established as an average temperature of pavement in Poland in winter, and the temperature $+18^\circ\text{C}$ as a sample temperature for the other seasons.

The choice of mode in which the load was applied depends on sample thickness, but in this case there was no clear recommendation. The mode of constant amplitude of load was applied, which is recommended for thicker asphalt pavements [11]. Frequency of testing was established according

Table 1. Load characteristics used in fatigue tests.

Load characteristics	Test temperature	
	-2°C	+18°C
Max. load – P_{max}	5,5 kN	2,5 kN
Min. load – P_{min}	0,5 kN	0,5 kN
Load amplitude – P_a	2,5 kN	1,0 kN
Mean load – P_m	3,0 kN	1,5 kN
Frequency – f	10 Hz	10 Hz
Coefficient of amplitude $R = P_{min}/P_{max}$	0,091	0,200

to the Polish standard [12], but fatigue threshold was defined as a number of load cycles necessary to decrease the sample initial stiffness modulus by half.

Load conditions were determined on the basis of preliminary static bending tests, accordingly to the temperature. The lower level of force amplitude was equal 0.5 kN for both temperatures. The upper level was calculated as the sum of the lower limit plus 50% of the maximum force. Characteristics of the load assumed for the tests are given in the table 1.

3 CHARACTERISTICS OF MATERIALS

The asphalt mixes for manufacturing of samples were taken from the asphalt mix plant. Each sample consisted of two asphalt mix layers combined with the bitumen, with the geosynthetics interlayer between them. Geosynthetics and bitumen used to soak and glue geosynthetics were delivered by the producers. In experimental investigations the following variables were assumed:

- type of geosynthetics (polyester nonwoven, polyester geocomposite, two types of geocomposites consisting of glass grid and polyester nonwoven),
- type of bitumen used for layers bonding (comparatively: pure bitumen D-70, two ordinary bitumen emulsions: K1-65 and K1-70 and bitumen emulsion K-1-65MP modified with the polymer),
- type of upper asphalt layer in samples (comparatively: two asphalt concretes with gradation 0/12,8 mm and 0/16 mm plus SMA (Stone Mastics Asphalt) 0/12,8 mm),
- various amounts of bitumen used for layers bonding.

The detailed data concerning the material characteristics are given in the report [1].

4 RESULTS OF FATIGUE LIFE TESTS

Before performing the fatigue tests, the apparent density and content of the air voids in compacted samples were determined. Then, the samples were submitted to the cyclic loading program, where number of cycles leading to fatigue and initial strain under bending of beams were measured.

The obtained results were submitted to the statistical processing [13], [14].

Selected results of testing are presented at the Figs 3–5.

Basing on the cyclic bending test results and their analysis, the following significant observations were formulated:

- Application of nonwoven in asphalt layers has no influence on fatigue characteristics; it is caused by the low stiffness modulus of nonwoven.

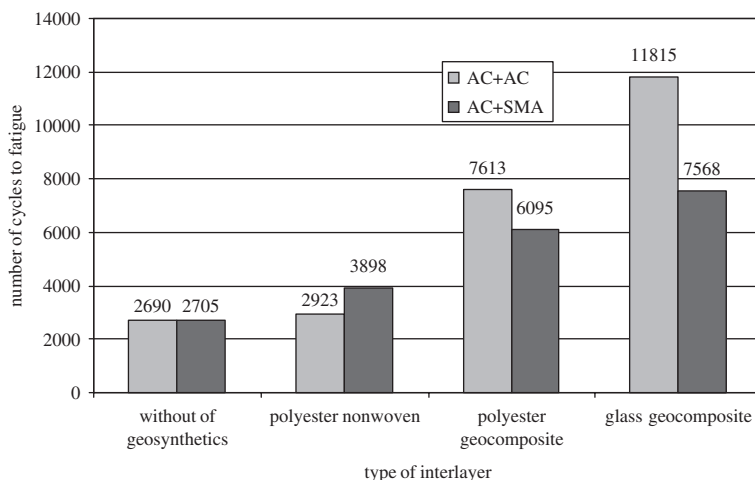


Figure 3. Dependence between interlayer type and fatigue for samples combined with 70°P bitumen, $T = +18^{\circ}\text{C}$.

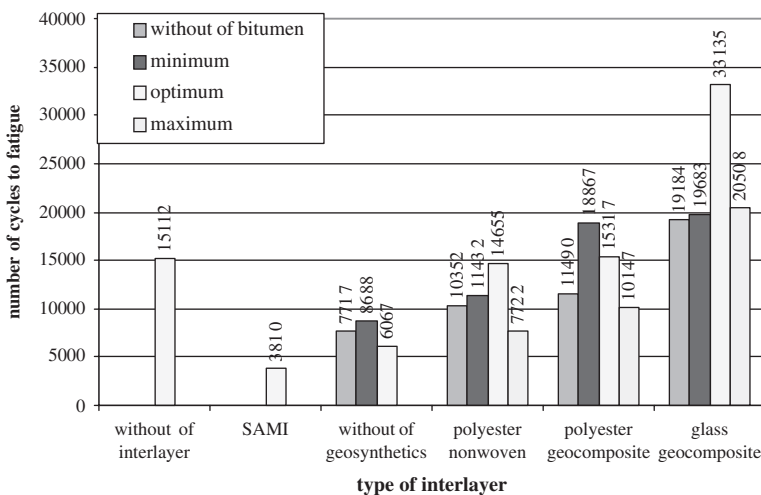


Figure 4. Fatigue life for AC 0/12,8 samples with various interlayer type and various amount of bitumen in interlayer, $T = +18^{\circ}\text{C}$.

- Effectiveness of application of geocomposites increases at the higher temperature (e.g. $+18^{\circ}\text{C}$), when the geocomposites stiffness modules achieve similar or higher values than the modules of asphalt layers. At the temperature $+18^{\circ}\text{C}$ all tested geocomposites give the essential increase of asphalt layers fatigue, the highest increase was observed for the geocomposites containing glass grid.
- It was proved that for geocomposites, the interlayer bonding realised by bitumen spreading has a strong influence on fatigue properties of layers.
- At the temperature -2°C the effect of geosynthetics application gives a weaker influence on fatigue properties.

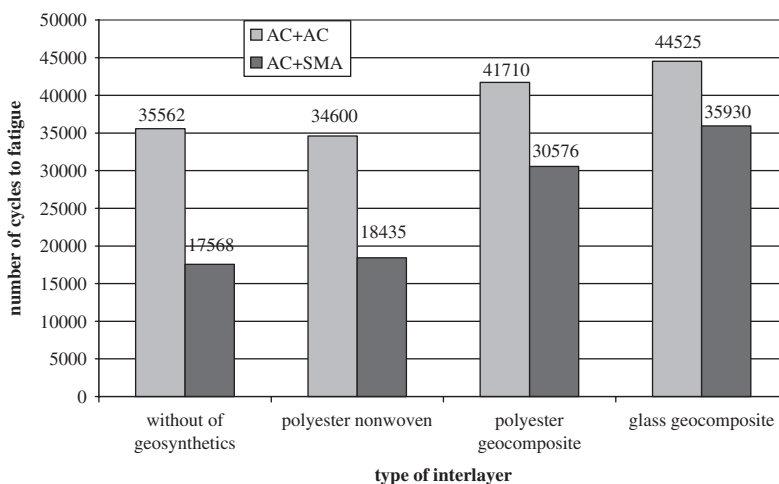


Figure 5. Dependence between interlayer type and fatigue life for samples glued by 70°P bitumen, $T = -2^{\circ}\text{C}$.

- At the constant amplitude of load, the proportion of durability of samples AC + AC and AC + SMA without geosynthetics, depends on temperature. At the room temperature number of load carried by samples were similar, while at the temperature -2°C the number of cycles leading to fatigue for the samples AC + AC were two times higher than for samples AC+SMA. The same conclusion could be drawn for samples with the nonwoven.

5 STATISTICAL ANALYSES OF FACTORS DETERMINING FATIGUE OF ASPHALT LAYERS WITH GEOSYNTHETICS

The aim of the present analyses is to formulate the regression dependence between interlayer bond characteristics, the geosynthetics stiffness, chosen characteristics of investigated samples, and their fatigue, which is expressed by the number of bending cycles needed to decrease the stiffness modulus by half.

The geosynthetics stiffness was represented by the stiffness modulus [MPa], whereas the interlayer bond was expressed by the shear strength [MPa] and the shear stiffness [N/mm/mm²].

The stiffness modulus for chosen geosynthetics was investigated in laboratory tests and its values are given in the paper [2]. The detailed structural characteristics of asphalt mixes are given in the report [1] and in the paper [2]. The investigated equations were analysed separately for the temperatures $+18^{\circ}\text{C}$ and -2°C .

The search of the regressive dependence between the fatigue durability and materials characteristics of tested samples was done by applying the computer program Statgraphics Plus v. 5.1. [14]. In the first step, the basic statistical characteristics were calculated e.g. mean values, standard deviation, skewness coefficient, kurtosis, as well as the normality of data distribution. Then, the correlation coefficients for tested characteristics, which describe their statistical significance and the correlation power, were determined. The regressive equations were formulated on the basis of multiple regression analysis.

For the proposed equations, the coefficient of determination (R^2) and corrected coefficient of determination (R_{kor}^2) were calculated. Then, an analysis of errors, referring to normality and independency of errors was carried out. For testing of the normality of errors, unusual residuals and influential points options were used. Independence of errors was tested by means of the Durbin-Watson statistic, which examines the residuals to determine if there is any significant correlation based on the order.

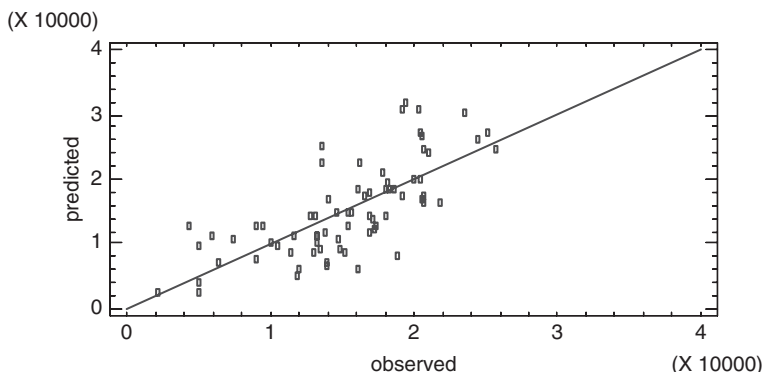


Figure 6. Dependence between tested and estimated number of cycles to fatigue for samples reinforced with geosynthetics.

5.1 Analyses of the fatigue test results at the temperature +18°C

For samples reinforced with geosynthetics the significant positive correlations were found between the number of cycles leading to fatigue and the stiffness of geosynthetics (the correlation coefficient $r=0,48$). Negative correlations between the number of cycles leading to fatigue and the volume of air voids ($r=-0,44$) as well as the initial tensile strain ($r=-0,65$) were estimated. The initial strain in the cyclic bending was positively correlated with the volume of air voids ($r=0,47$), while the shear strength ($r=-0,24$) and the stiffness of geosynthetics ($r=-0,14$) showed a negative correlation with the initial strain.

The obtained functional dependence, which gives the number of cycles leading to fatigue L , is presented in the equation (4), whereas fitting of the model is shown in the Fig. 6. Additionally, in the Fig. 7 the dependence between the number of cycles leading to fatigue, the initial tensile strain and the stiffness modulus of geosynthetics is presented.

$$L = 74505 - 1,14 \text{ E}8 * \varepsilon_0 + 7,35 * M \quad (4)$$

L is the number of cycles leading to fatigue of a sample [-], ε_0 is the initial tensile strain [$\mu\text{m}/\text{m}$], M is the geosynthetics modulus [MPa].

The calculated values of statistics: the corrected coefficient of determination – $R_{\text{kor}}^2 = 50,6\%$, the standard error of estimation – $\text{SSE} = 5055$, the mean absolute error – $\text{MAE} = 3840$, the Durbin-Watson statistic = $1,67 > 1,4$ – autocorrelation of residuals does not exist.

5.2 Analyses of fatigue test results at the temperature -2°C

For samples with geosynthetics, significant positive correlations were determined between the number of cycles leading to fatigue, the shear stiffness (the correlation coefficient $r=0,57$) and the stiffness modulus of geosynthetics ($r=0,36$).

The obtained functional dependence, which gives number of cycles resulting in fatigue L , is presented in the equation (5), whereas the fitting of model is shown in Fig. 8.

$$L = - 35681 + 23,01 * M + 15679 * S \quad (5)$$

L is the number of cycles resulting in fatigue of sample [-], M is the geosynthetics modulus [MPa], S is the shear stiffness [$\text{N}/\text{mm}/\text{mm}^2$].

The calculated values of statistics: the corrected coefficient of determination – $R_{\text{kor}}^2 = 52,6\%$, the standard error of estimation – $\text{SSE} = 10500$, the mean absolute error – $\text{MAE} = 8191$, the Durbin-Watson statistic = $1,68 > 1,4$ – autocorrelation of residuals does not exist.

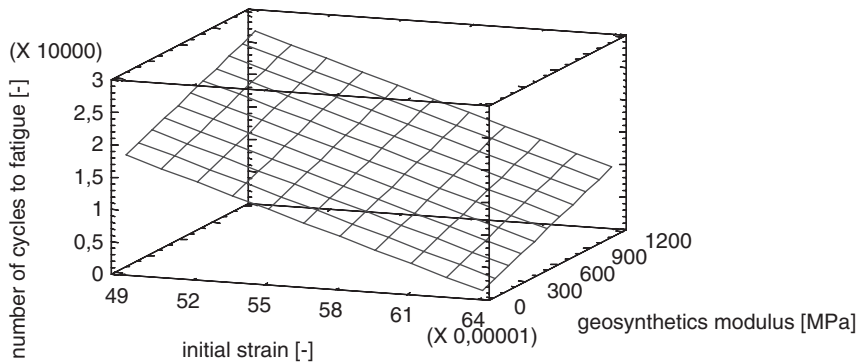


Figure 7. Dependence between the number of cycles to fatigue, the initial tensile strain and the stiffness modulus of geosynthetics.

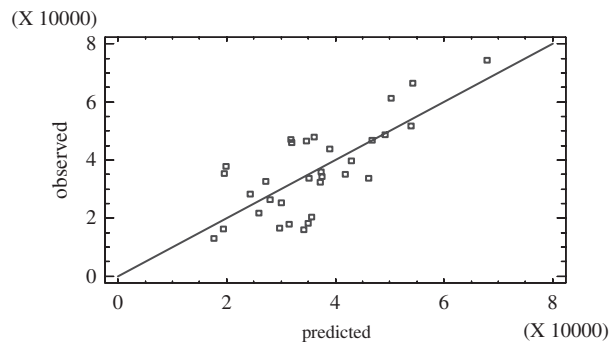


Figure 8. Dependence between tested and estimated number of cycles to fatigue for samples reinforced with geosynthetics.

5.3 Review of the regression analyses

- It was found that the mean of fatigue durability for samples with geocomposites is essentially higher than the fatigue durability for samples without geosynthetics or with nonwoven.
- For all samples reinforced with geosynthetics interlayer the durability increased with the augmentation of geosynthetics stiffness modulus as well as with the decrease of air voids amount and with the decrease of initial tensile strain in the cyclic bending.
- Geosynthetics have the effect on fatigue properties of asphalt concrete samples in the temperature $+18^{\circ}\text{C}$; the influence of the geosynthetics modulus on fatigue in this temperature was few times higher than in the temperature -2°C . It is caused by the variability of the asphalt concrete stiffness modulus in various temperatures, whereas, the stiffness modulus of geosynthetics is practically constant in the applied spectrum of temperature.
- For samples with geosynthetics tested in temperature -2°C , the fatigue depends on the geosynthetics modulus and the shear stiffness in geosynthetics interlayer, moreover, both parameters are positively correlated with the fatigue.
- The shear strength and the shear stiffness of the interlayer system, strongly related to the temperature as well as the geosynthetics modulus, considerably influence the fatigue of asphalt pavements.
- For samples tested in the temperature $+18^{\circ}\text{C}$, independently of the interlayer type, the positive correlation between the fatigue and the characteristics of interlayer bonding (e.g. shear strength

and shear stiffness) was found, while the initial tensile strain and the volume of air voids in samples were negatively correlated with the fatigue properties.

- Relation between the fatigue properties and the characteristics of interlayer bonding for samples with geosynthetics was weak (coefficient of determinations $R_{kor}^2 = 13,2 - 16\%$), whereas, for samples without geosynthetics, correlation between the fatigue and the shear strength exists clearly (coefficient of determination – $R_{kor}^2 = 36\%$).
- It was observed, that the shear strength is a better estimator of the fatigue in samples with small amount of saturating bitumen applied in the interlayer system (e.g. samples without geosynthetics, samples with polyester geocomposite), while in case of a higher amount of bitumen (samples with nonwoven or glass geocomposite), the fatigue is better correlated with the shear stiffness.

6 FINAL CONCLUSIONS

- The amount of bitumen applied to saturate and fix geosynthetics to asphalt layer, due to the influence on interlayer bonding, significantly changes fatigue properties of samples. Application of too little or too much of bitumen diminishes fatigue 1,5–2 times. For both testing temperatures a positive correlation between fatigue and the parameters of interlayer bonding (shear strength, shear stiffness) is significant.
- Nonwoven used in the asphalt layers structure, independently of testing temperature, does not increase fatigue significantly, thus, it could be used only as a stress relieving layer.
- Geocomposites could be used as reinforcement of asphalt pavements. Effectiveness of reinforcements depends on: (1) the transfer of load from asphalt layers to reinforcing elements due to the stiffness of bonding, (2) the ratio of stiffness modulus of reinforcement to the stiffness modulus of asphalt layers and (3) the durability of geosynthetics parameters during road service.
- Bonding between geosynthetics and asphalt layers can be improved by the application of geosynthetics initially impregnated with bitumen modified with polymer or with adhesive agent.

7 DIRECTION FOR FURTHER INVESTIGATIONS

Reinforcing of asphalt pavement with the geosynthetics interlayer is an open problem which concerns new geosynthetics generation, testing method, and theoretical analysis of modelling pavement behaviour. The further investigations include:

- Monitoring of a condition of asphalt pavements reinforced with geosynthetics. Observations of pavement conditions should be connected with investigations of interlayer bonding and geosynthetics behaviour.
- Investigations of effectiveness of new generations of geosynthetics (e.g. carbon grid, basalt grid, new types of glass geocomposites).
- Improvement of the adhesion of geosynthetics by use of a special adhesion agent.
- Improvement of the bitumen type used to apply glue geosynthetics to the bottom layer.
- Application of the FEM to elaborate the asphalt pavement model with geosynthetics interlayers.

ACKNOWLEDGEMENTS

The work has been carried out as a part of the research project for Polish Science Committee no 8.T07 E.043.21 “Influence of the Material Parameters on the Durability of Asphalt Mixtures in the Road Pavement Structures”.

REFERENCES

- [1] Grzybowska, W., Zieliński, P. i inni, 'Wpływ parametrów materiałowych na trwałość mieszanek mineralno-asfaltowych w nawierzchniach drogowych w różnych warunkach obciążeń', Projekt Badawczy Nr 8.TO7 E.043.21 finansowany przez Komitet Badań Naukowych w latach 2001–2003.
- [2] Zieliński, P., 'Wybrane zagadnienia trwałości nawierzchni asfaltobetonowej z geosyntetyczną warstwą pośrednią', Praca doktorska, Politechnika Krakowska 2004.
- [3] Button J., Lytton R.L., 'Evaluation of fabrics, fibers and grids in overlays', Proceedings of the Sixth International Conference Structural Design of Asphalt Pavements, Volume I, Delft, 1987.
- [4] Doligez D., Coppens M.H.M., 'Fatigue improvement of asphalt reinforced by glass fibre grid. Laboratory simulation and modeling of overlay systems', Proceedings of the Third International RILEM Conference, Reflective Cracking in Pavements, Maastricht, 1996.
- [5] Sprague C.J., Alen S., Tribbett W., 'Tensile Properties of Asphalt Overlay Geosynthetic Reinforcement', Proceedings of the the 1998 TRB Annual Meeting of the Transportation Research Board, Washington, DC, 1998.
- [6] De Bondt, A.H., 'Anti-Reflective Cracking Design of Reinforced Asphaltic Overlays', Ph.D. Thesis, Delft University of Technology, 1999.
- [7] De Bondt A.H., 'Effect of reinforcement properties,' Proceedings of the Fourth International RILEM Conference, Reflective Cracking in Pavements, Ottawa, 2000.
- [8] Tschegg E. K., 'Factors influencing the fracture behaviour of geosynthetics overlay system', Proceedings of the 4th International RILEM Conference on Reflective Cracking In Pavements, Research In Practice, Ottawa, Ontario, Canada, 2000, March 2000.
- [9] Jaecklin F.P., Scherer J., 'Asphalt reinforcing using glass fibre grid Glasphalt', Nicea 2002.
- [10] Sobhan K., Crooks T., Tandon V., and Mattingly S., 'Laboratory simulation of the growth and propagation of reflection cracks in geogrids reinforced asphalt overlays', Proceedings of the 5th International RILEM Conference on Cracking in Pavements, Mitigation, Risk Assessment and Prevention, Limoges, France, May 2004.
- [11] Judycki, J., 'Fatigue of asphalt mixes', University of Oulu, Finland 1991.
- [12] Katalog Wzmocnień i remontów nawierzchni podatnych i półsztywnych', IBDiM, opracowała Grupa Robocza pod kierunkiem prof. D. Sybilskiego, Warszawa, 2001.
- [13] Program komputerowy Statgraphics Plus v. 5.1', A Manugistics Inc. Product, Rockville, MD USA, 2000, Nr 537672031051732.
- [14] Dobosz, M., 'Wspomagana komputerowo statystyczna analiza wyników badań, Problemy współczesnej nauki, Teoria i zastosowania', STATYSTYKA, AOW EXIT, Warszawa, 2001.

On site validation and long term performance of anti-cracking interfaces

F. Vervaecke, J. Maeck & A. Vanelstraete
Belgian Road Research Center, Sterrebeek, Belgium

ABSTRACT: This paper deals with the results of an evaluation of different sites in Belgium where anti-cracking interfaces were used for the renovation of roads consisting of concrete cement slabs. Different interface systems were used including a SAMI, non-woven geotextiles impregnated with modified bitumen, grids and steel reinforcing nettings. Depending on the project, the reparations were executed recently to 16 years ago. The aim of this follow-up is to evaluate their long term performance.

This paper reports the results of yearly evaluations of experimental roads and other projects and gives insight in the reasons of failure of certain projects and the long term behaviour of these techniques. Most of the projects were already evaluated for the previous RILEM-conferences on cracking in pavements; the long term performance will be completed with the latest information and conclusions will be presented on the long term behaviour of the different anti-cracking systems.

1 INTRODUCTION

Belgium counts a lot of roads of concrete slabs built in the fifties and early sixties. By this time, many of these constructions are severely degraded and need to be repaired efficiently. Repairing cracked roads by only the application of an additional layer of asphalt is rarely a long-term efficient solution. Deficiencies in the old road are very rapidly reflected at the surface as a result of the combined effects of thermally induced stresses and traffic loading. These cracks are called reflective cracks. To extend the service lives of these road structures, interface systems are used for the prevention of reflective cracking.

During the last decade, The Belgian Road Research Centre had the opportunity to assist at the realisation of several sites where different anti-cracking techniques were used. This paper deals with the results of an evaluation of these sites in Belgium. The efficiency of the stabilisation of cement concrete plates and the interface systems such as a SAMI (stress absorbing membrane interlayer), a non-woven geotextiles impregnated with modified bitumen, geogrids and steel reinforcing nettings were investigated. In particular this paper gives an update of the results obtained from two experimental road sections and different other projects which were followed in time. The results from earlier observations were already described in previous papers (Decoene et al., 1993, Vanelstraete et al., 1996, Vanelstraete et al., 1996b, Vanelstraete et al., 1997, Vanelstraete et al., 2000, Vanelstraete et al., 2004). They showed the importance of the overlay thickness and gave evidence for the efficiency of crack and seat technique to prevent reflective cracking. Differences between different types of interfaces could not be observed in the earlier observations, since the experimental roads were still very “young” at that time. All results are updated in the present paper. The earlier conclusions are checked and extended.

For each project, the exact location of the reflective cracks and other type of damage was recorded. The transverse cracks were divided into three categories, depending on their length: cracks smaller

Table 1. Description of the four test sections for the experimental road of Berlare: with/without interface system, with/without crack and seating, with different vertical movements at the crack edges.

Section	Interlayer system	Crack and seat	Slab rocking
1	Steel reinforcement nettings	Yes	–
2a	Steel reinforcement nettings	No	±0.5 mm
2b	Steel reinforcement nettings	No	±1.0 mm
3	No	Yes	–
4a	No	No	±0.5 mm
4b	No	No	±1.0 mm

in length than 1/3, between 1/3 and 2/3, and between 2/3 and the full traffic lane width. Hence, the number of so-called “equivalent” reflected cracks can be deduced. This value takes into account that not all cracks have reached their full length. The number of equivalent reflected cracks is calculated as follows:

$$x_1.(1/6) + x_2.(3/6) + x_3.(5/6) \quad (1)$$

in which x_1 , x_2 , x_3 represent the number of cracks with length $\leq 1/3$; $> 1/3$ and $\leq 2/3$; $> 2/3$ of the traffic lane width, respectively. Knowing the number of original joints/cracks, the percentage of (equivalent) cracks reflected can be deduced.

2 LONG TERM BEHAVIOR OF TWO EXPERIMENTAL ROADS

2.1 *The experimental road of Berlare (1995)*

This experimental road concerns four test sections with or without steel reinforcing nettings on the same road. The traffic level is situated between 2000 and 8000 vehicles per day in each direction, with heavy traffic. In May 1995, the concrete cement slabs have been overlaid with 4 cm of split mastic asphalt (SMA). Different anti-cracking techniques were used. Parts are realised with/without interface, and with/without cracking and seating the concrete slabs. The different damage levels in the existing road were examined in detail i.e. the different vertical movements at the edges of the concrete slabs at passing of traffic. Therefore the faultimeter device developed at BRRC was used. The device is positioned at the two edges of successive slabs and the relative vertical displacement at passing of a known axle load is measured.

The steel reinforcing nettings were embedded in a slurry seal at a rate of 17 kg/m² prepared with elastomeric binder. An overview of the test section is presented in Table 1. These test sections were constructed in order to compare different rehabilitation techniques and to determine limits for the vertical movements at the crack edges above which the crack and seat technique is recommended.

Figure 1 gives an overview of the reflective cracking of the different test sections. No correlation has been noticed between the efficiency of the anti-cracking system and the magnitude of the slab rocking. In 2002 and 2006 some cracks, visible in previous inspections, disappeared and reappeared the next year. This effect can possibly be attributed to the temperature and humidity conditions at the day of inspection that differ from one year to the other.

From Figure 1, it is clear that in the case of the sections where the crack and seat stabilisation of the concrete slabs was not applied, the steel reinforcing netting delays the propagation of reflective cracking towards the surface. The highest efficiency against reflective cracking is however obtained when the crack and seat method is used to stabilize the concrete cement slabs. Even after a long period of 12 years after rehabilitation of the road, the amount of reflective cracks is below 10%. Up to this moment it was not possible to see a difference in the efficiency of crack and seat with and

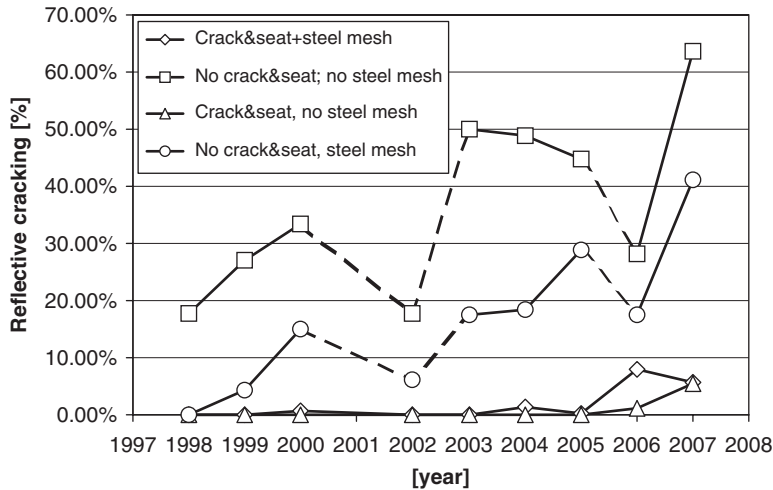


Figure 1. Results of the appearance of reflective cracks deduced from evaluations of the different test sections for the experimental road in Berlare rehabilitated in 1995. Sections were performed with/without crack and seat and with/without steel reinforcing netting.

without steel reinforcing netting, the reappearance is very low for both sections. We will continue to evaluate this test section the next years.

2.2 The experimental road of Sint-Pieters-Leeuw

Careful installation of interface systems is the key to their good performance, with specific rules to respect for each type of interface product. As a result of many difficulties encountered in the past with interface systems, detailed laying procedures for the different interlayer systems are specified in the Belgian standard tender specifications. An experimental road was constructed to evaluate these laying techniques and to compare the long term performance of different interface systems. This experimental road was realised in SintPieters-Leeuw in 1998 and was an initiative of the local authorities in order to choose the most appropriate reparation technique for the many cement concrete roads in this area. The Belgian Road Research Centre was in charge of the prior investigations, the evaluation of the laying procedure of these systems and the follow-up afterwards.

Prior to overlaying, measurements of slab rocking were performed with the faultimeter (Vanelstraete et al., 1996b). As the relative movements at the crack/joints were of the order of 1 mm and sometimes higher, it was decided to stabilize the slabs by injection. The crack and seat technique was not used for this road rehabilitation as nearby houses could possibly be affected by vibrations during the cracking of the concrete slabs. The bituminous overlay consists of a 5 cm thick SMA. Four different anti-cracking interfaces were applied on the cement concrete slabs: a SAMI, a non-woven impregnated with elastomeric binder, a glass fibre grid, steel reinforcing nettings and a reference section without interface system. Each section is about 100 m in length, in both directions. In the section of the steel netting a culvert was present under the existing road.

The laying procedure of interface systems comprises the following consecutive stages: the application of a fixing layer, the application of the interlayer product itself, the placement of a protective layer in some cases and the application of the bituminous overlay. Table 2 gives an overview of the laying procedure of the different sections, with the materials and quantities that were used and their sequence of placement.

The test sections were inspected each year. Figure 2 gives the results of the evaluations of the different test sections at different time intervals. It can be deduced that the investigated anti-cracking systems can be divided into two classes depending on their efficiency. A first class is formed by

Table 2. Overview of the laying techniques and materials for the different test sections on the experimental road of Sint-Pieters-Leeuw.

Step	Sami	Non-woven	Grid	Steel nettings	No interface
1	1.5 kg/m ² elastomeric binder	1.2 kg/m ² elastomeric binder	0.25 kg/m ² tack coat	0.15 kg/m ² tack coat	0.20 kg/m ² tack coat
2	9 kg/m ² 7/10 precoated chippings	non-woven	glass fibre grid	steel nettings	bituminous overlay
3	bituminous overlay	bituminous overlay	1.2 kg/m ² elastomeric binder	16 kg/m ² slurry seal with elastomeric binder	
4			6 kg/m ² 7/10 precoated chippings	0.2 kg/m ² tack coat	
5			bituminous overlay	bituminous overlay	

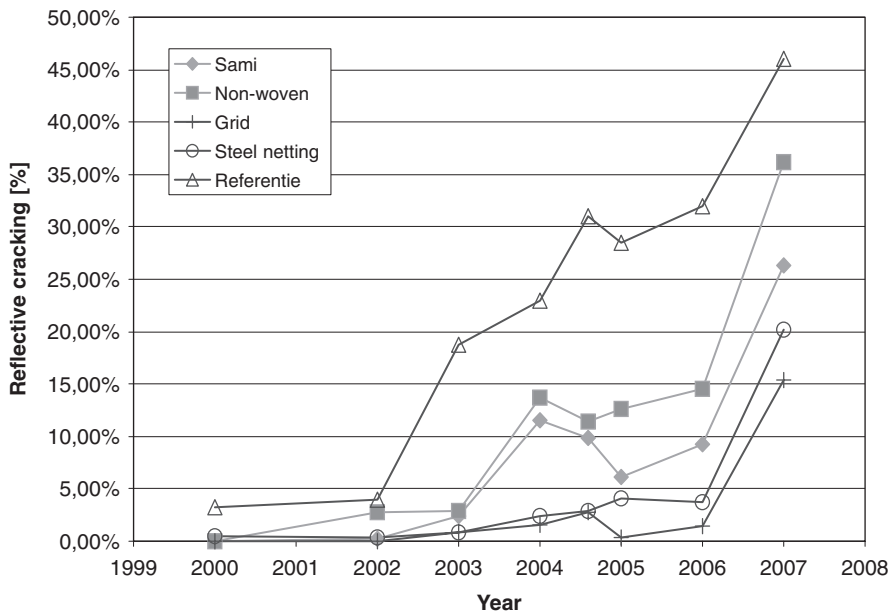


Figure 2. Results of the appearance of reflective cracks deduced from evaluations of the different test sections for the experimental road in Sint-Pieters-Leeuw rehabilitated in 1998.

the SAMI and non-woven which give both a considerable delay in the crack initiation. A second class which performs noticeably better than the first one, consists the grid and the steel reinforcing netting. Up to eight years after rehabilitation almost no cracks were visible with these interlayer systems.

For these sections, there is also no correlation visible between the height of the steps in the concrete and the crack initiation. On the other hand, there is a small trend visible that cracks initiate more easily at joints than at cracks. This might be explained by the fact that at cracks the load transfer can still have place due to aggregate interlock.

The inspections in June 2007, showed a serious growth of cracks in all sections. In order to have a complete view on the reflective crack occurrence at the surface, this test section will be inspected twice each year from new on.

3 LONG TERM EVALUATION OF INDIVIDUAL PROJECTS

The Belgian Road Research Centre has performed evaluations of several individual projects with interface systems (Decoene et al., 1993, Vanelstraete et al., 1996, Vanelstraete et al., 1996b, Vanelstraete et al., 1997, Vanelstraete et al., 2000, Vanelstraete et al., 2004). They concern overlays of cement concrete slabs, in most cases without foundation and with severe vertical movements (slab rocking) at the edges of the slabs.

Three different interface products have been placed: steel reinforcement nettings (either nailed or embedded in a slurry in order to fix it with the underlayer) and polyester nonwovens impregnated with bitumen. Table 3 gives for each of the projects the year of renovation, the type of interface, and the method of fixing with the underlayer. Other information such as overlay type and thickness, size of the project, traffic level in number of vehicles per day for each direction and original road structure can be found in (Vanelstraete et al., 2000). Table 3 gives also an overview of the results of the observed cracking, noted from 1994 to 2007. Additional information about the inspections is given further below.

3.1 *Project N415*

Since 2003, there is a drastic increase of the reflective cracking for this sixteen years old project. Until then, only limited amount of reflective cracks were observed. But it looks like the surface degrades fast once it started, over the last 4 years the reflective cracking increased from 30 to over 60%.

3.2 *Project N499*

On this 4 cm overlay with steel reinforcement nettings on heavily cracked cement concrete slabs all joints or old cracks reappeared as transverse reflective cracks after about ten years. The porous asphalt shows ravelling at a few places. Many cracks are double cracks, spaced about 2–3 cm from each other, especially in one road direction. The high percentage of reflective cracking is due to the limited 4 cm overlay thickness, combined with large vertical movements (slab rocking) at the edges of the concrete slabs. However, the fact that 100 % reflective cracking was observed after about ten years and not earlier, indicates that steel reinforcing nettings have been indeed efficient. Lower reflective cracking undoubtedly could be obtained by cracking and seating the slabs before overlaying and/or by increasing the overlay thickness.

3.3 *Project Aalter*

This fifteen years old project is seriously degrading now, with a percentage of reflective cracks of 72%. In contrast to the project N499, the slabs have been cracked and seated before overlaying and a 5 cm (levelling) course was placed in addition to the 4 cm thick top layer. These two facts undoubtedly lead to the high differences in reflective cracking between these projects.

3.4 *Project Genappe*

This project where impregnated non-wovens in polyester were applied, shows a lot of reflective cracking. The reflective cracks are double cracks, which were fine in the beginning phase, but have now evolved to narrow zones with loss of material between the adjacent cracks. There are several places with serious ravelling and even complete debonding of the 4 cm asphalt layer (where

Table 3. Summary of the results of the inspections (for further details about the description of the sites see (Vanelstraete et al., 2000)).

Project	Year repair	Crack and seat	Type of interlayer	Overlay	Equivalent reflected cracks in % (*)											
					1994	1995	1997	1999	2002	2003	2004	2005	2006	2007		
N415	1991	No	Steel reinforcement nettings, nailed	10 cm dense +4 cm porous bituminous mixture	no	3	11	14	30	36	48	55	63			
N499	1991	No	Steel reinforcement nettings, in slurry	4 cm porous bituminous mixture	11	37	68	75	91	93	100					
Aalter	1992	Yes	Steel reinforcement nettings, in slurry	9 cm dense bituminous mixture	no	0.1	5	10	33	36	46	52	56			
Genappe	1993	No	Non-woven polyester, 1.5 kg/m ² modif. Binder	4 cm asphalt layer		17	44	55	57	61	-	-	65			
N494 (A)	2003	Yes		4 cm dense bituminous mixture						no	no	0.5	7.5			
N494 (B)	2003	Yes	Steel reinforcement nettings, in slurry	6 cm dense mix and 4 cm SMA						no	no	no	no			

(*) Definition : see equation (1).

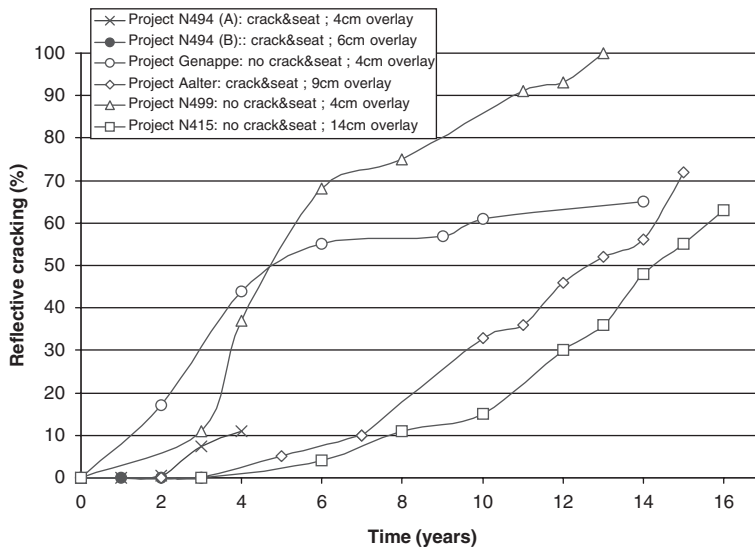


Figure 3. Overview of the reflective cracking in function of the number of years after rehabilitation of the different projects followed over time.

urgent repair is needed) and with a few zones already repaired. Better results undoubtedly could be obtained by cracking and seating the slabs before overlaying and/or by increasing the overlay thickness. After 2003 an extra overlay was applied but nevertheless the existing cracks reappeared almost completely in the 2007 inspection.

3.5 Project N494 (A)

In this four years old project, no anti-cracking interlayer was used to prevent reflective cracking. Moreover, only a small overlay thickness was used. As a consequence, already three years after rehabilitation, a considerable degree of reflective cracks is visible.

3.6 Project N494 (B)

In this four years old project, no reflective cracks are visible up to this moment. It has already been shown, that the combination of crack and seat, a steel reinforcing netting and a large overlay thickness is a very efficient way to overlay an existing road (section 2).

3.7 Conclusions

Figure 3 gives an overview of the reflective cracking of the different projects in function of the time after rehabilitation. Despite the fact that these are individual projects, with different structural designs and traffic conditions, some general trends are visible, which confirm previous conclusions:

- It can be seen that the thickness of the overlay plays a predominant role for the prevention of reflective cracking.
- The stabilisation of the cement concrete slabs by the crack and seat method is a very efficient way to decrease the appearance of reflective cracks after overlaying
- The interface systems seem to slow down the reflective cracking process, however there are limits to the vertical movements that can be supported.
- The use of an interface systems often leads to two adjacent cracks. In the initial phase they are very fine, but they then gradually evolve to small zones with loss of material.

4 CONCLUSIONS

The present paper describes the results of a long term evaluation of two experimental roads and six individual projects of overlays on cement concrete slabs on different roads, where different interface systems were used for prevention of reflective cracking.

From all investigated rehabilitations, it can be concluded that the crack and seat method is a very effective way to prevent reflective cracking. However, it is important to note that this technique leads to a reduced bearing capacity of the road. Hence, a control of the overall structural design is important when applying this technique. Also, the thickness of the overlay is of importance. The thicker the overlay, the more efficient it is against reflective cracking.

The follow up during 9 years of an experimental road where different interface systems (SAMI, non-woven, grid, steel reinforcing nettings) were applied, showed less reflective cracking on the sections with interface systems than on the reference section without interface. Moreover, the observations show there are two categories of materials with a different efficiency, in case of use on stabilised cement concrete slabs. On one hand a SAMI and a non-woven interface system delay the appearance of reflective cracks by a limited number of years. On the other hand, a steel reinforcement netting and geogrid are more efficient and delay the reflective cracking more.

REFERENCES

- Decoene Y., 1993. "Belgian applications of geotextiles to avoid reflective cracking in pavements", *Proceedings of the 2nd RILEM-Conference on Reflective Cracking in Pavements*, pp. 391–397.
- Vanelstraete A. and Decoene Y., 1996. "Behaviour of Belgian applications of geotextiles to avoid reflective cracking in pavements", *Proceedings of the 3rd RILEM-Conference on Reflective Cracking in Pavements*, Maastricht.
- Vanelstraete A. and Francken L., 1996. "On site behaviour of interface systems", *Proceedings of the 3rd RILEM-Conference on Reflective Cracking in Pavements*, Maastricht.
- Vanelstraete A., Francken L., Decoene Y., Veys J. and Delombaerde E., 1997. "On site behaviour of nonwovens and steel reinforcing nettings for the prevention of reflective cracking", *Revue Générale des Routes*, 2, pp. 54–57.
- Vanelstraete A. and Francken L., 2000. "On site behaviour of interface systems", *Proceedings of the 4th RILEM-Conference on Reflective Cracking in Pavements*, Ottawa.
- Vanelstraete, A., and De Visscher, J., 2004. "Long term performance on site of interface systems", *Proceedings of the 5th RILEM-Conference on Reflective Cracking in Pavements*, Limoges.
- Serfass J.-P., Bense P., Bonnot J., Samanos J., "A new type of ultrathin friction course", Transportation Research Board, Washington, January 1991.

Laboratory study of geogrid reinforcement in Portland cement concrete

X. Tang, G.R. Chehab & S. Kim

Pennsylvania State University, University Park, Pennsylvania, USA

ABSTRACT: The objective of this study is to investigate the behavior of geogrid reinforcement in Portland cement concrete (PCC) beams. The results from this study will pave the way for further investigation of using the geogrid as reinforcement in thin concrete overlays. Two geogrid products, for which the index material properties were obtained, are used for this study. The experiment comprises of four-point bending tests conducted on PCC beams without reinforcement, with one layer of geogrid-reinforcement, and with two layers. Results of testing and analysis showed substantial improvement in the response, particularly increase in ductility after crack initiation caused by flexural failure. Specimens reinforced with the stiff geogrids show higher energy-absorption capacity compared to that of flexible geogrids. Based on the study presented, it can be concluded that the placement of geogrids at the bottom of PCC beams for tensile reinforcement can provide post-cracking ductility and increase in loading capacity contingent upon the type and physical properties of geogrids used.

1 INTRODUCTION

Reinforcing steel bars have been conventionally used in reinforced Portland cement concrete pavements to provide the necessary strength required to endure stresses applied by moving loads. While steel-reinforced concrete is a functional and durable construction material given proper design and construction; however, several constraints often limit their use. Such limitations include physical constraints of placing the reinforcing steel bars in thin sections, such as concrete overlays and white-toppings, extensive time for construction, and concerns of steel corrosion (1, 2). Various remedies can be and are being adopted to mitigate steel corrosion through protective materials applied to the reinforcement directly or to the exposed concrete surface (2). Additionally, innovative and traditional materials are on the rise as alternatives to steel reinforcement, including fiber reinforced polymer (FRP) bars, tendons, and grids (3, 4, 5, 6).

The objective of this study is to assess the feasibility of using geogrids as potential reinforcements in thin concrete pavements and overlays to provide additional tensile strength and ductility. Of main importance is to study the ability of the geogrid to mitigate reflective cracking, and control the cracks once they have reflected by preventing them from widening. The work presented herein is a pilot study where the actions of the geogrids are first assessed while incorporated in concrete beams. As such, it is possible to assess, qualitatively and quantitatively, the behavior and mechanisms of reinforcement under controlled loading and environmental conditions. The findings can then be used in testing the geogrids in thin slabs under monotonic or moving load.

As reinforcing elements, geogrids have been mainly used in earthen structures, such as pavements, embankments, slopes, and retaining walls. By taking advantage of their high tensile strength, additional shear strength at the interface between geogrids and surrounding material is realized (8, 9). In geogrids manufacture, the generally used polymeric materials, high density polyethylene (HDPE), polypropylene (PP), and polyester (PET) offer excellent chemical resistance (10). This

Table 1. Concrete mix design (kg/m³).

Component	Material type	Content (kg/m ³)
Cement	ASTM Type III	480
Fine aggregates	River sand	670
Coarse aggregates	Crushed stone	1,000
Superplasticizer	Mid-range water-reducing admixture	9.6

makes geogrids a potential alternative of steel reinforcements in concrete, especially in thin sections and in architectural components such as arches where there might not be enough concrete cover and thus high resistance to corrosion is desirable.

An early research on cement composites reinforced by a stiff geogrid showed that the geogrid can provide considerable benefits when used as non-structural reinforcement under relatively light-loading conditions (11). Under dynamic loads, the stiff geogrid was even found comparable with steel reinforcement with respect to its structural performance (12).

This study on geogrid reinforcement for concrete focuses on the flexural behavior of concrete beams under a monotonic third-point loading. Two geogrid product types, stiff and flexible, are incorporated in concrete beams to provide tensile reinforcement in flexure. All beam specimens including the control beam (with no reinforcement) are cast using the same mix design and tested under monotonic loading. The inclusion of geogrids in the concrete beams shows significant benefits on post-cracking ductility. Additionally, a regain of strength is witnessed especially in concrete beams reinforced with two layers of geogrids. The stiff geogrid exhibits higher strain energy absorption capacity and provides additional post-cracking ductility to the beams as compared to the flexible geogrid.

2 EXPERIMENTAL INVESTIGATION

2.1 *Material properties*

The same mix design for the PCC mixtures (refer to Table 1) was used for all the specimens. In order to achieve high-strength concrete specimens, a low water to cement ratio of 0.37 was selected. A superplasticizer additive was added to obtain a high slump thus allowing the aggregates and cement paste to have adequate contact and interaction with the geogrids. A compressive strength of 58 MPa (8, 449 psi) was achieved at 21-days for the concrete mix tested per ASTM C 39.

The two biaxial geogrid products referred to as Grid A and Grid B, respectively, are shown in Figure 1. Grid A is composed of extruded PP sheets, while Grid B is composed of high tenacity PET multifilament yarns, woven into an open structure and coated with polyvinyl chloride (PVC) coating. The geogrids were tested for physical properties (details can be found in reference 13), including flexural rigidity, a critical property characterizing the tensile behavior of the geogrid in flexure. As per the results shown in Table 2, Grid A is classified as a stiff geogrid, while Grid B is classified as flexible (14).

2.2 *Specimen fabrication*

Figure 2 illustrates the schematic of the testing setup. All concrete beams are 15 cm × 15 cm × 56 cm (6 in × 6 in × 22 in) in dimension. A 3 mm wide, 6 mm (0.25 in) deep notch was sawed at the midpoint of the bottom face of the concrete beam (Figure 2) to promote flexural failure close to the mid-span of the beam. For casting the geogrid-reinforced concrete beams, a 5-cm concrete layer was first poured and compacted in the mold with a vibrator. The geogrid layer was then carefully installed and kept tight by being tied to the mold. Another concrete layer was cast above the geogrid (Figure 3). The mixtures were consolidated to the extent possible to ensure intermixing between

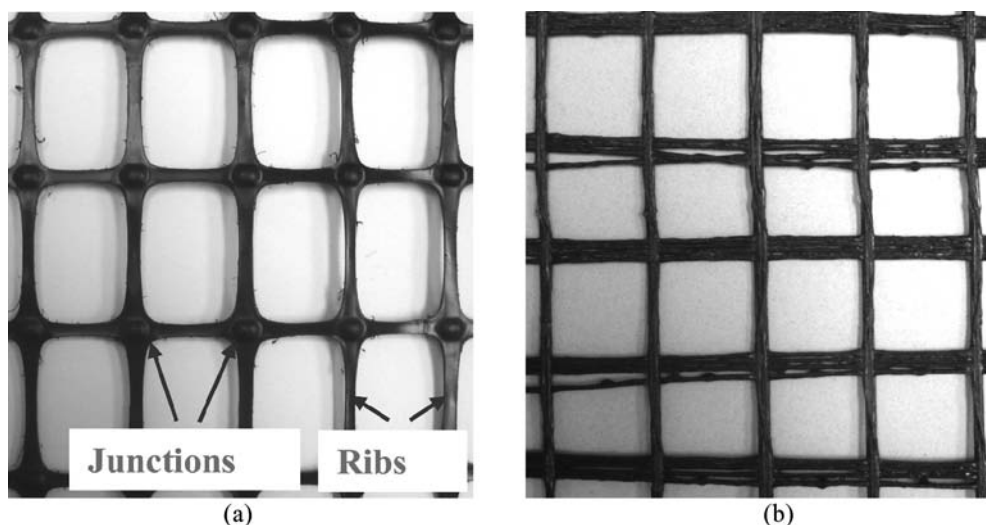


Figure 1. Geogrids used in the concrete beams: (a) Grid A; (b) Grid B.

Table 2. Tested geogrid index properties.

Index property	Testing method	Grid A		Grid B	
		MD*	TD**	MD	TD
Aperture size (mm)	Calipers	25.65	36.58	25.65	26.42
Mass per unit area (g/m ²)	ASTM D 5261	319.06		350.93	
Tensile strength at 2% strain (kN/m)		9.8	15.6	10.3	11.2
Tensile strength at 5% strain (kN/m)	ASTM D 6637	16.8	29.2	18.1	17.4
Ultimate tensile strength (kN/m)		23.9	32.9	39.5	52.8
Elongation at break (%)		20.6	10.9	10.5	12
Junction Strength (kN/m)	GRI GG2 (15)	17.7	28.1	7.4	7.1
Flexural rigidity (mg-cm)	ASTM D 1388, mod.	1429,355		452,671	
Torsional stiffness (cm-kg/degree)	COE/GRI GG9 (16)	7.50		3.43	

* MD: machine direction (along roll length).

** TD: cross-machine direction (along roll width).

the concrete layers above and below the geogrid. No separation or surface voids were observed after de-molding the specimens. For concrete beams reinforced with two layers of geogrids, after the installation of the bottom layer of geogrid, a 2.5-cm thick concrete layer was cast followed by placing the second layer of geogrid and another layer of concrete mixture. Specimens were then kept in an environmental chamber at a temperature of $23 \pm 5^\circ\text{C}$ and relative humidity greater than 95% to cure for 21 days before testing.

2.3 Testing and instrumentation

The tests were performed on a closed-loop hydraulic-driven 1MN (220kip) universal testing machine. A third-point monotonic load was applied via the loading head (Figure 1) at a rate of 0.02 mm/s. Mid-span displacement of the beam was measured by an extensometer mounted on a customized steel jig (Figure 4). Loading and mid-span deflection data were recorded using a 16 bit data acquisition system. Data was acquired until complete failure of the beam to investigate the effects of geogrid reinforcement on the post-cracking behavior.

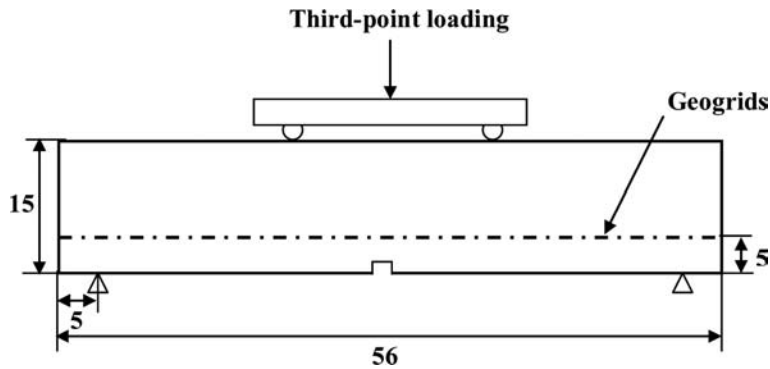


Figure 2. Geometry and configuration of the test setup, units in cm.

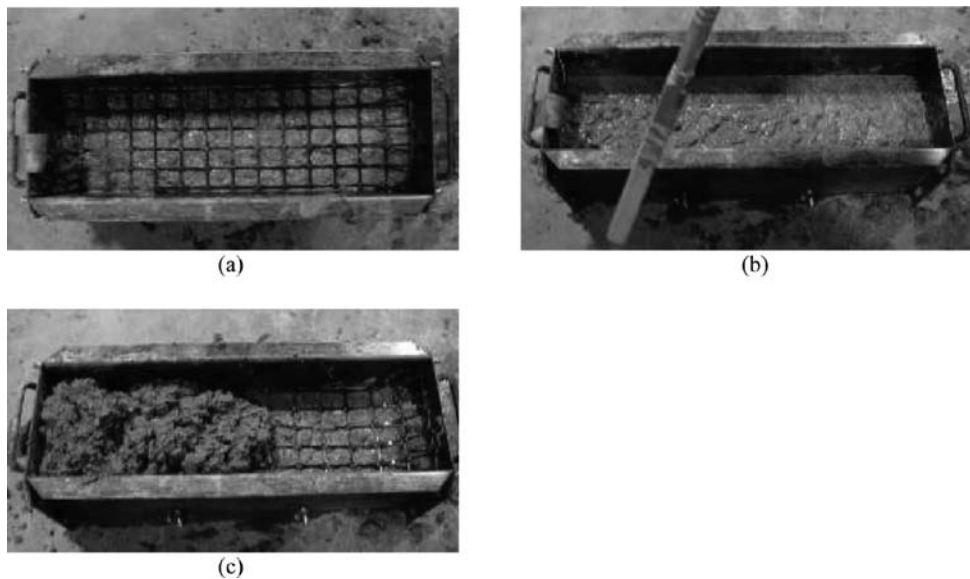


Figure 3. Casting geogrid-reinforced concrete beams: (a) Placement of the first 5-cm concrete layer; (b) place the geogrid; (c) cast the second layer of mixture.

3 RESULTS AND ANALYSIS

3.1 Effect of reinforcement on strength, ductility, and flexural energy absorption

Figure 5 presents the load-deflection behavior for the plain (control) and reinforced concrete beams in flexural tests. Both exhibit a sudden decrease in load immediately after initial cracking develops. While the failure mode and mechanism of the control beam follows a brittle and sudden failure given the lack of any reinforcement, the geogrid-reinforced specimens exhibits more ductility, delayed cracking, and an increase of strength after cracking.

Figure 5 also indicates that geogrid-reinforced specimens exhibit significant deformation before ultimate failure, most likely due to the geogrid's ductility, while the deformation of the control specimen is minimal as expected. The extensive post-cracking deformation of the concrete beams shows that the inclusion of geogrids provides certain post-cracking ductility, which is desirable in

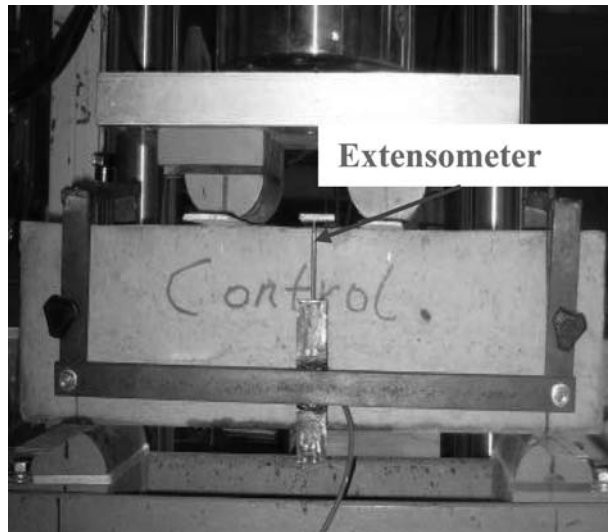


Figure 4. Concrete beam under loading and instrumented with an extensometer.

Table 3. Results of the tests.

Concrete beam type	Maximum load (kN)	Flexural strength (kPa)	Post-cracking maximum load (kN)	Accumulated Flexural energy (J)
Control	29.3	3987.1	N/A	N/A
Grid A_One Layer	26.7	3639.5	6.9	47.9
Grid B_One Layer	26.9	3662.1	7.0	44.5
Grid A_Two Layers	28.3	3856.2	15.5	162.1
Grid B_Two Layers	28.1	3829.6	12.9	112.4

most applications. In comparing Grid A and B, it is noted that concrete beams reinforced by Grid A exhibit more post-cracking ductility than that by Grid B.

The load-deflection curves for both one-layer and two-layer reinforced concrete are presented in Figure 6. Substantial improvement of post-cracking load capacity is achieved by including only one more layer of geogrids. In fact, for Grid A, the post-cracking load capacity of two-layer geogrid reinforced concrete beams is more than half of the maximum load causing the first crack as can be seen in Table 3, which indicates that the magnitude of the reinforcing- geogrids strength is somehow comparable with the maximum tensile load that the plain concrete can endure (refer to Table 2).

The flexural strength, R , is calculated from the following formula (17):

$$R = \frac{Pl}{bd^2} \quad (1)$$

where:

P is the maximum total load measured, units in kN;

l is the span length, 46 cm (18 in);

b is the specimen width, 15 cm (6 in);

d is the specimen height, 15 cm (6 in).

The calculated flexural strength is listed in Table 3. It is noted that the geogrid reinforcement does not necessarily increase the flexural strength, although the two-layer reinforced concrete possessed higher strength than the one-layer reinforced concrete.

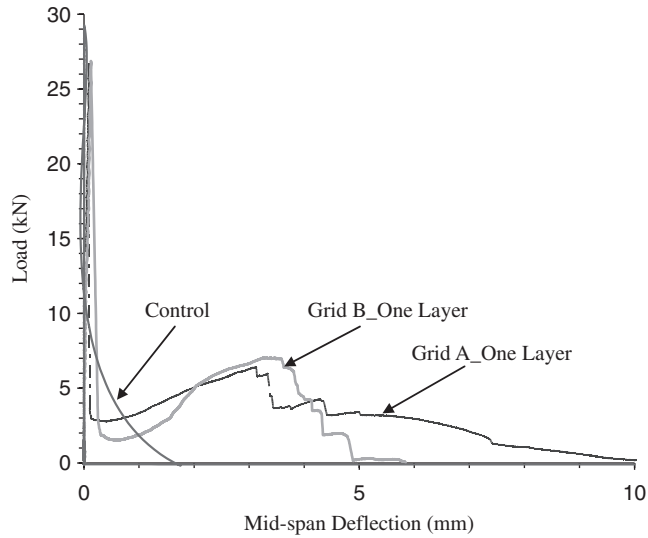


Figure 5. Load-displacement relationships for plain and reinforced concrete beams with one-layer goegrid.

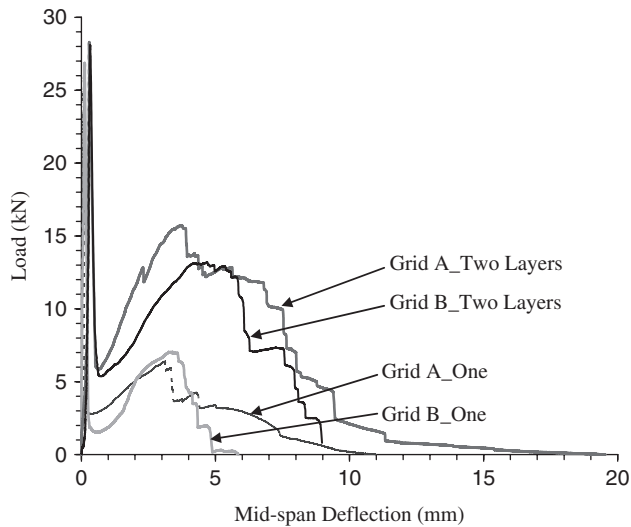


Figure 6. Load-displacements curves for reinforced concretes beams with one- and two-layer geogrids.

The area under the load-deflection curve in Figures 5 and 6 represents the static flexural energy absorption capacity of the concrete beams. Figure 7 shows that geogrid reinforcement in concrete beams leads to a substantial improvement in the total energy-absorption capacity. The specimen with Grid A exhibited higher overall energy-absorption capacity than that with Grid B.

3.2 Failure modes

The control and reinforced beams exhibit different failure modes as displayed in Figure 8 and Figure 9, respectively. Geogrids were mobilized at the time of crack initiation. For the reinforced concrete beams, there was extensive crack propagation with wide crack mouth opening before the

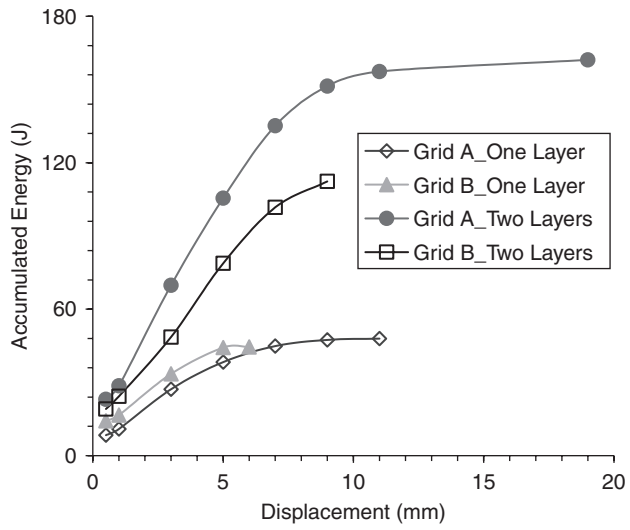


Figure 7. Accumulated energy in concrete beams against mid-span displacement.

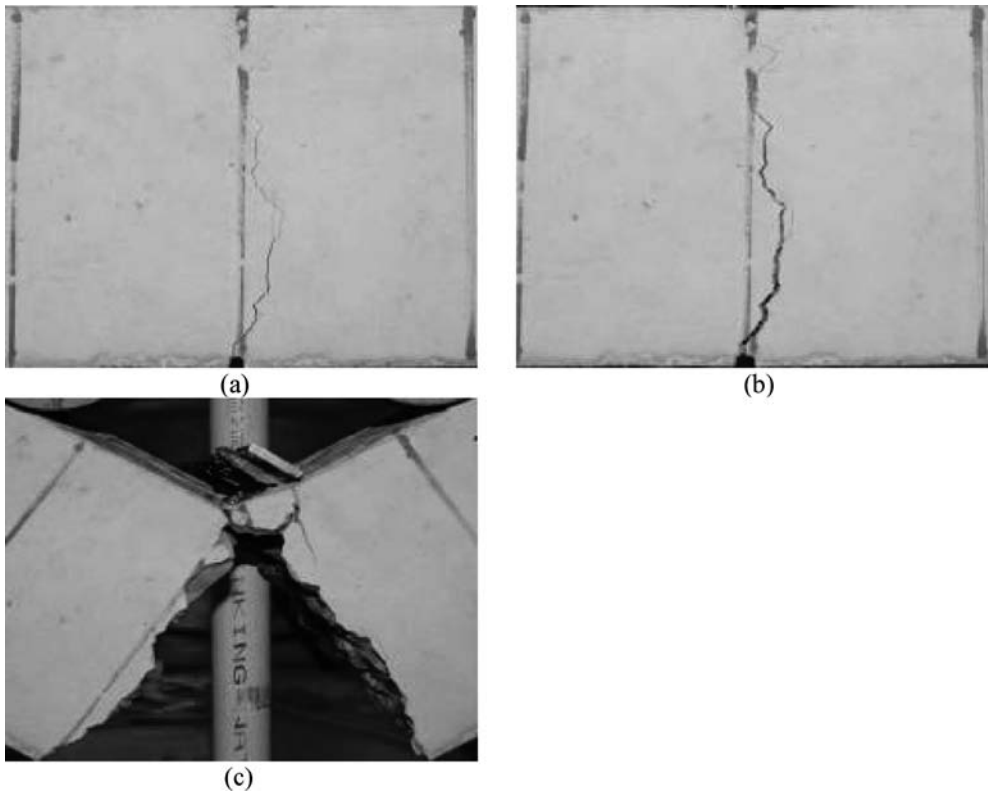


Figure 8. Failure mode of plain concrete beam: (a) Crack initiation; (b) Crack propagation; (c) Failure.

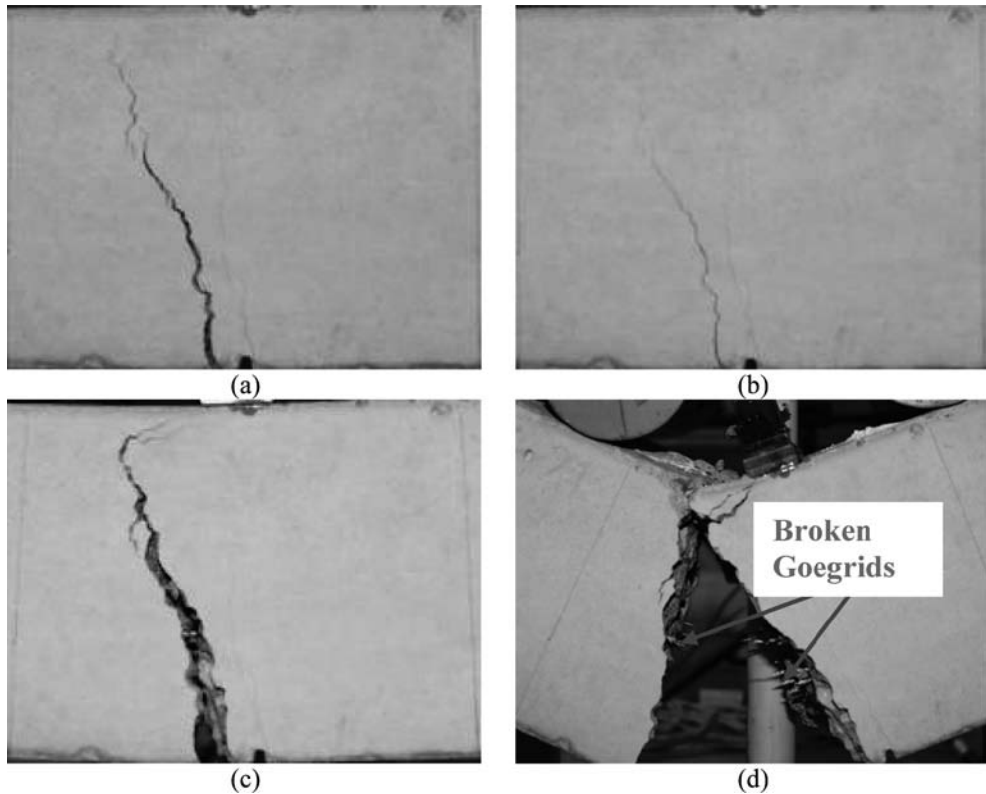


Figure 9. Failure mode of concrete beam reinforced by Grid B: (a) Crack initiation; (b) Crack propagation; (c) Crack with large CMOD; (d) Failure.

failure; while the plain concrete beam failed instantly. The additional phase of crack development demonstrated in Figure 9-c confirms a potential benefit of geogrid reinforcement on post-cracking behavior.

Upon initial cracking, most of the tensile force is transferred to the embedded geogrids at the crack. Based on pullout tests for geogrid-reinforced cement, it is found that geogrids with roughened surfaces are able to provide a resistance force to cause the failure of grid fracture instead of pullout failure (11). For the specimens consisting of coarse aggregates in this study, in addition to surface friction along the geogrid, the developed passive stress against the geogrid's bearing rib can produce adequate pullout resistance. Geogrids even without roughened surface therefore experienced fracture failure. Figure 10 shows different failure modes of Grid A and B. Grid A was torn apart mostly at ribs, while Grid B at junctions. This is possibly attributed to the significant difference in junction strength of Grid A and B as listed in Table 2.

4 CONCLUSIONS AND RECOMMENDATIONS

Plain and reinforced Portland cement concrete beams with the same mix design are tested under third-point monotonic loading. The results of this study show that the geogrid reinforcement adds a substantial post-cracking ductility to the concrete. Different failure modes are observed for plain versus geogrid-reinforced concrete beams. Reinforced beams exhibit extended crack propagation after crack initiation and before failure, while the plain concrete beams fail in a brittle mode

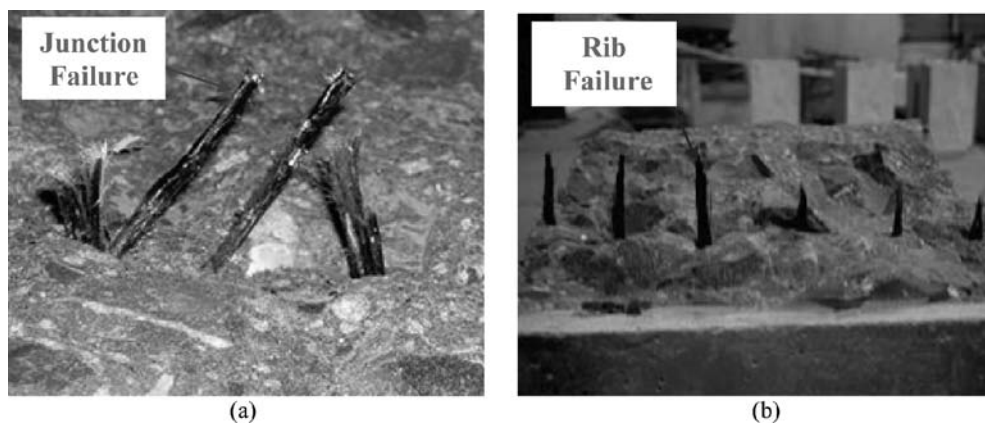


Figure 10. Different failure modes for geogrids: (a) Grid A failed at ribs; (b) Grid B failed at junctions.

instantaneously. The flexural strength of reinforced beams is not necessarily improved due to the inclusion of geogrids.

It is noted that the two types of geogrid reinforcement exhibit different mechanical behaviors in the flexural tests. Higher total energy-absorption capacity is witnessed in the concrete beam reinforced by the stiff geogrid. Furthermore, the specimens reinforced by the stiff geogrid exhibits more post-cracking ductility in both one-layer and two-layer cases. The difference in the performance for geogrids for the same concrete matrix indicates that the physical and mechanical properties of geogrids play an important role in the reinforcing effectiveness for concrete.

This study reveals the potential benefits of geogrids reinforcement for PCC. Nevertheless, various aspects associated with this study still need to be investigated, such as: the interlocking between geogrids and coarse aggregates in the concrete matrix, effects of the number and location of geogrid layers on the reinforcement performance and cracking propagation, and effects of the development length.

The contribution of geogrid reinforcement for PCC functionality and performance is promising for concrete overlay applications. Of particular benefit is their ability to control reflective cracking by absorbing concentrated stresses at the crack tips and delaying the crack propagation. Once cracks develop in the overlay, the geogrids are able to control the crack widening. Additional benefits of geogrids include lack of susceptibility to corrosion, ease of manufacture and handling, higher ratio of strength to weight, and lower costs. However, more research on the mechanisms of geogrid reinforcement needs to be performed on thin slabs under monotonic or moving loads.

ACKNOWLEDGEMENTS

The authors wish to thank R.M. Chacko and K. Grady for their assistance during the experiment. Thanks also go to the lab manager, Mr. Dan Fura, for his assistance making this study possible.

REFERENCES

- Nawy, E.G. *Reinforced Concrete: A Fundamental Approach*, 4th Edition, Prentice Hall, New Jersey, 2000.
 Clarke, J.L. *Alternative Materials for the Reinforcement and Prestressing of Concrete*, Blackie Academic and Professional, New York, 1993.
 Erki, M.A. and Rizkalla, S.H. FRP Reinforcement for Concrete Structures. *Concrete International*, Vol. 15, No. 6, 1993, pp. 48–53.
 Nanni, A. and Dolan, C.W. Fiber Reinforced Plastic Reinforcement for Concrete Structures, *Proceedings of the International Symposium on Fiber Reinforced Plastic Reinforcement for Concrete Structures*, American Concrete Institute, Detroit, MI, 1993.

- Banthia, N., Al-Asaly, M., and Ma.S. Behavior of Concrete Slabs Reinforced with Fiber-Reinforced Plastic Grid, *Journal of Materials in Civil Engineering*, Vol. 7, No. 4, 1995, pp. 252–257.
- Bakis, C.E., Bank, L.C., Brown, V.L., Cosenza, E., Davalos, J.F., Lesko, J.J., Machida, A. Rizkalla, S.H., Triantafillou, T.C. Fiber-Reinforced Polymer Composite for Construction – State-of-the-Art Review, *Journal of Composite for Construction*, Vol. 6, No. 2, 2002, pp. 73–87.
- Morris, M., Some of the Applications for Polymer Grids in Concrete, *Concrete*, Vol. 21, No. 2, 1987, pp. 25–26.
- Hass R., Wall, J., and Carroll, R.G. Geogrid Reinforcement of Granular Bases in Flexible Pavements. *Transportation Research Record 1188*, Transportation Research Board, National Research Council, Washington D.C., 1988, pp. 19–27.
- Perkins, S.W. Geosynthetic reinforcement of flexible pavements: laboratory based pavement test sections. *Report No. FHWA/MT-99-001/8138*, U.S. Department of Transportation, Federal Highway Administration, Washington, D.C., 1999.
- Shukla, S.K. *Geosynthetics and their Applications*, Thomas Telford, London, 2002.
- Swamy, R.N., Jones, R., and Oldroyd, P.N. The behavior of Tensar Reinforced Cement Composites under Static Loads. *Proceedings of the Conference on Polymer Grid Reinforcement in Civil Engineering*, Thomas Telford Publishing, London, 1984, pp. 222–232.
- Watson, A.J., Hobbs, B., and Oldroyd, P.N. The Behavior of Tensar Reinforced Cement Composites under Dynamic Loads. *Proceedings of the Conference on Polymer Grid Reinforcement in Civil Engineering*, Thomas Telford Publishing, London, 1984, pp. 233–242.
- Chehab, G.R., Palomino, A.M., and Tang, X. Laboratory evaluation and specification development for geogrids for highway engineering applications, *Report No. FHWA-PA-2007-009-050110*, Pennsylvania Department of Transportation, Harrisburg, PA, 2007.
- Koerner, R.M. *Designing with Geosynthetics*, 4th Edition, Prentice Hall, New Jersey, 1998.
- GRI Test Method GG2. *Standard Test Method for Individual Geogrid Junction Strength*, Geosynthetic Research Institute, Folsom, PA.
- GRI Test Method GG9. *Standard Test Method for Torsional Behavior of Bidirectional Geogrids When Subjected to In-Plane Rotation*, Geosynthetic Research Institute, Folsom, PA.
- ASTM C 78. Standard Test Method for Flexural Strength of Concrete (Using Simple Beam with Third-Point Loading), *Annual book of ASTM standards*, American Society for Testing and Materials (ASTM), West Conshohocken, PA, Vol. 4.02.

Performance and service life prediction of crack preventative joint systems

C. Recknagel, S. Pirskawetz & F. Lüddecke

Federal Institute for Materials Research and Testing (BAM), Berlin, Germany

ABSTRACT: The tactical arrangement of regular cracks in pavements – so-called joints – certainly represents an efficient crack preventative method to avoid uncontrolled pavement cracking. Tight sealing of this design element decisively influences pavement performance as well as service life although it accounts only for a small fraction of the total investment. Different from the existing predominantly empirical selection of joint or crack sealing systems a new approach is defined by engineering-related design based on a verified performance under relevant loading. A consequent realisation of this methodology demands the consideration of the required cyclic movement capacity as well as crucial climatic exposures – also referred to as ageing effects – during the verification of serviceability of these organic and predominantly thermo-plastic materials. Accordingly, a special testing method including loading function and adequate test equipment was developed at BAM able to activate the fundamental capability as well as the durability of crack and joint sealing systems. From the recorded characteristic test values the effective mechanical system behaviour, the expected maximum loading of the cohesive and adhesive bond and the restoring forces can be deduced. Additionally the cycle-dependent changes of the mechanical properties permit a service life prediction. Thus, the performance of the complete system is reproduced under realistic conditions. Constructional defects as well as material flaws can be detected and corrected. The methodology introduced will be discussed on various joint systems. With this tool, an appropriate technical design optimised for the performance of the required crack abating solution can be chosen.

1 INTRODUCTION

In search for an ideal technical system solution to prevent uncontrolled cracking of rigid pavements such as concrete pavements, but also for their maintenance or repair in the event of damage, have not led to any comprehensive or satisfyingly durable solutions to this problem even 80 years following the prevalence of industrialised road construction. A wide range of constructive, but also material approaches to solving the problem exist. The range of the constructive approaches extends from continuously reinforced concrete pavements without joints to pavements with expansion as well as contraction joints (dummy joints) combined using joint sealants up to pavements with unsealed joints. If the formation of joints is provided for in the pavement design and if they are to be sealed, then a multiplicity of joint filling systems is available. In the various national technical rules for the design and installation of crack preventative joint sealants, they are categorised according to a wide range of criteria (e.g. according to the material basis or their delivery form, according to installation technology, by the designated area of use, according to their flexibility or chemical resistance). At the same time, a special mechanical behaviour is assigned to each category, which is frequently assumed on a historical basis and as such, based on in some cases outdated or highly simplified conceptions of the product properties. However, these often empirical classifications and the associated conception regarding the system behaviour mark the technical rules to date.

The test tool kit provided for at present in the technical regulations for assessing the performance of the joint filling systems is generally also aligned with the level of knowledge adopted from the 70's and 80's. As a comprehensive analysis of literature concerning the national and international status of research and technology of qualifying joint filling systems in traffic areas demonstrated, until the end of the last century an evaluation of the real performance capacity of sealing materials as well as the system solution is only possible to a very limited extent [1].

Proof of the actual mechanical system behaviour under realistic loads as well as statements regarding durability (fatigue, climatic aging) is lacking for the most rules and regulations or is only present in part. In the view of the authors, an imbalance exists thus far between the address in terms of testing and the status quo of the products resp. possibilities of modern product development (e.g. focussed implementation of modifying polymers). Rather the evaluation of further developments with respect to materials or construction, but also a performance-based selection resp. design of a crack preventative joint filling system for its intended use requires performance-related testing. As such, it follows that the availability of appropriate test methods is regarded as a requirement for improved construction solutions with a greater degree of durability. This rating of the given situation is nearly congruent with conclusions published by Al-Quadi, Masson et al. (e.g. [2]; [3]) activating developments for performance-based material tests as well as system tests. Please find described herein our special evaluation approach focused on performance-related system testing.

In Germany, joints and cracks in road pavements are to be sealed with joint filling systems in order to secure their functionality and durability as well as to protect the lower layers of the pavement base. For this, directives concerning the design, installation and the evaluation of required performance characteristics for joints in motorways and federal highways are consolidated in the technical rules ZTV Fug-StB. Also with respect to these regulations, the fundamental knowledge as per [1] is based predominantly on experiences, which have been passed on and less on methodical tests oriented to performance. In the above-mentioned technical rules and regulations, a selection of materials and constructively different joint filling systems is designated for use on road with heavy vehicle traffic. The potential joint filling systems are categorised as follows and the following fundamental mechanical behaviour and generally performance requirements are attributed to them.

The current testing procedures required predominantly comprise material properties and only contain one method for indicating the extensibility of the overall system behaviour. An analysis of maintenance costs in 2005, which increased to around 1 billion euros (corresponds to approximately 19,000 euros per kilometre of federal highway), shows however that the system solutions for joint sealing often represent the crucial weaknesses in terms of durability and driving comfort in inflexible pavements. This also led the authors among other things to the fact that with the exception of a

Table 1. German joint filling sealants for motorway and highway pavements

Category of joint filling systems (abbr.)	Attributed system behaviour	General performance requirements
Thermoplastic sealants (hot applied)		
– plastic sealants (PS)	Plastic	up to 25% deformation capacity (5 mm); Minimum service life ≥ 5 years
– elastic sealants (ES)	Elastic	up to 35% deformation capacity (7 mm); Minimum service life ≥ 5 years
– crack renovating sealants (CS)	Plastic	up to 25% deformation capacity (5 mm); Minimum service life ≥ 2 years
Reactive sealants (RS) (cold applied)	Elastic	up to 25% deformation capacity (5 mm)*; Minimum service life ≥ 5 years
Preformed profiles (PP)	Elastic	up to 30% deformation capacity (6 mm); Minimum service life ≥ 5 years

* fuel – resistant

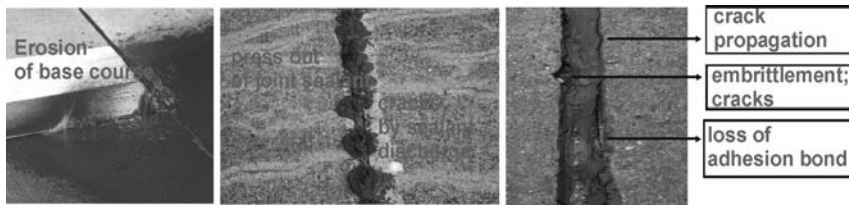


Figure 1. Typical joint damages.

test of the deformation capacity, methodically secured, comparable or differentiating statements on the real system behaviour and durability are not made during initial type testing. Rather, the cases of damage reported from actual practice indicate the necessity to enquire in a scientific manner empirically-derived construction principles and to orient the evaluation methodology of functionality and service life to a practical testing concept in order to address the actual behaviour and performance in use.

Besides a new approach for the material test on sealants – in a similar approach for quality assurance as mentioned in [3]; [5] – the development of a corresponding system test method was necessary for this. The following contribution describes the performance-related test methodology developed and the experiences resulting thus far in its application to different joint filling systems. The findings concerning the fundamental mechanical system behaviour identified will be discussed as well as the service life (durability) of the systems tested. Building on the mechanical system data collected, constructive empirical regulations can now also be verified in terms of their plausibility with numerical simulation tests.

2 PERFORMANCE-RELATED INVESTIGATION METHOD FOR JOINT FILLING SYSTEMS IN TRAFFIC AREAS

To conduct a performance-related investigation method, it was first necessary to determine the significant loads exerted on joint filling systems and also to stipulate the decisive evaluation criteria used in identifying the general functionality and durability. The significant loads decisive for functionality and durability (activation of the internal and external ageing effects) can be categorised in terms of influences from weather and traffic. Weather conditions constitute direct climatic and indirect mechanical loads (deformation) of the joint filling systems. Due to the thermo-plastic, thermo-viscoelastic or thermo-elastic behaviour of the different joint filling materials, the potential temperature conditions in use and their fluctuation are of particular significance. Fluctuation in temperatures results in deformation loads of the joint filling systems with simultaneously varied mechanical behaviour. In order to activate the internal ageing effects, the inserting of thermal and UV radiation (energy insert) is to be taken into consideration. Besides this ageing, but also the bond behaviour of the system is significantly influenced by air moisture or precipitation. The dynamic deformation associated with passing traffic is to be considered as significant influences on joint filling systems in pavements. An intensified load and activation of ageing processes (synergism) is to be expected based on the combined effect (superimposition) of the aforementioned loads. As such, a load function based on practice must take a superimposition of loads acting simultaneously into consideration.

With the assistance of the investigation method the following statements are to be acquired as performance-oriented criteria for evaluating the effects of significant loads triggering ageing effects on joint filling systems.

- **A** Demonstration of the serviceability (flexibility, cohesive and adhesive bonding)
- **B** Demonstration of durability (fatigue; load depending change in qualities)

An experimental rig was developed and built to replicate the decisive loads mentioned above.

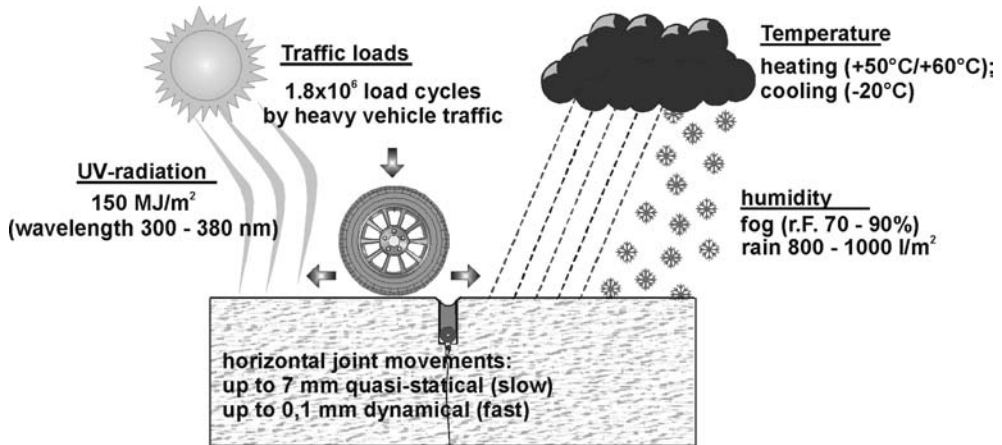


Figure 2. Schematic representation of decisive loads on joint filling systems (quantified according to German climatic, loading and construction conditions).

Based on the analysis of the decisive loads (see Fig. 2), a representative load function for joint filling systems was compiled adjusted for the conditions in the Germany highway network. During the process comprising 168 hours (1 cycle), the significant mechanical and climatic loads of one year are imposed on a sample in a time-lapsed manner. All in all the investigation method concerns a coupled test procedure controlled in terms of deformation and climate.

Phase	Simulated season	Deformation		Temperature	Air moisture	Rain cycles	UV-radiation
		static	dynamic				
1	spring	0 mm	± 0.1 mm f = 3 Hz	15°C	from 40% to 70%	0	100%
2	summer	-1.0 mm	± 0.1 mm f = 3 Hz	50°C	70%	11 × 1 min with 5 l/min	100%
3	autumn	0 mm	± 0.1 mm f = 3 Hz	15°C	from 70% to 20%	5 × 1 min with 5 l/min	100%
4	winter	+4.9 mm (PS) +6.9 mm (ES) +4.9 mm (CS) +4.9 mm (RS)	± 0.1 mm f = 3 Hz	-20°C	-	0	0
5	spring	0 mm	± 0.1 mm f = 3 Hz	15°C	20%	0	100%

The sample to be tested constitutes a true-to-scale section of a pavement joint. The bordering flanks may be finished in concrete or asphalt depending on the case of application.

3 TEST RESULTS FROM VARIOUS JOINT FILLING SYSTEMS

Due to their ongoing predominant use for concrete pavements in Germany, sealing compounds constituted the focus of the tests thus far. Different categories of systems as well as a number of

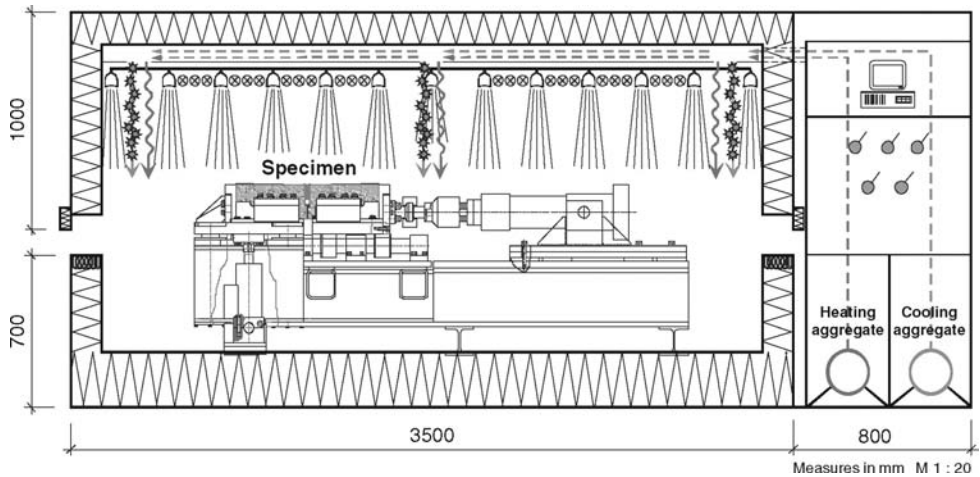


Figure 3. Functional principle of the new joint investigation method.

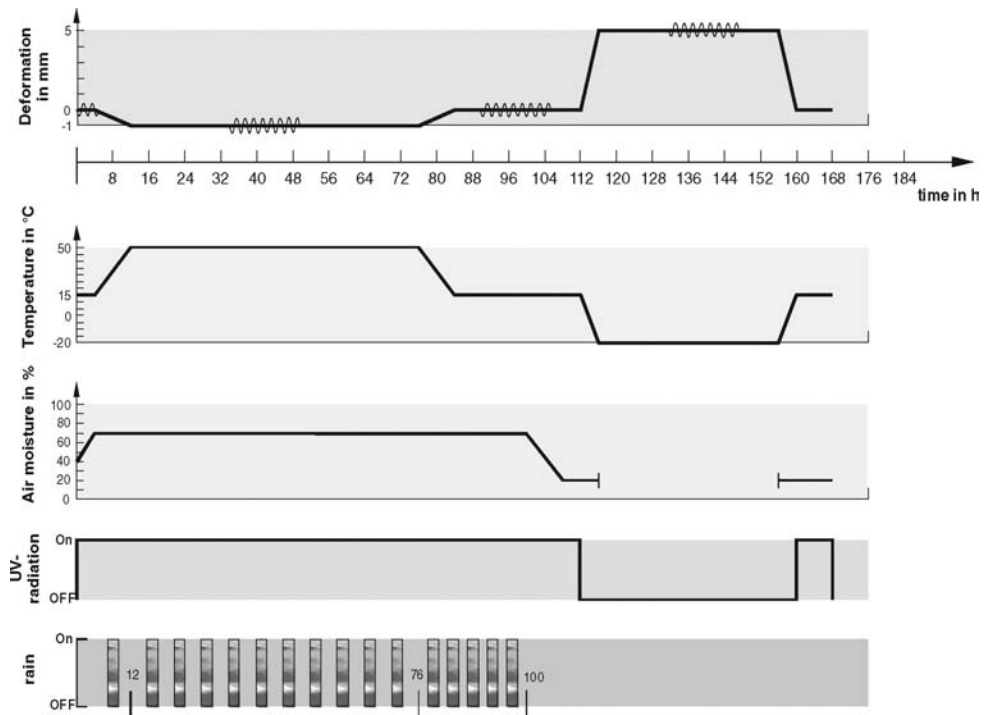


Figure 4. Simplified and time-lapsed load function for loads over the course of one year.

various products of selected categories were tested and compared. All systems tested were approved on the basis of the conventional test tools and are used in the highway network in accordance with current technical regulations. Each specimen was exposed to consecutive load cycles from the above-mentioned load function. The load function itself was adjusted to the performance requirements of each category pertaining to regulations with respect to the predefined deformations. The annual cycles of the load function were repeated at least corresponding to the required minimum duration (see table 1) resp. up to the loss of functionality (cracking, breaking, debonding). During

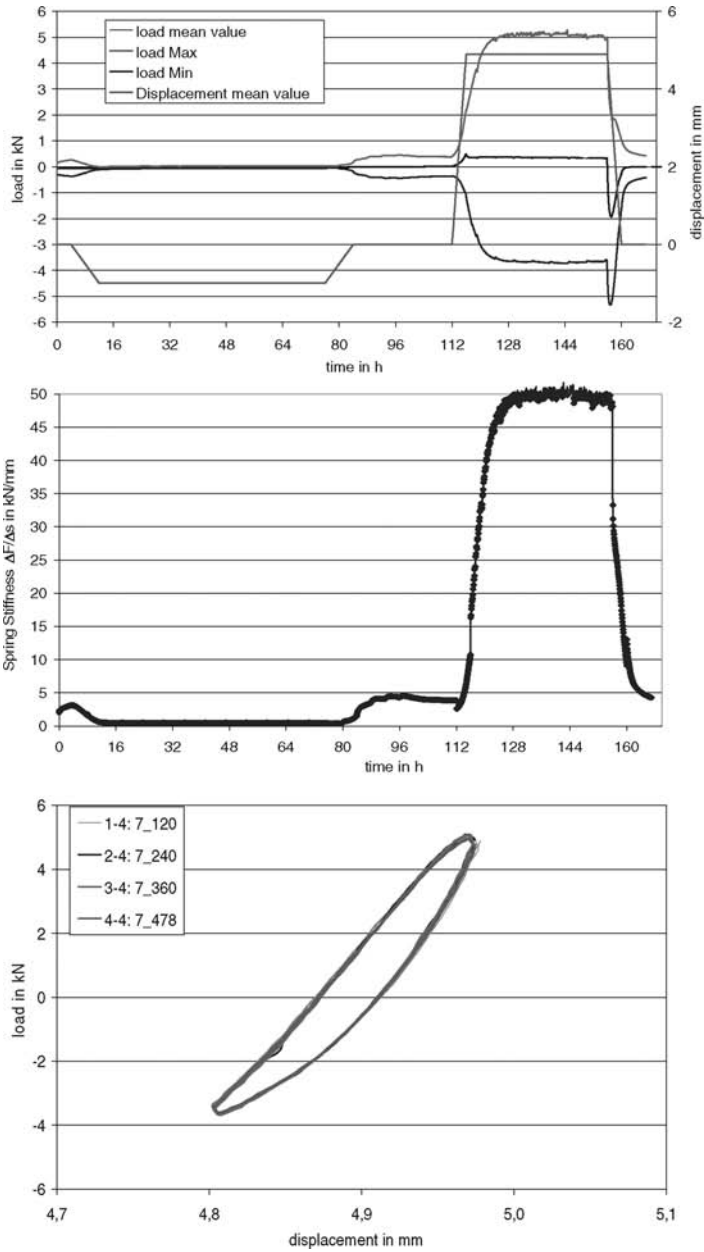


Figure 5. Typical progression of a load displacement, spring stiffness and energy absorption diagrams (hysteresis curve) over 1 loading cycle for a capable joint filling system.

the course of the trial, the forces F expended for the simulated static and dynamic deformations were recorded in separate force-displacement-diagrams. Besides this also the climactic parameters of temperature, moisture and radiation were recorded.

In addition, a visual inspection of the sample for cracks and debonding takes place. The parameters of mechanical stress σ , spring constant k and work performed W were continuously determined over the entire load cycle based on the data measured.

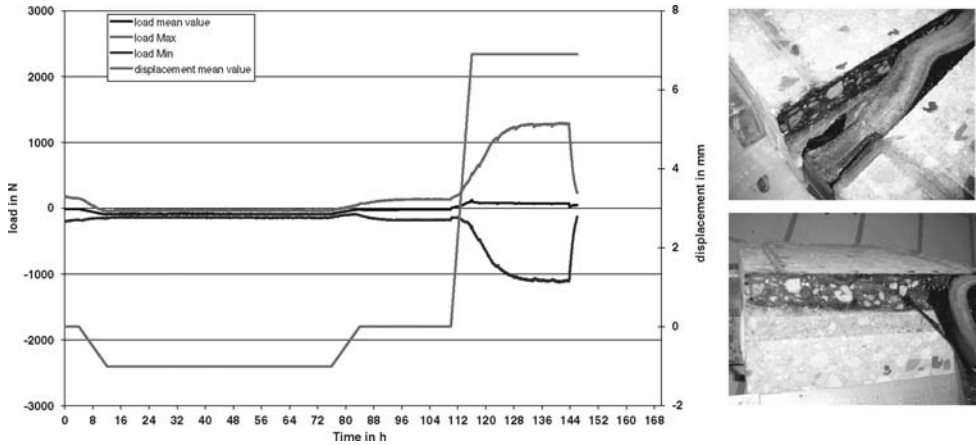


Figure 6. Typical force progression for spontaneous failures (crack resp. debonding).

$$\sigma = \frac{F}{l * d} \text{ in } [N / mm^2]$$

$$k = \frac{F_{\max} - F_{\min}}{s_{\max} - s_{\min}} \text{ in } [N / mm]$$

$$W = \int F \cdot ds \text{ in } [N * mm]$$

Normalised to an surface element of the bonding surface and as such comparable the parameters maximum stresses $\sigma_{A, \max}$, spring stiffness k_A of the system and work performed $W_{A, \max}$ are then analysed and discussed.

$$\sigma_{A, \max} = \frac{F_{\max}}{l * d} \text{ in } [N / mm^2]$$

$$k_A = \frac{k}{l * d} \text{ in } [N / mm^3]$$

$$W_A = \frac{W}{l * d} \text{ in } [N / mm]$$

Legend: F = load in [N]
 s = displacement in [mm]

l = length of the specimen's joint in [mm]
 d = height of the specimen's joint in [mm]

With the parameter $\sigma_{A, \max}$, the stress conditions resulting from the phase-dependent progression of the forces, which are decisive for the system and the adjacent surfaces to be bonded, are to be measured, whereupon information is provided concerning the loading of cohesive and adhesive bond. The spring constant k_A provides information concerning the temperature-dependent system stiffness of the respective product during the transition from season to season. With this parameter, it is possible to conduct more target-oriented parametric studies with the assistance of numerical calculations (FEM analysis) in a focussed manner for the decisive load condition at low temperatures during winter. The progression of the spring constant k_A returns in particular information regarding the system behaviour when subjected to rapidly occurring and often repeated dynamical movements. Constant changes in the progression at fixed seasonal conditions are to be interpreted as a measurement for mechanical fatigue behaviour. Based on the hysteresis curves departing from the shape resp. their fluctuation during the course of the test together with the course of the mean value load, information can be derived regarding the characteristic mechanical system behaviour. The area within the hysteresis curve constitutes a measurement for the capacity to partially absorb stresses imposed by means of dissipation – a source of informations about the mechanical behaviour also used in [4].

An analysis of the calculated parameters and their progression following the first load cycle serves to demonstrate the general functionality of the crack preventing system. According to the experiences collected, inappropriate material combinations or constructive problems of the system or faulty installation are already identified at this stage. The relative changes during the subsequent cycles then reflect the durability.

In this case: System failure caused by improper primer

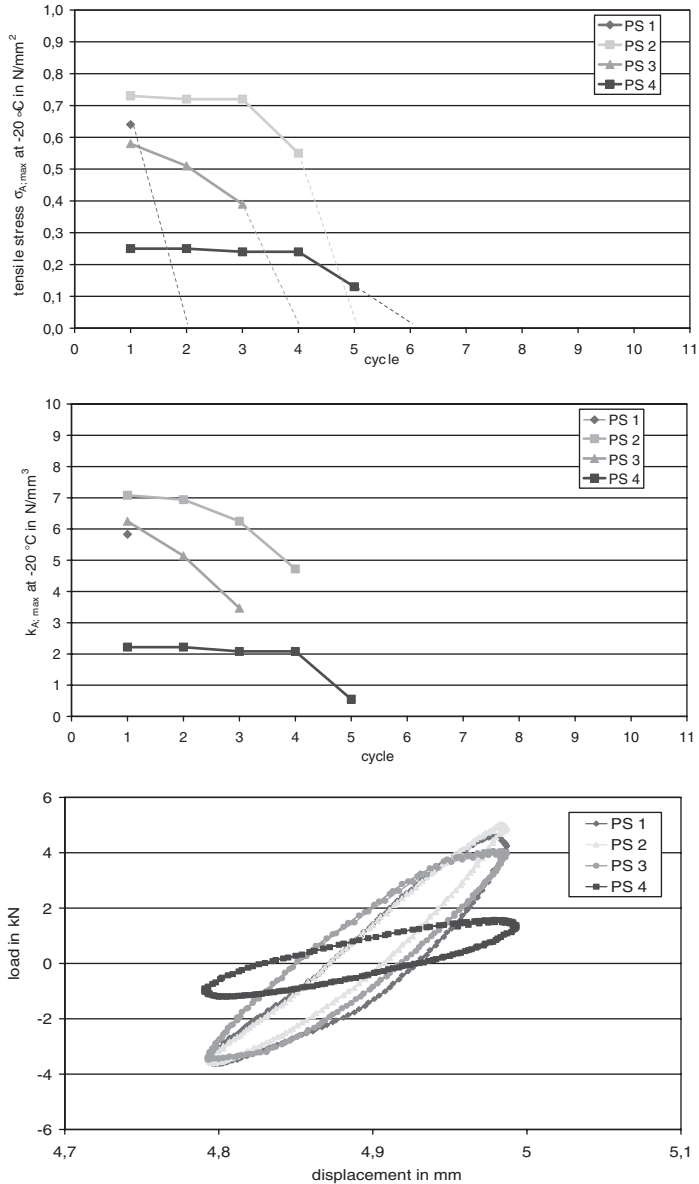


Figure 7. Characteristic mechanical data of various plastic sealants (PS) resulting from performance related system test.

A comparative test of 4 representative system products from the plastic sealants (PS) category returned a highly differentiated profile featuring a considerable range of varying functionality and in particular varying durability.

Contrary to formal categorisation, the systems PS tested demonstrate a mechanical behaviour, which can be generally designated as temperature-dependent viscoelastic behaviour. Both under slowly progressing deformations (magnitude and progression of intermediate force) and under rapidly repeated dynamic deformations (hysteresis curves with compression and extension forces), a part of the stresses imposed is absorbed by means of dissipation. However, an exceptionally elastic component exists, which on the one hand results in a permanent stress condition under a

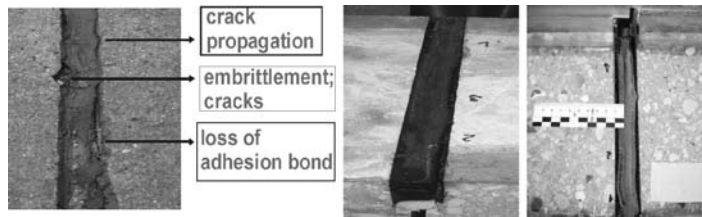


Figure 8. Typical failure profiles in the field (left); after loading in test (right).

static load and on the other, recovers stresses at a proportion of about 60% elastically in the event of dynamic deformations. This signifies that the mechanical categorisation does not captivate the existing system behaviour. Based on the diagrams of characteristic values recorded (Figure 7), it is apparent that the plastic sealants PS 1 to PS 3 are significantly different versus PS 4. The loads from these comparatively rigid products ($k_{A,cycle1}$ between 5.8 and 7.1) signify initial system stiffness E of some 130 to 155 N/mm².

This leads to stress conditions of 0.58 to 0.75 N/mm², whereupon the extension force represents the decisive system load stressing the cohesive and adhesive bond. All plastic sealants tested exhibit the capacity to partly absorb these loads by means of dissipation. As apparent in the shape and slope of the hysteresis curves, the system PS 4 demonstrates generally comparable behaviour, but is adjusted to be considerably softer. In this case, the special material formulation (combination of plastifying and elastifying modifications) has successfully reduced the stiffness and as such the resulting stress conditions – also especially in the sealed surfaces – to nearly one third. This is apparently the reason that the system PS 4 exhibits by far the highest durability of the plastic sealants tested. Only with this system could the formulated durability requirements for the minimum service life be demonstrated to be assured without detrimenting the functionality. The systems PS 2 and PS 3 from this category exhibited a failure in functionality after 3 resp. 4 annual cycles were simulated. The failure type as well as its visualisation detected in the outcome of the system tests demonstrated very positive compliance with the failure states known in practical experiences. The weakness of these systems was the insufficient bond to the neighbouring flanks, which was not of a durable nature.

The system PS 1 showed itself to be generally inappropriate for its intended use. Though the product was able to demonstrate the required deformation capacity over a short term, it was not capable of sustaining the loads over the course of a simulated year. In this case, the loads resulted in failures of the cohesive bond.

The universal applicability of the investigation method is to be demonstrated in the example of a comparative test of various categories of sealant compounds, plastic, elastic and reactive sealants. Based on the analysis of the characteristic mechanical values compared in Figure 9, it follows that the sealants of the type PS and ES cannot – contrary to their categorisation to present – be definitely attributed to the mechanical behaviour stipulated therein in terms of their mechanical behaviour. Rather, in both cases this appears to concern viscoelastic compounds, which exhibit solely a widely varying degree of stiffness (k_A) through various compound modifications. This is reflected in the stress conditions resulting from the deformations. It is shown that the ES sealants are to endure a stress level which is approximately 3 times less. This preserves the cohesive and adhesive bond and lastly results in a considerably longer service life, which was identified in the tests. Both system categories, however, exhibit similar damping properties when subject to dynamic deformation (area contained within the hysteresis curve W_A is equal in size). However, the large difference in stiffness effects that a greater deformation proportion is elastically restored when subject to a dynamic load in the case of the PS sealants than with the ES sealants so that one can even determine a mechanical behaviour opposite to that of the original categorisation. It becomes clear from the tests with respect to the PS systems that the general performance requirements to be evaluated are not fulfilled. In this case, new realistic areas of application must be defined for prolonged practical use. The basis for this may be further tests corresponding to the testing concept presented.

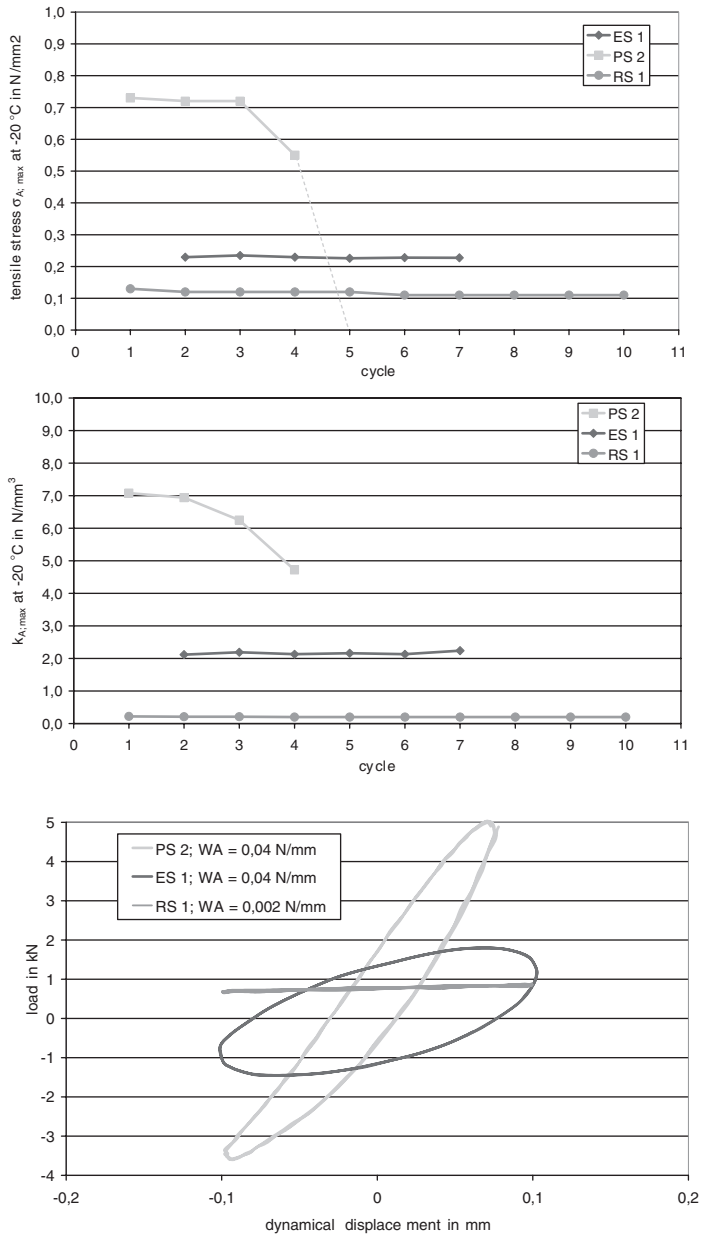
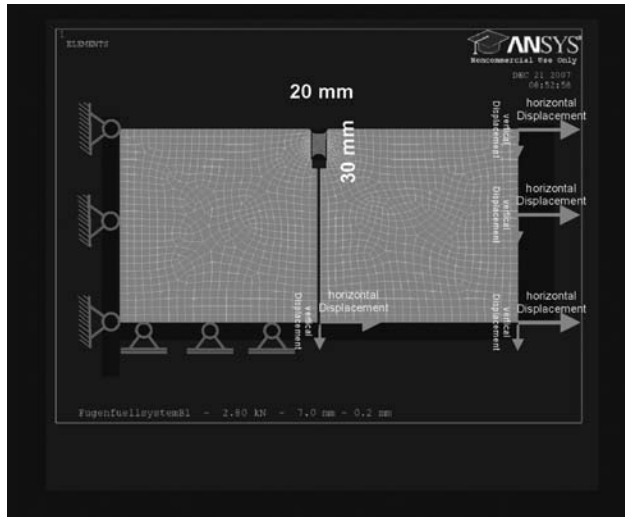


Figure 9. Characteristic mechanical data of several categories of sealants (PS; ES; RS) resulting from performance-related system test.

Compared to the PS and ES sealants discussed above, the RS sealant is the only system to demonstrate authentic elastic behaviour in the outcome of the investigations. Induced stresses are not absorbed (no damping by means of thermal conversion), but are on the basis of the reduced stiffness approximately 5 times less than with PS and even 2 times less than the ES. Force maxima and minima under quasi-static extension and superimposed dynamic extension and compression remain consistently in the tension section so that a permanent tension load prevails. A tension-compression alternate loading is as such not present. In the test, this system demonstrated the highest durability.



Poisson's ratio	Vertical displacement [mm]	Horizontal displacement [mm]	Tensile force in joint [kN]
0,3	7,0	0,2	2,8

Figure 10. Schematic representation of static model and loading parameters for FEM- Analysis of superposed deformations.

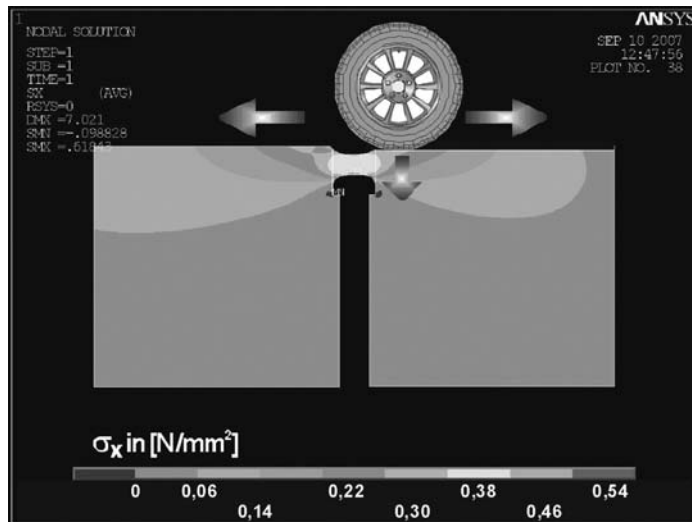


Figure 11. Stress distribution σ_x resulting from superimposed horizontal and vertical deformations for an ES sealant.

However, it is not to be ruled out that mechanical damages to the compound or imperfections especially in the bond area due to the permanent stress condition may result in rapid premature failure.

After the tests have shown that the conceptions to present concerning system behaviour and attributed performance categories have to be revised, a sustained requirement for the review and

evaluation of the design, constructive regulations and those relating to installation exists. On the basis of the characteristic mechanical data collected by means of the investigation method, the possibility now exists of doing so in a simplified initial approach with the assistance of a numerical simulation calculation (FEM analysis).

A current query constitutes for example proving the applicability and durability of ES sealants in zones subject to heavy vehicle traffic (transverse joints). There in addition to horizontal deformations also superimposed vertical deformations act on the system.

Opposite to the previous imaginations according to preliminary results of FEM-calculations, the resulting stress conditions are not significantly influenced even under superimposed horizontal and vertical deformation in comparison to the stress conditions resulting from loads simulated thus far in the new performance tests. This gives reason to evaluate these calculations in further practical system tests under simulated vertical and horizontal loads to clarify the conditions for a broader application of ES sealants.

4 SUMMARY

A newly developed test method of the German Federal Institute for Materials Research and Testing, BAM, has demonstrated its suitability for identifying the different mechanical behaviours of various types of joint filling systems and for differentiating them within the individual product groups. The test progression and failure profiles demonstrate proficient compliance with the occurrences observed in practice. As such, a tool kit exists for performing tests reflecting reality on crack preventative systems under reproducible conditions. Select influential parameters may be tested separately. The method enables the evaluation of constructive and material variations and in particular, provides information for estimating the durability to be expected.

LITERATURE

- [1] Recknagel; Vater; Mühlwinkel
Übersicht zum Stand der Forschung und Technik sowie der nationalen und internationalen Prüfvorschriften zum Alterungsverhalten von Fugenfüllsystemen in Verkehrsflächen [Overview regarding the status of research and engineering as well as the national and international testing regulations for the complex ageing behaviour of joint filling systems in pavements] 1997; Research report 08.146 on behalf of Federal Highway Research Institute; 159 p.
- [2] Al-Qadi, I.L.
Development of performance guidelines for the selection of bituminous hot-poured crack sealants General overview and short report about project TPF 5 (045) of University of Illinois 2007, see: www.ict.uiuc.edu
- [3] Masson; J.-F.
Bituminous Sealants for Pavement Joints and Cracks: Building the Basis for a performance-based Specification
3rd International Symposium on Durability of Building and Construction Sealants, RILEM Proceedings PRO 10, A.T. Wolf Ed. 2000, pp. 315–328.
- [4] Worms, Tanya; Shalaby, ahmed, Kavanagh, leonine
Accelerated Laboratory Evaluation of Joint Sealants under cyclic loads
2005; Paper presented at the “Annual Conference of the Transportation Association of Canada” (16 pages) See: www.tac-atc.ca/English/pdf/conf2005/s15/worms.pdf
- [5] Masson, J.-F., Collins, P.; Bundalo-Perc, S.; Woods, J.R.; Al-Qadi, I.
Variations in the composition and rheology of bituminous crack sealants for pavement maintenance (15 pages)
2005; Transportation Research Board, 84th Annual Meeting, Washington, D.C.
See: <http://irc.nrc-cnrc.gc.ca/ircpubs>

Anti-reflective cracking solutions for asphalt overlays: 8 years performance monitoring

M.L. Antunes & S. Fontul

Laboratório Nacional de Engenharia Civil, Portugal

A.M. Pinelo

Estradas de Portugal, Portugal

ABSTRACT: In Portugal, the advantages of anti-reflective cracking systems have proved to effectively slow down the appearance of cracking in semi-rigid pavements.

In 1997 the Portuguese road administration decided to study the performance of different anti-reflective cracking solutions placed on a damaged flexible pavement. Five different types of anti-reflective cracking solutions were applied on a test pavement and a study was performed by National Laboratory for Civil Engineering (LNEC), including the characterization of the existing pavement, the selection of test sections, the follow up of the construction and a long term performance study initiated after construction.

This paper highlights the main problems associated with the application of the different anti-reflective cracking systems, and presents the results achieved from performance monitoring of the in-service test sections. It was verified that after 8 years of service, the behaviour of test sections with distinct solutions was starting to differentiate.

1 INTRODUCTION

The use of anti-reflective cracking systems together with asphalt overlays has been used as one of the rehabilitation options for damaged asphalt pavements. The advantages of anti-reflective cracking systems for use in semi-rigid pavements have been studied in Portugal, through the performance monitoring of test sections where different solutions were studied (Quaresma, 1992, Quaresma et al 2000). However, the crack pattern of damaged asphalt pavements is quite different from the type of cracking that occurs in cement treated layers.

In 1997 the Portuguese road administration decided to study the performance of different anti-reflective cracking solutions placed on a damaged flexible pavement, through the construction of a test pavement where 5 different types of solutions were applied, resulting in 5 experimental sections for future pavement performance studies. This included a reference solution in which the asphalt overlay was placed without any anti-reflective cracking system.

The construction was followed up by LNEC, who also performed the structural characterization of the overlaid pavement, using FWD, core drilling and GPR tests. A long term performance study was initiated after construction. The monitoring activities comprised visual assessment of the pavement surface, rut depth measurement and FWD tests. At the end of a monitoring period of 8 years, new cores were extracted on selected locations, in order to assess the development of damage through the layers depth.

The following sections give a brief description of the test sections under study, highlight the problems associated with the practical implementation of the anti-reflective cracking techniques. The results from the monitoring activities performed within 8 years after construction are presented and discussed.



Figure 1. Pavement condition before rehabilitation.

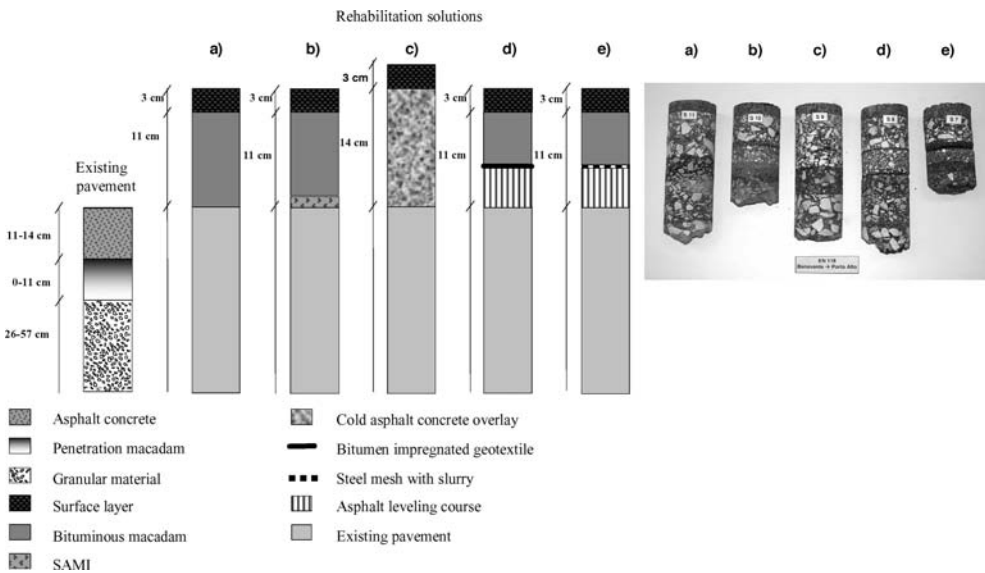


Figure 2. Composition of the existing pavement and rehabilitation solutions studied.

2 REHABILITATION WORKS AND SELECTION OF TEST SECTIONS

The test pavements with different anti-reflective cracking solutions were included in the rehabilitation works of the National Road EN 118, between km 28 + 100 and km 43 + 100. The overlay design was performed considering an equivalent number of 80 kN standard axle loads (ESAL) of 2.3×10^7 , during a design period of 10 years.

A detailed assessment of the pavement condition, together with FWD tests, was performed by LNEC before the rehabilitation works, under the frame of the research program (Antunes et al 2000). Before rehabilitation, the existing asphalt pavement was severely damaged, with extensive cracking, and wheel track rutting in some areas, Figure 1.

The test pavement comprised 5 different types of rehabilitation solutions, including a reference solution in which the asphalt overlay was placed without any anti-reflective cracking system. The composition of each pavement section is presented schematically in Figure 2. This Figure also shows the composition of the existing pavement before rehabilitation.



Figure 3. Details of the application of the geotextile and steel mesh.

Each of the above overlay solutions was applied on minimum extension of 500 m. The surface course was a thin open graded asphalt using modified bitumen, 0.03 m thick, applied throughout the whole extension. The main issues related to the application of the overlay solutions are briefly described below.

- a) *Asphalt Concrete* – This pavement corresponds to the “reference solution”, which includes a conventional asphalt concrete overlay, 0.11 m thick, under the surface course.
- b) *Stress Absorbing Membrane Interlayer (SAMI) with Modified Binder* – this type of solution comprises a thin asphalt layer with nominal thickness of 10 mm, with a very high modified binder content, which is placed between the existing pavement surface and the overlay, in order to delay reflective cracking.
- c) *Cold Asphalt Concrete Overlay* – this solution was selected on the basis that a cold asphalt concrete layer (using bitumen emulsion) would be “more flexible” than conventional hot mix asphalt, and therefore, have a better ability to “absorb” crack movements. Because this material was considered to have lower stiffness than hot mix asphalt, the overlay’s total thickness was higher than for the other types of solutions. Core drilling performed approximately one month after construction showed that, at that time, the cold asphalt was not cured yet, since it was not possible to retrieve a whole core.
- d) *Bitumen Impregnated Geotextile* – this anti-reflective cracking system consists essentially of the application of an abundant tack coat on the surface, followed by the placement of a geotextile (Figure 3a), which is therefore impregnated with the emulsion used in the tack coat. In this case, a modified bituminous emulsion was applied at a rate of 0.5 to 0.8 kg/m². The main issue associated with this technique is that the surface where it is applied must be leveled, and therefore, an asphalt leveling course had to be applied between the existing pavement and the geotextile. The total overlay thickness was kept at 0.11 m including the leveling course, plus 0.03 m surfacing. The practical application of this solution was found to be difficult on curves.
- e) *Steel Mesh with Slurry* – This anti-reflective cracking solution consists essentially on the placement of a steel mesh (“mesh track”, Figure 3b) on the pavement surface, followed by the spreading of a slurry seal at a rate of 17 to 25 kg/m². The slurry seal was produced with a modified bitumen emulsion. In order not to be dragged by the subsequent paving equipment, the end of the mesh is fixed to the surface with studs. As in the previous case, the application of this solution calls for a leveled surface in order to apply the mesh adequately, therefore a leveling course was applied. Apart from being difficult to apply on curves, the practical application of this solution was found to be somewhat labor-intensive.

Using the data collected before rehabilitation concerning visual condition of the existing pavement and FWD deflections, a set of 300 m long stretches that are identified in Table 1, were selected as *test sections* representing each of the solutions under study. The main criteria for selection of these sections was to have, as much as possible, similar initial conditions, in terms of surface

Table 1. Identification of test sections.

Sections	Rehabilitation solution	Remarks
1, 2	Asphalt concrete (reference)	Due to subsequent works, it was not possible to assess the surface condition of the section in 2005
3, 4	SAMI with modified binder	—
5, 6	Cold asphalt concrete overlay	—
7, 8	Bitumen impregnated geotextile	—
9, 10	Steel mesh with slurry	The location of the sections was conditioned by the need to choose a stretch with no sharp bends

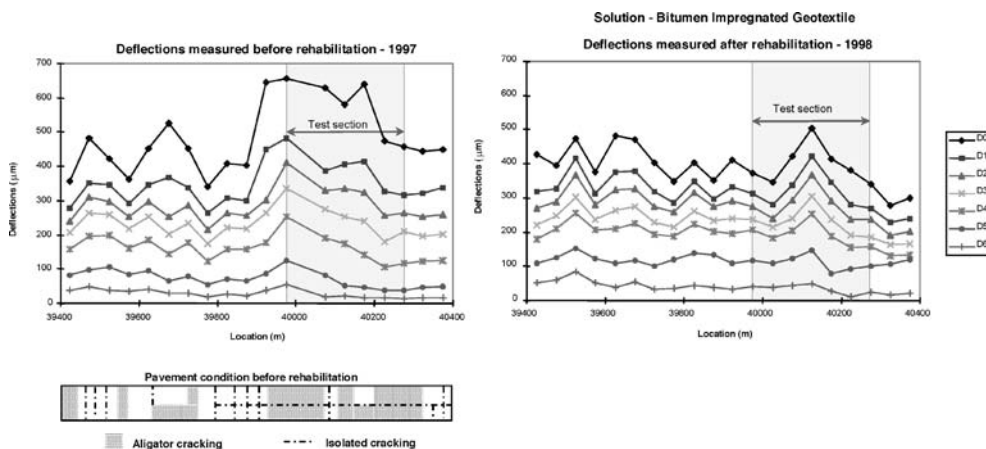


Figure 4. Example of results obtained before and after overlay (section 8: *geotextile*).

condition and deflections, in all test sections. In general, all the test sections were located in areas with severe alligator cracking. Each rehabilitation solution was represented by two test sections, one in each direction. Subsequent monitoring activities were restricted to these test sections.

3 CHARACTERIZATION OF TEST SECTIONS BEFORE AND AFTER REHABILITATION

Following the execution of the rehabilitation works, FWD tests were performed on the test sections. At this point, the improvement of the pavement’s response to the FWD load was expressed by a decrease in the average deflections in all sections, and also a decrease in their variability. In all test sections, the surface had no defects and no deformations.

Ground Penetration Radar (GPR) tests were also performed, in order to determine the overlay thickness. These GPR tests were complemented with core drilling, in order to calibrate the results (Fontul 2004, Fontul et al. 2007). All the cores showed a good condition of the overlay, and a good bond between layers. Exception is made to the cores extracted in the cold asphalt concrete sections, where the cold mixed asphalt could not be retrieved, since the curing process had not been finished yet. The overall conclusion from GPR tests was that the layer thickness had some variations, but it complied with the minimum values specified for the project.

Figure 4 presents an example of the results obtained for test section 8, where bitumen impregnated geotextile was used as anti-reflective cracking system. This Figure shows the pavement condition before overlay (bottom, left side), the FWD deflections measured before (left side) and after (right side) overlay. Figure 5 shows a core and a sample of the GPR output.

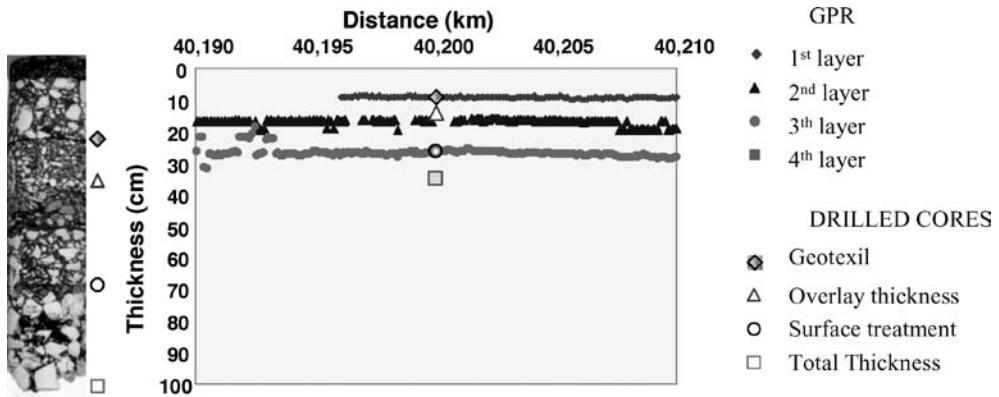


Figure 5. Example of GPR results and core extracted after overlay (section 8: *geotextile*).

Table 2. Layer thickness and backcalculated moduli before and after overlay.

Layer	Hot mix AC ⁽¹⁾	Cold mix AC ⁽²⁾	Existing asphalt	Unbound granular	Subgrade ⁽³⁾
Thickness (m)	4500–6400	2200–2300	1700–3800	260–400	50–75 ⁽⁴⁾
Moduli @20°C (MPa)	0.12–0.16	0.17	0.11–0.18	0.26–0.57	1.70–1.80

AC – Asphalt Concrete;

⁽¹⁾ – Sections 1 to 4 and 7 to 10;

⁽²⁾ – Sections 5 and 6;

⁽³⁾ – Refers to the upper layer of soil. A lower semi-infinite layer with a modulus of 1000 MPa was assumed.

⁽⁴⁾ – Except sections 9 and 10, where the subgrade had a higher moduli of 95 MPa.

Using the layer thickness derived from GPR results and cores and the FWD deflections, the layer moduli of the pavement sections before and after overlay were backcalculated. The results obtained are summarized in the Table above. Typical values for the Poisson's ratio of 0.40 for the soil and 0.35 for the unbound granular and asphalt layers were assumed.

4 PERFORMANCE MONITORING

The performance of the test sections was monitored by LNEC between 1998 and 2005 (Antunes & Fontul 2006), whereby the following activities were performed:

- Visual assessment of surface condition;
- Rut depth measurement in the outer wheel path, at 25 m intervals, using a 3 m straightedge;
- FWD testing in the outer wheel path, at 25 m intervals;
- Coring for assessment of bond between layers and crack development through the asphalt layers.

The visual assessment of the surface condition showed that in 2005, some longitudinal cracks started to show in the surface. The cold asphalt overlay sections were the ones with more cracking and the steel mesh sections had no cracking. However, it must be stressed that this latter sections were set in a better foundation, as already referred in the previous chapter. Apart from the steel mesh sections, the impregnated geotextile sections were the ones that exhibited less cracking.

Cores performed in 2005 on cracked areas showed that these cracks were initiated at the surface, but, in some cases, they were located above an existing crack from the old pavement. The photos shown in Figure 7 illustrate this issue. Another interesting aspect that arised from core drilling



Figure 6. Cores showing crack initiation at the surface and above an existing crack.

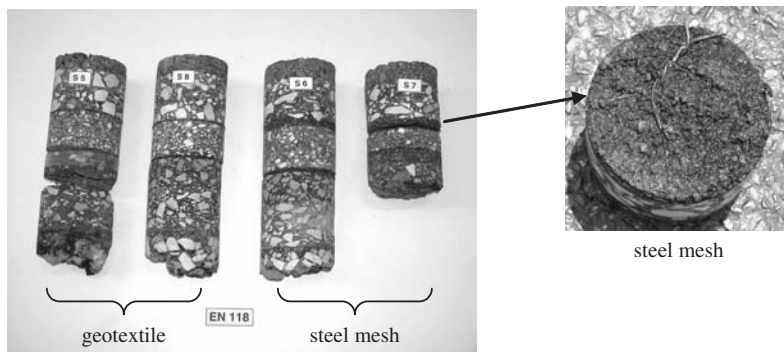


Figure 7. Cores showing bond braking at the interfaces.

in 2005 was that the bond between the layers in the geotextile and the steel mesh interfaces was braking (Figure 8).

The results obtained in the rut depth measurements, were averaged within each section, and they also show some differences between distinct rehabilitation solutions: the steel mesh with slurry had the best performance, and the bitumen impregnated geotextile sections were second best.

Figures 8 and 9 show the results obtained for rut depth and cracking of the test sections, respectively.

The deflections measured with the FWD showed that there was a decrease in the deflections measured in the cold asphalt concrete sections from 1998 to 2001, probably due to the curing of the cold mix asphalt. In general, there was no significant evolution between deflections measured in 2001 and 2005, except for the debonded geotextile and steel mesh sections, where there was an increase in the deflections. This increase was attributed to the lack of bond. In one of the geotextile sections where there was no debonding, the FWD deflections remained similar to the ones obtained in previous occasions.

The backcalculated E moduli for the overlay corresponding to the 1998, 2001 and 2005 FWD tests are presented in Figure 10. For the debonded sections, the overlay was split into two sublayers with the same modulus (above and below the interface) and a partial sleep interface was considered in the backcalculation procedure for the 2005 tests.

Finally, it must be referred that, based on the results from regular traffic counts performed by the Road Administration, the estimated number of 80 kN ESAL that occurred between 1998 and 2005 is around 3×10^7 , which is in the same order of magnitude as the design number of ESAL originally considered for a 10 years design period.

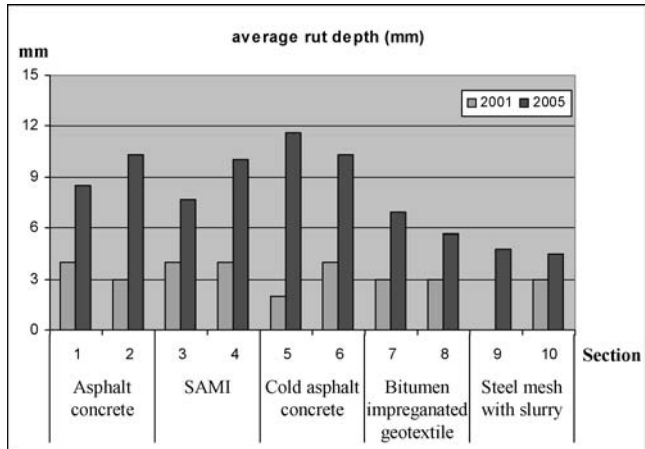


Figure 8. Surface condition per section: average rut depth evolution.

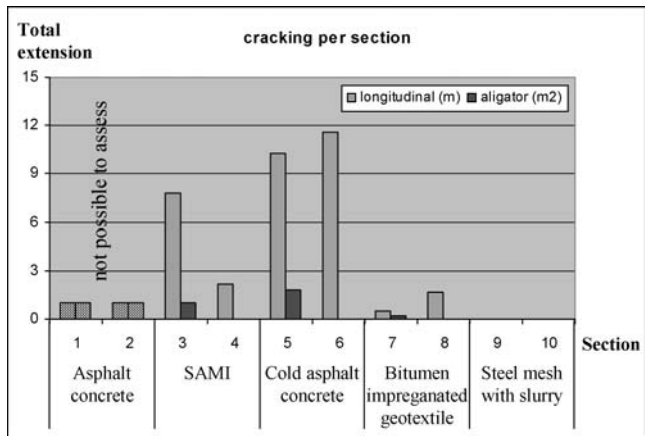


Figure 9. Surface condition per section: cracking in 2005.

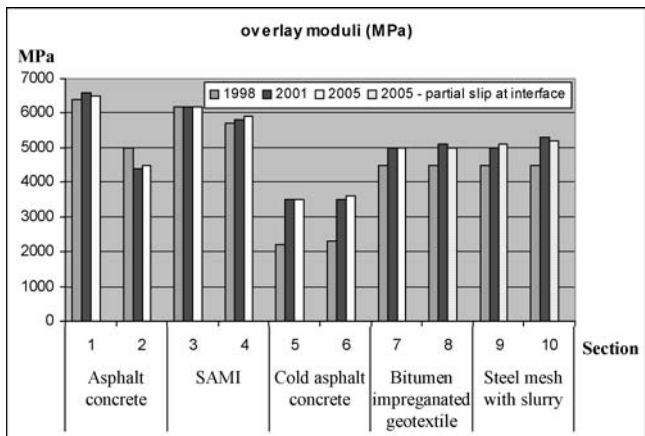


Figure 10. Structural response of the pavement sections during study- overlay moduli.

5 CONCLUSIONS AND FUTURE WORK

This paper presents the results achieved on an experimental study concerning the use of distinct rehabilitation solutions were applied on a deteriorated road pavement. These solutions included a number of distinct anti-reflective cracking techniques, such as SAMI, bitumen impregnated geotextile and steel mesh reinforcement. The use of a cold asphalt overlay was also tested, based on the assumption that a layer with lower stiffness would have a better ability to absorb crack movements.

The performance of the test sections was monitored by LNEC between 1998 and 2005, whereby the evolution of surface condition, rut depth and FWD deflections was assessed. The results from visual assessment of the surface condition and rut depth measurement showed that the section where cracking and rutting was developing faster was the one with the cold asphalt overlay, and the sections with better performance were the ones with bitumen impregnated geotextile and steel mesh reinforcements. The inspection of cores drilled in the test sections showed that the cracking observed was originated at the surface and also, that there was some debonding in the geotextile and steel mesh interfaces. The lack of bond seemed to be reflected in the FWD test results, since only the debonded sections presented an increase in the deflections between 2001 and 2005. The consideration of a partial slip at the debonded interfaces provided a good match between measured and theoretical deflections for the 2005 tests.

The interpretation of the results obtained in this experimental study using advanced analytical models is an interesting topic for future work. Issues such as the surface crack initiation and propagation or the development of rutting at distinct rates on different types of pavement sections can be further exploited with advanced modelling (Antunes 2005). The effect of interface conditions in the development of distresses is also an aspect for consideration.

REFERENCES

- Antunes, M.L. 2005. Advanced modelling of flexible pavements behaviour. Research Program for Research Coordination Degree. *LNEC Portugal*. (in Portuguese)
- Antunes, M.L. & Fontul, S. 2006. Anti-reflective cracking techniques for overlay of cracked flexible pavements . Test sections constructed at the EN 118 (km 28 + 100 to km 43 + 100), Final Report. *LNEC 255/06 Portugal*. (in Portuguese)
- Antunes, M.L., Fontul, S. & Pinelo, A. 2000. Anti-reflective cracking techniques for overlay of cracked flexible pavements. *CARRETERAS* 110, 53–68. (in Spanish)
- Fontul, S. 2004. Structural evaluation of flexible pavements using non-destructive tests. Ph.D. thesis. *University of Coimbra*, Portugal.
- Fontul, S., Antunes, M.L., Fortunato E. & Oliveira M. 2007. Practical application of GPR in transport infrastructure survey". *International Conference on Advanced Characterisation of Pavement and Soil Engineering Materials*, Athens, Greece.
- Quaresma, L.M. 1992 – Performance and modelling of a geotextile reinforced embankment constructed over soft soils. Thesis, *LNEC* (in Portuguese)
- Quaresma, L.M., Pinelo, A. & Fonseca, M.E. 2000 – Performance of road trials to prevent reflective cracking, *4th International RILEM Conference and Exhibition Reflective Cracking in Pavements*. Ottawa, Canada.

12. Field investigation of pavement cracking

Development of reflective cracking index to determine the effectiveness and service life of strip interlayer systems

I.L. Al-Qadi, J. Baek & W.G. Buttlar

University of Illinois at Urbana-Champaign, Urbana, Illinois, USA

ABSTRACT: A field crack survey and a forensic investigation as a part of interlayer assessment were conducted to evaluate the effectiveness of three strip interlayer systems applied in Illinois. Field coring revealed that reflective cracking may not always be located above a joint or an existing crack, but it is affected by the interlayer system used, bonding, and the overlay mixture characteristics. Cumulative transverse reflective crack data have been collected by visual survey over several years after overlay construction. Based on weighted reflective crack rate and considering crack extent and severity, a reflective crack index (RCI) is proposed to assess the efficiency and cost-effectiveness of an interlayer system. Among the interlayer systems, the interlayer stress absorbing composite (ISAC) system showed the best performance of the systems investigated in terms of the proposed RCI parameter and predicted service life. The other strip reflective crack control systems investigated showed some benefit in reducing reflective cracking amount and severity early in the overlay life.

1 INTRODUCTION

Although hot-mix asphalt (HMA) overlays are an effective rehabilitation strategy, their longevity is reduced as a result of reflective cracking. Discontinuities in existing pavements, such as joints, cracks, and/or patches, induce reflective cracking relatively early in the service life of the overlay (McDaniel and Bahia 2003, Zhou and Lijun 2002). Among several techniques to retard reflective cracking, interlayer systems have been widely used in the United States (Cleveland *et al.* 2002, Al-Qadi and Elseifi 2004). Various interlayer materials have been used as interlayer systems, including the following: Geosynthetics, geocomposite, steel reinforcement netting, and modified HMA. Interlayer system performance has been evaluated by field crack surveys, laboratory testing, accelerated pavement testing, and numerical analyses (Buttlar *et al.* 2000, Brown *et al.* 2001, Dempsey 2002, Zhou *et al.* 2004, Titi *et al.* 2003, Elseifi and Al-Qadi 2005). However, interlayer system effectiveness is still not well quantified due to a lack of understanding of the reflective cracking mechanism and because imperfect evaluation approaches are used. Life-cycle cost analysis (LCCA), supported by appropriate agency and user cost data, can be used to evaluate the cost-effectiveness of interlayer systems. This study introduces an interlayer system assessment approach and proposes a proper index that can be used to evaluate the cost-effectiveness of interlayer systems.

2 INTEGRATED INTERLAYER ASSESSMENT SYSTEM

The evaluation of interlayer system effectiveness requires an integrated method to understand the mechanism of reflective cracking and interlayer system effectiveness, collect field performance data, investigate various field conditions, and assess the cost-effectiveness. In an ongoing project sponsored by the Illinois Center for Transportation, a method to assess an interlayer assessment system has been developed by integrating four parts: field crack surveying, forensic investigation, numerical modeling, and life-cycle cost analysis (Figure 1). Based on preliminary results from

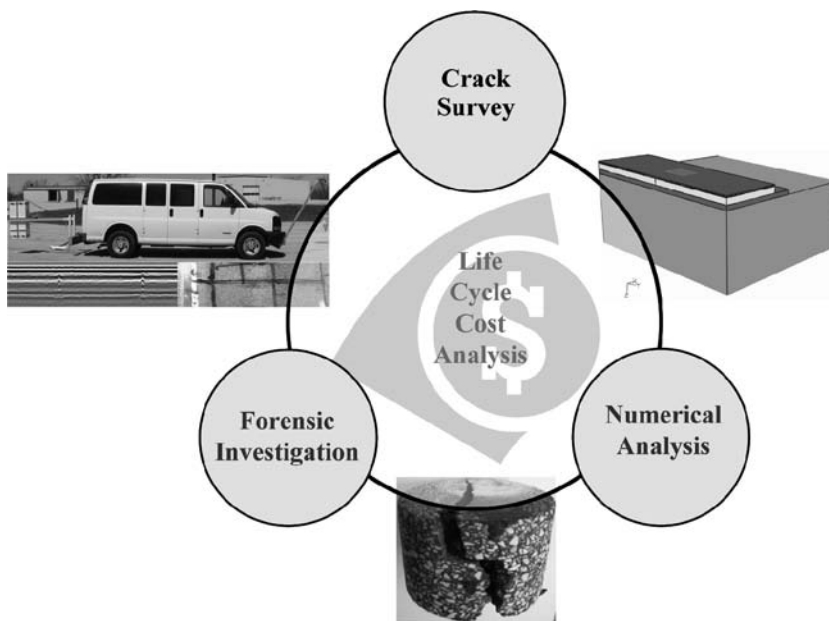


Figure 1. Integrated interlayer assessment system.

field crack surveys and forensic investigations, the interlayer assessment method is introduced in this study.

2.1 *Field crack survey*

To evaluate the performance of interlayer systems, pavement distress survey were conducted both visually (walking surveys) and using van-mounted video survey equipment. Transverse and longitudinal reflective cracking were the main distresses monitored in this study. Crack severity and extent were both collected. In order to distinguish reflective cracks from other types of transverse cracks, ground penetrating radar (GPR) was utilized to locate joints/cracks patches on pre-existing pavements. The GPR was also used to locate strip-type interlayer systems and to measure pavement layer thicknesses. The integrated GPR and video system used also provided safe and rapid reflective cracking surveys.

2.2 *Forensic investigation*

Field coring and laboratory testing was also used to better understand the mechanisms behind various reflective crack patterns observed in the field, such as crack offsetting and debonding, and to provide material and interface properties for numerical modeling. Four laboratory tests were utilized: Creep compliance (AASHTO T-322), complex modulus, fracture energy (ASTM D7313-06), interface shear strength; and permeability. Permeability testing was conducted on cores taken directly over reflective cracks, so that the retained waterproofing benefit of the interlayer system could be quantified.

2.3 *Numerical modeling*

Numerical modeling was used to identify the main factors affecting HMA overlay performance and the interaction between interlayer systems and overlays. Numerical modeling considered various overlay design parameters and field conditions such as overlay thickness, interlayer types, traffic, and climate. Using numerical analysis, reflective crack initiation and propagation mechanisms were

investigated. For instance, modeling was used to gain a better understanding of a crack offsetting phenomenon observed in the field, where cracks were found to propagate upwards from the edge of the strip reflective crack control treatment rather than directly over the existing PCC joint. A detailed description of the modeling performed is beyond the scope of this paper.

2.4 *Life-cycle cost analysis*

A rigorous life-cycle cost analysis will be performed using the data collected in this study, with the overall goal of evaluating the cost effectiveness of reflective crack control systems used in Illinois. Results from the aforementioned steps will also be used to develop a guide to assist pavement engineers in the selection of interlayer system to control reflective cracking, and will provide guidelines for optimized overlay thickness design and proper installation techniques.

3 FIELD TESTING

3.1 *Section descriptions*

Of the twenty-eight sites monitored as part of this study, two sections, Mattis Avenue in Champaign, Illinois and IL29 in Creve Coeur, Illinois were selected for detailed analysis in this paper. In these sections, three strip-type interlayers were installed on similar existing jointed concrete pavements (JCP) within the same climatic zone. Field crack surveys were conducted to monitor reflective cracks.

3.1.1 *Mattis Avenue: Champaign, Illinois*

Mattis Avenue, Champaign, Illinois has been the subject of reflective cracking studies since 2001. The original roadway is jointed plain concrete pavement (JPCP), which was constructed in 1966. The pavement received an HMA overlay in 2000. The length of resurfacing is 1.5 km between Kirby Avenue (STA. 5 + 00) and Springfield Avenue (STA. 53 + 83) in Champaign (Figure 2(a)). The overlay consists of 79-mm HMA (41-mm wearing surface and 38-mm leveling binder). Reflective cracking control interlayer system A strips were applied on northbound (STA. 5 + 00 to 9 + 00); system B strips were applied on southbound (9 + 00 to 35 + 00); and Interlayer Stress Absorbing Composite (ISAC) strips, which have a sandwich composition with asphalt binder between strong and soft geosynthetics, were applied on northbound (STA. 5 + 00 to 53 + 83) and southbound (STA. 35 + 00 to 53 + 83). System A is non-woven reinforcing fabric with a hot-asphalt binder; system B is a self-adhesive interlayer easy to attach to overlays (Buttler *et al.* 2000). An annual average daily traffic (AADT) of 15,000 with average daily truck traffic (ADTT) of 200 was reported in 2003.

3.1.2 *IL29, Creve Coeur, Illinois*

The second pavement section investigated is located on IL29 at Creve Coeur in Tazewell County, Illinois (Figure 2(b)). The existing pavement consists of six-lanes of jointed reinforced concrete pavement with 15-m joint spacing. This section was rehabilitated with a 57-mm-thick HMA overlay in 1997. The extent of resurfacing was 667m including on/off ramps of I-474 (STA. 7 + 470 to 7 + 800). The HMA overlay consists of 25 mm of wearing surface and 32 mm of leveling binder (Figure 2(b)). Two strip-type reflective control interlayer systems, ISAC and system B, were applied on the two inner lanes; and an unidentified area-type interlayer system was applied in the four outer lanes. Eleven ISAC and thirteen system B strips were installed over the joints. An AADT of 28900 was reported in 2003.

3.2 *Crack survey*

The quantity and severity of reflective cracks have been monitored by Illinois department of transportation since 2001 and 2000 for the sections on Mattis Avenue and IL29, respectively. The extent of the cracks was also recorded in 2006 and 2007 as part of this study. Crack severity is classified

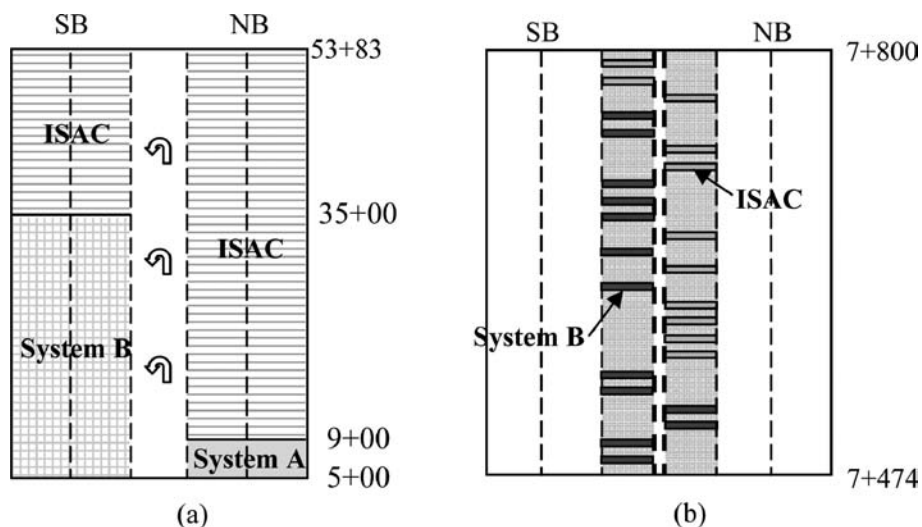


Figure 2. Section layout and pavement cross section: (a) Mattis Avenue and (b) IL29 Creve Coeur.

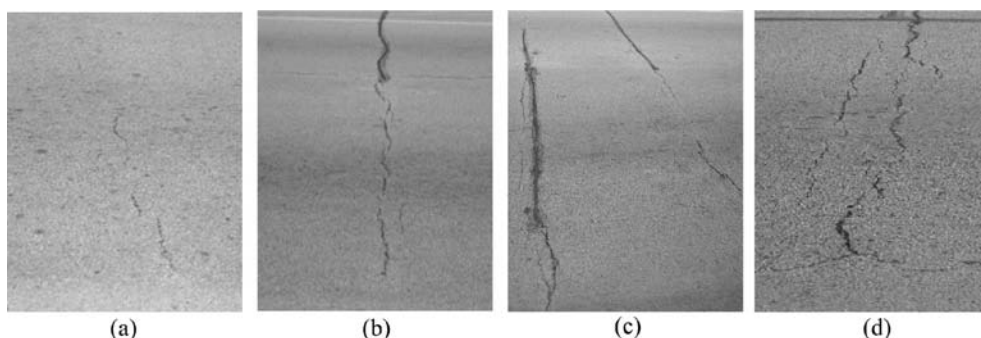


Figure 3. Crack type and severity (Mattis Avenue): (a) starting level, (b) sealed (upper) and unsealed (lower) low level; (c) sealed (left) and unsealed (right) medium level; and (d) high-level double reflective crack.

into four levels: starting, low, medium, and high based on the FHWA distress manual (Miller and Bellinger 2003). Figure 3 shows typical cracks in the Mattis Avenue section. The width of the starting-severity-level cracks (Figure 3(a)) was reported as 'hairline,' and had a length of less than 0.3 m. Most starting-severity-level cracks observed in this survey were located either under the wheel path or at lane edges. Two typical low-severity-level cracks are shown in Figure 3(b), with an average width of less than 6 mm; a portion of the crack had been routed and sealed. Routed and sealed cracks are considered low-severity when the seal is in good condition, and when no adjacent cracks exist. Figure 3(c) illustrates medium-severity-level reflective cracks, having a crack width between 6 mm and 19 mm. High-severity-level cracks either have a width greater than 19 mm or are adjacent to medium and/or high severity level cracks. Figure 3(d) shows high-severity level, double reflective cracking, which is sometimes referred to as band cracking. Visual surveys depend highly on environmental conditions, including angle and amount of sunlight, direction of survey, and ambient temperature.

3.3 Forensic investigation

Reflective crack paths and locations relative to PCC joints were investigated in selected areas via field coring. Reflective crack offset from the joint were noted at several coring locations. Figure 4

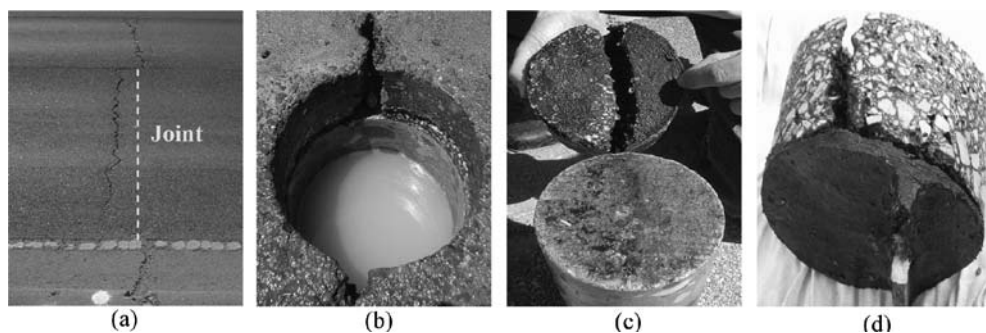


Figure 4. Reflective crack offset from a joint with strip interlayer: (a) reflective crack in southbound in IL29; (b) a core through the reflective crack; (c) a core with system B strip interlayer; and (d) debonding and reflective crack offset at Mattis Avenue.

shows a reflective crack, which was found to be offset from the PCC joint. In addition, the strip interlayer systems were found to be debonded at some locations, with cracks propagating upwards from the edge of the interlayer. These observations, made at both pavement sites, reinforce the importance of proper installation of interlayer systems. On the other hand, figure 4(d) shows a much smaller reflective cracking offset, this time 3 cm away from the PCC joint.

4 EVALUATION OF INTERLAYER SYSTEMS

4.1 *Reflective cracking index*

4.1.1 *Crack extent and severity*

Traditionally, interlayer system effectiveness has been assessed using measuring crack density, which is the number or length of cracks per unit length. The crack density approach has two main drawbacks. First of all, crack density may include other forms of transverse cracks, such as thermal cracking. For explicit evaluation of the ability of interlayer systems to resist reflective cracking, the location of joints, cracks, and or patches is needed to isolate reflective cracking from other forms of cracking. In the case of strip interlayer systems, it is appropriate to assume that all transverse cracks developed in the vicinity of underlying joints and cracks as reflective cracks.

The second drawback of the crack density approach is the exclusion of crack severity. Crack severity distributions in 2004 and 2007 at Mattis Avenue are compared in Figure 5. For system A, the total number of reflective cracks per 30 m in 2004 is similar to that in 2007. According to this approach, the overlay condition is similar. However, the majority of the cracks in 2004 were at the low-severity level; while medium-severity-level cracks were predominantly present in 2007. This suggests the need to develop an index which considers both crack extent and severity. The development of such an index is presented in the following section.

4.1.2 *Reflective cracking index*

A proposed reflective cracking index, reflective crack appearance ratio, R_{RCA} , calculates the average number of reflective cracks per joint/crack/patch (Baek et al. 2008). Adjacent or secondary reflective cracks are counted as one crack; while a patch with two discontinuities at its edges are counted as two. The upper limit of R_{RCA} , 1.0, means that reflective cracks occur at all joints. Figure 6 shows the comparison of R_{RCA} for the sections incorporating systems A, B, and ISAC on Mattis Avenue and for the sections incorporating system B and ISAC on IL29 Creve Coeur. For the section with system A on Mattis Avenue and for the section with system B on IL29 Creve Coeur, the R_{RCA} values reach the upper limit four years after overlay construction. Thus, R_{RCA} itself is inadequate to analyze the status of reflective cracking after a high degree of reflective cracking deterioration.

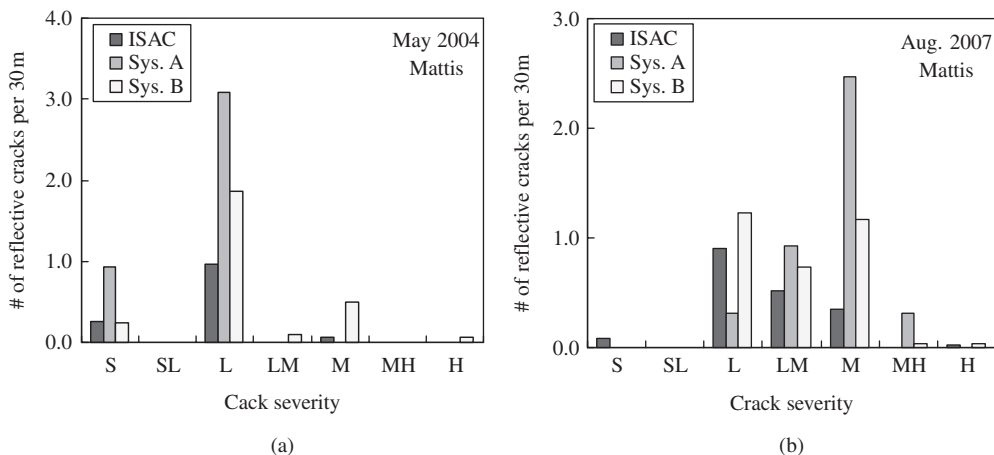


Figure 5. Reflective crack severity distributions in Mattis Ave.: (a) 2004 and (b) 2007.

Crack severity is added to R_{RCA} by means of a weighted function. The weighted function was determined from the Illinois condition rating system (CRS) value, which is computed from individual distress and is used to evaluate overall serviceability. Weighted reflective crack appearance ratio, R_{RCAW} , is obtained as follows (Baek *et al.* 2008):

$$R_{RCAW} = \frac{\sum_{i=1}^4 [W_i \times (N_{RC})_i]}{N_j} \quad (1)$$

where, R_{RCAW} = weighted reflective cracking appearance ratio; W_i = coefficient of a weight function for i th crack severity level (0.75, 1.5, 2.25, and 3.0 for starting-, low-, medium-, and high-severity level, respectively); $(N_{RC})_i$ = total number of i th severity reflective cracks; and N_j = total number of joints, patches, and existing cracks.

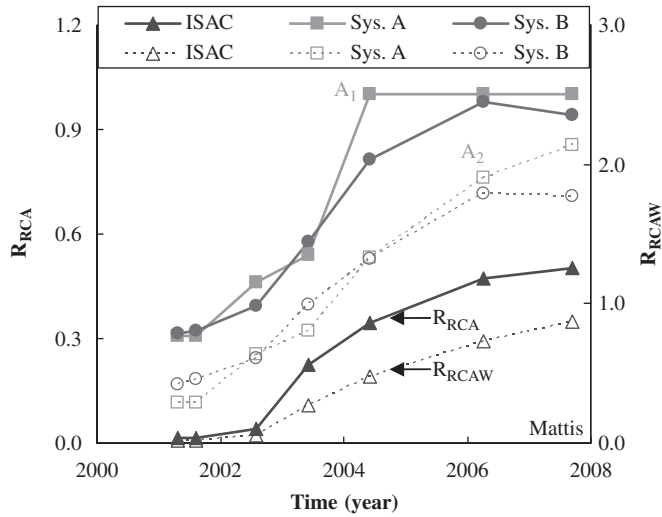
For $W_i = 1$, R_{RCAW} is identical to R_{RCA} , indicating uniform reflective cracking severity. However, R_{RCAW} is greater than R_{RCA} as the severity of reflective cracks increases. R_{RCA} and R_{RCAW} trends vary over time (Figure 6). While R_{RCAW} (curve A_2 in Figure 6(a)) has continued to increase on Mattis Avenue, R_{RCA} (curve A_1 in Figure 6(a)) has remained 1.0 since 2004. From both indices, R_{RCA} and R_{RCAW} , it can be observed that the extent of low-severity-level reflective cracks increased until four years; and after that, high-severity-level reflective cracks appeared. Similarly, the trends of curves B1 and B2 occur in Figure 6(b).

To quantify reflective cracking in a more convenient form, a reflective crack index (RCI) based on weighted reflective crack appearance ratio is proposed as follows:

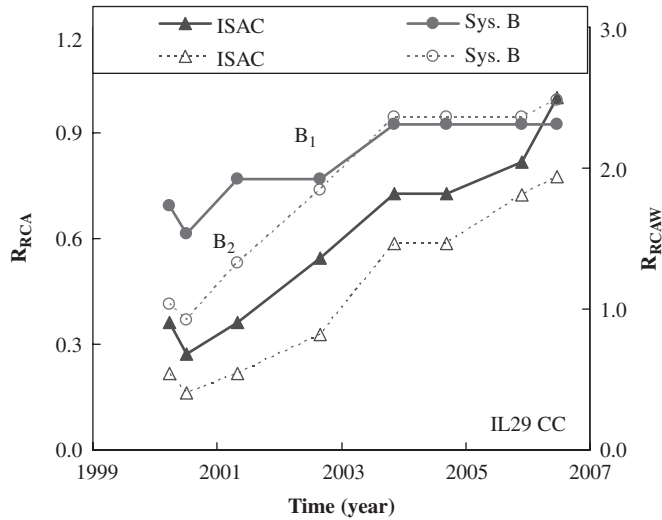
$$RCI = 100 - A_d \times R_{RCAW} = 100 \left(1 - \frac{R_{RCAW}}{3} \right) \quad (2)$$

where, A_d = a scale factor to adjust maximum RCI to 100.

The value of RCI ranges from 100 (no reflective cracks) to 0 (high-severity-level reflective cracks at every joint). Figure 7 presents the RCI variation with time for all interlayer systems at Mattis Avenue and IL29 Creve Coeur. Based on interlayer system types and pavement sections, RCIs decline at various rates. Using a simple linear regression model, the slope of RCI curve (RCI changing rate) can be determined. The regression curves show a goodness of fit for all interlayer systems at $R^2 > 0.9$. If RCI of 50 is assumed as a trigger value for reflective cracking repair; then the repair year for interlayer systems are 12.0 years and 7.3 years for the ISAC on Mattis Avenue and IL29 Creve Coeur, respectively; 4.5 years for the system A; and 4.9 years and 4.8 years for the



(a)



(b)

Figure 6. Reflective cracking appearance ratio over time with (bold) and without (dot) a weight function: (a) Mattis Avenue and (b) IL29 Creve Coeur.

system B on Mattis Avenue and IL29 Creve Coeur, respectively. Based on the repair year of the ISAC, the relative benefit of the ISAC system to the system B is 147% and 53%, on Mattis Avenue and IL29 Creve Coeur, respectively. The RCI estimated from uniform reflective crack appearance ratio ('x' symbols on Figure 7) shows an unreasonable trend (no degradation) after only 3.6 years of overlay construction. This supports the notion that crack severity should be considered in the analysis of reflective cracking.

4.2 Evaluation of interlayer systems

Analysis of variance (ANOVA) was performed on the RCI parameter to statistically examine the differences between interlayer systems. The p-values comparing the mean RCI for ISAC and

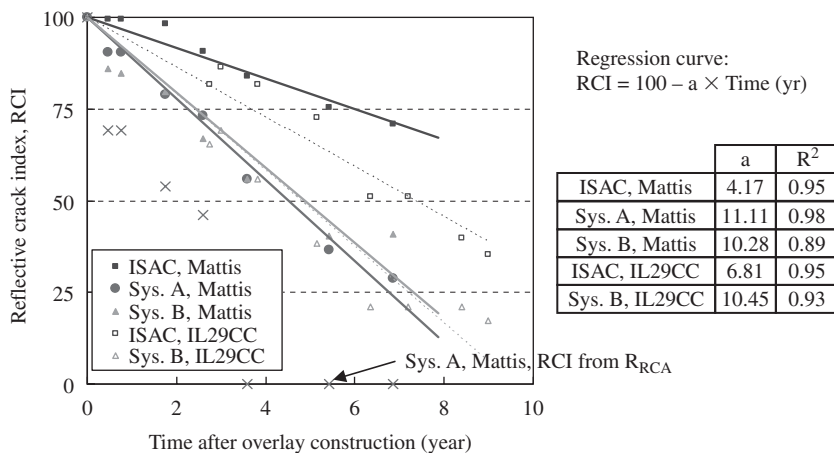


Figure 7. Reflective crack index (RCI) variations over time for the interlayer systems.

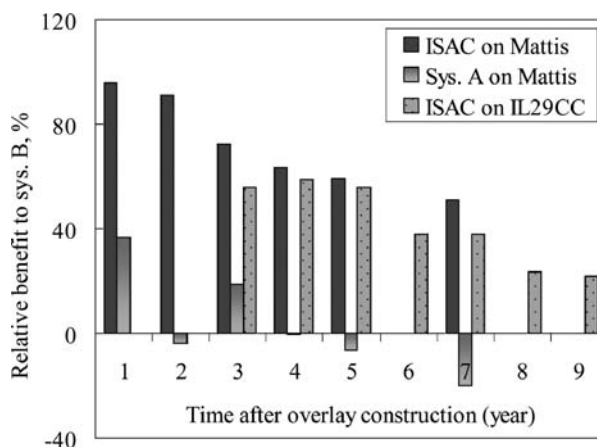


Figure 8. Relative benefits of interlayer systems compared to system B.

systems A and B on Mattis Avenue were 4.3% and 1.9%, respectively. For Creve Coeur, the p-value between the RCI values for ISAC and system B was 4.1%. In both cases, the RCI and, therefore, overlay performance was significantly better in the ISAC treated areas. On the other hand, the p-value of the mean RCIs for systems A and B on Mattis Ave. is 99.4%, indicating no significant difference between the two systems.

Figure 8 illustrates the relative benefit of ISAC and system A as compared to system B, using the R_{RCAW} parameter. In the case of ISAC, the relative benefit as compared to system B decreases with time, but even in the long term, it maintains a greater performance. At Mattis Avenue, after seven years, R_{RCAW} is 50% higher than system B, and for Creve Coeur, 21% higher even after nine years. On the contrary, system A shows some benefit at the beginning of the overlay life; but after four years, the benefit is less than system B. Overall, comparable performance is observed in systems A and B.

5 SUMMARY

The main purpose of the paper is to develop a method which is able to quantify the effectiveness of interlayer systems used in HMA overlays to retard reflective cracking. Field crack surveys

and forensic investigations on two sites, Mattis Avenue and IL29 Creve Coeur in Illinois, were conducted to investigate the effectiveness of three types of interlayer systems. It was often observed that reflective cracks were shifted from a PCC joint and developed from either an edge of a strip interlayer or at a distance from the joint due to possible debonding; which was clearly noted during the coring process.

This study proposes a reflective crack index (RCI) to evaluate the status of reflective cracking using a weighted reflective crack appearance ratio, R_{RCAW} in which reflective crack severity and extent are considered. Using the RCI, the effectiveness of interlayer systems was quantified and compared to the performance of interlayer system B. A total of 12.0 and 7.3 years were required for the RCI value to be reduced by 50% (the rehabilitation trigger level) when ISAC was used in pavement sections at Mattis Avenue and IL29 Creve Coeur, respectively. However, just under five years were required to reach the rehabilitation trigger level when other interlayer systems were used. This study concludes that for the three interlayer systems investigated, ISAC shows better performance and a potential to significantly increase the overlay service life against reflective cracking distress. However, since ISAC generally has a higher per unit length cost than the other systems investigated, a full life-cycle cost analysis will be required in order to fully assess the cost effectiveness of these systems.

ACKNOWLEDGMENTS

This publication is based on the preliminary results of ICT-R58, *Cost-Effectiveness and Performance of Overlay Systems in Illinois*. ICT-R58 is conducted in cooperation with the Illinois Center for Transportation and the Illinois Department of Transportation. The authors would like to acknowledge Joseph Vespa's support of the overlay systems research and the assistance of the following members of the Technical Review Panel for ICT-R58: Amy Schutzbach, David Lippert, James Trepanier, Aaron T. Toliver, and Patty Broers. The contents of this paper reflect the view of the authors, who are responsible for the facts and the accuracy of the data presented herein. The contents do not necessarily reflect the official views or policies of the Illinois Center for Transportation and the Illinois Department of Transportation. This paper does not constitute a standard, specification, or regulation. Trademark or manufacturers' names appear in this paper only because they are considered essential to the object of this document and do not constitute an endorsement of product by the Illinois Center for Transportation or the Illinois Department of Transportation.

REFERENCES

- Al-Qadi, I. L., and M. A. Elseifi. Field Installation and Design Considerations of Steel Reinforcing Netting to Reduce Reflection of Cracks. *Proceedings pro37: Cracking in Pavements: Mitigation, Risk Assessment and Prevention*. C. Petit, I. L. Al-Qadi, and A. Millien, Eds., Limoges, France, May 5–7, 2004, pp. 97–104.
- Cleveland, G. S., J. W. Button, and R. L. Lytton. *Geosynthetics in Flexible and Rigid Pavement Overlay Systems to Reduce Reflection Cracking*, Publication FHWA/TX-02/1777-1, FHWA, U.S. Department of Pavement, 2002.
- Baek, J., I.L. Al-Qadi, W. Xie, and W. G. Buttlar, In-Situ Assessment of Interlayer Systems to Abate Reflective Cracking in Hot-Mix Asphalt Overlays, . In *Transportation Research Record: Journal of the Transportation Research Board*, TRB, National Research Council, Washington, D.C., 2008.
- Brown, S. F., N. H. Thom, and P. J. Sanders. A Study of Grid Reinforced Asphalt to Combat Reflection Cracking. *Journal of Association of Asphalt Paving Technologists*, Vol. 73, 2001, pp. 543–571.
- Buttlar, W. G., D. Bozkurt, and B. J. Dempsey. Cost-Effectiveness of Paving Fabrics Used to Control Reflective Cracking. In *Transportation Research Record: Journal of the Transportation Research Board*, No. 1730, TRB, National Research Council, Washington, D.C., 2000, pp. 139–149.
- Dempsey, B. J. Development and Performance of Interlayer Stress Absorbing Composite in Asphalt Concrete Overlays. In *Transportation Research Record: Journal of the Transportation Research Board*, No. 1809, TRB, National Research Council, Washington, D.C., 2002, pp. 175–183.
- Elseifi, M. A., and I. L. Al-Qadi. Modeling of Strain Energy Absorbers for Rehabilitated Cracked Flexible Pavements. *Journal of Transportation Engineering*, Vol. 131, No. 9, 2005, pp. 653–661.

- McDaniel, R. S., and H. U. Bahia. Field Evaluation of Asphalt Additives to Control Rutting and Cracking. In *Transportation Research Record: Journal of the Transportation Research Board, No. 1853*, TRB, National Research Council, Washington, D.C., 2003, pp. 13–20.
- Miller, J. S., and W. Y. Bellinger. *Distress Identification Manual for the Long-term Pavement Performance Program (Fourth Revised Edition)*. Publication FHWA-RD-03-031, FHWA, U.S. Department of Transportation, 2003.
- Titi, H., M. Rasoulian, M. Martinez, B. Becnel, and G. Keel. Long-Term Performance of Stone Interlayer Pavement. *Journal of Transportation Engineering*, Vol. 129. Issue 2, 2003, pp. 118–126.
- Zhou, F., D. Chen, T. Scullion, and R. Williammee. Overlay Tester: a Simple Test to Evaluate the Reflective Cracking Resistance of Asphalt Mixtures. *Proceedings pro37: Cracking in Pavements: Mitigation, Risk Assessment and Prevention*. C. Petit, I. L. Al-Qadi, and A. Millien, Eds., Limoges, France, May 5–7, 2004, pp. 597–604.
- Zhou, F., and S. Lijun. Reflective Cracking in Asphalt Overlay on Existing PCC. *Proceedings of the Ninth International Conference on Design of Asphalt Pavements*. CD-ROM. Copenhagen, Denmark, 2002.

The use of digital image correlation for accurate determination of fracture energy density in Hot Mix Asphalt (HMA)

B. Birgisson

KTH, Royal Institute of Technology, Stockholm, Sweden

A. Montepara, E. Romeo, R. Roncella & G. Tebaldi

University of Parma, Italy

R. Roque

University of Florida, Gainesville, Florida, USA

ABSTRACT: Knowledge of the conditions governing the initiation and propagation of cracks in Hot Mix Asphalt (HMA) mixtures is a prerequisite for a comprehensive understanding of HMA cracking mechanisms. According to the “HMA Fracture Mechanics” pavement cracking model recently developed at the University of Florida, fundamental tensile failure limits of mixtures (fracture energy density and tensile strength) are identified as key parameters in defining the cracking resistance of HMA mixes.

A Digital Image Correlation (DIC) system, developed for the purpose of investigating the cracking behavior of HMA mixtures, has been applied to accurately determine fundamental tensile failure limits of SBS polymer modified mixes. The effect of modification on crack localization and crack growth was also investigated. One unmodified and four SBS polymer modified HMA mixes were tested performing both the Superpave IDT test and the Semi-Circular Bending (SCB) test. Tensile failure limits and cracking behavior of two of these mixes (the unmodified and a heavily SBS linear modified) were evaluated also from the Three Point Bending Beam (3PB) test. Full field strain maps indicate that the addition of SBS polymers in mixtures leads to more homogeneous stress states during tensile loading condition, resulting in high strains strongly localized up to the location of impending fracture.

1 INTRODUCTION

Knowledge of the conditions governing the initiation and propagation of cracks in Hot Mix Asphalt (HMA) mixtures is a prerequisite for a comprehensive understanding of asphalt pavement cracking mechanisms. In the last decades, several research efforts have been focused on the development of a reliable system to determine mixture’s resistance to crack development and propagation (1,2,3). A pavement cracking model developed by Zhang and Roque (4,1) has introduced the concept of a threshold as a failure criterion for the initiation and propagation of cracks. Based on this framework, two HMA tensile failure limits (namely the tensile strength and the fracture energy density) were found to be fundamental HMA properties, independent of specimen geometry and test configuration and not affected by polymer modification (5,6).

However, the evaluation of these fundamental HMA material properties rests on the accuracy of displacement and strain measurements.

The most common fracture tests performed on asphalt mixture specimens employ on-specimen mechanical strain measurement techniques (e.g. strain gauges and LVDTs). These devices are

simple to use, but their drawback is not being capable of accurately capturing localized or non-uniform strain distributions, thus not allowing for true point-wise analyses of a strain field. This prevents the exact determination of the important location of crack initiation, not easily allowing the determination of the strain values at the instance and location of which a crack initiates. Traditional on-specimen strain measurement techniques also do not provide flexibility, because the measurement location must be decided prior to the test. This precludes the possibility of a “back analysis” of the resulting strain field over an area of finite extent, and, above all, does not capture full field displacement/strain measurements in the specimen. In comparison, the detection of crack initiation in HMA specimens is simplified by field measurements of deformation over an area of finite extent, since typically cracks appear in somewhat non predictable locations.

During the last decade, several types of full deformation field measurement techniques have been proposed for composite material characterization (7). Since the advent of target location in digital or digitized images (8), alternatives based on analogue photogrammetry and vision metrology have also become viable (9). Digital image correlation was proposed in the 1980's (10,11,12) as an automated approach for the computation of surface strains and displacements. It was later advanced to study 2-D solid mechanics problems, being successfully applied to determine strains in specimens of resin films (13), fiber reinforced polymer composites (14,15), and concrete (16). Previous works conducted by Seo and Chehab (17,18) have successfully applied a Digital Image Correlation (DIC) technique to investigate asphalt mixture's fracture process zone at the crack tip as well as to extend the performance prediction of mixes to the postpeak region.

Recently, a system for non-contact and full strain field measurement was developed at the University of Parma (19,20) for the purpose of investigating the cracking behavior of hot mix asphalt mixtures (HMA). The DIC system has shown to overcome the shortcomings of traditional on-specimen strain measurement devices, achieving satisfactory accuracy compared to strain gauges. Furthermore, the new image correlation system has been proved of providing point-wise analysis, allowing for the exact determination of the location of crack initiation, and also for the calculation of strain values at the instance of crack initiation (6,20).

In this paper, the DIC technique was applied to accurately determine fundamental tensile failure limits of polymer modified HMA mixes. The effect of modification on crack localization and crack growth was also investigated. One unmodified and four SBS polymer modified HMA mixes were tested performing both the Superpave IDT test and the Semi-Circular Bending (SCB) test. Tensile failure limits and cracking behavior of two of these mixes (the unmodified and a heavily SBS linear modified) were evaluated also from the Three Point Bending Beam (3PB) test.

The results presented indicate that the DIC method allows for an easy and accurate determination of tensile failure limits for both soft and hard modified asphalt mixtures. Full field strain maps indicate that the addition of SBS polymers in mixtures leads to more homogeneous stress states during tensile loading condition, resulting in high strains strongly localized up to the location of impending fracture.

2 DIGITAL IMAGE CORRELATION (DIC) SYSTEM

The Digital Image Correlation (DIC) system was specifically developed for HMA strain estimation, taking into account both translations and rotations of the specimen as well as large deformations. The technique utilizes two or more digital images depicting at least partly the same scene; a matching algorithm automatically establishes correspondences between grey value windows extracted from the digital images.

A sophisticated image matching technique (Least Square Matching) (21,22) was employed for the purpose of providing matches with sub-pixel accuracy even in the case of large deformation. The DIC technique involves: specimen surface treatment, appropriate illumination, and a suitable equipment placement. A sequence of images is acquired with a digital camera Basler AF 101 (resolution 1300×1030 , focal length 8 mm, pixel size 6.7 micrometers, 12 fps@max resolution) during tensile fracture testing of HMA specimens. The optics adopted at maximum magnification

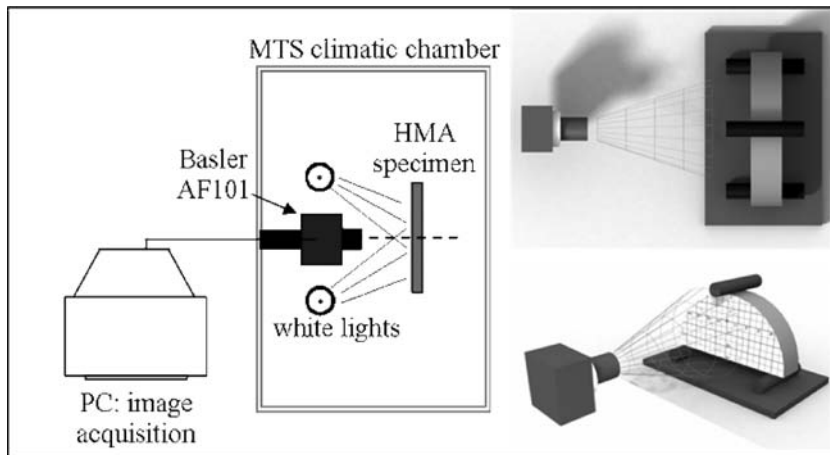


Figure 1. Digital image correlation system – Experimental setup.

allow 30 μm per pixel resolution. The camera which is directly connected with a personal computer, is located on a support inside a climatic chamber of a material testing system, focusing up to 3.5 cm from the area of most interest of the specimen (i.e. the most stressed area). A lighting system, created on purpose to properly illuminate the specimen inside the climatic chamber, is composed of 4 white lights which can be oriented according to the specimen shape and/or dimensions: two horizontal guide rails allow horizontal movements while two 20 cm eyelets in which the lights are embedded, allow vertical settings. The experimental setup is shown in Figure 1.

Before testing, the specimen requires a preliminary surface treatment to guarantee the success of the technique at the base of the image correlation method. This treatment consists of a homogeneous texture realized by a thin white painting overprinted by a speckle pattern of black obtained through manipulating the nozzle of the spray with proper pressure from a certain distance.

The camera was set up at a distance away from the specimen so that the resulting imaging window was focused on a 5×4 cm Region Of Interest (ROI) at around the location of maximum stress. The camera was set to acquire five frames per second (fps), which was found to allow for an optimal strain accuracy over time, processing time, and data storage.

A dense set of features, artificially generated on the specimen surface, is accurately tracked by the algorithm along the image sequence to obtain image coordinates. From the image coordinates, displacements and deformations can be evaluated in image space and, with an appropriate transformation, in object space.

The performance of the method was previously investigated by several tests resulting in a sub-micron measurement accuracy. For HMA tests, the capability of the method was valued comparing strains registered by a strain gauge with those estimated with the DIC method. Accuracies of 1/100 pixel were achieved.

3 MATERIALS AND TEST METHODS

Five 12.5-mm nominal maximum size asphalt mixtures were involved in this study. The mixes were composed by the same aggregate type and gradation but differently modified asphalt binders: one unmodified and four SBS polymer modified asphalts. Modified binders were obtained blending the unmodified one with different percentages of SBS cross-linked polymer or SBS linear polymer. A 3.5% of both cross-linked and linear polymers were added to the unmodified binder to obtain soft modified mixtures. Hard modified mixes were prepared blending the virgin binder with the maximum allowable percentage of polymer modifier to maintain asphalt stable, resulting in 5%

Table 1. Asphalt binder properties.

Asphalt binder	N	RM3.5	RM5.0	LM3.5	LM6.5
Performance grade Blend	PG 58-22 Unmodified	PG 64-22 N + 3.5% cross-linked	PG 70-22 N + 5.0% cross-linked	PG 70-22 N + 3.5% linear	PG 76-22 N + 6.5% linear
Un-aged asphalt					
Dynamic Shear (10 rad/sec) G*/sinδ, kPa	2.58 @ 58°C	2.46 @ 64°C	1.55 @ 70°C	1.40 @ 70°C	2.12 @ 76°C
RTFO aged residue					
Dynamic Shear (10 rad/sec) G*/sinδ, kPa	4.77 @ 58°C	4.64 @ 64°C	4.64 @ 70°C	2.35 @ 70°C	3.05 @ 76°C
PAV aged residue @100°C					
Creep Stiffness and m-value 60 sec.	179 and 0.353 @ -22°C	130 and 0.335 @ -22°C	147 and 0.323 @ -22°C	173 and 0.311 @ -22°C	150 and 0.324 @ -22°C

for the cross-linked polymer and 6.5% for the linear polymer. The SBS were blended with the base asphalt by the manufacturer using high shear milling. Details on the asphalt binder composition and PG grading test results are listed in Table 1. The mix design was conducted solely on the unmodified mixture according to the Marshall procedure, resulting in an optimum asphalt content of 5.2%. All the modified mixtures were prepared with the same effective asphalt content as the N2 unmodified one to assure that the SBS modifier was the only factor affecting the test results.

Cylindrical specimens were obtained compacting the mixes to 6 (± 0.5) percent air voids into 152 mm diameter specimens using the Pine Gyratory Compactor. Each specimen was then sawn to obtain two effective plates, each 30 mm thick discarding the top and the bottom plates for reducing density gradient effects. The slabs were compacted on a proper compactor (6) set to produce 300 mm long by 300 mm wide by 75 mm tall specimens. The slabs were then cut to produce beam specimens to the final dimension of 300 mm long by 75 mm tall by 100 mm wide.

Three different test methods, the Indirect Tensile Test (IDT), the Semi-Circular Bending Test (SCB) and the Three Point Bending Beam Test (3PB) were performed on three replicates at 10°C using an MTS closed-loop servo-hydraulic loading system. All the five mixes were tested performing both the IDT and SCB tests, while the 3PB test was performed using the unmodified (N) and the SBS linear hard modified (LM6.5) mixes. Details on the test procedure and strain field estimations are described by Birgisson et al (6).

4 EVALUATION OF TENSILE FAILURE LIMITS

“HMA Fracture Mechanics” is a visco-elastic fracture mechanics-based framework recently developed at the University of Florida (1,4) to describe the cracking behavior of HMA mixtures. The implication with this work is that changes in stiffness and strength are typically accommodated by changes in the visco-elastic properties of mixtures. This pavement cracking model has introduced the concept of the existence of a fundamental crack growth energy threshold below which damage is fully healable. If loading and healing conditions are such that the induced energy does not exceed the mixture threshold, then the mixture may never crack, regardless of the number of loads applied.

The Fracture Energy Density corresponds to that threshold required to fracture the mixture with a single load application. This parameter can be easily determined from the stress-strain response

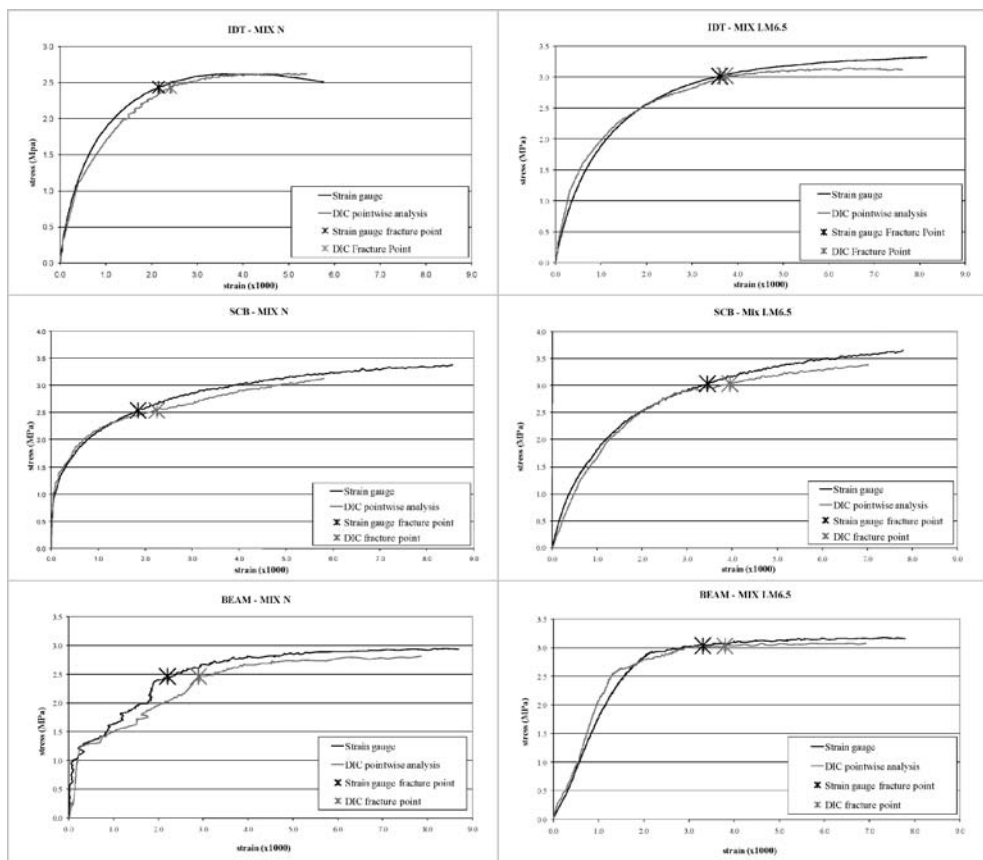


Figure 2. Comparison between pinpoint and average tensile stress-strain responses obtained from all tests for the unmodified and the SBS linear hard modified mixture.

of a tensile strength test as the area under the stress-strain curve at first fracture. Further details are discussed by Roque et al. (1).

In the test performed, strain values were estimated using the DIC System, at the specific point in which a crack has found to have visibly initiated, then fracture energy densities were computed as the resulting area under the tensile stress-strain curve up to the fracture point. Two different strain curves were estimated: a pinpoint one computed at the specific point in which a crack develops and the resulting mean strain value of the length covered by the strain gauge. The mean response was obtained interpolating all the strain values computed over the strain gauge length.

Figure 2 shows a comparison between pinpoint and average tensile stress-strain responses obtained from all the tests for the unmodified and the SBS linear hard modified mixtures. Tensile strengths and fracture energy densities for all the mixtures obtained from the three tests are shown in Figures 3 and 4, respectively.

From the results it can be observed how pinpoint tensile strengths do not significantly differ from those obtained with mean analysis. Conversely, fracture energy densities obtained at the specific point in which a crack has initiated are always about 20% higher than those evaluated along the strain gauge area. This means that tensile strains values obtained as average values along a finite area might be not totally representative of localized strains at impending fracture. Rather, it may be more appropriate to perform a point-wise analysis of localized strains at the point of impending fracture.

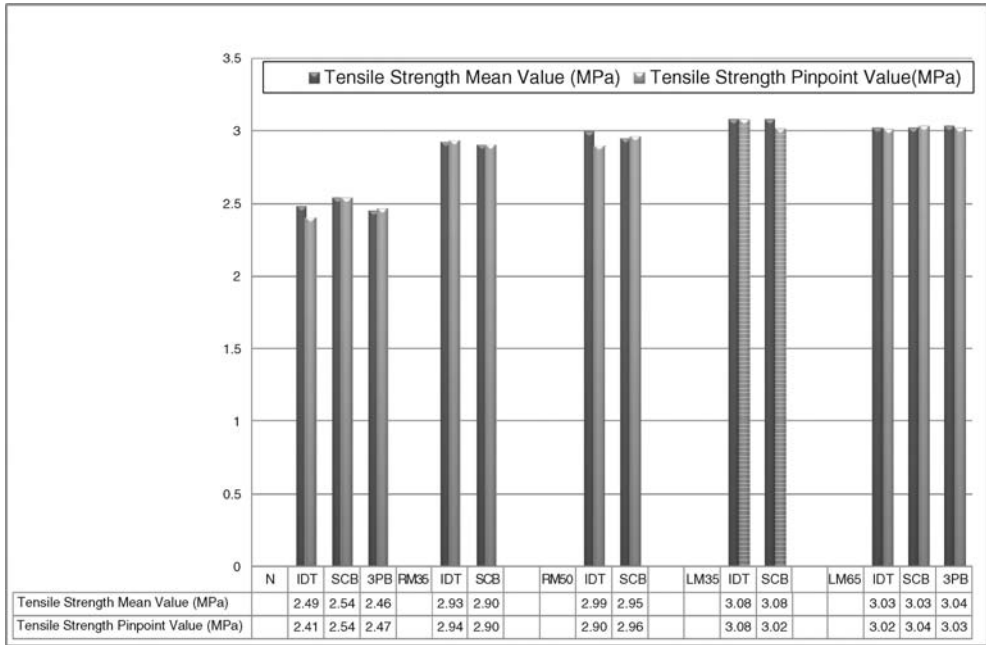


Figure 3. Comparison between pinpoint and mean tensile strengths of the five mixtures.

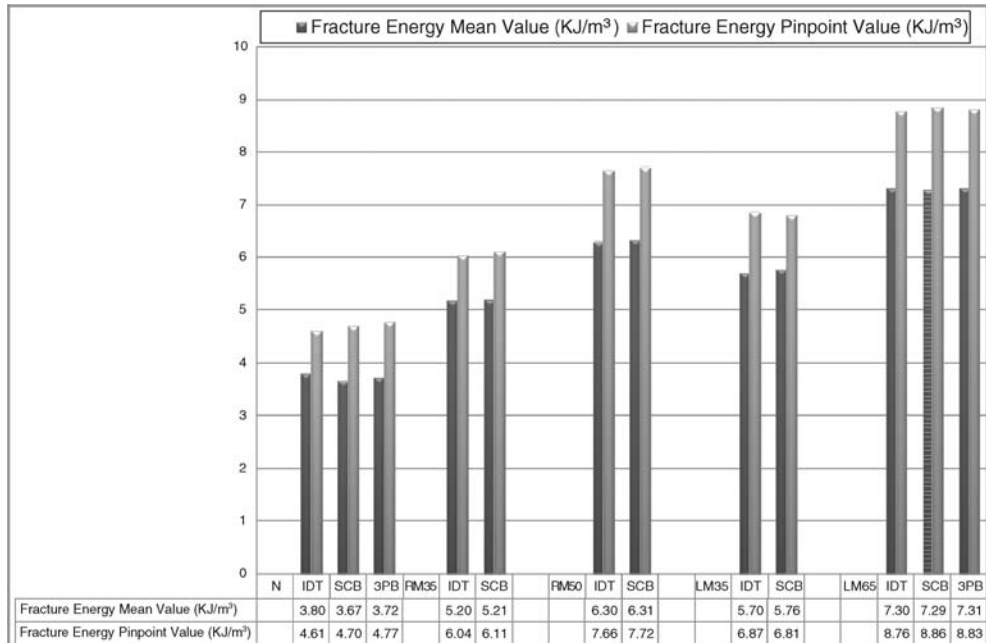


Figure 4. Comparison between pinpoint and mean fracture energy densities of the five mixtures.

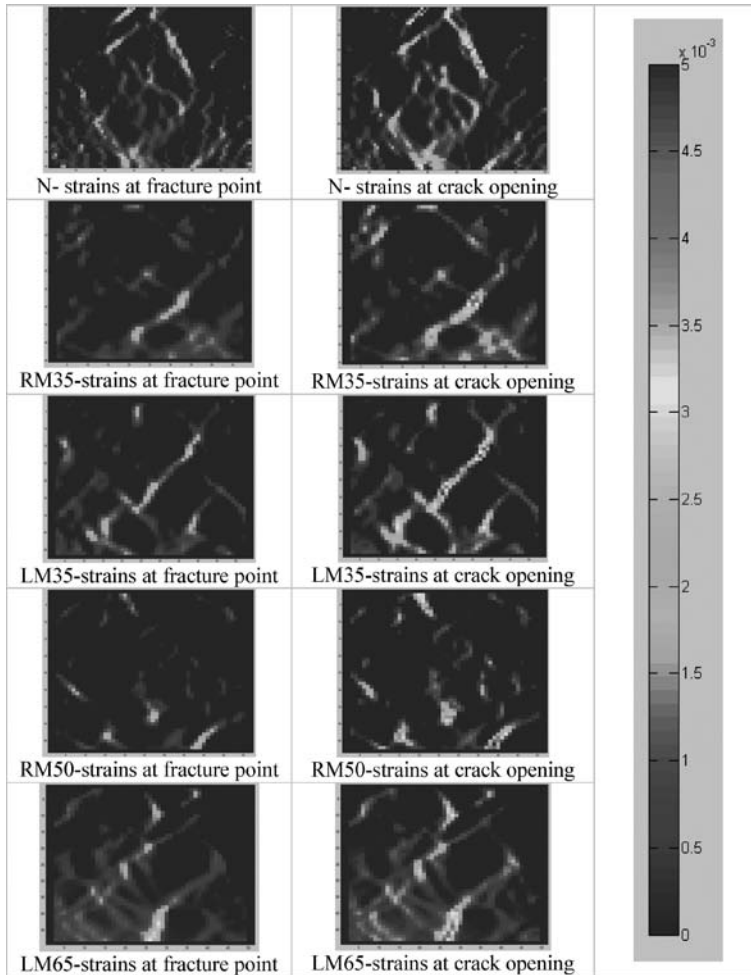


Figure 5. Full field strain maps during the IDT test for each mixture.

These results can lead to the possible conclusion that the effect of stress concentration due to the impending fracture requires the introduction of a specific damage or fracture model.

5 DIC FULL-FIELD ANALYSIS

One of the main advantages of the DIC System is its capability in capturing full-field strain map measurements, allowing for the detection of crack localization and for observations on crack initiation and growth. The measured horizontal strain map (from crack initiation to major crack opening) for the five mixtures during IDT and SCB are shown in Figures 5 and 6 respectively. The same results obtained for the unmodified and the linear SBS hard modified mixes during the 3PB test are shown in Figure 7. From full field strain maps it can be observed how tensile strains are greatly localized in the area in which a crack initiates. Moreover, it should be noted how SBS modified mixtures show high strains only up to the location of impending fracture, while the unmodified mix exhibits more location of high strain concentration both in the critical area and around the point of fracture. This means that the addition of polymers in mixtures leads to more

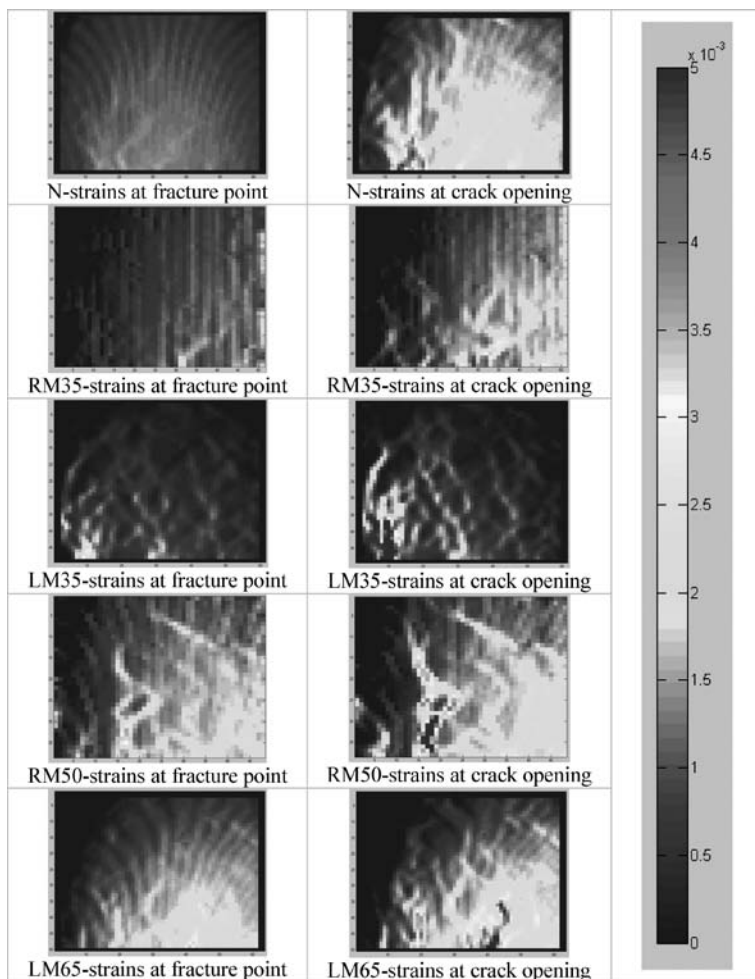


Figure 6. Full field strain maps during the SCB test for each mixture.

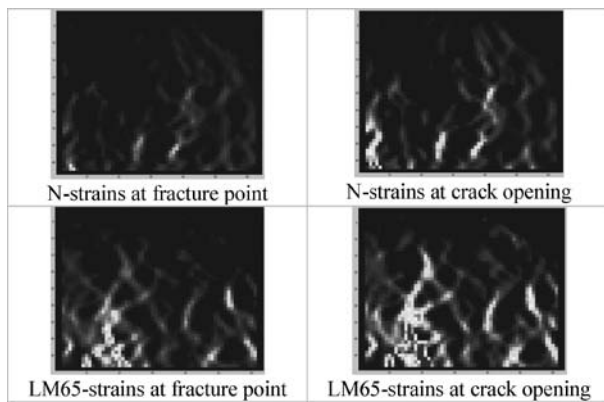


Figure 7. Full field strain maps during the 3PB test for two mixtures.

homogeneous stress states during tensile loading conditions. Finally, from the full field strain maps it's clearly evident that tensile strains develop around aggregates, while no strains are registered where a coarse aggregate exists.

6 SUMMARY AND CONCLUSIONS

A Digital Image Correlation (DIC) system for non-contact and full-field strain measurement was applied to accurately determine fundamental tensile failure limits of SBS polymer modified mixes and to investigate the effect of modification on crack localization and crack growth.

The system provides full-field strain analysis, thus not requiring the user to attempt to determine the location of crack initiation prior to the test or to mount multiple sensors on the specimen surface. Moreover, the new image correlation system provides point-wise analysis, allowing for the exact determination of the location of crack initiation, and also for the calculation of strain values at the instance of crack initiation.

One unmodified and four SBS polymer modified HMA mixes were tested performing both the Superpave IDT test and the Semi-Circular Bending (SCB) test. Tensile failure limits and cracking behavior of two of these mixes (the unmodified and a heavily SBS linear modified) were evaluated also from the Three Point Bending Beam (3PB) test.

Tensile failure limits of the mixes were estimated using the "HMA Fracture Mechanics" cracking model using the concept of a threshold as a failure criterion for the initiation and propagation of cracks.

The results indicate that fracture energy densities obtained at the specific point in which a crack has initiated are always about 20% higher than those evaluated along the strain gauge area. This means that tensile strains values obtained as average values along a finite area might be not totally representative of localized strains at impending fracture.

Moreover, full field strain maps indicate that the addition of SBS polymers in mixtures leads to more homogeneous stress states during tensile loading condition, resulting in high strains strongly localized up to the location of impending fracture. Finally, it's clearly evident that tensile strains develop around aggregates, while no strains are registered where a coarse aggregate exists.

REFERENCES

- [1] Roque R., Birgisson B., Sangpetgnam B., Zhang Z. Hot Mix Asphalt Fracture Mechanics: A Fundamental Crack Growth Law for Asphalt Mixtures. *Journal of the Association of Asphalt Paving Technologists*. Vol.71, 2002, pp. 816–827.
- [2] Wagoner M.P., Buttler W.G., Paulino G.H. Development of a Single-Edge Notched Beam Test for Asphalt Concrete Mixtures. *Journal of Testing and Evaluation*. Vol. 33:6, 2005.
- [3] Kim Y.R., Allen D.H., Little D.N. Damage-Induced Modeling of Asphalt Mixtures through Computational Micromechanics and Cohesive Zone. *Journal of Materials in Civil Engineering*. Vol. 17:5, 2005, pp. 477–484.
- [4] Roque R., Birgisson B., Sangpetgnam B., Zhang Z. Hot Mix Asphalt Fracture Mechanics: A Fundamental Crack Growth Law for Asphalt Mixtures. *Journal of the Association of Asphalt Paving Technologists*, Vol.71, 2002, pp. 816–827.
- [5] Birgisson B., Montepara A., Romeo E., Roque R., Roncella R., Tebaldi G. Determination of Fundamental Tensile Failure Limits of Mixtures. *Journal of the Association of Asphalt Paving Technologists*, Vol.76, 2007, (in press).
- [6] Birgisson B., Montepara A., Napier J.A.L., Romeo E., Roncella, Tebaldi G. Micromechanical Analyses for Measurement and Prediction of HMA Fracture Energy. *Journal of the Transportation Research Record*. No.1970: 186–195, 2006.
- [7] Grédiac M. The use of full-field measurement methods in composite material characterization: interest and limitations. *Composites, Part A: Applied Science and Manufacturing*, 35:751–761, 2004.
- [8] Van den Heuvel F., Kroon R. Digital Close-Range photogrammetry using artificial targets. *IAPRS* 29(5): 222–229, 1992.
- [9] Crippa B., Forlani G., de Haan A. Automatic deformation measurement from digital images. *Optical 3-D Measurement Techniques II*, Gruen/Kahmen (Ed's), Wichman Verlag, Karlsruhe: 557–563, 1993.

- [10] Chu T.C., Ranson W.F., Peters W.H., Sutton M.A. Applications of Digital-Image-Correlation Techniques to Experimental Mechanics. *Experimental Mechanics* 25(3):232–245, 1985.
- [11] Ranson W.F., Sutton M.A., Peters W.H.I. Holographic and Spackle Interferometry In *SEM Handbook of Experimental Mechanics*, New Jersey: Prentice-Hall, Inc: 388–429, 1987.
- [12] Bruck H.A., McNeill S.R., Sutton M.A., Peters W.H.I. Digital Image Correlation Using Newton-Raphson Method for a Partial Differential Correction. *Experimental Mechanics* 28(3):261–267, 1989.
- [13] Muszynski L., Wang F., Shaler S.M. Short Term Creep Tests on Phenol Resorcinol Formaldehyde (PRF) Resin Undergoing Moisture Cement. *Wood and Fiber Science* 34 (4):612–624, 2002.
- [14] Muszynski L., Lopez-Anido R., Shaler S.M. Image Correlation Analysis Applied to Measurement of Shear Strains in Laminated Composites. *SEM XI International Congress on Experimental Mechanics*, Orlando, FL, 2000.
- [15] Melrose P., Lopez-Anido R., Muszynski L. Elastic Properties of Sandwich Composite Panels using 3-D Digital Image Correlation with the Hydromat Test System. *SEM XI International Congress and Exposition on Experimental Mechanics and Applied Mechanics*, Costa Mesa, CA, 2004.
- [16] Choi S., Shah S.P. Measurement of Deformations on Concrete Subjected to Compression Using Imaging Correlation. *Experimental Mechanics*. Vol. 37(3), pp:307–313.
- [17] Seo Y., Kim Y.R., Witczak M.W., Bonaquist R. Application of the Digital Image Correlation Method to Mechanical Testing of Asphalt-Aggregate Mixtures *Transportation Research Record 1789*, TRB, National Research Council, Washington, D.C. pp. 162–172, 2002.
- [18] Chehab G.R., Seo Y., Kim Y.R. Viscoelastoplastic Damage Characterization of Asphalt–Aggregate Mixtures Using Digital Image Correlation. *International Journal of Geomechanics*, Vol. 7(2), pp:111–118, 2007.
- [19] Roncella R., Romeo E., Forlani F. Image Based Microstructural Analysis in Fracture Mechanics. *7th Optical 3-D Measurement Techniques*, 2005, Vienna, Austria.
- [20] Birgisson B., Montepara A., Romeo E., Roncella R., Napier J.A.L., Tebaldi G. Determination and Prediction of Crack Patterns in Hot Mix Asphalt (HMA) Mixtures. *Journal of Engineering Fracture Mechanics*. 2007 (in press).
- [21] Forstner W. On the geometric precision of digital image correlation. *IAPRS*, 1982, 24 (3):176–189.
- [22] Ackermann F. Digital image correlation: performance and potential application in photogrammetry”, *Photogrammetric record* 11(64):429–439, 1984.

Mitigating reflective cracking under Nevada's conditions

N.E. Morian

Nevada Department of Transportation, Carson City, Nevada, USA

E.Y. Hajj & P.E. Sebaaly

University of Nevada, Reno, Nevada, USA

ABSTRACT: This study was conducted to assess the effectiveness of the treatments applied by Washoe County, Nevada to mitigate reflective cracking which were limited to varying overlay thickness with either nonwoven geotextile fabrics, petromat, or no fabric placed over the original construction or reconstruction sections followed by an overlay. The overlay thicknesses varied from 37.5 to 63 mm (1.5 to 2.5 inches) without fabric placements and were limited to 50 mm (2 inches) with either fabric type. The performance of nearly 200 sections was analyzed in this study using the pavement condition index (PCI) from Micro PAVER, as well as three modified PCI values that were developed from fatigue cracking, longitudinal and transverse cracking, and a combination of both. The best performance of the treatments observed was petromat with a slurry seal placed between the initial construction and the overlay placement followed closely by the nonwoven fabric without prior slurry seals.

1 INTRODUCTION

Hot mixed asphalt (HMA) overlays are one of the commonly used methods for rehabilitating deteriorated pavements. A major type of distress influencing the life of an overlay is reflective cracking (Dempsey 2002). When asphalt overlays are placed over severely cracked pavements, cracks can reflect to the surface relatively quickly. Reflective cracking can allow water to percolate into pavement structure which can further damage the HMA by promoting the stripping of the asphalt binder from the aggregate. It can also significantly weaken the base and subgrade materials, leading to a catastrophic failure of the pavement structure.

The underlying cause of reflective cracking is the significant increase in the tensile stresses at the interface of the crack and the new HMA overlay due to discontinuity across the crack. The developed tensile stresses can rapidly exceed the tensile strength of the HMA overlay forming the crack, which quickly propagates to the surface. Combating reflective cracking can generally be achieved by either: (a) reducing the magnitude of the tensile stresses at the crack-overlay interface or (b) increasing the tensile strength of the HMA overlay.

Increasing the thickness of the HMA overlay reduces the magnitude of the tensile stresses at the crack-overlay interface for given traffic conditions. Fabrics and geotextiles increase the tensile strength of the HMA overlay as a whole. These materials have high tensile strengths and if they are effectively bonded to the HMA layer, can improve the tensile strength of the overlay. Selecting the best type of fabric or geotextile requires an in-depth assessment of their relative properties and their long-term performance.

The propagation of cracks through the new HMA layer is impacted by various factors such as: treatment of the cracks in the old pavement, the installation of a crack retarding techniques, properties of the new HMA mix, traffic loads, and environmental conditions. Traffic loads and environmental conditions are primarily fixed for a given project, which leaves crack treatment, retarding technique, and the design of the new mix as the three factors to be optimized.

A larger research project is being conducted to evaluate the techniques that have been used in the state of Nevada to mitigate reflective cracking. The objective of this portion of the study was to evaluate the various mitigation techniques previously used by Washoe County.

Based upon the referenced reports, it can be concluded that in most cases and in general terms, the use of paving fabrics have been found to be advantageous given the appropriate application and usage. In general, the proper overlay with fabric materials (Cleveland et al. 2002) must be used in the proper circumstances (Maxim 1997, Carmichael et al. 1999, Amini 2005, Sprague 2006, Button et al. 2007). Given the appropriate application, fabric treatments have been found to provide life cycle cost benefits (Buttlar et al. 1999, Carmichael et al. 1999, Amini 2005, Sprague 2006) by improving the overall performance of the overlaid pavement (Mascuana 1981, Buttlar et al. 1999, Amini 2005), by reducing the moisture conditions, or by being equivalent to additional overlay thickness in terms of cracking resistance (Maxim 1997, Carmichael et al. 1999), but not structural capacity (Carmichael et al. 1999). These considerations have included observation from the US, Europe, and South Africa.

2 WASHOE COUNTY PRACTICE

The Washoe County Engineering Department (WCED) has constructed several projects with and without geotextile fabrics in conjunction with HMA overlays over existing HMA pavements to mitigate reflective cracking and reduce moisture penetration into the pavement structure. This task of the study evaluates the performance of selected projects to examine the effectiveness of the geotextile fabrics on Washoe County roadways in northwestern Nevada, USA.

The information used in this analysis was obtained from a selective review of the Micro PAVER database maintained by the WCED as part of their pavement management system. The environmental conditions of the region can be characterized as a high desert, which generally indicates relatively low annual precipitation rates, generally around 250 mm (10 inches), but nearly all locations in the county below 500 mm (20 inches), except for the mountainous regions surrounding Lake Tahoe (Sierra Pacific 2007). Being a high desert, the area is subjected to relatively high summer temperatures, periodically over 38°C (100°F), and generally mild winters, usually not below -18°C (0°F). However, the region is subjected to significant daily temperature fluctuations varying by 17 to 22°C (30 to 40°F), but may exceed 25°C (45°F), between consecutive day and night temperatures throughout the year (NOAA 2007).

The overlays in this study without fabrics were specified to receive a tack coat of either SS-1 or SS-1h prior to the overlay. The overlays which used fabrics were specified to use 1.1 Liters per square meter (actual 0.25 gallons per square yard) of AR8000 applied before the fabric.

The overlay treatments were applied between 1988 and 2001. Overlays placed over previously overlaid pavements were not utilized in an effort to minimize the variability of the base pavement sections. The overlays were generally dense graded HMA with a 12.5 or 19 mm (0.50 or 0.75 inch) nominal maximum aggregate size with AC-20 or AR4000 unmodified binders (RTC 2007). The treatment sections were further divided by the placement of a slurry seal some years prior to the overlay. The nearly 200 utilized sections can be categorized as follows.

- NF-37.5: a 37.5 mm (1.5 inch) overlay over the existing pavement without fabrics.
- NF-50: a 50 mm (2.0 inch) overlay over the existing pavement without fabrics.
- NF-63: a 63 mm (2.5 inch) overlay over the existing pavement without fabrics.
- F-50: a 50 mm (2.0 inch) overlay over a nonwoven geotextile over existing pavement.
- F-50s: a 50 mm (2.0 inch) overlay over a nonwoven geotextile over the existing pavement that had been slurry sealed 4 to 6 years prior to the overlay.
- P-50: a 50 mm (2.0 inch) overlay over petromat over existing pavement.
- P-50s: a 50 mm (2.0 inch) overlay over petromat over the existing pavement that had been slurry sealed 3 to 5 years prior to the overlay placement.

The fabrics used were typically 136 gram per square meter (4 ounce per square foot) nonwoven geotextile fabrics. Petromat is a product produced by any number of suppliers, which generally includes similar weight fabrics that have been impregnated with asphalt binder.

The majority of the roadways under the county's direction are classified as minor arterials, collectors, and residential streets. After a general examination of the county's overlay program, all of the sections that met the selection criteria were utilized. The selected roadways were limited to the Reno/Sparks area to reduce, if not eliminate, the effects of differential environmental conditions and elevations, thus normalizing the environmental conditions as much as practical. Since specific traffic counts were not available for all the sections, the selection was limited to those classified as residential in function. The sections were also restricted in relative location to other roadways in terms of traffic flow. For instance, a main thoroughfare through town was not used, just as cul-de-sacs and dead ends were not utilized in the study.

No condition surveys were conducted on any of the sections as part of or specifically for this analysis. All of the information used in the analysis were obtained and compiled into the Micro PAVER software by WCED personnel as part of their standard maintenance program. Because many of the sections are no longer in physical existence, only in the MicroPAVER records, no field verification or material sampling was possible.

3 EVALUATION OF WASHOE COUNTY PROJECTS

3.1 *Data collection and processing*

Prior to data collection procedures, each portion of the subject roadways must be uniquely identified with network, branch, section, and sample unit designations. The main function of data collection procedures are the condition surveys, which are the visual condition surveys conducted on the designated sample units to provide an indication of the pavement's condition and thus its performance. These condition surveys are conducted periodically to identify the type, amount, and severity of the selected number of pavement distresses visible at the pavement surface. The distress types used are determined by the agency utilizing the software from the overall listing available in the software package. The cracking types, extent and severity used by WCED are defined in the Asphalt Distress Manual, Pavement Distress Identification Guide for Asphalt-Surfaced Roads and Parking Lots (USACE 1997).

In order to establish the desired historical performance records, the condition surveys are usually conducted on the same sample units each time, generally on 10% of the available sample units. The frequency of the inspections often depends upon the rate of pavement deterioration, which can be linked to traffic loading, environmental conditions, and the pavement condition itself. WCED typically conducted condition surveys used in this analysis every other year. There are exceptions to this timing, especially if any maintenance or other construction operations took place between the regularly scheduled inspections.

Once the information is accurately gathered, checked, and entered into Micro PAVER, the analyses can be performed by calculating the Pavement Condition Index (PCI). The PCI is a numerical indicator used to measure the condition of the pavement. The PCI values range from 100 for a roadway without any distresses to a value of 0 for a severely distressed and failed pavement. The PCI values are calculated for each section not each individual sample unit. Each PCI value is calculated by the Micro PAVER software (Shahin 2007). In the interest of space, the description of the calculations and the method for performing the calculations manually were left as a reference in ASTM D6433 (ASTM 2003). The analyzed treatment responses were those based upon the resulting PCI values for the respective test sections.

3.2 *Analysis criteria*

The analyses for the various sections were conducted utilizing the PCI values at four different ages with respect to the treatment date. The first PCI values were obtained as close as possible to, but

Table 1. Relative age characteristics of selected washoe county projects.

Treatment	Description	Number of projects		Project age, (years) relative to treatment application at			
				Year -1	Year +1	Year +3	Year +5
NF-37.5	No fabric + 37.5 mm overlay	52	Average	-1.2	1.6	3.6	5.5
			Minimum	-0.01	0.8	2.5	4.6
			Maximum	-2.7	2.2	4.2	6.7
NF-50	No fabric + 50 mm overlay	34	Average	-1.3	1.4	3.1	5.1
			Minimum	-0.16	0.6	2.7	4.7
			Maximum	-2.1	2.1	4.1	6.0
NF-63	No fabric + 63 mm overlay	39	Average	-1.3	1.1	3.1	5.0
			Minimum	-0.04	0.6	2.5	4.5
			Maximum	-3.0	2.2	4.2	6.0
F-50	Nonwoven fabric + 50 mm overlay	24	Average	-1.5	1.2	2.7	4.7
			Minimum	0.0	0.7	1.9	3.9
			Maximum	-3.0	1.9	3.9	5.8
F-50s	Nonwoven fabric + 50 mm overlay + prior slurry seal	11	Average	-1.1	0.8	3.0	5.1
			Minimum	-0.8	0.7	2.9	4.9
			Maximum	-3.1	1.0	3.2	5.2
P-50	petromat + 50 mm overlay	19	Average	-1.9	1.2	3.0	5.1
			Minimum	-0.9	0.7	1.9	4.3
			Maximum	-3.3	1.7	3.9	5.7
P-50s	petromat + 50 mm overlay + prior slurry seal	14	Average	-1.4	1.0	2.2	4.4
			Minimum	-0.3	0.8	1.6	3.8
			Maximum	-1.7	1.1	3.0	5.2

before the overlay placement, indicating the condition of the pavement before rehabilitation. The remaining PCI values were selected according to the available inspections based upon the relative dates from the overlay placement. Thus, the inspection dates used were from the year before and one, three, and five years after rehabilitation resulting in the respective designations of -1 PCI, 1 PCI, 3 PCI, and 5 PCI. These dates could not be selected at the exact time intervals due to the variable schedule of the inspection dates conducted about every other year. Therefore, the inspections used in the analyses had the timeframe variations noted in Table 1.

The specific criteria used in the analyses included the overall Pavement Condition Index, PCI, from Micro PAVER, as well as three modified PCI values based upon fatigue, longitudinal and transverse cracking, and a combination of both.

3.3 Field performance analysis of the selected Washoe County projects

The PCI values used in the analysis included the overall PCI calculations, which included all the identified distresses, and the three modified PCI values based upon the reported fatigue and longitudinal and transverse cracking as follows:

- PCI_{Ov} : the overall PCI value includes all of the distresses identified during the WCED surveys; including fatigue cracking, longitudinal and transverse cracking, block cracking, bleeding, rutting, bumps, sags, corrugation, depression, edge cracking, lane shoulder drop off, patching, utility cuts, polished aggregates, potholes, railroad crossings, shoving, slippage cracking, swelling, weathering, and raveling.
- PCI_{Fat} : a modified PCI value based solely on the fatigue cracking using the same sample units as the PCI_{Ov} , but ignoring all other identified distresses.
- PCI_{LT} : a modified PCI value based longitudinal and transverse cracking using the same sample units as the PCI_{Ov} , but ignoring all other identified distresses.

Table 2. Statistical analysis of the various treatments based on PCI_{Ov} .

At year -1	(NF-37.5)	(NF-50)	(NF-63)	(F-50)	(F-50s)	(P-50)	(P-50s)
NF-37.5	-	L	NS	L	L	L	L
NF-50	-	-	H	L	L	L	L
NF-63	-	-	-	L	L	L	L
F-50	-	-	-	-	L	L	NS
F-50s	-	-	-	-	-	NS	H
P-50	-	-	-	-	-	-	NS
At year +1	(NF-37.5)	(NF-50)	(NF-63)	(F-50)	(F-50s)	(P-50)	(P-50s)
NF-37.5	-	L	L	L	L	L	L
NF-50	-	-	NS	L	NS	L	NS
NF-63	-	-	-	L	NS	L	NS
F-50	-	-	-	-	NS	NS	NS
F-50s	-	-	-	-	-	NS	NS
P-50	-	-	-	-	-	-	NS
At year +3	(NF-37.5)	(NF-50)	(NF-63)	(F-50)	(F-50s)	(P-50)	(P-50s)
NF-37.5	-	NS	L	L	L	L	L
NF-50	-	-	L	L	L	L	L
NF-63	-	-	-	L	NS	NS	L
F-50	-	-	-	-	H	H	NS
F-50s	-	-	-	-	-	NS	L
P-50	-	-	-	-	-	-	L
At year +5	(NF-37.5)	(NF-50)	(NF-63)	(F-50)	(F-50s)	(P-50)	(P-50s)
NF-37.5	-	L	L	L	L	L	L
NF-50	-	-	NS	L	L	L	L
NF-63	-	-	-	L	NS	L	L
F-50	-	-	-	-	H	H	NS
F-50s	-	-	-	-	-	NS	L
P-50	-	-	-	-	-	-	L

- PCI_{FLT} : a modified PCI value that includes both fatigue and longitudinal and transverse cracking, but ignores all other distress measurements.

The modified PCI values, PCI_{Fat} , PCI_{LT} , and PCI_{FLT} , were calculated by the Micro PAVER software from their respective distress measurements utilizing all the same sample unit definitions and distress measurements as the overall PCI values. There are slight variations in the actual deduct values attributed to each distress, since the calculations did not include the other identified distresses in each section. These variations are both expected and deemed acceptable, since the three modified PCI values were intended to be used as an indicator of the amounts of fatigue cracking, longitudinal and transverse cracking, and the combined effects on a relative scale. They were not intended to state exactly how those distresses affected the overall PCI values, as that would not accurately represent the influence of the respective distresses independently either. Therefore, the modified PCI values should be considered as indicators only.

The performance of the various treatments were statistically compared to each others based on the average PCI values at the respective ages using the statistical analysis software SAS (Fernandez 2003). All statistical analyses were conducted at the 5% significance level ($\alpha = 0.05$) which means that for each comparison reported as significantly different or not, there is only a 5% chance that the statement is not true. The analyses were conducted utilizing the least square means methodology (LS Mean) in a two-way fixed factor analysis and incorporated the robust adjustment process to correct for normality. The analyses were conducted using each of the four PCI conditions as the responses. The condition of the section prior to the overlay, the -1 PCI values, and the time between the initial construction or reconstruction and the overlay placement were also considered as covariates. Tables 2 and 3 summarize the statistical comparisons between the various treatment means PCI_{Ov}

Table 3. Statistical analysis of the various treatments based on PCI_{LT}.

At year -1	(NF-37.5)	(NF-50)	(NF-63)	(F-50)	(F-50s)	(P-50)	(P-50s)
NF-37.5	-	L	L	H	L	NS	NS
NF-50	-	-	NS	H	L	H	NS
NF-63	-	-	-	H	L	H	NS
F-50	-	-	-	-	L	NS	L
F-50s	-	-	-	-	-	H	H
P-50	-	-	-	-	-	-	NS
At year +1	(NF-37.5)	(NF-50)	(NF-63)	(F-50)	(F-50s)	(P-50)	(P-50s)
NF-37.5	-	NS	L	L	NS	L	L
NF-50	-	-	NS	L	NS	L	NS
NF-63	-	-	-	NS	NS	NS	NS
F-50	-	-	-	-	NS	NS	NS
F-50s	-	-	-	-	-	NS	NS
P-50	-	-	-	-	-	-	NS
At year +3	(NF-37.5)	(NF-50)	(NF-63)	(F-50)	(F-50s)	(P-50)	(P-50s)
NF-37.5	-	L	L	L	L	L	L
NF-50	-	-	L	L	L	L	L
NF-63	-	-	-	NS	NS	NS	NS
F-50	-	-	-	-	H	NS	NS
F-50s	-	-	-	-	-	NS	L
P-50	-	-	-	-	-	-	NS
At year +5	(NF-37.5)	(NF-50)	(NF-63)	(F-50)	(F-50s)	(P-50)	(P-50s)
NF-37.5	-	L	L	L	L	L	L
NF-50	-	-	L	L	L	L	L
NF-63	-	-	-	L	NS	NS	L
F-50	-	-	-	-	H	H	NS
F-50s	-	-	-	-	-	NS	L
P-50	-	-	-	-	-	-	L

and PCI_{LT} values at the four relative ages. Comparisons of PCI_{Fat} have been excluded, due to all the comparisons being statistically the same with all the mean PCI_{Fat} values after the overlay placement exactly 100. Similarly, the PCI_{FLT} comparisons have also been excluded since they almost exactly mirror those of PCI_{LT}. The high, low, and not significant notations are provided as an indication of improvement, degradation, or insignificant differences. The following nomenclature is used in Tables 2 and 3.

- L – The PCI value listed in the row is significantly lower than the (column).
- H – The PCI value listed in the row is significantly higher than the (column).
- NS – The PCI value listed in the row is not significantly different from the (column).

Tables 4 and 5 summarize the statistical ranking of the various treatments based on the PCI_{Ov} and PCI_{LT}, respectively. Again the PCI_{Fat} and PCI_{FLT} comparisons have been omitted due to lack of significant differences. The effectiveness of the various treatments are evaluated based upon: the plots of the four mean PCI values as a function of the relative age, the rate of deterioration of the respective mean PCI values, the difference between the initial condition (i.e., PCI at year -1) and the pavement condition (i.e., mean PCI values) 5 years after treatment application, the mean PCI values 5 years after treatment application, as well as future projections of the condition of the respective treatments 10, 15, and 20 years after treatment application. The deterioration rate and the projected PCI values at 10, 15, and 20 years were predicted using a best fit linear model which assumed a constant rate of deterioration based upon the first five years of performance. Although a linear deterioration rate does not appropriately model the expected future performance, these analyses was used to differentiate between the deterioration rate as compared to the current

Table 4. Performance rankings based on PCI_{Ov} .

PCI _{Ov} ranking* based on						
Treatment	PCI _{Ov} rate of deterioration	PCI _{Ov} improvement	Year 5 PCI _{Ov}	Projected PCI _{Ov} values		
				10 years	15 years	20 years
NF-37.5	7	3	7	7	7	7
NF-50	6	2	6	6	6	6
NF-63	5	1	5	5	5	5
F-50	2	4	2	2	2	2
F-50s	4	7	4	4	4	4
P-50	3	6	3	3	3	3
P-50s	1	5	1	1	1	1

Table 5. Performance rankings based on PCI_{LT} .

PCI _{LT} ranking* based on						
Treatment	PCI _{LT} rate of deterioration	PCI _{LT} improvement	Year 5 PCI _{LT}	Projected PCI _{LT} values		
				10 years	15 years	20 years
NF-37.5	7	7	7	7	7	7
NF-50	6	5	6	6	6	6
NF-63	3	4	3	3	3	3
F-50	2	1	2	2	2	2
F-50s	4	6	5	4	4	4
P-50	5	3	4	5	5	5
P-50s	1	2	1	1	1	1

* Ranking from best to worst; i.e., the projects ranked as “1” had the best performance.

condition, i.e. to compare faster deterioration rates starting at higher PCI values to those with slower deterioration rates at lower initial PCI values.

3.3.1 Analysis based on PCI_{Ov}

By examining Figure 1 and Table 2, it becomes evident that the sections without fabric (NF-37.5, NF-50, and NF-63) resulted in statistically lower PCI values after the treatment, even though they initially started out with lower PCI values. It should be clarified that the PCI values after the treatment application have all been normalized to the initial condition (–1 PCI). The fabric and petromat treatments indicate significantly improved overall performance, with prior slurry sealing being beneficial to petromat and detrimental to the nonwoven fabric treatments. The petromat treatment with prior slurry seals (P-50s) exhibited statistically similar performance to the nonwoven fabric without the slurry seal (F-50). On the other hand, the petromat without the slurry (P-50) exhibited statistically similar performance to the nonwoven fabric with slurry seals (F-50s). Table 4 shows a common agreement between the ranking of deterioration rates and the 5, 10, 15, and 20 year PCI_{Ov} values, which generally indicates that the petromat with the prior slurry seal (P-50s) was the most effective treatment followed by the nonwoven fabric without prior slurry seals (F-50). These are followed by the P-50 and F-50s treatments, with the non fabric treatments not as effective as the four fabric treatments. The ranking is nearly reversed for the PCI improvement between the –1 and year 5 PCI values, suggesting the overall improvement may not be a sufficient indicator of treatment

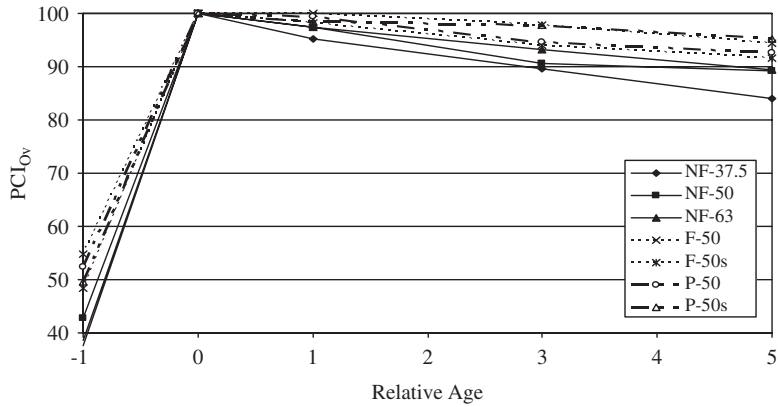


Figure 1. Statistical PCI_{Ov} values with relative age.

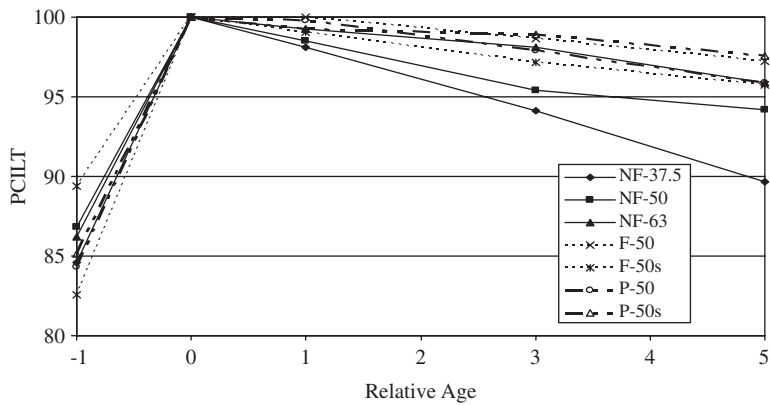


Figure 2. Statistical PCI_{LT} values with relative age.

effectiveness when based upon the overall pavement condition. This might also suggest that there are too many other distresses, other than fatigue, longitudinal, and transverse cracking, that influence the overall PCI values, thus further supporting the reasoning for the three modified PCI values.

3.3.2 Analysis of PCI_{Fat}

None of the treatments indicated any differences in fatigue performance as evidenced by the means of the PCI values after the treatment all being 100. Any comparisons that could be conducted similar to Table 4 would be limited to PCI improvements, which would be based on the initial condition and not performance. Therefore, the only significant finding based upon the PCI_{Fat} is that a five year assessment period is not long enough to make a determination in this study.

3.3.3 Analysis of PCI_{LT}

Figure 2 and Table 3 indicate the petromat with the slurry seal (P-50s) provided the best performance, followed closely by the nonwoven fabric without slurry seal (F-50). The 63 mm treatment without fabric appeared to perform better than the remaining two fabric sections. The nonfabric (NF-63), nonwoven fabric with slurry seal (F-50s), and the petromat without slurry seal (P-50) treatments all provided statistically similar performance. NF-37.5 and NF-50 treatments were again statistically the least effective treatments. Table 5 rankings generally agree according to deterioration rate, 5, 10, 15, and 20 year PCI_{LT} values, and the PCI improvement criteria.

3.3.4 Analysis of PCI_{FLT}

Because of the essentially nonexistent effects of fatigue cracking on the PCI_{FLT} values, the PCI_{FLT} values rank very similar to those of the PCI_{LT} values. Therefore, the analysis of the PCI_{FLT} values does not provide any additional information.

4 CONCLUSIONS FROM THE WASHOE COUNTY PROJECTS

The following general conclusions concerning the performance of reflective cracking treatments in Washoe County, Nevada are based on the combined analyses of distress data and PCI values. The following summaries should be viewed in light of the relative number of sections considered: 125 nonfabric sections, 35 with fabrics, and 23 with petromat.

- After the five year analysis period the average PCI_{OV} values for all treatments remained in the “Good” condition (i.e., PCI above 86) except for the NF-1.5 which remained “Satisfactory” (i.e., PCI from 71 to 85). These PCI condition categories are based upon the definitions incorporated in to the Micro PAVER program and are used by WCED.
- In terms of both PCI_{OV} and PCI_{LT} values, the best performance of the treatment types observed was the petromat with a slurry seal placed prior to the overlay placement (P-50s), followed by the nonwoven fabric without prior slurry seals (F-50).
- Based upon PCI_{OV} and PCI_{LT} values, the next beneficial treatments were the nonwoven fabric with prior slurry seals (F-50s) and the petromat without prior slurry seals (P-50).
- According to both PCI_{OV} and PCI_{LT} values, the least effective treatments were those without fabric placement. However, the 63 mm overlay without fabric (NF-63) can perform similar to the nonwoven fabric with prior slurry seals (F-50s) and the petromat without prior slurry seals (P-50) in terms of longitudinal and transverse cracking resistance. However, the overall pavement condition does not reflect such good performance by the 63 mm sections without fabric or petromat placements.

An alternative way of analyzing the effectiveness of the various treatments is to examine the time when cracks appeared at the pavement surface. Table 6 summarizes the number of projects that showed surface cracks within 1 year, between 1 and 3 years, and between 3 and 5 years from the time of construction with the following conclusions made.

- The nonfabric sections were not able to prevent the initiation of longitudinal and transverse cracking for the first year after the overlay placement. Most of the sections without fabric showed surface cracks within 1 to 3 years after construction. The number of sections with reflective cracking after 1 to 3 years of treatment application decreased with the increase of the overlay thickness. Specifically, the 63 mm overlay retarded reflective cracking on 38% of the sections for 3 to 5 years after construction compared to 26% and 13% of the sections for the 50 and 37.5 mm overlays without fabrics.
- In general, the fabric sections without the prior slurries retarded reflective cracking for 1 to 5 years after construction. About 42% of the nonslurried fabric sections exhibited longitudinal and transverse cracking within the 1 to 3 year timeframe. Additionally, almost half of the sections exhibited reflective cracking within the 3 to 5 year timeframe.
- In general, the fabric section with prior slurries retarded reflective cracking for 3 to 5 years after construction with only two sections showing reflective cracking within the first year after construction. Only one section of the nonslurried fabric sections exhibited reflective cracking within the 1 to 3 year timeframe. Additionally, almost half of the sections exhibited reflective cracking within the 3 to 5 year timeframe.
- In general, the petromat sections without the prior slurries retarded reflective cracking for 1 to 5 years. Over half of the nonslurried petromat sections (58%) exhibited reflective longitudinal and transverse cracking within 1 to 3 years. At the end of the five year analysis, only 11% of the nonslurried petromat sections remained without any cracks.

Table 6. Summary of the washoe county treatment performance.

Sections showing surface cracking (number/percentage)					
Treatment	Time to develop surface cracks				Number of projects
	<1 year	1–3 years	3–5 years	No cracks, 5 years	
<i>Fatigue cracking</i>					
NF-37.5	1/2%	4/8%	9/17%	38/73%	52
NF-50	1/3%	4/12%	5/15%	24/71%	34
NF-63	1/3%	4/10%	6/15%	28/72%	39
F-50	0/0%	1/4%	3/13%	20/83%	24
F-50s	0/0%	1/9%	1/9%	9/82%	11
P-50	0/0%	2/11%	4/21%	13/68%	19
P-50s	0/0%	0/0%	0/0%	14/100%	14
<i>Longitudinal and transverse cracking</i>					
NF-37.5	4/8%	40/77%	7/13%	1/2%	52
NF-50	5/15%	18/53%	9/26%	2/6%	34
NF-63	7/18%	12/31%	17/44%	3/8%	39
F-50	0/0%	10/42%	11/46%	3/13%	24
F-50s	2/18%	1/9%	5/45%	3/27%	11
P-50	0/0%	11/58%	6/32%	2/11%	19
P-50s	0/0%	4/29%	3/21%	7/50%	14
<i>Fatigue or longitudinal and transverse cracking</i>					
NF-37.5	4/8%	40/77%	7/13%	1/2%	52
NF-50	5/15%	19/56%	9/26%	1/3%	34
NF-63	7/18%	15/38%	15/38%	2/5%	39
F-50	0/0%	10/42%	11/46%	3/13%	24
F-50s	2/18%	1/9%	5/45%	3/27%	11
P-50	0/0%	11/58%	6/32%	2/11%	19
P-50s	0/0%	4/29%	3/21%	7/50%	14

- In general, the petromat sections with the slurries retarded reflective cracking for 1 to 5 years on half of the sections and for at least 5 years on the remaining half of the sections. Additionally, the slurried petromat sections never did develop fatigue cracking during the 5 year analysis period. About 29% of the nonslurried petromat sections exhibited reflective longitudinal and transverse cracking within the 1 to 3 year timeframe.

REFERENCES

- Amini, F., 2005. Potential Applications of Paving Fabrics to Reduce Reflective Cracking, Department of Civil and Environmental Engineering, Jackson State University.
- ASTM 2003. ASTM, D6433, Standard Practice for Roads and Parking Lots Pavement Condition Index Surveys, American Standards for Testing and Materials.
- Buttler, W.G., Dempsey, B.J., Bozkurt, D., 1999. Evaluation of Reflective Crack Control Policy, Final Report, Report No. ITRC FR95/96-4, Illinois Transportation Research Center, Department of Civil Engineering, University of Illinois at Urbana-Champaign, Urbana, Illinois.
- Button, J.W., Lytton, R.L., 2007. Guidelines for Using Geosynthetics with Hot Mix Asphalt Overlays to Reduce Reflective Cracking. In Transportation Research Board 2007 Annual Meeting CD-ROM. Transportation Research Board of the National Academies, Washington D.C.
- Carmichael III, R.F., Marienfeld, M.L., 1999. Synthesis and Literature Review of Nonwoven Paving Fabrics Performance in Overlays, In Transportation Research Record No. 1687, Geotechnical Aspects of Pavements, TRB National Research Council, Washington, D.C., pp. 112–124.
- Cleveland, G.S., Button, J.W., Lytton, R.L., 2002. Geosynthetics in Flexible and Rigid Pavement Overlay Systems to Reduce Reflection Cracking, Texas Transportation Institute, College Station, Texas.

- Dempsey, B.J., 2002. "Development and Performance of Interlayer Stress-Absorbing Composites in Asphalt Concrete Overlays," in *Transportation Research Record 1809*, TRB, National Research Council.
- Fernandez, G.C., 2003. *Data Mining using SAS Applications*. Chapman & HALL, Washington, D.C, 2003.
- Mascuana, I., 1981. An Evaluation of Engineering Fabric in Pavement Rehabilitation (IDH-21) Physical Research Report No. 88, State of Illinois Department of Transportation.
- Maxim Technologies, Inc., 1997. Nonwoven Paving Fabric Study, Final Report. Submitted to Industrial Fabrics Association International Geotextile Division.
- NOAA, 2007. Climate Description webpage, National Weather Service Forecast Office, Reno, Nevada, National Oceanic & Atmospheric Administration. http://www.wrh.noaa.gov/rev/climate/description_reno.php. Accessed March 19, 2007.
- RTC, 2007. Standard Specifications for Public Works Construction, Regional Transportation Commission (RTC) of Washoe County, 2007 and previous versions.
- Shahin, M.Y., 2007. MicroPAVER Homepage, US Army Engineer, Research and Development Center – Construction Engineering Research Laboratories – Department of Defense. <http://www.cecer.army.mil/paver/> Accessed March 19, 2007.
- Sierra Pacific, 2007. Washoe County Quality of Life webpage, Economic Development, Sierra Pacific Power Company, Reno, Nevada. <http://econdev.sierrapacific.com/sppc/county/washoe/quality.htm>. Accessed March 19, 2007.
- Sprague, C.J., 2006. Study of the Cost-Effectiveness of Various Flexible Pavement Maintenance Treatments, In *Transportation Research Circular, Maintenance Management 2006*, Presentations from the 11th AASHTO-TRB Maintenance Management Conference, Number E-C098, TRB, National Research Council, Washington D.C., pp. 45–53.
- USACE, 1997. Asphalt Distress Manual, Pavement Distress Identification Guide for Asphalt-Surfaced Roads and Parking Lots, US Army Corps of Engineers, Construction Laboratories, TR 97/104.

A practical methodology for the performance-based selection of bituminous mixtures for concrete overlays

T. Bennert & A. Maher

Center for Advanced Infrastructure and Transportation, Rutgers University, New Jersey, USA

ABSTRACT: Due to the majority of the PCC pavements in New Jersey being in average to poor condition, many HMA overlays are exposed to extreme movements (both vertical and horizontal). The combination of traffic- and environmentally-induced movements creates complex stresses and strains in the vicinity of expansion joints and cracks in the PCC reducing the life of the HMA overlay in the form of reflective cracking. To aid in mitigating the on-set of reflective cracking, a research effort was initiated to develop a methodology to select bituminous overlay materials that can withstand the excessive movements in composite pavement structures. The proposed performance-based method, consisting of field evaluations using the Falling Weight Deflectometer and Weigh-in-Motion Sensors, and laboratory testing using the Flexural Beam Fatigue and Overlay Tester is illustrated using the recent composite pavement overlay and early cracking failure of a test section on a state highway in New Jersey.

1 INTRODUCTION

Approximately 45% of the New Jersey Department of Transportation's (NJDOT) roadways are composite (hot mix asphalt overlying Portland cement concrete). Hot mix asphalt (HMA) is used as the overlying material because of its inexpensive nature when compared to most PCC rehabilitation/reconstruction alternatives. Unfortunately, the excessive underlying movements at the PCC joints typically results in premature transverse cracking, in the form of reflective cracking.

In the past, a number of reflective cracking mitigation methods have been attempted in New Jersey that ranged from paving fabrics/geosynthetics to asphalt interlayer mixes. Early field observations of the paving fabric/geosynthetic test sections showed initial promise, but transverse cracking soon developed after the first winter season. Poor performance of paving fabrics in cold season climates is in agreement with the recommendations of Button and Lytton (2007) who recommend that paving fabrics/geosynthetics perform better in warm to mild climates in mitigating reflective cracking.

A recent national survey conducted by Bennert and Maher (2007) indicated that many other state agencies located in the moderate to colder United States climates have also had minimal success with paving fabrics/geosynthetics in mitigating reflective cracking. However, both New Jersey and many other state agencies surveyed indicated that some success was found in the use of asphalt interlayer/stress-absorbing interlayers.

This paper summarizes a field and laboratory study on the use of a reflective crack relief interlayer-type mix to mitigate reflective cracking. The coupling of Falling Weight Deflectometer and Weigh-in-Motion sensors were used to measure applied loads and predict the associated vertical movements at the concrete slab joints. The Coefficient of Thermal Expansion (CTE) of the underlying PCC pavement was determined on extracted cores and used to estimate the potential horizontal movements due to expansion/contraction of the concrete slabs. The measured/calculated joint deflections were used in laboratory performance tests to evaluate the performance of different hot mix asphalt mixtures commonly used in New Jersey for overlaying concrete/composite pavements.

2 FIELD EVALUATION

A Field Evaluation program was put together to understand the functional performance of the underlying PCC pavement, especially at the PCC joint area. Traffic data is also essential so a proper understanding of the pavement loading conditions is known. Ignoring any of these most often results in early pavement failure.

2.1 General test site information

The test site for the study was New Jersey State Route 34 Northbound, between mileposts 0.3 and 7.6. Route 34 is a two-lane composite pavement, originally consisting of 228.6 mm of PCC overlaid with 63.5 to 150 mm of hot mix asphalt. The concrete pavement was constructed in 12.2 m slabs with 19 mm expansion joints and 31.75 mm diameter stainless steel dowel bars. The original bituminous overlay consisted of a 9.5 mm nominal aggregate gradation with an AC20 asphalt binder. The predominant pavement distress, as determined with a Visual Distress Survey, was reflective cracking (transverse), with minimal longitudinal cracking and rutting.

Under a maintenance resurfacing program, a reflective crack relief interlayer (RCRI) mix was specified to aid in mitigating the on-set of reflective cracking. The final pavement design consisted of milling to a constant depth of 76.2mm and then 114.3 mm of the bituminous overlay. Table 1 shows the different pavement sections, as designated based on milepost, and the final pavement design.

Both the 9.5 mm (9H76) and 12.5 mm (12M76) Superpave mixes contained a PG76-22 asphalt binder. The 12.5 mm Superpave mixture was designed using an N_{design} level of 75 gyrations, while the 9.5 mm Superpave mixture was designed using an N_{design} level of 100 gyrations. The RCRI mixture contained a highly polymerized asphalt binder specially designed for mitigating reflective cracking. The 9.5 mm and 12.5 mm Superpave mixtures are the most common asphalt overlay mixes used in New Jersey for composite pavement maintenance. The composite pavement is supported by an uncrushed gravel base layer, which rests on a silty sand subgrade soil.

2.2 Traffic loading

Portable Weigh-in-Motion Sensors (WIM) and Automatic Vehicle Classifiers (AVC) were used to measure the traffic stream and determine an Axle Load Spectra. The traffic data was collected over a seven-day period and averaged to provide weekly traffic loading conditions. A summary of the collected traffic is below:

- Average Daily Traffic (ADT) = 8,840 vehicles;
- 91.6% automobiles; 2.7% light trucks (FHWA Class 4 and 5); 5.7% Heavy Trucks (FHWA Class 6 and Greater);
- Automobile Axle Loads: Average = 16.9 kN;
- FHWA Class 4 and 5: Average = 59.2 kN; and
- FHWA Class 6 and Greater: Average = 57.8 kN.

Table 1. Final pavement thickness and mix selection.

Section	Surface course	Intermediate course	RCRI
MP 0.2 to 2.5	38.1 mm of NJDOT 9H76	50 mm of NJDOT 12M76	25 mm
MP 2.5 to 4.5	38.1 mm of NJDOT 9H76	76.2 mm of NJDOT 12M76	–
MP 4.5 to 7.2	38.1 mm of NJDOT 9H76	50 mm of NJDOT 12M76	25 mm

2.3 Field forensic testing

To establish laboratory test parameters that model expected field conditions, along with the collected traffic information, two essential field forensic tests were required; Falling Weight Deflectometer (FWD) and extracting cores of the PCC pavement.

2.3.1 Falling Weight Deflectometer testing

Falling Weight Deflectometer (FWD) testing was conducted before and after the transverse joint at three, increasing load magnitudes; 28.91, 44.48, and 71.17 kN. The FWD testing was used to assess the Load Transfer Efficiency (LTE) and the vertical deflections at the joint due to the applied loads. Vertical deflections at the joint were normalized to 40 kN for comparison purposes. The average results of the FWD testing for the different pavement sections are shown in Table 2.

The vertical deflection at the joint, measured immediately under the load plate, and the applied load were plotted against each other to generate a linear relationship between applied load and vertical deflection at the joint. Therefore, if applied load (or axle load) is known, then the resultant vertical joint deflection can be determined. This is schematically shown in Figure 1.

The applied load/vertical deflection relationship was developed and averaged using the FWD measurements taken within each test section. The resultant relationships are shown as Equations 1 through 3.

$$\text{MP 0.2 to 2.5: Joint Deflection} = 4.72779\text{E-}06(\text{Applied Load}) + 1.34363\text{E-}03 \quad (1)$$

$$\text{MP 2.5 to 4.5: Joint Deflection} = 5.12853\text{E-}06(\text{Applied Load}) + 9.18271\text{E-}03 \quad (2)$$

$$\text{MP 4.5 to 7.2: Joint Deflection} = 4.98799\text{E-}06(\text{Applied Load}) + 6.84053\text{E-}03 \quad (3)$$

Table 2. Average Falling Weight Deflectometer results.

Section	Load Transfer Efficiency (LTE)	Normalized Vertical Deflection
MP 0.2 to 2.5	71%	0.137 mm
MP 2.5 to 4.5	73%	0.163 mm
MP 4.5 to 7.2	85%	0.153 mm

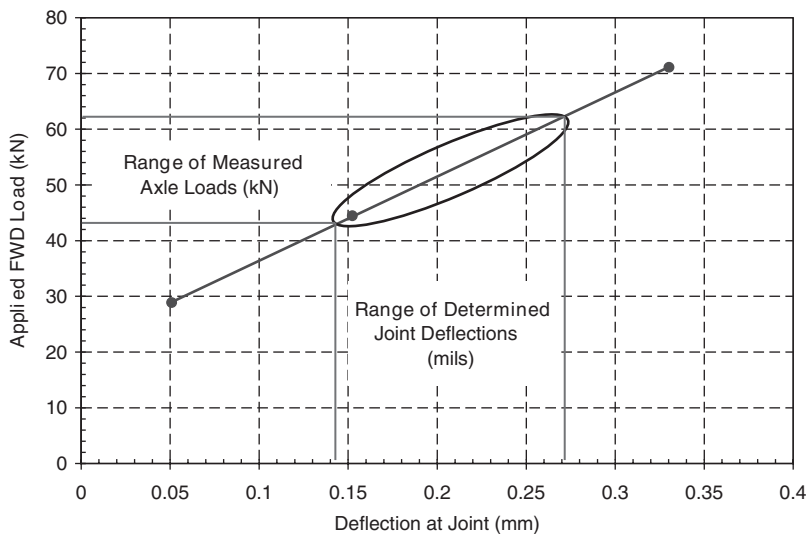


Figure 1. Generalized relationship between applied load and joint deflection.

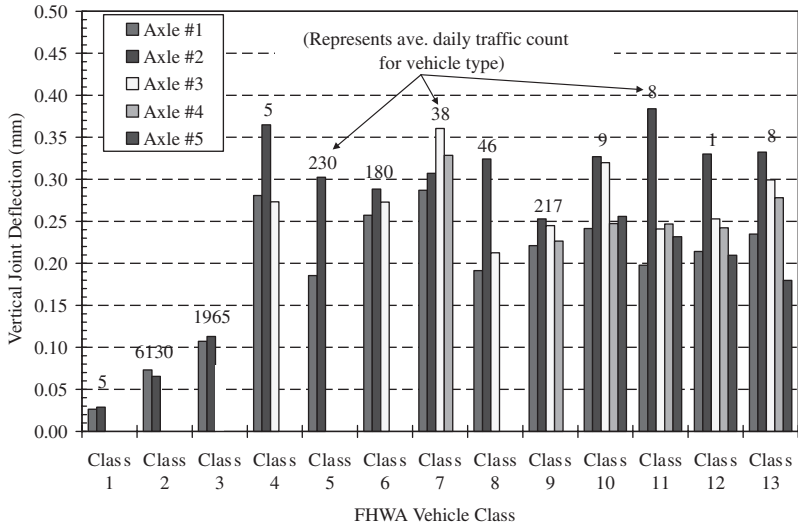


Figure 2. Daily deflection spectra for test section #1.

where, Joint Deflection is in millimeters (mm); and Axle Load is in Newtons (N).

Now that a relationship between applied load and joint deflection is established, the Axle Load Spectra can be directly inputted into any of the relationships shown above to establish a daily vertical Deflection Spectra of the PCC joints. Figure 2 is an example of the daily Deflection Spectra determined for MP 0.2 to 2.5. More detail on the use of the Deflection Spectra and how it can be applied to laboratory testing is discussed later in the paper.

2.3.2 Coring/concrete test results

Immediately after the FWD testing, full-depth pavement cores were taken for laboratory analysis. Of particular interest was the Coefficient of Thermal Expansion (CTE) of the underlying PCC pavement. The CTE is a parameter that, along with effective slab length (L_{eff}), maximum 24 hour temperature difference (ΔT), and the PCC/Base friction factor (β), can provide an estimate of the expected horizontal movement at the PCC slab joint (ΔL) due to daily temperature changes, as shown in Equation 4.

$$\Delta L = CTE(L_{eff})(\Delta T)(\beta) \quad (4)$$

Six cores were tested according to AASHTO TP60, “Standard Test Method for Coefficient of Thermal Expansion of Hydraulic Cement Concrete” and determined to have a CTE of $12.34E - 6 \text{ cm/cm/}^\circ\text{C}$, with a standard deviation of $0.28E - 6 \text{ cm/cm/}^\circ\text{C}$. The Enhanced Integrated Climatic Model, EICM (Larson and Dempsey, 2006) was used to estimate temperature profiles in the pavement since temperature probes were not installed at the site. Interpolated weather data from neighboring weather stations were used to generate 5 years (1998 and 2003) worth of historical climate information for the test site. The maximum 24-hour temperature difference determined at the surface of the PCC pavement for a 114.5 mm asphalt overlay was 6°C . The maximum 24-hour temperature difference was used for evaluation since this would create the greatest joint movement that would initiate cracking. A PCC/Base Friction Factor (β) was estimated from similar pavement materials/structures presented in the Long Term Pavement Project (LTPP) concrete pavement test sites (Khazanovich and Gotliff, 2002). This resulted in an average β assumed for the analysis was 0.73. Therefore, using Equation (1) and the appropriate input parameters, it was concluded that the maximum horizontal movement at the PCC joints that would be expected in a 24-hour period is 0.67 mm.

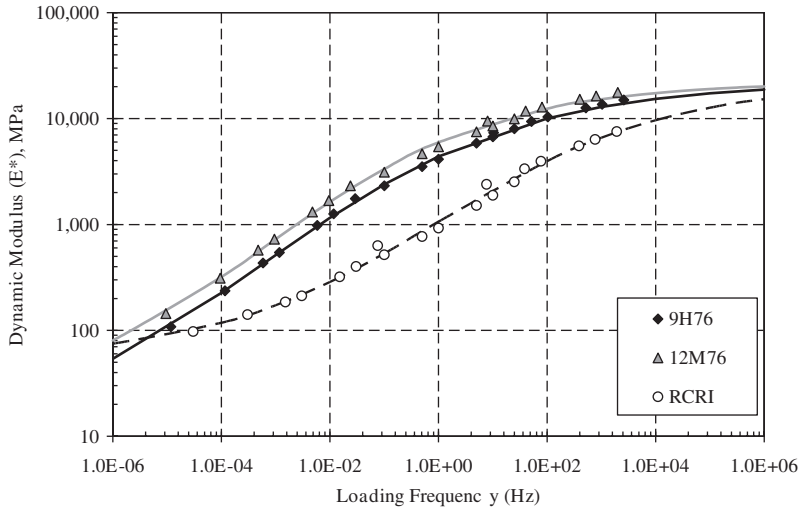


Figure 3. Master stiffness curve generated from loose mix.

3 LABORATORY EVALUATION

Typically, the vertical and horizontal deflections at the PCC joints initiate and perpetuate reflective cracking. The vertical deflection is a function of the daily traffic loading, while the horizontal deflection is a function of climatic loading (heating and cooling cycles). To simulate these movements in the laboratory, two different fatigue-type performance tests were conducted on loose mix sampled during the bituminous overlay construction; 1) Flexural Beam Fatigue test (AASHTO T321), and 2) TTI Overlay Tester (TxDOT Tex-248-F). Dynamic modulus testing, using an abbreviated version of AASHTO TP62, was also conducted on the different mixes to compare their stiffness properties and utilized the generated master stiffness curves to adjust for seasonal stiffness changes in the vertical deflection analysis.

3.1 Mixture stiffness – AASHTO TP62

Dynamic modulus and phase angle data were measured and collected in uniaxial compression following the method outlined in AASHTO TP62, *Standard Test Method for Determining Dynamic Modulus of Hot-Mix Asphalt Concrete Mixtures*. The data was collected at three temperatures; 4, 20, and 45°C (except for the RCRI which used 35°C), using loading frequencies of 25, 10, 5, 1, 0.5, 0.1, and 0.01 Hz. Samples were tested in triplicate after short-term oven aging following the procedures outlined in AASHTO R30, *Mixture Conditioning of Hot-Mix Asphalt (HMA)*. The reference temperature used for the generation of the master curves and the shift factors was 20°C. The resultant Master Stiffness curves are shown in Figure 3.

Review of the master stiffness curves clearly shows the difference in mixture stiffness, especially at the intermediate to lower test temperatures (mid to high loading frequency) between the Superpave dense-graded mixes (9H76 and 12M76) and the RCRI mix. Bituminous mixtures that are capable of obtaining lower stiffness properties at intermediate to low temperatures tend to be more resistant to cracking.

3.2 Flexural beam fatigue test – AASHTO T321

Flexural fatigue testing was conducted using the Flexural Beam Fatigue test procedure outlined in AASHTO T321, *Determining the Fatigue Life of Compacted Hot-Mix Asphalt (HMA) Subjected to Repeated Flexural Bending*). The applied tensile strain levels used for the fatigue evaluation were;

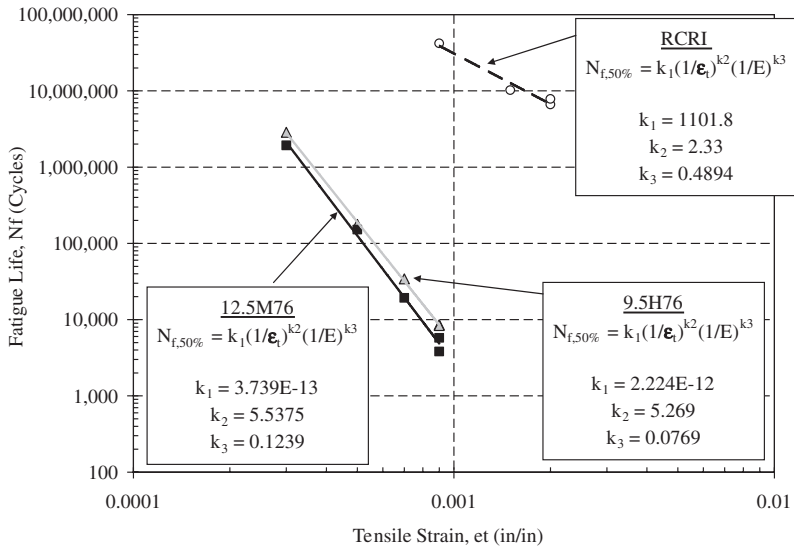


Figure 4. Fatigue life vs tensile strain.

300, 500, 700, and 900 micro-strains for the 9.5 and 12.5 mm Superpave mixtures and 900, 1500, and 2000 microstrains for the RCRI mixture. Samples were tested after short-term aging following the procedures outlined in AASHTO R30, *Mixture Conditioning of Hot-Mix Asphalt (HMA)*.

The test conditions utilized were those recommended by AASHTO T321 and were as follows:

- Test temperature = 15°C;
- Sinusoidal waveform;
- Strain-controlled mode of loading; and
- Loading frequency = 10 Hz;

Figure 4 illustrates the superior flexural fatigue resistance expected in the RCRI mixture over the Superpave dense-grade mixtures. The fatigue life regression equations shown in Figure 4 can now be used in conjunction with the master stiffness curves and the daily Deflection Spectra to predict the flexural fatigue life of the asphalt mixtures for the New Jersey test site.

3.3 TTI Overlay Tester (TxDOT Tex-248-F)

The TTI Overlay Tester (Fig. 5) is a test device that is has been gaining popularity (Zhou and Scullion, 2005) to evaluate the reflective crack resistance of bituminous mixtures. Originally developed by the Texas Transportation Institute, TTI (Germann and Lytton, 1979), the test device simulates the expansion and contraction movements at the PCC joint area. Although this test procedure is essentially a fatigue-type test, it currently represents the best method to truly simulate horizontal joint movements of PCC pavements.

The test was conducted using protocol established at TTI (Zhou and Scullion, 2005), although a test temperature of 15°C was used instead of 25°C. The horizontal deflection of 0.67 mm, determined from the Coefficient of Thermal Expansion testing on the PCC cores and the resulting joint deflection calculated using Equation 4, was used for the testing. The test results from the Overlay tester were:

- 12.5 mm Superpave Mixture: 22 Cycles
- 9.5 mm Superpave Mixture: 24 Cycles
- RCRI Mixture: 46,502 Cycles



Figure 5. TTI overlay tester and mounted test specimen.

It should be noted that the final test results of the RCRI mixture were extrapolated after testing was stopped at 3,000 cycles. The TTI Overlay Tester results again illustrate the superior fatigue resistance of the RCRI mixtures. Unfortunately, the Overlay Tester results for the two Superpave mixtures have been found to be typically for most dense-graded mixes specified by the New Jersey Department of Transportation (NJDOT). To put the Overlay Tester test results in perspective, albeit empirical, it would only take approximately 22 to 24 days of similar climatic conditions used in the Overlay Tester to initiate cracking at the bottom of the dense-graded bituminous layer.

4 DEFLECTION SPECTRA APPROACH FOR VERTICAL DEFLECTION FATIGUE ANALYSIS

The reflective cracking fatigue life evaluation using the Deflection Spectra is based on the cumulative fatigue damage concept originally developed by Miner (Yang, 1993), shown as Equation 5. Fatigue damage, D , is calculated as the ratio of the predicted number of traffic repetitions, n_i , to the allowable number of load repetitions, N_i .

The reflective cracking fatigue analysis using the Deflection Spectra is based on the cumulative damage concept originally developed by Miner (Yang, 1993), shown as Equation 5. The fatigue damage is calculated as the ratio of the predicted number of traffic repetitions to the allowable number of load repetitions. This is also the current fatigue cracking analysis format used in the Mechanistic Empirical Pavement Design Guide (ARA, 2004).

$$D = \sum_{i=1}^T \frac{n_i}{N_i} \quad (5)$$

where: D = damage; T = total number of periods; n_i = actual traffic for period i ; and N_i = allowable failure repetitions under conditions prevailing in period i .

The Deflection Spectra approach relies on the following pieces of information:

1. Measurement of axle load spectra from WIM and AVC sensors.
2. Relationship between applied load and joint deflection.

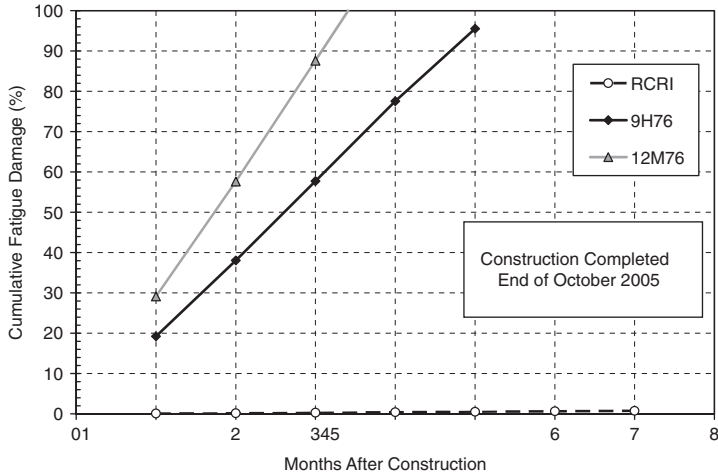


Figure 6. Fatigue life assessment using deflection spectra approach.

3. Fatigue life relationship of bituminous mixtures using the Flexural Beam Fatigue test.
4. Conversion of joint deflections to applied tensile micro-strain for the Flexural Beam Fatigue test.

Both 1), 2) and 3) were described earlier in the paper. The conversion of PCC vertical joint deflections to applied tensile micro-strain in the Flexural Fatigue Beam apparatus is accomplished by using the general equation of the test apparatus itself (Eq. 6). Equation 6 relates the test apparatus gauge length dimensions and vertical deflection of the test specimen itself to tensile micro-strain based on simple beam theory. By doing so, the vertical Deflection Spectra can be converted into micro-strain, which in turn can be inputted into the mixture specific, bituminous fatigue life equations shown in Figure 3 to determine the number of fatigue life repetitions until fatigue failure (N_i). The master stiffness curves (Fig. 2) of the bituminous mixtures are used to vary the mixtures modulus, E , due monthly temperature changes. The daily axle count is then used to determine n_i for that respective applied axle load. This allows for the determination of the Damage Ratio (n_i/N_i).

$$\varepsilon_t = \frac{12\delta h(1E6)}{(3G_o^2 - 4G_i^2)} \quad (6)$$

where: ε_t = applied tensile strain during Flexural Beam Fatigue test; δ = peak deflection of beam (or joint deflection); h = average height of Flexural Beam Fatigue specimen; G_o = outer gauge length of Flexural Beam Fatigue test; and G_i = inner gauge length of Flexural Beam Fatigue test

5 FIELD FATIGUE CRACKING MEASUREMENTS VS DEFLECTION SPECTRA APPROACH

The Deflection Spectra approach fatigue cracking predictions was compared to observed reflective cracking. Figure 6 shows the fatigue comparisons of the different asphalt mixtures. The Deflection Spectra approach predicted that the 12.5 mm Superpave mixture would begin to develop fatigue cracking three month after construction, while the 9.5 mm Superpave mix would develop fatigue cracking between five and six months after construction.



Figure 7. Premature reflective cracking between MP 0.2 and 2.5.

A visual distress survey was conducted five months after construction had been completed when premature cracking was observed during a routine drive-by. The one year crack count showed that:

- MP 0.2 to 2.5: 7.0% of transverse joint length had reflected through;
- MP 2.5 to 4.5: 3.6% of transverse joint length had reflected through; and
- MP 4.5 to 7.2: 0.33% of transverse joint length had reflected through.

Cores were taken through the cracks of the various test sections to assess the extent of the transverse crack. The higher amount of cracking between MP 0.2 to 2.5, an area with the RCRI material, was found to have several construction related issues that led to its premature failure. The three most severe being; 1) Insufficient thickness of the RCRI layer (typically <15.8 mm), 2) Higher than specified air voids in the RCRI mixture, and 3) Poor bonding between the surface and intermediate layers (Fig. 7). Therefore, the test section between MP 0.2 to 2.5 was considered to be an outlier in the comparison and not a true representative.

The Deflection Spectra approach was in relative agreement with the field observations of reflective cracking, although some cracks were observed in the RCRI section (Test Section #3), even though the joint conditions were better than the other two test sections. It is believed that this is due to an incompatibility between the flexural stiffness of the RCRI mixture and the dense-graded bituminous mixtures that overlaid it. Even though the RCRI was able to absorb a majority of the applied stress/strain occurring, the magnitude of tensile straining at the top of the RCRI layer was still enough to initiate cracking in the dense-graded mixtures.

6 SUMMARY AND CONCLUSIONS

A practical approach to HMA overlay material selection and performance evaluation has been presented. The combination of axle spectra and FWD test results to assess vertical joint deflection due to realistic traffic load spectra and the CTE test to determine the climatically induced horizontal deflections can provide pavement designers valuable information regarding bituminous mixture selection.

A new reflective crack fatigue life prediction method is proposed using joint deflection data from FWD testing, axle load spectra data, and laboratory test results from the Flexural Beam Fatigue and Dynamic Modulus test. The new method, called the Deflection Spectra Approach, predicted

fatigue lives for the various asphalt mixtures that were consistent with field observations. The method has the advantage over typical fatigue evaluation methods since tensile strains are being directly measured, instead of predicted based on elastic theory. The required information (axle load spectra, FWD testing, dynamic modulus, etc.) are also consistent with typical information collected for use with the Mechanistic-Empirical Pavement Design Guide Software. However, it should be noted that reflective cracking is a distress due to the coupled nature of vertical and horizontal deflections. Future analysis will concentrate on combining the affects of the vertical and horizontal fatigue distress.

More emphasis should also be placed on the asphalt mixtures that are used as overlays for RCRI mixtures. The Superpave dense-graded mixtures used to overlay the RCRI in the New Jersey Test Section had significantly higher stiffness and poorer fatigue resistance, essentially creating an incompatible system (i.e. – stiff over flexible). Research has begun to initiate a “Transitional Stiffness” type of design so incompatibility between bituminous mixtures does not occur.

REFERENCES

- Applied Research Associates, 2004, *Guide for the Mechanistic-Empirical Design of New and Rehabilitated Pavement Structures: Appendix II-1: Calibration of Fatigue Cracking Models for Flexible Pavements*, National Cooperative Highway Research Program, NCHRP, Transportation Research Board, National Research Council, 311 pp.
- Bennert, T. and Ali Maher, 2007, “Evaluation of the Current State of Flexible Overlay Design for Rigid/Composite Pavements in the United States”, Presented and Published at the 86th Annual Meeting of the Transportation Research Board, January 21st to 25th.
- Button, J. and R. Lytton, 2007, “Guidelines for Using Geosynthetics with Hot Mix Asphalt Overlays to Reduce Reflective Cracking”, Presented and Published at the 86th Annual Meeting of the Transportation Research Board, January 21st to 25th.
- Christensen, D.W., R. Bonaquist, and L.A. Cooley, Jr., 2006, *Quarterly Report for NCHRP Project 9-33, A Mix Design Manual for Hot Mix Asphalt*, National Cooperative Highway Research Program, Transportation Research Board, Washington, D.C.
- Distress Identification Manual for the Long-Term Pavement Performance Project, 4th Edition*, 2003, FHWA-RD-03-031, United States Department of Transportation, Federal Highway Administration, 169 pp.
- Germann, F.P. and R.L. Lytton, 1979, *Methodology for Predicting the Reflection Cracking Life of Asphalt Concrete Overlays*, Research Report FHWA/TX-79/09+207-5, College Station, Texas, March 1979.
- Khazanovich, L. and Alex Gotlif, 2002, *Evaluation of Joint and Crack Load Transfer – Final Report, FHWA-RD-02-088*, Federal Highway Administration, 118 pp.
- Larson, G. and B. Dempsey, 2006, *Enhanced Integrated Climatic Model, Version 3.2.*, Applied Research Associates (ARA).
- Yang, H.H., 1993, *Pavement Analysis and Design*, Prentice Hall, Englewood Cliffs, New Jersey.
- Zhou, F. and Tom Scullion, 2005, “Overlay Tester: A Simple Performance Test for Thermal Reflective Cracking”, *Journal of the Association of Asphalt Paving Technologists*, Vol. 74, pp. 443–484.
- Zhou, F., S. Hu, T. Scullion, M. Mikhail, and L. Walubita, 2007, “A Balanced Mix Design Procedure for Overlays”, *Journal of the Association of Asphalt Paving Technologists*, Vol. 76, pp. 430–465.

Case history on surface initiated cracks on urban thoroughfare pavements

L.A. Cooley, Jr.

Burns Cooley Dennis, Inc., Ridgeland, Mississippi, USA

I.L. Howard

Mississippi State University, Starkville, Mississippi, USA

G. Baumgardner

Paragon Technical Services, Inc., Jackson, Mississippi, USA

M. Ross

Public Works Department, Overland Park, Kansas, USA

ABSTRACT: This paper documents a forensic investigation into the cause(s) of premature surface-initiated cracks on thoroughfare pavements in overland Park, Kansas. Two issues were identified as the primary causes in the surface-initiated cracks: low in-place density and absorptive aggregates. Based upon the data and observations, it was recommended to increase the amount of oven aging prior to laboratory compaction of HMA. This recommendation was made to take into account the amount of asphalt absorbed by the aggregates. This paper also presents observations by the City of Overland Park after his recommendation was adopted. It is intended as a practical paper that highlights some causes of surface initiated cracks.

1 INTRODUCTION

The City of Overland Park, Kansas embarked on an initiative to improve the durability of its asphaltic concrete pavements in the late 1990s. Problems that were common with the older Marshall designed mixes included stripping, rutting and wide transverse cracks. The initial changes utilized the principles outlined in the Asphalt Institute's MS-2 (1997) which placed more emphasis on the volumetric properties of the hot mix asphalt (HMA). After several years of experience with HMA designed around volumetric properties, the City changed the specification to require the use of a Superpave gyratory compactor and mix design system. A design objective that is still important to the City is being able to use locally available materials. Unfortunately, local limestone aggregate tend to be more absorptive than is desirable. The locally available limestone aggregates are typically too soft to use design gyrations of 75 or more, but given the relatively low truck volumes on most streets will perform adequately in an otherwise well designed mix.

During 2004 and into 2005, the City became concerned with projects that exhibited widespread longitudinal cracking. The Public Works department felt that a thorough forensic analysis was necessary to establish the cause of the problem and to determine how the problem could be resolved.

1.1 Objectives

The primary objective of this investigation was to evaluate potential causes of premature longitudinal cracking experienced on the City of Overland Park's thoroughfares. Based upon the results of the investigation, recommendations were to be provided to minimize the occurrence of these cracks.



Figure 1. Cracking on Quivira Road.

2 SITE CONDITIONS

A site visit was conducted in April of 2005 in order to evaluate the condition of the roadways. During the site visit, the Overland Park Public Works Department led a guided tour of the City to evaluate various thoroughfare pavements that had experienced premature cracking. The following paragraphs present information on each of these pavements along with observations.

2.1 *Quivira Road from 135th street to 143rd Street*

Quivira Road, a four-lane divided thoroughfare, is a North-South connector located within the western part of Overland Park. The portion of the pavement in question was constructed during 1999 and 2000 (five years old). HMA used within the pavement structure was designed using 75 blows of the Marshall hammer. Cores obtained from Quivira Road indicated that the total pavement thickness was approximately 248 mm (10 in.).

At the time of the site visit, Quivira Road had experienced a moderate amount of longitudinal cracking and raveling. There was also loss of fines within the pavement surface. Cracks were occurring both within the wheel path and at the edge of the wheel path. Raveling was generally limited to areas near the cracks. Figure 1 illustrates the level of cracking and raveling within Quivira Road. Cores taken within Quivira Road indicated that the cracks were surface initiated and had progressed downward into the pavement structure.

2.2 *127th Street from Quivira Road to Switzer Road*

127th Street, a four-lane divided city street, is an East-West thoroughfare.. The portion of pavement evaluated during the site visit was constructed during 2000 and 2001 (four years old). According to the project specifications, the HMA mixture was designed in accordance with Marshall

methods using 75 blows per face. Cores taken from the roadway indicated that the pavement was approximately 241 mm (9.5 in.) in thickness.

At the time of the site visit, 127th Street had experienced a moderate amount of longitudinal cracking and raveling along with the loss of surface fines. The surface initiated cracks were located both within and outside the wheel path. Some of the cracks appeared to have asphalt binder that had migrated to the surface due to stripping of the asphalt binder from aggregates in underlying layers.

2.3 151st Street from Metcalf Avenue to Nall Avenue

151st Street, a four-lane divided city street, is an East-West thoroughfare in southern Overland Park. HMA used to construct the pavement structure was designed in accordance with Marshall methods using 75 blows per face. Construction of the pavement occurred during 2000 and 2001 (four years old). Cores taken from 151st Street indicated that the pavement structure was approximately 232 mm (9.1 in.) in thickness.

At the time of the site visit, 151st Street had experienced some longitudinal cracking, raveling and loss of surface fines. Longitudinal cracks were surface initiated with raveling occurring near the cracks. The longitudinal cracks were predominately between the wheel path and did not appear to be load associated.

2.4 127th Street from Pflumm Road to Quivira Road

The fourth project included in the site visit was 127th Street from Pflumm Road to Quivira Road, also a four-lane divided thoroughfare, traveling East-West. The portion of 127th Street evaluated was constructed in 2001 and 2002 (three years old). HMA mixtures used within the pavement structure were designed using 75 blows per face of the Marshall hammer. Cores taken from 127th Street indicated that the HMA portion of the pavement structure totaled approximately 267 mm (10.5 in.).

Similar to the previously discussed pavements, 127th Street from Pflumm to Quivira had experienced longitudinal cracking, raveling and loss of surface fines. Figure 2 illustrates the typical condition of the pavement at the time of the site visit. As shown in Figure 2, the longitudinal cracks were typically located within the wheel path; however, a core and evaluation of the pavement surface indicated that the cracks were surface initiated and traveled down into the pavement structure.

2.5 Santa Fe

Santa Fe is also a four-lane divided thoroughfare. The project included within the guided tour was constructed in 2004 (one year old). Specifications used for this construction project indicated that the Superpave mix design method was used to design all layers of HMA used in the pavement structure. Cores taken from Santa Fe show an approximate asphalt pavement thickness of 283 mm (11.1 in.) placed in four layers.

At the time of the site visit, only very minor surface distresses were observed. The pavement was experiencing some longitudinal cracking and loss of surface fines; however, raveling was not evident. Cracks within Santa Fe were hairline cracks and located at the edge of the wheel path. No cores were obtained within the hairline cracks, but it is assumed that the cracks were surface initiated.

3 POTENTIAL CAUSES OF CRACKING

Based upon the above discussion on observations during the site visit, the premature cracks observed within flexible pavements are primarily surface initiated cracks located both within and outside the wheel path. The depth at which the surface initiated cracks had propagated into the pavement structure varied depending upon the age of the pavement. Raveling was also observed on most of the pavements near the surface initiated cracks. All of the pavements also had loss of surface fines.



Figure 2. Cracking encountered on 127th Street.

The above described distresses indicate that the problems encountered are due to poor HMA durability. According to Gerritsen et al. (1987), the probable causes of surface initiated cracks are poor compaction, stiffening of the asphalt binder and/or low asphalt binder contents. Based upon the data accumulated for the five projects included in the guided tour, the pavements evaluated all had in-place air void contents above what would be desired. In-place air voids for nineteen cores from the five projects indicated that approximately 40 percent of these cores had in-place air void contents of 8 percent or less. Therefore, 60 percent of the cores had lower density than the Overland Park specifications of 92 percent of theoretical maximum (Rice) specific gravity. Even more troubling than 60 percent of the density measurements not meeting in-place density requirements is that these pavements ranged in age from 1 to 5 years. HMA pavements should densify under traffic resulting in lower in-place air voids after traffic has been applied.

3.1 *Evaluation of specifications*

The durability problems and lack of densification in the HMA pavements are likely related. Both appear to be caused by an insufficient volume of effective asphalt binder. The only systematic method of controlling the amount of effective asphalt binder (or at least the target binder volume) is during mix design. Therefore, the current version of the S-1, Overland Park Superpave Asphaltic Concrete Surface and Intermediate Course, specification was critiqued.

One method of critiquing a mix design specification is to evaluate HMA that has been produced using the specification. During the site visit, Overland Park supplied a significant amount of laboratory data for HMA produced for Overland Park construction projects.

Figure 3 illustrates data from a single contractor. On this figure are two different aggregate specific gravity values for mixtures produced during 2005. Aggregate specific gravities shown on Figure 3 include effective specific gravity and combined aggregate bulk specific gravity for each HMA sample tested from April 15, to May 23, of 2005. Data on Figure 3 are also divided into three subsets, signified by the vertical lines. All of the HMA samples represented on Figure 3 included the same fine aggregate sources, stockpiles and percentages. The purpose of dividing the samples

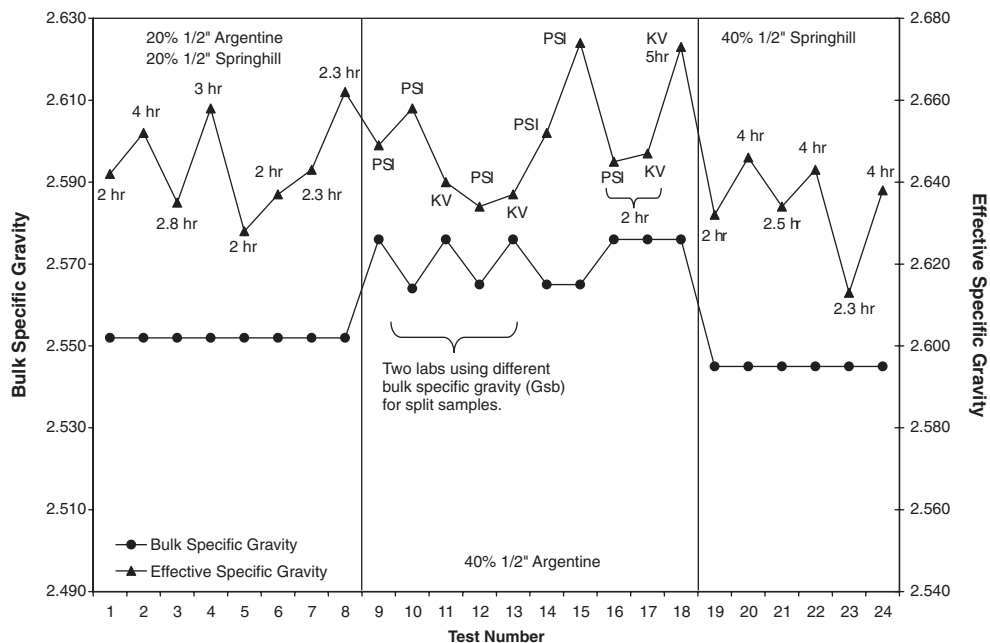


Figure 3. Bulk specific gravity and effective specific gravity data.

into three subsets is that three different coarse aggregate sources/proportions were utilized within each subset. Coarse aggregate for the first subset of data included two stockpiles: 1/2" Argentine and 1/2" Springhill. Both of these stockpiles were included at 20 percent of the total blend. Coarse aggregate for the second subset of data consisted of 1/2" Argentine, added at 40 percent of the total blend. The final subset of data had the coarse aggregate fraction provided by a 1/2" Springhill stockpile, at 40 percent of the total aggregate.

Two observations are noted from Figure 3. First is the variability in the effective specific gravity data within each data subset. As an example, observe the middle subset of data representing the HMA samples produced with 40 percent 1/2" Argentine coarse aggregates. All samples were supposedly allowed to cure (age) for 2 hours after production and prior to testing, except for the last data point which was aged for 5 hours. Neglecting the lone data point aged for 5 hours, the average effective specific gravity value is 2.648. The effective specific gravity ranged from a high of 2.674 to a low of 2.634 resulting in a range of 0.040. During normal HMA production, the effective specific gravity of aggregates should not vary significantly as long as materials do not change and samples are subjected to the same amount of aging prior to testing. A typical tolerance on effective specific gravity is ±0.012, or a range of 0.024. Comparing the typical allowable range of 0.024 to the 0.040 illustrates the amount of variability in the effective specific gravity data. If all of the samples were aged for two hours, as stated on the lab data sheets, then the materials, namely aggregates, must be changing in order to produce this amount of variability.

The second observation deals with the effect of curing time on the HMA sample test results. This effect is clearly seen when looking at the effective specific gravity data within the third subset of data (40 percent 1/2" Springhill). The six data points reflected in the third subset of data represent three HMA samples that were split with one sample aged for approximately two hours and one split aged for approximately four hours. In each instance, the effective specific gravity increased after four hours of aging when compared to the samples aged for two hours. The only explanation for the consistent increase in effective specific gravity after four hours of aging is that the extra two hours allowed for more asphalt binder to be absorbed by the aggregates. More asphalt binder absorbed into the aggregate results in an increase in aggregate effective specific gravity. Properties for these

Table 1. Properties of HMA split samples from third subset of data

Property	Sample 1		Sample 2		Sample 3	
	2 hr.	4 hr.	2.5 hr.	4 hr.	2 hr.	4 hr.
Asphalt Content, %	5.04	5.08	4.94	4.80	5.30	5.47
Rice Specific Gravity	2.451	2.458	2.448	2.461	2.434	2.440
Effective Specific Gravity	2.642	2.652	2.634	2.643	2.632	2.646
Air Voids, %	4.81	5.21	4.62	5.93	4.56	4.51
VMA, %	13.2	13.3	12.8	13.4	13.6	13.5
Eff. Asphalt Content, % (Mass)	3.73	3.63	3.63	3.35	4.03	3.99
Abs. Asphalt Content, % (Mass)	1.38	1.53	1.37	1.52	1.35	1.57
Eff. Asphalt Content, % (Volume)	8.37	8.13	8.17	7.47	9.00	8.95
Dust to Asphalt Ratio	1.34	1.35	1.40	1.52	1.39	1.20
Film Thickness, microns	7.49	7.03	6.84	6.17	7.30	7.60

samples are presented in Table 1. Of particular interest in Table 1 are the absorbed asphalt contents (by mass). For each of the three split samples, samples aged for four hours had approximately 0.2 percent more absorbed asphalt binder. This level of asphalt binder absorption increase, or more, is also likely occurring in the field, which indicates that the current two hour aging process included in the Overland Park specifications should be changed to four hours. Without aging the mixture in the lab to simulate the aging that occurs in the field, a HMA that has an insufficient volume of effective asphalt binder can result. Also of concern in Table 1 are the relatively low values for film thickness. Most literature recommends a minimum film thickness of 8 microns in order to provide a durable mixture. Film thicknesses shown in Table 1 all fall well below 8 microns.

3.2 Effective Asphalt Binder

Figure 3 and Table 1 suggest that the aggregates currently used with HMA produced for Overland Park absorb a significant amount of asphalt binder. Asphalt binder absorbed by aggregates does not provide benefit to an HMA pavement layer with respect to durability. Because of the relatively large amount of asphalt absorption, more than 2 hours is needed during both mix design and field production testing to result in mixture properties more closely resembling the pavement layer properties after construction is completed. Laboratory aging of HMA during mix design and field QC/QA testing should be increased from two hours to four hours. Based upon the data presented in Table 1, this should increase the amount of asphalt binder by an average of at least 0.2 percent. An average increase in asphalt binder of 0.2 for all HMA produced for Overland Park should significantly improve the durability of the City's flexible pavements.

Another method of evaluating whether the desired amount of asphalt binder is within a HMA mixture for durability is to determine the volume of effective asphalt binder. The percent volume of effective asphalt binder is the mathematical difference between the voids in mineral aggregates and air voids. Figure 4 illustrates a histogram of the percent volume of effective asphalt binder for data from 2005 production. The target percent volume of effective asphalt binder for this data should be 9.0 percent based upon the mix design criteria. This target was selected because all of the mixes included within Figure 4 were intermediate courses; therefore, subtracting a target air void content of 4.0 from the minimum VMA of 13.0 produces a percent effective volume of asphalt binder of 9.0 percent.

Figure 4 shows that for the 2005 data, half of the HMA samples did not have a sufficient volume of effective asphalt binder. As described previously, a significant amount of asphalt binder is absorbed by the aggregates when comparing mixes aged for two hours and mixes aged for four hours. Therefore, since the samples illustrated in Figure 4 were aged for only two hours, the percentage of samples having insufficient asphalt binder is actually higher than depicted on the figure. This further illustrates that more asphalt binder is needed for HMA produced for Overland Park.

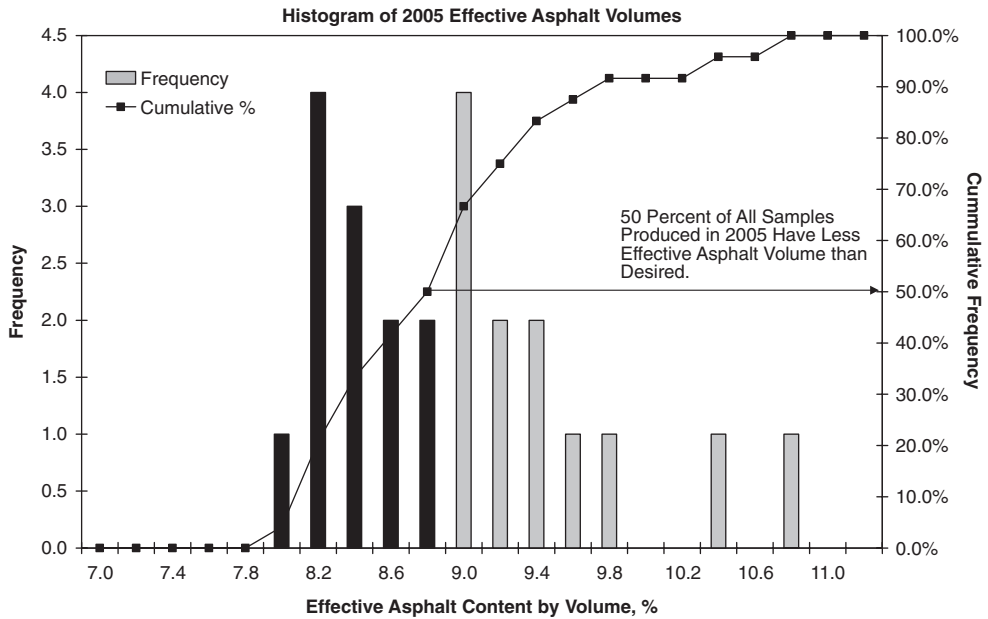


Figure 4. Effective asphalt volume data for 2005.

3.3 Pavement density specifications

As discussed previously, there was a lack of adequate density within the pavements experiencing premature cracking. Lack of adequate density results in both water and air being able to penetrate into the pavement. The presence of water in a pavement leads to an increased potential for moisture damage while excessive exposure to air increases the potential for oxidation of the asphalt binder.

The current density specifications for Overland Park are outlined in Sections 1.12 through 1.15 of S-1, Overland Park Superpave Asphaltic Concrete Surface and Intermediate Course. These specifications are somewhat contradictory, especially within Section 1.13. Within this section, the specification states that the "... contractor is responsible ..." for achieving the specified density level during construction. However, a significant portion of Section 1.12 and part of Section 1.13 uses language that specifies the type of rollers to be used, how to construct longitudinal and transverse joints, etc. Based upon conversations with local contractors and City employees, the current practice is that S-1 is used as a method specification. Method specifications provide details on the type of equipment and procedures for obtaining a desired quality characteristic. Method specifications place the onus on the specifying agency because the agency provides the procedures for obtaining the desired quality characteristic.

Our experiences indicate that for specifying pavement density, an end-result specification containing disincentives is a more effective tool for obtaining adequate density on construction projects. End-result specifications do not specify equipment or procedures, but rather define a quality characteristic that is required when the contractor concludes a day's production/construction. In order to develop an end-result specification, a desirable level of density is needed. For typical HMA having a dense gradation, an average 93 percent of theoretical maximum density should be the target density with the average not being lower than 92 percent.

Another concern with the specification for density was the locations that cores are to be obtained. Section S-1.14, Sampling Pavements for Density, states that "... two cores are to be from the lane being paved and one core centered on the longitudinal joint. ...". Section S-1.15 further states that "... the average of the three cores ..." shall be 92 to 96 percent of theoretical maximum density. It is generally not practical for core density data obtained on longitudinal joints to be averaged with cores obtained from mainline paving. The impracticality comes from the placement process. HMA

augered to the end of a screed typically becomes slightly segregated with the gradation of the mixture at the edge of the pavement coarser than the gradation of the mixture within the mainline. Therefore, averaging mainline cores and joint cores is in effect averaging dissimilar materials (populations). If longitudinal joints have posed a problem in the past, a density specification should be developed specifically for longitudinal joints.

3.4 Summary

The primary objective of this investigation was to evaluate potential causes of premature pavement cracking that occurred on the streets of Overland Park. Based upon cores taken from pavements experiencing the premature cracking, the cracks were not structural related cracks, (e.g., bottom-up fatigue) but rather surface-initiated cracks. The cracks were also longitudinal in nature which indicates that they were not caused by thermal conditions. Therefore, the surface initiated cracks are believed to be related to lack of durability within the placed HMA layers.

Based upon the data accumulated, there are two probable causes of the durability problems: lack of adequate density and low volumes of effective asphalt binder. With respect to adequate density, the City currently utilizes a cross between an end-result specification and a method specification. The City required 92 to 96% of theoretical maximum specific gravity for density; however, the City also specified the type of equipment and how to roll the pavement. Combination specifications such as this are very difficult to enforce and generally puts the contractor at a disadvantage. A simple end-result specification that contains a realistic minimum density requirement along with reasonable disincentives for not meeting the minimum requirement would better serve the City. Rigorous enforcement is also needed to confirm that the pavement meets requirements.

The most likely cause of the insufficient volume of asphalt binder was the highly absorptive nature of the aggregates used for HMA produced for Overland Park. For this reason, both mix design and field produced samples should be aged for four hours prior to testing. Increasing the aging time to four hours should increase the average asphalt binder content by at least 0.2 percent. For more problematic aggregates, the average increase in asphalt binder could be as much as 0.5 percent.

Another major concern is the variability of materials that are used to produce HMA for Overland Park. The circumstances existing at quarry sites near Overland Park promote the variability of materials; however, the control of HMA is very difficult due to the variability.

Because of the variability in materials, more frequent mix designs and/or mix design verifications are likely needed. An effective QC/QA program requires that the contractor have targets for producing the HMA. Arbitrarily targeting 4 percent air voids does not ensure that rut resistant and durable HMA is produced. Anytime that a stockpile is changed, the materials should be combined at the intended proportions and the properties of the mix checked prior to production. This is also true when proportions of the same stockpiles are significantly adjusted.

A target of 4 ± 1 percent air voids is adequate for HMA produced for Overland Park. For VMA, an allowable range of -0.5 to 2.0 should be utilized. Also, the effective specific gravity of the aggregate is a good tool for ensuring that materials are not changing during production. Control charts should be maintained and analyzed. Control charts for effective specific gravity will likely be the first indication that materials have changed. The importance of effective specific gravity is described later in this report. A reasonable tolerance to place on effective specific gravity is ± 0.012 .

4 CONCLUSIONS

As stated, the primary objective of this investigation was to determine the causes of premature cracking within flexible pavements in Overland Park, Kansas. The following are our conclusions for this project.

- A portion of the flexible pavements located in Overland Park, Kansas are experiencing premature cracking. The cracks are longitudinal and are occurring both within and outside the wheel path. These cracks are surface-initiated and are the results of a lack of durability.

- The lack of durability was caused by insufficient in-place density and insufficient effective asphalt binder.
- Effective specific gravity is a useful tool to determine when materials vary during the production of HMA.

5 RECOMMENDATIONS

Based upon the observations, data, and conclusions from this evaluation, the following are recommended.

- HMA should be aged for 4 hours during both mix design and field testing. During field testing, the mixture should be held at an elevated temperature for four hours after production.
- Develop and analyze control charts for the effective specific gravity of aggregates. A tolerance of ± 0.012 should be used for the control charts. If the effective specific gravity exceeds the tolerance, the aggregate specific gravity properties (namely bulk specific gravity) should be determined from the cold feed belt materials. If the bulk specific gravity value significantly differs from the job mix formula, verify that the produced HMA meets all properties of the S-1 specification.
- A recently verified job mix formula should be submitted prior to every construction project being started. The properties of the HMA should be verified anytime a stockpile is changed or the proportions of the stockpiles are significantly changed.
- More rigorous enforcement of the density specifications is needed. Longitudinal joint cores should not be averaged with mainline cores. Disincentives are recommended for density along with the more rigorous enforcement of the density specifications. The density specification should be enforced as an end-result specification.



Figure 5. Recent photograph of Overland Park thoroughfare.

6 UPDATE ON PERFORMANCE

The recommendation to increase the laboratory hold time to 4 hours from 2 hours was adopted very shortly after the field visit to Overland Park. The City discovered that by increasing the hold time, the asphalt mixtures tended to have volumetric properties that stayed more consistent from load to load, the that while the percent binder increased, the increase did not lead to problems in construction especially where the mix was not held in a silo for long periods of time. A visual inspection of several paving jobs that are now approaching two years of age shows that the change in design has appeared to have solved the surface cracking problem, and the surface raveling also has been eliminated. Figure 5 illustrates a recent picture of the first roadway paved after adopting this increase aging time (two years old). This figure shows no surface defects or cracking. Overland Park will continue to monitor this pavement, but our initial impression is that the problem has been largely solved. The widespread rutting, stripping and transverse cracking problems that we faced in the 1990's appear to have been eliminated.

REFERENCES

- (Asphalt Institute, 1997) "Mix Design Methods for Asphalt Concrete and Other Hot-Mix Types." Manual Series No. 2 (MS-2). The Asphalt Institute. Lexington, Kentucky.
- Gerritsen, A.H., van Gurp, C.A.P.M., van der Heide, J.P.J., Molenaar, A.A.A., and Pronk, A.C. (1987). "Prediction and Prevention of Surface Cracking in Asphaltic Pavements," *Proceedings of 6th International Conference on the Structural Design of Asphalt Pavements*, Ann Arbor, MI.

Investigation of transverse cracking of asphalt pavements in the North-Eastern Poland

M. Pszczoła, J. Judycki, & B. Dołżycki
Gdansk University of Technology, Gdansk, Poland

ABSTRACT: Transverse cracking is one of the most frequent type of distress on the Polish roads. The paper presents the results of investigation of transverse cracking on the roads of North – Eastern Poland. The research was carried out between 1999 and 2005. Based on the field investigations, the relationships between cracking frequency, represented by cracking index value and the selected features of asphalt pavements were established. The following features were considered: type of the base course (unbound aggregate or cement treated), thickness of asphalt pavement, thickness of asphalt layers, thickness of base course, type of subgrade soil, stiffness of asphalt layers defined by the resilient modulus, tensile strength of asphalt, pavement age and traffic volume. The relationship between the severity of transverse cracking and the type of the base course (unbound and cement treated) was also investigated.

1 INTRODUCTION

There are a number of causes of gradual deterioration of asphalt pavements, related to traffic and environmental factors. A typical manifestation of this gradual deterioration are transverse cracks, frequently found on the roads of Poland. It is commonly believed that these are reflective cracks, propagated from cracked hydraulically-bound base. Actually, the problem is more complex. According to data from literature and our own observations transverse cracks may also be caused by low-temperature cracking, as indicated by transverse cracks found on flexible pavements with asphalt layers underlain with unbound base course material. The objective of the paper is to present the results of investigation of transverse cracking and the relationships between cracking frequency and the selected features of asphalt pavements. Examples of typical transverse cracks, noted during field survey are presented in Figure 1.

2 EXPERIMENTAL PROGRAMME

2.1 *Test sections*

The survey was carried out on the national roads located in three provinces of north-eastern Poland: Pomorskie, Warminsko-Mazurskie and Podlaskie. For reliable evaluation of cracking intensity the sections were identified for detailed survey using random sampling technique. In the first step all the national roads within the limits of a given province were divided into 50 km segments. Then two numbers were selected randomly per each segment from the range 0 to 50. Each number corresponded to chainages, within which 500 m sections were identified for detailed investigation. Random function was used in the above described sampling technique. For the remainder segments (shorter than 50 km) one test section was selected for lengths below 25 km and two sections for lengths over 25 km. This sampling technique ensured random selection of the test sections throughout the entire length of all national roads within the limits of a given province.

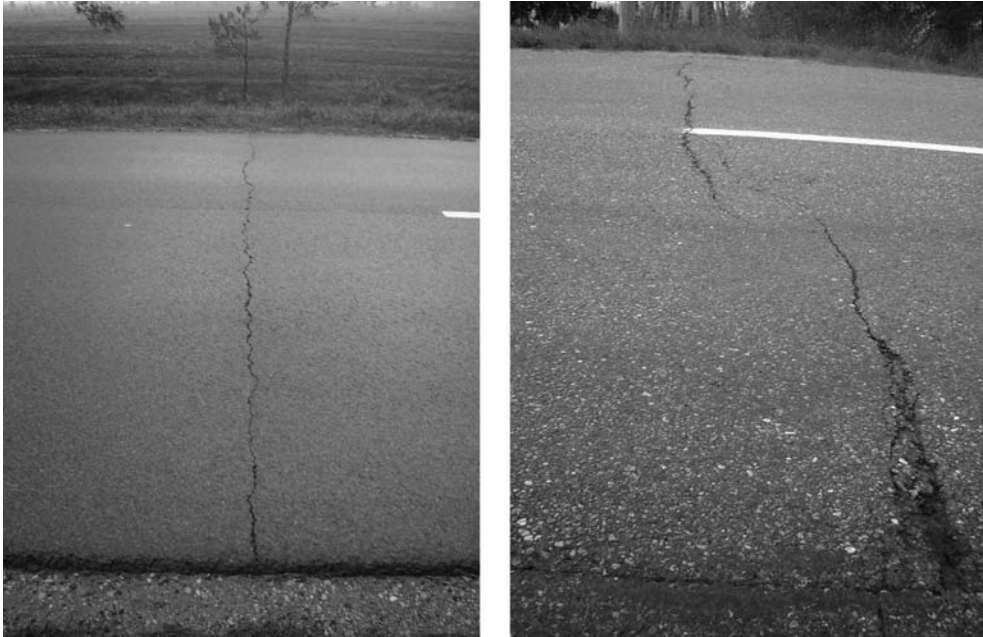


Figure 1. Typical transverse cracks noted during field survey, (left-hand side: regular transverse crack, right-hand side: irregular transverse crack).

The locations of the selected test sections were slightly shifted if they fell within city borders or in places with limited visibility distance due to horizontal and vertical alignment. The objective was to ensure safety to the persons carrying out the survey.

2.2 Testing methodology

For all the randomly selected test sections visual assessment was carried out along with determination of cracking index. The cracking index is defined as follows:

$$CI = S_1 + 0.5S_{1/2} + 0.25S_{1/4} \quad (1)$$

where: CI – cracking index – number of transverse cracks per 100 m length,
 S_1 – number of transverse cracks per roadway width, per 100 m length,
 $S_{1/2}$ – number of transverse cracks per half of roadway width, per 100 m length,
 $S_{1/4}$ – number of transverse cracks per quarter of roadway width, per 100 m length.

Then the sections were rated according to the obtained value of cracking index into four groups:

- Uncracked – index value below 0.2, this corresponding to less than one transverse crack per 500 m roadway length,
- Slightly cracked – index value between 0.2 and 1.0, this corresponding to not less than one and not more than five transverse cracks per 500 m roadway length,
- Moderately cracked – index value between 1.01 and 5.0, this corresponding to more than five transverse cracks and not more than twenty five transverse cracks per 500 m roadway length,
- Heavily cracked – index value over 5.01, this corresponding to more than twenty five transverse cracks per 500 m roadway length.

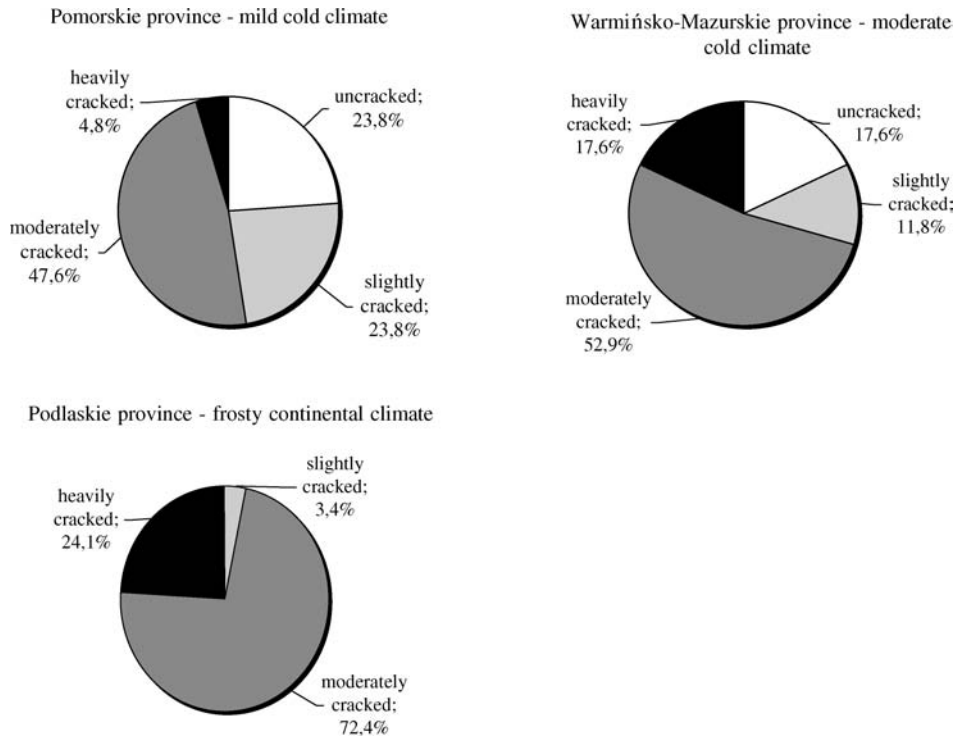


Figure 2. Percentage of sections with different severity of transverse cracking in the respective provinces.

On each test section cores were drilled through the road pavement. They were used for determining the pavement characteristics, as discussed in detail in section 4.

3 EVALUATION OF TRANSVERSE CRACKS

The survey, including determination of the severity of cracking covered 90 randomly selected test sections, including:

- 48 sections with flexible base course,
- 35 sections with rigid base course,
- 6 sections were excluded from the survey due to on-going maintenance or reconstruction work.

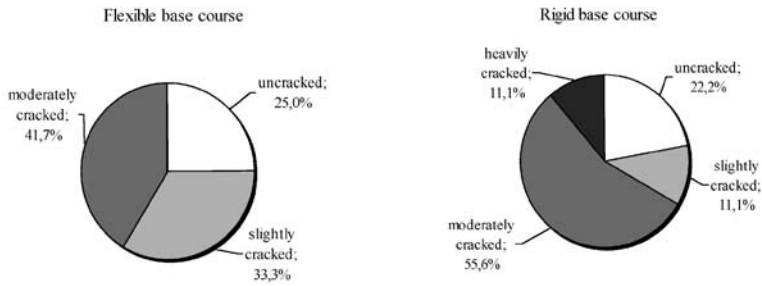
The survey was carried out in three provinces of northern and north-eastern Poland, where winters are influenced by various climatic factors:

- Pomorskie – within the range of the Baltic Sea (mild cold climate),
- Warmińsko-Mazurskie – combined effect of the Baltic Sea and continental climate (moderate cold climate),
- Podlaskie – within the range of continental climate (frosty continental climate).

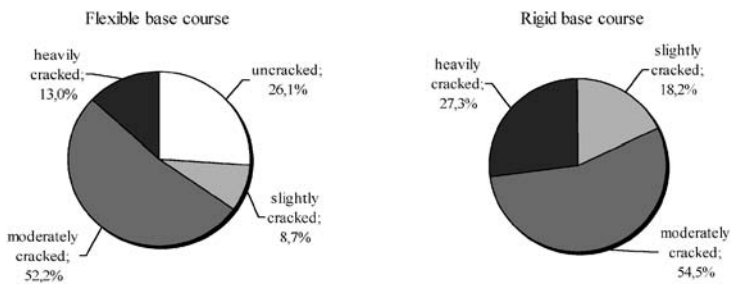
Figure 2 presents the percentage of sections with different severity of cracking in the respective provinces.

Figure 3 relates the frequency of transverse cracks to the base course design in the respective provinces. Flexible base course is built of unbound material, such as crushed aggregate, gravel, etc. On the other hand, rigid base course includes cement-bound materials, such as lean concrete, cement-treated aggregate and cement stabilized soil.

Pomorskie province – mild cold climate



Warmińsko-Mazurskie province – moderate cold climate



Podlaskie province – frosty continental climate

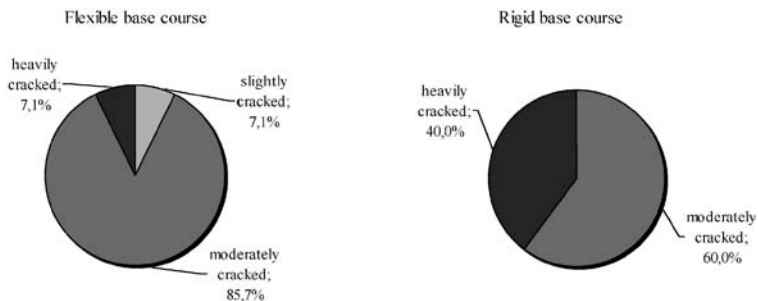


Figure 3. Transverse cracking intensity depending on base course design in the respective provinces.

Figure 4 provides an overall view on the severity of transverse cracking in the respective provinces for flexible and rigid pavements.

Having analysed the above relationships describing the severity of transverse cracking we note that:

1. Transverse cracking is quite frequent on the analysed national roads. The percentage of sections affected with transverse cracks (moderately and heavily cracked sections) ranged from 52.4% in Pomorskie province (mild cold climate), through 70.5% in Warmińsko-Mazurskie province (moderate cold climate), up to the considerable 96.6% in Podlaskie province (frosty continental climate). Thus, as we move north-east we find more sections affected with transverse cracks, accompanied with growing severity of cracking within each section. It is related to the effect of colder continental climate in the north-eastern part of Poland.

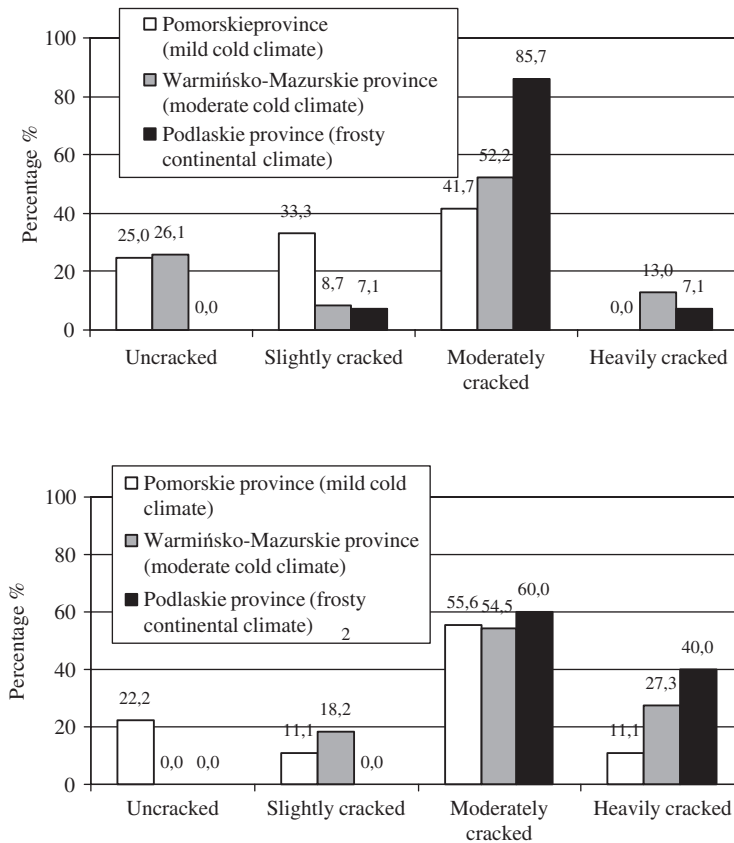


Figure 4. Severity of transverse cracking in the respective provinces for sections with different base course design: flexible (upper chart) and rigid (lower chart).

2. Transverse cracks occur irrespective of the base course construction: flexible or rigid. However, as it could have been reasonably expected the severity of cracking is greater on the sections where road construction incorporates cement-treated base.
3. Moderately cracked sections with 1–5 transverse cracks per 100 m length prevail among all the analysed sections.

4 INVESTIGATION OF RELATIONSHIPS BETWEEN TRANSVERSE CRACKING AND THE CHARACTERISTICS OF PAVEMENT

The test results were analysed to find a relationship between the transverse cracking index and the characteristics of pavement. Both field survey and laboratory testing data were used in the analysis, accompanied with record data on the age of pavement and volume of traffic. The following pavement characteristics were considered as having a potential effect on emergence of transverse cracks: thickness of pavement structure, thickness of asphalt courses, thickness of base course, resilient modulus in indirect tension test, indirect tensile strength, traffic volume and age of pavement.

Figures 5 through 11 show the relationships between the above mentioned factors and the value of cracking index.

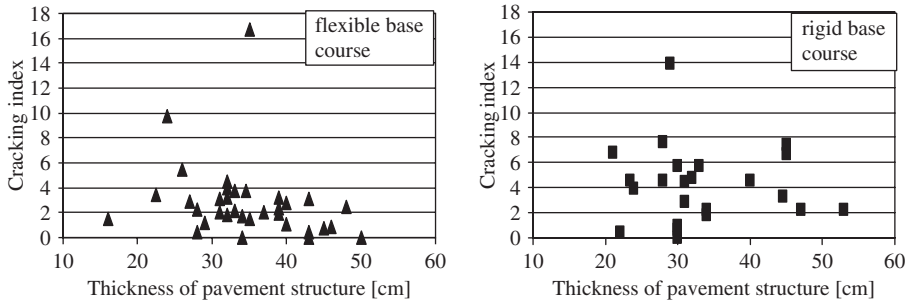


Figure 5. Relationship between the thickness of pavement structure and the value of cracking index.

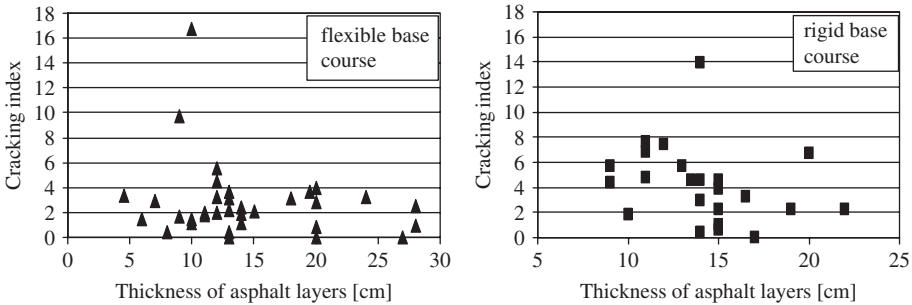


Figure 6. Relationships between the thickness of asphalt layers and the value of cracking index.

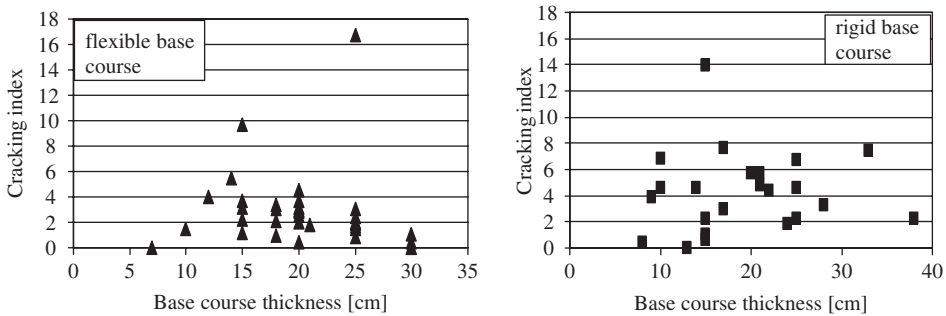


Figure 7. Relationships between the base course thickness and the value of cracking index.

Thickness of pavement structure – it includes the total thickness of asphalt layers and base course. It does not include the drainage layer thickness, which has been treated as part of improved subgrade.

Thickness of asphalt layers – is the total thickness of all bitumen-bound layers in pavement structure on a given section.

Base course thickness – it was determined both for flexible pavements without cement-treated bases and rigid with cement-treated bases.

Resilient modulus in indirect tension – the values of resilient modulus were established in laboratory testing of cores sampled from the asphalt surface. The tests were carried out in Nottingham Asphalt Tester (NAT) in controlled stress conditions at temperature -20°C .

Indirect tensile strength – determined in laboratory testing of cores sampled from the asphalt surface. The test was carried out in a press with a constant rate of movement of 50 mm/minute, at -20°C .

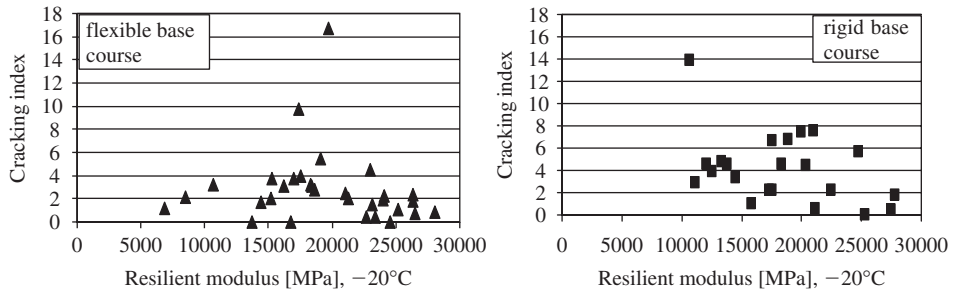


Figure 8. Relationships between the resilient modulus at -20°C and the value of cracking index.

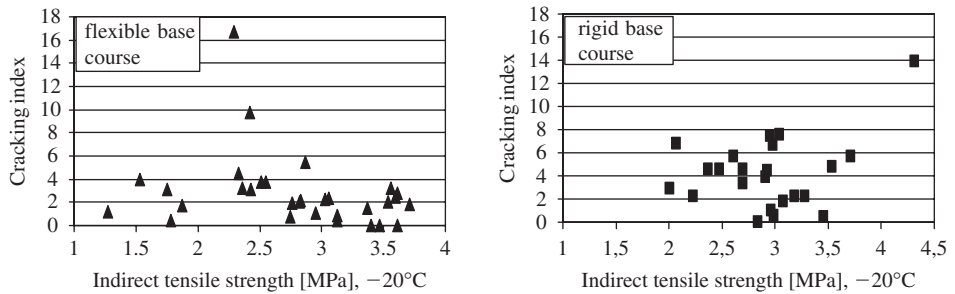


Figure 9. Relationships between the indirect tensile strength at -20°C and the value of cracking index.

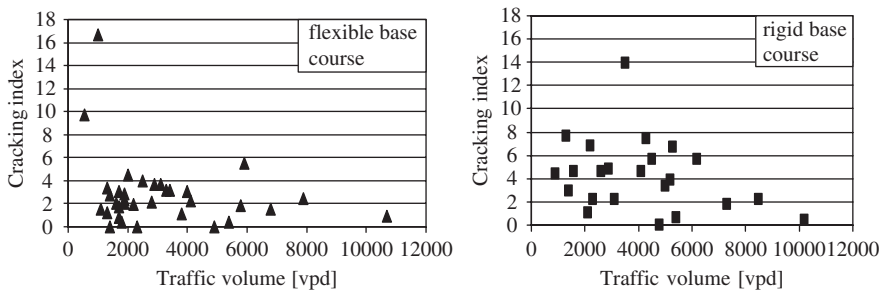


Figure 10. Relationships between the traffic volume and the value of cracking index.

Traffic volume – the average annual daily traffic in vehicles per day (vpd) from the general traffic survey carried out in 1995 were used in the analysis.

Age of pavement – has been taken as the number of years from the latest rehabilitation involving replacement of one or more asphalt courses.

The following conclusions have been drawn from the above relationships:

1. There is a certain relationship between the thickness of pavement structure and the value of cracking index, namely it slightly decreases with the increase in the thickness of pavement.
2. A similar relationship has been observed between the thickness of asphalt layers and the value of cracking index, namely it slightly decreases with the increase in thickness of asphalt surface.
3. Also the age of pavement has an effect on the value of cracking index with the value increasing with age – this has been observed for pavements with rigid base course construction.

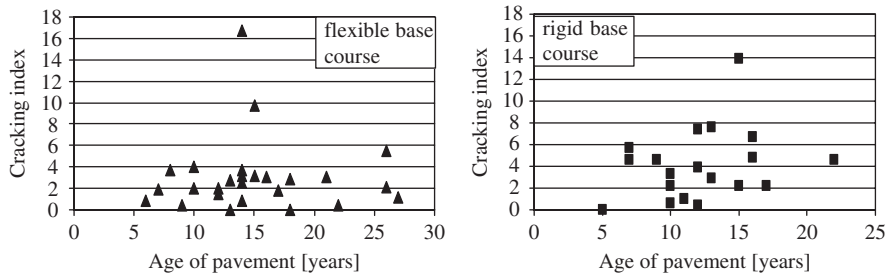


Figure 11. Relationships between the age of pavement and the value of cracking index.

- No clear relationships have been found between the cracking index and resilient modulus, indirect tensile strength at -20°C , base course thickness, both for rigid and flexible pavements and the volume of traffic.

5 CONCLUSIONS

Below are the conclusions from the field survey and tests, followed by the analysis of relationships between the severity of transverse and the pavement characteristics:

- Transverse cracks are frequent on the national roads in the three analysed provinces of the north-eastern Poland. The share of sections affected with cracking (at least one crack per 500 m of roadway length) varied between the provinces and ranged from 76.2% in the Pomorskie province (mild cold climate), through 82.4% in Warminsko-Mazurskie province (moderate cold climate), up to the considerable 100% in Podlaskie province (frosty continental climate). Thus, the number of sections affected with transverse cracks and the severity of cracking increases in the north-eastern direction. It is related to the effect of colder continental climate in the north-eastern part of Poland.
- Transverse cracks occur on pavements with rigid (cement-treated) and flexible base courses, the latter most often built of crushed stone. Accordingly, there are two cracking mechanisms involved: propagation from rigid base and thermal shrinkage of asphalt layers due to low temperatures. The values of cracking index show that severity of transverse cracking is greater on pavements with rigid base courses.
- Upon considering the pavement characteristics we note that the value of cracking index, representing the number of transverse cracks per 100 m roadway length:
 - decreases with the increase of the thickness of pavement structure,
 - decreases with the increase of the thickness of asphalt layers,
 - increases with the age of pavement,
 - shows no clear relationship with the resilient modulus, indirect tensile strength at -20°C , base course thickness both for rigid and flexible pavements and also the volume of traffic.

REFERENCES

- Dołżycki B., Alenowicz J. 2001. *Research on Transverse Cracking of Asphalt Pavements in the Northern and North-Eastern Poland*, 7th International Conference 'Durable and Save Road Pavements', Kielce.
- Judycki J., Dołżycki B. 2000. *Field Investigations on Transverse Cracks in Asphalt Pavements*, unpublished report for the Polish road network authority GDDKiA, Gdansk University of Technology, Gdansk.
- Judycki J., Alenowicz J., Dołżycki B. 2000. *Research on Transverse Cracks in Pavements in Northern Poland*, 6th International Conference 'Durable and Save Road Pavements', Kielce.
- Pszczółka M. 2006 'Low Temperature Cracking of Asphalt Layers of Pavements', Ph.D. thesis, Gdansk University of Technology, Gdansk.

Evaluation of relationships between deflection-based indices and flexible pavement cracking field performance

S.W. Haider & K. Chatti

Michigan State University, East Lansing, Michigan, USA

ABSTRACT: The use of the Falling Weight Deflectometer (FWD) has become an integral part of pavement management and rehabilitation. The deflection basins obtained along the length of a pavement section capture most of the variability in the overall strength of the pavement structure and thus encompass variation in the material properties and structural aspects. This variability can contribute to different cracking performance levels within the same pavement section. Therefore, the deflection variation within a section can be used to ascertain its overall future performance. Although considerable research have been conducted on relating deflections basin parameters (DBP) to flexible pavement performance using mechanistic-based analyses, they are limited in scope because of inadequate field validation and the complex interactions of structural and site factors. This paper evaluates the apparent relationships between response and performance of in-service flexible pavements using various DBPs and cracking types: fatigue, longitudinal (wheel-path and non-wheel-path) and transverse cracking. The data from the SPS-1 experiment of the LTPP program was used for this purpose where experiment sections were constructed in different site conditions (subgrade type and climate). It was found that the relationships between DBPs and cracking types are fairly good within a pavement section or site; however correlations become weak for network level analysis. The approach described in the paper can lead to some allowable variation limits for deflections within a pavement section, thus making the procedure very helpful for field quality control in the context of performance-based specifications.

1 INTRODUCTION

1.1 *Background*

Pavement performance encompasses growth of several distresses (e.g. cracking and rutting) and roughness over time. Pavement response to load plays an important role in explaining the distress mechanism. The primary pavement responses are stress, strain and deformations at a particular location within a pavement system (see Figure 1a). Because of the difficulty in measuring stresses and strains in an existing pavement, the primary responses are typically calculated using linear elastic layered solutions for design purposes. While these analytical procedures are based on several simplified assumptions, the actual field conditions can pose many other challenges due to intricate material behavior, load characteristics and other boundary conditions. For pavement evaluation purposes, the surface deflections are the main pavement response which can be measured in the field under prevailing conditions. However, surface deflections are not considered as a primary response causing distresses in a layered pavement system. Surface deflections on a layered system are a poor substitute for stress and strains. From the analytical view point (Boussinesq's equations for stress/strain and deflection) surface deflection alone is poorly correlated to the stresses and strains, which are considered more fundamental responses to characterize the pavement performance. One can have multiple pavement thickness combinations with varying layer moduli which may have similar surface deflections but significantly different stress/strain (Ullidtz 1998).

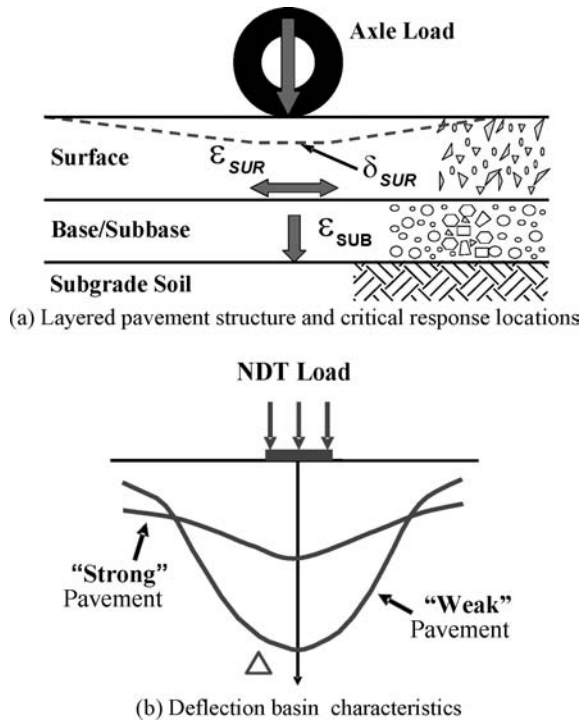


Figure 1. Flexible pavement primary response for explaining distress mechanisms and deflection basin under load.

Due to ease of measuring and efficiency, the use of nondestructive deflection testing has become an essential part of pavement evaluation, rehabilitation and management process. The falling weigh deflectometer (FWD) test can effectively simulate the actual wheel loadings on a pavement structure and can capture the essential pavement structural response in terms of surface deflections. The curvature of the deflection basin is generally related to pavement structural strength i.e., higher deflections and steep curvature indicate a weaker pavement while low deflection and low curvature are signs of a stronger pavement structure (see Figure 1b). Typically, for a known pavement cross-section, the surface deflection obtained from FWD testing have been used to back-calculate the in-situ material properties (layer moduli) for a layered system. Once the in-situ layer moduli are estimated, the forward analysis methods are used to calculate the critical responses (stresses and strains), which explain the mechanism of a particular distress and are used to predict pavement deterioration by using respective performance models (e.g., fatigue cracking). Hence, the whole process is complicated and requires technical expertise and sound engineering judgment. On the other hand, simplified methods of relating surface deflections or deflection-based indices (DBI) to performance have evolved due to their more practical nature and ease of use. The main assumption in the development of such tools is that the DBIs are related to the primary pavement responses (stress and strain) and are therefore indirectly related to pavement performance. This paper explores this basic assumption by relating several DBIs to pavement cracking by considering the SPS-1 experiment in-service pavements available in the long-term pavement performance (LTPP) database. All cracking types (fatigue, longitudinal and transverse cracking) were considered.

1.2 Literature review

Previous research at Delft University of Technology (Molenaar 2002) has shown that there exists a direct relationship between tensile strain at the bottom and the top of the asphalt layer and the

surface curvature index (SCI) as shown by Equations 1 and 2, respectively. The relationships shown are applicable to flexible pavements having asphalt thickness greater than 150 mm.

$$\log \varepsilon_{bottom} = 0.481 + 0.881 \times \log SCI \quad (1)$$

$$\varepsilon_{top} = 194.9 - 20.78 \times SCI^{0.5} \quad (2)$$

$$SCI = d_0 - d_{300} \quad (3)$$

where d_0 = deflection at the center of the loading plate; d_{300} = deflection 300 mm from the center of the loading plate.

Based on theoretically developed synthetic database, Kim et al. (Kim and Ranjithan 2000) concluded that tensile strain at the bottom of an asphalt layer is very strongly correlated to asphalt layer thickness and base damage index (BDI). This relationship for pavements with aggregate base has the following form:

$$\log(\varepsilon_{ac}) = 1.078 \cdot \log(BDI) + 0.180 \cdot \log(H_{ac}) + 2.772 \quad (4)$$

$$BDI = d_{300} - d_{600} \quad (5)$$

where d_{300} = deflection 300 mm from the center of the loading plate; d_{600} = deflection 600 mm from the center of the loading plate; H_{ac} = thickness of the AC layer in mm.

The same researchers have identified methods for assessing pavement layer condition based on deflection measurements and have correlated surface deflection to layer condition and distress (Kim and Ranjithan 2000). The approach utilized in this study was to generate a synthetic database of primary responses for a variety of pavement sections by using a nonlinear, dynamic finite element program. The synthetic database was analyzed to identify deflection basin parameters that have significant influence in the prediction of critical pavement responses in flexible pavements (Xu et al. 2002). Similarly, prediction methods were developed for the remaining life of flexible pavements using FWD multi-load levels deflections (Park and Kim 2003).

Kim and Ranjithan (2000) concluded that for full depth and aggregate base pavements, E_{ac} ¹ can be used as an indicator to detect cracking and stripping in the AC layer. BDI ² and ε_{abc} ³ were found to be good condition indicators for base layer condition, while BCI ⁴, ε_{sg} ⁵, SSR ⁶ and E_{sg} ⁷ appeared to be good condition indicators for the subgrade. For intact pavements, the pavement overall fatigue cracking and rutting potentials are mainly controlled by ε_{ac} , ε_{abc} and ε_{sg} . For full depth and aggregate base pavements, the analysis from both synthetic data and field data showed that SCI ⁸ can be used to predict the AC modulus. Also, a high correlation was found between BDI and ε_{ac} .

A recent study (Stubstad et al. 2002) on evaluating the feasibility of using FWD deflection data to characterize the pavement construction quality using the SPS-1 data concluded that "FWD can be effectively used to assist in the characterization of pavement quality for new or reconstructed pavements during construction". Furthermore, "quality" can be directly equated to stiffness or modulus, and to other deflection-based parameters. It is therefore expected that these parameters should correlate to the future performance of pavements.

¹ AC modulus

² $BDI = D_{12} - D_{24}$ (Base Damage Index)

³ Compressive strain at top of base layer

⁴ $BCI = D_{24} - D_{36}$ (Base curvature index)

⁵ Compressive strain at top of subgrade

⁶ $SSR = \sigma_d/q_u$ (Stress parameter for rutting potential of subgrade)

⁷ Resilient modulus for subgrade

⁸ $SCI = D_0 - D_{12}$ (Surface curvature index)

Equation (6) can be used to calculate the area under the deflection basin using the first four sensors equally spaced at 300 mm from each other (AASHTO 1993; Stubstad et al. 2002).

$$Area = 6 \left[1 + 2 \left(\frac{d_1}{d_o} \right) + 2 \left(\frac{d_2}{d_o} \right) + \left(\frac{d_3}{d_o} \right) \right] \quad (6)$$

where Area = the “Area” within 900 mm of the deflection basin; d_o = FWD deflection measured at the center of load plate; d_1 = FWD deflection measured at 300 mm from the center of plate; d_2 = FWD deflection measured at 600 mm from the center of plate; d_3 = FWD deflection measured at 900 mm from the center of plate.

A maximum value of 36 is possible for “Area” when all the deflections are the same in Equation (6). This will represent a very stiff pavement (extreme value). It was found using the forward analysis (Stubstad et al. 2002) that when all the layers in a flexible pavement were assumed to have the same modulus, the “Area” term is always equal to 11.037. Therefore, it was concluded that if FWD deflection measurements carried out in the field result in an “Area” value close to 11.037, then the effective modulus of the upper layer is identical to that of the underlying layer(s). Hence, this particular value of “Area” can be used as a cutoff in order to ascertain whether the upper layer has a higher stiffness than the underlying layer(s).

The surface modulus at the center of the circular plate may be calculated by using Boussinesq’s solution for semi-infinite half space by using Equation (7).

$$E_o = \frac{2(1-\nu^2)\sigma_o a}{d_o} \quad (7)$$

where E_o = surface modulus; σ_o = peak stress from FWD impact load under loading plate; d_o = peak surface deflection at center of load plate; a = radius of FWD loading plate; ν = poisson’s ratio of the semi-infinite half space; “2” in above equation is a factor for uniform stress distribution (Ullidtz 1998).

The problem arising from an unknown stress distribution for Equation (7) may be solved by measuring the deflections at different distances from the center of the load (Ullidtz 1987). Measuring the deflections at several distances (as is the case with FWD) also serves as a check on the assumption that the subgrade is a linear elastic semi-infinite space. In that case the moduli calculated at different distances must be identical, otherwise the subgrade is either non-linear or it consists of different layers, as shown in Equation (8).

$$E_i = \frac{(1-\nu^2)\sigma_o a^2}{(r_i d_i)} \quad (8)$$

where E_i = surface modulus; d_i = Surface deflection at distance “ i ” from center of load plate; r_i = distance from the center of the load where d_i is measured.

The surface modulus represents a composite or effective modulus of all the layers under the FWD loading plate. Based on Equations (6) and (7), the following equations were derived by Stubstad et al. (2002).

$$AF = \left[\frac{(k_2 - 1)}{\left(k_2 - \left(\frac{Area}{k_1} \right) \right)} \right]^2 \quad (9)$$

where AF = area factor, i.e. the “improvement” in AREA from 11.037 squared; k_1 = 11.037 (the Area when the stiffness of the upper layers is the same as that of the lower layers; k_2 = 3.262

(Maximum possible improvement in Area = 36/11.037). Equation (10) can effectively be used to approximate the relative stiffness of the upper (bound) layers in the pavement cross section.

$$ES = \left[E_o AF (k_3) \left\{ \left(\frac{1}{AF} \right)^{-1} \right\} \right] \quad (10)$$

where ES = effective stiffness of upper (bound) layers; E_o = as defined by Equation (7); AF = as defined by Equation (9); k_3 = thickness of upper layer/load plate diameter = $h_1/(2a)$.

Utilizing similar FWD deflection characteristics and DBIs, a forward-calculation approach was also developed by Stubstad et al. (2006a; 2006b). The pavement layer moduli are estimated directly from the load and deflection data using closed-form formulae rather than iterations.

In summary, the DBIs presented above are correlated to primary pavement response at different locations in a pavement structure. Therefore, it will be useful to explore direct relationships between DBIs and expected pavement performance in terms of cracking. These apparent relationships were explored by using the SPS-1 experiment sections from the LTPP database.

2 DEFLECTION AND PERFORMANCE DATA USED FOR ANALYSES

The SPS-1 experiment was designed to study the effects of structural and design features on the new flexible pavement performance and response. There are twelve pavement sections constructed at each site with varying structural factors. The experiment design allows the investigation of the effects of HMA layer thickness (102 vs. 178 mm), base type (dense-graded aggregate base, DGAB vs. asphalt-treated, ATB, vs. ATB/DGAB), base thickness (203, 305 and 406 mm), and in-pavement drainage (Yes vs. No) on performance under different site conditions defined by subgrade type [Fine (F) vs. Coarse (C)] and climate [Wet Freeze (WF) vs. Wet No-Freeze (WNF) vs. Dry Freeze (DF) vs. Dry No-Freeze (DNF)]. The comprehensive design matrix has 288 factor-level combinations from six independent factors. However, there are only 192 factor-level combinations available, making the SPS-1 experiment a fractional factorial design (Haider 2005). The details of the SPS-1 experiment and its status can be found elsewhere (Chatti et al. 2005).

The average age of test sections in the SPS-1 experiment was 7 years with a range of 3 to 11 years. Considering most pavements are designed for a life of 20 years, these pavements are “fairly young” and high levels of distresses are not expected. Thus, all conclusions from the analyses presented in this paper should be interpreted as “mid-term” performance findings.

FWD deflections were collected on each pavement twice a year (Schmalzer 2006) while distress extent and severity were also collected on an annual basis (Miller and Bellinger 2003). The cracking performance data at the latest age available in the database (Release 17.0) were extracted for each pavement section while the first deflection measurements (just after opening to traffic), when the original pavement was intact and new, were considered in this analysis.

3 APPARENT RELATIONSHIP BETWEEN DEFLECTION BASED INDICES AND CRACKING

In this section, the observations regarding apparent relationships between flexible pavement response (FWD deflection and DBIs) and observed pavement performance are presented. To provide a predictive capability of the future level of performance, the initial average deflections or DBIs of pavements were related to the future cracking performance. Predictive relationships were established based on bivariate correlation analyses at the site level, and by employing scatter plots on data from all sections at the network level.

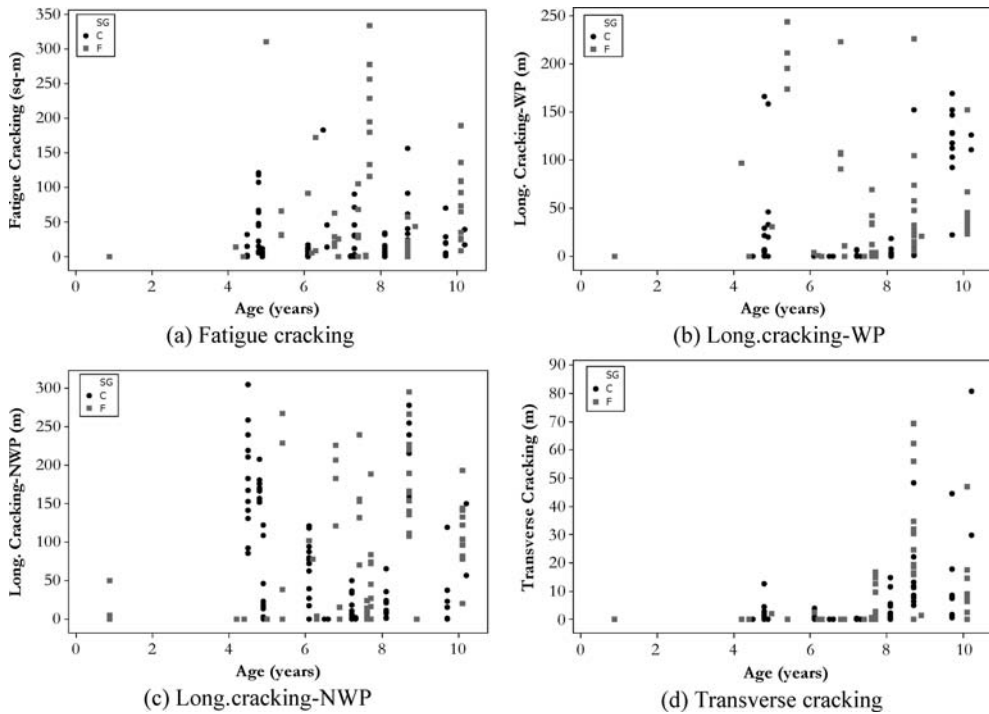


Figure 2. Relationships between age and different cracking performances.

3.1 Project level predictive relationships

This section summarizes the findings regarding predictive relationships between initial response (FWD deflection or deflection-based indices) and future pavement performance (fatigue, longitudinal and transverse cracking), at the site level. Various deflection-based indices (Kim and Ranjithan 2000; Stubstad et al. 2002) were calculated based on the individual deflection basins within each pavement section; these indices include:

- *AREA* (the area under first three feet of deflection basin),
- *SCI* – Surface Curvature Index,
- *BDI* – Base Damage Index,
- d_0 (peak deflection under the load),
- d_6 (farthest deflection at 1500 mm away from the load),
- *ES* (effective stiffness of upper (bound) layer), and
- E_g (subgrade modulus calculated by using Equation (8) from surface deflection at 900 mm from load).

Bivariate correlation analyses between the initial response parameters (deflections or deflection basin parameters) and the cracking performance were conducted for all the sites within the SPS-1 experiment. The latest performance for each section within the SPS-1 experiment was used in these analyses. The effect of temperature on the measured deflection was taken into account by applying a temperature correction (Lukanen et al. 2000). It should be noted that for a given site; age, traffic, construction, material properties and environment are the same and thus this provides a good opportunity for seeking apparent relationships.

Figure 2 shows the cracking performance for all pavement sections in the SPS-1 experiment design as of Release 17.0 of the LTPP database. It can be seen that fatigue and transverse cracking

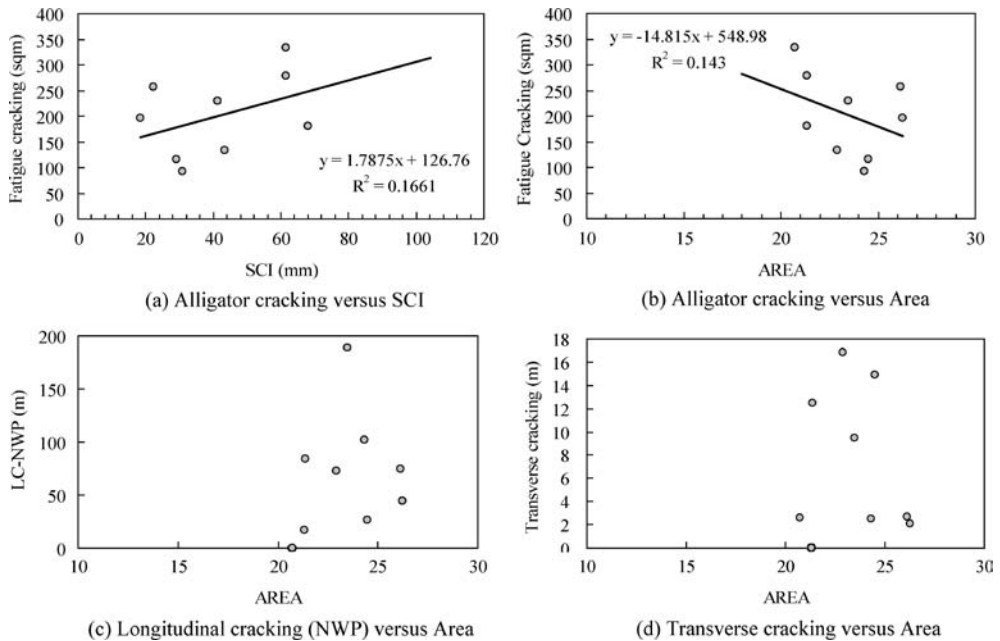


Figure 3. Example relationships between DBI and cracking performance for Kansas site (20).

are somewhat age dependent while longitudinal cracking (WP and NWP) are not. Figure 3 shows examples of bivariate relationships between SCI and AREA and different cracking types. The site in the state of Kansas (20) was chosen for this example because of high extent of cracking at the site. It can be seen that for the sections in this site, initial SCI and initial AREA have a slight association ($\rho = 0.4$) with future fatigue cracking, such that the higher the SCI or the lower the AREA, the higher the observed cracking. The probability of longitudinal and transverse cracking is higher if AREA is more than 20 for the pavements at site in Kansas (20) (see Figures 3c and 3d).

Table 1 presents summaries of correlation coefficients from the bivariate analyses between cracking and various deflection parameters for all the sites. The results in Table 1 show that fifteen out of seventeen sites have a consistent trend of relationship between AREA, BDI, d_o and future fatigue cracking. Also, fourteen out of seventeen sites have a positive association between SCI and fatigue cracking. In general, AREA, SCI, BDI and d_o have reasonable associations with fatigue cracking for all the sites in SPS-1 experiment. Pavements that have more fatigue cracking had higher initial SCI or BDI, and lower AREA. Reasonable apparent relationships between AREA and various cracking performance measures were found within sites that have shown considerable level of cracking.

Results in Table 2 show poor correlation and no consistent trend for longitudinal or transverse cracking. This is expected for non-load-related cracking (LC-NWP and TC); for LC-WP, none of the DBIs showed a good correlation.

3.2 Network level predictive relationships

This section summarizes the findings of apparent relationships between initial response (FWD deflection or DBIs) and future cracking based on data from all the test sections in the experiment. Recognizing the difficulties in seeking such associations, the relationships were explored using bivariate scatter plots between selected response parameters and cracking performance for all the sections.

Table 1. Summary of correlations between DBPs and fatigue cracking.

LTPP	Site, State	Area	ES	E _{sg}	d0	d6	SCI	BDI	Zone	SG
1	Alabama	-0.79	-0.64	-0.08	0.72	-0.27	0.75	0.73	WNF	F
4	Arizona	-0.13	0.06	0.53	-0.10	-0.55	-0.03	-0.03	DNF	C
5	Arkansas	-0.07	-0.19	-0.54	0.34	0.59	0.17	0.34	WF	C
10	Delaware	-0.93	-0.65	-0.04	0.72	-0.03	0.93	0.73	WF	C
12	Florida	-0.40	-0.40	0.14	0.50	-0.12	0.46	0.55	WNF	C
19	Iowa	-0.45	-0.09	0.05	0.41	0.15	0.55	0.49	WF	F
20	Kansas	-0.38	-0.25	-0.14	0.33	-0.01	0.41	0.30	WF	F
26	Michigan	0.48	0.42	0.21	-0.42	-0.03	-0.46	-0.45	WF	F
30	Montana	-0.36	-0.58	-0.74	0.53	0.83	0.34	0.42	DF	C
31	Nebraska	-0.79	-0.64	-0.37	0.90	0.43	0.94	0.91	WF	F
32	Nevada	-0.49	-0.31	0.10	0.38	-0.17	0.41	0.29	DF	C
35	New Mexico	0.19	0.33	-0.14	0.31	-0.01	-0.14	0.60	DNF	F
39	Ohio	-0.66	-0.44	-0.43	0.58	0.20	0.63	0.63	WF	F
40	Oklahoma	-0.47	-0.59	-0.16	0.25	-0.05	0.28	0.28	WNF	C
48	Texas	-0.48	-0.57	-0.49	0.74	0.65	0.78	0.58	WNF	C
51	Virginia	-0.72	-0.58	-0.32	0.75	0.04	0.79	0.75	WNF	F
55	Wisconsin	-0.46	-0.37	-0.02	0.38	0.04	0.51	0.22	WF	C
(-)ρ		15	14	12	2	9	3	2		
(+)ρ		2	3	5	15	8	14	15		
Mean		-0.41	-0.32	-0.14	0.43	0.10	0.43	0.43		
Std		0.36	0.34	0.32	0.33	0.35	0.38	0.33		
CoV		0.89	1.03	2.21	0.76	3.55	0.89	0.76		

Table 2. Summary of correlations between DBPs and longitudinal and transverse cracking.

LTPP	Site	State	Long cracking (WP)					Long. cracking (NWP)					Trans. cracking			Zone	SG
			Area	ES	E _{sg}	SCI	BDI	Area	ES	SCI	BDI	Area	SCI	BDI			
1	Alabama		0.38	0.62	0.40	-0.19	-0.17	-0.09	-0.22	0.09	0.08	-0.55	0.37	0.38	WNF	F	
4	Arizona		-0.22	-0.40	-0.46	0.22	0.22	-0.59	-0.47	0.55	0.54	-0.78	0.95	0.95	DNF	C	
5	Arkansas		-0.10	-0.14	0.37	-0.09	-0.25	0.52	0.50	-0.44	-0.33	0.09	0.02	0.23	WF	C	
10	Delaware		-	-	-	-	-	0.29	0.52	-0.21	-0.24	0.00	0.00	0.00	WF	C	
12	Florida		0.16	-0.06	-0.28	-0.01	0.08	-0.52	-0.47	0.26	0.29	-0.26	0.18	0.18	WNF	C	
19	Iowa		-0.50	-0.13	0.03	0.55	0.49	-0.11	-0.01	-0.05	-0.08	0.24	-0.28	-0.34	WF	F	
20	Kansas		0.05	-0.08	0.01	-0.14	-0.19	0.22	0.03	-0.17	-0.19	-0.10	0.09	0.23	WF	F	
26	Michigan		-	-	-	-	-	0.77	0.82	-0.64	-0.63	0.00	0.00	0.00	WF	F	
30	Montana		-0.18	-0.26	-0.28	0.07	0.13	0.18	0.08	-0.23	-0.22	-0.50	0.46	0.45	DF	C	
31	Nebraska		-0.60	-0.46	-0.16	0.57	0.60	-0.57	-0.48	0.76	0.71	0.00	0.00	0.00	WF	F	
32	Nevada		0.12	-0.08	0.27	-0.23	-0.11	-0.34	-0.32	0.27	0.25	-0.50	0.62	0.70	DF	C	
35	New Mexico		0.20	0.45	-0.02	-0.10	0.80	0.42	0.60	-0.38	0.70	0.08	-0.01	0.57	DNF	F	
39	Ohio		-0.53	-0.47	-0.61	0.54	0.60	-0.02	0.12	0.00	-0.05	0.00	0.00	0.00	WF	F	
40	Oklahoma		-0.33	0.08	0.87	-0.20	-0.22	0.29	0.12	-0.47	-0.46	0.28	-0.06	-0.07	WNF	C	
48	Texas		0.01	-0.12	-0.26	0.13	0.06	0.03	-0.24	0.13	0.19	0.00	0.00	0.00	WNF	C	
51	Virginia		-0.65	-0.44	-0.27	0.84	0.75	-0.46	-0.43	0.41	0.47	-0.63	0.83	0.74	WNF	F	
55	Wisconsin		-	-	-	-	-	-0.48	-0.36	0.47	0.26	0.00	0.00	0.00	WF	C	
(-)ρ			8	11	8	7	5	9	9	9	8	7	3	2			
(+)ρ			6	3	6	7	9	8	8	8	9	4	8	9			
Mean			-0.16	-0.11	-0.03	0.14	0.20	-0.03	-0.01	0.02	0.08	-0.16	0.19	0.24			
Std			0.33	0.32	0.39	0.35	0.38	0.42	0.42	0.40	0.40	0.32	0.34	0.35			
CoV			2.11	3.04	14.79	2.50	1.91	16.69	31.25	18.83	5.24	2.06	1.82	1.46			

Note: The SPS-1 pavements at Louisiana site (22) are young and did not exhibit any significant cracking, and therefore are not included in this analysis.

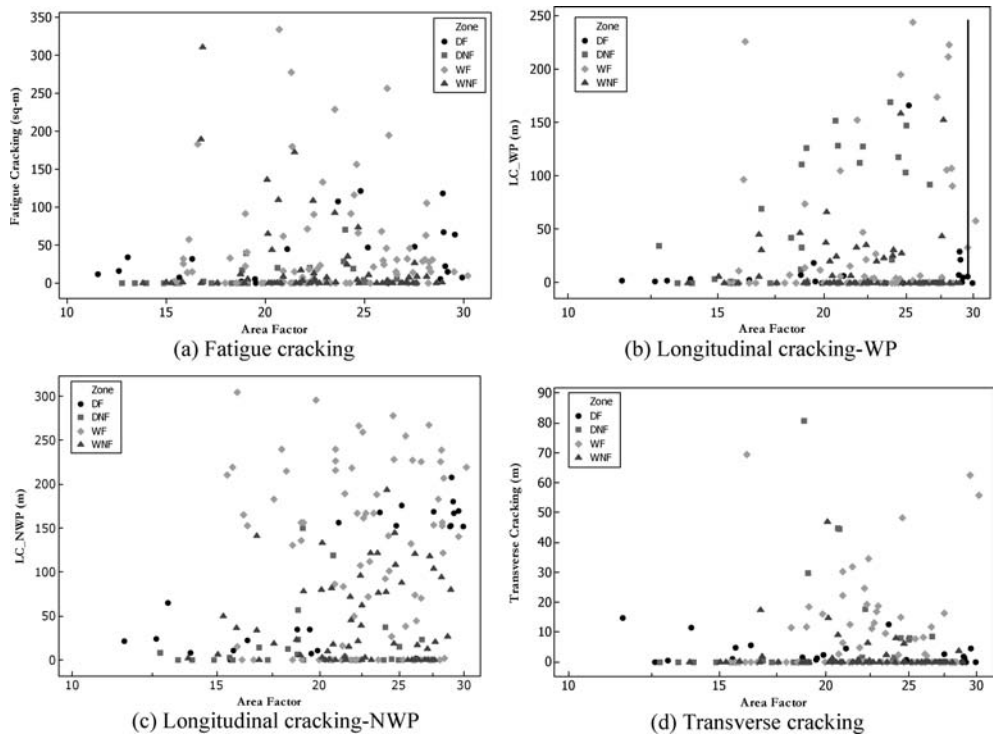


Figure 4. Example plots between Area and cracking performance at the network level.

Though the sites differ in age, traffic, climate, and materials this analysis is intended to use the wealth of data from all the sections in the experiment. Moreover, the variation in age of the sites may not be very critical at this point in time as no definitive trends were observed between pavement age and performance (see Figure 2). Also, it is assumed in this analysis that deflection basin parameters will “characterize” the structural features such as HMA surface thickness, base type and base thickness. In other words, pavement response was assumed to be strongly correlated with the structural capacity of the pavement. In order to account for the effects of subgrade type and climate, relationships were explored for different subgrade soil types (fine- and coarse-grained soils) and climates (WF, WNF, DF and DNF).

Figure 4 shows scatter plots between AREA and the various cracking distresses. All figures show a high level of scatter. For fatigue cracking (Figure 4a) there is an indication of a downward trend as AREA increases. The reverse trend can be seen for longitudinal cracking-WP (Figure 4b) and transverse cracking (Figure 4d). For longitudinal cracking-NWP, there is no trend (Figure 4c). This could imply that this distress type is not load-related and probably caused by the environment.

4 CONCLUSIONS

Based on simple analysis to seek apparent relations and trends between initial pavement response parameters (deflections and DBI) and future observed cracking performance in flexible pavements, the following preliminary conclusions can be made.

At the project level, generally, AREA, SCI, BDI and d_0 have shown reasonable correlations with fatigue cracking for sections in most of the sites in the SPS-1 experiment (where sufficient distress has occurred). In most of the sites, pavements with higher initial SCI, BDI or d_0 , or lower initial

AREA were found to have more fatigue cracking. No apparent relations or trends were observed for longitudinal and transverse cracking.

At the overall network level, the scatter was very high. However some weak downward trend was seen with increasing AREA for fatigue cracking. The opposite trend with increasing AREA was observed for longitudinal cracking-WP and transverse cracking. No apparent relation was observed between AREA and longitudinal cracking-NWP, implying that this distress could be independent of the pavement structural capacity.

Deflection-based criteria to predict pavement performance are very uncertain at the network level. The amount of uncertainty or variance in the deflections on flexible pavement is contributed by many unexplained factors. The spatial variability may show the relative strength and the weakness along the pavement at the project level and hence such relationships between initial deflection-based parameters and future performance may be very useful for quality control/assurance, especially in the context of performance-related specifications. However, it may not be possible to predict the performance with any reliability at the network level.

REFERENCES

- AASHTO. (1993). "Guide for Design of Pavement Structures." American Association of State Highway and Transportation Officials, Washington, DC.
- Chatti, K., Buch, N., Haider, S. W., Pulipaka, A., Lyles, R. W., Gilliland, D., and Desaraju, P. (2005). "Final Report, LTPP Data Analysis: Influence of Design and Construction Features on the Response and Performance of New Flexible and Rigid Pavements." *NCHRP Project 20-50 (10/16)*, NCHRP Web Document 74, NCHRP, Washington DC.
- Haider, S. W. (2005). "The Use of Long-Term Pavement Performance Data for Quantifying the Relative Effects of Structural and Environmental factors on the Response and Performance of New Flexible Pavements," Ph.D. Dissertation, Michigan State University, East Lansing.
- Kim, R. Y., and Ranjithan, S. R. (2000). "Assessing Pavement Layer Condition Using Deflection Data." *NCHRP 10-48*, Department of Civil Engineering, North Carolina State University.
- Lukanen, E. O., Stubstad, R., and Briggs, R. (2000). "Temperature Predictions and Adjustment Factors for Asphalt Pavements." *FHWA-RD-98-085*, FHWA, Washington DC.
- Miller, J. S., and Bellinger, W. Y. (2003). "Distress Identification Manual." FHWA-RD-03-031.
- Molenaar, A. A. A. (2002). "Structural Evaluation and Strengthening of Flexible Pavements using Deflection Measurements and Visual Condition Surveys." Lecture Notes, Delft University of Technology.
- Park, H. M., and Kim, Y. R. (2003). "Prediction of Remaining Life of Asphalt Pavement using FWD Multiloading Level Deflections." *TRB*.
- Schmalzer, P. N. (2006). "LTPP Manual for Falling Weight Deflectometer Measurements, Version 4.1." *FHWA-HRT-06-132*, Federal Highway Administration, Office of Infrastructure Research and Development, McLean, Virginia.
- Stubstad, R. N., Jiang, Y. J., Clevenson, M. L., and Lukanen, E. O. (2006a). "Review of the long-term pavement performance backcalculation results - Final Report." *FHWA-RD-05-150*, FHWA, Washington DC.
- Stubstad, R. N., Jiang, Y. J., and Lukanen, E. O. (2006b). "Guidelines for review and evaluation of backcalculation results." *FHWA-RD-05-152*, FHWA, Washington DC.
- Stubstad, R. N., Lukanen, E. O., Tayabji, S. D., and Clevenson, M. L. (2002). "LTPP Data Analysis: Feasibility of Using FWD Deflection Data to Characterize Pavement Construction Quality." *NCHRP Project 20-50(9)*, *Final Report*.
- Ullidtz, P. (1987). *Pavement Analysis*, Elsevier Science Publisher B.V., Amsterdam, The Netherlands.
- Ullidtz, P. (1998). *Modeling Flexible Pavement Response and Performance*, Narayana Press, Gylling, Denmark.
- Xu, B., Ranjithan, S. R., and Kim, Y. R. (2002). "A New Condition Assessment Procedure for Asphalt Layers Using FWD Deflection." *Transportation Research Board*.

13. Pavement cracking detection

Photogrammetric pavement detection system

T. Lovas, I. Kertész, I. Fi & A. Barsi

Budapest University of Technology and Economics, Budapest, Hungary

ABSTRACT: This paper introduces a complex, low-cost road pavement measurement system designed primarily for pothole and crack detection. The onboard system is composed of a GPS/INS navigation unit, an image acquisition module, and a photogrammetric and image-processing subsystem. Due to the use of structured light and the availability of accurate navigation data, the 3D coordinates of the road points, in the form of cross profiles, as well as the size and location of the potholes, can be derived from the images at cm-level relative accuracy. For the road classification the International Roughness Index (IRI) can be derived. This paper also discusses the potential future developments of the system; it reports on the initial investigations of applying single camera with laser line projection which can significantly simplify the overall procedure.

1 INTRODUCTION AND CONCEPT

In the well-motorized countries the transportation authorities spend significant amounts of money to road constructions and road pavement maintenance. The roads are aging; the maintenance works have to keep pace with the new constructions. The traffic delays are mostly caused by road closures, this topic is always highlighted in the news. Therefore, the optimized scheduling became extremely important, the authorities tend to turn to new technologies in order to map the actual condition of the road pavement and decide upon the priorities of the scheduled maintenance works.

Since road engineering is one of the most extended engineering field, many “traditional” road surveying methods used for construction and maintenance planning. As most of the maintenance works are scheduled based on experiences, the road conditions are often classified by visual observations. The number of potholes, the length and type of the cracks, and lane grooves are clear indicators of the overall road condition.

However, there are a few autonomous (or at least semi-autonomous) systems in use, e.g. the Swedish RST (<http://www.opq.se>) or the Mandli Roadview (<http://www.mandli.com>): both systems are able to measure the cross- and longitudinal profiles of the roads; moreover, Mandli is collecting digital images about the road surface.

The authors also reported about the results in the major mapping and remote sensing conferences (e.g. International Society for Photogrammetry and Remote Sensing, American Society for Photogrammetry and Remote Sensing).

This paper discusses the structure and results of the original system, the potential of the entry-level IMUs (inertial measurement unit) in mobile mapping and introduces the latest concept with the initial test results.

2 SYSTEM COMPONENTS

Our basic idea was to create a road pavement detection system, which uses optical sensors for measuring the longitudinal and cross sections of the roads and the pavement anomalies (potholes, wide cracks). Figure 1 shows how the system components are linked to each other. The sensor

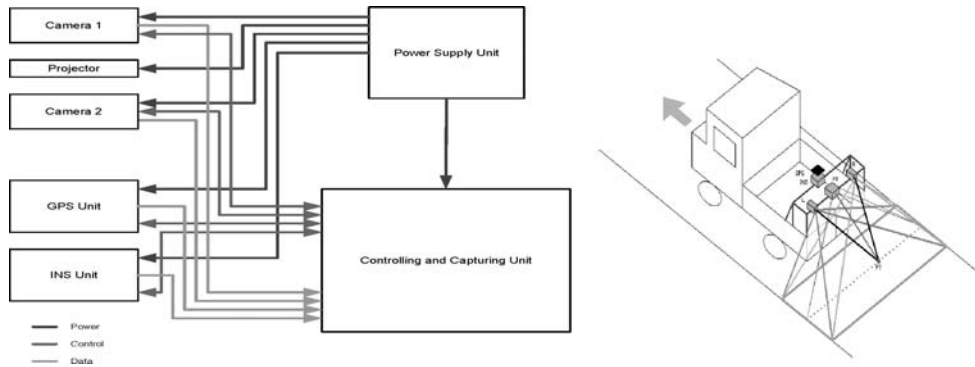


Figure 1. The main components of the system.



Figure 2. The instrument platform mounted on the pickup and the controlling environment.

component consists of two cameras (Sony XCD-SX910) synchronized by external trigger and laser projectors, the location component contains an integrated GPS/INS (Global Positioning System / Inertial Navigation System) unit (Crossbow NAV420CA).

The cameras are capturing downward images about the pavement at a rate of 5 fps. 20 individual laser projectors provide the equally spaced marker points located perpendicular to the traveling direction on the surface. Therefore, the 3D coordinates of the points can be computed by evaluating equations of geometric constraints.

The georeferenced position and orientation of the camera pair are provided by the integrated GPS/INS system. The NAV420CA system consists of a navigation grade GPS receiver, an entry-level IMU (Inertial Measurement Unit), and a built-in Kalman-filter. The accuracy of the positioning by the GPS module is about 3 m CEP, whereas the random walk of the IMU is about $4.5^\circ/\text{hr}^{1/2}$ (Barsi et al. 2005).

The cameras have 1280 by 960 pixel resolution which results in 3 mm ground pixel size, which enable not only the detailed surface description but the scar and crack detection from the images, too. The camera location assures the full lane-width visibility, covering 3.5 m wide area. The cameras are linked by FireWire to the laptop mounted in the cab (Fig. 2).

3 INITIAL RESULTS

The system will be used by the transportation authorities and intended to replace the existing road measurement technologies. There are several types of end products obtained by the developed

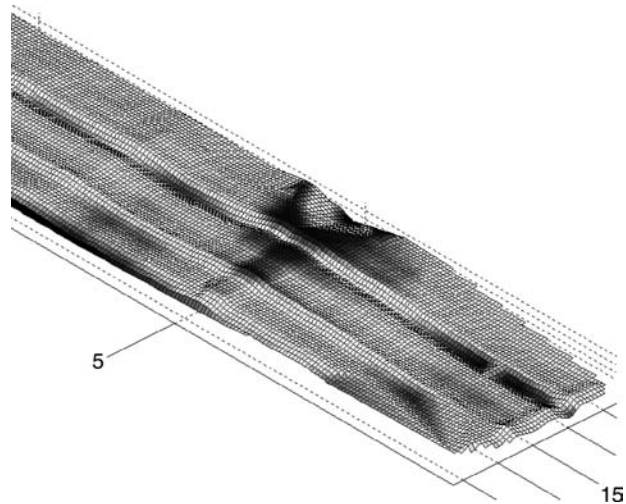


Figure 3. Pavement surface model.

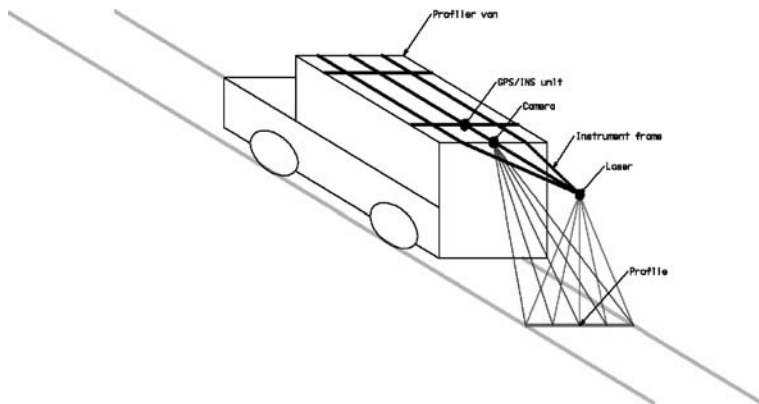


Figure 4. The concept of the second version.

system. The two main categories are: elevation information of the road surface and images about the pavement. From the elevation data of the projected points the cross and longitudinal sections of the road surface can be computed. If the point arrays are linked together, the digital surface model of the road can be created and enhanced on demand with the gradient values (Fig. 3). Using the optical images for crack detection is considered as a completely separate category. Applying well-known image processing algorithms, the length of the cracks can be computed.

4 V2 – BASIC CONCEPT

The idea behind the second version is measuring height in a single image by profile detection. If a straight line is projected on a smooth surface and an image is taken from oblique camera position, the line appears straight on the image (Fig. 4).

In case of height change (an object or pothole, for example), the image of the line seems straight only from top view, but it's broken from any oblique view point (Fig. 5).

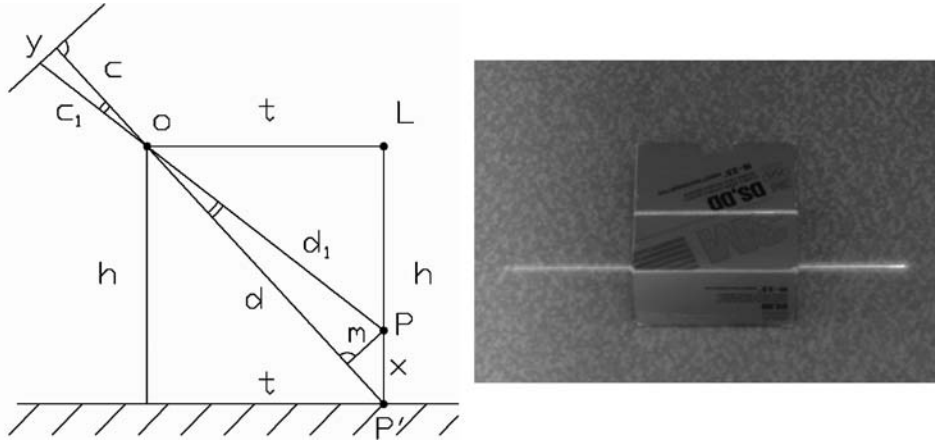


Figure 5. The basic concept of measuring height (x) in a single image taken from oblique viewpoint.

Based on similar triangles clear correspondence can be defined between y and x , which is a quadratic equation. For x the function is the following:

$$x = f(h, t, c, y) \quad (1)$$

During the calibration, the camera focal length is considered as constant. So the only inputs of calibration are the h and t values.

This system can be considered much robust compared to the previous version, since it avoids stereo imagery. Moreover, in this concept every single points of the projected line can be evaluated and measured (note, that previously separated points have been projected); therefore it enables much higher resolution for the road surface model. The surface resolution depends on the camera cross-directional resolution. Initially only a single line is projected onto the surface, later, if higher measurement speed is needed, more lines can be projected simultaneously.

5 FIRST TESTS WITH V2: CONCEPT PROOF

In the first phase the image processing module has been developed. For the concept proof an industrial laser line projector and an industrial digital camera were used, the same equipments are intended to apply in the final version. The laser projector is a 5 mW, 660 nm Lasiris laser diode, with special optic for the structured light. The imaging unit is a The Imaging Source DFK 41F02 color camera with 1280×960 resolution and 7.5 fps image acquisition speed.

The laser projector was mounted vertically (perpendicularly to the surface); the projected line was captured by the camera from the oblique position of about 45 degrees.

In all cases the objects have been moved towards the camera, perpendicularly to the projected line. Sequences of camera images were the inputs of the overall object reconstruction procedure. In all images the red laser stripe was extracted by filtering and binary image morphology, and then the y image coordinates of the laserline were computed.

The accuracy of the reconstructed object depends on the capturing resolution (number of images per object) and the calibration parameters (camera height, object distance). In the following the computed cross sections and the reconstructed object are shown (Fig. 6).

As it can be seen in Figure 6, the detected object is nicely reconstructed. The accuracy of the height measurement ensures adequate solution for road condition detection, since the final purpose is measuring the height differences on the road surface and deriving the IRI number for dedicated road segments.

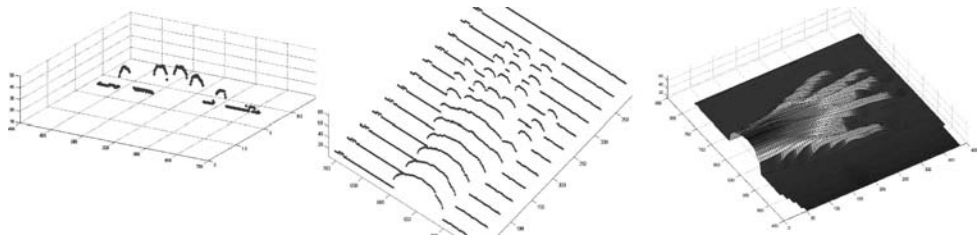


Figure 6. Computed cross sections and the reconstructed model of a hand.

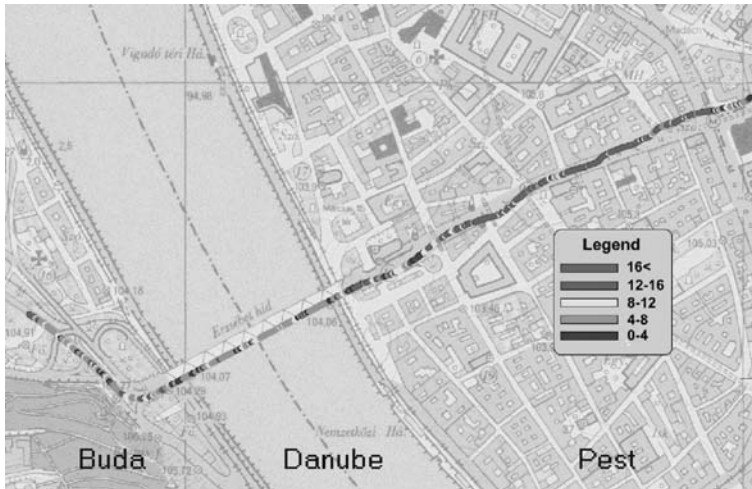


Figure 7. IRI map derived from laser markers below the tires. (light is for good, dark for bad status)

6 DERIVING THE INTERNATIONAL ROUGHNESS INDEX

The IRI measurement has m/km (sometimes mm/m) or in/mi units. The determination of IRI can be easily done from the intersected surface points; only the longitudinal profile has to be used. The most relevant place of road roughness is exactly under the tires, therefore the four (2 left and 2 right) markers in line with the tires have been selected for IRI calculations. The IRI values are calculated for all four points, samples taken in every 80 cm (at a speed of 4 m/s [15 km/h]) along the road, then their average are ordered to the analyzed road segment.

A further software module has been developed, which produces IRI files (reports) and IRI maps. In Figure 7 the effect of the recently finished road reconstruction on the bridge and the lack of it on the east (Pest) side can be clearly seen.

The IRI calculation is done at the highest resolution, but of course the values can be aggregated arbitrary.

An additional experiment was also performed: the potential of vertical acceleration directly in IRI calculation i.e. how can IRI be derived from the single vertical acceleration measurements. To test this hypothesis, regular gridded vertical acceleration values were interpolated, then they were integrated into vertical movements, and at the end the IRI-calculations were performed as (Sayers & Karamihas 1998) refers. The IRI-values are calculated for 2 m long segments. Since only a single IMU was applied in the vehicle, no smoothing (e.g. averaging) was needed (compared to the previously mentioned “optical” IRI method).

Considering different pavement types the IRI-diagrams can be compared (Fig. 8).

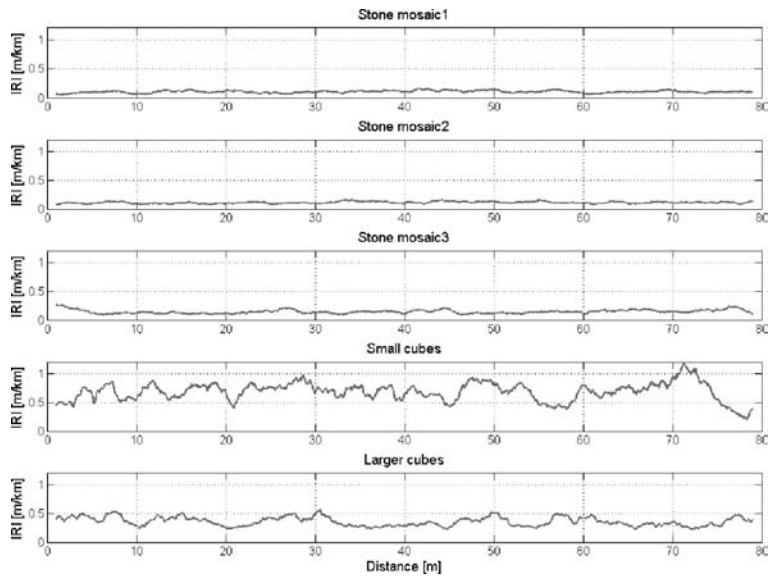


Figure 8. IRI-values calculated directly from vertical acceleration measurements on different pavement types.

Table 1. Basic statistics of IRI on different pavement types (derived from Figure 8 diagrams).

Pavement type	Mean	Std deviation
Stone mosaic1	0.1041	0.0195
Stone mosaic2	0.1095	0.0164
Stone mosaic3	0.1416	0.0317
Small cubes	0.6795	0.1586
Large cubes	0.3543	0.0775

The most important statistics of the IRI-values are in the Table 1.

The standardized IRI values for airport runways and superhighways are 0.5–2.0, 1.5–3.5 for new pavement, 2.5–5.5 for older pavement, 4.0–11.0 for damaged pavement and 8.0–20.0 m/km for rough unpaved roads. Comparing the IRI values of Figure 7, relative good fitting can be noticed: the renewed pavement on the bridge has an average IRI value of 4 m/km, whilst the older road segment on the east river side has about 16 m/km. Especially this latter value points out that our system requires a calibration run to get the mathematical formula to assign the IRI observations to the standardized evaluation.

Figure 8 illustrates the IRI diagrams for the investigated pavement types, calculated from the raw vertical acceleration measurements.

The first three pavement types are the smooth surfaces; they have an average IRI value of about 0.1 with a relatively small (<0.05) standard deviation. Compared to this, the last two pavements are worse as the observed higher IRI values (0.3 and 0.6) with larger standard deviation (>0.05) clearly indicate it.

Although there are numerically greater differences between our mean IRI values and the standardized ones, the tendency is obvious: the worse road gets higher IRI measures. This solution also cannot avoid the calibration procedure.

7 CONCLUSIONS

In this paper we presented a concept study and our initial results of the developed pavement detection system. Digital cameras capture the images of the road pavement which is lit by structured light. The exterior orientation parameters of the images are provided by a GPS/INS navigation system, which enables the pavement surface generation at good accuracy. Applying a special diffuse illumination, the small anomalies of the pavement, such as scars and potholes, can also be detected. In the context of this effort we developed a road profile and surface generation module which input the profiles formed from the marker points. This CAD-based module not only computes the profiles from the given points, but generates a road surface model that represents the pavement condition and can be used for maintenance assessment, scheduling, and planning.

The investigations and tests described in this paper proved that the proposed single-camera detection method assures robust solution for road surface generation. Applying a single imaging unit simplifies the georeferencing and avoids the complicated calculation and calibration of two cameras which have to be synchronized. Using line projection instead of laser point array enables measuring all point heights along the profile, therefore the surface model resolution depends only on the horizontal resolution of the camera. This concept also has further potential in development, e.g. applying multiple projected lines in order to allow higher measurement speed, and also leaves open the possibility of using the camera images for additional purposes, such as crack detection, which is a critical issue regarding road condition detection.

The described mobile mapping system and the provided surface data can be used for deriving the IRI for the particular road segments, which is used by the transportation authorities for road pavement classification.

The next step in development is creating the engineering prototype of the road detection system; the camera, the laser projector, the control unit, and the navigation system are to be mounted on a vehicle and the next tests are to be carried out in the environment of the final system, i.e. on the roads.

REFERENCES

- Sayers, W. M. & Karamihas, M. S. (1998): *The Little Book of Profiling; Basic Information about Measuring and Interpreting Road Profiles*, The Regent of the University of Michigan
- Crossbow (2004): *Nav420 Series User's Manual*, Document 7430-0121-01
- Toth, C. & Grejner-Brzezinska, D. (2004): *Redefining the Paradigm of Modern Mobile Mapping: An Automated High-precision Road Centerline Mapping System*, *Photogrammetric Engineering and Remote Sensing*, Vol. 70, No. 6, pp. 685–694
- Barsi, A., Fi, I., Lovas, T., Mélykúti, G., Takács, B., Toth, C., Tóth, Z. (2005): *Mobile Pavement Measurement System: A Concept Study*, *Proc. ASPRS Annual Conference, Baltimore, USA*, May 7–11, p. 8
- Barsi, A., Fi, I., Mélykúti, G., Lovas, T., Tóth, Z. (2005): *Road pavement detection – Developing mobile mapping system at BME*, in Hungarian, *Mélyépitő Tükörkép Magazin*, Budapest, pp. 32–33
- Kertész, I. (2005): *Geoinformational analysis of GPS/INS systems*, *Proc. Scientific Student Conference*, p. 38.
- Barsi, A., Lovas, T., Kertész, I. (2006): *The Potential of Low-End IMUs for Mobile Mapping Systems*, *International Archives of Photogrammetry and Remote Sensing*, Vol. XXXVI, Part 1/A+B, p. 4
- Barsi, A., Lovas, T., Toth, C.K. (2006): *Positioning with mobile mapping system*, in Hungarian, *Geodézia és Kartográfia*, Budapest, Vol. LVIII, No. 4, pp. 3–8
- Kertész, I. & Barsi, A. (2007): *Inertial measurements in mobile mapping*, in Hungarian, *Geomatikai Közlemények*, Sopron
- Lovas, T., Kertész, I., Fi, I., Barsi, A. (2007): *New Concept of Profile Based Pavement Measurement System*, *Proc. ASPRS Annual Conference, Tampa, USA*, May 7–11, p. 6

Automated cracking survey

K.C.P. Wang, W. Gong & Z. Hou

University of Arkansas, Fayetteville, Arkansas, USA

ABSTRACT: Despite tremendous difficulties for developing automated data collection and interpretation of pavement surface cracks, there have been progresses made in recent years in both hardware and software technologies for data collection and crack analysis. This paper attempts to present the status of developments, such as laser based imaging with low power consumption and shadow-free characteristics, and real-time and fully automated analysis. A special focus is on the Automated Distress Analyzer (ADA) that was developed at the University of Arkansas. Challenges in computing resources and algorithm development will be discussed. In addition, data is presented comparing fully automated real-time results from ADA and results from manual surveys.

1 INTRODUCTION

Pavement condition survey is a critical process for roadway agencies to accomplish the tasks of performance measurement, maintenance, rehabilitation, and reconstruction of the transportation facilities. Traditional survey is conducted through manual observation in the field. It is hazardous, error-prone, lack of consistence, and time and cost consuming. Many existing systems can automatically collect the data (Wang, 2000). However, they share common characteristics of limited automation level on the data analysis. Analyzing the data collected manually is a painstaking task considering the large amount of data for visual inspection.

The challenge of the automated data analysis is the extraction and recognition of the features of interest from the images by computer. The automated recognition is mostly based on pattern recognition and image processing techniques. A recent report on automated cracking survey (McGhee, 2004) presented comparison of data between the results from an automated system and the results from manual surveys. The conclusion of the report is that there are still large differences between them. For nearly a decade, the researchers at the University of Arkansas worked on the Digital Highway Data Vehicle (DHDV) and the related real-time cracking software, the Automated Distress Analyzer (ADA). This paper attempts to present the development of DHDV, the use of the Laser Road Imaging System (LRIS) for image capture, and ADA, and discuss two popular cracking protocols that are being deployed in the US and Europe.

2 DESCRIPTION OF HARDWARE SYSTEM

The Digital Highway Data Vehicle (DHDV) has evolved into a new platform with laser based imaging technology for pavement surface data collection. The DHDV is multi-functional and includes a sub-system for pavement surface imaging, a sub-system for Right-Of-Way imaging, and a sub-system of laser road profiling. Figure 1 illustrates the basic components and data flow of DHDV.

The pavement imaging sub-system includes two line scan cameras and two laser sensors pointing downward on the pavement. Together, the two cameras capture about 4-meter wide pavement with 1-mm resolution at speeds over 100 KPH. The images are in 8-bit gray scale. An Automated Distress

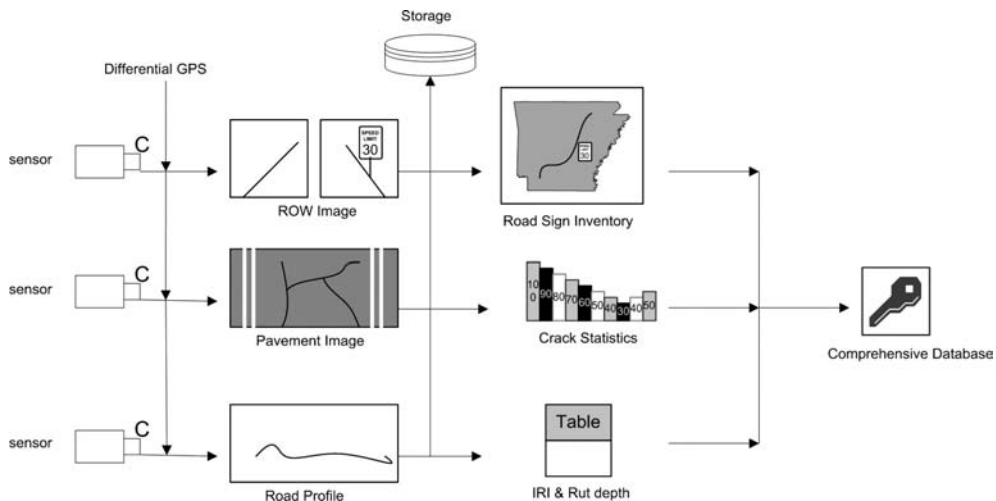


Figure 1. Dataflow of the DHDV System.

Analyzer (ADA) is developed to conduct the real-time automated distress detection and analysis of the pavement images. Four types of cracks (longitudinal, transverse, alligator and block) are detected and classified. Geometry information of individual cracks and their positions are streamed into a real-time database. The ReportWriter software compiles the cracking information in the database into various indexing formats, such as the AASHTO interim protocol, Cracking Indicator (CI), TxDOT method, UK SCANNER, and Pavement Condition Index (PCI). Custom protocol can also be developed into the ReportWriter.

For several decades, the data collection industry of roadway pavements struggled to provide high-quality and shadow free images. The implementation of digital image collection in recent years did not help ease the problem. Unnaturally darker areas in images are caused by the shadowing effect due to sun's relative orientation to the data collection vehicle. For example, trees, power lines, buildings, and mountain slopes can cause the darker areas. Even the data collection vehicle's own shadow can appear in images. Shadows in pavement images can render that portion of image not usable for survey as the details are not visible. If the details of the shadowed area are legible for survey, the un-shadowed area would be too bright and not legible for survey. As automated interpretation techniques also rely on high image quality to produce correct results, the shadow problem in pavement images present difficulties for both manual and automated processes. Many data collection vehicles had to operate at night to eliminate shadows and provide uniform images with light-emitting devices.

Since early 2006, laser was successfully implemented as the illuminating device to capture pavement images by the Canadian company INO in Quebec. The underlying principle is to illuminate the pavement surface with a laser line light within a narrow spectrum that sun light has limited energy influence. Camera lens is outfitted with a filter that only allows energy in the narrow spectrum to pass through. The end result is that the camera can only receive information reflected from the pavement surface in the narrow spectrum. The two major advantages of this technique are (1) shadow free images are obtained all the time, day or night, (2) energy consumption is limited to 200 watts or less. Systems based on traditional lighting techniques require thousands of watts of energy, still not able to rid of the shadowing problem.

The new INO system is called Laser Road Imaging System (LRIS), consisting of two high resolution line-scan cameras and two laser emitters to image 4-meter wide pavement surface with 1-mm resolution at speeds surpassing 100 KPH. In Figure 2, the LRIS system uses both high speed/high resolution line-scan cameras in conjunction with high power laser line projectors that are aligned in the same plane in a symmetrically crossed optical configuration. The laser used in LRIS

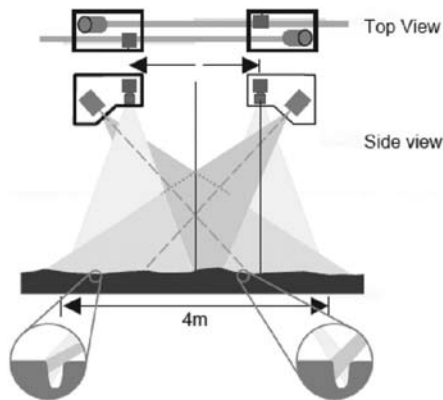


Figure 2. DHDV with LRIS in Operation.

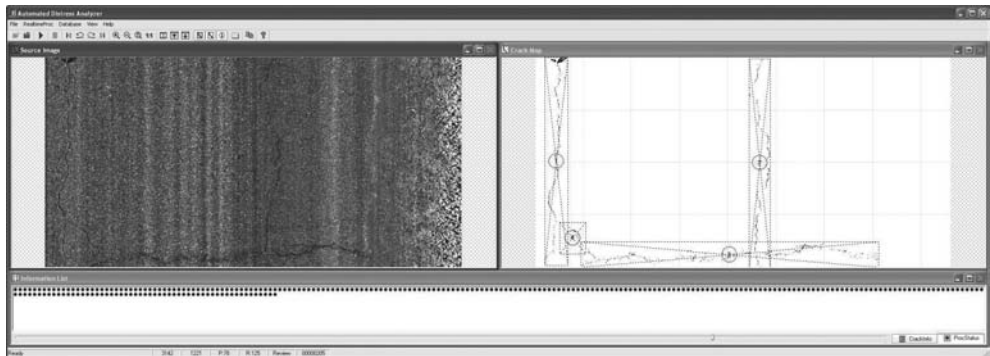


Figure 3. Automated Distress Analyzer.

has a wavelength of 800 nm to 580 nm which belongs to class IIIb. This particular configuration offers several advantages as compared to more traditional imaging techniques. It is compact (20 kg total weight), power efficient (<250 W), and immune to shade and ambient illumination change. The most important feature of the system is that this optical configuration increases the visibility of even the smallest cracks by using the incident illumination angle of the laser to cause the cracks to project shadows.

A Real-time distress analyzer, Automated Distress Analyzer (ADA), shown in Figure 3, was developed which provides the real time analysis of the longitudinal, transverse, alligator, and block crack. The detected cracks in the images are highlighted in a bounding box in the crack map. The length, width, direction, type, and other information of the cracks are imported to utility software, ReportWriter. The crack statistics of the target road is provided in a graph, an Excel file, or database file.

3 AUTOMAED INTERPRETATION FOR CRACKS

In order to achieve rapid execution of algorithms on image compression and image analysis, parallel processing techniques are used in the DHDV to maintain real-time operation of data acquisition and processing.

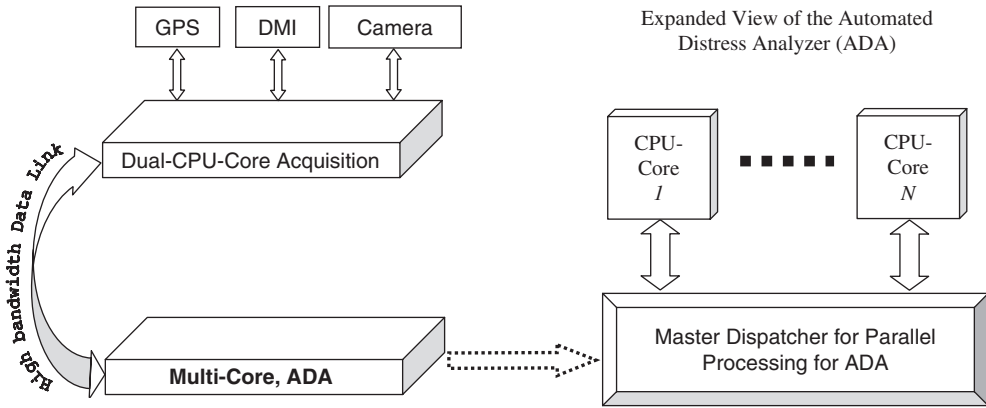


Figure 4. The Framework of the Data Acquisition and Processing.



Figure 5. Integrated MHIS Deluxe for Distress Editing and Information Presentation.

At the macro level, Figure 4 illustrates the data acquisition and processing in a parallel environment. A dual-CPU multi-core computer is used for data acquisition of GPS data, DMI data, images from the digital camera, and data from other sensors. These data sets are moved to another multi-core CPU computer in real-time for the distress analyzer through a gigabit data path. There is a project manager or master dispatcher for parallel processing, which coordinates the processing of images among the n processor cores. The current implementation uses two CPUs for the distress analyzer. In the near future, a single multi-CPU and multi-core computer will be deployed to conduct the entire processes of data acquisition and processing.

Figure 5 illustrates an integrated multi-media highway information system (MHIS) Deluxe that presents all DHDV collected data sets in a geo-referenced environment. A key feature of MHIS Deluxe is its capability to add non-cracking distresses and edit existing cracks through a CAD like tool palette.

4 EXPERIMENT DATA

When geometry and positioning information of cracks are known, the next logic step is to compile the information into an engineering index for pavement management purposes. In the past decades, roadway agencies in the world were devising and implementing their own definitions of distress indices or indicators. Universal Cracking Indicator (CI) was devised by William D. Paterson of

World Bank (Paterson, 1994). Its simplicity makes it appropriate to be used to test the validity of ADA. It is dimensionless. It produces a single number to indicate the severity of pavement cracking as follows:

$$CI = 100[l_L w_L + l_A w_A + l_T w_T] / A$$

l : Length of the crack (m)

w : Width of the crack (mm)

l_L : Longitudinal crack

l_A : Alligator crack

l_T : Transverse crack

A : Total pavement surface area (m²)

Seven sets of experiment data are presented in this paper. The original pavement images are collected using the DHDV equipped with LRIS. ADA processes the pavement images and the cracks are automatically detected and presented in the form of location, geometry and orientation. The ReportWriter software then processes results from ADA and produces crack statistics. Several distress protocols are implemented in ReportWriter such as UK SCANNER, ASSHTO, World Bank CI, Texas DOT protocol etc. The CI method is used in this study.

The manual results are obtained by carefully examining the results from ADA and correcting the erroneous detections, including deleting false alarms and adding missed cracks. Diversity of pavement location, road condition, characteristics are considered when choosing the sampling data sets. There are seven databases presented here for seven pavement sections: five for urban road, two for rural road.

The seven figures show the comparison results. The X-axis shows the section number, with 100 meters for each section. Y-Axis shows the CI index for the sections. All seven datasets generally show consistency between the manual rating and the automated rating. The error percentage is less than 1% for most of the comparisons. However, dataset 4 and dataset 5 have error percentage about 20%–50%. These two datasets are taken from the roads in the City of Los Angeles where some roads are severely deteriorated. From the raw images, a large amount of man-made objects, trash, and marking can be seen. These contents pose tremendous challenges to the automatic algorithms and become a next research project.

5 CONCLUSIONS

The pavement data collection industry finally has obtained a hardware that is able to capture 1-mm details of pavement in digital format at highway speed without influence of sun light and free of shadows. This dramatic development has further encouraged developers to produce working systems for automated interpretation, and generation of crack maps of pavement surfaces. Due to the technical complexity of definitions and varying needs of highway agencies, it appears that a universally accepted standard for cracking index is not likely. This paper attempts to correlate the fully automated real-time results from ADA with results of manual processing based on the CI index. It is conclusive that ADA results meet the manual results very well. It should be noted that there have been two major efforts of developing cracking protocols in the US (AASHTO Interim Protocol) and United Kingdom (UK SCANNER) that have received certain level of acceptance in a number of agencies. The authors will present more data analysis based on the two protocols in the near future.

REFERENCES

AASHTO, Standard Practice for Quantifying Cracks in Asphalt Pavement Surface, AASHTO Designation: PP44,00, 2001

McGhee Kenneth, H. (2004), NCHRP SYNTHESIS 334, Automated Pavement Distress Collection Techniques, a Synthesis of Highway Practice, National Cooperative Highway Research Program, Washington, D.C.

Paterson, W.D. Proposal of Universal Cracking Indicator for Pavements. Transportation Research Record 1455, pp. 69–75, TRB, National Research Council, Washington, D.C., 1994.

SCANNER Surveys for Local Roads, Specification Vol. 2, Specification for Services, July 2005, Halcrow Group Limited.

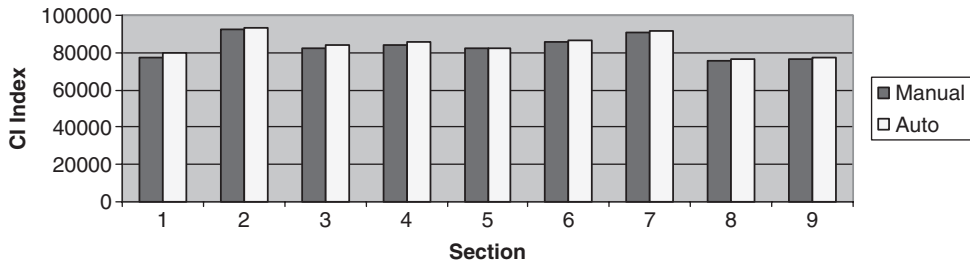
Strategic Highway Research Program (SHRP), National Research Council (1993 and 2003), Distress Identification Manual for the Long-Term Pavement Performance Program (2003 Fourth Revised Edition)

Wang, K.C.P. (2000) “Design and Implementation of Automated Systems for Pavement Surface Distress Survey”, ASCE Journal of Infrastructure Systems, Vol. 6, No1, March, pp. 24–32

Data Set 1

Location: Baton Rouge, LA, Suburban; Length: 900 meters
 General Pavement Condition: Poor
 Foreign Object on Pavement Surface: Clean, with some oil streaks
 Survey Time: ADA, 1.5-min; Manual 10-hr

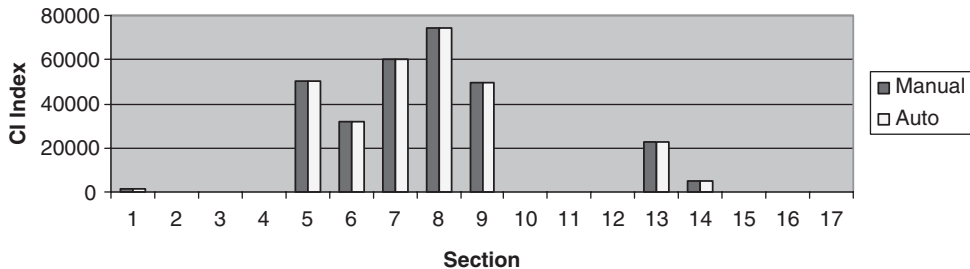
BatonRouge, LA, 74 wb, 2006-06-28



Data Set 2

Location: Baton Rouge, LA, Suburban; Length: 1700 meters
 General Pavement Condition: Poor
 Foreign Object on Pavement Surface: Clean, with oil streaks on road, trash, seam between shoulder and ground
 Survey Time: ADA, 3-min; Manual 10-hr

BatonRouge, LA, 74eb, 2006-06-28



Data Set 3

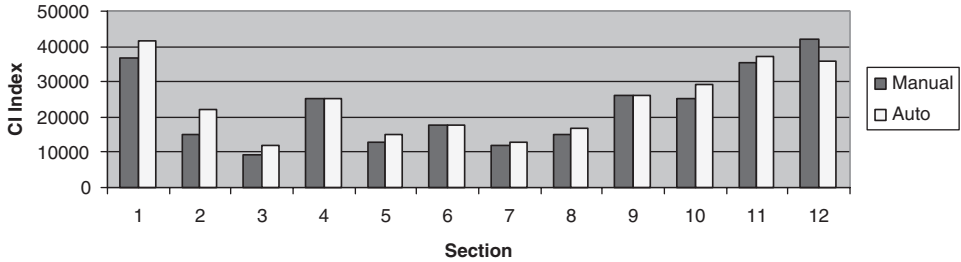
Location: Fayetteville, AR, urban; Length: 1200 meters

General Pavement Condition: Poor

Foreign Object on Pavement Surface: Clean, with man holes

Survey Time: ADA, 2-min; Manual 6-hr

Fayetteville, AR, 15th Street, 2007-09-13



Data Set 4

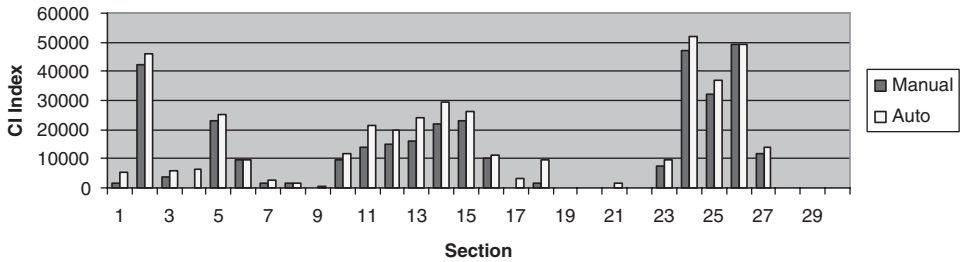
Location: Los Angeles, CA, Urban; Length: 3000 meters

General Pavement Condition: Poor

Foreign Object on Pavement Surface: Dirty, with man holes, seams between asphalt and curb, debris, railroad tracks

Survey Time: ADA, 5-min; Manual 20-hr

Los Angeles, CA, 7th Street, 2007-11-29



Data Set 5

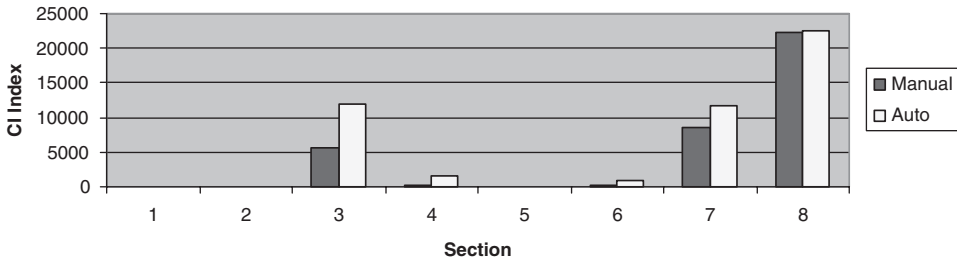
Location: Los Angeles, CA, Urban; Length: 800 meters

General Pavement Condition: Fair

Foreign Object on Pavement Surface: Clean, with manholes, seams between asphalt and curb, debris, railroad tracks, cuts on asphalt

Survey Time: ADA, 1.5-min; Manual 1.5-hr

Los Angeles, CA, 1st Street, 2007-12-19



Data Set 6

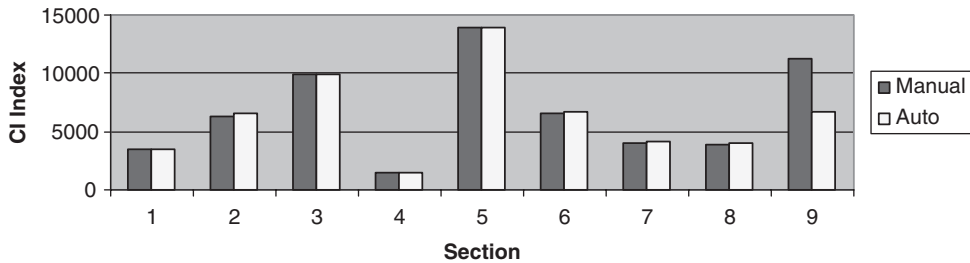
Location: College Station, TX, Urban; Length: 900 meters

General Pavement Condition: Fair

Foreign Object on Pavement Surface: Clean, with some oil from median reflectors, seams between asphalt and curb

Survey Time: ADA, 1.5-min; Manual 2.5-hr

College Station, TX, WellBorn Rd, 2006-08-10



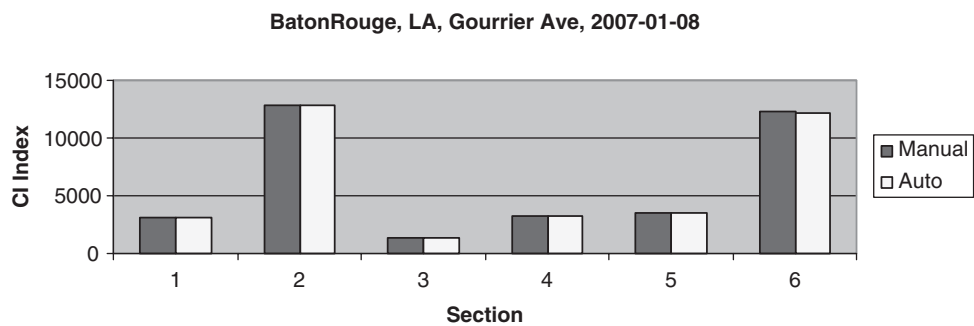
Data Set 7

Location: Baton Rouge, LA, Urban; Length: 600 meters

General Pavement Condition: Fair

Foreign Object on Pavement Surface: Clean, with seams between asphalt and curb

Survey Time: ADA, 1-min; Manual 2-hr



Crack detection and classification in asphalt pavement using image processing

A. Hassani & H. Ghasemzadeh Tehrani

Tarbiat Modares University, Tehran, Iran

ABSTRACT: Road surface cracking is a major and extent type of distress in both rigid and flexible pavements. Crack detection and their classification are very important in pavement management systems. This paper, proposed a method based on road surface image processing. Some of the image characteristics including vertical histogram, horizontal histogram, vertical proximity and horizontal proximity are calculated. By using these parameters an image categorized into free crack, longitudinal, transverse, block and alligator cracks. In some cases, block and alligator cracks have a near properties and method need to use a fuzzy algorithm for judgment. The main advantage of fuzzy algorithm is considering uncertainty nature of crack patterns. The proposed method is very easy, fast with a high accuracy.

Keywords: road crack, image processing, fuzzy, pattern recognition.

1 INTRODUCTION

Road and highway networks are a major asset in all countries. Billion of dollars are needed for current road maintenance every year. Thus, road authorities need accurate, confidential and up-to-date information on the network pavement condition for managing these assets efficiently. Conventional method for road pavement evaluation is manual. The manual methods are very costly, time consuming, dangerous, labor intensive and subjective [1]. These factors cause an approach to automatic monitoring and non-destructive testing for road pavement evaluation. This approach started by measuring roughness and then continued by considering other distress types. Currently, there are many types of equipment for rapid monitoring and evaluating of road pavements such as Swedish PAVUE, CSIRO crack detection system, Dynatest productions, ARAN productions and so on. They are very powerful tools but they only produce surface cracking map and can not classify cracks.

As the papers show, many researchers have studied recognition and classification of road surface cracks. Imaging method is widely used in which a visual digital image from the surface is analyzed to identify surface distresses.

Because of uncertainty in crack patterns, some papers have proposed methods based on fuzzy theory and fuzzy logic [1, 2, 3, 4]. As the brain can detect the distress on the road easily by seeing them, some researchers tried artificial intelligence method such as neural networks and neuro-fuzzy systems to classify the distress on the roads [5, 6, 7]. Others also applied for crack detection and classification [8, 9, 1, 11, 12].

Authors have proposed three methods for crack detection and crack classification in digital images [13, 14 15, 16]. Firstly, an algorithm for classifying cracks in pre-processed images was proposed based on fuzzy membership functions. This method is very simple and too fast. The method consider crack pattern uncertainty for judgment, specially in the case of block cracks with high severity and alligator cracks with low or medium severity, But this method can not detect free crack images and its accuracy is not in agreement completely [13, 16].

Secondly, a method was proposed by using artificial neural network. A multi layer perceptron (MLP) network was learned to classify cracks in the road surface digital images. The MLP method

is not as simple as fuzzy algorithm, but it can use for identifying any kind of distresses and their corresponding severity. The problem with MLP method is the size of image. As the size of image increase, the number of neurons will be high and the network diverges [14, 16].

Thirdly, a region growing classifier (RGC) was proposed for crack identification. The basic idea in the RGC method is to segment underlying image into some disjoint regions or segments based on pixel grey level characteristics and then count the number of regions which are produced as the desirable output. These regions may be small neighborhoods or even single pixels. RGC method is the process of joining neighboring pixels into larger regions based on image properties. This method has a good accuracy but it is a deterministic method and can not consider uncertainty in different type of crack patterns [15, 16].

This paper presents a method, classifying road cracks by combining two approaches. At the first, some of image characteristics including vertical histogram, horizontal histogram, vertical proximity and horizontal proximity are used to identify cracks in the image. Finally, in some cases, such as block or alligator cracks fuzzy algorithm is used.

2 IMAGE CHARACTERISTICS

A digital handy cam is used to take road surface images. The degree of handy cam with horizontal axes is 30 degree and it is 1.5 meter above the surface. The original image has 640 by 480 pixels. Each image shows a 1.2 m × 1.2 m of road surface. The performed results showed that images taken in sunny weather two or three hours after raining were the best, as the gray level of the cracks is much different from the background of surface. As such all pixels should be located in two groups, namely background and crack pixels. Thus, a computer program is written to change each image to gray scale, and then by using proper threshold all images changed to a binary image. Proper threshold is chosen by investigating more than 500 images.

From the pre-processed input image two kinds of histograms are calculated, a vertical histogram ($Vh(j)$) and a horizontal histogram ($Hh(i)$). The vertical and horizontal histogram of a binary image is defined as the number of non-zero values in each column and row respectively. Based on these definitions for a given “n.m” image equation (1) and (2) are introduced.

$$Vh(j) = \sum_{i=1}^n I(i, j) \quad (1)$$

$$Hh(i) = \sum_{j=1}^m I(i, j) \quad (2)$$

To find a way for using the ability of histogram method, we propose the mean value of each vertical histogram (μ_v) and horizontal histogram (μ_h) as follows:

$$\mu_v = [\sum_{j=1}^m Vh(j)] / m \quad (3)$$

$$\mu_h = [\sum_{i=1}^n Hh(i)] / n \quad (4)$$

One advantage of using the mean value of histogram is that it gives a position invariant measure of the input image because if the crack is shifted across the horizontal or vertical direction, then μ_v and μ_h are not changed. We can also define the proximity measure as a vertical proximity and horizontal proximity. The proximity is computed by accumulating the difference between adjacent histogram values. Low level of proximity indicates that there is little difference between any of the columns or rows for the input image. The vertical proximity (Ω_v) and the horizontal proximity (Ω_h) can be calculated as follows:

$$\Omega_v = \sum_{j=1}^m |Vh(j+1) - Vh(j)| \quad (5)$$

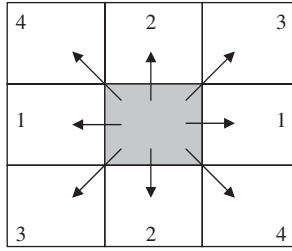


Figure 1. Different directions of crack development.

$$\Omega h = \sum_{i=1}^n |Hh(i+1) - Hh(i)| \quad (6)$$

We categorize the images in five groups including free crack, longitudinal, transverse, block and alligator crack. At least 100 images are taken for each group. Our study shows that μ_v and μ_h are less than 0.5 for free crack images. Further, for longitudinal and transverse crack images μ_v and μ_h are from 1 to 10. For longitudinal cracks, the vertical proximity is greater than horizontal proximity and for transverse cracks; the vertical proximity is less than horizontal proximity.

If the μ_v and μ_h are greater than 10 then image may be a block or alligator crack. Clear block cracks have μ_v and μ_h less than 15 and clear alligator cracks have μ_v and μ_h greater than 35. Otherwise, the image shows a block crack (with medium or high severity) or an alligator crack (with medium or low severity). In such cases, the image characteristic ranges are similar for both cracks and there is an uncertainty at the judgment. In this situation, we propose using fuzzy algorithm for crack classifying.

3 FUZZY ALGORITHM

Different types of cracks are developed in different directions as shown in figure 1. The longitudinal cracks are developed in direction 1, transverse cracks are developed in direction 2, block cracks are developed in direction 1 and 2, alligator cracks are developed in direction 3 and 4. In each binary image, the pixels with gray level 1 are count in four directions. The percent of new element in each direction (p_1, p_2, p_3, p_4) shows the kind of crack. All images were categorized and then P_i values were calculated. P_i values were used for develop a set of membership functions. These functions indicate the image membership for each category and intersection of all functions shows the image classification. Based on our experience the membership functions for block and alligator cracks are provided and shown in Figure 2 [13].

According to Bellman and Zadeh law, the minimum of membership is chosen as intersection [17]. Figure 3 shows the decision making flowchart.

4 EXPERIMENTAL RESULT

Some images are reviewed in this section for describing the method. Figure 4 shows an image with $\mu_h = 2.2$, $\mu_v = 3.2$, $\Omega h = 40$ and $\Omega v = 93$. Based on our flowchart, this image represents a longitudinal crack, as it is seen.

Figure 5 shows an image with $\mu_h = 43$, $\mu_v = 63$, $\Omega h = 1936$ and $\Omega v = 1229$. According to our flowchart, this image is categorized as an alligator crack, as it is seen.

Figure 6 shows an image with $\mu_h = 19$, $\mu_v = 28$, $\Omega h = 982$ and $\Omega v = 845$. In this case, we need to use fuzzy algorithm. In this image, percent of new elements at each directions are as follow

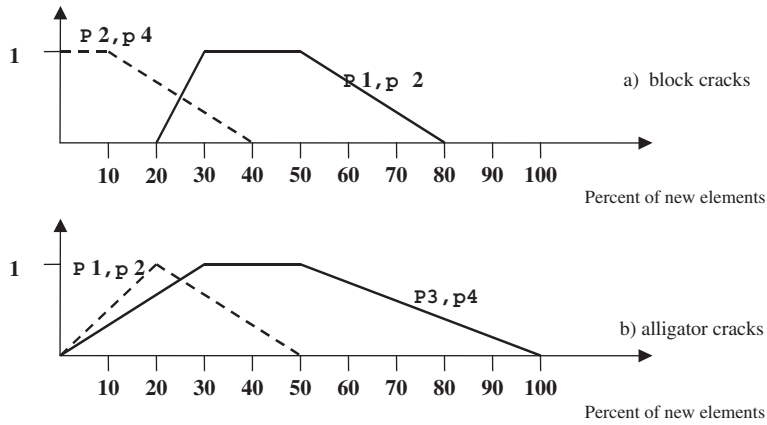


Figure 2. Membership functions for (a) block cracks and (b) alligator cracks.

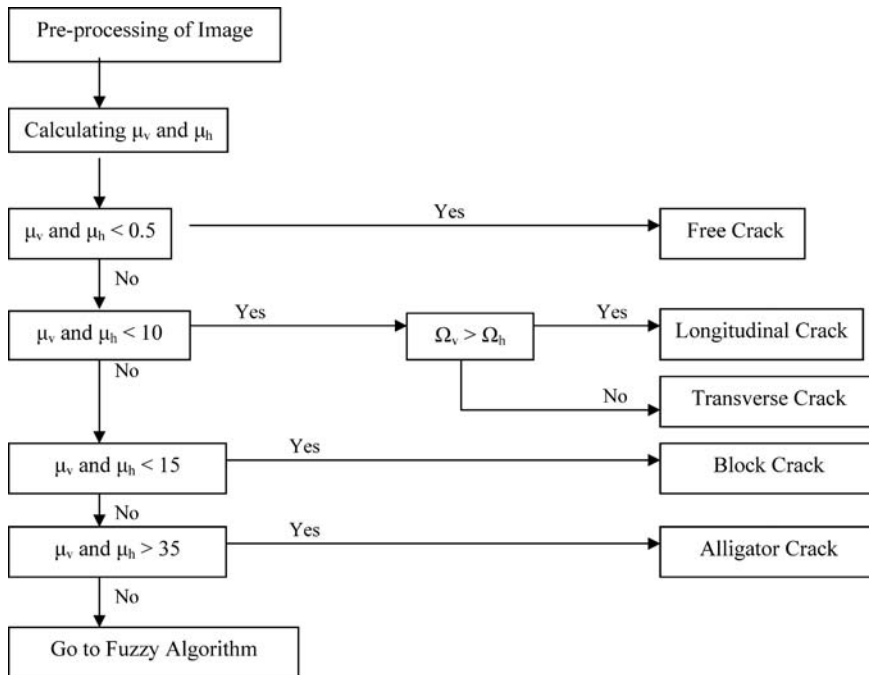


Figure 3. Decision making flowchart.

$p_1 = 39\%$, $p_2 = 31\%$, $p_3 = 18\%$ and $p_4 = 12\%$. The membership degree intersection of image for block cracking is 0.73 and for alligator cracking is 0.33. So, this image represents a block crack. Comparing 0.33 and 0.73 indicates the uncertainty nature of crack pattern.

5 CONCLUSIONS

Pavement cracks are major and extensive distresses. Crack identification and classification with manual methods are very costly, time consuming, dangerous, labor intensive and subjective. There

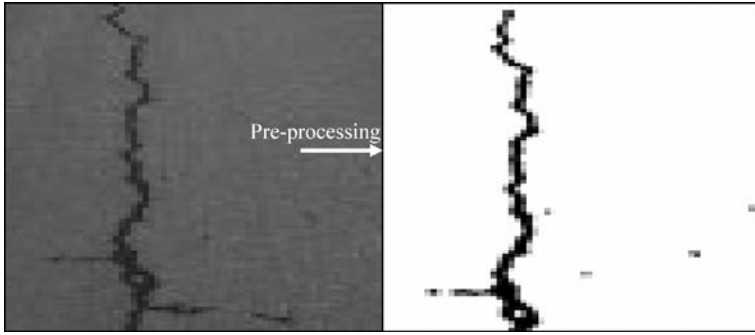


Figure 4. Longitudinal crack.

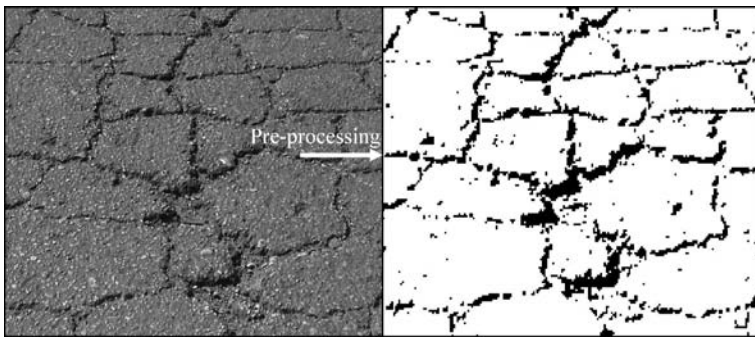


Figure 5. Alligator crack.

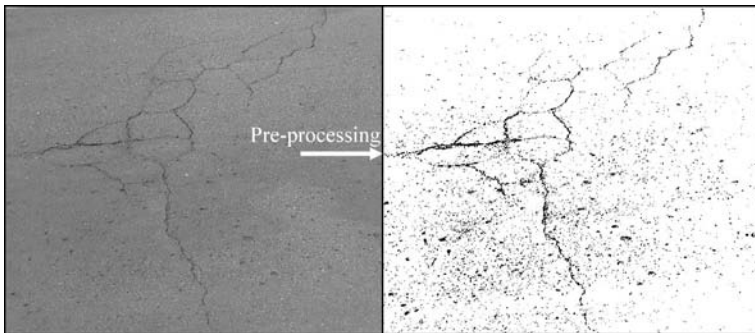


Figure 6. Block crack.

are many types of equipment for rapid monitoring and evaluating of road pavement but they only produce surface cracking map and can not classify cracks.

In this paper, we reviewed our previous methods for crack detection and classification in digital images. Then, we proposed a new method with combination some of them. As the experimental results show, this method is free from disadvantages of other previous methods. This method is simple and fast and so the hardware implementation is easy with low cost. It's accuracy in our images is more than 95% and provides a reliable and confidential results.

REFERENCES

1. H.D. Cheng, et al. (1999) *Novel Approach to Pavement Cracking Detection Based on Fuzzy Set Theory*. Journal of Computing in Civil Eng. Vol: 13, No: 4, pp: 270–280.
2. D. Kaur, D. Tekkedil (2000) *Fuzzy Expert System for Asphalt Pavement Performance Prediction*. IEEE Intelligent Transportation Systems Proceeding. Pp: 428–433.
3. C.J. Chao, F.P. Cheng (1998) *Fuzzy Pattern Recognition Model for Diagnosing Cracks in RC Structures*. Journal of Computing in Civil Eng. Vol: 12, No: 2, pp: 111–119.
4. B. Ravi and M.H. Ang (2000) *Fuzzy Logic Based Character Recognizer*. Proceeding of the Computing Science Congress (PCSC).
5. D. Kaur, E. Chao (1999) *Applying Neuro-Fuzzy Techniques for Intelligent Highway Pavement Performance Prediction Model*. IEEE, Vol: 5, pp: 922–924.
6. N.K. Kasabov (1998) *Foundations of Neural Networks, Fuzzy Systems and Knowledge Engineering*, MIT Press, Second Printing.
7. Y. Liu et al (2001) *Inspection of Defects in Optical Fibers Based on Back Propagation Neural Networks*. Elsevier Journal of Optics Communications. Vol: 198.
8. T. Tomikawa (1999) *A Study of Road Crack Detection by Meta-Genetic algorithm*. IEEE AFRICON, Vol: 1.
9. K. Sarabandi and E.S. Li (2000) *Polarimetric Characterization of Debris and Faults in the Highway Environmental at Millimeter Wave Frequencies*. IEEE Transactions on Antennas and Propagation. Vol: 48, No: 11.
10. A.C. Heath, et al. (2003) *Modeling Longitudinal, Corner and Transvers Cracking in Jointed Concrete Pavements*. The International Journal of Pavement Eng. Vol: 4, No: 1, pp: 51–58.
11. C. Scheffy and E. Diaz (1999) *Asphalt Concrete Fatigue Crack Monitoring and Analysis Using Digital Image Analysis Techniques*. International Conference on Accelerated Pavement Testing, Reno, Nevada.
12. J. Ze et al (1997) *Content-Based Image Indexing and Searching Using Daubechies Wavelets*. International Journal of Digital Libraries, pp: 311–328.
13. H. Ghasemzadeh Tehrani and H. Toosian Shandiz (2005) *Fuzzy Algorithm for Classification of Road Crack Pre-Processed Digital Images*. 3rd International Iranian Conference on Machine Vision and Image Processing. Tehran, Iran.
14. H. Toosian Shandiz and H. Ghasemzadeh Tehrani (2005) *Using Multi Layer Perceptron Network to Classify Road Cracks*. 6th WSEAS International Conference on Neural Network, Fuzzy Systems and Evolutionary Computing. Lisbon, Portugal.
15. H. Toosian Shandiz and H. Ghasemzadeh Tehrani (2005) *Road Surface Crack Identification by Using Different Classifiers on Digital Images*. 5th WSEAS International Conference on Systems. Corfu, Greece.
16. H. Toosian Shandiz and H. Ghasemzadeh Tehrani (2005) *Comparing Different Methods in Road Surface Crack Identification and Classification*. WSEAS Transaction on Information Science and Applications. Issue 9, Vol: 2, pp: 1393–1412.
17. R.E. Bellman and L.A. Zadeh (1970) *Decision Making in a Fuzzy Environment*. Management Science, pp: 4–17.

*14. Cracking control in concrete
and bridge decks*

Experimental and numerical simulation study on the crack of steel orthotropic bridge deck pavement

W. Xu & X.-N. Zhang

China University of Technology, China

ABSTRACT: Cracking is the main distress of pavement on steel orthotropic bridge deck. The crack of pavement on steel orthotropic bridge deck is surveyed in China and the character of cracks is analyzed. The strain state of pavement on steel orthotropic bridge deck is measured in site of Queshi Bridge in China. The strain state of pavement on steel orthotropic bridge deck under static vehicle load and dynamic vehicle are measured by strain gauges. The results of measurements show that the asphalt deck pavement is of viscoelastic character evidently. The stress state and strain distribution of deck pavement under the tire load are studied through finite element method. And the results of numerical simulation analysis and experimental measurement are compared, which shows that numerical simulation analysis can accord with experimental measurement well. Four types of pavement material are designed and the anti cracking performance is compared through fatigue test.

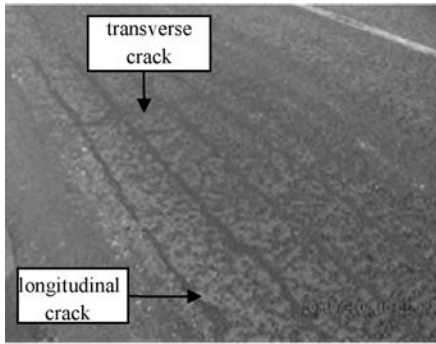
1 INTRODUCTION

The problem of Cracking in pavement on steel orthotropic bridge deck has not been solved well for about 20 years in China. For about 3–5 years the pavement on steel orthotropic bridge deck will be replaced usually in China, which has big influence on traffic function of the bridge. There are about ten big steel bridges to be built in recent years in China, and the cracking is an urgent problem to be solved for the high temperature and heavy traffic condition (Hu, Qian & Huang 2001). There are several reasons for the cracking, such as overload, the stiffness of bridge deck and pavement material performances are weak (Li, Deng & Zhou 2001). While empirical and mechanics design models do exist for the design of ordinary pavements, there is no universally accepted model for the design of surfacing on orthotropic steel bridges now. There is a need for a new design procedure for surfacing on orthotropic steel decks. Such a procedure should be based on a proper understanding of the behavior of the different materials involved, as well as the stress state of the pavement on bridge deck (Medani 2001).

2 THE CHARACTER OF THE CRACKING ON STEEL ORTHOTROPIC BRIDGE DECK PAVEMENT

2.1 *Character of the cracking*

The character of the cracking on the typical steel orthotropic bridge deck pavement was surveyed in China. Cracking of guss asphalt concrete pavement is shown in Figure 1a, cracking of SMA concrete pavement is shown in Figure 1b, Figure 1c, cracking of rubber modified asphalt concrete pavement is shown in Figure 1d, and cracking of epoxy asphalt concrete pavement is shown in Figure 1e. The crack shape includes transverse crack, longitudinal crack, net crack, and local circle crack. The longitudinal crack is the main style crack in the surveyed deck pavement. The transverse crack often happens along with sliding longitudinally of the deck pavement. The cracks observed most happen in the right lane (used mainly by trucks). Most of the cracking occurs above the



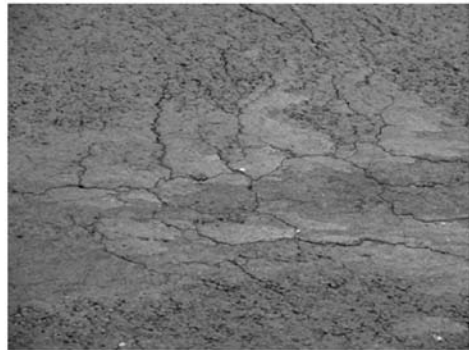
a: Guss asphalt



b: SMA longitudinal crack



c: SMA transverse crack



d: Rubber modified asphalt



e: Epoxy asphalt

Figure 1. The character of the cracking on steel orthotropic bridge deck.

longitudinal or transverse stiffeners. Local circle crack occurs in epoxy asphalt concrete pavement, which often leading to pothole. Cracking is probably the most occurring type of damage on asphalt surfacing of orthotropic steel bridges in the surveyed bridge deck. There are more cracking in the lane with low speed traffic than the lane with high speed traffic.

2.2 Analyses of the cracking

The orthotropic deck consists of a deck plate supported into mutually perpendicular directions by a system of transverse crossbeams and longitudinal stiffeners. The stress analysis results show that

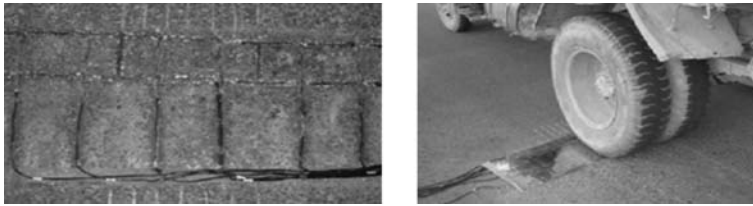


Figure 2. Scheme of strain measurement of the pavement on bridge deck.

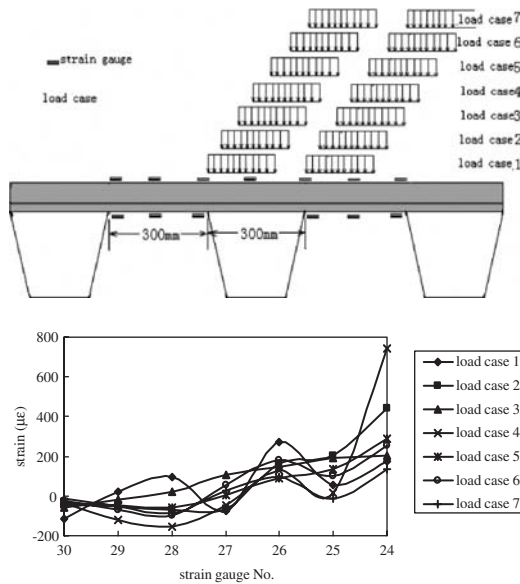


Figure 3. Strain of the pavement for seven load cases under static loading.

the tensile strain located at upside of surfacing above the upper edge of web plate of rib is the dominating design factor for surfacing (Medani 2002 & Hulsey, Yang & Raad 1999). The shape of cracking shows that fatigue cracking of deck pavement is caused by repeated stresses induced by traffic. Some cracking may due to exceptionally high stresses, induced by heavy traffic exceeding the material's tensile or shear strength. Sliding cracking happens when the binding failed between the pavement and steel deck. Ch epoxy asphalt shows the best anti-cracking performance among different pavement material.

3 MEASUREMENT OF THE STRAIN STATE OF PAVEMENT ON STEEL ORTHOTROPIC BRIDGE DECK

3.1 Scheme of measurement

The stain gauges are bound in the cut groove of 5 mm depth in the SBS SMA pavement on steel orthotropic bridge deck of Qeshi Bridge in China shown in Figure 2. And the strain gauges are covered with a thin steel plate cover of 1 mm thickness to protect signal lines.

3.2 Analysis of the measurement data

The transverse strain of pavement is measured under seven load cases in static loading tests shown in Figure 3. Maximum strain occurs above the longitudinal or transverse stiffeners. The strain of

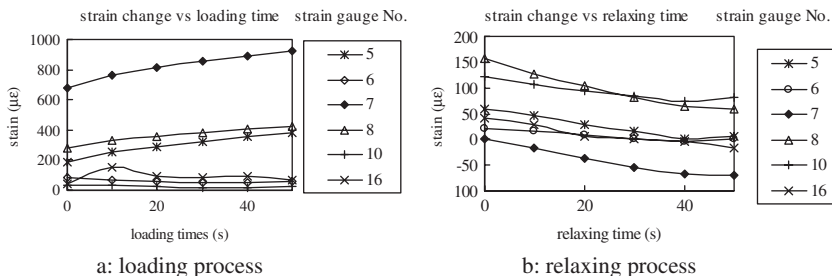


Figure 4. Strain of the pavement change in the process of loading and relaxing.

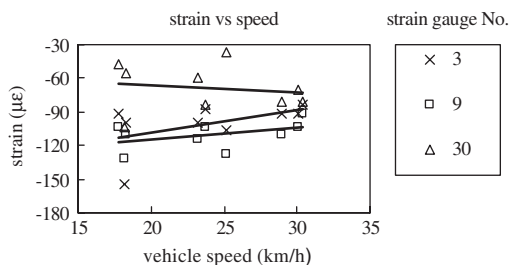


Figure 5. The relation of the pavement strain with loading vehicle speed.

pavement is in the process of increasing along with loading when the loading vehicle stops on the test position and in the process of decreasing after unloading shown in Figure 4. The strain of pavement will become smaller along with the increasing of loading vehicle speed in dynamic loading tests shown in Figure 5. The results of measurements show that the asphalt deck pavement is of viscoelastic character evidently.

4 NUMERICAL SIMULATION ANALYSIS OF STRESS STATE OF PAVEMENT

The surfacing and orthotropic steel deck constitute a composite structure bearing tire load. The mechanics analysis has to be made on this composite structure to understand the performance requirement and design target for surfacing material. The computing model is built by shell cell for beam and link cell for cable. Accurate results of surfacing strain state can be pulled out from analysis on this finite element model.

The finite element model has large numbers of element if computing the local effect under tire load in details by the whole bridge model. And this big finite element model has a very high requirement on the computer and the computing efficiency is low. The independent bridge beam section can not represent the integrity of the whole bridge structure and boundary condition. The submodeling of finite element method is used to solve this problem in this paper (Xu, Li & Zhang 2004). The spatial view for distribution of transverse strain of the surfacing is shown in Figure 6. The strain distribution shows that peak value of tensile strain is located at upside of surfacing above the upper edge of stiffeners, which is in the same law with measurement data.

And the results of numerical simulation analysis and experimental measurement are compared shown in Figure 7, which shows that numerical simulation analysis can accord with experimental measurement well.

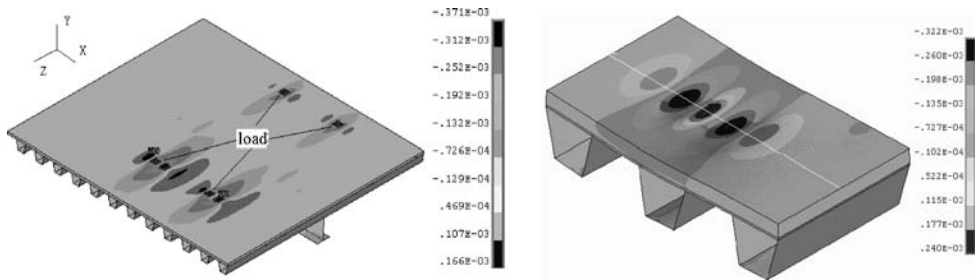


Figure 6. The spatial view of transversal tensile strain distribution in computational model.

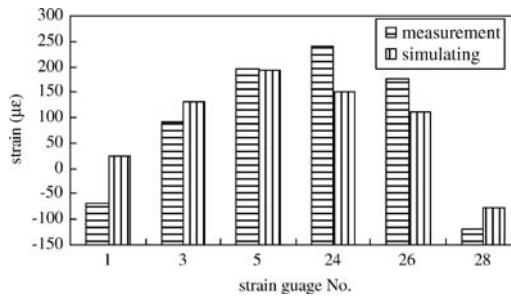


Figure 7. Compare of the pavement strain between measurement and simulating.

5 FATIGUE TEST ON PAVEMENT MATERAIL

The survey, measurement and simulating calculation results show that the transverse strain has the dominantly effect on the cracking of deck surfacing. The fatigue test was done to evaluate the fatigue performance and flexural stiffness of different material such as epoxy asphalt, SBS SMA, guss asphalt. The fatigue test model is four point bending beam. The stress state of the specimen can simulate the stress state of the deck pavement. The model of fatigue test is strain control and the load frequency is 10Hz and the temperature is 15°.

The test results of fatigue life of four kinds of pavement material are shown in Figure 8. That shows Ch epoxy asphalt has best fatigue performance, and Ta epoxy asphalt and guss asphalt have the lowest fatigue performance.

The bending modulus of the specimen at 15° shows that the Ta epoxy asphalt has the highest flexural stiffness 13.70 GPa and the SBS SMA has the lowest modulus 3.28 GPa. The modulus changes curves along with temperature are shown in Figure 9 which shows that the flexural stiffness of the specimen is influenced evidently by temperature and the flexural stiffness of the specimen comes down when temperature increases. Especially the flexural stiffness of guss asphalt and SBS SMA drop quickly along with the temperature increasing.

The pavement with high flexural stiffness will lower the strain level since the surfacing and orthotropic steel deck constitute a composite structure bearing tire load. The Ch epoxy asphalt has higher flexural stiffness in the usual temperature range and best fatigue performance and performs excellent in practice.

6 CONCLUSIONS

Longitudinal cracking is the main distress of pavement on steel orthotropic bridge deck. The pavement need has reliable anti fatigue performance and binding strength to steel deck.

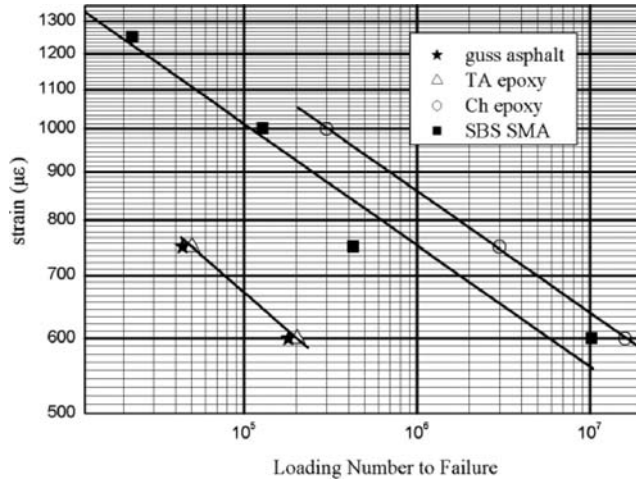


Figure 8. Compare of the fatigue performance of four kinds of materials.

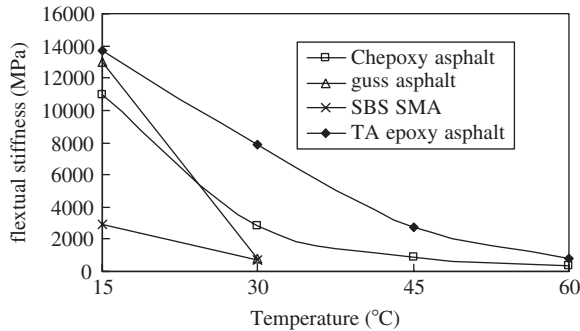


Figure 9. Compare of the flexural stiffness of four kinds of materials.

The survey, measurement and simulating calculation analysis results show that the tensile strain located at upside of surfacing above the upper edge of stiffeners is the dominating factor for surfacing design.

The results of measurements show that the asphalt deck pavement is of viscoelastic character evidently. The loading time and vehicle speed will affect the strain level of pavement and performance of pavement.

The fatigue test shows that Ch epoxy asphalt mixture has higher modulus and the longest fatigue life. Ch epoxy asphalt pavement performs excellent in practice under high temperature and heavy traffic. Ch epoxy asphalt pavement is a practical way to solve the cracking under China condition from six years application experience. But the long time performance of epoxy asphalt pavement in China still need longer time to test.

REFERENCES

- Hulsey J Leroy, Yang Liao & Raad Lutfi. 1999. Wearing surfaces for orthotropic steel bridge decks. *Transportation Research Record* 1999(1654): 141-150.
- Hu Guangwei, Qian Zhendong & Huang Wei. 2001. Structural optimum design of the second system of orthotropic steel bridge. *Journal of Southeast University (Natural Science Edition)* 31(3): 76-78.

- Li Chang, Deng Xuejun & Zhou Shizhong. 2001. Analysis of the deck pavement on steel box bridge. *Journal of Southeast University (Natural Science Edition)* 31(6): 14–17.
- Medani T. O. 2001. Asphalt surfacing applied to orthotropic steel bridge decks, a literature study Netherlands: Road and Railroad Research Laboratory of Delft University of Technology (Report No: 7-01-127-1).
- Medani T. O, Scarpas A & Kolstein M H, et al. 2002. Design aspects of wearing courses on orthotropic steel bridge decks. *Proceedings of the 9th International Conference on Asphalt Pavements (ICAP)*. Copenhagen, Denmark: 1–5.
- Xu Wei, Li Zhi & Zhang Xiaoning. 2004. Application of submodeling method for analysis for deck structure of diagonal cable-stayed bridge with long span. *China Civil Engineering Journal* 37(6): 30–34.

Cracking of wearing courses on steel orthotropic bridge decks

X. Chen, W. Huang, J. Yang, X. Wang & G. Cheng

Southeast University, Nanjing, China

ABSTRACT: Asphalt surfacing on steel orthotropic decks act compositely with the steel deck plate and must be regarded as an integral part of the structural deck system. It should be watertight, develop no cracks and well bonded to steel deck plate, besides providing a smooth riding surface with high skid resistance for the driver. Cracking of the asphalt surfacing on steel decks will do great harm not only to the surfacing itself but also to the steel structure. This paper reported in-site crack survey on wearing surfaces of more than ten bridges, including gussasphalt, SMA with polymer modified asphalt and epoxy asphalt. It is found that all cracks are top-down cracking. The cracks were classified into four types according to its characters of geometry and location, with the names of regular cracks, short hair cracks, bubble cracks and slippage cracks. Causes of the cracking of asphalt surfacing on steel orthotropic decks were discussed. Regular cracking is believed to be a fatigue matter according to 3-D Finite Element Analysis. Short hair cracking and bubble cracking are mainly related to construction defects, while slippage cracking is primarily due to the interlayer lack of bonding strength and shear resistance.

Keywords: Steel bridge, orthotropic decks, wearing courses, cracking, classification, causes.

1 INTRODUCTION

An orthotropic steel deck plate requires a wearing surfacing for skid resistance, for smooth riding, and for corrosion protection. The wearing surfacing is subjected to the heavy impact of loaded truck wheels imposed by the passage of millions of trucks during the several decades of its service life. Asphalt surfacing on steel orthotropic decks act compositely with the steel deck plate and must be regarded as an integral part of the structural deck system[1–3]. It should be watertight, develop no cracks and well bonded to steel deck plate[3–8].

Several asphalt surfacing systems, including gussasphalt, SMA with polymer modified asphalt and epoxy asphalt, have been used as wearing surfacing for orthotropic steel deck plate bridges around the world. Their performances vary from excellent to poor depending largely on local climate, deck plate flexibility, volume of heavy truck traffic, and, in particular, the type and thickness of the surfacing[8–16]. Cracking, potholes, rutting, corrugating and shoving, de-bonding are the main distresses of deck pavement. The latter four distresses mainly depend on the characters of asphalt mixture as well as bonding membrane and can be avoided by proper material selection, while cracking lies not only on materials' performances but also on structure characteristic and in return has many bad effects on the structure[3]. Moisture and water can penetrate into interlayer and the surface of steel deck through cracks, which may decrease the bonding strength and composite action between asphalt surfacing and steel deck, finally lead to the failure of the whole surfacing system and meanwhile, shorten the fatigue of the welded joints of steel decks. It is important to recognize the cracks properly and take an immediate and suitable preventive repair or preservation action when the deck pavements were found cracked. However, there is no detailed report on the cracks of deck pavement.

A long-term survey project on the conditions of deck pavement was conducted with the help of Construction Headquarters of Yangtze River Bridge in Jiangsu. Over ten bridges were inspected

by the engineers of the Road and Bridge Laboratory of Southeast University, with a frequency of 4–6 times per year. This paper reported the survey results on the cracking of asphalt surfacing on long-spanned steel bridges. The cracks were studied with phenomenological and theoretical methods. Cracks were classified into four types, with the names of slippage cracks, fatigue cracks, short hair cracks and bubble cracks. Their characteristics and propagations were summarized, and the causes were discussed. It is believed that bubble cracking is caused by buried volatiles such as water or moisture, while short hair cracks is caused by some unknown construction defects. It can be concluded that regular cracking is caused by repeated wheel loading, and slippage cracking occurs due to a weak interlayer and unstable wearing course under high temperature.

2 CLASSIFICATION OF THE CRACKS

It is interesting that only top-down cracks were observed and there are no bottom-up cracks found. Based on its characters on geometry and positions, the cracks are classified into four groups—regular cracks, short hair cracks, bubble cracks and slippage cracks. Regular cracks were observed in pavement of gussasphalt or SMA near the longitudinal or transverse stiffeners of the deck plate, while for epoxy asphalt surfacing develops mainly irregular hair cracks and bubble cracks, slippage cracks were only found in SMA with polymer modified asphalt.

2.1 *Regular cracks*

Most regular cracks occur in the pavement of gussasphalt and SMA near the longitudinal or transverse stiffeners of the deck plate. According to the long-term observation, the propagation of regular cracks can be characterized into four stages before net cracks form:

- (1) short longitudinal cracks occur at ribs or the girders, as shown in Fig 1a.
- (2) short transverse cracks initiate nearby the cross beam or diaphragms adjacent the transverse cracks, as shown in Fig 1b.
- (3) longitudinal cracks propagate in length and more H-shape cracks occur, as shown in Fig 1c.
- (4) orthogonal cracks propagate in length, as shown in Fig 1d.

The longitudinal cracks will soon propagate into parallel cracks and net cracks or alligators if there are not properly sealed, as shown in Fig 2. Himeno K. et al.[13] has reported another type of longitudinal cracks of asphalt surfacing which occur in between the trough of ribs, as shown in Fig 3. Yet this type of cracks has not been observed during the survey.

2.2 *Short hair cracks*

Short hair cracks were mostly observed at the surface of epoxy asphalt in steel bridges. Although those cracks seem to be irregular, the lengths of the cracks are all short than 30 cm with a width less than 2 mm and a depth less than 2 cm.

2.3 *Bubble cracks*

Bubble cracks are characterized with short radial cracks in at least three directions of about 10–15 cm length, as shown in Fig 5. Ring cracks will appear around the radial cracks due to repeated wheel loading and dynamic water pressure; pothole will finally be formed if there is no timely patch, as shown in Fig 6. Generally, bubble cracks may appear in any asphalt surfacing with the air void lower than 3% such as gussasphalt and epoxy asphalt. But it is surprising that only the deck pavement of epoxy asphalt were observed with this type of cracks.

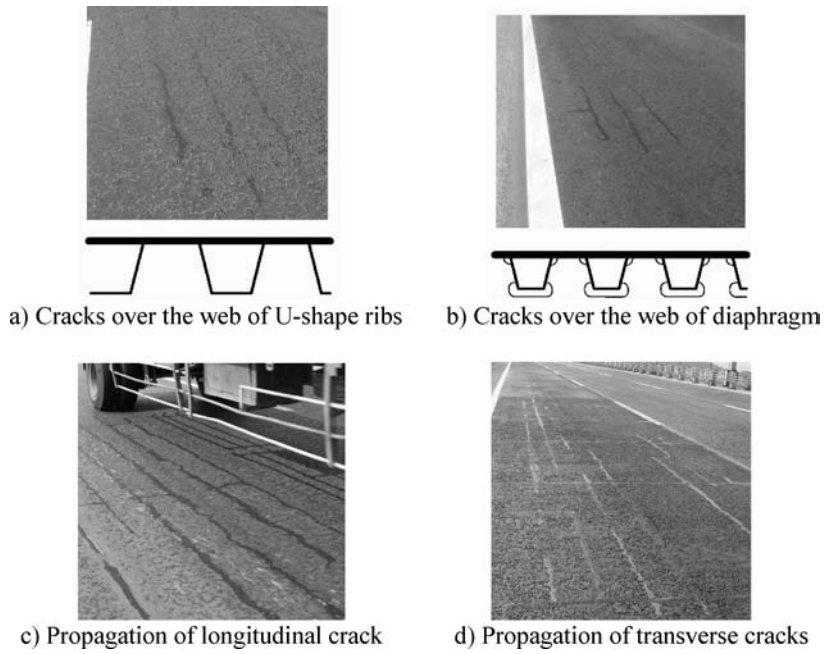


Figure 1. Surface crack in gussasphalt.

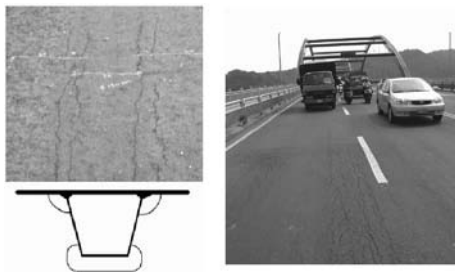


Figure 2. Parallel cracks and alligators.

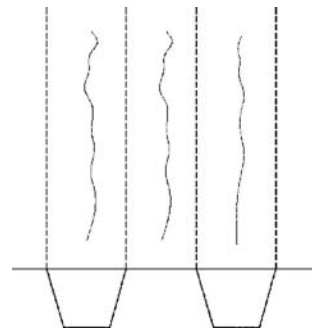


Figure 3. Cracks in between ribs.



Figure 4. Disordered short hair cracks.

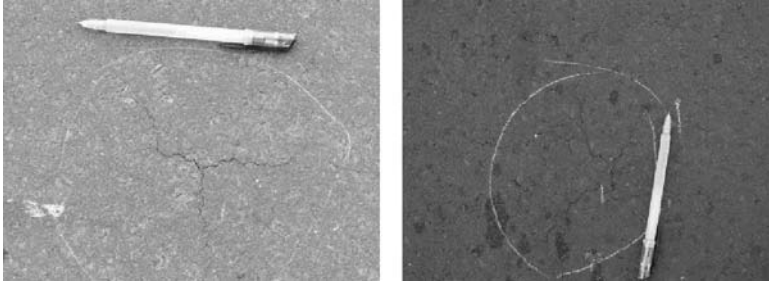


Figure 5. Bubble cracks.

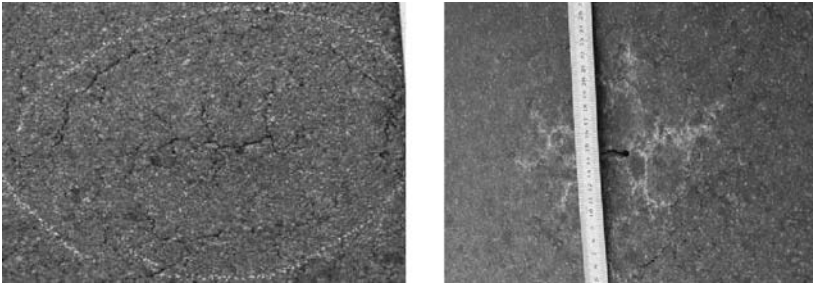


Figure 6. Development of ring cracks and pothole.



Figure 7. Slippage cracks.

2.4 Slippage cracks

Slippage cracks can be easily recognized as large U-shape cracks occur with the corrugation and shoving of the asphalt surfacing. The cracks generally have a width of 2 cm to 10 cm covering one or two lanes.

3 DISCUSSION ON THE CAUSES OF THE CRACKS

3.1 Theoretical analysis on regular cracks

It is known that the responses of asphalt surfacing on steel orthotropic decks under wheel loading are complex with localization, and strongly dependent on the geometry of the decks, position of the wheels, wheel footprints, composite action and other uncertain factors[3][17–19]. The critical loading condition for the asphalt is a double tired vehicle wheel straddles the trough edge of the rib, as show in Figure 8. 3-D FEA results show that max transverse tensile stress occurs at the top

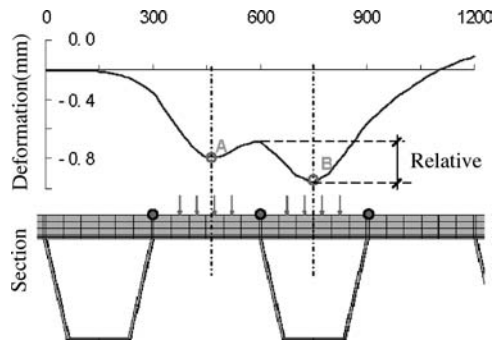


Figure 8. Local deflexion responses of deck pavement under critical load position.

of pavement over webs of U-shape ribs adjacent to wheel load, seen as Fig 8, and for longitudinal tensile stress, the max value occurs at the top of pavement over webs of diaphragms near to wheel load. Consequent longitudinal and transverse cracks will occur after numerous traffic loadings or if the pavement lack of enough fatigue resistance. Another cause of transverse cracks is thermal cracking according to Huang W [16].

3.2 Discussion on the causes of the cracks other than regular cracks

Bubble cracks are caused by moisture as it is a impossible mission to get rid of the effects of any type of moisture. Water on the cables or tower and sweat may drop into the mixture and evaporate during the paving process. As gussasphalt is paved with a thickness of 5 cm and a temperature of 180–200 centigrade, the dropped water or sweat can be fully evaporated, which makes the bubbles be easily found and repaired during construction. But for epoxy asphalt, the pavement cool down rapidly as the paving thickness is only a half of gussasphalt and the mixture's temperature is at 110–121 centigrade. The moisture cannot fully evaporate to form visible bubbles, that is to say, most bubbles can not be found before the pavement is compacted or cool down. When the temperature of deck pavement is higher enough, the moisture existed in the concrete will swell, producing large volume expansion and tensile pressures, which leads to the cracks combined with wheel loading.

The short hair cracks should be caused by some unknown construction defects and be independent with mixture properties as they appear randomly without any propagations. Further studies should be launched to explore the relations between the cracks and the paving technologies.

The causes of slippage cracks lie in three factors according to Chen and Huang et al.[9]:

- (1) Primarily, the waterproofing and bonding membrane lack of bonding strength and shear resistance;
- (2) Secondly, the wearing courses of asphalt mixture short in high temperature stabilities;
- (3) Tertiarily, hot summer and frequently braking in the downslop.

4 CONCLUSIONS

This paper has presented a brief discussion on the cracking of the asphalt surfacing on steel orthotropic bridge decks based on a 6-year-long survey. The cracks of asphalt surfacing on steel orthotropic decks are classified into regular crack, short hair crack, bubble crack and slippage crack according to their geometry or positions. The propagation and development of each type of cracks are summarized, as well as their causes. It is believed that bubble cracking be caused moisture, while short hair cracks is caused by some unknown construction defects. It can be concluded that regular cracking is caused by repeated wheel loading, and slippage cracking occurs due to a weak interlayer and unstable wearing coursed under high temperature. Further studies can be done to

assess the influences of different type of cracks on the wearing course as well as on the steel bridge decks to provide a operational guide.

REFERENCES

- AASHTO, 'LRFD Bridge Design Specifications', American Association of State Highway and Transportation Officials, Washington, D.C., 1994
- Medani T.O., Scarpas A., et al., 'Design aspects for wearing courses on orthotropic steel bridge decks'. Netherlands: Delft University of Technology, 2003
- CHEN X.H., 'Fatigue characteristics of deck pavement on steel orthotropic bridge decks based on composite beam', A dissertation submitted to Southeast University for the Academic Degree of Doctor of Engineering, 2006, April, Nanjing, Southeast University(in Chinese)
- Stefan Bild, 'Durability design criteria for bituminous pavements on orthotropic steel bridge decks'. *Can J Civ Eng*, 1987(14): 41–48
- T. O. Medani, 'Asphalt surfacing applied to orthotropic steel bridge decks(A literature review)'. Delft University of Technology, Report 7-01-127-1, March, 2001
- Chen X.H., Huang W., Wang J.W., 'On design methods of asphalt mixture for the steel orthotropic decks on long-spanned steel box girder bridge', *Highway*, 2004, (8): 34–38(in Chinese)
- Charles S., Tim I., 'The influence of wearing surfacing on the performance of orthotropic steel plate decks', TRB 2004 Annual Meeting CR-ROM
- Huang W., Ji Lin., Cheng G., et al., 'Runyang construction series: asphalt surfacing for steel orthotropic decks', 1st Ed (Beijing, Communication, 2005) (in Chinese)
- Chen X.H., Huang W., Cheng G., et al., 'Cracking causes of gussasphalt on steel orthotropic bridge decks', *Journal of Transportation Engineering*, 2005, 21(4): 490–494(in Chinese)
- Mo Y.S., Wang H., 'On the causes of the distresses of asphalt mixture on steel bridge decks', *Highway Engineering of Middle South*, 2001, 26(1): 56–60(in Chinese)
- Xie X.J., 'Reparation on the deck pavement of Hai Cang steel bridge in Xiamen', *Material Developing and Applying*, 2004, 19(5): 39–41(in Chinese)
- Hiromitsu N., Takara O., Koji G., 'The structural evaluation for an asphalt pavement on a steel plate deck'. Engineering Research Laboratory, Taiyu Kensetsu Co. Ltd. Nagoya, Japan, 2003
- Himeno, K., Nishizawa, T., Uchida, K., et al., 'Longitudinal surface cracking in asphalt pavements on steel bridge decks using energy dissipation theory', Procs. 2nd JAPAN/CHINA Workshop on Pavement Technologies, Tokyo, pp. 293–302, Nov., 2003
- Roman W., 'Structural behaviour of surfacings on steel orthotropic decks and considerations for practical design', *Structural Engineering International*. 2002 No. 2: 124–129
- Ylva E., Pereric W., 'Polymer modified waterproofing and pavement system for the High Coast Bridge in Sweden(research, testing and experience)', Swedich National Road and Transport Research Institute, VTI Rapport 430A–2001
- Xu A.M., Zhang C.G., Zhou Z.Y., 'Damage conditions and the rehabilitation strategies of deck pavement on Kuandu Bridge', *Taiwan Highway Engineering*, 2004 31(4): 13–29
- Huang, W. 'The design principle and methods of asphalt surfacing on steel decks', 1st Ed(Beijing, Communication, 2006)(in Chinese)
- Qian Z.D., Huang W., 'Effects of parameters of asphalt concrete surfacing on mechanical property of paving layer', *Journal of Southeast University(English Edition)*, 2003, 19(3): 79–82
- Guan Y.S., Chen X.H., Yao B., 'Fatigue performance of pavement on steel deck with variable thickness'. 3rd China-Japan Workshop on Pavement Technologies, China, Nanjing, 2005, November.

Author Index

- Abd El Halim, A.O. 357
Akkaya, Y. 179
Akram, T. 529
Al-Qadi, I.L. 563, 661, 801
Allen, D.H. 295, 599
Ammendola, R. 539
Antunes, M.L. 791
Arnaud, L. 261
Artamendi, I. 417
- Baek, C. 315
Baek, J. 563, 801
Bahia, H.U. 469
Bai, B.-Q. 617
Baladi, G.Y. 529
Balay, J.M. 13, 55, 671
Barsi, A. 873
Baumgardner, G. 843
Bažant, Z.P. 137
Bennert, T. 833
Birgisson, B. 811
Bodin, D. 13
Bouhas, F. 609
Braham, A.F. 369
Brake, N.A. 155
Breitenbücher, R. 127
Bressette, T. 45
Buonsanti, M. 587
Buttlar, W.G. 369, 683, 801
- Cebon, D. 627
Chabot, A. 13, 55, 671
Chaignon, F. 721
Chatti, K. 155, 861
Chaverot, P. 457
Chehab, G.R. 769
Chehab, G.R. 721
Chen, X. 907
Cheng, G. 907
Ciampa, D. 201
Clyne, T. 405
Collop, A. 395
Cominoli, L. 89
Coni, M. 271
- Cooley, L.A. 843
- Dai, P. 229
Daranga, C. 469
Dave, E.V. 369
Davis, L. 703
de Bondt, A.H. 437
de Freitas, F.A.C. 295
de Larrard, F. 671
Delaporte, B. 457
Deloffre, L. 13
Dendurant, J. 703
Di Benedetto, H. 283, 457
Diakhaté, M. 649
Dołżycki, B. 853
Dong, Z.-J. 387
Doré, G. 447
- Easa, S. 357
El-Desouky, A. 357
Feng, Z. 575
Ferron, R.P. 179
Fi, I. 873
Fontul, S. 791
Fratta, D. 469
- Gauthier, G. 457
Ghasemzadeh Tehrani, H. 891
Gibson, N. 35, 405
Gibson, N.H. 305
Goacolou, H. 649
Gong, W. 881
Gong, W.-Q. 387
Guddati, M.N. 315, 575
Guissi, G. 447
Guo, E.H. 25
- Haider, S.W. 155, 529, 861
Hajj, E.Y. 821
Hansen, W. 119
Harvey, J. 741
Harvey, J.T. 3, 45
Hassani, A. 891
Himeno, K. 509
- Hook, K.D. 713
Hoover, C.G. 137
Hornych, P. 13
Hou, Z. 881
Houel, A. 261
Howard, I.L. 843
Hu, S. 333, 637
Hu, X. 333, 345, 637
Huang, W. 907
Huang, X.-M. 327
Hussain, A. 529
- Isola, R. 271
Jia, L. 345
Jones, D. 45, 741
Judycki, J. 853
- Kabir, M.D. 427
Kannekanti, V. 69
Kertész, I. 873
Kerzreho, J.P. 13
Khalid, H.A. 417
Khedoe, R.N. 481
Kim, S. 769
Kim, Y.-R. 295, 599
Kim, Y.R. 315, 575
Kogo, K. 509
Kohler, E. 69
Kutay, M.E. 305
Kwon, S.H. 179
- la Agostinacchio, M. 201
Labuz, J.F. 501
Lee, K. 315
Leng, Z. 661
Leonardi, G. 587
Li, Q. 211
Li, Q.-F. 327
Li, X. 501
Little, D.N. 575
Loizos, A. 519
Losa, M. 239
Lovas, T. 873
Lu, H. 221
Lüddecke, F. 779

Maeck, J. 491, 761
 Maher, A. 833
 Marasteanu, M. 405, 469
 Marasteanu, M.O. 501
 McDowell, G. 395
 Meda, A. 89
 Millien, A. 55, 609, 649
 Minhoto, M.J.C. 551
 Mohammad, L.N. 427
 Molenaar, A.A.A. 189, 251, 481
 Montepara, A. 811
 Morian, N.E. 821
 Moro, A. 539
 Mostafa, A. 357
 Nantung, T. 109
 Newbolds, S.A. 167
 Nguyen, M.L. 283
 Ni, F.-J. 211

 Ojo, J.O. 469
 Olek, J. 167
 Olita, S. 201
 Oliveira, J.R.M. 271
 Ozer, H. 661

 Pais, J.C. 551
 Palacios, C. 721
 Papavasiliou, V. 519
 Paulino, G.H. 369, 683
 Penman, J. 713
 Pereira, P.A.A. 551
 Perraton, D. 447
 Petch, F. 25
 Petit, C. 609
 Petit, Ch. 55, 649
 Phelipot-Mardelé, A. 649
 Pierre, P. 447
 Pinelo, A.M. 791
 Pirkawetz, S. 779
 Plizzari, G.A. 89

 Portas, S. 271
 Portillo, O. 627
 Pouteau, B. 649, 671
 Powell, R.B. 731
 Praticò, F.G. 239, 539
 Pszczoła, M. 853
 Pu, B. 189
 Pérez, S.A. 55

 Qi, X. 35

 Raoufi, K. 109
 Recknagel, C. 779
 Ricalde, L. 25
 Roesler, J.R. 79
 Romeo, E. 811
 Roncella, R. 811
 Roque, R. 811
 Ross, M. 843

 Saadeh, S. 427
 Salama, H. 155
 Sauzeat, C. 283
 Schlangen, E. 119
 Scopelliti, F. 587
 Sebaaly, P.E. 821
 Shah, S.P. 179
 Shitangkoon, W. 695
 Sievering, C. 127
 Soares, R.F. 599
 Subramanian, V. 315
 Sun, L. 333, 345

 Tamagny, P. 55
 Tan, Y.-Q. 387
 Tang, X. 769
 Tayabji, S.D. 145
 Tebaldi, G. 811
 Thompson, M. 721
 Tsai, B.-W. 741
 Turos, M. 405
 Tyson, S.S. 145

 Ullidtz, P. 741
 Underwood, B.S. 315

 Van Rompu, J. 457
 van Rooijen, R.C. 437
 Vanelstraete, A. 491, 761
 Velásquez, R. 405
 Vervaecke, F. 491, 761
 v.d. Ven, M.F.C. 481
 Vázquez, J.R. 99

 Walubita, L.F. 333
 Wang, D. 79
 Wang, K.C.P. 881
 Wang, P. 327
 Wang, X. 907
 Wei, Y. 119
 Weiss, J. 109
 Wen, H. 695
 Wendling, L. 55, 283
 Wu, J. 395
 Wu, R.Z. 3

 Xu, H.-N. 387
 Xu, W. 899

 Yang, J. 221, 229, 907
 Yang, Y. 221, 229
 Yang, Z.-T. 327
 Yin, H.M. 683
 Youtcheff, J. 35, 305
 Yu, B. 229
 Yu, H.T. 145

 Zeghal, M. 379
 Zhang, P. 575
 Zhang, X.-N. 899
 Zhou, F. 637
 Zieliński, P. 751
 Zofka, A. 369

Internationally, much attention is given to causes, prevention, and rehabilitation of cracking in concrete, flexible, and composite pavements. The Sixth RILEM International Conference on Cracking in Pavements (Chicago, June 16-18, 2008) provided a forum for discussion of recent developments and research results. This book is a collection of papers from the Conference, and includes contributions on a variety of topics:

- Modeling of the initiation and propagation of pavement cracking
- Top-down and bottom-up fatigue cracking mechanisms
- Laboratory testing techniques and evaluation effectiveness
- Construction approaches and their relation to crack development
- Crack surveys and nondestructive evaluation
- In-situ experimental studies: field construction and rehabilitation techniques to inhibit pavement cracking
- Performance of crack preventative techniques and pavement service life prediction
- Interlay system effectiveness
- Pavement cracking evaluation using accelerated pavement testing
- Hot-mix asphalt overlay characterization
- Pavement interface modeling and testing
- Laboratory and field model validation
- Low-temperature cracking mechanisms and field studies
- Cracking in semi-rigid and stabilized pavement layers
- Analytical and experimental investigations of concrete joints
- White topping performance

Pavement Cracking: Mechanisms, Modeling, Detection, Testing, and Case Histories is particularly of interest to academics, researchers, and practitioners involved in pavement mechanics and performance.



CRC Press
Taylor & Francis Group
an informa business
www.crcpress.com

6000 Broken Sound Parkway, NW
Suite 300, Boca Raton, FL 33487
270 Madison Avenue
New York, NY 10016
2 Park Square, Milton Park
Abingdon, Oxon OX14 4RN, UK



an **informa** business